

# RELATIVISTIC HYDRODYNAMICS

---

Luciano Rezzolla | Olindo Zanotti

OXFORD

# Relativistic Hydrodynamics

Luciano Rezzolla

*Institute for Theoretical Physics, Frankfurt am Main, Germany  
Albert Einstein Institute, Potsdam, Germany*

Olindo Zanotti

*Laboratory of Applied Mathematics  
University of Trento, Italy*

OXFORD  
UNIVERSITY PRESS

**OXFORD**  
UNIVERSITY PRESS

Great Clarendon Street, Oxford, OX2 6DP,  
United Kingdom

Oxford University Press is a department of the University of Oxford.  
It furthers the University's objective of excellence in research, scholarship,  
and education by publishing worldwide. Oxford is a registered trade mark of  
Oxford University Press in the UK and in certain other countries

© Luciano Rezzolla and Olindo Zanotti 2013

The moral rights of the authors have been asserted

First Edition published in 2013

Impression: 1

All rights reserved. No part of this publication may be reproduced, stored in  
a retrieval system, or transmitted, in any form or by any means, without the  
prior permission in writing of Oxford University Press, or as expressly permitted  
by law, by licence or under terms agreed with the appropriate reprographics  
rights organization. Enquiries concerning reproduction outside the scope of the  
above should be sent to the Rights Department, Oxford University Press, at the  
address above

You must not circulate this work in any other form  
and you must impose this same condition on any acquirer

Published in the United States of America by Oxford University Press  
198 Madison Avenue, New York, NY 10016, United States of America

British Library Cataloguing in Publication Data  
Data available

Library of Congress Control Number: 2013936269

ISBN 978–0–19–852890–6

Printed and bound by  
CPI Group (UK) Ltd, Croydon, CR0 4YY

Links to third party websites are provided by Oxford in good faith and  
for information only. Oxford disclaims any responsibility for the materials  
contained in any third party website referenced in this work.

*To Carolin, Anna, Emilia and Dominik*

*To my wife Luana*

# Preface

Relativistic hydrodynamics is an incredibly successful framework to describe the dynamics of matter from scales as small as those of colliding elementary particles, up to the largest scales in the universe. This general framework is constructed around the concept of a *fluid* as a system whose large-scale properties can be described effectively without having to worry about the features that the constituent elements have at much smaller length-scales. It is in fact possible to introduce a “*fluid element*” as a local collection of particles so numerous that the dynamics of the individual particles cannot be followed, but large enough to guarantee homogeneity within the element. The properties of neighbouring fluid elements, which can be different and even discontinuous, represent then the global properties of the fluid. This elementary framework can be used to describe with remarkable precision what we observe, for instance, when colliding two heavy ions moving at near the speed of light, when studying venous hemodynamics or racing sailing boats, or even when explaining the most catastrophic events from the remote corners of the universe.

If hydrodynamics establishes a connection between the microscopic and the macroscopic properties of a system, when does hydrodynamics become *relativistic*? In practice, the adjective “*relativistic*” can be applied equally to the microscopic and to the macroscopic level and emerges in at least three different contexts, which however are not mutually exclusive. The first one is related mostly to the microscopic description and applies when the velocities of the constituent particles within a fluid element are very close to the speed of light, or, equivalently, when their Lorentz factor is significantly larger than one. This microscopic condition then leads to a series of specific thermodynamic properties at a macroscopic level, which are reflected by the equation of state. The second context applies instead when the Lorentz factor of the bulk, macroscopic motion of the fluid is significantly larger than one, quite independently of the properties of the fluid at a microscopic level (indeed the constituent particles within the fluid element can have very small velocities). The third and final context emerges in all those situations in which the macroscopic gravitational field is strong enough to require a description in terms of general relativity. In this latter case, no assumption is made about the velocity of the fluid, which can even be at rest as, for instance, in a stationary relativistic star.

The mathematical complexity of general-relativistic hydrodynamics has often induced authors to concentrate on the mathematical aspects of the theory, detaching it from the physical contexts in which the equations find a concrete application, or from the techniques for actually performing calculations. Examples in this respect are the pioneering work of Lichnerowicz (1967), *Relativistic Hydrodynamics and Magnetohydrodynamics*, or the classic monograph of Anile (1989), *Relativistic Fluids and Magneto-fluids*. We here propose a rather different approach to relativistic hydrodynamics by providing an up-to-date, lively and approachable introduction to the mathematical formalism, the numerical techniques and the numerous applications of relativistic hydrodynamics. Numerous figures and diagrams, and a variety of examples and exercises guide the reader through the different parts of the book.

To reflect this multi-pronged approach to relativistic hydrodynamics, the book is organised in three distinct, but tightly knit parts. In the first one, in Chapters 2–4 we introduce the mathematical aspects of relativistic hydrodynamics, touching on fundamental topics such as kinetic theory, the concept of the equations of state, fundamental theorems and results, and the properties of linear and nonlinear waves in fluids, from sound waves to shocks and rarefaction waves. The first part is then concluded with two advanced topics, in Chapters 5–6, about the treatment of relativistic reaction fronts and non-ideal fluids, the discussion of which is found mostly in research papers. All of these concepts pave the way for the two following parts of the book. The second part, Chapters 7–10, discusses the various formulations of the Einstein–Euler equations that are particularly suited for numerical solution. This is followed by an introductory but complete description of those numerical methods adopted for the solution of the relativistic hydrodynamic equations, going from the traditional finite-difference approaches to the more advanced high-resolution shock-capturing methods, and to the more sophisticated high-order methods. Finally, the third part, Chapters 11–12, is devoted to physical and astrophysical applications of relativistic hydrodynamics. This part is naturally divided into the discussion of fluids which are non-selfgravitating and of fluids whose dynamics requires also the solution of the Einstein equations. Two topics which however are not discussed in this book are turbulence and fluid instabilities. This is a little unfortunate, but is due partly to space constraints and partly to the fact that these topics have not yet reached sufficient maturity in relativistic regimes.

The book is especially recommended to astrophysicists and particle physicists, but also to applied mathematicians interested in the properties of hyperbolic equations. The reader will be assumed to have prior knowledge of related mathematical methods, up to the level expected of a physics undergraduate or a beginning graduate student. An introductory Chapter 1 is dedicated to general relativity, but this serves mainly as a reference to the equations used in the rest of the book and as a pointer to textbooks in which these topics are covered in detail.

Our final remark here is about how “wet” the fluids in this book are. It is often said, in fact, that people working in fluid dynamics are divided into two categories: those for whom fluids are “dry” and those for whom fluids are “wet”.<sup>1</sup> This somewhat bizarre definition aims to categorise the two different approaches to hydrodynamics as being, respectively, either an arena for studying nonlinear partial differential equations or a powerful framework for describing nature. For us, fluids are definitely wet, but here the mathematical beauty of differential equations is not washed out.

Luciano Rezzolla  
*Potsdam*

Olindo Zanotti  
*Trento*

*August 2013*

<sup>1</sup>This definition is due to R. Feynman, who titled Chapter 40 of Vol. 2 of *The Feynman Lectures on Physics* as “*The flow of dry water*” (Feynman, 1964). The intention there was to emphasise the idealised physical conditions behind potential flow, for which there is a sophisticated mathematical framework and a well-developed literature, but also scarce physical realism.

## Acknowledgements

Writing this book has been one of those ideas taken on a momentary lapse of reason and then regretted for the uncountable hours spent honouring the initial commitment.

This book is the result of what we have learnt during the last 20 years through our own research, the literature, the lectures given in different universities and schools, and, more pleasantly, through discussions with colleagues and friends. All of them have contributed to this effort more than they know, starting from those that have first introduced us to the subject: John Miller, Marcello Anile, Fernando de Felice, José Mariá Ibáñez, José Mariá Martí, and Toni Font. We are also indebted to Ernazar Abdikamalov, Marek Abramowicz, Bobomurat Ahmedov, Miguel Alcubierre, Miguel-Angel Aloy, Nils Andersson, Marcus Ansorg, Luis Anton, Dinshaw Balsara, Enrico Barausse, Thomas Baumgarte, Nigel Bishop, Carles Bona, Alfio Bonanno, Silvano Bonazzola, Bernd Brügmann, Marco Bruni, Joan Centrella, Cecilia Chirenti, Riccardo Ciolfi, Frederic Daigne, Thibault Damour, Peter Diener, Harry Dimmelmeier, Kyriaki Dionysopoulou, Orhan Dönmez, Yoshiharu Eriguchi, Valeria Ferrari, Bruno Giacomazzo, Eric Gourgolhon, Leonardo Gualtieri, Ian Hawke, Scott Hughes, Hans-Thomas Janka, Thorsten Kellermann, Kostas Kokkotas, Pablo Laguna, Fred Lamb, Luis Lehner, Lee Lindblom, Frank Löffler, Richard Matzner, Juan Antonio Miralles, Phillip Mösta, Pedro Montero, Ewald Müller, Ingo Müller, Ilia Musco, Alessandro Nagar, David Neilsen, Christian Ott, Carlos Palenzuela, Ornella Pantano, Tsvi Piran, Denis Pollney, José Pons, Christian Reisswig, Constanze Roedig, Erik Schnetter, Bernard Schutz, Ed Seidel, Jennifer Seiler, Stu Shapiro, Masaru Shibata, Nikolaos Stergioulas, Béla Szilágyi, Saul Teukolsky, Kip Thorne, Manuel Tiglio, Aaryn Tonita, Kōji Uryū and Shin'ichirou Yoshida.

We are also particularly grateful to Dana Alic, Luca Baiotti, Francesco Becattini, Roberto De Pietri, Luca Del Zanna, Michael Dumbser, Filippo Galeazzi, Arturo Hidalgo, Pasi Huovinen, José Luis Jaramillo, Wolfgang Kastaun, José Mariá Ibáñez, Antonio Marquina, José Mariá Martí, John Miller, Francesco Pannarale, David Radice, Dirk Rischke, Armen Sedrakian, Christian Schell, Daniel Siegel, Kentaro Takami and Eleuterio Toro, for their careful reading of the book and the numerous suggestions that have improved it. LR also thanks the Institut des Hautes Études Scientifiques (IHES) in Bur-sur-Yvette (France) and the Departamento de Astronomia y Astrofísica (DAA) in Valencia (Spain) for the kind hospitality during the visits when parts of this book were being written.

Last but not least we thank Oxford University Press and in particular Sönke Adlung for his continuous support and advice during the writing of this book.

# 1

## A Brief Review of General Relativity

---

### 1.1 Why this chapter?

This book is about the physics of relativistic hydrodynamics, that is, about the physical properties of fluids in those conditions in which the relativistic corrections play a fundamental role. As mentioned in the preface, this can occur either because the bulk velocity of the flow is comparable with the speed of light, or when the spacetime curvature is large.<sup>1</sup> In astrophysical compact objects, such as black holes and neutron stars, both of these conditions are usually met.

In order to introduce the reader to the properties and subtleties of relativistic hydrodynamics, we will present in the following sections a brief summary of the basic aspects of Einstein's theory of general relativity. The purpose of this chapter, however, is not just that of introducing a set of mathematical tools that will be used extensively in the following parts of the book. Rather, it will serve to build the *forma mentis*, that is, the frame of mind necessary to understand in detail the physics of relativistic hydrodynamics. In particular, we need to abandon the *Newtonian* perception of the laws of physics that we experience every day,<sup>2</sup> and build a new intuition that will serve us when understanding the behaviour of fluids in relativistic regimes.

We should note that the material presented here does not attempt, in any way, to provide a systematic or complete introduction to the theory of general relativity. Many textbooks are already available on this subject and books such as *A First Course in General Relativity* by Schutz (1985), *Introducing Einstein's Relativity* by d'Inverno (1992), or *Gravity: an Introduction to Einstein's General Relativity* by Hartle (2003) represent excellent starters for students at the undergraduate level. The interested reader can then find more material in classic texts such as *Gravitation* by Misner et al. (1973), or in more advanced monographs such *General Relativity* by Wald (1984), *Relativity on Curved Manifolds* by de Felice and Clarke (1990), or *Classical Fields: General Relativity and Gauge Theory* by Carmeli (2001).

Rather than aiming at completeness, the content of this chapter provides those basic concepts and mathematical tools that will be used extensively in the other chapters of this book. In addition, because our main interest here is to discuss the “physical” aspects of relativistic hydrodynamics, our language will be favouring a more pragmatic description of concepts and tools, leaving aside the more mathematical aspects of the theory. As a result, we will not indulge in listing and proving theorems, which can be found in books such as *The Large Scale Structure of Spacetime* by Hawking and Ellis (1973), or in *Relativistic Fluids and Magnetohydrodynamics* by Müller and Müller (1974).

<sup>1</sup>Of course, the presence of a large spacetime curvature also implies in general that the flow velocities are close to that of light, but counterexamples can easily be produced, e.g., a static star.

<sup>2</sup>Hereafter we will consider *Newtonian* to be any description which is *non-relativistic*. In practice, a Newtonian regime is characterised by weak gravitational fields, i.e.,  $GM/(c^2r) \ll 1$  and small velocities, i.e.,  $v/c \ll 1$ .

## 4 A Brief Review of General Relativity

*fluids* by Anile (1989), that give general relativity its mathematical solidity and beauty. The reader can rest assured that all of the material presented here can be cast in more rigorous terms if needed or necessary.

We should also emphasise that our introduction to general relativity is based on a balance between the *differential-geometry* approach, that has become the most effective one in all modern presentations, and the more traditional *coordinate-components* approach. Indeed, while the geometrical approach is rather elegant and powerful in expressing in a compact way the physical meaning of the theory, if pushed too far, it may become cryptic. On the other hand, a certain amount of coordinate representation of vectors, tensors and equations is absolutely necessary, especially for physicists with practical problems in mind.

### Notation

Throughout, we will use a spacelike signature  $(-, +, +, +)$  and a system of geometrised units in which  $G = c = 1$ , although when needed we will also indicate the speed of light,  $c$ , explicitly. We will indicate with a boldface any tensor, *e.g.*,  $\mathbf{V}$  and with the standard arrow any three-dimensional vector or operator, *e.g.*,  $\vec{v}$  and  $\vec{\nabla}$ . Four-dimensional covariant and partial derivatives will be indicated in general with  $\nabla_\mu$  and  $\partial_\mu$ , but other symbols may be introduced for less common definitions, or when we want to aid the comparison with classical Newtonian expressions. Within the standard convention of a summation of repeated indices, Greek letters will be taken to run from 0 to 3, while Latin indices run from 1 to 3. Finally, a list of errata will be kept updated on our personal webpages.

## 1.2 The concept of spacetime

An important first step towards a proper understanding of general relativity, and hence of relativistic hydrodynamics, consists in abandoning the Galilean idea of an *absolute space* and of an *absolute time*. This, in turn, implies the rather revolutionary suggestion of abandoning the idea of space and time as the elements of a fixed background, an overall construct against which all the processes take place. Rather, we need to think of space and time as dynamical constituents of the laws of nature and, as such, deeply influenced by them. This revolutionary idea is of course at the very heart of general relativity and surely among the most influential scientific achievements of the twentieth century.

Abandoning the idea of an absolute space and of an absolute time inevitably introduces a new concept, that of *spacetime*, a single four-dimensional object  $\mathcal{S}$ , which, however, should not be regarded just as an arena for the processes of a given physical system, but rather as a dynamical field that participates in the evolution of the physical system itself. The basic elements of this apparently abstract object are called *events* and may appear equally abstract but really should not. We surely are very familiar with the concept of “*something being somewhere*” as this becomes part of our perception of the world already as infants. Similarly, the concept of event could be associated with the idea of “*something happening somewhere*”, such as a photon from the Sun that reaches our retina at dawn. Relativists, therefore, like to think of events as “points”  $\mathcal{P}$  in the spacetime  $\mathcal{S}$ , and their existence as elements of the spacetime is *independent* of the choice made for locating them at a given spatial position and at a given

time. Events are therefore elements of the spacetime in their own right, whose dynamics is regulated by the laws of physics.

With this in mind, we can now think about how to relate events. If an event should be thought of as “something happening somewhere”, then two or more events can be related (*e.g.*, through the laws of physics) and put into a “*sequence of events*” that, in the case in which the sequence is ordered using time as a parameter, are then said to belong to a *worldline*. Also in this case, the apparently abstract notion of worldline has indeed a rather familiar interpretation and we can think of the route on a map (*e.g.*, the one we take when going to work from home) as our worldline in spacetime describing our motion. The subtlety here is that while the route on the map connects different (spatial) points that we occupy at different times, the worldline connects different events of spacetime, that is, those we have occupied when going from home to work. An obvious consequence of the definition of worldline given above is that in the absence of an absolute time and an absolute space, any choice in the ordering of the events can only be “arbitrary” (or rather relative!) as many possible and equivalent ones can be made over the same set of events. This result, however, should not be seen as a limitation, but as an important feature of the new picture of space and time that is rooted in general relativity. Concepts such as that of simultaneity are not lost in general, but need to be expressed properly. This is part of what we will do in the following sections.

### 1.3 Spacetime as a manifold

We have just seen that general relativity proposes the idea of describing physical phenomena as a collection of *events*, forming a four-dimensional continuum, the *spacetime*. The most appropriate mathematical concept to characterise the spacetime is that of a differentiable *manifold*,  $\mathcal{M}$ , which combines the notions of topological space and that of differentiability. Namely, by saying that the spacetime, as a collection of events, is a topological space, we are providing information on how different regions of this continuum are connected to each other. Moreover, as will become apparent when we talk about the equivalence principle, general relativity requires that different events of the spacetime allow for disjoint local neighbourhoods. Hence, the corresponding topological space needs to be a *Hausdorff topological space*. In addition to the topological structure, we need to endow the spacetime with a differential structure through a *continuous parameterisation* in terms of coordinates to be assigned to each of the events. Such parameterisations are performed through functions of class  $C^\ell$ , with  $\ell \geq 2$ , that map the local neighbourhoods of each event onto  $\mathbb{R}^4$ . Hence, a differentiable manifold is a Hausdorff topological space locally diffeomorphic to  $\mathbb{R}^n$ . Simple mathematical examples of a manifold are the surface of a three-dimensional sphere (*i.e.*, a “*two-sphere*”), or any  $m$ -dimensional hyperplane in an  $n$ -dimensional space, where  $m \leq n$ .

A vast mathematical literature is available to discuss the definitions and properties of topological spaces and of manifolds, and we will not enter into such details here, referring the reader to the discussions in de Felice and Clarke (1990) and Frankel (2004). For all practical purposes, we can here think of a manifold  $\mathcal{M}$  as a “*container of parameterised events*”, those that make up the four-dimensional spacetime, and whose parameterisations are functions differentiable to some degree.

The number of independent parameters needed to single out an event in  $\mathcal{M}$  represents the *dimension* of the manifold and the choice made for these parameters will represent the

## 6 A Brief Review of General Relativity

choice made for the *coordinates* needed to cover the manifold, one choice among the infinite possible ones. An obvious example of such coordinates is the longitude and the latitude used to determine the position of a point on a two-sphere such as the Earth. In practice, we need to define a rule that maps a point of the manifold  $\mathcal{M}$ , *i.e.*, an event, into the  $n$ -dimensional real space  $\mathbb{R}^n$ . This rule is called a *mapping* and corresponds to the selection of a coordinate system that will cover a *part* or *all* of the spacetime.

A number of further comments may be useful at this point:

- (i) The mapping discussed above can be viewed as a one-to-one association of the points of the manifold with the points of the Euclidean space of the correct number of dimensions. This correspondence is a useful one but needs to be handled with care. More specifically, it highlights that at least *locally* the manifold looks like a Euclidean space.<sup>3</sup> However, it also hides the fact that the *global* topology of the manifold can be very different from the Euclidean one. A torus lends itself as a useful example of a manifold: neither its surface nor its global topology is Euclidean, yet a small area of its surface can be mapped, at least locally, to a Euclidean space: that of the plane tangent to it.
- (ii) While there are infinite possible choices for the coordinates to cover a given manifold, not all of them are equally good. Some of them may be degenerate for some choice of coordinates and a good part of the mathematical analysis of the solution of the Einstein equations consists in determining the coordinate system that best highlights the physical content of the solution (see also the discussion in Section 1.6). A useful example in this context is again offered by the spherical coordinate system,  $(\theta, \phi)$ , on a two-sphere. This is clearly degenerate at the poles, which can be mapped with an infinite set of values, *i.e.*, those having  $\theta = 0, \pi$  and  $\phi \in [0, 2\pi]$ .
- (iii) Each coordinate system covering a certain region of the spacetime is called a *patch* or a *chart*, and two different charts may or may not overlap. An *atlas* of the manifold is any union of charts that covers the entire manifold.
- (iv) As commented above, an essential property of manifolds in general relativity is that they are *differentiable*, in the sense that the local mapping from the manifold to  $\mathbb{R}^n$  must be differentiable. A two-sphere is an example of a differentiable manifold; a cone is not, as it contains a point, *i.e.*, its vertex, which cannot be mapped in a differentiable manner into  $\mathbb{R}^n$ .

### 1.3.1 Coordinates

The idea of a spacetime (the container of all events), as of a manifold (a space covered with coordinates), is very attractive from a *geometrical* point of view, but it may also be a source of concern from the *physical* point of view, as the arbitrariness in the choice of coordinates may entail the loss of physical information. However, this is a false concern and coordinate-independent *measurements*, that is, measurements that will yield the same result in all coordinate systems, can be made. Similarly, it is still possible to derive coordinate-independent *equations* even when the spacetime is treated as a manifold. The theory of general relativity is indeed all about how to do this and we will progressively learn it in the course of this chapter.

<sup>3</sup>We will return to this point from a physical viewpoint in Section 1.5.

The first step in this learning process consists of becoming familiar with the basic objects of a manifold, *i.e.*, curves, scalars and vectors, and on how they transform when going from one system of coordinates to another one. Hereafter, we will assume that  $\mathcal{M}$  has four dimensions (three spatial dimensions and one temporal one) but, as mathematicians like to emphasise, the generalisation to an  $N$ -dimensional manifold is straightforward.

Consider therefore the spacetime to be covered by two sets of coordinates,<sup>4</sup>  $\{x^\mu\}$  and  $\{x^{\mu'}\}$ ,<sup>5</sup> or equivalently, consider two different mappings  $\Phi$  and  $\Phi'$  of the differentiable manifold  $\mathcal{M}$  into  $\mathbb{R}^4$ . Each point  $\mathcal{P}$  in  $\mathcal{M}$  is therefore represented by two different sets of four numbers  $\{x_\mathcal{P}^\mu\}$  and  $\{x_{\mathcal{P}'}^{\mu'}\}$ . A *coordinate transformation*  $\{x^\mu\} \rightarrow \{x^{\mu'}\}$  at  $\mathcal{P}$  is then expressed in terms of four functions  $f^\mu$ , which are single-valued, continuous and differentiable, such that

$$x_{\mathcal{P}}^{\mu'} = f^{\mu'}(x^1, x^2, x^3, x^4) \Big|_{\mathcal{P}} = f^{\mu'}(\boldsymbol{x}) \Big|_{\mathcal{P}}, \quad (1.1)$$

where we have indicated with  $\boldsymbol{x}$  the four coordinates  $x^\mu$ , thus adopting a convention we will use in the rest of the book, and in which we indicate with boldface a generic object in  $\mathcal{M}$ . Because our manifold is differentiable, the coordinate transformation need not be restricted at  $\mathcal{P}$ , *i.e.*,

$$x^{\mu'} = f^{\mu'}(\boldsymbol{x}), \quad (1.2)$$

and should be invertible, so that  $\boldsymbol{f}^{-1}$  is the *inverse* coordinate transformation  $\{x^{\mu'}\} \rightarrow \{x^\mu\}$  and

$$x^\mu = (f^{-1})^\mu(\boldsymbol{x}'), \quad (1.3)$$

with the combined operation  $\boldsymbol{f} \circ \boldsymbol{f}^{-1}$  being the identity, *i.e.*,  $x^\mu = x^\mu(x^{\mu'}) = x^\mu(x^{\mu'}(x^\mu))$ . As an instructive example, we can use the familiar two-dimensional manifold represented by a plane and consider the two sets of coordinates  $\{x^\mu\} = (x, y)$  and  $\{x^{\mu'}\} = (r, \theta)$  so that

$$\boldsymbol{f} : \begin{cases} x = r \cos \theta \\ y = r \sin \theta, \end{cases} \quad \boldsymbol{f}^{-1} : \begin{cases} r = (x^2 + y^2)^{\frac{1}{2}} \\ \theta = \tan^{-1}\left(\frac{y}{x}\right), \end{cases} \quad (1.4)$$

and if  $\boldsymbol{f} \circ \boldsymbol{f}^{-1}$  is applied, for instance, to the first set of coordinates, this then yields the identity  $x = (x^2 + y^2)^{\frac{1}{2}} \cos[\tan^{-1}(y/x)] = x$ .

Exploiting again the fact that the manifold is differentiable, we can differentiate the coordinates  $\boldsymbol{x}'$  with respect to the coordinates  $\boldsymbol{x}$  and obtain the  $4 \times 4$  *transformation matrix*

<sup>4</sup>Note that we indicate coordinates as  $\{x^\mu\}$ , *i.e.*, between curly brackets, to emphasise the fact that we are really considering four different numbers at each point of the manifold.

<sup>5</sup>A subtle issue of notation arises here. In principle, the new coordinate system should be indicated as  $\{(x')^\mu\}$ , but this notation is clearly overly complicated. Similarly, notations of the type  $\{x'^\mu\}$  or  $\{x^{\mu'}\}$  could create confusion between the prime, which is used to mark a different coordinate system, and the index  $\mu$ . Hence, we opt for the more convenient (although not mathematically rigorous) notation of  $\{x^{\mu'}\}$ .

## 8 A Brief Review of General Relativity

$$\Lambda^{\mu'}_{\mu} := \frac{\partial x^{\mu'}}{\partial x^{\mu}} = \begin{pmatrix} \frac{\partial x^{0'}}{\partial x^0} & \frac{\partial x^{0'}}{\partial x^1} & \frac{\partial x^{0'}}{\partial x^2} & \frac{\partial x^{0'}}{\partial x^3} \\ \frac{\partial x^{1'}}{\partial x^0} & \frac{\partial x^{1'}}{\partial x^1} & \frac{\partial x^{1'}}{\partial x^2} & \frac{\partial x^{1'}}{\partial x^3} \\ \frac{\partial x^{2'}}{\partial x^0} & \frac{\partial x^{2'}}{\partial x^1} & \frac{\partial x^{2'}}{\partial x^2} & \frac{\partial x^{2'}}{\partial x^3} \\ \frac{\partial x^{3'}}{\partial x^0} & \frac{\partial x^{3'}}{\partial x^1} & \frac{\partial x^{3'}}{\partial x^2} & \frac{\partial x^{3'}}{\partial x^3} \end{pmatrix}, \quad (1.5)$$

whose determinant

$$J' := \left| \frac{\partial x^{\mu'}}{\partial x^{\mu}} \right| \quad (1.6)$$

is also called the *Jacobian* of the coordinate transformation  $\mathbf{f}$  in (1.2). If  $J'$  is nonzero everywhere, we can solve Eq. (1.2) and obtain the inverse transformation (1.3). If, on the contrary,  $J' = 0$  at a point, the transformation is said to be *singular* there. Similarly, we can differentiate the coordinates  $\mathbf{x}$  with respect to the coordinates  $\mathbf{x}'$  and obtain the  $4 \times 4$  inverse-transformation matrix

$$\Lambda^{\mu}_{\mu'} := \left( \frac{\partial x^{\mu}}{\partial x^{\mu'}} \right). \quad (1.7)$$

At this point, using the chain rule for partial derivatives, it is not difficult to show that the two matrices (1.5) and (1.7) are inverses of one another, *i.e.*,

$$\Lambda' \Lambda = \mathbb{1}, \quad (1.8)$$

where  $\Lambda'$ ,  $\Lambda$  and  $\mathbb{1}$  are shorthand for  $\Lambda^{\mu'}_{\mu}$ ,  $\Lambda^{\mu}_{\mu'}$  and the unit matrix, respectively. A direct consequence of the relation (1.8) is that the two Jacobians are reciprocals of each other, *i.e.*,  $J = 1/J'$  (see Problem 1). It is a useful exercise to apply relations (1.5) and (1.7) to the coordinate systems (1.4) to derive, for instance, that

$$\Lambda' = \Lambda^{\mu'}_{\mu} = \begin{pmatrix} \frac{\partial r}{\partial x} & \frac{\partial r}{\partial y} \\ \frac{\partial \theta}{\partial x} & \frac{\partial \theta}{\partial y} \end{pmatrix}, \quad (1.9)$$

and

$$\Lambda = \Lambda^{\mu}_{\mu'} = \begin{pmatrix} \frac{\partial x}{\partial r} & \frac{\partial x}{\partial \theta} \\ \frac{\partial y}{\partial r} & \frac{\partial y}{\partial \theta} \end{pmatrix}, \quad (1.10)$$

with  $J' = 1/(x^2 + y^2)^{1/2} = 1/J$ .

### 1.3.2 Curves and paths

Having introduced the concept of coordinate systems and of coordinate transformations, we next consider the simplest object in the manifold  $\mathcal{M}$  that will ultimately lead to the definition of a tensor.

Consider therefore in the spacetime  $\mathcal{S}$  a continuous series of events  $\mathcal{P}_1, \dots, \mathcal{P}_N, \dots$ , which are related in some way. We have already discussed in Section 1.2 that we can relate or order these events and that the result is a worldline when the ordering parameter is the time coordinate  $t$ . We will now extend this idea and consider events which are not necessarily related through time, but through a more generic parameter  $\lambda$ . The resulting object is then called a *curve*  $\mathcal{C}$  and is therefore a mapping of an interval  $I = [a, b] \cap \mathbb{R}$  into a set of points with coordinates  $\{x^\mu\}$ , *i.e.*,

$$\text{curve } \mathcal{C} : \{x^\mu(\lambda), \text{ with } \lambda \in I \cap \mathbb{R}\}. \quad (1.11)$$

It is quite apparent that the same set of points in  $\mathcal{S}$  can be parameterised in an infinite number of different ways by suitably changing the parameter  $\lambda$ . This consideration helps us distinguish a *path*, *i.e.*, as the set of events in  $\mathcal{S}$ , from the *curve* through these events. While the path is an intrinsic object in the spacetime  $\mathcal{S}$ , the curve depends both on the parameter  $\lambda$  and on the coordinates chosen for the chart of the manifold  $\mathcal{M}$ . A change of the parameterisations  $\lambda$  will lead to a new curve passing through the same path in  $\mathcal{S}$  and having the same coordinate representation in  $\mathcal{M}$  (in this case it is called an *image*). However, a change of coordinates can lead to a new curve passing through the same path in  $\mathcal{S}$ , but clearly not to the same coordinate representation in  $\mathcal{M}$ . In other words, the concept of a path is much more fundamental than that of a curve and of an image, and we can construct two curves

$$\text{curve } \mathcal{C}' : \{x^\mu(\lambda'), \text{ with } \lambda' \in I' \cap \mathbb{R}\}, \quad (1.12)$$

and

$$\text{curve } \mathcal{L}' : \{x^{\mu'}(\lambda'), \text{ with } \lambda' \in I' \cap \mathbb{R}\}, \quad (1.13)$$

such that they cover the same path in  $\mathcal{S}$ , with  $\mathcal{C}$  and  $\mathcal{C}'$  having the same image, but with  $\mathcal{C}$  and  $\mathcal{L}'$  having a different one.

Finally, we can extend the concept of curve to that of a *surface* if there is more than one parameter, *i.e.*,

$$\text{surface } \mathcal{H} : \{x^\mu(\lambda^1, \lambda^2), \text{ with } \lambda^1, \lambda^2 \in I \cap \mathbb{R}\}. \quad (1.14)$$

The surface is then a *hypersurface* of the manifold if the number of parameters is equal to the dimensions of the manifold minus one, *i.e.*, three in the case of our four-dimensional spacetime.

### 1.3.3 Tangent vectors

All of the concepts introduced so far about curves and surfaces can be viewed as the building blocks necessary for the introduction of the very important and useful concept of the *tangent vector* to a curve  $\mathcal{C}$ . Indeed, bearing in mind that a curve is just a collection of points, each marked by a set of coordinates and ordered with a parameter  $\lambda$ , the tangent vector is simply a measure of how the coordinates change along the curve. In other words, given a coordinate

## 10 A Brief Review of General Relativity

system  $\{x^\mu\}$  in a manifold  $\mathcal{M}$  and a curve  $\mathcal{C} : \{x^\mu(\lambda), \lambda \in I\}$  in  $\mathcal{M}$ , its *tangent vector*  $\mathbf{V}_\mathcal{P}$  at a point  $\mathcal{P}$  along  $\mathcal{C}$  is then simply defined as the set of four numbers

$$V_\mathcal{P}^\mu := \left. \frac{dx^\mu}{d\lambda} \right|_{\mathcal{P}}. \quad (1.15)$$

Note that a curve has a unique tangent at  $\mathcal{P}$  and even if two curves may exist that have the same tangent at  $\mathcal{P}$ , they will either be different elsewhere or identical everywhere. Since the point  $\mathcal{P}$  is totally generic, we can write the general expression for the tangent vector  $\mathbf{V}$  to a curve  $\mathcal{C}$  as

$$V^\mu := \frac{dx^\mu}{d\lambda}. \quad (1.16)$$

Attention should be paid to the distinction between the vector as a geometrical object,  $\mathbf{V}$ , and its representation in a specific coordinate system, in which case we should really talk of the vector *components*  $V^\mu$ .

The importance of expression (1.16) is that it gives us the possibility of defining a geometrical quantity in terms of its transformation properties under a change of coordinates. Indeed, we can consider a new coordinate system  $\{x^{\mu'}\}$  and calculate, using expressions (1.2), the components that the *same* tangent vector  $\mathbf{V}$  assumes in the new coordinate system

$$V^{\mu'} := \frac{dx^{\mu'}}{d\lambda} = \sum_{\mu=0}^3 \frac{\partial x^{\mu'}}{\partial x^\mu} \frac{dx^\mu}{d\lambda} = \sum_{\mu=0}^3 \frac{\partial x^{\mu'}}{\partial x^\mu} V^\mu, \quad (1.17)$$

where the second equality simply exploits the definition of a differential

$$dx^{\mu'} = \sum_{\mu=0}^3 \frac{\partial x^{\mu'}}{\partial x^\mu} dx^\mu, \quad (1.18)$$

and the last equality in (1.17) is just the result of the definition (1.16).

Because good notation is important and this is particularly so in general relativity, we can simplify expression (1.17) firstly by adopting Einstein's summation convention, that is we can assume there is an implicit summation between 0 and 3 every time an index appears twice, and, secondly, by using the more compact expression (1.5) for the transformation matrix, *i.e.*,

$$V^{\mu'} = \Lambda_{\mu'}^\mu V^\mu. \quad (1.19)$$

A few considerations should be made about expression (1.19). The first one is that  $\mu$  is the index involved in the summation (or contraction) and, as such, it appears once as an upper (*i.e., contravariant*) index in  $V^\mu$  and once as a lower (*i.e., covariant*) index in  $\Lambda_{\mu'}^\mu$ . This index is then called a *dummy* to distinguish it from the *free* index  $\mu'$  that appears as the non-contracted index on either side of expression (1.19). Verifying that there are the same number of free indices on either side of an equality is the simplest way to check that it is not, at least mathematically, incorrect (of course, it can be incorrect for many other reasons!).

Expression (1.19) is very general and represents the *transformation rule* of what is properly referred to as a *contravariant vector*.<sup>6</sup> In essence, the four equations (1.19) tell us how

<sup>6</sup>Unfortunately, the nomenclature is not unique and some authors refer to  $V^\mu$  simply as a *vector*.

to compute the components of the generic vector  $\mathbf{V}$  in the coordinate system  $\{x^{\mu'}\}$  once we know them in the coordinate system  $\{x^\mu\}$ .

We can extend expression (1.19) to the case of a *composite coordinate transformation*, that is, by considering two coordinate transformations: first a coordinate transformation from  $\{x^\mu\}$  to a new one  $\{x^{\mu'}\}$  and then a subsequent one to  $\{x^{\mu''}\}$ , *i.e.*,

$$\{x^\mu\} \rightarrow \{x^{\mu'}\} \rightarrow \{x^{\mu''}\}, \quad (1.20)$$

and view it as a single coordinate transformation

$$\{x^\mu\} \rightarrow \{x^{\mu''}\}, \quad (1.21)$$

so that the (contravariant) vector will transform as

$$V^{\mu''} = \Lambda^{\mu''}_{\mu'} V^{\mu'} = \Lambda^{\mu''}_{\mu'} \Lambda^{\mu'}_{\mu} V^{\mu} = \Lambda^{\mu''}_{\mu} V^{\mu}. \quad (1.22)$$

Using the introductory work done in the previous section, we can write the *inverse transformation rule* to (1.19) as

$$V^\mu = \Lambda^\mu_{\mu'} V^{\mu'}. \quad (1.23)$$

In practice, the four equations (1.23) tell us how to compute the components of the vector  $\mathbf{V}$  in the coordinate system  $\{x^\mu\}$  once we know them in the coordinate system  $\{x^{\mu'}\}$ . Equally natural, it will appear that the two transformation matrices are inverses of each other, or equivalently, that

$$\Lambda^{\mu'}_{\mu} \Lambda^{\mu}_{\nu'} = \delta^{\mu'}_{\nu'} = \begin{cases} 0 & \text{if } \mu' \neq \nu' \\ 1 & \text{if } \mu' = \nu' \end{cases}, \quad (1.24)$$

and that the same must hold for the inverse transformation, *i.e.*,

$$\Lambda^\mu_{\mu'} \Lambda^{\mu'}_{\nu} = \delta^\mu_\nu = \begin{cases} 0 & \text{if } \mu \neq \nu \\ 1 & \text{if } \mu = \nu \end{cases}. \quad (1.25)$$

Note that both (1.24) and (1.25) are true provided that the Jacobians are non-singular, *i.e.*, that

$$\det(\Lambda^{\mu'}_{\mu}) \neq 0 \quad \text{and} \quad \det(\Lambda^\mu_{\mu'}) \neq 0. \quad (1.26)$$

The second equalities appearing in the two expressions (1.24) and (1.25) represent the definition of the *Kronecker delta*, an object that will be used extensively in the rest of the book.

Before concluding this section it may be useful to take a step back and go rapidly through the logical sequence we have followed. We have first considered a generic set of points related through a parameter, *i.e.*, a *curve* in a manifold, then introduced the *tangent vector* to it at a generic point  $\mathcal{P}$  and learnt how this geometrical object changes under a coordinate transformation. This leads us now to the more general concept of a vector and thus to the definition of the *tangent space* to a manifold  $\mathcal{M}$  at a point  $\mathcal{P}$  as the space of all the (contravariant) vectors at  $\mathcal{P}$ .

## 12 A Brief Review of General Relativity

### 1.3.4 Gradients of a function

Any generic vector can be built upon the concept of a curve. We can see this by going back to the definition (1.11) of the curve  $\mathcal{C}$  in the manifold and by introducing a scalar function  $\phi$ , that is, a real-valued function mapping any point  $\mathcal{P}$  of coordinates  $x^\mu(\lambda)$  in  $\mathcal{M}$  to a real number  $\phi(x^\mu(\lambda))|_{\mathcal{P}}$ . We can now calculate how the function varies along the curve  $\mathcal{C}$  simply as<sup>7</sup>

$$\frac{d\phi}{d\lambda} = \frac{\partial\phi}{\partial x^\mu} \frac{dx^\mu}{d\lambda} = \frac{\partial\phi}{\partial x^\mu} V^\mu = U_\mu V^\mu. \quad (1.27)$$

The second equality in (1.27) is simply the definition of the tangent vector we have already encountered in (1.16), while the third equality represents the *definition* of the *gradient of the function*  $\phi$

$$U_\mu := \frac{\partial\phi}{\partial x^\mu} = (\tilde{d}\phi)_\mu, \quad (1.28)$$

whose free index *must* be a lower (*i.e.*, a *covariant*) index, as this represents the feature that distinguishes it from the vector  $U^\mu$ .

To better appreciate why the index in  $U_\mu$  must be a lower one, we can study how this geometrical object behaves under a coordinate transformation and thus classify it accordingly. Once again, if  $U_\mu$  are the components of this object in a coordinate system  $\{x^\mu\}$ , the components it will assume in the coordinate system  $\{x^{\mu'}\}$  are

$$U_{\mu'} := \frac{\partial\phi}{\partial x^{\mu'}} = \frac{\partial\phi}{\partial x^\mu} \frac{\partial x^\mu}{\partial x^{\mu'}} = U_\mu \frac{\partial x^\mu}{\partial x^{\mu'}}. \quad (1.29)$$

Stated differently, the transformation rules of the gradient of a function  $\phi$  are simply

$$(\tilde{d}\phi)_{\mu'} = \frac{\partial x^\mu}{\partial x^{\mu'}} (\tilde{d}\phi)_\mu, \quad (1.30)$$

and they can be used as the *definition* of a *covariant vector* or *covector*.<sup>8</sup>

Note that the transformation (1.30) is the *inverse* of the transformation rule seen for the components of vectors [*cf.*, (1.19)]. The reason for this comes from the fact that vectors and covectors are *dual* to each other, so that the space of all covectors is a *dual space* to the tangent space introduced in the previous section.<sup>9</sup> Because this is an important and deep link between vectors and covectors we will discuss it further in the following sections. As for contravariant vectors, also for a covariant vector we can derive the inverse transformation and easily obtain

$$(\tilde{d}\phi)_\mu = \frac{\partial x^\mu}{\partial x^{\mu'}} (\tilde{d}\phi)_{\mu'}. \quad (1.31)$$

The careful reader may have wondered why we have not written Eq. (1.30) simply as

<sup>7</sup>In principle we should have considered (1.27) as defined at  $\mathcal{P}$  in the curve [as done in (1.15)] and then extended it to a generic point; in practice, we have removed the intermediate step and anticipated the general expression.

<sup>8</sup>Some authors refer to this object as a *one-form*.

<sup>9</sup>In Section 1.3.5 we will see that the components of covectors transform in the same way as coordinate basis vectors (hence the prefix “co”), while the components of contravariant vectors transform in the opposite way (hence the prefix “contra”).

$$(\tilde{d}\phi)_{\mu'} = \Lambda^{\mu}_{\mu'} (\tilde{d}\phi)_{\mu}, \quad (1.32)$$

and, similarly, why we have not written Eq. (1.31) as

$$(\tilde{d}\phi)_{\mu} = \Lambda^{\mu'}_{\mu} (\tilde{d}\phi)_{\mu'}. \quad (1.33)$$

The reason behind this choice is that the matrix notation suggested by (1.32) or (1.33) is potentially misleading if one takes  $\Lambda^{\mu}_{\mu'}$  in (1.32) as the same matrix that appears in (1.23). This becomes quite clear if we go back to the example of the coordinate transformation described in Section 1.3.2. Indeed, when we transform the gradient of a scalar from  $(x, y)$  to  $(r, \theta)$  components, the correct matrix to use in (1.32) and that multiplies the column vector  $(\tilde{d}\phi)_{\mu}$  is

$$\Lambda^{i'}_j = \begin{pmatrix} \frac{\partial x}{\partial r} & \frac{\partial y}{\partial r} \\ \frac{\partial x}{\partial \theta} & \frac{\partial y}{\partial \theta} \end{pmatrix}, \quad (1.34)$$

which is the transpose of the matrix defined in (1.10). In the rest of the chapter, we will use the symbol  $\Lambda^{\mu'}_{\mu}$  just as a shorthand for  $\partial x^{\mu'}/\partial x^{\mu}$ , and the symbol  $\Lambda^{\mu}_{\mu'}$  just as a shorthand for  $\partial x^{\mu}/\partial x^{\mu'}$ , while, if one wishes to interpret them as matrix symbols, care must be taken on whether they are applied to vectors or to covectors.

### 1.3.5 A geometrical view of vectors and covectors

We can collect the concepts discussed so far to reach a unified description of both contravariant and covariant vectors. In particular, we can use the definition of the gradient along a curve (1.27) and rewrite it as

$$\frac{d\phi}{d\lambda} = \frac{dx^{\mu}}{d\lambda} \frac{\partial\phi}{\partial x^{\mu}} = V^{\mu} (\tilde{d}\phi)_{\mu}, \quad (1.35)$$

so that a contravariant vector  $\mathbf{V}$  can be regarded as a geometrical object tangent to the curve with parameter  $\lambda$  and that measures  $d\phi/d\lambda$  for any scalar function  $\phi$  along the curve. In this way, the vector can be seen as an object in itself, independent of any coordinate system, and which defines, at least in a certain neighbourhood, the curve to which it is tangent. Its (contravariant) components  $V^{\mu}$  give a measure of the change of the coordinates along that curve and these are strictly related to the choice made for the coordinate system; a different coordinate system will yield a different set of components, as well as different function gradients  $(\tilde{d}\phi)_{\mu}$ .

Of course, we can also do without a scalar function  $\phi$  in (1.35) and view a vector as the object defined by

$$\mathbf{V} := \frac{d}{d\lambda} = V^{\mu} \frac{\partial}{\partial x^{\mu}} = V^{\mu} \mathbf{e}_{\mu}, \quad (1.36)$$

where we have introduced the symbols

$$\mathbf{e}_{\mu} := \frac{\partial}{\partial x^{\mu}} = \partial_{\mu} \quad (1.37)$$

## 14 A Brief Review of General Relativity

to indicate four *basis vectors*  $\{e_\mu\}$  along the directions defined by the coordinates  $\{x^\mu\}$ .<sup>10</sup> Such a basis of vectors, which is tightly related to the coordinates adopted, is also known as the *coordinate basis*. In this way, expression (1.36) simply states that  $\mathbf{V}$  is the composition of the contravariant components  $V^\mu$  along the coordinate directions.

The definition (1.36) for a vector may appear as very geometrical and unconventional but this is just a wrong impression. In fact, if we consider a three-dimensional manifold and associate the directional derivatives  $\{\partial/\partial x^i\}$  with the *basis vectors*  $\{\vec{e}_i\}$  of classical vector calculus, it is then clear that expression (1.36) indeed *coincides* with the one in which three-dimensional vectors (or *three-vectors*) are introduced in traditional textbooks in physics or linear algebra, *i.e.*,

$$\begin{aligned}\vec{V} &= V^i \vec{e}_i = V^x \vec{e}_x + V^y \vec{e}_y + V^z \vec{e}_z \\ &= V^r \vec{e}_r + V^\theta \vec{e}_\theta + V^\phi \vec{e}_\phi = \dots,\end{aligned}\quad (1.38)$$

when  $\vec{V}$  is expressed in a Cartesian coordinate system (second equality) or in a spherical polar one (third equality), or in any other coordinate basis. This new view of a vector is also useful to introduce a new view of a covector. Indeed, we can go back to the definition (1.35) and now think of the covariant vector  $\tilde{d}$  as an operator  $\tilde{d}(\cdot)$  acting on a vector and such that when applied to  $\mathbf{V}$  it returns a *single* real number,<sup>11</sup> *i.e.*,

$$\tilde{d}(\mathbf{V}) = V^\mu d_\mu. \quad (1.39)$$

When seen as an operator acting on vectors, the covector is then a linear operator, *i.e.*,

$$\text{if } \tilde{d} = a \tilde{p} + b \tilde{q}, \quad \text{then } \tilde{d}(\mathbf{V}) = a \tilde{p}(\mathbf{V}) + b \tilde{q}(\mathbf{V}), \quad (1.40)$$

where  $a$  and  $b$  are constant coefficients. In addition, it is linear in its arguments, *i.e.*,

$$\tilde{d}(a \mathbf{V} + b \mathbf{U}) = a \tilde{d}(\mathbf{V}) + b \tilde{d}(\mathbf{U}). \quad (1.41)$$

This geometrical interpretation of vectors and covectors is indeed a *unifying* one. In such a view, a vector  $\mathbf{V}$  defines a curve to which it is tangent, while a covector  $\tilde{d}$  defines the gradient of a scalar function along the same curve. Furthermore, a covector acting on a vector produces a coordinate-independent number and thus a relativistic *invariant*. This is such an important property that is worth proving it by starting from expression (1.39) in a coordinate system  $\{x^{\mu'}\}$ , *i.e.*,

$$\begin{aligned}\tilde{d}(\mathbf{V}) &= V^{\mu'} d_{\mu'} = (\Lambda^{\mu'}_{\nu} V^\nu)(\Lambda^\nu_{\mu'} d_\mu) \\ &= \Lambda^\mu_{\mu'} \Lambda^{\mu'}_{\nu} V^\nu d_\mu \\ &= \delta^\mu_{\nu} V^\nu d_\mu = V^\mu d_\mu.\end{aligned}\quad (1.42)$$

This invariance applies also to the definition (1.36) of a vector and allows us to derive the transformation rule for the basis vectors

<sup>10</sup>We indicate *basis vectors* as  $\{e_\mu\}$ , *i.e.*, between curly brackets, to emphasise the fact that we are really considering four such vectors. Hence, the lower index in (1.37) does *not* denote the different components of *one* basis vector, but it distinguishes the *four* different vectors composing the basis.

<sup>11</sup>We reserve boldface font with a tilde, *e.g.*,  $\tilde{p}$ , to indicate a covector as an operator and normal font with a lower index, *e.g.*,  $p_\mu$ , to indicate its components.

$$\begin{aligned}\mathbf{V} &= V^{\mu'} e_{\mu'} = V^{\mu} e_{\mu} \\ &= \Lambda^{\mu}_{\nu'} V^{\nu'} e_{\mu} = \Lambda^{\mu}_{\nu'} V^{\mu'} e_{\mu},\end{aligned}\quad (1.43)$$

so that, collecting the components of  $\mathbf{V}$ , we obtain

$$V^{\mu'} (e_{\mu'} - \Lambda^{\mu}_{\mu'} e_{\mu}) = 0, \quad (1.44)$$

and thus for any non-trivial  $\mathbf{V}$

$$e_{\mu'} = \Lambda^{\mu}_{\mu'} e_{\mu}. \quad (1.45)$$

Although expression (1.45) is *not* a component transformation, it is impossible not to recognise the similarity between (1.45) and the transformation rule for the components of a covector (1.32). It is therefore customary to say that basis vectors transform as the components of covectors and in the “opposite way” to the component of vectors. Note that opposite is in quotes because if we read the vector transformation (1.45) as the matrix representation of a change of basis, then the corresponding matrix representation (1.19) adopts the inverse of the *transpose* matrix used in (1.45) and not just the inverse matrix (see the discussion in Section 1.3.4).

Finally, having introduced the basis vectors, it is also natural to define the *basis covectors* simply as those covectors dual to basis vectors, *i.e.*,

$$\tilde{\omega}^{\mu}(e_{\nu}) = \delta^{\mu}_{\nu}, \quad (1.46)$$

thus stating that a vector basis  $\{e_{\nu}\}$  induces a unique covector basis  $\{\tilde{\omega}^{\mu}\}$ , and that any covector  $\tilde{\mathbf{p}}$  can be expressed as

$$\tilde{\mathbf{p}} = p_{\mu} \tilde{\omega}^{\mu}. \quad (1.47)$$

To prove that (1.46) is correct, we can simply use (1.36) and (1.47) to obtain that

$$\begin{aligned}p_{\mu} V^{\mu} &= \tilde{\mathbf{p}}(\mathbf{V}) = p_{\mu} \tilde{\omega}^{\mu}(\mathbf{V}) \\ &= p_{\mu} \tilde{\omega}^{\mu}(V^{\nu} e_{\nu}) \\ &= p_{\mu} V^{\nu} \tilde{\omega}^{\mu}(e_{\nu}) = p_{\mu} V^{\nu} \delta^{\mu}_{\nu}.\end{aligned}\quad (1.48)$$

### 1.3.6 Tensors

The definitions of vectors and covectors introduced in the previous sections have paved the way to the content of this section. They have been introduced to define geometrical objects that are independent of any coordinate system and we have learnt that when a coordinate system is introduced and changed, these contravariant and covariant vectors transform according to the simple rules (1.19) and (1.30).

There are at least two aspects of vectors (either contra- or covariant ones) that are quite apparent. The first one is that we need not restrict ourselves to the idea of a vector defined at a point. Rather, we can think of a whole region of the manifold  $\mathcal{M}$  and assign, through a

## 16 A Brief Review of General Relativity

smooth differentiable function, a vector at each point of this region, thus building a so-called *vector field*

$$f: \{\mathcal{P} \in \mathcal{M} \rightarrow V^\mu(\mathcal{P})\}, \quad \text{and} \quad g: \{\mathcal{P} \in \mathcal{M} \rightarrow U_\mu(\mathcal{P})\}, \quad (1.49)$$

where  $V^\mu(\mathcal{P}), U_\mu(\mathcal{P})$  are the values of the vector field at  $\mathcal{P}$ . Furthermore, the vector field is said to be *differentiable* if its components are differentiable functions of the coordinates in all coordinate systems. The second aspect is that vectors represent only the simplest elements of a more general class of geometrical objects, *i.e.*, *tensors*. As for contravariant and covariant vectors, in fact, also tensors can be viewed as geometrical objects which are entirely *defined* in terms of the properties under a coordinate transformation.

Coherent with this approach, we define a *contravariant tensor of rank 2* (or tensor of contravariant rank 2) as a geometrical object  $T$ , whose components transform according to the following rule when going from one coordinate system  $\{x^\mu\}$  to a new one  $\{x^{\mu'}\}$ <sup>12</sup>

$$T^{\mu' \nu'} = \frac{\partial x^{\mu'}}{\partial x^\mu} \frac{\partial x^{\nu'}}{\partial x^\nu} T^{\mu\nu} = \Lambda^{\mu'}_{\mu} \Lambda^{\nu'}_{\nu} T^{\mu\nu}. \quad (1.50)$$

Similarly, we define a *covariant tensor of rank 2* (or tensor of covariant rank 2) as a geometrical object  $T$ , whose components transform according to the following rule when going from  $\{x^\mu\}$  to  $\{x^{\mu'}\}$ <sup>13</sup>

$$T_{\mu' \nu'} = \frac{\partial x^\mu}{\partial x^{\mu'}} \frac{\partial x^\nu}{\partial x^{\nu'}} T_{\mu\nu} = \Lambda^\mu_{\mu'} \Lambda^\nu_{\nu'} T_{\mu\nu}. \quad (1.51)$$

If the coordinates are regular, both expressions (1.50) and (1.51) will admit inverse transformations and these can be deduced straightforwardly from the corresponding expressions (1.23) and (1.31). Equally natural is then to define a *mixed tensor* as a geometrical object having *both* contravariant and covariant components, so that, for instance, we can define the following mixed tensor of type (4, 2) (*i.e.*, of contravariant rank 4 and covariant rank 2),  $R^{\alpha\beta\gamma\delta}_{\mu\nu}$ , whose transformation properties when going from  $\{x^\mu\}$  to  $\{x^{\mu'}\}$  are simply given by<sup>14</sup>

$$R^{\alpha'\beta'\gamma'\delta'}_{\mu'\nu'} = \Lambda^{\alpha'}_{\alpha} \Lambda^{\beta'}_{\beta} \Lambda^{\gamma'}_{\gamma} \Lambda^{\delta'}_{\delta} \Lambda^{\mu}_{\mu'} \Lambda^{\nu}_{\nu'} R^{\alpha\beta\gamma\delta}_{\mu\nu}, \quad (1.52)$$

and the inverse transformation will be

$$R^{\alpha\beta\gamma\delta}_{\mu\nu} = \Lambda^{\alpha}_{\alpha'} \Lambda^{\beta}_{\beta'} \Lambda^{\gamma}_{\gamma'} \Lambda^{\delta}_{\delta'} \Lambda^{\mu}_{\mu'} \Lambda^{\nu}_{\nu'} R^{\alpha'\beta'\gamma'\delta'}_{\mu'\nu'}. \quad (1.53)$$

Expressions (1.52) and (1.53) serve here just as examples and it is not difficult to imagine that it is possible to build tensors with an arbitrary number of contravariant and covariant components. It is indeed possible to construct a *vector space*  $V_n^m$  as the set of all tensors of type  $(m, n)$  so that, for instance,  $R^{\alpha\beta\gamma\delta}_{\mu\nu} \in V_2^4$ .

Given that vectors and covectors can now be viewed as tensors of special type [*i.e.*, of type (1, 0) and (0, 1), respectively] we can also exploit the decomposition into basis vectors (1.36)

<sup>12</sup>Some authors refer to this object as a  $\begin{pmatrix} 2 \\ 0 \end{pmatrix}$  tensor.

<sup>13</sup>Some authors refer to this object as a  $\begin{pmatrix} 0 \\ 2 \end{pmatrix}$  tensor. Furthermore, if the tensor is antisymmetric [see Eq. (1.56) for a definition] it is also referred to as a *two-form*.

<sup>14</sup>Some authors refer to this object as a  $\begin{pmatrix} 4 \\ 2 \end{pmatrix}$  tensor.

and covectors (1.47) to express a generic mixed vector also as a geometric object which is coordinate independent. Restricting for simplicity to a mixed tensor of type (1, 1), this would yield

$$\mathbf{R} = R^\mu{}_\nu e_\mu \otimes \tilde{\omega}^\nu, \quad (1.54)$$

where the symbol  $\otimes$  denotes the *outer product*. Note that this operator is *not* commutative, *i.e.*,  $e_\mu \otimes \tilde{\omega}^\nu \neq \tilde{\omega}^\nu \otimes e_\mu$ , so that the two tensors  $\mathbf{R} = R^\mu{}_\nu e_\mu \otimes \tilde{\omega}^\nu$  and  $\tilde{\mathbf{R}} = \tilde{R}_\nu{}^\mu \tilde{\omega}^\nu \otimes e_\mu$  are effectively two distinct tensors.

In analogy with what was done for vectors, we can introduce the concept of a *tensor field* by associating a tensor of type  $(m, n)$  to any point  $\mathcal{P}$

$$f: \{\mathcal{P} \in \mathcal{M} \longrightarrow V^{\alpha\beta\dots}_{\mu\nu\dots}(\mathcal{P})\}, \quad (1.55)$$

where  $V^{\alpha\beta\dots}_{\mu\nu\dots}(\mathcal{P})$  are the values of the tensor field at  $\mathcal{P}$ . Also in this case, the tensor field is said to be differentiable if its components are differentiable functions of the coordinates in all coordinate systems. Hereafter, we will always consider tensor fields although we will refer to them simply as tensors.

In general, if a tensor has  $N$  *indices* and is defined in a manifold of  $D$  *dimensions*, it will have  $D^N$  components, so that in the four-dimensional manifold we are interested in here, we can think of tensors as being matrices having 4, 16, 64 or 256 components according to whether their rank is 1, 2, 3 or 4, respectively.<sup>15</sup> Of course there is no reason to expect them to be all independent. Indeed, as we will discuss in the following section, several constraints can restrict the number of independent components.

We conclude this section with a note on the nomenclature. Differences are in fact still present among different authors, so that the same object can be named in four or five different ways. Here are some examples and a simple summary:

- $V^\mu$ : contravariant vector, or vector, or contravariant tensor of rank 1, or tensor of type  $(1, 0)$ , or  $\begin{pmatrix} 1 \\ 0 \end{pmatrix}$  tensor.
- $V_\mu$ : covariant vector, or covector, or covariant tensor of rank 1, or tensor of type  $(0, 1)$ , or  $\begin{pmatrix} 0 \\ 1 \end{pmatrix}$  tensor, or one-form.
- $V_{\mu\nu}$ : covariant tensor of rank 2, or tensor of type  $(0, 2)$ , or  $\begin{pmatrix} 0 \\ 2 \end{pmatrix}$  tensor.<sup>16</sup>
- $V^{\mu\nu}{}_{\alpha\beta\gamma\delta}$ : mixed tensor of contravariant rank 2 and covariant rank 4, or tensor of type  $(2, 4)$ , or  $\begin{pmatrix} 2 \\ 4 \end{pmatrix}$  tensor.

### 1.3.7 Tensor algebra

Any use of general relativity inevitably involves a certain amount of tensor manipulations and it is therefore a good idea to become familiar with the basic operations of tensor algebra, which will ultimately lead to tensor calculus in Section 1.5. Besides the linearity property already

<sup>15</sup>Despite this freedom of building tensors of arbitrary rank, we will not discuss here tensors with rank higher than 4.

<sup>16</sup>The tensor is also called a two-form if it is antisymmetric, *i.e.*, if it obeys the definition in Eq. (1.56).

## 18 A Brief Review of General Relativity

seen for covectors in (1.39), that extends trivially when  $\mathbf{V}$  and  $\tilde{d}\phi$  are seen as tensors, we list below some of the most important properties of tensors as well as of tensor operations.

(i) *Zero tensor*: If a tensor has all of its components zero in one coordinate system, it is said to be the *zero tensor* and its components will be zero in all coordinate systems.

(ii) *Identical tensors*: If two tensors of the same type have all of their components equal in one coordinate system they are said to be *identical* and will have the same components in all coordinate systems.

(iii) *Scalar function*: The multiplication of a scalar field  $\phi$  with a tensor of a given type will yield a new tensor of the same type, *i.e.*, if  $\mathbf{X} \in \mathbf{V}_n^m$  and  $\mathbf{Y} := \phi \mathbf{X}$ , then  $\mathbf{Y} \in \mathbf{V}_n^m$ .

(iv) *Addition*: The addition of two tensors of the same type yields a new tensor of the same type, *i.e.*, if  $\mathbf{X}, \mathbf{Y} \in \mathbf{V}_n^m$  and  $\mathbf{Z} := \mathbf{X} + \mathbf{Y}$ , then  $\mathbf{Z} \in \mathbf{V}_n^m$ .

(v) *Multiplication*: The multiplication of two tensors of any type yields a new tensor whose type is the sum of the two types (*i.e.*, the sum of the corresponding contravariant and covariant ranks) and which is also called the *outer product* of the two tensors, *e.g.*, if  $\mathbf{X} \in \mathbf{V}_n^m, \mathbf{Y} \in \mathbf{V}_q^p$  and  $\mathbf{Z} := \mathbf{X} \otimes \mathbf{Y}$ , then  $\mathbf{Z} \in \mathbf{V}_{n+q}^{m+p}$ . Using a component notation in which, say,  $m = q = 2$ , and  $n = p = 1$ , then  $Z_{\lambda\mu\nu}^{\alpha\beta\gamma} = X_{\lambda}^{\alpha\beta} Y_{\mu\nu}^{\gamma}$ .

(vi) *Contraction*: Contraction on a pair of indices of a tensor of type  $(m, n)$  yields a new tensor of type  $(m - 1, n - 1)$ , *i.e.*,  $Z_{\gamma\mu\nu}^{\alpha\beta\gamma} = Z_{\mu\nu}^{\alpha\beta}$ .

(vii) *Symmetries and antisymmetries*: A generic tensor of type  $(m, n)$  is said to be *symmetric* on any pair of indices  $p$  and  $q$  (either both covariant or contravariant) if its components do not change under the exchange of these two indices. Conversely, it is said to be *antisymmetric* (or skew) if its sign changes under the exchange of the two indices. As an example, consider for simplicity  $m = 0, n = 2$ , then

$$Z_{\mu\nu} : \text{symmetric} \iff Z_{\mu\nu} = Z_{\nu\mu}, \quad (1.56)$$

$$Z_{\mu\nu} : \text{antisymmetric} \iff Z_{\mu\nu} = -Z_{\nu\mu}. \quad (1.57)$$

As a result of (1.56)–(1.57) it is possible to construct a symmetric or antisymmetric tensor from an arbitrary one, *i.e.*,

$$Z_{(\mu\nu)} := \frac{1}{2} (Z_{\mu\nu} + Z_{\nu\mu}), \quad Z_{[\mu\nu]} := \frac{1}{2} (Z_{\mu\nu} - Z_{\nu\mu}), \quad (1.58)$$

where the round and square brackets are used to highlight symmetric and antisymmetric indices, respectively. As an obvious consequence of (1.58), an arbitrary tensor can always be decomposed into its symmetric and antisymmetric parts, *i.e.*,

$$Z_{\mu\nu} = Z_{(\mu\nu)} + Z_{[\mu\nu]}. \quad (1.59)$$

Expressions (1.58) can be extended to tensors of arbitrary rank and, for example, the symmetric and antisymmetric expressions for a tensor of type  $(0, 3)$  is given by the permutations of the three indices

$$Z_{(\mu\nu\gamma)} := \frac{1}{3!} (Z_{\mu\nu\gamma} + Z_{\nu\mu\gamma} + Z_{\gamma\mu\nu} + Z_{\mu\gamma\nu} + Z_{\nu\gamma\mu} + Z_{\gamma\nu\mu}), \quad (1.60)$$

$$Z_{[\mu\nu\gamma]} := \frac{1}{3!} (Z_{\mu\nu\gamma} - Z_{\nu\mu\gamma} + Z_{\gamma\mu\nu} - Z_{\mu\gamma\nu} + Z_{\nu\gamma\mu} - Z_{\gamma\nu\mu}). \quad (1.61)$$

The last of these properties gives us the opportunity to introduce the *Levi-Civita tensor*, which is an extension to four dimensions of the well-known Levi-Civita symbol  $\epsilon_{ijk}$ . More specifically, given a tensor<sup>17</sup>  $g$  of type  $(0, 2)$  and with determinant  $g$ , i.e.,  $g := \det(g_{\mu\nu})$ , we define the Levi-Civita tensor as<sup>18</sup>

$$\epsilon_{\alpha\beta\gamma\delta} := -\sqrt{-g} \eta_{\alpha\beta\gamma\delta}, \quad (1.62)$$

$$\epsilon^{\alpha\beta\gamma\delta} := \frac{1}{\sqrt{-g}} \eta^{\alpha\beta\gamma\delta}, \quad (1.63)$$

where  $\eta_{\alpha\beta\gamma\delta}$  is the “totally antisymmetric symbol” defined as<sup>19</sup>

$$\eta_{\alpha\beta\gamma\delta} := \begin{cases} +1 & \text{if } [\alpha\beta\gamma\delta] \text{ is an even permutation of } 0123, \\ -1 & \text{if } [\alpha\beta\gamma\delta] \text{ is an odd permutation of } 0123, \\ 0 & \text{if } [\alpha\beta\gamma\delta] \text{ are not all different.} \end{cases} \quad (1.64)$$

In addition, the contraction of two Levi-Civita tensors leads to additional *permutation tensors*

$$\epsilon^{\alpha\beta\gamma\delta} \epsilon_{\lambda\mu\nu\delta} = -1! \delta_{\lambda\mu\nu}^{\alpha\beta\gamma}, \quad (1.65)$$

$$\epsilon^{\alpha\beta\gamma\delta} \epsilon_{\lambda\mu\gamma\delta} = -2! \delta_{\lambda\mu}^{\alpha\beta}, \quad (1.66)$$

$$\epsilon^{\alpha\beta\gamma\delta} \epsilon_{\lambda\beta\gamma\delta} = -3! \delta_{\lambda}^{\alpha}, \quad (1.67)$$

$$\epsilon^{\alpha\beta\gamma\delta} \epsilon_{\alpha\beta\gamma\delta} = -4!, \quad (1.68)$$

where the permutation tensors are just extensions of the *Kronecker delta*  $\delta_{\beta}^{\alpha}$ , i.e.,

$$\delta_{\lambda\mu}^{\alpha\beta} = \begin{vmatrix} \delta_{\lambda}^{\alpha} & \delta_{\mu}^{\alpha} \\ \delta_{\lambda}^{\beta} & \delta_{\mu}^{\beta} \end{vmatrix} = \delta_{\lambda}^{\alpha} \delta_{\mu}^{\beta} - \delta_{\mu}^{\alpha} \delta_{\lambda}^{\beta}, \quad (1.69)$$

$$\delta_{\lambda\mu\nu}^{\alpha\beta\gamma} = \begin{vmatrix} \delta_{\lambda}^{\alpha} & \delta_{\mu}^{\alpha} & \delta_{\nu}^{\alpha} \\ \delta_{\lambda}^{\beta} & \delta_{\mu}^{\beta} & \delta_{\nu}^{\beta} \\ \delta_{\lambda}^{\gamma} & \delta_{\mu}^{\gamma} & \delta_{\nu}^{\gamma} \end{vmatrix} = \delta_{\lambda}^{\alpha} (\delta_{\mu}^{\beta} \delta_{\nu}^{\gamma} - \delta_{\nu}^{\beta} \delta_{\mu}^{\gamma}) - \delta_{\mu}^{\alpha} (\delta_{\lambda}^{\beta} \delta_{\nu}^{\gamma} - \delta_{\nu}^{\beta} \delta_{\lambda}^{\gamma}) + \delta_{\nu}^{\alpha} (\delta_{\lambda}^{\beta} \delta_{\mu}^{\gamma} - \delta_{\mu}^{\beta} \delta_{\lambda}^{\gamma}).$$

As a final and important remark on tensors and tensor algebra, it is worth underlining why we are so interested in tensors. As mentioned repeatedly in this chapter, in general relativity we are interested in defining quantities which are independent of any specific choice made for

<sup>17</sup>In Section 1.3.8 we will recognise that this tensor is actually the metric tensor and it is necessary to transform  $\epsilon$  as a tensor.

<sup>18</sup>Unfortunately different authors have different sign conventions about the Levi-Civita tensor. For example, Misner et al. (1973) define  $\epsilon^{\alpha\beta\gamma\delta} := -\eta^{\alpha\beta\gamma\delta}/\sqrt{-g}$ , but we here follow the notation which is more commonly used in recent research work, as in, e.g., Giacomazzo and Rezzolla (2007). Note also that the use of the metric determinant in (1.62) and (1.63) is essential for  $\epsilon$  to transform as a tensor.

<sup>19</sup>Note that because  $\eta_{\alpha\beta\gamma\delta}$  is *not* a tensor, its lower indices are not to be meant as covariant indices but just a sequence of numbers; for this reason  $\eta_{\alpha\beta\gamma\delta} = \eta^{\alpha\beta\gamma\delta} = [\alpha\beta\gamma\delta]$ .

## 20 A Brief Review of General Relativity

the coordinate system covering the manifold. We have seen that tensor components are very much dependent on this choice, but tensors and most importantly *tensor equations* are not. As a representative example we may consider the following tensor equation in the coordinate system  $\{x^\mu\}$

$$G^\mu{}_\nu = kT^\mu{}_\nu, \quad (1.70)$$

where  $k$  is just a constant and we may think of the tensor components  $G^\mu{}_\nu$  as representing, for instance, a differential operator of some kind. To derive the form that Eqs. (1.70) take in the new coordinate system  $\{x^{\mu'}\}$  is, by now, straightforward and just requires using the proper transformation for each side of Eqs. (1.70), *i.e.*,

$$\Lambda^\mu{}_{\mu'} \Lambda^{\nu'}{}_\nu G^{\mu'}{}_{\nu'} = k \Lambda^\mu{}_{\mu'} \Lambda^{\nu'}{}_\nu T^{\mu'}{}_{\nu'}, \quad (1.71)$$

so that a simple grouping of terms leads to

$$\Lambda^\mu{}_{\mu'} \Lambda^{\nu'}{}_\nu (G^{\mu'}{}_{\nu'} - kT^{\mu'}{}_{\nu'}) = 0. \quad (1.72)$$

Since (1.72) must hold for any coordinate transformation, it follows that

$$G^{\mu'}{}_{\nu'} = kT^{\mu'}{}_{\nu'}, \quad (1.73)$$

which has exactly the same form as Eqs. (1.70). In other words, tensor equations are said to be *covariant* in the sense that they assume the *same form* in any coordinate system. As a result, if they are true (or satisfied) in one coordinate system, then they are true in all coordinate systems. The covariance of tensor equations represents a very important property of tensors and is deeply rooted in the theory of general relativity. We close this section by recommending Ohanian (1976), for an interesting discussion about the distinction between covariance and invariance in general relativity.

### 1.3.8 The most important tensor: the metric

An operation we have not yet discussed is how to compute the *scalar product* between two vectors and hence how to measure the modulus of a single vector. Both things, namely, the scalar product and the calculation of the modulus, require that the spacetime is endowed with an operator  $\mathbf{g}$ , a symmetric tensor of type  $(0, 2)$ , that, when acting on two generic vectors  $\mathbf{U}$  and  $\mathbf{V}$ , yields a number, *i.e.*,

$$\mathbf{g}(\mathbf{U}, \mathbf{V}) = \mathbf{U} \cdot \mathbf{V} = g_{\mu\nu} U^\mu V^\nu. \quad (1.74)$$

The expression above is indeed the definition of the scalar product between two vectors, and when it is zero, the two vectors are said to be *orthogonal*. In the same way in which we have shown that  $\tilde{d}(\mathbf{V})$  is coordinate independent [*cf.* Eq. (1.42)], we can prove that the scalar product (1.74) is also invariant, that is,  $g_{\mu\nu} U^\mu V^\nu = g_{\mu'\nu'} U^{\mu'} V^{\nu'}$ . The definition of the modulus (or length) of a generic vector  $\mathbf{V}$  follows as a special case of (1.74) and corresponds to the scalar product of the vector with itself, *i.e.*,

$$\mathbf{g}(\mathbf{V}, \mathbf{V}) = \mathbf{V} \cdot \mathbf{V} := \mathbf{V}^2 := g_{\mu\nu} V^\mu V^\nu. \quad (1.75)$$

We can now go back to the ideas developed in Section 1.3 and think of the spacetime as a manifold  $\mathcal{M}$  in which we have laid out some coordinate system. Given two events  $\mathcal{P}$  at

$\{x^\mu\}_{\mathcal{P}}$  and  $\mathcal{Q}$  at  $\{x^\mu\}_{\mathcal{Q}}$  in  $\mathcal{M}$ , we may want to measure their squared infinitesimal *spacetime interval* (or *line element*),  $ds^2$ , in terms of the infinitesimal displacement vector  $\mathbf{dx}$ , whose components are simply  $dx^\mu := \{x^\mu\}_{\mathcal{P}} - \{x^\mu\}_{\mathcal{Q}}$ . Being nothing more than a scalar product, such a distance will be *independent* of the coordinate system chosen and given by

$$ds^2 := \mathbf{dx} \cdot \mathbf{dx} = g_{\mu\nu} dx^\mu dx^\nu. \quad (1.76)$$

Because of the role played in measuring the distances in expression (1.76), the symmetric tensor  $\mathbf{g}$  is referred to as the *metric tensor* (or simply metric) and it represents the single most important tensor in general relativity. The *signature* of the metric tensor is then defined as the number of positive, negative and zero eigenvalues of the metric.

Once a coordinate system is chosen to locate and *order* events in the spacetime, the metric tensor allows us to determine the *distance* between them and thus make physical *measurements*. While expression (1.76) is restricted to infinitesimal distances, its extension to finite distances is straightforward and thus the *proper distance* between two events along a curve  $\mathcal{C}$  can be written as

$$\ell := \int_{\mathcal{C}} \sqrt{ds^2} = \int_{\mathcal{C}} \sqrt{g_{\mu\nu} dx^\mu dx^\nu}. \quad (1.77)$$

We can easily recognise in expression (1.76) the very familiar Pythagoras' theorem applied in spacetimes that are not necessarily Euclidean. To make this correspondence more transparent, let us consider the two points  $\mathcal{P}$  and  $\mathcal{Q}$  belonging to a three-dimensional spacetime and calculate their distance respectively as

$$ds^2 = dx^2 + dy^2 + dz^2 \quad (1.78)$$

$$= d\rho^2 + \rho^2 d\phi^2 + dz^2 \quad (1.79)$$

$$= dr^2 + r^2 d\theta^2 + r^2 \sin^2 \theta d\phi^2 = dr^2 + r^2 d\Omega^2. \quad (1.80)$$

The three expressions presented above refer to the *same* distance (*i.e.*, they yield the *same* number) and appear to be different simply because they employ three different coordinate systems, namely: a Cartesian one  $(x, y, z)$  in (1.78), a cylindrical one  $(\rho, \phi, z)$  in (1.79) and a spherical polar  $(r, \theta, z)$  one in (1.80). Clearly, each choice of coordinates will select a new form for the metric tensor which will be  $g_{ij} = \text{diag}(1, 1, 1)$  in (1.78), or  $g_{ij} = \text{diag}(1, \rho^2, 1)$  in (1.79), and finally  $g_{ij} = \text{diag}(1, r^2, r^2 \sin^2 \theta)$  in (1.80). The example (1.78) is also useful to emphasise that Cartesian coordinates are rather special, as the metric in it assumes the simplest possible form, *i.e.*,  $|g_{\mu\nu}| = \delta_{\mu\nu}$ .

The determinant of the metric is denoted by  $g := \det(g_{\mu\nu})$  and, among its many uses, it serves to define the *proper volume* element as the integral over a four-dimensional hypersurface  ${}^4\Sigma$ , *i.e.*,

$$\mathcal{V}_p := \int_{{}^4\Sigma} \sqrt{-g} d^4x. \quad (1.81)$$

Furthermore, the metric is said to be *non-singular* if  $g \neq 0$  everywhere in the mapping. When this is the case,  $g_{\mu\nu}$  admits an inverse  $g^{\mu\nu}$  such that

$$g^{\mu\nu} g_{\mu\gamma} = \delta_\gamma^\nu. \quad (1.82)$$

Exploiting the property (1.82), we can use the metric to *raise* and *lower* the indices in tensors by contracting the tensor with the metric or its inverse. In this operation the contracted

## 22 A Brief Review of General Relativity

(dummy) index is lost and the remaining index of the metric is either lowered (when the metric is used in the contraction) or raised (when the inverse is used). As an example, for a tensor  $T$  of type (2, 2), the contractions with the metric and its inverse lead to

$$g_{\alpha\beta} T^{\alpha\delta}_{\mu\nu} = T^{\delta}_{\beta\mu\nu}, \quad \text{and} \quad g^{\mu\delta} T^{\alpha\beta}_{\mu\nu} = T^{\alpha\beta\delta}_{\nu}, \quad (1.83)$$

or, more generally for a tensor of arbitrary type,

$$g_{\alpha\beta} T^{\cdots\alpha\cdots} = T^{\cdots\beta\cdots}, \quad \text{and} \quad g^{\alpha\beta} T^{\cdots\cdots\alpha\cdots} = T^{\cdots\cdots\beta\cdots}. \quad (1.84)$$

Two special cases of the contraction with the metric appear in the case of a tensor of rank 2, where the contraction leads either to the *trace* if the tensor is symmetric, or to zero if the tensor is antisymmetric,<sup>20</sup> *i.e.*,

$$g^{\mu\nu} Z_{\mu\nu} = g^{\mu\nu} Z_{(\mu\nu)} = Z^\mu_\mu := \text{tr}(Z^{\mu\nu}). \quad g^{\mu\nu} Z_{\mu\nu} = g^{\mu\nu} Z_{[\mu\nu]} = 0. \quad (1.85)$$

The property of raising and lowering the indices is not just a convenient way of doing tensor algebra, but it also highlights that the metric can be used to *map vectors into covectors*. To appreciate this, let us recall the considerations about (1.74) and view the metric as an operator acting on two vectors. Furthermore, let us fix one of these vectors, say  $\mathbf{U}$ , and consider it as an operator needing one additional vector to produce a number, *i.e.*,

$$\mathbf{g}(\mathbf{U}, \cdot) = \mathbf{g}(\cdot, \mathbf{U}) = \tilde{\mathbf{U}}(\cdot), \quad (1.86)$$

where the first equality emphasises the symmetry of the operator in “filling” one of the two slots. We could now have both sides of (1.86) acting on a vector  $\mathbf{V}$  and they will, of course, yield the same number, *i.e.*,

$$\mathbf{g}(\mathbf{U}, \mathbf{V}) = U_\mu V^\mu, \quad \text{and} \quad \tilde{\mathbf{U}}(\mathbf{V}) = U_\mu V^\mu. \quad (1.87)$$

In essence, expression (1.86) states that the metric can be used to map a vector  $\mathbf{U}$  into a covector  $\tilde{\mathbf{U}}$  whose components will be  $U_\mu$ . Similarly, the inverse of the metric  $\mathbf{g}^{-1}$  will induce a mapping of a covector into a vector, thus completing the picture and, once again, stating the *duality* between vectors and covectors. Additional insight about the meaning of the metric tensor is achieved if we rewrite the scalar product as

$$\mathbf{U} \cdot \mathbf{V} = g_{\mu\nu} U^\mu V^\nu = (U^\mu e_\mu) \cdot (V^\nu e_\nu) = U^\mu V^\nu (e_\mu \cdot e_\nu), \quad (1.88)$$

from which we can deduce that

$$g_{\mu\nu} = \mathbf{g}(e_\mu, e_\nu) = e_\mu \cdot e_\nu. \quad (1.89)$$

Put differently, the metric components of a given coordinate system represent the scalar products of its basis vectors. Furthermore, if the basis vectors are such that  $|e_\mu \cdot e_\nu| = \delta_{\mu\nu}$ , then the corresponding basis is said to be an *orthonormal basis* (see also the discussion at the end of Section 1.5.1).

<sup>20</sup>It is a simple exercise to show that the contraction of two tensors of any rank, which involves at least two indices that are symmetric in one tensor and antisymmetric in the other, is zero, *e.g.*,  $T^{\alpha\beta[\gamma\delta]\cdots\epsilon} R_{\mu\nu(\gamma\delta)\cdots\rho} = 0$ .

### 1.3.9 Splitting a tensor through a vector

A useful application of tensor algebra that we will exploit also when describing the kinematic properties of a fluid in Section 3.1.1, is the possibility of splitting a generic tensor of rank 2 in directions parallel and perpendicular to a given vector. Consider a vector field  $\mathbf{U}$ , which has unit norm, *i.e.*,  $\mathbf{U} \cdot \mathbf{U} = -1$ , and define a *projection operator* (or *projection tensor*)  $\mathbf{h}$  orthogonal to  $\mathbf{U}$  as the tensor with components

$$h_{\mu\nu} := g_{\mu\nu} + U_\mu U_\nu, \quad (1.90)$$

which satisfies the following identities

$$h_{\mu\nu} U^\mu = 0, \quad h_\mu^\lambda h_{\lambda\nu} = h_{\mu\nu}, \quad h_\mu^\mu = 3. \quad (1.91)$$

With this operator it is then possible to split, for example, any vector field  $\mathbf{V}$  into a part parallel to  $\mathbf{U}$  and a part orthogonal to  $\mathbf{U}$ , *i.e.*,

$$\mathbf{V}^\mu = AU^\mu + B^\mu, \quad (1.92)$$

where the term  $A = -U_\mu V^\mu$  is the component of  $\mathbf{V}$  along  $\mathbf{U}$ , while the term  $B^\mu = h_\nu^\mu V^\nu$  is the component of  $\mathbf{V}$  in the space orthogonal to  $\mathbf{U}$ . Similarly, it is possible to split a covariant tensor  $\mathbf{W}$  of rank 2 by applying the projection tensor separately on each component of the tensor to obtain

$$W_{\mu\nu} = AU_\mu U_\nu + B_\mu U_\nu + U_\mu C_\nu + Z_{\mu\nu}, \quad (1.93)$$

where

$$A := W_{\mu\nu} U^\mu U^\nu, \quad B_\mu := -h_\mu^\alpha W_{\alpha\beta} U^\beta, \quad (1.94)$$

$$C_\nu := -h_\nu^\alpha W_{\beta\alpha} U^\beta, \quad Z_{\mu\nu} := h_\mu^\alpha h_\nu^\beta W_{\alpha\beta}. \quad (1.95)$$

We can further decompose  $Z_{\mu\nu}$  into its symmetric and skew parts as in expression (1.59), and also note that

$$Z_{(\mu\nu)} = h_{(\mu}^\alpha h_{\nu)}^\beta W_{\alpha\beta} = h_\mu^\alpha h_\nu^\beta W_{(\alpha\beta)} = W_{\langle\mu\nu\rangle} + \frac{1}{3} W_{\alpha\beta} h^{\alpha\beta} h_{\mu\nu}, \quad (1.96)$$

$$Z_{[\mu\nu]} = h_{[\mu}^\alpha h_{\nu]}^\beta W_{\alpha\beta} = h_\mu^\alpha h_\nu^\beta W_{[\alpha\beta]}, \quad (1.97)$$

where  $W_{\langle\mu\nu\rangle}$  in (1.96) is the trace-free, symmetric and spatial part of the tensor  $\mathbf{W}$ , namely:

$$W_{\langle\mu\nu\rangle} := h_\mu^\alpha h_\nu^\kappa W_{(\alpha\kappa)} - \frac{1}{3} W_{\alpha\kappa} h^{\alpha\kappa} h_{\mu\nu}. \quad (1.98)$$

As a result, the decomposition (1.93) can be written in the so-called irreducible form as

$$W_{\mu\nu} = AU_\mu U_\nu + B_\mu U_\nu + U_\mu C_\nu + \frac{1}{3} W_{\alpha\beta} h^{\alpha\beta} h_{\mu\nu} + W_{\langle\mu\nu\rangle} + h_\mu^\alpha h_\nu^\beta W_{[\alpha\beta]}. \quad (1.99)$$

Although we have not yet introduced the mathematical tool necessary to perform derivatives in a way that does not depend on the specific coordinates chosen (*i.e.*, in a covariant manner), we have enough mathematical tools to say something about the simplest four-dimensional spacetime, the flat one.

## 1.4 Flat spacetime: special relativity

Let us consider two *inertial* frames, namely, two reference frames,  $\mathcal{O}$  and  $\mathcal{O}'$ , moving at *constant speed* (or *boost*), relative to each other.<sup>21</sup> Because this speed is purely spatial and hence a three-vector, we will indicate it as the *three-velocity*,  $\vec{V}$ , with components given by<sup>22</sup>

$$V^i := \frac{dx^i}{dt}, \quad (1.100)$$

where, we recall, the Latin index runs from 1 to 3 and  $t$  is the time or zeroth coordinate. Hereafter, we will consider  $\vec{V}$  to be aligned with the  $x$ -axis of the frames  $\mathcal{O}$  and  $\mathcal{O}'$ , so that  $V^i = (V^x, 0, 0) = (V, 0, 0)$ . In Newtonian physics, the correct physical transformations among these two frames are given by the *Galilean transformations*, *i.e.*,

$$x' = x - Vt, \quad (1.101)$$

$$t' = t, \quad (1.102)$$

with respect to which the laws of Newtonian dynamics are invariant.<sup>23</sup> The idea that something was wrong with this description came to Einstein after realising that Maxwell's equations are not invariant under the Galilean transformations (1.101)–(1.102) [see, *e.g.*, Preti *et al.* (2009) for a historical perspective]. Special relativity was developed to solve this inconsistency and resulted in the first theory of spacetime as a whole entity. In spite of its numerous experimental validations, it has a clear axiomatic structure, being based on the following assumptions (axioms):

1. There is no privileged inertial reference frame and the laws of physics are invariant when changing among (inertial) reference frames.
2. The speed of light  $c$  is the maximum speed at which physical bodies and physical perturbations can move or propagate.

Note that, as a consequence of the second assumption, and because the speed of light enters explicitly in the Maxwell equations,  $c$  must be the same in all (inertial) reference frames. The topological and differential structure of special relativity is the same as the Newtonian structure, but with a different definition of distance, namely with a different metric. In Cartesian coordinates, the metric tensor  $g_{\mu\nu}$  of the special-relativistic spacetime, known as the *Minkowski* spacetime, is simply given by

$$g_{\mu\nu} = \eta_{\mu\nu} = \begin{pmatrix} -1 & 0 & 0 & 0 \\ 0 & 1 & 0 & 0 \\ 0 & 0 & 1 & 0 \\ 0 & 0 & 0 & 1 \end{pmatrix} = \eta^{\mu\nu}. \quad (1.103)$$

<sup>21</sup>Equivalently, an inertial frame can be defined as the frame where the Galilean “principle of inertia” holds, *i.e.*, a frame where a body not subject to any force will maintain its status of uniform motion.

<sup>22</sup>Our convention of setting  $c = 1$  is not particularly convenient in this section as it hides the fact that the time coordinate  $t$  should really be read as  $ct$  and where any velocity  $V$  should really be seen as  $V/c$ . We encourage the reader to always bear this in mind.

<sup>23</sup>A physical law is invariant with respect to a given transformation if it maintains the same mathematical form and if the physical constants appearing in it do not change their values.

This metric is also commonly referred to as the *flat-spacetime* metric, due to the fact that the corresponding curvature is zero everywhere (see Section 1.5.5). The line element (1.76) induced by the metric (1.103) is then simply given by

$$ds^2 = g_{\mu\nu} dx^\mu dx^\nu = -dt^2 + dx^2 + dy^2 + dz^2. \quad (1.104)$$

Of course, in the same flat spacetime, a different system of coordinates, *e.g.*, a spherical polar system, will have a metric tensor which is different from the one in (1.103). However, an important property of flat spacetimes (that we will not prove) is that independently of the coordinate system used to cover the manifold, there is always a *global* coordinate transformation that allows one to express the metric in the form (1.103).

We still have to find out what are the correct transformations replacing the Galilean transformations (1.101)–(1.102), and which are at the heart of special relativity. Besides expressing the change from the frame  $\mathcal{O}$  to the frame  $\mathcal{O}'$  and fulfilling the constraint of the invariance of the line element, *i.e.*,  $ds^2 = ds'^2$  (see Section 1.3.8), these transformations must also satisfy another condition. We should ask, in fact, that the interval  $ds^2$  does not change value under the change of reference frame *and* that it maintains the same form, *i.e.*,  $ds'^2 = -dt'^2 + dx'^2 + dy'^2 + dz'^2$ . This second condition is necessary because otherwise there would be a way to distinguish among different inertial frames. Imposing these conditions then leads to the so-called *Lorentz transformations* (Landau and Lifshitz, 1975)

$$x' = W(x - Vt), \quad (1.105)$$

$$t' = W(t - Vx), \quad (1.106)$$

where

$$W := \frac{1}{\sqrt{1 - V^i V_i}} = \frac{1}{\sqrt{1 - V^2}} \quad (1.107)$$

is the *Lorentz factor*,<sup>24</sup> and is constrained to be between 1 (for  $V = 0$ ) and infinity (for  $V \rightarrow 1$ ). Using expression (1.5), we can derive the prototype matrix for the coordinate transformation of vectors in special relativity, namely, the *Lorentz transformation matrix* (*cf.*, Section 1.3.2)

$$\Lambda^{\mu'}_\mu = \begin{pmatrix} W & -WV & 0 & 0 \\ -WV & W & 0 & 0 \\ 0 & 0 & 1 & 0 \\ 0 & 0 & 0 & 1 \end{pmatrix}, \quad (1.108)$$

where we stress once again that in this case a coordinate transformation is equivalent to a change of inertial reference frames. Note that the matrix in (1.108) is symmetric, hence equal to its transpose, and with unit determinant, hence with an inverse that is obtained by simply changing  $V$  into  $-V$ . This inverse can be used in the transformation law (1.45), to find the unit basis vectors of observer  $\mathcal{O}'$  in terms of the unit basis vectors of the original observer  $\mathcal{O}$ .

<sup>24</sup>Note that in most textbooks the Lorentz factor is indicated by “ $\gamma$ ”, but we here adopt a notation that will be useful when discussing the numerical solution of the relativistic-hydrodynamic equations in Chapter 9.

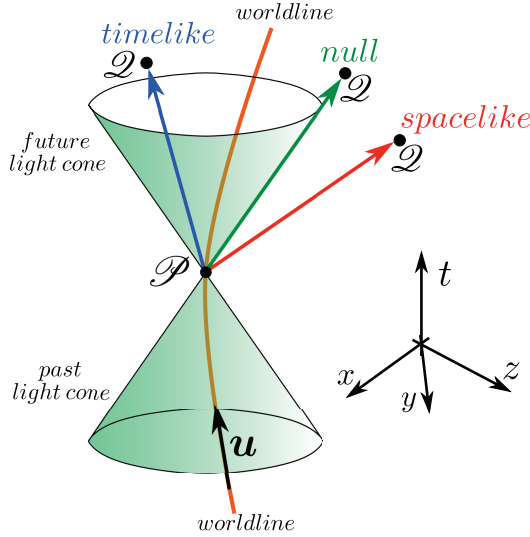


**Fig. 1.1** Schematic diagram of the future and past light cone emanating from the event  $\mathcal{P}$ . Shown with a brown line is the worldline of an observer with four-velocity  $u$ , while different colours represent vectors between the events  $\mathcal{P}$  and  $\mathcal{Q}$ , which are either timelike (i.e.,  $U \cdot U < 0$ ), null (i.e.,  $U \cdot U = 0$ ), or spacelike (i.e.,  $U \cdot U > 0$ ).

All of the important novelties that special relativity introduces with respect to Newtonian dynamics, such as the relative notion of *simultaneity*, the *Lorentz length contraction*, or the *time dilation* (and many more), can be easily derived from the transformations (1.105) and (1.106). For conciseness we will not discuss these properties here, assuming that the reader is either already familiar with them, or that these properties can be easily found in the numerous textbooks on special relativity. We will introduce, however, the distinction between *timelike*, *spacelike* and *null* (or *null-like*) intervals, because of the relevance that these concepts have even in more general spacetimes.

More specifically, two events  $\mathcal{P}$  and  $\mathcal{Q}$  are said to be *timelike separated* if their interval  $ds^2 < 0$ , in the sense that in every reference frame the spatial distance between the two events,  $dl = \sqrt{dx^2 + dy^2 + dz^2}$ , can always be covered by an object moving at a physical velocity  $v < c$  during the time interval  $dt = |t_{\mathcal{P}} - t_{\mathcal{Q}}|$ . When the interval between the two events is  $ds^2 = 0$ , the events are said to be *null separated*, and they can be causally connected only through light rays. Taken any event  $\mathcal{P}(x^i, t)$  in spacetime, light rays then define a *past* or a *future light cone*, depending on whether they converge or emanate from  $\mathcal{P}$ . Finally, the two events  $\mathcal{P}$  and  $\mathcal{Q}$  are said to be *spacelike separated* if their interval  $ds^2 > 0$ , implying that in every reference frame the spatial distance  $dl$  between the two events is always larger than the distance that light can travel during the time interval  $dt = |t_{\mathcal{P}} - t_{\mathcal{Q}}|$ . This is shown in Fig. 1.1, which gives a schematic view of the future and past light cones emanating from the event  $\mathcal{P}$ . Two events are said to be *causally connected* only if they lie in each other's light cone.

We can extend the classification about intervals also to vectors, so that an arbitrary four-vector  $\mathbf{U}$  will be referred to as *timelike*, *null*, or *spacelike*, according to whether  $\mathbf{U} \cdot \mathbf{U} < 0$ ,  $\mathbf{U} \cdot \mathbf{U} = 0$  or  $\mathbf{U} \cdot \mathbf{U} > 0$ , respectively. Examples of such vectors are also shown with different colours in Fig. 1.1.

If two events are timelike separated, then the minimum time interval  $d\tau$  between them is the one reported by the observer that assigns to the events the same spatial coordinates, *i.e.*,  $dx = dy = dz = 0$ , so that  $ds^2 = -dt^2 = -d\tau^2$ . Because of the invariance of the line element, this condition must hold true also in any other difference frame, where it takes the form

$$-d\tau^2 = ds^2 = -dt^2 + dx^2 + dy^2 + dz^2, \quad (1.109)$$

thus implying that

$$d\tau = \frac{dt}{W} < dt. \quad (1.110)$$

Because  $\tau$  is the time of an observer as measured, say, from his comoving clock, it is usually referred to as the *proper time*.

We conclude this section with the definition of one of the most important tensors in hydrodynamics: the *four-velocity* vector  $\mathbf{u}$

$$u^\mu := \frac{dx^\mu}{d\tau}, \quad (1.111)$$

which can be recognised as the tangent to the curve span by the parameter  $\tau$  [*cf.* Eq. (1.15)], *e.g.*, a particle worldline if  $\mathbf{u}$  is the particle four-velocity. Furthermore, because of the definition of proper time  $\tau$  in (1.109), it is easy to conclude that the four-velocity must satisfy the normalisation condition

$$u^\mu u_\mu = -1. \quad (1.112)$$

Expressions (1.112) and (1.111) are general, in the sense that will be valid also in the curved spacetimes we will introduce in the next section, and will be important in the remainder of the book too. The relation between the velocity four-vector  $\mathbf{u}$  and the corresponding velocity three-vector  $\vec{v}$  is easy to establish and is expressed through the components of the four-velocity as<sup>25</sup>

$$u^\mu = W(1, v^i), \quad u_\mu = W(-1, v^i), \quad (1.113)$$

with  $W := (1 - v^i v_i)^{-1/2}$ , so that the three-velocity can also be expressed as<sup>26</sup>

$$v^i = \frac{u^i}{u^0} = v_i. \quad (1.114)$$

Note that in the reference frame in which the particle is at rest,  $u^i = v^i = 0$ , the four-velocity has components  $u^\mu = (u^0, 0, 0, 0) = (1, 0, 0, 0)$ . As a result, in the rest frame of the particle,

<sup>25</sup> Because it will turn out to be useful in Section 3.5, when discussing the Newtonian limit of the relativistic-hydrodynamic equations, we report below the expressions for the four-velocity where the speed of light appears explicitly, *i.e.*,  $u^\mu = (W, Wv^i/c)$  and  $u_\mu = (-W, Wv^i/c)$ . Note also that all the velocities here should be meant as “relative” velocities, *e.g.*, with respect to a static observer with four-velocity  $U^\mu = \delta_0^\mu$ .

<sup>26</sup>See Eq. (7.22) in Section 7.22 for the corresponding general-relativistic expressions.

## 28 A Brief Review of General Relativity

the four-velocity is oriented along the time basis vector, *i.e.*,  $\mathbf{u} = \mathbf{e}_t$ . Assuming now again a reference frame  $\mathcal{O}'$  moving under a boost of velocity  $V$  along the  $x$ -direction relative to the frame  $\mathcal{O}$ , so that the three-velocity of a given particle is  $\vec{v} = d\vec{x}/dt$  in  $\mathcal{O}$  and  $\vec{v}' = d\vec{x}'/dt'$  in  $\mathcal{O}'$ , the three-velocities will obey the *relativistic velocity composition laws*

$$v^x = \frac{v^{x'} + V}{1 + v^{x'}V}, \quad v^y = \frac{Wv^{y'}}{1 + v^{x'}V}, \quad v^z = \frac{Wv^{z'}}{1 + v^{x'}V}. \quad (1.115)$$

It is easy to recognise that expressions (1.115) reduce to the well-known *Galilean velocity composition law*, *i.e.*,  $v^x = v^{x'} + V$ ,  $v^y = v^{y'}$ , etc., for  $V \ll 1$ .

If  $m$  is the *rest mass*<sup>27</sup> of a particle, then we can introduce its *four-momentum* as

$$\mathbf{p} := m\mathbf{u}, \quad (1.116)$$

so that its components are given by

$$p^\mu = mW(1, v^i), \quad p_\mu = mW(-1, v^i), \quad (1.117)$$

satisfying the normalisation condition  $p^\mu p_\mu = -m^2$ . Finally, we define the *relativistic energy* as

$$E := mW, \quad (1.118)$$

which coincides with the zeroth component of the four-momentum, *i.e.*,

$$p^0 = E = -p_0, \quad (1.119)$$

and is such that

$$E^2 = m^2 + p^2, \quad (1.120)$$

where  $p^2 := p^i p_i$ . A Taylor series expansion in the dimensionless parameter  $v := (v^i v_i)^{1/2}$  is very helpful in clarifying how the new definition of energy in Eq. (1.118) differs from the equivalent one in Newtonian physics. It is in fact easy to derive that

$$E = m \left( 1 + \frac{1}{2}v^2 + \frac{3}{8}v^4 + \dots \right) = m + \frac{1}{2}mv^2 + \mathcal{O}(v^4). \quad (1.121)$$

While the second term on the right-hand side of Eq. (1.121) is the well-known Newtonian kinetic energy, the first term is fundamentally novel and absent in Newtonian physics. It represents the so-called *rest energy* of the particle (see also the discussion in Section 3.5)

$$E_0 = m, \quad (1.122)$$

which is nonzero even if the particle has zero velocity (hence the name). The difference  $E - E_0$  can be regarded as the relativistic kinetic energy, and is given by

$$E - E_0 = m(W - 1). \quad (1.123)$$

Note that when  $v = 1$ , both the momentum and the energy of the particle diverge, reflecting the fact that no object with finite mass can move at the speed of light. However, motion at the

<sup>27</sup>As is customary in relativity, we define “rest mass” as the mass of a particle in a reference frame comoving with it. This definition helps in distinguishing it from the more general “mass”, which includes also gravitational contributions (see Problem 9 of Chapter 11 and the discussion in Chapter 12).

speed of light is possible for particles with zero mass, *e.g.*, photons. For such particles, Eq. (1.120) still holds, but reduces to<sup>28</sup>

$$p = E. \quad (1.124)$$

Note that the four-velocity (1.111) cannot be defined for a photon (as for any massless particle) since these move along null worldlines, hence with zero proper time and separation,  $d\tau^2 = -ds^2 = -dx \cdot dx = 0$ . This is equivalent to saying that there is no frame which is comoving with the photon and thus in which the photon is at rest.

## 1.5 Curved spacetimes: general relativity

As discussed in the previous section, special relativity relies on the existence of *inertial frames*, that is, of frames moving at constant velocity and such that they can always be covered with coordinates where proper distances and proper times do not depend on position. While special relativity and its predictions have been validated uncountable times in high-energy laboratory experiments, where gravity does not play an important role, it is clear that some of the axiomatic foundations of special relativity are not compatible with the presence of a gravitational field. We will not discuss here the experimental evidence in support of this statement [*e.g.*, the Eötvös experiment or the Global Positioning System (GPS) of satellites], but it is sufficient to realise that the equations of Newtonian dynamics are not invariant under Lorentz transformations (invariance of the Maxwell equations was a fundamental requirement in the development of special relativity). As a result, the gravitational interactions must necessarily appear through an extension of the laws of physics as proposed by special relativity. As we will show below, this effectively amounts to the extension of the concept of spacetime as a flat manifold over to that of a curved manifold.

Historically, the starting point of the development of the theory of general relativity was represented by the formulation of the so-called *equivalence principle*.<sup>29</sup> In its “strong” formulation, the equivalence principle states that *the laws of physics in a free-falling frame are the same as those in an inertial frame*. Such a formulation comes from the evidence that, at least locally, it is not possible to distinguish through physical experiments and measurements, an inertial frame from one in which gravity has been “removed” by the free fall.<sup>30</sup> In both frames, in fact, the motion of the body does not depend on its mass. The essence of the principle is therefore that gravity prevents the existence of an inertial frame and the way to produce an inertial frame is that of removing gravity by being in free fall. There is also a “weak” formulation of the equivalence principle, which instead makes a complementary statement: *the laws of physics in a non-inertial (accelerated) frame are the same as those in a frame immersed*

<sup>28</sup>In units in which the speed of light is not set to one, expressions (1.118)–(1.124) given above should read:  $p^\mu p_\mu = -m^2 c^2$ ,  $E = mWc^2$ ,  $E^2 = m^2 c^4 + p^2 c^2$ ,  $E = mc^2 + mv^2 + \mathcal{O}(v^4/c^4)$ ,  $E_0 = mc^2$ , and  $p = E/c$ , respectively.

<sup>29</sup>Several formulations of the equivalence principle are actually possible and the experimental validation of this principle through sophisticated experiments in space is a very active field of research (Will, 1992).

<sup>30</sup>Note that, as stated, the equivalence principle is valid if the frame is freely falling with constant acceleration, that is, in a *uniform* gravitational field. Such a gravitational field is of course an idealisation that does not exist in practice. For a gravitational field which is *non-uniform*, as all the ones known, the equivalence principle is, strictly speaking, not valid, since the appearance of tidal effects will allow one to distinguish gravitational effects from those of a freely falling frame.

### 30 A Brief Review of General Relativity

*in a gravitational field.* The essence of this second formulation is instead that a gravitational field has the same manifestation of a non-inertial (*i.e.*, accelerated) reference frame.

Following this logic, the route to the inclusion of gravitational effects starts from the analysis of non-inertial frames and, more specifically, from their important property of being described by a metric that cannot be cast in diagonal form. The equivalence principle can then be used to deduce that the manifestation of a gravitational field can be associated with a metric tensor which is no longer diagonal and cannot be diagonalised. An example may help clarify this point. Let us assume that in a flat spacetime covered with Cartesian coordinates we perform a change of reference frame through a coordinate transformation, from an inertial frame into another frame that rotates rigidly with angular velocity  $\Omega$  about the  $z$ -axis, *i.e.*,

$$x = x' \cos(\Omega t) - y' \sin(\Omega t), \quad y = x' \sin(\Omega t) + y' \cos(\Omega t), \quad (1.125)$$

$$z = z', \quad t = t'. \quad (1.126)$$

The new frame is certainly non-inertial (Coriolis and centrifugal forces appear) and the metric in these new coordinates changes from the diagonal expression in (1.103) to the non-diagonal form expressed by the line element

$$ds'^2 = -[1 - \Omega^2(x'^2 + y'^2)]dt^2 + dx'^2 + dy'^2 + dz'^2 - 2\Omega y'dx'dt + 2\Omega x'dy'dt. \quad (1.127)$$

Hence, a non-inertial frame, which we have just seen could be related to a gravitational field, can also be associated with a non-diagonal metric. This example is useful to conjecture that even a gravitational field can be described as a deviation of the metric from the simple flat-spacetime form (1.103). In this way, gravity should no longer be thought of in terms of a “force”, but, rather, simply as the manifestation of the curvature of spacetime.

Note that this line of argument can be slippery. In the example above, in fact, the spacetime is always flat independently of the reference frame and it is therefore always possible to go from the metric (1.127), back to a metric which is diagonal and with constant coefficients. This is not possible in a genuinely curved spacetime and it is indeed *this* property that distinguishes a curved spacetime, which can always be treated as locally flat, from a globally flat spacetime.<sup>31</sup>

We can now collect all of the considerations made above and, in particular, that of the metric as a tensor describing the gravitational field, to provide a mathematically precise definition of non-flat spacetime. More specifically, we define as a *curved spacetime* a manifold where for any point  $\mathcal{P}$  of the manifold it is possible to define a set of coordinates  $x^\mu$  such that the metric assumes the form

$$g_{\mu\nu}(x^\mu) = \eta_{\mu\nu} + \mathcal{O}((x^\mu)^2). \quad (1.128)$$

In other words, while a curved spacetime can appear as locally flat in the neighbourhood of *any* point, *i.e.*, with  $g_{\mu\nu}(\mathcal{P}) = \eta_{\mu\nu}(\mathcal{P})$ , it cannot be locally flat at *all* points. This conclusion and the weakness of the gravitational field on Earth also explain the success of special relativity in providing a highly accurate description of the physics on the small distance scales of any laboratory experiment.

<sup>31</sup>We recall that when we introduced the concept of manifold in Section 1.3, we stressed that locally, *i.e.*, in a sufficiently small neighbourhood of any point, the manifold is like a Euclidean space and can be approximated by the tangent plane at that point.

Having introduced the concept of curved spacetimes we next have to learn how to perform derivatives in such a spacetime and this is the subject of the next two sections.

### 1.5.1 Lie derivative

A first useful concept when discussing derivatives in curved spacetimes is that of the *Lie derivative* of a vector field with respect to another vector field. In order to introduce this new differential operator, we first need to associate to any vector field  $\mathbf{V}(x^\mu)$  a family of curves  $\mathcal{C}_V$ , called the *congruence* of  $\mathbf{V}$ , having  $\mathbf{V}$  as a tangent vector, *i.e.*,

$$V^\mu(x) = \frac{dx^\mu}{d\lambda}, \quad (1.129)$$

where  $\lambda$  is a parameter varying along the curve. Secondly, we note that the congruence provides a mapping  $\phi_\lambda$  of the manifold into itself. In fact, at any point  $\mathcal{P}$  of the manifold there is one and only one curve of the congruence passing through it. Therefore, the point  $\mathcal{P}$  can be mapped into the point  $\mathcal{Q}$ , by *dragging*  $\mathcal{P}$  along the curve of the congruence to which it belongs, *i.e.*,

$$\mathcal{Q} = \phi_\lambda(\mathcal{P}), \quad (1.130)$$

where  $\mathcal{P} = \mathcal{C}(\lambda_0)$ ,  $\mathcal{Q} = \mathcal{C}(\lambda_0 + \lambda)$ ,  $\mathcal{C}$  being the curve of the congruence through  $\mathcal{P}$  and  $\mathcal{Q}$ . Of course the mapping (1.130) can drag not only points but also a whole curve, which is just a collection of points. Suppose now there is a second vector field  $\mathbf{U}$  with its associated congruence  $\mathcal{C}_U$ . The basic idea of the Lie derivative of a vector field  $\mathbf{U}$  with respect to the vector field  $\mathbf{V}$  is that of comparing the vector  $\mathbf{U}(\mathcal{Q})$  with the vector that is obtained after dragging  $\mathbf{U}(\mathcal{P})$  along the congruence of  $\mathbf{V}$ . Namely the Lie derivative of  $\mathbf{U}$  along  $\mathbf{V}$  is

$$\mathcal{L}_V \mathbf{U} = \lim_{\lambda \rightarrow 0} \frac{\mathbf{U}(\mathcal{Q}) - \phi_\lambda^*(\mathbf{U}(\mathcal{P}))}{\lambda} = \lim_{\lambda \rightarrow 0} \frac{\mathbf{U}(\phi_\lambda(\mathcal{P})) - \phi_\lambda^*(\mathbf{U}(\mathcal{P}))}{\lambda}, \quad (1.131)$$

where  $\phi_\lambda^*(\mathbf{U}(\mathcal{P}))$  is the vector obtained by taking the tangent in  $\mathcal{P}$  to the curve of the congruence  $\mathcal{C}_U$  and dragging it from  $\mathcal{P}$  to  $\mathcal{Q}$ . A schematic view of the two congruences of curves and of the corresponding tangent vectors is shown in Fig. 1.2.

In coordinate components, the dragging (1.130) translates into a standard coordinate transformation:

$$\mathcal{P}(x) \longrightarrow \mathcal{Q}(x') \quad (1.132)$$

$$x^\mu \longrightarrow x^{\mu'} = x^\mu + \lambda V^\mu, \quad (1.133)$$

where  $\lambda V^\mu$  is the change of coordinates along the curve. Since the derivative of  $x^{\mu'}$  is<sup>32</sup>

$$\partial_\nu x^{\mu'} = \delta_\nu^\mu + \lambda \partial_\nu V^\mu, \quad (1.134)$$

it follows that the vector  $U^\mu$  transforms as

$$U^{\mu'}(x') = \Lambda^\mu_\nu U^\nu = U^\mu(x) + \lambda U^\nu(x) \partial_\nu V^\mu. \quad (1.135)$$

<sup>32</sup>Hereafter, we will indicate partial derivatives in a more compact form as  $\partial_\mu := \partial/\partial x^\mu$ .

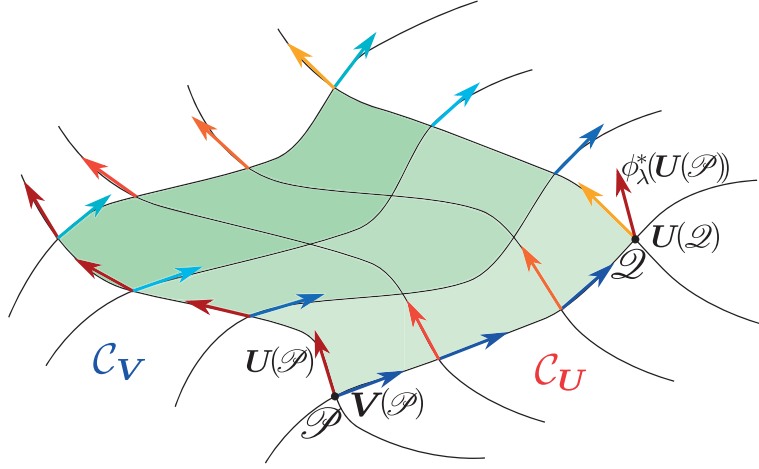


**Fig. 1.2** Schematic diagram of the congruences of curves  $\mathcal{C}_U$  and  $\mathcal{C}_V$ , having respectively the vector fields  $\mathbf{U}$  and  $\mathbf{V}$  as tangents. Note the difference between the vector field  $\mathbf{U}(\mathcal{Q})$  at the event  $\mathcal{Q}$  (dark red) and the dragged equivalent  $\phi_\lambda^*(\mathbf{U}(\mathcal{P}))$  of  $\mathbf{U}(\phi_\lambda(\mathcal{P}))$  at the event  $\mathcal{P}$  (light orange).

On the other hand,  $U^{\mu'}(x')$  on the left-hand side of (1.135) can also be calculated through a Taylor expansion as

$$U^{\mu'}(x') = U^{\mu'}(x) + \lambda V^\nu \partial_\nu U^\mu + \mathcal{O}(\lambda^2), \quad (1.136)$$

and combining the last two equations we obtain

$$U^\mu = U^{\mu'} + \lambda (V^\nu \partial_\nu U^\mu - U^\nu \partial_\nu V^\mu). \quad (1.137)$$

If we now refer back to the definition (1.131), we deduce that the Lie derivative of the vector field in contravariant and covariant coordinate components is given by

$$(\mathcal{L}_V \mathbf{U})^\mu = V^\nu \partial_\nu U^\mu - U^\nu \partial_\nu V^\mu, \quad (1.138)$$

$$(\mathcal{L}_V \mathbf{U})_\mu = V^\nu \partial_\nu U_\mu + U_\nu \partial_\mu V^\nu. \quad (1.139)$$

What we have found for a vector field can be specialised to scalar fields and generalised to any tensor field. For example, in the case of a scalar function  $\phi$  and a generic tensor  $\mathbf{T}$ , we can repeat the arguments above and find

$$\mathcal{L}_\phi \mathbf{V} \mathbf{T} = \phi \mathcal{L}_V \mathbf{T}, \quad (1.140)$$

$$\mathcal{L}_V \phi = V^\nu \partial_\nu \phi_\nu = \frac{d\phi}{d\lambda}, \quad (1.141)$$

where the second identity is simply the derivative of the scalar field along the congruence of  $\mathbf{V}$ , thus highlighting that the Lie derivative can be considered as the generalisation to an arbitrary manifold of the *convective derivative* of a scalar field along a curve [see also Eq. (1.176)].

It is clear from the definition (1.131) that the Lie derivative is a linear operator, that is, given two generic tensors  $\mathbf{Y}$ , and  $\mathbf{Z}$ , the Lie derivative of their linear combination is

$$\mathcal{L}_{\mathbf{V}}(aY^{\alpha\nu} + bZ^{\beta\nu}) = a\mathcal{L}_{\mathbf{V}}Y^{\alpha\nu} + b\mathcal{L}_{\mathbf{V}}Z^{\beta\nu}, \quad (1.142)$$

where  $a$  and  $b$  are two constant real coefficients. Similarly, the standard Leibniz rules for derivatives follow, namely

$$\mathcal{L}_{\mathbf{V}}(Z^{\mu\nu}Y_{\alpha\beta}) = \mathcal{L}_{\mathbf{V}}(Z^{\mu\nu})Y_{\alpha\beta} + Z^{\mu\nu}\mathcal{L}_{\mathbf{V}}Y_{\alpha\beta}. \quad (1.143)$$

Furthermore, the Lie derivative maps a tensor of type  $(m, n)$  into another tensor of the same type, so that, for a generic tensor of rank  $(1, 1)$ , the Lie derivative in coordinate components is

$$\mathcal{L}_{\mathbf{V}}T_{\beta}^{\alpha} = V^{\mu}\partial_{\mu}T_{\beta}^{\alpha} - T_{\beta}^{\mu}\partial_{\mu}V^{\alpha} + T_{\mu}^{\alpha}\partial_{\beta}V^{\mu}. \quad (1.144)$$

Finally, we note that expression (1.138) can also be written in a more compact form as

$$\mathcal{L}_{\mathbf{V}}\mathbf{U} = [\mathbf{V}, \mathbf{U}], \quad (1.145)$$

where we have omitted the component form.  $[\mathbf{V}, \mathbf{U}]$  is referred to as *Lie brackets* and is a basic element of the Lie algebra (de Felice and Clarke, 1990). The Lie brackets can also be used to highlight an important property about the *coordinate basis*  $e_{\mu} = \partial_{\mu}$ . In general, in fact, the Lie brackets of any two basis vectors can be written in terms of the same basis as

$$[e_{\mu}, e_{\nu}] = C_{\mu\nu}^{\lambda}e_{\lambda}, \quad (1.146)$$

where the components  $C_{\mu\nu}^{\lambda}$ , which are not components of a tensor, are named *structure coefficients*. It can be proven [see, *e.g.*, de Felice and Clarke (1990)] that a basis of vectors is a *coordinate basis* if and only if all of its structure coefficients vanish.

Following the definition  $e_{\mu} = \partial_{\mu}$  [*cf.*, Eq. (1.37)], coordinate bases can be constructed for any coordinate system, so that, for example,  $\{e_t, e_x, e_y, e_z\} = \{\partial_t, \partial_x, \partial_y, \partial_z\}$  is the coordinate basis in the case of Cartesian coordinates, and  $\{e_t, e_r, e_{\theta}, e_{\phi}\} = \{\partial_t, \partial_r, \partial_{\theta}, \partial_{\phi}\}$  is the coordinate basis for spherical polar coordinates. Obviously, the components of a coordinate basis are just  $e_{\mu}^{\nu} = \delta_{\mu}^{\nu}$  when computed with respect to their same basis, but not all coordinate bases are orthonormal, that is, not all bases are such that  $e_{\mu} \cdot e_{\nu} \neq \eta_{\mu\nu}$ . Indeed, when using curvilinear coordinates, even in a flat spacetime, coordinate bases are in general *not* orthonormal, but can be easily cast in such a form after a suitable normalisation. Considering for example the coordinate basis  $\{e_t, e_r, e_{\theta}, e_{\phi}\}$ , we can construct an orthonormal basis  $\{e_{\hat{t}}, e_{\hat{r}}, e_{\hat{\theta}}, e_{\hat{\phi}}\}$  as

$$e_{\hat{t}} = e_t, \quad e_{\hat{r}} = e_r, \quad (1.147)$$

$$e_{\hat{\theta}} = \frac{1}{r}e_{\theta}, \quad e_{\hat{\phi}} = \frac{1}{r \sin \theta}e_{\phi}, \quad (1.148)$$

which is now manifestly orthonormal, *i.e.*,  $e_{\hat{\mu}} \cdot e_{\hat{\nu}} = \eta_{\hat{\mu}\hat{\nu}}$ . Furthermore, if the first component of an orthonormal basis is given by a four-velocity, *e.g.*, that of an observer, then the

### 34 A Brief Review of General Relativity

corresponding basis is called a *tetrad*, and it plays a fundamental role in the theory of measure within general relativity, since measurements made in a tetrad are equivalent to those in an inertial frame (de Felice and Clarke, 1990; Carmeli, 2001). The important property of the new orthonormal basis (1.147)–(1.148) is that it is not a coordinate basis, since it cannot be generated by a simple coordinate transformation from a Cartesian coordinate system, or, equivalently, since it has nonzero structure coefficients, *e.g.*,

$$C_{\hat{r}\hat{\theta}}^\theta = [\mathbf{e}_{\hat{r}}, \mathbf{e}_{\hat{\theta}}]^\theta = (\mathcal{L}_{\mathbf{e}_{\hat{r}}} \mathbf{e}_{\hat{\theta}})^\theta = \mathbf{e}_{\hat{r}}^\nu \partial_\nu \mathbf{e}_{\hat{\theta}}^\theta - \mathbf{e}_{\hat{\theta}}^\nu \partial_\nu \mathbf{e}_{\hat{r}}^\theta = \delta_r^\nu \partial_\nu \left( \frac{1}{r} \right) = -\frac{1}{r^2} \neq 0. \quad (1.149)$$

For this reason, a basis like (1.147)–(1.148) is referred to as a *non-coordinate basis*. Hereafter we will indicate an orthonormal basis with a “hat” over the covariant index.

#### 1.5.2 Covariant derivative and Christoffel symbols

When building a new differential operator extending to curved spacetimes the concept of the partial derivative, we know exactly what properties it should have. Namely, when acting on a tensor this new operator should yield another tensor. Partial derivatives do so, but only for coordinate transformations that are linear. However, under more generic conditions, *i.e.*, for nonlinear transformations, the result of a partial derivative does not behave like a tensor. This can be seen by considering, for instance, the transformation

$$V^{\mu'} = \Lambda_{\mu}^{\mu'} V^\mu, \quad (1.19)$$

and then taking its partial derivative with respect to the new coordinates  $\{x^{\mu'}\}$  to obtain

$$\partial_{\beta'} V^{\mu'} = \partial_\mu x^{\mu'} \partial_{\beta'} V^\mu + \left( \partial_\mu \partial_{\beta'} x^{\mu'} \right) V^\mu. \quad (1.150)$$

If the coordinate transformation  $\{x^\mu\} \rightarrow \{x^{\mu'}\}$  is nonlinear, the second term on the right-hand side of Eq. (1.150) will not vanish and the partial derivatives of the vector components will not transform like a tensor. Fortunately, constructing a differential operator with the required properties is not particularly difficult and we can start by considering a vector field  $\mathbf{U}$  and a set of basis vectors  $\{\mathbf{e}_\mu\}$  in which to express its components, *i.e.*,  $\mathbf{U} = U^\mu \mathbf{e}_\mu$  [*cf.*, Eq. (1.36)]. We next take a derivative of such a vector field simply as

$$\partial_\nu \mathbf{U} = \partial_\nu U^\mu \mathbf{e}_\mu + U^\mu \partial_\nu \mathbf{e}_\mu, \quad (1.151)$$

where we can think of the term  $\partial_\nu \mathbf{e}_\mu$  as of a vector written in terms of the same basis vectors  $\{\mathbf{e}_\mu\}$ , *i.e.*,

$$\partial_\nu \mathbf{e}_\mu = \Gamma_{\mu\nu}^\lambda \mathbf{e}_\lambda, \quad (1.152)$$

and where it is easy to realise that the coefficients  $\Gamma_{\mu\nu}^\lambda$  simply vanish in a flat spacetime covered with Cartesian coordinates, since in that case the basis vectors are constants. Note that if the same flat spacetime is covered with a different set of coordinates, *e.g.*, spherical polar,

then the corresponding coefficients will not vanish. As a result, the vanishing of the coefficients  $\Gamma_{\mu\nu}^\lambda$  cannot provide, per se, an indication of the flatness of the spacetime. Combining now Eq. (1.151) with (1.152), we obtain

$$\partial_\nu \mathbf{U} = (\partial_\nu U^\mu + \Gamma_{\nu\lambda}^\mu U^\lambda) \mathbf{e}_\mu = (\nabla_\nu U^\mu) \mathbf{e}_\mu, \quad (1.153)$$

so that the components of the vector field  $\partial_\nu \mathbf{U}$ , namely what is between the brackets in (1.153), define the *covariant derivative* of  $U^\mu$ , i.e.,<sup>33</sup>

$$\nabla_\nu U^\mu := \partial_\nu U^\mu + \Gamma_{\nu\lambda}^\mu U^\lambda. \quad (1.154)$$

The coefficients  $\Gamma_{\nu\lambda}^\mu$  are called *affine connection coefficients* or *Christoffel symbols*, and cannot represent the components of a tensor, since they vanish in a specific coordinate system (the Cartesian system in flat spacetime) while they can be different from zero in another coordinate system. Indeed, it is easy to verify that under a general coordinate transformation the Christoffel symbols change as

$$\Gamma_{\beta'\gamma'}^{\alpha'} = \Lambda_{\alpha}^{\alpha'} \Lambda_{\beta'}^{\beta} \Lambda_{\gamma'}^{\gamma} \Gamma_{\beta\gamma}^{\alpha} + \Lambda_{\alpha}^{\alpha'} \partial_{\beta'} \partial_{\gamma'} x^{\alpha}, \quad (1.155)$$

from which it follows that they behave like a tensor only for linear transformations, such as the Lorentz transformations. On the other hand, the covariant derivative defined by expression (1.154) does define the components of a tensor since they have been built so as to represent the components of the vector field in (1.153). Also note that since a scalar function cannot be decomposed in terms of basis vectors, the covariant derivative of a scalar function  $\phi$  coincides with the standard partial derivative, i.e.,

$$\nabla_\mu \phi = \partial_\mu \phi. \quad (1.156)$$

We can now use the property (1.156) and the definition (1.154) of the covariant derivative of the contravariant vector  $U^\mu$  to obtain the covariant derivative of the covariant vector  $U_\mu$  (see Problem 2)

$$\nabla_\nu U_\mu = \partial_\nu U_\mu - \Gamma_{\mu\nu}^\lambda U_\lambda. \quad (1.157)$$

Similar manipulations allow us to find the covariant derivative of mixed tensors of any type. For instance, for tensors of type  $(1, 1)$  and  $(0, 2)$  we find

$$\nabla_\mu T_\beta^\alpha = \partial_\mu T_\beta^\alpha + \Gamma_{\nu\mu}^\alpha T_\beta^\nu - \Gamma_{\beta\mu}^\nu T_\nu^\alpha, \quad (1.158)$$

$$\nabla_\mu T_{\alpha\beta} = \partial_\mu T_{\alpha\beta} - \Gamma_{\alpha\mu}^\nu T_{\nu\beta} - \Gamma_{\beta\mu}^\nu T_{\alpha\nu}. \quad (1.159)$$

Interestingly, if we now turn back to the transformation law (1.155), we realise that the anti-symmetric part of the Christoffel symbols,  $\Gamma_{[\mu\nu]}^\gamma$ , is a tensor. Furthermore, when a coordinate

<sup>33</sup>Another notation is often used to express the covariant derivative in which the nabla symbol is replaced by a semicolon, while the partial derivative is simply indicated with a comma, i.e.,  $U_{;\nu}^\mu = U_{,\nu}^\mu + \Gamma_{\nu\lambda}^\mu U^\lambda$  [see, e.g., Misner et al. (1973)].

### 36 A Brief Review of General Relativity

basis is considered, this antisymmetric part of the Christoffel symbols is used to define a tensor, called the *torsion* *i.e.*,

$$\mathcal{T}_{\mu\nu}^\alpha := 2\Gamma_{[\mu\nu]}^\alpha. \quad (1.160)$$

In its original formulation, general relativity assumed spacetimes with torsion-free connections. In the Einstein–Cartan theory, on the other hand, an attempt is made to introduce a torsion through the density spin of elementary particles. However, in the following we will consider just torsion-free spacetimes, for which the Christoffel symbols are symmetric in their covariant indices. This implies, for instance, that in the Lie derivative (1.138) we can replace partial derivatives with covariant derivatives, namely

$$(\mathcal{L}_V U)^\mu = V^\nu \nabla_\nu U^\mu - U^\nu \nabla_\nu V^\mu, \quad (1.161)$$

hence obtaining an important relation between the Lie and the covariant derivatives. Since we can write the covariant derivative of a generic vector  $A$  in the two equivalent forms

$$\nabla_\lambda A_\mu = \nabla_\lambda (g_{\mu\nu} A^\nu) = A^\nu \nabla_\lambda g_{\mu\nu} + g_{\mu\nu} \nabla_\lambda A^\nu, \quad (1.162)$$

and since we built the covariant derivative to be a tensor, we can express (1.162) also as

$$\nabla_\lambda A_\mu = g_{\mu\nu} \nabla_\lambda A^\nu. \quad (1.163)$$

From Eqs. (1.162) and (1.163) it follows immediately that

$$\nabla_\lambda g_{\mu\nu} = 0. \quad (1.164)$$

The invariance of the metric with respect to covariant derivatives can be used to compute the Christoffel symbols entirely in terms of the metric coefficients. In fact, a tedious but straightforward calculation of (1.164) through (1.159) allows one to find that

$$\Gamma_{\beta\gamma}^\alpha = \frac{1}{2} g^{\alpha\delta} (\partial_\gamma g_{\delta\beta} + \partial_\beta g_{\delta\gamma} - \partial_\delta g_{\beta\gamma}). \quad (1.165)$$

The form of the covariant derivative of a four-vector (1.157) and the explicit expression for the Christoffel symbols (1.165) allow us to derive an important identity for the four-divergence of a vector, namely

$$\nabla_\mu U^\mu = \frac{\partial_\mu (\sqrt{-g} U^\mu)}{\sqrt{-g}}, \quad (1.166)$$

where again  $g := \det(g_{\mu\nu})$  and where we have exploited the properties of the Christoffel symbols with two contracted indices, *i.e.*,

$$\Gamma_{\mu\nu}^\nu = \frac{1}{2} g^{\nu\delta} \partial_\mu g_{\nu\delta} = \frac{\partial_\mu (\sqrt{-g})}{\sqrt{-g}}. \quad (1.167)$$

Expression (1.166) is also known as the *divergence formula* and is considerably simpler to compute since it involves only partial derivatives.

In the general case, because for each value of the upper index there are 10 different couples of values of the lower indices, there will be 40 different values of  $\Gamma_{\mu\nu}^\gamma$ , which are however not

all independent. The vanishing of the Christoffel symbols also offers the opportunity for an important remark. Suppose in fact that the Christoffel symbols in a coordinate system  $x^\mu$  at a given point  $x_0$  are nonzero, *i.e.*,  $\Gamma_{\lambda\kappa}^\mu(x_0) \neq 0$ . It is a simple exercise to show that if the following coordinate transformation is performed (see Problem 6)

$$x^{\mu'} = x^\mu - x_0^\mu + \frac{1}{2}\Gamma_{\alpha\beta}^\mu(x_0)(x^\alpha - x_0^\alpha)(x^\beta - x_0^\beta), \quad (1.168)$$

then the Christoffel symbols in the new coordinates vanish at the point  $x'_0$ , *i.e.*,  $\Gamma_{\lambda'\kappa'}^\mu(x'_0) = 0$ . This result is not particularly surprising since we have already discussed that a curved spacetime can appear locally flat, and hence with vanishing Christoffel coefficients, in the neighbourhood of *any* point. Hence, the vanishing of the Christoffel symbols simply implies that a locally flat form of the metric has been found at that point. What is important, however, is that in a curved spacetime this property cannot be extended to *all* points, so that a coordinate transformation of the type (1.168) will yield nonzero Christoffel symbols at any other point which is not  $x'_0$ . Once again, this basic property is a manifestation of the equivalence principle and thus of the possibility of having a local frame which is inertial and thus as if free-falling. This possibility cannot be extended to the whole manifold.

### 1.5.3 Symmetries and Killing vector fields

Symmetries play a fundamental role in physics and general relativity is no exception. To appreciate the importance of such symmetries, let us consider a spacetime that has some symmetry responsible for the invariance of the equations under the action of a one-parameter group  $\mathcal{G}$ . In this case, it is possible to associate to  $\mathcal{G}$  a vector field  $\xi$  such that the vector-field lines of  $\xi$  correspond to the trajectories (or *orbits*) of  $\mathcal{G}$ . As an example, if the spacetime is stationary, then  $\mathcal{G} = (\mathbb{R}, +)$  and the equations are invariant under translations along timelike curves, *i.e.*, they are time independent. Similarly, if the spacetime is axisymmetric, then  $\mathcal{G} = \text{SO}(2)$  and the equations are invariant under rotations around some axis, *i.e.*, they are independent of the angle describing rotations around the axis. Killing vector fields highlight the symmetries of the spacetime and, as we will comment further in the following section, they provide a powerful tool when dealing with conserved quantities associated to those symmetries.

Moving now to definitions, a vector field  $\xi$  is said to be a *Killing field* if the metric is Lie dragged along the congruence of  $\xi$ , *i.e.*, if  $\mathcal{L}_\xi g = 0$ . In component form, this translates into the condition

$$\mathcal{L}_\xi g_{\mu\nu} = \xi^\alpha \partial_\alpha g_{\mu\nu} + g_{\mu\alpha} \partial_\nu \xi^\alpha + g_{\alpha\nu} \partial_\mu \xi^\alpha = 0. \quad (1.169)$$

The vector field  $\xi$  is also referred to as the *generator* of the associated symmetry group  $\mathcal{G}$ . Equation (1.169) easily provides a covariant characterisation of the existing symmetries. Indeed, if we replace the partial derivatives  $\partial_\nu \xi^\alpha$  by means of (1.154), and we use the property  $\nabla_\mu g_{\alpha\beta} = 0$  [*cf.* Eq. (1.164)], we then obtain the following *Killing equations*

$$\nabla_{(\mu} \xi_{\nu)} = 0. \quad (1.170)$$

Equations (1.170) are first-order linear differential equations for the Killing vectors and they determine the *isometries* of the spacetime. For instance, assume that we choose a coordinate

### 38 A Brief Review of General Relativity

system such that  $\xi^\mu = (1, 0, 0, 0)$  is a Killing vector. Then, from (1.169) we obtain that the metric is time independent, *i.e.*,

$$\partial_t g_{\mu\nu} = 0. \quad (1.171)$$

In general, when the Killing vector is a coordinate basis vector, then the metric does not depend on the corresponding coordinate, which is also called a *cyclic coordinate*. For instance, in some of the spacetime metrics of physical interest that we consider in Section 1.7, the coordinates  $t$  and  $\phi$  are cyclic. Hence, they admit at least two Killing vectors  $\eta$  and  $\xi$  such that  $\eta^\mu = \delta_t^\mu$  and  $\xi^\mu = \delta_\phi^\mu$ , and whose scalar products yield directly the related components of the metric tensor, *i.e.*,

$$\eta^\mu \eta_\mu = g_{tt}, \quad \xi^\mu \xi_\mu = g_{\phi\phi}, \quad \eta^\mu \xi_\mu = g_{t\phi}. \quad (1.172)$$

Of course, the presence of a Killing vector is a *coordinate-independent* property of the spacetime, while the fact that a coordinate is cyclic is indeed due to a particular choice of the coordinates. However, given a Killing vector, we can always find a suitable system of coordinates such that the Killing vector coincides with one of the coordinate basis vectors. It can also be proven that an  $N$ -dimensional spacetime admits at most  $N(N + 1)/2$  independent Killing vectors, all of which are effectively present only when the curvature of the spacetime is constant<sup>34</sup> (de Felice and Clarke, 1990). This is the case, for instance, of the flat spacetime and of the Friedmann–Robertson–Walker (FRW) spacetime treated in Section 1.7.3.

We close this section by reporting, without a proof, two fundamental relations that hold in a spacetime admitting two Killing vectors  $\eta$  and  $\xi$ , and that will become useful in Section 11.6.1, *i.e.*,

$$\eta^\mu \nabla_\mu \eta_\nu = -\frac{1}{2} \nabla_\nu (\eta^\mu \eta_\mu), \quad \xi^\mu \nabla_\mu \xi_\nu = -\frac{1}{2} \nabla_\nu (\xi^\mu \xi_\mu). \quad (1.173)$$

In addition, if the two Killing vectors  $\eta$  and  $\xi$  commute, namely, if [*cf.* Eq. (1.145)]

$$\mathcal{L}_\eta \xi = \mathcal{L}_\xi \eta = 0, \quad (1.174)$$

then the following relation also holds

$$\eta^\mu \nabla_\mu \xi_\nu = \xi^\mu \nabla_\mu \eta_\nu = -\frac{1}{2} \nabla_\nu (\xi^\mu \eta_\mu). \quad (1.175)$$

#### 1.5.4 Geodesic equation

A concept that will be useful in several other parts of the book and that combines many of the concepts introduced so far is that of a geodesic. Let us therefore consider a vector field  $\mathbf{U}$  on the manifold  $\mathcal{M}$  and a curve  $\mathcal{C}$  with a tangent vector  $\mathbf{V}$ . We can then define the *convective derivative* of  $\mathbf{U}$  along  $\mathbf{V}$  as

<sup>34</sup>A manifold admitting all the possible  $N(N + 1)/2$  Killing vectors is called *maximally symmetric*.

$$\begin{aligned} \left( \frac{D\mathbf{U}}{D\lambda} \right)^\mu &:= (\nabla_{\mathbf{V}} \mathbf{U})^\mu \\ &= V^\nu \nabla_\nu U^\mu = V^\nu \partial_\nu U^\mu + \Gamma_{\alpha\nu}^\mu U^\alpha V^\nu, \end{aligned} \quad (1.176)$$

where  $\lambda$  is the parameter along the curve  $\mathcal{C}$  and where we have used the symbol  $D/D\lambda$  to emphasise that this should be regarded as the extension of the covariant derivative along the direction selected by the vector field  $\mathbf{V}$ . Note that if the vector  $\mathbf{U}$  is just a scalar function  $\phi$ , then the convective derivative (1.176) coincides with a Lie derivative of  $\phi$  along  $\mathbf{V}$ , *i.e.*,

$$\frac{D\phi}{D\lambda} = V^\nu \partial_\nu \phi = \frac{d\phi}{d\lambda} = \mathcal{L}_{\mathbf{V}} \phi. \quad (1.177)$$

The convective derivative allows us to define the very important concept of *parallel transport* and we will say that  $\mathbf{U}$  is *parallel transported* along the curve  $\mathcal{C}$  with tangent vector  $\mathbf{V}$  if

$$\nabla_{\mathbf{V}} \mathbf{U} = 0. \quad (1.178)$$

Stated differently, a vector field is parallel transported if it is moved from  $\mathcal{P}_1$  to  $\mathcal{P}_2$  along  $\mathcal{C}$  and it coincides there with the vector field at  $\mathcal{P}_1$ . The concept of parallel transport naturally leads to the definition of a special curve, namely the one that parallel-transports its own tangent vector, *i.e.*,

$$\nabla_{\mathbf{V}} \mathbf{V} = 0 \iff V^\nu \nabla_\nu V^\mu = 0. \quad (1.179)$$

To better grasp the implication of Eq. (1.179), it is useful to think of flat spacetime, where the line that parallel transports its tangent vector is simply a straight line. In that case, in fact, the tangent vector remains parallel to itself as it is slid along the straight line. Equation (1.179) represents therefore the extension to a generic curved spacetime of the concept of “straight line”, which are then called *geodesic curves* or *geodesics*.

Since  $\mathbf{V}$  is a tangent vector, it can be written as  $V^\mu = dx^\mu/d\lambda$  [cf., Eq. (1.16)], and from Eq. (1.179) we obtain

$$V^\alpha \nabla_\alpha V^\mu = V^\alpha (\partial_\alpha V^\mu + \Gamma_{\alpha\beta}^\mu V^\beta) = \frac{dV^\mu}{d\lambda} + \Gamma_{\alpha\beta}^\mu V^\alpha V^\beta = 0, \quad (1.180)$$

which directly provides the *geodesic equation*, or, equivalently, the equation of a geodesic curve, *i.e.*,

$$\frac{d^2 x^\mu}{d\lambda^2} + \Gamma_{\alpha\beta}^\mu \frac{dx^\alpha}{d\lambda} \frac{dx^\beta}{d\lambda} = 0. \quad (1.181)$$

The parameter  $\lambda$ , which could represent the proper time in a timelike curve, is also referred to as the *affine parameter* of the geodesic, where the name comes from the fact that equation (1.181) is invariant under an affine transformation in which  $\lambda \rightarrow \lambda' = a\lambda + b$ , with  $a$  and  $b$  two constant coefficients.

The geodesic equation (1.181) could also be derived following an alternative approach. Just as a straight line in flat spacetime represents the curve of extremal length, so we can

## 40 A Brief Review of General Relativity

require that the geodesic curve represents the curve of extremal length between two points  $\mathcal{P}_1$  and  $\mathcal{P}_2$  in a generic curved spacetime, *i.e.*,  $\delta\mathcal{S} = 0$ , where (Stephani, 1977)

$$\mathcal{S} := \int_{\mathcal{P}_1}^{\mathcal{P}_2} 2\mathcal{L}d\lambda = \int_{\mathcal{P}_1}^{\mathcal{P}_2} ds = \int_{\mathcal{P}_1}^{\mathcal{P}_2} \sqrt{|g_{\mu\nu}dx^\mu dx^\nu|} = \int_{\mathcal{P}_1}^{\mathcal{P}_2} \sqrt{|g_{\mu\nu}\dot{x}^\mu \dot{x}^\nu|} d\lambda, \quad (1.182)$$

with  $\dot{x}^\mu := dx^\mu/d\lambda$  and with  $\mathcal{L} = \mathcal{L}(x^\mu, \dot{x}^\mu, \lambda)$  being the *Lagrangian*. An important consequence of this different derivation is that there can be only one geodesic curve connecting two different points.

Assume now that the curve  $\mathcal{C}$  is the worldline of a particle of mass  $m$ , and is parameterised by the proper time, so that the tangent vector is actually the four-velocity of the particle. In this case, the resulting geodesic is the curve along which the four-acceleration of the particle vanishes, that is, along which the particle is in free fall. This is quite simple to deduce if we consider a flat spacetime in Cartesian coordinates, where the geodesic equation simply reduces to

$$\frac{d^2x^\mu}{d\lambda^2} = \frac{F^\mu}{m} = 0, \quad (1.183)$$

where  $F^\mu$  are the components of a *four-force*. We have therefore reached two important conclusions. The first one is that geodesics are indeed the trajectories of freely falling particles, that is, of particles not subject to “net forces”. The second result, which will be further discussed in Section 3.1.1, is that the four-acceleration of the particle, which is defined as the convective derivative of the four-velocity, is zero along the geodesics, namely

$$a^\mu = u^\nu \nabla_\nu u^\mu = 0. \quad (1.184)$$

It is also useful to set a connection between the notion of geodesic curves derived in this section, with that of Killing symmetries introduced in the previous one. We can do this by noting that if  $\xi$  is a Killing vector and  $\mathbf{u}$  the tangent vector to a geodesic, then Eq. (1.184) implies that

$$\mathcal{L}_{\mathbf{u}}(u_\mu \xi^\mu) = \nabla_{\mathbf{u}}(u_\mu \xi^\mu) = 0, \quad (1.185)$$

that is, the scalar quantity  $\mathbf{u} \cdot \xi$  is conserved along the geodesic<sup>35</sup>. Indeed geodesic equations are useful to highlight that the presence of Killing vectors is related to physical conservation laws. This property is already expressed in Eq. (1.185), but it becomes clearer if we consider the geodesic equation (1.179) and contract it with a given Killing vector field  $\xi_\nu$ , to find

$$\xi_\nu V^\mu \nabla_\mu V^\nu = V^\mu \nabla_\mu (\xi_\nu V^\nu) - V^\mu V^\nu \nabla_\mu \xi_\nu = 0. \quad (1.186)$$

Since the term  $V^\mu V^\nu \nabla_\mu \xi_\nu = V^\mu V^\nu \nabla_{(\mu} \xi_{\nu)}$  vanishes because of the Killing equations (1.170), we immediately deduce that the quantity  $\xi_\mu V^\mu$  is conserved along the geodesic. This result has a beautiful physical interpretation. Namely, when the metric does not depend on a given coordinate, as is the case for the time and for the azimuthal coordinates in a stationary and axisymmetric spacetime, then a test particle moving with velocity  $V^\mu$  along a geodesic has both  $V_t$  and  $V_\phi$  conserved. Since a particle follows a geodesic only if it does not experience any force other than gravity, it is natural to associate to  $V_t$  and  $V_\phi$  the constants of the motion, *i.e.*, the energy and the angular momentum.

<sup>35</sup>In Section 3.4 we will discuss how to extend this conservation also to the case of fluids [*cf.*, Eq. (3.72)].

### 1.5.5 The Riemann tensor

Although the metric tensor is certainly the most important tensor in general relativity, it alone cannot be used to deduce if a spacetime is flat or curved. We have already mentioned in fact that while a flat spacetime in Cartesian coordinates has a very simple metric tensor with constant coefficients [*cf.*, Eq. (1.103)], the same spacetime will have a more complex metric tensor when the manifold is covered with other coordinates, *e.g.*, spherical polar coordinates. Intuitively, a measure of the curvature will have to depend on how the metric tensor changes across spacetime (*i.e.*, will have to be proportional to derivatives of the metric) and that these changes will have to be quadratic, for a simple analogy with the Gaussian (intrinsic) curvature of surfaces. Hence, this simple line of argument already provides us with the indication that the curvature tensor will have to have the dimensions of the inverse of a length squared and be an object of the type

$$(\text{curvature tensor}) \propto f[(\partial \mathbf{g})^2, \partial^2 \mathbf{g}]. \quad (1.187)$$

A more precise definition can be made after exploiting many of the mathematical tools developed so far and, in particular, the concept of the covariant derivative along a curve. Consider an arbitrary vector field  $\mathbf{A}$  and two congruences of curves  $\mathcal{C}_U$  and  $\mathcal{C}_V$ , having  $\mathbf{U}$  and  $\mathbf{V}$  as tangent vector fields, respectively. Given the value of the vector field at a point  $\mathcal{P}$ , *i.e.*,  $\mathbf{A}(\mathcal{P})$ , we can evaluate it also at another point  $\mathcal{Q}$ , after having dragged it first along the congruence  $\mathcal{C}_U$  and then along the congruence  $\mathcal{C}_V$ . The result of this transport can then be compared at  $\mathcal{Q}$  with the equivalent one obtained after having dragged first along  $\mathcal{C}_V$  and then along  $\mathcal{C}_U$ . In a flat spacetime the two dragged vectors will be identical, but this cannot be the case in a curved spacetime and, indeed, the difference can be used to measure the curvature of the spacetime. This comparison is shown schematically in Fig. 1.3, which reports the two congruences of curves and the corresponding tangent vectors. Note that the vector  $\mathbf{A}(\mathcal{P})$  will have two different images at the new point  $\mathcal{Q}$  and the differences measure the curvature of the manifold.

Straightforward but lengthy calculations involving the definitions of the covariant derivative (1.154) and of the convective derivative (1.176) yield the following expressions for the commutation of the second covariant derivative of a generic four-vector  $\mathbf{A}$  (these are also known as the *Ricci identities*)

$$\nabla_{[\mu} \nabla_{\nu]} A_\alpha = \frac{1}{2} R^\beta_{\alpha\nu\mu} A_\beta, \quad (1.188)$$

$$\nabla_{[\mu} \nabla_{\nu]} A^\alpha = \frac{1}{2} R^\alpha_{\beta\mu\nu} A^\beta, \quad (1.189)$$

where<sup>36</sup>

$$R^\mu_{\nu\alpha\beta} := \partial_\alpha \Gamma^\mu_{\nu\beta} - \partial_\beta \Gamma^\mu_{\nu\alpha} + \Gamma^\mu_{\lambda\alpha} \Gamma^\lambda_{\nu\beta} - \Gamma^\mu_{\lambda\beta} \Gamma^\lambda_{\nu\alpha}, \quad (1.191)$$

is the *Riemann tensor* or *curvature tensor*, which is  $\mathcal{O}((\partial \mathbf{g})^2, \partial^2 \mathbf{g})$  as expected in (1.187).

<sup>36</sup>Expressions (1.188) and (1.189) can also be extended to spacetimes with nonzero torsion,  $\mathcal{T}$ , in which case they assume the form

$$\nabla_{[\mu} \nabla_{\nu]} A_\alpha = \frac{1}{2} R^\beta_{\alpha\nu\mu} A_\beta + \frac{1}{2} \mathcal{T}^\beta_{\mu\nu} \nabla_\beta A_\alpha, \quad \nabla_{[\mu} \nabla_{\nu]} A^\alpha = \frac{1}{2} R^\alpha_{\beta\mu\nu} A^\beta + \frac{1}{2} \mathcal{T}^\beta_{\mu\nu} \nabla_\beta A^\alpha. \quad (1.190)$$

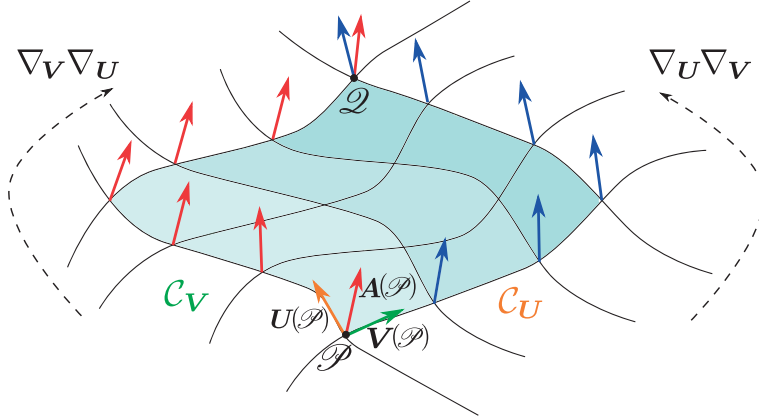


**Fig. 1.3** Schematic diagram of the differences in the vector  $\mathbf{A}$  when transported from point  $\mathcal{P}$  to point  $\mathcal{Q}$  first along the congruence  $\mathcal{C}_U$  and then along  $\mathcal{C}_V$ , or vice versa. The two corresponding vectors are then compared at point  $\mathcal{Q}$  and the differences are a measure of the curvature of the manifold, as expressed by the Riemann tensor.

The route outlined above is not the only one to derive the expression of the Riemann tensor, and a more physically oriented one is also possible, which best highlights the connection between the curvature and the appearance of tidal forces due to a gravitational field. To see this, we first need to compute the second convective derivative of a generic vector field  $\mathbf{A}$  along a geodesic with tangent vector  $\mathbf{u}$ . This is easily done by extending the definition of a first derivative (1.176) to obtain

$$\frac{D^2 A^\mu}{D\lambda^2} = \frac{D}{D\lambda} \left( \frac{DA^\mu}{D\lambda} \right) = u^\nu \nabla_\nu \left( \frac{DA^\mu}{D\lambda} \right) = u^\nu \nabla_\nu (u^\kappa \nabla_\kappa A^\mu). \quad (1.192)$$

Using now the definition of the geodesic equation (1.179), we can expand (1.192) through the standard rules of the covariant derivative, to find

$$\begin{aligned} \frac{D^2 A^\mu}{D\lambda^2} = & \frac{d^2 A^\mu}{d\lambda^2} + A^\nu u^\alpha u^\beta \partial_\beta \Gamma_{\nu\alpha}^\mu + 2\Gamma_{\nu\alpha}^\mu u^\nu \frac{dA^\alpha}{d\lambda} + \\ & + \Gamma_{\nu\beta}^\mu \Gamma_{\alpha\rho}^\beta A^\alpha u^\rho u^\nu - \Gamma_{\nu\alpha}^\mu \Gamma_{\gamma\rho}^\nu A^\alpha u^\gamma u^\rho, \end{aligned} \quad (1.193)$$

where we have introduced

$$\frac{dA^\mu}{d\lambda} := u^\nu \partial_\nu A^\mu. \quad (1.194)$$

We next consider two point-like particles which are close to each other and freely falling, that is, following two geodesics having the same parameter  $\lambda$  (e.g., the proper time). In a flat spacetime, they will move along straight lines and hence their separation, which could be measured through the displacement vector  $\xi^\mu$  between the two geodesics, is obviously constant (parallel lines do not intersect in flat spacetime). However, this is not the case if the spacetime is curved and we can measure the variations in the displacement vector by simply looking at the two geodesics, which will have the form

$$\frac{d^2x^\mu}{d\lambda^2} + \Gamma_{\alpha\beta}^\mu \frac{dx^\alpha}{d\lambda} \frac{dx^\beta}{d\lambda} = 0, \quad (1.195)$$

$$\frac{d^2(x^\mu + \xi^\mu)}{d\lambda^2} + \Gamma_{\alpha\beta}^\mu(x + \xi) \frac{d(x^\alpha + \xi^\mu)}{d\lambda} \frac{d(x^\beta + \xi^\mu)}{d\lambda} = 0. \quad (1.196)$$

Taking now the difference between expressions (1.195) and (1.196), and expanding to first order in the displacement so that  $\Gamma_{\alpha\beta}^\mu(x + \xi) = \Gamma_{\alpha\beta}^\mu(x) + \xi^\nu \partial_\nu \Gamma_{\alpha\beta}^\mu + \mathcal{O}(\xi^2)$ , we obtain

$$\frac{d^2\xi^\mu}{d\lambda^2} = -2\Gamma_{\nu\beta}^\mu u^\nu \frac{d\xi^\beta}{d\lambda} - u^\nu u^\alpha \xi^\beta \partial_\beta \Gamma_{\nu\alpha}^\mu + \mathcal{O}(\xi^2). \quad (1.197)$$

Expression (1.197) can then be used to compute the second convective derivative of the displacement vector  $\xi^\mu$ , following the functional form obtained in Eq. (1.193) for the generic four-vector  $A^\mu$ , to finally obtain

$$\frac{D^2\xi^\mu}{D\lambda^2} = R_{\nu\alpha\beta}^\mu u^\nu u^\alpha \xi^\beta, \quad (1.198)$$

where the (1, 3) rank tensor  $R_{\nu\alpha\beta}^\mu$  in (1.198) is the same Riemann tensor defined by (1.191).

Equation (1.198), which for obvious reasons is called the *geodesic-deviation* equation, provides a very important result as it states that neighbouring geodesics change their separation in an accelerated manner if the Riemann tensor is nonzero.<sup>37</sup> As a result, a typical manifestation of a gravitational field, namely, the appearance of tidal forces, is now simply seen as a geometrical effect due to a nonzero curvature of the spacetime. The Riemann tensor, therefore, serves as a probe not only of the curvature of the spacetime, but also of the presence of a gravitational field, as the two are effectively indistinguishable. This is shown schematically in Fig. 1.4, which reports the separation four-vector  $\xi$  between the geodesics of two free-falling particles with tangent vector  $u$ . The left panel refers to a flat spacetime, *i.e.*, where  $R_{\nu\alpha\beta}^\mu = 0$ , in which case the separation does not change and the geodesics are parallel straight lines. The right panel refers instead to a curved spacetime, *i.e.*, where  $R_{\nu\alpha\beta}^\mu \neq 0$ , such as the one produced by a selfgravitating body, in which case the separation vector undergoes an acceleration as it moves in the gravitational field [*cf.* Eq. (1.198)].

We have already discussed that if the spacetime is flat, then there is a coordinate system in which the Christoffel symbols vanish *globally* in the spacetime. Hence, from Eq. (1.191) the Riemann tensor also vanishes, and, being a tensor, it will vanish in any other coordinate system. The opposite is also true, namely, if the Riemann tensor is *globally* zero in the spacetime, then from Eq. (1.198) it follows that the separation between any two geodesics will not change and hence that the spacetime is flat. Note however that if the Christoffel symbols vanish only *locally*, this does not necessarily imply that the Riemann tensor will be zero at that point, since the latter depends also on the derivatives of the Christoffel symbols. Hence, it is always possible to disentangle the effects of a true gravitational field from those produced by a non-inertial reference frame (*i.e.*, the one that leads to a locally flat spacetime), simply by checking whether the Riemann tensor there is zero or not.

When written as a tensor of type (0, 4), the Riemann tensor shows the following important algebraic symmetry properties:

<sup>37</sup>If the Riemann tensor is itself dynamical, *i.e.*, is a function of time, the equation of geodesic deviation (1.198) can be used to determine the effects of weak gravitational radiation on a free-falling test particles [see, *e.g.*, Misner et al. (1973)].

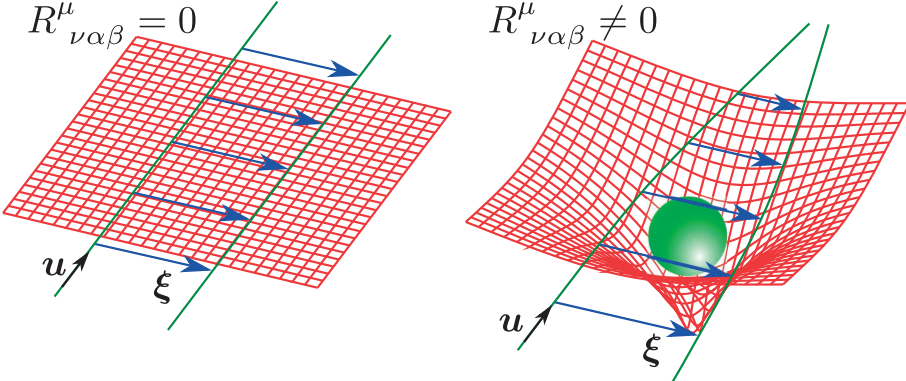


**Fig. 1.4** Schematic diagram of the deviation of two geodesics as measured through the separation four-vector  $\xi$  between the geodesics of two free-falling particles with tangent vector  $u$ . The left panel refers to a flat spacetime, i.e.,  $R_{\nu\alpha\beta}^{\mu} = 0$ , when the separation does not change and the geodesics are parallel straight lines. The right panel refers instead to a curved spacetime such as the one produced by a selfgravitating body, and in this case the separation vector changes along the geodesics [cf. Eq. (1.198)], which are no longer parallel.

- It is symmetric under exchange of the first and the second pair of indices

$$R_{\alpha\beta\gamma\delta} = R_{\gamma\delta\alpha\beta}. \quad (1.199)$$

- It is antisymmetric in the first pair of indices

$$R_{\alpha\beta\gamma\delta} = -R_{\beta\alpha\gamma\delta}. \quad (1.200)$$

- It is antisymmetric in the second pair of indices

$$R_{\alpha\beta\gamma\delta} = -R_{\alpha\beta\delta\gamma}. \quad (1.201)$$

- It is antisymmetric in the last three indices (these are also known as the first *Bianchi identities*)

$$R_{\alpha[\beta\gamma\delta]} = 2(R_{\alpha\beta\gamma\delta} + R_{\alpha\delta\beta\gamma} + R_{\alpha\gamma\delta\beta}) = 0. \quad (1.202)$$

Because of all of these symmetries, the independent components of the Riemann tensor in an  $N$ -dimensional manifold are not  $N^4$ , but only  $N^2(N^2 - 1)/12$ ; as a result, in a standard four-dimensional spacetime, only 20 of the 256 components of the Riemann tensor are independent. Contractions of the indices of the Riemann tensor are obviously possible, but there is only one which is non-trivial and generates a symmetric tensor of rank 2, called the *Ricci tensor*, namely

$$R_{\mu\nu} := g^{\alpha\beta} R_{\alpha\mu\beta\nu} = R_{\mu\beta\nu}^{\beta} = \partial_{\lambda}\Gamma_{\mu\nu}^{\lambda} - \partial_{\nu}\Gamma_{\mu\lambda}^{\lambda} + \Gamma_{\mu\nu}^{\lambda}\Gamma_{\lambda\beta}^{\beta} - \Gamma_{\mu\beta}^{\lambda}\Gamma_{\nu\lambda}^{\beta}, \quad (1.203)$$

where the last equality comes after resorting to definition (1.191). We can further contract the Ricci tensor to obtain its trace, which is also called the *curvature scalar* or *Ricci scalar*, and is given by

$$R := g^{\mu\nu} R_{\mu\nu} = R^\mu_\mu. \quad (1.204)$$

Since it is constructed directly from the Riemann tensor, also the Ricci tensor and the Ricci scalar have the dimensions of the inverse of a length squared. Note also that the Ricci scalar should not be confused with another scalar that can be obtained after the contraction of two Riemann tensors, *i.e.*,

$$\mathcal{C} := R^{\mu\nu\lambda\kappa} R_{\mu\nu\lambda\kappa}. \quad (1.205)$$

Such a scalar, which now has the dimensions of the inverse of a length to the fourth power, is usually referred to as the *curvature invariant* and is very useful in providing a sensitive and pointwise measure of the curvature of the spacetime, thus probing the existence of physical singularities (see Section 1.7.1). To fix ideas and gain some more intuition on the properties of the Riemann tensor, let us compute its components for the simplest curved space, *i.e.*, that confined on the surface of a two-sphere  $\mathcal{S}$ . If  $R_s$  is the radius of such a two-sphere, the corresponding line element will be given by

$$ds^2 = R_s^2 (d\theta^2 + \sin^2 \theta d\phi^2), \quad (1.206)$$

so that the metric has components

$$g_{ij} = \begin{pmatrix} R_s^2 & 0 \\ 0 & R_s^2 \sin^2 \theta \end{pmatrix}, \quad g^{ij} = \begin{pmatrix} R_s^{-2} & 0 \\ 0 & (R_s^2 \sin^2 \theta)^{-1} \end{pmatrix},$$

and the only nonzero Christoffel symbols are

$$\Gamma_{\theta\theta}^r = -\sin \theta \cos \theta, \quad \Gamma_{r\theta}^\theta = \cot \theta. \quad (1.207)$$

It is straightforward to calculate that the only nonzero components of the Riemann tensor on the two-sphere are

$$R_{\theta\theta r}^r = -\frac{1}{R_s^2} g_{\theta\theta} = -\sin^2 \theta, \quad R_{\theta\theta r}^r = \frac{1}{R_s^2} g_{rr} = 1, \quad (1.208)$$

while the Ricci scalar is simply  $R = 1/R_s^2$ . The importance of expressions (1.208) is in highlighting that the curvature tensor is simply proportional to the inverse square of the local *curvature radius* and thus, independently of the dimensions of the manifold, it is possible to associate the curvature tensor at a given point to the inverse square of the radius of the sphere osculating at that point. For any two-sphere with constant radius  $R_s$ , expressions (1.208) are easily extended to

$$R_{\mu\beta\nu}^\alpha = \frac{1}{R_s^2} (\delta_\beta^\alpha g_{\mu\nu} - \delta_\nu^\alpha g_{\mu\beta}). \quad (1.209)$$

In addition to the symmetry properties above, the Riemann tensor also obeys a set of differential relations (these are also known as the second *Bianchi identities*)

$$\nabla_{[\mu} R_{\nu\alpha]\beta\gamma} = 0, \quad (1.210)$$

## 46 A Brief Review of General Relativity

$$\nabla_{[\mu} R_{\nu\alpha\beta]\gamma} = 0. \quad (1.211)$$

Contracting the Bianchi identity (1.210) twice, we obtain an important result that will be used often hereafter, namely, the *contracted Bianchi identities*

$$\nabla_\mu \left( R^{\mu\nu} - \frac{1}{2} g^{\mu\nu} R \right) = \nabla_\mu G^{\mu\nu} = 0, \quad (1.212)$$

where we have introduced the divergence-free, second-rank symmetric tensor

$$G^{\mu\nu} := R^{\mu\nu} - \frac{1}{2} g^{\mu\nu} R, \quad (1.213)$$

which is also known as the *Einstein tensor*.

As a final remark we note that the Ricci tensor has  $N(N+1)/2$  independent components and hence the Riemann tensor has a number of independent components larger than those of the Ricci tensor on a manifold with dimension  $N > 3$ . Furthermore, the Riemann tensor also admits a decomposition in terms of another tensor, called the *Weyl tensor*, which is defined as

$$C^\mu_{\nu\alpha\beta} := R^\mu_{\nu\alpha\beta} - \frac{2}{N-2} \left( \delta^\mu_{[\alpha} R_{\beta]\nu} + g_{\nu[\beta} R^\mu_{\alpha]} \right) + \frac{2R}{(N-1)(N-2)} \delta^\mu_{[\alpha} g_{\beta]\nu}. \quad (1.214)$$

The Weyl tensor vanishes in any  $N \leq 3$  dimensional manifold, is trace-free and has the same symmetry properties as the Riemann tensor. In analogy with the Riemann tensor, the Weyl tensor expresses the tidal forces experienced by a body moving in a gravitational field (*i.e.*, in a curved spacetime). Differently from the curvature tensor, however, the Weyl tensor provides information on how the shape of the body is distorted by the tidal force and not on how the volume of the body changes. The Weyl tensor is particularly useful in the calculation of the gravitational radiation produced in numerical-relativity simulations via the Newman–Penrose formalism, which provides a convenient representation for a number of radiation-related quantities in terms of spin-weighted scalars (Newman and Penrose, 1962).

## 1.6 Einstein equations

In Newtonian gravity the equation relating the gravitational potential  $\phi$  to the mass density  $\rho$  representing the source of the field, is the *Poisson equation*

$$\nabla^2 \phi = 4\pi G \rho, \quad (1.215)$$

which is a second-order partial differential equation in the unknown potential  $\phi$  and where  $\nabla^2$  is the *Laplacian operator* (or Laplacian). Since the main idea of general relativity is that the gravitational field is a geometrical entity, it follows that the metric coefficients  $g_{\mu\nu}$  should be regarded as the new dynamical variables of the gravitational field. By analogy with the Newtonian limit, we expect that the new equations of the gravitational field, namely the *Einstein equations*, will contain derivatives of the metric tensor no higher than the second. Moreover,

the new equations must retain the same form no matter which coordinate system one chooses. Therefore, they must involve tensors, and the most natural tensor that generalises the mass density on the right-hand side of (1.215) is the *energy-momentum* (or *stress-energy*) *tensor*  $T^{\mu\nu}$  that will be extensively discussed in Chapter 2. This line of argument suggests therefore the following form for the Einstein equations

$$G_{\mu\nu} = \kappa T_{\mu\nu}, \quad (1.216)$$

where  $\kappa$  is a proportionality constant, while the tensor  $G_{\mu\nu}$  should have the following dependence on the metric  $g$  and its derivatives

$$G_{\mu\nu} = G_{\mu\nu}(g, \partial g, \partial^2 g), \quad (1.217)$$

in analogy with the corresponding Newtonian expression. Moreover, since the source of the field will have to satisfy some conservation laws of the type  $\nabla_\mu T^{\mu\nu} = 0$ , we also expect from (1.216) that  $\nabla_\mu G^{\mu\nu} = 0$ . Although within a purely geometrical context, we have already built a tensor with all of these properties, namely, the *Einstein tensor*, whose definition is given by Eq. (1.213).

Since the covariant derivative of the metric is identically zero [*cf.*, Eq. (1.164)], the addition to the Einstein tensor of a term proportional to the metric tensor does not change its four-divergence, *i.e.*,  $\nabla_\mu(G^{\mu\nu} + \Lambda g^{\mu\nu}) = 0$ , where  $\Lambda$  is a constant. Historically, this constant was introduced by Einstein to obtain a static cosmological solution and was named, for this reason, the *cosmological constant*. More recently, the cosmological constant has seen renewed interest for the possibility of leading to an accelerated cosmological expansion, as astronomical observations indeed suggest (Riess *et al.*, 1998; Perlmutter *et al.*, 1999). We will not discuss here the cosmological implications of a nonzero  $\Lambda$ , nor the difficulty of calculating its value within the standard model of particle physics, but the interested reader can find an exhaustive discussion in the monograph of Ellis *et al.* (2012). Given the minuteness of the cosmological constant on the scales of astrophysical compact objects, it is a very good approximation to consider  $\Lambda = 0$  for all of the considerations we will make in this book, although we will continue to report it below for completeness.

Collecting all terms, we can write the Einstein equations as

$$G_{\mu\nu} + \Lambda g_{\mu\nu} = R_{\mu\nu} - \frac{1}{2}R g_{\mu\nu} + \Lambda g_{\mu\nu} = \frac{8\pi G}{c^4} T_{\mu\nu}, \quad (1.218)$$

where we have temporarily reintroduced the factors  $G$  and  $c$ , while the factor  $8\pi$  is required by the weak-field limit of Newtonian gravity (Misner *et al.*, 1973).

A more rigorous derivation of the Einstein equations is of course possible and involves the definition of a suitable action of the gravitational field (*i.e.*, the *Einstein–Hilbert action*) and then the application of the principle of least action [see, *e.g.*, de Felice and Clarke (1990) and also the discussion in Section 3.10]. However, the choice of a “good” action for the gravitational field requires a heuristic line of argument similar to the one outlined above, and it will not be discussed here.

Taking now the trace of the Einstein equations (1.218), we find that

$$R = -8\pi \left( T - \frac{\Lambda}{2\pi} \right), \quad (1.219)$$

## 48 A Brief Review of General Relativity

so that the Einstein equations can also be written as

$$R_{\mu\nu} = 8\pi \left( T_{\mu\nu} - \frac{1}{2} T g_{\mu\nu} + \frac{1}{4\pi} \Lambda g_{\mu\nu} \right), \quad (1.220)$$

which helps in highlighting the tight connection (indeed the strict equivalence!) between the geometry of the spacetime on the left-hand side of (1.220), with its mass-energy content on the right-hand side.<sup>38</sup> This is one of the fundamental aspects of general relativity.

From a more mathematical point of view, the Einstein equations consist of 10 second-order, nonlinear, partial differential equations in the metric terms  $g_{\mu\nu}$ . The independent ones, however, are just six, due to the constraint  $\nabla_\mu G^{\mu\nu} = 0$ . This result reflects the fact that there are exactly four degrees of freedom among the 10 components of the metric tensor. These have nothing to do with gravity and are just due to an arbitrary, but unavoidable, choice of the coordinates used to express the metric, *i.e.*, the *gauge freedom*. The fact that the Einstein equations are nonlinear, while making their analytical solution a daunting task, also implies that there is no superposition principle for (strong) gravitational fields. In other words, the sum of two solutions of the Einstein equations is not a solution. Even in a vacuum spacetime, where  $T_{\mu\nu} = 0$  and the Einstein equations become simply  $R_{\mu\nu} = 0$ , this elementary appearance hides 10 nonlinear partial differential equations. The only trivial solution to the Einstein equations is the one relative to flat spacetime, in which case  $T_{\mu\nu} = 0$  and all of the components of the Riemann and Einstein tensor are identically zero.

A fundamental difference between the Einstein equations and those of other field theories, such as, for instance, electromagnetism, is that they also contain information about the equations of motion for the sources of the curvature. This is evident when taking the four-divergence of the Einstein equations (1.218), which ultimately states that the motion of matter cannot be determined arbitrarily but has to follow the conservation laws  $\nabla_\mu T^{\mu\nu} = 0$ . In electromagnetism, on the other hand, the Maxwell equations do not prescribe the motion of the charges, whose dynamics must be solved separately using the Lorentz force.

Of course, much more could be said about the Einstein equations, although this would defy the idea of a brief review of general relativity which embodies the spirit of this chapter. The Einstein equations will be the focus of much of Chapter 7, which is dedicated to the different formulations that have been proposed over the years as best suited for a numerical solution.

## 1.7 Spacetimes of astrophysical relevance

Besides leading to one of the most fascinating sets of equations in mathematical physics, the nonlinearity of the Einstein equations also has the important consequence that only very few exact solutions are known that are astrophysically relevant and these are usually obtained under restricted conditions and special symmetries, either in time, in space or in spacetime. In this section we will discuss a few of the most celebrated exact solutions of the Einstein equations, two of which refer to black holes and one to a cosmological model. In the first

<sup>38</sup>Although it is expected that only a quantum description of gravity, which is yet to be found, will be able to provide a convincing explanation of the origin of the cosmological constant, it can already be considered now as an additional contribution to the energy-momentum tensor in the form  $T_{\mu\nu}^\Lambda := -(\Lambda/8\pi)g_{\mu\nu}$ .

case we will neglect the cosmological constant as this is not expected to provide an important contribution on the length-scales of astrophysical black holes, while we will retain it when discussing cosmological solutions. As for the rest of the chapter, our treatment will be merely that of a brief review, referring the interested reader to the more advanced textbooks of Misner *et al.* (1973), or of Poisson (2004).

### 1.7.1 Non-rotating black holes: the Schwarzschild solution

The easiest among the exact solutions of the Einstein equations was derived by Schwarzschild just a few months after the derivation of the Einstein equations (Schwarzschild, 1916). It provides their solution in a spacetime which is spherically symmetric, static<sup>39</sup> and in vacuum. It is universally known as the *Schwarzschild solution* and its relevance is emphasised in an important theorem by G. Birkhoff<sup>40</sup> who proved in 1923 that the Schwarzschild solution is the *only* solution of the Einstein equations in a spherically symmetric spacetime in vacuum. As a result, the Schwarzschild solution is also the solution in the exterior regions of a spherically symmetric relativistic star, quite independently of whether it is static or oscillating radially (Birkhoff, 1923).

In spherical polar coordinates,  $(t, r, \theta, \phi)$ , the line element in *Schwarzschild coordinates* is given by

$$ds^2 = - \left(1 - \frac{2M}{r}\right) dt^2 + \left(1 - \frac{2M}{r}\right)^{-1} dr^2 + r^2(d\theta^2 + \sin^2 \theta d\phi^2), \quad (1.221)$$

where  $M$  is the total mass-energy, *i.e.*, the gravitational mass, of the system. Note that because the spacetime described by the metric (1.221) is curved, the corresponding spherical coordinates are not the ordinary spherical coordinates in flat spacetime. As an example, the proper length of the circumference centred at  $r = 0$  and on the  $\theta = \pi/2$  (equatorial) plane is  $C_{\text{circ}}(r) := \oint \sqrt{g_{\phi\phi}} d\phi$ , while the proper radial distance between two points on two radial shells at coordinate radii  $r_1$  and  $r_2$  is

$$\int_{r_1}^{r_2} \sqrt{g_{rr}} dr = \int_{r_1}^{r_2} (1 - 2M/r)^{-1/2} dr > r_2 - r_1, \quad (1.222)$$

thus showing that the increase in the proper radial distance is larger than the increase in the coordinate distance. Moreover, if two events have the same spatial coordinates, namely, if  $dr = d\theta = d\phi = 0$ , the coordinate time interval  $dt$  between the two events is different from the corresponding proper time interval  $d\tau$  and their ratio is

$$\frac{dt}{d\tau} = \frac{1}{(1 - 2M/r)^{1/2}} \geq 1. \quad (1.223)$$

In other words, at finite distances from the origin, the coordinate time runs slower than the proper time. Suppose now there are two clocks placed at  $r_1$  and  $r_2$ , with  $r_1 < r_2$ , each of

<sup>39</sup>We recall that a *static* solution of the Einstein equations is one in which the metric components are neither dependent on time nor are affected by a time reversal, *i.e.*, by a coordinate transformation  $t \rightarrow -t$ .

<sup>40</sup>Recent historical investigations by Voje Johansen and Ravndal (2006) have revealed that this theorem was actually discovered and published two years earlier by an unknown Norwegian physicist, J. T. Jebsen (Jebsen, 1921). Regrettably, to avoid confusion we will continue to refer to it as “Birkhoff’s theorem”.

## 50 A Brief Review of General Relativity

them sending two light signals that reach an observer at infinity with the same separation  $dt$ , namely

$$d\tau_1 = (1 - 2M/r_1)^{1/2} dt, \quad d\tau_2 = (1 - 2M/r_2)^{1/2} dt. \quad (1.224)$$

The ratio between the two proper times is then

$$\frac{d\tau_2}{d\tau_1} = \frac{(1 - 2M/r_2)^{1/2}}{(1 - 2M/r_1)^{1/2}}, \quad (1.225)$$

which, translated into frequency measurements, implies that

$$\frac{\nu_1}{\nu_2} = \frac{(1 - 2M/r_2)^{1/2}}{(1 - 2M/r_1)^{1/2}} \approx 1 - \frac{M}{r_2} + \frac{M}{r_1} > 1. \quad (1.226)$$

This is the well-known *gravitational redshift*, by means of which a photon decreases its frequency as it moves out of the gravitational potential well. As photons are characterised by having  $ds^2 = 0$ , for radially moving photons we obtain  $dr/dt = \pm(1 - 2M/r)$ , where the  $+$  sign is for outgoing photons, while the  $-$  sign is for ingoing ones. Hence, unlike in flat spacetime, where  $dr/dt = \pm 1$ , the worldlines of photons in the  $(t, r)$  plane are no longer straight lines. In addition, from the first equality in Eq. (1.226) it is easy to realise that when  $r_1 \rightarrow 2M$ , then  $\nu_1/\nu_2 \rightarrow \infty$ , or, equivalently, that  $\nu_2 \rightarrow 0$ . This result reflects the fact that the surface at the *Schwarzschild radius*,  $r = 2M$ , represents a special but regular surface in the Schwarzschild solution, such that photons cannot propagate outwards. This surface, which is mathematically defined as the one at which the metric function  $g_{tt} = 0$ , separates the spacetime into two regions which are causally disconnected and is for this reason referred to as the *event horizon*. Furthermore, since light can only be absorbed by this surface, the Schwarzschild solution is also known as the *Schwarzschild black-hole* solution.

It should be noted that although the metric (1.221) is singular at  $r = 2M$ , this singularity is just in the choice of coordinates used to cover the spacetime and is not a physical one. Recognising this fact has profoundly changed our understanding of the Schwarzschild solution. Support for this conclusion can be obtained by computing the curvature invariant (1.205) for the Schwarzschild spacetime, *i.e.*,  $\mathcal{C} = 48M^2/r^6$ , which is finite at  $r = 2M$  and diverges only for  $r \rightarrow 0$ , which represents the physical *singularity* of the solution. Indeed, coordinates that are better suited to reflect the properties of the spacetime near the horizon, *e.g.*, the Kruskal coordinates, or the Eddington–Finkelstein coordinates, can remove the coordinate singularity at  $r = 2M$  [see, *e.g.*, de Felice and Clarke (1990) or d’Inverno (1992)]. A more detailed discussion of the properties of the event horizon can be found in a number of textbooks, *e.g.*, Misner *et al.* (1973), or Poisson (2004).

The motion of test particles of rest mass  $m$  in the Schwarzschild spacetime can be deduced after solving the geodesic equations (1.181). We will not provide here the details of the derivation, which however can be found in many textbooks, *e.g.*, d’Inverno (1992). In practice, one of the simplest routes is to use a variational approach in terms of the Lagrangian introduced in (1.182) and adopt the proper time  $\tau$  as affine parameter

$$2L = \mathcal{L}^2 = g_{\mu\nu}\dot{x}^\mu\dot{x}^\nu = - \left(1 - \frac{2M}{r}\right)\dot{t}^2 + \left(1 - \frac{2M}{r}\right)^{-1}\dot{r}^2 + r^2(\dot{\theta}^2 + \sin^2\theta\dot{\phi}^2), \quad (1.227)$$

from which we derive the following *Euler–Lagrange equations*

$$\frac{d}{d\tau} \left[ \left( 1 - \frac{2M}{r} \right) \frac{dt}{d\tau} \right] = 0, \quad (1.228)$$

$$\frac{d}{d\tau} \left[ \left( 1 - \frac{2M}{r} \right)^{-1} \frac{dr}{d\tau} \right] = r \left[ \left( \frac{d\theta}{d\tau} \right)^2 + \sin^2 \theta \left( \frac{d\phi}{d\tau} \right)^2 \right], \quad (1.229)$$

$$\frac{d}{d\tau} \left( r^2 \frac{d\theta}{d\tau} \right) = r^2 \sin \theta \cos \theta \left( \frac{d\phi}{d\tau} \right)^2, \quad (1.230)$$

$$\frac{d}{d\tau} \left( r^2 \sin^2 \theta \frac{d\phi}{d\tau} \right) = 0. \quad (1.231)$$

Equations (1.228) and (1.231) essentially state that  $t$  and  $\phi$  are ignorable coordinates and allow us to define two *constants of motion*, namely,  $\tilde{E} := E/m$  as the specific energy of the particle, and  $\tilde{\ell} := p_\phi$  as the specific azimuthal angular momentum. Furthermore, because of spherical symmetry, we can consider any initial orbital plane as the equatorial plane, *i.e.*, set  $\theta = \pi/2$  and  $d\theta/d\tau = 0$  initially. It then follows from Eq. (1.230) that  $d^2\theta/d\tau^2$  also vanishes and thus  $\theta$  will remain constant, as expected for planar motion.<sup>41</sup> As a result, the geodesic equations for a massive particle in the Schwarzschild spacetime reduce to<sup>42</sup>

$$\frac{dt}{d\tau} = \left( 1 - \frac{2M}{r} \right)^{-1} \tilde{E}, \quad (1.232)$$

$$\frac{dr}{d\tau} = \left[ \tilde{E}^2 - \left( 1 - \frac{2M}{r} \right) \left( 1 + \frac{\tilde{\ell}^2}{r^2} \right) \right]^{1/2}, \quad (1.233)$$

$$\frac{d\theta}{d\tau} = 0, \quad (1.234)$$

$$\frac{d\phi}{d\tau} = \frac{\tilde{\ell}}{r^2}. \quad (1.235)$$

The analysis of the radial equation (1.233) is particularly illuminating, as it highlights the difference with respect to the Newtonian case. We can in fact rewrite (1.233) simply as

$$\left( \frac{dr}{d\tau} \right)^2 = \tilde{E}^2 - V^2(r), \quad (1.236)$$

where we have defined the *effective potential*  $V$  as

$$V(r) := \left( 1 - \frac{2M}{r} \right)^{1/2} \left( 1 + \frac{\tilde{\ell}^2}{r^2} \right)^{1/2}, \quad (1.237)$$

which reduces to the Newtonian effective potential at large distances,<sup>43</sup> namely

<sup>41</sup>Indeed, if the orbit was not planar it would precess around a direction, breaking the assumption of spherical symmetry.

<sup>42</sup>Equation (1.233) can be easily derived after realising that  $2L = -m^2$  and using Eqs. (1.232) and (1.235).

<sup>43</sup>Note that the constant 1 in the potential does not disturb the solution, having no effect on the equations of motion.

## 52 A Brief Review of General Relativity

$$V(r) \approx \left(1 - \frac{M}{r}\right) \left(1 + \frac{\tilde{\ell}^2}{2r^2}\right) = 1 - \frac{M}{r} + \frac{\tilde{\ell}^2}{2r^2} + \mathcal{O}\left(\frac{1}{r^3}\right) := V_N. \quad (1.238)$$

The radial equation (1.233) is also useful to classify the different types of orbits which are possible and which will essentially depend on the number of maxima and minima the effective potential will have for a given value of the specific angular momentum (if  $\tilde{\ell} = 0$  the orbit is simply radial and will connect any radial point with the origin). Let us assume, for the time being, that the specific angular momentum is such that it yields an effective potential with a local maximum with  $V > 1$ , and local minimum, just as illustrated in the left panel of Fig. 1.5, which refers to  $\tilde{\ell}/M = 4.1$ . In this case, using the specific energy  $\tilde{E}$  as a decreasing parameter, the orbits can be:

- *capture orbit*: no intersection is possible between the effective potential and a constant-energy level. No matter how large the angular momentum, there is always a value of the energy that makes the particle reach the origin. This is to be contrasted with the Newtonian case, where the effective potential diverges as  $r \rightarrow 0$ , and thus no matter how small (but nonzero) the angular momentum, a particle in a Newtonian orbit will never reach the origin (*i.e.*, the Newtonian potential has a zero *capture cross-section*).
- *circular, unstable orbit*: this is located at the local maximum of the effective potential,  $r_{\text{circ},u}$ , where  $dr/d\tau = 0$ , and is such that any perturbation will move the particle either to smaller or to larger radii.
- *hyperbolic, unbound orbits*: these correspond to orbits of particles with energies at spatial infinity larger than one (*i.e.*, with positive velocity), that move towards the origin till reaching a minimum radial position at which  $dr/d\tau = 0$ , *i.e.*, a *turning point*, from where they return to infinity.
- *parabolic, bound orbit*: this corresponds to an orbit of a particle with energy at spatial infinity equal to one (*i.e.*, at rest), that moves towards the origin till reaching a *turning point*,  $r_b$ . For  $\tilde{\ell}/M = 4$ , the turning point coincides with the unstable circular orbit  $r_{\text{circ},u}$  and is located at  $4 M$  (see below).
- “*elliptic*”, *bound orbits*: these correspond to orbits with energies at spatial infinity less than one (*i.e.*, bound particles) that have two turning points at  $r_1$  and  $r_2$ .<sup>44</sup>
- *circular, stable orbit*: this is located at the local minimum of the effective potential,  $r_{\text{circ},s}$ , where  $dr/d\tau = 0$ , and is such that any small perturbation away from the stable orbit will move the particle back to it.

The values of the specific angular momentum for which the effective potential shows both local minima and maxima, *i.e.*, for which  $\partial_r V(r) = 0$ , and thus for which circular orbits exist, is given by

$$\tilde{\ell}^2 = \frac{Mr^2}{r - 3M}. \quad (1.239)$$

To ensure that the right-hand side is positive, such extremal points exist only for  $\tilde{\ell}/M \geq 2\sqrt{3}$ . Furthermore, for  $\tilde{\ell}_{\text{ms}}/M = 2\sqrt{3} \simeq 3.46$ , the stable and unstable circular orbits coincide,

<sup>44</sup>Note that these orbits are not closed because of the advance of the periastron, another general-relativistic effect of the motion in a gravitational field (Misner *et al.*, 1973). Hence, the defining property of these orbits is that of having two turning points and not that of being closed ellipses.

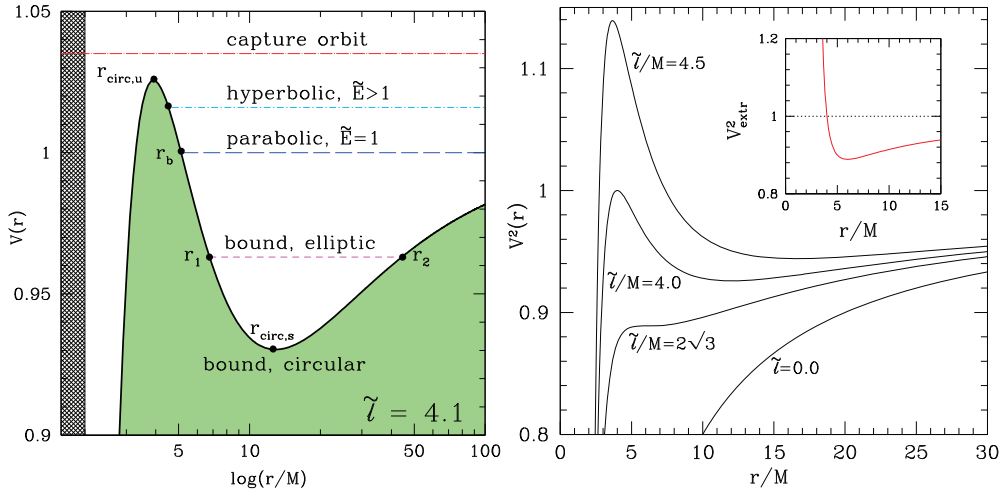


**Fig. 1.5** *Left panel:* Effective potential  $V(r)$  for a value  $\tilde{\ell}/M = 4.1$  of the specific angular momentum. Shown are the different types of orbits allowed: capture, marginally bound, marginally stable, elliptic and circular, as determined by the different values of the energy above the green dashed area. Shown as black shading is the region inside the horizon, with the radial scale set to be logarithmic. *Right panel:* Effective potential  $V(r)$  of the Schwarzschild metric for some values of the angular momentum  $\tilde{\ell}$ . The inset shows the value of the effective potential at the local extrema and it should be noted that the radial scale is linear.

leading to an *inflection point* at the radius  $r_{\text{ms}} = 6M$ , which is also called the *marginally stable radius*. The corresponding orbit is also known as the *innermost stable circular orbit* or *ISCO* and because this represents the smallest possible radius for a stable circular orbit, it is often taken to mark the inner edge of an accretion disc around a black hole (see also Section 11.8). A marginally stable orbit can be defined also for a massless particle, *e.g.*, a photon, in which case it is given by  $r_{\text{ph}} = 3M$ , and is usually referred to as the “*light ring*”.

The variation of the effective potential with the specific angular momentum is illustrated in the right panel of Fig. 1.5, while the inset shows the values of the effective potential at the local extrema (which coincide with the energies of the unstable circular orbits), and is given by

$$V_{\text{extr}}^2(r) = \frac{4M^2(r/2M - 1)^2}{r(r - 3M)}. \quad (1.240)$$

Setting  $V_{\text{extr}}(r) = 1$  will mark the position of the *marginally bound orbit*,  $r_{\text{mb}} = 4M$ , namely, the smallest radius for a bound, circular but unstable orbit. A particle leaving spatial infinity at rest (*i.e.*, with  $\tilde{E} = 1$ ), will move on a parabolic orbit down to  $r = r_{\text{mb}}$ , where it can remain on a circular orbit but in unstable equilibrium.

In summary, unstable circular orbits exist for

$$3M = r_{\text{ph}} \leq r < r_{\text{ms}} = 6M, \quad \iff \quad 2\sqrt{3} \leq \tilde{\ell}/M < \infty, \quad (1.241)$$

while stable circular orbits exist for

$$6M = r_{\text{ms}} \leq r < \infty, \quad \iff \quad 2\sqrt{3} \leq \tilde{\ell}/M < \infty. \quad (1.242)$$

Using Eq. (1.240), it is not difficult to estimate that the energy corresponding to the ISCO is  $\tilde{E}_{\text{ms}} = \sqrt{8/9} \simeq 0.943$ , and this apparently simple result calls for an important comment. Consider, in fact, a particle progressively moving from a circular orbit to a neighbouring one and losing part of its energy in the transition (*e.g.*, a fluid element in an accretion disc). The total energy that can be lost when inspiralling from spatial infinity down to the ISCO is  $\Delta E = (1 - \tilde{E}_{\text{ms}}) \simeq 0.057$ , implying an efficiency in the conversion of the binding energy of  $\simeq 6\%$ . When comparing this with the efficiency of nuclear fission (*i.e.*,  $\sim 0.1\%$ ) or of nuclear fusion (*i.e.*,  $\sim 0.4\%$ ), it becomes clear that accretion onto a black hole represents one of the most efficient processes to extract energy. As we will comment in the following section, this efficiency can be further increased in the case of a rotating black hole.

### 1.7.2 Rotating black holes: the Kerr solution

In 1963, that is, almost 50 years after Schwarzschild's work, Kerr found a stationary solution to the Einstein equations in vacuum, which describes the spacetime of a black hole of total mass  $M$  and angular momentum  $J$  (Kerr, 1963). This solution, which is also known as the *Kerr black-hole* solution and was later proven to be unique (Robinson, 1975), reduces to the Schwarzschild solution in the limit of zero angular momentum. Since it includes the contributions of rotation, the Kerr black hole is not spherically symmetric, but axisymmetric about the direction of the angular momentum vector of the black hole; furthermore, it is no longer a static solution, but a stationary one.<sup>45</sup> Due to the ubiquitous presence of rotation in astrophysical systems, this solution is considered to be the most realistic for studying any physical process that takes place in the vicinity of a black hole. Unfortunately, no analogue to *Birkhoff's theorem* exists for the Kerr solution, which is unique in vacuum, but whose exterior in non-vacuum spacetimes depends on the properties of the matter source, *e.g.*, mass and angular momentum distribution in the case of a relativistic star.

We will not show here the details of the derivation of the Kerr metric, which is rather involved in its original form, and for which we recommend reading Carmeli (2001) and de Felice and Clarke (1990). However, we will present an abridged derivation which is not often found in textbooks. The starting point consists in exploiting the symmetries of the spacetime and choose a coordinate system  $(t, x^1, x^2, \phi)$ , where  $x^1$  and  $x^2$  are generic coordinates, and write the line element as

$$ds^2 = P dt^2 + 2Q dt d\phi + \varrho d\phi^2 + e^{2\mu} [(dx^1)^2 + (dx^2)^2], \quad (1.243)$$

where  $P, Q, \varrho$  and  $\mu$  are functions of  $x^1$  and  $x^2$  alone. The corresponding Einstein equations reduce to a single equation, known as the *Ernst equation* (Ernst, 1968), given by

$$(\xi \bar{\xi} - 1) \nabla^\alpha (\nabla_\alpha \xi) = 2\bar{\xi} (\nabla_\alpha \xi) (\nabla^\alpha \xi), \quad (1.244)$$

where  $\xi$  is a complex function of  $x^1$  and  $x^2$ , while  $\bar{\xi}$  denotes complex conjugation. Spheroidal coordinates  $(t, \chi, \zeta, \phi)$  represent a convenient set of coordinates for the solution of the Ernst equation and these are related to the usual cylindrical coordinates  $(t, R, z, \phi)$  as

<sup>45</sup>The metric components are still independent of time but the solutions are affected by a time reversal, *i.e.*, by a coordinate transformation  $t \rightarrow -t$ .

$$R = \sqrt{(M^2 - a^2)(\chi^2 - 1)(1 - \zeta^2)}, \quad (1.245)$$

$$z = \sqrt{M^2 - a^2}\chi\zeta, \quad (1.246)$$

where, for the time being,  $a$  is just a constant coefficient. Adopting such coordinates and a considerable amount of algebra, it is possible to express the Kerr metric as

$$ds^2 = -P^{-1} \left[ (M^2 - a^2)e^{2\gamma'} \left( \frac{d\chi^2}{\chi^2 - 1} + \frac{d\zeta^2}{1 - \zeta^2} \right) + R^2 d\phi^2 \right] + P(dt - hd\phi)^2, \quad (1.247)$$

where

$$r := \sqrt{M^2 - a^2}\chi + M, \quad \theta := \cos^{-1}\zeta, \quad (1.248)$$

$$P := - \left( 1 - \frac{2Mr}{\Sigma^2} \right), \quad \Sigma^2 := r^2 + a^2 \cos^2\theta, \quad (1.249)$$

$$h := - \frac{2Mar \sin^2\theta}{\Sigma^2 - 2Mr}, \quad \gamma' := \ln \left[ (M^2 - a^2)^{-1/2} (\Sigma^2 - 2Mr)^{1/2} \right]. \quad (1.250)$$

Denoting as  $J$  the angular momentum associated with the spacetime (1.247), leads to a straightforward interpretation of the parameter  $a$  as the angular momentum per unit mass,  $a := J/M$ . Since the parameter  $a$  in geometrised units has the dimensions of a length, it is useful to introduce the so-called dimensionless *spin parameter*,  $a_* := J/M^2 = a/M$ , which is bound to be  $-1 \leq a_* \leq 1$ .

The most common form in which the Kerr metric is used (although not necessarily the most convenient) adopts the so-called *Boyer–Lindquist coordinates*  $(t, r, \theta, \phi)$ , where the spherical coordinates  $r$  and  $\theta$  are related to the spheroidal coordinates  $\chi$  and  $\zeta$  through Eqs. (1.248). In these coordinates the Kerr metric reads

$$ds^2 = - \left( 1 - \frac{2Mr}{\Sigma^2} \right) dt^2 - \frac{4Mar}{\Sigma^2} \sin^2\theta dt d\phi + \frac{\Sigma^2}{\Delta} dr^2 + \Sigma^2 d\theta^2 + \frac{A}{\Sigma^2} \sin^2\theta d\phi^2, \quad (1.251)$$

where

$$\Delta := r^2 - 2Mr + a^2, \quad A := (r^2 + a^2)^2 - a^2 \Delta \sin^2\theta, \quad (1.252)$$

and where (1.251) now reduces to the Schwarzschild metric (1.221) when  $a = 0$ .

Unlike in the Schwarzschild solution, where the surfaces of infinite redshift and of the event horizon coincide, the Kerr solution has two surfaces of infinite redshift, again obtained by imposing  $g_{tt} = 0$ , and are given by the condition

$$r_{s,\pm} = M \pm \sqrt{M^2 - a^2 \cos^2\theta}. \quad (1.253)$$

The event horizons, on the other hand, can be determined from the divergence of the metric function  $g_{rr}$  and thus from setting  $\Delta = 0$ , which then yields the two surfaces

$$r_{eh,\pm} = M \pm \sqrt{M^2 - a^2}, \quad (1.254)$$

where the  $\pm$  sign denotes the outer (+) and inner (−) event horizon, respectively. Note that in the Schwarzschild limit  $r_{eh,-} = 0$ , and  $r_{eh,+} = 2M$ , as expected (see also Fig. 1.6).

## 56 A Brief Review of General Relativity

The region between  $r_{s,+}$ , which is also called the *ergosphere*, and  $r_{eh,+}$  is also referred to as the *ergoregion*, since no static observers (*i.e.*, observers seen as non-rotating from infinity) can exist and the whole spacetime is dragged into synchronous *corotation* by the black hole. This purely relativistic effect, which is also known as *frame dragging*, does not apply only to the ergoregion (where the corotation is unavoidable even for photons), but extends to the whole spacetime, although it becomes progressively weaker far from the black hole. As a result, an observer with zero angular momentum at infinity, or Zero Angular Momentum Observer (ZAMO) in the definition of Bardeen *et al.* (1972), will not move radially towards the black hole, but will be set into rotation as seen from infinity. The corresponding four-velocity in Boyer–Lindquist coordinates is given by

$$u^\mu = \left( \frac{A}{\Delta \Sigma^2} \right)^{1/2} (1, 0, 0, \omega), \quad (1.255)$$

where

$$\omega := \frac{2Mar}{A} \propto \frac{a}{r^3} \quad (1.256)$$

is the ZAMO angular velocity, which falls off as  $1/r^3$  away from the black hole and is obviously zero for a non-rotating (Schwarzschild) black hole. The importance of the ergosphere lies in that it can host physical processes that extract rotational energy from the black hole, as first shown by Penrose (1969) using test particles, and subsequently by Blandford and Znajek (1977), who addressed the question of whether the rotational energy of an isolated black hole can be extracted efficiently by a magnetic field fed by an accretion disc.

As for the Schwarzschild solution, neither the infinite-redshift surface nor the event-horizon surface represent physical singularities of the Kerr spacetime, and the calculation of the curvature invariant tensor can easily prove this. Also for the Kerr solution, in fact, the coordinate singularity at the event horizon can be removed through a coordinate transformation that can be defined in terms of the one-forms

$$dt' = dt + \frac{2Mr}{\Delta} dr, \quad d\phi' = d\phi + \frac{a}{\Delta} dr, \quad (1.257)$$

or, more explicitly, through the coordinate transformation

$$t' = t + 2M \int \frac{r dr}{r^2 - 2Mr + a^2}, \quad \phi' = \phi + a \int \frac{dr}{r^2 - 2Mr + a^2}. \quad (1.258)$$

In the new coordinates  $(t', r, \theta, \phi')$ , called the *Kerr–Schild coordinates*, the line element reads

$$\begin{aligned} ds^2 = & -(1 - B) dt'^2 - 2Ba \sin^2 \theta dt' d\phi' + 2Bdt' dr - 2a(1 + B) \sin^2 \theta dr d\phi' \\ & + (1 + B) dr^2 + \Sigma^2 d\theta^2 + \frac{A \sin^2 \theta}{\Sigma^2} d\phi'^2, \end{aligned} \quad (1.259)$$

where  $B := 2Mr/\Sigma^2$ , and where the spatial part of the metric is no longer diagonal. The only physical singularity of the Kerr spacetime, independently of whether it is written in the form (1.251) or (1.259), is at  $\Sigma^2 = r^2 + a^2 \cos^2 \theta = 0$ , namely, at  $r = 0$  and  $\theta = \pi/2$ . Note,

however, that this result can be misleading if we incorrectly interpret the Boyer–Lindquist coordinates as standard spherical coordinates, since it seems to imply that it is possible to reach the point  $r = 0$  without crossing any singularity through trajectories at  $\theta \neq \pi/2$ . This incorrect conclusion is avoided if a better set of coordinates is used near the origin and, in particular, after performing an additional coordinate transformation to the Kerr–Schild Cartesian coordinates  $(t, x, y, z)$ , defined as

$$x := \sqrt{r^2 + a^2} \sin \theta \cos \left[ \phi' - \arctan \left( \frac{a}{r} \right) \right], \quad (1.260)$$

$$y := \sqrt{r^2 + a^2} \sin \theta \sin \left[ \phi' - \arctan \left( \frac{a}{r} \right) \right], \quad (1.261)$$

$$z := r \cos \theta, \quad (1.262)$$

$$t := t', \quad (1.263)$$

such that the condition  $\Sigma^2 = 0$  is expressed as

$$\frac{x^2 + y^2}{r^2 + a^2} + \frac{z^2}{r^2} = 1. \quad (1.264)$$

Equation (1.264) shows that all the points in the  $z = 0$  plane (*i.e.*, the equatorial plane) with  $x^2 + y^2 \leq a^2$  have  $r = 0$ , implying that the physical singularity is actually represented by a ring in these coordinates. This ring singularity reduces to the  $r = 0$  Schwarzschild singularity in the limit of vanishing black-hole spin. Because of its relevance in numerical calculations, we report below the form of the line element in the Kerr–Schild Cartesian coordinates

$$ds^2 = -dt^2 + dx^2 + dy^2 + dz^2 + \frac{2Mr^3}{r^4 + a^2z^2} \left[ dt + \frac{r(x\,dx + y\,dy)}{a^2 + r^2} + \frac{a(y\,dx - x\,dy)}{a^2 + r^2} + \frac{z}{r}dz \right]^2. \quad (1.265)$$

As done for the Schwarzschild spacetime, it is possible to study the geodesic motion of test particles in the Kerr metric to gain insight into its properties. The particle motion in this case is far more complicated and, in addition to the energy and angular momentum, a new constant of motion appears, *i.e.*, the *Carter constant* (Carter, 1968). Furthermore, the motion is planar only in the case of equatorial orbits, whose qualitative properties remain similar to the ones already encountered for a Schwarzschild spacetime. The geodesic motion within the Kerr metric has been extensively investigated in the literature and we refer the interested reader to Bardeen *et al.* (1972) or de Felice (1980) for a more extended discussion. We here limit ourselves to pointing out that for each value of the black-hole spin  $a/M$ , marginally bound orbits can be found at

$$r_{mb,\pm} = 2M \mp a + 2M^{1/2} (M \mp a)^{1/2}, \quad (1.266)$$

where the  $\pm$  sign in  $r_{mb,\pm}$  refers to particles which are either in prograde (*i.e.*, corotating) or retrograde (*i.e.*, counter-rotating) orbits, respectively. Similarly, for each value of the black-hole spin  $a/M$ , stable circular orbits exist from spatial infinity down to the *marginally stable orbit*, or ISCO, given by

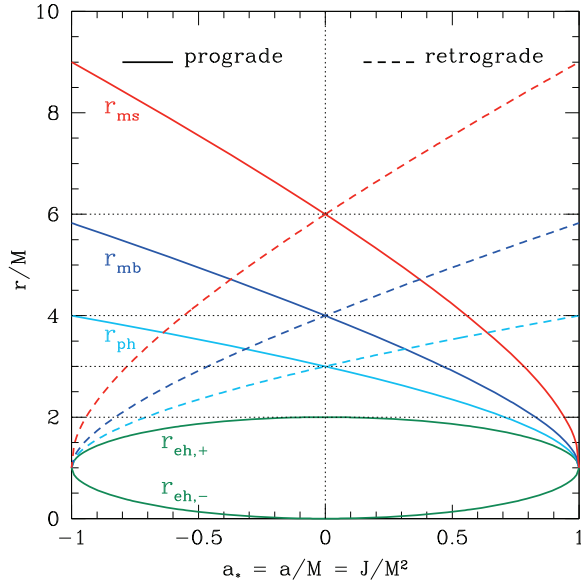


**Fig. 1.6** Relevant radii for equatorial orbits in a Kerr spacetime. Shown as a function of the dimensionless spin of the black hole,  $a/M$ , are respectively: the radii of the outer and inner event horizons  $r_{\text{eh},\pm}$ , the radii of the marginally stable photon orbits  $r_{\text{ph}}$ , the radii of the marginally bound photon orbits  $r_{\text{mb}}$ , and the radii of the marginally stable orbits  $r_{\text{ms}}$ . Continuous and dashed lines help distinguish between prograde and retrograde orbits, respectively.

$$r_{\text{ms},\pm} = r_{\text{ISCO}} = M \left[ 3 + Z_2 \mp \sqrt{(3 - Z_1)(3 + Z_1 + 2Z_2)} \right], \quad (1.267)$$

where

$$Z_1 := 1 + (1 - a^2)^{1/3} \left[ (1 + a)^{1/3} + (1 - a)^{1/3} \right], \quad (1.268)$$

$$Z_2 := \sqrt{3a^2 + Z_1^2}. \quad (1.269)$$

Figure 1.6 shows a useful summary of the relevant radii for equatorial orbits in a Kerr spacetime. Reported as a function of the dimensionless spin of the black hole,  $a/M$ , are respectively: the radii of the outer and inner event horizons  $r_{\text{eh},\pm}$ , the radii of the marginally stable photon orbits  $r_{\text{ph}}$ , the radii of the marginally bound photon orbits  $r_{\text{mb}}$ , and the radii of the marginally stable orbits  $r_{\text{ms}}$ . Continuous and dashed lines help distinguish between prograde and retrograde orbits, respectively. Note that for  $a/M = 1$ , i.e., for an *extremal Kerr black hole*, a number of radii for prograde orbits tend to coincide, i.e.,  $r_{\text{ms}} = r_{\text{ph}} = r_{\text{eh},+} = M$  (obviously, the same happens for retrograde orbits around black holes with  $a/M = -1$ ). Since stable circular orbits exist down to the horizon, they can have there extremely small energies and as small as  $\hat{E}_{\text{ms}} = 0.577$ . As a result, a particle accreting from spatial infinity down to the ISCO of an extremal Kerr black hole will have lost an amount of energy

$E = (1 - \tilde{E}_{\text{ms}}) = 0.43$ , implying a conversion of  $\sim 43\%$  of the binding energy. This enormous efficiency explains why models of accretion discs onto Kerr black holes represent the best candidates to explain the vast amounts of energy radiated in *active galactic nuclei* (AGN) (see also Sections 11.8 and 11.9).

### 1.7.3 The Friedmann–Robertson–Walker metric

Since the Einstein equations are meant to describe any gravitational interaction, they will apply not only to compact objects such as the black holes discussed in the previous section, but also to the universe as a whole. The starting point in deriving the equations describing the dynamics of the universe must obviously be set by cosmological observations. These provide evidence that, at least on sufficiently large scales, the universe is isotropic and thus, by virtue of the *cosmological principle* homogeneous.<sup>46</sup> In addition, the observations indicate that the universe is expanding (Hubble, 1926) and actually in an accelerated manner (Riess et al., 1998; Perlmutter et al., 1999).

The most general metric accounting for these constraints, derived by Friedman (1922), Robertson (1935) and Walker (1935), and thus is known as the *Friedmann–Robertson–Walker (FRW)* metric

$$ds^2 = -dt^2 + a^2(t) \left[ \frac{dr^2}{1 - \kappa r^2} + r^2(d\theta^2 + \sin^2 \theta d\phi^2) \right]. \quad (1.270)$$

Though impressively simple, the metric above represents the starting point of modern cosmology. First of all, we note that the time–time covariant component of the metric is  $g_{tt} = -1$ , thus implying that the coordinate time,  $t$ , is also the proper time measured by a clock comoving with the galaxies in their expansion (this is also known as the *comoving gauge*). The fact that all of the mixed time–space components  $g_{ti}$  vanish is a necessary (and sufficient) condition for making all of these comoving clocks synchronizable, as required by a sensible definition of the global coordinate time  $t$  [see, e.g., Landau and Lifshitz (1975) and also Section 12.4.1 for the application to gravitational collapse]. The synchronisation can be physically conceived by assuming that all the observers set their proper time to an assigned number when the background homogeneous density reaches a given value that is the same for all observers.

The spatial part of the metric (1.270) is expressed through the conformal factor<sup>47</sup>  $a(t)$ , which can be used to rescale spatial distances. As such, this factor accounts for the expansion or contraction of the universe and is therefore named the *scale factor* (not to be confused with the spin parameter of a rotating black hole introduced in Section 1.7.2), and its dynamics is obviously determined by the Einstein equations, as we will show below. The constant  $\kappa$ , on the other hand, can assume values  $0, \pm 1$  and measures the constant curvature of the purely spatial metric. At any given epoch, in fact, the curvature has to be the same in all spatial positions, hence constant in space, if the assumption of isotropy is to be preserved. A value  $\kappa = 0$  refers to a flat spatial line element and the resulting universe is *flat* and *open*. A value  $\kappa = 1$ , instead,

<sup>46</sup>The cosmological principle (which is supported by observations but remains fundamentally an assumption), states that when observed on a sufficiently large scale, the properties of the universe are the same for all observers. Viewed differently, the cosmological principle is the extension of the *Copernican principle*, in which we do not occupy a special position in the universe.

<sup>47</sup>See also Eq. (3.157) for a definition of conformally related metrics.

## 60 A Brief Review of General Relativity

corresponds to a *positive* spatial curvature, describing a *closed* universe with finite volume but no boundaries, in analogy with a two-sphere. Finally, a value  $\kappa = -1$  represents a universe that has *negative* spatial curvature and is *open*, with overall properties that are more similar to those of Euclidean space.

Note that the metric (1.270) provides only a kinematic description of the spacetime in accordance with the cosmological assumptions discussed above. However, when combined with the Einstein equations and the conservation of energy  $\nabla_\mu T^{\mu\nu} = 0$ , the unknown scale factor  $a(t)$  and the curvature constant  $\kappa$  can be related to the energy content of the universe and the resulting equations are known as the *Friedmann equations*

$$H^2 := \left( \frac{\dot{a}}{a} \right)^2 = \frac{8}{3}\pi(e + e_\Lambda) - \frac{\kappa}{a^2}, \quad (1.271)$$

$$\frac{\ddot{a}}{a} = -\frac{4}{3}\pi(e + 3p - 2e_\Lambda), \quad (1.272)$$

$$\dot{e} + 3H(e + p) = 0, \quad (1.273)$$

where the dot indicates a derivative with respect to the cosmological time,  $t$ , and  $H = H(t)$  is the “*Hubble parameter*”, having the dimensions of the inverse of time. Note that in deriving Eqs. (1.271) and (1.272) we have assumed that the energy–momentum tensor appearing in the Einstein equations is that of a perfect fluid with total energy density  $e$  and pressure  $p$  (see Section 3.2). In addition, following the discussion in Section 1.6, we have associated to the *cosmological constant*  $\Lambda$  an effective energy density  $e_\Lambda := \Lambda/(8\pi)$ .

Using Eq. (1.271), we can express the curvature of spacetime also as

$$\frac{\kappa}{a^2} = H^2 \left( \frac{e + e_\Lambda}{e_c} - 1 \right) = H^2 (\Omega_m + \Omega_\Lambda - 1), \quad (1.274)$$

where

$$e_c := \frac{3H^2}{8\pi}, \quad \Omega_m := \frac{e}{e_c}, \quad \Omega_\Lambda := \frac{e_\Lambda}{e_c}. \quad (1.275)$$

Here,  $e_c$  is the *critical energy density*, while  $\Omega_m$  and  $\Omega_\Lambda$  are the normalised energy density of the “matter” (*i.e.*, including the contributions coming from radiation) and of the cosmological constant, respectively. In practice,  $e_c$  can be used to determine whether the curvature of the space is closed ( $\kappa = 1$ ), flat ( $\kappa = 0$ ) or open ( $\kappa = -1$ ), according to whether the *density parameter*  $\Omega := \Omega_m + \Omega_\Lambda$  assumes values that are greater than, equal to, or less than one. It is also possible to associate an effective energy density to the spatial curvature, *i.e.*, define  $e_\kappa := -3\kappa/(8\pi a^2)$  and its corresponding normalised value is  $\Omega_\kappa := e_\kappa/e_c = -\kappa/(aH)^2$ , so that Eq. (1.274) can be written as

$$1 = \Omega_\Lambda + \Omega_m + \Omega_\kappa \simeq 0.685 + 0.315 + 0.000. \quad (1.276)$$

The second equality in expression (1.276) reports the present estimates of the various densities based on multiple astronomical observations, such as those of the cosmic microwave background (Planck Collaboration *et al.*, 2013). Interestingly, about 70% of the energetic content of the universe is in a form which cannot be associated to ordinary matter and is for this

reason commonly referred to as “*dark energy*”. Note also that the matter contributions to the critical density can be distinguished into those associated to baryonic matter,  $\Omega_b$  and those associated to “*dark matter*”,  $\Omega_{dm}$ , *i.e.*, matter whose origin is presently unknown and whose presence cannot be deduced from the luminosity but only through its gravitational influence (hence the name). Also in this case, multiple astronomical observations converge to yield:  $\Omega_m = \Omega_b + \Omega_{dm} \simeq 0.05 + 0.26 \simeq 0.31$ . Equation (1.272) also highlights that different cosmological models, or simply different dynamical properties within the same model, can be obtained for different values of the cosmological constant and for different “equations of state” of the fluid filling the universe, that is, for different prescriptions between the pressure and the energy density (see also the discussion in Section 2.4). Models with zero cosmological constant are collectively known as *Friedmann models*, while the presence of a nonzero cosmological constant will lead to the *Lemaitre models*; the most celebrated of such models are the *de Sitter* and *anti-de Sitter models*, which are empty universes, *i.e.*, with  $e = 0 = p$ , but with cosmological constant which is  $\Lambda > 0$  and  $\Lambda < 0$ , respectively [see, *e.g.*, Coles and Lucchin (2002), Ellis *et al.* (2012), for a more systematic presentation of the properties of the different cosmological models].

## 1.8 Gravitational radiation

When considering the Einstein equations (1.218) as a set of second-order partial differential equations it is not easy to predict that there exist solutions behaving as waves. Indeed, the concept of gravitational waves as solutions of the Einstein equations written as linear and homogeneous wave equations is valid only under some rather idealised assumptions, such as a vacuum and asymptotically flat spacetime, a linearised regime for the gravitational fields and suitable gauges. If these assumptions are removed, the definition of gravitational waves becomes much more difficult, although still possible (see Section 7.2.5). It should be noted, however, that in this respect gravitational waves are not peculiar. Any wave-like phenomenon, in fact, can be described in terms of homogeneous wave equations only under simplified assumptions, such as those requiring a uniform “background” for the fields propagating as waves (see also Section 4.3.1 for a discussion on sound waves).

These considerations suggest that the search for wave-like solutions to the Einstein equations should be made in a spacetime with very modest curvature and with a line element which is that of flat spacetime but for small deviations of nonzero curvature, *i.e.*,

$$g_{\mu\nu} = \eta_{\mu\nu} + h_{\mu\nu} + \mathcal{O}((h_{\mu\nu})^2), \quad (1.277)$$

where the linearised regime is guaranteed by the fact that  $|h_{\mu\nu}| \ll 1$ . Before writing the linearised version of the Einstein equations (1.218) it is necessary to derive the linearised expression for the Christoffel symbols. In a Cartesian coordinate basis (such as the one we will assume hereafter), we recall that the general expression for the affine connection is given by Eq. (1.165), where the partial derivatives are readily calculated as

$$\partial_\beta g_{\nu\alpha} = \partial_\beta \eta_{\nu\alpha} + \partial_\beta h_{\nu\alpha} = \partial_\beta h_{\nu\alpha}. \quad (1.278)$$

As a result, the linearised Christoffel symbols become

## 62 A Brief Review of General Relativity

$$\Gamma^\mu_{\alpha\beta} = \frac{1}{2}\eta^{\mu\nu}(\partial_\beta h_{\nu\alpha} + \partial_\alpha h_{\nu\beta} - \partial_\nu h_{\alpha\beta}) = \frac{1}{2}(\partial_\beta h^\mu_\alpha + \partial_\alpha h^\mu_\beta - \partial^\mu h_{\alpha\beta}). \quad (1.279)$$

Note that the operation of lowering and raising the indices in expression (1.279) is not made through the metric tensors  $g_{\mu\nu}$  and  $g^{\mu\nu}$  but, rather, through the spacetime metric tensors  $\eta_{\mu\nu}$  and  $\eta^{\mu\nu}$ . This is just the consequence of the linearised approximation and, despite this, the spacetime is really curved!

Once the linearised Christoffel symbols have been computed, it is possible to derive the linearised expression for the Ricci tensor which takes the form

$$R_{\mu\nu} = \partial_\alpha \Gamma^\alpha_{\mu\nu} - \partial_\nu \Gamma^\alpha_{\mu\alpha} = \frac{1}{2}(\partial_\alpha \partial_\nu h_\mu^\alpha + \partial_\alpha \partial_\mu h_\nu^\alpha - \partial_\alpha \partial^\alpha h_{\mu\nu} - \partial_\mu \partial_\nu h), \quad (1.280)$$

where

$$h := h^\alpha_\alpha = \eta^{\mu\alpha} h_{\mu\alpha} \quad (1.281)$$

is the trace of the metric perturbations. The resulting Ricci scalar is then given by

$$R := g^{\mu\nu} R_{\mu\nu} \simeq \eta^{\mu\nu} R_{\mu\nu}. \quad (1.282)$$

Making use of (1.280) and (1.282), it is possible to rewrite the Einstein equations (1.218) in a linearised form as

$$\partial^\alpha \partial_\nu h_{\mu\alpha} + \partial^\alpha \partial_\mu h_{\nu\alpha} - \partial_\alpha \partial^\alpha h_{\mu\nu} - \partial_\mu \partial_\nu h - \eta_{\mu\nu}(\partial^\alpha \partial^\beta h_{\alpha\beta} - \partial^\alpha \partial_\alpha h) = 16\pi T_{\mu\nu}. \quad (1.283)$$

Although linearised, the Einstein equations (1.283) do not yet seem to suggest a wave-like behaviour. A good step in the direction of unveiling this behaviour can be made if we introduce a more compact notation, which makes use of “trace-free” tensors defined as

$$\bar{h}_{\mu\nu} := h_{\mu\nu} - \frac{1}{2}\eta_{\mu\nu}h, \quad (1.284)$$

where the “bar-operator” in (1.284) can be applied to any symmetric tensor so that, for instance,  $\bar{R}_{\mu\nu} = G_{\mu\nu}$ , and also iteratively, *i.e.*,  $\bar{h}_{\mu\nu} = h_{\mu\nu}$ .<sup>48</sup> Using this notation, the linearised Einstein equations (1.283) take the more compact form

$$-\partial^\alpha \partial_\alpha \bar{h}_{\mu\nu} - \eta_{\mu\nu} \partial^\alpha \partial^\beta \bar{h}_{\alpha\beta} + \partial^\alpha \partial_\mu \bar{h}_{\nu\alpha} = 16\pi T_{\mu\nu}, \quad (1.285)$$

where the first term on the left-hand side of (1.285) can be easily recognised as the *Dalambertian* (or wave) operator, *i.e.*,  $\partial_\alpha \partial^\alpha \bar{h}_{\mu\nu} = \square \bar{h}_{\mu\nu}$ . At this stage, we can exploit the gauge freedom inherent in general relativity (see also below for an extended discussion) to recast Eqs. (1.285) in a more convenient form. More specifically, we exploit this gauge freedom by choosing the metric perturbations  $h_{\mu\nu}$  so as to eliminate the terms in (1.285) that spoil the wave-like structure. Most notably, the metric perturbations can be selected so that

$$\partial_\alpha \bar{h}^{\mu\alpha} = 0. \quad (1.286)$$

Making use of the gauge (1.286), which is also known as the *Lorenz*<sup>49</sup> (or Hilbert) *gauge*, the linearised field equations take the form

<sup>48</sup>Note that the “bar” operator can in principle be applied also to the trace so that  $\bar{h} = -h$ .

<sup>49</sup>Although most books report this as the Lorentz gauge, it is actually due to Ludvig V. Lorenz, who is often confused with Hendrik A. Lorentz. At the risk of creating confusion, we will refer to it as the Lorenz gauge.

$$\square \bar{h}_{\mu\nu} = -16\pi T_{\mu\nu}, \quad (1.287)$$

that, in vacuum reduce to the desired result

$$\square \bar{h}_{\mu\nu} = 0. \quad (1.288)$$

Equations (1.288) show that, in the Lorenz gauge, the metric perturbations propagate as waves distorting flat spacetime.

The simplest solution to the linearised Einstein equations (1.288) is that of a plane wave of the type

$$\bar{h}_{\mu\nu} = A_{\mu\nu} \exp(i\kappa_\alpha x^\alpha), \quad (1.289)$$

where of course we are interested only in the real part of (1.289), with  $A$  being the *amplitude tensor*, and  $\kappa$  a null four-vector, *i.e.*,  $\kappa^\alpha \kappa_\alpha = 0$ . In such a solution, the plane wave (1.289) travels in the spatial direction  $\vec{k} = (\kappa_x, \kappa_y, \kappa_z)/\kappa^0$  with frequency  $\omega := \kappa^0 = (\kappa^j \kappa_j)^{1/2}$ . Note that the amplitude tensor  $A$  has in principle  $16 - 6 = 10$  independent components, but it is easy to conclude that there are only two independent components corresponding to the dynamical degrees of freedom of general relativity. The reduction of independent components can be explained simply. Firstly,  $A$  and  $\kappa$  cannot be arbitrary if they have to describe a plane wave; as a result, an orthogonality condition between the two quantities will constrain four of the ten components of  $A$  [see condition (a) below]. Secondly, while a global Lorenz gauge has been chosen [*cf.*, Eq. (1.286)], this does not completely fix the coordinate system of a linearised theory. A residual ambiguity, in fact, is preserved through arbitrary *gauge changes*, *i.e.*, through infinitesimal coordinate transformations that are not entirely constrained, even if a global gauge has been selected. To better appreciate this, consider an infinitesimal coordinate transformation in terms of a small but otherwise arbitrary displacement four-vector  $\xi$

$$x^{\alpha'} = x^\alpha + \xi^\alpha. \quad (1.290)$$

Applying this transformation to the linearised metric (1.277) generates a “new” metric tensor that, to the lowest order, is

$$g_{\mu'\nu'}^{\text{new}} = \eta_{\mu\nu} + h_{\mu\nu}^{\text{old}} - \partial_\nu \xi_\mu - \partial_\mu \xi_\nu, \quad (1.291)$$

so that the “new” and “old” perturbations are related by the following expression

$$h_{\mu'\nu'}^{\text{new}} = h_{\mu\nu}^{\text{old}} - \partial_\nu \xi_\mu - \partial_\mu \xi_\nu, \quad (1.292)$$

or, alternatively, by

$$\bar{h}_{\mu'\nu'}^{\text{new}} = \bar{h}_{\mu\nu}^{\text{old}} - \partial_\nu \xi_\mu - \partial_\mu \xi_\nu + \eta_{\mu\nu} \partial_\alpha \xi^\alpha. \quad (1.293)$$

Requiring now that the new coordinates satisfy the condition (1.286) of the Lorenz gauge  $\partial^\alpha \bar{h}_{\mu\alpha}^{\text{new}} = 0$ , forces the displacement vector to be solution of the homogeneous wave equation

$$\partial_\beta \partial^\beta \xi^\alpha = 0. \quad (1.294)$$

As a result, the plane-wave vector with components

$$\xi^\alpha := -iC^\alpha \exp(i\kappa_\beta x^\beta) \quad (1.295)$$

generates, through the *four* arbitrary constants  $C^\alpha$ , a gauge transformation that changes arbitrarily *four* components of  $A$  in addition to those coming from the condition  $A \cdot \kappa = 0$ . Effectively, therefore,  $A_{\mu\nu}$  has only  $10 - 4 - 4 = 2$  linearly independent components, corresponding

## 64 A Brief Review of General Relativity

to the number of degrees of freedom in general relativity (Misner *et al.*, 1973). Note that these considerations are not unique to general relativity and similar arguments can also be made in classical electrodynamics, where the Maxwell equations are invariant under transformations of the vector potentials of the type  $A_\mu \rightarrow A_{\mu'} = A_\mu + \partial_\mu \Psi$ , where  $\Psi$  is an arbitrary scalar function, so that the corresponding electromagnetic tensor is  $F_{\mu'\nu'}^{\text{new}} = \partial_{\nu'} A_{\mu'} - \partial_{\mu'} A_{\nu'} = F_{\mu'\nu'}^{\text{old}}$ . Similarly, in a linearised theory of general relativity, the gauge transformation (1.292) will preserve the components of the Riemann tensor, *i.e.*,  $R_{\alpha\beta\mu\nu}^{\text{new}} = R_{\alpha\beta\mu\nu}^{\text{old}} + \mathcal{O}(R^2)$ .

To summarise, it is convenient to constrain the components of the amplitude tensor through the following conditions:

- (a): *orthogonality condition*: four components of the amplitude tensor can be specified if  $\mathbf{A}$  and  $\boldsymbol{\kappa}$  are chosen to be orthogonal, *i.e.*,  $A_{\mu\nu}\kappa^\nu = 0$ .
- (b): *global Lorentz frame*: just like in special relativity, a global Lorentz frame relative to an observer with four-velocity  $\mathbf{u}$  can be defined. In this case, three<sup>50</sup> components of the amplitude tensor can be specified after selecting a four-velocity  $\mathbf{u}$  orthogonal to  $\mathbf{A}$ , *i.e.*,  $A_{\mu\nu}u^\nu = 0$ .
- (c): *infinitesimal gauge transformation*: one final component of the amplitude tensor can be eliminated after selecting the infinitesimal displacement vector  $\xi^\mu = iC^\mu \exp(i\kappa_\alpha x^\alpha)$  so that  $A_{\mu}^\mu = 0$ .

Conditions (a), (b) and (c) define the so-called *transverse–traceless* (TT) *gauge*, which represents a most convenient gauge for the analysis of gravitational waves. To appreciate the significance of these conditions, consider them implemented in a reference frame which is globally at rest, *i.e.*, with four-velocity  $u^\alpha = (1, 0, 0, 0)$ , where the amplitude tensor must satisfy:

(a):

$$A_{\mu\nu}\kappa^\nu = 0 \quad \iff \quad \partial^j h_{ij} = 0, \quad (1.296)$$

*i.e.*, the spatial components of  $h_{\mu\nu}$  are *divergence-free*.

(b):

$$A_{\mu\nu}u^\nu = 0 \quad \iff \quad h_{\mu t} = 0, \quad (1.297)$$

*i.e.*, only the spatial components of  $h_{\mu\nu}$  are *nonzero*, hence the *transverse* character of the TT gauge.

(c):

$$A_{\mu}^\mu = 0 \quad \iff \quad h = h_j^j = 0, \quad (1.298)$$

*i.e.*, the spatial components of  $h_{\mu\nu}$  are *trace free* hence the *trace-free* character of the TT gauge. Because of this, and only in this gauge,  $\bar{h}_{\mu\nu} = h_{\mu\nu}$

Two important remarks should be made at this point. The first is that the assumption of linearity makes the use of the TT gauge completely general. Any linear gravitational wave, in fact, can be decomposed into a linear superposition of planar waves. Because the conditions (1.297)–(1.298) are linear in  $h_{\mu\nu}$ , any of the composing planar waves can be chosen to satisfy (1.297)–(1.298), which, as a result, are satisfied also by the original gravitational wave. The second remark is that, because the gravitational radiation reflects the two degrees of freedom

<sup>50</sup>Note that the orthogonality condition fixes three and not four components since one further constraint needs to be satisfied, *i.e.*,  $\kappa^\mu A_{\mu\nu}u^\nu = 0$ .

of general relativity, it is always possible to decompose a gravitational wave into two linearly polarised plane waves or into two circularly polarised plane waves. These two polarisation modes are then referred to as “plus” (+) and “cross” ( $\times$ ) because of the distortions they introduce on a ring of freely falling particles, and identify the gravitational-wave *polarisation amplitudes*  $h_+$  and  $h_\times$  [see, e.g., Misner et al. (1973)].

The accurate determination of the gravitational-radiation content of the simulated space-times represents a delicate and yet fundamental aspect of any modelling of sources of gravitational waves. At least two different methods are possible and in use in modern numerical-relativity calculations. The first one based on the Newman–Penrose formalism, which provides a convenient representation for a number of radiation-related quantities through spin-weighted scalars (Newman and Penrose, 1962). In particular, the curvature scalar

$$\psi_4 := -C_{\alpha\beta\gamma\delta}n^\alpha\bar{m}^\beta n^\gamma\bar{m}^\delta \quad (1.299)$$

is defined as a particular component of the Weyl curvature tensor  $C_{\alpha\beta\gamma\delta}$  [cf., Eq. (1.214)] projected onto a given null frame  $\{\mathbf{l}, \mathbf{n}, \mathbf{m}, \bar{\mathbf{m}}\}$ , where the bar indicates the complex conjugate. In practice, in numerical calculations adopting a 3+1 decomposition of spacetime (cf., Section 7.1), a polar orthonormal basis is defined in the three-space  $(\mathbf{e}_\hat{r}, \mathbf{e}_\hat{\theta}, \mathbf{e}_\hat{\phi})$ , centred on a Cartesian origin and with poles along, say, the  $z$ -axis. The normal to the spatial hypersurface defines a timelike vector  $\mathbf{e}_{\hat{t}}$ , from which the null frame is constructed as

$$\mathbf{l} = \frac{1}{\sqrt{2}}(\mathbf{e}_{\hat{t}} - \mathbf{e}_{\hat{r}}), \quad \mathbf{n} = \frac{1}{\sqrt{2}}(\mathbf{e}_{\hat{t}} + \mathbf{e}_{\hat{r}}), \quad \mathbf{m} = \frac{1}{\sqrt{2}}(\mathbf{e}_{\hat{\theta}} - i\mathbf{e}_{\hat{\phi}}). \quad (1.300)$$

The gravitational-wave *polarisation amplitudes*  $h_+$  and  $h_\times$  are then related to  $\psi_4$  by simple time integrals (Teukolsky, 1973)

$$\ddot{h}_+ - i\ddot{h}_\times = \psi_4, \quad (1.301)$$

where the double over-dot stands for the second-order time derivative.

The second method employed in numerical calculations is instead based on the measurements of the non-spherical gauge-invariant perturbations of a Schwarzschild black hole. In practice, a set of “observers” is placed on two-spheres of fixed Schwarzschild radius where gauge-invariant quantities are extracted. These are the odd-parity (or axial) current multipoles  $Q_{\ell m}^\times$  and even-parity (or polar) mass multipoles  $Q_{\ell m}^+$  of the metric perturbation (Moncrief, 1974; Abrahams and Price, 1996). The variables  $Q_{\ell m}^+$  and  $Q_{\ell m}^\times$  are then related to the gravitational-wave amplitudes  $h_+$  and  $h_\times$  as (Nagar and Rezzolla, 2005)

$$h_+ - ih_\times = \frac{1}{\sqrt{2}r} \sum_{\ell, m} \left( Q_{\ell m}^+ - i \int_{-\infty}^t Q_{\ell m}^\times(t') dt' \right) {}_{-2}Y^{\ell m}, \quad (1.302)$$

where  ${}_{-2}Y^{\ell m}$  are the  $s = -2$  spin-weighted spherical harmonics and  $(\ell, m)$  are the indices of the angular decomposition. We will encounter again both the  $\psi_4$  scalar and the gauge-invariant variables  $Q_{\ell m}^+$  and  $Q_{\ell m}^\times$ , in Chapter 12, when discussing the gravitational-wave emission from binary systems of neutron stars.

A final comment should be reserved for “gravitational-wave astronomy”, that is, the use of the gravitational radiation produced by astrophysical compact objects, to deduce, learn about and predict the properties of astronomical objects. This is an area of research that is becoming increasingly large and important, as introduced in a number of recent monographs by Maggiore (2007), Creighton and Anderson (2012), and Blair et al. (2012).

## 1.9 Further reading

- Carmeli, M. (2001). *Classical Fields: General Relativity and Gauge Theory*. World Scientific, River Edge, NJ.
- d’Inverno, R. (1992). *Introducing Einstein’s Relativity*. Oxford University Press, Oxford.
- de Felice, F. and Clarke, C. J. S. (1990). *Relativity on Curved Manifolds*. Cambridge University Press, Cambridge.
- Frankel, T. (2004). *The Geometry of Physics: An Introduction*. Cambridge University Press, Cambridge.
- Hartle, J. B. (2003). *Gravity: An Introduction to Einstein’s general relativity*. Addison Wesley, San Francisco.
- Landau, L., Lifshitz, E. M. (1975). *The Classical Theory of Fields*. Course of Theoretical Physics, Vol. 2. Butterworth-Heinemann, Oxford.
- Misner, C. W., Thorne, K. S., and Wheeler, J. A. (1973). *Gravitation*. W. H. Freeman, San Francisco.
- Schutz, B. F. (1985). *A First Course in General Relativity*. Cambridge University Press, Cambridge.

## 1.10 Problems

1. Apply relations (1.5) and (1.7) to the coordinate systems  $\{x^\mu\} = (x, y)$  and  $\{x^{\mu'}\} = (r, \theta)$  to derive the explicit expressions of the matrix (1.9) and of its inverse (1.10), i.e.,

$$\Lambda^{\mu'}_\mu = \begin{pmatrix} \frac{x}{(x^2 + y^2)^{1/2}} & \frac{y}{(x^2 + y^2)^{1/2}} \\ -\frac{y}{x^2 + y^2} & \frac{x}{x^2 + y^2} \end{pmatrix},$$

and

$$\Lambda = \Lambda^\mu_{\mu'} = \begin{pmatrix} \cos \theta & -r \sin \theta \\ \sin \theta & r \cos \theta \end{pmatrix}.$$

2. Use the definition of the covariant derivative of the contravariant vector  $U^\mu$ , Eq. (1.154), to obtain the covariant derivative of the covariant vector  $U_\mu$ , Eq. (1.157) [Hint: recall that, for a scalar function, the covariant and partial derivative coincide, and that the scalar product of two vector fields  $\mathbf{U}$  and  $\mathbf{V}$  is a scalar function!].

3. Consider the two-sphere with metric

$$ds^2 = r^2 (d\theta^2 + \sin^2 \theta d\phi^2),$$

and compute the Christoffel symbols in this geometry.

4. Show that, if  $U^\mu U_\mu$  is a constant, then all of the following are scalar invariants

$$\frac{dU^0 dU^1 dU^2}{U_3} = \frac{dU^0 dU^1 dU^3}{U_2} = \frac{dU^0 dU^2 dU^3}{U_1} = \frac{dU^1 dU^2 dU^3}{U_0}.$$

5. Use the definition (1.131) to show that the Lie derivative is a linear operator, namely  $\mathcal{L}_{\mathbf{V}}(\alpha \mathbf{U} + \beta \mathbf{W}) = \alpha \mathcal{L}_{\mathbf{V}} \mathbf{U} + \beta \mathcal{L}_{\mathbf{V}} \mathbf{W}$ .

6. Show that the Christoffel symbols can be reduced to zero at a given point through the coordinate transformation (1.168).

7. Compute the second convective derivative (1.193) of a generic vector field  $A^\mu$  along a geodesic with tangent vector  $V^\nu$ .

8. Consider the metric

$$ds^2 = e^{-2f(\sigma)} (-dt^2 + dx^2 + dy^2 + dz^2),$$

where  $f$  is an arbitrary function and  $\sigma^2 = t^2 - (x^2 + y^2 + z^2)$ . Show that such a metric is invariant under Lorentz transformations.

9. Compute the Riemann tensor of the Friedman Robertson Walker metric (1.270), and show that  $R = 0$  is a curvature singularity for the cosmological spacetime, the so-called *big bang*.

## 2

# A Kinetic-Theory Description of Fluids

---

### 2.1 On the fluid approximation

Given a collection of  $N$  free particles interacting through some coupling, there are a number of different ways to describe the dynamics of the system.<sup>1</sup> These approaches can be distinguished in terms of the dimensionless ratio  $\mathcal{R} := \lambda_{\text{DB}}/\ell$ , where  $\lambda_{\text{DB}}$  is the *de Broglie wavelength* associated to each particle and  $\ell$  is the typical inter-particle separation. In this way, if the system has  $\mathcal{R} \gtrsim 1$ , then the waveforms of the various particles overlap and a quantum-mechanical description is necessary, with the system being described by the  $N$ -particle wavefunction evolving in time following the Schrödinger equation. On the other hand, if the system is such that  $\mathcal{R} \ll 1$ , then the wavefunctions of the different particles are widely separated, the quantum interference is not important, and the individual wave packets evolve according to the Schrödinger equation in an isolated fashion, moving like classical particles. This result, which is known as the *Ehrenfest's theorem*, asserts that the states of the system are prescribed by the positions and the velocities of the  $N$  particles, and that the time evolution is described by the laws of classical mechanics.

Of course, if  $N$  is very large, it is not realistic to solve the equations of motion for all of the particles and it is more useful to switch to a statistical approach in terms of a *distribution function*  $f(t, \vec{x}, \vec{u})$ , which expresses the particle *number density* at time  $t$  within the six-dimensional *phase space*  $(\vec{x}, \vec{u})$  (hereafter we will assume  $\vec{x}$  to be the coordinate position in a three-dimensional space and  $\vec{u}$  the corresponding coordinate velocity). The dynamics of the system is then described via the evolution of the distribution function  $f(t, \vec{x}, \vec{u})$ , which can change in time either through a simple advection in phase space when no collisions occur among the particles, or in more complex manners when the collisions are present and strongly influence the evolution. In the case of systems composed of electrically neutral particles such as the ones of interest here,<sup>2</sup> the equation expressing these changes is the *Boltzmann equation*, which represents the cornerstone of statistical physics and will be discussed in detail in this chapter. There are two important extensions of this equation to systems in which the collisions are absent and are replaced by long-range forces. More precisely, in plasmas subject *only* to Coulomb forces, the Boltzmann equation is replaced by the *Vlasov–Maxwell* equation, while

<sup>1</sup>The adjective “free” is used here to indicate that the particles are not themselves part of a rigid ordered structure such as, for instance, a lattice in a solid.

<sup>2</sup>Most astrophysical fluids are indeed ionised plasmas, which are however globally and locally neutral, where by “locally” we mean on scales larger than the Debye length. Hence, as long as the electromagnetic fields are comparatively small and the Debye scale is much smaller than the size of the problem, these plasmas can be treated as effectively neutral (quasi-neutral) fluids (Choudhuri, 1998).

it becomes the *Einstein–Vlasov* equation when the long-range forces are gravitational and are treated within general relativity [see Rendall (2004) for a review].

An additional description of a system of  $N$  free particles is also possible and is of particular relevance for this book. This description becomes possible when the number  $N$  of the free particles is so large and the system extends over a length-scale  $L$  so much larger than  $\ell$  (and of course much larger than  $\lambda_{\text{DB}}$ ), that the dynamics of the individual particles cannot be followed, not even in statistical terms. In this case, which would correspond to  $\mathcal{R} \lll 1$  in the classification above, the collective dynamics of the system can be conveniently approximated by a continuous description in terms of a so-called “*fluid*”. The validity of the “*fluid description*” can be measured in terms of the dimensionless *Knudsen number*  $K_n := \ell/L$ , which should be  $K_n \lll 1$  for a fluid continuum and is, for example,  $K_n \sim 0.005$  for air at room temperature. When a fluid description is possible, the system can then be described in terms of quantities averaged over representative “*elements*”, which are large enough to contain a high number of particles, and small enough to guarantee homogeneity within the element. As a result, in each of these fluid elements the particles have the same velocity on average and are in thermodynamic equilibrium.<sup>3</sup>

Despite the fuzziness of its definition, the fluid description is extremely powerful as it allows one to describe the state of the system in terms of a few scalar functions (not even necessarily continuous) defined at each point in space. For a single-component fluid, for example, these functions correspond to two thermodynamic variables, *e.g.*, pressure and temperature, and the velocity field. The evolution laws that can be derived for this continuum are then called the *hydrodynamic equations* and have a vast range of applications, since they can be used to describe in an *effective* manner an enormous phenomenology ranging from meteorology, over to heavy-ion collisions and relativistic astrophysics.

This chapter illustrates how the foundations of the fluid description can be found in statistical mechanics and in particular in kinetic theory. We will assume that the reader is familiar with the basic concepts of thermodynamics and start with a discussion of the *Newtonian* kinetic theory, which will pave the way to the presentation of the *relativistic* extension of the theory. The fundamental concept of the *equilibrium distribution* function will then be used to introduce the notion of the “*equation of state*”, for which we will present a variety of examples for fluids under different physical conditions. The reader with a keener interest in the statistical-physics aspects of the topics covered in this chapter will find more details in the excellent monographs of Huang (1987) and of Cercignani and Kremer (2002).

Note that in this chapter we will break our standard notation and use the speed of light,  $c$ , explicitly, rather than using units in which  $c = 1$ . This choice will help to highlight the role played by the speed of light within the kinetic theory and to facilitate the physical interpretation of several new quantities. With the exception of Section 3.5, in all other chapters of the book we will use units in which  $c = 1$ .

<sup>3</sup>The definition given above of fluids encompasses equally well both *gases* and *liquids*, where the latter are defined as *incompressible fluids*. Hereafter, we will consider only *compressible fluids* and, because there is really no distinction in our framework, simply call “*fluid*” also what is sometimes referred to as “*gas*”.

## 2.2 Newtonian kinetic theory

### 2.2.1 The Boltzmann equation

The Newtonian (*i.e.*, non-relativistic) kinetic theory represents the simplest and yet non-trivial framework within which we can build a complete description of a system of interacting particles. As will become evident, many of the concepts and techniques derived here will be present also within a relativistic regime.

We start by introducing the definition of the *distribution function*  $f(t, \vec{x}, \vec{u})$  of a physical system composed of particles of the same species that are indistinguishable, *i.e.*, of a single-component system with no internal degrees of freedom, and characterised by the same rest mass  $m$ , *i.e.*, the *particle mass*. (The generalisation to a multicomponent system is simple and consists in considering a distinct distribution function for each component and for the exchange terms among the different components; see Section 3.11.) The distribution function is then defined as the probability that a particle has, at time  $t$ , a velocity<sup>4</sup>  $\vec{u}$  in the velocity-space element  $d^3u$  at  $\vec{u}$  and a position  $\vec{x}$  in the coordinate volume element  $d^3x$  at  $\vec{x}$ . In other words,  $f(t, \vec{x}, \vec{u}) d^3x d^3u$  is the number of particles in the region of phase space spanned by the six-dimensional volume  $d^3x d^3u$ . The total number of particles of the system,  $N$ , is then just the integral of the distribution function over the six-dimensional phase space, *i.e.*,

$$N = \int_{-\infty}^{\infty} d^3x \int_{-\infty}^{\infty} d^3u f(t, \vec{x}, \vec{u}) = \int f(t, \vec{x}, \vec{u}) d^3x d^3u. \quad (2.1)$$

For this approach to be meaningful it is necessary that the volume elements  $d^3x$  are large enough to contain a very large number of particles ensuring a small statistical variance and yet small enough with respect to the size of the system so that they can be considered as “points” in phase space and the continuum approach is justified. Conditions of this type are easily met for standard fluids on Earth; in ordinary physical conditions, in fact, a gas contains  $\sim 3 \times 10^{19}$  molecules per cubic centimetre. If we take  $d^3x \sim 10^{-10} \text{ cm}^{-3}$ , which is small enough to be considered as a point, we find that in this element  $d^3x$  there are  $\sim 10^9$  molecules. The aim of kinetic theory, and ours in this section, is to find the equations determining the evolution of the distribution function  $f(t, \vec{x}, \vec{u})$ . In addition, should an equilibrium state exist for the system, we are interested in computing the *equilibrium distribution* function, *i.e.*, the time-independent distribution function  $f_0 := f(\vec{x}, \vec{u})$  describing the thermodynamic properties of the system.

A fundamental qualitative difference in the evolution of the distribution function will be introduced by the possibility that particles can interact (either in binary or multiple interactions) and thus change their position in phase space. These interactions take the generic name of “*collisions*” and Fig. 2.1 illustrates the qualitative differences they introduce. The left panel of the figure reports the trajectories in phase space [for simplicity we consider just its cross-section in three dimensions  $(t, x, u_x)$ ] of two particles, 1 and 2, in the absence of collisions. Each particle remains in the corresponding plane in momentum space and has a simple linear trajectory in spatial space, which intersects with the other one at the collision event. The

<sup>4</sup>Given the simplicity of our single-component system, at any time in the discussion in this section we can replace the velocity vector  $\vec{u}$  with the specific linear momentum  $\vec{p}/m$ .

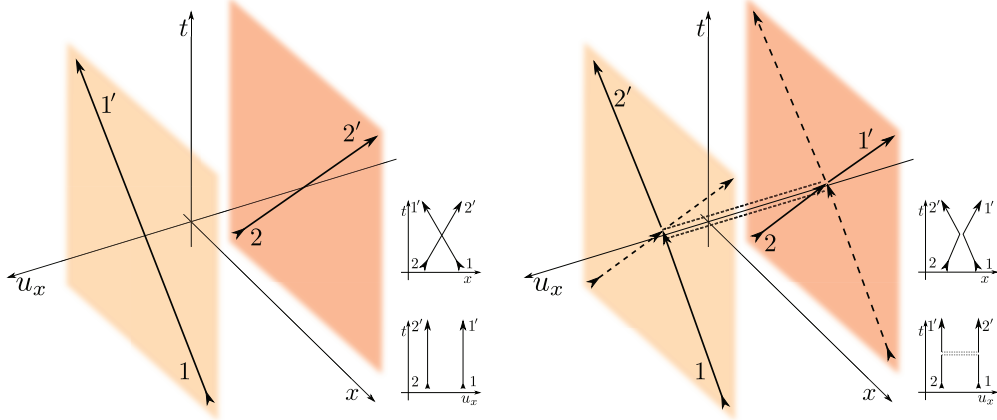


**Fig. 2.1** Schematic diagram of the trajectories in a three-dimensional  $(t, x, u_x)$  cross-section of phase space. The left panel refers to the absence of collisions, when the particles remain in the corresponding plane in momentum space and have simple linear trajectories in spatial space intersecting at the collision event [see the corresponding  $(t, x)$  and  $(t, u_x)$  sections on the bottom right]. The right panel refers to the presence of an *elastic collision*, where, after the collision, the planes in momentum space are exchanged, while in the spatial space the worldlines undergo a rapid change [see the sections on the bottom right].

corresponding sections are shown with the two small  $(t, x)$  and  $(t, u_x)$  insets on the bottom right of the panel. This behaviour should be contrasted with the one shown in the right panel, where the particles undergo an *elastic collision*.<sup>5</sup> In this case, after the collision, the planes in momentum space containing the particles' trajectories are exchanged, while in the spatial space the worldlines undergo a rapid change at the collision event. Also in this case, the corresponding sections are shown with the two small  $(t, x)$  and  $(t, u_x)$  insets on the bottom right of the panel.

Let us start by considering the less realistic but simpler case in which *no collisions* are present, but where an external force  $\vec{F}$  is present (e.g., a gravitational force), which is applied on each particle and let  $m$  be the mass of the particle.<sup>6</sup> In the absence of collisions, all particles in the six-dimensional phase-space cell at  $(\vec{x}, \vec{u})$  would travel after a time  $dt$  into the cell at  $(\vec{x} + \vec{u} dt, \vec{u} + \vec{F}/m dt)$  with volume element  $d^3x' d^3u'$ .

In the absence of collisions, the number of particles in each cell is therefore an invariant

$$f(t + dt, \vec{x} + \vec{u} dt, \vec{u} + \vec{F}/m dt) d^3x' d^3u' = f(t, \vec{x}, \vec{u}) d^3x d^3u, \quad (2.2)$$

with particles moving from one cell of the phase space to the neighbouring one and, at the same time, being replaced by particles from nearby cells. This change of position and velocity can also be seen as a simple coordinate transformation

$$\vec{x}' = \vec{x} + \vec{u} dt, \quad (2.3)$$

<sup>5</sup>A collision is said to be elastic if the relative velocity of the particles involved in the collision changes sign after the collision, while keeping its modulus constant. A collision where the modulus changes is said *inelastic*.

<sup>6</sup>It is important that the force  $\vec{F}$  is not the one resulting by the interaction between particles via elastic collisions. The inclusion of such forces will be considered in Eq. (2.8).

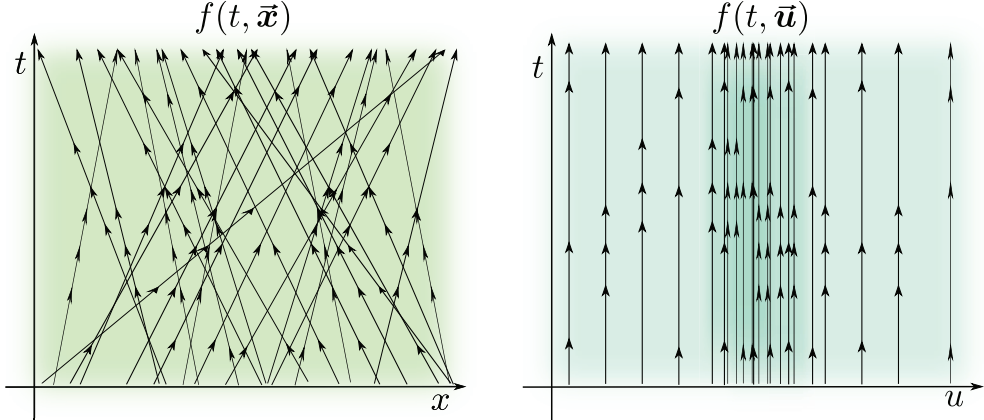


**Fig. 2.2** Schematic diagram of the trajectories in phase space for a set of particles obeying the *collisionless* Boltzmann equation. The left panel reports the worldlines of the particles and the evolution of the spatial distribution  $f(t, \vec{x})$  with a green colour. The right panel reports the trajectories of the particles in velocity space and the evolution of the velocity distribution  $f(t, \vec{u})$  with a blue colour. Note that both distributions remain constant in time and that we have assumed for simplicity that  $\vec{F} = 0$ . This figure should be contrasted with Fig. 2.3.

$$\vec{u}' = \vec{u} + (\vec{F}/m) dt, \quad (2.4)$$

whose Jacobian has determinant  $J = 1 + \mathcal{O}(dt^2)$  [see, e.g., Reif (1965) for a detailed derivation]. Stated differently,  $J = 1$  is correct up to and including first-order terms in the infinitesimal time interval  $dt$ , thus implying that  $d^3x' d^3u' = J d^3x d^3u = d^3x d^3u + \mathcal{O}(dt^2)$ . Hence, a Taylor series expansion of the left-hand side of (2.2) truncated to first order in  $dt$  gives

$$\frac{\partial f}{\partial t} + \vec{u} \cdot \vec{\nabla}_\vec{u} f + \frac{\vec{F}}{m} \cdot \vec{\nabla}_{\vec{u}} f = 0, \quad (2.5)$$

where the  $i$ -th component of the gradient  $\vec{\nabla}_{\vec{u}}$  of  $f$  is simply given by  $\partial f / \partial u^i$ . Equation (2.5) is the famous *collisionless Boltzmann equation* and it expresses the conservation of the distribution function in the absence of collisions. This becomes evident when writing  $\vec{F}/m = \partial \vec{p} / \partial t = \dot{\vec{p}}$  and  $\vec{u} = \partial \vec{x} / \partial t = \dot{\vec{x}}$ , so that (2.5) is simply given by

$$\frac{d}{dt} f(t, \vec{x}, \vec{p}/m) = \frac{\partial f}{\partial t} + \dot{\vec{x}} \cdot \frac{\partial f}{\partial \vec{x}} + \dot{\vec{p}} \cdot \frac{\partial f}{\partial \vec{p}} = 0. \quad (2.6)$$

Figure 2.2 offers a schematic diagram of the trajectories in phase space for a set of particles obeying the collisionless Boltzmann equation. The left panel, in particular, shows the trajectories of the particles in space (*i.e.*, their worldlines) and with a green colour the evolution of the spatial distribution  $f(t, \vec{x})$ . The right panel, instead, reports the trajectories of the particles in velocity space and with a blue colour the evolution of the velocity distribution  $f(t, \vec{u})$ . As commented above, note that the absence of collisions prevents particles from changing their velocities when their worldlines intersect.

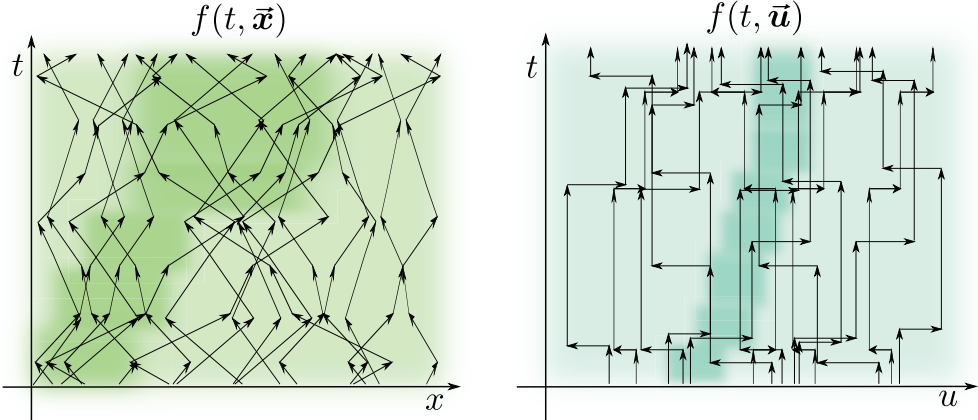


**Fig. 2.3** Schematic diagram of the trajectories in phase space for a set of particles obeying the *collisional* Boltzmann equation. The left panel reports the worldlines of the particles and the evolution of the spatial distribution  $f(t, \vec{x})$  with a green colour. The right panel reports the trajectories of the particles in velocity space and the evolution of the velocity distribution  $f(t, \vec{u})$  with a blue colour. Note that also in this case we have assumed  $\vec{F} = 0$ , but here the distributions undergo an evolution till reaching an equilibrium distribution  $f_0$  (see Section 2.2.2). This figure should be contrasted with Fig. 2.2.

We can now move to a more realistic scenario and consider a large set of particles which interact with each other, but only through *binary elastic collisions* produced by some short-range force among the particles. As shown in the right panel of Fig. 2.1, some of these collisions will have the effect of altering the simple advection of particles from one cell to the neighbouring one expressed by (2.2). In fact, particles will be moved via collisions to the cell at  $(\vec{x} + \vec{u} dt, \vec{u} + \vec{F}/m dt)$  which were not previously contained in the cell at  $(\vec{x}, \vec{u})$ . Similarly, other collisions will prevent some of the particles that were in the cell at  $(\vec{x}, \vec{u})$  from being advected to the neighbouring cell at  $(\vec{x} + \vec{u} dt, \vec{u} + \vec{F}/m dt)$ . Overall, this collision-modified advection can be expressed by correcting Eq. (2.2) as

$$f(t + dt, \vec{x} + \vec{u} dt, \vec{u} + \vec{F}/m dt) d^3x' d^3u' = f(t, \vec{x}, \vec{u}) d^3x d^3u + \Gamma(f) d^3x d^3u dt, \quad (2.7)$$

where  $\Gamma(f) d^3x d^3u$  expresses the net change, per unit time, of the number of particles in the cell around  $(\vec{x}, \vec{u})$  as caused by collisions. Correspondingly, Eq. (2.5) needs to be modified into what is known as the classical full (or collisional) *Boltzmann equation* (Boltzmann, 1872)

$$\frac{\partial f}{\partial t} + \vec{u} \cdot \vec{\nabla}_x f + \frac{\vec{F}}{m} \cdot \vec{\nabla}_{\vec{u}} f = \Gamma(f) = \left( \frac{\partial f}{\partial t} \right)_{\text{coll}}. \quad (2.8)$$

Figure 2.3 provides a schematic diagram of the trajectories in phase space for a set of particles obeying the (collisional) Boltzmann equation. Note that in this case, the presence of collisions introduces changes in the particle worldlines and velocities at each collision. Furthermore, as we will see later on, if the system is out of equilibrium, the distribution functions undergo an evolution both in spatial space and in velocity space till they attain the equilibrium value  $f_0$  (see Section 2.2.2).

## 74 A Kinetic-Theory Description of Fluids

The term  $\Gamma(f) = (\partial f / \partial t)_{\text{coll}}$  is usually referred to as the *collision integral* and accounts for the effect of collisions via an integral involving  $f$  and depending on the nature of the interaction between particles. In the simplest case in which only binary collisions are considered between particles with velocities  $\vec{u}_1$  and  $\vec{u}_2$  and no external force is present, the collision integral accounts for the net number of particles entering and leaving the reference volume in phase space and thus takes the form<sup>7</sup>

$$\left( \frac{\partial f}{\partial t} \right)_{\text{coll}} = \int d^3 u_2 \int d\Omega \sigma(\Omega) |\vec{u}_1 - \vec{u}_2| (f'_2 f'_1 - f_2 f_1) = \Gamma(f), \quad (2.9)$$

where  $f_{1,2} := f(t, \vec{x}, \vec{u}_{1,2})$ ,  $f'_{1,2} := f(t, \vec{x}, \vec{u}'_{1,2})$  are the distribution functions before and after the collision at time  $t$  and position  $\vec{x}$ ,<sup>8</sup> while  $\sigma(\Omega)$  is the differential cross-section over the solid angle  $d\Omega$  of the short-range interaction responsible for the collisions. It follows then that the Boltzmann equation (2.8) with the collision integral (2.9) is a (nonlinear) integro-differential equation and the problem of the kinetic theory amounts to finding a solution to this equation, which requires, in general, a numerical approach.

A notable exception is the *Fokker–Planck equation*, which is given by the Boltzmann equation (2.8) in a gravitational potential  $\phi$ , so that  $\vec{F}/m = -\vec{\nabla}\phi$ , and the collision integral can be expressed in terms of diffusion coefficients, thus making the Fokker–Planck equation a partial differential equation and not an integro-differential equation. The Fokker–Planck equation is widely used to model gravitational systems of dense stellar systems, such as globular clusters [see, e.g., Binney and Tremaine (1987) for an extended discussion]. An equation similar to (2.8) was proposed by Uehling and Uhlenbeck (1933) for the description of a quantum gas, where only the collision term  $\Gamma$  has to be changed to account for the quantum degeneracy of the particles.

Whatever distribution function may be the solution of Eq. (2.8), it is possible to define the *averaged value* of any quantity  $\psi$  with respect to the distribution function  $f$  as

$$\langle \psi \rangle := \frac{1}{n} \int \psi f d^3 u, \quad (2.10)$$

where  $n$  is the *number density*, i.e., the number of particles per unit volume, which, from Eq. (2.1), is simply given by the normalisation conditions

$$n = \int f d^3 u, \quad N = \int n d^3 x. \quad (2.11)$$

Note that  $n$  has the dimensions of  $[L]^{-3}$  and thus any average quantity  $\langle \psi \rangle$  has the same dimensions as  $\psi$ . A very relevant example of the use of (2.10) is provided by the *mean macroscopic velocity*  $\vec{v}$ , defined as the first moment of the distribution

$$\vec{v} := \langle \vec{u} \rangle = \frac{1}{n} \int \vec{u} f d^3 u. \quad (2.12)$$

Since the averaged vector  $\vec{v}$  indicates a global direction of motion (in contrast to the local velocity vector  $\vec{u}$ ), it is also referred to as the *fluid velocity*. This is such an important concept

<sup>7</sup>It is a useful exercise to show that the terms proportional to  $f_2 f_1$  and  $f'_2 f'_1$  are proportional to the number of particles that leave or enter, respectively, the volume element  $d^3 x d^3 u$  in phase space (Cercignani and Kremer, 2002).

<sup>8</sup>The subscripts “1” and “2” refer to the particles undergoing the collision, while unprimed and primed variables refer to quantities before and after the collision.

that it deserves a comment, although we will have the opportunity of remarking on this point also elsewhere in this book. When adopting a fluid description to discuss the dynamics of a collection of particles, it is essential to distinguish the local dynamics of the constituents, *e.g.*, the velocity  $\vec{u}$ , from the global dynamics of the whole collection, *i.e.*, the flow velocity  $\vec{v}$ . Indeed, apart from a static fluid, for which the fluid velocity  $\vec{v} = 0$  (*e.g.*, a fluid in a box), the flow velocity represents a fundamental reference with respect to which we measure the properties of the system. Such properties, in fact, should be independent of the translational state of the set of particles.

### 2.2.2 The $H$ -theorem

We have so far introduced the concept of a distribution function and discussed the partial differential equations that prescribe its evolution with and without collisions [Eqs. (2.5) and (2.8), respectively]. However, we have not yet discussed the properties of the *equilibrium distribution function*, that is of the solution of the transport Boltzmann equation (2.8) representing an asymptotic state of the system and hence independent of time. In the next section we will discuss the most important of such distribution functions for a simple monatomic fluid, but before doing that it is useful to review here a theorem, *i.e.*, the  *$H$ -theorem*, which gives a condition for the functional form of the equilibrium distribution, provides a definition of the *entropy* of the fluid, and a microscopic derivation of the second law of thermodynamics.

There are several texts where this theorem is discussed in greater detail [*see, e.g.*, Pitaevskii and Lifshitz (1981), Huang (1987) and Cercignani and Kremer (2002)] and here we will discuss only the most salient aspects of the proof, highlighting the aspects of the theorem that are relevant for our subsequent discussion. We start by recalling that  $\Gamma(f)$ , as expressed in Eq. (2.9), represents the collision integral in the simplest case in which there are only binary collisions and no external force is present. Let us also denote the *equilibrium distribution*, which is of course uniform and stationary, by  $f_0(\vec{u})$ , so that, by construction

$$\frac{\partial f_0}{\partial t} = \Gamma(f_0) = 0. \quad (2.13)$$

The proof of the classical  $H$ -theorem then amounts to showing that the condition (2.13) is fully equivalent to the condition

$$f_0(\vec{u}'_2)f_0(\vec{u}'_1) - f_0(\vec{u}_2)f_0(\vec{u}_1) = 0, \quad (2.14)$$

which provides then the functional form of the sought-after equilibrium function. To proceed with the proof we start by recalling Eq. (2.9) and evaluating it for the equilibrium function so that we have

$$\frac{\partial f_0}{\partial t} = \int d^3 u_2 \int d\Omega \sigma(\Omega) |\vec{u}_1 - \vec{u}_2| [f_0(\vec{u}'_2)f_0(\vec{u}'_1) - f_0(\vec{u}_2)f_0(\vec{u}_1)] = 0, \quad (2.15)$$

where  $\vec{u}_1$  and  $\vec{u}_2$  are the velocities of the particles undergoing the collisions, and where  $\vec{u}_1$  is considered fixed. Clearly, given that  $f_0(\vec{u}'_2)f_0(\vec{u}'_1) - f_0(\vec{u}_2)f_0(\vec{u}_1)$  is part of the integrand in Eq. (2.15), it follows that (2.14) is a sufficient condition for (2.13).

## 76 A Kinetic-Theory Description of Fluids

Proving that (2.14) is also a necessary condition for (2.13) is more involved and requires the definition of a new quantity

$$H(t) := \int f(t, \vec{u}) \ln(f(t, \vec{u})) d^3 u, \quad (2.16)$$

where  $f(t, \vec{u})$  is the distribution function at time  $t$  and thus satisfying

$$\frac{\partial f(t, \vec{u}_1)}{\partial t} = \int d^3 u_2 \int d\Omega \sigma(\Omega) |\vec{u}_1 - \vec{u}_2| [f(\vec{u}'_2) f(\vec{u}'_1) - f(\vec{u}_2) f(\vec{u}_1)]. \quad (2.17)$$

Taking now the time derivative of (2.16) we obtain

$$\frac{dH(t)}{dt} = \int \frac{\partial f(t, \vec{u})}{\partial t} [1 + \ln(f(t, \vec{u}))] d^3 u, \quad (2.18)$$

from which it is easy to deduce that if  $\partial f / \partial t = 0$ , then also  $dH/dt = 0$ , that is,  $dH/dt = 0$  is a necessary condition for  $\partial f / \partial t = 0$ . What we need now is to show that the condition (2.14) is indeed equivalent to  $dH/dt = 0$ . We do this by substituting (2.17) in the integrand of (2.18) to obtain

$$\frac{dH(t)}{dt} = \int d^3 u_1 \int d^3 u_2 \int d\Omega \sigma(\Omega) |\vec{u}_1 - \vec{u}_2| (f'_2 f'_1 - f_2 f_1) (1 + \ln f_1), \quad (2.19)$$

where, for compactness, we have set  $f'_{1,2} = f(\vec{u}'_{1,2})$ , which should be the same if we swapped  $\vec{u}_1$  with  $\vec{u}_2$ , since the cross-section  $\sigma(\Omega)$  is invariant under this change. We can therefore consider the half-sum of the corresponding expressions and write it as

$$\frac{dH(t)}{dt} = \frac{1}{2} \int d^3 u_1 \int d^3 u_2 \int d\Omega \sigma(\Omega) |\vec{u}_2 - \vec{u}_1| (f'_2 f'_1 - f_2 f_1) [2 + \ln(f_1 f_2)]. \quad (2.20)$$

Now, since for each collision there is an inverse collision with the same cross-section, the integral (2.20) is invariant under change of  $\vec{u}_1, \vec{u}_2$  with  $\vec{u}'_1, \vec{u}'_2$  and consequently of the distribution functions  $f_2, f_1$  with  $f'_2, f'_1$ , and we can rewrite it as

$$\frac{dH(t)}{dt} = \frac{1}{2} \int d^3 u'_1 \int d^3 u'_2 \int d\Omega \sigma'(\Omega) |\vec{u}'_2 - \vec{u}'_1| (f_2 f_1 - f'_2 f'_1) [2 + \ln(f'_1 f'_2)]. \quad (2.21)$$

At this point we can note that

$$d^3 u'_1 d^3 u'_2 = d^3 u_1 d^3 u_2, \quad |\vec{u}_2 - \vec{u}_1| = |\vec{u}'_2 - \vec{u}'_1|, \quad \sigma(\Omega) = \sigma'(\Omega), \quad (2.22)$$

so that we can take the half-sum of (2.20) and (2.21) to obtain the needed expression

$$\begin{aligned} \frac{dH(t)}{dt} &= \frac{1}{4} \int d^3 u_1 \int d^3 u_2 \int d\Omega \sigma(\Omega) |\vec{u}_2 - \vec{u}_1| (f'_2 f'_1 - f_2 f_1) [\ln(f_1 f_2) - \ln(f'_1 f'_2)], \\ &= \frac{1}{4} \int d^3 u_1 \int d^3 u_2 \int d\Omega \sigma(\Omega) |\vec{u}_1 - \vec{u}_2| f'_2 f'_1 [(1-x) \ln x], \end{aligned} \quad (2.23)$$

where  $x := (f_1 f_2) / (f'_1 f'_2)$ . The integrand of (2.23) is never positive for  $x \geq 0$ , leading to the result that

$$\frac{dH}{dt} \leq 0. \quad (2.24)$$

Furthermore, since  $dH/dt = 0$  only when  $(f'_2 f'_1 - f_2 f_1) = 0$ , Eq. (2.23) proves the needed condition, namely that  $\partial f / \partial t = 0$  implies  $dH/dt = 0$ . Since this result holds for arbitrary initial conditions, including those of the equilibrium distribution,  $dH/dt = 0$  is also equivalent to  $f_0(\vec{u}'_2) f_0(\vec{u}'_1) - f_0(\vec{u}_2) f_0(\vec{u}_1) = 0$ , thus proving Eq. (2.14). In summary, we have shown that

$$f'_1 f'_2 - f_1 f_2 = 0 \iff \Gamma(f) = 0 \iff \frac{dH}{dt} = 0. \quad (2.25)$$

As anticipated above, there are several reasons why the  $H$ -theorem is important in a kinetic theory of fluids, and we can now discuss them in more detail. Firstly, through Eq. (2.14) it gives a condition for the functional form of the equilibrium distribution. The condition (2.13) can in fact be written as

$$\ln(f_0(\vec{u}'_1)) + \ln(f_0(\vec{u}'_2)) = \ln(f_0(\vec{u}_1)) + \ln(f_0(\vec{u}_2)), \quad (2.26)$$

thus expressing the equilibrium distribution function as a conservation law among the quantities before and after the collision. If  $\chi_j(\vec{u})$  is one of the  $N$  conserved quantities associated with the particle with velocity  $\vec{u}$  and such that  $\chi_j(\vec{u}_1) + \chi_j(\vec{u}_2)$  is conserved during a collision, then the most generic solution to Eq. (2.14) is

$$\ln(f_0(\vec{u})) = \sum_{j=1}^N \chi_j(\vec{u}). \quad (2.27)$$

For a simple classical monatomic fluid, the quantities to be conserved during collisions are the total momentum, the kinetic energy and the particle number, so that the equilibrium distribution will have the generic form

$$\ln(f_0(\vec{u})) = -A(\vec{u} - \vec{u}_0)^2 + \ln C, \quad (2.28)$$

or, equivalently,

$$f_0(\vec{u}) = C e^{-A(\vec{u} - \vec{u}_0)^2}. \quad (2.29)$$

As we will discuss in the next section, the functional form (2.29) can be used to derive the equilibrium distribution function in the case of a monatomic fluid of identical particles not subject to external forces. Secondly, the  $H$ -theorem provides, through expression (2.16), a definition for the *entropy* of the fluid in a volume  $V$

$$S(t) := -k_B V H(t) = -k_B V \int f(t, \vec{x}, \vec{u}) \ln(f(t, \vec{x}, \vec{u})) d^3 u, \quad (2.30)$$

and indeed  $H$  is the symbol originally adopted by Boltzmann for the entropy, from which the name of the theorem follows; in the next section we will use Eq. (2.30) to compute the entropy of a monatomic fluid in equilibrium.

## 78 A Kinetic-Theory Description of Fluids

Thirdly, the  $H$ -theorem provides, through expressions (2.30) and (2.24), a microscopic derivation of the second law of thermodynamics and hence a kinetic explanation of why entropy cannot decrease. Finally, it highlights the fact that if the system is momentarily set out of equilibrium,<sup>9</sup> so that  $dH/dt \neq 0$ , then the collisions in the system will bring it back to equilibrium, *i.e.*,  $dH/dt = 0$ , via (2.24) till the equilibrium condition is found again. Note that these considerations also imply that  $H$  is not necessarily a continuous function of time and therefore that the *irreversibility* of the transformation (2.24) is meant only in a statistical sense. It is always possible to imagine a configuration of the system which produces an increase of  $H$  at least locally in time; however, the role of the collisions in the Boltzmann equation is exactly that of ensuring that the subsequent evolution will lead to a decrease in  $H$ .

### 2.2.3 The moment equations

We continue our investigation of a single-component system with no internal degrees of freedom by extending the statistical and microscopic description based on the Boltzmann equation to derive the macroscopic equations which we can use when we want to describe our collections of particles as a fluid. To do this we need to introduce quantities which are *collisionally invariant*, that is, quantities that are conserved in binary collisions; of course mass, linear momentum and energy do satisfy such conservation laws in this simple system and are therefore collisionally invariant. The mathematical definition of collisional invariance is then rather straightforward and we can say that the generic quantity  $\psi$  has the property of being collisionally invariant if [see Section 5.2 of Huang (1987) for a proof]

$$\int \Gamma(f)\psi d^3u = 0, \quad (2.31)$$

where  $\Gamma$  is the *collision integral* in the Boltzmann equation (2.8). In other words, if we multiply the Boltzmann equation (2.8) by a collisionally invariant  $\psi$  and integrate over  $d^3u$ , the contribution of the collision term vanishes and we obtain the following *conservation* or (classical) *transport equation* for the density  $n\langle\psi\rangle$  (Huang, 1987)

$$\frac{\partial(n\langle\psi\rangle)}{\partial t} + \frac{\partial(n\langle u_i \psi \rangle)}{\partial x_i} - n \left\langle u_i \frac{\partial\psi}{\partial x_i} \right\rangle - \frac{n}{m} \left\langle F_i \frac{\partial\psi}{\partial u_i} \right\rangle - \frac{n}{m} \left\langle \frac{\partial F_i}{\partial u_i} \psi \right\rangle = 0, \quad (2.32)$$

where  $n\langle\psi\rangle = \langle n\psi \rangle$  because  $n$  does not depend on  $\vec{u}$ , and where we have selected a Cartesian coordinate system, which we will maintain for the rest of the chapter.<sup>10</sup> In Eq. (2.32) the quantity

$$\phi_i := n\langle u_i \psi \rangle = \int u_i \psi f d^3u \quad (2.33)$$

<sup>9</sup>Here the adjective “momentarily” emphasises the fact that, on average, the system is not subject to an external force.

<sup>10</sup>If  $\{\mathbf{e}_1, \mathbf{e}_2, \mathbf{e}_3\}$  are the unit vectors in a Cartesian coordinate system  $\{x^k\}$  and  $\{\mathbf{g}_1, \mathbf{g}_2, \mathbf{g}_3\}$  the corresponding unit vectors in a generic curvilinear coordinate system  $\{\xi^i\}$  (*e.g.*, a spherical polar system), then  $\mathbf{e}_i = J_{ik}\mathbf{g}_k$ , where  $J_{ik} := \partial\xi_i/\partial x_k$  is the Jacobian of the transformation matrix between the two coordinate systems, with  $i$  and  $k$  being indices of columns and rows, respectively. Using this relation between the basis vectors it is then possible to derive expressions for the differential operators acting on scalars and vectors in the coordinate system  $\{\xi^i\}$  [*see, e.g.*, Choudhuri (1998) for some explicit expressions and the discussion at the end of Section 1.3.5].

defines the *transport flux* of  $\psi$ , *i.e.*, the amount of  $\psi$  transported per unit time and unit area along the direction  $i$ . At this point, after assuming  $\vec{F}$  to be independent of velocity, we can replace  $\psi$  in Eq. (2.32) with the collisional invariants  $m$ ,  $mu_j$  and  $\frac{1}{2}m|\vec{u} - \vec{v}|^2$ , respectively, to find the following three equations

$$\frac{\partial \rho}{\partial t} + \frac{\partial(\rho v_i)}{\partial x_i} = 0, \quad (2.34)$$

$$\frac{\partial(\rho v_j)}{\partial t} + \frac{\partial(\rho v_i v_j)}{\partial x_i} + \frac{\partial P_{ij}}{\partial x_i} - \frac{\rho}{m} F_j = 0, \quad (2.35)$$

$$\frac{\partial(\rho \epsilon)}{\partial t} + \frac{\partial(\rho \epsilon v_i)}{\partial x_i} + \frac{\partial q_i}{\partial x_i} + P_{ij} \Lambda^{ij} = 0, \quad (2.36)$$

where, using the first equation, the last two can also be written in the more common form

$$\frac{\partial v_j}{\partial t} + v_i \frac{\partial v_j}{\partial x_i} + \frac{1}{\rho} \frac{\partial P_{ij}}{\partial x_i} - \frac{1}{m} F_j = 0, \quad (2.37)$$

$$\frac{\partial \epsilon}{\partial t} + v_i \frac{\partial \epsilon}{\partial x_i} + \frac{1}{\rho} \frac{\partial q_i}{\partial x_i} + \frac{1}{\rho} P_{ij} \Lambda^{ij} = 0. \quad (2.38)$$

There are a number of new quantities introduced in the equations above that need a definition. The first one is the *density*, or mass per unit volume,

$$\rho := nm, \quad (2.39)$$

a quantity that we will encounter repeatedly in the rest of the book, and whose conservation is expressed by Eq. (2.34), where we have used the property  $\langle m \rangle = m$ , as we are considering a fluid of identical particles.

Equation (2.35) expresses instead the conservation of linear momentum through the evolution of the *momentum flux*  $\rho v_j$  (*i.e.*, the rate of change of linear momentum per unit time and unit area), where the symmetric tensor  $P_{ij}$ , referred to as the *pressure tensor*, is defined through the peculiar velocities of the particles as

$$P_{ij} := \rho \langle (u_i - v_i)(u_j - v_j) \rangle = \rho \langle u_i u_j \rangle - v_i v_j. \quad (2.40)$$

The pressure tensor  $P_{ij}$  is a generalisation of the isotropic pressure scalar and accounts for the transport of linear momentum. It is nonzero even when the fluid is at rest ( $\vec{v} = 0$ ) and should be contrasted with the term  $\rho v_i v_j$  in Eq. (2.35), which represents instead the transport of linear momentum associated with a global mass flow and which therefore vanishes if  $\vec{v} = 0$ .

Equation (2.36), on the other hand, expresses the evolution of the *specific internal energy* of the fluid, defined as

$$\epsilon := \frac{1}{2} \langle |\vec{u} - \vec{v}|^2 \rangle = \frac{1}{2n} \int |\vec{u} - \vec{v}|^2 f d^3 u. \quad (2.41)$$

Equation (2.36) contains another symmetric second-order tensor, the *strain tensor*  $\Lambda_{ij}$ , defined as

$$\Lambda_{ij} := \frac{1}{2} \left( \frac{\partial v_i}{\partial x_j} + \frac{\partial v_j}{\partial x_i} \right), \quad (2.42)$$

which describes the rate of *strain* in the fluid (see also Fig. 3.2 for a schematic diagram). Note that, unlike the *kinetic energy*,  $\frac{1}{2}\rho v^i v_i$ , the specific internal energy is not related to the macroscopic bulk motion of the fluid. Rather, it accounts for the “internal” motions of the particles and it depends on factors such as the intermolecular potentials, the vibrational states, etc., or, simply, on the state of agitation of the molecules. Finally, we define the *heat flux* vector as

$$\vec{q} := \frac{1}{2} \rho \langle (\vec{u} - \vec{v}) |\vec{u} - \vec{v}|^2 \rangle, \quad (2.43)$$

that is zero only for uniform velocity distributions, in which case  $\vec{u} = \vec{v}$ .

Equations (2.34)–(2.36) are often referred to as the *moment equations* of the Boltzmann equation because they can be obtained by multiplying the Boltzmann equation by the zeroth, the first and the second powers of the velocity, and integrating over the velocity space. The same equations, but for multicomponent systems, are reported by Battaner (1996).

Before concluding this section, two remarks are worth making. The first one is about the differential operator acting on the first two terms in Eqs. (2.37)–(2.38), which is usually called the *Lagrangian derivative* (or *convective derivative* or *material derivative*), since it describes the changes as measured by a *Lagrangian observer*, *i.e.*, an observer moving with the fluid velocity  $\vec{v}$ <sup>11</sup>

$$\frac{D}{Dt} := \left( \frac{\partial}{\partial t} + \vec{v} \cdot \vec{\nabla} \right) = \left( \frac{\partial}{\partial t} + \vec{v} \cdot \frac{\partial}{\partial \vec{x}} \right), \quad (2.44)$$

where the second equality is valid only in a Cartesian coordinate system. The integral curves of the differential equation  $Dx^i/Dt = v^i$  represent the trajectories of the fluid elements as they evolve in time. We call these spacetime trajectories *fluidlines*, since they represent for fluid elements the equivalent of the *worldlines* for test particles. In addition, we refer to the spatial projections of the fluidlines as *streamlines* (or *flowlines*), so that a flow is called *laminar* if the streamlines do not intersect and the flow is *stationary* if the streamlines do not change in time. Note also that while streamlines can be closed, fluidlines cannot, and that the four-velocity  $\vec{u}$  is the tangent vector for fluidlines, while the three-velocity  $\vec{v}$  is the tangent vector for streamlines. Although Newtonian, these definitions extend unmodified also to a relativistic context and a schematic representation of streamlines and fluidlines is shown in Fig. 2.4.

The second remark is that the moment equations are of very limited practical importance, since they include quantities such as the tensors  $P_{ij}$ ,  $\Lambda_{ij}$  etc., that are unknown unless one solves the Boltzmann equation to obtain the distribution function. If, on the other hand, the distribution function is locally of equilibrium (such as the local Maxwellian that we will introduce in the next section), then Eqs. (2.34)–(2.36) yield a genuine system of *hydrodynamic equations*.

<sup>11</sup>The concept of a Lagrangian observer should be contrasted with that of an *Eulerian observer*, who is instead at a fixed spatial location; see Section 7.1.

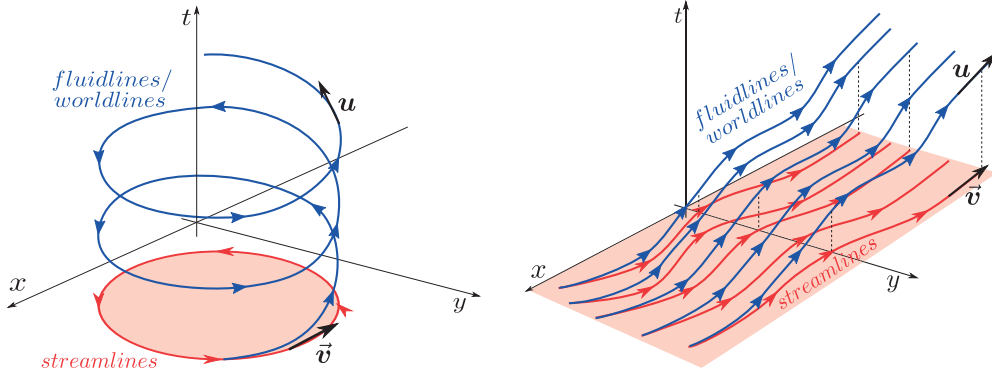


**Fig. 2.4** Schematic diagram illustrating the differences between the fluidlines (or worldlines) and their spatial projections, *i.e.*, the streamlines. Note that streamlines can be closed, while the worldlines cannot (in general), and that the flow is laminar if the streamlines do not intersect. Note also that the four-velocity  $\mathbf{u}$  is the tangent vector for fluidlines, while the three-velocity  $\vec{v}$  is the tangent vector for streamlines.

## 2.2.4 The Maxwell–Boltzmann equilibrium distribution

The equilibrium distribution function describing single-component systems, *e.g.*, a monatomic<sup>12</sup> fluid of identical particles, for which the effects of external forces are negligible, *i.e.*,  $\vec{F} = 0$ , is represented by the *Maxwell–Boltzmann distribution*. In such conditions, we can exploit the results of the *H*-theorem discussed in Section 2.3.3, and search for a distribution function in the form (2.29). The unknown coefficients can be determined after using the following integral identities

$$\int_{-\infty}^{\infty} e^{-A\bar{u}^2} d^3u = \frac{\pi^{3/2}}{A^{3/2}}, \quad \int_{-\infty}^{\infty} \bar{u} e^{-A\bar{u}^2} d^3u = 0, \quad \int_{-\infty}^{\infty} \bar{u}^2 e^{-A\bar{u}^2} d^3u = \frac{3}{2} \frac{\pi^{3/2}}{A^{5/2}}, \quad (2.45)$$

to compute the particle number density  $n$  as defined by Eq. (2.11). In this way we obtain that

$$A = \frac{3}{4\epsilon}, \quad C = n \left( \frac{3}{4\pi\epsilon} \right)^{3/2}. \quad (2.46)$$

Recalling now that a *classical monatomic fluid* obeys the following (experimental) laws

$$\epsilon = \frac{3}{2} \frac{k_B T}{m}, \quad p = \frac{2}{3} \frac{\epsilon}{nm} = nk_B T, \quad (2.47)$$

where  $T$  is the *temperature* and  $k_B = 1.3807 \times 10^{-16}$  erg K<sup>-1</sup> is the *Boltzmann constant*, we can write the explicit expression for the *Maxwell–Boltzmann distribution* (or simply *Maxwellian*) as

<sup>12</sup>Particles (atoms) in a monatomic fluid have only translational motions, thus corresponding to three degrees of freedom. In polyatomic fluids particles (molecules) also have rotational and vibrational degrees of freedom, and the associated energies.

$$f_0(\vec{u}) = n \left( \frac{m}{2\pi k_B T} \right)^{3/2} \exp \left( -\frac{m(\vec{u} - \vec{v})^2}{2k_B T} \right). \quad (2.48)$$

Clearly, the distribution (2.48) satisfies the condition  $\partial f_0 / \partial t = 0$  and represents the distribution function of the velocity *vector*,  $\vec{u}$  [not to be confused with the distribution function for the velocity *norm*,  $|\vec{u}|$ , which we will instead discuss to derive the average velocity in (2.57)], of a monatomic fluid in equilibrium and not subject to external forces.

It is useful to distinguish expression (2.48), which is usually referred to as the *absolute Maxwellian*, from the corresponding distribution function in which the three thermodynamic quantities  $n$ ,  $T$  and  $\vec{u}$  are functions of time and space, *i.e.*,

$$f(t, \vec{x}, \vec{u}) = n(t, \vec{x}) \left( \frac{m}{2\pi k_B T(t, \vec{x})} \right)^{3/2} \exp \left( -\frac{m(\vec{u}(t, \vec{x}) - \vec{v})^2}{2k_B T(t, \vec{x})} \right). \quad (2.49)$$

The distribution (2.49) is referred to as the *local Maxwellian* and, when considered at different times, describes the transition through a sequence of local quasi-equilibrium states that lead to the state of constant macroscopic thermodynamic variables in (2.48). The interested reader will find additional details on this aspect in Liboff (2003).

Having now an equilibrium distribution function, we can afford a number of considerations. First, it is possible to extend the average (2.12) and compute the velocity variance or *root mean square velocity*  $\vec{v}_{\text{rms}}$  as

$$\vec{v}_{\text{rms}}^2 := \langle \vec{u}^2 \rangle = \frac{1}{n} \int \vec{u}^2 f d^3 u. \quad (2.50)$$

Note that in analogy with (2.12), Eq. (2.50) represents the second moment of the distribution function  $f$ . Using now the identities (2.45) and the Maxwell–Boltzmann distribution  $f_0$ , it is possible to rewrite (2.50) as

$$\langle \vec{u}^2 \rangle = \frac{3k_B T}{m} - \langle \vec{u} \rangle^2 = \frac{3k_B T}{m} - \vec{v}^2, \quad (2.51)$$

and thus obtain a “kinetic expression” for the temperature  $T$ , that is an expression in terms of the microscopic and statistical properties of the system

$$T = \frac{m}{3k_B} (\langle \vec{u}^2 \rangle - \langle \vec{u} \rangle^2) = \frac{m}{3k_B} (\vec{v}_{\text{rms}}^2 - \vec{v}^2). \quad (2.52)$$

Equation (2.52) hints at two important remarks. First of all, it clarifies that the temperature as a thermodynamic quantity really reflects a measure of the kinetic energy associated with the velocity dispersion in the system; in a system without a preferred translational velocity (*i.e.*,  $\vec{v}$ ), this measure is simply given by the root mean square velocity. Second, for a generic system which is also “flowing” globally in some direction, the definition of the temperature takes into account this motion by removing the temperature associated with the global motion (*i.e.*,  $\propto \vec{v}^2$ ). Hence, any sensible measurement of the properties of a fluid system needs to be performed in a reference frame that is (instantaneously) *comoving* with it, *i.e.*, in its local Lorentz rest frame. We will return to this point later on in this book.

There are a few more quantities that are worth computing from the Maxwell–Boltzmann distribution function and to do this it is better to express the distribution not in terms of the velocity vector  $\vec{u}$ , but rather in terms of the velocity norm  $u := |\vec{u}|$ . Bearing in mind that for any distribution function

$$\int_{-\infty}^{\infty} f(\vec{u}) d^3u = \int_0^{2\pi} d\phi \int_0^{\pi} \sin \theta d\theta \int_0^{\infty} u^2 f(u) du = 4\pi \int_0^{\infty} u^2 f(u) du, \quad (2.53)$$

it is possible to express the distribution function for  $f_0(\vec{u})$  in terms of the distribution of the velocity norm for a system of particles with zero translational velocity, *i.e.*, to write the following identity  $f_0(\vec{u}) d^3u = f_0(u) u^2 du d\theta d\phi$ , where

$$f_0(u) = 4\pi n u^2 \left( \frac{m}{2\pi k_B T} \right)^{3/2} \exp \left( -\frac{mu^2}{2k_B T} \right). \quad (2.54)$$

Using now the distribution function (2.54) and the results on the  $H$ -theorem, we can compute the equilibrium entropy of a monatomic fluid of  $N$  particles occupying a finite volume  $V$  as [*cf.* Eq. (2.30)]

$$\begin{aligned} S &:= -k_B V H_0 = -k_B \frac{N}{n} \int f_0 \ln(f_0) d^3u \\ &= \frac{3}{2} N k_B \ln \left( p V^{5/3} \right) + \text{const.}, \end{aligned} \quad (2.55)$$

where we have used the identity

$$H_0 = 4\pi \int_0^{\infty} u^2 f_0 \ln(f_0) du = n \left\{ \ln \left[ n \left( \frac{m}{2\pi k_B T} \right)^{3/2} \right] - \frac{3}{2} \right\}. \quad (2.56)$$

We can also compute the *average speed* as

$$v := \langle u \rangle = \frac{4\pi}{n} \int_0^{\infty} u^3 f_0 du = \left( \frac{8k_B T}{\pi m} \right)^{1/2}. \quad (2.57)$$

Similarly, it is possible to compute the *most probable velocity* in the system  $u_p$  as the one corresponding to the maximum of the distribution function; a little bit of algebra then yields

$$u_p = \left( \frac{2k_B T}{m} \right)^{1/2}. \quad (2.58)$$

Note that although  $(\langle \vec{u}^2 \rangle)^{1/2}$ ,  $\langle u \rangle$  and  $u_p$  correspond to three distinct measures of the velocities in the system, they are all of the order of  $\sqrt{k_B T/m}$ . To fix ideas, for a fluid of oxygen molecules at room temperature, the representative velocity is  $\sim \sqrt{k_B T/m} \simeq 10^5 \text{ cm s}^{-1}$  and we show in Fig. 2.5 examples of the Maxwell–Boltzmann distribution at different temperatures when the number density is taken to be  $n = 1.0 \times 10^{19} \text{ cm}^{-3}$ . It is also useful to compute the temperature at which relativistic corrections are needed, *i.e.*, when  $k_B T/m \simeq c^2$ ; using the same oxygen molecule, it is easy to realise that this happens for  $T \simeq 10^{13} \text{ K}$ .

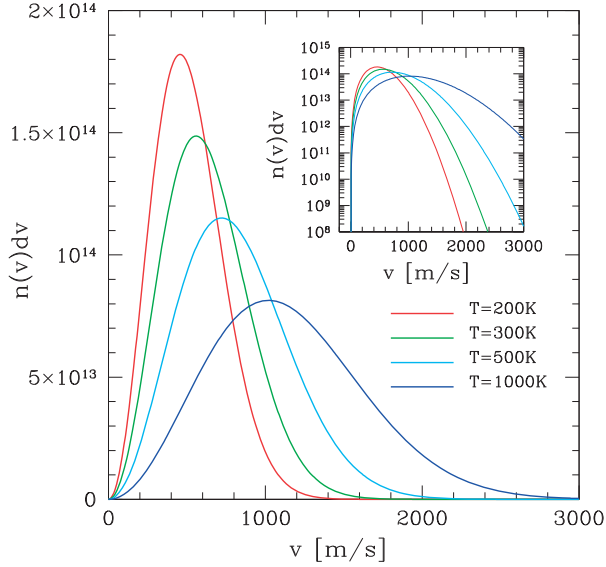


**Fig. 2.5** Examples of the Maxwell–Boltzmann distribution (2.54) at different temperatures for a fluid of molecular oxygen with constant number density  $n = 1.0 \times 10^{19} \text{ cm}^{-3}$ . The inset shows the distributions on a logarithmic scale.

As a final remark for this section, we note that an alternative expression for the temperature is given by

$$T = \frac{mn}{3k_B} \int (\vec{u} - \vec{v})^2 f_0 d^3 u = \frac{m}{3k_B} \langle (\vec{u} - \vec{v})^2 \rangle. \quad (2.59)$$

Although Eq. (2.59) is of course equivalent to Eq. (2.52), it has the advantage of highlighting that the temperature is effectively a measure of the *variance* of the particle’s velocity relative to an average translational one (Problem 1 is dedicated to showing the equivalence between the two expressions).

### 2.2.5 The zero-order approximation: perfect fluids

As mentioned in the previous section, the moment equations (2.34)–(2.36) are general but of limited use if we do not know the distribution function of the particles in the system. However, we can assume that such a distribution function is given by the Maxwell–Boltzmann distribution and hence work within the so-called *zero-order approximation*. Hence, we can compute  $\Lambda_{ij}$ ,  $q_i$  and  $P_{ij}$  in Eqs. (2.34)–(2.36) after setting  $f(t, \vec{x}, \vec{u}) \simeq f_0(t, \vec{x}, \vec{u})$ , where  $f_0(t, \vec{x}, \vec{u})$  is the Maxwell–Boltzmann distribution (2.48).

There are two key assumptions underlying the *zero-order approximation*. The first one is that there is a large number of collisions between particles within the system. This happens when the *mean free path*  $\ell_{\text{mfp}}$ , that is, the average distance covered by a particle between two collisions, is much smaller than the typical length-scale  $L$  of the system or, equivalently, when

the *Knudsen number* is  $K_n \ll 1$  [see Section 2.1]. Such fluids are commonly referred to as *collisional fluids* to distinguish them from *collisionless fluids*, for which either the mean free path is much larger than  $L$  or the mean time between collisions is much longer than the typical time-scale of the system.

The second assumption is that, as a result of these frequent collisions, the system will reach a local equilibrium approximated by the local Maxwellian (2.49) on a time-scale of the order of  $\ell_{\text{mfp}}/v$ , where  $v$  is the typical particle velocity. This assumption expresses the concept of *Local Thermodynamic Equilibrium (LTE)*, *i.e.*, an idealisation that allows us to use the moment equations and the local Maxwellian distribution function to calculate transport fluxes and then obtain a dynamical theory for the system. This thermodynamic equilibrium is however valid only locally and the distribution function can depend on temperature, density and average velocity that vary slowly in space and time. It is indeed the possibility of defining such spatial and temporal scales below which our system is in LTE, that allows us to make use of the hydrodynamic description.

With this clarification in mind, we now use the local Maxwellian distribution (2.49) to calculate some of the quantities appearing in the moment equations. We begin by calculating  $P_{ij}$  and  $\vec{q}$  from their definitions (2.40) and (2.43) as

$$P_{ij} = \rho \left( \frac{m}{2\pi k_B T} \right)^{3/2} \int w_i w_j \exp \left( -\frac{mw^2}{2k_B T} \right) d^3 w, \quad (2.60)$$

$$\vec{q} = \frac{\rho}{2} \left( \frac{m}{2\pi k_B T} \right)^{3/2} \int \vec{w} w^2 \exp \left( -\frac{mw^2}{2k_B T} \right) d^3 w, \quad (2.61)$$

where we have introduced the *peculiar velocity*

$$\vec{w} := \vec{u} - \vec{v}, \quad w := |\vec{w}|. \quad (2.62)$$

Given that the integration is performed in the whole range of velocities, the integral vanishes when the integrand is an odd function of  $w$ . This immediately implies that the energy flux  $\vec{q} = 0$ , while

$$P_{ij} = p \delta_{ij}, \quad (2.63)$$

where

$$p = \frac{1}{3} \rho \left( \frac{m}{2\pi k_B T} \right)^{3/2} \int w^2 \exp \left( -\frac{mw^2}{2k_B T} \right) d^3 w = nk_B T \quad (2.64)$$

is the *isotropic pressure* which, by construction, satisfies the pressure law (2.47) for monatomic fluids.

It is important to remark that the concept of isotropic pressure, which appears very obvious in our daily experience, is effectively the result of considering a Maxwell–Boltzmann distribution in which the pressure tensor  $P_{ij}$  is diagonal with diagonal elements given by  $p$ . In more generic situations, however, such as those involving viscous fluids and discussed in the following section, the pressure tensor can be arbitrarily complex, giving rise to non-isotropic transport of linear momentum.

## 86 A Kinetic-Theory Description of Fluids

We are now ready to express the system (2.34)–(2.36) as a closed system of equations governing the dynamics of the fluid. We start with the equation of conservation of mass, or *continuity equation* (2.34), which we write in vector form as

$$\frac{\partial \rho}{\partial t} + \vec{\nabla} \cdot (\rho \vec{v}) = 0. \quad (2.65)$$

Next, by substituting  $P_{ij}$  in Eq. (2.37) and writing it in vector form we obtain the equation of conservation of linear momentum, or *Euler equations*

$$\frac{\partial \vec{v}}{\partial t} + (\vec{v} \cdot \vec{\nabla}) \vec{v} = -\frac{1}{\rho} \vec{\nabla} p + \frac{\vec{F}}{m}. \quad (2.66)$$

Finally, by replacing  $\vec{q}$  and  $\epsilon$  in Eq. (2.38), we obtain the equation of conservation of energy, or *internal energy equation*

$$\rho \left( \frac{\partial \epsilon}{\partial t} + \vec{v} \cdot \vec{\nabla} \epsilon \right) + p \vec{\nabla} \cdot \vec{v} = 0, \quad (2.67)$$

where we have used  $P_{ij} \Lambda^{ij} = p \vec{\nabla} \cdot \vec{v}$ . Equations (2.65)–(2.67) represent a system of five equations describing the evolution of the five independent variables of the system: the three components of the fluid velocity  $\vec{v}$  and two out of three thermodynamic variables  $\rho$ ,  $p$  and  $\epsilon$ , with the third one being computed via a relation involving two of these variables, *i.e.*, via an equation of state.

The equation for the specific internal energy, (2.67), can be used to derive an equation for the evolution of the *Newtonian total energy density*  $e_N$ , which includes an internal-energy contribution ( $\propto \rho \epsilon$ ) and a kinetic energy one ( $\propto \rho \vec{v}^2$ ), *i.e.*,

$$e_N := \rho \epsilon + \frac{1}{2} \rho \vec{v}^2. \quad (2.68)$$

To this extent, it is necessary to multiply the momentum equation (2.66) by  $\vec{v}$ , which, after exploiting the continuity equation, yields

$$\frac{\partial}{\partial t} \left( \frac{1}{2} \rho \vec{v}^2 \right) + \vec{\nabla} \cdot \left( \frac{1}{2} \rho \vec{v}^2 \vec{v} \right) + \vec{v} \cdot \vec{\nabla} p = \frac{\rho}{m} \vec{F} \cdot \vec{v}. \quad (2.69)$$

Adding now (2.69) to (2.67), and using once again the continuity equation, we finally obtain the conservation equation for the total energy density

$$\frac{\partial}{\partial t} \left( \frac{1}{2} \rho \vec{v}^2 + \rho \epsilon \right) + \vec{\nabla} \cdot \left[ \left( \frac{1}{2} \rho \vec{v}^2 + \rho \epsilon + p \right) \vec{v} \right] = \frac{\rho}{m} \vec{F} \cdot \vec{v}, \quad (2.70)$$

where the term  $(\frac{1}{2} \rho \vec{v}^2 + \rho \epsilon + p) \vec{v}$  represents the flux of energy per unit surface and per unit time, *i.e.*, the *Newtonian energy flux density vector*. Equations (2.65)–(2.66) and (2.70) represent the building blocks of classical (Newtonian) hydrodynamics<sup>13</sup> and because of their non-linear nature, they rarely yield exact solutions. There are however some interesting analytic

<sup>13</sup>It is not uncommon that Eqs. (2.65)–(2.66) and (2.70) are indicated simply as the “*Euler equations*”. However, because the latter refer only to the conservation of momentum, hereafter we will distinguish the “*hydrodynamic equations*” (which express the conservation of mass, momentum and energy) from the “*Euler equations*”. This distinction will be kept also when extending these concepts to a relativistic framework.

examples that can be obtained in rather general conditions of stationarity, or of irrotational flow, that we will consider in detail in the following chapter, both in Newtonian and in relativistic regimes.

We conclude with an important remark on the title of this section. Hereafter we will define *perfect fluids* as those fluids described by the moment equations (2.34)–(2.36) in the zero-order approximation given by the equilibrium distribution (2.48). As a consequence, perfect fluids are such that the viscous effects and heat fluxes are zero, and the pressure tensor is diagonal. In Section 2.3.6 we will see that the same properties will continue to be present also when extending the concept of perfect fluids to a relativistic regime.

### 2.2.6 The first-order approximation: non-perfect fluids

As an improvement over the zero-order approximation we can consider averaging over a distribution function  $g(t, \vec{x}, \vec{u}) = f(t, \vec{x}, \vec{u}) - f_0(t, \vec{x}, \vec{u})$ , where  $f(t, \vec{x}, \vec{u})$  is the exact distribution and  $f_0(t, \vec{x}, \vec{u})$  the usual Maxwell–Boltzmann one. This is also known as the *first-order approximation* and provides a description for *non-perfect fluids*. In this case, the true distribution function has to be expanded in powers of  $\ell_{\text{mfp}}/L$  through the so-called *Chapman–Enskog expansion* (Chapman and Cowling, 1970) so as to obtain the *Navier–Stokes equations*, which extend the perfect-fluid equations (2.65)–(2.67) to the case of true transport phenomena. We will not provide here a detailed derivation of these equations, mostly because while the derivation of the inviscid relativistic hydrodynamic equations exploits several analogies with the Newtonian treatment, the same is not true in the viscous case. In fact, the derivation of the relativistic equations for non-perfect fluids follows a different strategy and a comparison with the Newtonian framework is more misleading than illuminating. This will become apparent in Chapter 6, where we specifically treat the case of non-perfect fluids in relativity.

Nevertheless, given the importance of these equations, which are widely used in classical hydrodynamics, we report them below as an extension of Eqs. (2.65)–(2.67) to fluids that are not perfect, and we will re-encounter them in Chapter 6 when taking the Newtonian limit of the corresponding equations of relativistic hydrodynamics (see Section 6.4.2).

An essential first step in formulating the Navier–Stokes equations is the generalisation of the pressure tensor to include, in addition to the inviscid diagonal part  $p\delta_{ij}$ , also a viscous contribution, namely

$$P_{ij} := p\delta_{ij} - S_{ij}, \quad (2.71)$$

where the symmetric tensor  $S_{ij}$  is referred to as the *viscous stress tensor*, or simply *stress tensor*. This is defined as

$$\begin{aligned} S_{ij} &:= \eta \left[ \frac{\partial v_j}{\partial x_i} + \frac{\partial v_i}{\partial x_j} - \frac{2}{3} \left( \frac{\partial v_k}{\partial x_k} \right) \delta_{ij} \right] + \zeta \left( \frac{\partial v_k}{\partial x_k} \right) \delta_{ij} \\ &= 2\eta \Lambda_{ij} + \left( \zeta - \frac{2}{3}\eta \right) \theta \delta_{ij}, \end{aligned} \quad (2.72)$$

where we have introduced the fluid *expansion scalar* (or simply *expansion*; see also Fig. 3.2 for a schematic diagram)

$$\theta := \frac{\partial v_k}{\partial x_k}. \quad (2.73)$$

## 88 A Kinetic-Theory Description of Fluids

The coefficients  $\eta$ ,  $\zeta$  and  $\lambda := \zeta - \frac{2}{3}\eta$ , appearing in (2.72) to parameterise the rate of strain and the fluid expansion are usually referred to as the coefficients of *shear*, *bulk* and *dilatational viscosity*, respectively.<sup>14</sup> Note also that the stress and the strain tensors,  $S_{ij}$  and  $\Lambda_{ij}$ , are not independent and that the former is a more general tensor, with its diagonal terms accounting also for the changes related to the expansion, which are absent in the strain tensor.

The evolution equations derived from the moment equations (2.34)–(2.36) in the first-order approximation are then given by

$$\text{(continuity equation)} \quad \frac{\partial \rho}{\partial t} + \frac{\partial(\rho v_i)}{\partial x_i} = 0, \quad (2.74)$$

$$\begin{aligned} \text{(Navier-Stokes equation)} \quad & \frac{\partial v_j}{\partial t} + v_i \frac{\partial v_j}{\partial x_i} + \\ & \frac{1}{\rho} \left\{ \frac{\partial p}{\partial x_j} - \frac{\partial}{\partial x_i} \left[ \eta \left( \frac{\partial v_j}{\partial x_i} + \frac{\partial v_i}{\partial x_j} - \frac{2}{3} \delta_{ij} \frac{\partial v_k}{\partial x_k} \right) + \zeta \left( \frac{\partial v_k}{\partial x_k} \right) \delta_{ij} \right] \right\} - \frac{1}{m} F_j = 0, \end{aligned} \quad (2.75)$$

$$\begin{aligned} \text{(heat-conduction equation)} \quad & \frac{\partial \epsilon}{\partial t} + v_i \frac{\partial \epsilon}{\partial x_i} + \frac{1}{\rho} \frac{\partial q_i}{\partial x_i} + \frac{1}{\rho} P_{ij} \Lambda^{ij} = \\ & \frac{\partial \epsilon}{\partial t} + v_i \frac{\partial \epsilon}{\partial x_i} + \frac{1}{\rho} \frac{\partial q_i}{\partial x_i} + \frac{p}{\rho} \left( \frac{\partial v_k}{\partial x_k} \right) - \frac{2\eta}{\rho} \Lambda_{ij} \Lambda^{ij} - \frac{1}{\rho} \left( \zeta - \frac{2}{3}\eta \right) \left( \frac{\partial v_k}{\partial x_k} \right)^2 = 0. \end{aligned} \quad (2.76)$$

Note that in deriving the *heat-conduction equation* (2.76), only terms containing first-order derivatives have been retained. In addition, if we write the *heat flux* in what is also known as the *Fourier law*, *i.e.*, as

$$\vec{q} = -\kappa \vec{\nabla} T, \quad (2.77)$$

where  $\kappa$  is the coefficient of *thermal conductivity*, we find that for a static and incompressible fluid, *i.e.*,  $\vec{u} = 0$ ,  $\theta = 0$ , the heat-conduction equation (2.76) reduces to

$$\frac{\partial T}{\partial t} = \frac{2m}{3k_B\rho} \vec{\nabla} \cdot (\kappa \vec{\nabla} T) = \frac{2m\kappa}{3k_B\rho} \nabla^2 T, \quad (2.78)$$

which is the well-known *heat-diffusion equation* (see also Section 6.6.2 for its extension to a relativistic regime). It should be remarked that since we have neglected terms containing derivatives of order higher than the first, the second equality in (2.78) is correct even when the thermal conductivity  $\kappa$  is not uniform in space [see the discussion in Huang (1987)].

The introduction of the thermal conductivity  $\kappa$  and of the viscosity coefficients  $\eta$ ,  $\zeta$ , gives us the opportunity to clarify the different definitions of a fluid that are possible in combination with the different values assumed by  $\kappa$ ,  $\eta$ ,  $\zeta$ . We will hereafter define respectively as *perfect*, *non-perfect*, *inviscid* and *viscous* fluids with the following properties

<sup>14</sup>Note that some authors, most notably Landau and Lifshitz (1980), define the *stress tensor*  $\tilde{\Sigma}_{ij}$  as the opposite of the pressure tensor, *i.e.*,  $\tilde{\Sigma}_{ij} := -P_{ij}$ .

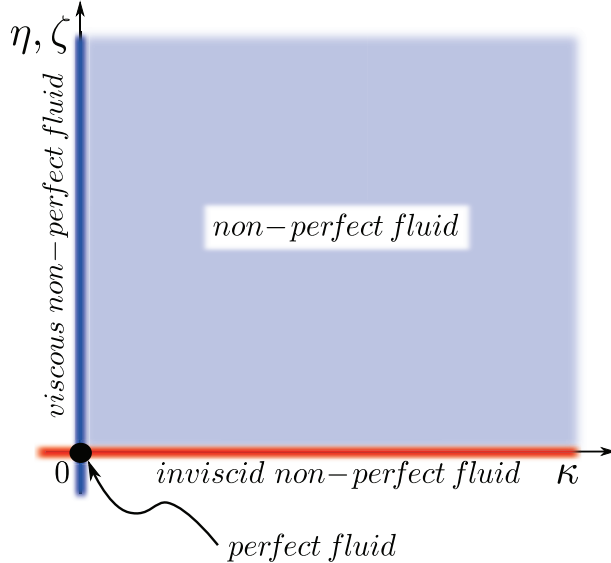


**Fig. 2.6** Schematic classification of fluids according to the values of the thermal conductivity  $\kappa$  and of the viscosity coefficients  $\eta, \zeta$ . Note that non-perfect fluids collect a large class of fluids and that a perfect fluid represents a rather special subclass [see also the scheme (2.79)].

$$\begin{aligned}
 \kappa = 0, \text{ and } \eta = 0, \text{ and } \zeta = 0 : & \quad \text{perfect fluid;} \\
 \kappa \neq 0, \text{ or } \eta \neq 0, \text{ or } \zeta \neq 0 : & \quad \text{non-perfect fluid;} \\
 \kappa \neq 0; \quad \eta = 0, \text{ and } \zeta = 0 : & \quad \text{inviscid non-perfect fluid;} \\
 \kappa = 0; \quad \eta \neq 0, \text{ or } \zeta \neq 0 : & \quad \text{viscous non-perfect fluid.}
 \end{aligned} \tag{2.79}$$

As summarised in the scheme above and in Fig. 2.6, a perfect fluid has all coefficients that are zero (hence it is “perfect”) and represents a very specific subclass of fluids, which are in general non-perfect. Indeed, it is sufficient that only one of these coefficients is nonzero for the fluid to be “non-perfect”. Also, while an inviscid fluid and a viscous fluid are both non-perfect fluids, they will have different dynamics since the first one has a diagonal stress tensor.<sup>15</sup>

### 2.3 Relativistic kinetic theory

The origin of relativistic kinetic theory dates back to 1911, when Jüttner (1911) derived the Maxwell–Boltzmann equilibrium distribution for a relativistic fluid. Fundamental references on the relativistic formulation of kinetic theory are the monographs by Stewart (1971), Ehlers (1971) and Groot *et al.* (1980), or, more recently, those by Mueller and Ruggeri (1998), Cercignani and Kremer (2002), and Liboff (2003). In the following we present the basic concepts

<sup>15</sup>In view of the similarities with the properties of ideal gases, some authors call “ideal fluids” what we refer to as perfect fluids. Here, instead, we call “ideal fluids” those fluids that obey the “ideal-fluid” equation of state presented in Section 2.4.6. Also, some authors use “dissipative fluid” as a synonym of non-perfect fluid, although this is not entirely correct since a non-perfect fluid can be simply inviscid and non-dissipative (see Fig. 2.6).

## 90 A Kinetic-Theory Description of Fluids

of relativistic kinetic theory in flat spacetime providing an amount of detail sufficient to preserve a consistent picture of the kinetic approach to relativistic fluids, but omitting most of the proofs and mathematical details, which can however be found in the references listed above.

### 2.3.1 The relativistic Boltzmann equation

We start by indicating with  $x^\mu$  and  $p^\mu = mcu^\mu = (p^0, p^i)$  the spacetime coordinates and the four-momentum<sup>16</sup> of a particle of rest mass  $m$ , the latter normalised such that  $p^\mu p_\mu = -m^2c^2$ . As in the Newtonian description, a distribution function  $f$  can be defined such that the quantity

$$f d^3x d^3p = f dx^1 dx^2 dx^3 dp^1 dp^2 dp^3 \quad (2.80)$$

gives the number of particles in a given volume element in the six-dimensional phase space  $d^3x d^3p$ . Consider now an observer  $\mathcal{O}'$  comoving with the particle, and a second observer  $\mathcal{O}$  moving with a speed  $\vec{v}$  with respect to  $\mathcal{O}'$ , where we assume that the three-vector  $\vec{v}$  is aligned with the  $x$ -axis. As a result of the Lorentz contraction of lengths that follows from (1.105), one can find that the proper volume  $d^3x'$  measured by  $\mathcal{O}'$  is given by

$$d^3x' = W d^3x, \quad (2.81)$$

where  $W$  is the Lorentz factor between the two observers (see Section 1.4), and that (see Problem 4 of Chapter 1)

$$\frac{d^3p'}{p_{0'}} = \frac{d^3p}{p_0}, \quad (2.82)$$

namely, that the ratio  $d^3p/p_0$  is a *Lorentz invariant*. Using now the standard transformation law  $p_\mu = \Lambda^{\nu'}_\mu p_{\nu'}$  with  $\Lambda^{\nu'}_\mu$  given by the Lorentz matrix (1.108), and recalling that  $p'_x = 0$  in the local Lorentz rest frame, we obtain  $p_{0'} = p_0/W$ . Finally, combining (2.81) with (2.82), we obtain the desired result that

$$d^3x' d^3p' = d^3x d^3p. \quad (2.83)$$

Stated differently, while  $d^3x$  is not a Lorentz invariant, the product  $d^3x d^3p$  is a Lorentz invariant; furthermore, given that the two observers must agree on the number of particles in the volume element, *i.e.*,

$$f'(\mathbf{x}', \mathbf{u}') d^3x' d^3p' = f(\mathbf{x}, \mathbf{u}) d^3x d^3p, \quad (2.84)$$

the distribution function  $f$  itself must also be a Lorentz invariant, *i.e.*,

$$f'(\mathbf{x}', \mathbf{u}') = f(\mathbf{x}, \mathbf{u}). \quad (2.85)$$

The *relativistic Maxwell–Boltzmann equation* can then be obtained under the same assumptions made for the Newtonian case and it reads

<sup>16</sup>Note that our notation here is different from that of Cercignani and Kremer (2002), who, besides having a different notation for many thermodynamic quantities, use a signature  $(+, -, -, -)$ , defining  $u^\mu = W(c, v^i)$ ,  $u_\mu = W(c, -v^i)$ , while the four-momentum is still defined as  $p^\mu := mu^\mu$  [*cf.* Eqs. (1.113) and (1.117)]. As a result, in the notation of Cercignani and Kremer (2002):  $u^\mu u_\mu = c^2$  and  $p^\mu p_\mu = m^2c^2$ , while in our notation we have  $u^\mu u_\mu = -c^2$  and  $p^\mu p_\mu = -m^2c^2$ .

$$p^\mu \frac{\partial f}{\partial x^\mu} + m \frac{\partial(F^\mu f)}{\partial p^\mu} = \Pi(f), \quad (2.86)$$

where  $F^\mu$  is the four-force acting on a particle, that may or may not depend on the four-momentum  $p^\mu$ , while the scalar  $\Pi$  is the relativistic generalisation of the *collision integral* and is generally given by (Cercignani and Kremer, 2002)

$$\Pi(f) := \left( \frac{\partial f}{\partial t} \right)_{\text{coll}} = \int \frac{d^3 p_2}{(p_2)^0} \int d\Omega \sigma(\Omega) K (f'_2 f'_1 - f_2 f_1), \quad (2.87)$$

where

$$K := \sqrt{(p_1)^\alpha (p_2)_\alpha - m^4 c^4}. \quad (2.88)$$

Equation (2.86), first obtained by Lichnerowicz and Marrot (1940), reduces to Eq. (2.8) in the non-relativistic limit and, as any other equation in tensorial form, is covariant. Note that the collisionless Maxwell–Boltzmann equation, namely (2.86) with  $\Pi = 0$ , can be understood as the conservation of  $f$  along the particle trajectories in phase space

$$\frac{d}{d\lambda} f(x^\mu(\lambda), p^\mu(\lambda)) = 0, \quad (2.89)$$

where  $\lambda$  is the affine parameter along the particle trajectory. Equation (2.89) is of course conceptually identical to the corresponding Newtonian one (2.6) and summarises the thesis of *Liouville's theorem*, namely, that the density of points in phase space is constant along the trajectories in phase space, or equivalently, that the density of points in phase space moves as an incompressible fluid (Huang, 1987; Cercignani and Kremer, 2002).

### 2.3.2 Relativistic transport fluxes

Before going into the relativistic extension of the  $H$ -theorem discussed in Section 2.2.3, we introduce the *relativistic transport fluxes* of a generic rank- $k$  tensor  $\mathbf{G}$ , i.e.,  $\phi^\mu(\mathbf{G})$ , as [cf. Eq. (2.33)]

$$\phi^{\mu \alpha_1 \dots \alpha_k}(\mathbf{G}) = \int G^{\alpha_1 \dots \alpha_k} p^\mu f \frac{d^3 p}{p^0}, \quad (2.90)$$

where  $G^{\alpha_1 \dots \alpha_k}$  are the contravariant components of  $\mathbf{G}$ . Note that, although in special relativity the speed of light is the largest possible velocity, the spatial components of the four-momentum are not upper-bounded and are given by  $p^i = W m v^i$ , where as usual the Lorentz factor is defined as  $W := 1/\sqrt{1 - v^i v_i/c^2}$ . Hence,  $p^i \rightarrow \pm\infty$  as  $v^i \rightarrow \pm c$ , and the integral in (2.90) is therefore meant to cover momenta that are arbitrarily large.

As a first example, we can set  $k = 0$  and  $\mathbf{G} := c \mathbf{1}$ , with  $\mathbf{1}$  the unit tensor, so as to obtain from (2.90) the *first moment* of the distribution function, or *number-density current* four-vector

$$N^\mu := c \int p^\mu f \frac{d^3 p}{p^0}. \quad (2.91)$$

The above definition makes it clear that the number density  $n$  is actually the zeroth (contravariant) component of the number-density current, i.e.,

## 92 A Kinetic-Theory Description of Fluids

$$N^0 = c \int f d^3 p = cn, \quad (2.92)$$

while the spatial (contravariant) components of the number-density current are given by

$$N^i = c \int p^i f \frac{d^3 p}{p^0} = c^2 \int W m v^i f \frac{d^3 p}{E} = \int v^i f d^3 p, \quad (2.93)$$

where we have used  $p^0 = E/c$  and  $E = Wmc^2$ . Hence,  $N^i$  is the flux of particle number per unit time and unit area along the  $i$ -th spatial direction. Directly related to the first moment is the *rest-mass density current*, which is defined as

$$J^\mu := m N^\mu = mc \int p^\mu f \frac{d^3 p}{p^0}, \quad (2.94)$$

and this is the tensor we will routinely employ when considering rest-mass conservation within the equations of relativistic hydrodynamics.

Proceeding in a similar way, setting  $k = 1$  and  $\mathbf{G} := c\mathbf{p}$  we obtain the *second moment* of the distribution function, also called the *energy-momentum tensor* (or *stress-energy tensor*)

$$T^{\mu\nu} := c \int p^\mu p^\nu f \frac{d^3 p}{p^0}, \quad (2.95)$$

which therefore measures the flux of  $\mu$ -momentum across a surface at  $x^\nu = \text{const.}$ , *i.e.*, in the  $\nu$ -direction. Finally, setting  $k = 2$  and  $\mathbf{G} := c\mathbf{p} \otimes \mathbf{p}$  we obtain the *third moment* of the distribution,<sup>17</sup> defined as

$$F^{\mu\nu\sigma} := c \int p^\mu p^\nu p^\sigma f \frac{d^3 p}{p^0}. \quad (2.96)$$

We could continue along these lines and construct moments of higher orders in the hierarchy by simply adding the number of momenta in the integral and increasing the rank of the corresponding tensor.<sup>18</sup> However, the physical interpretation of these higher moments also becomes increasingly obscure and so the third moment is also the highest of the moments usually considered. We will encounter  $F^{\mu\nu\sigma}$  again when discussing the properties of non-perfect fluids in Chapter 6 (see Section 6.6.3), where its physical interpretation will be given.

Although we have not yet discussed an explicit expression for the energy-momentum tensor, and this will happen only in Section 3.2 when discussing relativistic perfect fluids, it is useful to discuss what are called the *energy conditions*, that is, some very generic conditions that the energy-momentum tensor should fulfill so that the matter it describes behaves in a way that matches our experimental experience. These conditions will then have a direct impact on the properties of some equations of state. However, to express these conditions we need to anticipate here a result that will be properly discussed only in Section 3.2, namely, that the

<sup>17</sup>Moments of order higher than the second do not have a proper name.

<sup>18</sup>Note that the dimensions of the moments increase with the order, so that  $[N^\mu] = L^{-3}$ ,  $[T^{\mu\nu}] = L^{-2}$ , and  $[F^{\mu\nu\sigma}] = L^{-1}$ , etc.

energy density of the fluid as measured by an observer comoving with it is given by the contraction of the energy-momentum tensor with the fluid four-velocity [*cf.*, Eq. (3.40)], *i.e.*,

$$T_{\mu\nu}u^\mu u^\nu = \frac{1}{m^2 c^2} T_{\mu\nu} p^\mu p^\nu. \quad (2.97)$$

Being an energy density, the quantity in (2.97) should be positive for any reasonable classical matter and this condition can be expressed more generically in terms of the so-called *weak energy condition*

$$T_{\mu\nu}\xi^\mu \xi^\nu \geq 0, \quad (2.98)$$

where  $\xi$  is a generic future-directed timelike four-vector. A condition that is more stringent (hence stronger) than (2.98) is usually referred to as the *strong energy condition*, which instead requires that

$$T_{\mu\nu}\xi^\mu \xi^\nu \geq -\frac{1}{2} T^\alpha_\alpha, \quad (2.99)$$

where now  $\xi$  is taken to be a *unit* timelike four-vector. Considering, for instance, the case in which  $\xi$  is given by the fluid four-velocity, expression (2.99) translates into the condition that not only is the energy density positive, but also it is larger than the opposite of the pressure [*cf.*, Eq. (2.287)]. Despite their names, the strong and the weak energy conditions are totally independent. The latter, however, is not independent of another condition, named the *dominant energy condition*, which requires instead that the quantity  $-T_{\mu\nu}\xi^\mu$  should be a future-directed timelike or null four-vector, *i.e.*,

$$-T_{\mu\nu}\xi^\mu = Au_\nu + Bk_\nu, \quad (2.100)$$

where  $A, B > 0$  and  $k$  is a null vector, *i.e.*,  $k^\mu k_\mu = 0$ . Also in this case, we can make better sense of this condition when  $\xi$  is the four-velocity of an observer. Since the quantity  $-T_{\mu\nu}\xi^\mu$  represents the energy-momentum four-current density measured by this observer, the dominant energy condition (2.100) expresses the fact that the energy flow of the matter cannot be observed to move at speeds larger than the speed of light. A tedious calculation then shows that the dominant energy condition implies the weak energy condition.

Expression (2.99) also has a direct impact on the Einstein equations (1.218), which can be rewritten as

$$R_{\mu\nu}u^\mu u^\nu = \frac{8\pi G}{c^4} \left( T_{\mu\nu} - \frac{1}{2} T g_{\mu\nu} \right) u^\mu u^\nu = \frac{8\pi G}{c^4} \left( T_{\mu\nu} u^\mu u^\nu + \frac{1}{2} T^\alpha_\alpha \right). \quad (2.101)$$

Hence, the strong energy condition is equivalent to the positivity condition for the Ricci tensor  $R_{\mu\nu}u^\mu u^\nu \geq 0$ , which is often used in the proofs of the singularity theorems (Wald, 1984) [see also Section 2.4.9 for the discussion of the energy conditions in the case of a fluid].

### 2.3.3 The relativistic $H$ -theorem

We next switch to the proof of the *relativistic  $H$ -theorem* which, as its Newtonian counterpart, plays an important role in relativistic statistical physics, providing a microscopic derivation

## 94 A Kinetic-Theory Description of Fluids

of the second law of thermodynamics through the extension of the definition of the *entropy* of the fluid in terms of an *entropy four-current*. The logic of the proof is very similar to the one developed for the Newtonian case and, more specifically, we seek a relation between the kernel of the relativistic collision integral,  $\Pi(f)$ , and the time derivative of the “ $H$ ” quantity [in the Newtonian case we have shown that  $f'_1 f'_2 - f_1 f_2 = 0 \iff \Gamma(f) = 0 \iff dH/dt = 0$ , cf., Eq. (2.25)]. We therefore define the following scalar

$$\psi := \left[ \ln(fA_H) - \left(1 + \frac{1}{fB_H}\right) \ln(1 + fB_H) \right], \quad (2.102)$$

where  $A_H$  and  $B_H$  are two constant coefficients whose explicit expression will be presented in Section 2.3.6 [cf., Eq. (2.133)] but that, for the time being, we will leave unspecified. Using (2.102), it is possible to define the four-vector  $H^\mu$  as the relativistic extension of the scalar quantity  $H$  introduced in (2.16), as

$$H^\mu := \int p^\mu f \psi \frac{d^3 p}{p^0} = \int p^\mu f \left[ \ln(fA_H) - \left(1 + \frac{1}{fB_H}\right) \ln(1 + fB_H) \right] \frac{d^3 p}{p^0}, \quad (2.103)$$

and prove that (Cercignani and Kremer, 2002)

$$\frac{\partial H^\mu}{\partial x^\mu} = \vartheta \leq 0, \quad (2.104)$$

where the quantity  $\vartheta$  is defined as

$$\begin{aligned} \vartheta := & \frac{1}{4} \int d\Omega \sigma(\Omega) \int \frac{d^3 p_1}{(p_1)^0} \frac{d^3 p_2}{(p_2)^0} K f_1 f_2 \ln \left[ \frac{f'_1 f'_2 (1 + f_1 B_H)(1 + f_2 B_H)}{f_1 f_2 (1 + f'_1 B_H)(1 + f'_2 B_H)} \right] \\ & \times (1 + f'_1 B_H)(1 + f'_2 B_H) \left[ 1 - \frac{f'_1 f'_2 (1 + f_1 B_H)(1 + f_2 B_H)}{f_1 f_2 (1 + f'_1 B_H)(1 + f'_2 B_H)} \right]. \end{aligned} \quad (2.105)$$

The proof of the inequality in (2.104) is rather simple to obtain after recalling that the distribution functions are always non-negative and that

$$\begin{cases} (1-x) \ln x < 0 & \text{for all } x > 0 \text{ and } x \neq 1, \\ (1-x) \ln x = 0 & \text{for } x = 1, \end{cases}$$

where  $x = f'_1 f'_2 (1 + f_1 B_H)(1 + f_2 B_H) / [f_1 f_2 (1 + f'_1 B_H)(1 + f'_2 B_H)]$ . As a result,  $\vartheta = 0$  if and only if

$$f'_1 f'_2 (1 + f_1 B_H)(1 + f_2 B_H) - f_1 f_2 (1 + f'_1 B_H)(1 + f'_2 B_H) = 0. \quad (2.106)$$

Clearly, the condition (2.106) is only a sufficient condition for the vanishing of the relativistic collision integral,  $\Pi(f)$ , but, as in the Newtonian case, it is possible to show that it is also a necessary condition and that it applies only for the equilibrium distribution. Both proofs are rather lengthy and will be omitted here for compactness, but the interested reader can find them in Cercignani and Kremer (2002).

Two interesting considerations can be made at this point. The first one is that we can define another four-vector

$$\mathcal{S}^\mu := -k_B c H^\mu = -k_B c \int p^\mu f \left[ \ln(f A_H) - \left(1 + \frac{1}{f B_H}\right) \ln(1 + f B_H) \right] \frac{d^3 p}{p^0}, \quad (2.107)$$

which, in analogy with the Newtonian expression (2.30), can be shown to correspond to the *entropy current* four-vector. The second consideration is that when comparing the condition (2.106) with the Newtonian equivalent (2.25) it is suggestive to think that the constant coefficient  $B_H$  must somehow account for the relativistic or quantum-mechanical corrections to the properties of the fluid. This will be discussed after introducing the relativistic equilibrium distributions in Section 2.3.6.

#### 2.3.4 The relativistic moment equations

Following a procedure similar to the one that allowed us to derive the Newtonian transport equation (2.32), we multiply the relativistic Maxwell–Boltzmann equation (2.86) by the generic tensor  $\mathbf{G} = \mathbf{G}(x^\mu, p^\mu)$ , assumed to be conserved in a binary collision, and integrate with respect to the invariant element  $d^3 p / p^0$  to obtain

$$\int G^{\alpha_1 \dots \alpha_k} \left( p^\mu \frac{\partial f}{\partial x^\mu} + m F^\mu \frac{\partial f}{\partial p^\mu} \right) \frac{d^3 p}{p^0} = 0, \quad (2.108)$$

where the right-hand side is zero as a consequence of  $\mathbf{G}$  being a collisionally invariant and where we have assumed that the external four-force  $F^\mu$  does not depend on the four momentum, *i.e.*,  $\partial F^\mu / \partial p^\mu = 0$ .

The first term on the left-hand side of (2.108) can then be rewritten as

$$\int G^{\alpha_1 \dots \alpha_k} p^\mu \frac{\partial f}{\partial x^\mu} \frac{d^3 p}{p^0} = \frac{\partial}{\partial x^\mu} \int G^{\alpha_1 \dots \alpha_k} p^\mu f \frac{d^3 p}{p^0} - \int p^\mu f \frac{\partial G^{\alpha_1 \dots \alpha_k}}{\partial x^\mu} \frac{d^3 p}{p^0}, \quad (2.109)$$

while the second term on the left-hand side of (2.108) has the equivalent form

$$m \int G^{\alpha_1 \dots \alpha_k} F^\mu \frac{\partial f}{\partial p^\mu} \frac{d^3 p}{p^0} = m \left( \int \frac{\partial (G^{\alpha_1 \dots \alpha_k} F^\mu f)}{\partial p^\mu} \frac{d^3 p}{p^0} - \int F^\mu f \frac{\partial G^{\alpha_1 \dots \alpha_k}}{\partial p^\mu} \frac{d^3 p}{p^0} \right). \quad (2.110)$$

Now, the first integral on the right-hand side of (2.110) can be transformed into a volume integral in momentum space by virtue of the divergence theorem and is effectively zero since we are assuming that  $F^\mu$  is independent of  $p^\mu$  and the distribution function will have to vanish for infinite values of the four momentum, *i.e.*,  $f \rightarrow 0$  for  $p^i \rightarrow \pm\infty$ .

Collecting together the different pieces, we derive the *relativistic conservation* or *transport equation* for the flux of  $\mathbf{G}$  as

$$\frac{\partial}{\partial x^\mu} \int G^{\alpha_1 \dots \alpha_k} p^\mu f \frac{d^3 p}{p^0} - \int \left( p^\mu \frac{\partial G^{\alpha_1 \dots \alpha_k}}{\partial x^\mu} + m F^\mu \frac{\partial G^{\alpha_1 \dots \alpha_k}}{\partial p^\mu} \right) f \frac{d^3 p}{p^0} = 0, \quad (2.111)$$

which represents the relativistic extension of the conservation equation (2.32). The importance of the covariant formulation of Eq. (2.111) is that it is now straightforward to obtain the

## 96 A Kinetic-Theory Description of Fluids

equations for the different moments. More specifically, after replacing  $G^{\alpha_1 \dots \alpha_k}$  with  $c$  we obtain directly the continuity equation

$$\frac{\partial J^\mu}{\partial x^\mu} = mc \frac{\partial}{\partial x^\mu} \int p^\mu f \frac{d^3 p}{p^0} = 0. \quad (2.112)$$

Similarly, when we replace  $G^{\alpha_1 \dots \alpha_k}$  with the four-vector  $cp^\nu$  we readily derive the conservation equation of energy and momentum

$$\frac{\partial T^{\mu\nu}}{\partial x^\mu} = c \frac{\partial}{\partial x^\mu} \int p^\mu p^\nu f \frac{d^3 p}{p^0} = c \int m F^\nu f \frac{d^3 p}{p^0}. \quad (2.113)$$

As was the case in Newtonian kinetic theory, it is important to remark that Eqs. (2.112)–(2.113) have little practical use as long as an equilibrium distribution function  $f$  is not known. For this reason, and as we have done in the non-relativistic case, we first need to consider relativistic equilibrium distribution functions and, within the zero-order approximation, characterise perfect fluids in a relativistic framework. However, it is also possible to follow a more intuitive approach, which does not resort to a kinetic description and bypasses the definition of a relativistic equilibrium distribution function. This will be the focus of Section 3.2, where we introduce the definitions of the rest-mass density current and of the energy–momentum tensor of perfect fluids.

### 2.3.5 The general-relativistic hydrodynamic equations

Although we have just remarked that Eqs. (2.112) and (2.113) are not very useful for a practical solution as long as the distribution function  $f$  on their right-hand sides remains unknown, their tensor formulation can be exploited to obtain a fully general-relativistic expression for the hydrodynamic equations.

We do this by recalling that the rest-mass density current and the energy–momentum tensor represent the flux of rest mass and the flux of four-momentum. We can therefore enforce the conservation of rest mass and energy–momentum by imposing that the corresponding total net fluxes across a closed three-surface,  $\Sigma$ , vanish. In a flat spacetime, these conditions are simply expressed as

$$\int_{\Sigma} J^\mu l_\mu d^3 x = 0, \quad (2.114)$$

$$\int_{\Sigma} T^{\mu\nu} l_\mu d^3 x = 0, \quad (2.115)$$

where  $l_\mu$  is the unit normal to the three-dimensional surface  $\Sigma$ . Using now Gauss divergence theorem we can transform the surface integrals (2.114)–(2.115) into volume integrals as

$$\int \nabla_\mu J^\mu d^4 x = 0, \quad (2.116)$$

$$\int \nabla_\nu T^{\mu\nu} d^4 x = 0. \quad (2.117)$$

The integral conservation laws (2.114)–(2.115) can also be trivially cast into differential form by noting that the arbitrariness in the choice of the volume element in spacetime implies that they are satisfied only if

$$\nabla_\mu J^\mu = 0, \quad (2.118)$$

$$\nabla_\nu T^{\mu\nu} = 0. \quad (2.119)$$

The differential conservation laws (2.118)–(2.119) represent the *general-relativistic hydrodynamic equations* for a *generic* fluid and express the conservation of rest mass, *i.e.*, Eq. (2.118), and the conservation of energy and linear momentum *i.e.*, Eq. (2.119). Although they have been derived in flat spacetime, the covariance of their tensor formulation guarantees they have the same form also in a general curved spacetime. Indeed, recalling the properties of the Einstein tensor as stated by the *contracted Bianchi identities*, *i.e.*,  $\nabla_\mu G^{\mu\nu} = 0$  [cf., Eq. (1.212)] and the form of the Einstein equations (1.218), the conservation equation (2.119) can be seen as a mere consequence of the *Bianchi identities*. Whether to interpret the conservation of the energy–momentum tensor from a purely geometrical point of view as a consequence of a tensor identity, or from a physical point of view as the extension to a fluid framework of a kinetic theory description is, to a large extent, a matter of taste. The equivalence of these two views is embodied in the Einstein equations (1.218) and any distinction for the most “natural” interpretation is of little use.

What we find important is that, at least in principle, relativistic kinetic theory provides us with the mathematical tools necessary to compute the expressions for the rest-mass density current  $\mathbf{J}$  and for the energy–momentum tensor  $\mathbf{T}$  via the definitions (2.94) and (2.95), respectively. However, as we will discuss in Section 3.2, alternative and more intuitive routes are possible to obtain expressions for these tensors in the case of perfect fluids.

### 2.3.6 Relativistic equilibrium distributions

When looking for an equilibrium distribution function that is a solution of the relativistic Maxwell–Boltzmann equation (2.86), attention needs to be paid to whether or not quantum effects should be taken into account, as they change the form of the collision term  $\Pi(f)$ . The distinction is however rather simple and the fluids will be referred to as *non-degenerate* or *degenerate* according to whether quantum effects can be neglected or not, leading in this latter case to a pressure that is not dependent on temperature. This classification will be discussed in more detail in Section 2.4 (see Table 2.1), but it is sufficient to anticipate here that the most obvious manifestation of the importance of quantum effects in a degenerate relativistic fluid is that the pressure is in general independent of the temperature. On the other hand, this is not the case for a non-degenerate relativistic fluid, for which thermal effects are important and the pressure does depend on the temperature.

The derivation of the equilibrium distribution functions in these two cases follows the lines sketched in Section 2.2.4 for the Maxwell–Boltzmann distribution, and for compactness will not be reported here, referring the interested reader to Landau and Lifshitz (1980), Reichl (1998) and Cercignani and Kremer (2002) for additional details.

Considering first the case of a *non-degenerate fluid*, the equilibrium distribution in the absence of external forces is given by

## 98 A Kinetic-Theory Description of Fluids

$$f_0(\mathbf{p}) = \left( \frac{g_s}{h_p^3} \right) \frac{1}{\exp(-\alpha_f - c p^\mu u_\mu / k_B T)}, \quad (2.120)$$

where  $g_s$  is the *degeneracy factor*, accounting for the internal (spin) degrees of freedom, and defined as

$$g_s = \begin{cases} 2s + 1 & \text{for } m \neq 0, \\ 2s & \text{for } m = 0, \end{cases} \quad (2.121)$$

where  $m$  is the rest mass of the particle and “s” its spin.<sup>19</sup> Note that in Eq. (2.120)  $p^\mu$  refers to the four-momentum of the *constituent* particles, *i.e.*,  $p^\mu = mcU^\mu$ , while  $u^\mu$  is the four-velocity of the *fluid*, so that  $p^\mu u_\mu \neq -mc$ .

Expression (2.120) represents the relativistic generalisation of the Maxwell–Boltzmann distribution (2.48) and is also known as the *Maxwell–Jüttner distribution* function. The thermodynamic quantity  $\alpha_f$  appearing in (2.120) measures the degree of degeneracy of the fluid (see Section 2.4), is referred to as the *fugacity*, and is a pure number defined as<sup>20</sup>

$$\alpha_f := \frac{m}{k_B T} \left( \frac{e + p}{\rho} - Ts \right), \quad (2.122)$$

where

$$\rho := nm \quad (2.123)$$

represents now the *rest-mass density* [*cf.* Eq. (2.39)], while

$$e := \rho(c^2 + \epsilon) \quad (2.124)$$

is the (total) *energy density*,  $e/\rho = c^2 + \epsilon$  the *specific energy*, and

$$s := \frac{S}{Nm} \quad (2.125)$$

is the *specific entropy*, *i.e.*, the entropy per unit mass [not to be confused with the spin “s” of the constituent particles as in (2.121)]. The fugacity is more commonly expressed in connection with the *Gibbs free energy*  $G$  through the relation

$$\alpha_f = \frac{G}{Nk_B T} = \frac{\mu}{k_B T}, \quad (2.126)$$

where

$$\mu := \frac{G}{N} = \left( \frac{\partial G}{\partial N} \right)_{T,p} \quad (2.127)$$

is the (relativistic) *chemical potential*, measuring the energy increase/decrease per unit increase/decrease of particle number. Note that because the relativistic energy density includes

<sup>19</sup>For point-like particles the degeneracy factor reflects degeneracy introduced by the spin, while for molecules it reflects the internal degrees of freedom of the molecule. For a photon, for instance,  $g_s = 2$  to account for the two possible polarisation states. Similarly,  $g_s = 2$  also for an electron, in order to account for the two spin states.

<sup>20</sup>In statistical mechanics it is also common to define instead as fugacity the quantity  $\exp(\alpha_f)$ ; see, *e.g.*, Huang (1987).

also the contribution coming from the rest-mass density, the relativistic chemical potential will differ from the corresponding Newtonian quantity  $\mu_N$ , since it includes the contribution of the rest mass, *i.e.*,  $\mu = \mu_N + mc^2$ .

If we now choose a reference frame comoving with the fluid, such that  $u_\mu = (-1, 0, 0, 0)$ , the term in the exponential of (2.120) is  $-cu_\mu p^\mu = wmc^2$ , where  $w$  is the Lorentz factor of the constituent particles with respect to the comoving frame, *i.e.*,  $w := 1/\sqrt{1 - V^i V_i/c^2}$ . In this case, the Maxwell–Jüttner distribution (2.120) can be rewritten as

$$f_0(p) = \left( \frac{g_s}{h_p^3} \right) \exp(\alpha_f) \exp \left( -\sqrt{1 + \frac{p^2}{m^2 c^2}} \frac{mc^2}{k_B T} \right), \quad (2.128)$$

where we have used the relation  $p^2 = m^2 c^2 (w^2 - 1)$  between the Lorentz factor and the momentum of the constituent particles. Expression (2.128) can be converted into a distribution of the Lorentz factor  $f_0(w)$  using the identity  $f_0(p) 4\pi p^2 dp = f_0(w) dw$ , from which we obtain

$$f_0(w) = \left( \frac{g_s}{h_p^3} \right) 4\pi m^3 c^3 w (w^2 - 1)^{1/2} \exp(\alpha_f) \exp \left( -\frac{wmc^2}{k_B T} \right). \quad (2.129)$$

Finally, after specialising to the case of a non-degenerate relativistic fluid [*cf.*, Eq. (2.182)], the distribution (2.129) further reduces to

$$f_0(w) = \frac{\zeta_c n}{K_2(\zeta_c)} w (w^2 - 1)^{1/2} \exp(-w\zeta_c), \quad (2.130)$$

where we have introduced the *relativistic coldness* (or simply coldness)

$$\zeta_c := \frac{mc^2}{k_B T} \quad (2.131)$$

as a measure of the thermal energy of the fluid, while  $K_2(\zeta_c)$  is a modified Bessel function of the second type (see Section 2.4.2). As an illustrative example, we have reported in Fig. 2.7 the Maxwell–Jüttner distribution (2.130) of an electron fluid at different temperatures and for different values of  $\zeta_c$ .

We next consider the case of a *degenerate fluid* and start accounting for quantum effects by recalling that the classical volume element in phase space  $d^3x d^3p$  should now be replaced by its semi-classical equivalent  $d^3x d^3p/h_p^3$ , where  $h_p = 6.626 \times 10^{-27}$  erg s is the Planck constant. Because of the invariance expressed by Eq. (2.83), also  $g_s d^3x d^3p/h_p^3$  will be a Lorentz invariant and thus can be interpreted as the number of available quantum states in the volume element  $d^3x d^3p$ . The number of particles in one particular quantum state, *i.e.*, the occupation number, depends on whether the particle does or does not obey Pauli's exclusion principle. In quantum mechanics particles are distinguished into bosons and fermions according to whether they are described by the Bose–Einstein or by the Fermi–Dirac statistics. In fact, bosons, for which the same quantum state can be occupied in arbitrary numbers (*e.g.*, by a Bose–Einstein condensate), have integer spin numbers and include, *e.g.*, photons, gluons, mesons (pions and kaons), and nuclei with even atomic mass number, *e.g.*, helium-4. On the other hand, fermions, for which the same quantum state can be occupied by one particle at

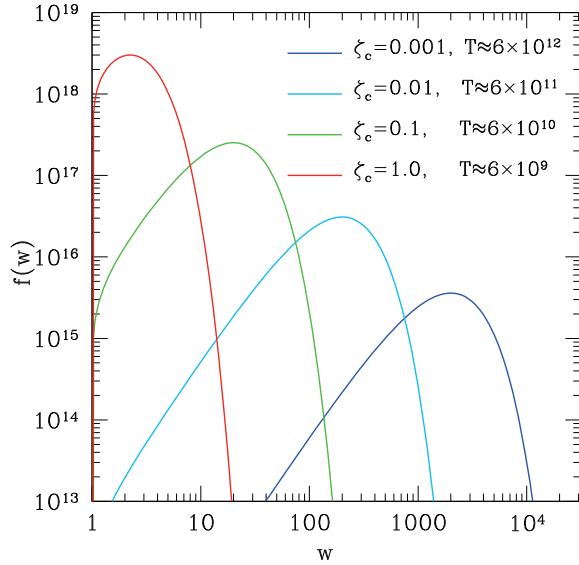


**Fig. 2.7** Examples of the Maxwell-Jüttner distribution (2.130) for a fluid of electrons with  $n = 1.0 \times 10^{19} \text{ cm}^{-3}$  and at different values of the relativistic coldness  $\zeta_c$ . Note that  $w$  is the Lorentz factor of the constituent particles with respect to the frame comoving with the fluid, which is also the frame where the distribution function is measured.

most, have half-integer spin numbers and include, *e.g.*, leptons (electrons, neutrinos, muons and taus), baryons (neutrons, protons and lambda particles) and nuclei with odd atomic mass number, *e.g.*, helium-3.

As a result, a degenerate fluid will have two distinct equilibrium distributions depending on whether the particles are bosons or fermions. Fortunately, however, both distributions are given by the same generic expression

$$\begin{aligned} f_0(\mathbf{p}) &= \left( \frac{g_s}{h_p^3} \right) \frac{1}{\exp(-\alpha_f - cp^\mu u_\mu/k_B T) \pm 1} \\ &= \left( \frac{g_s}{h_p^3} \right) \frac{1}{\exp[(E - \mu)/k_B T] \pm 1}, \end{aligned} \quad (2.132)$$

where the + and - signs apply in the case of fermions and bosons, respectively, while  $-cu_\mu p^\mu = E = wmc^2$  [note that also in this case attention must be paid to the fact that  $\mathbf{p}$  refers to the constituent particles while  $\mathbf{u}$  refers to the fluid four-velocity; *cf.*, Eq. (2.120)]. Expression (2.132) will be used extensively in Section 2.4 to introduce the properties of a number of non-degenerate and degenerate relativistic fluids.

A bit of algebra and the knowledge of the relativistic equilibrium distributions (2.132) allows us now to derive the explicit form of the coefficients  $A_H$  and  $B_H$  which we have introduced in Section 2.3.3 when discussing the relativistic formulation of the  $H$ -theorem, namely,

$$A_H := \frac{h_P^3}{g_s}, \quad B_H := \varepsilon \frac{h_P^3}{g_s}, \quad (2.133)$$

where  $\varepsilon$ , not to be confused with the specific energy  $\epsilon$ , selects the actual distribution function to be adopted, *i.e.*,

$$\varepsilon = \begin{cases} +1 & \text{for the Fermi-Dirac statistics,} \\ -1 & \text{for the Bose-Einstein statistics,} \\ 0 & \text{for the Maxwell-Jüttner statistics.} \end{cases} \quad (2.134)$$

In this way we can rewrite the expression for the entropy current (2.107) as

$$\mathcal{S}^\mu = s\rho u^\mu = \int p^\mu f \left[ -k_B c \ln \left( \frac{fh_P^3}{g_s} \right) + k_B c \left( 1 + \frac{g_s}{\varepsilon f h_P^3} \right) \ln \left( 1 + \frac{\varepsilon f h_P^3}{g_s} \right) \right] \frac{d^3 p}{p^0}. \quad (2.135)$$

We conclude this section with an important remark. In analogy with the Newtonian treatment, we define as *relativistic perfect fluids* those fluids described by the moment equations (2.112) and (2.113) in the zero-order approximation given by the equilibrium distributions (2.120) or (2.132). As a result, also *relativistic perfect fluids are such that the viscous effects and heat fluxes are zero, and the pressure tensor is diagonal*.

### 2.3.7 The laws of thermodynamics

The laws of thermodynamics provide important information about the changes in the thermodynamic properties of the system as it evolves from one state to another one in quasi-equilibrium. Given a fluid element at any given time, there will be a certain number of thermodynamic quantities (*e.g.*,  $n$ ,  $\rho$ ,  $p$ ,  $e$ ,  $T$ ,  $\epsilon$ ,  $s$ ,  $\mu$ , etc.) defined at that event and measured in the fluid's Lorentz rest frame. Not all of the thermodynamic potentials are independent and indeed it can be shown that the thermodynamic state of a single-component fluid can be expressed in terms of only two independent parameters, *e.g.*,  $\rho$  and  $\epsilon$  or  $e$  and  $T$ .

Because of the equivalence principle, the *first law of thermodynamics* in the fluid rest frame is the same as the first law in flat spacetime, and basically states the conservation of the *internal energy*,  $U := \rho e V = N m e$ . The internal energy can then change either because of a heat exchange,  $dQ := T dS$ , or because of the work done,  $p dV$ , or because of the creation/destruction of its constituents,  $\mu dN$ , that is (Stewart, 1971)

$$dU = T dS - p dV + \mu dN, \quad (2.136)$$

where  $N$  is the number of particles and  $\mu := (\partial G / \partial N)_{T,p}$  is the corresponding chemical potential [*cf.* Eq. (2.127)].<sup>21</sup> Note that while the differential operator on the left-hand side of

<sup>21</sup>In the more generic situation in which the fluid is composed of several components, *i.e.*, a *multicomponent fluid* or *multiphase* (see Section 2.136), the first law should be trivially extended as  $dU = T dS - p dV + \sum_i \mu_i dN_i$ , where  $N_i$  are the number of particles of the  $i$ -th species and  $\mu_i := (\partial G / \partial N_i)_{T,p}$  is the corresponding chemical potential.

(2.136) is *exact* (the energy changes are independent of the path followed between the two states), the differentials on the right-hand side are not [the changes in heat and work depend on the path; see Landau and Lifshitz (1980) for a discussion]. For simplicity of notation we will not make this distinction hereafter.

In the simpler case in which the fluid is composed of one type of particle only and its number is conserved, *i.e.*,  $dN = 0$ , Eq. (2.136) reduces to

$$d\epsilon = Tds - pd\left(\frac{1}{\rho}\right), \quad (2.137)$$

where, we recall,  $\epsilon, T, s, p$  and  $\rho$  represent, respectively, the specific internal energy, the temperature, the specific entropy, the pressure and the rest-mass density; furthermore, the quantity  $1/\rho$  is often referred to as the *specific volume*. Because it will be useful later on, we can also express the internal energy as a function of the variables  $V, S$  and  $N$ , *i.e.*, given a constant coefficient  $\lambda$  we express  $U$  as

$$U(\lambda V, \lambda S, \lambda N) = \lambda U(V, S, N). \quad (2.138)$$

After differentiating with respect to  $\lambda$ , taking  $\lambda = 1$  and using the first law (2.136), we obtain

$$U = -pV + TS + \mu N. \quad (2.139)$$

Differentiating (2.139) and using again the first law, we obtain the desired alternative expression

$$Vdp = SdT + Nd\mu, \quad (2.140)$$

which now relates the changes in the pressure with the changes in the temperature and chemical potentials.

Introducing the relativistic *specific enthalpy* defined as [*cf.*, Eq. (2.124)]

$$h := \frac{e + p}{\rho} = c^2 + \epsilon + \frac{p}{\rho}, \quad (2.141)$$

it is possible to write the first law (2.137) as the alternative and handy expressions

$$dp = \rho dh - \rho Tds, \quad (2.142)$$

$$de = hdp + \rho Tds, \quad (2.143)$$

which are sometimes presented in terms of the number density  $n$  as (Misner *et al.*, 1973)

$$dp = \frac{n}{N} (dH - TdS), \quad (2.144)$$

$$de = \frac{1}{N} (Hdn + nTds), \quad (2.145)$$

where

$$H := Nmh = \frac{N(e + p)}{n} = V(e + p) \quad (2.146)$$

is the *enthalpy*.

All of the above equations are of course valid both in a Newtonian and in a relativistic framework, but care must be paid when switching between Newtonian and relativistic quantities. In particular the Newtonian *total* energy density  $e_N$  includes internal and kinetic contributions [*cf.*, Eq. (2.68)], and is different from the corresponding relativistic quantity, which includes instead the internal (thermal) contribution ( $\propto \rho\epsilon$ ) and the rest-mass energy contribution ( $\propto \rho c^2$ ) [*cf.*, Eq. (2.124)]. Similarly, the *Newtonian specific enthalpy* is defined as

$$h_N := \epsilon + \frac{p}{\rho}, \quad (2.147)$$

and therefore lacks the contribution coming from the rest-mass energy density [*cf.*, Eq. (2.141)].

To see how the *second law of thermodynamics* can be expressed in terms of the entropy current  $S^\mu$ , whose explicit microscopic definition was given in Eq. (2.135), we proceed as follows. We first define the total entropy  $S$  by integrating over a spacelike surface  $\Sigma$ , *i.e.*,

$$S(\Sigma) := \int_{\Sigma} S^\mu l_\mu d^3x. \quad (2.148)$$

Next, because the second law of thermodynamics requires that  $S$  is a non-decreasing function of time, such that  $S(\Sigma') - S(\Sigma) \geq 0$  for every surface  $\Sigma'$  to the future of  $\Sigma$ , we make use of Gauss divergence theorem to convert the flux integral into a volume integral, requiring therefore that

$$S(\Sigma') - S(\Sigma) = \int \nabla_\mu S^\mu d^4x \geq 0. \quad (2.149)$$

Since  $\Sigma$  and  $\Sigma'$  are completely arbitrary, the second law of thermodynamics is equivalent to imposing

$$\nabla_\mu S^\mu \geq 0. \quad (2.150)$$

The condition of non-decreasing entropy flux (2.150) is also known as the (*maximum*) *entropy principle* (Liu *et al.*, 1986). In Section 2.3.3 we have discussed how the definition of the entropy has a microscopic nature and is related to the properties of the collision integral. The vanishing of the latter is also equivalent to the vanishing of the four-divergence in Eq. (2.150), and is thus attained only for a relativistic equilibrium distribution.

We will get back to the second law of thermodynamics in two subsequent parts of the book: first, in Section 3.3, where we will show that perfect fluids are *adiabatic fluids*, that is, their specific entropy  $s$  is conserved along the fluidlines [*cf.*, Eq. (3.61)]; second, in Chapter 6, where we will discuss the form of the entropy current  $S^\mu$  in a hydrodynamic theory of non-perfect fluids that is relativistically consistent.

## 2.4 Equations of state

Our discussion about the kinetic-theory description of fluids should have clarified by now that the properties of a fluid system can be fully determined if an equilibrium function is known. In particular, all thermodynamic quantities can be computed and these, together with

the moment equations, provide all the information needed. In practice, however, the distribution function is rarely known or is often too complicated to compute via the collisional Boltzmann equation. In these cases, one needs to resort to phenomenological expressions that relate quantities appearing in the energy-momentum tensor and in particular the pressure  $p$  to the other hydrodynamic variables, such as the rest-mass density or the specific internal energy, *i.e.*,  $p = p(\rho, \epsilon)$ . Such expressions are called *equations of state* and play a fundamental role in any hydrodynamic description not only because they provide a *closure relation* in the set of hydrodynamics equations [*cf.*, discussion made after Eqs. (2.65)–(2.67)], but also because they represent the realism in the description of a given physical system. Indeed, our ability to reproduce the dynamics of a realistic configuration rests ultimately on the equation of state that describes the physical properties of the system.

Given the considerations above, it is natural to conclude that there will be as many equations of state as the different physical systems that one can construct (this is in part the case of the equations of state describing nuclear matter in neutron stars). Fortunately, there are some general classes of equations of state that describe fluids with properties that are most commonly encountered in nature and that we will present in detail in the following sections.

We start with the simplest of the equations of state, that is, the one with vanishing pressure,  $p = 0$ . The corresponding fluid, which is commonly referred to as a *dust* or a *pressureless fluid*, represents the limit in which the constitutive elements of the fluid do not have any interaction, so that the system is intrinsically collisionless.<sup>22</sup> Although apparently very simple, such an approximation is often a good one in cosmological fluids, and large  $N$ -body simulations of collisionless dark matter exploit it extensively.

Next we consider those equations of state which are of greatest importance for relativistic fluids and consider, in particular, both non-degenerate and degenerate fluids, either of fermions or of bosons. The general procedure consists in substituting the equilibrium distributions (2.120) and (2.132) into the general expressions (2.91)–(2.95), to obtain explicit expressions for the number density, energy density and pressure [*cf.*, Eqs. (3.43)–(3.45) in Section 3.2], and then by taking the corresponding limits, if any, for the relevant quantities of that physical regime. When doing so, the particle number density, the energy density or the pressure are written in terms of integrals of the type

$$\int \chi f \frac{d^3 p}{p^0} = \int_0^\pi \sin \theta d\theta \int_0^{2\pi} d\phi \int_0^\infty \chi |\vec{p}|^2 f \frac{d|\vec{p}|}{p^0}, \quad (2.151)$$

where  $\chi$  represents some combination of the momenta and where we have used the relation  $d^3 p = |\vec{p}|^2 d|\vec{p}| \sin \theta d\theta d\phi$ , with  $|\vec{p}|^2 := p^i p_i$  [*cf.*, Eq. (2.53)]. A few tricks will come in handy when deriving an equation of state. In particular, we can introduce the *dimensionless momentum* defined as

$$\cosh x := \frac{p^0}{mc}, \quad (2.152)$$

with  $x \in [0, \infty)$  and such that from the normalisation condition  $p^\mu p_\mu = -(p^0)^2 + |\vec{p}|^2 = -m^2 c^2$ , we can deduce

<sup>22</sup>Note that a collisionless fluid is not necessarily a pressureless one and that in general the pressure of a collisionless fluid is nonzero. An extension of a dust fluid to the case in which the only interaction is gravity will be presented in Section 12.4.1.

**Table 2.1** Schematic classification of fluids as non-degenerate/degenerate and as non-relativistic/relativistic in terms of the fugacity  $\alpha_f$  and of the coldness  $\zeta_c$ .

$\alpha_f \ll 1, \zeta_c \gg 1:$	non-degenerate, non-relativistic
$\alpha_f \ll 1, \zeta_c \ll 1:$	non-degenerate, relativistic
$\alpha_f \gg 1, \zeta_c \gg 1:$	degenerate, non-relativistic
$\alpha_f \gg 1, \zeta_c \ll 1:$	degenerate, relativistic

$$|\vec{p}|^2 = (p^0)^2 - m^2 c^2 = m^2 c^2 (\cosh^2 x - 1) = m^2 c^2 \sinh^2 x. \quad (2.153)$$

By differentiating the first and the last terms in (2.153) it follows that

$$\frac{d|\vec{p}|}{p^0} = dx. \quad (2.154)$$

Using now the general expression (2.132) for the equilibrium distributions and selecting the local Lorentz rest frame to compute the scalar product  $p^\mu u_\mu$ , we readily obtain that  $cp^\mu u_\mu = cp^0 u_0 = mc^2 \cosh x$ , so that we can finally rewrite (2.151) as

$$\int \chi f \frac{d^3 p}{p^0} = 4\pi \frac{g_s}{h_p^3} m^2 c^2 \int_0^\infty \frac{\chi \sinh^2(x)}{\exp(-\alpha_f + \zeta_c \cosh x) + \varepsilon} dx, \quad (2.155)$$

where again  $\varepsilon$  distinguishes the different distribution functions [*cf.*, Eq. (2.134)]. It should be noted that when computing the thermodynamic quantities of the system, one often encounters integrals of hyperbolic functions and exponential functions which have the typical form<sup>23</sup>

$$\mathcal{I}_n(\alpha_f, \zeta_c) := \int_0^\infty \frac{\cosh(nx)}{\exp(-\alpha_f + \zeta_c \cosh x) + \varepsilon} dx. \quad (2.156)$$

Although the calculation of the integrals (2.156) cannot be done analytically in most cases, the *fugacity*,  $\alpha_f$ , and the *coldness*,  $\zeta_c$ , provide us with useful measures of the importance of, respectively, quantum and relativistic corrections to the behaviour of the fluid. In fact, when  $\alpha_f \ll 1$ , quantum effects are unimportant [the terms  $\pm 1$  in the denominator of (2.132) can be neglected] and the fluid is then *non-degenerate*, while, when  $\alpha_f \gg 1$ , quantum effects are important and the fluid is then *degenerate* (see Table 2.1). On the other hand, when  $\zeta_c \gg 1$ , the rest-mass energy is much larger than the thermal energy and the fluid is *non-relativistic*, while, when  $\zeta_c \ll 1$ , the opposite is true and the fluid is *relativistic* (see Table 2.1). To fix ideas, it is useful to recall that an electron at room temperature has  $\zeta_c \approx 10^7$ , while it has  $\zeta_c \approx 6 \times 10^{-3}$  at  $T = 10^{12}$  K.

Before discussing the properties of different fluids, it is useful to introduce some quantities that will play an important role in the subsequent discussion. The first one is the *specific heat*,

<sup>23</sup>Do not confuse the index  $n$  of the integral  $\mathcal{I}_n$  with the particle number density  $n$ .

## 106 A Kinetic-Theory Description of Fluids

expressing the amount of heat per unit mass,  $dq := dQ/m$ , that is necessary to increase the temperature of a physical system by a given amount  $dT$ , *i.e.*,

$$c_{\text{heat}} := \frac{dq}{dT}. \quad (2.157)$$

From Eq. (2.137), it follows that  $dq = Tds = d\epsilon - p/\rho^2 d\rho$  and therefore that

$$c_{\text{heat}} = \frac{1}{dT} \left\{ \left( \frac{\partial \epsilon}{\partial T} \right)_\rho dT + \left[ \left( \frac{\partial \epsilon}{\partial \rho} \right)_T - \frac{p}{\rho^2} \right] d\rho \right\}, \quad (2.158)$$

where we have assumed  $T$  and  $\rho$  as independent variables. When the process of heat exchange is performed at constant volume, *i.e.*, with  $d\rho = 0$ , the corresponding *specific heat at constant volume* is given by

$$c_v := \left( \frac{\partial \epsilon}{\partial T} \right)_V = T \left( \frac{\partial s}{\partial T} \right)_V. \quad (2.159)$$

On the other hand, when the heat exchange is performed at constant pressure, the *specific heat at constant pressure* is expressed as

$$c_p := c_v + \left[ \left( \frac{\partial \epsilon}{\partial \rho} \right)_T - \frac{p}{\rho^2} \right] \left( \frac{\partial \rho}{\partial T} \right)_p = \left( \frac{\partial h}{\partial T} \right)_p = T \left( \frac{\partial s}{\partial T} \right)_p, \quad (2.160)$$

where the second and the third equalities follow directly from the first law of thermodynamics as written in (2.142). In other words, when the temperature of the system is changed, the two specific heats measure the changes in the total energy at constant volume and in the enthalpy at constant pressure, respectively. In general, most bodies have positive specific heats but there is nothing that prevents specific heats from being negative. A classical example is represented by stars, which, when contracting because of cooling via radiative losses, decrease their total energy while increasing their temperature.

Using the last two equalities in (2.159) and (2.160) it is also possible to write that (Landau and Lifshitz, 1980)

$$c_p - c_v = -T \left( \frac{\partial p}{\partial T} \right)_p^2 / \left( \frac{\partial p}{\partial V} \right)_T > 0, \quad (2.161)$$

where the inequality comes from  $(\partial p/\partial V)_T < 0$ , *i.e.*, the pressure decreases in the isothermal expansion of a fluid. As a result,  $c_p > c_v$  in a classical fluid. A useful quantity derived from the specific heats is their ratio, also known as the *adiabatic index*, and defined as

$$\gamma := \frac{c_p}{c_v} > 1. \quad (2.162)$$

In the following sections we will see in detail how the adiabatic index changes in the case of fluids in different regimes where either relativistic or quantum-mechanical corrections are important, but we can already anticipate two important values assumed by the adiabatic index. The first one is relative to a *classical monatomic fluid* with pressure  $p = nk_B T$

[cf., Eq. (2.47)<sub>2</sub>]<sup>24</sup>, which in Section 2.4.3 we will see to be close to a non-degenerate and non-relativistic fluid. In this case, if  $m$  is the mass of the constituent particles, it is possible to show that  $(\partial\epsilon/\partial\rho)_T = 0$  and  $(\partial\rho/\partial T)_p = -\rho/T$ , so that expression (2.160) becomes

$$c_p = c_v + \frac{k_B}{m}, \quad (2.163)$$

and the adiabatic index can be calculated to be

$$\gamma = 1 + \frac{k_B}{mc_v}. \quad (2.164)$$

Moreover, because the specific heats are constant and given by

$$c_p = \left(\frac{5}{2}\right) \frac{k_B}{m} \quad c_v = \left(\frac{3}{2}\right) \frac{k_B}{m}, \quad (2.165)$$

the adiabatic index (2.164) is simply given by<sup>25</sup>

$$\gamma = \frac{5}{3}. \quad (2.166)$$

The second relevant limit of the adiabatic index is instead offered by an *ultrarelativistic fluid* of massless particles, which we will introduce in Section 2.4.4 and for which

$$\gamma = \frac{4}{3}. \quad (2.167)$$

As we will see repeatedly in the following sections, the adiabatic index is often in the range given by expressions (2.166) and (2.167).

Another quantity that will play an important role in the remainder of this book is the relativistic *sound speed*, whose definition is given by

$$c_s^2 := \left(\frac{\partial p}{\partial e}\right)_s, \quad (2.168)$$

where we have assumed that  $p = p(e, s)$ . We will encounter expression (2.168) again when studying the linear perturbations of the relativistic-hydrodynamic equations and it will be shown there that it is not just a thermodynamic identity, but it measures the speed at which linear *sound waves* propagate (see Section 4.3.1). It is useful to relate (2.168) to its Newtonian counterpart, which is instead defined as (Landau and Lifshitz, 1980)

$$(c_s^2)_N := \left(\frac{\partial p}{\partial \rho}\right)_s, \quad (2.169)$$

<sup>24</sup>Hereafter we will indicate as  $(X)_n$  the  $n$ -th equation of number X.

<sup>25</sup>For a diatomic fluid, that is, a fluid composed of molecules with two atoms of the same type, e.g., H<sub>2</sub>, O<sub>2</sub>, N<sub>2</sub>,  $c_p = (7/2)k_B/m$ ,  $c_v = (5/2)k_B/m$ , and thus the adiabatic index is  $\gamma = 7/5$ .

and to do this we use Eq. (2.143) written now as

$$h = \left( \frac{de}{d\rho} \right)_s = \left( \frac{\partial e}{\partial \rho} \right)_s , \quad (2.170)$$

so that we immediately deduce

$$c_s^2 = \frac{1}{h} (c_s^2)_N . \quad (2.171)$$

Definitions (2.168) and (2.169) allow us once again to remark that in a relativistic framework the energy density plays the role played by the rest-mass density in a Newtonian regime (see the discussion in Section 2.3.7). Furthermore, as we will see in Section 3.5, in the Newtonian limit  $h \rightarrow 1$  [cf., Eq. (3.84)], as required by (2.171).

For a generic equation of state of the kind  $p = p(\rho, \epsilon)$ , which is also the kind most commonly found in practical calculations, Eqs. (2.168) and (2.170) can be combined to yield a relation which will turn out to be useful when discussing the formulations of the equations suited for numerical calculations (see Section 7.3.3)

$$c_s^2 = \frac{1}{h} \left( \frac{dp}{d\rho} \right)_s = \left( \frac{d \ln h}{d \ln \rho} \right)_s , \quad (2.172)$$

$$= \frac{1}{h} \left[ \left( \frac{\partial p}{\partial \rho} \right)_\epsilon + \frac{d\epsilon}{d\rho} \left( \frac{\partial p}{\partial \epsilon} \right)_\rho \right] = \frac{1}{h} \left[ \left( \frac{\partial p}{\partial \rho} \right)_\epsilon + \frac{p}{\rho^2} \left( \frac{\partial p}{\partial \epsilon} \right)_\rho \right] . \quad (2.173)$$

Equation (2.168) can also be used to introduce the concept of “convexity/non-convexity” of an equation of state. Following Menikoff and Plohr (1989), and more recently Ibáñez *et al.* (2012b), we can determine the convexity/non-convexity of an equation of state by examining the convexity of *isentropes* (*i.e.*, the curves of constant entropy) in the  $(p, 1/\rho)$  plane. In particular, we can introduce the “fundamental derivative”

$$\mathcal{G} := -\frac{1}{2} V \frac{(\partial^2 p / \partial V^2)_s}{(\partial p / \partial V)_s} = \frac{1}{2} \frac{V^2}{\gamma p} \left( \frac{\partial^2 p}{\partial V^2} \right)_s = \frac{1}{2} \left( 1 + \gamma + \frac{\partial \ln \gamma}{\partial \ln \rho} \Big|_s \right) , \quad (2.174)$$

and then define an equation of state to be *convex (non-convex)* if (Ibáñez *et al.*, 2012b)<sup>26</sup>

$$\mathcal{G} > \frac{3}{2} c_s^2 , \quad \left( \mathcal{G} < \frac{3}{2} c_s^2 \right) . \quad (2.175)$$

Besides expressing a condition on the amount of concavity of isentropes in the  $(p, 1/\rho)$  plane, the definition above allows one to distinguish between equations of state with markedly different fluid behaviours. Fluids following convex equations of state, in fact, are such that their fluid elements increase their specific volume and decrease their pressure when overtaken by a rarefaction wave (*i.e.*, rarefaction waves are “expansive”); similarly, they are compressed

<sup>26</sup>The condition (2.175) represents the extension to relativistic hydrodynamics of the equivalent condition for Newtonian fluids derived by Menikoff and Plohr (1989) and stating that a Newtonian equation of state is *convex (non-convex)* if  $\mathcal{G} > 0$  ( $\mathcal{G} < 0$ ).

when overtaken by a compression wave (*i.e.*, compression waves are “compressive”).<sup>27</sup> Conversely, fluids following non-convex equations of state are such that their fluid elements behave rather “anomalously”, that is, they are compressed by rarefaction waves and rarefied by compression waves. It is not difficult to show that a sufficient condition for an equation of state to be convex is that the sound speed increases with increasing energy density, *i.e.*, that  $(d^2p/de^2)_s > 0$ . Indeed, this latter condition is reminiscent of the corresponding Newtonian condition  $(d^2p/d\rho^2)_s > 0$ , which is sometimes used as a definition of a convex equation of state.

### 2.4.1 Degenerate relativistic fluid

As a first and illustrative example of an equation of state, we derive explicit expressions of the most relevant thermodynamic quantities relative to a *degenerate relativistic fluid*, that is, a fluid for which the particle motions are close to the speed of light and quantum effects also need to be taken into account. We start from the particle number density, which can be obtained from the definition (2.92) and after using the distribution function for a degenerate fluid (2.132)

$$n = \int p^0 f \frac{d^3p}{p^0} = 4\pi \frac{g_s}{h_p^3} m^3 c^3 \int_0^\infty \frac{\sinh^2 x \cosh x}{\exp(-\alpha_f + \zeta_c \cosh x) + \varepsilon} dx. \quad (2.176)$$

Since  $\sinh^2 x \cosh x = \frac{1}{4}(\cosh(3x) - \cosh x)$ , the above integral can be rewritten as

$$n = 4\pi \frac{g_s}{h_p^3} m^3 c^3 \frac{1}{4} (\mathcal{I}_3 - \mathcal{I}_1) = \frac{\pi g_s m^3 c^3}{h_p^3} (\mathcal{I}_3 - \mathcal{I}_1), \quad (2.177)$$

where the integrals  $\mathcal{I}_n$  follow the definition given by (2.156) and need in general to be computed numerically.

A similar procedure can be followed also for the other thermodynamic quantities, with some additional algebra that involves manipulations of the hyperbolic functions. Omitting the details of the derivations, which however can be found, for instance, in Cercignani and Kremer (2002), we simply report the final expressions as<sup>28</sup>

$$e = 4\pi \frac{g_s}{h_p^3} m^4 c^5 \frac{1}{8} (\mathcal{I}_4 - \mathcal{I}_0) = \frac{\pi g_s m^4 c^5}{2 h_p^3} (\mathcal{I}_4 - \mathcal{I}_0), \quad (2.179)$$

$$p = 4\pi \frac{g_s}{h_p^3} m^4 c^5 \frac{1}{24} (\mathcal{I}_4 - 4\mathcal{I}_2 + 3\mathcal{I}_0) = \frac{\pi g_s m^4 c^5}{6 h_p^3} (\mathcal{I}_4 - 4\mathcal{I}_2 + 3\mathcal{I}_0). \quad (2.180)$$

<sup>27</sup>A detailed discussion of compression and rarefaction waves will be presented in Sections 4.4.2 and 4.4.3.

<sup>28</sup>To facilitate the comparison with the corresponding expressions that Cercignani and Kremer (2002) report in terms of quantities per particle, we recall the following simple transformations:

$$(\dots)_{\text{specific}} = \frac{1}{m} (\dots)_{\text{per-particle}}, \quad (\dots)_{\text{density}} = n (\dots)_{\text{per-particle}}, \quad (2.178)$$

where the dots represent either the energy, the entropy, the enthalpy, etc.

## 110 A Kinetic-Theory Description of Fluids

Equations (2.177)–(2.180) are a set of thermodynamic relations of the kind  $n = n(\mu, T)$ ,  $e = e(\mu, T)$ ,  $p = p(\mu, T)$ , where the chemical potential  $\mu = \alpha_f k_B T$  can be seen to express the degree of degeneracy and how much the fluid is relativistic [cf., Eq. (2.126)].

### 2.4.2 Non-degenerate relativistic fluid

The properties of a *non-degenerate relativistic fluid* can be obtained either directly from the Maxwell–Jüttner distribution function (2.120), or from the degenerate relativistic fluid in the limit in which  $\alpha_f \ll 1$ . In both cases, the relevant integral (2.156) tends to a modified Bessel function of the second type  $K_n(\zeta_c)$ , namely

$$\begin{aligned}\mathcal{I}_n(\alpha_f, \zeta_c) &\approx \exp(\alpha_f) \int_0^\infty \cosh(nx) \exp(-\zeta_c \cosh x) dx \\ &= \exp(\alpha_f) K_n(\zeta_c),\end{aligned}\quad (2.181)$$

where the approximation sign is indeed an equality when  $\varepsilon = 0$  in the general distribution (2.156) (*i.e.*, for the Maxwell–Jüttner distribution). The resulting basic thermodynamic quantities that are obtained in this way are

$$n = 4\pi \frac{g_s m^3 c^3}{h_p^3} \frac{K_2}{\zeta_c} \exp(\alpha_f), \quad (2.182)$$

$$e = nmc^2 \left( \mathcal{G} - \frac{1}{\zeta_c} \right), \quad (2.183)$$

$$p = nmc^2 \frac{1}{\zeta_c} = nk_B T, \quad (2.184)$$

$$s = \frac{k_B}{m} \left[ \ln \left( 4\pi \frac{g_s m^3 c^3}{h_p^3} \right) + \ln \frac{K_2}{n \zeta_c} + \zeta_c \mathcal{G} \right], \quad (2.185)$$

where

$$\mathcal{G}(\zeta_c) := \frac{K_3(\zeta_c)}{K_2(\zeta_c)}. \quad (2.186)$$

An important property of this fluid is that the pressure is directly proportional to the particle density and to the temperature in a way that we will encounter also in the non-relativistic regime (see Section 2.4.3). It has become customary to refer to the fluid in this regime as a *Synge fluid* (Synge, 1957; Lanza *et al.*, 1985) and we note that, as is apparent from (2.183) and (2.184), the quantity  $\mathcal{G}$  is actually related to the enthalpy density through the relation

$$\rho c^2 \mathcal{G} = e + p = \rho h = H/V. \quad (2.187)$$

There are of course a number of mathematical properties concerning the functions  $K_n(\zeta_c)$ , among which we will only report the most relevant ones [see, *e.g.*, Abramowitz and Stegun (1968) for a complete list]

$$\frac{d}{d\zeta_c} (\zeta_c^{-n} K_n(\zeta_c)) = -\zeta_c^{-n} K_{n+1}(\zeta_c), \quad \frac{d}{d\zeta_c} (\zeta_c^n K_n(\zeta_c)) = -\zeta_c^n K_{n-1}(\zeta_c), \quad (2.188)$$

$$K_{n+1}(\zeta_c) = K_{n-1}(\zeta_c) + \frac{2n}{\zeta_c} K_n(\zeta_c), \quad (2.189)$$

from which it follows, for instance, that

$$\frac{d\mathcal{G}}{d\zeta_c} = \mathcal{G}^2 - \frac{5\mathcal{G}}{\zeta_c} - 1. \quad (2.190)$$

In turn, this allows us to compute the sound speed as (Anile, 1989)<sup>29</sup>

$$c_s^2 = \frac{\zeta_c(d\mathcal{G}/d\zeta_c)}{\mathcal{G}(\zeta_c^2\mathcal{G} + 1)} = \frac{\zeta_c\mathcal{G}^2 - 5\mathcal{G} - \zeta_c}{\mathcal{G}(\zeta_c^2\mathcal{G} + 1)}, \quad (2.191)$$

as well as the specific heats per particle as

$$\tilde{c}_v = \left( \frac{\partial(e/n)}{\partial T} \right)_V = k_B[\zeta_c^2(1 - \mathcal{G}^2) + 5\mathcal{G}\zeta_c - 1], \quad (2.192)$$

$$\tilde{c}_p = \left( \frac{\partial(hm)}{\partial T} \right)_p = k_B[\zeta_c^2(1 - \mathcal{G}^2) + 5\mathcal{G}\zeta_c]. \quad (2.193)$$

Although these specific heats depend on the temperature and therefore are not constant, it is still possible to define an effective adiabatic index as

$$\tilde{\gamma} := 1 + \frac{p}{\rho\epsilon} = \frac{c^2(\mathcal{G}(\zeta_c) - 1)}{\epsilon} = \frac{\zeta_c(\mathcal{G}(\zeta_c) - 1)}{\zeta_c\mathcal{G}(\zeta_c) - \zeta_c - 1}. \quad (2.194)$$

This parameter is reminiscent of the adiabatic index since

$$\frac{4}{3} \leq \tilde{\gamma} \leq \frac{5}{3}, \quad (2.195)$$

so that in the limit of  $\zeta_c \gg 1$ ,  $\tilde{\gamma} \rightarrow 5/3$ , which is the adiabatic index of a classical monatomic fluid [cf., Eq. (2.166)], while in the limit  $\zeta_c \ll 1$ ,  $\tilde{\gamma} \rightarrow 4/3$ , which is instead the adiabatic index of an ultrarelativistic fluid [cf., Eq. (2.167)].

### 2.4.3 Non-degenerate non-relativistic fluid

*Non-degenerate non-relativistic fluids* are those we are exposed to in our daily experience and have an accurate description already within classical statistical mechanics, where they are also referred to as *classical fluids*. In practice, the equation of state for such a fluid within relativistic kinetic theory can be obtained as the limit of the degenerate relativistic fluid in the case of small fugacity and large coldness, *i.e.*, when  $\alpha_f \ll 1$  and  $\zeta_c \gg 1$ . In this case, the Bessel functions can be approximated as (Abramowitz and Stegun, 1968)

$$K_n(\zeta_c) \approx \sqrt{\frac{\pi}{2\zeta_c}} \exp(-\zeta_c) \left[ 1 + \frac{4n^2 - 1}{8\zeta_c} + \frac{(4n^2 - 1)(4n^2 - 9)}{2(8\zeta_c)^2} + \dots \right], \quad (2.196)$$

<sup>29</sup>Note that expression (2.191) corrects a typo in Anile (1989).

## 112 A Kinetic-Theory Description of Fluids

so that, for instance,  $\mathcal{G} = K_3/K_2 \approx 1 + 5/(2\zeta_c)$  and the corresponding thermodynamic quantities are

$$n = 4\pi \frac{g_s}{h_p^3} \sqrt{2mk_B T^3} \exp(\alpha_f + \zeta_c) \frac{3}{8}\pi, \quad (2.197)$$

$$e = nmc^2 + \frac{3}{2}nk_B T \left( 1 + \frac{5}{4\zeta_c} + \dots \right), \quad (2.198)$$

$$p = nk_B T, \quad (2.199)$$

$$s = \frac{k_B}{m} \left\{ \ln \frac{T^{3/2}}{n} - \ln \left[ \frac{h_p^3}{g_s(2\pi m k_B)^{3/2}} \right] + \frac{5}{2} \right\} + \frac{k_B}{m} \left( \frac{15}{4\zeta_c} + \dots \right), \quad (2.200)$$

where it is easy to isolate the relativistic corrections at first-order in  $\zeta_c$  from the corresponding classical-fluid expressions (note that the corrections to the pressure are of order higher than the first). Using (2.198) and (2.199) it is also simple to see that the internal energy density is  $e - nmc^2 = nmc = \frac{3}{2}p$ , a result we have already derived in (2.47)<sub>2</sub>.

As done in the previous section, we can compute the specific heats as

$$c_V = \frac{3}{2}k_B \left( 1 + \frac{5}{2\zeta_c} + \dots \right), \quad c_p = \frac{5}{2}k_B \left( 1 + \frac{3}{2\zeta_c} + \dots \right), \quad (2.201)$$

so that the adiabatic index in this case is given by

$$\gamma = \frac{c_p}{c_V} = \frac{5}{3} \left( 1 - \frac{1}{\zeta_c} + \dots \right), \quad (2.202)$$

which should be compared with the result anticipated in Eq. (2.166) for a classical monatomic fluid, *i.e.*,  $\gamma = 5/3$ .

### 2.4.4 Ultrarelativistic fluid

Equations of state for ultrarelativistic perfect fluids are found in those physical conditions which limit to a vanishing coldness  $\zeta_c \ll 1$ . This is the case of fluids at very high temperature or, more generically, if the internal energy is much larger than the rest-mass energy, as in the case of neutrinos or (in the limit) of photons. Under these conditions, the number density can be obtained by going back to the general expression (2.176) and by performing an additional change of variable in the integral, that is, by introducing  $z := \zeta_c \cosh x$ , and by taking  $(z/\zeta_c)^2 \approx \cosh^2 x - 1$  because of the assumption of  $\zeta_c \ll 1$ . This then leads to the following expressions

$$n = 4\pi \frac{g_s}{h_p^3} \left( \frac{k_B T}{c} \right)^3 \int_0^\infty \frac{z^2}{\exp(-\alpha_f + z) + \varepsilon} dz, \quad (2.203)$$

$$e = 4\pi \frac{g_s}{h_p^3} c \left( \frac{k_B T}{c} \right)^4 \int_0^\infty \frac{z^3}{\exp(-\alpha_f + z) + \varepsilon} dz, \quad (2.204)$$

$$p = \frac{1}{3} 4\pi \frac{g_s}{h_p^3} c \left( \frac{k_B T}{c} \right)^4 \int_0^\infty \frac{z^3}{\exp(-\alpha_f + z) + \varepsilon} dz, \quad (2.205)$$

which already show two important properties of ultrarelativistic fluids, *i.e.*,

$$p = \frac{1}{3} e, \quad (2.206)$$

and

$$c_s^2 = \frac{1}{3}. \quad (2.207)$$

Note that Eqs. (2.203)–(2.205) have been derived for a *degenerate ultrarelativistic fluid*. The corresponding expression for a *non-degenerate ultrarelativistic fluid* can be obtained starting from Eqs. (2.182)–(2.184) and then by considering the limit  $\zeta_c \ll 1$ . In this case, in fact, the Bessel functions can be approximated as (Abramowitz and Stegun, 1968)

$$K_2(\zeta_c) \approx \frac{2}{\zeta_c^2}, \quad K_3(\zeta_c) \approx \frac{8}{\zeta_c^3}, \quad (2.208)$$

so that  $\mathcal{G} = h/c^2 \approx 4/\zeta_c$ . As a result, Eqs. (2.182)–(2.184) for a non-degenerate ultrarelativistic fluid become

$$n = 8\pi \frac{g_s}{h_p^3} \left( \frac{k_B T}{c} \right)^3 \exp(\alpha_f), \quad (2.209)$$

$$e = 3nk_B T, \quad (2.210)$$

$$p = nk_B T = \frac{1}{3} e, \quad (2.211)$$

$$\bar{s} = -k_B \left\{ \ln \left[ \frac{n}{8\pi g_s} \left( \frac{h_p c}{k_B T} \right)^3 \right] - 4 \right\}, \quad (2.212)$$

where  $\bar{s} = S/N$  represents the *entropy per particle*. From the expressions above we obtain the heat capacities per particle as

$$c_V = 3k_B, \quad c_p = 4k_B, \quad (2.213)$$

which gives an adiabatic index

$$\gamma = \frac{4}{3}, \quad (2.214)$$

which of course coincides with the result anticipated in Eq. (2.167).

### 2.4.5 Degenerate Fermi fluid

To describe the properties of a *degenerate Fermi fluid* we can recall the number density for a degenerate relativistic fluid (2.176) and rewrite it in such a way as to highlight the competition of different terms in the denominator, *i.e.*,

$$n = 4\pi \frac{g_s}{h_p^3} m^3 c^3 \int_0^\infty \frac{\sinh^2 x \cosh x}{\exp(-\alpha_f + \zeta_c) \exp(\zeta_c \cosh x - \zeta_c) + 1} dx. \quad (2.215)$$

As mentioned in Section 2.4, the degenerate and relativistic regime is obtained for large fugacity and small coldness, *i.e.*, when  $\alpha_f \gg 1$ , and  $\zeta_c \ll 1$ , so that the exponential term  $\exp(-\alpha_f + \zeta_c)$  in Eq. (2.215) is vanishingly small. In this case, it is possible to define as *completely degenerate Fermi* a fluid in which  $\exp(-\alpha_f + \zeta_c) \rightarrow 0$  and the denominator in (2.215) will be equal to unity up to a critical dimensionless momentum  $x_F$ , where the term  $\exp(\zeta_c \cosh x - \zeta_c)$  diverges. In this limit, the particle number density reduces from expression (2.215) to

$$n = 4\pi \frac{g_s}{h_p^3} m^3 c^3 \int_0^{x_F} \sinh^2 x \cosh x dx, \quad (2.216)$$

where [cf., Eq. (2.152)]

$$x_F = \cosh^{-1} \left( \frac{p_F^0}{mc} \right) = \cosh^{-1} \sqrt{1 + \frac{p_F^2}{m^2 c^2}}. \quad (2.217)$$

The quantity  $p_F := |\vec{p}_F|$  is called the *Fermi momentum*<sup>30</sup> and reflects the property that fermions will fill all of the quantum states with  $p \leq p_F$ , and none of the states with  $p > p_F$ . By direct integration of (2.216) and using similar considerations also for the energy density and the pressure, one obtains (Cercignani and Kremer, 2002)

$$n = \frac{4\pi}{3} \frac{g_s}{h_p^3} m^3 c^3 z^3, \quad (2.218)$$

$$e = \frac{\pi}{6} \frac{g_s}{h_p^3} m^4 c^5 \mathcal{F}_1(z), \quad (2.219)$$

$$p = \frac{\pi}{6} \frac{g_s}{h_p^3} m^4 c^5 \mathcal{F}_2(z), \quad (2.220)$$

where now  $z := p_F/mc$  is the dimensionless Fermi momentum, while the two auxiliary functions  $\mathcal{F}_1(z)$  and  $\mathcal{F}_2(z)$  are given by

$$\mathcal{F}_1(z) := 3z(2z^2 + 1)\sqrt{z^2 + 1} - 3\sin^{-1} z, \quad (2.221)$$

$$\mathcal{F}_2(z) := z(2z^2 - 3)\sqrt{z^2 + 1} + 3\sin^{-1} z. \quad (2.222)$$

Equations (2.218)–(2.220) therefore provide all the information needed to characterise a strongly degenerate Fermi fluid. They can be further distinguished in the two opposite regimes of a non-relativistic ( $z \ll 1$ ) and of an ultrarelativistic ( $z \gg 1$ ) fluid, for which well-defined

<sup>30</sup>In Eq. (2.217),  $p_F^0$  represents the (contravariant) time component of the Fermi four-momentum  $\vec{p}_F$ .

expansions of the functions  $\mathcal{F}_1(z)$  and  $\mathcal{F}_2(z)$  exist. More specifically, for  $x \ll 1$  or  $p_F \ll mc$ , which corresponds to a *completely degenerate non-relativistic Fermi fluid*, it is possible to obtain (Cercignani and Kremer, 2002)

$$e = nmc^2 + \frac{3}{10} \left( \frac{3h_P^3}{4\pi m^{3/2} g_s} \right)^{2/3} n^{5/3} \left[ 1 - \frac{5}{28} \left( \frac{3h_P^3}{4\pi g_s} \right)^{2/3} \frac{n^{2/3}}{m^2 c^2} + \dots \right], \quad (2.223)$$

$$p = \frac{1}{5} \left( \frac{3h_P^3}{4\pi m^{3/2} g_s} \right)^{2/3} n^{5/3} \left[ 1 - \frac{5}{14} \left( \frac{3h_P^3}{4\pi g_s} \right)^{2/3} \frac{n^{2/3}}{m^2 c^2} + \dots \right]. \quad (2.224)$$

Similarly, for  $x \gg 1$  or  $p_F \gg mc$ , which corresponds to a *completely degenerate ultrarelativistic Fermi fluid*, one obtains

$$e = \frac{3}{4} \left( \frac{3c^3 h_P^3}{4\pi g_s} \right)^{1/3} n^{4/3} \left[ 1 - \left( \frac{4\pi g_s}{3h_P^3} \right)^{2/3} \frac{m^2 c^2}{n^{2/3}} + \dots \right], \quad (2.225)$$

$$p = \frac{1}{4} \left( \frac{3c^3 h_P^3}{4\pi g_s} \right)^{1/3} n^{4/3} \left[ 1 - \left( \frac{4\pi g_s}{3h_P^3} \right)^{2/3} \frac{m^2 c^2}{n^{2/3}} + \dots \right], \quad (2.226)$$

so that, as seen for an ultrarelativistic fluid, the pressure and energy density are related as [*cf.* Eq. (2.206)]

$$p \approx \frac{1}{4} \left( \frac{3c^3 h_P^3}{4\pi g_s} \right)^{1/3} n^{4/3} \approx \frac{1}{3} e. \quad (2.227)$$

Note that in both the non-relativistic and in the ultrarelativistic limit, the energy density and the pressure are functions only of the particle number density and not of the temperature.<sup>31</sup>

Although extreme, the conditions that lead to a completely degenerate Fermi fluid are rather common in nature and in particular in astrophysics. These conditions, for instance, regulate the hydrostatic equilibrium of *white dwarfs*, stars with a size comparable to that of the Earth, but with a mass as large as that of the Sun, that represent the end-state of many stellar-evolution scenarios (Shapiro and Teukolsky, 1983). In 1930 Chandrasekhar used the properties of a degenerate relativistic Fermi fluid to infer a limit to the maximum mass that a white dwarf can have, which is approximately  $1.4 M_\odot$  (Chandrasekhar, 1931), and is known as the *Chandrasekhar mass*.

#### 2.4.6 Ideal fluid

The equation of state of a classical monatomic fluid,  $p = nk_B T$  [*cf.* Eq. (2.47)<sub>2</sub>], that we have found to be valid also for non-degenerate relativistic fluids (see Section 2.4.2), for non-degenerate non-relativistic fluids (see Section 2.4.3) and for non-degenerate ultrarelativistic fluids (see Section 2.4.4), becomes the prototype of a more general behaviour of an equation

<sup>31</sup>Using a less restrictive assumption on the properties of the denominator of (2.215) one obtains the definition of a *strongly degenerate Fermi fluid*, for which the pressure and energy density depend not only on the particle number density but also on the temperature [see, *e.g.*, Cercignani and Kremer (2002) for details].

## 116 A Kinetic-Theory Description of Fluids

of state in which the pressure can be expressed in terms of the rest-mass density and of the temperature (or specific internal energy). Recalling that the first law of thermodynamics for a transformation at constant volume of a monatomic fluid of rest mass  $m$  is simply given by  $d\epsilon = c_v dT$  [cf., Eqs. (2.137) and (2.159)], it is possible to write for a fluid at constant specific heat  $c_v$  that  $\epsilon = c_v T$ . Furthermore, using the result obtained in Section 2.4, where it was shown that for a monatomic fluid  $k_B/c_v = m(\gamma - 1)$ , where  $\gamma$  is the *adiabatic index* of the fluid, the equation of state  $p = nk_B T$  can be written as

$$p(\rho, \epsilon) = \rho\epsilon(\gamma - 1), \quad (2.228)$$

or, equivalently, when expressed in terms of the specific enthalpy, as [cf., Eq. (2.141)]

$$h = c^2 + \gamma\epsilon. \quad (2.229)$$

The equation of state (2.228) is widely adopted in numerical simulations and it is commonly referred to as the *ideal-fluid* (or  $\Gamma$ -*law*) *equation of state*. This nomenclature, however, is somewhat confusing, as it seems to imply that it is the correct equation of state for any perfect fluid.<sup>32</sup> Rather, as noted above, it is a suitable expression only for fluids that are non-degenerate and relativistic, or non-degenerate and non-relativistic, or non-degenerate and ultrarelativistic. We therefore *define* as “ideal fluid” any fluid whose equation of state can be written as Eq. (2.228).

Although not evident at first glance, the ideal-fluid equation of state is not compatible with arbitrary values of the adiabatic index in a relativistic framework. This fact was first noticed by Taub (1948), who showed that, to be consistent with relativistic kinetic theory, the specific enthalpy must satisfy *Taub’s inequality*

$$\left(h - \frac{p}{\rho}\right) \left(h - 4\frac{p}{\rho}\right) \geq c^4. \quad (2.230)$$

It is not difficult to show that Taub’s inequality is fulfilled for any value of  $p/\rho$  when  $\gamma = 4/3$ , while it cannot be satisfied for any positive value of  $p/\rho$  when  $\gamma = 5/3$  [see, e.g., Mignone and McKinney (2007) for a recent discussion]. This problem can be circumvented by adopting an equation of state that satisfies the condition (2.230) with the equals sign, and closely follows the  $\gamma = 4/3$  law in the limit of high temperatures, while reducing to the  $\gamma = 5/3$  law in the cold-fluid limit. This modified ideal-fluid equation of state is therefore expressed as

$$p = \frac{1}{3} \left( \frac{\epsilon + 2}{\epsilon + 1} \right) \rho\epsilon, \quad (2.231)$$

where the corresponding sound speed is given by

$$c_s^2 = \frac{p(5\rho h - 8p)}{3\rho h(\rho h - p)}, \quad (2.232)$$

while the specific enthalpy can be expressed in terms of the ratio  $p/\rho$  as (Mathews, 1971)

<sup>32</sup>This is particularly the case for those authors who do not distinguish between perfect fluids and ideal fluids.

$$h = \frac{5p}{2\rho} + \sqrt{c^4 + \left(\frac{3p}{2\rho}\right)^2}. \quad (2.233)$$

Such an approach was first proposed by Mathews (1971) and it has been recently adopted in numerical simulations (Mignone and McKinney, 2007). The sound speed corresponding to the ideal-fluid equation of state (2.228) can be calculated rather easily after using expression (2.173), so as to obtain

$$c_s^2 = \frac{\gamma\epsilon(\gamma-1)}{c^2 + \gamma\epsilon} = \left(\frac{h - c^2}{h}\right)(\gamma-1) = \frac{\gamma p}{\rho h}. \quad (2.234)$$

When the fluid is ultrarelativistic, thus with an adiabatic index  $\gamma = 4/3$  and characterised by having  $\epsilon \gg 1$ , expression (2.234) yields the well-known result that  $c_s^2 \rightarrow (\gamma-1)$ , which in turn implies  $c_s^2 \leq 1/3$ .

We also note that it is possible to exploit the equivalence  $p = nk_B T = \rho\epsilon(\gamma-1)$  to derive a direct expression of the temperature in terms of the internal energy as

$$T = \frac{m}{k_B}(\gamma-1)\epsilon = \frac{m}{k_B}\left(\frac{p}{\rho}\right), \quad (2.235)$$

providing a particularly convenient estimate of the temperature (which is not routinely computed in numerical simulations) in terms of the specific internal energy (which is instead an evolved variable in numerical simulations; see Section 7.3.3).

To conclude this section it is useful to remark that the concept of adiabatic index is more general than the one introduced with the definition (2.162) as ratio of the specific heats. Indeed, for an ideal fluid undergoing an isentropic process, namely, a process for which  $ds = 0$ , it is possible to show that the following three relations hold, of which only two are independent [see, e.g., Reif (1965)]

$$pV^\gamma = \text{const.}, \quad (2.236)$$

$$p^{(1-\gamma)/\gamma}T = \text{const.}, \quad (2.237)$$

$$V^{\gamma-1}T = \text{const.} \quad (2.238)$$

From these relations it is then possible to define three different indices  $\Gamma_1, \Gamma_2, \Gamma_3$  such that

$$\Gamma_1 := \left(\frac{\partial \ln p}{\partial \ln \rho}\right)_s, \quad (2.239)$$

$$\frac{\Gamma_2 - 1}{\Gamma_2} := \left(\frac{\partial \ln T}{\partial \ln p}\right)_s, \quad (2.240)$$

$$\Gamma_3 - 1 := \left(\frac{\partial \ln T}{\partial \ln \rho}\right)_s, \quad (2.241)$$

which all coincide and are equal to the adiabatic index (2.162) for an ideal fluid, *i.e.*,  $\Gamma_1 = \Gamma_2 = \Gamma_3 = \gamma$ . In Section 2.4.8 we will see that this is not the case for a fluid composed of photons.

### 2.4.7 Polytropic fluid

Another large class of equations of state that is widely used in the modelling of astrophysical objects and in numerical calculations is the one associated to *polytropic*<sup>33</sup> thermodynamic transformations, that is, to transformations of the type  $pV^\Gamma = \text{const}$ . The corresponding *polytropic equation of state* is expressed as

$$p(\rho) = K\rho^\Gamma = K\rho^{1+1/N_p}, \quad (2.242)$$

and is also the prototypical barotropic equation of state, where  $K$  is a constant and is called the *polytropic constant*, while  $N_p = 1/(\Gamma - 1)$  is called the *polytropic index* and  $\Gamma$  the *polytropic exponent*.

Polytropic equations of state are used to model the behaviour of matter under a wide range of different physical conditions (Horedt, 2004), including the interiors of neutron stars. Indeed, as discussed in Section (2.4.5), completely degenerate non-relativistic/relativistic fluids are good examples of fluids obeying this class of equation of state. As a first approximation, in fact, a completely degenerate non-relativistic *electron* fluid, such as the one described by Eq. (2.224) truncated at first order, corresponds to a polytropic equation of state with exponent  $\Gamma = 5/3$  (index  $N_p = 3/2$ ) and polytropic constant  $K = \frac{1}{5} [(3h_p^3)/(8\pi m_e^4)]^{2/3}$ . Similarly, a completely degenerate ultrarelativistic *electron* fluid, such as the one described by Eq. (2.226) truncated at first order, corresponds to a polytropic equation of state with  $\Gamma = 4/3$  ( $N_p = 3$ ) and  $K = \frac{1}{4} [(3c^3 h_p^3)/(8\pi m_e^4)]^{1/3}$ .

A useful property of polytropic equations of state is the flexibility which pivots fully around  $K$  and  $N_p$ . In particular, since the polytropic constant  $K$  has the dimensions of  $[L]^{2/N_p}$ , it is easy to either perform calculations in terms of dimensionless quantities *e.g.*, by setting (Cook *et al.*, 1992)

$$\rho \rightarrow \bar{\rho} = K^{N_p} \rho, \quad M \rightarrow \bar{M} = K^{-N_p/2} M, \quad (2.243)$$

or to rescale all quantities obtained with a set of values of  $K, N_p$  to a different one. More specifically, since in geometrised units all quantities can be written in terms of lengths, if  $L_1$  is a length-scale obtained with  $K_1$  and  $\Gamma_1$ , then the corresponding length-scale  $L_2$  obtained with  $K_2$  and  $\Gamma_2$  is simply

$$L_2 = \left( \frac{K_2^{N_2}}{K_1^{N_1}} \right)^{1/2} L_1 = \left[ \frac{K_2^{1/(\Gamma_2-1)}}{K_1^{1/(\Gamma_1-1)}} \right]^{1/2} L_1. \quad (2.244)$$

Note that since the pressure is a function of the rest-mass density only, a polytropic equation of state does not provide any information about the properties of the specific internal energy, which is unconstrained. As a result, it is perfectly reasonable to assume that  $\epsilon = 0$ .<sup>34</sup>

Although a polytropic equation of state is of a more general type than the ideal-fluid one, the latter coincides with the former in the case of isentropic transformations, *i.e.*, when  $ds = 0$ .

<sup>33</sup>The name polytropic emphasises the many “directions” (*i.e.*, *tropos*) in which such a transformation can take place.

<sup>34</sup>A fluid obeying the ideal-fluid equation of state with  $\epsilon = 0$  would also have a zero temperature and could provide a reasonable model for a cold and old neutron star.

To see this, we start by differentiating expression (2.228) for the ideal-fluid equation of state to obtain

$$dp = (\gamma - 1) \left( \frac{p}{\rho} + \epsilon \right) d\rho = \gamma \left( \frac{p}{\rho} \right) d\rho, \quad (2.245)$$

where we have expressed the first law of thermodynamics (2.137) with  $ds = 0$  as

$$\rho d\epsilon = \frac{p}{\rho} d\rho. \quad (2.246)$$

Integrating Eq. (2.245) we deduce that

$$p = K \rho^\gamma, \quad (2.247)$$

which is similar but distinct from (2.242) and of course the two equations of state coincide when  $\Gamma = \gamma$ . Put differently, a polytropic equation of state is equivalent to an ideal-fluid equation of state *only* under those *isentropic transformations* for which the *adiabatic index* of the fluid  $\gamma$  is the same as the *adiabatic index of the polytrope*  $\Gamma$ . In practice, numerical simulations employing a polytropic equation of state make the implicit assumption that  $\Gamma = \gamma$ , so that the internal energy can be computed by integrating Eq. (2.246) to obtain the algebraic expression (hereafter we will assume that  $\Gamma = \gamma$ )

$$\epsilon = \frac{K \rho^{\Gamma-1}}{\Gamma - 1}, \quad (2.248)$$

where  $\Gamma > 1$  [cf., Eq. (2.162)]. Similarly, it is possible to derive an explicit expression for the sound speed by direct differentiation of (2.242) to obtain  $dp = (\Gamma p / \rho) d\rho$ , so that the general definition (2.168) yields

$$c_s^2 = \frac{\Gamma p}{\rho h} = \frac{\Gamma(\Gamma - 1)p}{\rho(\Gamma - 1) + \Gamma p} = \left( \frac{1}{\Gamma K \rho^{\Gamma-1}} + \frac{1}{\Gamma - 1} \right)^{-1}. \quad (2.249)$$

Three important remarks are needed at this point. First, since the sound speed measures the *compressibility* or *stiffness* of the fluid [cf., Eq. (2.172)], it is easy to use expressions (2.234) and (2.249) to relate the stiffness of the equation of state with the adiabatic index  $\Gamma$ . Larger values of the adiabatic index will correspond, on the whole, to a *stiff* equation of state (*i.e.*, one in which small changes in the density lead to large changes in the pressure), while smaller values will refer to a *soft* equation of state (*i.e.*, one in which small changes in the density lead to small changes in the pressure).<sup>35</sup>

The second remark is to emphasise that the polytropic constant  $K$  introduced in (2.242) is more than just a constant and is indeed related to the entropy of the flow along the fluidlines. To show this point, let us relax, for the time being, the hypothesis of isentropy, and express

<sup>35</sup>Note that stiffness in polytropic relativistic stars can be a slippery concept. As an example, for any fixed  $K$ , a star with  $\Gamma \gtrsim 2$  (hence with a stiff equation of state) will be more compact than one constructed with  $\Gamma \lesssim 2$  (hence with a soft equation of state) and having the same gravitational mass. In other words, a polytropic star with a stiff equation of state will be even more compressed than one with a soft equation of state. The opposite is true when realistic equations of state are considered, in which case the star will be more compact if the equation of state is softer.

the first law of thermodynamics as  $Tds = d\epsilon - (p/\rho^2)d\rho$ , and use the expression for the temperature (2.235) to obtain

$$\frac{m}{k_B}ds = \frac{d\epsilon}{\epsilon(\Gamma-1)} - \frac{d\rho}{\rho} = d\left[\ln\left(\frac{\epsilon^{1/(\Gamma-1)}}{\rho}\right)\right]. \quad (2.250)$$

The equation above can be thought of as being valid for each element in the fluid and can be integrated to yield

$$s = \frac{k_B}{m} \left[ \ln\left(\frac{K}{\Gamma-1}\right)^{1/(\Gamma-1)} + \tilde{K} \right] = \left(\frac{k_B}{m}\right) \frac{\ln K}{\Gamma-1}, \quad (2.251)$$

where we have used expression (2.248) to rewrite the specific internal energy, and where  $\tilde{K}$  is an integration constant that we have chosen to be  $\tilde{K} := \ln(\Gamma-1)/(\Gamma-1)$ . Equation (2.251) shows that, for each fluid element, the polytropic constant is directly proportional to the specific entropy along its fluidline and thus constant if the fluid element undergoes an isentropic transformation. At the same, the condition (2.251) is purely local and does not require the polytropic constant to be the same across the fluid. It is only if  $K$  is constant across the fluid, that the fluid is isentropic. These considerations reflect the fact that perfect fluids are intrinsically *adiabatic fluids*, *i.e.*, the specific entropy is conserved along the fluidline, but not necessarily *isentropic fluids*, *i.e.*, the specific entropy is the same across the whole fluid [see also the discussion in Section 3.3 and compare Eqs. (3.61) and (3.62)]. All numerical implementations of the polytropic equation of state (2.242) assume that  $K$  is the same across the fluid and hence that the fluid is isentropic (see also the discussion in Section 3.8).

The equivalence between the ideal-fluid and the polytropic equation of state holds when the transformation is isentropic, but this requirement can be easily violated in a fluid, where nonlinear waves and shock-discontinuities can be produced easily (see Chapter 6). When this happens, that is when the flow is no longer *smooth*, the two equations of state will have a significantly different behaviour. The ideal-fluid equation of state, in fact, allows for a local increase of the entropy across the shock, so that kinetic energy is transformed *irreversibly* into internal energy through what is commonly referred to as “*shock heating*” (see Section 4.4.3 for a discussion of the increase of entropy across a shock).<sup>36</sup> The polytropic equation of state, on the other hand, cannot break the isentropy condition (at least as long as  $K$  is kept constant) and hence does not allow for the development of genuine shocks, but only for very large gradients (see Section 4.3.1 for the physical conditions defining a shock).<sup>37</sup>

Polytropic equations of state can be formulated also in terms of a sequence of relations of the type (2.242), with suitable conditions of continuity at the joining pressures or rest-mass densities. The resulting equation of state is called *piecewise polytropic* and is expressed as

$$p(\rho) = \bigcup_{i=1}^I p_i(\rho) = \bigcup_{i=1}^I K_i \rho^{\Gamma_i}, \quad (2.252)$$

<sup>36</sup>Note that the conversion of kinetic energy into internal energy occurs also in smooth compressions (expansions), but is, in these cases, isentropic and thus *reversible*.

<sup>37</sup>In simulations employing an ideal-fluid equation of state, the quantity  $p/\rho^\Gamma$  is computed to monitor the local growth of entropy [*cf.*, Eq. (2.251)].

where each “piece” of the polytropic equation of state is valid only in a given range of densities  $\bar{\rho}_i \leq \rho \leq \bar{\rho}_{i+1}$ , where  $\bar{\rho}_i$  is the  $i$ -th transition rest-mass density. Expression (2.252) needs to guarantee that the pressure and the energy density are continuous at the transition points and the first of these conditions is enforced by requiring that  $p_i(\bar{\rho}_i) = p_{i+1}(\bar{\rho}_i)$ , *i.e.*,

$$K_i \bar{\rho}_i^{\Gamma_i} = K_{i+1} \bar{\rho}_i^{\Gamma_{i+1}}, \quad (2.253)$$

which highlights that if the two polytropic constants are the same across the junction, the pressure is generally discontinuous. The continuity of the energy density is instead enforced through the definition of suitable jump conditions which can be calculated via the first law of thermodynamics for a perfect fluid (2.137)

$$d\left(\frac{e}{\rho}\right) = d\epsilon = \frac{p}{\rho^2} d\rho. \quad (2.254)$$

Integrating (2.254) we obtain that the energy density can be expressed as

$$e_i(\rho) = \rho(1 + A_i) + \frac{K_i}{\Gamma_i - 1} \rho^{\Gamma_i}, \quad (2.255)$$

where we have fixed the integration constants by requiring that  $e/\rho \rightarrow 1$  in the limit  $\rho \rightarrow 0$ . The coefficients  $A_i$  can therefore be fixed after requiring the continuity of the energy density across a transition in rest-mass density, *i.e.*,  $e_i(\bar{\rho}_i) = e_{i+1}(\bar{\rho}_i)$ . If  $A_0$  corresponds to  $\bar{\rho}_0 = 0$ , all the other coefficients are given by

$$A_i = \frac{e_{i-1}(\bar{\rho}_{i-1})}{\bar{\rho}_{i-1}} - 1 - \frac{K_i}{\Gamma_i - 1} \bar{\rho}_{i-1}^{\Gamma_i-1}. \quad (2.256)$$

A little bit of algebra then allows us to derive also the expressions for the specific internal energy and for the specific enthalpy as

$$\epsilon_i(\rho) = A_i + \frac{K_i}{\Gamma_i - 1} \rho^{\Gamma_i-1}, \quad (2.257)$$

$$h_i(\rho) = 1 + A_i + \frac{\Gamma_i K_i}{\Gamma_i - 1} \rho^{\Gamma_i-1}, \quad (2.258)$$

where, of course,  $h_i(\bar{\rho}_i) = h_{i+1}(\bar{\rho}_i)$ . In general, piecewise polytropic equations of state can represent useful parameterisations of fluids with complex nuclear equations of state, such as those encountered in stellar cores (Janka *et al.*, 1993) or in neutron stars (Read *et al.*, 2009a). It should be noted that since at the transition point we have imposed the condition that the pressure and energy density are only continuous, the corresponding sound speed may be discontinuous, *i.e.*, in general  $(c_s)_i(\bar{\rho}_i) \neq (c_s)_{i+1}(\bar{\rho}_i)$ . In practice, however, the discontinuities are small enough that they do not seem to result in a serious problem in numerical simulations (Read *et al.*, 2009b).

An important aspect of the use of the polytropic and of the ideal-fluid equations of state emerges when considering those physical systems in which both of them are used at the same time in the so-called *hybrid equation of state*. There are physical systems, in fact, for which the pressure and the specific internal energy can be expressed as the sum of a “cold” contribution,

obeying the polytropic equation of state,<sup>38</sup> and of a “thermal” contribution obeying the ideal-fluid equation of state. The resulting pressure and specific internal energies are then expressed as

$$p = p_c + p_{\text{th}} = K\rho^{\Gamma_c} + \rho\epsilon_{\text{th}}(\Gamma_{\text{th}} - 1), \quad (2.259)$$

$$\epsilon = \epsilon_c + \epsilon_{\text{th}} = \frac{K\rho^{\Gamma_c-1}}{\Gamma_c - 1} + \epsilon_{\text{th}}. \quad (2.260)$$

Hybrid equations of state are used, for instance, to study the collapse of a stellar core (Janka *et al.*, 1993; Zwerger and Müller, 1997), or to simulate the merger of a binary system of neutron stars (Shibata *et al.*, 2005). In both cases, it is necessary to couple the dynamics of a fluid which is essentially cold (*e.g.*, a collapsing stellar core prior to the bounce or two neutron stars before their merger) with the one which has been heated via shocks, which have dissipated kinetic energy into internal energy (*e.g.*, the post-shock region or a hypermassive neutron star). In practice, numerical simulations generally evolve the total specific energy  $\epsilon$ , from which it is simple to compute the thermal component as  $\epsilon_{\text{th}} = \epsilon - \epsilon_c$  and thus complete the calculation of the total pressure. Note that  $\Gamma_c$  and  $\Gamma_{\text{th}}$  should not be the same and indeed the cold polytropic part can itself be the result of a piecewise combination.

We cannot conclude this section without an example that will be useful to clarify the ideas. Let us consider therefore the case of a hybrid equation of state, in which the cold part is made up of two different polytropic pieces, *i.e.*, a “hybrid” *piecewise polytropic equation of state*. Such an example is not purely academic, since it could provide, for instance, the description of a fluid which is non-relativistic (*i.e.*,  $\Gamma_1 = 5/3$ ) at low density, while being relativistic (*i.e.*,  $\Gamma_2 = 4/3$ ) at higher densities. At the same time, the inclusion of the thermal contribution can account for effects which may arise due to heating via shocks. We start by writing the cold part of the pressure as

$$p_c = \begin{cases} K_1\rho^{\Gamma_1}, & \text{for } \rho \leq \bar{\rho} \\ K_2\rho^{\Gamma_2}, & \text{for } \rho \geq \bar{\rho}, \end{cases} \quad (2.261)$$

where  $K_{1,2}$  and  $\Gamma_{1,2}$  are the polytropic constants and indices, respectively. As noted above, continuity in the pressures at the transition density,  $p_{c,1}(\bar{\rho}) = p_{c,2}(\bar{\rho})$ , requires that  $K_2 = K_1\bar{\rho}^{\Gamma_1-\Gamma_2}$  [*cf.*, Eq. (2.253)]. Imposing further that the specific internal energies are continuous at the transition density, *i.e.*,  $\epsilon_{c,1}(\bar{\rho}) = \epsilon_{c,2}(\bar{\rho})$ , and after a bit of algebra, we obtain that the polytropic (cold) part of the specific internal energy is

$$\epsilon_c = \begin{cases} \frac{K_1}{\Gamma_1 - 1}\rho^{\Gamma_1-1}, & \text{for } \rho \leq \bar{\rho} \\ \frac{K_2}{\Gamma_2 - 1}\rho^{\Gamma_2-1} + \frac{(\Gamma_2 - \Gamma_1)K_1}{(\Gamma_2 - 1)(\Gamma_1 - 1)}\bar{\rho}^{\Gamma_1-1} & \text{for } \rho \geq \bar{\rho}. \end{cases} \quad (2.262)$$

Finally, we can derive the expression for the total pressure  $p = p_c + p_{\text{th}}$  as

<sup>38</sup>In the simulation of neutron-star binaries, the polytropic component is often replaced by a cold, realistic equation of state; see Bauswein *et al.* (2010) for a recent extensive analysis.

$$p = \left( \frac{\Gamma - \Gamma_{\text{th}}}{\Gamma - 1} \right) K_1 \bar{\rho}^{\Gamma_1 - \Gamma} \rho^\Gamma - \frac{(\Gamma_{\text{th}} - 1)(\Gamma - \Gamma_1)}{(\Gamma_1 - 1)(\Gamma_2 - 1)} K_1 \bar{\rho}^{\Gamma_1 - 1} \rho + \rho \epsilon (\Gamma_{\text{th}} - 1), \quad (2.263)$$

where  $\Gamma = \Gamma_1$  for  $\rho \leq \bar{\rho}$  and  $\Gamma = \Gamma_2$  for  $\rho \geq \bar{\rho}$ . A bit more algebra allows one to verify that  $p = K_1 \rho^{\Gamma_1} + \rho \epsilon_{\text{th}} (\Gamma_{\text{th}} - 1)$  and  $p = K_2 \rho^{\Gamma_2} + \rho \epsilon_{\text{th}} (\Gamma_{\text{th}} - 1)$  for  $\rho \leq \bar{\rho}$  and  $\rho \geq \bar{\rho}$ , respectively. This hybrid and piecewise polytropic equation of state has been used extensively in the study of stellar-core collapse (Dimmelmeier *et al.*, 2002).

#### 2.4.8 Radiation fluid

A particularly interesting fluid is one which is composed of photons, which, we recall, follow the Bose–Einstein statistics. If the radiation field is not in vacuum but rather tightly coupled with matter through scattering and absorption processes, the behaviour of the *photon fluid* mimics very closely that of a more standard fluid of massive particles. In particular, in 1900 Planck found that the energy density per unit frequency (measured therefore in  $\text{erg cm}^{-3} \text{Hz}^{-1}$  in cgs units) of a radiation field in thermodynamic equilibrium within a cavity at temperature  $T$  is given by [*cf.*, Eqs. (2.155)–(2.134)]

$$e_R(\nu, T) = \left( \frac{8\pi h_p}{c^3} \right) \frac{\nu^3}{\exp(h_p \nu / k_B T) - 1}, \quad (2.264)$$

where  $\nu$  is the frequency of the radiation, while  $h_p = 6.62607 \times 10^{-27} \text{erg s}$  is the Planck constant. If we divide Eq. (2.264) by the energy of a photon,  $E = h_p \nu$ , we readily obtain the number density of photons with frequency in the range  $(\nu, \nu + d\nu)$ , as

$$n(\nu) d\nu = \left( \frac{8\pi}{c^3} \right) \frac{\nu^2 d\nu}{\exp(h_p \nu / k_B T) - 1}. \quad (2.265)$$

The corresponding *mean intensity*, measured in  $\text{erg cm}^{-2} \text{s}^{-1} \text{Hz}^{-1}$ , is then given by the *Planck function*

$$B(\nu, T) := \frac{c}{4\pi} e_R(\nu, T) = \left( \frac{2h_p}{c^2} \right) \frac{\nu^3}{\exp(h\nu / k_B T) - 1}, \quad (2.266)$$

which is also commonly referred to as *black-body radiation*. If we now integrate (2.264) with respect to frequency and recall that the *Bose–Einstein integral* is

$$\int_0^\infty \frac{x^3}{\exp(x) - 1} dx = \frac{\pi^4}{15}, \quad (2.267)$$

we immediately obtain that the energy density of the photon fluid in thermodynamic equilibrium, or *thermal radiation energy density*, is simply proportional to the fourth power of the temperature, namely, that

$$e_R(T) = a_R T^4, \quad (2.268)$$

where

$$a_R := \frac{8\pi^5 k_B^4}{15h_p^3 c^3} = 7.56 \times 10^{-15} \text{erg cm}^{-3} \text{K}^{-4} \quad (2.269)$$

## 124 A Kinetic-Theory Description of Fluids

is called the *radiation constant*.<sup>39</sup> Proceeding in a similar way, and bearing in mind that the thermal radiation is necessarily isotropic, it is possible to compute the corresponding thermal radiation pressure as

$$p_R(T) = \frac{1}{3}a_R T^4 = \frac{1}{3}e_R(T), \quad (2.270)$$

thus reproducing the equation of state of an ultrarelativistic fluid encountered in Section 2.4.4.

A few remarks are worth making at this point. First, in the case of a photon fluid (or of any ultrarelativistic fluid with massless constituents), the concept of specific enthalpy, *i.e.*, of enthalpy per unit mass, obviously ceases to be valid. Nevertheless, it is still possible to define a *radiation enthalpy*, which is trivially given by

$$H_R = (e_R + p_R)V = \frac{4}{3}e_R V. \quad (2.271)$$

Second, although single photons move at the speed of light, it is possible to define the four-velocity of the radiation field as that of the matter fluid with which it is coupled, and thus define an energy–momentum tensor for a radiation fluid  $T_R^{\mu\nu}$ , in analogy to that of a perfect fluid (see Section 3.2). Finally, the equation of state (2.270) can also be obtained by considering that in the case of photons the energy–momentum tensor can be written as  $T_R^{\mu\nu} = \sum_* k^\mu k^\nu$ , where the sum is meant to be over all photons with unit wavenumber  $k_\mu$ . Since  $k^\mu k_\mu = 0$  and the photon fluid is isotropic, the energy–momentum tensor will be diagonal and with zero trace, *i.e.*,  $T_R^{\mu\nu} g_{\mu\nu} = -e_R + 3p_R = 0$ , thus leading again to (2.270).

The analogies between a photon fluid and a standard fluid of massive particles can further be appreciated by writing the first law of thermodynamics (2.136) for the radiation field as<sup>40</sup>

$$TdS = d(e_R V) + p_R dV = d(a_R T^4 V) + \frac{1}{3}a_R T^4 dV, \quad (2.272)$$

from which it follows that

$$dS = d\left(\frac{4}{3}a_R T^3 V\right), \quad (2.273)$$

and thus that the entropy and the *entropy density*,  $\tilde{s}$ , are given by

$$S = \frac{4}{3}a_R T^3 V, \quad \tilde{s} := \frac{S}{V} = \frac{4}{3}a_R^{1/4} e^{3/4} \propto e^{3/4}. \quad (2.274)$$

Hence, in the case of isentropic transformations, Eq. (2.274) implies that  $T^3 V = \text{const.}$ , or, equivalently, that  $p_R V^{4/3} = \text{const.}$  In this way, we have just found that the photon fluid behaves as a polytrope with adiabatic index  $\Gamma = 4/3$ .

<sup>39</sup>The radiation constant  $a_R$  is related to the *Stefan–Boltzmann constant*,  $\sigma_{SB}$ , via the relation  $a_R = 4\sigma_{SB}/c$ .

<sup>40</sup>Note that for a radiation field, as for an ultrarelativistic fluid, the rest-mass energy density is not defined, while the internal-energy density coincides with the energy density.

When the radiation field is in thermal equilibrium with a fluid obeying the ideal-fluid equation of state, the energy densities simply add [*cf.*, Eq. (2.235)] and the total energy density is given by

$$e = e_M + e_R = \rho \left[ c^2 + \frac{nk_B T}{\rho(\gamma - 1)} \right] + a_R T^4, \quad (2.275)$$

where the indices “*M*” and “*R*” refer to the matter and radiation fluids, respectively. The corresponding equation of state of the mixture is given simply by

$$p = p_M + p_R = nk_B T + \frac{1}{3} a_R T^4, \quad (2.276)$$

so that, if we now introduce the parameter  $\alpha$

$$\alpha := \frac{p_R}{p_M}, \quad (2.277)$$

the total pressure can be rewritten simply as<sup>41</sup>

$$p = p_M (1 + \alpha). \quad (2.278)$$

The parameter  $\alpha$  allows us to scan the range of possible behaviours ranging from the fluid-pressure-dominated regime (*i.e.*,  $\alpha \rightarrow 0$ ), over to the radiation-dominated regime (*i.e.*,  $\alpha \rightarrow \infty$ ). In Section 2.4.6 we introduced three different definitions of the adiabatic index  $\gamma$  in terms of the indices  $\Gamma_1, \Gamma_2, \Gamma_3$ , and we also showed that they all coincide in an ideal fluid. However, under more general conditions, such as those encountered in a fluid-plus-radiation field, the three adiabatic indices defined by (2.239)–(2.241) differ. In this case, and under the further assumption that the perfect fluid is monatomic ( $\gamma = c_p/c_v = 5/3$ ), it is possible to show that (Mihalas and Mihalas, 1984)

$$\Gamma_1 = \frac{5/2 + 20\alpha + 16\alpha^2}{(3/2 + 12\alpha)(1 + \alpha)} \leq \frac{5}{3}, \quad (2.279)$$

$$\frac{\Gamma_2 - 1}{\Gamma_2} = \frac{1 + 5\alpha + 4\alpha^4}{5/2 + 20\alpha + 16\alpha^2} \leq \frac{2}{5}, \quad (2.280)$$

$$\Gamma_3 - 1 = \frac{1 + 4\alpha}{3/2 + 12\alpha} \leq \frac{2}{3}. \quad (2.281)$$

In this way, expressions (2.279)–(2.281) highlight that a photon fluid in thermal equilibrium with a monatomic ideal fluid behaves effectively as a polytrope with adiabatic index  $\Gamma_1 \rightarrow 4/3$  in the radiation-dominated regime, while it behaves effectively as a polytrope with adiabatic index  $\Gamma_1 \rightarrow 5/3$  in the fluid-pressure-dominated regime.

The equations describing the dynamics of a fully coupled mixture of matter and radiation fluids will be presented in Section 3.11.1, when discussing the dynamics of multifluids.

<sup>41</sup>A different parameterisation is sometimes used in terms of the ratio between the total pressure and the fluid pressure, *i.e.*,  $\beta = p_M/p = 1/(1 + \alpha)$ .

### 2.4.9 Dark-energy fluid

Over the last decade, a number of astronomical observations reporting the dependence on cosmological redshift of the apparent magnitudes for a sample of supernovae Ia, have shown that the universe is in a phase of accelerated expansion (Riess *et al.*, 1998; Perlmutter *et al.*, 1999). In particular, the observations indicate that, although the total density parameter of the universe is  $\Omega_{tot} \approx 1$  [cf., Eq. (1.276)], its baryonic content can account for only  $\sim 5\%$  of the total energy density, namely  $\Omega_b \approx 0.05$  (Planck Collaboration *et al.*, 2013). The remaining non-baryonic part is represented by what are now usually referred to as the *dark-matter* component, accounting for  $\Omega_{dm} \approx 0.26$ , and the *dark-energy* component, accounting for  $\Omega_{de} \approx 0.7$  [cf., Eq. (1.276)]. Although both “dark”, in the sense that their existence is revealed not through radiation but through gravitational effects, the dark matter is assumed to cluster on sub-megaparsec scales and has been invoked to explain the rotation curves of galaxies, while the dark energy is assumed to permeate the whole universe and is the ultimate cause for the accelerated expansion.

Recall that the evolution equations for the scale factor  $a$  in FRW solution (1.272) can be written as

$$\frac{\ddot{a}}{a} = -\frac{4}{3}\pi(e + 3p), \quad (2.282)$$

so that an accelerated expansion of the universe is possible if the right-hand side of the Friedmann equation (2.282) is negative. The attempt to reproduce this behaviour has led to the heuristic definition of an equation of state for a *dark-energy fluid* in the simple form

$$p = w(z)e, \quad (2.283)$$

where  $z$  is the *cosmological redshift* and the coefficient  $w(z)$  has been introduced to parameterise our “ignorance” about the properties of the effective fluid associated with the dark-energy component. The dependence in Eq. (2.283) on the cosmological redshift  $z$  is commonly expressed via a Taylor expansion around the present value  $z = 0$ , so that

$$w = w_0 + w_1(1 - a) = w_0 + w_1 \left( \frac{z}{1+z} \right), \quad (2.284)$$

where  $w_0$  and  $w_1$  represent the values of the coefficient at the present time and its variation with redshift  $z$ , respectively. Present cosmological observations seem to indicate  $w_0 \approx -1$  and  $w_1 \approx 0$ , thus indicating that the dark energy does not vary considerably over time. For simplicity, hereafter we will neglect these corrections and simply consider  $w = w_0$ . Note that Eq. (2.283) is entirely phenomenological as it does not have the explicit microscopic description that we have discussed so far for the other relativistic fluids (the only exceptions being the values  $w = 0$  and  $w = 1/3$ , see below). Therefore, the determination via astronomical observations of the coefficient  $w$  is one of the most challenging tasks of modern cosmology.

Since our interest here is to discuss the properties of this type of fluid more than to assess its cosmological relevance, we start by considering the sound speed associated with (2.283), which is simply given by

$$c_s^2 = w, \quad (2.285)$$

and thus defined only for  $w \geq 0$ . Considering therefore the equation of state (2.283) with  $w = \text{const.}$ , we can translate the *weak*, the *strong* and the *dominant* energy conditions, *i.e.*, Eqs. (2.98), (2.99) and (2.100), respectively, into the following conditions

$$\text{weak condition : } e + p \geq 0, e \geq 0 \iff w \geq -1, \quad (2.286)$$

$$\text{strong condition : } e + p \geq 0, e + 3p \geq 0, \iff w \geq -\frac{1}{3}, \quad (2.287)$$

$$\text{dominant condition : } e \geq |p|, \iff -1 \leq w \leq 1. \quad (2.288)$$

In other words, a negative-pressure fluid with  $-1/3 \leq w \leq 0$  is certainly unusual, but it still satisfies the strong energy condition, although only negative values of  $w$  with  $w < -1/3$  can be employed to produce an accelerated expansion [*cf.* Eq. (2.282)]. Even in this case, the fluid satisfies the dominant energy condition as long as  $w \geq -1$ .

Within a cosmological context, the different values of  $w$  reflect either different phenomenological states of matter responsible for the expansion of the universe ( $w \geq 0$ ), or account for different dynamical dark-energy models that have been proposed over the years ( $w < 0$ ). The latter can be roughly divided in two categories: those with  $-1 < w < 0$ , which include *quintessence* and *k-essence*, and those with  $w < -1$ , which include the *phantom models* [see, *e.g.*, Ellis *et al.* (2012) for a discussion].

The relevant limiting cases offered by the equation of state (2.283) can therefore be summarised as follows:

- $w = 1$ .

This represents the case of an *ultrastiff fluid* and is therefore usually referred to as an *ultrastiff equation of state*. Because the corresponding sound speed  $c_s^2 = 1$  is the largest that is possible to reach without violating special relativity, such an equation of state is also the stiffest possible and the fluid is also referred to as *incompressible*. It has been proposed as a possible description of the very early universe but it is not clear whether it corresponds to a physically realistic fluid.

- $w = 1/3$ .

This of course represents the case of an *isotropic radiation fluid* with sound speed  $c_s^2 = 1/3$  and it has been discussed in detail in Section 2.4.8.

- $w = 0$ .

This represents the case of a zero-pressure or *dust fluid*, whose sound speed is  $c_s^2 = 0$ . It represents a good approximation for the dynamics of baryonic and of cold dark matter at late times in the universe and, as we will discuss in more detail in Section 3.3, the equations of motion reduce to simple geodesics [*cf.* Eq. (3.55) in Section 3.3].

- $w = -1$ .

This represents the case of a *cosmological constant* and is a rather exceptional type of fluid. Firstly, it does satisfy (although only marginally) the weak energy condition ( $e \geq 0$  and  $e + p = 0$ ) but it does not satisfy the strong energy condition ( $e + 3p = -2e < 0$ ). Secondly, having zero specific enthalpy, the momentum equation does not constrain the

associated four-velocity [cf., Eqs. (3.55)]. Thirdly, the energy conservation equation implies that  $e$  is not only conserved but actually constant [cf., Eq. (3.57)], so that it is natural to associate the energy density of this dark energy with the actual cosmological constant, *i.e.*,  $e \propto \Lambda$  (see Section 1.7.3). Finally, since this type of fluid does not support classical perturbations, it does not have a sound speed.

In addition to the dark-energy fluids described by the equation of state (2.283), another cosmological fluid, the *Chaplygin fluid*, has been considered as a potential candidate for unified dark-matter and dark-energy models (Kamenshchik *et al.*, 2001). The Chaplygin fluid has an equally simple equation of state of the type

$$p = -\frac{A}{e}, \quad (2.289)$$

where  $A > 0$ . The corresponding energy density can be shown to evolve as [cf., Eq. (3.58)]

$$e = \sqrt{A + B(1+z)^6}, \quad (2.290)$$

where  $0 < B < A$ , so that the sound speed of a Chaplygin fluid is

$$c_s^2 = \frac{A}{A + B(1+z)^6}. \quad (2.291)$$

At early times, when  $z \gg 1$ ,  $e \rightarrow \sqrt{B}(1+z)^3$ , and the Chaplygin fluid behaves like a pressureless fluid with  $c_s^2 \approx 0$ . On the other hand, at late times, when  $z \rightarrow 0$ ,  $e \rightarrow \sqrt{A}$ ,  $p \rightarrow -\sqrt{A} = -e$  and  $c_s^2 \approx 1$ , so that the Chaplygin fluid behaves like dark energy with  $w \approx -1$  (Sapone, 2010). Although modifications of (2.289) of the type  $p = -A/e^C$  have been proposed recently, various observational data obtained from the cosmic microwave background radiation and from high-redshift supernovae of type Ia seem to exclude the Chaplygin fluid as a valid candidate for dark energy, setting a constraint of  $|C| < 10^{-5}$  at a 95% confidence level (Sandvik *et al.*, 2004).

#### 2.4.10 Newtonian and relativistic barotropic fluids

While Sections 2.4.1–2.4.9 have introduced some of the most relevant equations of state, this final section is dedicated to clarifying some subtleties about relativistic barotropic fluids that often risk being confused. In *Newtonian hydrodynamics*, a large class of equations of state are referred to as *barotropic* to reflect the condition that the pressure is a function uniquely of the (rest-mass) density, *i.e.*,

$$p = p(\rho). \quad (2.292)$$

This definition has a transparent physical meaning and essentially implies that *surfaces at constant density coincide with surfaces at constant pressure* or, equivalently, that such surfaces have parallel gradients, *i.e.*,  $\vec{\nabla}p = k\vec{\nabla}\rho$ . The extension of this definition to *relativistic hydrodynamics* is not unique, but it is convenient to define as *barotropic* a relativistic fluid such that the energy density is a function of the pressure *only* (Anile, 1989)<sup>42</sup>

<sup>42</sup>Note that some authors use the condition  $e = e(\rho)$  to define a fluid as barotropic (Gourgoulhon, 2006; Andersson and Comer, 2007).

$$e = e(p), \quad (2.293)$$

so that, assuming that such a relation is invertible, the pressure is a function of the energy density *only*

$$p = p(e). \quad (2.294)$$

In other words, in a relativistic barotropic fluid *isobaric surfaces coincide with surfaces at constant energy density*. Using this definition it is then clear that a dark-energy fluid, a photon fluid, and also a non-degenerate ultrarelativistic fluid or a completely degenerate ultrarelativistic Fermi fluid, *are* barotropic (see Sections 2.4.1–2.4.5). On the other hand, a degenerate and non-degenerate relativistic fluid, a non-degenerate non-relativistic fluid, or any degenerate Fermi fluid which is not ultrarelativistic, *are not* barotropic (see Sections 2.4.1–2.4.5).

The properties of an ideal fluid are less obvious and indeed an ideal fluid is in general not a barotropic fluid, although it could be, at least in one case. More specifically, we have seen that for such a fluid the pressure is  $p = p(\rho, \epsilon) \propto \rho\epsilon \propto e - \rho$ , which, in general, is *not* a function of the energy density only (but see the exception below). The properties of a polytropic fluid  $p = p(\rho)$  also require some special care. In the case in which it models a fluid with  $\epsilon = 0$ , the energy density coincides with the rest-mass density (*i.e.*,  $e = e(\rho)$ ) and the polytropic fluid is then obviously barotropic, since  $p = p(\rho) = p(e)$ . However, if the fluid has a *nonzero* specific internal energy, then a polytropic fluid is barotropic only if  $\epsilon = \epsilon(\rho)$ . In this case, in fact,  $e = e(\rho)$ , from which  $\rho = \rho(e)$ , and thus  $p = p(e)$ . Note that both an ideal fluid and a polytropic fluid become barotropic under the same requirement, namely  $\epsilon = \epsilon(\rho)$ , and this is the only case in which an ideal fluid is barotropic.<sup>43</sup>

The properties of a polytropic fluid with specific internal energy  $\epsilon = \epsilon(\rho)$  give us the opportunity for an additional comment. Starting from the first law of thermodynamics, a bit of algebra allows one to deduce that (see Problem 8)

$$d\rho \left( \frac{\partial \epsilon}{\partial \rho} - \frac{p}{\rho^2} \right) = Tds, \quad (2.295)$$

thus expressing that a polytropic equation of state is isentropic (*i.e.*,  $ds = 0$ ) if and only if

$$\frac{\partial \epsilon}{\partial \rho} = \frac{p}{\rho^2}. \quad (2.296)$$

The expression above clarifies that a polytropic fluid is *not* necessarily an isentropic fluid and that the additional condition (2.296) must be satisfied by the specific internal energy. Since we have seen in Section 2.4.7 that a polytropic equation of state is equivalent to an ideal-fluid equation of state for those isentropic transformations for which the adiabatic index of the fluid  $\gamma$  coincides with the adiabatic index of the polytrope  $\Gamma$ , it does not come as a surprise that the condition (2.296) is satisfied when the specific internal energy is expressed as in Eq. (2.248), *i.e.*,  $\epsilon = K\rho^{\Gamma-1}/(\Gamma - 1)$ . In fact, a polytropic fluid which is also isentropic can *only* have a specific energy density expressed as in Eq. (2.248). Should a transformation (*e.g.*, the development of a shock wave) lead to a violation of (2.248), this transformation

<sup>43</sup>If an ideal fluid has  $\epsilon = \epsilon(\rho)$ , then  $p = p(\rho, \epsilon) = p(\rho)$ , but this does not force the ideal fluid to be polytropic. Any functional dependence other than  $p = K\rho^\Gamma$  could be used in principle.

### **130** *A Kinetic-Theory Description of Fluids*

must be accompanied by an increase of entropy. Conversely, if in a numerical simulation the constraint (2.248) is imposed, then conservation of entropy is automatically guaranteed (Font *et al.*, 2002).

## 2.5 Further reading

- Cercignani, C. and Kremer, G. M. (2002). *The Relativistic Boltzmann Equation: Theory and Applications*. Birkhäuser, Boston.
- Ehlers, J. (1971). *General Relativity and Kinetic Theory*. In General Relativity and Cosmology, 1–70. Proceedings of the Varenna Summer School on Relativistic Astrophysics. Academic Press, New York.
- Huang, K. (1987). *Statistical Mechanics*. Second Edition. John Wiley, New York.
- Landau, L. D. and Lifshitz, E. M. (1980). *Statistical Physics*. Course of Theoretical Physics, Vol. 5. Butterworth-Heinemann, Oxford.
- Liboff, R. L. (2003). *Kinetic Theory: Classical, Quantum, and Relativistic Descriptions*. Springer, Berlin.
- Pitaevskii, L. P. and Lifshitz, E. M. (1981). *Physical Kinetics*. Course of Theoretical Physics, Vol. 10. Pergamon Press, Oxford.
- Reif, F. (1965). *Fundamentals of Statistical and Thermal Physics*. McGraw-Hill, Boston.
- Stewart, J. M. (1971). *Non-equilibrium Relativistic Kinetic Theory*. Volume 10, Lecture Notes in Physics, Springer, Berlin.

## 2.6 Problems

1. Derive the *transport equation* for the volume density  $n\langle\psi\rangle$  given by Eq. (2.32).
2. Derive the Newtonian conservation equations (2.34)–(2.36) expressing the conservation of number density, momentum and energy, respectively.
3. Derive the explicit expression for the *Maxwell–Boltzmann distribution* given by Eq. (2.48).
4. Show that Eqs. (2.52) and (2.59) are equivalent.
5. Show that Eq. (2.70) can also be written as

$$\frac{D}{Dt} \left( \frac{1}{2} \rho \vec{v}^2 + \rho \epsilon \right) + \left( \frac{1}{2} \rho \vec{v}^2 + \rho \epsilon + p \right) \vec{\nabla} \cdot \vec{v} = \rho \vec{v} \cdot \left( \frac{\vec{F}}{m} - \frac{1}{\rho} \vec{\nabla} p \right).$$

6. Show that the equation of state of a non-degenerate relativistic fluid discussed in Section 2.4.2 can be approximated by the fitting formula

$$\frac{p}{e+p} = 0.36y + 0.036346y^2 - 0.088763y^3 - 0.047698y^4 - 0.083547y^5 + 0.073662y^6,$$

where  $y = \zeta_c^{-1}/(0.36 + \zeta_c^{-1})$ . Compute how good this approximation is by comparing it with Eqs. (2.182)–(2.184). For more details see Service (1986).

7. Use Eq. (2.264) and Eq. (2.265) to show that the mean energy per photon of a radiation field in thermodynamic equilibrium within a cavity at temperature  $T$  is given by  $2.7k_B T$ .
8. Assuming that the fluid is isentropic, *i.e.*,  $ds = 0$  and follows a polytropic equation of state, *i.e.*,  $p = p(\rho)$ , derive expression (2.295).

# 3

## Relativistic Perfect Fluids

---

Having laid out the foundations of relativistic hydrodynamics from relativistic kinetic theory, we are now ready to construct the mathematical framework that is behind relativistic perfect fluids, that is, fluids for which viscous effects and heat fluxes are zero, and the pressure tensor is diagonal. Starting from the definition of the kinematic elements of a perfect fluid and of the building block of relativistic hydrodynamics, namely, the energy–momentum tensor, we will explore the numerous forms that the equations of relativistic hydrodynamics assume under a variety of conditions. While some of these conditions reflect simplifying assumptions, *e.g.*, that the flow is either stationary, or irrotational, or isentropic, the resulting analytic solutions will provide us with a very valuable insight that we will exploit when discussing more complex and realistic conditions. Finally, a part of this chapter will be dedicated to more advanced topics, such as the derivation of the relativistic hydrodynamic equations from variational principles or an introduction to the properties of multicomponent fluids. While some of the topics covered in this chapter are best suited to readers with a mathematical inclination, they will help us build a more complete mathematical framework of relativistic perfect fluids which combines relativistic kinetic theory with field theory.

### 3.1 Kinematic properties of fluids

#### 3.1.1 Kinematic shear, expansion and vorticity

Before discussing the properties of relativistic perfect fluids, it is useful to introduce some quantities that describe the kinematic properties of any fluid, irrespective of their equations of state or of the state of motion. The first fundamental kinematic quantity of the fluid is obviously its *four-velocity*,  $\mathbf{u}$ , whose contravariant components in a coordinate system  $x^\mu = (t, \mathbf{x}^i)$  are given by

$$u^\mu := \frac{dx^\mu}{d\tau}, \quad (1.111)$$

where  $\tau$  is the fluid *proper time*, that is, the proper time of an observer comoving with the fluid (see Section 1.4). The second fundamental quantity is instead given by the fluid (kinematic) *four-acceleration*,  $\mathbf{a}$ , whose contravariant components are defined as (see Section 1.5.4)

$$a^\mu := u^\nu \nabla_\nu u^\mu. \quad (3.1)$$

Both the four-velocity and the four-acceleration satisfy two fundamental relations, which will be important for the derivation of several results in this chapter. These are the normalisation condition

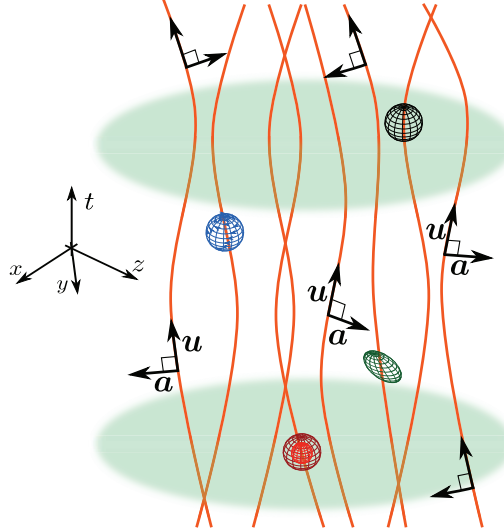


**Fig. 3.1** Schematic spacetime diagram illustrating the worldlines of fiducial fluid elements, together with the local four-velocity vector and acceleration four-vector. Also shown are wireframe spheres for the various kinematic tensors that can be associated to a fluid element (see Fig. 3.2).

$$\mathbf{u} \cdot \mathbf{u} = u^\mu u_\mu = -1, \quad (3.2)$$

and the orthogonality condition

$$\mathbf{a} \cdot \mathbf{u} = a^\mu u_\mu = 0, \quad (3.3)$$

which is easy to prove after taking the covariant derivative of (3.2) to obtain the identity

$$u^\mu \nabla_\nu u_\mu = 0. \quad (3.4)$$

Figure 3.1 offers a schematic spacetime diagram illustrating the worldlines of fiducial fluid elements and the local four-velocity vector (which is tangent to the worldline) and the local acceleration four-vector (which is orthogonal to the four-velocity). Also shown are wireframe spheres representing the various kinematic tensors that can be associated to a fluid element and that will be introduced below (*cf.*, Fig. 3.2).

As already done in Section 1.4, we can write the components of the four-velocity (1.111) in full generality as

$$u^\mu = u^0 \left( 1, \frac{dx^i}{dt} \right) = u^0 (1, v^i), \quad (3.5)$$

where  $t$  is instead the *coordinate time*. All the kinematic properties of the fluid can be expressed in terms of the vectors  $\mathbf{u}$  and  $\mathbf{a}$ . In order to show this, we introduce the definition of the *displacement vector*  $\xi^\mu$  as the four-vector connecting two fluid elements that are infinitesimally close, as they move along their worldlines, which, in general, will not be geodesics. The

rate of change of the displacement vector is given by  $u^\mu \nabla_\mu \xi^\nu$ , but because  $\xi$  is Lie dragged along  $\mathbf{u}$ , i.e.,  $\mathcal{L}_\mathbf{u} \xi = 0$ , we have (see Section 1.5.1)

$$u^\mu \nabla_\mu \xi^\nu = \xi^\mu \nabla_\mu u^\nu, \quad (3.6)$$

and therefore

$$\dot{\xi}^\mu := u^\nu \nabla_\nu \xi^\mu = \xi^\nu \nabla_\nu u^\mu. \quad (3.7)$$

Note that, according to the definition introduced in Section 1.5.4, Eq. (3.7) represents the *convective derivative* of the displacement vector  $\xi^\mu$  along the vector  $\mathbf{u}$ , i.e., along the fluid worldlines.<sup>1</sup> As discussed in Section 2.2.3 in a Newtonian context, we can regard the integral curves of the differential equation  $\dot{\xi}^\mu = \text{const.}$  as the *fluidlines* of the various fluid elements, and thus the *streamlines* as the spatial projections of such integral curves (see Fig. 2.4). Using now the *irreducible decomposition* (1.99), which holds for any  $\binom{0}{2}$  tensor, and applying it to  $\nabla_\nu u_\mu$ , we obtain

$$\dot{\xi}_\mu = \xi^\nu \nabla_\nu u_\mu = \left( \omega_{\mu\nu} + \sigma_{\mu\nu} + \frac{1}{3} \Theta h_{\mu\nu} - a_\mu u_\nu \right) \xi^\nu, \quad (3.8)$$

where

$$h_{\mu\nu} := g_{\mu\nu} + u_\mu u_\nu \quad (3.9)$$

is the *projection tensor*, which projects any tensor on the hypersurface orthogonal to  $u^\mu$  (see Section 1.3.9 for some of the properties of  $\mathbf{h}$ ). In essence, using simple kinematic arguments, we have shown that the covariant derivative of the four-velocity can be decomposed into the following “*irreducible tensorial parts*”

$$\nabla_\nu u_\mu = \omega_{\mu\nu} + \sigma_{\mu\nu} + \frac{1}{3} \Theta h_{\mu\nu} - a_\mu u_\nu, \quad (3.10)$$

where these irreducible tensorial parts are defined as

$$\omega_{\mu\nu} := h^\alpha_\mu h^\beta_\nu \nabla_{[\beta} u_{\alpha]} = \nabla_{[\nu} u_{\mu]} + a_{[\mu} u_{\nu]}, \quad (3.11)$$

$$\sigma_{\mu\nu} := \nabla_{(\mu} u_{\nu)} = \nabla_{(\mu} u_{\nu)} + a_{(\mu} u_{\nu)} - \frac{1}{3} \Theta h_{\mu\nu}, \quad (3.12)$$

$$\Theta := h^{\mu\nu} \nabla_\nu u_\mu = \nabla_\mu u^\mu. \quad (3.13)$$

As a result, the tensor  $\omega_{\mu\nu}$ , which is called the *kinematic vorticity tensor* (or *twist*), is the antisymmetric part of the covariant derivative of the four-velocity, computed in the space orthogonal to  $\mathbf{u}$ . Similarly, the tensor  $\sigma_{\mu\nu}$ , which is called the *shear tensor*, is the trace-free symmetric part of the covariant derivative of the four-velocity, again computed in the orthogonal space. Finally, the scalar  $\Theta$ , which is called the *expansion scalar* (or simply *expansion*),

<sup>1</sup>A mathematically more precise statement is that Eq. (3.7) is the convective derivative of the displacement vector  $\xi$  along the congruence of the fluid worldlines with tangent vector field  $\mathbf{u}$ .

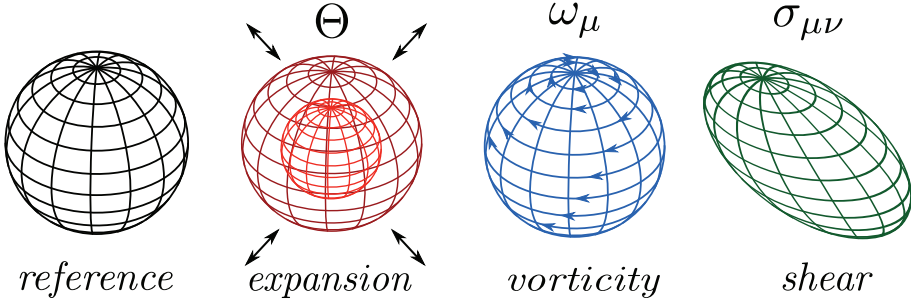


**Fig. 3.2** Schematic diagram illustrating the physical interpretation of the action of the various kinematic tensors on a fluid element idealised as a reference sphere on the left. The action of the expansion  $\Theta$  changes the volume of the sphere but preserves the principal axes. The action of the kinematic vorticity vector  $\omega_\mu$  introduces a rotation around a fixed axis. The action of the shear tensor  $\sigma_{\mu\nu}$  distorts the sphere but preserves the volume and the principal axes of the sphere [cf., Fig. 3.1].

is the four-divergence of the four-velocity. By construction, the following relations hold for the kinematic tensors,

$$\omega_{(\mu\nu)} = \sigma_{[\mu\nu]} = 0, \quad \sigma^\mu{}_\mu = 0, \quad \omega_{\mu\nu} u^\nu = 0 = \sigma_{\mu\nu} u^\nu, \quad (3.14)$$

and consequently also

$$\omega_{\mu\nu} h^{\mu\nu} = 0, \quad \sigma_{\mu\nu} h^{\mu\nu} = 0. \quad (3.15)$$

As for their Newtonian counterparts, the importance of these quantities is in providing us with specific and distinct information about the possible types of fluid motion. For example, if we consider a fluid element as approximated by an ellipsoid, then the kinematic vorticity tensor will describe rigid rotations of the principal axis of the ellipsoid with respect to the local inertial rest frame. Its dual in the comoving frame determined by  $u^\mu$  defines a *kinematic vorticity four-vector*

$$\omega^\mu := {}^*\omega^{\mu\nu} u_\nu = \frac{1}{2} \epsilon^{\mu\nu\alpha\beta} \omega_{\alpha\beta} u_\nu, \quad (3.16)$$

where  ${}^*\omega^{\mu\nu}$  is the dual tensor of  $\omega_{\mu\nu}$  (not to be confused with  $\omega^{\mu\nu}$ ) and  $\epsilon^{\mu\nu\alpha\beta}$  is the Levi-Civita tensor, whose properties have been illustrated in Section 1.3.7.

The shear tensor, on the other hand, describes pure deformations and the three eigenvalues of  $\sigma^{\mu\nu}$  are the rate of change of the axial lengths of the ellipsoid as it evolves. The trace-free character of the shear tensor reflects the property that this deformation takes place while maintaining the volume of the ellipsoid constant. Finally, the expansion describes changes of the ellipsoid that are only in the volume, but not in shape. All of these quantities are schematically shown in Fig. 3.2, which provides a physical interpretation of the expansion  $\Theta$ , of the kinematic vorticity four-vector  $\omega_\mu$ , and of the shear tensor  $\sigma_{\mu\nu}$  for a fluid element idealised as a wireframe sphere. Shown on the left is the reference fluid element.

### 3.1.2 Evolution laws of the kinematic quantities

An evolution law can be derived for each of the kinematic quantities introduced above after following a simple strategy. First, in a spacetime without torsion we can express the fact that covariant derivatives do not commute as [cf., Eq. (1.188)]

$$\nabla_\mu \nabla_\nu u_\lambda - \nabla_\nu \nabla_\mu u_\lambda = R^\kappa_{\lambda\nu\mu} u_\kappa, \quad (3.17)$$

where  $R^\kappa_{\lambda\nu\mu}$  is the Riemann tensor [cf., Eq. (1.191)], which allows us to write

$$\begin{aligned} u^\mu \nabla_\mu \nabla_\nu u_\lambda &= R^\kappa_{\lambda\nu\mu} u_\kappa u^\mu + u^\mu \nabla_\nu \nabla_\mu u_\lambda \\ &= R_{\mu\nu\lambda}{}^\kappa u^\mu u_\kappa + \nabla_\nu (u^\mu \nabla_\mu u_\lambda) - (\nabla_\nu u^\mu)(\nabla_\mu u_\lambda). \end{aligned} \quad (3.18)$$

Using the decomposition (3.10), the equation above can be written equivalently as

$$u^\mu \nabla_\mu \left( \sigma_{\lambda\nu} + \omega_{\lambda\nu} + \frac{1}{3} \Theta h_{\lambda\nu} - a_\lambda u_\nu \right) = R_{\mu\nu\lambda}{}^\kappa u^\mu u_\kappa + \nabla_\nu a_\lambda - (\nabla_\nu u^\mu)(\nabla_\mu u_\lambda). \quad (3.19)$$

Taking now respectively the antisymmetric part, the symmetric part and the trace of (3.19), we obtain the evolution laws of the kinematic vorticity, of the shear and of the expansion (see Problem 2), *i.e.*,

$$\begin{aligned} u^\mu \nabla_\mu \omega_{\lambda\nu} &= -\frac{2}{3} \Theta \omega_{\lambda\nu} + 2\omega_{\gamma[\lambda} \sigma^{\gamma}_{\nu]} + u^\mu \nabla_\mu (a_{[\lambda} u_{\nu]}) + \nabla_{[\nu} a_{\lambda]} \\ &\quad + \sigma_{\gamma[\lambda} u_{\nu]} a^\gamma - \omega_{\gamma[\lambda} u_{\nu]} a^\gamma + \frac{1}{3} \Theta a_{[\lambda} u_{\nu]}, \end{aligned} \quad (3.20)$$

$$\begin{aligned} u^\mu \nabla_\mu \sigma_{\lambda\nu} &= -\frac{2}{3} \Theta \sigma_{\lambda\nu} - \sigma_{\lambda\kappa} \sigma^{\kappa}_{\nu} - \omega_{\lambda\kappa} \omega^{\kappa}_{\nu} + \frac{2}{3} h_{\lambda\nu} (\sigma^2 - \omega^2) \\ &\quad + C_{\mu\nu\lambda\kappa} u^\mu u^\kappa + \frac{1}{2} \left( h_{\lambda\mu} h_{\nu\kappa} R^{\mu\kappa} - \frac{1}{3} h_{\lambda\nu} h_{\mu\kappa} R^{\mu\kappa} \right) \\ &\quad - \frac{1}{3} h_{\lambda\nu} \nabla_\mu a^\mu - \frac{1}{3} \Theta a_{(\lambda} u_{\nu)} + u^\mu \nabla_\mu a_{(\lambda} u_{\nu)} + \nabla_{(\nu} a_{\lambda)} \\ &\quad + \sigma_{\gamma(\lambda} u_{\nu)} a^\gamma - \omega_{\gamma(\lambda} u_{\nu)} a^\gamma, \end{aligned} \quad (3.21)$$

$$u^\mu \nabla_\mu \Theta = -R_{\mu\nu} u^\mu u^\nu - 2(\sigma^2 - \omega^2) - \frac{1}{3} \Theta^2 + \nabla_\mu a^\mu, \quad (3.22)$$

where  $R_{\mu\nu}$  is the Ricci tensor [cf., Eq. (1.203)],  $\sigma$  and  $\omega$  are the *shear scalar* and the *vorticity scalar*, *i.e.*,

$$\sigma^2 := \frac{1}{2} \sigma_{\mu\nu} \sigma^{\mu\nu}, \quad \omega^2 := \frac{1}{2} \omega_{\mu\nu} \omega^{\mu\nu}, \quad (3.23)$$

while  $C_{\mu\nu\lambda\kappa}$  is the Weyl tensor [cf., Eq. (1.214)]. Note that in deriving (3.20)–(3.22) we have used the identities

$$\begin{aligned} (\nabla_\nu u^\mu) (\nabla_\mu u_\lambda) &= \sigma_{\gamma\lambda} \sigma^\gamma_\nu - 2\omega_{\gamma[\lambda} \sigma^\gamma_{\nu]} + \omega_{\lambda\gamma} \omega^\gamma_\nu + \frac{2}{3}\Theta\sigma_{\lambda\nu} + \frac{2}{3}\Theta\omega_{\lambda\nu} \\ &\quad + \frac{1}{9}\Theta^2 h_{\lambda\nu} - \sigma_{\gamma\lambda} u_\nu a^\gamma + \omega_{\gamma\lambda} u_\nu a^\gamma - \frac{1}{3}\Theta a_\lambda u_\nu, \end{aligned} \quad (3.24)$$

$$(\nabla_\nu u^\mu) (\nabla_\mu u^\nu) = 2(\sigma^2 - \omega^2) + \frac{1}{3}\Theta^2. \quad (3.25)$$

It is easier to appreciate the dynamical implications of Eqs. (3.20)–(3.22) through a few simple examples. First of all, we can consider the equation for the kinematic vorticity (3.20) under the assumption of geodesic motion, *i.e.*,  $a^\mu = 0$ , in which case the evolution of the vorticity four-vector is given by (see Problem 3)

$$\dot{\omega}^\mu := u^\nu \nabla_\nu \omega^\mu = -\frac{2}{3}\Theta\omega^\mu + \sigma^\mu_\nu \omega^\nu. \quad (3.26)$$

Equation (3.26) highlights that the geodesic motion will be irrotational, *i.e.*,  $\omega^\mu = 0$ , if the kinematic vorticity is initially zero; stated differently, vortices cannot be created in a flow which is initially irrotational. In Section 3.7 we will reconsider the definition of vorticity, expanding it from its purely kinematic context, and discussing how it relates to the properties of an irrotational flow.

As another representative example, we can replace the Ricci tensor in Eq. (3.22) via the Einstein equations (1.220) and assume that the energy–momentum tensor is that of dust, *i.e.*, with  $p = 0$  and  $T^{\mu\nu} = eu^\mu u^\nu$ . In this case, the equations of motion are simply the geodesic equations and Eq. (3.22) becomes

$$\dot{\Theta} := u^\mu \nabla_\mu \Theta = 2(\omega^2 - \sigma^2) - \frac{1}{3}\Theta^2 - 4\pi e, \quad (3.27)$$

which is the so-called *Raychaudhuri equation*, and determines the rate of change of the cross-sectional area orthogonal to the bundle of geodesics, each of which can be thought of as representing the worldline of a fluid element. Equation (3.27) then clarifies that a decelerated expansion, *i.e.*,  $\dot{\Theta} < 0$ , is produced by an initial nonzero expansion, or by the interplay between the shear and the vorticity via the term  $\propto (\omega^2 - \sigma^2) < 0$ , or by the “attractive” action of gravity via the energy density  $e$ . On the other hand, an accelerated expansion, *i.e.*,  $\dot{\Theta} > 0$ , could be generated by vorticity, which plays here the role of a Newtonian centrifugal force, when it dominates over shear and gravity.

## 3.2 Mass current and energy–momentum of perfect fluids

Although Eq. (2.95) is a perfectly consistent definition of the energy–momentum tensor, it is also strictly connected with the definition of an equilibrium distribution function, which needs to be properly computed. In what follows we discuss a straightforward and intuitive approach to obtain an explicit expression for the energy–momentum tensor of perfect fluids without having to consider a form for the distribution function.

We start by recalling that in Newtonian kinetic theory, perfect fluids are those described by an equilibrium distribution function which, when expressed in terms of the “flow” velocity, *i.e.*, the local average of the velocities of all the particles comprising the “fluid element”, are characterised by an isotropic pressure tensor and by a vanishing energy flux (see Section 2.2.5). Both properties should be preserved when extending the definition of perfect fluids to a relativistic regime. Also in this case we need to consider our measurements to be made by an observer that is momentarily comoving with the fluid element, *i.e.*, in the fluid-element’s Lorentz rest frame. Of course, also in a relativistic regime this choice does not prevent the individual particles from having a nonzero velocity with respect to such an element.

The simplest quantity to determine is the *rest-mass density current*, namely [*cf.* Eq. (2.94)]

$$J^{\hat{\mu}} : \text{flux of rest-mass current density in the } \hat{\mu}\text{-direction,}$$

where we have indicated with “hats” the vector components computed in the local rest frame of a comoving observer. Since we want the comoving observer to measure a zero flux of matter along any direction, the components of this rest-mass density current are simply given by

$$J^{\hat{\mu}} = (\rho, 0, 0, 0). \quad (3.28)$$

Similarly, recalling that the energy-momentum tensor expresses [*cf.* Eq. (2.95)]

$$T^{\hat{\mu}\hat{\nu}} : \text{flux of } \hat{\mu}\text{-momentum in the } \hat{\nu}\text{-direction,}$$

we can compute the expressions for the energy-momentum tensor by simply requiring that it satisfies the conditions described above, *i.e.*,

$$\begin{aligned} T^{\hat{0}\hat{0}} &: \text{total energy density,} \\ T^{\hat{0}\hat{i}} &: \text{flux of energy density in } \hat{i}\text{-th direction,} \\ T^{\hat{i}\hat{0}} &: \text{flux of } \hat{i}\text{-momentum in } \hat{0}\text{-th direction (}\hat{i}\text{-momentum density),} \\ T^{\hat{j}\hat{i}} &: \text{flux of } \hat{j}\text{-th component of momentum density in } \hat{i}\text{-th direction .} \end{aligned}$$

This is indeed shown in Fig. 3.3, which offers a schematic view of the different components of the energy-momentum tensor and the corresponding physical meaning. Note that if  $E$  is the average relativistic energy of the particles in the fluid, so that  $E = \langle p^{\hat{0}} \rangle$ , and requiring that  $T^{\hat{\mu}\hat{\nu}}$  is a symmetric tensor, the components of the energy-momentum tensor should be given by

$$\begin{aligned} T^{\hat{0}\hat{0}} &= n\langle p^{\hat{0}} \rangle = e, \\ T^{\hat{0}\hat{i}} &= T^{\hat{i}\hat{0}} = 0, \\ T^{\hat{j}\hat{i}} &= T^{\hat{i}\hat{j}} = 0, & \text{for } i \neq j \\ T^{\hat{j}\hat{i}} &= p, & \text{for } i = j \end{aligned} \quad (3.29)$$

or, when expressed in matrix form,

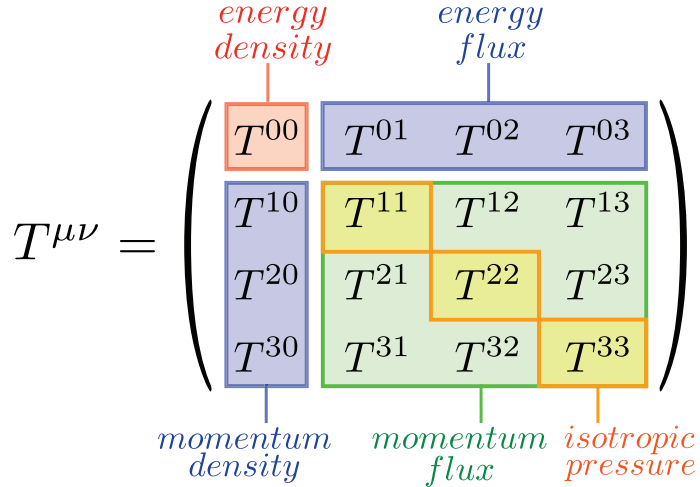


**Fig. 3.3** Schematic diagram illustrating the different parts composing the energy–momentum tensor of a perfect fluid in the local rest frame of a comoving observer. Note the location of the *energy density*  $T^{00}$  (red), of the *energy flux*  $T^{0i}$  (light blue), of the *momentum density*  $T^{i0}$  (light blue), of the *momentum flux*  $T^{ij}$  (green), and of the *isotropic pressure*  $T^{ii}$  (orange).

$$T^{\hat{\mu}\hat{\nu}} = T_{\hat{\mu}\hat{\nu}} = \begin{pmatrix} e & 0 & 0 & 0 \\ 0 & p & 0 & 0 \\ 0 & 0 & p & 0 \\ 0 & 0 & 0 & p \end{pmatrix}. \quad (3.30)$$

By construction, the quantity  $e$  introduced above represents, the (*total*) *energy density* of the fluid and hence it is the sum of the rest-mass energy density and of the internal energy density<sup>2</sup>

$$e := \frac{Nm}{V} (1 + \epsilon) = \rho (1 + \epsilon). \quad (3.31)$$

In the discussion above we have made two implicit assumptions which are useful to discuss in more detail. First, we have assumed that the energy–momentum tensor is symmetric but we have not discussed the grounds for this assumption. While its symmetry is already dictated by construction [*cf.* Eq. (2.95)], it is also not difficult to realise that a tensor which measures the flux of momentum must be symmetric. If this was not the case, in fact, the asymmetry would introduce local torques on the fluid element (a permutation of the spatial indices can be thought of as a rotation), which would diverge in the continuum limit. Second, we have assumed that all the diagonal terms in the spatial part of  $T^{\hat{\mu}\hat{\nu}}$  are the same and equal to the pressure  $p$ . This assumption, which characterises what are defined as *isotropic*

<sup>2</sup>Because the contribution of the rest-mass energy may otherwise be lost, we recall that the definition of the energy density in a system of units in which  $c \neq 1$  is  $e := \rho (c^2 + \epsilon)$  [*cf.* Eq. (2.124)]. Also, note that we use a notation which is close to the standard Newtonian one and thus indicate the rest-mass density and the energy density as  $\rho$  and  $e$ , respectively. However, this is not the only notation in relativistic hydrodynamics and other authors indicate the rest-mass density as  $\rho_0$  and the energy density as  $\rho$ .

*perfect fluids*, is indeed a very reasonable one and validated by the experimental behaviour of classical fluids. However, the isotropy condition is not strictly necessary and it is possible to construct *anisotropic perfect fluid* by simply combining the energy-momentum tensors of two perfect fluids (Letelier, 1980). For such fluids, therefore, the energy-momentum tensor is still diagonal but with a form

$$(T^{\hat{\mu}\hat{\nu}})_{\text{anisotropic}} = (T_{\hat{\mu}\hat{\nu}})_{\text{anisotropic}} = \begin{pmatrix} e & 0 & 0 & 0 \\ 0 & p_r & 0 & 0 \\ 0 & 0 & p_t & 0 \\ 0 & 0 & 0 & p_t \end{pmatrix}, \quad (3.32)$$

where  $p_r$  and  $p_t$  are the *radial pressure* and the *tangential pressure*, respectively, and where in general  $p_r > p_t$ . Anisotropic perfect fluids are often used in the construction of relativistic models of exotic relativistic stars (Mak and Harko, 2003; Cattoen *et al.*, 2005; Chirenti and Rezzolla, 2007), and as toy models for stellar-core collapse calculations (Ibáñez and Miralles, 1985).

We can now rewrite the tensor components (3.28) and (3.30) in terms of the four-velocity  $u^{\hat{\mu}} = (1, 0, 0, 0)$  of the fluid in the comoving frame to find

$$J^{\hat{\mu}} = \rho u^{\hat{\mu}}, \quad (3.33)$$

and

$$T^{\hat{\mu}\hat{\nu}} = e u^{\hat{\mu}} u^{\hat{\nu}} + p (\eta^{\hat{\mu}\hat{\nu}} + u^{\hat{\mu}} u^{\hat{\nu}}). \quad (3.34)$$

We can now exploit the requirement of covariance to generalise (3.33) and (3.34) to any other frame as

$$J^\mu = \rho u^\mu, \quad (3.35)$$

$$T^{\mu\nu} = e u^\mu u^\nu + p (g^{\mu\nu} + u^\mu u^\nu) = (e + p) u^\mu u^\nu + p g^{\mu\nu}, \quad (3.36)$$

where  $J^\mu J_\mu = -\rho^2$  and the energy-momentum tensor has trace  $T^\mu_\mu = 3p - e$ . At the same time, we can follow the intuitive decomposition of the energy-momentum tensor made in (3.29) and use the projection tensor  $\mathbf{h}$  defined as  $h^\mu_\nu := u^\mu u_\nu + \delta^\mu_\nu$  [*cf.*, Eq. (3.9)] to define the derived quantities<sup>3</sup>

$$L_{\mu\nu} := h^\alpha_\mu h^\beta_\nu T_{\alpha\beta}, \quad (3.37)$$

$$L_\mu := -h^\alpha_\mu u^\beta T_{\alpha\beta}, \quad (3.38)$$

$$L := L^\mu_\mu, \quad (3.39)$$

$$e := u^\alpha u^\beta T_{\alpha\beta}. \quad (3.40)$$

In this way,  $L_{\mu\nu}$  represents the total projection of the energy-momentum tensor in the hyperplane orthogonal to  $\mathbf{u}$  and hence it represents the fully spatial *stress tensor*, with  $L_{\mu\nu} u^\mu = 0$  [*cf.*, the Newtonian equivalent (2.71)]. Similarly,  $L_\mu$  is the *spatial momentum density* and since  $\mathbf{h}$  and  $\mathbf{u}$  are orthogonal (*i.e.*,  $\mathbf{h} \cdot \mathbf{u} = 0$ ), also  $L_\mu u^\mu = 0$ . Finally, the energy density,  $e$ , can be regarded as the projection along the fluid four-velocity of the energy-momentum tensor.

<sup>3</sup>Note that the definitions (3.37)–(3.40) are similar but distinct from the 3+1 projections (7.76)–(7.79). In fact, while the former are obtained with a projector orthogonal to the *four-velocity*  $\mathbf{u}$ , the latter are obtained with a projector orthogonal to the *normal* to a spacelike hypersurface  $\mathbf{n}$  (see Section 7.2.2).

## 142 Relativistic Perfect Fluids

Using these definitions, we can build the general expression for the energy–momentum tensor of a generic fluid (*i.e.*, not necessarily a perfect one) and decompose it in terms of parts which are parallel and orthogonal to  $\mathbf{u}$  as [*cf.*, Eq. (6.13) for the explicit expression in the case of a non-perfect fluid]

$$T_{\mu\nu} = eu_\mu u_\nu + 2u_{(\mu}L_{\nu)} + L_{\mu\nu}, \quad (3.41)$$

whose trace is given by  $T^\mu_\mu = L^\mu_\mu - e = L - e$ . A bit of straightforward algebra then shows that, for a perfect fluid

$$L_\mu = 0, \quad L_{\mu\nu} = ph_{\mu\nu}, \quad L = 3p. \quad (3.42)$$

Now that we have the explicit expressions for the rest-mass density current (3.35) and for the energy–momentum tensor (3.36), we can write explicit relations between the thermodynamic quantities  $n, e, p$  and the distribution function  $f$ . With a little bit of algebra, it is not difficult to obtain that [*cf.*, the definitions (2.91)–(2.95)]

$$\rho = -u_\mu J^\mu = -mu_\mu \int p^\mu f \frac{d^3p}{p^0}, \quad (3.43)$$

$$e = u_\mu u_\nu T^{\mu\nu} = u_\mu u_\nu \int p^\mu p^\nu f \frac{d^3p}{p^0}, \quad (3.44)$$

$$p = \frac{1}{3} (\eta_{\mu\nu} + u_\mu u_\nu) T^{\mu\nu} = \frac{1}{3} (\eta_{\mu\nu} + u_\mu u_\nu) \int p^\mu p^\nu f \frac{d^3p}{p^0}. \quad (3.45)$$

In addition, we can go back to the energy conditions discussed in Section 2.3.2 and realise that the weak energy condition (2.98) relative to an observer with four-velocity  $\mathbf{u}$  translates into the condition

$$T_{\mu\nu} u^\mu u^\nu = e \geq 0, \quad (3.46)$$

while the strong energy condition (2.99) implies that

$$2T_{\mu\nu} u^\mu u^\nu + T^\alpha_\alpha = e + 3p \geq 0. \quad (3.47)$$

We note that given that all the quantities on the right-hand side of the energy–momentum tensor (3.36) are measured in a frame comoving with the fluid, the corresponding expressions for an observer moving with four-velocity  $\mathbf{u}'$  are simply obtained via a Lorentz transformation of the tensor  $T^{\mu\nu}$ . As an example, the corresponding total energy density and pressure will be given by

$$e' = u'_\mu u'_\nu T^{\mu\nu} = W^2 (e + v^2 p), \quad (3.48)$$

$$p' = \frac{1}{3} (\eta_{\mu\nu} + u'_\mu u'_\nu) T^{\mu\nu} = \frac{1}{3} W^2 [ev^2 + p(3 - 2v^2)], \quad (3.49)$$

where  $W = (1 - v^2)^{-1/2}$  is the Lorentz factor of the observer with four-velocity  $u'^\mu$  relative to the fluid. There are two interesting consequences of Eqs. (3.48)–(3.49). The first one is that a fluid, which is measured to behave like *dust* in the comoving frame, *i.e.*, with  $p = 0$ , will

have a nonzero pressure as measured by an observer in a different frame, *i.e.*,  $p' \neq 0$ . The second one is that in the limit of ultrarelativistic flows (see Section 2.4.4)

$$\lim_{v \rightarrow 1} \frac{p'}{e'} = \frac{1}{3}. \quad (3.50)$$

This means that, whatever the equation of state in the comoving frame, the fluid will behave as a fluid of photons as seen by the observer moving at a velocity approaching the speed of light.

As a final remark we stress that, as anticipated in Section 2.4.8, in the case of a photon fluid in which the photons are in thermodynamic equilibrium with an ordinary material fluid, the energy-momentum tensor of the radiation field can be obtained by just replacing the comoving energy density and pressure of the fluid with those of the radiation field (Hsieh and Spiegel, 1976), namely,

$$T_R^{\mu\nu} = (e_R + p_R)u^\mu u^\nu + p_R g^{\mu\nu} = p_R (4u^\mu u^\nu + g^{\mu\nu}). \quad (3.51)$$

The total energy-momentum tensor will then be given by the sum of (3.51) with the energy-momentum tensor of the standard fluid (3.36).

### 3.3 Hydrodynamics equations of perfect fluids

In Section 2.3.5 we have derived the general-relativistic hydrodynamic equations for a *generic fluid* either as integral conservation laws (2.114)–(2.115), or as differential conservation laws (2.118)–(2.119). We can now specialise the form of these equations to the case of *perfect fluids* by exploiting the definitions of the rest-mass density current and of the energy-momentum tensor given in Eqs. (3.35) and (3.36), respectively. In this way, we obtain that the general-relativistic conservation of rest mass is given by

$$\nabla_\mu J^\mu = \nabla_\mu (\rho u^\mu) = u^\mu \nabla_\mu \rho + \rho \nabla_\mu u^\mu = 0, \quad (3.52)$$

and by the conservation of energy and momentum

$$\nabla_\mu T^{\mu\nu} = \nabla_\mu [(e + p) u^\mu u^\nu + p g^{\mu\nu}] = 0. \quad (3.53)$$

Equations (3.52)–(3.53) are five equations in the six unknowns represented by: the three components of the four-velocity [the fourth one is obtained through the normalisation (3.2)], the rest-mass density and two thermodynamic quantities, say, the pressure and internal energy density. As discussed in Section 2.4, an equation of state relating the pressure to other thermodynamic quantities, *e.g.*,  $p = p(\rho)$ , or  $p = p(\rho, \epsilon)$ , is necessary to close the system of equations. We postpone to Chapter 7 the discussion of the mathematical properties and in particular of the hyperbolic character of Eqs. (3.52)–(3.53), as such a discussion will be particularly relevant for the numerical solution of these equations. Similarly, a complementary derivation of the relativistic-hydrodynamic equations from a variational principle will be presented in Section 3.10. Here instead we will concentrate in casting the equations in a form that will be useful in the remainder of the chapter.

## 144 Relativistic Perfect Fluids

The four equations expressing the conservation of energy and momentum, *i.e.*,  $\nabla \cdot \mathbf{T} = 0$ , can be further decomposed into three *momentum-conservation equations* and into one *energy-conservation equation*, after projecting the four-divergence in the direction orthogonal to the four-velocity and along it. More specifically, recalling that  $u^\nu \nabla_\nu (u^\mu) u_\mu = a^\mu u_\mu = 0$ , we can write the projection of Eqs. (3.53), *i.e.*,  $\mathbf{h} \cdot \nabla \cdot \mathbf{T} = 0$ , as

$$\begin{aligned} h^\nu_{\lambda} \nabla_\mu T^{\mu\lambda} &= h^\nu_{\lambda} [u^\lambda u^\mu \nabla_\mu (\rho h) + \rho h u^\mu \nabla_\mu u^\lambda + \rho h \Theta u^\lambda + g^{\lambda\mu} \nabla_\mu p] \\ &= \rho h u^\mu \nabla_\mu u^\nu + h^\nu_{\lambda} g^{\lambda\mu} \nabla_\mu p = 0, \end{aligned} \quad (3.54)$$

from which it follows that

$$u^\mu \nabla_\mu u_\nu + \frac{1}{\rho h} h^\mu_{\nu} \nabla_\mu p = 0. \quad (3.55)$$

Equations (3.55) represent the relativistic version of the *Euler equations* [*cf.* Eq. (2.66)]. Since the first term is nothing but the fluid acceleration  $a_\nu = u^\mu \nabla_\mu u_\nu$ , the equations of motion (3.55) can be written in a form resembling Newton's second law as [a closer comparison with the Newtonian limit of (3.55) will be presented in the following section]

$$\rho h a^\mu = -(g^{\mu\nu} + u^\mu u^\nu) \nabla_\nu p, \quad (3.56)$$

where the acceleration is proportional to the pressure gradient, and the enthalpy density  $\rho h$  provides the inertial contribution of the rest mass. Not surprisingly, Eqs. (3.55) reduce to simple geodetic equations ( $a_\nu = 0$ ) in the case of a uniform pressure or pressureless fluid [*cf.* Eq. (1.179)].

Similarly, we can write the projection of Eq. (3.53) along  $\mathbf{u}$ , *i.e.*,  $\mathbf{u} \cdot \nabla \cdot \mathbf{T} = 0$ , and obtain

$$u^\mu \nabla_\mu e + \rho h \Theta = 0, \quad (3.57)$$

which represents the relativistic version of the *energy-conservation equation*; and also in this case a closer comparison with the corresponding Newtonian expression will be presented in the following section. Equation (3.57) can also be cast in a different form by recalling that the continuity equation (3.52) provides an explicit expression for the expansion  $\Theta$  as

$$\Theta = -\frac{1}{\rho} u^\mu \nabla_\mu \rho, \quad (3.58)$$

so that we can express the energy conservation as

$$u^\mu \nabla_\mu e - h u^\mu \nabla_\mu \rho = 0. \quad (3.59)$$

In analogy with the corresponding Newtonian expression, Eq. (3.58) also provides us with a straightforward definition of an *incompressible fluid* as a fluid with zero expansion, *i.e.*,

$$\Theta = 0 = u^\mu \nabla_\mu \rho. \quad (3.60)$$

We conclude this section with an important remark. If we recall the first law of thermodynamics in the form given by (2.143), we find that the energy-conservation equation (3.59) also implies that *perfect fluids are adiabatic*, *i.e.*,

$$u^\mu \nabla_\mu s = 0, \quad (3.61)$$

that is, the specific entropy  $s$  is conserved along the fluidlines. Furthermore, a perfect fluid will be said to be *isentropic* if

$$\nabla_\mu s = 0, \quad (3.62)$$

that is, if, in addition to being adiabatic, the specific entropy is constant throughout the entire fluid. Clearly, a fluid that is isentropic is also adiabatic, but the opposite is not true.

It should be noted that although several ordinary flows are essentially isentropic, we will rarely need the condition (3.62) when considering the rather generic classes of flows discussed in Sections 3.6–3.7. In addition, the conservation of specific entropy along fluidlines in (3.61) will be valid as long as the flow is continuous. In the presence of shocks, in fact, Eq. (3.61) will cease to be valid and entropy will be produced as a result of the irreversibility of the processes occurring across the shock (see the discussion in Section 4.4.3).

### 3.4 Perfect fluids and symmetries

In Section 1.5.3 we have discussed that if the spacetime has some symmetry which is responsible for the invariance of the equations under a symmetry group  $\mathcal{G}$ , then it is possible to associate to  $\mathcal{G}$  a Killing vector field  $\xi$ , whose vector lines correspond to the trajectories of  $\mathcal{G}$ . Although generic spacetimes will not have any symmetry, it is often instructive to consider those spacetimes which do possess one or more Killing vector fields. In this case, if the energy-momentum tensor  $T$  satisfies the conservation equation (3.53), then also the four-vector  $Q := T \cdot \xi$  satisfies a conservation law, *i.e.*,

$$\nabla_\mu Q^\mu = \nabla_\mu (T^{\mu\nu} \xi_\nu) = 0. \quad (3.63)$$

The proof is straightforward since Eq. (3.63) can be rewritten as

$$\nabla_\mu Q^\mu = T^{\mu\nu} \nabla_\mu \xi_\nu = T^{\mu\nu} \nabla_{(\mu} \xi_{\nu)} = 0, \quad (3.64)$$

where we have exploited the symmetry properties of the energy-momentum tensor, *i.e.*, that  $T^{\mu\nu} \nabla_{[\mu} \xi_{\nu]} = 0$ , as well as Eq. (1.170), which is valid for any Killing vector.

It should be emphasised that the symmetries of the spacetime need not be shared by the fluid. Indeed, generic fluid motions will not preserve any symmetry even when occurring in a spacetime that does have symmetries.<sup>4</sup> Nevertheless, it is interesting to consider those cases in which *also* the fluid is invariant under the same symmetry group  $\mathcal{G}$  of the spacetime, that is, when the fluid motion shares the same symmetries of the spacetime. Mathematically, this is expressed by the condition (Gourgoulhon, 2006)

$$\mathcal{L}_\xi(\mathbf{B}) = 0, \quad (3.65)$$

where  $\xi$  is a Killing vector field and  $\mathbf{B}$  is any tensor field associated with the fluid, *e.g.*, pressure, density, rest-mass density current, etc. As we will show below, it is possible in these cases to derive elegant and generic expressions for the equations of motion.

<sup>4</sup>As a simple and relevant example, we will discuss in Section 11.5 the motion of a moving fluid in a Schwarzschild black-hole spacetime and show that the flow can be non-stationary and asymmetric despite the spacetime being static and spherically symmetric.

## 146 Relativistic Perfect Fluids

Let us start therefore from the momentum-conservation equation in the form given by (3.55), which can also be written as

$$\rho u^\mu \nabla_\mu (hu_\nu) - \rho u_\nu u^\mu \nabla_\mu h = -\nabla_\nu p - u_\nu u^\mu \nabla_\mu p. \quad (3.66)$$

Recalling now the first law of thermodynamics in the form given by (2.142) and that a perfect fluid is also adiabatic and thus with  $u^\mu \nabla_\mu s = 0$ , we find that (3.66) can be expressed as

$$u^\mu \nabla_\mu (hu_\nu) = -\frac{\nabla_\nu p}{\rho}. \quad (3.67)$$

The expression above for the Euler equations can be further manipulated exploiting the relation between the Lie derivative and the fluid four-acceleration<sup>5</sup> [cf., Eqs. (3.1)–(3.4)]

$$\mathcal{L}_u u_\nu = u^\mu \nabla_\mu u_\nu + u_\mu \nabla_\nu u^\mu = u^\mu \nabla_\mu u_\nu, \quad (3.68)$$

so that Eq. (3.67) can also be written as

$$\mathcal{L}_u (hu_\mu) = -\frac{1}{\rho} \nabla_\mu p - \nabla_\mu h. \quad (3.69)$$

By contracting the left-hand side of Eq. (3.69) with a generic Killing vector  $\xi^\mu$ , we obtain

$$\begin{aligned} \xi^\mu \mathcal{L}_u (hu_\mu) &= \mathcal{L}_u (hu_\mu \xi^\mu) - hu_\mu \mathcal{L}_u \xi^\mu \\ &= \mathcal{L}_u (hu_\mu \xi^\mu) - hu^\mu u^\gamma \nabla_{(\gamma} \xi_{\mu)} \\ &= \mathcal{L}_u (hu_\mu \xi^\mu), \end{aligned} \quad (3.70)$$

where in the second line we have used the Killing equation (1.170) to remove the second term on the right-hand side. As a result, Eq. (3.69) is equivalent to

$$\mathcal{L}_u (hu_\mu \xi^\mu) = -\frac{\xi^\mu \nabla_\mu p}{\rho} - \xi^\mu \nabla_\mu h = -\frac{1}{\rho} \mathcal{L}_\xi p - \mathcal{L}_\xi h, \quad (3.71)$$

which is a general equation of motion for a fluid in a spacetime with Killing vector field  $\xi$ . This equation can be further simplified if we make the *additional* assumption that the fluid shares the same symmetries of the spacetime and thus use the condition (3.65) with  $\mathcal{L}_u p = 0$  and  $\mathcal{L}_u h = 0$ , to finally obtain

$$\mathcal{L}_u (hu_\mu \xi^\mu) = \nabla_u (hu_\mu \xi^\mu) = 0. \quad (3.72)$$

Equation (3.72) expresses therefore that if  $\xi$  is a symmetry generator of the spacetime and if the fluid shares the same symmetry, then the scalar quantity  $hu \cdot \xi$  is conserved along the fluidlines. Note the similarity between expression (3.72) and the corresponding equation (1.185) along geodesic trajectories, *i.e.*,  $\mathcal{L}_u (u_\mu \xi^\mu)$ . The difference is clearly introduced by the fact that a non-trivial fluid has non-uniform pressure and hence the quantity conserved is

<sup>5</sup>For the sake of simplicity, we employ here a notation that is intentionally not rigorous, so that we indicate as  $\mathcal{L}_u u_\nu$  what should more properly be written as  $(\mathcal{L}_u u)_\nu$ .

not  $\mathbf{u} \cdot \boldsymbol{\xi}$ , but its inertial equivalent  $hu \cdot \boldsymbol{\xi}$ . Only when the fluid is not subject to accelerations, that is, when the pressure is uniform, do the two expressions coincide.

As a useful example of the implications of expression (3.72), let us consider the case in which the Killing vector expresses the invariance for rotation around a given axis, *i.e.*,  $\boldsymbol{\xi} = \partial_\phi$ , where we have used a standard polar spherical coordinate system  $x^\mu = (t, r, \theta, \phi)$  (another example of a stationary Killing vector will be discussed in Section 3.6.2.). As a result, Eq. (3.72) implies that in this case  $\xi^\mu = (0, 0, 0, 1)$  and

$$hu_\mu \xi^\mu = hu_\phi = \text{const.} \quad (3.73)$$

The quantity  $hu_\phi$  represents therefore the specific angular momentum of the fluid, as it is simple to realise when considering the limit to the corresponding Newtonian expression, *i.e.*,  $hu_\phi \rightarrow \Omega r^2$ , where  $\Omega = d\phi/dt$ .

### 3.5 The Newtonian limit of the hydrodynamic equations

The comparison between Eqs. (3.52)–(3.53) and their Newtonian counterparts (2.65)–(2.67) can be instructive to highlight the structural differences that are introduced by a relativistic formulation of hydrodynamics. However, before going into the details of the derivation, it is useful to remark that the Newtonian “limit” of the relativistic-hydrodynamic equations should not be intended as a rigorous mathematical limit. This is because special and general relativity introduce genuinely new aspects, which are not present in the Newtonian formulation and hence cannot be recovered through a simple mathematical limit. Two important examples in this regard are the contributions of the *rest mass* and of the *rest energy*, which are both absent in Newtonian physics and that will need to be added/removed when going from one theory to the other one.<sup>6</sup>

Let us assume therefore that there is a Newtonian gravitational field with potential  $\phi$  solution of the Poisson equation  $\nabla^2 \phi = 4\pi G\rho$  [*cf.* Eq. (1.215)] and that this is weak (*i.e.*,  $|\phi| \ll 1$ ) and static, so that it is possible to find a coordinate system  $x^\alpha = (t, x^i)$  such that the metric components take the form (note that in contrast with the rest of the chapter, in this section we will retain explicitly the speed of light,  $c$ , as this will help us keep track of the order of different terms in an expansion in terms of the normalised fluid velocity  $v/c$ )

$$ds^2 = - \left( 1 + 2 \frac{\phi}{c^2} \right) c^2 dt^2 + \left( 1 - 2 \frac{\phi}{c^2} \right) \eta_{ij} dx^i dx^j, \quad (3.74)$$

where  $\eta_{ij}$  is the flat three-metric [*cf.* Eq. (1.103)]. If we define<sup>7</sup> as  $v^i = dx^i/dt$  the components of the fluid velocity  $\vec{v}$  with respect to the inertial frame defined by the coordinates  $x^\alpha$  in (3.74) (these coordinates become inertial in the limit  $\phi/c^2 \rightarrow 0$ ), then the Newtonian limit is obtained by additionally requiring that  $|\vec{v}|/c \ll 1$ . Using the normalisation condition for the four-velocity (1.112) and the expression for the four-velocity components (3.5), we can

<sup>6</sup>As mentioned in Chapter 1, in Newtonian physics mass and energy are two distinct quantities and the rest mass does not contribute to the energy budget as it does in special and general relativity.

<sup>7</sup>Note that the indices of  $v^i$  are lowered via the flat metric  $v_i = \eta_{ij} v^j$ .

## 148 Relativistic Perfect Fluids

express  $u^0$  in terms of  $\phi$  and  $\vec{v}$ . To first order in  $\phi$  and  $v_j v^j$ , we can write (see footnote 25 in Section 1.4)

$$u^0 \simeq 1 - \frac{\phi}{c^2} + \frac{1}{2} \frac{v_j v^j}{c^2}, \quad u^0 \frac{v^i}{c} \simeq \frac{v^i}{c} + \mathcal{O}\left(\frac{v^i v_j v^j}{c^3}\right). \quad (3.75)$$

As a result, the contravariant components of the four-velocity vector in the Newtonian limit are given by

$$u^\alpha \simeq \left( u^0, \frac{v^i}{c} \right) = \left( 1 - \frac{\phi}{c^2} + \frac{1}{2} \frac{v_j v^j}{c^2}, \frac{v^i}{c} \right), \quad (3.76)$$

while the corresponding covariant components are obtained after contracting with the metric (3.74) to obtain

$$u_\alpha \simeq \left( u_0, \frac{v_i}{c} \right) = \left( -1 - \frac{\phi}{c^2} - \frac{1}{2} \frac{v_j v^j}{c^2}, \frac{v_i}{c} \right). \quad (3.77)$$

We can now consider the Newtonian limit of the relativistic-hydrodynamic equations by starting from the continuity equation (3.52) and recognising that the operator  $u^\mu \nabla_\mu$  reduces to the convective (or Lagrangian) derivative in the Newtonian framework, *i.e.*,

$$u^\mu \nabla_\mu \longrightarrow \frac{D}{Dt} := \frac{\partial}{\partial t} + \vec{v} \cdot \vec{\nabla}, \quad (3.78)$$

since

$$u^\mu \nabla_\mu = \frac{u^0}{c} \frac{\partial}{\partial t} + u^i \frac{\partial}{\partial x^i}, \quad (3.79)$$

and we can use expressions (3.76) and (3.77) to express the differential operators at  $\mathcal{O}(v^2/c^2)$  as

$$\frac{u^0}{c} \frac{\partial}{\partial t} \simeq \frac{1}{c} \frac{\partial}{\partial t}, \quad (3.80)$$

$$u^i \frac{\partial}{\partial x^i} \simeq \frac{v^i}{c} \frac{\partial}{\partial x^i}. \quad (3.81)$$

Similarly, the term  $\nabla_\mu u^\mu$  can be expressed as

$$\nabla_\mu u^\mu = \frac{1}{c} \frac{\partial u^0}{\partial t} + \frac{\partial u^i}{\partial x^i} \simeq \frac{1}{c} \frac{\partial v^i}{\partial x^i} = \frac{1}{c} \theta, \quad (3.82)$$

where  $\theta$  is the Newtonian expansion for the fluid expansion in the three-dimensional space [*cf.*, Eq. (2.73)]. Collecting all these results, the Newtonian limit of Eq. (3.52) is given by

$$\frac{D\rho}{Dt} + \rho(\vec{\nabla} \cdot \vec{v}) = 0, \quad (3.83)$$

which obviously coincides with the expression (2.65) introduced in Section 2.2.5.

Next, we consider the case of the momentum-conservation equations (3.55), whose Newtonian limit deserves some comments. We recall that when discussing in Section 2.2.1 the Boltzmann equation within a Newtonian framework, and subsequently the moment equations

in Section 2.2.3, we have introduced the concept of *external forces*. These are long-range forces, whose strength decreases slowly with the distance between the fluid elements, but which are still significant on distances comparable with the characteristic size of the fluid. The typical example of an external force is represented by the gravitational force, but other important examples are electromagnetic forces (which act when the fluid has a net electromagnetic charge) and the “fictitious” forces (such as the centrifugal or Coriolis force), which appear when the fluid motion is described in a non-inertial (*e.g.*, rotating) reference frame. The important difference between the Newtonian description discussed above and the relativistic one is that, if present, the gravitational forces (and the possible fictitious forces) are no longer external forces but are accounted for by the curvature of spacetime. Recognising therefore that in a non-relativistic regime  $\epsilon \ll c^2$  (*i.e.*, the energy density of the fluid is essentially given by the rest-mass density) and  $p/\rho \ll c^2$  (*i.e.*, the pressure contribution to the energy density is negligible), the Newtonian limit of the specific enthalpy and of the second term in Eq. (3.55) are given respectively by<sup>8</sup>

$$h = c^2 + \epsilon + \frac{p}{\rho} \longrightarrow c^2, \quad (3.84)$$

$$\frac{1}{\rho h} h_{\mu\nu} \nabla^\mu p \longrightarrow \frac{1}{\rho c^2} \left( \partial_j p + \frac{v_j}{c^2} \partial_t p + \frac{v_j v_i}{c^2} \partial_i p \right) \simeq \frac{1}{\rho c^2} \partial_j p. \quad (3.85)$$

It should be remarked that although there exists a perfectly well-defined Newtonian specific enthalpy  $h_N := \epsilon + p/\rho$  [*cf.* Eq. (2.147)], this does not represent the Newtonian limit of the relativistic specific enthalpy, which is instead given by (3.84). As commented above, the reason for this difference is the absence in Newtonian physics of the rest energy  $E_0 = mc^2$  [*cf.* Eq. (1.122)].

Collecting the results in Eqs. (3.84) and (3.85) and considering the presence of an external force of gravitational origin, we can derive the Newtonian limit of the momentum-conservation equation (3.55) as

$$\frac{\partial \vec{v}}{\partial t} + (\vec{v} \cdot \vec{\nabla}) \vec{v} + \frac{1}{\rho} \vec{\nabla} p + \vec{\nabla} \phi = 0, \quad (3.86)$$

where the term  $\vec{\nabla} \phi$  has been introduced to account for the acceleration due to the external and conservative forces.

A similar approach can finally be followed also for the relativistic energy-conservation equation (3.57), whose Newtonian limit follows directly from (3.78) and from the mapping of the energy density and enthalpy density to their Newtonian limits, *i.e.*,

$$e \rightarrow w_N = \rho \epsilon, \quad \rho h \rightarrow \rho c^2, \quad (3.87)$$

to yield

$$\rho \frac{D\epsilon}{Dt} + p \vec{\nabla} \cdot \vec{v} = 0, \quad (3.88)$$

which coincides with Eq. (2.67). Finally, we report the Newtonian limit of the adiabatic property of perfect fluids (3.61), which is given by

<sup>8</sup>Note that the limit in (3.84) expresses the fact that in a Newtonian fluid the only term playing the role of inertia is represented by the rest-mass density, *i.e.*,  $\rho h \rightarrow \rho c^2$  [*cf.* Eq. (3.87)<sub>2</sub>].

## 150 Relativistic Perfect Fluids

$$\frac{\partial s}{\partial t} + v^i \frac{\partial s}{\partial x^i} = 0. \quad (3.89)$$

We will use this equation in Section 4.1.1 when discussing quasi-linear hyperbolic systems of partial differential equations.

Because the hydrodynamic equations for perfect fluids play such an important role both in classical and in relativistic regimes, we conclude this section by reporting them below and side by side for a direct comparison that helps in highlighting the analogies.

relativistic	Newtonian
$u^\mu \nabla_\mu \rho + \rho \nabla_\mu u^\mu = 0,$	$\partial_t \rho + v^i \partial_i \rho + \rho \partial_i v^i = 0,$
$u^\mu \nabla_\mu u_\nu + \frac{1}{\rho h} h^\mu_\nu \nabla_\mu p = 0,$	$\partial_t v^i + v^j \partial_j v^i + \frac{1}{\rho} \partial_i p + \partial_i \phi = 0,$
$u^\mu \nabla_\mu e + \rho h \nabla_\mu u^\mu = 0,$	$\partial_t \left( \frac{1}{2} \rho v^i v_i + \rho \epsilon \right) + \partial_i \left[ \left( \frac{1}{2} \rho (v^i v_i) + \rho \epsilon + p \right) v^i \right] + \rho v^i \partial_i \phi = 0,$
$u^\mu \nabla_\mu s = 0,$	$\partial_t s + v^i \partial_i s = 0,$
$p = p(\rho, \varepsilon, \dots),$	$p = p(\rho, \varepsilon, \dots).$

## 3.6 Stationary flows

As mentioned in Section 2.2.5, the complex and nonlinear character of the (relativistic) hydrodynamic equations makes the derivation of analytic solutions very difficult, even when symmetries are present. Nevertheless, there are regimes in which the equations simplify sufficiently that integrals of motion can be found analytically. One such example is that of *stationary flows*, for which all time derivatives can be neglected. In the following two sections we will review the basic features of stationary flows in Newtonian and relativistic regimes and provide some useful examples of their application.

### 3.6.1 Bernoulli's theorem

Let us first consider the classical (Newtonian) formulation of Bernoulli's theorem, which provides a simple characterisation of the flow when stationarity is reached. The starting point is the Euler equations in the case when the external force field is conservative, *i.e.*, Eq. (3.86). For stationary flows, *i.e.*, when  $\partial/\partial t = 0$ , this equation simplifies to

$$(\vec{v} \cdot \vec{\nabla}) \vec{v} = -\vec{\nabla} \phi - \frac{\vec{\nabla} p}{\rho}, \quad (3.90)$$

which is equivalent to

$$\vec{\nabla} \left( \frac{1}{2} \vec{v}^2 \right) - \vec{v} \times (\vec{\nabla} \times \vec{v}) = -\vec{\nabla} \phi - \frac{\vec{\nabla} p}{\rho}. \quad (3.91)$$

Let us now consider the first law of thermodynamics in the form given by (2.142), where we replace the differential of the (relativistic) specific enthalpy with the corresponding Newtonian quantity, *i.e.*,  $dh \rightarrow dh_N = d(\epsilon + p/\rho)$ .<sup>9</sup> Making the additional assumption that the flow is adiabatic, that is,  $Ds/Dt = \vec{v} \cdot \vec{\nabla} s = 0$ , we can deduce that

$$\frac{Dh_N}{Dt} = \frac{1}{\rho} \frac{Dp}{Dt}, \quad (3.92)$$

which, again for a stationary flow, reduces to

$$(\vec{v} \cdot \vec{\nabla}) h_N = \frac{1}{\rho} \vec{v} \cdot \vec{\nabla} p. \quad (3.93)$$

We now evaluate Eq. (3.91) along the direction given by  $\vec{v}$ , and, after using Eq. (3.93), we obtain

$$(\vec{v} \cdot \vec{\nabla}) \left( \frac{1}{2} \vec{v}^2 + \phi + h_N \right) = (\vec{v} \cdot \vec{\nabla}) \left( \frac{1}{2} \vec{v}^2 + \phi + \epsilon + \frac{p}{\rho} \right) = 0, \quad (3.94)$$

which, since we are assuming the flow to be stationary, reduces to

$$\frac{D}{Dt} \mathcal{B}_N = \frac{D}{Dt} \left( \frac{1}{2} \vec{v}^2 + \phi + \epsilon + \frac{p}{\rho} \right) = 0. \quad (3.95)$$

The equation above is called the *Bernoulli equation* and proves the thesis of the classical *Bernoulli's theorem*, namely, that the quantity

$$\mathcal{B}_N := \frac{1}{2} \vec{v}^2 + \phi + h_N, \quad (3.96)$$

which is called the *Bernoulli's constant*, is constant along the streamlines. Because the flow is stationary, the streamlines coincide with the fluidlines (see Fig. 2.4). Of course, the Bernoulli's constant should really be thought of as a scalar quantity which can vary across the fluid, while it is preserved along fluidlines.

In several Newtonian applications in which changes in the thermal state of the fluid can be neglected, *i.e.*,  $\epsilon = \text{const.}$ , the Bernoulli equation takes the more familiar form

$$\frac{1}{2} \rho \vec{v}^2 + \rho |\vec{g}| z + p = \text{const.}, \quad (3.97)$$

where  $\vec{g}$  is the gravitational acceleration and  $z$  is the flow height. The practical applications of the Bernoulli equation (3.97) in hydraulics and engineering applications are numerous and an extended discussion can be found in the classical text by Lamb (1993).

<sup>9</sup>Note that both the differential of the specific enthalpy and that of the pressure in (2.142) are exact, and that although the specific enthalpy tends to the rest energy density in the Newtonian limit, *i.e.*,  $h \rightarrow 1$ , its differential is nonzero, *i.e.*,  $dh \rightarrow dh_N$ .

### 3.6.2 Relativistic Bernoulli theorem

The relativistic generalisation of Bernoulli's theorem is rather straightforward after the discussion made in Section 3.4. In fact, to deduce the consequences of the assumption of stationarity on the equation of motion we simply have to select as Killing vector the one expressing the invariance for translations along the  $t$ -direction, *i.e.*,  $\xi = \partial_t$ . As a result, the contravariant components of  $\xi$  will be given by  $\xi^\mu = (1, 0, 0, 0)$  and using Eq. (3.72) we readily obtain

$$\mathcal{L}_u(\mathcal{B}) = \mathcal{L}_u(hu_t) = 0. \quad (3.98)$$

Equation (3.98) is called the *relativistic Bernoulli equation* and proves the thesis of the *relativistic Bernoulli's theorem*, namely, that the quantity

$$\mathcal{B} := hu_\mu \xi^\mu = hu_t = \text{const.} \quad (3.99)$$

is Lie-dragged along the fluidlines and represents therefore the *relativistic Bernoulli's constant*. The Newtonian limit of (3.98) is easily recovered if we replace  $u_t$  with the expression given by (3.77), namely

$$\left(1 + \epsilon + \frac{p}{\rho}\right) \left(1 + \phi + \frac{1}{2}\vec{v}^2\right) = \text{const.}, \quad (3.100)$$

and recall that the Newtonian limit of Eq. (3.100) cannot contain the contribution relative to the rest energy, *i.e.*, the term  $\mathcal{O}(1)$ . As a result, the Newtonian limit of Eq. (3.100) at  $\mathcal{O}(\vec{v}^2)$  is

$$\left(\frac{1}{2}\vec{v}^2 + \phi + \epsilon + \frac{p}{\rho}\right) + \text{higher-order terms} = \text{const.}, \quad (3.101)$$

which coincides with the form given by Eq. (3.95). In Section 11.9.2, we will discuss two models that use the relativistic Bernoulli equation (3.98) to explain the very high Lorentz factors observed in astrophysical jets.

## 3.7 Irrotational flows

Another class of simple flows which serve as a basic approximation to model more general flows are the so-called *irrotational flows* or *potential flows*, and are defined as those flows which have zero kinematic vorticity and are inviscid (*i.e.*, of perfect fluids). In the following two sections we will review the basic features of irrotational flows in Newtonian and relativistic regimes and provide some useful examples of their application.

### 3.7.1 Newtonian irrotational flows

The starting point is the definition of the Newtonian *vorticity vector*

$$\vec{\omega}_{\text{N}} := \vec{\nabla} \times \vec{v}, \quad (3.102)$$

which then allows us, after taking the curl of the Euler equations (2.66), to derive the following evolution equation for the vorticity

$$\frac{\partial \vec{\omega}_N}{\partial t} = \vec{\nabla} \times (\vec{v} \times \vec{\omega}_N) - \vec{\nabla} \times \left( \frac{\vec{\nabla} p}{\rho} \right). \quad (3.103)$$

Note that the second term on the right-hand side of (3.103) vanishes in three important cases:

1. when the fluid is isentropic, because then  $\vec{\nabla} p/\rho = \vec{\nabla} h$  and  $\vec{\nabla} \times \vec{\nabla} h = 0$ ;
2. when the fluid is barotropic, *i.e.*, when  $p = p(\rho)$ , since then  $\vec{\nabla} p$  and  $\vec{\nabla} \rho$  are parallel;<sup>10</sup>
3. when the fluid is incompressible, because then  $\rho = \text{const.}$  and  $\vec{\nabla} \times \vec{\nabla} p = 0$ .<sup>11</sup>

In these cases, the equation for the vorticity evolution (3.103) reduces to

$$\frac{\partial \vec{\omega}_N}{\partial t} = \vec{\nabla} \times (\vec{v} \times \vec{\omega}_N), \quad (3.104)$$

thus implying that any flow which is initially *irrotational*, *i.e.*,  $\vec{\omega}_N = 0$ , will remain irrotational also at any later time. Stated differently, no matter how complex the dynamics of the flow may be, vortices cannot be created if they are initially absent. Furthermore, if vortices are present, they can only be advected along the flow. A derived quantity is the *vortensity*, which is simply given by the ratio of the vorticity and the mass density, *i.e.*,  $\vec{\mathcal{V}} := \vec{\omega}_N/\rho$ . The vortensity is often used in the analysis of rotating flows in protoplanetary discs (Ou *et al.*, 2007).

The class of irrotational flows has the important advantage that in this case the velocity field  $\vec{v}$  has zero curl and it is therefore possible to introduce a scalar quantity  $\varphi$ , also referred to as the *velocity potential*, and defined as

$$\vec{v} := \vec{\nabla} \varphi(t, \vec{r}). \quad (3.105)$$

The flow is therefore fully determined by the scalar function  $\varphi$  and is referred to as a *potential flow*. If we further consider fluids that are incompressible everywhere and at all times, *i.e.*,  $\vec{\nabla} \cdot \vec{v} = 0$ , the determination of the velocity field follows from the continuity equation and amounts to computing the velocity potential  $\varphi(\vec{r})$  satisfying the following Laplace equation

$$\vec{\nabla} \cdot \vec{\nabla} \varphi(\vec{r}) = \Delta \varphi(\vec{r}) = 0. \quad (3.106)$$

The elliptic equation above has a unique solution even in domains that are not simply connected (see the example below) provided that suitable boundary conditions are specified. Equation (3.106) is most commonly employed to study the fluid flow past an obstacle (either in motion or at rest), for which the appropriate boundary condition is that the component of the velocity normal to the surface of the obstacle is zero, *i.e.*,  $\vec{v}_n = \partial \varphi / \partial n = 0$ , where  $n := |\vec{n}|$  and  $\vec{n}$  is the local unit normal to the body surface. The point in the flow where  $\vec{v} = 0$  is also known as the *stagnation point* and corresponds to the point where the pressure is largest in the absence of external gravitational forces [*cf.*, the Bernoulli equation (3.97)].

Because of their mathematical appeal, potential flows have been the subject of extended mathematical analyses (Chorin and Marsden, 1979; Meyer, 1999). At the same time, however,

<sup>10</sup>A fluid for which  $\vec{\nabla} p$  and  $\vec{\nabla} \rho$  are not parallel and thus the vector product  $\vec{\nabla} p \times \vec{\nabla} \rho \neq 0$  is also referred to as a *baroclinic fluid*.

<sup>11</sup>Note that in an incompressible fluid  $\vec{\nabla} p$  could well be nonzero.

they are rather idealised and lack important physical effects, such as the possibility of developing turbulent flows, which is a common feature of realistic flows, or the inclusion of viscous effects, which introduce substantial differences even in laminar flows.<sup>12</sup>

### 3.7.2 Kelvin–Helmholtz theorem

Before switching to the relativistic formulation of irrotational flows, we discuss an important theorem that regulates the dynamics of perfect fluids that obey Eq. (3.104), that is, of perfect fluids that are either barotropic, or isentropic, or incompressible. Considering a generic loop  $\Gamma$  of particles in such a fluid and defining  $\mathcal{C}$ , the *circulation* of  $\vec{v}$ , as

$$\mathcal{C}_N := \oint_{\Gamma} \vec{v} \cdot d\vec{l}, \quad (3.107)$$

the *Kelvin–Helmholtz theorem* states that [Helmholtz, 1858; Kelvin, 1867; Batchelor, 2000]

$$\frac{D}{Dt} \mathcal{C}_N := \frac{D}{Dt} \oint_{\Gamma} \vec{v} \cdot d\vec{l} = 0. \quad (3.108)$$

Equation (3.108) therefore expresses the *law of conservation of circulation* along the fluid-lines. The proof of the theorem is rather simple if we bring the differential operator inside the integral and let it act separately on the two terms of the circulation, *i.e.*,

$$\begin{aligned} \frac{D}{Dt} \oint_{\Gamma} \vec{v} \cdot d\vec{l} &= \oint_{\Gamma} \left( \frac{D}{Dt} \vec{v} \right) \cdot d\vec{l} + \oint_{\Gamma} \vec{v} \cdot \left( \frac{D}{Dt} d\vec{l} \right) \\ &= \int_{\Sigma} \vec{\nabla} \times \left( \frac{D}{Dt} \vec{v} \right) \cdot d\vec{S} + \oint_{\Gamma} \vec{v} \cdot d\vec{v}, \end{aligned} \quad (3.109)$$

where we have used Stokes' theorem to replace the first circulation integral into a surface flux through the open surface  $\Sigma$  enclosed by the loop  $\Gamma$  (see Fig. 3.4). It is then not difficult to realise that the second term in the last line of Eq. (3.109) is zero, since the line integral can be rewritten as

$$\oint_{\Gamma} \vec{v} \cdot d\vec{v} = \frac{1}{2} \oint_{\Gamma} d\vec{v}^2 = 0, \quad (3.110)$$

and the line integral of any exact differential over a closed contour is zero. Moreover, the momentum-conservation equation (3.86) in the absence of external forces implies that the Lagrangian time derivative can be written as  $D\vec{v}/Dt = -\vec{\nabla}p/\rho$ , so that Eq. (3.109) simplifies to

$$\frac{D}{Dt} \oint_{\Gamma} \vec{v} \cdot d\vec{l} = - \int_{\Sigma} \vec{\nabla} \times \left( \frac{\vec{\nabla}p}{\rho} \right) \cdot d\vec{S}. \quad (3.111)$$

As discussed in Section 3.7.1, the term  $\vec{\nabla} \times (\vec{\nabla}p/\rho)$  vanishes under the same assumptions in which (3.104) holds, namely, when the fluid is either isentropic, or barotropic, or incompressible. Under these conditions, and after using Stokes' theorem, we can express the Kelvin–Helmholtz theorem in the alternative formulation

<sup>12</sup>In view of their idealised character, R. Feynman defined these fluids as “dry”; see *The Feynman Lectures on Physics*, Vol. 2, Chapter 40 (Feynman, 1964).

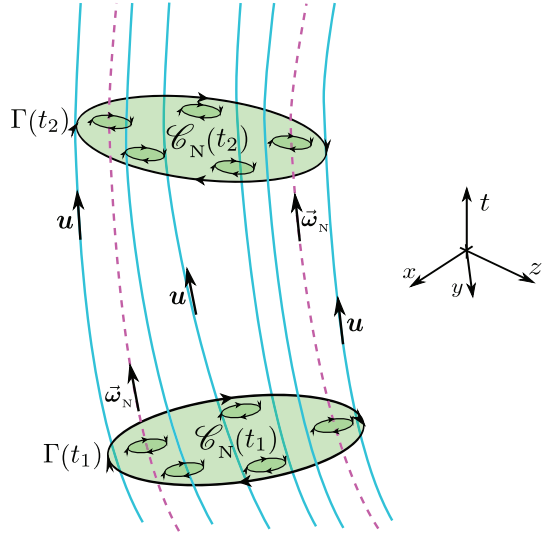


**Fig. 3.4** Schematic spacetime diagram illustrating the essence of the Kelvin–Helmholtz theorem. Show with blue solid lines are the fluidlines of fiducial fluid elements with tangent vector  $\mathbf{u}$ , while the purple dashed lines represent two vortex lines with tangent vector  $\vec{\omega}_N$ . The circulation  $\mathcal{C}_N$  is shown at two different times,  $t_1$  and  $t_2$ , along two loops  $\Gamma(t_1)$  and  $\Gamma(t_2)$  advected with the fluid.

$$\frac{D}{Dt} \mathcal{C}_N := \frac{D}{Dt} \int_{\Sigma} \vec{\omega}_N \cdot d\vec{S} = 0. \quad (3.112)$$

Expression (3.112) states therefore that in an irrotational flow the circulation is conserved and the number of *vortex lines*, i.e., the trajectories of vortices, crossing any element of area moving with the fluid remains constant in time.<sup>13</sup> This is shown schematically in the spacetime diagram in Fig. 3.4, which reports with blue solid lines the fluidlines of fiducial fluid elements with tangent vector  $\mathbf{u}$ , while with purple dashed lines it shows two vortex lines with tangent vector given by the local vorticity  $\vec{\omega}_N$ . The circulation  $\mathcal{C}_N$  is shown as computed at two different times,  $t_1$  and  $t_2$ , along two loops  $\Gamma(t_1)$  and  $\Gamma(t_2)$  advected with the fluid. In essence, therefore, the Kelvin–Helmholtz theorem then states that  $\mathcal{C}_N(t_2) = \mathcal{C}_N(t_1)$  and that the number of vortices in the areas limited by  $\Gamma(t_1)$  and  $\Gamma(t_2)$  is conserved.

### 3.7.3 Relativistic vorticity

In contrast to the Newtonian framework, in relativity the *kinematic vorticity tensor* defined in Section (3.1.1) [cf., Eq. (3.11)] does not provide a full account of the properties of relativistic vorticity. We introduce therefore the additional concept of the *vorticity tensor* (or *circulation tensor*, or *vorticity two-form*) through the definition

$$\begin{aligned} \Omega_{\mu\nu} &:= 2\nabla_{[\nu} w_{\mu]} \\ &= \nabla_\nu(hu_\mu) - \nabla_\mu(hu_\nu) = \partial_\nu(hu_\mu) - \partial_\mu(hu_\nu), \end{aligned} \quad (3.113)$$

<sup>13</sup>In turn, a vortex is loosely defined as a localised region of the fluid with nonzero vorticity.

## 156 Relativistic Perfect Fluids

where  $w$  is the *enthalpy current* (or *specific four-momentum*) and is defined as<sup>14</sup>

$$w^\mu := hu^\mu. \quad (3.114)$$

Note that the *vorticity tensor*  $\Omega$  is similar but distinct from the *kinematic vorticity tensor*  $\omega$ , which we have defined in Eq. (3.11), when introducing the kinematic characterisation of a fluid. The difference is of course in the inclusion of the inertial role played by the specific enthalpy  $h$  in the definition (3.113), which leads to a number of important results that we will encounter in the following sections. For the time being, let us remark that a flow with zero kinematic vorticity does not imply a zero vorticity tensor, and vice versa. This conclusion can be easily reached after deriving the following algebraic expression relating the vorticity tensor with the kinematic vorticity, *i.e.*,

$$\Omega_{\mu\nu} = 2h(\omega_{\mu\nu} - a_{[\mu}u_{\nu]} + u_{[\mu}\nabla_{\nu]}\ln h). \quad (3.115)$$

Equation (3.115) thus shows that *only* for a “test fluid” (*i.e.*, a fluid for which  $e = 0 = p$  and  $h = 1$ ) in geodetic motion (*i.e.*,  $a_\mu = 0$ ), the two tensors are directly proportional, differing by a factor of 2, *i.e.*,  $\Omega_{\mu\nu} = 2\omega_{\mu\nu}$ .

Next, we derive an important identity, first introduced by Lichnerowicz (1967), and involving the vorticity tensor. More precisely, after contracting (3.113) with  $u^\nu$  and using the momentum-conservation equation (3.66), we obtain

$$\Omega_{\mu\nu}u^\nu = \nabla_\mu h - \frac{1}{\rho}\nabla_\mu p. \quad (3.116)$$

Expressing now the first law of thermodynamics as [*cf.*, (2.142)]

$$\rho\nabla_\mu h - \nabla_\mu p = \rho T\nabla_\mu s, \quad (3.117)$$

we can write the identity (3.116) as

$$\Omega_{\mu\nu}u^\nu = T\nabla_\mu s. \quad (3.118)$$

Equation (3.118) is also known as the *Carter–Lichnerowicz equation* of motion, from Lichnerowicz, who first proposed it (Lichnerowicz, 1967), and Carter, who extended it to *multicomponent fluids* (or *multifluids*) [see, *e.g.*, Carter and Gaffet (1988), Carter (1989) and Section 3.11 for a discussion]. Since it has been derived from Eq. (3.66), it essentially represents an alternative formulation of the momentum-conservation equation. Yet, the Carter–Lichnerowicz equation deserves a few important remarks. First, if we define as *irrotational* a fluid with zero vorticity tensor, *i.e.*,  $\Omega = 0$ , then expression (3.118) immediately implies that *irrotational perfect fluids are isentropic*.<sup>15</sup> This is an important result, which does not have a Newtonian counterpart (since the Newtonian vorticity is a purely kinematic concept)

<sup>14</sup>Since in the Newtonian limit  $h \rightarrow 1$ , both the enthalpy current  $w$  and the four-velocity  $u$  have the same Newtonian limit and can be considered relativistic generalisations of the three-velocity  $\vec{v}$ .

<sup>15</sup>Of course a fluid which is isentropic does not necessarily have zero vorticity. A simple counterexample is a uniformly rotating star at zero temperature: it is isentropic but it has a nonzero vorticity.

and which nicely complements the similar implication of Eq. (3.61), that *perfect fluids are adiabatic*. Second, if a Killing vector  $\xi$  exists, its contraction with the vorticity (3.115) yields

$$\xi^\mu \Omega_{\mu\nu} = 2\xi^\mu \nabla_{[\nu} w_{\mu]} = \partial_\nu(h u_\mu \xi^\mu) - h u_\mu \partial_\nu \xi^\mu - \xi^\mu \partial_\mu(h u_\nu). \quad (3.119)$$

Assuming now that the fluid obeys the same symmetries of  $\xi$ , then Eq. (3.65) with  $B = hu$  implies that

$$\nabla_\nu(h u_\mu \xi^\mu) = 0. \quad (3.120)$$

In other words, in the case of irrotational flow in a spacetime with nonzero Killing vector fields, the quantity  $hu \cdot \xi$  is conserved not only along fluidlines [*cf.*, Eq. (3.72)], but it is also the same from one fluidline to another. Finally, we note that a comparison between the left-hand side of expression (3.118) with the corresponding contraction of the kinematic vorticity tensor (3.14)<sub>3</sub>, highlights that the vorticity tensor and the four-velocity are in general not orthogonal, *i.e.*,  $u^\mu \Omega_{\mu\nu} \neq 0$ , with the only exception being offered by an isentropic fluid. We will go back to expression (3.118) when discussing in Section 3.7.5 the relativistic Kelvin–Helmholtz theorem.

The Newtonian limit of the Carter–Lichnerowicz equation (3.118) is straightforward to derive and is given by

$$\frac{\partial \vec{v}}{\partial t} + \vec{\nabla} \left( \frac{1}{2} \vec{v}^2 + \epsilon + \frac{p}{\rho} + \phi \right) - \vec{v} \times (\vec{\nabla} \times \vec{v}) = T \vec{\nabla}_S, \quad (3.121)$$

which is also known as the *Crocco* equation of motion (Oleinik and Samokhin, 1999).

### 3.7.4 Relativistic irrotational flows

In close analogy with what was done for the kinematic vorticity, a *vorticity four-vector* can be defined as

$$\Omega^\mu := {}^*\Omega^{\mu\nu} u_\nu = \frac{1}{2} \epsilon^{\mu\nu\alpha\beta} \Omega_{\alpha\beta} u_\nu, \quad (3.122)$$

where

$${}^*\Omega^{\mu\nu} := \frac{1}{2} \epsilon^{\mu\nu\alpha\beta} \Omega_{\alpha\beta} \quad (3.123)$$

is the dual tensor of  $\Omega_{\mu\nu}$  (not to be confused with  $\Omega^{\mu\nu}$ ) and  $\epsilon^{\mu\nu\alpha\beta}$  are the components of the Levi–Civita tensor [*cf.*, Eq. (1.63)]. It is then straightforward to deduce that the four-vectors  $\Omega$  and  $u$  are orthogonal, *i.e.*,

$$\Omega^\mu u_\mu = 0. \quad (3.124)$$

For a generic fluid, the vorticity vector is nonzero and obeys the following evolution equation

$$\begin{aligned} \dot{\Omega}^\mu &:= u^\gamma \nabla_\gamma \Omega^\mu = u^\gamma \nabla_\gamma \left[ \frac{1}{2} \epsilon^{\mu\nu\alpha\beta} \Omega_{\alpha\beta} u_\nu \right] \\ &= u^\gamma \nabla_\gamma \left[ \frac{1}{2} \epsilon^{\mu\nu\alpha\beta} 2h (\omega_{\alpha\beta} - a_\alpha u_\beta + u_\alpha \nabla_\beta \ln h) u_\nu \right] \\ &= 2u^\gamma \nabla_\gamma (h\omega^\mu), \end{aligned} \quad (3.125)$$

## 158 Relativistic Perfect Fluids

where on the right-hand side of (3.125) we have made use of the kinematic vorticity tensor  $\omega_{\alpha\beta}$  and of the kinematic vorticity four-vector  $\omega^\mu$  defined by Eq. (3.16), and exploited the relation  $\epsilon^{\mu\nu\alpha\beta} u_\alpha u_\nu = 0 = \epsilon^{\mu\nu\alpha\beta} u_\beta u_\nu$ . The evolution equation for the vorticity vector (3.125) can be compared with the corresponding evolution equation (3.26) for the kinematic vorticity vector  $\omega^\mu$ . Also in this case, we can conclude that the vorticity vector will remain zero if it is initially zero over a finite domain around any point. On the other hand, in a relativistic framework a uniform vorticity (*i.e.*,  $\nabla_\nu \omega^\mu = 0$ ) will no longer guarantee that the vorticity will not change in time.

The definition (3.113) also clarifies that if the vorticity is zero, *i.e.*,  $\Omega_{\mu\nu} = 0$ , then the velocity of a relativistic (isentropic) perfect fluid can be expressed as the gradient of a *relativistic velocity potential* function, in close analogy with the corresponding concept in Newtonian hydrodynamics (Moncrief, 1980). More specifically, the *enthalpy current*  $w_\mu$  can be expressed, at least locally, as the gradient of a potential  $\Psi$ <sup>16</sup>

$$w_\mu = h u_\mu = \nabla_\mu \Psi. \quad (3.126)$$

Note that the definition above becomes a global one if the region of spacetime occupied by the fluid is simply connected and should be contrasted with the corresponding non-relativistic expression (3.105). Using now the continuity equation (3.52), we arrive at the general potential flow equation on an arbitrary background spacetime

$$\nabla_\mu \left[ \left( \frac{\rho}{h} \right) \nabla^\mu \Psi \right] = 0, \quad (3.127)$$

where  $\rho$  can be expressed as a function of  $h$  (see the *thermodynamic square* in Appendix B)

$$\rho = \left( \frac{\partial p}{\partial h} \right)_s, \quad (3.128)$$

once the equation of state is specified for the pressure  $p$ . The specific enthalpy, on the other hand, can be obtained after expressing the four-velocity as  $u_\mu = \nabla_\mu \Psi / h$  and imposing the normalisation condition  $u^\mu u_\mu = -1$ , so as to obtain

$$h = (-g^{\mu\nu} \nabla_\mu \Psi \nabla_\nu \Psi)^{1/2}. \quad (3.129)$$

Equation (3.127) is in general a nonlinear equation in  $\Psi$  and can also be written in a more compact form as

$$\nabla^\mu \nabla_\mu \Psi + \left( \frac{1}{c_s^2} - 1 \right) (\nabla_\mu \ln h) \nabla^\mu \Psi = 0, \quad (3.130)$$

where we have used the fact that the partial derivative can be replaced by a full differential, *i.e.*,  $dh/d\rho$  and where we have used expression (2.172) to write the differentials in terms of the sound speed. The nonlinear equation (3.130) reduces to a linear equation when  $h \propto \rho$ ,

<sup>16</sup>Of course the covariant derivative of a scalar function is simply given by the partial derivative and hence Eq. (3.126) should be read as  $w_\mu = \partial_\mu \Psi$ . For simplicity, however, hereafter we will not distinguish between  $\partial_\mu \Psi$  and  $\nabla_\mu \Psi$ , preferring the latter for a more uniform notation.

that is, when considering the ultrastiff equation of state  $p = e$  (see Section 2.4.9) and when  $e \propto \rho^2$ . In this case, in fact, the speed of sound is equal to the speed of light and Eq. (3.130) transforms into a linear equation for a massless scalar field

$$\nabla_\mu \nabla^\mu \Psi = 0, \quad (3.131)$$

which needs to be solved with the appropriate initial and boundary conditions.

The condition of irrotational flow is not completely idealised and indeed it represents a typical condition for the description of *superfluids* such as He-3, for which a zero vorticity and the lack of viscosity is simply the result of quantum effects. It is then possible to show that the fact that all particles are identical leads to an extra equation expressing the vanishing of the vorticity. As discussed by Schutz and Sorkin (1977), this condition is basically equivalent to a Noether theorem from the invariance of the Lagrangian against exchanging identical particles which are all in the same quantum state. Another interesting application of relativistic potential flow is offered by the study of the stationary accretion problem onto a black hole, which was first investigated by Petrich *et al.* (1988), and that we will discuss in detail in Section 11.5.1.

### 3.7.5 Relativistic Kelvin–Helmholtz theorem

A property that relativistic irrotational fluids share with their Newtonian counterparts is that, if the vorticity vanishes at some initial hypersurface, it will vanish at all future times. This is expressed by the *relativistic Kelvin–Helmholtz theorem*, which states that if  $\Gamma$  is a generic loop of particles in a perfect fluid, so that the *relativistic circulation*  $\mathcal{C}$  is defined as [*cf.*, the corresponding Newtonian expression (3.107)]

$$\mathcal{C} := \oint_{\Gamma} h u_\alpha dx^\alpha, \quad (3.132)$$

then this quantity is conserved along fluidlines, that is

$$u^\mu \nabla_\mu \mathcal{C} := u^\mu \nabla_\mu \oint_{\Gamma} h u_\alpha dx^\alpha = 0, \quad (3.133)$$

[*cf.*, Eq. (3.108) for the corresponding Newtonian expression]. Although the rigorous proof of this theorem will not be particularly important for the remainder of the book, we will derive it here for completeness and for its elegance. In doing this we will follow the route suggested by Katz (1984).

The starting point in the proof is expression (3.118), which we use after contracting it with the four-velocity  $u^\mu$  and by exploiting the antisymmetry of the vorticity tensor. In this way, we directly obtain the conservation law of the specific entropy along the fluidlines [*cf.*, Eq. (3.61)]

$$T u^\mu \nabla_\mu s = 0. \quad (3.134)$$

Recalling now the definition (3.122) of the vorticity four-vector, we can contract Eq. (3.118) with  $\epsilon^{\alpha\beta\mu\nu} \nabla_\nu s$ , so as to obtain

$$\epsilon^{\alpha\beta\mu\nu} \Omega_{\mu\delta} u^\delta \nabla_\nu s = \epsilon^{\alpha\beta\mu\nu} T \nabla_\mu s \nabla_\nu s = 0, \quad (3.135)$$

where the last equality follows immediately from the symmetry properties of the Levi-Civita tensor [*cf.*, Eq. (1.62)]. We now rewrite the left-hand side of Eq. (3.135) in terms of the vorticity tensor as

$$\begin{aligned} \frac{1}{2}\epsilon^{\alpha\beta\mu\nu}\epsilon_{\mu\gamma\rho\sigma}{}^*\Omega^{\rho\sigma}u^\gamma\nabla_\nu s &= -\frac{1}{2}\delta_{\gamma\rho\sigma}^{\alpha\beta\nu}{}^*\Omega^{\rho\sigma}u^\gamma\nabla_\nu s \\ &= -(u^{\alpha*}\Omega^{\beta\nu} + u^{\nu*}\Omega^{\alpha\beta} + u^{\beta*}\Omega^{\nu\alpha})\nabla_\nu s, \end{aligned} \quad (3.136)$$

where we have used (1.65) and where the second term on the last equality is zero because of (3.134). As a result, we obtain

$$-u^{\alpha*}\Omega^{\nu\beta}\nabla_\nu s + u^{\beta*}\Omega^{\nu\alpha}\nabla_\nu s = 0. \quad (3.137)$$

Contracting with  $u^\beta$ , using the definition of the vorticity four-vector (3.122) and the normalisation condition for the four-velocity, we can rewrite (3.137) as

$$u^\alpha\Omega^\beta\nabla_\beta s = {}^*\Omega^{\alpha\beta}\nabla_\beta s = \epsilon^{\alpha\beta\mu\nu}\nabla_\mu(hu_\nu)\nabla_\beta s. \quad (3.138)$$

If we now take the four-divergence of the right-hand side of (3.138), we obtain

$$\begin{aligned} \nabla_\alpha[\epsilon^{\alpha\beta\mu\nu}\nabla_\mu(hu_\nu)\nabla_\beta s] &= \epsilon^{\alpha\beta\mu\nu}\nabla_{[\alpha}\nabla_{\mu]}(hu_\nu)\nabla_\beta s \\ &= \frac{1}{2}(\epsilon^{\alpha\beta\mu\nu}R^\delta{}_{\nu\mu\alpha})hu_\delta\nabla_\beta s = 0, \end{aligned} \quad (3.139)$$

where we have used the commutation properties of the covariant derivative, Eq. (1.188), and exploited the symmetries of the Riemann tensor.

As a result, also the four-divergence of the left-hand side of (3.138) is zero, thus yielding the *conservation law*

$$\nabla_\alpha(u^\alpha\Omega^\beta\nabla_\beta s) = 0. \quad (3.140)$$

Equation (3.140), together with the continuity equation (3.52), allows us to state the conservation of the scalar quantity  $\Phi$  along the fluidlines

$$\rho u^\mu\nabla_\mu\Phi = 0, \quad \text{where} \quad \Phi := \frac{1}{\rho}\Omega^\mu\nabla_\mu s. \quad (3.141)$$

The function  $\Phi$  is also referred to as the *relativistic potential vorticity* and is therefore the extension to a relativistic regime of the equivalent Newtonian quantity

$$\phi := \frac{1}{\rho}(\vec{\nabla} \times \vec{u}) \cdot \vec{\nabla} s. \quad (3.142)$$

Both quantities are conserved along the motion of the fluid and, indeed, the conservation of the relativistic potential vorticity represents a fundamental piece of this proof, to which we will get back later on.

Let us now consider a set of comoving coordinates  $\tilde{x}^\mu$  as the remaining part of the proof is particularly simple in this reference frame. Of course, because of Eq. (3.134), the specific

entropy  $s$  represents an excellent first choice for one such set of coordinates and the remaining two, which we name  $a$  and  $b$ , are chosen so that, by construction, they are advected, *i.e.*,

$$u^\mu \nabla_\mu a = 0 = u^\mu \nabla_\mu b. \quad (3.143)$$

Contracting (3.137) with  $\nabla_\mu a$ , we obtain in view of Eq. (3.143) that

$${}^*\Omega^{\alpha\beta} \nabla_\alpha s \nabla_\beta a = 0. \quad (3.144)$$

Because  $s, a$  and  $b$  are all advected with the fluid, the vector  $\epsilon^{\alpha\beta\mu\nu} \nabla_\beta s \nabla_\mu a \nabla_\nu b$  will also be advected and hence parallel to the fluid four-velocity  $u^\alpha$ . We can therefore constrain the choice of  $a$  and  $b$  by requiring that

$$u^\alpha = \frac{1}{\rho} \epsilon^{\alpha\beta\mu\nu} \nabla_\beta s \nabla_\mu b \nabla_\nu a, \quad (3.145)$$

thus leading to our set of comoving coordinates  $\tilde{x}^\mu := (t, s, a, b)$ , in which, by construction, the fluid will be spatially bounded. We next consider a flow in which two-dimensional surfaces with constant specific entropy  $s$  at a fixed time  $t$  cut through the fluid and are cylinder-like. Each of such surfaces will produce a tube as it evolves in time and thus a cylinder in the  $(t, s)$  subspace. Now let  $\ell(s)$  be one of the curves where one such  $(t, s)$ -tube intersects the boundary of the fluid and  $\Gamma(s)$  any closed curve around the same  $(t, s)$ -cylinders. Denoting then with  $\sigma$  the surface between  $\ell(s)$  and  $\Gamma(s)$ , we can use Green's theorem to write the relativistic circulation  $\mathcal{C}$  as

$$\mathcal{C} = \oint_{\Gamma} h u_\mu dx^\mu = \oint_{\ell} h u_\mu dx^\mu + \oint_{\sigma} \Omega_{\mu\nu} dx^{[\mu} dx^{\nu]}. \quad (3.146)$$

It now appears clear why we have chosen comoving coordinates. Since  $dt = 0 = ds$  on  $\sigma$ , this implies that the surface element  $dx^{[\mu} dx^{\nu]}$  can be written as

$$\begin{aligned} dx^{[\mu} dx^{\nu]} &= \frac{1}{2} \frac{\partial(x^\mu, x^\nu)}{\partial(a, b)} da db = \frac{1}{4} \epsilon^{\mu\nu\alpha\beta} \frac{\partial(t, s)}{\partial(x^\alpha, x^\beta)} J da db \\ &= \frac{1}{2} \eta^{\mu\nu\alpha\beta} \partial_\alpha t \partial_\beta s J da db, \end{aligned} \quad (3.147)$$

where  $J := \det(\partial x^\mu / \partial \tilde{x}^\mu)$  and  $\partial_\alpha t$  is related to  $u_\alpha$  and the four-velocity in the comoving frame  $\tilde{u}_\alpha$ . The relation between the two four-velocities is then given by the simple coordinate transformation

$$u_\mu = \tilde{u}_\nu \partial_\mu \tilde{x}^\nu = \tilde{u}_0 \partial_\mu t + \tilde{u}_i \partial_\mu \tilde{x}^i. \quad (3.148)$$

We can now contract (3.145) with  $\rho\sqrt{-g} u_\alpha$  to obtain an expression for  $\rho\sqrt{-g}$  in comoving coordinates

$$\rho\sqrt{-g} = -\epsilon^{\alpha\beta\mu\nu} u_\alpha \nabla_\beta s \nabla_\mu b \nabla_\nu a = \tilde{u}_0 \epsilon^{\alpha\beta\mu\nu} \nabla_\alpha t \nabla_\beta s \nabla_\mu a \nabla_\nu b = \tilde{u}_0 J^{-1}. \quad (3.149)$$

Let us now contract (3.147) and use, in turn, Eqs. (3.122), (3.148), and (3.149), to finally obtain

$$\begin{aligned}
\Omega_{\mu\nu} dx^{[\mu} dx^{\nu]} &= \frac{1}{2} \Omega_{\mu\nu} \eta^{\mu\nu\alpha\beta} \partial_\alpha t \partial_\beta s J da db = {}^*\Omega^{\alpha\beta} \sqrt{-g} \partial_\alpha t \partial_\beta s J da db \\
&= {}^*\Omega^{\alpha\beta} \rho^{-1} (\rho \sqrt{-g} J \partial_\alpha t) \partial_\beta s da db = {}^*\Omega^{\alpha\beta} \rho^{-1} (-\tilde{u}_0 \partial_\alpha t) \partial_\beta s da db \\
&= -\rho^{-1} {}^*\Omega^{\alpha\beta} \partial_\alpha s (u_\beta - \tilde{u}_i \partial_\beta \tilde{x}^i) da db.
\end{aligned} \tag{3.150}$$

Since the  $\tilde{x}^\mu$  coordinates are comoving, we can exploit their property (3.144) to deduce that

$${}^*\Omega^{\mu\nu} \partial_\mu s \partial_\nu \tilde{x}^i = 0, \tag{3.151}$$

so that expressing everything in terms of the vorticity vector and the potential vorticity, Eq. (3.150) reduces to

$$\Omega_{\mu\nu} dx^{[\mu} dx^{\nu]} = \frac{1}{\rho} \Omega^\mu \nabla_\mu s da db = \Phi da db. \tag{3.152}$$

We are now ready to go back to the circulation integral (3.146), which we can therefore rewrite as

$$\oint_{\Gamma} h u_\alpha dx^\alpha = \oint_{\ell} h u_\alpha dx^\alpha + \oint_{\sigma} \Phi da db, \tag{3.153}$$

and evaluate its variation along the fluidlines, *i.e.*,

$$\begin{aligned}
u^\mu \nabla_\mu \oint_{\Gamma} h u_\alpha dx^\alpha &= u^\mu \nabla_\mu \oint_{\ell} h u_\alpha dx^\alpha + u^\mu \nabla_\mu \oint_{\sigma} \Phi da db \\
&= u^\mu \nabla_\mu \oint_{\ell} h u_\alpha dx^\alpha.
\end{aligned} \tag{3.154}$$

It is now clear why the result (3.141)<sub>1</sub> about the conservation of the potential vorticity was important. It allows us to set to zero the second term in Eq. (3.154), which therefore states that the circulation along *any* contour  $\Gamma(s)$  that moves uniformly along the fluidlines is conserved if the circulation along the boundary contours  $\ell(s)$  is conserved. However, we can consider the case in which the two contours  $\Gamma$  and  $\ell$  coincide and hence conclude that

$$u^\mu \nabla_\mu \oint_{\Gamma} h u_\alpha dx^\alpha = 0. \tag{3.155}$$

This is indeed what we wanted to prove. Of course, all the implications of the Kelvin–Helmholtz theorem discussed in Section 3.7.2 within a Newtonian framework apply unmodified also in a relativistic context.

### 3.8 Isentropic flows

We have seen that the isentropy condition of a fluid is a sufficient condition for the adiabaticity, but not a necessary one: an adiabatic fluid may be non-isentropic [*cf.*, Eqs. (3.61) and (3.62)]. Although still rather idealised, the simplicity of isentropic flows provides us with two results

that are worth discussing. The first one can be derived starting again from the momentum-conservation equation (3.55), which, for an isentropic fluid, can be written as

$$u^\mu \nabla_\mu u^\nu = -h^{\mu\nu} \nabla_\mu \ln h, \quad (3.156)$$

where, as usual,  $\nabla$  is the covariant derivative with respect to the metric  $\mathbf{g}$ . Consider now the *conformally related* metric<sup>17</sup>

$$\bar{g}_{\mu\nu} := h^2 g_{\mu\nu}, \quad \bar{g}^{\mu\nu} := h^{-2} g^{\mu\nu}, \quad (3.157)$$

where the conformal factor is given by the specific enthalpy. It is a straightforward exercise of tensor algebra to derive that the Christoffel symbols in the two metrics are related through the transformation (see Problem 5)

$$\bar{\Gamma}^\alpha_{\beta\gamma} = \Gamma^\alpha_{\beta\gamma} + \frac{1}{h} (\delta^\alpha_\beta \nabla_\gamma h + \delta^\alpha_\gamma \nabla_\beta h - g_{\beta\gamma} g^{\alpha\mu} \nabla_\mu h), \quad (3.158)$$

and thus that the corresponding covariant derivatives can be written as

$$\begin{aligned} u^\mu \bar{\nabla}_\mu u_\nu &= u^\mu \nabla_\mu u_\nu - \frac{1}{h} (\delta^\alpha_\nu \nabla_\mu h + \delta^\alpha_\mu \nabla_\nu h - g_{\nu\mu} g^{\alpha\beta} \nabla_\beta h) u^\mu u_\alpha \\ &= u^\mu \nabla_\mu u_\nu + \frac{1}{h} \nabla_\nu h. \end{aligned} \quad (3.159)$$

A little more tensor algebra and the momentum-conservation equation (3.156) allows us to rewrite expression (3.159) as

$$u^\mu \bar{\nabla}_\mu u_\nu = -u_\nu u^\mu \nabla_\mu \ln h = k u_\nu, \quad (3.160)$$

where  $k := -u^\mu \nabla_\mu \ln h$ . Equation (3.160) is effectively a geodesic equation, since the tangent vector  $\mathbf{u}$  is parallel transported to another vector which is just its multiple, *i.e.*,  $\nabla_u \mathbf{u} = k \mathbf{u}$ . In other words, we have just shown that in an isentropic flow, the *fluidlines*  $u^\mu = dx^\mu/d\lambda$  coincide with the geodesic lines in the conformal metric  $\bar{g}_{\mu\nu}$  (Anile, 1989). Besides the mathematical elegance of this result, it is suggestive to think that in a metric in which inertial effects are mapped out via the conformal transformation (3.157), fluid elements move just as if they were test particles, hence along geodesics.

The second interesting result is that the *enthalpy current*  $\mathbf{w}$  [*cf.* Eq. (3.114)] is conserved along the fluidlines in the conformal metric (3.157), that is

$$w^\mu \bar{\nabla}_\mu w_\nu = 0. \quad (3.161)$$

The proof is rather simple and follows directly from the definition of the current  $\mathbf{w}$  and from expression (3.160), *i.e.*,

<sup>17</sup>We recall that two (four-)metrics  $\mathbf{g}$  and  $\bar{\mathbf{g}}$  are said to be *conformally related* if they can be written as  $\bar{g}_{\mu\nu} = \Omega^n g_{\mu\nu}$ , with  $n$  an arbitrary constant coefficient. In this case,  $\bar{\mathbf{g}}$  is said to be the *conformal metric* of the *physical metric*  $\mathbf{g}$ , and  $\Omega$  the *conformal factor* (see also Section 7.2.3 for some applications of conformal metrics).

$$\begin{aligned}
w^\mu \bar{\nabla}_\mu w_\nu &= hu^\mu (h \bar{\nabla}_\mu u_\nu + u_\nu \bar{\nabla}_\mu h) \\
&= h^2 u^\mu \bar{\nabla}_\mu u_\nu + hu_\nu u^\mu \nabla_\mu h \\
&= -h^2 \frac{u_\nu}{h} u^\mu \nabla_\mu h + hu_\nu u^\mu \nabla_\mu h = 0.
\end{aligned} \tag{3.162}$$

Equally simple is to derive that

$$\bar{g}^{\mu\nu} w_\mu w_\nu = -1, \tag{3.163}$$

so that

$$w^\mu \bar{\nabla}_\nu w_\mu = 0. \tag{3.164}$$

Equation (3.164) should be compared with the similar expression (3.4) derived at the beginning of the chapter in terms of the four-velocity vector. We can also recall the definition of the vorticity tensor in Eq. (3.113) to realise that

$$\Omega_{\mu\nu} = \bar{\nabla}_\nu w_\mu - \bar{\nabla}_\mu w_\nu = \nabla_\nu w_\mu - \nabla_\mu w_\nu, \tag{3.165}$$

and after using Eqs. (3.161) and (3.164), we obtain the desired result that, for an isentropic flow,  $w^\mu \Omega_{\mu\nu} = 0$  [*cf.*, Eq. (3.118)]. As a final remark we note that the enthalpy current and the vorticity tensor can be shown to obey the so-called *Helmholtz equations*

$$w^\mu \bar{\nabla}_\mu \Omega_{\alpha\beta} + (\bar{\nabla}_\alpha w^\mu) \Omega_{\mu\beta} + (\bar{\nabla}_\beta w^\mu) \Omega_{\alpha\mu} = 0. \tag{3.166}$$

The proof of these identities can be found in Lichnerowicz (1967).

### 3.9 A velocity-potential approach to relativistic hydrodynamics

An alternative formulation of the equation of relativistic hydrodynamics is possible when the latter is treated as a nonlinear relativistic field theory for five coupled scalar fields, whose Lagrangian density is simply the fluid pressure (Schutz, 1970). This approach stems from the work of Seliger and Whitham in Newtonian hydrodynamics, who derived an expression for the velocity vector in terms of three scalar fields and obtained in this way a variational principle in classical mechanics (Seliger and Whitham, 1968). This approach was then extended to a relativistic regime by Schutz (1970) and derived independently by Schmid (1970). According to this representation, one first defines the scalar functions  $\phi$  and  $\theta$  as (Schutz, 1970)

$$u^\mu \nabla_\mu \phi := -h, \tag{3.167}$$

$$u^\mu \nabla_\mu \theta := T, \tag{3.168}$$

where, as usual,  $T$  and  $h$  are the temperature and the specific enthalpy, respectively. In addition to Eqs. (3.167) and (3.168), the formulation requires the conservation of the rest-mass density and of the specific entropy, as expressed by the continuity equation (3.52) and by the adiabatic condition (3.61). Having made these assumptions, we can define the vector

$$W_\nu := hu_\nu - \nabla_\nu \phi - \theta \nabla_\nu s, \tag{3.169}$$

which is, by construction, orthogonal to  $u^\nu$ , *i.e.*,  $u^\nu W_\nu = 0$ . Next, we compute its Lie derivative along the fluidlines as

$$\begin{aligned}\mathcal{L}_u(W_\nu) &= u_\nu \mathcal{L}_u h + h \mathcal{L}_u u_\nu - \mathcal{L}_u(\nabla_\nu \phi) - \nabla_\nu s \mathcal{L}_u \theta - \theta \mathcal{L}_u(\nabla_\nu s) \\ &= u_\nu u^\mu \nabla_\mu h + h u^\mu \nabla_\mu u_\nu + \nabla_\nu h - T \nabla_\nu s,\end{aligned}\quad (3.170)$$

where we have used the definition of the Lie derivative of a covariant vector [*cf.* Eq. (1.139)], the two definitions (3.167) and (3.168), as well as the property that  $u_\mu \nabla_\nu u^\mu = 0$ , [*cf.* Eq. (3.4)]. Using now the first law of thermodynamics in the form given by (2.142), we can rewrite the right-hand side of (3.170) as

$$\mathcal{L}_u(h u_\nu - \nabla_\nu \phi - \theta \nabla_\nu s) = u^\mu \nabla_\mu (h u_\nu) + \frac{\nabla_\nu p}{\rho} = 0, \quad (3.171)$$

where the last equality is implied by the momentum-conservation equation in the form given by (3.67). We have therefore reached the conclusion that

$$\mathcal{L}_u \mathbf{W} = 0, \quad (3.172)$$

that is, in a perfect fluid the vector  $\mathbf{W}$  is Lie-dragged along  $\mathbf{u}$ . Since Pfaff's theorem of differential forms states that four scalar functions (potentials) are sufficient to describe the four-velocity, we can express the vector  $W_\mu$  in terms of two additional potentials  $\alpha$  and  $\beta$ , such that  $W_\mu = \alpha \nabla_\mu \beta$  and we can invert the definition (3.169) to express the four-velocity in terms of the six potentials  $h, \phi, s, \alpha, \beta, \theta$  as (Schutz, 1970)

$$u_\mu = \frac{1}{h} (\nabla_\mu \phi + \alpha \nabla_\mu \beta + \theta \nabla_\mu s). \quad (3.173)$$

Note that, because of the orthogonality condition between  $\mathbf{W}$  and  $\mathbf{u}$ , and because of the condition (3.172), the scalar functions  $\alpha$  and  $\beta$  are constrained to satisfy the constraints

$$u^\mu \nabla_\mu \alpha = 0, \quad u^\mu \nabla_\mu \beta = 0. \quad (3.174)$$

In addition, the normalisation condition of the four-velocity (3.2) provides one more constraint between the specific enthalpy and the potentials

$$h^2 = -g^{\mu\nu} (\nabla_\mu \phi + \alpha \nabla_\mu \beta + \theta \nabla_\mu s) (\nabla_\nu \phi + \alpha \nabla_\nu \beta + \theta \nabla_\nu s). \quad (3.175)$$

The end-result of this derivation is that we have formulated the relativistic-hydrodynamic equations as a standard conservation equation for the rest-mass density and a set of evolution equations along the fluidlines of six scalar functions or *potentials*:  $h, s, \alpha, \beta, \phi, \theta$ , *i.e.*,

$$\nabla_\mu (\rho u^\mu) = 0, \quad (3.176)$$

$$u^\mu \nabla_\mu s = 0, \quad (3.177)$$

$$u^\mu \nabla_\mu \alpha = 0, \quad (3.178)$$

$$u^\mu \nabla_\mu \beta = 0, \quad (3.179)$$

$$u^\mu \nabla_\mu \phi = -h, \quad (3.180)$$

$$u^\mu \nabla_\mu \theta = T. \quad (3.181)$$

Equations (3.176)–(3.181) provide the *velocity-potential formulation* of the equations of hydrodynamics. Note that they are not just an equivalent formulation of the hydrodynamic equations discussed so far but they rather offer a different viewpoint of the dynamics of a fluid. Indeed, they transform the fluid four-velocity from its intuitive role of a primary fluid quantity to a less intuitive, secondary quantity derived from primary potentials. The velocity-potential approach changes the traditional framework in which the fluid is fully determined by two scalar quantities (*i.e.*, two thermodynamic variables) and one vector (*i.e.*, the three-velocity), to build a new one in which there are six basic scalar functions determined at each point in the fluid. Hence, the four-velocity is not regarded as a vector field in spacetime, but rather as the gradient of a set of scalar functions, whose values change in space and time throughout the fluid. The novelty of this approach also brings a number of new considerations that have to do with: (1) the physical interpretation of the potentials; (2) the determination of the “gauge-freedom” intrinsic to the use of potentials; (3) the definition of the initial-value problem. Most of these considerations are nicely presented by Schutz (1970), which we report here, slightly elaborating them.

Let us start therefore with point (1). The easiest way to build physical intuition about the four new potentials  $\alpha, \beta, \phi, \theta$  is to realise that we can combine the new definition of the four-velocity (3.173) with the definition (3.113) so as to express both the vorticity tensor and the vorticity four-vector in terms of the velocity potentials, *i.e.*,

$$\Omega_{\mu\nu} = 2\nabla_{[\nu}w_{\mu]} = 2\nabla_{[\nu}\alpha\nabla_{\mu]}\beta + 2\nabla_{[\nu}\theta\nabla_{\mu]}s, \quad (3.182)$$

$$\Omega^\mu = \frac{1}{2}\epsilon^{\mu\nu\kappa\lambda}\Omega_{\kappa\lambda}u_\nu = \epsilon^{\nu\mu\lambda\kappa}(\nabla_\lambda\alpha\nabla_\kappa\beta + \nabla_\lambda\theta\nabla_\kappa s)u_\nu. \quad (3.183)$$

Expression (3.183) becomes more transparent if we evaluate it in the fluid local rest frame, in which  $g_{\mu\nu} = \eta_{\mu\nu} = (-1, 1, 1, 1)$ , the enthalpy current and the four-velocity have zero spatial components, *i.e.*,  $w^0 = -w_0 = h$ ,  $u^0 = -u_0 = 1$ ,  $w^i = w_i = 0$ ,  $u^i = u_i = 0 = v^i = v_i$ , and  $\epsilon^{\nu\mu\lambda\kappa}u_\nu = \epsilon^{0ijk}u_0 = \epsilon^{ijk}$ . As a result, the vorticity vector has only spatial components and these are given by

$$\Omega^i = \epsilon^{ijk}(\nabla_j\alpha\nabla_k\beta + \nabla_j\theta\nabla_k s), \quad (3.184)$$

or, in vector notation,<sup>18</sup>

$$\vec{\Omega} = \vec{\nabla}\alpha \times \vec{\nabla}\beta + \vec{\nabla}\theta \times \vec{\nabla}s, \quad (3.185)$$

where as usual  $\vec{\Omega}$  is the spatial part of  $\Omega$ . Let us consider expression (3.185) in two simple but instructive cases. First, if the flow is isentropic, *i.e.*,  $\vec{\nabla}s = 0$  [*cf.*, Eq. (3.62)], then surfaces of constant  $\alpha$  and  $\beta$  intersect along vortex lines and these are advected with the flow, since  $\nabla_u\alpha = 0 = \nabla_u\beta$ . In other words, the vorticity vector is always orthogonal to the plane containing the local gradients of the potentials  $\alpha$  and  $\beta$ . Second, if  $\alpha = \text{const.}$ ,  $\beta = \text{const.}$ , but  $s \neq \text{const.}$ , then again surfaces of constant  $\theta$  and  $s$  intersect along vortex lines which, however, are not advected but modified by the temperature, since  $\nabla_u\theta = T$ . Note that if the flow is isentropic and built to be irrotational (*e.g.*, by setting the gradients of  $\alpha$  and  $\beta$  to be parallel,

<sup>18</sup> Expression (3.185) highlights the similarities between the velocity potentials and the *Euler potentials*  $\alpha$  and  $\beta$ , sometimes considered to express magnetic fields as  $\vec{B} = \vec{\nabla}\alpha \times \vec{\nabla}\beta$  (Stern, 1970). A well-known drawback of Euler potentials is that they are not uniquely defined: any new potential  $\alpha'$  which differs by a function of  $\beta$  will yield the same magnetic field.

i.e.,  $\nabla_\mu \beta = k \nabla_\mu \alpha$ , where  $k$  is a constant), then the second term on the right-hand side of the definition (3.182) can be cast as another gradient of a scalar function and be effectively absorbed by the first term. As a result, the expression reduces to  $h u_\mu = \nabla_\mu \Psi$ , as expected for irrotational (isentropic) flows [cf., Eq. (3.126)].

Next, let us consider point (2) and discuss whether the representation in terms of the potential is unique. Clearly, since we have six potentials to fix the five degrees of freedom of the fluid, one of them must be totally arbitrary. This “gauge freedom” cannot involve  $h$  and  $s$  since they measure the thermodynamic (or “gauge-invariant”) properties of the fluid. This leaves us with the potentials  $\alpha, \beta, \phi, \theta$ , and the gauge freedom is therefore reflected in the fact that for any choice we can make of them at an initial time, we can find an equivalent set of potentials  $\alpha', \beta', \phi', \theta'$ , which will give the same four-velocity  $u$ . More precisely, two sets of velocity potentials are said to be *equivalent* if they yield the same four-velocity for any fixed state of the fluid. Using again the limiting case of isentropic flow, the gauge freedom amounts to choosing  $\alpha, \beta$  and  $\alpha', \beta'$  in such a way that their gradients rotate in the plane orthogonal to  $\vec{\Omega}$ , which is of course unaffected by such rotation. The *equivalence transformations* by means of which one set of potentials is transformed into another one are presented in Schutz (1970), but the salient aspect of these transformations is that the initial value of any one potential may be chosen arbitrarily and the remaining three are then *constrained* but *not determined* by the physical state of the fluid, i.e., by  $u, h, s$ .

Finally, let us consider point (3) and discuss how to define and solve the initial-value problem on a spatial hypersurface  $\Sigma$ . In practice two routes are possible (Schutz, 1970). In the first one it is sufficient to define at the initial time the values of the rest-mass density  $\rho$  and of six potentials  $h, s, \alpha, \beta, \phi, \theta$  (from what was said above, one of the last four can be chosen arbitrarily), but not of their derivatives. Of course the choice of  $\beta, \phi$  is not unique as arbitrary constants can be added to them without affecting the four-velocity. In the second route, on the other hand, it is possible to distinguish between “initial-value variables”, that is, variables which are entirely advected with the flow, such as  $\alpha, \beta, s$ ,<sup>19</sup> from the “dynamical variables”, such as  $\theta$  and  $h$ , whose evolution is determined by the thermodynamic conditions of the fluid. In this second case, it is sufficient to define, together with  $\rho$ , the initial values of the four potentials  $\alpha, \beta, \phi, \theta$  (again, one of which can be chosen arbitrarily), and the derivatives of any two potentials in the direction orthogonal to  $\Sigma$ . This breakup of variables has an intuitive justification but, again, it is not unique nor necessarily the simplest. Indeed, this is one of the limitations of the velocity-potential formulation, that has so far found only limited numerical applications, e.g., by Mann (1985).

While both of these approaches provide a solution of the initial-value problem for the potentials, and hence fully describe the thermodynamic state of the fluid and its four-velocity at the initial time, the opposite mapping is not straightforward. Stated differently, if the initial physical state is known in terms of the variables  $u, h, s$  (as it is usually the case in practical applications), the differential nature of the relation (3.173) makes it difficult to perform the inverse mapping from the velocity space over that of the velocity potentials.

As a concluding remark in this section we note that the velocity-potential formulation of relativistic hydrodynamics can also be written in a fully conservative form (see Section 7.3), that is, in a form involving only four-divergences of currents densities. This can be achieved

<sup>19</sup>As expressed by Eqs. (3.177)–(3.179), the quantities  $\alpha, \beta, s$ , can be considered as Lagrangian tracers of the fluid, so that a fluid element will always carry along its initial values of  $\alpha, \beta$  and  $s$ .

after introducing the derived quantities

$$\tilde{\alpha} := \rho\alpha, \quad \tilde{\beta} := \rho\beta, \quad \tilde{s} := \rho s, \quad (3.186)$$

$$\tilde{\phi} := \rho\phi, \quad \tilde{\theta} := \rho\theta, \quad (3.187)$$

so that Eqs. (3.176)–(3.181) are equivalent to

$$\nabla_\mu(\rho u^\mu) = 0, \quad (3.188)$$

$$\nabla_\mu(\tilde{s} u^\mu) = 0, \quad (3.189)$$

$$\nabla_\mu(\tilde{\alpha} u^\mu) = 0, \quad (3.190)$$

$$\nabla_\mu(\tilde{\beta} u^\mu) = 0, \quad (3.191)$$

$$\nabla_\mu(\tilde{\phi} u^\mu) = -\rho h, \quad (3.192)$$

$$\nabla_\mu(\tilde{\theta} u^\mu) = \rho T. \quad (3.193)$$

In the case of a monatomic ideal fluid, the last two equations (3.192)–(3.193) can also be combined into a single equation as

$$\begin{aligned} \nabla_\mu[(\tilde{\theta} - \tilde{\phi})u^\mu] &= \rho(T + h) = e + p + \rho T \\ &= \rho + p \left[ \frac{m}{k_B} + \frac{\gamma}{\gamma - 1} \right] \\ &= \rho \left[ 1 + K\rho^{\Gamma-1} \left( \frac{\Gamma k_B + m(\Gamma - 1)}{(\Gamma - 1)k_B} \right) \right], \end{aligned} \quad (3.194)$$

where in the second and third lines we have considered respectively the case of an ideal-fluid equation of state with adiabatic index  $\gamma$  [cf., Eq. (2.235)], or a polytropic equation of state with index  $\Gamma$  [cf., Eq. (2.247)]. The formulation of Eqs. (3.188)–(3.193) is particularly suited to be employed by finite-volume numerical methods for the solution of conservation laws (see Chapter 9).

### 3.10 A variational principle for relativistic hydrodynamics

The equations of relativistic hydrodynamics, which we have so far derived in terms of conservation laws within a relativistic Boltzmann-equation approach (see Section 2.3.4), or within a macroscopic description of a fluid (see Section 3.3), can also be derived from a purely variational principle, at least for perfect fluids. There are a number of different routes to this derivation, starting from the historical one of Taub (1954), up to more recent derivations, which have then found application in development of the mathematical description of *multifluids* and non-perfect fluids (Carter, 1973; Hawking and Ellis, 1973; Carter, 1989) [see, e.g., the recent review by Andersson and Comer (2007)]. Apart for minor adjustments in the notation and in the signature, hereafter we will follow closely the first derivation of Taub (1954), as this is particularly straightforward to discuss and it fits nicely with the velocity-potential approach described in the previous section.

Our goal in this section is therefore to show that it is possible to obtain, through the extremal variation of a suitable action, the Einstein field equations

$$R_{\mu\nu} - \frac{1}{2}g_{\mu\nu}R = 8\pi T_{\mu\nu}, \quad (1.218)$$

and the equations of motion [*cf.*, Eq. (3.53)]

$$\nabla_\mu T^{\mu\nu} = 0, \quad (3.195)$$

for a fluid with four-velocity satisfying the normalisation condition expressed by Eq. (3.2) and whose rest mass (particle number) is conserved, *i.e.*, for which [*cf.*, Eq. (3.52)]

$$\nabla_\mu(\rho u^\mu) = 0 = \nabla_\mu(nu^\mu). \quad (3.196)$$

The energy-momentum tensor and the specific enthalpy of such a fluid will then turn out to have the standard definitions [*cf.*, Eq. (3.36)]

$$T_{\mu\nu} := \rho h u_\mu u_\nu + p g_{\mu\nu}, \quad (3.197)$$

$$h := 1 + \epsilon + \frac{p}{\rho}. \quad (2.141)$$

If  $L_{\text{fluid}}$  is the fluid Lagrangian density (Misner *et al.*, 1973), so that the fluid contribution to the total Lagrangian is defined as

$$\mathcal{L}_{\text{fluid}} = \sqrt{-g} L_{\text{fluid}} := \sqrt{-g} \left[ R - 2\kappa\rho(1 + f + \frac{1}{2}\lambda g_{\mu\nu}u^\mu u^\nu) \right], \quad (3.198)$$

that is, as a function only of the fluid rest-mass density  $\rho$ , of its temperature  $T$ , of its four-velocity  $u^\mu$ , and of the metric  $g_{\mu\nu}$ , then we will show that Eqs. (1.218) are obtained through the variation of  $g_{\mu\nu}$ . Similarly, we will show that the equations of motion (3.195) [with definitions (3.197)–(2.141)] are obtained through the variation of  $\rho$ ,  $T$  and of the fluid worldlines, when the conditions (3.2)–(3.196) are also satisfied. We start therefore by considering the *action*

$$\mathcal{S} = \int \left[ R - 2\kappa\rho \left( 1 + f + \frac{1}{2}\lambda g_{\mu\nu}u^\mu u^\nu \right) \right] \sqrt{-g} d^4x, \quad (3.199)$$

where  $\kappa$  is a constant,  $\lambda$  is a Lagrange multiplier to be determined so as to satisfy the normalisation condition (3.2),  $g := \det(g_{\mu\nu})$ , and  $f$  is the *specific Helmholtz free energy*, defined as

$$f := \epsilon - sT, \quad (3.200)$$

with  $s$  being the familiar specific entropy. The integral in (3.199) is to be performed on the portion of the spacetime spanned by the worldlines of the fluid elements and is assumed to have compact support.

Taking  $\rho$  and  $T$  as independent thermodynamic quantities, the variation of the Helmholtz free energy is given by

$$df = \left( \frac{\partial \epsilon}{\partial \rho} - T \frac{\partial s}{\partial \rho} \right) d\rho + \left( \frac{\partial \epsilon}{\partial T} - s - T \frac{\partial s}{\partial T} \right) dT, \quad (3.201)$$

and, using the first law of thermodynamics in the form [cf., Eq. (2.137)]

$$Tds = d\epsilon + pd \left( \frac{1}{\rho} \right), \quad (3.202)$$

such a variation can be simplified to

$$df = \left( \frac{p}{\rho^2} \right) \delta\rho - sdT. \quad (3.203)$$

As mentioned above, we need to consider the variation of the worldlines of fluid elements, which we write as

$$x^\mu = x^\mu(u, v, w, s) = x^\mu(x^{\mu'}), \quad (3.204)$$

where  $u$ ,  $v$ ,  $w$ , and  $s$  are variables distinguishing one such worldline, and where  $s$ , in particular, can be taken to be the *proper time* along the worldline.<sup>20</sup> As a result, the fluid four-velocity can be written as

$$u^\mu = \frac{\partial x^\mu}{\partial s}, \quad (3.205)$$

and the variation of the velocity four-vector  $\delta u$  is directly related to the variation  $\delta x$  in the worldlines, *i.e.*,

$$\delta u^\mu = \delta \left( \frac{\partial x^\mu}{\partial s} \right) = \frac{\partial(\delta x^\mu)}{\partial s}. \quad (3.206)$$

For all practical purposes, the construction (3.204) can be thought of as a coordinate transformation between the coordinate system  $\{x^\mu\}$  and the coordinate system of the labels of the worldline  $\{x^{\mu'}\} = \{u, v, w, s\}$ , so that we can evaluate the Lagrangian in terms of the new coordinate system indicated with primed quantities as

$$\mathcal{S} = \mathcal{S}' = \int \left[ R' - 2\kappa\rho'(1 + f' + \frac{1}{2}\lambda g_{\mu'\nu'}u^{\mu'}u^{\nu'}) \right] \sqrt{-g'} du dv dw ds, \quad (3.207)$$

leaving to standard coordinate transformations the passage from one set of coordinates to the other. As an example, we can evaluate the determinant of the new, primed metric, simply as

$$\sqrt{-g'(x^{\mu'})} = \sqrt{-g(x^\mu)} \eta_{\alpha\beta\mu\nu} \frac{\partial x^\alpha}{\partial u} \frac{\partial x^\beta}{\partial v} \frac{\partial x^\mu}{\partial w} \frac{\partial x^\nu}{\partial s}, \quad (3.208)$$

where  $\eta_{\alpha\beta\mu\nu}$  is the totally antisymmetric symbol [cf., Eq. (1.64)]. In the new coordinate system, the mass (particle-number) conservation equation (3.195) will take the form

<sup>20</sup>Do not confuse the variables  $u, v, w, s$  along the worldline with other quantities introduced in other parts of the book, *e.g.*, the velocity or the specific entropy.

$$\frac{1}{\sqrt{-g'}} \partial_{\mu'} (\sqrt{-g'} \rho' u^{\mu'}) = 0, \quad (3.209)$$

and, after multiplying it by  $\sqrt{-g'} du dv dw ds$  and integrating over the four-dimensional volume spanned by the fluid worldlines, it can be expressed as

$$\int \partial_{\mu'} (\sqrt{-g'} \rho' u^{\mu'}) du dv dw ds = 0. \quad (3.210)$$

Equation (3.210) is equivalent to the statement that the three-dimensional integral

$$\int \sqrt{-g} \rho u^\delta \eta_{\alpha\beta\gamma\delta} \frac{\partial x^\alpha}{\partial u} \frac{\partial x^\beta}{\partial v} \frac{\partial x^\gamma}{\partial w} du dv dw \quad (3.211)$$

is independent of  $s$ . Stated differently, the condition of mass conservation (3.196) is equivalent to the condition that

$$\rho' \sqrt{-g'(x^{\mu'})} = \rho \sqrt{-g(x^\mu)} \eta_{\alpha\beta\gamma\delta} \frac{\partial x^\alpha}{\partial u} \frac{\partial x^\beta}{\partial v} \frac{\partial x^\gamma}{\partial w} \frac{\partial x^\delta}{\partial s} = M(u, v, w), \quad (3.212)$$

where  $M(u, v, w)$  is independent of  $s$  and thus a property of the fluid that does not change along the bundle of worldlines considered. This fact allows us to express the variations in the rest-mass density  $\delta\rho$  in terms of the metric and of the variations in the fluid elements paths. Setting in fact  $\delta M = 0$ , Eq. (3.212) implies that

$$\frac{\delta\rho}{\rho} - \frac{1}{2} g^{\mu\nu} \delta g_{\mu\nu} - \frac{1}{\sqrt{-g}} \partial_\mu (\sqrt{-g} \delta x^\mu) = 0, \quad (3.213)$$

where we have used the fact that the determinant of the Jacobian of the transformation (3.204) is given by

$$J := \eta_{\alpha\beta\gamma\delta} \frac{\partial x^\alpha}{\partial u} \frac{\partial x^\beta}{\partial v} \frac{\partial x^\gamma}{\partial w} \frac{\partial x^\delta}{\partial s}, \quad (3.214)$$

and its relative variation is then

$$\frac{\delta J}{J} = -\nabla_\mu (\delta x^\mu). \quad (3.215)$$

Similarly, the relative variations in the rest-mass density in the primed coordinate system are given by

$$\frac{\delta\rho'}{\rho'} - \frac{1}{2} g^{\mu'\nu'} \delta g_{\mu'\nu'} - \frac{1}{\sqrt{-g'}} \partial_{\mu'} (\sqrt{-g'} \delta x^{\mu'}) = 0, \quad (3.216)$$

where

$$\delta x^{\mu'} = \frac{\partial x^{\mu'}}{\partial x^\nu} \delta x^\nu, \quad (3.217)$$

and

$$\delta g_{\mu'\nu'} = \frac{\partial x^\alpha}{\partial x^{\mu'}} \frac{\partial x^\beta}{\partial x^{\nu'}} \delta g_{\alpha\beta}. \quad (3.218)$$

Note that while  $g_{\mu'\nu'}$  is the metric tensor in the primed coordinate system and can be computed from  $g_{\mu\nu}$  via an ordinary coordinate transformation [cf., Eq. (1.5)]

$$g_{\mu'\nu'} = \Lambda^\alpha_{\mu'} \Lambda^\beta_{\nu'} g_{\alpha\beta} = \frac{\partial x^\alpha}{\partial x^{\mu'}} \frac{\partial x^\beta}{\partial x^{\nu'}} g_{\alpha\beta}, \quad (3.219)$$

the quantity  $\delta g_{\mu'\nu'}$  represents the variation of the metric tensor in the primed coordinate system. An additional variation is possible and is the result of the variation of the fluid worldlines. We indicate this special variation as

$$\delta_x(g_{\mu'\nu'}) := \nabla_{\mu'}(\delta x_{\nu'}) + \nabla_{\nu'}(\delta x_{\mu'}), \quad (3.220)$$

where the covariant derivatives are computed in the primed coordinate system and  $\delta x_{\mu'}$  are the covariant components of the variations  $\delta x^{\mu'}$ .

We are now ready to take the variations of the action (3.207), which, after some algebra, leads to the expression

$$\begin{aligned} \delta S = \int \left\{ \left( R^{\mu'\nu'} - \frac{1}{2} g^{\mu'\nu'} R' \right) [\delta g_{\mu'\nu'} + \nabla_{\nu'}(\delta x_{\mu'}) + \nabla_{\mu'}(\delta x_{\nu'})] \right. \\ \left. - 2\kappa\rho \left[ \left( \frac{p}{(\rho')^2} \delta\rho' - s' \delta T' \right) + \frac{1}{2} \lambda u^{\mu'} u^{\nu'} \delta g_{\mu'\nu'} \right. \right. \\ \left. \left. + \lambda g_{\mu'\nu'} u^{\mu'} u^{\nu'} \nabla_\alpha(\delta x^{\nu'}) \right] \right\} \sqrt{-g'} du dv dw ds, \end{aligned} \quad (3.221)$$

and where we have used the well-known relation [see, e.g., Misner et al. (1973)]

$$\delta(\sqrt{-g}) = \frac{1}{2} \sqrt{-g} g^{\mu\nu} \delta g_{\mu\nu} = -\frac{1}{2} \sqrt{-g} g_{\mu\nu} \delta g^{\mu\nu}. \quad (3.222)$$

Enforcing now the constraint  $\delta M = 0$  via expression (3.216), we can eliminate the term in  $\delta\rho'$  and write (3.221) as

$$\begin{aligned} \delta S = \int \left\{ \left( R^{\mu'\nu'} - \frac{1}{2} g^{\mu'\nu'} R' - \kappa \Theta^{\mu'\nu'} \right) [\delta g_{\mu'\nu'} + 2\nabla_{\nu'}(\delta x_{\mu'})] \right. \\ \left. + 2\kappa\rho s' \delta T' \right\} \sqrt{-g'} du dv dw ds, \end{aligned} \quad (3.223)$$

where we have defined  $\Theta^{\mu\nu}$  as the new (but rather familiar) quantity

$$\Theta^{\mu'\nu'} := \lambda \rho u^{\mu'} u^{\nu'} + p g^{\mu'\nu'}. \quad (3.224)$$

It is also convenient to introduce a new scalar quantity  $\varrho$ , which does not have an obvious physical interpretation, but can be defined in terms of the equation

$$\delta T' = u^{\mu'} \nabla_{\mu'}(\delta \varrho') = \frac{\partial(\delta \varrho')}{\partial s}, \quad (3.225)$$

so that, using the additional identities

$$\begin{aligned}
 \delta_x(g_{\mu'\nu'}u^{\mu'}u^{\nu'}) &= \delta_x(g_{\mu\nu}u^\mu u^\nu) \\
 &= u^\mu u^\nu \left( \frac{\partial g_{\mu\nu}}{\partial x^\alpha} \right) \delta x^\alpha + 2g_{\mu\nu}u^\nu \left( \frac{\partial \delta x^\mu}{\partial s} \right) \\
 &= u^\mu u^\nu \left( \frac{\partial g_{\mu\nu}}{\partial x^\alpha} \right) \delta x^\alpha + 2g_{\mu\nu}u^\nu u^\alpha \left( \frac{\partial \delta x^\mu}{\partial x^\alpha} \right) \\
 &= 2g_{\mu\nu}u^\nu u^\alpha \nabla_\alpha(\delta x^\mu) = 2g_{\mu'\nu'}u^{\nu'}u^{\alpha'}\nabla_{\alpha'}(\delta x^{\mu'}) ,
 \end{aligned} \tag{3.226}$$

the variation of the action (3.223) can be integrated by parts and rewritten as

$$\begin{aligned}
 \delta\mathcal{S} = \int \left[ \left( R^{\mu'\nu'} - \frac{1}{2}g^{\mu'\nu'}R' - \kappa\Theta^{\mu'\nu'} \right) \delta g_{\mu'\nu'} + \kappa\nabla_{\nu'}(\Theta^{\mu'\nu'})\delta x_{\mu'} \right. \\
 \left. - 2\kappa\nabla_{\mu'}(\rho's'u^{\mu'})\delta\theta' \right] \sqrt{-g'} du dv dw ds .
 \end{aligned} \tag{3.227}$$

As usual, we have considered variations that vanish on the three-dimensional surface bounding the region of integration. As a result, the variations of the action leading to an extremum, *i.e.*,  $\delta\mathcal{S} = 0$ , are given by<sup>21</sup>

$$R^{\mu\nu} - \frac{1}{2}g^{\mu\nu}R = \kappa\Theta^{\mu\nu}, \tag{3.228}$$

$$\nabla_\mu\Theta^{\mu\nu} = 0, \tag{3.229}$$

$$\nabla_\mu(\rho su^\mu) = 0, \tag{3.230}$$

where we have not used primed quantities since Eqs. (3.228)–(3.230) are tensor equations. The last one, in particular, can be rewritten after using the condition of mass conservation (3.195) as

$$\rho u^\mu \nabla_\mu s = 0, \tag{3.231}$$

which we recognise to be the condition of adiabaticity that we have already encountered in Section 3.3 when discussing perfect fluids [*cf.*, Eq. (3.61)]. Similarly, after recalling that  $u^\mu \nabla_\nu u_\mu = 0$  [*cf.*, Eq. (3.4)], Eq. (3.229) can be cast as

$$\rho u^\nu \nabla_\nu(\lambda u^\mu) = -g^{\mu\nu} \partial_\nu p, \tag{3.232}$$

which is still not fully determined since we do not yet have a final expression for the Lagrange multiplier  $\lambda$ . We therefore compute the latter imposing the requirement that the normalisation condition (3.2) is satisfied, namely that

$$-\frac{1}{2}\lambda\rho d(g_{\mu\nu}u^\mu u^\nu) = dp + \rho g_{\mu\nu}u^\mu u^\nu d\lambda = dp + \rho g_{\mu\nu}u^\mu u^\nu u^\alpha \partial_\alpha \lambda, \tag{3.233}$$

<sup>21</sup>Clearly, if restricted to a vacuum spacetime, we have here simply re-derived the classical *Einstein–Hilbert action* leading to the Einstein equations in vacuum (Misner *et al.*, 1973).

where we have defined  $d\phi := u^\mu \partial_\mu \phi$ . Using now the first law of thermodynamics (3.202) in the form

$$\frac{dp}{\rho} = d\epsilon + d\left(\frac{p}{\rho}\right) - Tds, \quad (3.234)$$

we rewrite (3.233) as

$$-\frac{1}{2}\lambda\rho d(g_{\mu\nu}u^\mu u^\nu) = \rho \left[ d\epsilon + d\left(\frac{p}{\rho}\right) \right] + \rho g_{\mu\nu}u^\mu u^\nu d\lambda, \quad (3.235)$$

and thus

$$d\lambda = d\epsilon + d\left(\frac{p}{\rho}\right), \quad (3.236)$$

which can be easily integrated to yield

$$\lambda = 1 + \epsilon + \frac{p}{\rho}. \quad (3.237)$$

Note that the first term on the right-hand side of (3.237) is an integration constant (being  $c^2$  in a system of units in which  $c \neq 1$ ), obtained so as to recover the correct expression for the energy-momentum tensor when  $p = 0$ .

This completes our derivation, since we have shown that, after setting  $\kappa := 8\pi$ , Eqs. (3.228), (3.229), (3.224) and (3.237) are equivalent to Eqs. (1.218), (3.195), (3.197) and (2.141), respectively. In other words, we have shown that if we use as variables  $\rho$ ,  $T$  and  $g_{\mu\nu}$ , and apply the variational principle  $\delta\mathcal{S} = 0$  to the Lagrangian (3.199), with variations of the particle paths such that the normalisation condition (3.198) is satisfied and the Lagrangian multiplier is given by (3.237), then we obtain the Einstein field equations and the equations of conservation of energy and momentum for a perfect fluid with energy-momentum tensor given by (3.197).

Two final remarks before concluding. First, as discussed by Schutz (1970), a variational formulation of the relativistic hydrodynamics equations is possible also within the velocity-potential approach discussed in Section 3.9 and it coincides with the one suggested by Taub (1954). In this case, the action takes the simpler form [*cf.*, Eqs. (3.198)]

$$\mathcal{S} = \int (R + 16\pi p) \sqrt{-g} d^4x, \quad (3.238)$$

that is, with the fluid contribution to the Lagrangian density being given simply by the fluid pressure [*cf.*, Eqs. (3.199)]

$$\mathcal{L}_{\text{fluid}} = \sqrt{-g} L_{\text{fluid}} := \sqrt{-g} p. \quad (3.239)$$

Other fluid Lagrangian densities expressed in terms of the fluid energy density have also been proposed (Carter, 1989) and used in the study of multicomponent fluids (Carter and Langlois, 1998; Langlois *et al.*, 1998). Second, we recall that, in addition to a derivation from a variational principle, the equations of relativistic hydrodynamics for perfect fluids have also been cast in a Hamiltonian formulation. The interested reader will find more details in Schutz (1971), Künzle and Nester (1984), Holm (1989), and Comer and Langlois (1994).

### 3.11 Perfect multifluids

We have so far considered a fluid description in which the fluid is composed of indistinguishable particles of the same type. This is of course a very good first approximation, which is widely used for the vast majority of research in relativistic hydrodynamics, but an approximation nevertheless. In practice, most fluids are a mixture of different fluid species, which are compenetrating and interacting, therefore composing a perfect *multicomponent fluid*, or simply a *multifluid*. In what follows we briefly discuss the main properties of such mixtures, distinguishing the case of *coupled multifluids* from that of *interacting multifluids*. We note that it is in principle also possible to consider *multicomponent non-interacting* fluids – as a mixture of fluids which interact only gravitationally and therefore with each component having its own four-velocity. Fluids of this type are sometimes considered within a cosmological context (Krasinski, 1997), where it is reasonable to consider fluids that are essentially pressureless dusts and that influence each other's dynamics only via gravity, *e.g.*, a mixture of dark-matter fluids [see, *e.g.*, Bolejko and Lasky (2008) for some recent work].

#### 3.11.1 Coupled multifluids

Going beyond the single-fluid approximation is not particularly difficult for perfect fluids and indeed it can be very simple in the case in which the fluids are *coupled*. In this case, in fact, the exchange of momentum through the collisions (that are given mostly by two-body interactions), taking place among the different constituents of the multifluid, is such that all the different fluid species have the *same* four-velocity.<sup>22</sup>

In this case, the energy–momentum tensor of the multifluid is just a linear combination of the energy–momentum tensors of the single species. In other words, for a fluid composed of  $N_s$  different species, each with rest-mass density  $\rho_i$ , elementary mass  $m_i$ , specific internal energy  $\epsilon_i$ , and pressure  $p_i$ , and all with the same four-velocity  $u^\mu$ , the total energy–momentum tensor is simply given by

$$\begin{aligned} T^{\mu\nu} &= (e + p)u^\mu u^\nu + pg^{\mu\nu} \\ &= \sum_i^{N_s} T_i^{\mu\nu} = \sum_i^{N_s} (e_i + p_i)u^\mu u^\nu + p_i g^{\mu\nu}, \end{aligned} \quad (3.240)$$

where the total fluid quantities are simple linear combinations of those of the constituents

$$\rho = \sum_i^{N_s} \rho_i = \sum_i^{N_s} n_i m_i, \quad e = \sum_i^{N_s} e_i = \sum_i^{N_s} \rho_i(1 + \epsilon_i), \quad p = \sum_i^{N_s} p_i. \quad (3.241)$$

It should be noted that even in the case of a coupled multifluid, each of the constituents will have its own sound speed defined as [*cf.*, Eq. (2.168)]

$$c_{s,i}^2 = \left( \frac{\partial p_i}{\partial e_i} \right)_s, \quad (3.242)$$

<sup>22</sup>Multifluids of this type are sometimes also referred to as *multicomponent single fluids* (Andersson and Comer, 2007).

## 176 Relativistic Perfect Fluids

which may depend on some common thermodynamic quantity (*e.g.*, temperature), but does not depend on the relative state of motion of the different components. This will be another difference with respect to interacting multifluids.

The linearity in the rest-mass density implies that its global conservation equation is simply given by the combination of the conservation equations for each constituent, *i.e.*,

$$\nabla_\mu(n_i m_i u^\mu) = 0, \quad \forall i, \quad (3.243)$$

while the conservation of the energy and momentum is given by the conservation of the total one, taken as a sum of the different contributions, each of which can, but does not need to, be conserved. As a result, the conservation equations become [*cf.*, Eqs. (2.118)–(2.119)]

$$\nabla_\mu J^\mu = 0 = \sum_i^{N_s} \nabla_\mu(n_i m_i u^\mu), \quad (3.244)$$

$$\nabla_\mu T^{\mu\nu} = 0 = \sum_i^{N_s} \nabla_\mu T_i^{\mu\nu}. \quad (3.245)$$

A useful example of a coupled multifluid is offered by the case in which a photon fluid is tightly interacting with a fluid of ordinary matter, as for instance in the early stages of the cosmological hot big bang (Peebles, 1993). As remarked in Section 2.4.8, in the case in which the photon fluid is mixed with a perfect fluid, the pressures and energy densities simply add [*cf.*, Eqs. (2.275)–(2.276)] and, in the radiation-dominated regime, the mixture can be described as a polytrope with adiabatic index  $\Gamma = 4/3$ .

We can therefore introduce the total energy–momentum tensor  $T^{\mu\nu}$  of a matter fluid coupled with a radiation field as

$$T^{\mu\nu} = T_M^{\mu\nu} + T_R^{\mu\nu}, \quad (3.246)$$

where the first term is the ordinary energy–momentum tensor of matter [*cf.*, Eq. (3.36)]

$$T_M^{\mu\nu} = \rho h u^\mu u^\nu + p g^{\mu\nu}, \quad (3.247)$$

while the second term describes instead the radiation field and is given by (Mihalas and Mihalas, 1984)

$$T_R^{\alpha\beta} = \int I_\nu N^\alpha N^\beta d\nu d\Omega. \quad (3.248)$$

The quantity  $I_\nu = I_\nu(x^\alpha, N^i, \nu)$  in (3.248) is referred to as the *specific intensity* of the radiation,<sup>23</sup> while  $N^\alpha$  is the four-vector defining the photon propagation direction and is defined as

$$N^\alpha := \frac{p^\alpha}{h_p \nu}, \quad (3.249)$$

where  $p^\alpha$  is the photon four-momentum. On the other hand,  $h_p$  and  $\nu$  are, respectively, the Planck constant and the photon frequency as measured in the comoving frame of the fluid, *i.e.*,

<sup>23</sup>We note that  $I_\nu$  is an energy flux per unit time, frequency and solid angle, so that in cgs units it has dimensions of erg cm<sup>-2</sup> s<sup>-1</sup> Hz<sup>-1</sup> sr<sup>-1</sup>.

$$\nu := -\frac{1}{h_p} (\mathbf{p} \cdot \mathbf{u}) . \quad (3.250)$$

Since both  $\nu d\nu d\Omega$  and  $I_\nu/\nu^3$  are relativistic invariants [see, e.g., the discussion in Cercignani and Kremer (2002) and Rybicki and Lightman (1986)], their product with the tensor  $p^\alpha p^\beta$  is still a tensor, and indeed it provides the integrand of Eq. (3.248).

In the frame comoving with the fluid, it is possible to use the four-vector  $N$  to expand the radiation intensity in *moments* of the radiation field. This approach is conceptually and mathematically equivalent to the one discussed in Section 2.3.2 when discussing the relativistic transport fluxes in terms of moments of a given distribution function [*cf.*, Eq. (2.90)]. As a result, the first three elements of this expansion have a straightforward physical interpretation and are given respectively by the *radiation energy density*

$$e_R := \int I_\nu d\nu d\Omega , \quad (3.251)$$

by the *radiation flux*

$$F_R^\alpha := h_\beta^\alpha \int I_\nu N^\beta d\nu d\Omega , \quad (3.252)$$

where the tensor  $h^{\mu\nu} = g^{\mu\nu} + u^\mu u^\nu$  is the usual projection onto the space orthogonal to  $u^\mu$  [*cf.*, Eq. (3.9)], and by the *radiation stress tensor*

$$P_R^{\alpha\beta} := \int I_\nu N^\alpha N^\beta d\nu d\Omega . \quad (3.253)$$

In terms of such moments the radiation energy-momentum tensor  $T_R^{\mu\nu}$  can be rewritten as (Hsieh and Spiegel, 1976)

$$T_R^{\mu\nu} = (e_R + p_R) u^\mu u^\nu + F_R^\mu u^\nu + u^\mu F_R^\nu + p_R g^{\mu\nu} , \quad (3.254)$$

where  $p_R$  is the radiation pressure. The full set of equations describing the dynamics of a generic (*i.e.*, not necessarily coupled) matter-radiation multifluid is

$$\nabla_\mu (\rho u^\mu) = 0 , \quad (3.255)$$

$$\nabla_\mu T^{\mu\nu} = 0 , \quad (3.256)$$

$$\nabla_\mu T_R^{\mu\nu} = -G_R^\nu . \quad (3.257)$$

While Eqs. (3.255) and (3.256) represent respectively the continuity equation and the energy-momentum conservation equations, Eq. (3.257) describes the evolution of the radiation field, where  $G_R^\mu$  is the *radiation four-force density*. The latter depends on the physical interaction between matter and radiation and is therefore specific to the problem considered. This tensor is given in full generality by (Mihalas and Mihalas, 1984)

$$G_R^\mu := \int (\chi_\nu I_\nu - \eta_\nu) N^\mu d\nu d\Omega , \quad (3.258)$$

where

$$\chi_\nu := \chi_\nu^t + \chi_\nu^s, \quad (3.259)$$

$$\eta_\nu := \eta_\nu^t + \eta_\nu^s \quad (3.260)$$

are the total *opacity* and *emissivity* coefficients,<sup>24</sup> each containing a thermal contribution, indicated with the superscript “*t*”, and a scattering contribution, indicated with a superscript “*s*”.

The condition of *coupling* between matter and radiation fluids is then translated into the condition that the radiation field is perfectly isotropic in the comoving frame of the fluid, so that  $p_R = e_R/3$  [cf. Eq. (2.270)] and the radiation flux is zero, *i.e.*,  $F_R^\mu = 0$ . These conditions are also referred to as those of an *optically thick regime* and follow therefore in the conservation equations (3.244).<sup>25</sup> This regime is to be contrasted with the opposite one, referred to as the *optically thin regime*, in which the matter and radiation fluids are *decoupled*, photons freely stream away from the matter fluid, both the opacity and the emissivity coefficients are zero and so is the radiation four-force, *i.e.*,  $G_R^\mu = 0$ .

Just as the hydrodynamic equations can be obtained as the moments of the Maxwell–Boltzmann equation, it can be shown that the *radiation-hydrodynamic equations* can be obtained as the moments of the radiation transfer equation, with the additional complication that the distribution function depends both on the frequency and on the direction of the photons [see, *e.g.*, Mihalas and Mihalas (1984) and Pomraning (1973) for a systematic introduction to the problem]. Because of these difficulties, and even though the mathematical infrastructure for radiation hydrodynamics has already been laid out by Thorne in the 1980s (Thorne, 1981), progress in the numerical solution of generic dynamical situations in general-relativistic regimes has proceeded slowly. In an astrophysical context, relevant achievements have been obtained over the years by Rezzolla and Miller (1994), Janka and Mueller (1995), Mezzacappa *et al.* (2001), Liebendörfer *et al.* (2005), and more recently by Mueller *et al.* (2010).

Quite recently, several attempts have been made (Farris *et al.*, 2008; Zanotti *et al.*, 2011; Shibata *et al.*, 2011) to model radiation fluids in relativistic regimes by adopting a conservative formulation of the equations in the 3 + 1 decomposition of spacetime (see Section 7.1 for the definition). When an optically thick regime is considered, a number of assumptions can be made. In particular, although the radiation field is essentially isotropic in the frame comoving with the fluid, *i.e.*,  $p_R \approx e_R/3$ , the radiation flux is allowed to assume non-vanishing values, with the constraint that it is very small, *i.e.*,  $F_R^i/e_R \ll 1$ . In addition, it is often assumed that: (*i*) the scattering is isotropic and coherent; (*ii*) the thermal emissivity and the thermal opacity coefficients are related to the Planck black-body function  $B_\nu$  [cf., Eq. (2.266)] through Kirchhoff’s law  $\eta_\nu^t = B_\nu \chi_\nu^t$  (Rybicki and Lightman, 1986); (*iii*) electrons and ions are maintained at the same temperature; and (*iv*) the opacity coefficients are independent of frequency. Under these assumptions, the radiation four-force has a simple expression and can be written in covariant form as (Farris *et al.*, 2008; Zanotti *et al.*, 2011)

$$G_R^\mu = \chi^t (e_R - a_R T^4) u^\mu + (\chi^t + \chi^s) F_R^\mu, \quad (3.261)$$

<sup>24</sup>Note that although both are referred to as “coefficients”,  $\chi_\nu$  and  $\eta_\nu$  really have different units. The dimensions of  $\chi_\nu$  are  $\text{cm}^{-1}$ , while those of  $\eta_\nu$  are  $\text{erg cm}^{-3} \text{s}^{-1} \text{Hz}^{-1} \text{sr}^{-1}$ .

<sup>25</sup>Of course, in this case one cannot define a rest-mass density for the photon component, but one can nevertheless define a number density of photons.

where  $T$  is the temperature of the fluid and  $a_R$  is the radiation constant. Applications of this approach to study the radiative emission from matter accreting onto a moving black hole have been presented recently by Zanotti *et al.* (2011).

### 3.11.2 Interacting multifluids

#### **Basic concepts.**

The dynamics of *interacting* perfect multifluids is intrinsically different from that of *coupled* ones, since in the former case the different fluid components each have a *different* four-velocity.<sup>26</sup> As we will see, this is a fundamental difference, which only slightly complicates the treatment, while introducing new properties of the fluid, some of which may be counter-intuitive. For simplicity, we will consider here only the best-studied case of a two-component multifluid and although this is only the simplest extension of the single fluid, it is not devoid of practical applications. Indeed, a two-fluid model of interacting fluids is often employed when describing superfluidity in neutron stars.

In fact, the neutrons present in neutron stars are expected to be superfluid [see, *e.g.*, Baym *et al.* (1969)] and this property is at the base of what is the most accredited explanation for the “glitches” in radio pulsars [see, *e.g.*, Shapiro and Teukolsky (1983), Chamel and Haensel (2008)]. Because of their superfluidity (and thus lack of viscosity), neutrons in the crust and in the stellar outer core represent the “first” fluid in a two-fluid system and are expected to move freely through the other main fluid components of a neutron star interior, *i.e.*, protons, electrons, muons and the heavier nuclei in the crust. All of these other components are instead expected to be coupled together by viscosity and magnetic field and thus represent the “second” fluid in the two-fluid description. The interaction between these two fluids is offered by the strong nuclear force acting between protons and neutrons and will lead to important and qualitatively new effects in the dynamics of these two fluids (Vardanyan and Sedrakian, 1981; Mendell, 1991; Sedrakian and Sedrakian, 1995).

The study of equilibrium configurations of superfluid neutron stars in a two-fluid framework has made considerable progress in recent years both in Newtonian gravity [see, *e.g.*, Prix *et al.* (2002)], as well as in general relativity [see, *e.g.*, Prix *et al.* (2005)]. Here we will not discuss the results of these calculations, but only introduce the basic elements of the mathematical framework that has been employed to describe an interacting two-fluid system, reviewing the work developed by Carter, Langlois and collaborators, who have used an elegant variational principle (Carter and Gaffet, 1988; Comer and Langlois, 1994; Carter and Langlois, 1998). In addition, we will consider only the simplest case of this framework, that is, the one in which the fluids are not conducting, are at zero temperature, and there are no dissipative forces between them. This restricted scenario is a reasonable starting point to study cold superfluid neutron stars.

An annoying complication in describing multicomponent fluids is already evident from expressions (3.240), namely, that a new index needs to be introduced to distinguish the different components. This inevitably makes the notation heavier and sometimes hard to read. Here, we will introduce a notation which does not make use of new letters to distinguish the same

<sup>26</sup>Multifluids of this type as sometimes also referred to as *multicomponent multifluids* (Andersson and Comer, 2007).

quantity in the different components, nor uses indices which could be confused with some of the quantities or be exchanged for contracted indices. Rather, we introduce the indices “1” and “2” to distinguish the two components and always represent them as lower indices, exploiting the metric tensor to keep the tensor indices as contravariant indices. This notation leads to a more transparent interpretation of the results and it can be easily extended to more than two components.

We start by introducing the two *number densities* or *particle currents*  $j_1$  and  $j_2$ , which are simply defined as

$$j_1^\mu := n_1 u_1^\mu, \quad j_2^\mu := n_2 u_2^\mu, \quad (3.262)$$

and where each of the two four-velocities  $\mathbf{u}_1$  and  $\mathbf{u}_2$  satisfies the normalisation condition [cf., Eq. (3.2)]

$$\mathbf{u}_1 \cdot \mathbf{u}_1 = g_{\mu\nu} u_1^\mu u_1^\nu = -1, \quad \mathbf{u}_2 \cdot \mathbf{u}_2 = g_{\mu\nu} u_2^\mu u_2^\nu = -1. \quad (3.263)$$

Note that the particle current of each fluid is related to the corresponding rest-mass density current introduced in Section 3.2 through the corresponding elementary mass, *i.e.*, [cf., Eq. (3.35)]

$$\mathbf{J}_i = \rho_i \mathbf{u}_i = m_i \mathbf{j}_i. \quad (3.264)$$

Next, we use the normalisation conditions (3.263) to introduce three scalar quantities related to the contractions of the particle currents, *i.e.*,

$$n_{11}^2 := -g_{\mu\nu} j_1^\mu j_1^\nu = n_1 n_1, \quad (3.265)$$

$$n_{22}^2 := -g_{\mu\nu} j_2^\mu j_2^\nu = n_2 n_2, \quad (3.266)$$

$$n_{12}^2 := -g_{\mu\nu} j_1^\mu j_2^\nu = -n_1 n_2 (g_{\mu\nu} u_1^\mu u_2^\nu), \quad (3.267)$$

where it should be noted that while  $n_{11}^2 = n_1 n_1 = (n_1)^2$  and  $n_{22}^2 = n_2 n_2 = (n_2)^2$  simply represent the squares of the two number densities, the mixed contraction of the currents is not proportional, in general, to the product of the number densities, *i.e.*,  $n_{12}^2 \neq n_1 n_2$ . Indeed, this is the case *only* for *comoving* fluids, *i.e.*, when  $\mathbf{u}_1 = \mathbf{u}_2$ , and Eq. (3.267) then reads  $n_{12}^2 = n_1 n_2$ . This is a novel and obviously relativistic feature of interacting two-fluid systems.

The Lagrangian density of the system  $\mathcal{L}$  will be a linear function of the two particle currents and can be written as (Carter and Gaffet, 1988)

$$\mathcal{L}(j_1^\mu, j_2^\mu) = -\mathcal{E}(n_{11}^2, n_{22}^2, n_{12}^2), \quad (3.268)$$

where  $\mathcal{E}(n_{11}^2, n_{22}^2, n_{12}^2)$  is a thermodynamic potential representing the total energy density of the multifluid and is therefore determined by the equation of state. The variation of the Lagrangian density with respect to the particle currents can be used to define the *conjugate four-momenta*  $\mathbf{p}_1$  and  $\mathbf{p}_2$ , *i.e.*,

$$d\mathcal{L} = g_{\mu\nu} (p_1^\mu dj_1^\nu + p_2^\mu dj_2^\nu). \quad (3.269)$$

In a single-component perfect fluid or in a coupled multifluid these conjugate four-momenta are simply given by the fluid four-momentum per unit mass and unit volume and are therefore *parallel* to the fluid four-velocity, *i.e.*,

$$\mathbf{p}_i = \frac{\mathbf{J}_i}{m_i} = \mathbf{j}_i = n_i \mathbf{u}_i . \quad (3.270)$$

This property ceases to be true if the fluids are interacting. In particular, these conjugate four-momenta can also be expressed in terms of a  $2 \times 2$  symmetric *mass matrix* (or *entrainment matrix* in the case in which one of the two fluids is a superfluid)  $\mathcal{K}_{ij}$  such that

$$p_1^\mu = \mathcal{K}_{11} j_1^\mu + \mathcal{K}_{12} j_2^\mu = \mathcal{K}_{11} n_1 u_1^\mu + \mathcal{K}_{12} n_2 u_2^\mu , \quad (3.271)$$

$$p_2^\mu = \mathcal{K}_{21} j_1^\mu + \mathcal{K}_{22} j_2^\mu = \mathcal{K}_{21} n_1 u_1^\mu + \mathcal{K}_{22} n_2 u_2^\mu . \quad (3.272)$$

Expressions (3.271)–(3.272) summarise an important qualitative difference introduced by interacting multifluids, which deserves a special remark. In general, the four-momentum of a given component is *not parallel* to the corresponding four-velocity. This is a consequence of the fact that, in general, the mass matrix  $\mathcal{K}_{ij}$  is non-diagonal and hence the particle current of fluid “1” imparts a certain momentum also on fluid “2”, and vice versa. This is the most evident (and somewhat counter-intuitive) manifestation of the interaction between the two fluids. Note also that because the mass matrix is the result of the microphysical exchanges between the two fluids, this effect is not a purely relativistic one and is already present in a Newtonian description of multifluids, as we will discuss later on. Clearly, in the limit in which the mass matrix  $\mathcal{K}_{ij}$  is diagonal, *i.e.*, when  $\mathcal{K}_{12} = 0 = \mathcal{K}_{21}$ , we recover all of the properties we have already encountered for single perfect fluids or with coupled multifluids, with  $\mathbf{p}_1 \propto \mathbf{u}_1$  and  $\mathbf{p}_2 \propto \mathbf{j}_2$ .

Since the mass matrix reflects microphysical interactions, it is useful to define it in terms of the partial derivatives of the total energy density with respect to the contracted particle currents

$$\mathcal{K}_{11} := 2 \frac{\partial \mathcal{E}}{\partial n_{11}^2} , \quad (3.273)$$

$$\mathcal{K}_{22} := 2 \frac{\partial \mathcal{E}}{\partial n_{22}^2} , \quad (3.274)$$

$$\mathcal{K}_{12} := \frac{\partial \mathcal{E}}{\partial n_{12}^2} = \mathcal{K}_{21} . \quad (3.275)$$

At the same time, the components of the mass matrix (3.273)–(3.275) can have a more direct physical interpretation if we introduce the *multifluid relative velocity*  $\Delta$  as the norm of the four-velocity of fluid “1” in the rest frame of fluid “2”, *i.e.*,

$$\Delta^2 := 1 - \left( \frac{n_1 n_2}{n_{12}^2} \right)^2 , \quad (3.276)$$

so that when the fluids are comoving, *i.e.*, when  $n_{12}^2 \rightarrow n_1 n_2$  [*cf.* Eq. (3.267)], then the relative velocity  $\Delta \rightarrow 0$ , as it should for two fluids that share the same four-velocity. We can now express the total energy density  $\mathcal{E}(n_{11}^2, n_{22}^2, n_{12}^2)$  also in terms of the relative velocity  $\Delta$ , *i.e.*,  $\mathcal{E}(n_{11}^2, n_{22}^2, \Delta^2)$ , so that the first law of thermodynamics can be expressed as (Carter and Gaffet, 1988)

$$d\mathcal{E} = \mu_1 dn_1 + \mu_2 dn_2 + \mathcal{A} d\Delta^2 , \quad (3.277)$$

where  $\mu_1$  and  $\mu_2$  are the chemical potentials and  $\mathcal{A}$  is the *entrainment function*, or *coupling scalar*, and measures the interaction among the two fluids, such that  $\mathcal{A} \rightarrow 0$  for coupled multi-fluids. If this interaction is due to superfluidity, it is customary to introduce the dimensionless *entrainment parameters* defined as

$$\chi_1 := \frac{2\mathcal{A}}{n_1 m_1}, \quad \chi_2 := \frac{2\mathcal{A}}{n_2 m_2}. \quad (3.278)$$

Using now Eq. (3.277) and a little algebra, we can express the chemical potentials directly in terms of the mass matrix and of the coupling scalar

$$\mu_1 = \frac{1}{n_1} (\mathcal{K}_{11} n_{11}^2 + \mathcal{K}_{12} n_{12}^2), \quad (3.279)$$

$$\mu_2 = \frac{1}{n_2} (\mathcal{K}_{22} n_{22}^2 + \mathcal{K}_{12} n_{12}^2), \quad (3.280)$$

$$\mathcal{A} = \frac{1}{2} \mathcal{K}_{12} n_1 n_2 W_\Delta^3 = \frac{1}{2} \mathcal{K}_{12} n_{12}^2 W_\Delta^2, \quad (3.281)$$

where we have defined  $W_\Delta$  as the Lorentz factor of the relative velocity  $\Delta$ , *i.e.*,

$$W_\Delta := \frac{1}{(1 - \Delta^2)^{1/2}} = \frac{n_{12}^2}{n_1 n_2}, \quad (3.282)$$

which has been used in deriving the last equality in (3.281). Note that using Eqs. (3.273)–(3.275), the Lorentz factor can also be seen as the contraction of the conjugate four-momenta in the two fluids, *i.e.*,  $W_\Delta = -g_{\mu\nu} p_1^\mu p_2^\nu$ .

We can now invert Eqs. (3.279)–(3.281) to obtain explicit expressions for the components of the mass matrix

$$\mathcal{K}_{11} = \frac{1}{n_{11}^2} \left( n_1 \mu_1 - \frac{2\mathcal{A}}{W_\Delta^2} \right), \quad (3.283)$$

$$\mathcal{K}_{22} = \frac{1}{n_{22}^2} \left( n_2 \mu_2 - \frac{2\mathcal{A}}{W_\Delta^2} \right), \quad (3.284)$$

$$\mathcal{K}_{12} = \frac{1}{n_{12}^2} \left( \frac{2\mathcal{A}}{W_\Delta^2} \right) = \frac{1}{n_1 n_2} \left( \frac{2\mathcal{A}}{W_\Delta^3} \right). \quad (3.285)$$

In the limit in which  $\mathcal{A} \rightarrow 0$ , the components of the mass matrix simplify to  $\mathcal{K}_{11} = \mu_1/n_1$ ,  $\mathcal{K}_{22} = \mu_2/n_2$ , and  $\mathcal{K}_{12} \rightarrow 0$ , so that the conjugate four-momenta reduce to [*cf.*, Eqs. (3.271)–(3.272)]

$$p_1^\nu = \mu_1 u_1^\nu, \quad (3.286)$$

$$p_2^\nu = \mu_2 u_2^\nu, \quad (3.287)$$

as expected for coupled multi-fluids. In addition, expressions (3.279)–(3.281) and the first law of thermodynamics (3.277) allow us also to introduce a *generalised pressure* (Langlois *et al.*, 1998)

$$\Psi = -\mathcal{E} + n_1 \mu_1 + n_2 \mu_2, \quad (3.288)$$

so that expressions (3.283)–(3.285) can be used to obtain the following thermodynamic identities

$$\mathcal{E} + \Psi = -g_{\mu\nu}(j_1^\mu p_1^\nu + j_2^\mu p_2^\nu) \quad (3.289)$$

$$= \mathcal{K}_{11} n_{11}^2 + 2\mathcal{K}_{12} n_{12}^2 + \mathcal{K}_{22} n_{22}^2, \quad (3.290)$$

and

$$\mu_1 := -g_{\alpha\beta} u_1^\alpha p_1^\beta, \quad \mu_2 := -g_{\alpha\beta} u_2^\alpha p_2^\beta. \quad (3.291)$$

It should be noted that also in the case of an interacting multifluid, each of the constituents will have its own sound speed, whose definition, however, is more involved since it depends also on the particle currents of the other components. A possible prescription on how to calculate the sound speeds using a local plane-wave analysis is discussed by Andersson and Comer (2007), while the study of the damping of sound waves in superfluid nucleon–hyperon matter, where it is used to describe the interior of neutron stars, can be found in Kantor and Gusakov (2009).

To fix ideas about the properties of interacting multifluids discussed so far, we can consider the simple case of a “polytropic two-fluid”, that is, a two-component interacting multifluid where each component follows a polytropic equation of state of the type [*cf.* Eq. (2.242)]  $p_i \propto K_i \rho_i^{\Gamma_i}$ , with  $i = 1, 2$ , so that the corresponding energy density will be given by (Prix *et al.*, 2005)

$$\mathcal{E} = n_1 m_1 + n_2 m_2 + \frac{1}{2} K_1 n_1^{\Gamma_1} + \frac{1}{2} K_2 n_2^{\Gamma_2} + K_{12} n_1^{\Gamma_3} n_2^{\Gamma_4} + K_\Delta n_1^{\Gamma_5} n_2^{\Gamma_6} \Delta^2. \quad (3.292)$$

The first two terms on the right-hand side of Eq. (3.292) clearly account for the rest-mass contribution to the energy density, while the third and fourth terms provide the internal-energy contribution [*cf.* Eq. (2.248) for an ordinary fluid]. Lastly, the fifth and sixth terms account respectively for the “symmetry-energy”, which is proportional to  $K_{12}$ , and for the “entrainment energy”, which is proportional to the coefficient  $K_\Delta \Delta^2$  as defined in (3.292). Assuming for simplicity that  $\Gamma_1 = \Gamma_2 = 2$  and  $\Gamma_3 = \Gamma_4 = \Gamma_5 = \Gamma_6 = 1$ , the generic expression (3.292) becomes<sup>27</sup>

$$\mathcal{E} = \rho + \Psi, \quad (3.293)$$

where the generalised pressure is therefore

$$\Psi = \frac{1}{2} K_1 n_1^2 + \frac{1}{2} K_2 n_2^2 + K_{12} n_1 n_2 + K_\Delta n_1 n_2 \Delta^2. \quad (3.294)$$

Finally, we can recast the quantities introduced so far in terms of this equation of state to express the two chemical potentials as (Prix *et al.*, 2005)

$$\mu_1 = m_1 + K_1 n_1 + (K_{12} + K_\Delta \Delta^2) n_1, \quad (3.295)$$

$$\mu_2 = m_2 + K_2 n_2 + (K_{12} + K_\Delta \Delta^2) n_2, \quad (3.296)$$

<sup>27</sup>This equation of state has been employed by Prix *et al.* (2005) to compute numerically the equilibrium configurations of rotating and superfluid relativistic stars.

and the entrainment coefficients as

$$\chi_1 = \frac{2\mathcal{A}}{n_1 m_1} = \frac{2K_\Delta}{m_1} n_2, \quad \chi_2 = \frac{2\mathcal{A}}{n_2 m_2} = \frac{2K_\Delta}{m_2} n_1, \quad (3.297)$$

where

$$\mathcal{A} = K_\Delta n_1 n_2. \quad (3.298)$$

### Equations of motion.

Using the background material presented so far to discuss the properties of a two-component multifluid, we can now finally focus our attention on the equations of motion. For this we introduce the energy–momentum tensor of the interacting multifluid as (Carter and Langlois, 1998)

$$T^{\mu\nu} = j_1^\mu p_1^\nu + j_2^\mu p_2^\nu + \Psi g^{\mu\nu}, \quad (3.299)$$

which is non-manifestly symmetric unless we impose the additional condition

$$j_1^{[\mu} p_1^{\nu]} = j_2^{[\nu} p_2^{\mu]}. \quad (3.300)$$

The dynamics of the interacting multifluid is then expressed via the conservation equations of particle currents

$$\nabla_\mu j_1^\mu = 0, \quad \nabla_\mu j_2^\mu = 0, \quad (3.301)$$

and through the usual conservation of energy and momentum  $\nabla_\mu T^{\mu\nu} = 0$ . Using the conditions (3.301), and taking a covariant derivative of the constraint (3.300), it is possible to show that the conservation of energy and momentum is equivalent to the following combined conditions for each of the two components of the multifluid

$$n_1^\mu (g_{\alpha\nu} \nabla_\mu p_1^\alpha - g_{\alpha\mu} \nabla_\nu p_1^\alpha) = 0, \quad (3.302)$$

$$n_2^\mu (g_{\alpha\nu} \nabla_\mu p_2^\alpha - g_{\alpha\mu} \nabla_\nu p_2^\alpha) = 0. \quad (3.303)$$

We conclude this section by reporting the Newtonian expressions of the hydrodynamic equations for multicomponent fluids, which can be of help in highlighting the differences with respect to the hydrodynamic equations of single-component fluids [these equations can be found in a number of works and we refer to Mendell (1991) and Sedrakian and Sedrakian (1995) for their application to the properties of superfluid neutron stars]. More specifically, we consider a simple two-component multifluid, with number density  $n_1$  and  $n_2$ , and conjugate momenta [*cf.*, Eqs. (3.271)–(3.272)]

$$\vec{p}_1 = \mathcal{K}_{11} \vec{j}_1 + \mathcal{K}_{12} \vec{j}_2 = \mathcal{K}_{11} n_1 \vec{v}_1 + \mathcal{K}_{12} n_2 \vec{v}_2, \quad (3.304)$$

$$\vec{p}_2 = \mathcal{K}_{22} \vec{j}_2 + \mathcal{K}_{12} \vec{j}_1 = \mathcal{K}_{22} n_2 \vec{v}_2 + \mathcal{K}_{12} n_1 \vec{v}_1, \quad (3.305)$$

where  $\vec{p}_i = \vec{J}_i/m_i = \vec{j}_i = n_i \vec{v}_i$ . As in the relativistic case, the relation between the momenta and the velocities is mediated by the mass matrix, whose Newtonian components are given by

$$\mathcal{K}_{11} = \frac{1}{n_1^2} (m_1 n_1 - 2\mathcal{A}), \quad (3.306)$$

$$\mathcal{K}_{22} = \frac{1}{n_2^2} (m_2 n_2 - 2\mathcal{A}), \quad (3.307)$$

$$\mathcal{K}_{12} = \frac{2\mathcal{A}}{n_1 n_2}, \quad (3.308)$$

and where  $\mathcal{A}$  is, again, the coupling scalar ( $\mathcal{A} \rightarrow 0$  four coupled multifluids). In this framework, the Newtonian equations for the conservation of particle numbers will be given by the familiar expressions in Cartesian coordinates

$$\partial_t n_1 + \partial_i (n_1 v_1^i) = 0, \quad (3.309)$$

$$\partial_t n_2 + \partial_i (n_2 v_2^i) = 0, \quad (3.310)$$

while the corresponding equations for the conservation of linear momentum are expressed as (Andersson and Comer, 2001) [see, *e.g.*, Sedrakian and Sedrakian (1995) for a different but equivalent form]

$$\begin{aligned} \partial_t \left[ v_1^i + \frac{2\mathcal{A}}{n_1 m_1} (v_2^i - v_1^i) \right] + v_1^j \partial_j \left[ v_1^i + \frac{2\mathcal{A}}{n_1 m_1} (v_2^i - v_1^i) \right] + \\ + \delta^{ij} \partial_j \left( \phi + \frac{\mu_1}{m_1} \right) + \frac{2\mathcal{A}}{n_1 m_1} \delta^{ij} \delta_{kl} (v_2^l - v_1^l) \partial_j v_1^k = 0, \end{aligned} \quad (3.311)$$

$$\begin{aligned} \partial_t \left[ v_2^i + \frac{2\mathcal{A}}{n_2 m_2} (v_1^i - v_2^i) \right] + v_2^j \partial_j \left[ v_2^i + \frac{2\mathcal{A}}{n_2 m_2} (v_1^i - v_2^i) \right] + \\ + \delta^{ij} \partial_j \left( \phi + \frac{\mu_2}{m_2} \right) + \frac{2\mathcal{A}}{n_2 m_2} \delta^{ij} \delta_{kl} (v_1^l - v_2^l) \partial_j v_2^k = 0, \end{aligned} \quad (3.312)$$

where  $\mu_1$  and  $\mu_2$  are the two Newtonian chemical potentials and  $\phi$  is the total gravitational potential, satisfying the Poisson equation [*cf.* Eq. (1.215)]

$$\nabla^2 \phi = \partial_i \partial^i \phi = 4\pi G (n_1 m_1 + n_2 m_2). \quad (3.313)$$

A quick inspection of Eqs. (3.311) and (3.312) reveals that when  $\mathcal{A} = 0$  they coincide and reduce to the corresponding expression for a single-component fluid [*cf.* Eq. (3.86)]. On the other hand, for genuine interacting multifluids, *i.e.*, when  $\mathcal{A} \neq 0$ , they show that the momentum of one of the components can change in time simply as a consequence of a nonzero relative velocity with respect to the other one. Finally, the energy conservation equation will have the simple form

$$\partial_t \mathcal{E} = \partial_i (Q_0^i + Q^i), \quad (3.314)$$

where  $\mathcal{E}$  is the total energy density, which can be expressed as (Sedrakian and Sedrakian, 1995)

$$\mathcal{E} = \frac{1}{2} (\mathcal{K}_{11} \vec{v}_1 \cdot \vec{v}_1 + 2\mathcal{K}_{12} \vec{v}_1 \cdot \vec{v}_2 + \mathcal{K}_{22} \vec{v}_2 \cdot \vec{v}_2) + \mathcal{E}_0 , \quad (3.315)$$

with  $\mathcal{E}_0$  being the internal energy density. The energy flux terms  $\vec{Q}_0$  and  $\vec{Q}$  appearing on the right-hand side of Eq. (3.314), represent the channels in which the fluid may change energy via non-dissipative processes (this is the flux associated to  $\vec{Q}_0$  and accounts for the advection of energy), or via dissipative processes (this is the flux associated to  $\vec{Q}$  and accounts for radiative or viscous losses). Explicit expressions for  $\vec{Q}_0$  and  $\vec{Q}$  can be found, for example, in Sedrakian and Sedrakian (1995), where  $\vec{Q}$  involves losses due to thermal conductivity, shear viscosity, vortex dissipation and electromagnetic interactions in superfluid neutron stars.

### 3.12 Further reading

- Andersson, N. and Comer, G. L. (2007). *Relativistic Fluid Dynamics: Physics for Many Different Scales*. Living Rev. Relativ., 10, 1.
- Anile, A. M. (1989). *Relativistic Fluids and Magneto-fluids*. Cambridge University Press, Cambridge.
- Ehlers, J. (1971). *General Relativity and Kinetic Theory*. In General Relativity and Cosmology, 1–70. Proceedings of the Varenna Summer School on Relativistic Astrophysics. Academic Press, New York.
- Gourgoulhon, É. (2006). *An Introduction to Relativistic Hydrodynamics*. EAS Publications Series, **21**, 43–79.
- Landau, L. D. and Lifshitz, E. M. (1987). *Fluid Mechanics*. Course of Theoretical Physics, Vol. 6. Butterworth-Heinemann, Oxford.
- Lichnerowicz, A. (1967). *Relativistic Hydrodynamics and Magnetohydrodynamics*. Benjamin, New York.
- Mihalas, D. and Mihalas, B. (1984). *Foundations of Radiation Hydrodynamics*. Dover, New York.
- Schutz, B. F and Sorkin R. (1977). Variational aspects of relativistic field theories, with application to perfect fluids. *Ann. Phys.*, **107**, 1–43.
- Synge, J. L. (1957). *The Relativistic Gas*. North-Holland, Amsterdam.
- Synge, J. L. (2002). “Golden Oldie”: Relativistic Hydrodynamics. *Gen. Rel. Grav.*, **34**, 2177–2216.

### 3.13 Problems

1. Use the definitions (3.11)–(3.13) to show that

$$\begin{aligned}\sigma_{\alpha\beta}\sigma^{\alpha\beta} &= \frac{1}{2} \left( \nabla_\mu a^\mu + a^2 - \frac{2}{3} \Theta^2 \right), \\ \omega_{\alpha\beta}\omega^{\alpha\beta} &= \frac{1}{2} (a^2 - \nabla_\mu a^\mu),\end{aligned}$$

thus concluding that the term  $2(\omega^2 - \sigma^2)$  entering the Raychaudhuri equation (3.27) is actually

$$2(\omega^2 - \sigma^2) = \frac{1}{3} \Theta^2 - \nabla_\mu a^\mu.$$

2. Derive Eqs. (3.20)–(3.22) by taking the antisymmetric part, the symmetric part and the trace of (3.19). [Hint: when computing (3.20) note that  $R_{\mu[\nu\kappa]\lambda} u^\mu u^\lambda = 0$ ,  $\sigma^\lambda_{[\mu} \sigma_{\nu]\lambda} = 0$ ,  $\omega^\lambda_{[\mu} \omega_{\nu]\lambda} = 0$ . Moreover, (3.22) has to be used in order to obtain (3.21).]
3. Derive Eq. (3.26), valid for geodesic motion, starting from (3.20) and using the definition of the kinematic vorticity vector (3.16). [Hint: note that  $\omega_{\mu\nu} = \epsilon_{\mu\nu\lambda\kappa} \omega^\lambda u^\kappa$ ]. Then, show that (3.26) can also be rewritten as

$$\dot{\omega}^\mu = -\Theta \omega^\mu + \omega^\nu \nabla_\nu u^\mu,$$

and combine the above equation with the continuity equation  $\nabla_\mu (\rho u^\mu) = 0$  to obtain

$$u^\mu \nabla_\mu \left( \frac{\omega^\nu}{\rho} \right) = \frac{\omega^\mu}{\rho} \nabla_\mu u^\nu.$$

This equation presents a strong formal analogy with the Newtonian

$$\frac{D}{Dt} \left( \frac{\vec{B}}{\rho} \right) = \left( \frac{\vec{B}}{\rho} \cdot \vec{\nabla} \right) \vec{v},$$

and it suggests that, to a certain extent, the vorticity behaves like a magnetic field.

4. Derive Eq. (3.83) and Eq. (3.86).
5. Using the conformal transformation (3.157), derive expression (3.158) for the conformal Christoffel symbols and expression (3.159) for the covariant derivative relative to the conformal metric  $\bar{g}$ .
6. Prove that the time variation of the kinetic energy per unit mass of a fluid particle is given by the expression

$$\frac{D}{Dt} \left( \frac{1}{2} \vec{v}^2 \right) = \vec{g} \cdot \vec{v} - \frac{1}{\rho} \vec{v} \cdot \vec{\nabla} p.$$

7. Prove that the time variation of the specific internal energy of a fluid particle is given by the following two equivalent expressions

$$\frac{D\epsilon}{Dt} + p \frac{D(1/\rho)}{Dt} = 0,$$

$$\frac{D\epsilon}{Dt} + \frac{p}{\rho} \theta = 0.$$

8. Prove that

$$\nabla_\mu \omega^\mu = 2\dot{u}_\mu \omega^\mu.$$

The above expression is surprising to some extent, given that in Newtonian hydrodynamics the vorticity is divergence free. However, the equation above also strengthens the analogy of the vorticity vector with the magnetic field, since in relativistic magnetohydrodynamics a similar expression can be obtained with the four-vector magnetic field replacing  $\omega^\mu$ .

# 4

## Linear and Nonlinear Hydrodynamic Waves

---

Much of the complexity, but also much of the beauty of hydrodynamic flows, rests on the nonlinearity of the equations and on the development under generic conditions of nonlinear waves and possibly of discontinuities in the flow. This chapter is dedicated to the analysis of the conditions under which these waves can be produced and of the flow properties across such waves. Attention will also be paid to the study of the building block of many numerical algorithms for the solution of the hydrodynamic equations, namely, the Riemann problem. The chapter will be completed by two sections covering more advanced topics, such as the stability of nonlinear waves and the properties of discontinuous solutions in full general relativity. These sections are admittedly more informative than formative, but the interested reader can use them as an introduction to topics normally treated in more advanced research papers.

### 4.1 Hyperbolic systems of partial differential equations

#### 4.1.1 Quasi-linear formulation

Before discussing in detail linear and nonlinear waves in relativistic hydrodynamics, it is useful to analyse the mathematical properties of the equations, as these are fundamental to understanding the propagation of linear waves in perfect fluids and their development into nonlinear waves. However, we will not dive immediately into the relativistic framework, but start by considering the set of Newtonian hydrodynamic equations, which is far simpler to write and analyse. We recall therefore that in Chapters 2 and 3 we have derived the Newtonian equations of conservation of mass, momentum and energy in the absence of external forces. In Cartesian coordinates they are [*cf.*, Eqs. (3.83), (3.86), and (3.89)]

$$\partial_t \rho + v^i \partial_i \rho + \rho \partial_i v^i = 0, \quad (3.83)$$

$$\partial_t v^i + v^j \partial_j v^i + \frac{1}{\rho} \partial_i p = 0, \quad (3.86)$$

$$\partial_t s + v^i \partial_i s = 0. \quad (3.89)$$

These equations can be written in compact matrix form as

$$\partial_t \mathbf{U} + \mathbf{A} \cdot \nabla \mathbf{U} = 0, \quad \iff \quad \partial_t U_J + (A^i)_{JK} \partial_i U_K = 0, \quad (4.1)$$

where the summation is taken from 1 to 3 for the index  $i$  and from 1 to 5 for the indices  $J$  and  $K$ . The components of the vector  $\mathbf{U}_J$ , with  $J = 1, \dots, 5$ , are defined such that (Anile, 1989)

$$\mathbf{U} := (\rho, v^i, s)^T, \quad (4.2)$$

where  $T$  denotes transposition and  $\mathbf{U}$  is referred to as the *state vector*. The three  $5 \times 5$  matrices  $A^i$  in (4.1) can be written explicitly to have components (Anile, 1989)

$$A^1 := \begin{pmatrix} v^1 & \rho & 0 & 0 & 0 \\ \frac{1}{\rho} c_s^2 & v^1 & 0 & 0 & \frac{1}{\rho} \partial_s p \\ 0 & 0 & v^1 & 0 & 0 \\ 0 & 0 & 0 & v^1 & 0 \\ 0 & 0 & 0 & 0 & v^1 \end{pmatrix}, \quad A^2 := \begin{pmatrix} v^2 & 0 & \rho & 0 & 0 \\ 0 & v^2 & 0 & 0 & 0 \\ \frac{1}{\rho} c_s^2 & 0 & v^2 & 0 & \frac{1}{\rho} \partial_s p \\ 0 & 0 & 0 & v^2 & 0 \\ 0 & 0 & 0 & 0 & v^2 \end{pmatrix}, \quad (4.3)$$

$$A^3 := \begin{pmatrix} v^3 & 0 & 0 & \rho & 0 \\ 0 & v^3 & 0 & 0 & 0 \\ 0 & 0 & v^3 & 0 & 0 \\ \frac{1}{\rho} c_s^2 & 0 & 0 & v^3 & \frac{1}{\rho} \partial_s p \\ 0 & 0 & 0 & 0 & v^3 \end{pmatrix}, \quad (4.4)$$

where we have used the condition that in Newtonian hydrodynamics the sound speed is defined as  $(c_s^2)_N := (\partial p / \partial \rho)_s$  [cf., Eq. (2.169)] and we have adopted an equation of state  $p = p(\rho, s)$ .

In a similar way, also the equations of relativistic hydrodynamics that express the conservation of rest mass,  $\nabla_\mu(\rho u^\mu) = 0$ , and of energy and momentum,  $\nabla_\mu T^{\mu\nu} = 0$  [cf., Eqs. (2.118)–(2.119)], can be cast in compact matrix form after introducing the (relativistic) state vector, which has now six components and is given by (Anile, 1989)<sup>1</sup>

$$\mathbf{U} := (u^\mu, e, s)^T, \quad (4.5)$$

so that Eqs. (2.118)–(2.119) are equivalent to

$$\mathcal{A} \cdot \nabla \mathbf{U} = 0, \quad \iff \quad (\mathcal{A}^\mu)_{JK} \nabla_\mu U_K = 0, \quad (4.6)$$

<sup>1</sup>An analysis similar to the one presented here for the state vector (4.2) can be found in Font *et al.* (1994), where a different state vector,  $\mathbf{U} = (\rho, v^i, \epsilon)^T$ , was adopted. This choice is closer to the one used in numerical calculations (see Chapter 9), but it also results in a less compact characteristic matrix. Uniquely for this reason we follow the approach of Anile (1989). Note also that the six quantities (4.5) are not all independent because of the normalisation condition  $u^\mu u_\mu = -1$ , and the independent quantities are effectively only five (see also footnote 7).

where the summation is taken from 0 to 3 for the index  $\mu$  and from 1 to 6 for the indices  $J$  and  $K$ ; the latter is also referred to as the *order* of the quasi-linear system.<sup>2</sup> The  $6 \times 6$  matrices  $(\mathcal{A}^\mu)_{JK}$  have components given by (Anile, 1989)

$$\mathcal{A}^\mu = \begin{pmatrix} \rho h u^\mu \delta_\beta^\alpha & h^{\alpha\mu} c_s^2 & h^{\alpha\mu} \partial_s p \\ \rho h \delta_\beta^\mu & u^\mu & 0^\mu \\ 0_\beta^\mu & 0^\mu & u^\mu \end{pmatrix}, \quad (4.7)$$

where  $h^{\mu\alpha} = g^{\alpha\mu} + u^\alpha u^\mu$  is the usual projection tensor orthogonal to  $\mathbf{u}$  [cf., Eq. (3.9)], and where we have used the result that in relativistic hydrodynamics the sound speed is  $c_s^2 = (\partial p / \partial e)_s$ . The other entries in (4.7) are just shorthand for the zero vector and matrix, respectively, *i.e.*,

$$0^\mu := 0, \quad 0_\beta^\mu := (0, 0, 0, 0), \quad (4.8)$$

whereas  $\rho h u^\mu \delta_\beta^\alpha$  is to be read as a  $4 \times 4$  diagonal matrix with elements  $\rho h u^\mu$  (see Problem 1).

Equations (4.6) represent a set of partial differential equations whose properties can be better assessed after we recast them in a first-order (in time) form, *i.e.*, when we write them as

$$\partial_t \mathbf{U} + \mathbf{A} \cdot \nabla \mathbf{U} = \mathbf{S}, \quad (4.9)$$

where  $\mathbf{A} = \mathbf{A}(\mathbf{U})$  and where the “source term”  $\mathbf{S}$  can depend on  $\mathbf{U}$  but not on its derivatives.<sup>3</sup> In full generality, the system of equations (4.9) is said to be *linear with constant coefficients* if all the elements  $a_{JK}$  of the matrix  $\mathbf{A}$  and all the elements  $s_J$  of the vector  $\mathbf{S}$  are constant. If instead  $a_{JK} = a_{JK}(x, t)$  and  $s_J = s_J(x, t)$ , where  $x$  represents the spatial coordinates, then the system is said to be *linear with variable coefficients*. Finally, if the matrix  $\mathbf{A}$  is a function of the vector  $\mathbf{U}$ , the system is then said to be *nonlinear*, although the standard (and somewhat misleading) mathematical denomination is that of *quasi-linear* system.

More importantly, the system (4.9) is said to be *hyperbolic*<sup>4</sup> if the matrix of coefficients  $\mathbf{A}$  is diagonalisable with a set of real *eigenvalues*  $\lambda_1, \dots, \lambda_N$  and has a corresponding set of  $N$  linearly independent *right eigenvectors*  $\mathbf{R}^{(1)}, \dots, \mathbf{R}^{(N)}$  such that<sup>5</sup>

$$\mathbf{A} \mathbf{R}^{(i)} = \lambda_i \mathbf{R}^{(i)}, \quad (4.10)$$

and

$$\Lambda := \mathbf{R}^{-1} \mathbf{A} \mathbf{R} = \text{diag}(\lambda_1, \dots, \lambda_N) \quad (4.11)$$

is the (diagonal) matrix of eigenvalues, while  $\mathbf{R}$  is the *right-eigenvector matrix*, that is, a matrix with columns that are given by the right eigenvectors  $\mathbf{R}^{(1)}, \dots, \mathbf{R}^{(N)}$ .

<sup>2</sup>In expression (4.6) we do not contract the indices  $K$  to emphasise that this is a matrix operation and not a contraction of tensors; however, an implicit sum is present over  $K$ .

<sup>3</sup>As for ordinary differential equations, the system (4.9) is said to be *homogeneous* if  $\mathbf{S} = 0$ .

<sup>4</sup>Note that we follow here a nomenclature that is customary in hydrodynamics, see, *e.g.*, Anile (1989), LeVeque (2002), or Toro (2009). Other authors, however, and especially in numerical relativity, *e.g.*, Alcubierre (2008), call “strongly hyperbolic” what we have here defined to be “hyperbolic”. Since the mathematical definitions are the same, the difference merely reduces to adding the adjective “strong” when referring to a hyperbolic system.

<sup>5</sup>In Eq. (4.10) we use the notation  $\mathbf{R}^{(i)}$  to remark that this is not a component of a tensor contracted with  $\lambda_i$ , but rather the  $i$ -th column vector of the matrix  $\mathbf{R}$ .

Additional definitions of system (4.9) are possible on the basis of the properties of the eigenvalues and eigenvectors. More specifically, the system is said to be *strictly hyperbolic* if the matrix  $\mathbf{A}$  has a set of eigenvalues that are real and also distinct, while it is said to be *symmetric hyperbolic* if the matrix  $\mathbf{A}$  is symmetric,<sup>6</sup> i.e.,  $\mathbf{A} = \mathbf{A}^T$ . Finally, the system is said to be *weakly hyperbolic* if the matrix  $\mathbf{A}$  has a set of real eigenvalues but is not diagonalisable, so that it does not have a complete set of eigenvectors.

The importance of determining the degree of hyperbolicity of a set of partial differential equations is related to the concept of *well-posedness*. We recall that given the system of partial differential equations (4.9), the *Cauchy* or *initial-value problem* consists in finding a solution at an arbitrary time  $t$ , i.e.,  $\mathbf{U}(x, t)$ , once the solution is known at an initial time  $t = 0$ , i.e.,  $\mathbf{U}(x, t = 0)$ , which is also referred to as the *initial data*. We also recall that a system of partial differential equations is defined as “well-posed” if its solutions depend continuously on the initial data, so that small variations will lead to small variations in the solutions. Mathematically, this condition is expressed by requiring that for any component  $u = u(t, x)$  of the vector  $\mathbf{U}$ , any norm  $\|\cdot\|$  of the solution at an arbitrary time  $t$  is bounded by some exponential of the initial data, i.e.,

$$\|u(x, t)\| \leq ke^{at}\|u(x, 0)\|, \quad (4.12)$$

where  $k$  and  $a$  are two constants. Hence, in a well-posed problem, the norm of the solutions grows, at most, exponentially. This is clearly a prerequisite for any system whose solution should be computed numerically. A fundamental property of *hyperbolic equations* is that they are *well-posed*, hence suitable for a numerical solution [see, e.g., Reula (1998) for an extended discussion].

Let us now go back to the relativistic-hydrodynamic equations and determine whether the system (4.6) represents a set of equations that is strictly hyperbolic in the time direction defined by the unit (timelike) four-vector  $\xi$ , where  $\xi^\mu\xi_\mu = -1$ . To establish this, we first need to take the matrix  $\mathcal{A}$  with coefficients (4.7), and then contract it with  $\xi_\mu$  to obtain the *characteristic matrix*

$$\mathcal{A}^\mu\xi_\mu = \begin{pmatrix} \rho ha\delta_\beta^\alpha & h^{\alpha\mu}\xi_\mu c_s^2 & h^{\alpha\mu}\xi_\mu\partial_s p \\ \rho h\xi_\beta & a & 0^\mu \\ 0_\beta^\mu & 0^\mu & a \end{pmatrix}, \quad (4.13)$$

where  $a := u^\mu\xi_\mu$ . At this point, the hyperbolicity of the system (4.6) is obtained if the following two conditions are met (Anile, 1989; Font *et al.*, 1994):

$$(i) \det(\mathcal{A}^\mu\xi_\mu) \neq 0;$$

$$(ii) \text{for any unit spacelike four-vector } \zeta \text{ such that } \zeta^\mu\xi_\mu = 1 \text{ and } \zeta^\mu\xi_\mu = 0, \text{ the } \textit{eigenvalue problem}$$

$$\mathcal{A}^\mu(\zeta_\mu - \lambda\xi_\mu)\mathbf{R} = 0 \quad (4.14)$$

has only real eigenvalues,  $\lambda_1, \dots, \lambda_6$ , and a corresponding set of six linearly independent right eigenvectors  $\mathbf{R}^{(1)}, \dots, \mathbf{R}^{(6)}$ .

<sup>6</sup>Since it is symmetric, the matrix  $\mathbf{A}$  is always diagonalisable with real eigenvalues, so that symmetric hyperbolic systems are also hyperbolic; the opposite is of course not true.

A bit of algebra and a good dose of patience allows one to show that the determinant of the characteristic matrix is given by Anile (1989) (see Problem 1).

$$\det(\mathcal{A}^\mu \xi_\mu) = (\rho h a)^4 (a^2 - c_s^2 h^{\mu\nu} \xi_\mu \xi_\nu) \neq 0, \quad (4.15)$$

which is always true, since  $0 < c_s^2 \leq 1$  and  $\xi$  is timelike. Hence, condition (i) holds for the system of relativistic-hydrodynamic equations. To show that also condition (ii) holds, let us consider the equation

$$\det(\mathcal{A}^\mu \phi_\mu) = (\rho h u^\mu \phi_\mu)^4 [(u^\mu \phi_\mu)^2 - c_s^2 h^{\mu\nu} \phi_\mu \phi_\nu] = 0, \quad (4.16)$$

where  $\phi_\mu := \zeta_\mu - \lambda \xi_\mu$  is a four-vector such that if  $\lambda$  is the velocity of a perturbation in the arbitrary direction  $x^1$ , then  $\phi_\mu = (-\lambda, 1, 0, 0)$ . Stated differently, if we express the four-vector  $\phi_\mu$  in terms of the gradient of a scalar function  $\phi = \phi(x^\nu)$ , such that  $\phi_\mu = \nabla_\mu \phi$ , then  $\phi_\mu$  represents the local normal to the hypersurface  $\phi(x^\nu) = 0$ . Such a hypersurface is also referred to as the *characteristic hypersurface* (Anile, 1989). For simplicity, we evaluate Eq. (4.16) in the comoving frame, *i.e.*,  $u^\mu = \delta_0^\mu$ , so that the content of the square brackets is

$$[(\zeta_0 - \lambda \xi_0)^2 - c_s^2 (|\vec{\zeta}| - \lambda |\vec{\xi}|)^2] = 0, \quad (4.17)$$

where  $|\vec{\zeta}|^2 := \zeta_i \zeta^i$  and  $|\vec{\xi}|^2 = \xi_i \xi^i$ . Equation (4.17) is a second-order equation in  $\lambda$  with a discriminant that is positive as long as  $\xi$  and  $\zeta$  are timelike and spacelike, respectively. In this case, the corresponding solutions  $\lambda_\pm$  are real and distinct with corresponding linearly independent right eigenvectors given by

$$\mathbf{R}^{(\pm)} = \begin{pmatrix} -h^{\mu\nu}(\zeta_\nu - \lambda_\pm \xi_\nu) c_s^2 \\ \rho h u^\nu (\zeta_\nu - \lambda_\pm \xi_\nu) \\ 0 \end{pmatrix}. \quad (4.18)$$

Similarly, requiring that in Eq. (4.16) the term  $(u^\mu \phi_\mu)^4 = 0$  implies that

$$\lambda_i = \frac{u^\mu \zeta_\mu}{u^\mu \xi_\mu} \quad \text{for } i = 1, 2, 3, 4, \quad (4.19)$$

thus yielding an eigenvalue of multiplicity four.<sup>7</sup> The corresponding four linearly independent right eigenvectors  $\mathbf{R}^{(i)}$  are then easy to derive and given by (Anile, 1989)

$$\mathbf{R}^{(1)} = (u^\mu, 0, 0)^T, \quad \mathbf{R}^{(2)} = (v_2^\mu, 0, 0)^T, \quad (4.20)$$

$$\mathbf{R}^{(3)} = (v_3^\mu, 0, 0)^T, \quad \mathbf{R}^{(4)} = (0^\mu, -\partial_s p, c_s^2)^T, \quad (4.21)$$

where  $v_2^\mu$  and  $v_3^\mu$  are two linearly independent vectors orthogonal to  $u^\mu$  and  $\phi_\mu$ .

In summary, we have just shown that the system of relativistic-hydrodynamic equations (4.6) satisfies both conditions (i) and (ii), namely, that it has a set of six real eigenvalues,

<sup>7</sup> Because of the normalisation condition  $u^\mu u_\mu = -1$ , the multiplicity of the degenerate eigenvalue can be reduced from four to three [see Eq. (7.238)].

i.e.,  $\lambda_{\pm}$ ,  $\lambda_i$ , and six linearly independent right eigenvectors, i.e.,  $\mathbf{R}^{(\pm)}$ ,  $\mathbf{R}^{(i)}$ . Note that because the eigenvalue (4.19) has multiplicity larger than one and is therefore called *degenerate*, the relativistic-hydrodynamic equations are *not* a strictly hyperbolic system. This is true even if a different state vector is adopted, like the one presented in Section 7.3.3. However, this degeneracy does not affect the character of the equations, which are nevertheless hyperbolic because they always admit a complete set of eigenvectors.<sup>8</sup>

Once again let us take an illustrative example to fix ideas. Consider therefore a flat space-time with a Cartesian coordinate system, so that the four-velocity is given by  $u^\mu = W(1, v^i)$ , and concentrate on one direction only i.e.,  $x^1 = x$  (similar expressions can be obtained also for the other directions). In this case,  $\xi^\mu = (-1, 0, 0, 0)$ ,  $\zeta^\mu = (0, 1, 0, 0)$ , and the condition (4.14) then reduces to

$$(\mathcal{A}^0 - \lambda \mathcal{A}^1) \mathbf{R} = 0. \quad (4.22)$$

Lengthy but otherwise straightforward algebra then leads to the following *eigenvalues* (Anile, 1989; Font *et al.*, 1994)

$$\lambda_0 := v^x, \quad (4.23)$$

$$\lambda_{\pm} := \frac{1}{1 - v^2 c_s^2} \left( v^x (1 - c_s^2) \pm c_s \sqrt{(1 - v^2) [1 - (v^x)^2 - ((v^y)^2 + (v^z)^2) c_s^2]} \right), \quad (4.24)$$

where  $\lambda_0$  is a quadruple solution. The eigenvalues  $\lambda_0$  and  $\lambda_{\pm}$  are said to refer to the *matter* (or *material waves*) and to the *acoustic waves*, respectively. The reason for this denomination becomes obvious when considering the situation in which  $v^x = 0 = v$ , so that  $\lambda_0 = 0$ , and  $\lambda_{\pm} = \pm c_s$  (see also the discussion in Section 4.3.1). A particularly interesting limit of the eigenvalues (4.23)–(4.24) is that in which the fluid flow is one-dimensional, i.e.,  $v = v^x$ ,  $v^y = 0 = v^z$ , in which case they reduce to

$$\lambda_0 = v, \quad \lambda_{\pm} = \frac{v \pm c_s}{1 \pm vc_s} \stackrel{\text{N}}{=} v \pm c_s, \quad (4.25)$$

where the last equality, indicated with “ $\stackrel{\text{N}}{=}$ ”, refers to the Newtonian limit. In this case the eigenvalues are just the laws of velocity composition for waves moving with velocity  $\pm c_s$  with respect to the bulk flow velocity  $v$ . Note that the eigenvalues  $\lambda_{\pm}$  become degenerate<sup>9</sup> in the limit  $c_s \ll |v|$ , i.e.,  $\lambda_{\pm} \approx v$ .

#### 4.1.2 Conservative formulation

If the matrix  $\mathbf{A}(\mathbf{U})$  in (4.9) is the *Jacobian* of a *flux vector*  $\mathbf{F} = \mathbf{F}(\mathbf{U})$  with respect to the state vector  $\mathbf{U}$ , namely, if we can write

$$\mathbf{A}(\mathbf{U}) = \frac{\partial \mathbf{F}}{\partial \mathbf{U}}, \quad (4.26)$$

<sup>8</sup>This behaviour can be compared with what happens in relativistic (ideal) magnetohydrodynamics, where there are additional degenerate eigenvalues, whose corresponding eigenvectors are zero. In that case, special “normalisation” techniques must be adopted to provide a set of eigenvectors which remains complete even in the presence of degeneracies, thus preserving the hyperbolic character of the equations (Anton, 2008).

<sup>9</sup>More precisely, in the limit  $c_s \ll |v|$ , the eigenvalues are said to be *linearly degenerate*, where the precise definition is rather involved and can be found in LeVeque (2002).

## 196 Linear and Nonlinear Hydrodynamic Waves

then the homogeneous system (4.9) can be written in what is called *conservative form*, that is, in a form in which the change in time of  $\mathbf{U}$  over any finite volume is only due to its flux across the boundaries of the volume, *i.e.*,

$$\partial_t \mathbf{U} + \boldsymbol{\nabla} \mathbf{F} = 0. \quad (4.27)$$

In this case, the state vector  $\mathbf{U}$  is referred to as the vector of *conserved variables*. Note that the prescription (4.26) is not unique and in general there can be several flux vectors  $\mathbf{F}$  that could be mathematically compatible with the same matrix  $\mathbf{A}$ .

In the case of the relativistic-hydrodynamic equations, the simplest route to the derivation of a conservative formulation (4.27) consists in starting from the original covariant equations (3.52), (3.55), and (3.57), and suitably combining them. Such a derivation will be shown in full detail for the general-relativistic framework within the 3+1 decomposition in Section 7.3.3, but it is instructive to do it also here, in the simpler case of a one-dimensional flow in a flat spacetime, as this result will soon be used in Section 4.2.2.

We consider therefore a flow with four-velocity  $u^\mu = W(1, v, 0, 0)$  in a Cartesian coordinate system and start from the continuity equation (3.52), which is indeed already in the required form, and can be expanded as

$$\partial_t D + \partial_x(Dv) = 0, \quad (4.28)$$

where we have introduced the *conserved rest-mass density*,<sup>10</sup>  $D := \rho W$ . On the other hand, the momentum equation follows directly from (3.53), assuming the free index  $\nu = x$ , so as to obtain

$$\partial_t(\rho h W^2 v) + \partial_x(\rho h W^2 v^2 + p) = 0, \quad (4.29)$$

which, after introducing the *conserved momentum*  $S := \rho h W^2 v$  [not to be confused with the entropy introduced in Eq. (2.30)], we rewrite as

$$\partial_t S + \partial_x(Sv + p) = 0. \quad (4.30)$$

Similarly, the energy equation follows from (3.53), assuming the free index  $\nu = t$ , to find

$$\partial_t(\rho h W^2 - p) + \partial_x(\rho h W^2 v) = 0, \quad (4.31)$$

and therefore

$$\partial_t E + \partial_x S = 0, \quad (4.32)$$

where we have introduced the *conserved energy*  $E := \rho h W^2 - p$ . When collected, Eqs. (4.28), (4.30) and (4.32) form a system of conservation laws in the form (4.27), with state vector and fluxes given respectively by

$$\mathbf{U} = \begin{pmatrix} D \\ S \\ E \end{pmatrix}, \quad \mathbf{F} = \begin{pmatrix} Dv \\ Sv + p \\ S \end{pmatrix}. \quad (4.33)$$

<sup>10</sup>Note that despite the denomination,  $D$  is measured by an Eulerian observer who is *not at rest* with the fluid. See Section 7.1 for the definition of such an observer.

Once the conservative form of the equations is known, it is in principle possible to recover the quasi-linear form in an unambiguous way via the Jacobian (4.26). However, a fundamental complication is given by the fact that the fluid *primitive variables*  $p, \rho, v$  and  $\epsilon$ , which hereafter we will consider as the components of the state vector  $\mathbf{V}$ , cannot be obtained analytically from the state vector  $\mathbf{U}$ . In other words, while the relation  $\mathbf{U} = \mathbf{U}(\mathbf{V})$  is known analytically, the inverse  $\mathbf{V} = \mathbf{V}(\mathbf{U})$  is not and thus the operation  $\partial\mathbf{F}/\partial\mathbf{U}$  cannot be performed. However, a simple strategy can be followed that, starting from the conservative form, yields the quasi-linear form for *any set of primitive variables*  $\mathbf{V}$ , and, at the same time, provides a relation among the eigenvectors in different set of variables. To illustrate this procedure, which can be found also in Huynh (1995), let us consider again Eq. (4.27) and use the chain rule to rewrite it as

$$\frac{\partial\mathbf{U}}{\partial t} + \frac{\partial\mathbf{F}}{\partial x} = \frac{\partial\mathbf{U}}{\partial\mathbf{V}} \frac{\partial\mathbf{V}}{\partial t} + \frac{\partial\mathbf{F}}{\partial\mathbf{V}} \frac{\partial\mathbf{V}}{\partial x} = 0. \quad (4.34)$$

After multiplying the second equality in (4.34) by the matrix  $(\partial\mathbf{U}/\partial\mathbf{V})^{-1}$ , we obtain a quasi-linear form of the equations

$$\frac{\partial\mathbf{V}}{\partial t} + \mathbf{A}_p \frac{\partial\mathbf{V}}{\partial x} = 0, \quad (4.35)$$

where we have defined

$$\mathbf{A}_p := \left( \frac{\partial\mathbf{U}}{\partial\mathbf{V}} \right)^{-1} \frac{\partial\mathbf{F}}{\partial\mathbf{V}}. \quad (4.36)$$

Equation (4.35) expresses a first important result: namely, that by starting from the knowledge of the vector flux  $\mathbf{F}$  it is possible to obtain a quasi-linear homogeneous form such as the one in Eq. (4.9) in terms of *a generic set of primitive variables*  $\mathbf{V}$ , and with the matrix  $\mathbf{A}_p$  being given by Eq. (4.36). In the case of the relativistic-hydrodynamic equations, since they are hyperbolic, the matrix  $\mathbf{A}_p$  is diagonalisable, with a set of eigenvalues  $\lambda_p$  and corresponding matrix of right eigenvectors  $\mathbf{R}_p$ , such that  $\mathbf{A}_p = \mathbf{R}_p \Lambda_p \mathbf{R}_p^{-1}$ . In this case, Eq. (4.35) can be written as

$$\begin{aligned} \frac{\partial\mathbf{V}}{\partial\mathbf{U}} \frac{\partial\mathbf{U}}{\partial t} + \mathbf{R}_p \Lambda_p \mathbf{R}_p^{-1} \frac{\partial\mathbf{V}}{\partial\mathbf{U}} \frac{\partial\mathbf{U}}{\partial x} &= 0 = \frac{\partial\mathbf{U}}{\partial t} + \left( \frac{\partial\mathbf{V}}{\partial\mathbf{U}} \right)^{-1} \mathbf{R}_p \Lambda_p \mathbf{R}_p^{-1} \frac{\partial\mathbf{V}}{\partial\mathbf{U}} \frac{\partial\mathbf{U}}{\partial x} \\ &= \frac{\partial\mathbf{U}}{\partial t} + \mathbf{A} \frac{\partial\mathbf{U}}{\partial x} = 0, \end{aligned} \quad (4.37)$$

where we have defined

$$\mathbf{R} := \frac{\partial\mathbf{U}}{\partial\mathbf{V}} \mathbf{R}_p, \quad \mathbf{R}^{-1} := \mathbf{R}_p^{-1} \left( \frac{\partial\mathbf{U}}{\partial\mathbf{V}} \right)^{-1}, \quad (4.38)$$

$$\mathbf{A} := \mathbf{R} \Lambda \mathbf{R}^{-1}, \quad \Lambda := \Lambda_p. \quad (4.39)$$

Equations (4.38)–(4.39) express identities that deserve some additional comment. First, even if the flux vector depends on the primitive variables, *i.e.*,  $\mathbf{F} = \mathbf{F}(\mathbf{V})$ , rather than on the conserved ones, *i.e.*,  $\mathbf{F} = \mathbf{F}(\mathbf{U})$ , it is possible to obtain a quasi-linear form of the relativistic-hydrodynamic equations in terms of the conserved variables  $\mathbf{U}$ , with the matrix  $\mathbf{A}$  given by Eq. (4.39). Second, the matrix of eigenvectors  $\mathbf{R}$  in the conserved variables  $\mathbf{U}$  can be obtained

from the matrix of eigenvectors  $\mathbf{R}_p$  in the primitive variables  $\mathbf{V}$  via Eq. (4.38). Finally, and more importantly, while the eigenvectors change when going from one quasi-linear form to another one expressed for a different set of variables, the eigenvalues remain the same, and are given, for a one-dimensional flow, by Eq. (4.25).

As an example, and because this will become relevant for Section 4.2.2, let us apply these results to the case in which the vector of primitive variables is chosen to have components  $\mathbf{V} = (\rho, v, p)^T$ . A direct application of (4.36) with a flux vector given by (4.33) then yields

$$\mathbf{A}_p = \begin{pmatrix} v & \frac{\rho}{1 - v^2 c_s^2} & -\frac{v}{hW^2(1 - v^2 c_s^2)} \\ 0 & \frac{v(1 - c_s^2)}{1 - v^2 c_s^2} & \frac{1}{\rho h W^4 (1 - v^2 c_s^2)} \\ 0 & \frac{\rho h c_s^2}{1 - v^2 c_s^2} & \frac{v(1 - c_s^2)}{1 - v^2 c_s^2} \end{pmatrix}, \quad (4.40)$$

where the eigenvalues  $\lambda_0, \lambda_{\pm}$  are, as mentioned above, again expressed by Eq. (4.25), and the corresponding right eigenvectors are given by

$$\mathbf{R}_p^{(-)} = \begin{pmatrix} -\rho W^2 / c_s \\ 1 \\ -\rho h W^2 c_s \end{pmatrix}, \quad \mathbf{R}_p^{(0)} = \begin{pmatrix} 1 \\ 0 \\ 0 \end{pmatrix}, \quad \mathbf{R}_p^{(+)} = \begin{pmatrix} \rho W^2 / c_s \\ 1 \\ \rho h W^2 c_s \end{pmatrix}. \quad (4.41)$$

All of these results will have important implications in Chapter 9, when discussing the different formulations used when solving the equations numerically.

## 4.2 Linear and nonlinear behaviour

### 4.2.1 Characteristic equations for linear systems

An important feature of hyperbolic systems is that they typically describe physical processes involving wave motion or advective transport, and as will become clear in Chapter 9, the condition of reality for the eigenvalues is associated with the existence of propagating waves. To better appreciate the relation between a hyperbolic set of equations and the propagation of waves, it is convenient to consider the set of equations (4.9) as hyperbolic and linear, namely when the matrix  $\mathbf{A}$  has coefficients that are all *constant*. Under these conditions, we define the so-called *characteristic vector*, *i.e.*, the vector of *characteristic variables*, as

$$\mathbf{W} := \mathbf{R}^{-1} \mathbf{U}, \quad (4.42)$$

where the matrix of the eigenvectors  $\mathbf{R}$  is also constant. Multiplying now the homogeneous form of Eq. (4.9) by  $\mathbf{R}^{-1}$  we obtain

$$\mathbf{R}^{-1} \partial_t \mathbf{U} = \partial_t (\mathbf{R}^{-1} \mathbf{U}) = \partial_t \mathbf{W}, \quad (4.43)$$

$$\mathbf{R}^{-1} \mathbf{A} \nabla \mathbf{U} = \mathbf{R}^{-1} \mathbf{A} \mathbf{R} \nabla \mathbf{W} = \boldsymbol{\Lambda} \nabla \mathbf{W}, \quad (4.44)$$

so that Eq. (4.9) can be rewritten as

$$\partial_t \mathbf{W} + \boldsymbol{\Lambda} \nabla \mathbf{W} = 0. \quad (4.45)$$

Equations (4.45) are called *characteristic equations*<sup>11</sup> and state that the characteristic vector  $\mathbf{W}$  is conserved along the directions given by the eigenvalues of  $\mathbf{A}$ , *i.e.*,

$$\frac{d\mathbf{W}}{dt} = 0 = \partial_t \mathbf{W} + \boldsymbol{\Lambda} \partial_{\vec{x}} \mathbf{W} = 0, \quad (4.46)$$

along

$$\boldsymbol{\Lambda} = \frac{\partial \vec{x}}{\partial t}, \quad (4.47)$$

where  $\{x^j\}$  are the coordinates of the spatial section of an otherwise arbitrary coordinate system. The fact that  $\boldsymbol{\Lambda}$  is diagonal has two important consequences. The first one is that Eqs. (4.46) are effectively a set of  $N$  decoupled ordinary differential equations along the directions

$$\boldsymbol{\lambda}_{(i)} = \frac{\partial \vec{x}_{(i)}}{\partial t}, \quad (4.48)$$

which are then referred to as the *characteristic curves* (or simply *characteristics*). The second relevant implication is that Eqs. (4.45) provide a system of  $N$  independent linear advection equations, one for each component of the characteristic vector  $\mathbf{W}$  (see Section 4.2.3 for details on the advection equation). As such, the solution of  $W^i$  at any (future) position  $(x^j, t)$  is given simply by the spacetime translation of the initial data, *i.e.*,  $W^i(x^j, t) = W^i(x^j - \lambda_i t, 0)$ . Once the solution is known in terms of the characteristic vector  $\mathbf{W}$ , it is then straightforward to find it in terms of the original state vector  $\mathbf{U}$ . In fact, using Eq. (4.42) to derive that  $\mathbf{U} := \mathbf{R} \mathbf{W}$ , we can write the solution at any position  $(x^j, t)$  as (see the discussion below in Section 4.2.3)

$$\mathbf{U}(x^j, t) = \sum_{i=1}^N W^i(x^j, t) \mathbf{R}^{(i)} = \sum_{i=1}^N W^i(x^j - \lambda_i t, 0) \mathbf{R}^{(i)}. \quad (4.49)$$

The relevant result expressed by Eq. (4.49) is that, once the characteristic vector  $\mathbf{W}$  at the *initial time* is known, *i.e.*,  $\mathbf{W}(x^j, 0)$ , then the state vector  $\mathbf{U}(x^j, t)$  can be computed at *any* spatial position and at *any* time. This possibility represents of course a very powerful tool, which is however limited to those situations in which the characteristic curves do not intersect and thus the solution (4.49) is not double-valued. In practice, therefore, the use of Eq. (4.49)

<sup>11</sup>Note that Eq. (4.16), introduced in the previous section, represents a mathematically more elegant, but physically less transparent, definition of characteristic equations (Anile, 1989).

is restricted only to *linear systems* of hyperbolic equations, although the numerical solution of nonlinear system is sometimes addressed by resorting to a linearisation of the quasi-linear form (see Section 9.3.3). In such cases, suitable averages are performed to make the matrix  $\mathbf{A}$  constant, and numerical methods based on adaptations of Eq. (4.49) can be used even in the nonlinear case (Toro, 2009). A detailed discussion of the physical relevance of characteristics and different properties in linear and quasi-linear systems will be made in Section 4.2.3.

#### 4.2.2 Riemann invariants

Since the characteristic vector  $\mathbf{W}$  is conserved along the characteristic curves as long as they do not intersect, its components can be associated to physical scalar quantities that are conserved through the corresponding waves and that can therefore be used to describe the fluid properties in certain portions of the flow. As we will discuss below, additional scalar quantities with a clear physical interpretation can be found that are conserved for a certain class of waves. To explore this concept further, let us go back to the general form of the relativistic-hydrodynamic equations (4.6) and let us consider them for the simpler but representative case of one-dimensional flows. We further assume we are dealing with a solution  $\mathbf{U}(x, t)$  that is a smooth function of the type  $\mathbf{U} = \mathbf{U}(\varphi(x, t))$ , where  $\varphi(x, t)$  is called the *characteristic phase* and is a suitable function of class  $\mathcal{C}^1$  (Anile, 1989). We then rewrite Eqs. (4.6) as

$$\mathcal{A}^t \partial_t \mathbf{U} + \mathcal{A}^x \partial_x \mathbf{U} = 0, \quad (4.50)$$

or, equivalently, as

$$(\mathcal{A}^t \varphi_t + \mathcal{A}^x \varphi_x) \frac{d\mathbf{U}}{d\varphi} = 0, \quad (4.51)$$

where  $\varphi_i := \partial_i \varphi$ . Since we want to consider the non-trivial case in which  $d\mathbf{U}/d\varphi \neq 0$ , the phase  $\varphi(x, t)$  must satisfy the characteristic equation

$$\det(\mathcal{A}^t \varphi_t + \mathcal{A}^x \varphi_x) = 0. \quad (4.52)$$

Introducing now the speed

$$\lambda := -\frac{\varphi_t}{\varphi_x} = -\frac{\partial x}{\partial t}, \quad (4.53)$$

Eq. (4.52) becomes

$$\det(\mathcal{A}^t - \lambda \mathcal{A}^x) = 0, \quad (4.54)$$

where, we recall,  $\mathcal{A}^t$  and  $\mathcal{A}^x$  are two  $6 \times 6$  matrices in the case of the relativistic-hydrodynamic equations [cf., Eq. (4.7)]. Indicating with  $\lambda_i$ , where  $i = 1, \dots, 6$ , the eigenvalues and with  $\mathbf{R}^{(i)}$  the corresponding right eigenvectors, it follows that  $d\mathbf{U}/d\varphi$  must be proportional to  $\mathbf{R}^{(i)}$

$$\frac{d\mathbf{U}}{d\varphi} = \pi \mathbf{R}^{(i)}, \quad (4.55)$$

where  $\pi$  is just a proportionality factor. Smooth solution of this kind are called *simple waves* and a proper discussion about them is deferred to Section 4.4.1.

Equations (4.55) are a set of  $6 \times 6$  ordinary differential equations of the type

$$\frac{dU^1}{R_1^{(i)}} = \frac{dU^2}{R_2^{(i)}} = \dots = \frac{dU^6}{R_6^{(i)}}, \quad (4.56)$$

where we have assumed that  $\mathbf{U} = (U^1, \dots, U^6)^T$ . If we express, say,  $U^1 = U^1(\varphi)$  as an arbitrary function of the phase  $\varphi$ , then the solution of the system of equations (4.56) allows us to express  $U^2, \dots, U^6$  as a function of  $U^1$ . For each eigenvalue  $\lambda_i$ , the solution of the system (4.56) is equivalent to the determination of  $6 - 1 = 5$  first integrals  $\mathcal{J}_1^{(i)}(\mathbf{U}), \dots, \mathcal{J}_5^{(i)}(\mathbf{U})$ , which are called *Riemann invariants*, associated to the eigenvalue  $\lambda_i$ . As follows from Eq. (4.56), the Riemann invariants are scalar quantities that are conserved along the curves  $\mathbf{U} = \mathbf{U}(\varphi)$ , where now  $\varphi$  can be seen to be the parameter of the curves. Note a Riemann invariant is not only constant along each of the integral curves, but also takes the same value on all of the integral curves within a simple wave, thus being constant in both space and time.

For each such curve, the tangent vector,  $dU^i/d\varphi$ , is always parallel to the eigenvector with eigenvalue  $\lambda_i$ . These curves are called *integral curves* (LeVeque, 2002) and because they are defined in the space of the solution  $\mathbf{U}$ , they should not be confused with the characteristic curves, which are instead defined in the space  $(x, t)$ , i.e., in spacetime. As long as simple waves describe a smooth flow and do not break into discontinuous waves, their characteristic curves are just *straight lines*. This latter property follows immediately from the fact that along the  $i$ -th characteristic,  $\varphi = \text{const.}$ , and thus  $\mathbf{U}(\varphi) = \text{const.}$  On the other hand, it is also true that  $\lambda_i = \lambda_i(\mathbf{U}) = \text{const.}$ , so that

$$\frac{dx}{dt} = \lambda_i(\mathbf{U}) = \text{const.}, \quad (4.57)$$

that is, the characteristics are straight lines. Note that this property holds true only in special regions of the flow where Riemann invariants exist.

Let us again fix ideas with a simple example and compute the relativistic *Riemann invariants* in the case of one-dimensional special-relativistic motion (Taub, 1948; Anile, 1989). To this end, we can apply Eq. (4.56) after adopting the quasi-linear form of the equations in terms of the primitive variables  $\mathbf{V} = (\rho, v, p)$ , of the matrix  $\mathbf{A}$  given by (4.40) and of the eigenvectors given by Eq. (4.41). For instance, if we consider the matter wave with eigenvalue  $\lambda_0 = v$ , a direct application of Eq. (4.56) allows us to find that  $dp = 0 = dv$ , thus concluding that both pressure and velocity are the associated Riemann invariants. The full set of Riemann invariants computed after following the same logic for each of the eigenvalues can be reported schematically as<sup>12</sup>

<sup>12</sup>The standard but confusing convention is to associate the Riemann invariants  $\mathcal{J}_{\pm}$  to the characteristics  $\lambda_{\mp}$  and not to  $\lambda_{\pm}$ .

Eigenvalue	Differential relation	Riemann invariant	
$\lambda_- = \frac{v - c_s}{1 - vc_s}$	$ds = 0, \quad W^2 dv + \frac{c_s}{\rho} d\rho = 0$	$s, \mathcal{J}_+$	
$\lambda_0 = v$	$dp = 0, \quad dv = 0$	$p, v$	
$\lambda_+ = \frac{v + c_s}{1 + vc_s}$	$ds = 0, \quad W^2 dv - \frac{c_s}{\rho} d\rho = 0$	$s, \mathcal{J}_-$	(4.58)

where

$$\mathcal{J}_\pm := \frac{1}{2} \ln \left( \frac{1+v}{1-v} \right) \pm \int \frac{c_s}{\rho} d\rho = \text{const.} \quad (4.59)$$

Note that provided the flow is isentropic, the two Riemann invariants  $\mathcal{J}_+$  and  $\mathcal{J}_-$  are constant along the characteristics with slopes  $\lambda_+$  and  $\lambda_-$ , respectively, (see Problem 2).

Equation (4.59) is used, for instance, in the solution of the Riemann problem when rarefaction waves are produced (see Section 4.4.2). In this case, the characteristic phase is given by

$$\varphi = x - \left( \frac{v \pm c_s}{1 \pm vc_s} \right) t, \quad (4.60)$$

where the  $\pm$  sign refers to right/left propagating waves. As a result, once we specify an arbitrary profile for the velocity  $v$  as a function of  $\varphi$  (this could be, for instance, the initial data in an initial-value problem)

$$v = f(\varphi) = f \left( x - \left( \frac{v \pm c_s}{1 \pm vc_s} \right) t \right), \quad (4.61)$$

then the energy-density profile can be computed simply from the integration of (see Problem 3)

$$\int \frac{c_s}{e+p} de = \pm \frac{1}{2} \ln \left( \frac{1+v}{1-v} \right) + \text{const.} \quad (4.62)$$

Let us consider, for example, the cosmological and barotropic equation of state (2.283) for a dark-energy fluid (see Section 2.4.9),  $p = we$ , so that  $c_s = \sqrt{w}$ . Expression (4.62) can then be readily integrated to yield the following relation between the energy density and the fluid velocity

$$e = e_0 \left( \frac{1+v}{1-v} \right)^{\pm(1+w)/(2\sqrt{w})}. \quad (4.63)$$

The solution (4.63) can be used, for instance, to study the nonlinear development of acoustic waves in the early universe and indicates that, for a right/left-propagating wave,  $e \rightarrow \infty$  as  $v \rightarrow \pm 1$ .

As a concluding note we remark that the Riemann invariants are not Lorentz invariants (Anile, 1989). Considering in fact a Lorentz transformation of the type

$$v' = \frac{v + \beta}{1 + v\beta}, \quad (4.64)$$

the Riemann invariants will be transformed as

$$\mathcal{J}'_{\pm} = \mathcal{J}_{\pm} + \frac{1}{2} \ln \left( \frac{1 + \beta}{1 - \beta} \right). \quad (4.65)$$

Of course since  $\beta = \text{const.}$ , also  $\mathcal{J}'_{\pm} = \text{const.}$ , and indeed they will still be Riemann invariants in the boosted frame, although with a form different from  $\mathcal{J}_{\pm}$ .

### 4.2.3 Characteristic curves and caustics

There is no better way to understand the mathematical and physical implications of the characteristic curves and their relation with the emergence of nonlinear effects in the hydrodynamic equations, than to consider a couple of simple but representative examples. We start therefore from the most elementary *linear* hyperbolic equation in one spatial dimension: the Newtonian *advection equation* with *constant advection velocity*  $v$ . In a Cartesian coordinate system, this equation is easily derived from the general expression (4.9) when setting  $\mathbf{U} \rightarrow u$ ,  $\mathbf{A} \rightarrow v$  and  $\mathbf{S} = 0$ , *i.e.*,

$$\partial_t u + v \partial_x u = 0, \quad (4.66)$$

with generic initial conditions given by

$$u_0(x) := u(x, 0). \quad (4.67)$$

It is easy to realise that Eq. (4.66) is linear and in conservative form [*cf.* Eq. (4.27)], and that the Jacobian has only one component, which is also its eigenvalue, namely,  $\lambda = v = \text{const.}$ , which represents the *characteristic speed*. In other words, for the linear advection equation (4.66) the characteristic speed coincides with the advection velocity, that is, the velocity at which the solution  $u(t, x)$  is translated in spacetime. Let us now interpret the characteristics as *curves* in the spacetime  $(x, t)$ . For this we recognise that the total rate of change of  $u$  is

$$\frac{du}{dt} = \frac{\partial u}{\partial t} + \frac{dx}{dt} \frac{\partial u}{\partial x}, \quad (4.68)$$

and it is therefore zero along the direction set by the characteristic, *i.e.*,

$$\frac{du}{dt} = 0, \quad (4.69)$$

along the *characteristic curve*

$$\frac{dx}{dt} = \lambda = \text{const.} \quad (4.70)$$

As a result,  $u$  is constant along the curve  $x = x(t)$  with *constant slope*  $\lambda$  in the  $(t, x)$  plane. Furthermore, since the solution is the same along the characteristic curve  $x(t) = x_0 + \lambda t$ , the

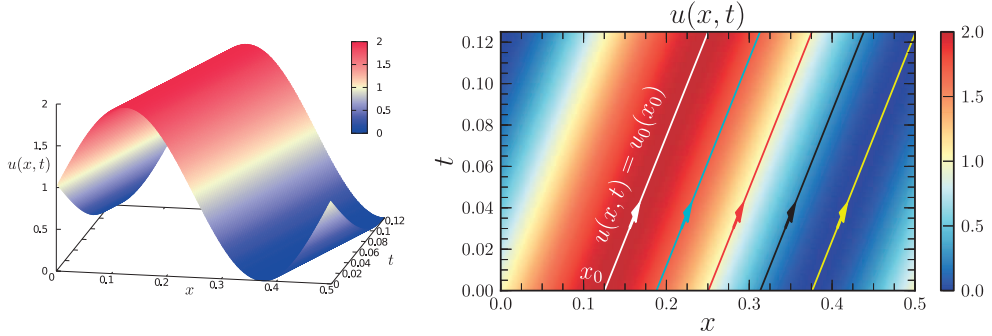


**Fig. 4.1** Spacetime representation of the solution of the one-dimensional advection equation (4.66) with  $v = 1$  and initial data  $u_0(x) = \sin(4\pi x) + 1$ . The left panel reports a three-dimensional view of the solution, which is simply translated in spacetime along the direction  $x = t$ . The right panel reports instead a map view of the solution and of the characteristics curves, which are straight lines with unit slope and always parallel (no caustics are produced). The linear behaviour of the advection equation should be contrasted with the nonlinear behaviour of the Burgers equation shown in Fig. 4.2 for the same initial data.

solution at any arbitrary position  $(x, t)$  can be readily computed from the initial solution  $u_0$  as the one at which the characteristic curve intersects the  $x$ -axis at  $t = 0$  (see the right panel of Fig. 4.1), *i.e.*,

$$u(x, t) = u_0(x_0) = u_0(x - \lambda t). \quad (4.71)$$

Two important remarks on the properties of linear hyperbolic equations can be made at this point. First, since in this case the characteristic speed is constant along a characteristic curve, the latter is a straight line everywhere. Second, since the characteristic speed is the same everywhere, the characteristic curves are always parallel and thus never produce *caustics* (*i.e.*, never intersect) in the  $(x, t)$  plane. Figure 4.1 summarises much of what has been discussed so far and provides a spacetime representation of the solution of the one-dimensional advection equation (4.66) with initial data  $u_0(x) = \sin(4\pi x) + 1$ . The left panel reports a three-dimensional view of the solution, which is simply translated in space and time along the direction  $x/t = v = 1$ , while the right panel shows a map view of the solution and of the characteristics curves. As commented above, the solution at any point in this diagram can be derived from the initial solution through the same characteristic line.

We now turn to consider *nonlinear* hyperbolic equations and many of the new properties that emerge in this case can be appreciated by studying another elementary equation in one spatial dimension, namely, the Newtonian inviscid *Burgers equation*. Again, this equation can be easily derived from the general expression (4.9) when setting  $\mathbf{U} \rightarrow u$ ,  $\mathbf{A} \rightarrow u$  and  $\mathbf{S} = 0$ , *i.e.*,<sup>13</sup>

$$\partial_t u + u \partial_x u = 0. \quad (4.72)$$

<sup>13</sup>The (viscous) Burgers equation is a simple extension of (4.72) and is given by  $\partial_t u + u \partial_x u = \eta \partial_x^2 u$ , where  $\eta$  accounts, for instance, for a viscous dissipative process.

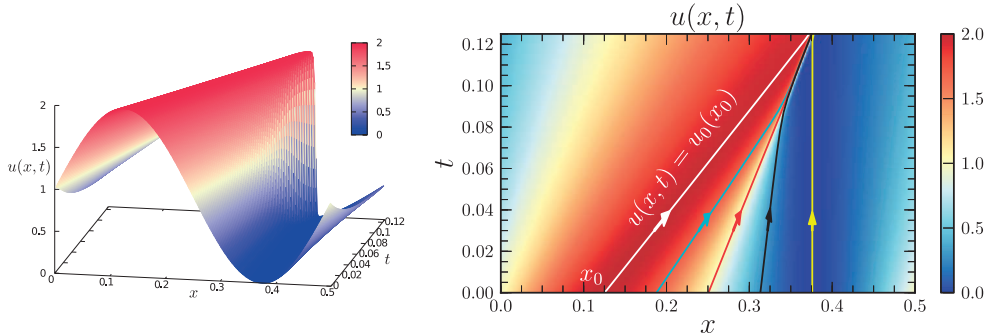


**Fig. 4.2** Spacetime representation of the solution of the one-dimensional inviscid Burgers equation (4.72) with initial data  $u_0(x) = \sin(4\pi x) + 1$ . The left panel reports a three-dimensional view of the solution, which shows the steepening and the formation of a shock discontinuity at  $t \simeq 0.08$ . The right panel reports instead a map view of the solution and of the characteristics curves, which are still straight lines, but no longer parallel; these lines intersect in a caustic corresponding to the formation of a shock. The nonlinear behaviour of the Burgers equation should be contrasted with the linear behaviour of the advection equation shown in Fig. 4.1 for the same initial data.

In other words, the only difference between the advection equation (4.66) and the Burgers equation (4.72) is that  $v = \text{const.}$  has been replaced by  $u = u(x, t)$ . This substitution, however, is far from being trivial and Eq. (4.72) is more than an academic example. Indeed, it can be thought to represent the one-dimensional Euler equations for a fluid with negligible pressure gradients and external forces [*cf.*, Eq. (2.66)]; in this sense, the Burgers equation already incorporates the nonlinear properties of the more complex hydrodynamic equations.

Equation (4.72) is already in a quasi-linear form [*cf.*, Eq. (4.9)] where  $A = u(x, t)$  and the single eigenvalue is also  $\lambda = u(x, t)$ . It is then easy to realise that the characteristic curves are still straight lines, which however are no longer parallel. Equation (4.68), in fact, still vanishes along the characteristic curve which now has slope  $u$ , *i.e.*,

$$\frac{dx}{dt} = \lambda = u(x, t) = \text{const.} \quad (4.73)$$

Since  $u(x, t)$  is constant along the curve  $\lambda$  in the  $(t, x)$  plane the characteristics are straight lines, but their slope is not the same everywhere. This implies that different parts of the solutions will propagate at different speeds, thus leading either to compressions or to rarefactions in the fluid. It is then easy to conclude that those parts of the solution that have larger characteristic speeds will tend to overtake those with smaller speeds, eventually leading to caustics in the characteristic curves. This is indeed shown in Fig. 4.2, which represents the equivalent of Fig. 4.1, but for the Burgers equation. Also in this case, the left panel shows a three-dimensional view of the solution of Eq. (4.72) with initial data  $u_0(x) = \sin(4\pi x) + 1$ , while the right panel reports a map view of the solution and of the characteristics curves. Note that the parts of the solution above/below 1 have characteristic curves with slopes larger/smaller than 1, indicating that while they all move to larger values of  $x$ , the latter ones move much more slowly (if at all). As a result, the characteristics will eventually intersect in a caustic.

Calculating when this intersection will happen is not too difficult and can be done by considering Eq. (4.71) for the *implicit Burgers equation*, *i.e.*, when writing the solution as

$$u(x, t) = u_0(x - \lambda t) = u_0(x - u(x, t)t), \quad (4.74)$$

where we have used the result that the characteristic is  $\lambda = u(x, t)$ . Taking a time derivative then yields the implicit equation

$$\partial_t u(x, t) = \partial_x u_0[-u(x, t) - t \partial_t u], \quad (4.75)$$

which can be solved for the time derivative to obtain

$$\partial_t u(x, t) = -\frac{u(x, t) \partial_x u_0}{1 + t \partial_x u_0}. \quad (4.76)$$

The caustic will appear when the right-hand side of (4.76) diverges and thus at a time

$$\tau_c = -\frac{1}{\min(\partial_x u_0)} = \frac{1}{4\pi} \simeq 0.08, \quad (4.77)$$

where the final result is obtained for the specific initial data chosen and is reported in Fig. 4.2.

This phenomenology is clearly independent of the initial data chosen and is usually referred to as *wave steepening* to emphasise the fact that given *any smooth initial data*, the gradients of the solution of a nonlinear hyperbolic equation will increase progressively, eventually leading to a multi-valued solution and hence to a *shock wave* unless dissipative processes intervene (see also Section 4.4.3 for an extended discussion of discontinuities in hydrodynamic flows).<sup>14</sup> The properties of nonlinear hyperbolic equations discussed above are summarised in Fig. 4.2, where both the wave-steepening (left panel) and the intersection of the characteristic curves (right panel) are shown rather clearly. As we will discuss extensively in the following, wave steepening and shock formation are very common situations in the evolution of inviscid compressible flows.

#### 4.2.4 Domain of determinacy and region of influence

In addition to coinciding with the directions of propagation of acoustic disturbances and being locally tangent to the fluidlines, the characteristic curves also provide the basic tools for a rigorous definition of causally connected regions within the fluid, applying equally well to a Newtonian and to a relativistic framework. Furthermore, as we will show in Sections 4.8 and 5.5, they can be used to investigate the causal structure of nonlinear waves and reaction fronts. We recall that in the general case of nonlinear systems of hyperbolic equations the characteristics are curved lines, although they reduce to straight lines when the solution is only composed of simple waves, as discussed in Section 4.2.2.

Given the hydrodynamic equations as a quasi-linear set of hyperbolic differential equations and taking an event  $\mathcal{P}(x, t)$  in the spacetime  $(x, t)$ , it is possible to define as *domain*

<sup>14</sup>A notable counterexample exists to this otherwise general statement. This is offered by initial data which is monotonically increasing; in this case, in fact, all characteristics diverge from each other and no steepening can take place. This wave is what will be referred to as a rarefaction wave in Section 4.4.2.

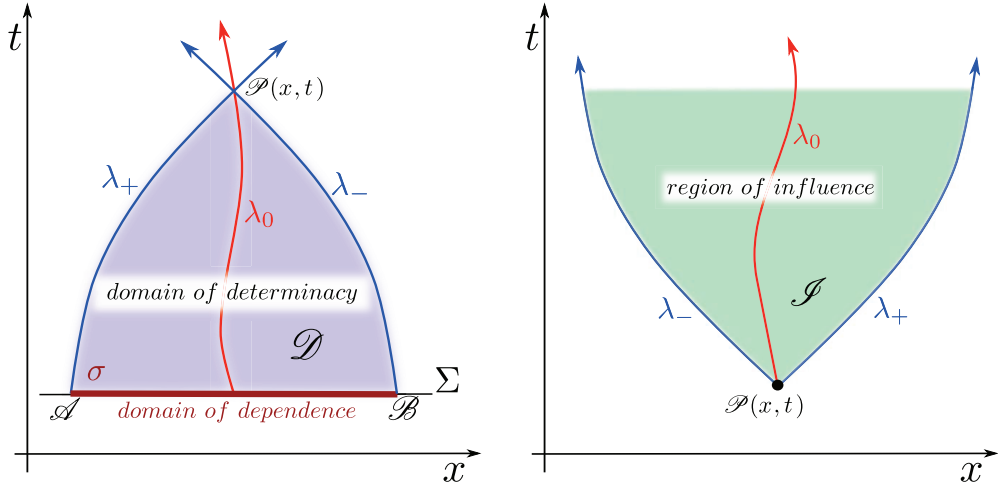


**Fig. 4.3** *Left panel:* Schematic representation of the “domain of dependence” (indicated with a heavy line  $\sigma$ ) and of the “domain of determinacy” (indicated with the shaded area region  $\mathcal{D}$ ) of an event  $\mathcal{P}(x, t)$ . Indicated with  $\lambda_+$ ,  $\lambda_-$  and  $\lambda_0$  are the forward, the backward and the advective characteristics, respectively. *Right panel:* “region of influence” (indicated with the shaded area  $\mathcal{I}$ ) of the event  $\mathcal{P}(x, t)$  from where the three characteristics are emitted.

of dependence of  $\mathcal{P}(x, t)$  the portion  $\sigma$  of the  $t = 0$ -hypersurface  $\Sigma$  delimited by the events  $\mathcal{A}$  and  $\mathcal{B}$  (see the left panel of Fig. 4.3, where for simplicity we consider a one-dimensional section of the spatial sector of the spacetime). On this line it is possible to specify the *Cauchy data* for the event  $\mathcal{P}$ , that is, the set of possible initial conditions from which the solution at  $\mathcal{P}$  of the hyperbolic differential equations depends.<sup>15</sup> Associated with the domain of dependence is the *domain of determinacy* (sometimes also referred to as the *future domain of dependence*), which is the region of spacetime  $\mathcal{D}$  limited by the domain of dependence and by the *forward*,  $\lambda_+$ , and the *backward*,  $\lambda_-$ , characteristics issued respectively from  $\mathcal{A}$  and  $\mathcal{B}$ . As indicated by its name, the solution at any point in the domain of determinacy is fully determined by the initial data assigned on the domain of dependence (Courant and Hilbert, 1962; Coulson and Jeffrey, 1977). Similarly, if the Cauchy data is assigned only at a single point  $\mathcal{P}(x, t)$  of the domain of dependence, the solution will then be determined only at that point  $\mathcal{P}(x, t)$ , which, in turn, will influence, but not determine, the solution on a larger region. It is then defined as the *region of influence* of the event  $\mathcal{P}(x, t)$ , the region of spacetime  $\mathcal{I}$  included between the characteristic curves diverging from the point  $\mathcal{P}(x, t)$  (see the right panel of Fig. 4.3).

Of course, much of what was discussed above on the mathematical definitions of the domain of determinacy and of the region of influence is deeply rooted in the relativistic concept of causality in vacuum spacetimes discussed in Section 1.4, where the characteristic speeds are given simply by the speed of light and are always straight lines. The important difference here is that the concept of causality refers uniquely to the properties of the fluid as embedded

<sup>15</sup>The domain of dependence and the Cauchy data are often (and easily) confused. Note that the first one refers to a portion of the  $t = 0$  hypersurface, while the second one represents the actual initial solution  $u_0$  specified on this portion.

in a causally connected spacetime, thus leading to the presence of a double-cone structure, in which the *sound cone* is always contained within the *light cone* (see Fig. 1.1). Furthermore, this description of causality based on the fluid characteristic speeds applies unmodified also to a Newtonian description of the fluid, despite the fact that the propagation speeds of Newtonian gravitational perturbations can be unbounded.

### 4.3 Linear hydrodynamic waves

#### 4.3.1 Sound waves

We have seen in Section 2.4 that for any equation of state it is possible to define the *sound speed* as  $c_s^2 := (\partial p / \partial e)_s$  [cf., Eq. (2.168)], but we have treated such a definition mostly as a relation among thermodynamic quantities. We have also seen in Section 4.1 that, when considering the eigenvalues for the relativistic-hydrodynamic equations relative to a one-dimensional fluid flow, these correspond to the relativistic velocity-composition expression of the fluid velocity and of the sound speed [cf., Eq. (4.25)]. We have knowledgeably named the corresponding waves as *acoustic waves*. We will now show that, consistently with the previous definitions, the sound speed is effectively the velocity at which linear perturbations in a uniform fluid propagate.

Consider therefore a stationary and uniform perfect fluid in a flat spacetime and obeying the special-relativistic laws of conservation of energy and momentum (3.53)<sup>16</sup>

$$\nabla_\mu T^{\mu\nu} = 0. \quad (4.78)$$

Assuming for simplicity that the flow is one-dimensional (*i.e.*, for  $\mu = 0, 1$ ), we rewrite Eqs. (4.78) in a Cartesian coordinate system as

$$\partial_t [(e + pv^2) W^2] + \partial_x [(e + p) W^2 v] = 0, \quad (4.79)$$

$$\partial_t [(e + p) W^2 v] + \partial_x [(ev^2 + p) W^2] = 0, \quad (4.80)$$

where  $u^\mu = W(1, v)$  and  $W = (1 - v^2)^{-1/2}$  is the familiar Lorentz factor. If  $e_0, p_0$  and  $v_0 = 0$  are, respectively, the energy density, the pressure and the velocity of the unperturbed fluid (for simplicity we are assuming that the fluid is at rest), we can then introduce perturbations of the type

$$e = e_0 + \delta e, \quad p = p_0 + \delta p, \quad v = v_0 + \delta v = \delta v, \quad (4.81)$$

where we have truncated to first order in the perturbation since we are interested in the *linear* regime of the hydrodynamic equations. Substituting Eqs. (4.81) in the conservation equations (4.79) we can rewrite them as

$$\partial_t(\delta e) + (e_0 + p_0)\partial_x(\delta v) = 0, \quad (4.82)$$

<sup>16</sup>We use the covariant derivative in Eq. (4.78) to allow for coordinates that are not Cartesian.

$$\partial_t(\delta v) + \frac{1}{(e_0 + p_0)} \partial_x(\delta p) = 0, \quad (4.83)$$

where  $\partial_t e_0 = 0 = \partial_x e_0$  and  $\partial_t p_0 = 0 = \partial_x p_0$  since the unperturbed fluid is stationary and uniform. Taking a time derivative of (4.82) and a space derivative of (4.83), it is then possible to combine them into the wave equation

$$\partial_t^2(\delta e) - c_s^2 \partial_x^2(\delta e) = 0, \quad (4.84)$$

where we have used the result that  $c_s^2 = \delta p / \delta e$  since the fluid is perfect and hence adiabatic, with the specific entropy conserved along fluidlines [*cf.* Eq. (3.61)]. Equation (4.84) (a similar equation can be written in terms of  $\delta p$ ) represents our desired result: it states that, independently of the equation of state considered, perturbations in a uniform fluid satisfy a wave equation and propagate at the speed of sound. These are therefore *acoustic* or *sound waves*

## 4.4 Nonlinear hydrodynamic waves

### 4.4.1 Simple waves and discontinuous waves

In Section 4.2.2 we have defined simple waves as smooth solutions of the hydrodynamic equations of the type  $\mathbf{U} = \mathbf{U}(\varphi(x, t))$ . Moreover, we have also shown that simple waves are always associated to a single eigenvalue, for which some quantities of the flow, *i.e.*, the Riemann invariants, are conserved along the corresponding integral curves. Indeed, simple waves in one-dimensional flows are quite generically characterised by having two of the three Riemann invariants that are constant in space and time (Anile *et al.*, 1983).

Note however that the existence of Riemann invariants is a necessary but not sufficient condition for the presence of a simple wave. Stated differently, there are Riemann invariants even in the case of non-smooth solutions which we will encounter, for instance, in the case of a contact discontinuity (see Section 4.4.4). At the same time, the study of the inviscid Burgers equation in Section 4.2.3 has revealed how a quasi-linear hyperbolic equation can have characteristics that converge into caustics and thus lead to nonlinear steepening of the data which is initially smooth. Both of these two basic properties of one-dimensional flows lead us to the definition of the two building blocks of a generic perfect-fluid flow, namely, *simple waves* and *discontinuous waves*.

A theorem by Friedrichs states that “any one-dimensional smooth solution neighbouring a constant state must be a simple wave” (Courant and Hilbert, 1962; Anile, 1989). In other words, simple waves are solutions (often exact) of quasi-linear equations representing travelling waves and can be considered as the nonlinear analogue of the linear sound waves discussed in Section 4.3.1. These regions are always adjacent to a flow region of constant state. Examples of simple waves are compression or *rarefaction waves*, and we have already discussed one such wave when deriving the solution (4.63), while a more detailed discussion of rarefaction waves will be made in the following Section 4.4.2. A systematic investigation of relativistic simple waves and of their literature can be found in the book of Anile (1989).

Similarly, a *discontinuous wave* (or *discontinuity surface*) is defined as a region of the flow in which some of the fluid properties (*e.g.*, velocity, rest-mass density, energy) can be non-continuous across a surface of infinitesimal width. It is of utmost importance to emphasise that this concept of “discontinuity” is just a *shortcoming* of our fluid description on sufficiently small length-scales. From a microscopical (kinetic) point of view, in fact, the physical properties across a hydrodynamic discontinuity surface are perfectly continuous, although they experience very large gradients over extremely short length-scales. Within these regions, they are subject to complex irreversible thermodynamic processes caused by dissipation and heat conduction. However, outside those regions, the flow is much more regular and is usually governed by the standard laws of adiabatic reversible hydrodynamics.

At the same time, the use of discontinuities provides us with a very convenient mathematical *simplification* as it does not require a complex description of these large gradients, but, rather, provides us with the handy tool of the *junction conditions*, which greatly simplify the problem (see Section 4.4.3). This approximation is extremely good under the following two conditions:

- (i) when the discontinuity front has a constant width  $\Delta_s$  which is of the order of the mean free path of the particles in the fluid and much smaller than the typical length-scale for the variation of the flow variables away from the discontinuity, *i.e.*,

$$\Delta_s \approx \ell_{\text{mfp}} \ll \frac{\phi}{\partial_x \phi}, \quad (4.85)$$

where again  $\ell_{\text{mfp}}$  is the mean free path and  $\phi$  is a representative scalar property of the fluid;

- (ii) when the dissipative (*i.e.*, either radiative or viscous) time-scale  $\tau$  is much shorter than the one set by the motion of the front, namely, when

$$\tau \ll \frac{\phi}{\partial_t \phi}. \quad (4.86)$$

When the conditions (4.85)–(4.86) are not satisfied, the use of discontinuous waves in hydrodynamic flows is dubious if not incorrect.

Broadly speaking, discontinuous waves can be distinguished in *contact waves*, which are surfaces separating two parts of a fluid without any flow through the surface, and in *shock fronts* and *reaction fronts*, which are instead discontinuity surfaces that are crossed by a fluid flow. As far as the terminology is concerned, we here follow the convention of Landau and Lifshitz (1980) and denote by “discontinuous wave” just the discontinuity *surface*, so that “wave” and “front” become equivalent terms for us. Other authors, however [*e.g.*, Courant and Friedrichs (1976)] call a “discontinuous wave” the flow *region* comprising the discontinuity surface and its downstream flow.

In the following sections we will review the main aspects of the relativistic theory of hydrodynamic waves first developed by Taub (1948). In the rest of the chapter we will limit the analysis to a perfect *test fluid* in a flat spacetime and to flows that are one-dimensional in the  $x$ -direction of a Cartesian coordinate system. This choice is merely due to simplicity and the analysis of relativistic nonlinear waves reported below can be easily generalised not only to a general curved spacetime, but also to any metric theory of gravity admitting local

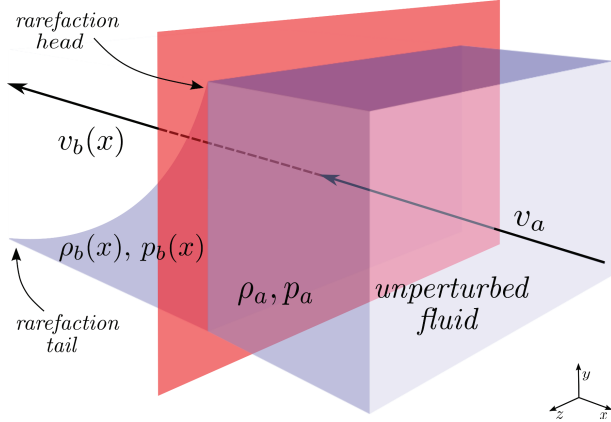


**Fig. 4.4** Schematic representation of the fluid properties  $p$  and  $\rho$  as measured in a frame comoving with the head of a rarefaction wave, for a right-propagating rarefaction wave.

Lorentz frames in which the non-gravitational laws of physics assume their standard special-relativistic form. There is only one circumstance in which the general-relativistic treatment of the junction conditions across a discontinuity surface needs particular care and this happens when there is a phase interface which has intrinsic physical properties (*e.g.*, surface energy or surface tension). In this case the discontinuity surface becomes a *singular hypersurface* and its influence on the local curvature of spacetime should be taken into account through the Gauss–Codazzi equations. We will discuss this case in detail in Section 4.9.

#### 4.4.2 Rarefaction waves

Rarefaction waves are simple waves characterised by the fact that the pressure and rest-mass density of the fluid decrease in the region where the wave propagates. Being simple waves, they are adjacent to a region of constant state and their Riemann invariants are those associated with the sonic eigenvalues, namely  $s = \text{const.}$  and  $\mathcal{J}_\pm = \text{const.}$ , which are all conserved across the wave (see Section 4.2.2). As a result, rarefaction waves are isentropic solutions. They have a *head*, which represents the portion of the wave propagating at the largest velocity in the unperturbed medium, and a *tail*, which represents instead the portion of the wave propagating at the smallest velocity. A schematic representation of the profiles of the pressure and rest-mass density is shown in Fig. 4.4, as measured in a frame comoving with the head of a right-propagating rarefaction wave.

An important property of simple waves in general, and of rarefaction waves in particular, is that they can be written in a *self-similar* form. While we postpone an extended analysis of self-similar motion to Section 11.1, it is sufficient to recall here that in a one-dimensional self-similar solution all of the fluid quantities depend on  $x$  and  $t$  through the *similarity variable*  $\xi := x/t$ .

To derive the properties of rarefaction waves we assume a four-velocity  $u^\mu = W(1, v, 0, 0)$ , where, as usual,  $W$  is the Lorentz factor of the flow, so that the continuity and the momentum equations (3.52) and (3.55) can be written as

$$\partial_t(\rho W) + \partial_x(\rho W v) = 0, \quad (4.87)$$

$$W\partial_t(Wv) + Wv\partial_x(Wv) = -\frac{1}{\rho h} [\partial_x p + W^2 v \partial_t p + W^2 v^2 \partial_x p]. \quad (4.88)$$

We now express the partial derivatives in terms of the similarity variable as

$$\partial_t = -\left(\frac{\xi}{t}\right)\frac{d}{d\xi}, \quad \partial_x = \left(\frac{1}{t}\right)\frac{d}{d\xi}, \quad (4.89)$$

so that we can write the adiabaticity condition (3.61) as

$$(v - \xi)\frac{ds}{d\xi} = 0, \quad (4.90)$$

and the conservation equations (4.87)–(4.88) as

$$(v - \xi)\frac{d\rho}{d\xi} + \rho[W^2 v(v - \xi) + 1]\frac{dv}{d\xi} = 0, \quad (4.91)$$

$$\rho h W^2(v - \xi)\frac{dv}{d\xi} + (1 - v\xi)\frac{dp}{d\xi} = 0. \quad (4.92)$$

The energy-conservation equation, on the other hand, can be derived trivially from the first law of thermodynamics in the case of isentropic flows and is written as [*cf.*, Eq. (2.172)]

$$\frac{dp}{d\xi} = hc_s^2 \frac{d\rho}{d\xi}. \quad (4.93)$$

The self-similar solution is obtained after imposing the condition that the determinant of the system (4.91)–(4.93) vanishes, which gives the following expression for the local sound speed within the rarefaction wave, from the tail to the head, *i.e.*,

$$c_s^2 = \left(\frac{v - \xi}{1 - v\xi}\right)^2 \implies c_s = \left|\frac{v - \xi}{1 - v\xi}\right| = \frac{|v - \xi|}{1 - v\xi} = \pm \frac{v - \xi}{1 - v\xi}. \quad (4.94)$$

The plus sign is chosen for the case in which  $v > \xi$ , hence when the rarefaction wave propagates to the left with respect to the fluid, *i.e.*, a left-propagating wave, and which we will hereafter indicate as “ $\mathcal{R}_-$ ”. Similarly, the minus sign corresponds to the rarefaction wave propagating to the right relative to the fluid, *i.e.*, a right-propagating wave, which we will indicate as “ $\mathcal{R}_+$ ”. Expression (4.94) can be inverted to express the similarity variable across the rarefaction wave as

$$\xi = \frac{v \mp c_s}{1 \mp vc_s}, \quad (4.95)$$

and hence the speeds at which the head and the tail move. Note that in (4.95) the minus and plus signs have the opposite meaning to that in (4.94). As an example, if the unperturbed fluid is at rest, *i.e.*,  $v = 0$ , then the head of the rarefaction will be moving at the sound speed, *i.e.*,  $\xi_{\text{head}} = \mp c_s$ , where the minus and plus signs refer to waves propagating to the left and to the right, respectively. Similarly, if  $\bar{v} \neq 0$  is the velocity of the fluid after it has crossed the rarefaction wave, then the tail of the rarefaction will have speed  $\xi_{\text{tail}} = (\bar{v} \mp c_s)/(1 \mp \bar{v}c_s)$ .

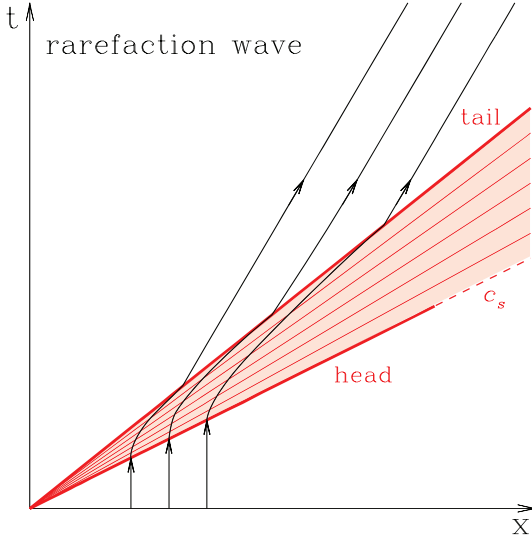


**Fig. 4.5** Fluidlines in an Eulerian frame of representative fluid elements across a right-propagating rarefaction wave. Indicated are the head, the tail (thick red solid lines) and the simple wave between the two, with characteristics indicated with thin solid lines. Note that the separation of the fluid elements increases across the rarefaction, that the characteristics are straight lines, and that the head of the rarefaction moves at the speed of sound (red dashed line) since the unperturbed fluid is at rest. Note also that the axes are not to scale and it is only the relative differences in the slopes that matters here.

Figure 4.5 shows the fluidlines in an Eulerian frame of representative fluid elements across a right-propagating rarefaction wave. The head and tail of the rarefaction are indicated with thick red solid lines, while characteristics (which are straight lines) in the simple wave between the two are shown with thinner lines. Note that the separation of the fluid elements increases across the rarefaction and that the head of the rarefaction moves at the speed of sound (red dashed line) since the unperturbed fluid is at rest. It is worth remarking that the slopes in the  $(t, x)$  plane do not represent realistic speeds and that it is only the relative differences in the slopes that matters.

We can further manipulate the system (4.91)–(4.93) to find an expression involving only differentials [*cf.* Eq. (4.55)], *i.e.*,

$$W^2 dv \pm \frac{c_s}{\rho} d\rho = 0. \quad (4.96)$$

The integration of (4.96), which we have already encountered in Section 4.2.1 [*cf.* Eq. 4.60], leads to the *Riemann invariant*

$$\mathcal{J}_\pm = \frac{1}{2} \ln \left( \frac{1+v}{1-v} \right) \pm \int \frac{c_s}{\rho} d\rho = \text{const.}, \quad (4.97)$$

which is of course conserved across the rarefaction wave. In the specific case when the equation of state is of polytropic type,  $p = K\rho^\Gamma$  [*cf.* Eq. (2.242)], Eq. (4.97) can be rewritten as

$$\left(\frac{1+v}{1-v}\right) \left[\frac{(\Gamma-1)^{1/2} + c_s}{(\Gamma-1)^{1/2} - c_s}\right]^{\pm 2/(\Gamma-1)^{1/2}} = \text{const.}, \quad (4.98)$$

which, in turn, allows us to express the flow velocity behind the head of the rarefaction  $v_b(x)$  as a function of pressure there,  $p_b(x)$  (hereafter we will use the indices “ $a$ ” and “ $b$ ” to represent quantities on either side of a wave), *i.e.*,

$$v_b(x) = \frac{(1+v_a)A_{\pm}(p_b) - (1-v_a)}{(1+v_a)A_{\pm}(p_b) + (1-v_a)}, \quad (4.99)$$

where  $v_a = \text{const.}$  is the velocity in the unperturbed fluid and the quantity  $A_{\pm}(p)$  in (4.99) is defined as (Martí and Müller, 1994)

$$A_{\pm}(p) := \left\{ \left[ \frac{(\Gamma-1)^{1/2} - c_s(p)}{(\Gamma-1)^{1/2} + c_s(p)} \right] \left[ \frac{(\Gamma-1)^{1/2} + c_s(p_a)}{(\Gamma-1)^{1/2} - c_s(p_a)} \right] \right\}^{\pm 2/(\Gamma-1)^{1/2}}. \quad (4.100)$$

The calculation of the pressure behind the rarefaction’s head,  $p_b(x)$ , will require the solution of a Riemann problem, and we will get back to this in Section 4.5. We can now use expression (4.99) to write a Lorentz-invariant expression for the relative velocity across a rarefaction wave (*i.e.*, the relative velocity of the fluid “ahead of the head” and “behind the tail” of the rarefaction wave), which will turn out to be useful when discussing the solution of the Riemann problem in Section 4.5

$$v_{ab} = \frac{v_a - v_b}{1 - v_a v_b} = \frac{1 - A_{\pm}(p_b)}{1 + A_{\pm}(p_b)}. \quad (4.101)$$

#### 4.4.3 Shock waves

Discontinuous waves, such as *shocks waves*, can form from compressive motions even from initially smooth data. After introducing a local Lorentz frame comoving with the shock front, we can think of it as a planar discontinuity surface which divides the three-space into a region *ahead* of the shock (or *upstream*), from which the fluid enters the shock front, and a region *behind* the shock (or *downstream*), in which the fluid moves away from the shock front. This is reported schematically in Fig. 4.6, which shows the fluid properties  $p$ ,  $\rho$  and  $v$  as measured in the shock frame for a right-propagating shock wave.

As also anticipated above, the presence of the discontinuity prevents the use of relativistic-hydrodynamic equations (2.118) and (2.119) at the shock location, which can however be replaced by suitable *junction conditions*, the so-called relativistic *Rankine–Hugoniot conditions*.

These are simple algebraic expressions that involve quantities on both sides of the shock and that ensure the conservation of rest mass, energy and momentum across the discontinuity. Deriving such conditions in covariant form is particularly simple and can be done as follows. We first rewrite Eqs. (2.118)–(2.119) in the equivalent forms

$$\nabla_{\mu}(\rho u^{\mu} f) = \rho u^{\mu} \nabla_{\mu} f, \quad (4.102)$$

$$\nabla_{\mu}(T^{\mu\nu} \lambda_{\nu}) = T^{\mu\nu} \nabla_{\mu} \lambda_{\nu}, \quad (4.103)$$

where  $f$  and  $\lambda_{\mu}$  are an arbitrary function and vector field, respectively. Next, we integrate Eqs. (4.102)–(4.103) over an arbitrary four-dimensional volume  $\mathcal{V}$  comprising the hypersurface  $\Sigma$

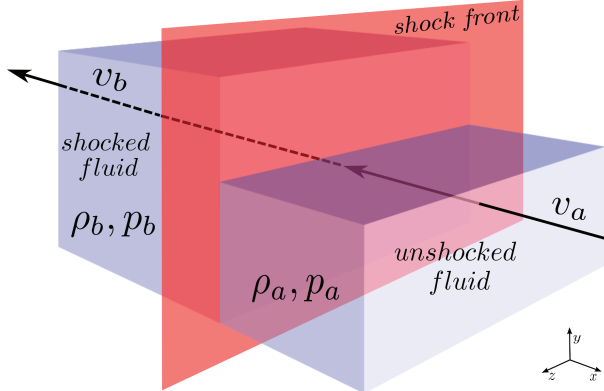


**Fig. 4.6** Schematic representation of the fluid properties,  $p$ ,  $\rho$  and  $v$  as measured in the shock frame for a right-propagating shock wave.

which is the history of a two-dimensional spacelike surface representing the shock front. This is possible even if there are discontinuities of the fluid variables across  $\Sigma$ . By doing so, and after applying Stokes' theorem, we obtain

$$\int_{\mathcal{V}} \nabla_\mu (\rho u^\mu f) d^4x = \int_{\mathcal{V}} \rho u^\mu \nabla_\mu f d^4x = \oint_{\mathcal{S}} \rho u^\mu f n_\mu dV, \quad (4.104)$$

$$\int_{\mathcal{V}} \nabla_\mu (T^{\mu\nu} \lambda_\nu) d^4x = \int_{\mathcal{V}} T^{\mu\nu} \nabla_\mu \lambda_\nu d^4x = \oint_{\mathcal{S}} T^{\mu\nu} \lambda_\nu n_\mu dV, \quad (4.105)$$

where the surface integrals are performed over the closed hypersurface  $\mathcal{S}$  with unit spacelike normal  $n_\mu$  enclosing the four-dimensional volume  $\mathcal{V}$ . Let us now focus on the second equalities in (4.104) and (4.105) and consider the limit in which the four-dimensional volume  $\mathcal{V}$  shrinks to zero while comprising a portion  $\Sigma'$  of the three-dimensional worldtube relative to the shock front. In this limit, the four-dimensional volume integrals in (4.104) and (4.105) vanish, while the surface integrals reduce to the computation of the integrand on both sides of the shock front, namely,

$$\int_{\Sigma'} f [\rho u^\mu] n_\mu dV = 0, \quad (4.106)$$

$$\int_{\Sigma'} \lambda_\mu [T^{\mu\nu}] n_\nu dV = 0, \quad (4.107)$$

where we have introduced the *double-bracket notation* (see Problem 6 for some identities of the double brackets)

$$[Q] := Q_a - Q_b, \quad (4.108)$$

to denote the jump of the generic quantity  $Q$  across the shock front. Given the arbitrariness of both  $f$  and  $\lambda_\mu$  in (4.106) and (4.107), they can be satisfied only if

$$[\![\rho u^\mu]\!] n_\mu = 0, \quad (4.109)$$

$$[\![T^{\mu\nu}]\!] n_\nu = 0, \quad (4.110)$$

which represent therefore the relativistic *Rankine–Hugoniot junction conditions* (or *jump conditions*) across the shock front. Additional conditions can be obtained to express the jumps across the shock of first- and second-order derivatives of the energy–momentum tensor, *i.e.*, of the quantities  $[\![\nabla_\mu T_\beta^\alpha]\!]$  and  $[\![\nabla_\mu \nabla_\nu T_\beta^\alpha]\!]$ , which are referred to as the first-order and second-order *compatibility conditions*. We will not make use of such expressions here, but the interested reader will find a detailed discussion of their properties in Anile (1989).

Evaluating Eqs. (4.109)–(4.110) in the shock-front rest frame, where  $n_\mu = (0, 1, 0, 0)$ , they take the form

$$\rho_a u_a^x = \rho_b u_b^x, \quad T_a^{xx} = T_b^{xx}, \quad T_a^{tx} = T_b^{tx}, \quad (4.111)$$

or, equivalently,

$$J := \rho_a W_a v_a = \rho_b W_b v_b, \quad (4.112)$$

$$\rho_a h_a W_a^2 v_a^2 + p_a = \rho_b h_b W_b^2 v_b^2 + p_b, \quad (4.113)$$

$$\rho_a h_a W_a^2 v_a = \rho_b h_b W_b^2 v_b, \quad (4.114)$$

where  $J$  is also referred to as the relativistic *mass flux*. It is also convenient to rewrite the continuity equation (4.112) and the conservation of energy (4.113) as a single expression involving the mass flux across the shock front, *i.e.*,

$$[\![J^2]\!] = 0, \quad J^2 = - \frac{[\![p]\!]}{[\![h/\rho]\!]}. \quad (4.115)$$

Similarly, by using the continuity equation (4.112), we can rewrite the conservation of momentum (4.114) as

$$[\![hW]\!] = 0. \quad (4.116)$$

Multiplying now Eq. (4.115) by  $(h_a/\rho_a + h_b/\rho_b)$  and combining it with (4.112) we obtain

$$(h_b W_b v_b)^2 - (h_a W_a v_a)^2 = - \left( \frac{h_a}{\rho_a} + \frac{h_b}{\rho_b} \right) [\![p]\!]. \quad (4.117)$$

We then take the square of expression (4.116) and subtract it from (4.117) to obtain the expression for the *Taub adiabat*

$$[\![h^2]\!] = \left( \frac{h_a}{\rho_a} + \frac{h_b}{\rho_b} \right) [\![p]\!], \quad (4.118)$$

which represents the relativistic generalisation of the classical *Hugoniot adiabat* for Newtonian shock fronts. Equations (4.112), (4.115) and (4.118) are collectively referred to as *Taub's junction conditions* for shock waves and are the relativistic generalisation of the corresponding Rankine–Hugoniot junction conditions for Newtonian shocks (Courant and Friedrichs, 1976).

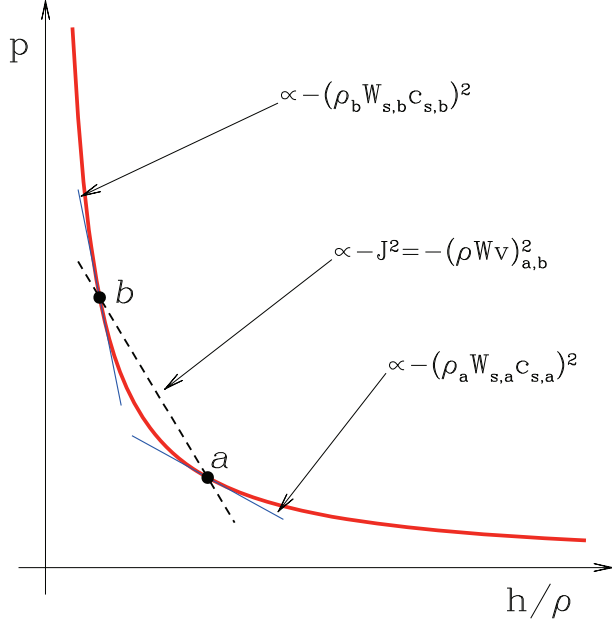


**Fig. 4.7** Schematic representation of the Taub adiabat in the  $(p, h/\rho)$  plane (red solid line).  $a$  and  $b$  represent the states ahead and behind the shock and the slope of the chord between the two is proportional to the mass flux across the shock. Similarly, the slope of the adiabat at the two states is proportional to the local sound speed, which will be clearly larger for shocked states that have larger pressures and densities.

The classical Hugoniot adiabat is readily obtained from (4.118) after recalling that in the Newtonian limit  $h_N = 1 + \epsilon + p/\rho \approx 1$  [cf., Eq. (2.147)], and that  $\llbracket h^2 \rrbracket \approx 2 \llbracket \epsilon + p/\rho \rrbracket$ , so that the Newtonian limit of the Taub adiabat (4.118) is given by

$$\left[ \left[ \epsilon + \frac{p}{\rho} \right] \right] = \frac{1}{2} \left( \frac{1}{\rho_a} + \frac{1}{\rho_b} \right) \llbracket p \rrbracket , \quad (4.119)$$

and obviously coincides with the Hugoniot adiabat (Landau and Lifshitz, 1980).

When considered in the  $(p, h/\rho)$  plane, the Taub adiabat provides a simple and graphical representation of the fluid properties across a shock. In this plane, in fact, the *Taub adiabat* can be seen as the curve that joins the states ahead and behind a shock wave, as shown in Fig. 4.7. Once the state “ $a$ ” of the fluid ahead of the front is assigned in terms of a pressure  $p_a$  and of the ratio  $h_a/\rho_a$ , the condition (4.118) constrains the allowed states of the fluid in the shocked region “ $b$ ” to lie on the adiabat. In analogy with the corresponding Newtonian result (Landau and Lifshitz, 1980), the chord joining the two states is proportional to the square of the mass flux, so that for the same initial state  $a$ , a new state  $b$  at larger pressure will also be accompanied by a larger mass flux across the shock [cf., Eq. (4.115) and see Fig. 4.7]. Note also that from the definition of the sound speed

$$c_s^2 := \left( \frac{\partial p}{\partial e} \right)_s , \quad (2.168)$$

and recalling that for isentropic transformations  $de = hd\rho$  [cf., Eqs. (2.143) and (2.172)], we obtain

$$\frac{dp}{d(h/\rho)} = -\frac{\rho^2 c_s^2}{1 - c_s^2} = -\rho^2 W_s^2 c_s^2 , \quad (4.120)$$

where  $W_s^2 := (1 - c_s^2)^{-1}$ . Equation (4.120) shows that the slope at any point on the Taub adiabat is necessarily negative and that it is proportional to the local sound speed, which, in turn, will be larger for shocked states that have larger pressures and densities (see Fig. 4.7).

As a concrete example of how to use Taub's adiabat, we can consider an ideal-fluid equation of state, so that the pressure and rest-mass density can be related as (see Section 2.4.6)

$$\rho = \frac{\gamma p}{(\gamma - 1)(h - 1)} . \quad (4.121)$$

Using the adiabat (4.118), it is easy to show that the specific enthalpy in the shocked region,  $h_b$ , can be computed as a function of  $p_b$  after solving the quadratic equation

$$\left[ 1 + \frac{(\gamma - 1)p_a}{p_b} \right] h_b^2 - \frac{(\gamma - 1) \llbracket p \rrbracket}{p_b} h_b - \frac{(\gamma - 1) \llbracket p \rrbracket}{p_a} h_a - \left[ 1 + \frac{(\gamma - 1)p_b}{p_a} \right] h_a^2 = 0 . \quad (4.122)$$

Another important curve in the  $(p, h/\rho)$  plane is represented by the *Poisson adiabat*, which is instead the curve of constant entropy connecting  $(p_a, h_a/\rho_a)$  and  $(p_b, h_b/\rho_b)$ . It is possible to show that the Poisson and the Taub adiabat through a given state have the same first and second derivatives at that state [see Thorne (1973) for a proof and Fig. 4.8 for a graphical representation for a convex equation of state] and that, apart from non-convex equations of state (see Section 2.4), the second derivative of the Taub adiabat is always positive (Ibáñez *et al.*, 2012b). Moreover, for *weak shocks* (or *weak discontinuities*), that is, for discontinuities in which the states ahead and behind the shock are not very different,<sup>17</sup> the jumps in the specific entropy and in the pressure scale according to (Thorne, 1973)

$$\llbracket s \rrbracket = \left[ \frac{1}{12hT} \left( \frac{\partial^2(h/\rho)}{\partial p^2} \right)_s \right]_a \llbracket p \rrbracket^3 + \mathcal{O}(\llbracket p \rrbracket^4) . \quad (4.123)$$

The importance of Eq. (4.123) rests on the fact that, although only slightly, the entropy across a shock must change. Because the second law of thermodynamics requires that this change can only be an increase, we obtain a fundamental relation for shock waves, *i.e.*,

$$s_b > s_a . \quad (4.124)$$

The inequality (4.124) reflects the complex irreversible processes that take place in the small region of the shock front and allows one to exclude as unphysical those shocks which do not

<sup>17</sup>Loosely speaking, the flow across a weak discontinuity is continuous but has derivatives of some order which are not continuous.

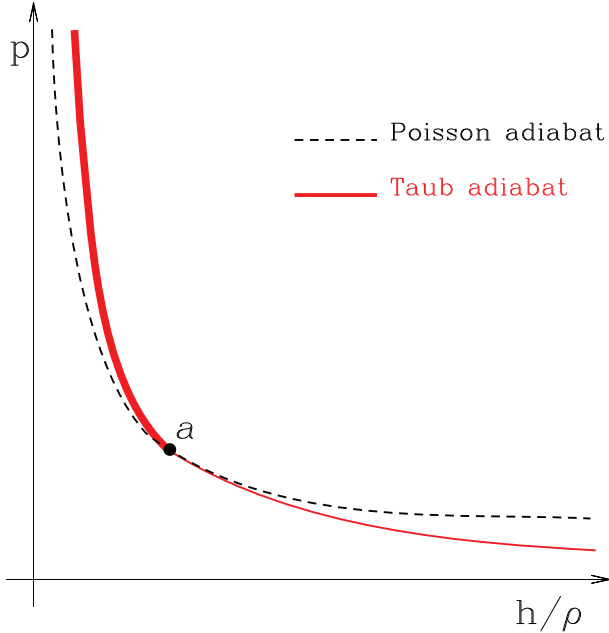


**Fig. 4.8** Schematic representation of the Taub adiabat (solid line) and of the Poisson adiabat (red dashed line) in the  $(p, h/\rho)$  plane. The two adiabats have the same second derivatives at the initial state  $a$ . Because entropy must increase across the shock, the Poisson adiabat selects the upper branch of the Taub adiabat as the physical one (thick red solid line).

produce an entropy increase. Using now expressions (4.123) and (4.124) we can deduce that also the pressure has to increase across the shock, *i.e.*,

$$p_b > p_a, \quad (4.125)$$

or, equivalently, that the state  $b$  must be above the state  $a$  on the  $(p, h/\rho)$  plane. When combined, the conditions (4.124) and (4.125) state that the Poisson adiabat selects the “physical” branch of the Taub adiabat as the one that always lies above the constant-entropy curve (see Fig. 4.8).

Combining now Eqs. (4.118) and (4.125) we also deduce that

$$h_b > h_a, \quad (4.126)$$

and since  $h_a/\rho_a > h_b/\rho_b$ , we can conclude that the rest-mass density must increase even more than  $h$  increases, namely

$$\rho_b > \rho_a. \quad (4.127)$$

An important piece of information that can be extracted from the study of the Taub adiabat is given by the magnitudes of the flow velocities on either side of the shock and how they

compare with the local sound speeds. First, we note that making use of the momentum equation (4.113) and of the conditions (4.125)–(4.127) we deduce that the modulus of the velocity across the shock must decrease, *i.e.*,

$$|v_b| < |v_a|. \quad (4.128)$$

Furthermore, using (4.120) together with the condition (4.128), it is easy to show that the flow entering a shock front is always *supersonic* and, similarly, that the flow out of it is necessarily *subsonic*,<sup>18</sup> *i.e.*,

$$v_a \geq c_{sa} \quad (\propto \text{tangent at } a), \quad (4.129)$$

$$v_b \leq c_{sb} \quad (\propto \text{tangent at } b), \quad (4.130)$$

where  $c_{sa}$  and  $c_{sb}$  are the sound speeds ahead and behind the shock, respectively.

To summarise, across a shock, the following must happen: *the entropy, the enthalpy, the pressure, and the rest-mass density must increase, while the velocity relative to the shock must decrease*. Furthermore, the flow is *supersonic ahead of the shock and subsonic behind it*, with the *mass flux* and the *entropy jump* increasing for states “further-up” on the physical branch of the Taub adiabat (see Figs. 4.7 and 4.8). The results just found remain valid also for *strong shocks*, for which the jumps in the states ahead and behind the shock can be arbitrarily large. A comprehensive analysis of the properties of strong shocks can be found in Lichnerowicz (1967).

A spacetime representation of a shock is shown in Fig. 4.9, which reports in an Eulerian frame the fluidlines of representative fluid elements across a right-propagating supersonic shock wave. Indicated are the shock front (thick red solid line) and the sound speed (red dashed line). Note that the separation of the fluid elements decreases across the shock as a result of the compression [*cf.* Eq. (4.127)] and that since the unperturbed fluid is at rest, the shock moves at supersonic speed (compare the slope of the shock with that of the sound speed shown as a reference). Also in this case, the axes are not to scale and it is only the relative differences in the slopes that is important.

The junction conditions (4.112)–(4.114) can be manipulated to yield a number of useful relations (see Problem 4). For instance, they can be used to express velocities on either side of the front in terms of the physical state there, *i.e.*,

$$v_a^2 = \frac{(p_a - p_b)(e_b + p_a)}{(e_a - e_b)(e_a + p_b)}, \quad (4.131)$$

$$v_b^2 = \frac{(p_a - p_b)(e_a + p_b)}{(e_a - e_b)(e_b + p_a)}, \quad (4.132)$$

while the relative velocity of the fluid ahead and behind the shock is

$$v_{ab} := \frac{v_a - v_b}{1 - v_a v_b} = \sqrt{\frac{(p_a - p_b)(e_a - e_b)}{(e_a + p_b)(e_b + p_a)}}. \quad (4.133)$$

<sup>18</sup>The proof is even simpler when looking at Fig. 4.7 and comparing the slopes of the tangents at  $a$  and  $b$  with the slope of the chord between  $a$  and  $b$ .

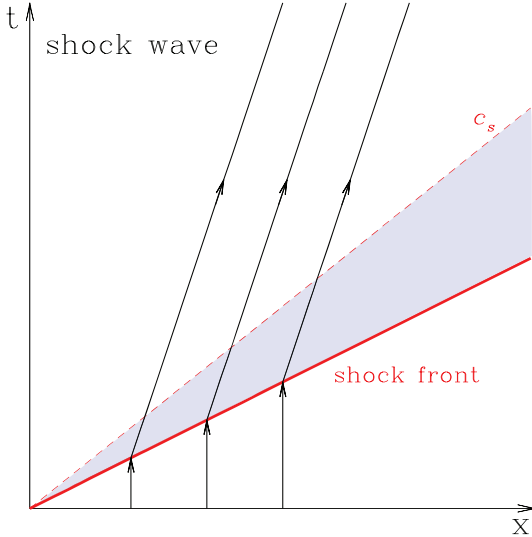


**Fig. 4.9** Fluidlines in an Eulerian frame of representative fluid elements across a right-propagating supersonic shock wave. Indicated are the shock front (thick red solid line) and the sound speed (red dashed line). Note that the separation of the fluid elements decreases across the shock and that since the unperturbed fluid is at rest, the shock moves at supersonic speed. Note that the axes are not to scale and it is only the relative differences in the slopes that matters here.

Similarly, it is possible to compute the ratio of the velocities and their product, *i.e.*,

$$\frac{v_a}{v_b} = \frac{e_b + p_a}{e_a + p_b}, \quad v_a v_b = \frac{p_a - p_b}{e_a - e_b}. \quad (4.134)$$

Expressions (4.134) can be manipulated further in the simpler case of an ultrarelativistic fluid with  $p = e/3$  and  $c_s = 1/\sqrt{3}$  (see Section 2.4.4), so that they become

$$v_a = \left( \frac{3e_b + e_a}{3e_a + e_b} \right) v_b, \quad v_a = \frac{1}{3v_b}, \quad (4.135)$$

while the Lorentz factors relative to  $v_a$  and  $v_b$  in Eqs. (4.135) are given by

$$W_a^2 = \frac{3}{8} \left( \frac{3e_a + e_b}{e_a} \right), \quad (4.136)$$

$$W_b^2 = \frac{3}{8} \left( \frac{3e_b + e_a}{e_b} \right), \quad (4.137)$$

$$W_{ab}^2 = \frac{(3e_a + e_b)(3e_b + e_a)}{16e_1e_2} = \frac{4}{9} W_a^2 W_b^2, \quad (4.138)$$

with the additional property that

$$W_a^2 - 2W_{ab}^2 + W_b^2 = 1. \quad (4.139)$$

Note that once the states ahead and behind the shock are known, it is simple to compute the velocity at which the shock front is actually moving in the Eulerian frame. For this it is

sufficient to bear in mind that the mass flux  $J$  defined in (4.112) is also an invariant under Lorentz boosts in the  $x$ -direction, so that it can be equally expressed as

$$J := \rho_a W_a W_s (V_s - v_a) = \rho_b W_b W_s (V_s - v_b), \quad (4.140)$$

where  $V_s$  is the shock velocity,  $W_s = (1 - V_s^2)^{-1/2}$  the corresponding Lorentz factor, and the velocities  $v_a$ ,  $v_b$  in (4.140) are now also measured in the Eulerian frame. We can therefore invert expression (4.140) to obtain

$$V_s^\pm = \frac{\rho_a^2 W_a^2 v_a \pm |J| \sqrt{J^2 + \rho_a^2}}{\rho_a^2 W_a^2 + J^2}, \quad (4.141)$$

where the  $\pm$  sign refers to shock waves propagating to the right or to the left, respectively, and where  $J$  is given by (4.112), thus involving only quantities that are ahead or behind the shock front. As an example, if  $v_a = 0$ , then  $W_a = 1$  and the shock velocity is simply given by  $V_s^\pm = \rho_b W_b v_b / (\rho_b W_b \pm \rho_a)$  (see Problem 5). Finally, it is instructive to consider the expressions that Eqs. (4.134) and (4.135) assume in the limiting situations of *weak shocks* and of *strong shocks*, respectively. More specifically, for weak shocks  $e_b \sim e_a$  and from (4.135) it is possible to deduce that for an ultrarelativistic fluid

$$v_a \rightarrow c_{sa} = c_s, \quad v_b \rightarrow c_{sb} = c_s, \quad (4.142)$$

that is, an asymptotically weak shock wave tends to a sound wave. On the other hand, in the case of strong shocks with  $e_b \rightarrow \infty$  (*i.e.*, the state  $b$  moves on the diverging part of the Taub adiabat) then expressions (4.135) reveal that

$$v_a \rightarrow 1, \quad v_b \rightarrow \frac{1}{3}. \quad (4.143)$$

Since in the ultrarelativistic case  $c_s \rightarrow 1/\sqrt{3}$ , the ratio  $v_b/c_{sb} \leq 1$ , confirming that the shocked region remains subsonic, even for strong shocks moving at  $V_s \rightarrow 1$ .

#### 4.4.4 Contact discontinuities

Contact discontinuities can be regarded as special cases of shock waves and are characterised by the absence of a mass flux across the discontinuous wave, *i.e.*,  $\llbracket J \rrbracket = 0$ . From the general definition (4.115) it follows that this condition can take place only if  $\llbracket p \rrbracket = 0$ , which, in turn, implies from (4.118) that  $\llbracket h \rrbracket = 0$  and  $\llbracket \rho \rrbracket \neq 0$ . Finally, (4.131) and (4.132) imply that  $\llbracket v \rrbracket = 0$ , namely, that the velocities on either side of the discontinuity front are the same. As a result, *velocity and pressure are continuous across a contact discontinuity, while the rest-mass density is discontinuous*, *i.e.*,

$$\llbracket p \rrbracket = 0 = \llbracket h \rrbracket = \llbracket v \rrbracket, \quad \llbracket \rho \rrbracket \neq 0. \quad (4.144)$$

Contact discontinuities admit (trivial) Riemann invariants, which are given by the pressure and the velocity, as discussed in Section 4.2.2 [*cf.*, (4.58)]. As a concluding remark we note that in multidimensional flows, the contact discontinuity may also have a component of the velocity which is tangential to it and it may be discontinuous across the discontinuity. A more detailed discussion of this point will be presented in Section 4.7.

## 4.5 The Riemann problem

All of the nonlinear waves considered so far appear in the solution of the so-called *Riemann problem*, which consists in determining the flow pattern that develops in the presence of constant and discontinuous initial data. This problem was first addressed by Riemann more than 150 years ago and has become the prototype of the initial-value problem for nonlinear hyperbolic systems of partial differential equations with discontinuous initial conditions (see Section 9.1).

From a mathematical point of view, the Riemann problem for a general nonlinear hyperbolic system, such as the one expressed by (4.9), is an initial-value problem with initial conditions given by

$$\mathbf{U}(x, 0) = \begin{cases} \mathbf{U}_L & \text{if } x < 0, \\ \mathbf{U}_R & \text{if } x > 0, \end{cases} \quad (4.145)$$

where  $\mathbf{U}_L$  and  $\mathbf{U}_R$  are two constant values, named “left” and “right” states, respectively.<sup>19</sup> Depending on the particular set of hyperbolic equations considered, different wave structures will emerge in the solution.

The mathematical definition of the Riemann problem given above also has a direct physical interpretation. Consider, in fact, a fluid filling a tube and consisting of an initial “left” state and an initial “right” state, each having prescribed and different values of uniform pressure, rest-mass density and velocity. The two discontinuous states are initially separated by a planar membrane at position  $x = 0$  at time  $t = 0$ , which is then removed instantaneously. The conclusion reached by Riemann in Newtonian hydrodynamics is that the one-dimensional flow that develops when the barrier is removed will lead to four different and distinct solutions. All of the solutions are composed of nonlinear waves, in the form of either shock waves, rarefaction waves, or contact discontinuities, that propagate in opposite directions and join the two unperturbed left and right states. Schematically, starting from a configuration with a left ( $L$ ) and a right ( $R$ ) state at  $t = 0$ , the fluid solution for any  $t > 0$  can be represented as

$$L \ R, \quad \text{at } t = 0, \quad (4.146)$$

$$L \mathcal{W}_{\leftarrow} L_* \mathcal{C} R_* \mathcal{W}_{\rightarrow} R, \quad \text{at } t > 0, \quad (4.147)$$

where  $\mathcal{W}$  denotes a shock or a rarefaction wave that propagates towards the left ( $\leftarrow$ ) or the right ( $\rightarrow$ ) with respect to the initial discontinuity, while  $L_*$  and  $R_*$  are the new hydrodynamic states that form behind the two waves propagating in opposite directions. These waves are separated by a contact discontinuity  $\mathcal{C}$  and therefore have the same values of the velocity and of the pressure  $p_* = p_{L_*} = p_{R_*}$ , but different values of the rest-mass density.

This is shown schematically in Fig. 4.10, which reports the spacetime diagram, or “*Riemann fan*”, for the evolution of a generic Riemann problem. Shown as areas shaded in red and blue are the unperturbed left and right states,  $L$  and  $R$ , while shown as shaded in light yellow and blue are the new starred states,  $L_*$  and  $R_*$ . Also shown are the three different waves separating these states, namely the left-going wave  $\mathcal{W}_{\leftarrow}$  (red solid line), the contact discontinuity  $\mathcal{C}$  (green dashed line) and the right-going wave  $\mathcal{W}_{\rightarrow}$  (blue solid line).

<sup>19</sup>Expression (4.145) should be compared with the definition of the generalised Riemann problem, Eq. (10.75).

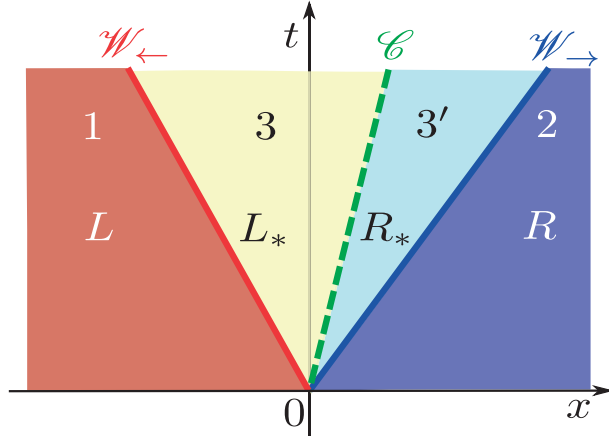


**Fig. 4.10** Spacetime diagram, or “Riemann fan”, of the evolution of a generic Riemann problem from  $L R$  at  $t = 0$  to  $L \mathcal{W}_- L_* \mathcal{C} R_* \mathcal{W}_+ R$  at  $t > 0$ . Shown as shaded areas are the unperturbed left,  $L$  (or 1), and right states,  $R$  (or 2), as well as the new starred states,  $L_*$  (or 3) and  $R_*$  (or 3'). Three different waves separate these states, with  $\mathcal{W}_-$  (red solid line),  $\mathcal{C}$  (green dashed line) and  $\mathcal{W}_+$  (blue solid line) being the left-going wave, the contact discontinuity and the right-going wave, respectively. This figure should be compared with the corresponding one for a generalised Riemann problem, Fig. 10.4.

It should be noted that the generic “three-waves” solution discussed above can be distinguished as three different “wave patterns”

(i) two shock waves, one moving towards the initial left state, and the other towards the initial right state:

$$L \mathcal{S}_- L_* \mathcal{C} R_* \mathcal{S}_+ R, \quad (4.148)$$

or simply  $\mathcal{S}_- \mathcal{C} \mathcal{S}_+$ ;

(ii) one shock wave and one rarefaction wave, the shock moving towards the initial right state, and the rarefaction towards the initial left state or vice versa:

$$L \mathcal{R}_- L_* \mathcal{C} R_* \mathcal{S}_+ R, \quad (4.149)$$

$$L \mathcal{S}_- L_* \mathcal{C} R_* \mathcal{R}_+ R, \quad (4.150)$$

or simply  $\mathcal{R}_- \mathcal{C} \mathcal{S}_+$  and  $\mathcal{S}_- \mathcal{C} \mathcal{R}_+$ ;

(iii) two rarefaction waves, one moving towards the initial left state, and the other towards the initial right state:

$$L \mathcal{R}_- L_* \mathcal{C} R_* \mathcal{R}_+ R, \quad (4.151)$$

or simply  $\mathcal{R}_- \mathcal{C} \mathcal{R}_+$ .

Representative examples of these wave patterns are shown in Fig. 4.11 For each panel, the top part shows the rest-mass density profile (black solid line) at a given time as obtained from the numerical solution of the Riemann problem, while the bottom part reports the corresponding spacetime diagram up to the given time. We note that, because the left and right states in a

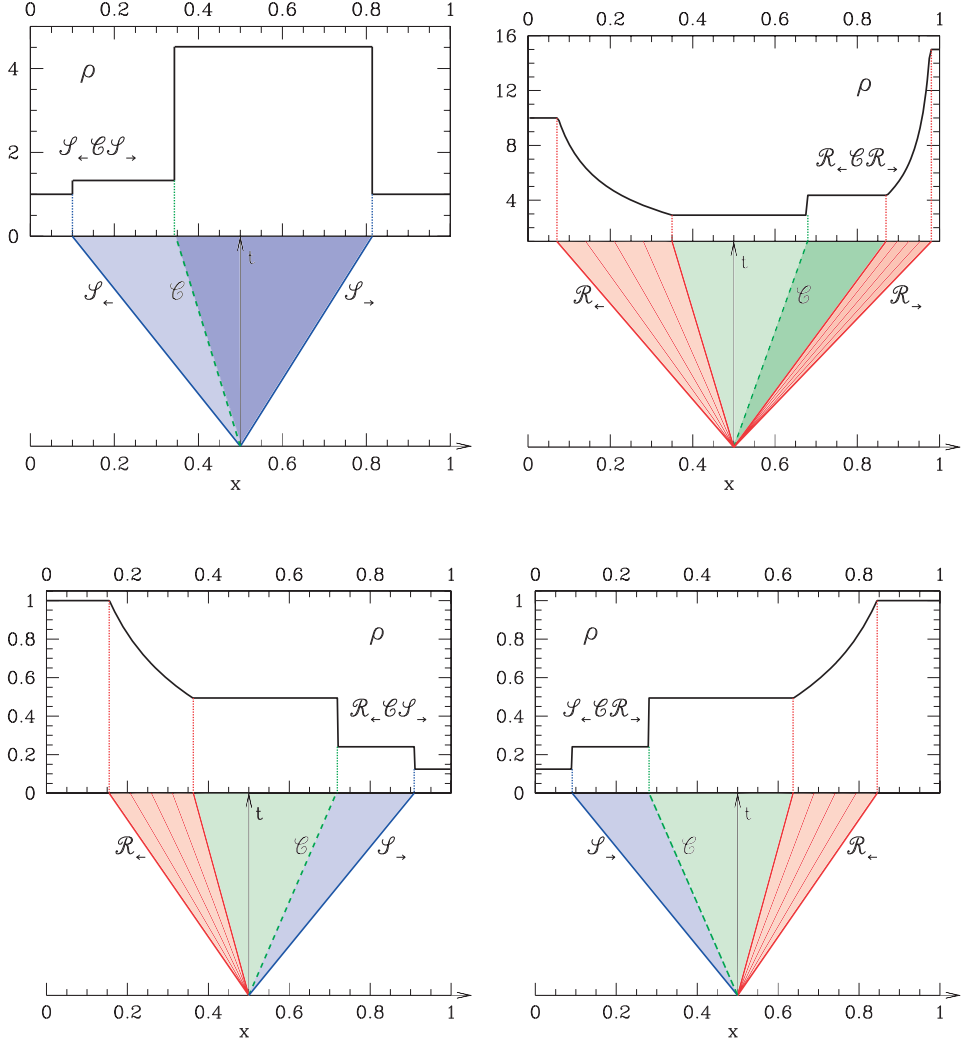


**Fig. 4.11** Examples of the development of a Riemann problem. For each panel, the top part shows the rest-mass density profile (black solid line) at a given time, while the bottom part reports the corresponding spacetime diagram up to the given time. Indicated are the shock fronts  $\mathcal{S}_\rightarrow$ ,  $\mathcal{S}_\leftarrow$  (blue solid lines), the contact discontinuities  $\mathcal{C}$  (green dashed lines), and the rarefaction waves  $\mathcal{R}_\rightarrow$ ,  $\mathcal{R}_\leftarrow$  (red solid lines). The top panels refer to  $\mathcal{S}_\leftarrow \mathcal{C} \mathcal{S}_\rightarrow$  and  $\mathcal{R}_\leftarrow \mathcal{C} \mathcal{R}_\rightarrow$  wave patterns, while the bottom panels refer to  $\mathcal{R}_\leftarrow \mathcal{C} \mathcal{S}_\rightarrow$  and  $\mathcal{S}_\leftarrow \mathcal{C} \mathcal{R}_\rightarrow$  wave patterns (cf., Fig. 4.12).

Riemann problems are constant, the characteristics emerging from  $x = 0.5$  at time  $t = 0$  have constant slopes and are therefore straight lines, even for systems of nonlinear equations such as the relativistic-hydrodynamic equations. Indicated are the shock fronts  $\mathcal{S}_\rightarrow$ ,  $\mathcal{S}_\leftarrow$  (solid blue lines), the contact discontinuities  $\mathcal{C}$  (dashed green lines), and the rarefaction waves  $\mathcal{R}_\rightarrow$ ,  $\mathcal{R}_\leftarrow$  (solid red lines). The top left panel refers to a  $\mathcal{S}_\leftarrow \mathcal{C} \mathcal{S}_\rightarrow$  wave pattern, with initial data

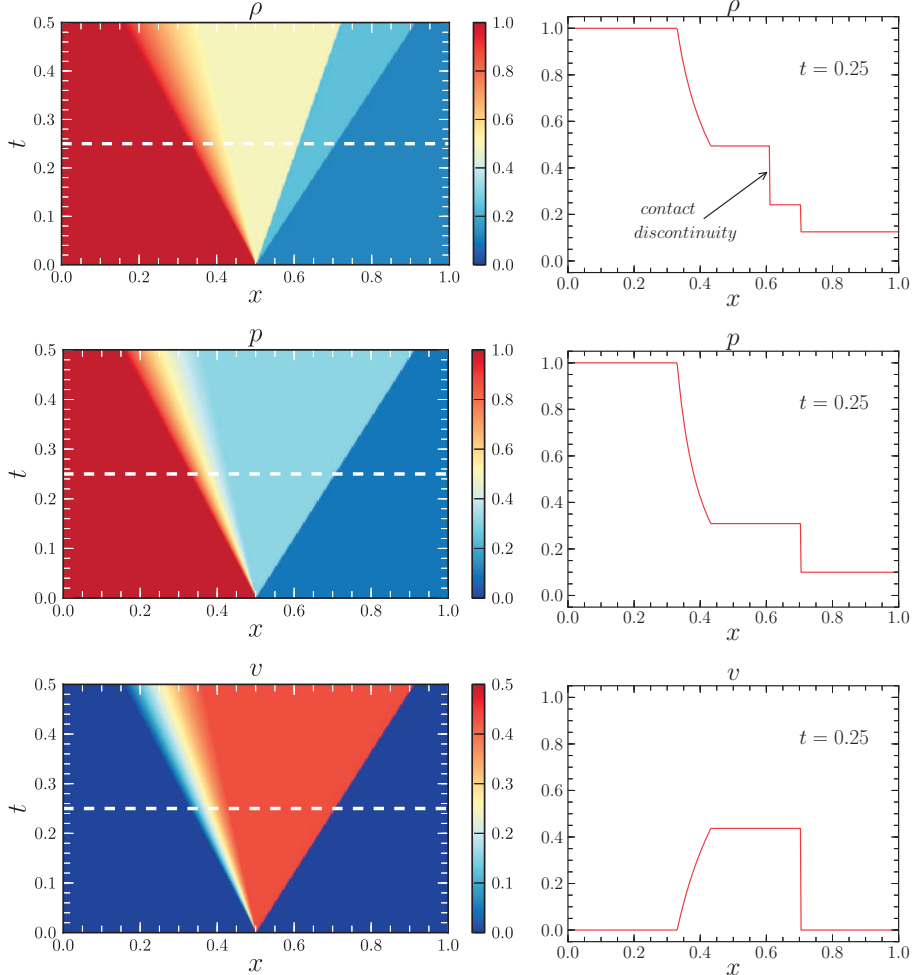


**Fig. 4.12** *Left panels:* Spacetime diagrams for the development of nonlinear waves in the numerical solution of a Riemann problem evolving into a  $\mathcal{R}_\leftarrow \mathcal{C} \mathcal{S}_\rightarrow$  wave pattern (Sod problem, cf., bottom left panel of Fig. 4.11). Shown from the top are the rest-mass density, the pressure and the velocity. *Right panels:* The corresponding profiles at  $t = 0.25$  of the evolution.

$p_L = 10$ ,  $\rho_L = 1$ ,  $v_L = 0$  and  $p_R = 1$ ,  $\rho_R = 1$ ,  $v_R = -0.9$ , while the top right panel refers to a  $\mathcal{R}_\leftarrow \mathcal{C} \mathcal{R}_\rightarrow$  wave pattern, with initial data  $p_L = 10$ ,  $\rho_L = 10$ ,  $v_L = -0.4$  and  $p_R = 10$ ,  $\rho_R = 15$ ,  $v_R = 0.8$ . Similarly, the bottom left panel shows a  $\mathcal{R}_\leftarrow \mathcal{C} \mathcal{S}_\rightarrow$  wave pattern, with initial data  $p_L = 1$ ,  $\rho_L = 1$ ,  $v_L = 0$  and  $p_R = 0.1$ ,  $\rho_R = 0.125$ ,  $v_R = 0$  (this is known as the *Sod problem* and its numerical solution is also shown in Fig. 4.12), while the bottom right panel refers to a  $\mathcal{S}_\leftarrow \mathcal{C} \mathcal{R}_\rightarrow$  wave pattern, with the same initial data as in the bottom left panel, but with the  $L$  and  $R$  states inverted. In all cases, we have adopted an ideal-fluid equation of state [cf., Eq. (2.228)] with adiabatic index  $\gamma = 5/3$ .

In addition to the “snapshots” illustrated in Fig. 4.11, we have reported in the left panels of Fig. 4.12 the spacetime diagrams for the development of nonlinear waves as obtained from the *numerical* solution of a Riemann problem evolving into a  $\mathcal{R}_\leftarrow \mathcal{C} \mathcal{S}_\rightarrow$  wave pattern; the corresponding initial data is that of the Sod problem (see the bottom panels of Fig. 4.11) for an ideal-fluid equation of state [cf., Eq. (2.228)] with  $\gamma = 5/3$ . Shown from the top are the rest-mass density, the pressure and the velocity, respectively. The right panels, on the other hand, show the corresponding profiles at  $t = 0.25$  of the evolution (this time is indicated with a dashed white line in the left panels). Note the appearance of a contact discontinuity in the rest-mass density, which is absent in the evolution of the pressure and of the velocity.

Hereafter, we will use a more compact notation and simply indicate as  $2\mathcal{S}$ ,  $\mathcal{SR}$  and  $2\mathcal{R}$  a two-shock, a shock–rarefaction and a two-rarefaction wave pattern, respectively. Furthermore, we will use numbers to indicate the different states in the Riemann fan, so that the general wave-pattern evolution (4.146)–(4.147) is equivalent to

$$L \ R, \quad \text{at } t = 0, \quad (4.152)$$

$$1 \mathcal{W}_\leftarrow 3 \mathcal{C} 3' \mathcal{W}_\rightarrow 2, \quad \text{at } t > 0. \quad (4.153)$$

Finally, we will adopt a convention in which  $p_1 > p_2$ , with the  $x$ -axis being normal to the discontinuity surface being positively oriented from 1 to 2.

## 4.6 Solution of the one-dimensional Riemann problem

The general solution of the Riemann problem cannot be given in closed analytic form, even for one-dimensional Newtonian flows.<sup>20</sup> Although no general analytic solution is known, it is possible to solve the Riemann problem numerically to any required accuracy. In this sense, the Riemann problem is said to have been solved *exactly*, even though the solution is actually not analytical. In Newtonian hydrodynamics, the exact solution of the one-dimensional Riemann problem was first found by Courant and Friedrichs (1948), while in special-relativistic hydrodynamics, the so-called *shock-tube problem* (which is basically a particular case of the  $\mathcal{R}_\leftarrow \mathcal{C} \mathcal{S}_\rightarrow$  Riemann problem discussed above) was first solved by Thompson (1986). However, it is only with Martí and Müller (1994) that the first general solution of the one-dimensional special-relativistic Riemann problem was obtained, and later with Rezzolla and Zanotti (2001) that an improved approach to the solution was derived.

Hereafter, we will concentrate on one-dimensional problems, *i.e.*, on flows which do not have velocity components tangent to the initial discontinuity, so that the four-velocity is given by

$$u^\mu := W(1, v^x, 0, 0) = W(1, v, 0, 0), \quad (4.154)$$

where, to keep the notation compact, we have indicated  $v = v^x$ ; this notation will need to be extended when dealing with multidimensional velocity fields in Section 4.7. We have seen in the previous section that once two initial states are specified, the evolution of the Riemann problem leads to the formation of one of the three possible wave patterns. In practice, the exact solution of the Riemann problem is obtained through the following three steps:

<sup>20</sup>As a notable exception, an analytic solution has been found recently by Mach and Piętka (2010) in the special case of an equation of state for a relativistic dark-energy fluid  $p = we$  (see Section 2.4.9).

1. On the basis of the initial conditions, determine the wave pattern that will be produced. This can be done following a relativistic version of the Newtonian recipe suggested by Landau and Lifshitz (1987), that is, after looking at the relativistic, frame-independent expression for the relative velocity between the two unperturbed initial states,  $(v_{12})_0$ , and by comparing it with three limiting values  $(\tilde{v}_{12})_{\mathcal{S}}$ ,  $(\tilde{v}_{12})_{\mathcal{R}}$ ,  $(\tilde{v}_{12})_{\mathcal{B}}$ . These values mark the transition from one wave pattern to another one, and that are directly computed from the initial conditions (Rezzolla and Zanotti, 2001).
2. Using the continuity of the pressure and velocity across the contact discontinuity separating regions 3 and 3', compute the pressure in the region between the two nonlinear waves,  $p_*$ , as the root of the nonlinear equation

$$v_{12}(p_*) - (v_{12})_0 = 0, \quad (4.155)$$

where  $v_{12}(p_*)$  has a functional form that is *different* for each of the *three* possible wave patterns, but is now known through step 1.

3. Once  $p_* = p_3 = p_{3'}$  is known, complete the solution of the Riemann problem by determining all the other quantities in states 3 and 3'. The specific enthalpy  $h_b$  behind a shock wave follows from Eq. (4.118), which in turn allows us to compute the rest-mass density through (4.121). On the other hand, given the isentropic character of the flow within the rarefaction, the density behind a rarefaction wave follows immediately from the pressure via an equation of state.

Undoubtedly, the first of the three steps listed above is the one requiring the most care and before entering the details of how to compute the limiting velocities, we should note that the validity of the approach detailed above rests on two important facts. First, that the function  $v_{12} = v_{12}(p_*)$  increases monotonically with  $p_*$ . Second, that this function is composed of three branches, corresponding to the three possible wave patterns that join smoothly at the limiting values  $(\tilde{v}_{12})_{\mathcal{S}}$ ,  $(\tilde{v}_{12})_{\mathcal{R}}$ ,  $(\tilde{v}_{12})_{\mathcal{B}}$  [see, e.g., Rezzolla and Zanotti (2001) for a mathematical proof]. An example of the monotonicity is shown in Fig. 4.13 for some representative initial data. More specifically, we report the relative velocity  $v_{12}$  as a function of the pressure at the contact discontinuity and as the continuous joining of three different curves describing the relative velocity corresponding respectively to two shocks (red dashed line), one shock and one rarefaction wave (black dotted line), and two rarefaction waves (blue continuous line). The joining of the curves is indicated with filled dots and the inset shows a magnification where we have also indicated with filled squares the limiting values for the relative velocities  $(\tilde{v}_{12})_{\mathcal{S}}$ ,  $(\tilde{v}_{12})_{\mathcal{R}}$ ,  $(\tilde{v}_{12})_{\mathcal{B}}$ .

#### 4.6.1 Limiting relative velocities

We next proceed with showing how the limiting relative velocities can be calculated in different reference frames, specialising, when necessary, our expressions to the case of an ideal-fluid equation of state  $p = \rho\epsilon(\gamma - 1)$  [*cf.* Eq. (2.228)]. Because the remainder of this section is somewhat technical and reported here for completeness, it can be skipped without any conceptual loss.

We start by remarking that although the values of  $(v_{12})_0$  are relativistic invariants under a Lorentz boost in the  $x$ -direction, there exists a reference frame which is better suited to

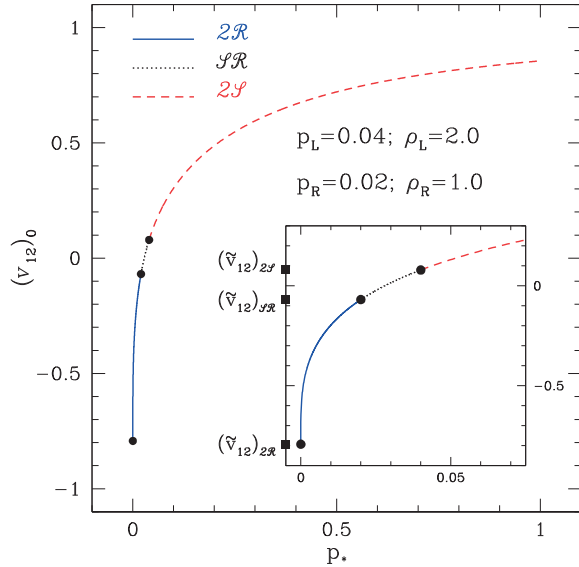


**Fig. 4.13** Relative velocity between the two initial states 1 and 2 as a function of the pressure at the contact discontinuity. The curve shown is given by the continuous joining of three different curves describing the relative velocity corresponding respectively to two shocks (red dashed line), one shock and one rarefaction wave (black dotted line), and two rarefaction waves (blue continuous line). Filled dots mark the joining of the curves, while the inset shows a magnification with filled squares showing the limiting values for the relative velocities [adapted from Rezzolla and Zanotti (2001)].

evaluate this quantity. In the reference frame of the contact discontinuity, in fact, the normal velocities behind the nonlinear waves are zero by definition (*i.e.*,  $v_{3,\mathcal{C}} = 0 = v_{3',\mathcal{C}}$ ) and the relative velocities across the nonlinear waves measured in this reference frame will be

$$(v_{13}),_{\mathcal{C}} := \frac{v_{1,\mathcal{C}} - v_{3,\mathcal{C}}}{1 - (v_{1,\mathcal{C}})(v_{3,\mathcal{C}})} = v_{1,\mathcal{C}}, \quad (4.156)$$

$$(v_{23'}),_{\mathcal{C}} := \frac{v_{2,\mathcal{C}} - v_{3',\mathcal{C}}}{1 - (v_{2,\mathcal{C}})(v_{3',\mathcal{C}})} = v_{2,\mathcal{C}}. \quad (4.157)$$

Because of their invariance, the normal velocity jumps across the nonlinear waves measured in the Eulerian frame can be expressed as

$$v_{13} = \frac{v_1 - v_3}{1 - v_1 v_3} = (v_{13}),_{\mathcal{C}} = v_{1,\mathcal{C}}, \quad (4.158)$$

$$v_{23'} = \frac{v_2 - v_{3'}}{1 - v_2 v_{3'}} = (v_{23'}),_{\mathcal{C}} = v_{2,\mathcal{C}}. \quad (4.159)$$

As a result, the relative normal-velocity function between the two initial states 1 and 2 can be written as

$$v_{12}(p_*) = (v_{12}),_{\mathcal{C}} = \frac{v_{1,\mathcal{C}} - v_{2,\mathcal{C}}}{1 - (v_{1,\mathcal{C}})(v_{2,\mathcal{C}})}. \quad (4.160)$$

## 230 Linear and Nonlinear Hydrodynamic Waves

In the rest of this section we will consider the three different wave patterns that can be produced and we will repeatedly evaluate expression (4.160) making use of (4.158) and (4.159).

**Two shock waves:**  $1 \mathcal{S}_\leftarrow 3 \mathcal{C} 3' \mathcal{S}_\rightarrow 2$ .

This wave pattern, represented in the top left panel of Fig. 4.11, is characterised by a value of the pressure downstream of the shocks which is larger than the pressures in the unperturbed states, *i.e.*,  $p_3 > p_1 > p_2$ . By simply applying Eq. (4.133) to the shock front propagating towards the left and evaluating it in the reference frame of the contact discontinuity, we can write the velocity ahead of the left- and right-propagating shocks as

$$v_{1,\mathcal{C}} = \sqrt{\frac{(p_3 - p_1)(e_3 - e_1)}{(e_1 + p_3)(e_3 + p_1)}}, \quad v_{2,\mathcal{C}} = -\sqrt{\frac{(p_3 - p_2)(e_{3'} - e_2)}{(e_2 + p_3)(e_{3'} + p_2)}}. \quad (4.161)$$

Equations (4.161) can now be used to derive the relativistic expression for the relative velocity of the flow ahead of the two shocks  $(v_{12})_{2,\mathcal{S}}$  through (4.160). It is possible to prove that the resulting expression is a monotonically increasing function of  $p_3$  [see, *e.g.*, Rezzolla and Zanotti (2001) for a proof]. As a result, the value of  $(v_{12})_{2,\mathcal{S}}$  can be used to build a criterion for the occurrence of two shocks propagating in opposite directions. Because  $p_1$  is the smallest value that the pressure at the contact discontinuity  $p_3$  can take, the limiting value for the two shock wave branch can therefore be expressed as

$$(\tilde{v}_{12})_{2,\mathcal{S}} = \lim_{p_3 \rightarrow p_1} (v_{12})_{2,\mathcal{S}}. \quad (4.162)$$

Evaluating the limit (4.162) basically involves calculating the limits of  $v_{1,\mathcal{C}}$  and  $v_{2,\mathcal{C}}$  for  $p_3$  tending to  $p_1$ . Both these limits are straightforward to calculate and are

$$\lim_{p_3 \rightarrow p_1} v_{1,\mathcal{C}} = 0, \quad (4.163)$$

$$\lim_{p_3 \rightarrow p_1} v_{2,\mathcal{C}} = -\sqrt{\frac{(p_1 - p_2)(\hat{e} - e_2)}{(\hat{e} + p_2)(e_2 + p_1)}}, \quad (4.164)$$

where we have defined

$$\hat{e} := \hat{h}\hat{\rho} - p_1 = \hat{h}\frac{\gamma p_1}{(\gamma - 1)(\hat{h} - 1)} - p_1, \quad (4.165)$$

and  $\hat{h}$  is the only positive root of the Taub adiabat (4.118) [*cf.*, the equivalent expression (4.122)]

$$\left[1 + \frac{(\gamma - 1)(p_2 - p_3)}{\gamma p_3}\right]\hat{h}^2 - \frac{(\gamma - 1)(p_2 - p_3)}{\gamma p_3}\hat{h} + \frac{h_2(p_2 - p_3)}{\rho_2} - h_2^2 = 0, \quad (4.166)$$

when  $p_3 \rightarrow p_1$ . As a result, we can conclude that two shocks will form if

$$(v_{12})_0 > (\tilde{v}_{12})_{2,\mathcal{S}} := \sqrt{\frac{(p_1 - p_2)(\hat{e} - e_2)}{(\hat{e} + p_2)(e_2 + p_1)}}. \quad (4.167)$$

**One shock and one rarefaction wave:**  $1 \mathcal{R}_\leftarrow 3 \mathcal{C} 3' \mathcal{S}_\rightarrow 2$ .

This wave pattern is characterised by  $p_1 > p_3 > p_2$  and is shown in the bottom left panel of Fig. 4.11. Evaluating expression (4.101) in the reference frame comoving with the contact discontinuity, we can evaluate the flow velocity ahead of the rarefaction wave to be

$$v_{1,\mathcal{C}} = \frac{1 - A_+(p_3)}{1 + A_+(p_3)}, \quad (4.168)$$

where we have used the quantity [cf., Eq. (4.100)]

$$A_+(p_3) := \left\{ \left[ \frac{(\gamma - 1)^{1/2} - c_s(p_3)}{(\gamma - 1)^{1/2} + c_s(p_3)} \right] \left[ \frac{(\gamma - 1)^{1/2} + c_s(p_1)}{(\gamma - 1)^{1/2} - c_s(p_1)} \right] \right\}^{2/(\gamma-1)^{1/2}}. \quad (4.169)$$

The flow velocity ahead of the shock front can be derived as before and is given by Eq. (4.161). When combined with expression (4.168), it can be used to derive the relativistic expression for the relative velocity of the fluids ahead of the shock and ahead of the rarefaction wave  $(v_{12})_{\mathcal{S}\mathcal{R}}$ . As for  $(v_{12})_{\mathcal{S}\mathcal{R}}$ , it can be shown that  $(v_{12})_{\mathcal{S}\mathcal{R}}$  is a monotonically increasing function of  $p_3$  (see Fig. 4.13). The limiting value for the one-shock and one-rarefaction branch can therefore be expressed as

$$(\tilde{v}_{12})_{\mathcal{S}\mathcal{R}} = \lim_{p_3 \rightarrow p_2} (v_{12})_{\mathcal{S}\mathcal{R}}. \quad (4.170)$$

In the limit  $p_3 \rightarrow p_2$ , the right-propagating shock is suppressed, i.e.,  $v_{3'} \rightarrow v_2$ , so that

$$\lim_{p_3 \rightarrow p_2} v_{2,\mathcal{C}} = 0, \quad (4.171)$$

and

$$(\tilde{v}_{12})_{\mathcal{S}\mathcal{R}} = \lim_{p_3 \rightarrow p_2} v_{1,\mathcal{C}} = \frac{1 - A_+(p_3)}{1 + A_+(p_3)} \Big|_{p_3=p_2}. \quad (4.172)$$

Therefore, the criterion for the relative velocity for having one shock and one rarefaction wave is

$$(\tilde{v}_{12})_{\mathcal{S}\mathcal{R}} < (v_{12})_0 \leq (\tilde{v}_{12})_{\mathcal{S}\mathcal{R}}. \quad (4.173)$$

We note that in the limit,  $p_3 \rightarrow p_2$ , regions 1 and 2 are connected by a single rarefaction wave. In this case, the sound speed can be computed using  $p_3 = p_2$  and  $\rho_3 = \rho_1(p_2/p_1)^{1/\gamma}$ . Finally, note that this is the only wave pattern in which  $v_1$  and  $v_2$  have the same sign and therefore includes the classical *shock-tube problem*, where  $v_1 = v_2 = 0$ .

**Two rarefaction waves:**  $1 \mathcal{R}_\leftarrow 3 \mathcal{C} 3' \mathcal{R}_\rightarrow 2$ .

This wave pattern is characterised by  $p_1 > p_2 > p_3$  and is shown in the top right panel of Fig. 4.11. In principle, it could even lead to a vacuum region, i.e.,  $\rho_3 = 0$ , behind the rarefaction waves if the waves are sufficiently strong. Using the same procedure followed so far, we can determine the fluid velocities ahead of the two rarefaction waves respectively as

$$v_{1,\mathcal{C}} = -\frac{A_+(p_3) - 1}{A_+(p_3) + 1}, \quad (4.174)$$

$$v_{2,\mathcal{C}} = \frac{1 - A_-(p_{3'})}{1 + A_-(p_{3'})}, \quad (4.175)$$

where

$$A_-(p_{3'}) := \left\{ \left[ \frac{(\gamma - 1)^{1/2} - c_s(p_{3'})}{(\gamma - 1)^{1/2} + c_s(p_{3'})} \right] \left[ \frac{(\gamma - 1)^{1/2} + c_s(p_2)}{(\gamma - 1)^{1/2} - c_s(p_2)} \right] \right\}^{-2/(\gamma-1)^{1/2}}. \quad (4.176)$$

Note that we have indicated with  $c_s(p_{3'})$  the sound speed in region  $3'$ , which differs from that in region  $3$  because of the jump in the rest-mass densities  $\rho_3$  and  $\rho_{3'}$ . The relative velocity built using (4.174) and (4.175) is then

$$(v_{12})_{\mathcal{R}} = -\frac{A_+(p_3) - A_-(p_{3'})}{A_+(p_3) + A_-(p_{3'})}. \quad (4.177)$$

As for the relative velocities of the previous wave patterns, it can be shown that  $(v_{12})_{\mathcal{R}}$  is a monotonically increasing function of  $p_3$  (see Fig. 4.13), so that the criterion for the occurrence of two rarefaction waves can be expressed as

$$(v_{12})_{\mathcal{R}}|_{p_3=0} < (v_{12})_0 \leq (v_{12})_{\mathcal{R}}|_{p_3=p_2} = (\tilde{v}_{12})_{\mathcal{R}}. \quad (4.178)$$

Since  $A_-(p_3 = p_2) = 1$ , the upper limit for (4.178) coincides with the lower limit for (4.173). The condition (4.178) can also be expressed in a more useful form as

$$-\frac{\mathcal{S}_1 - \mathcal{S}_2}{\mathcal{S}_1 + \mathcal{S}_2} < (v_{12})_0 \leq -\frac{1 - A_+(p_2)}{1 + A_+(p_2)}, \quad (4.179)$$

where the constants  $\mathcal{S}_1$  and  $\mathcal{S}_2$  are shorthand for

$$\mathcal{S}_1 := \left[ \frac{(\gamma - 1)^{1/2} + c_s(p_1)}{(\gamma - 1)^{1/2} - c_s(p_1)} \right]^{2/(\gamma-1)^{1/2}}, \quad (4.180)$$

$$\mathcal{S}_2 := \left[ \frac{(\gamma - 1)^{1/2} + c_s(p_2)}{(\gamma - 1)^{1/2} - c_s(p_2)} \right]^{-2/(\gamma-1)^{1/2}}. \quad (4.181)$$

A comment should be made in the case in which the two rarefaction waves leave behind them a region with zero density and pressure. This situation occurs only when the fluids in regions 1 and 2 are moving sufficiently fast in opposite directions. In practice, this happens whenever the relative velocity between the two states ahead of the rarefaction waves is less than or equal to the lower limit for  $(v_{12})_{\mathcal{R}}$ , *i.e.*,

$$(v_{12})_0 \leq (\tilde{v}_{12})_{\mathcal{R}} := -\frac{\mathcal{S}_1 - \mathcal{S}_2}{\mathcal{S}_1 + \mathcal{S}_2}. \quad (4.182)$$

Note that when a vacuum is produced,  $v_{12}$  is no longer dependent on  $p_3$  and this branch of the curve cannot be plotted in Fig 4.13.

To recap: expressions (4.167), (4.173) and (4.179) provide the limiting values against which to compare the initial relative velocity  $(v_{12})_0$  and determine the wave pattern that will develop from initial states. This completes step 1 of the procedure and allows for the calculation of the nonlinear equation (4.155) in step 2, which represents the heart of the solution of the exact Riemann problem.

### Other approaches.

As a concluding remark we emphasise that besides being elegant and leading to a more efficient algorithm in which no trial-and-error is required, knowledge of the wave pattern and hence step 1 is not strictly necessary. Indeed, in the first solution of the relativistic Riemann problem by Martí and Müller (1994), the pressure  $p_*$  is computed not as the root of (4.155), but rather as the root of

$$v_3(p_*) - v_{3'}(p_*) = 0, \quad (4.183)$$

which is a direct consequence of the absence of a pressure jump at the contact discontinuity between 3 and 3'. In this case, the solution of the Riemann problem can be seen geometrically as the determination, in the  $(v, p)$  plane of possible solutions, of the two waves (one moving to the right and one to the left) passing through the initial states. An example of this is shown in the left panel of Fig. 4.14, which refers to two initial states given by  $p_1 = 20$ ,  $\rho_1 = 10$ ,  $v_1 = -0.5$ ,  $p_2 = 10$ ,  $\rho_2 = 1$ ,  $v_2 = 0.6$  (blue circle and red square, respectively), for an ideal-fluid equation of state [*cf.* Eq. (2.228)] with  $\gamma = 5/3$ . In this specific case, the solution is represented by two rarefaction waves, propagating towards the left,  $\mathcal{R}_\leftarrow$ , and towards the right,  $\mathcal{R}_\rightarrow$ . The intersection of these two waves passing through the initial states marks the pressure,  $p_*$ , and the velocity,  $v_*$ , in the unknown regions 3 and 3'.

The wave pattern is then found only after solving Eq. (4.183), by comparing the computed pressure  $p_*$  with the two initial values  $p_1$  and  $p_2$ .<sup>21</sup> The reason why it is possible to solve Eq. (4.183) without knowing what is the analytic form of  $v_3(p_*)$  and  $v_{3'}(p_*)$  (*i.e.*, not knowing the wave pattern that will be produced) becomes clear after looking at the right panel of Fig. 4.14, where we have plotted  $v_3(p_*) - v_{3'}(p_*)$  as a function of the unknown pressure  $p_*$ .

This function, whose root provides the solution, is given by the continuous joining of three branches, corresponding to the three possible wave patterns. Remarkably, it can be shown to be a function of class  $\mathcal{C}^1$ , so that even if one starts from an initial guess  $p_0$  which belongs to the wrong branch (empty circle in Fig. 4.14) and thus assuming a wrong wave pattern, a standard root-finding algorithm will converge to the correct solution  $p_*$  (filled circle) thanks to the smoothness of the function  $v_3(p_*) - v_{3'}(p_*)$  (Zanotti, 2002).

## 4.7 Solution of the multidimensional Riemann problem

In the most general case, the fluid four-velocity on either side of the initial discontinuity can also have tangential components, that is, components in directions orthogonal to the discontinuity normal and thus of the generic form

<sup>21</sup>Indeed, if  $p_* > \max(p_1, p_2)$ , then two shocks will be produced; if instead  $\min(p_1, p_2) < p_* < \max(p_1, p_2)$ , then one shock and one rarefaction will be produced; finally, if  $p_* < \min(p_1, p_2)$ , then two rarefaction waves will be produced.

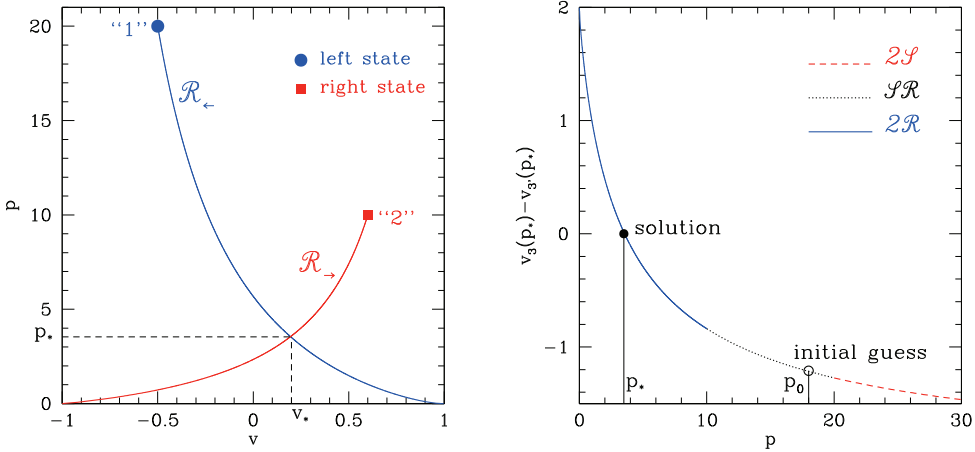


**Fig. 4.14** *Left Panel:* Solution of the Riemann problem in the  $(v, p)$  plane with initial conditions given by  $p_1 = 20$ ,  $\rho_1 = 10$ ,  $v_1 = -0.5$ ,  $p_2 = 10$ ,  $\rho_2 = 1$ ,  $v_2 = 0.6$  (blue circle and red square) for an ideal-fluid equation of state with  $\gamma = 5/3$ . The solution consists of two rarefaction waves, propagating towards the left,  $\mathcal{R}_{\leftarrow}$ , and towards the right,  $\mathcal{R}_{\rightarrow}$ . The intersection of the two curves selects the pressure,  $p_*$ , and velocity,  $v_*$ , in the unknown region 3 and 3'. *Right Panel:* Relative velocity  $v_3(p_*) - v_{3'}(p_*)$  as a function of the pressure. The curve is given by the smooth joining of three different branches, corresponding to the three possible wave patterns. The initial conditions are the same as those in the left panel and the unknown pressure  $p_*$  falls in the branch corresponding to two rarefaction waves. The smoothness of the function guarantees the convergence to the correct  $p_*$  even if the initial guess  $p_0$  belongs to the wrong branch [adapted from Zanotti (2002)].

$$u^\mu := W(1, v^x, v^y, v^z), \quad (4.184)$$

where

$$v^2 := v^i v_i = (v^x)^2 + (v^y)^2 + (v^z)^2, \quad W^2 = (1 - v^2)^{-1}. \quad (4.185)$$

We can then introduce the *tangential velocity* as

$$v^t := [(v^y)^2 + (v^z)^2]^{1/2}, \quad (4.186)$$

which satisfies the relativistic constraint  $(v^t)^2 + (v^x)^2 \leq 1$ . The extension of the approach presented in the previous section to the case when tangential velocities are present is relatively straightforward and the solution of the Riemann problem can still be obtained following steps 1–3 discussed in the previous section. Furthermore, the fundamental equation (4.155), as well as all expressions (4.156)–(4.182), remain unmodified but for the trivial change  $v \rightarrow v^x$ . Other non-trivial modifications will involve the changes of quantities across nonlinear waves and will be discussed in the following Sections 4.7.1–4.7.3. The reader not interested in the details of the derivation can skip these sections and move directly to Section 4.7.4.

However, before diving into the details it is useful to anticipate the most important result: *nonzero tangential velocities can affect the solution of the Riemann problem and cause*

a transition from one wave pattern to another. More specifically, by varying the tangential velocities on either side of the initial discontinuity while keeping the remaining state vectors unchanged, the nonlinear waves involved in the solution of the Riemann problem can change from rarefaction waves to shock waves and vice versa. This is a purely relativistic feature introduced by the Lorentz factor and it marks an important difference with respect to Newtonian hydrodynamics, where the wave pattern of the Riemann problem does not depend on the tangential component of the flow (Rezzolla and Zanotti, 2002; Rezzolla *et al.*, 2003).

#### 4.7.1 Jumps across a shock wave

Calculating the jump conditions in the rest frame of the shock front is not particularly advantageous when tangential velocities are present. In this case, in fact, the velocity jump across the shock cannot be expressed as an algebraic relation among the thermodynamic quantities across the shock [*cf.* Eqs. (4.161)]. Rather, the ratio of the velocities ahead and behind the shock front needs to be found as roots of a nonlinear equation (Königl, 1980). For this reason it is more convenient to use the Rankine–Hugoniot conditions in the Eulerian reference frame. In particular, these conditions can be written as (Pons *et al.*, 2000)

$$[\![v^x]\!] = -\frac{J}{W_s} \left[ \frac{1}{\rho W} \right], \quad (4.187)$$

$$[\![p]\!] = \frac{J}{W_s} [\![hWv^x]\!], \quad (4.188)$$

$$[\![hWv^y]\!] = 0 = [\![hWv^z]\!], \quad (4.189)$$

$$[\![v^x p]\!] = \frac{J}{W_s} \left[ hW - \frac{p}{\rho W} \right]. \quad (4.190)$$

In expressions (4.187), (4.188) and (4.190),  $J$  represents the mass flux across the shock [*cf.* Eq. (4.140)], which is an invariant under Lorentz boosts in the  $x$ -direction.

We can now exploit Eqs. (4.187)–(4.190) to express the normal velocity of the fluid on the back of the shock front in terms of the pressure as

$$v_b^x = \frac{h_a W_a v_a^x + W_s (p_b - p_a)/J}{h_a W_a + (p_b - p_a)[W_s v_a^x/J + 1/(\rho_a W_a)]}, \quad (4.191)$$

where  $W_s := (1 - V_s^2)^{-1/2}$  is the Lorentz factor of the shock velocity  $V_s$  [*cf.* Eq. (4.141)]. Besides providing the jump in the normal velocity across a shock wave, expression (4.191) states that the two regions of the flow across the shock wave are coupled through a Lorentz factor which is built also in terms of the tangential velocities. This is a purely relativistic feature and an important difference from Newtonian hydrodynamics. One of the consequences of this coupling can be deduced immediately from expressions (4.189), indicating that only the ratio  $v^y/v^z$  remains unchanged through shocks, *i.e.*,

$$[\![v^y/v^z]\!] = 0, \quad [\![v^y]\!] \neq 0, \quad [\![v^z]\!] \neq 0. \quad (4.192)$$

As a result, the tangential velocity three-vector does not rotate across the shock, but it can change its norm. This property, which applies also across rarefaction waves, represents a major difference from the behaviour of the tangential three-velocity vector across Newtonian nonlinear waves, which neither rotates, nor changes its norm, *i.e.*,

$$\llbracket v^y \rrbracket \stackrel{N}{=} 0 \stackrel{N}{=} \llbracket v^z \rrbracket . \quad (4.193)$$

#### 4.7.2 Jumps across a rarefaction wave

As discussed in Section 4.4.2, it is convenient when considering a rarefaction wave to introduce the self-similar variable  $\xi := x/t$ , in terms of which similarity solutions to the hydrodynamic equations can be found. The extension of expression (4.95) to the multidimensional case is given by (Pons *et al.*, 2000)

$$\xi = \frac{v^x(1 - c_s^2) \pm c_s \sqrt{(1 - v^2)[1 - v^2 c_s^2 - (v^x)^2(1 - c_s^2)]}}{1 - v^2 c_s^2} , \quad (4.194)$$

which reduces to (4.95) when  $v^x = v$ . In the case of a perfect fluid, the isentropic character of the flow allows us to calculate the velocity on the back of the wave as a solution of an ordinary differential equation

$$\frac{dv^x}{dp} = \frac{1}{\rho h W^2} \frac{(1 - \xi v^x)}{(\xi - v^x)} , \quad (4.195)$$

which can be solved to calculate the normal fluid velocity at the tail of the rarefaction wave. In practice it is more convenient to make use of constraints such as those in expressions (4.189) (which remain valid also across a rarefaction wave) and express Eq. (4.195) in a different way. After defining  $\mathcal{A} := h_a W_a v_a^t = h_b W_b v_b^t$ , the tangential velocity along a rarefaction wave can be expressed as (Pons *et al.*, 2000)

$$(v^t)^2 = \mathcal{A}^2 \left[ \frac{1 - (v^x)^2}{h^2 + \mathcal{A}^2} \right] , \quad (4.196)$$

so that it is possible to eliminate the dependence on  $v^t$  from Eq. (4.194). From the definition of the Lorentz factor and Eq. (4.196), it is straightforward to obtain

$$W^2 = \frac{h^2 + \mathcal{A}^2}{h^2[1 - (v^x)^2]} , \quad (4.197)$$

and after some algebra we obtain

$$\frac{1 - \xi v^x}{\xi - v^x} = \pm \frac{\sqrt{h^2 + \mathcal{A}^2(1 - c_s^2)}}{h c_s} , \quad (4.198)$$

so that Eq. (4.195) can finally be written as

$$\frac{dv^x}{1 - (v^x)^2} = \pm \frac{\sqrt{h^2 + \mathcal{A}^2(1 - c_s^2)}}{(h^2 + \mathcal{A}^2)} \left( \frac{dp}{\rho c_s} \right) . \quad (4.199)$$

Note that in this way we have isolated the thermodynamic quantities on the right-hand side of (4.199) and the kinematic ones on the left-hand side, which can then be integrated analytically.

For some particular cases, *e.g.*, when the sound speed is constant, also the right-hand side can be integrated analytically, but this is not true for a generic equation of state. The velocity at the tail of the rarefaction wave can then be obtained directly as

$$v_b^x = \tanh \mathcal{B} , \quad (4.200)$$

where

$$\mathcal{B} := \frac{1}{2} \log \left( \frac{1 + v_a^x}{1 - v_a^x} \right) \pm \int_{p_a}^{p_*} \frac{\sqrt{h^2 + \mathcal{A}^2(1 - c_s^2)}}{(h^2 + \mathcal{A}^2)} \left( \frac{dp}{\rho c_s} \right) . \quad (4.201)$$

Here,  $h = h(p, s)$ ,  $\rho = \rho(p, s)$  and  $c_s = c_s(p, s)$ ; furthermore, the isentropic character of rarefaction waves allows one to fix  $s = s_a$ .

### 4.7.3 Limiting relative velocities

Also in a multidimensional context, the first step in the solution of the Riemann problem consists in calculating the relative normal velocity across the two initial states and comparing it with the limiting relative velocities for each of the three possible wave patterns. In practice, this amounts to calculating Eq. (4.160) making use of expressions (4.158) and (4.159). The limiting velocities will be different from the ones encountered in the one-dimensional case in Section 4.6 and, more importantly, they will depend on the tangential velocity, as we will discuss below.

**Two shock waves:**  $1 \mathcal{S}_- 3 \mathcal{C} 3' \mathcal{S}_+ 2$ .

In this case, the general expression for the relative normal velocities between the two initial states  $(v_{12}^x)_{2,\mathcal{S}}$ , can be calculated from (4.160) with the velocities behind the shock waves  $v_3^x$  and  $v_{3'}^x$  being determined through the jump condition (4.191). Because  $p_1$  is the smallest value that the pressure at the contact discontinuity  $p_3$  can take, the limiting value for the two shock wave branch  $(\tilde{v}_{12}^x)_{2,\mathcal{S}}$  can be expressed as [*cf.*, Eq. (4.162)]

$$(\tilde{v}_{12}^x)_{2,\mathcal{S}} = \lim_{p_3 \rightarrow p_1} (v_{12}^x)_{2,\mathcal{S}} . \quad (4.202)$$

Evaluating the limit (4.202) basically involves calculating the limits of  $v_{1,\mathcal{C}}^x$  and  $v_{2,\mathcal{C}}^x$  for  $p_3$  tending to  $p_1$ . Both these limits are straightforward to calculate and are given by

$$\lim_{p_3 \rightarrow p_1} v_{1,\mathcal{C}}^x = 0 , \quad (4.203)$$

$$\lim_{p_3 \rightarrow p_1} v_{2,\mathcal{C}}^x = \frac{v_2^x - \bar{v}_{3'}^x}{1 - v_2^x \bar{v}_{3'}^x} , \quad (4.204)$$

where  $\bar{v}_{3'}^x$  is simply the value of  $v_3^x$  for  $p_3 = p_1$ , *i.e.*,

$$\bar{v}_{3'}^x := \lim_{p_3 \rightarrow p_1} v_{3'}^x . \quad (4.205)$$

Using now the limits (4.203)–(4.204) and some lengthy but straightforward algebra, we obtain the limiting relative velocity for the two-shock branch as

$$(\tilde{v}_{12}^x)_{\mathcal{S}} = - \lim_{p_3 \rightarrow p_1} v_{2,\mathcal{C}}^x = \frac{(p_1 - p_2)(1 - v_2^x \bar{V}_s)}{(\bar{V}_s - v_2^x)\{h_2 \rho_2 (W_2)^2 [1 - (v_2^x)^2] + p_1 - p_2\}}, \quad (4.206)$$

where  $\bar{V}_s$  is the velocity of the shock wave propagating towards the right when  $p_3 \rightarrow p_1$  (Rezzolla et al., 2003). Note that  $(\tilde{v}_{12}^x)_{\mathcal{S}}$  does not depend on the initial velocity in the state 1.

**One shock and one rarefaction wave:**  $1 \mathcal{R}_\leftarrow 3 \mathcal{C} 3' \mathcal{S}_\rightarrow 2$ .

Also in this case, the limiting velocity  $(v_{12}^x)_{\mathcal{SR}}$  can be calculated from (4.160) with  $v_3^x$  being determined through the jump condition (4.191), and with  $v_3^x$  from the numerical integration of equation (4.195) in the range  $[p_1, p_3]$ . Because  $p_2$  is now the lowest pressure in the unknown region behind the two nonlinear waves, the limiting value for the one-shock and one-rarefaction branch  $(\tilde{v}_{12}^x)_{\mathcal{SR}}$  can be expressed as

$$(\tilde{v}_{12}^x)_{\mathcal{SR}} = \lim_{p_3 \rightarrow p_2} (v_{12}^x)_{\mathcal{SR}}. \quad (4.207)$$

In the limit  $p_3 \rightarrow p_2$ , the right-propagating shock is suppressed,  $v_{3'}^x \rightarrow v_2^x$ , so that

$$\lim_{p_3 \rightarrow p_2} v_{2,\mathcal{C}}^x = 0, \quad (4.208)$$

and

$$(\tilde{v}_{12}^x)_{\mathcal{SR}} = \lim_{p_3 \rightarrow p_2} v_{1,\mathcal{C}}^x. \quad (4.209)$$

Defining now

$$\mathcal{B}_1 := \frac{1}{2} \log \left( \frac{1 + v_1^x}{1 - v_1^x} \right), \quad (4.210)$$

and using Eq. (4.200), we obtain the limiting relative velocity for the shock–rarefaction branch as

$$(\tilde{v}_{12}^x)_{\mathcal{SR}} = \lim_{p_3 \rightarrow p_2} \tanh(\mathcal{B}_1 - \mathcal{B}) = \tanh \left( \int_{p_1}^{p_2} \frac{\sqrt{h^2 + \mathcal{A}_1^2(1 - c_s^2)}}{(h^2 + \mathcal{A}_1^2)\rho c_s} dp \right), \quad (4.211)$$

where  $\mathcal{A}_1 := h_1 W_1 v_1^t$  and the integral should be evaluated numerically. Note that  $(\tilde{v}_{12}^x)_{\mathcal{SR}}$  does not depend on the initial velocity in state 2.

**Two rarefaction waves:**  $1 \mathcal{R}_\leftarrow 3 \mathcal{C} 3' \mathcal{R}_\rightarrow 2$ .

Finally, the limiting velocity  $(v_{12}^x)_{\mathcal{RR}}$  can be calculated from (4.160) with the velocities behind the waves being calculated using (4.200) and (4.201). Since the lowest value of the pressure behind the tails of the rarefaction waves is zero, the limiting value for the two-rarefaction branch  $(\tilde{v}_{12}^x)_{\mathcal{RR}}$  is given by

$$(\tilde{v}_{12}^x)_{\mathcal{RR}} = \lim_{p_3 \rightarrow 0} (v_{12}^x)_{\mathcal{RR}}. \quad (4.212)$$

Proceeding as in the case of a shock–rarefaction wave pattern, we can express  $(\tilde{v}_{12}^x)_{\mathcal{RR}}$  as

$$(\tilde{v}_{12}^x)_{\mathcal{RR}} = \frac{\bar{v}_{1,\mathcal{C}}^x - \bar{v}_{2,\mathcal{C}}^x}{1 - (\bar{v}_{1,\mathcal{C}}^x)(\bar{v}_{2,\mathcal{C}}^x)}, \quad (4.213)$$

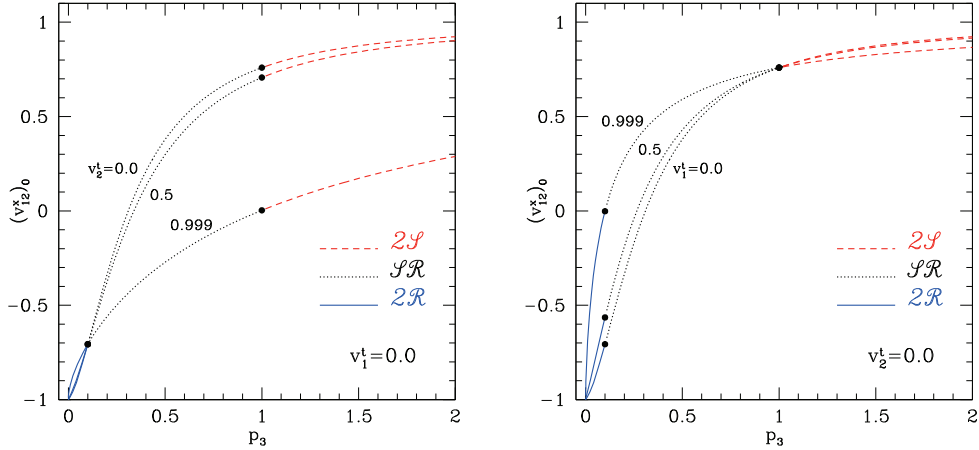


**Fig. 4.15** Relative normal velocity between the two initial states as a function of the pressure at the contact discontinuity with initial conditions given by the Sod problem with  $\gamma = 5/3$ . The different line types mark the different branches corresponding to two shock waves (red dashed line), one shock and one rarefaction wave (black dotted line), and two rarefaction waves (blue solid line), respectively. Note how the functional behaviour is modified when only one of the initial tangential velocities is varied ( $v_2^t$  for the left panel and  $v_1^t$  for the right one) while all the other components of the initial state vectors are left unchanged [adapted from Rezzolla *et al.* (2003)].

where

$$\bar{v}_{1,\mathcal{C}}^x := \tanh \left( \int_{p_1}^0 \frac{\sqrt{h^2 + \mathcal{A}_1^2(1 - c_s^2)}}{(h^2 + \mathcal{A}_1^2)\rho c_s} dp \right), \quad (4.214)$$

$$\bar{v}_{2,\mathcal{C}}^x := \tanh \left( \int_0^{p_2} \frac{\sqrt{h^2 + \mathcal{A}_2^2(1 - c_s^2)}}{(h^2 + \mathcal{A}_2^2)\rho c_s} dp \right), \quad (4.215)$$

and where  $\mathcal{A}_2 := h_2 W_2 v_2^t$ . Note that  $(\tilde{v}_{12}^x)_{\mathcal{R}}$  depends both on  $v_1$  and  $v_2$  and marks the transition to a wave pattern having two rarefaction waves separated by vacuum.

#### 4.7.4 Relativistic effects in multidimensional Riemann problems

As anticipated in Section 4.7, the tangential velocities are responsible for a purely relativistic effect and can cause a transition from one wave pattern to another (Rezzolla and Zanotti, 2002; Rezzolla *et al.*, 2003). To illustrate this, let us restrict our attention to a situation in which the tangential velocity of only one of the two initial states is varied. This is simpler than the general case as it basically represents a one-dimensional cross-section of the three-dimensional parameter space, but it maintains all of the relevant properties. The two panels of Fig. 4.15 show the relative normal velocity for the same initial conditions of the Sod problem (Sod, 1978) where either  $v_1^t$  or  $v_2^t$  is varied while all the other quantities of the initial state vectors are left unchanged. Different line types mark the different branches (joined at the filled dots)

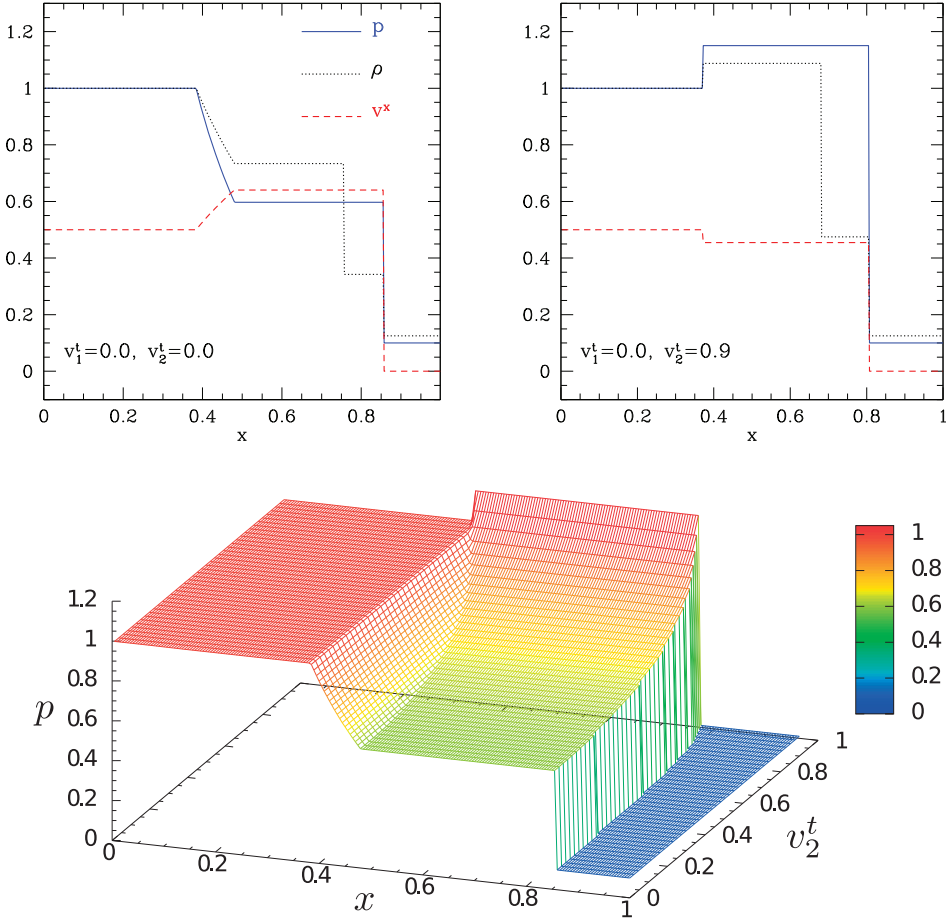


**Fig. 4.16** *Top panels:* Transition from a  $\mathcal{SR}$  wave pattern to a  $2\mathcal{S}$  pattern. The initial state vectors are identical except for the values of  $v_2^t$ . Blue solid, black dotted and red dashed lines refer to pressure, rest-mass density and normal velocity, respectively. *Bottom panel:* Transition from a  $\mathcal{SR}$  wave pattern to a  $2\mathcal{S}$  pattern, shown by reporting the pressure profile as a function of  $v_2^t$  [adapted from Rezzolla et al. (2003)].

describing the relative velocity corresponding to two shock waves ( $2\mathcal{S}$ , red dashed line), one shock and one rarefaction wave ( $\mathcal{SR}$ , black dotted line), and two rarefaction waves ( $2\mathcal{R}$ , blue solid line), respectively. Both panels of Fig. 4.15 indicate that when tangential velocities are present, the relative normal velocity  $(v_{12}^x)_0$  is a function of  $p_3$ , and also of  $v_1^t$  and  $v_2^t$ .

Now consider, for instance, initial conditions in which the normal velocities are chosen to be  $v_1^x = 0.5$ ,  $v_2^x = 0.0$ , and there are no tangential velocities. In this case,  $(v_{12}^x)_0 = 0.5$  and the left panel of Fig. 4.15 then shows that the solution to the Riemann problem falls in the  $\mathcal{SR}$  branch, hence producing a wave pattern consisting of a shock and a rarefaction wave moving in opposite directions. This is shown in more detail in the left panel of Fig. 4.16 where

the different types of line show the solution of the Riemann problem at a time  $t > 0$  for the pressure, the rest-mass density and the velocity, respectively. However, if we now maintain the *same* initial conditions but allow for nonzero tangential velocities in state 2, then the left panel of Fig. 4.15 shows that the solution of the Riemann problem can fall in the  $\mathcal{2S}$  branch, hence producing a wave pattern consisting of two shock waves moving in opposite directions. This is shown in the right panel of Fig. 4.16, which illustrates the solution of the same Riemann problem but with initial tangential velocities  $v_1^t = 0.0$  and  $v_2^t = 0.9$ . Note that, except for the tangential velocities, the solutions in Figs. 4.16 have the same initial state vectors but different intermediate ones (*i.e.*,  $p_3$ ,  $\rho_3$ ,  $\rho_{3'}$ , and  $v_3^x$ ).

What is reported in Fig. 4.16 is just an example, but it shows that a change in the tangential velocities can produce a *smooth transition from one wave pattern to another while maintaining the rest of the initial states unmodified* (Rezzolla and Zanotti, 2002; Rezzolla *et al.*, 2003). Furthermore, because the coupling among the different states is produced by the Lorentz factors, the effect is not sensitive to the sign chosen for the tangential velocity. Of course, the transition does not need to always produce a solution consisting of two shock waves. Suppose, in fact, that the normal velocities are now chosen to be  $v_1^x = 0.0$ ,  $v_2^x = 0.5$ .

We can repeat the considerations made above and start by examining the wave pattern produced when there are zero tangential velocities. In this new setup,  $(v_{12}^x)_0 = -0.5$  and the right panel of Fig. 4.15 shows that the solution of the Riemann problem still falls in the  $\mathcal{SR}$  branch (*cf.*, dashed line), with the corresponding solution at a time  $t > 0$  being presented in the left panel of Fig. 4.17 (note that the wave patterns in Figs. 4.16 and 4.17 both consist of a shock and a rarefaction wave, but have alternating initial normal velocities).

However, when nonzero tangential velocities are now considered in state 1, the right panel of Fig. 4.15 shows that  $(v_{12}^x)_0$  can fall in the  $\mathcal{2R}$  branch, hence producing a wave pattern consisting of two rarefaction waves moving in opposite directions. The solution to this Riemann problem is shown in the right panel of Fig. 4.17, where we have chosen initial tangential velocities  $v_1^t = 0.999$  and  $v_2^t = 0.0$ . It should be noted that in this case too, except for the tangential velocities, the solutions in the two panels of Fig. 4.17 have the same initial state vectors but different intermediate ones.

Two relevant limits are worth considering. The first one is for the relative velocity  $(\tilde{v}_{12}^x)_{\mathcal{SR}}$  when the tangential velocity in state 2 is allowed to be arbitrarily large. In this case, it is possible to show that (Rezzolla *et al.*, 2003)

$$\lim_{W_2 \rightarrow \infty} (\tilde{v}_{12}^x)_{\mathcal{SR}} = 0. \quad (4.216)$$

The implications of this result are made clear in the left panel of Fig. 4.15, where the right solid dot tends to zero as  $W_2 \rightarrow \infty$ , while the left one does not vary. A direct consequence of (4.216) is that, given a Riemann problem having initial state vectors with positive relative normal velocity and producing a  $\mathcal{SR}$  wave pattern, it is *always* possible to transform it into a  $\mathcal{2S}$  wave pattern by increasing the value of the initial tangential velocity in the state of initial lower pressure. In a similar way, it is possible to show that (Rezzolla *et al.*, 2003)

$$\lim_{W_1 \rightarrow \infty} (\tilde{v}_{12}^x)_{\mathcal{SR}} = 0, \quad (4.217)$$

which can again be inferred from the right panel of Fig. 4.15, where the left solid dot converges to zero as  $W_1 \rightarrow \infty$ , while the right one does not vary. Overall, expressions (4.216)

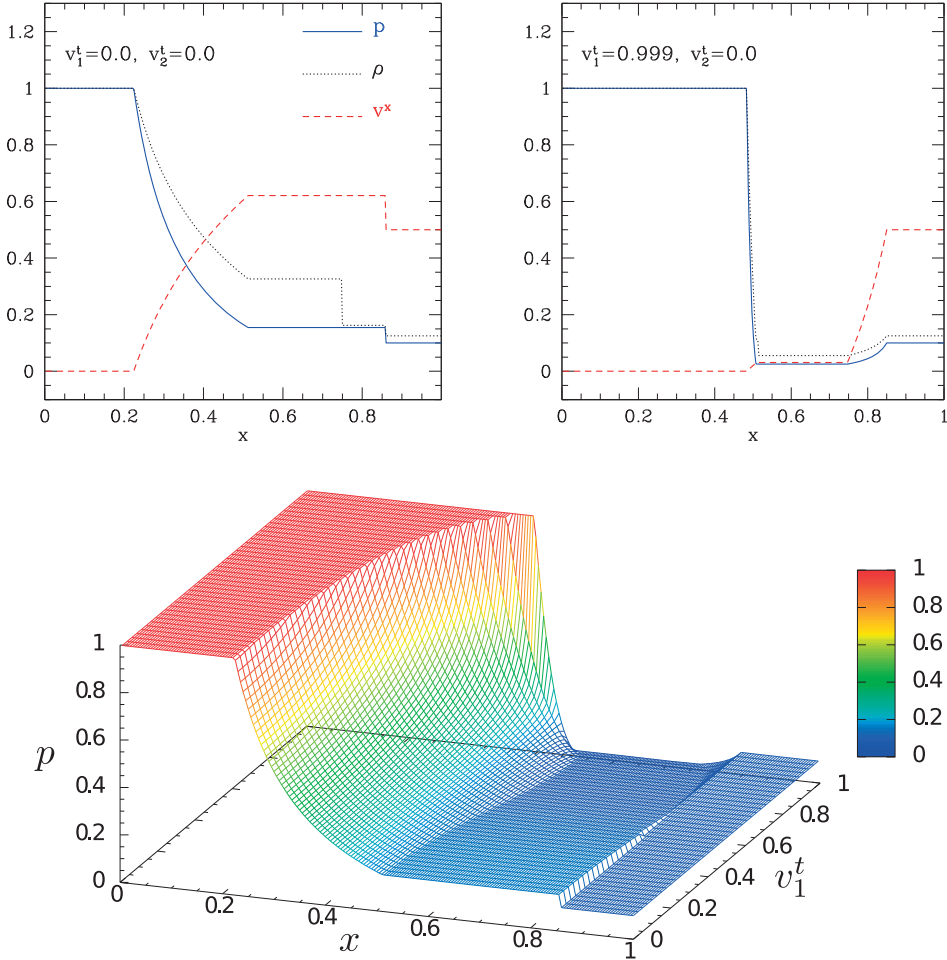


**Fig. 4.17** *Top panels:* Transition from a  $\mathcal{SR}$  wave pattern to a  $\mathcal{2R}$  pattern. The initial state vectors are identical except for the values of  $v_1^t$ . Blue solid, black dotted and red dashed lines refer to pressure, rest-mass density and normal velocity, respectively. Note that in the top right panel the left-propagating rarefaction wave covers a very small region of the flow and is closely followed by the contact discontinuity. *Bottom panel:* Transition from a  $\mathcal{SR}$  wave pattern to a  $\mathcal{2R}$  pattern, shown by reporting the pressure profile as a function of  $v_1^t$  [adapted from Rezzolla et al. (2003)].

and (4.217) indicate that for tangential velocities assuming increasingly larger values, the  $\mathcal{SR}$  branch of the  $v_{12}^x$  curve spans a progressively smaller interval of relative normal velocities. When the tangential velocities reach their asymptotic values, the  $\mathcal{SR}$  branch reduces to a point. Note also that there exists a set of initial conditions for which these new relativistic effects cannot occur. These initial conditions are those in which  $v_1^x = v_2^x$  as in the classic “shock-tube” problem, where  $v_1^x = 0 = v_2^x$ . In these cases, in fact,  $(v_{12}^x)_0 = 0$  and, because

of the limits (4.216) and (4.217), the solution of the Riemann problem will be given by a wave pattern consisting of a shock and a rarefaction wave, independently of the values of the tangential velocities.

Because the effects discussed here have a purely special-relativistic origin they might conflict with our physical intuition, especially when the latter is based on knowledge of the Riemann problem in Newtonian hydrodynamics. However, the behaviour reported here is typical of those special-relativistic phenomena involving Lorentz factors including also tangential velocities, *e.g.*, the relativistic transverse Doppler effect. An astrophysical application of the relativistic effects discussed here has been made recently by Aloy and Rezzolla (2006), who have exploited it to produce a powerful hydrodynamic booster that could be at work in relativistic jets (see Section 11.9.2).

#### 4.7.5 Shock-detection techniques

It may sometimes be useful to determine accurately the location of a shock within a numerical calculation and several different methods are possible to do this, with varying degrees of precision. The simplest method, often adopted in artificial-viscosity numerical methods (see Section 8.4), is to look at where the density undergoes large variations and thus at where an artificial viscosity should be added to the pressure. A second method just measures the spatial gradients of the rest-mass density and interprets them as ‘‘shocks’’ once above a certain threshold. Finally, another method marks a given region as a shocked one if  $\vec{\nabla} \cdot \vec{v} < 0$  and if the pressure difference between the monitored zone and at least one of its neighbours exceeds the difference expected from the Rankine–Hugoniot jump conditions for a shock of a pre-specified minimum *Mach number*. The latter is defined as the relativistic generalisation of the corresponding Newtonian quantity<sup>22</sup> and thus as the ratio between the local fluid velocity,  $v$ , and the local sound speed,  $c_s$ , *i.e.*,

$$\mathcal{M} := \frac{Wv}{W_s c_s}, \quad (4.218)$$

where  $W$  and  $W_s$  are the Lorentz factors associated respectively to  $v$  and  $c_s$ , *i.e.*,  $W := (1 - v^2)^{-1/2}$ , and  $W_s := (1 - c_s^2)^{-1/2}$ . While more robust than the previous two, also the latter prescription is not very accurate and all the methods discussed so far can fail to detect shocks unless they are very strong.

A much more accurate shock detector can be built on the basis of the limiting relative velocities discussed in the previous sections.<sup>23</sup> To illustrate the logic of this shock detector let us suppose that along a given direction, say the  $x$ -direction, two adjacent fluid elements 1 and 2 manifest a jump in the hydrodynamic quantities, such as pressure, rest-mass density and velocity, thus reproducing the typical conditions of a local Riemann problem. A shock front will then be produced if the wave pattern generated by the Riemann problem contains at least one shock wave, while the other wave can be a rarefaction wave. As discussed in Section 4.7.3, there is a simple criterion for predicting the occurrence of a wave pattern containing a shock

<sup>22</sup>The Newtonian expression of the Mach number is simply given by  $\mathcal{M}_N := v/c_s$ .

<sup>23</sup>A similar detector can be prescribed also for non-relativistic flows; the interested reader can find a detailed discussion in the appendix of Zanotti *et al.* (2010).

wave and this amounts to the requirement that the relative velocity between the two states 1 and 2 (*i.e.*, between two adjacent fluid cells) is larger than a threshold value

$$v_{12} > (\tilde{v}_{12})_{\mathcal{SR}} = \tanh \left( \int_{p_1}^{p_2} \frac{\sqrt{h^2 + \mathcal{A}_1^2(1 - c_s^2)}}{(h^2 + \mathcal{A}_1^2)\rho c_s} dp \right), \quad (4.219)$$

where  $v_{12} := (v_1 - v_2)/(1 - v_1 v_2)$  and  $(\tilde{v}_{12})_{\mathcal{SR}}$  is taken from expression (4.211). If, on the other hand, the relative velocity  $v_{12}$  is smaller than  $(\tilde{v}_{12})_{\mathcal{SR}}$ , then no shock wave can be produced and the wave pattern of the corresponding Riemann problem consists of two rarefaction waves propagating in opposite directions. Note that the integral (4.211) effectively provides the minimum value for the occurrence of a wave pattern containing a single shock wave. In the limit of  $(\tilde{v}_{12})_{\mathcal{SR}} \rightarrow v_{12}$ , in fact, the pressure jump across the shock wave becomes vanishingly small and a single rarefaction wave joining  $p_1$  and  $p_2$  propagates in the direction opposite to that of the vanishing shock wave.

The procedure described above is completely general and can be used to build an efficient and accurate shock detector even in a curved spacetime. However, two subtleties should also be taken into account. The first one is that, for generic spacetimes and coordinates systems, the velocity field  $v^j$  should be projected in a local tetrad via a transformation of the type

$$\hat{v}^i = M_j^i v^j, \quad (4.220)$$

with  $M_j^i$  given by (Pons *et al.*, 1998)

$$M_j^i = \begin{pmatrix} \sqrt{\gamma_{11}} & (-\gamma^{12}\gamma_{22} + \gamma^{13}\gamma_{23})/(\gamma^{11}\sqrt{\gamma_{22}}) & -\gamma^{13}\sqrt{\gamma_{22}\gamma_{33} - (\gamma_{23})^2}/(\gamma^{11}\sqrt{\gamma_{22}}) \\ 0 & \sqrt{\gamma_{22}} & 0 \\ 0 & \gamma_{23}/\sqrt{\gamma_{22}} & \sqrt{\gamma_{22}\gamma_{33} - (\gamma_{23})^2}/\sqrt{\gamma_{22}} \end{pmatrix}, \quad (4.221)$$

where  $\gamma_{ij}$  is the spatial part of the metric tensor in a 3+1 decomposition of spacetime (see Section 7.1). The second subtlety concerns the fact that, because the shock detector validates the inequality (4.219), it can be arbitrarily sensitive. Although this certainly represents an advantage, one often wishes to disregard very weak shocks, which can be easily filtered out by making the condition (4.219) somewhat more restrictive and by requiring therefore that a shock is detected if

$$v_{12} > \tilde{v}_{12} = (\tilde{v}_{12})_{\mathcal{SR}} + \chi [(\tilde{v}_{12})_{\mathcal{PS}} - (\tilde{v}_{12})_{\mathcal{SR}}], \quad (4.222)$$

where  $(\tilde{v}_{12})_{\mathcal{PS}}$  is given by expression (4.206). Because  $(\tilde{v}_{12})_{\mathcal{PS}} \geq (\tilde{v}_{12})_{\mathcal{SR}}$ , any value of  $\chi$  between 0 and 1 will effectively raise the threshold for the detection of the shocks, filtering out the weakest ones.

A practical example of the implementation and effectiveness of the shock-detector recipe discussed above is shown in Fig. 4.18, where we report the rest-mass density distribution (left panel) and shock structure (right panel) on the equatorial plane of an accretion disc responding to a moving black hole (Zanotti *et al.*, 2011). The rest-mass density is plotted on a logarithmic

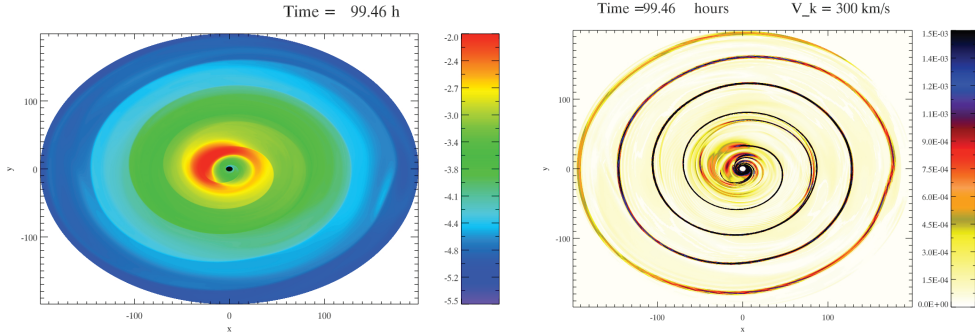


**Fig. 4.18** Logarithm of the rest-mass density distribution (left panel) and shock structure indicated by the values  $S_d > 0$  (right panel) on the equatorial plane of an accretion disc responding to a moving black hole. It is very difficult to determine the presence and position of the shock by simply looking at the density distribution. [From Zanotti *et al.* (2010), reproduced with permission © ESO.]

scale and in cgs units, while the shock structure is obtained by plotting the quantity  $S_d := \max\{0, v_{12}^x - \tilde{v}_{12}^x, v_{12}^y - \tilde{v}_{12}^y\}$ , whereby shock waves can form in regions where  $S_d > 0$ . The black hole is moving with velocity  $V_k = 300 \text{ km s}^{-1}$  towards the disc and, although it is not yet interacting directly with the matter in the disc, it induces the development of spiral shock waves as the disc attempts to readjust itself to the new and moving source of gravitational potential [more details on these calculations and the astrophysical implications can be found in Zanotti *et al.* (2011)]. The two panels in Fig. 4.18 highlight that it is very hard to locate a shock by simply looking at the density distribution or even at its gradients, but also that the shock detector discussed above provides a simple recipe for a sharp detection of large-scale shocks.

## 4.8 Stability of shock waves

The study of the stability of generic discontinuity surfaces is as complex and vast as it is important. While much of this type of study is nowadays carried out through fully nonlinear numerical simulations [see, e.g., Mach (2012)], there are some basic aspects of the stability of shock waves that are worth mentioning. Our discussion here, which will be relevant also for the analysis of the stability of reaction fronts in Section 5.5, is meant mostly as a pointer to the relevant literature.

Let us therefore start by discussing the concept of “evolutionarity” of a discontinuity surface (either a shock front or a reaction front) and the validity of a linear stability analysis. A discontinuity surface is said to be *evolutionary* if any infinitesimal perturbation of the initial state produces only an infinitesimal change in the flow over a sufficiently short time interval (Landau and Lifshitz, 1987). Stated differently, if a discontinuity is evolutionary, it can be momentarily perturbed and these perturbations have a regular evolution in time, on sufficiently short time-scales. However, an evolutionary front is not necessarily a stable front, since it might develop instabilities over a long enough time-scale. In order to establish whether an evolutionary front is also hydrodynamically stable, a detailed perturbative stability analysis is

necessary. However, even perturbative analyses, especially if only linear, are not guaranteed to describe the effective behaviour of a perturbed discontinuity surface. It is in fact possible that the modes that are found to be unstable in the perturbative analysis are ultimately controlled by intervening nonlinear effects, which would limit the energy transfer into the unstable modes and counteract their growth.

To determine whether a shock front (or a reaction front) is evolutionary it is sufficient to determine its *degree of under-determinacy*,  $\mathcal{D}_u$ , which is a measure of the number of free parameters which could be associated with a small perturbation of the front (Landau and Lifshitz, 1987; Burstein *et al.*, 1978).<sup>24</sup> These are determined as the difference between the number of unknown parameters associated with the front and the number of boundary conditions that the perturbation has to satisfy. In general, the unknown parameters are given by the number of acoustic perturbations that can be transmitted from the front, *i.e.*,  $\lambda_{\pm}^{a,b}$ , and by the entropy perturbations propagated in the downstream region of the flow, *i.e.*,  $\lambda_0^{a,b}$ , where again the indices “ $a$ ” and “ $b$ ” refer to the states ahead and behind the front, respectively. On the other hand, the boundary conditions are always three and given by the conservation across the discontinuity of rest mass, energy and momentum. The logic behind this counting is that if there are more parameters than those that can be constrained by the boundary conditions, then there is no expectation that these unconstrained parameters should remain bounded.

To fix ideas, we can consider the usual one-dimensional flow with a left-propagating discontinuity surface along the  $x$ -direction.<sup>25</sup> The number of free parameters can then be computed by considering a reference frame comoving with the shock front and by counting how many of the characteristics satisfy the conditions of moving away from the front. Using therefore the expressions for the eigenvalues derived in Eq. (4.25), these conditions, for a left-propagating shock, amount to requiring that [see, *e.g.*, Landau and Lifshitz (1987) and Seibert (1985) for a Newtonian equivalent]

$$\lambda_0^a > 0, \quad \lambda_{\pm}^a = \frac{v_a \pm c_{sa}}{1 \pm v_a c_{sa}} < 0, \quad (4.223)$$

$$\lambda_0^b > 0, \quad \lambda_{\pm}^b = \frac{v_b \pm c_{sb}}{1 \pm v_b c_{sb}} > 0. \quad (4.224)$$

Figure 4.19 can be of help in making this counting. It shows the spacetime diagrams and characteristics for the various combinations of velocities across a left-propagating shock front, as measured in the front rest frame. For each panel, the thick red line shows the worldline of the front, while the black solid lines represent the worldlines of a fiducial fluid element,  $\lambda_0^{a,b}$ . Similarly, blue solid lines indicate the characteristic curves,  $\lambda_{\pm}^{a,b}$ , while the dashed lines show the sound speed in the frame of the front and limit the sound cone (red shaded area). A quick look at the figure then reveals that, for instance, in the case of a shock front which is supersonic relative to the medium ahead and subsonic relative to the medium behind, the condition (4.223) is satisfied only by  $\lambda_0^a$ , while the condition (4.224) is satisfied by  $\lambda_0^b$  and  $\lambda_+^b$ . Hence there will be three free parameters matching the three boundary conditions represented

<sup>24</sup>An alternative but equivalent necessary condition for a shock to be evolutionary has been proposed by Lax (Lax condition) and requires that for a hyperbolic system of order  $N$ , the number of outgoing waves should be  $N - 1$  (Jeffrey, 1976; Anile, 1989; Falle and Komissarov, 2001).

<sup>25</sup>This choice is different from the one shown in Fig. 4.6, but more convenient here.

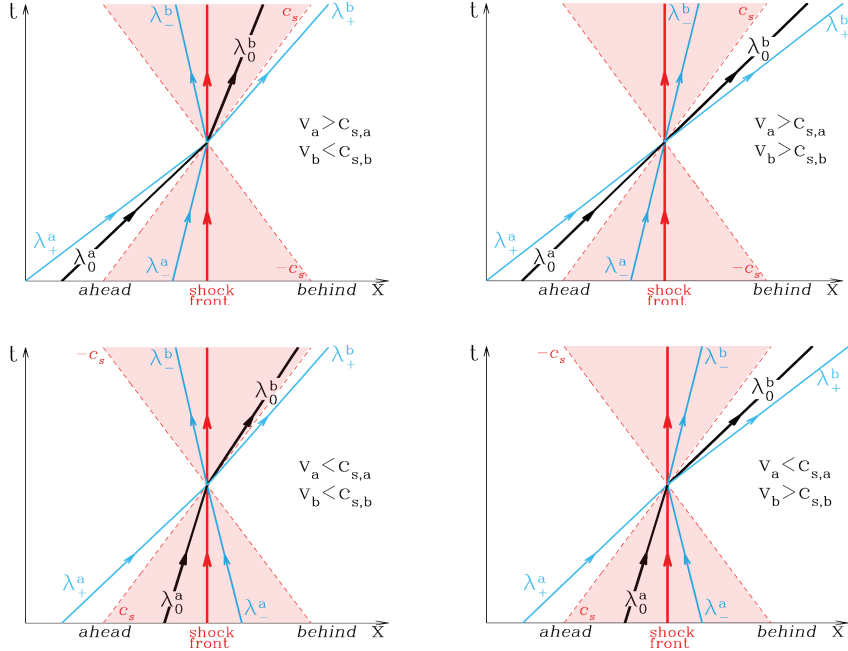


**Fig. 4.19** Spacetime diagrams and characteristics of the various types of shock fronts when considered as left-propagating. All velocities are measured in the shock rest frame and while the top row refers to supersonic flows ahead of the front, the bottom one refers to subsonic flows. For each panel, the thick red and black solid lines represent the worldlines of the front and of a fiducial fluid element,  $\lambda_0^{a,b}$ , respectively, while blue solid lines indicate the characteristic curves,  $\lambda_{\pm}^{a,b}$ , and the dashed lines show the sound speed in the frame of the front (assumed to be the same on either side of the front for simplicity).

by the conservation of mass, momentum and energy across the shock, thus yielding a zero degree of under-determinacy.

A comprehensive overview of the propagated perturbations and of corresponding degrees of under-determinacy for the different combinations of flow velocities is summarised in Table 4.1. The important result is therefore that *only* the conditions  $v_a > c_{sa}$ ,  $v_b < c_{sb}$ , which we had already selected in Section 4.4.3 as representative of a physically realistic shock [*cf.* Eq. (4.129)], provide a zero degree of under-determinacy and thus an *evolutionary shock front*. We remark that  $\mathcal{D}_u = 0$  is only a necessary but not sufficient condition for a shock to be evolutionary. All other combinations of the flow velocities do not even lead to necessary conditions for a shock to be evolutionary.

We have already hinted that a shock that is evolutionary could become unstable with respect to small perturbations of the discontinuity surface, which would then appear as “*corrugations*” of the front, that is, with the normal to the shock surface being no longer along the direction of propagation of the shock (see Fig. 5.6). We postpone to Section 5.5 a complete linear-perturbation analysis of the stability of a discontinuity surface, which will be relevant both for a shock front and for a reaction front. We here mention, however, the intuitive definition of corrugation stability introduced by Whitham for non-relativistic fluids and according

**Table 4.1** Perturbation types as propagated from a frame comoving with the various possible fronts and their associated degree of underterminacy.

Upstream velocity	Downstream velocity	Propagated perturbations	Degree of under-determinacy
$v_a > c_{sa}$	$v_b < c_{sb}$	$\lambda_0^a, \lambda_0^b, \lambda_+^b$	$3 - 3 = 0$
$v_a > c_{sa}$	$v_b > c_{sb}$	$\lambda_0^a, \lambda_-^b, \lambda_0^b, \lambda_+^b$	$4 - 3 = 1$
$v_a < c_{sa}$	$v_b < c_{sb}$	$\lambda_-^a, \lambda_0^a, \lambda_0^b, \lambda_+^b$	$4 - 3 = 1$
$v_a < c_{sa}$	$v_b > c_{sb}$	$\lambda_-^a, \lambda_0^a, \lambda_-^b, \lambda_0^b, \lambda_+^b$	$5 - 3 = 2$

to which a corrugated shock front is *stable* if the shock velocity decreases where the front is expanding and increases where it is contracting (Whitham, 1974).

In other words, consider a corrugated front with parts which are propagating at speeds larger than the unperturbed speed (convex part of the front) and parts which are propagating at speeds smaller than the unperturbed speed (concave part of the front). Such a corrugation will be smoothed out if the shock front slows down in the convex part and speeds up in the concave part. Should this happen, the shock front will be stable, while it will be unstable if the opposite is true. The importance of this criterion is that it is purely local (convexities and concavities are evaluated locally on the front) and is fully nonlinear, hence not requiring an expansion and linearisation of the equations. Anile and Russo (1986) have then cast this definition of stability into a more rigorous form and extended it to the case of relativistic fluids. In addition, they have performed a linear stability analysis, similar to the one we will carry out in Section 5.5.1, and confirmed the results obtained within the corrugation-stability analysis (Anile and Russo, 1987). The summary of these results is therefore the following: *an evolutionary shock front (i.e., with  $v_a > c_{sa}, v_b < c_{sb}$ ) is stable to linear perturbations and to corrugations*. A complete account of the basic results of the stability of relativistic shocks can also be found in the work of Russo and Anile (1987) and of Anile (1989). Finally, we note that, at least for ultrarelativistic fluids, it is possible to write necessary and sufficient conditions for a shock wave not to decay into a number of different discontinuity surfaces (Gorenstein and Zhdanov, 1987). These conditions, however, do not provide information about the stability of the shock or about its evolution when it is subject to corrugations.

We conclude this section with a simple but non-trivial question: how far can a shock propagate? A shock that is evolutionary and stable, in fact, will nevertheless be damped as a result of the dissipative processes taking place across it. As a consequence, the jump of the physical quantities across the shock will in general be a decreasing function of time. Determining the *shock damping* time-scale is of course of great importance in those situations in which the successful propagation of a shock is responsible for a physical process, *e.g.*, in a supernova explosion or for the perturbations travelling along relativistic extragalactic jets. Unfortunately, the complexity of these scenarios is such that the damping time is in general the end-result

of a combination of physical effects that need to be taken into account simultaneously and properly balanced. However, there are specific illustrative situations where progress can be made without much effort. As an example, in the case of a planar one-dimensional shock, the initial *damping time*,  $\tau_D$ , can be expressed in terms of the initial velocity jump across the shock as (Liang and Baker, 1977; Anile *et al.*, 1980)

$$\tau_D := \left( \frac{\llbracket v \rrbracket}{\delta \llbracket v \rrbracket} \right)_{t=0}, \quad (4.225)$$

where  $\delta \llbracket \phi \rrbracket := \llbracket \partial_t \phi \rrbracket + V_s \llbracket v^i \partial_i \phi \rrbracket$  is the *Thomas derivative* of a discontinuous scalar function  $\phi$  [see, *e.g.*, Anile (1989) for a discussion]. Hence, once the initial velocity jump across the shock is chosen, the damping time is fully determined. Note also that if  $c_s = 1$ , then  $V_s = 1$  and  $\delta \llbracket v \rrbracket = 0$ , so that  $\tau_D \rightarrow \infty$ , *i.e.*, the shock moves at the speed of light and is not damped. For less extreme conditions and simple initial data, *e.g.*, triangular or sine waves, the *quality factor*  $\mathcal{Q}$  (*i.e.*, the inverse of the damping time) is given by (Anile *et al.*, 1983; Lanza *et al.*, 1985)

$$\begin{aligned} \mathcal{Q} &:= 1/\tau_D \simeq \mathcal{O}(\llbracket v \rrbracket) && \text{for } \llbracket v \rrbracket \rightarrow 0, \\ \mathcal{Q} &:= 1/\tau_D \simeq \mathcal{O}(1 - \llbracket v \rrbracket) && \text{for } \llbracket v \rrbracket \rightarrow 1. \end{aligned} \quad (4.226)$$

Interestingly, the damping time diverges in the case of very weak shocks (*i.e.*,  $\llbracket v \rrbracket \rightarrow 0$ ), and also of ultrastrong shocks (*i.e.*,  $\llbracket v \rrbracket \rightarrow 1$ ). While the former result is rather easy to understand (the smaller the shock strength the smaller the entropy increase across it), the latter is less intuitive and has to do with the fact that as  $\llbracket v \rrbracket$  tends to 1, also  $V_s$  tends to the speed of light, so that it becomes increasingly difficult for dissipative processes to be effective. Clearly, these are rather idealised results and what should be learnt from the scaling in expressions (4.226) is that the damping time is in general a non-trivial function of the shock strength and has a local minimum, which numerical calculations in simplified scenarios suggest to be  $\tau_D \approx 10\text{--}100$  for  $\llbracket v \rrbracket \approx 0.4\text{--}0.5$  (Anile *et al.*, 1983; Lanza *et al.*, 1985).

## 4.9 General-relativistic discontinuities

Our treatment so far of nonlinear hydrodynamic waves and of discontinuity surfaces has been made under the assumption that the spacetime is flat but, more importantly, that the mass/energy associated with the fluid is so small that it does not change the spacetime curvature. Under these conditions, the fluid can be considered as a *test fluid* whose dynamics on a fixed background spacetime can be calculated without having to evolve the Einstein equations. However, when the fluid's contribution to the spacetime curvature can no longer be neglected, a different approach needs to be considered, in which possible discontinuities in the energy-momentum tensor are properly taken into account.

This problem was first addressed by Israel in the late 1960s (Israel, 1966; Israel, 1967) who, starting from the Gauss–Codazzi formalism (Hawking and Ellis, 1973; Misner *et al.*, 1973), developed the so-called *singular-hypersurface method*. This method has since found a number of applications in astrophysics (Smoller and Temple, 1995) and especially in cosmology, where it has been employed to study the motion of a shell in a dust universe (Maeda

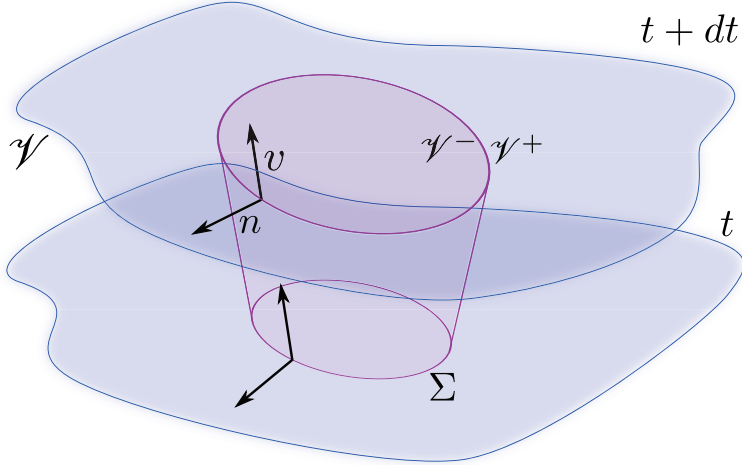


**Fig. 4.20** Schematic spacetime diagram of an expanding closed singular hypersurface  $\Sigma$  as it evolves from a spacelike hypersurface at time  $t$  to a subsequent one at time  $t + dt$ . (For convenience, one spatial dimension has been suppressed and the singular hypersurface is considered as closed.)  $n$  is the spacelike unit four-vector normal to the hypersurface and  $v$  is the timelike unit four-vector tangent to it.

and Sato, 1983; Lake and Pim, 1985), or the dynamics of bubbles in early-universe phase transitions (Maeda, 1986; Miller and Pantano, 1989; Rezzolla and Miller, 1994).

To appreciate the essence of the problem, it is sufficient to recall briefly the Einstein equations,  $G_{\mu\nu} = 8\pi T_{\mu\nu}$  [cf., Eqs. (1.220)], and realise that a discontinuity in the Einstein tensor,  $G_{\mu\nu}$ , is inevitable if there is a discontinuity in the energy-momentum tensor,  $T_{\mu\nu}$ . Since the Einstein tensor is a combination of first- and second-order derivatives of the metric tensor [cf., Eq. (1.203)], its discontinuity does not imply a discontinuity in the metric, but only in its first (or second) derivatives. The singular-hypersurface method provides therefore a mathematical framework to relate the discontinuities in the energy-momentum tensor to discontinuities in the curvature and in what follows we will review its most salient aspects. Before doing that, however, we should remark once again that the singular behaviour of matter at a discontinuity is only a shortcoming of the fluid description and not a manifestation of singular behaviour of physics (see Section 4.4.1). On sufficiently small scales, in fact, the properties of matter and of spacetime are perfectly continuous, although with very large changes over very small length-scales.

Within the singular-hypersurface approach, the evolution of a genuine discontinuity surface, or *singular surface*, can be described in terms of a three-dimensional timelike hypersurface  $\Sigma$  (*i.e.*, the worldtube of the discontinuity surface) which divides the four-dimensional spacetime  $\mathcal{V}$  into the two regions  $\mathcal{V}^+$  and  $\mathcal{V}^-$ , as shown in Fig. 4.20. Using the terminology of the previous sections, these regions can be thought of as representing the portions of the spacetime “ahead” and “behind” the travelling discontinuity surface. The basic idea in the singular-hypersurface approach is then that of “cutting out” the region of spacetime containing the hypersurface  $\Sigma$ , where junction conditions across the surface can provide suitable solutions, and of adopting the standard techniques of continuum relativistic hydro-

namics everywhere else. The form of the junction conditions across a discontinuity surface for special-relativistic fluids has been presented in Section 4.4.3 [*cf.*, Eqs. (4.109)–(4.110)], and these need to be suitably extended when applied across an interface treated as a singular hypersurface.

First of all we need to impose junction conditions on the metric to guarantee that proper measurements match across the singular hypersurface. In other words, the measurements of proper times and proper lengths made by two observers, located on either side of  $\Sigma$ , must match (May and White, 1967). This amounts to requiring that the observers measure the same invariant interval  $ds^2$  and hence that

$$[\![ds^2]\!] = 0, \quad (4.227)$$

where now the double brackets do not refer to jumps across a discontinuity on a spacelike two-dimensional surface [*cf.*, Eq. (4.108)], but as the jumps across  $\Sigma$  in the two submanifolds  $\mathcal{V}^+$  and  $\mathcal{V}^-$ , *i.e.*,  $[\![\Phi]\!] := \Phi^+ - \Phi^-$ , where  $\Phi^\pm$  are values of a generic quantity  $\Phi$  on either side of  $\Sigma$ .<sup>26</sup> In the simple case of a spherically symmetric metric in the generic form

$$ds^2 = -a^2 dt^2 + b^2 dr^2 + R^2 d\Omega^2, \quad (4.228)$$

the condition (4.227) is equivalent to requiring that

$$[\![a^2 dt^2 - b^2 dr^2 - R^2 d\Omega^2]\!] = 0. \quad (4.229)$$

Since  $4\pi R^2$  is the proper area of a spherical shell at a given time and this quantity must be continuous across  $\Sigma$ , we can write

$$[\![4\pi R^2]\!] = 0. \quad (4.230)$$

From this it is easy to rewrite (4.229) as the two distinct equations

$$[\![R]\!] = 0, \quad (4.231)$$

$$[\![f^2]\!] = [\![a^2 - b^2 \dot{r}^2]\!] = 0, \quad (4.232)$$

where  $\dot{r} := dr/dt$ . Since  $Rd\Omega$  represents the “circumferential” proper length, Eq. (4.231) simply expresses the fact that two metre rods lying parallel to the singular surface can be brought into contact there and be directly compared by the observers on either side. Finally, from the continuity of any  $R$  at any time  $t$ , we can deduce the additional metric junction condition

$$[\![\frac{dR}{dt}]\!] = [\![\dot{R}]\!] = [\![\partial_t R + \dot{r} \partial_r R]\!] = 0. \quad (4.233)$$

Next, we need to consider the junction conditions for the energy and momentum across  $\Sigma$ . To this end we introduce the unit spacelike four-vector  $\mathbf{n}$  normal to the timelike hypersurface  $\Sigma$  dividing the four-dimensional spacetime  $\mathcal{V}$  into  $\mathcal{V}^+$  and  $\mathcal{V}^-$ , *i.e.*,

$$n_\mu n^\mu = 1. \quad (4.234)$$

Similarly, we can introduce the unit timelike four-vector  $\mathbf{v}$  tangent to  $\Sigma$ , *i.e.*,  $v^\mu v_\mu = -1$ ,  $v^\mu n_\mu = 0$  (see Fig. 4.20).

<sup>26</sup>Because the concept of “ahead” and “behind” are not useful in the context of a singular hypersurface, we will use here the indices + and – to mark quantities on either side of  $\Sigma$ .

Being embedded in a higher dimensional spacetime, the hypersurface will have an extrinsic curvature  $K_{\alpha\beta}$  defined as<sup>27</sup>

$$K_{\alpha\beta} = \tilde{h}_{\alpha}^{\mu} \tilde{h}_{\beta}^{\nu} \nabla_{(\mu} n_{\nu)} , \quad (4.235)$$

where  $\tilde{h}_{\alpha\beta} := g_{\alpha\beta} - n_{\alpha} n_{\beta}$  is the projection operator on  $\Sigma$  and describes its three-geometry. We can introduce the symbol  $\tilde{\nabla}$  to denote the covariant derivative with respect to  $\tilde{h}$  in analogy with the symbol  $\nabla$  that we commonly use to denote the covariant derivative with respect to  $g$  [cf., Eq. (1.153)]. From the *Gauss–Codazzi equations* we can write (Israel, 1966)

$${}^{(3)}R + K_{\alpha\beta} K^{\alpha\beta} - K^2 = -2G_{\alpha\beta} n^{\alpha} n^{\beta} , \quad (4.236)$$

$$\tilde{\nabla}_{\beta} K_{\alpha}^{\beta} - \tilde{\nabla}_{\alpha} K = G_{\mu\nu} \tilde{h}_{\alpha}^{\mu} n^{\nu} , \quad (4.237)$$

where  $K := K_{\alpha}^{\alpha}$  is the trace of the extrinsic curvature and  ${}^{(3)}R$  is the Ricci scalar of the three-dimensional geometry  $\tilde{h}$ . Defining now as  $K_{\alpha\beta}^+$  and  $K_{\alpha\beta}^-$  the extrinsic curvatures of  $\Sigma$  in the two submanifolds  $\mathcal{V}^+$  and  $\mathcal{V}^-$ , we will say that  $\Sigma$  is a *singular hypersurface* representing the time evolution of a *surface layer* if  $K_{\alpha\beta}^+ \neq K_{\alpha\beta}^-$ . Conversely,  $\Sigma$  will be denoted simply as a hypersurface representing the time evolution of a *boundary surface* if  $K_{\alpha\beta}^+ = K_{\alpha\beta}^-$ . A typical example of a surface layer is the phase interface in general-relativistic first-order phase transitions and, in this case, the energy–momentum tensor in  $\mathcal{V}$  has a  $\delta$ -function singularity on  $\Sigma$ .

Let us now introduce the following two quantities  $S_{\alpha\beta}$  and  $\tilde{K}_{\alpha\beta}$  defined as

$$-8\pi \left( S_{\alpha\beta} - \frac{1}{2} h_{\alpha\beta} S \right) := \llbracket K_{\alpha\beta} \rrbracket , \quad (4.238)$$

$$2\tilde{K}_{\alpha\beta} := \{ \{ K_{\alpha\beta} \} \} , \quad (4.239)$$

where  $S := S_{\alpha}^{\alpha}$  and where we have introduced the additional double-bracket notation  $\{ \{ \Phi \} \} := \Phi^+ + \Phi^-$ . We then interpret  $S_{\alpha\beta}$ , which is nonzero only on  $\Sigma$ , as the energy–momentum tensor of the matter in the discontinuity surface, *i.e.*, the *surface energy tensor*, thus embodying the physical properties of the singular hypersurface (Israel, 1966). As a result,  $S_{\alpha\beta}$  can also be defined as

$$S_{\alpha\beta} = \lim_{\varepsilon \rightarrow 0} \int_{-\varepsilon}^{+\varepsilon} T_{\mu\nu} \tilde{h}_{\alpha}^{\mu} \tilde{h}_{\beta}^{\nu} dx , \quad (4.240)$$

where  $x$  is a Gaussian coordinate in the direction of  $\mathbf{n}$ , with  $x = 0$  on  $\Sigma$  [see, *e.g.*, Misner *et al.* (1973)], while  $T^{\mu\nu}$  is the usual energy–momentum tensor. Making use of the Einstein equations (1.218), and of Eqs. (4.236)–(4.239), we obtain

$${}^{(3)}R + \tilde{K}_{\alpha\beta} \tilde{K}^{\alpha\beta} - \tilde{K}^2 = -16\pi^2 \left( S_{\alpha\beta} S^{\alpha\beta} - \frac{1}{2} S^2 \right) - 8\pi \{ \{ T^{\alpha\beta} n_{\alpha} n_{\beta} \} \} , \quad (4.241)$$

$$\tilde{\nabla}_{\beta} \tilde{K}_{\alpha}^{\beta} - \tilde{\nabla}_{\alpha} \tilde{K} = 4\pi \{ \{ T^{\mu\nu} n_{\mu} h_{\nu\alpha} \} \} , \quad (4.242)$$

<sup>27</sup>For an easier comparison with the original work, we here follow the definition of the extrinsic curvature given by Israel (1966), which differs in sign from the more standard one that we will adopt in Chapter 7 [cf., Eq. (7.60)].

$$\tilde{K}_{\alpha\beta}S^{\alpha\beta} = \llbracket T^{\alpha\beta}n_\alpha n_\beta \rrbracket , \quad (4.243)$$

$$\tilde{\nabla}_\beta S^\beta_\alpha = - \llbracket T^{\mu\nu}n_\mu h_{\nu\alpha} \rrbracket . \quad (4.244)$$

Equations (4.241) and (4.242) can be regarded as the standard Hamiltonian and momentum constraints of a 3+1 decomposition of spacetime (see Section 7.1) when considered in a fictitious spacetime  $\tilde{V}$  in which  $\tilde{K}_{\alpha\beta}$  is the mean curvature of  $\Sigma$  (Maeda, 1986). On the other hand, Eqs. (4.243) and (4.244), together with the Einstein equations (1.218), are sufficient to describe the evolution of the singular surface and will account for the conservation of energy and momentum across  $\Sigma$ .

Next, it is convenient to use an orthonormal tetrad and to assume that the system under consideration has a planar or spherical symmetry, so that there exist two orthogonal Killing vectors  $e_{(A)}$ , with  $A = 2, 3$ , and the complete tetrad is then given by  $(v^\alpha, n^\alpha, e_{(A)}^\alpha)$ . Assuming that the matter in  $\mathcal{V}$  can be treated as a perfect fluid, the expressions for the energy-momentum tensors in the singular surface and in the two submanifolds  $\mathcal{V}^+$  and  $\mathcal{V}^-$  will be

$$S_{\alpha\beta} = (\gamma_\Sigma + \tilde{\sigma})v_\alpha v_\beta + \gamma_\Sigma h_{\alpha\beta}, \quad (4.245)$$

$$(T_F^{\alpha\beta})^\pm = (e^\pm + p^\pm)u^\alpha u^\beta + p^\pm(g^{\alpha\beta})^\pm, \quad (4.246)$$

where  $\gamma_\Sigma$  is the *surface energy* and  $\tilde{\sigma}$  is the bidimensional “tangential pressure”, or more simply the opposite of the surface tension, *i.e.*,  $\tilde{\sigma} := -\sigma$ .<sup>28</sup>

Projecting (4.244) along each of the directions of the orthonormal tetrad  $(v, n, e_{(A)})$  yields

$$\tilde{\nabla}_\alpha[(\gamma_\Sigma + \tilde{\sigma})v^\alpha] - v^\alpha\tilde{\nabla}_\alpha\tilde{\sigma} = \llbracket (e + p)(u^\alpha n_\alpha)(u^\beta v_\beta) \rrbracket , \quad (4.248)$$

$$(\gamma_\Sigma + \tilde{\sigma})n_\alpha v^\beta\tilde{\nabla}_\beta v^\alpha = 0, \quad (4.249)$$

$$(\gamma_\Sigma + \tilde{\sigma})e_{(A)}^\alpha v^\beta\tilde{\nabla}_\beta v_\alpha = 0, \quad (4.250)$$

where all of the fluid quantities are evaluated on the hypersurface  $\Sigma$ . Because of the definition of the unit vector  $v$ , its acceleration on  $\Sigma$  vanishes, *i.e.*,

$$v^\beta\tilde{\nabla}_\beta v^\alpha = 0, \quad (4.251)$$

and, as a consequence, (4.249) and (4.250) are trivially satisfied. It follows then that the only non-trivial equation is (4.248), which represents the energy conservation across  $\Sigma$ .

It should be noted that Eq. (4.251) is true only on  $\Sigma$ , and that, in general, the acceleration vector in  $\mathcal{V}$  is not zero, *i.e.*,

$$\frac{dv^\alpha}{d\tau} := v^\beta\nabla_\beta v^\alpha = -n^\alpha v^\mu v^\nu K_{\mu\nu}, \quad (4.252)$$

<sup>28</sup>In the case of a spherical bubble in a quark-gluon plasma [see, *e.g.*, Rezzolla *et al.* (1995)] the surface energy is defined as

$$\gamma_\Sigma := \sigma - T \left( \frac{\partial \sigma}{\partial T} \right)_A, \quad (4.247)$$

where  $T$  is the temperature and  $\sigma$  is the *surface tension* and is given by the change per unit area  $A$  of the *Helmholtz free energy*, *i.e.*,  $\sigma := \partial F / \partial A$  [*cf.* Eq. (3.200)].

where  $\tau$  is the proper time of an observer on  $\Sigma$ . Using (4.245) and (4.252), the left-hand side of equation (4.243) can be rewritten as

$$\begin{aligned}\tilde{K}_{\alpha\beta}S^{\alpha\beta} &= \left[ \left[ \gamma_{\Sigma} v^{\alpha} v^{\beta} + \tilde{\sigma} e_{(A)}^{\alpha} e_{(A)}^{\beta} \right] \right] \tilde{K}_{\alpha\beta} \\ &= -\frac{\gamma_{\Sigma}}{2} \left\{ \left\{ n_{\alpha} \frac{dv^{\alpha}}{d\tau} \right\} \right\} + \tilde{\sigma} \tilde{K}_{\alpha\beta} e_{(A)}^{\alpha} e_{(A)}^{\beta}.\end{aligned}\quad (4.253)$$

In the spherically symmetric line element (4.228), it is simple to write the second contraction on the right-hand side of (4.253) as

$$\tilde{K}_{\alpha\beta} e_{(A)}^{\alpha} e_{(A)}^{\beta} = K^{\theta}_{\theta} + K^{\phi}_{\phi} = n^{\alpha} \partial_{\alpha} (\ln R), \quad (4.254)$$

from which Eq. (4.243) further reduces to

$$\left\{ \left\{ -\frac{\gamma_{\Sigma}}{2} n_{\alpha} \frac{dv^{\alpha}}{d\tau} + \tilde{\sigma} n^{\alpha} \partial_{\alpha} (\ln R) \right\} \right\} = \left[ \left[ (e + p)(u^{\alpha} n_{\alpha})^2 + p \right] \right]. \quad (4.255)$$

In summary, Eqs. (4.248) and (4.255) represent the time-dependent part of the Einstein equations evaluated across a singular spherically symmetric hypersurface  $\Sigma$ . These ensure the conservation of energy and momentum across such a hypersurface and prescribe its evolution in time. The specialisation of expressions (4.248) and (4.255) to the case of a spherical expanding hadron bubble in a quark–gluon plasma can be found in Rezzolla *et al.* (1995) and Rezzolla and Miller (1996).

#### 4.10 Further reading

- Anile, A. M. (1989). *Relativistic Fluids and Magneto-fluids*. Cambridge University Press, Cambridge.
- Courant, R. and Friedrichs, K. O. (1976). *Supersonic Flows and Shock Waves*. Springer, Berlin.
- Font, J. A. (2008). Numerical Hydrodynamics and Magnetohydrodynamics in General Relativity. *Living Rev. Relativ.*, **11**, 7.
- Landau, L. D. and Lifshitz, E. M. (1987). *Fluid Mechanics*. Course of Theoretical Physics, Vol. 6. Butterworth-Heinemann, Oxford.
- LeVeque, R. J. (2002). *Finite Volume Methods for Hyperbolic Problems*. Cambridge University Press, Cambridge.
- Martí, J. M. and Müller, E. (2003). Numerical Hydrodynamics in Special Relativity. *Living Rev. Relativ.*, **6**, 7.
- Whitham, G. B. (1974). *Linear and Nonlinear Waves*. Pure and applied mathematics. John Wiley, New York.

## 4.11 Problems

1. Using the characteristic matrix (4.13)

$$\begin{aligned} \mathcal{A}^\mu \xi_\mu &= \begin{pmatrix} \rho h a \delta_\beta^\alpha & h^{\alpha\mu} \xi_\mu c_s^2 & h^{\alpha\mu} \xi_\mu \partial_s p \\ \rho h \xi_\beta & a & 0^\mu \\ 0_\beta^\mu & 0^\mu & a \end{pmatrix} \\ &= \begin{pmatrix} \rho h a & 0 & 0 & 0 & h^{0\mu} \xi_\mu c_s^2 & h^{0\mu} \xi_\mu \partial_s p \\ 0 & \rho h a & 0 & 0 & h^{1\mu} \xi_\mu c_s^2 & h^{1\mu} \xi_\mu \partial_s p \\ 0 & 0 & \rho h a & 0 & h^{2\mu} \xi_\mu c_s^2 & h^{2\mu} \xi_\mu \partial_s p \\ 0 & 0 & 0 & \rho h a & h^{3\mu} \xi_\mu c_s^2 & h^{3\mu} \xi_\mu \partial_s p \\ \rho h \xi_0 & \rho h \xi_1 & \rho h \xi_2 & \rho h \xi_3 & a & 0 \\ 0 & 0 & 0 & 0 & 0 & a \end{pmatrix}, \end{aligned}$$

where  $a := u^\mu \xi_\mu$ , derive the eigenvalues (4.15).

2. Prove that in a rarefaction wave  $\mathcal{J}_+$  ( $\mathcal{J}_-$ ) is constant along the characteristic  $\lambda_+$  ( $\lambda_-$ ), namely that

$$\left[ \partial_t + \left( \frac{v + c_s}{1 + vc_s} \right) \partial_x \right] \mathcal{J}_+ = 0, \quad \left[ \partial_t + \left( \frac{v - c_s}{1 - vc_s} \right) \partial_x \right] \mathcal{J}_- = 0.$$

[Hint: Assume  $\mathcal{J}_\pm$  as given by

$$\mathcal{J}_\pm = \frac{1}{2} \ln \left( \frac{1+v}{1-v} \right) \pm \frac{1}{\sqrt{\Gamma-1}} \ln \left( \frac{\sqrt{\Gamma-1} + c_s}{\sqrt{\Gamma-1} - c_s} \right)$$

and exploit the continuity and momentum equations as resulting from the system (4.35) with  $A_p$  given by (4.40). Also use the property  $\partial_i p = hc_s^2 \partial_i \rho$ , which is valid for isentropic flows.]

3. Using the differential relation

$$W^2 dv \pm \frac{c_s}{\rho} d\rho = 0,$$

and exploiting the isentropic character of simple waves, derive Eq. (4.59), showing that it is equivalent to (4.62).

4. Using the junction conditions (4.131)–(4.132), and under the assumption of a highly relativistic shock, *i.e.*,  $W_a \gg 1$ ,  $p_a = 0$ ,  $e_a = \rho_a$ ,  $p_b = e_b/3$ , show that  $e_b = 2W_a^2 e_a$ . This proves that the energy density in the shocked fluid scales like the square of the Lorentz factor of the shock front (with respect to the unshocked fluid).
5. Using the junction condition (4.140), compute the mass flux  $J$  such that the shock velocity  $V_s$  is twice the velocity  $v_a$  in the unshocked region. Compare it with the corresponding Newtonian mass flux. Which of the two is larger for the same value of  $v_a$ ?
6. Verify that the double brackets satisfy the following identities:
  - (i)  $\alpha \llbracket A \rrbracket = \llbracket \alpha A \rrbracket$ , if and only if  $\llbracket \alpha \rrbracket = 0$ ;
  - (ii)  $\llbracket A + B \rrbracket = \llbracket A \rrbracket + \llbracket B \rrbracket$ ;
  - (iii)  $\llbracket A B \rrbracket \neq \llbracket A \rrbracket \llbracket B \rrbracket$ ;
  - (iv)  $\llbracket A \rrbracket \llbracket B \rrbracket = \llbracket B \rrbracket \llbracket A \rrbracket$ ;
  - (v)  $\llbracket A^2 \rrbracket \neq \llbracket A \rrbracket^2$ .
7. Write a numerical code that solves the one-dimensional Riemann problem according to the procedure described in Section 4.6.

# 5

## Reaction Fronts: Detonations and Deflagrations

---

A large part of the mathematical framework developed in the previous chapter for the study of the properties and dynamics of shock waves can be applied also when chemical or physical changes take place in the fluid as it crosses the discontinuity surface. This chapter is dedicated to the analysis of relativistic reaction fronts, either deflagrations or detonations, and to the study of their stability under different conditions.

### 5.1 Basic properties of reaction fronts

Within a Newtonian treatment, reaction fronts are discontinuities in the flow that are described as moving surfaces by means of which a suitable fluid mixture undergoes a *chemical transformation*, with release of energy and heat [see, *e.g.*, Courant and Friedrichs (1976), Landau and Lifshitz (1987), Burstein *et al.* (1978), Fickett and Davis (1979), and Buckmaster *et al.* (1983)]. As a result of the transformation, the fluid behind the reaction front can be either compressed and decelerated (*i.e.*, in detonations) or decompressed and accelerated (*i.e.*, in deflagrations). The study of the microphysics in the narrow region where the reaction processes take place is extremely complicated and an exhaustive theory of it within the context of relativistic reaction fronts has not yet been reached. Nevertheless, just as for shock waves, a satisfactory hydrodynamic description of reaction fronts can be achieved when these are treated as idealised discontinuity surfaces of infinitesimal and constant width, across which rapid changes in the fluid properties take place. As already discussed in Section 4.4.1 for generic fluid discontinuities, also the theory of reaction fronts represents a good approximation as long as the front has a thickness which is much smaller than the typical length-scale of the variation of the flow variables and if the thermal and the viscous time-scales are much smaller than that set by the motion of the front, *i.e.*, as long as conditions (4.85)–(4.86) are satisfied. Hereafter, we will assume that these requirements are met also when dealing with reaction fronts and, hence, that a hydrodynamic description is the most adequate.

In this respect, reaction fronts are very similar to shock fronts and can be essentially described by using the same mathematical theory developed for shocks in the previous chapter (see Section 4.4.3). However, in two important respects reaction fronts and shock fronts differ. The first one is that, as a result of the reaction taking place at the reaction front, the fluids on either side of the front are *chemically and physically different*. This is not the case for a shock front, for which the fluid changes its energy density and entropy (it is compressed and decelerated), but the irreversible processes occurring across the front do not produce a change in its

chemical and physical properties, and the same equation of state will hold on either side of the shock. Conversely, for a reaction front, the irreversible processes taking place at the front do produce an intrinsic change in the chemical and physical properties of the fluid. As a result, fluid elements on either side of a reaction front are described by different equations of state, each accounting for the different molecular binding energies (in the case of a non-relativistic fluid) or for the different number of degrees of freedom or vacuum energies (in the case of a relativistic fluid). The second important aspect in which reaction fronts differ from shock fronts is that the flow behind the former is not necessarily in a constant state, but, as we will see below, can also be represented by a rarefaction wave.

Relativistic reaction fronts have been considered in recent years in a number of different scenarios, which would not be possible to review in detail here. These involve:

- the hydrodynamics of the phase interface during cosmological first-order phase transitions, *e.g.*, Steinhardt (1982), Gyulassy *et al.* (1984), Kurki-Suonio (1985), Miller and Pantano (1989), Rezzolla *et al.* (1995) (see also the discussion in Sections 11.1.2, 11.1.3);
- the collision of relativistic heavy ions, *e.g.*, Huovinen and Ruuskanen (2006), Ollitrault (2008), Romatschke (2010) (see also the discussion in Section 11.10);
- the generation of a gravitational-wave background resulting from phase transitions in the early universe, *e.g.*, Caprini *et al.* (2008) and Leitao *et al.* (2012);
- the burning of a neutron star into a quark or a hybrid star, with the consequent emission of gravitational and electromagnetic waves, *e.g.*, Tokareva *et al.* (2005) and Drago *et al.* (2007), Herzog and Röpke (2011);
- the explosion mechanisms in Type Ia supernovae and the related emission of electromagnetic radiation and the ejection of heavy elements, *e.g.*, Hoefflich *et al.* (1998), Calder *et al.* (2007), Jordan *et al.* (2008) and Ciaraldi-Schoolmann *et al.* (2009).

In what follows we will review the most salient aspects of detonations and deflagrations, and of their stability properties.

## 5.2 Reaction adiabat

Given the numerous similarities, the analysis of reaction fronts proceeds in close analogy to that of shock fronts and we can therefore start directly from the equations of conservation of rest mass, momentum and energy across the reaction front [*cf.*, Eqs. (4.109) and (4.110)] for one-dimensional flows in special relativity (also in this case, the extension to multidimensional and curved spacetimes is straightforward). In this way we will obtain again an adiabat in the  $(p, h/\rho)$  plane, which is however referred to as the *reaction adiabat*, to distinguish it from the analogous but distinct *Taub adiabat*. Indeed, although the reaction adiabat has the same functional form as the Taub adiabat (4.118), it represents *only* the state behind the front, while the state ahead of the front lies on a Taub adiabat proper.

To discuss in more detail the properties of the fluid on either side of a reaction front it is convenient to introduce the *compression coefficient* (Danielewicz and Ruuskanen, 1987; Bonometto and Pantano, 1993)

$$x := \frac{\rho_b h_b W_b^2 v_b^2}{\rho_a h_a W_a^2 v_a^2}, \quad (5.1)$$

## 260 Reaction Fronts: Detonations and Deflagrations

where, as usual,  $\rho$ ,  $h$ ,  $v$ , and  $W$  represent respectively the rest-mass density, the specific enthalpy, the fluid velocity and the corresponding Lorentz factor, while the indices  $a$  and  $b$  refer to the fluid ahead and behind the *reaction front*. The denomination in (5.1) derives from the fact that, in the Newtonian limit, the compression coefficient represents simply the ratio of the two densities, *i.e.*,

$$x \stackrel{\text{N}}{=} \frac{\rho_b v_b^2}{\rho_a v_a^2} \stackrel{\text{N}}{=} \frac{\rho_a}{\rho_b}, \quad (5.2)$$

where we have used the Newtonian continuity of mass across the front,  $\rho_a v_a = \rho_b v_b$ . Adopting the definition (5.1) and a bit of algebra, we can rewrite the Taub adiabat (4.118) as (see Problem 1)

$$\rho_b h_b x - \rho_a h_a + (p_a - p_b)(1 + x) = 0, \quad (5.3)$$

which represents the expressions for the *reaction adiabat* once a prescription to describe the chemical/physical transition to the state behind has been chosen. We can also use the laws of conservation of momentum and energy (4.113)–(4.114) to obtain the additional inequalities which must be satisfied across the front (see Problem 2)

$$\frac{x(p_a - p_b)}{x - 1} = \rho_b h_b W_b^2 v_b^2 > 0, \quad (5.4)$$

$$\frac{p_a - p_b}{x - 1} = \rho_a h_a W_a^2 v_a^2 > 0, \quad (5.5)$$

$$\frac{p_a - p_b}{v_b - v_a} = \rho_a h_a W_a^2 v_a > 0 \quad \text{if } v_a > 0. \quad (5.6)$$

Inequalities (5.4)–(5.6) distinguish the reaction adiabat as two different branches: the *detonation* branch and the *deflagration* branch, with physical conditions given by

$$p_a < p_b, \quad v_a > v_b, \quad x < 1 : \quad \text{detonations}, \quad (5.7)$$

$$p_a > p_b, \quad v_a < v_b, \quad x > 1 : \quad \text{deflagrations}. \quad (5.8)$$

These branches are illustrated in Fig. 5.1, which shows the Taub adiabat (blue dashed line) and reaction adiabat (red solid line) for a generic reaction front. The state ahead of the reaction front, “ $a$ ”, lies on the Taub adiabat and can be connected to the state behind the front, “ $b$ ” (not indicated in the figure), which lies instead on the reaction adiabat. As for shocks, the slope of the chord connecting the two states is proportional to the mass flux across the reaction front, *i.e.*,  $-J^2 = -(\rho_a W_a v_a)^2 = -(\rho_b W_b v_b)^2$ , and the local tangents at  $a$  and  $b$  are proportional to the local sound speeds (see Fig. 4.7). For mass fluxes which are not imaginary, the chord between the two adiabats then selects two branches, which are relative to detonations and deflagrations, respectively. The states on each branch are further distinguished into *weak* and *strong* reaction fronts, with *Chapman–Jouguet* detonations and deflagrations distinguishing the two classes (marked as C–J in Fig. 5.1). The part of the reaction adiabat between the two branches indicated with a dotted line in Fig. 5.1 refers to a non-physical region since the mass flux is imaginary there [*cf.* Eq. (4.115)].

Many of the properties of the different classes of reaction fronts can be derived by simply looking at different slopes in Fig. 5.1. Let us start from the slope of the tangent at  $a$  on the Taub adiabat (light-blue solid line): we have seen that this slope is proportional to the sound

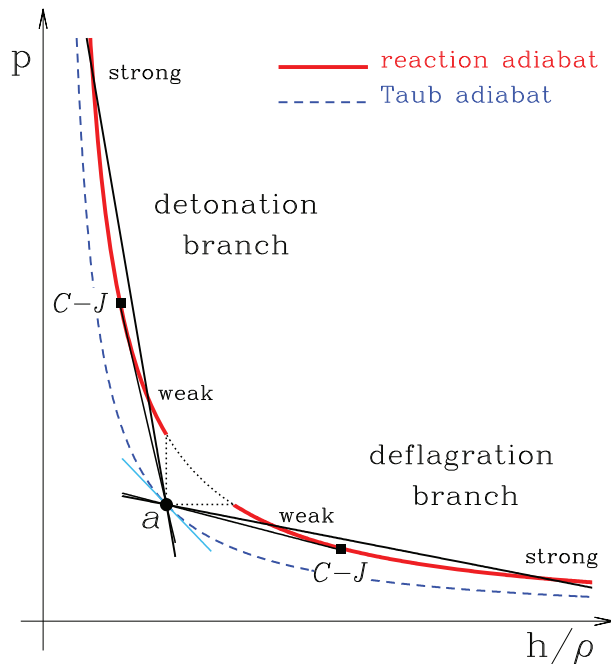


**Fig. 5.1** Taub and reaction adiabats for a generic reaction front. The state ahead of the reaction front  $a$  lies on the Taub adiabat (blue dashed line) and can be connected to the state behind the front  $b$  (not indicated), which lies instead on the reaction adiabat (red solid line). The slope of the chord connecting the two states is proportional to the mass flux across the reaction front and the local tangents at  $a$  and  $b$  are proportional to the local sound speeds (see Fig. 4.7). The reaction adiabat selects two branches which are relative to detonations and deflagrations, with each branch further distinguishing weak and strong reaction fronts, and with Chapman–Jouguet detonations/deflagrations separating the two classes (marked as C–J). The part of the reaction adiabat between the two branches indicated with a dotted line refers to a non-physical region with imaginary mass flux.

speed of the fluid ahead of the front,  $c_{sa}$ . A simple comparison with the slope of the chords on the detonation branch, which have slopes proportional to the velocities ahead of the front, leads us to the conclusion that  $v_a > c_{sa}$  for all states  $b$  on the detonation branch. Stated differently, detonations always move *supersonically* relative to the fluid ahead. In addition, we can deduce that the chord which is also tangent to the detonation branch will select the slowest detonation wave and, by definition, will have the velocity of the fluid behind the front that is equal to the local sound speed, *i.e.*,  $v_b = c_{sb}$  (see Fig. 4.7). Such reaction fronts are referred to as *Chapman–Jouguet detonations* and represent a very special class of detonations, as we will further discuss in Section 5.3. It is equally simple to conclude that states “above” the Chapman–Jouguet detonation (*i.e.*, with  $p > p_{C-J}$ ) will be characterised by  $v_b < c_{sb}$ , while states “below” by  $v_b > c_{sb}$ . These are referred to as *strong* and *weak detonations*, respectively (see Fig. 5.1).

Using the same logic, we can compare the slope of the chords on the deflagration branch

**Table 5.1** Main fluid properties for the different types of reaction front. Note that detonations are always supersonic relative to the fluid ahead and that deflagrations are always subsonic. Chapman–Jouguet detonations and deflagrations are instead characterised by sonic flows behind. Note that weak reaction fronts are those for which the velocities ahead and behind the front are either both subsonic (weak deflagrations) or supersonic (weak detonations).

	Detonations ( $p_a < p_b$ , $v_a > v_b$ )	Deflagrations ( $p_a > p_b$ , $v_a < v_b$ )
Weak	$v_a > c_{sa}$ , $v_b > c_{sb}$	$v_a < c_{sa}$ , $v_b < c_{sb}$
Chapman–Jouguet	$v_a > c_{sa}$ , $v_b = c_{sb}$	$v_a < c_{sa}$ , $v_b = c_{sb}$
Strong	$v_a > c_{sa}$ , $v_b < c_{sb}$	$v_a < c_{sa}$ , $v_b > c_{sb}$

and deduce that  $v_a < c_{sa}$  for all states  $b$  on the deflagration branch. In other words, deflagrations always move *subsonically* relative to the fluid ahead. In addition, we can deduce that the chord which is also tangent to the deflagration branch will select the fastest deflagration wave and, by definition, will have the velocity of the fluid behind equal to the local sound speed, *i.e.*,  $v_b = c_{sb}$ . Such reaction fronts are referred to as *Chapman–Jouguet deflagrations*. Finally, we can conclude that states “above” the Chapman–Jouguet deflagration will be characterised by  $v_b < c_{sb}$ , while states “below” by  $v_b > c_{sb}$ . These are referred to as *weak deflagrations* and *strong deflagrations*, respectively (see Fig. 5.1).

The classification of the various reaction fronts is summarised in Table 5.1 and a useful mnemonic rule is to remember that *weak* reaction fronts are those for which the velocities ahead and behind the front are either both subsonic (*i.e.*, weak deflagrations) or supersonic (*i.e.*, weak detonations). The following sections are devoted to a brief review of the main properties of detonation and deflagration fronts, while Sections 11.1.2 and 11.1.3 will explore the fluid properties across these fronts when the flow is assumed to be spherically symmetric and self-similar.

### 5.3 Relativistic detonations

As mentioned above, detonation fronts propagate supersonically relative to their medium ahead, so that no causal influence from the front is possible on the upstream region of the flow, which, therefore, cannot be perturbed (see also Section 5.5 for a discussion of the causal structure of reaction fronts). If initially at rest, the fluid crossed by a detonation front is compressed, heated and set into motion, while the flow immediately behind the front is characterised by a region in which the fluid is smoothly decompressed and decelerated. This *rarefaction wave* is therefore limited by a supersonic “head” and by a “tail”, which instead moves at the local sound speed in the case in which the velocity is zero at the downstream boundary of the flow. A schematic spacetime diagram of a detonation front is shown in Fig. 5.2, which reports with a heavy red line the worldline of the detonation front, while the thin solid lines with arrows

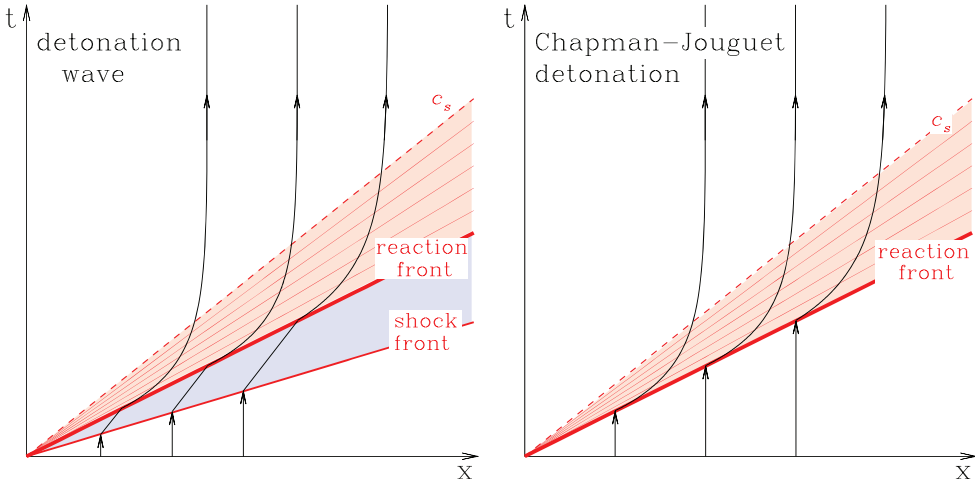


**Fig. 5.2** Schematic spacetime diagram of a one-dimensional flow across a detonation wave. The heavy red line traces the worldline of the detonation front, while the thin solid lines with arrows represent the worldline of fiducial fluid elements which are initially and eventually at rest. Also shown with red thin solid lines are the characteristics in the rarefaction wave following the reaction front, with the tail of the rarefaction being indicated with a red dashed line moving at the local sound speed  $c_s$ . The left panel refers to a detonation which is preceded by a shock across which the fluid is accelerated up to the reaction front, where it is decompressed in a rarefaction wave. The right panel refers to a Chapman–Jouguet detonation, in which the shock and the reaction front merge and are followed by a rarefaction wave (see also the bottom row of Fig. 11.3 for the solution relative to a spherical self-similar expanding detonation).

represent the worldlines of fiducial fluid elements that are initially and eventually at rest. Also shown with red thin solid lines behind the reaction front are the characteristics in the rarefaction fan, whose tail moves at the local sound speed  $c_s$  as a *weak discontinuity* and is indicated with a red dashed line. The left panel, in particular, refers to a detonation that is preceded by a shock across which the fluid is compressed and accelerated to a constant velocity up to the reaction front, where it encounters a rarefaction wave and is decompressed. The right panel, on the other hand, refers to a Chapman–Jouguet detonation, in which the shock and the reaction front merge and are followed by a rarefaction wave. The profiles for the velocity and the energy density relative to a spherical self-similar expanding detonation can be found in Fig. 11.3, within the discussion of self-similar flows.

As shown in Table 5.1, detonations can be distinguished according to the magnitude of the fluid velocities on either side of the detonation front when these are compared with the local sound speed. In this sense, are defined as *weak*, *strong* and *Chapman–Jouguet*, those detonations having respectively supersonic, subsonic, and sonic downstream flows. A formal similarity exists between detonations and another class of reaction fronts called *condensation discontinuities*, which in a Newtonian framework, are discontinuity surfaces across which a supersaturated vapour undergoes a phase transformation becoming a condensed vapour (*e.g.*, the small droplets of fog). Condensation discontinuities are reaction fronts because they do not simply result from the compression of a fluid across a shock wave, which, in general produces

a local increase of the temperature larger than the local increase of the degree of supersaturation. Rather, condensation discontinuities are exothermic processes and it is the release of the latent heat that induces the condensation of the supersaturated vapour; as a result, they can take place only in fluids with sufficiently large heat capacities. Because of their similarities with detonations, the description of condensation discontinuities uses the same formal description of detonation waves (Landau and Lifshitz, 1987; Thompson *et al.*, 1986), and they have been considered in connection with cosmological first-order phase transitions (Applegate and Hogan, 1985; Laine, 1994).

Important features of detonations can be deduced by counting the number of “unknowns” that are typical of the hydrodynamic solution of a detonation wave. In general, we need to calculate the energy densities and the velocities on each side of the discontinuity surface and the velocity  $v_{\text{det}}$  at which the detonation moves relative to an Eulerian frame. There are therefore five unknowns, *i.e.*,  $e_a$ ,  $v_a$ ,  $e_b$ ,  $v_b$  and  $v_{\text{det}}$ , that can be balanced by the three equations expressing the conservation of rest mass, energy and momentum across the reaction front. If one of the two states, *e.g.*, the unperturbed one, is specified, then the dynamics of a detonation wave is fully determined.

As mentioned earlier, a special class of detonations is the one in which the velocity out of the reaction front equals the local sound speed, namely Chapman–Jouguet detonations. These detonations, we recall, are the slowest of all possible detonations and represent a particularly relevant class of reaction fronts, whose peculiar nature is emphasised by the “*Chapman–Jouguet hypothesis*”. According to this hypothesis, detonations in chemical combustion should occur *only* under the form of Chapman–Jouguet detonations and a proof of this can be found in Courant and Friedrichs (1976) or in Landau and Lifshitz (1987) for an ideal self-similar Newtonian detonation. Although non-relativistic detonations in chemical combustion often appear accompanied by nonlinear effects such as transverse shock waves or turbulence (Fickett and Davis, 1979), the Chapman–Jouguet hypothesis is generally verified to a good approximation, with detonation fronts which although complicated, propagate at a constant velocity close to the theoretical Chapman–Jouguet value (Lewis and Elbe, 1987; Williams, 1965; Engquist *et al.*, 1988). However, because of the differences between chemical combustions and phase transitions, the validity of the Chapman–Jouguet hypothesis cannot be easily extended to a relativistic regime, *e.g.*, in the context of cosmological phase transitions (Laine, 1994; Kurki-Suonio and Laine, 1995).

Another important property of Chapman–Jouguet detonations is that the entropy of the fluid behind the front is at a *minimum* [see, *e.g.*, Anile (1989) for a proof]. To appreciate the physical consequences of this result it is useful to make use of Fig. 5.3, which is similar to Fig. 5.1, but concentrates on the detonation branch. Also in this case, the state ahead of the detonation front,  $a$ , lies on the Taub adiabat (blue dashed line) and can be connected to the state behind the front,  $b$ , on the reaction adiabat (red solid line). A strong detonation can then be seen as a sequence of transformations from state  $a$  to state  $c$  and then to state  $b$ . More specifically, we can consider a detonation front as a region of finite width across which the reaction takes place and whose forward-moving surface is represented by a shock front moving into the unreacted fluid (Landau and Lifshitz, 1987). In this picture, we can then think that, as the fluid moves across the shock wave, it is heated and compressed and thus is effectively moving on the chord  $ac$  from the state  $a$ , over to the state  $c$ . Here, the physical conditions are such that the reaction can take place, with the latent heat of the reaction

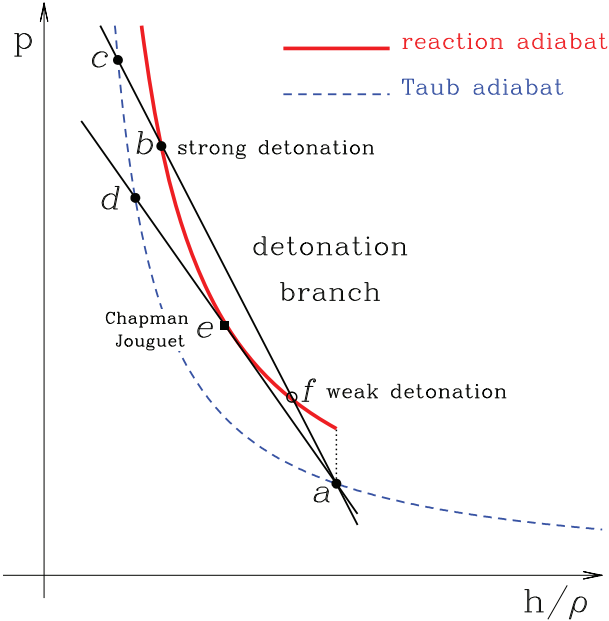


**Fig. 5.3** Taub and reaction adiabats for a generic detonation front. As in Fig. 5.1, the state ahead of the detonation front,  $a$ , lies on the Taub adiabat (blue dashed line) and can be connected to the state behind the front,  $b$ , on the reaction adiabat (red solid line). A strong detonation can be seen as a sequence of transformations from state  $a$  to state  $c$  and then to state  $b$ . Also shown is a Chapman–Jouguet detonation,  $e$ , for which  $v_a > c_{sa}, v_b = c_{sb}$  and the entropy of the medium behind the reaction front is at a minimum. As a result, the state  $f$ , representing weak detonations, cannot be achieved in a detonation which releases energy.

being released, and with the fluid expanding and reducing its pressure, which is however larger than the unreacted one. This reaction and expansion process is therefore equivalent in the  $(p, h/\rho)$  plane to a transition from point  $c$ , over to the final state  $b$  along the chord  $cb$ , which will be representative of a strong detonation. Also shown in Fig. 5.3 is the Chapman–Jouguet detonation,  $e$ , which can be thought of as the result of the transition  $a-d-e$ . Since a Chapman–Jouguet detonation produces a reacted fluid with the minimum entropy, the state  $f$ , which does satisfy the same conservation laws as state  $b$ , would have an entropy smaller than the minimum one, *i.e.*, that of the Chapman–Jouguet detonation, and cannot therefore be reached via a transition from the state  $a$ . Stated differently, weak detonations are not physically possible in reaction fronts which are exothermic, *e.g.*, in chemical burning.

In Section 5.5.1, we will prove that strong and Chapman–Jouguet detonations are evolutionary and linearly stable to corrugations of the detonation front.

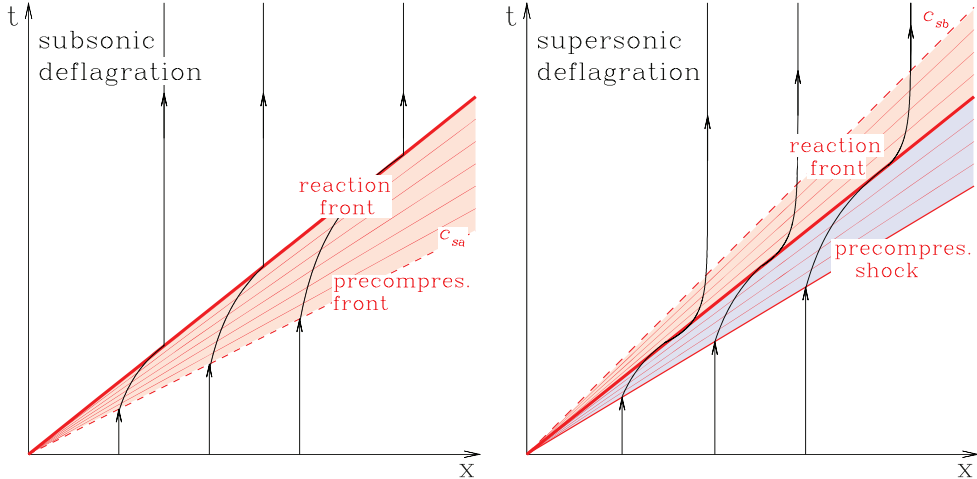


**Fig. 5.4** Schematic spacetime diagram of a one-dimensional flow across deflagration waves. The heavy red line traces the worldline of the reaction front, while the thin solid lines with arrows represent the worldline of fiducial fluid elements which are initially and eventually at rest. Also shown with red thin solid lines are the characteristics in the rarefaction or compression waves following or preceding the reaction front. A red dashed line indicates the local sound speed  $c_s$ . The left panel refers to a (subsonic) deflagration, which is preceded by a precompression wave whose leading edge is a weak discontinuity moving at the local sound speed  $c_{sa}$  for an unperturbed medium which is at rest (see also the top row of Fig. 11.3 for the solution relative to a spherical self-similar expanding deflagration). The right panel, on the other hand, refers to a supersonic deflagration, which is preceded by a shock front and is followed by a rarefaction wave (see also the third row of Fig. 11.3 for the solution relative to a spherical self-similar expanding supersonic deflagration).

## 5.4 Relativistic deflagrations

Deflagration waves have been extensively investigated within the classical theory of combustion and laminar flames. As mentioned above, deflagration fronts move subsonically relative to their medium ahead, so that the reaction front can perturb the unreacted fluid by means of a *precompression wave* travelling ahead of the deflagration front. The leading edge of the precompression wave is either a weak discontinuity moving at the local sound speed  $c_{sa}$  if the reaction front is subsonic, or a shock front moving supersonically if the reaction front is supersonic. The role of the precompression wave is that of accelerating, compressing and heating the fluid before it is swept by the deflagration front, thus establishing suitable hydrodynamic and chemical conditions under which the reaction can take place. It should be emphasised that the fluid undergoes a chemical or physical transformation only when it is swept by the deflagration front and that no chemical transformation takes place in the precompression front.

A schematic spacetime diagram of a one-dimensional flow across two representative deflagration waves is shown in Fig. 5.4, where the heavy red line traces the worldline of the reaction front moving at  $v_{\text{def}}$ , while the thin solid lines with arrows represent the worldline of fiducial fluid elements, which are initially and eventually at rest. Also shown with red thin solid lines are the characteristics in the rarefaction or compression waves following or preced-

ing the reaction front, while the red dashed line indicates the local sound speed  $c_s$ . The left panel refers to a *subsonic deflagration*, which is preceded by a precompression wave whose leading edge is a weak discontinuity moving at the local sound speed  $c_{sa}$  for an unperturbed medium which is at rest. The one-dimensional profiles for the velocity and the energy density relative to a self-similar spherically expanding deflagration can be found in the top row of Fig. 11.3 and will be discussed in greater detail in Section 11.1.1 when introducing self-similar flows.

As in the case of detonations, also deflagrations can be further distinguished into *weak*, *strong* and *Chapman–Jouguet deflagrations* according to whether the fluid velocity behind the deflagration front is supersonic, subsonic, or sonic, respectively. Indeed, much of the analysis made in the previous section about detonations can be extended also to deflagrations, so that, for instance, it is possible to show that Chapman–Jouguet deflagrations are the fastest among deflagrations and that they produce a reacted fluid with maximum entropy (Anile, 1989). Similarly, it can be shown that, in analogy with weak detonations, also strong deflagrations are not physically possible in reaction fronts which are intrinsically exothermic. There are a number of ways of proving this result for chemical combustion. A first approach treats the combustion front as a changing mixture of the reacted and unreacted fluid and concludes that strong deflagrations would include regions of negative entropy production and therefore are not possible (Courant and Friedrichs, 1976). Other proofs involve instead the investigation of the stability properties of a strong deflagration (see next section) and show that if a strong deflagration could be momentarily produced, it would be unstable and would then split into a rarefaction wave and a weak deflagration (Landau and Lifshitz, 1987; Laine, 1994). Interestingly, since strong deflagrations are not physically possible in chemical combustion, it is then possible to exclude also weak detonations (which we have already discarded in the previous section using entropy minimisation arguments) when the latter are considered as equivalent to a shock front followed by a strong deflagration (Courant and Friedrichs, 1976).

A particularly interesting class of deflagrations is the one in which the reaction front is preceded by a shock front and is followed by a rarefaction wave whose tail moves at the sound speed of the reacted medium  $c_{sb}$ . These are called *supersonic deflagrations* and an example is shown in the right panel of Fig. 5.4. Also in this case the one-dimensional profiles of a self-similar spherically expanding supersonic deflagration can be found in the third row of Fig. 11.3. A member of this class of supersonic deflagrations is the one composed of a Chapman–Jouguet deflagration, thus with  $v_b = c_{sb}$ , which is then followed by a rarefaction wave. These solutions have been studied extensively in relation to a cosmological quark–hadron phase transition (Kurki-Suonio and Laine, 1995). It should be noted that a supersonic deflagration could eventually evolve into a detonation if the deflagration front were to coalesce with its precompression shock. This could happen, for instance, when the strength of the precompression shock front increases so much that its speed would equal that of a detonation front (Courant and Friedrichs, 1976). A similar mechanism, the so-called *deflagration-to-detonation transition* or *DDT*, is often invoked to explain white dwarfs exploding as Type Ia supernovae. In this case, a turbulent mixing of the unreacted and reacted fluids on either side of an active deflagration front is invoked to accelerate a subsonic reaction front and merge it with the supersonic shock front ahead of it (Khokhlov, 1991; Khokhlov *et al.*, 1997). Recent numerical simulations seem to support the actual occurrence of this mechanism in Type Ia supernovae [see, *e.g.*, Jordan *et al.* (2008) and Ciaraldi-Schoolmann *et al.* (2009)].

Because of the higher number of discontinuity surfaces that could be present in a deflagration, the counting of the unknowns in the hydrodynamic solution of a deflagration front is somewhat more elaborate than for detonations. Nevertheless, it is straightforward to show that in the case of a subsonic deflagration wave there are 10 different unknowns, *i.e.*,  $e$  and  $v$  ahead of the precompression front (2),  $e$  and  $v$  behind the precompression front (2), the speed of the precompression front  $V_s$  (1), the energy densities and velocities on either side of the reaction front  $e_a, v_a, e_b, v_b$  (4), and the speed of the reaction front  $v_{\text{def}}$  (1). A similar count in the case of a supersonic deflagration leads to 12 unknowns since, in addition to the 10 described above, it is necessary to add the energy density behind the tail of the rarefaction wave and its velocity (Kurki-Suonio, 1985). The junction conditions across the discontinuity surfaces together with the boundary and initial conditions allow us to determine nine of the unknowns for a subsonic deflagration and 11 of the unknowns for a supersonic deflagration. As a result, deflagration waves represent intrinsically *under-determined* fronts and this reflects the impossibility of defining the velocity of the reaction front from the initial conditions and the conservation equations alone (Landau and Lifshitz, 1987). An additional equation is therefore required to close the system, which is usually defined through the microphysical description of the processes taking place at the reaction front and effectively expresses the rate at which the reaction takes place across the front. Because of its microscopic nature, this equation can represent the most important but also the most uncertain aspect in the hydrodynamic treatment of a deflagration wave.

## 5.5 Stability of reaction fronts

As discussed in the case of shocks waves, an aspect which deserves great attention when studying the evolution of a *thermodynamically stable* reaction front (*i.e.*, of a front which satisfies conservation laws and can be momentarily produced) is that of *hydrodynamic stability*. For this purpose, stability analyses are carried out to establish whether, once the front is produced, it can evolve in time without radically changing its properties. Stability analyses of reaction fronts represent a large area of research, both from the experimental and the theoretical point of view, with a number of important results having been established especially within a linear regime. In analogy with what was done in Section 4.8 for shock fronts, our study of the stability of reaction fronts will first consider the causal structure of the different types of fronts that can be produced and then analyse in detail the linear stability properties of either relativistic detonation fronts (see Section 5.5.1) or of relativistic deflagration fronts (see Section 5.5.2). As we will discuss below, much of what was presented for the stability of detonations applies unmodified also to shock fronts and therefore completes the analysis started in Section 4.8.

Also for reaction fronts, the concept of the “degree of under-determinacy”  $\mathcal{D}_u$  continues to be valid and measures the number of free parameters which could be associated with a small perturbation of the front (Landau and Lifshitz, 1987; Burstein *et al.*, 1978). We recall that the degree of under-determinacy is computed as the difference between the number of perturbations that can be transmitted from the front and the number of boundary conditions that the perturbations have to satisfy, *i.e.*, the conservation across the discontinuity of rest mass, energy and momentum. A reaction front with a zero degree of under-determinacy is then said to be an *evolutionary reaction front* and it can be shown to be linearly stable. Note

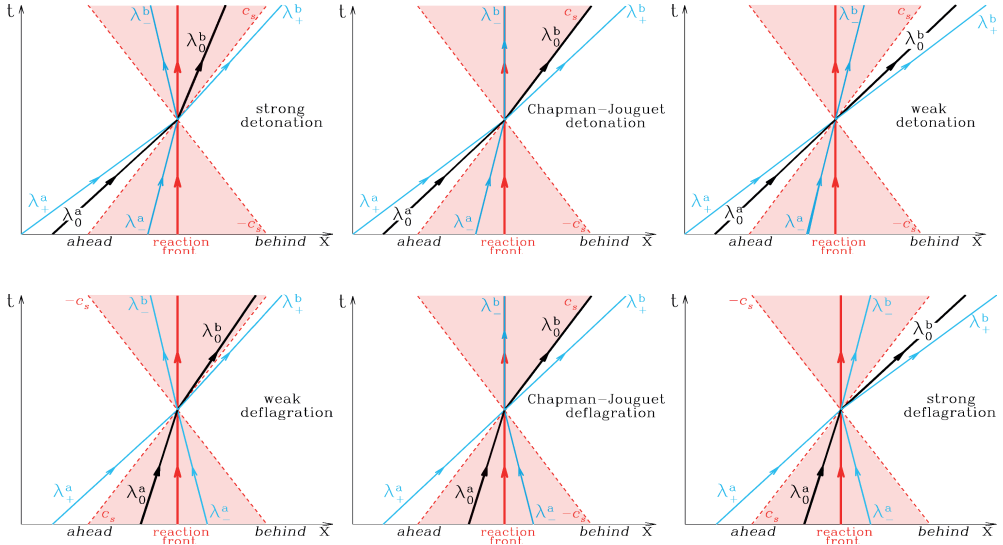


**Fig. 5.5** Spacetime diagrams and characteristics of the various types of reaction front when considered as left-propagating. The top row refers to detonations, while the bottom row refers to deflagrations. For each of the six panels, the thick red and black solid lines represent the worldlines of the front and of a fiducial fluid element, respectively, while blue solid lines indicate the characteristic curves,  $\lambda_{\pm}^{a,b}$ , and the dashed lines show the sound speed in the frame of the front (assumed to be the same on either side of the front).

that a reaction front with a nonzero degree of under-determinacy can still be made evolutionary if an additional boundary condition is specified. Such a boundary condition usually prescribes the velocity of the reaction front and is a function of the thermodynamic variables on either side.

The calculation of the perturbations that can leave the reaction front can be done in full analogy with the logic detailed in Section 4.8 for shock fronts and is therefore given by the same conditions that we report again here

$$\lambda_0^a > 0, \quad \lambda_{\pm}^a = \frac{v_a \pm c_{sa}}{1 \pm v_a c_{sa}} < 0, \quad (4.223)$$

$$\lambda_0^b > 0, \quad \lambda_{\pm}^b = \frac{v_b \pm c_{sb}}{1 \pm v_b c_{sb}} > 0. \quad (4.224)$$

Also in this case, the counting can be helped with the graphical representation given in Fig. 5.5, where detonations are reported in the top row, while deflagrations are shown in the bottom row. The figure consists of six different spacetime diagrams showing the spacetime causal structure of the different types of reaction fronts summarised in Table 5.1. All panels are referred to the front rest frame, with the thick red and black solid lines representing the worldlines of the front and of a fiducial fluid element  $\lambda_0^{a,b}$ , respectively. Also shown with blue solid lines are the characteristic curves  $\lambda_{\pm}^{a,b}$ , while the dashed lines show the sound speed in

the frame of the front and limiting the sound cone.<sup>1</sup>

After a careful look at Fig. 5.5, it is then easy to realise that the condition (4.223) is satisfied only by the characteristic  $\lambda_0^a$  when the medium ahead of a reaction front is supersonic (*i.e.*, for detonations), while it is satisfied by the characteristics  $\lambda_-^a$  and  $\lambda_0^a$  when the medium ahead of a reaction front is subsonic (*i.e.*, deflagrations). Similarly, the condition (4.224) is satisfied by the characteristics  $\lambda_0^b$  and  $\lambda_+^b$  for strong and Chapman–Jouguet detonations, as well as for weak and Chapman–Jouguet deflagrations. In addition, the condition is satisfied also by the characteristics  $\lambda_-^b$  for weak detonations and strong deflagrations.

The causal connection between the front and the medium behind in the case of subsonic downstream flows (*i.e.*, for strong detonations and weak deflagrations) has the important consequence that the medium behind can respond to any perturbation produced by the front and it can, at least in principle, counteract the growth of a developing instability. This back-reaction could then appear as nonlinear effects that tend to saturate the oscillations, which would be present but not grow without bounds. This might be at the origin of the formation of the typical corrugated but stable cellular flames observed in laboratory experiments of weak deflagrations (Markstein, 1951; Buckmaster *et al.*, 1983). Conversely, the lack of causal connection between the front and the medium behind in the case of supersonic downstream flows (*i.e.*, for weak detonations and strong deflagrations) establishes that the products of the reaction cannot mediate or suppress a potential perturbation in the reaction front, which can grow unbounded and lead to an instability.

As done in Section 4.8, we provide in Table 5.2 a summary of the propagated perturbations and of the corresponding degrees of under-determinacy for the different types of reaction fronts. Once again, it is useful to remark that  $\mathcal{D}_u = 0$  is only a necessary but not sufficient conditions for a reaction front to be evolutionary. The important result that can be deduced from Table 5.2 is therefore that only the conditions  $v_a > c_{sa}$ ,  $v_b \leq c_{sb}$  provide a zero degree of under-determinacy and thus only *strong and Chapman–Jouguet detonations are evolutionary reaction fronts*. On the other hand, as mentioned above, if an additional boundary condition is specified to express the velocity of the reaction front, then a degree of under-determinacy of order one can be reduced to zero, thus making also *weak deflagrations* (but also weak detonations and strong deflagrations) *evolutionary reaction fronts*.

In summary, the analysis of the causal structure of reaction fronts has revealed that if the flow downstream of a reaction front is supersonic, as for weak detonations and strong deflagrations, any perturbation in the front cannot be mediated and is free to grow unbounded. Hence, such reaction fronts, which in Sections 5.3 and 5.4 we have already been shown to be unphysical on the basis of entropy considerations, would be, in addition, also not evolutionary.

The line of argument followed so far has the strength of being non-perturbative and hence of being valid also in a nonlinear regime. On the other hand, it has the considerable limitation of not being conclusive about the stability of the other classes of reaction fronts, namely weak deflagrations, strong detonations and Chapman–Jouguet deflagrations/detonations. As we will see in the following sections, a perturbative approach which is considerably more involved is necessary in these cases. The results of the perturbation analyses, that we anticipate here, reveal that *strong and Chapman–Jouguet detonations are stable to linear perturbations and to corrugations*. In addition, *weak and Chapman–Jouguet deflagrations could be stable to*

<sup>1</sup>For simplicity we assume the sound speeds are the same on either side of the front but we recall they are generally different.

**Table 5.2** Perturbation types as propagated from a frame comoving with the various possible reaction fronts and their associated degree of under-determinacy.

Reaction front	Propagated perturbations	Degree of under-determinacy
Strong detonations	$\lambda_0^a, \lambda_0^b, \lambda_+^b$	$3 - 3 = 0$
C-J detonations	$\lambda_0^a, \lambda_0^b, \lambda_+^b$	$3 - 3 = 0$
Weak detonations	$\lambda_0^a, \lambda_-^b, \lambda_0^b, \lambda_+^b$	$4 - 3 = 1$
Weak deflagrations	$\lambda_-^a, \lambda_0^a, \lambda_0^b, \lambda_+^b$	$4 - 3 = 1$
C-J deflagrations	$\lambda_-^a, \lambda_0^a, \lambda_0^b, \lambda_+^b$	$4 - 3 = 1$
Strong deflagrations	$\lambda_-^a, \lambda_0^a, \lambda_-^b, \lambda_0^b, \lambda_+^b$	$5 - 3 = 2$

*linear perturbations and to corrugations* if a suitable boundary condition is specified for the velocity of the reaction front.

The following two sections are rather technical and they can be skipped without serious conceptual losses. However, they report techniques for the linear stability analysis which are completely general and apply unmodified to shock fronts, and, with minimal modifications, also to deflagrations. Additional details not reported here can be found in Rezzolla (1996b).

### 5.5.1 Stability of detonations

The stability of classical detonation fronts has been studied quite extensively in the one-dimensional and linear regime [see, e.g., D'yakov (1954), Kontorovich (1958), Erpenbeck (1962), Landau and Lifshitz (1987) and Lee and Stewart (1990)] and attempts were recently made to extend these analyses within a weakly nonlinear theory [see, e.g., Roytburd (1991) for a list of useful references] or to a relativistic regime (Rezzolla, 1996b).

In what follows we will first present the linearised relativistic-hydrodynamic equations for a one-dimensional flow in a flat spacetime and then examine the stability of a generic discontinuity front with respect to corrugations. This will be done by requiring that the perturbed hydrodynamic equations are compatible with the conservation of energy and momentum across a front subject to a corrugation perturbation.

#### **Linearised relativistic-hydrodynamic equations.**

Let us consider the usual flat spacetime in Cartesian coordinates  $(t, x, y, z)$  and a frame comoving with the planar discontinuity surface which is at rest on the  $(y, z)$  plane. Let us also assume that there are no three-velocity components tangent to the front, so that the flow has

**272 Reaction Fronts: Detonations and Deflagrations**

four-velocity  $u^\mu = W(1, v^x, 0, 0)$ , where, as usual,  $W^2 := [1 - (v^x)^2]^{-1}$  is the Lorentz factor and  $v^x > 0$ , *i.e.*, that the front is left-propagating in an Eulerian system.<sup>2</sup> The relativistic-hydrodynamic equations (4.78) will then describe the properties of the flow and represent the “zeroth-order” equations. These can be perturbed via the introduction, on either side of the front, of small perturbations of the type

$$p \rightarrow p' = p + \delta p, \quad u^\mu \rightarrow u'^\mu = u^\mu + \delta u^\mu, \quad (5.9)$$

where  $u'^\mu := W(1 + W^2 v^x \delta v^x, v^x + W^2 \delta v^x, \delta v^y, 0)$ .<sup>3</sup> As a result, the perturbed expressions of the relativistic-hydrodynamic equations are (see Problem 3)

$$\rho h c_s^2 (W^2 v^x \partial_t \delta v^x + W^2 \partial_x \delta v^x + \partial_y \delta v^y) + \partial_t \delta p + v^x \partial_x \delta p = 0, \quad (5.10)$$

$$\rho h W^2 (\partial_t \delta v^x + v^x \partial_x \delta v^x) + v^x \partial_t \delta p + \partial_x \delta p = 0, \quad (5.11)$$

$$\rho h W^2 (\partial_t \delta v^y + v^x \partial_x \delta v^y) + \partial_y \delta p = 0, \quad (5.12)$$

which can also be written in a more compact form as

$$(\mathbf{C}_t \partial_t + \mathbf{C}_x \partial_x + \mathbf{C}_y \partial_y) \delta \mathbf{U} = 0, \quad (5.13)$$

where

$$\mathbf{C}_t := \begin{pmatrix} 1 & \rho h W^2 c_s^2 v^x & 0 \\ v^x & \rho h W^2 & 0 \\ 0 & 0 & \rho h W^2 \end{pmatrix}, \quad \mathbf{C}_x := \begin{pmatrix} v^x & \rho h W^2 c_s^2 & 0 \\ 1 & \rho h W^2 v^x & 0 \\ 0 & 0 & \rho h W^2 v^x \end{pmatrix}, \quad (5.14)$$

$$\mathbf{C}_y := \begin{pmatrix} 0 & 0 & \rho h c_s^2 \\ 0 & 0 & 0 \\ 1 & 0 & 0 \end{pmatrix}, \quad (5.15)$$

and  $\delta \mathbf{U}$  is the state vector for the perturbations, *i.e.*,  $\delta \mathbf{U} := (\delta p, \delta v^x, \delta v^y)^T$ . The most general solution of (5.13) has the form

$$\delta \mathbf{U}(t, x, y) = \mathbf{A}(x) e^{-i(\omega t + ky)}, \quad (5.16)$$

with the eigenfrequency  $\omega$  being a complex number, the wavenumber  $k$  a real number, and the vector  $\mathbf{A}$  can be expressed as

<sup>2</sup>This choice is different from the one shown in Fig. 4.6, but more convenient here since it leads to positive velocities relative to the reaction front.

<sup>3</sup>In addition to considering no background flow in the  $z$ -direction, also the perturbations are assumed to be planar and hence with  $\delta v^z = 0$ .

$$\mathbf{A}(x) := \sum_{j=1}^3 (c_j \mathbf{L}^{(j)}) e^{-i(l_j x)}. \quad (5.17)$$

Here,  $l_j$  are the complex eigenvalues of the characteristic equation (5.13),  $\mathbf{L}^{(j)}$  are the corresponding eigenvectors and  $c_j$  are three real constant coefficients. Substituting the ansatz (5.16) in (5.13), leads to a homogeneous system of equations whose coefficients are collected in the characteristic matrix

$$\mathbf{D} := (\mathbf{C}_t \omega + \mathbf{C}_x l + \mathbf{C}_y k). \quad (5.18)$$

The eigenvalues  $l_j$  can then be found by setting to zero the determinant of  $\mathbf{D}$ , which then leads to the dispersion relation (see Problem 4)

$$\det(\mathbf{D}) = (lv^x + \omega) [(lv^x + \omega)^2 - (\omega v^x + l)^2 c_s^2 - (1 - (v^x)^2) k^2 c_s^2] = 0, \quad (5.19)$$

with roots

$$l_1 = -\frac{\omega}{v^x}, \quad (5.20)$$

$$l_{2,3} = \frac{1}{(v^x)^2 - c_s^2} \left\{ (c_s^2 - 1)\omega v^x \pm c_s [1 - (v^x)^2] \left[ \omega^2 + \frac{((v^x)^2 - c_s^2)}{1 - (v^x)^2} k^2 \right]^{1/2} \right\}. \quad (5.21)$$

Note that the singularity at the sonic point in the eigenvalues  $l_{2,3}$  is only an apparent one as it becomes clear when solving Eq. (5.19) directly with  $v^x = c_s$ . In this case, in fact, there are only two roots and the new eigenvalues, which we denote with a bar, are regular and given by

$$\bar{l}_1 = l_1, \quad \bar{l}_2 = \frac{c_s k^2}{2\omega} - \frac{(1 + c_s^2)}{2c_s} \omega. \quad (5.22)$$

Given this singular behaviour near the sonic point, it is more convenient to expand the eigenvalues near the sound speed and write the velocity normal to the reaction front as

$$v^x = c_s + \varepsilon, \quad (5.23)$$

with  $\varepsilon$  being positive and in the range  $0 < \varepsilon < 1 - c_s$  in the supersonic upstream region of the flow, *i.e.*, for  $x < 0$ , and in the range  $-c_s < \varepsilon < 1 - c_s$  in the downstream region, *i.e.*, for  $x > 0$ .<sup>4</sup> Making use of (5.23), it is possible to expand both the numerators and the denominators of the eigenvalues (5.20) and (5.21) around the sonic velocity so as to obtain the new eigenvalue expressions

$$\tilde{l}_1 \cong -\frac{\omega}{c_s + \varepsilon}, \quad (5.24)$$

$$\tilde{l}_2 \cong -\frac{1}{\varepsilon(2c_s + \varepsilon)} \left\{ \omega \left( 1 + c_s^2 - \frac{k^2 c_s^2}{\omega^2} \right) \varepsilon + \omega c_s \left[ 1 - \frac{k^2}{2\omega^2} + \frac{k^4 c_s^2}{2\omega^4 (1 - c_s^2)} \right] \varepsilon^2 \right\}, \quad (5.25)$$

<sup>4</sup>The downstream flow can either be supersonic, as in weak and Chapman–Jouguet detonations, hence with  $0 \leq \varepsilon < 1 - c_s$ , or subsonic, as in strong detonations, hence with  $-c_s < \varepsilon < 0$ .

$$\begin{aligned}\tilde{l}_3 \cong \frac{1}{\varepsilon(2c_s + \varepsilon)} & \left\{ 2\omega c_s(c_s^2 - 1) + \omega \left( 3c_s^2 - 1 - \frac{k^2 c_s^2}{\omega^2} \right) \varepsilon \right. \\ & \left. + \omega c_s \left[ 1 - \frac{k^2}{2\omega^2} + \frac{k^4 c_s^2}{2\omega^4(1 - c_s^2)} \right] \varepsilon^2 \right\}.\end{aligned}\quad (5.26)$$

Although truncated at  $\mathcal{O}(\varepsilon^2)$ , the eigenvalues (5.24)–(5.26) are suitable for a generic value of the fluid velocity near the interface and provide a starting point for the stability analysis of both shocks and reaction fronts (see also Section 5.5). Note that  $\tilde{l}_2$  is not singular for  $\varepsilon \rightarrow 0$  and that it reduces to  $\tilde{l}_2$  at first order; for this reason the second-order term needs to be retained. This is not the case for  $\tilde{l}_3$ , which represents the singular root of (5.21) and for which the first-order expansion is, in fact, sufficient.

Next, it is necessary to find the form of the eigenvectors  $\mathbf{L}^{(j)}$  contained in (5.17). This requires solving the matrix equation

$$\begin{pmatrix} (\omega + \tilde{l}v^x) & \rho h W^2 (\omega v^x + \tilde{l}) c_s^2 & \rho h c_s^2 k \\ (\omega v^x + \tilde{l}) & \rho h W^2 (\omega + \tilde{l}v^x) & 0 \\ k & 0 & \rho h W^2 (\omega + \tilde{l}v^x) \end{pmatrix} \begin{pmatrix} \mathbf{L}^{(1)} \\ \mathbf{L}^{(2)} \\ \mathbf{L}^{(3)} \end{pmatrix} = 0,\quad (5.27)$$

where  $\tilde{\mathbf{l}} = (\tilde{l}_1, \tilde{l}_2, \tilde{l}_3)$ , which leads to the following eigenvectors

$$\mathbf{L}^{(1)} = \begin{pmatrix} 0 \\ 1 \\ -\frac{\tilde{l}_1}{k} \end{pmatrix}, \quad \mathbf{L}^{(n)} = \begin{pmatrix} 1 \\ -\frac{(\omega v^x + \tilde{l}_n)}{\rho h W^2 (\omega + \tilde{l}_n v^x)} \\ -\frac{k}{\rho h W^2 (\omega + \tilde{l}_n v^x)} \end{pmatrix}, \quad n = 2, 3.\quad (5.28)$$

We now determine the values of the coefficients  $c_j$  for which the solution (5.16), with eigenvalues (5.24)–(5.26) and eigenvectors (5.28), satisfies the necessary boundary conditions. More specifically, if there are growing instabilities, the effects of these should be limited in space and not extend to infinity, so that

$$\lim_{x \rightarrow \pm\infty} |\delta \mathbf{U}(t, x, y)| = 0.\quad (5.29)$$

After a bit of algebra it is possible to verify that *ahead* of the front, that is for  $0 < \varepsilon < 1 - c_s$ , the following conditions hold for the imaginary (Im) part of the eigenfrequencies and eigenvectors

$$\begin{aligned}\text{Im}(\omega) > 0 & \quad \text{iff} \quad \text{Im}(\tilde{l}_1) < 0, \\ \text{Im}(\omega) > 0 & \quad \text{iff} \quad \text{Im}(\tilde{l}_2) < 0, \\ \text{Im}(\omega) > 0 & \quad \text{iff} \quad \text{Im}(\tilde{l}_3) < 0,\end{aligned}\quad (5.30)$$

and for the region *behind* the front, that is for  $-c_s < \varepsilon \leq 0$ , the following conditions hold

$$\text{Im}(\omega) > 0 \quad \text{iff} \quad \text{Im}(\tilde{l}_1) < 0,$$

$$\begin{aligned} \operatorname{Im}(\omega) > 0 &\quad \text{iff} \quad \operatorname{Im}(\tilde{l}_2) < 0, \\ \operatorname{Im}(\omega) > 0 &\quad \text{iff} \quad \operatorname{Im}(\tilde{l}_3) > 0. \end{aligned} \quad (5.31)$$

In order for the limits (5.29) to be satisfied, it is necessary that  $\operatorname{Im}(\tilde{l}_j) > 0$ , or that the corresponding coefficients  $c_j$  are zero for  $x < 0$  and that  $\operatorname{Im}(\tilde{l}_j) < 0$ , or  $c_j = 0$  for  $x > 0$ . For modes with  $\operatorname{Im}(\omega) > 0$  we then have

- (a)  $c_1 = 0, c_2 = 0, c_3 = 0$  for  $x < 0$  and  $\varepsilon > 0$ , (all detonations)
  - (b)  $c_1 \neq 0, c_2 \neq 0, c_3 = 0$  for  $x > 0$  and  $\varepsilon \leq 0$ , (strong, C-J det.)
  - (c)  $c_1 \neq 0, c_2 \neq 0, c_3 \neq 0$  for  $x > 0$  and  $\varepsilon > 0$ . (weak det.)
- (5.32)

In other words, the conditions (5.32) express that no perturbations can grow ahead of the detonation front, *i.e.*,  $\delta\mathbf{U}(t, x, y) = 0$  for  $x < 0$ , while this is not necessarily the case for the positive  $x$  half-plane, where growing modes are allowed to exist. In fact, only one coefficient needs to be zero in the case of strong and Chapman–Jouguet detonations, and none in the case of weak detonations. This latter result represents an important difference between strong and weak detonations and will be further discussed below. The condition (5.32)<sub>(a)</sub> on the coefficients  $c_j$  has its physical interpretation in the fact that in the negative  $x$  half-plane the flow is supersonic and “entering” the front and, as a consequence, no acoustic signal (and therefore no perturbation) can be transmitted upstream of this flow. This can also be seen in the top row of Fig. 5.5, which shows that the characteristics ahead of the front,  $\lambda_-^a, \lambda_0^a, \lambda_+^a$ , all have a positive slope in the case of detonations.

#### **Corrugation instability of strong detonations.**

We next discuss the *corrugation instability* of relativistic strong detonation fronts. The first step consists in establishing the correct eigenvalues to choose. Using the conditions (5.30)–(5.31), together with (5.32), it is then evident that the eigenvalues  $\tilde{l}_1, \tilde{l}_2$  (and the corresponding eigenvectors) should be used in the case of strong and Chapman–Jouguet detonations ( $\varepsilon \leq 0$ ) while all of the eigenvalues  $\tilde{l}_1, \tilde{l}_2, \tilde{l}_3$  would need to be used in the case of weak detonations ( $\varepsilon > 0$ ). The second step consists in requiring that the perturbed hydrodynamic equations satisfy junction conditions at the front expressing the conservation of energy and momentum, respectively [*cf.* Eqs. (4.112)–(4.114)]. We recall that these junction conditions are expressed in the front rest frame and that the latter coincides with the coordinate frame only when the front is unperturbed. Let us now suppose that the front position is perturbed in the  $y$ -direction with a harmonic perturbation of the type (see Fig. 5.6)

$$\Delta = \Delta_0 e^{-i(\omega t + ky)}, \quad (5.33)$$

where  $\Delta$  has the dimensions of length, and let us calculate the resulting form of the perturbed junction conditions. For this purpose it is convenient to introduce two unit and orthogonal three-vectors,  $\vec{n}$  and  $\vec{t}$ , that are normal and tangent to the front, respectively (see Fig. 5.6). To first order in the perturbation, they have components

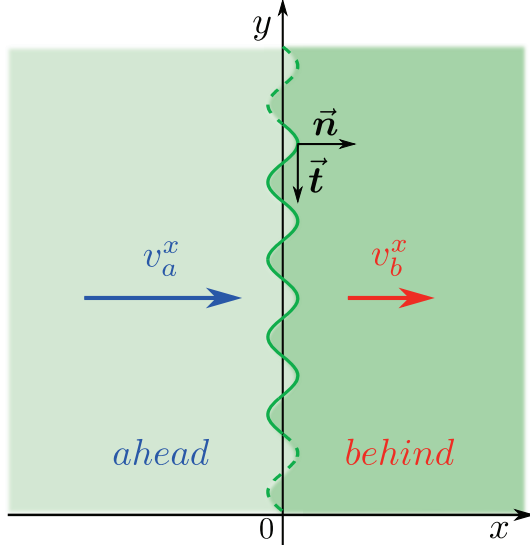


**Fig. 5.6** Schematic representation of a corrugated left-propagating detonation front. The diagram refers to a frame comoving with the front, which is initially at  $x = 0$ . Shown are the orthogonal unit three-vectors normal,  $\vec{n}$ , and tangent,  $\vec{t}$ , to the discontinuity surface. The detonation is assumed to be strong and hence with  $v_a^x > c_{sa}$ ,  $v_b^x < c_{sb} = c_{sa}$ .

$$\vec{n} := \left( 1, -\frac{\partial \Delta}{\partial y}, 0 \right) = (1, ik\Delta, 0), \quad \vec{t} := \left( \frac{\partial \Delta}{\partial y}, 1, 0 \right) = (-ik\Delta, 1, 0). \quad (5.34)$$

Next, we evaluate the perturbed expressions for the fluid velocities on either side of the front as measured in the front rest frame. For this purpose, we need to perform a relativistic boost with velocity equal to that of the detonation front, *i.e.*,

$$\vec{v}_{\text{det}} := (\partial_t \Delta) \vec{n} = (-i\omega \Delta) \vec{n}, \quad (5.35)$$

so as to obtain the following expressions for the perturbed normal and tangential velocities relative to the front

$$\vec{v}_j' \cdot \vec{n} = \left( \frac{v_j^x + \delta v_j^x + i\omega \Delta}{1 + i\omega v_j^x \Delta}, \delta v_j^y, 0 \right) \cdot \vec{n} \cong v_j^x + \delta v_j^x + \frac{i\omega \Delta}{W_j^2}, \quad (5.36)$$

$$\vec{v}_j' \cdot \vec{t} \cong \delta v_j^y - ik v_j^x \Delta, \quad j = 1, 2, \quad (5.37)$$

and to which corresponds a perturbed Lorentz factor

$$\delta W_j \cong W_j^3 v_j^x \left( \delta v_j^x + \frac{i\omega \Delta}{W_j^2} \right), \quad j = 1, 2. \quad (5.38)$$

It is now convenient to introduce the new state vector of the perturbations near the front in the downstream region of the flow

$$\delta\mathbf{V}_b(t, y) := (\delta p_b, \delta v_b^x, \delta v_b^y)^T, \quad (5.39)$$

where, as discussed above, each component of the corresponding state vector  $\mathbf{V}_a(t, y)$  is automatically zero. Making use of expressions (5.36)–(5.38) in the jump conditions (4.112)–(4.114) and recalling that the perturbed tangential velocity will be continuous across the front, *i.e.*,  $\llbracket v^y \rrbracket = 0$ , it is possible to write out the perturbed junction conditions and to use the resulting system of three equations to derive the components of  $\delta\mathbf{V}_b(t, y)$ . Note that if a surface tension  $\sigma$  is present (as in the case of a phase interface), it is necessary to modify the momentum balance across the front to take account of this contribution (Zeldovich *et al.*, 1985). On the other hand, the energy balance at the front is unaffected by a constant surface tension (Miller and Pantano, 1989). This additional term appears in the expressions for the negative  $x$  half-plane with the form  $\simeq \sigma(\partial_y^2 - \partial_t^2)\Delta$ , where the first term is related to the surface curvature, while the second is related to its “inertia”. Omitting here the lengthy algebra, the three components of  $\delta\mathbf{V}_b(t, y)$  are found to be (see Problem 5)

$$\delta p_b = \frac{1 + v_b^2}{\Gamma_- + \Gamma_+ v_b^2} \left[ 2i\omega\rho_b h_b \frac{(v_a - v_b)(1 - v_a v_b)}{(1 + v_b^2)} \frac{W_b^2 v_b}{v_a} + \sigma(\omega^2 - k^2) \right] \Delta, \quad (5.40)$$

$$\delta v_b^x = -\frac{1 - v_b^2}{\Gamma_- + \Gamma_+ v_b^2} \left[ i\omega \frac{(v_a - v_b)(1 - v_a v_b)}{v_a} \Gamma_+ + \sigma(\omega^2 - k^2) \frac{\Theta_b}{\rho_b h_b} v_b \right] \Delta, \quad (5.41)$$

$$\delta v_b^y = -ik\Delta(v_a - v_b), \quad (5.42)$$

where

$$\Gamma_{\pm} := (1 \pm \Theta_b W_b^2 v_b^2), \quad \Theta_b := \frac{\delta(\rho_b h_b)}{\delta p_b} = 1 + \frac{1}{c_{sb}^2}, \quad (5.43)$$

and, for compactness, we have written  $v_a := v_a^x$ ,  $v_b := v_b^x$  for the zeroth-order velocities. Expressions (5.40)–(5.42) represent the special-relativistic generalisation of the equivalent expressions discussed by Landau and Lifshitz (1987) and reduce to these when the Newtonian limit is taken.

It is important to remark that the term

$$\Gamma_- + \Gamma_+ v_b^2 = 1 + v_b^2(1 - \Theta_b) \quad (5.44)$$

in the denominators of (5.40)–(5.41) vanishes whenever  $v_b = c_{sb}$ , giving a singular behaviour for Chapman–Jouguet detonations, in analogy to what happens in the Newtonian case (Landau and Lifshitz, 1987). Great care must be taken when discussing these limiting cases, but some physical insight into the properties of Chapman–Jouguet detonations can already be gained when inverting expressions (5.40)–(5.41) in terms of the perturbation  $\Delta$ . In this case, in fact, we could conclude that the corrugations produced on a Chapman–Jouguet detonation front by perturbations in the downstream fluid variables are always zero and independent of

the strength of the perturbations (*i.e.*, independent of the magnitude of  $\delta V_b$ ). In other words, we would conclude that *Chapman–Jouguet detonations are stable against linear perturbations*. We will later see that the same conclusion can be drawn also from the study of the full dispersion relation.

We can continue with our stability analysis and derive a dispersion relation after requiring that the hydrodynamic perturbations present in the fluid adjacent to the phase interface are compatible and coincide with the perturbations produced by the corrugations of the front, *i.e.*,

$$\delta \mathbf{U}(t, 0^+, y) := \sum_{j=1}^3 (c_j \mathbf{L}^{(j)}) e^{-i(\omega t + ky)} = \delta \mathbf{V}_b(t, y). \quad (5.45)$$

Writing out (5.45) explicitly yields a system of three equations with unknowns given by the coefficients  $c_j$ , and by the amplitude of the surface displacement  $\Delta_0$ . Whether Eqs. (5.45) are sufficient to determine the dispersion relation depends on the number of nonzero coefficients  $c_j$  or, equivalently, on the degree of under-determinacy of the detonation front. In the case of a strong or Chapman–Jouguet detonation, there exist three free parameters (corresponding to the unknowns  $c_1, c_b$  and to  $\Delta_0$ ) and the front then has zero degree of under-determinacy (see Table 5.2). In this case, Eq. (5.45) has a solution provided that the determinant of the matrix of coefficients vanishes, *i.e.*, that

$$\det \begin{pmatrix} 0 & 1 & \delta p_b \\ 1 & -\frac{(\omega v^x + \tilde{l}_2)}{W_b^2 \rho_b h_b (\omega + \tilde{l}_2 v^x)} & \delta v_b^x \\ -\frac{\tilde{l}_1}{k} & -\frac{k}{W_b^2 \rho_b h_b (\omega + \tilde{l}_2 v^x)} & \delta v_b^y \end{pmatrix} = 0.$$

After some algebra, the general form of the dispersion relation is found to be (see Problem 6)

$$\begin{aligned} & \frac{\rho_b h_b}{\Gamma_- + \Gamma_+ v_b^2} \left\{ \frac{(v_a - v_b)}{v_a} \left[ \omega^3 \frac{(1 - v_a v_b)(\Gamma_+ - 2W_b^2 v_b^2)}{v_b} + \omega^2 (1 - v_a v_b)(\Gamma_+ - 2W_b^2) \tilde{l}_2 \right. \right. \\ & + \omega \left[ 2v_b(1 - v_a v_b) - v_a (\Gamma_- + \Gamma_+ v_b^2) \right] W_b^2 k^2 - W_b^2 v_a v_b k^2 (\Gamma_- + \Gamma_+ v_b^2) \tilde{l}_2 \Big] i \\ & \left. \left. + \sigma \frac{(\omega^2 - k^2)}{\rho_b h_b} \left[ \omega^2 (\Theta_b - 1 - v_b^2) - \frac{\omega}{v_b} (\Gamma_- + \Gamma_+ v_b^2) \tilde{l}_2 + (1 + v_b^2) k^2 \right] \right\} = 0, \end{aligned} \quad (5.46)$$

which provides a relation  $\omega = \omega(k)$  once the free variables  $v_a, v_b, c_{sb}$  and  $\sigma/(\rho_b h_b)$  are specified.

Similarly, we can consider the case of a weak detonation, for which there exist four free parameters (corresponding to the unknowns  $c_1, c_2, c_3$  and  $\Delta_0$ ) and this forces the introduction of a suitable fourth boundary condition in order to make the solution fully determined. In this respect, weak detonations are similar to weak deflagrations and in order to be fully determined,

they require an equation describing the microscopic burning mechanism or, in the case of phase transitions, the rate of transformation of the old phase into the new one. This feature of weak detonations does not allow for a general discussion of their stability properties but only to a case-by-case one, restricting the analysis to those specific situations in which the fourth boundary condition can be expressed. For this reason, in the following we limit ourselves only to the discussion of the stability properties of Chapman–Jouguet and strong detonations.

Recalling the definition (5.25) of  $\tilde{l}_2$ , it is possible to see that a strong detonation naturally evolves into a Chapman–Jouguet detonation when the velocity behind the front passes from being subsonic to being equal to the sound speed. This is the case which we will discuss first by setting  $\varepsilon = 0$  and  $v_b = c_s$  (hereafter  $c_s := c_{sb}$ ), so that Eq. (5.46) reduces to

$$\frac{\rho_b h_b}{\Gamma_- + \Gamma_+ c_s^2} \left\{ i \frac{(v_a - c_s)}{v_a} \left[ 2\omega^3 \frac{(1 - v_a c_s)}{c_s} + 2\omega(1 - v_a c_s) W_b^2 c_s k^2 \right] + \sigma \frac{(\omega^2 - k^2)}{\rho_b h_b} \left[ \omega^2 \frac{(1 + c_s^2)}{W_b^2 c_s^2} + (1 + c_s^2) k^2 \right] \right\} = 0. \quad (5.47)$$

The dispersion relation (5.47) does not contain the eigenvalue  $\tilde{l}_2$  (which is always multiplied by vanishing terms) and to avoid a singular behaviour, the content of the curly brackets in (5.47) has to be zero, that is,

$$(\omega^2 + W_b^2 c_s^2 k^2) \left[ 2i\omega \frac{(v_a - c_s)(1 - v_a c_s)}{v_a c_s} + \sigma \frac{(\omega^2 - k^2)}{W_b^2 c_s^2 h_b} \right] = 0. \quad (5.48)$$

Equation (5.48) has the four distinct roots given by

$$\omega_{1,2} = \pm i W_b c_s k, \quad (5.49)$$

$$\begin{aligned} \omega_{3,4} = - \frac{W_b^2 c_s \rho_b h_b}{v_a \sigma} & \left\{ i(v_a - c_s)(1 - v_a c_s) \right. \\ & \left. \mp \left[ \left( \frac{v_a \sigma}{W_b^2 c_s \rho_b h_b} \right)^2 k^2 - (v_a - c_s)^2 (1 - v_a c_s)^2 \right]^{1/2} \right\}. \end{aligned} \quad (5.50)$$

Not all of these roots are physically acceptable. For instance,  $\omega_1$  has a positive imaginary part and would lead to an exponentially growing unstable mode. It should therefore be rejected since it does not have a dissipative cutoff at short wavelengths. It is well known, in fact, that the surface energy associated with a perturbation of amplitude  $\Delta$  is proportional to  $\sigma k^2 \Delta^2$  and a cutoff wavenumber, above which instabilities are not allowed, is necessary to avoid accumulation of infinite energies at high frequencies. The physical processes which operate this limitation depend on the specific situation under examination and can be either dissipative effects, such as a fluid viscosity, or can be the consequence of surface tension. However, the root  $\omega_1$  does not contain any contribution coming from the surface tension and this has the consequence that even an infinitely stiff front (*i.e.*, one with  $\sigma \rightarrow \infty$ ) would appear to be unstable at all wavelengths. This behaviour suggests that the roots  $\omega_1$  and  $\omega_2$  cannot provide a physical description of detonation fronts and should be discarded. Further arguments supporting this choice can be found in Rezzolla (1996b).

After some algebraic manipulations, whose details can be found in Rezzolla (1996b), it is possible to show that the other two roots  $\omega_{3,4}$ , which are clearly dependent on  $\sigma$ , have negative imaginary parts and therefore lead to stable solutions. Hence, as anticipated already, also a rigorous linear stability analysis shows that *Chapman–Jouguet detonations are stable against linear perturbations*. When applied to the cosmological quark–hadron transition, this view is in agreement with fully nonlinear calculations of the relativistic-hydrodynamics equations coupled to a scalar field with a quartic self-interaction potential regulating the transition (Fragile and Anninos, 2003). Although the calculations showed rather complex behaviour, no sign of hydrodynamic instability was found during this transition period, at least for the choice of parameters, scalar-field interaction potential, equation of state, and grid resolutions investigated by Fragile and Anninos (2003).

The situation is not very different when strong detonations are considered. In this case, however, all of the expressions in the dispersion relation (5.46) need to be expanded around the sound speed, with terms up to second order being retained. This is because Chapman–Jouguet detonations and strong detonations are indistinguishable to first order and a second-order expansion is thus necessary. The complete general dispersion relation, which results from lengthy algebraic manipulations, can be found in Rezzolla (1996b) and consists of a seventh-order equation in  $\omega$  with complex coefficients. The roots of such a dispersion relation can be computed only numerically and after all the parameters have been specified, *e.g.*,  $v_a$  and  $\varepsilon$ . In that case, only the solution of the complete polynomial allows one to deduce a consistent picture of the functional dependence of the growth rate on the wavenumber  $k$ . Any analysis of the dispersion relation in the long- and short-wavelength limits, in fact, can easily give rise to misleading outcomes.

Overall, the calculations of the roots of the dispersion relation for representative strong detonations occurring in ultrarelativistic fluids indicate that there is always a root of the dispersion relation which has positive imaginary part, while all of the others have either negative or constant imaginary part (Rezzolla, 1996b). The associated growth rate is independent of  $\sigma$ , increases linearly with the wavenumber  $k$  and produces a divergence at high frequencies. The behaviour of this root is clearly analogous to that of the unstable mode contained in the root  $\omega_1$  of the dispersion relation (5.48) and, in analogy with what was deduced for Chapman–Jouguet detonations, it should be discarded. As a result, we conclude that also *strong detonations are stable against linear perturbations* and in this respect they resemble Chapman–Jouguet detonations to which they reduce for  $\varepsilon \rightarrow 0$ . As discussed in Section 4.8, a similar result has been obtained for standard shocks by Anile and Russo (1986) and by Anile and Russo (1987), who have shown that an evolutionary front is also stable with respect to corrugations.

Finally, before turning to the discussion of the stability of deflagration fronts, a comment should be made on strong detonations and on the possibility of employing them for studying the growth of new-phase bubbles during cosmological phase transitions. We have just proved that strong detonations are both evolutionary and stable with respect to corrugation instabilities. However, as already discussed in Section 5.3, entropy minimisation arguments indicate that such flow configurations cannot be realised in practice. In addition, they cannot be employed as solutions to describe the self-similar growth of a spherical bubble in a phase transition. Proofs of this have been given by Landau and Lifshitz (1987) for non-relativistic planar and spherical fronts, by Steinhardt (1982) for relativistic spherical fronts, and by Laine (1994) for the case of relativistic planar fronts.

### 5.5.2 Stability of deflagrations

The linear stability of classical planar deflagration fronts was first studied by Landau (1944), who showed that at linear order in the perturbations a “slow combustion front” (*i.e.*, a weak deflagration) is unstable at any wavelength. This result was compatible with the observed irregularities in propagating planar combustion fronts and indicated that higher-order effects were probably responsible for the saturation of the oscillations and the production of the globally stable cellular fronts. In his derivation, Landau concentrated on a weak deflagration and made use of the hypothesis of continuity of the pressure field across the deflagration front. This approximation allowed him to reduce to zero the degree of under-determinacy of the front and to obtain the solution of the problem. Such a choice is certainly reasonable when the fluid is not relativistic and the perturbations produced at the front are not so significant so as to alter the continuity of the pressure across the front. However, when the fluid is relativistic, this approximation ceases to be a good one and the problem needs to be solved taking into account the pressure variation along with the conservation of momentum across the front.

A linear stability analysis of relativistic deflagration fronts would resemble closely the one presented in the previous section, but with some important differences emerging because of the different causal structure between deflagrations and detonations. In particular, it is necessary to reconsider the values of the coefficients  $c_j$  of the solution (5.17) that satisfy the boundary conditions (5.29). In the case of a deflagration, in fact, the solution of the perturbed hydrodynamic equations does not extend to infinity only if

- (a)  $c_1 = 0, c_2 = 0, c_3 \neq 0$  for  $x < 0$  and  $\varepsilon \leq 0$ , (all deflagrations)
- (b)  $c_1 \neq 0, c_2 \neq 0, c_3 = 0$  for  $x > 0$  and  $\varepsilon \leq 0$ , (weak, C–J def.)
- (c)  $c_1 \neq 0, c_2 \neq 0, c_3 \neq 0$  for  $x > 0$  and  $\varepsilon > 0$ . (strong def.)

(5.51)

A first consequence of the conditions (5.51)<sub>(a)</sub> is that it is no longer possible to assume the perturbed state vector of the fluid ahead  $\delta\mathbf{V}_a(t, y)$  to be identically zero (as we have done for detonations) since there exists at least one coefficient which does not need to be zero. This can also be appreciated by noting that in the bottom row of Fig. 5.5 the backward characteristic  $\lambda_-^a$  always has a negative slope in the case of deflagrations. A second consequence concerns the degree of under-determinacy of a deflagration, which is always larger than zero. In particular, the degree of under-determinacy of a weak or Chapman–Jouguet deflagration is one, since there are four different parameters (*i.e.*,  $c_3$  ahead of the front,  $c_1$  and  $c_2$  behind the front and  $\Delta_0$ ) that need to be specified, while it is two for a strong deflagration, since there are five different parameters (*i.e.*,  $c_3$  ahead of the front,  $c_1$ ,  $c_2$  and  $c_3$  behind the front and  $\Delta_0$ ) which could be associated with a small perturbation of the front [see the summary in (5.2)].

As discussed in Section 5.5, a finite degree of under-determinacy of weak and Chapman–Jouguet deflagrations prevents a *general* discussion of their stability properties, leaving space only for a case-by-case study. In particular, this is possible in those situations in which an additional (*i.e.*, a fourth) boundary condition, usually prescribing the velocity of the deflagration front, can be specified. Attempts at the study of the linear stability properties of relativistic weak deflagrations as phase interfaces during cosmological phase transitions have been carried out in the past both in the limit of small velocities (Link, 1992; Kamionkowski and Freese,

1992) and in the case of large velocities (Huet *et al.*, 1993). Unfortunately, the results obtained from these analyses are often in conflict and this is due mainly to the strong dependence of the stability properties on the form chosen for the boundary condition expressing the rate at which the transition proceeds. These examples, however, are useful to emphasise the most relevant result for this section and, namely, that *weak and Chapman–Jouguet deflagrations could be stable to linear perturbations and to corrugations* if a suitable boundary condition is specified for the velocity of the reaction front.

## 5.6 Further reading

- Anile, A. M. (1989). *Relativistic Fluids and Magneto-fluids*. Cambridge University Press, Cambridge.
- Burstein, S. Z., Lax, P.D., and Sod, G.A (1978). *Lectures on combustion theory*. New York University, Courant Mathematics and Computing Laboratory.
- Courant, R. and Friedrichs, K. O. (1976). *Supersonic Flows and Shock Waves*. Springer, Berlin.
- Fickett, W. and Davis, C. (1979). *Detonation: Theory and Experiment*. Dover, New York.
- Landau, L. D. and Lifshitz, E. M. (1987). *Fluid Mechanics*. Course of Theoretical Physics, Vol. 6. Butterworth-Heinemann, Oxford.
- Whitham, G. B. (1974). *Linear and nonlinear waves*. Pure and Applied Mathematics. John Wiley, New York.

## 5.7 Problems

1. Derive the expression for the reaction adiabat (5.3) [Hint: start from the expression for the Taub adiabat (4.118) and use the definition (5.1) for the compression factor].
2. Derive the inequalities (5.4)–(5.6) across a reaction front [Hint: start from the laws of conservation of momentum and energy (4.114)–(4.113)].
3. Derive the expressions of the perturbed relativistic-hydrodynamic equations (5.10)–(5.12).
4. Derive the dispersion relation (5.19) [Hint: start from the perturbed relativistic-hydrodynamic equations (5.10)–(5.12) and write them in the matrix form (5.13). Introduce the ansatz (5.16) to derive the new matrix (5.18), whose determinant will yield the desired solution].
5. Derive the expressions for the components (5.40)–(5.42) of the perturbation vector (5.39) in the downstream region of a corrugated front [Hint: start from the jump conditions (4.112)–(4.114) to obtain expressions (5.36)–(5.38); exploit the fact that the perturbed tangential velocity will be continuous across the front].
6. Using the matrix of coefficients (5.46), derive the dispersion relation (5.46) by setting its determinant to zero.

# 6

## Relativistic Non-Perfect Fluids

---

With a few exceptions, all of our discussion of relativistic hydrodynamics has so far concentrated on relativistic perfect fluids, which, we recall, are defined as those fluids for which viscous effects and heat fluxes are zero, and the pressure tensor is diagonal (see the discussion in Sections 2.2.5 and 2.3.6). While this is an approximation that works well for most fluids under generic conditions, it clearly becomes a poor approximation when the thermodynamic (*i.e.*, microscopic) time-scales are comparable to the dynamic (*i.e.*, macroscopic) ones, and thus when the assumption of local thermodynamic equilibrium breaks down. When this happens, the perfect-fluid description needs to be extended through the inclusion of dissipative terms and energy fluxes, thus leading to the relativistic hydrodynamics of *non-perfect fluids*. By construction, therefore, non-perfect fluids are those fluids with nonzero viscous and thermal-conductivity coefficients [*cf.*, the fluid classification in the scheme (2.79) and in Fig. 2.6].

In Newtonian physics, this extension is complex but straightforward, and it leads to the replacement of the Euler and energy equations with the corresponding Navier–Stokes and heat-conduction equations, accounting respectively for the conservation of momentum and energy (see Section 2.2.6). The mathematical character of these new equations is no longer *hyperbolic*, having gained a *parabolic* character, that is, possessing characteristics with infinite speeds (see Section 6.5.1). While this new character is perfectly compatible with the laws of Newtonian physics, it is inconsistent even with special relativity, since all speeds must be finite and smaller than that of light. As a result, and as will become clear in the following sections, the relativistic generalisation of the relativistic-hydrodynamic equations is far from being straightforward and requires the definition of suitable theories of non-perfect fluids that are causal and based on what is known as Extended Irreversible Thermodynamics.

### 6.1 On the four-velocity of a non-perfect fluid

As for perfect fluids, also for non-perfect fluids the energy–momentum tensor represents one of the building blocks of any hydrodynamic treatment. However, before deducing the expression for the energy–momentum tensor of non-perfect fluids, it is important to note that even the simple definition of four-velocity is not straightforward in the case of non-perfect fluids. In the case of a relativistic perfect fluid, it was possible to consider the fluid as moving with a precise bulk velocity and hence define a frame which is momentarily comoving with it.<sup>1</sup>

<sup>1</sup>Also for a Newtonian perfect fluid one can think that the mean macroscopic velocity, *i.e.*, the first moment of the distribution function [*cf.*, Eq. (2.12)], coincides everywhere with the local velocity, leading to a zero net heat flux [*cf.*, Eq. (2.43)].

On the other hand, when viscosity and heat conduction are present, the definition of the local rest frame of the fluid becomes ambiguous. This can be seen from the fact that the rest-mass density current  $J^\mu$ , the energy–momentum tensor  $T^{\mu\nu}$  and the entropy current  $S^\mu$  should now be treated as primary field variables, with no *a priori* relation to the four-velocity of the fluid and no reference to any rest frame. This uncertainty should in principle be solved by resorting to kinetic theory and by performing a suitable calculation of the moments of the distribution function. Such an approach has been recently followed by Tsumura *et al.* (2007), who derived the general-relativistic hydrodynamic equations for a non-perfect fluid starting from the Boltzmann equation.<sup>2</sup> Traditionally, however, a more (macroscopic) “hydrodynamic” approach has been adopted, in which the equations of motion

$$\nabla_\mu J^\mu = 0, \quad (2.118)$$

$$\nabla_\mu T^{\mu\nu} = 0, \quad (2.119)$$

and the second law of thermodynamics or (*maximum*) *entropy principle*

$$\nabla_\mu S^\mu \geq 0, \quad (2.150)$$

have been used to derive expressions for  $J^\mu$ ,  $T^{\mu\nu}$  and  $S^\mu$  that are relativistically consistent and expressed in terms of a yet-undefined four-velocity  $u^\mu$ .

Within this approach, there are two natural ways to define the four-velocity  $u$ . The first one uses a unit timelike vector that is parallel to  $\mathbf{J}$  and that we will indicate as  $\mathbf{u}_N$ , *i.e.*,  $J^\mu = \rho u_N^\mu$  and  $\mathbf{u}_N \cdot \mathbf{u}_N = -1$ . The second possibility uses the so-called “eigenvector” of the energy–momentum tensor  $\mathbf{T}$ , namely, the unit timelike four-vector  $\mathbf{u}_E$  parallel to  $\mathbf{T} \cdot \mathbf{u}_E$ , *i.e.*,  $u_E^\mu = \kappa T^\mu_\nu u_E^\nu$  and  $\mathbf{u}_E \cdot \mathbf{u}_E = -1$ . These two options coincide for a perfect fluid, since in that case the four-velocity defining the rest-mass density current  $J^\mu$  is also an eigenvector of  $T^{\mu\nu}$ , *i.e.*,  $u^\mu = -(1/e)T^{\mu\nu}u_\nu$ . As a result,  $\mathbf{u}_N$  and  $\mathbf{u}_E$  are identical for a perfect fluid and parallel to  $\mathbf{S}^\mu$ , thus defining a unique hydrodynamic four-velocity  $u$ .

On the other hand, non-perfect fluids have vectors  $u_E^\mu$  and  $u_N^\mu$  that are in general different and related in a form of the type (Israel, 1976)

$$u_E^\mu = u_N^\mu + \frac{q^\mu}{e + p} + \text{higher-order terms}, \quad (6.1)$$

where  $q^\mu$  is a four-vector that we will later see to be the *heat flux* (see Section 6.2 below). In general, we can work under the assumption that the additional dissipative properties of non-perfect fluids can be cleanly distinguished from those pertaining to perfect fluids and hence consider the rest-mass density current and energy–momentum tensor as the linear combination of two contributions, *i.e.*, as

$$J^\mu = J_{\text{PF}}^\mu + J_{\text{NPF}}^\mu, \quad (6.2)$$

$$T^{\mu\nu} = T_{\text{PF}}^{\mu\nu} + T_{\text{NPF}}^{\mu\nu}, \quad (6.3)$$

where the indices “PF” and “NPF” refer to the perfect and non-perfect fluid contributions, respectively. Note that  $J_{\text{PF}}^\mu$  and  $T_{\text{PF}}^{\mu\nu}$  are given respectively by Eq. (3.35) and (3.36), where we

<sup>2</sup>Unfortunately, an approach of this type is not useful when modelling ultrarelativistic fluids, such as the quark–gluon plasma, where the particle interactions cannot be described in terms of classical collisions. In these cases, in fact, field-theory approaches represent the best option.

are still free to adopt either  $u_N^\mu$  or  $u_E^\mu$  for the four-velocity. This ambiguity can be resolved by imposing constraints on the non-perfect fluid terms  $J_{\text{NPF}}^\mu$  and  $T_{\text{NPF}}^{\mu\nu}$ , keeping in mind that, whatever the final choice for the four-velocity  $u$ , the total rest-mass density current  $J^\mu$  must be parallel to  $u_\mu$ . A first possibility was suggested by Landau and Lifshitz (1987), who defined the fluid four-velocity as  $u^\mu = u_E^\mu$ . The resulting frame is called the *Landau frame* or *energy frame* (hence the index  $E$ ) and it represents the frame in which there is no net energy flux, *i.e.*, the frame defined by the conditions

$$J_{\text{NPF}}^\mu (u_\mu)_E = J_{\text{NPF}}^\mu u_\mu = 0, \quad (6.4)$$

$$T_{\text{NPF}}^{\mu\nu} (u_\mu)_E = T_{\text{NPF}}^{\mu\nu} u_\mu = 0. \quad (6.5)$$

In this frame the rest-mass density current is not parallel to the four-velocity and is given by [cf., Eq. (6.2)]

$$J^\mu = \rho u_N^\mu = \rho u_E^\mu - \frac{q^\mu}{h}, \quad (6.6)$$

where, as usual,  $h = (e+p)/\rho$  is the specific enthalpy [cf., Eq. (2.141), where however  $c \neq 1$ ], and where we have used Eq. (6.1). The presence of the heat flow in (6.6) will introduce an extra term in the continuity equation (2.118).

A second possibility was suggested instead by Eckart (1940), who defined the fluid four-velocity as  $u^\mu = u_N^\mu$ . The resulting frame is called the *Eckart frame* or *particle frame* (hence the index  $N$ ) and corresponds to the frame in which there is no dissipative contribution to the rest-mass density current and to the energy density, *i.e.*,

$$J_{\text{NPF}}^\mu = 0, \quad (6.7)$$

$$T_{\text{NPF}}^{\mu\nu} (u_\mu)_N (u_\nu)_N = T_{\text{NPF}}^{\mu\nu} u_\mu u_\nu = 0. \quad (6.8)$$

Clearly, in the Eckart frame the rest-mass density current is parallel to the four-velocity and the continuity equation retains the same expression as for a perfect fluid.

In the rest of the chapter we will adopt the Eckart frame, mainly for its pedagogical advantages and because the continuity equation assumes a simple form. However, we should also make two remarks. The first one is that for systems with vanishing net baryon number, as approximately realised in relativistic heavy ion collisions at very high energies, the Eckart frame is not well defined (the quark contribution to the energy flux diverges in the limit of vanishing baryon number density) and the Landau frame is preferred (Danielewicz and Gyulassy, 1985). The second remark is that, as recently shown by Tsumura *et al.* (2007), both the Landau frame and the Eckart frame can be regarded as two special cases of a wider class of frames in which the relativistic-hydrodynamic equations of non-perfect fluids can be written.

## 6.2 The energy-momentum tensor of non-perfect fluids

The distinction made in Eq. (6.3) between the parts of the energy-momentum tensor that are relative to the “perfect part” of the fluid from those that are relative to the “non-perfect part” does not provide any useful information *per se*, as we have not yet defined the properties of

$T_{\text{NPF}}^{\mu\nu}$ . This can be done after splitting the dissipative contribution to the energy–momentum tensor into two parts as

$$T_{\text{NPF}}^{\mu\nu} = \mathcal{S}^{\mu\nu} + T_{\text{flux}}^{\mu\nu}, \quad (6.9)$$

where  $\mathcal{S}^{\mu\nu}$  accounts for the *viscous* contributions and is referred to as the *viscous stress tensor*, while  $T_{\text{flux}}^{\mu\nu}$  describes the generation of *energy fluxes* within the Eckart frame. In Chapter 2 we wrote the Newtonian viscous stress tensor  $\mathcal{S}_{ij}$  in terms of the Newtonian strain tensor  $\Lambda_{ij}$  as

$$\begin{aligned} \mathcal{S}_{ij} &:= \eta \left[ \partial_i v_j + \partial_j v_i - \frac{2}{3} \theta \delta_{ij} \right] + \zeta \theta \delta_{ij} \\ &= 2\eta \Lambda_{ij} + \left( \zeta - \frac{2}{3} \eta \right) \theta \delta_{ij}, \end{aligned} \quad (2.72)$$

where  $\theta := \partial_k v^k$  is the Newtonian fluid expansion. A naive generalisation of this tensor to a relativistic framework would amount to writing

$$-\mathcal{S}_{\mu\nu} = 2\eta \sigma_{\mu\nu} + \left( \zeta - \frac{2}{3} \eta \right) \Theta g_{\mu\nu}, \quad (6.10)$$

where  $\eta$  and  $\zeta$  are the *shear viscosity* and the *bulk viscosity* (see Section 2.2.6). In expression (6.10) we have used some of the quantities already introduced in Section 3.1.1, namely

$$\sigma_{\mu\nu} := \nabla_{(\mu} u_{\nu)} = \nabla_{(\mu} u_{\nu)} + a_{(\mu} u_{\nu)} - \frac{1}{3} \Theta h_{\mu\nu}, \quad (3.12)$$

and

$$\Theta := h^{\mu\nu} \nabla_\nu u_\mu = \nabla_\mu u^\mu, \quad a^\mu := u^\nu \nabla_\nu u^\mu, \quad (3.13)$$

which, we recall, are the (relativistic) *shear tensor*, the *expansion scalar*, and the *four-acceleration*, respectively. However, as will be shown below, such a choice would also imply superluminal propagation speeds and thus is not a satisfactory one. The correct definition, although admittedly not a very transparent one, is instead given by

$$\mathcal{S}^{\mu\nu} = \pi^{\mu\nu} + \Pi h^{\mu\nu}, \quad (6.11)$$

where  $\pi^{\mu\nu}$  is called the *anisotropic stress tensor*,  $\Pi$  is the *viscous bulk pressure* (or “dynamic pressure” or “non-equilibrium pressure”), and  $h_{\mu\nu} := g_{\mu\nu} + u_\mu u_\nu$  is the standard projection tensor orthogonal to the four-velocity  $u$  [cf., Eq. (3.9)]. Note that all tensors in (6.11) are *symmetric*.

Next, we have to fix a form for the heat-flow tensor  $T_{\text{flux}}^{\mu\nu}$  in (6.9), which can be obtained by recalling that in the Newtonian framework the heat flow in the comoving frame is described by a three-vector  $\vec{q}$ , whose components give the rate of energy flow per unit area along each coordinate axis. In the Eckart frame, the *heat flux* four-vector will therefore be given by<sup>3</sup>

$$q^\mu = (0, q^i), \quad (6.12)$$

where we have marked with a “hat” the spatial indices of the heat-flux four-vector to emphasise that this is evaluated in the frame comoving with the fluid (see Section 3.2 for an analogous discussion for the energy–momentum tensor). Recalling now that the flux of energy density along a generic  $i$ -direction is expressed by the components  $T^{\hat{0}i}$  of the energy–momentum

<sup>3</sup>In a notation in which the speed of light is not set to one, the heat flux has components  $q^\mu = (0, \hat{q}^i/c)$ .

tensor, we conclude that in the comoving frame  $T_{\text{flux}}^{\hat{i}\hat{i}} = q^{\hat{i}}$ , while in any other frame it should be given by<sup>4</sup>  $T_{\text{flux}}^{\mu\nu} = q^\mu u^\nu + q^\nu u^\mu$ . Collecting the different contributions identified so far, the full energy-momentum tensor in the *Eckart frame* can be written explicitly as [cf., Eq. (3.41) in Section 3.2, where a similar decomposition was already proposed]

$$\begin{aligned} T^{\mu\nu} &= T_{\text{PF}}^{\mu\nu} + T_{\text{NPF}}^{\mu\nu} \\ &= eu^\mu u^\nu + (p + \Pi)h^{\mu\nu} + q^\mu u^\nu + q^\nu u^\mu + \pi^{\mu\nu}. \end{aligned} \quad (6.13)$$

In the construction of the energy-momentum tensor (6.13) we have made the implicit assumption that the state of the fluid is close to a fictitious local thermodynamic equilibrium state characterised by the local equilibrium scalars  $n$ ,  $e$ ,  $p$ ,  $s$ , and  $T$ , representing the usual particle number density, the energy density, the specific entropy and the temperature, respectively. In the frame with four-velocity  $u^\mu = u_N^\mu$ , the number and energy densities coincide with the local equilibrium values and only the pressure deviates from the equilibrium value,  $p_{\text{eq}}$ , while the viscous bulk pressure measures how large this deviation is, *i.e.*,  $\Pi = p - p_{\text{eq}}$ .

Collectively,  $\Pi$ ,  $q^\mu$  and  $\pi^{\mu\nu}$  are named *thermodynamic fluxes* and they account for the deviations of the fluid from a perfect fluid. These terms can be formally recovered from the energy-momentum tensor as

$$q^\mu := -h^\mu_\alpha T^{\alpha\nu} u_\nu, \quad (6.14)$$

$$p + \Pi := \frac{1}{3} h_{\mu\nu} T^{\mu\nu}, \quad (6.15)$$

$$\pi^{\mu\nu} := h^\mu_\alpha h^\nu_\beta T^{\alpha\beta} - (p + \Pi)h^{\mu\nu}, \quad (6.16)$$

and they satisfy the following properties (see Problem 1)

$$u_\nu \pi^{\mu\nu} = 0, \quad \pi^\mu_\mu = 0, \quad (6.17)$$

$$q^\mu u_\mu = 0, \quad u_\mu q^\nu \nabla_\nu u^\mu = 0. \quad (6.18)$$

It is also sometimes useful to define the covariant derivative  $\mathcal{D}$  in the space orthogonal to the four-velocity  $u$ , which is obtained after projecting all free indices of the corresponding ordinary covariant derivative  $\nabla$ . As a result, for either a scalar, a vector or a tensor, this derivative will be expressed as

$$\mathcal{D}_\mu f := h^\nu_\mu \nabla_\nu f, \quad (6.19)$$

$$\mathcal{D}_\mu A_\nu := h^\alpha_\mu h^\beta_\nu \nabla_\alpha A_\beta, \quad (6.20)$$

$$\mathcal{D}_\lambda A_{\mu\nu} := h^\alpha_\lambda h^\beta_\mu h^\gamma_\nu \nabla_\alpha A_{\beta\gamma}. \quad (6.21)$$

In the following sections we will refer to *constitutive equations* as those equations relating the thermodynamic fluxes to the kinematic properties of the fluid and we will soon discuss how the development of a consistent relativistic theory of non-perfect fluids depends on the choice of such equations.

<sup>4</sup>Note that a simpler definition of the type  $T_{\text{flux}}^{\mu\nu} = q^\mu u^\nu$  would not lead to a symmetric energy-momentum tensor.

## 6.3 Hydrodynamic equations of non-perfect fluids

### 6.3.1 The general form of the momentum and energy equations

As mentioned in Section 6.1, the use of the Eckart frame through the constraints (6.7) and (6.8) has the important advantage that in the continuity equation (2.118), the total rest-mass density current  $J^\mu$  is proportional to the four-velocity only. On the other hand, the substantially different form of the energy-momentum tensor (6.13) does introduce important new terms in the form of the momentum and of the energy equations for non-perfect fluids. To highlight them, we start by writing explicitly the conservation laws (2.119) to obtain

$$\begin{aligned}\nabla_\nu T^{\mu\nu} &= u^\mu u^\nu \nabla_\nu (e + p + \Pi) + (e + p + \Pi)(u^\mu \Theta + a^\mu) + g^{\mu\nu} \nabla_\nu (p + \Pi) \\ &\quad + q^\mu \Theta + u^\nu \nabla_\nu q^\mu + q^\nu \nabla_\nu u^\mu + u^\mu \nabla_\nu q^\nu + \nabla_\nu \pi^{\mu\nu} = 0.\end{aligned}\quad (6.22)$$

Next, and as done for perfect fluids, we derive the momentum equation after projecting Eq. (6.22) in the space orthogonal to  $\mathbf{u}$ , i.e.,  $\mathbf{h} \cdot \nabla \cdot \mathbf{T} = 0$ , to find (see Problem 2)

$$\begin{aligned}(e + p + \Pi)a_\mu + \mathcal{D}_\mu(p + \Pi) + \mathcal{D}_\nu \pi^\nu_\mu + a^\nu \pi_{\mu\nu} + h^\nu_\mu u^\gamma \nabla_\gamma q_\nu \\ + \left( \omega_{\mu\nu} + \sigma_{\mu\nu} + \frac{4}{3} \Theta h_{\mu\nu} \right) q^\nu = 0,\end{aligned}\quad (6.23)$$

where  $\omega_{\mu\nu} := h^\alpha_\mu h^\beta_\nu \nabla_{[\beta} u_{\alpha]}$  is the antisymmetric *vorticity tensor* (see Section 3.1.1). Note that in deriving expression (6.23) we have used the properties expressed by (6.17), the irreducible decomposition (3.10), and we have exploited the following identity for the anisotropic stress tensor (see Problem 1)

$$h^\gamma_\mu \nabla_\nu \pi^{\mu\nu} = \mathcal{D}^\mu \pi^\gamma_\mu + a^\mu \pi^\gamma_\mu , \quad (6.24)$$

which can be easily proved with the help of some tensor algebra. Similarly, we can write the projection of Eq. (6.22) along  $\mathbf{u}$ , i.e.,  $\mathbf{u} \cdot \nabla \cdot \mathbf{T} = 0$ , to obtain the energy equation as (see Problem 4)

$$u^\mu \nabla_\mu e + (e + p + \Pi)\Theta + 2q_\mu a^\mu + \mathcal{D}^\mu q_\mu + \pi^{\mu\nu} \sigma_{\mu\nu} = 0 , \quad (6.25)$$

where we have used the additional identities

$$\nabla_\mu q^\mu = \mathcal{D}_\mu q^\mu + a^\mu q_\mu , \quad (6.26)$$

$$u_\nu \nabla_\mu \pi^{\mu\nu} = -\pi^{\mu\nu} \nabla_\mu u_\nu = -\pi^{\mu\nu} \sigma_{\mu\nu} , \quad (6.27)$$

which again follow from (6.18) and the irreducible decomposition (3.10).

Clearly, the non-perfect fluid conservation equations (6.23) and (6.25) reduce to the corresponding perfect-fluid expressions (3.55) and (3.57) in the limit of  $\Pi \rightarrow 0$ ,  $q^\mu \rightarrow 0$  and  $\pi^{\mu\nu} \rightarrow 0$ .

### 6.3.2 The equilibrium state

As discussed in Section 2.3.7, when irreversible processes are present, the entropy is no longer conserved, but grows according to the second law of thermodynamics

$$\nabla_\mu \mathcal{S}^\mu \geq 0. \quad (2.150)$$

Equation (2.150) becomes a strict equality in the case of a perfect fluid, whose entropy current is then defined simply as  $\mathcal{S}^\mu = s\rho u^\mu$ . However, for relation (2.150) to be strictly nonzero, the entropy current must have an additional contribution in terms of the four-vector  $R^\mu$  with nonzero divergence such that<sup>5</sup>

$$\mathcal{S}^\mu = s\rho u^\mu + \frac{R^\mu}{T}, \quad (6.28)$$

where the temperature  $T$  in (6.28) is defined through the first law of thermodynamics (2.143), namely as

$$T = \frac{1}{\rho} \left( \frac{\partial e}{\partial s} \right)_\rho. \quad (6.29)$$

The dissipative part  $R^\mu$  in (6.28) is assumed to be a function of the thermodynamic fluxes  $\Pi$ ,  $q^\mu$ ,  $\pi^{\mu\nu}$ , and obviously it must vanish for a perfect fluid. We also know from the discussion in Chapter 2 that an *equilibrium state* is characterised by the absence of true *transport phenomena*, and therefore by having  $\Pi$ ,  $q^\mu$  and  $\pi^{\mu\nu}$  all equal to zero. As a result, and surely not surprisingly, the equilibrium state corresponds to a vanishing entropy-production rate, namely

$$\text{equilibrium state} \iff \Pi = q^\mu = \pi^{\mu\nu} = 0 \iff \nabla_\mu \mathcal{S}^\mu = 0. \quad (6.30)$$

In the following, we will show how two equivalent approaches to the description of non-perfect fluids, namely *Classical (or Standard) Irreversible Thermodynamics* (CIT) and *Extended Irreversible Thermodynamics* (EIT), differ in prescribing the four-vector  $R^\mu$  while maintaining the same properties for the equilibrium state.

## 6.4 Classical Irreversible Thermodynamics (first-order theories)

The first formulation of the relativistic-hydrodynamic equations for non-perfect fluids was proposed by Eckart (1940) and was later slightly modified by Landau and Lifshitz (1987) through the introduction of a different fluid frame (see the discussion in Section 6.1). Such theories represent the simplest covariant generalisations of the Navier–Stokes and Fourier equations of Newtonian non-perfect fluids [*cf.*, Eqs. (2.75) and (2.77)]. They are usually referred to as *Classical (or Standard) Irreversible Thermodynamics* (CIT), where the adjective “classical”, however, should not be understood as “Newtonian”, since the formulations are indeed fully relativistic. Although CIT suffers from at least two undesired properties that we will discuss in detail in Section 6.5, it has played an important role in paving the way to more consistent theories, and so we will review it in the following sections adopting, in particular, Eckart’s formulation.

<sup>5</sup>If the fluid is composed of massless particles, the definition (6.28) should be replaced by  $\mathcal{S}^\mu = \tilde{s}u^\mu + R^\mu/T$ , where  $\tilde{s}$  is the entropy density.

### 6.4.1 The constitutive equations

CIT assumes a *linear* dependence of the four-vector  $R^\mu$  on the thermodynamic fluxes. In other words, the entropy current contains no terms higher than the first one in the deviations from equilibrium. Because of this, CIT is said to belong to the generic class of *first-order theories* of relativistic dissipative hydrodynamics, to distinguish it from those theories, such as the one discussed in Section 6.6.1, where higher-order contributions are also considered. Within a first-order theory, it is not difficult to show that the most generic four-vector  $R^\mu$  in the entropy current (6.28) that can be built from the thermodynamic fluxes  $\Pi, q^\mu, \pi^{\mu\nu}$  and the four-velocity  $u^\mu$  is given by

$$R^\mu = f_1 \Pi u^\mu + f_2 q^\mu, \quad (6.31)$$

where  $f_1$  and  $f_2$  are thermodynamic functions of the number density  $n$  and of the energy density,  $e$ . A series of constraints on these thermodynamic functions can be easily derived. First, the *entropy density*, which is defined as

$$-\mathcal{S}^\mu u_\mu := s\rho + f_1 \Pi, \quad (6.32)$$

must have a maximum in the equilibrium state. Hence, it must be stationary with respect to variations in the thermodynamic flux given by the viscous bulk pressure  $\Pi$ , *i.e.*,

$$\frac{\partial}{\partial \Pi} (-\mathcal{S}^\mu u_\mu) \Big|_{\text{equil.}} = 0, \quad (6.33)$$

from which we immediately deduce that  $f_1 = 0$ . Second, since we know that in the rest frame of the fluid the heat flux has components  $q^\mu/T := (0, \vec{q}/T)$ , which represents the entropy current due to the heat flow only, we immediately deduce that the second free function has to be  $f_2 = 1$ . As a result, in CIT the entropy current (6.28) will have to take the form

$$\mathcal{S}^\mu = s\rho u^\mu + \frac{q^\mu}{T}. \quad (6.34)$$

We can now compute the entropy-generation rate as

$$\begin{aligned} T\nabla_\mu \mathcal{S}^\mu &= T\nabla_\mu \left( s\rho u^\mu + \frac{q^\mu}{T} \right) \\ &= T\rho u^\mu \nabla_\mu s + \nabla_\mu q^\mu - q^\mu \nabla_\mu \ln T \\ &= -\Pi\Theta - (\mathcal{D}_\mu \ln T + a_\mu)q^\mu - \pi^{\mu\nu}\sigma_{\mu\nu}, \end{aligned} \quad (6.35)$$

where we have used the continuity equation (3.52), the first law of thermodynamics in the form (2.143), the energy equation (6.25), the property (6.26), and the fact that at the equilibrium the energy-conservation equation (3.57) holds.

If we now require that the entropy four-divergence (6.35) satisfies the condition of being non-negative [*cf.* Eq. (2.150)], we find that the simplest relation between the thermodynamic fluxes and the thermodynamic forces  $\Theta, \mathcal{D}_\mu \ln T + a_\mu$  and  $\sigma_{\mu\nu}$ , is a linear one and is given by

$$\Pi = -\zeta\Theta, \quad (6.36)$$

$$q_\mu = -\kappa T(\mathcal{D}_\mu \ln T + a_\mu), \quad (6.37)$$

$$\pi_{\mu\nu} = -2\eta\sigma_{\mu\nu}, \quad (6.38)$$

where  $\kappa$  is non-negative and accounts for the *thermal conductivity*. Altogether,  $\kappa$ ,  $\zeta$ , and  $\eta$ , are known as the *transport coefficients* (see Section 2.2.6), while Eqs. (6.36)–(6.38) are referred to as the *constitutive equations* of CIT, also known as *Eckart's theory* of Relativistic Irreversible Thermodynamics (Eckart, 1940). The momentum and energy equations (6.23) and (6.25), together with the definitions (6.36)–(6.38), represent a complete set for the description of relativistic non-perfect fluids in a first-order theory. Note that Eq. (6.37) points to a purely relativistic property: the heat flux, in fact, is nonzero even for a zero temperature gradient, simply as a consequence of the acceleration of the fluid. Fortunately, this contribution is rather small in general, especially if the fluid motion is almost geodetic and is often neglected in practice (see the discussion in Section 11.8.5).

We can exploit the constitutive equations (6.36)–(6.38) to further characterise the properties of the *equilibrium state*. We know in fact that at equilibrium all the terms  $\Pi$ ,  $q^\mu$  and  $\pi^{\mu\nu}$  must vanish, so that Eqs. (6.36)–(6.38) imply the following conditions at equilibrium

$$\Theta = 0, \quad (6.39)$$

$$\mathcal{D}_\mu T + Ta_\mu = 0, \quad (6.40)$$

$$\sigma_{\mu\nu} = 0. \quad (6.41)$$

When combined with the continuity equation (3.52), with the momentum-conservation equation (6.23), and with the energy-conservation equation (6.25), Eqs. (6.39)–(6.41) lead to the following conditions

$$u^\mu \nabla_\mu \rho = 0, \quad (6.42)$$

$$u^\mu \nabla_\mu e = 0, \quad (6.43)$$

$$(e + p)a_\mu + \mathcal{D}_\mu p = 0. \quad (6.44)$$

As a result, we can use the definition (3.12) of the shear tensor and the condition that it must vanish at equilibrium, to find that

$$\begin{aligned} \frac{\nabla_\mu u_\nu}{T} + \frac{\nabla_\nu u_\mu}{T} + \frac{a_\mu u_\nu}{T} + \frac{a_\nu u_\mu}{T} &= \\ \nabla_\mu \left( \frac{u_\nu}{T} \right) + \nabla_\nu \left( \frac{u_\mu}{T} \right) + u_\nu \frac{\nabla_\mu T}{T^2} + u_\mu \frac{\nabla_\nu T}{T^2} - u_\nu \frac{\mathcal{D}_\mu T}{T^2} - u_\mu \frac{\mathcal{D}_\nu T}{T^2} &= \\ \nabla_\mu \left( \frac{u_\nu}{T} \right) + \nabla_\nu \left( \frac{u_\mu}{T} \right) &= 0, \end{aligned} \quad (6.45)$$

where we have replaced  $a_\mu$  using Eq. (6.40) and used the fact that  $u^\mu \nabla_\mu T = 0$ . The last condition follows directly from Eqs. (6.42) and (6.43) since the temperature  $T$  depends only on  $\rho$  and  $e$  through the equation of state. We have therefore reached the conclusion, expressed by Eq. (6.45), that at the equilibrium the vector field  $u^\mu/T$  is a *Killing vector field* [cf., Eq. (1.170)]. In addition, after combining Eq. (6.40) and Eq. (6.43), it is easy to find that

$$\nabla_\mu p - \frac{e + p}{T} \nabla_\mu T = 0, \quad (6.46)$$

which, using the first law of thermodynamics in the form (2.142), implies that the fluid *fugacity*, as defined in Eq. (2.122) in terms of the particle mass  $m$  and of the Boltzmann constant  $k_B$ , must be constant, *i.e.*,

$$\rho T \nabla_\mu \alpha_f = \frac{m}{k_B} \rho T \nabla_\mu \left( \frac{e+p}{\rho T} - s \right) = \frac{m}{k_B} \left( \nabla_\mu p - \frac{e+p}{T} \nabla_\mu T \right) = 0. \quad (6.47)$$

To summarise: the requirement that the fluid is in an *equilibrium state* is equivalent to assuming that the thermodynamics fluxes  $\Pi$ ,  $q^\mu$ , and  $\pi^{\mu\nu}$  vanish, that  $u^\mu/T$  is a Killing vector field, and that the fugacity is constant. Because these properties pertain to the equilibrium state, they remain valid even in the framework of EIT, which we will introduce later on in Section 6.6.

#### 6.4.2 The Newtonian limit: Navier–Stokes and heat conduction

The purpose of this section is to show how Eqs. (6.23) and (6.25), together with the constitutive relations (6.36)–(6.38), reduce to Eqs. (2.74)–(2.76), *i.e.*, to the *Navier–Stokes equations*, in the Newtonian limit. In Section 3.5 we have already considered the Newtonian limit of the relativistic-hydrodynamic equations for a perfect fluid and made several comments on the behaviour of the four-velocity in this limit. Many of those comments are relevant also here and we summarise them by recalling that if contributions  $\mathcal{O}(v^2)$  are neglected, the four-velocity components have the Newtonian limits<sup>6</sup>

$$u^\alpha \rightarrow (1, v^i), \quad u_\alpha \rightarrow (-1, v_i), \quad u^\mu \nabla_\mu \rightarrow \frac{\partial}{\partial t} + \vec{v} \cdot \vec{\nabla}. \quad (3.76)$$

With this in mind, we can consider the momentum equation (6.23), replacing the viscous bulk pressure  $\Pi$  via Eq. (6.36), and the anisotropic stress tensor  $\pi_{\mu\nu}$  via Eq. (6.38), while keeping  $q^\mu$  generic. We therefore obtain

$$(e+p)a_\mu + \mathcal{D}_\mu p - \zeta \Theta a_\mu - \mathcal{D}_\mu(\zeta \Theta) - 2\mathcal{D}_\nu(\eta \sigma^\nu_\mu) - 2\eta a^\nu \sigma_{\mu\nu} + h^\nu_\mu u^\gamma \nabla_\gamma q_\nu + \left( \omega_{\mu\nu} + \sigma_{\mu\nu} + \frac{4}{3} \Theta h_{\mu\nu} \right) q^\nu = 0, \quad (6.48)$$

and a bit of tensor algebra will also allow us to deduce the following identities (see Problem 4)

$$-\zeta \Theta a_\mu - \mathcal{D}_\mu(\zeta \Theta) = -\nabla_\mu(\zeta \Theta) - u^\nu \nabla_\nu(\zeta \Theta u_\mu), \quad (6.49)$$

$$-2\mathcal{D}_\nu(\eta \sigma^\nu_\mu) - 2\eta a^\nu \sigma_{\mu\nu} = -2\nabla_\nu(\eta \sigma^\nu_\mu) + 2\eta u_\mu \sigma^{\alpha\beta} \sigma_{\alpha\beta}. \quad (6.50)$$

We can therefore cast the momentum-conservation equation (6.23) in the form

$$(e+p)a_\mu + h^\nu_\mu \nabla_\nu p - \nabla_\mu(\zeta \Theta) - u^\nu \nabla_\nu(\zeta \Theta u_\mu) - 2\nabla_\nu(\eta \sigma^\nu_\mu) + 2\eta u_\mu \sigma^{\alpha\beta} \sigma_{\alpha\beta} + h^\nu_\mu u^\gamma \nabla_\gamma q_\nu + \left( \omega_{\mu\nu} + \sigma_{\mu\nu} + \frac{4}{3} \Theta h_{\mu\nu} \right) q^\nu = 0. \quad (6.51)$$

At this point, recalling the definition of the shear tensor  $\sigma_{\mu\nu}$  as given by Eq. (3.12) and the Newtonian limit of the pressure four-divergence [*cf.* Eq. (3.85)], we can easily isolate the (spatial) Newtonian limit of the different terms in Eq. (6.51) to obtain

<sup>6</sup>Note that differently from Section 3.5, here we have set  $c = 1$ .

$$(e + p)a_\mu \longrightarrow \rho \left( \frac{\partial}{\partial t} + v^i \frac{\partial}{\partial x^i} \right) v_j, \quad \mathcal{D}_\mu p \longrightarrow \frac{\partial}{\partial x^j} p, \quad (6.52)$$

$$\nabla_\mu(\zeta\Theta) \longrightarrow \frac{\partial}{\partial x^j} \left( \zeta \frac{\partial v_k}{\partial x_k} \right) = \frac{\partial}{\partial x^j} (\zeta\theta), \quad (6.53)$$

$$-2\nabla_\nu(\eta\sigma^\nu{}_\mu) \longrightarrow -\frac{\partial}{\partial x^i} \left[ \eta \left( \frac{\partial v_j}{\partial x_i} + \frac{\partial v_i}{\partial x_j} \right) \right] + \frac{2}{3} \frac{\partial}{\partial x^i} \left( \eta \frac{\partial v_k}{\partial x_k} \delta_{ij} \right), \quad (6.54)$$

and

$$u^\gamma \nabla_\gamma(\zeta\Theta u_\mu) \longrightarrow 0, \quad \sigma^{\alpha\beta} \sigma_{\alpha\beta} \longrightarrow 0, \quad (6.55)$$

$$h^\nu{}_\mu u^\gamma \nabla_\gamma q_\nu \longrightarrow 0, \quad \left( \frac{4}{3}\Theta h_{\mu\nu} + \sigma_{\mu\nu} + \omega_{\mu\nu} \right) q^\nu \longrightarrow 0, \quad (6.56)$$

where the terms (6.55)–(6.56) vanish because  $\mathcal{O}(v^2)$ . After collecting the remaining non-vanishing terms in Eq. (6.51), we obtain that the Newtonian limit of the momentum-conservation equation (6.23) becomes (see Problem 5)

$$\begin{aligned} & \frac{\partial v_j}{\partial t} + v_i \frac{\partial v_j}{\partial x_i} \\ & + \frac{1}{\rho} \left\{ \frac{\partial p}{\partial x_j} - \frac{\partial}{\partial x_i} \left[ \eta \left( \frac{\partial v_j}{\partial x_i} + \frac{\partial v_i}{\partial x_j} - \frac{2}{3} \delta_{ij} \frac{\partial v_k}{\partial x_k} \right) + \zeta \left( \frac{\partial v_k}{\partial x_k} \right) \delta_{ij} \right] \right\} = 0, \end{aligned} \quad (6.57)$$

which clearly coincides with the Navier–Stokes equations (2.75) after an external force term  $F_j/m$  is added.

Next, we consider the energy equation (6.25), which, in view of the constitutive equations, can now be written in the more convenient form

$$u^\mu \nabla_\mu e + \Theta(e + p) - \zeta\Theta^2 + 2q_\mu a^\mu + \mathcal{D}^\mu q_\mu - 2\eta\sigma^{\mu\nu} \sigma_{\mu\nu} = 0. \quad (6.58)$$

We now recall that the Newtonian limit of the relativistic energy density  $e$  is the (classical) internal energy density, *i.e.*,  $e \longrightarrow w_N = \rho\epsilon$  [cf., Eq. (3.87)]<sup>7</sup> and use the identity (see Problem 3)

$$2q_\mu a^\mu + \mathcal{D}^\mu q_\mu = q_\mu a^\mu + \nabla_\mu q^\mu, \quad (6.59)$$

to rewrite Eq. (6.58) as

$$\rho u^\mu \nabla_\mu \epsilon + p\Theta - \zeta\Theta^2 + q_\mu a^\mu + \nabla_\mu q^\mu - 2\eta\sigma^{\mu\nu} \sigma_{\mu\nu} = 0. \quad (6.60)$$

Again, we now consider the Newtonian limit of each term in Eq. (6.60) and obtain the following set of limits

$$\rho u^\mu \nabla_\mu \epsilon \longrightarrow \rho \left( \frac{\partial \epsilon}{\partial t} + v_i \frac{\partial \epsilon}{\partial x_i} \right), \quad p\Theta \longrightarrow p \frac{\partial v_i}{\partial x_i}, \quad (6.61)$$

<sup>7</sup>We recall that the Newtonian total energy density also contains contributions from the kinetic energy density  $e_N := \rho\epsilon + \frac{1}{2}\rho v^2$  [cf., Eq. (2.68)].

$$-\zeta\Theta^2 \longrightarrow -\zeta \left( \frac{\partial v_i}{\partial x_i} \right)^2, \quad \nabla_\mu q^\mu \longrightarrow \frac{\partial q_i}{\partial x_i}, \quad (6.62)$$

$$\sigma_{\mu\nu} \longrightarrow \Lambda_{ij} - \frac{1}{3} \left( \frac{\partial v_k}{\partial x_k} \right) \delta_{ij}, \quad q_\mu a^\mu \longrightarrow 0, \quad (6.63)$$

$$-2\eta\sigma^{\mu\nu}\sigma_{\mu\nu} \longrightarrow -2\eta\Lambda_{ij}\Lambda^{ij} - \frac{2}{3}\eta \left( \frac{\partial v_i}{\partial x_i} \right)^2. \quad (6.64)$$

Finally, collecting all the various terms, we can write the Newtonian limit of the energy-conservation equation (6.60) as

$$\frac{\partial \epsilon}{\partial t} + v_i \frac{\partial \epsilon}{\partial x_i} + \frac{1}{\rho} \frac{\partial q_i}{\partial x_i} + \frac{p}{\rho} \left( \frac{\partial v_i}{\partial x_i} \right) - \frac{2\eta}{\rho} \Lambda_{ij}\Lambda^{ij} - \frac{1}{\rho} \left( \zeta - \frac{2}{3}\eta \right) \left( \frac{\partial v_i}{\partial x_i} \right)^2 = 0, \quad (6.65)$$

which clearly coincides with the *heat-conduction equation* reported in (2.76).

## 6.5 The importance of a causal theory

### 6.5.1 Parabolic versus hyperbolic

Most of the calculations of relativistic non-perfect fluids to date have employed the formulation of CIT presented in the previous section. The physical description that results from these assumptions has been undoubtedly useful and has led to a large bulk of scientific work in many different areas. The classical theory of relativistic accretion discs, for example, which we will briefly review in Section 11.8, has been developed within this framework.

However, CIT has several undesirable features, some of which will be investigated in this section. By far the most significant one is the algebraic nature of the constitutive equations (6.36)–(6.38), namely, the fact that thermodynamic fluxes react *instantaneously* to the corresponding thermodynamic forces, which, in turn, is responsible for the propagation of signals at infinite speeds. To appreciate the consequences of this behaviour, it is easier to start from a purely Newtonian framework and consider the Newtonian *heat-flux law* or *Fourier law*

$$\vec{q} = -\kappa \vec{\nabla} T, \quad (2.77)$$

whose relativistic counterpart is given by Eq. (6.37). As shown in Section 2.2.6 for the Newtonian case, such a relation leads to a diffusion equation for the temperature [*cf.*, Eq. (2.78)],

$$\partial_t T = \frac{2m\kappa}{3k_B\rho} \nabla^2 T = \chi_t \nabla^2 T. \quad (6.66)$$

From a mathematical point of view, Eq. (6.66) is of *parabolic type*, that is, using the terminology introduced in Chapter 4, it can be cast in a first-order-in-time form of the type (4.9), where the matrix of coefficients is diagonalisable with a set of *divergent* eigenvalues. From a physical point of view, a parabolic character implies that disturbances propagate at infinite

speeds, so that the heat flux changes *instantaneously* with the changes to the temperature gradients. On the other hand, in any realistic physical theory with finite propagation speeds, we expect that if a thermodynamic force is switched on/off, a *relaxation time* will lapse before the corresponding thermodynamic flux is switched on/off. In our example, if  $\vec{\nabla}T$  is set to zero at time  $t \geq 0$ , and if  $\vec{q}_0$  is the heat flux at  $t = 0$ , then we would heuristically expect that  $\vec{q}$  does not go to zero immediately, but that it decays over a time-scale  $\tau_r$  following a law of the type

$$\vec{q} = \vec{q}_0 \exp\left(-\frac{t}{\tau_r}\right). \quad (6.67)$$

In order to account for this relaxation feature, and well before EIT was developed, Cattaneo (1948) modified the Fourier law (2.77) by using the kinetic theory of gases to obtain

$$\tau_r \partial_t \vec{q} + \vec{q} = -\kappa \vec{\nabla}T. \quad (6.68)$$

This expression leads to a hyperbolic equation for the temperature, *i.e.*, the “*telegraph*” equation<sup>8</sup>

$$\tau_r \partial_t^2 T + \partial_t T - \chi_t \nabla^2 T = 0, \quad (6.69)$$

which describes the propagation of a *thermal wave* in the  $x$ -direction, *i.e.*,

$$T \propto \exp[i(\vec{k} \cdot \vec{x} - \omega t)], \quad (6.70)$$

where  $\vec{k}$  is the *wavevector* and  $\omega$  is the frequency of the signal. The dispersion relation resulting from (6.70) is

$$k^2 = \frac{\omega}{\chi_t} (\omega \tau_r + i), \quad (6.71)$$

so that the *phase velocity* is (Anile *et al.*, 1998)

$$v_{\text{ph}} := \text{Re}\left(\frac{\omega}{k}\right) = \left[ \frac{2\chi_t \omega}{\omega \tau_r + \sqrt{1 + \omega^2 \tau_r^2}} \right]^{1/2}, \quad (6.72)$$

and the travelling wave can also be expressed as

$$T \propto \exp\left(-\frac{t}{2\tau_r}\right) \exp\left[i\left(\vec{k} \cdot \vec{x} - \left(\chi \tau_r k^2 - 1\right) \frac{t}{2\tau_r}\right)\right]. \quad (6.73)$$

which highlights the fact that the wave decays exponentially (first exponential) and propagates with a dispersion (second term in second exponential)<sup>9</sup>.

At low frequencies, *i.e.*, for  $\omega \tau_r \ll 1$ , the phase velocity (6.72) of the hyperbolic theory reduces to  $v_{\text{ph}} \simeq \sqrt{2\chi_t \omega}$ . On the other hand, in the high-frequency limit, *i.e.*, for  $\omega \tau_r \gg 1$ , expression (6.72) reduces to  $v_{\text{ph}} \simeq \sqrt{\chi_t / \tau_r}$ , which is the propagation speed of thermal pulses, also known as the *second sound speed*. This result was first discovered experimentally by Peshkov (1944) in helium II and later confirmed in solids through several experiments.

<sup>8</sup>The most general expression for the telegraph equation includes also a term linear in the temperature, which we omit here as it does not contribute to the line of reasoning followed here.

<sup>9</sup>It was by suitably tuning  $\chi$  and  $\tau_r$  so as to reduce dispersion and by setting amplifiers at intermediate stations that signals could be transmitted along the telegraph lines.

In summary: a distinctive feature of first-order theories, including the original formulation by Eckart (1940) and that by Landau and Lifshitz (1987), is that they do not allow for the existence of the relaxation time  $\tau_r$  for dissipative processes, namely the time taken by the system to return to its equilibrium state. However, it is exactly in the transition to equilibrium that hyperbolic and parabolic-type theories differ most significantly. It follows that if one wishes to study a dissipative process over time-scales  $\lesssim \tau_r$ , it is essential to assume a “hyperbolic viewpoint”, whereas for processes occurring on time-scales  $\gg \tau_r$ , a “parabolic viewpoint” may represent a reasonable approximation.

### 6.5.2 Non-causality of Classical Irreversible Thermodynamics

The pathology highlighted in the parabolic form of the Newtonian heat-diffusion equation (6.66) becomes evident also when considering the relativistic counterparts given by Eqs. (6.23) and (6.25), in combination with the constitutive equations (6.36)–(6.38). To show the non-causality of these equations and to keep the expressions as simple as possible, we consider small perturbations in a physical system that is initially in equilibrium. Furthermore, we focus on the case of a non-perfect fluid at rest in a flat spacetime and with a zero viscous pressure,  $\Pi$ , and a zero heat flux,  $q^\mu$  (Romatschke, 2010). In this case, Eqs. (6.23) and (6.25) reduce to

$$(e + p)a_\mu + \mathcal{D}_\mu p - 2\mathcal{D}_\nu(\eta\sigma^\nu_\mu) - 2\eta a^\nu\sigma_{\mu\nu} = 0, \quad (6.74)$$

$$u^\nu\nabla_\nu e + \Theta(e + p) - 2\eta\sigma^{\mu\nu}\sigma_{\mu\nu} = 0, \quad (6.75)$$

where we have used Eq. (6.38). In addition, we assume that the flow is one-dimensional in the  $x$ -direction and that the perturbation affects only the energy density and the fluid velocity, *i.e.*,

$$e = e_0 + \delta e(t, x), \quad u^\mu = u_0^\mu + \delta u^\mu(t, x), \quad (6.76)$$

where the lower index “0” refers to the equilibrium state, so that  $u_0^\mu = (1, 0, 0, 0)$ , and  $\delta u^\mu = (0, \delta u, 0, 0)$ . After retaining only the linear terms in the perturbed form of (6.74), we obtain a parabolic evolution law for the perturbation  $\delta u$ , *i.e.*,

$$\partial_t\delta u - \frac{\eta}{e_0 + p_0}\partial_x^2\delta u = 0 + \mathcal{O}(\delta^2). \quad (6.77)$$

As is customary in perturbative analysis, we assume that the perturbation has a simple harmonic behaviour of the type

$$\delta u(t, x) \propto \exp(-\omega t + ikx), \quad (6.78)$$

where  $\omega$  is the frequency of the perturbation (in general a complex number), while  $k$  is the wavenumber in the  $x$ -direction. A bit of additional algebra allows us to find that the dispersion relation of the perturbed system is

$$\omega = \frac{\eta}{e_0 + p_0}k^2, \quad (6.79)$$

which can be used to estimate the *group velocity* of the mode with wavenumber  $k$ , *i.e.*, the speed of diffusion of the mode, as

$$v_{\text{gr}}(k) = \frac{d\omega}{dk} = \frac{2\eta}{e_0 + p_0} k. \quad (6.80)$$

Since this diffusion speed depends linearly on the wavenumber, it will inevitably become superluminal for sufficiently high  $k$ , thus violating causality. While this result is acceptable within a Newtonian description, it is clearly unsatisfactory within a relativistic theory in which all signals must be contained in the light cone.

As a concluding remark for this section we should stress that non-causality is not the only drawback that plagues CIT. Another pitfall, which is potentially even more serious, is represented by the fact these first-order theories can be shown to be *unstable*, that is, such that small and spatially bounded departures from an equilibrium state can diverge exponentially over a very short time. This aspect of CIT was pointed out by Hiscock and Lindblom (1985), who carried out a linear stability analysis for a non-selfgravitating special-relativistic fluid in a spatially homogeneous equilibrium state. Under rather generic and reasonable conditions it was found that the dispersion relation governing the evolution of the Fourier components of the perturbations always contains exponentially growing modes. In addition, the unstable modes were shown to exist for all wavenumbers and to have ridiculously large growth rates. As an example, plain water at room temperature and pressure was predicted to be unstable with a time-scale of  $\sim 10^{-34}$  s (Hiscock and Lindblom, 1985).

## 6.6 Extended Irreversible Thermodynamics (second-order theories)

A number of approaches have been developed over the years to overcome the *non-causal* features of CIT and to derive a relativistic description of non-perfect fluids which would not violate the causality restrictions imposed by general relativity, while at the same time removing the instability problem of the equilibrium states. The central idea behind these theories is to *extend* the space of variables of conventional theories by treating the dissipative quantities, *i.e.*, the heat flux, shear and bulk stresses, etc., as conserved variables of the ideal fluid, thus restoring causality under a wide range of conditions. The resulting equations are hyperbolic in nature and can be interpreted as evolution equations for the dissipative variables which describe how the “*extended fluxes*” evolve from an initial state to a final state. There is, of course, a price to pay in this extension and amounts to a more involved theory from a mathematical point of view and in a large number of variables and parameters, not all of which have a transparent physical interpretation.

A non-relativistic extended theory was first proposed by Mueller (1967), and was later generalised to the relativistic framework by Israel (1976) and Stewart (1977).<sup>10</sup> These approaches are usually referred to as Extended Irreversible Thermodynamics (EIT) and they will be introduced in Section 6.6.1, although the denomination *Causal Thermodynamics* is often used as a synonym. Starting from these earlier works, the mathematical properties of the new theory have been progressively explored and extended, leading to the class of *divergence-type theories*, which are, by construction, covariant and hyperbolic. These more modern approaches have also gone under the new denomination of *Rational Extended Thermodynamics (RET)*,

<sup>10</sup>A pioneering investigation within the relativistic regime was first proposed by I. Müller in his doctoral thesis (Mueller, 1966).

in order to highlight the rigorous (*i.e.*, “rational”) approach followed in obtaining the constitutive equations as opposed to the heuristic attempts of the early versions. RET, which will be briefly discussed in Section 6.6.3, was first introduced in a Newtonian framework by Liu and Mueller (1983) and in a relativistic framework by Liu *et al.* (1986). A full account of this modern approach can be found in the monographs by Mueller and Ruggeri (1998) and Jou *et al.* (2009).

### 6.6.1 The Israel–Stewart formulation

As first argued by Mueller (1967) and later by Israel (1976), the entropy current as given by Eq. (6.28) is too simplistic. This view is supported by kinetic theory, which argues for an expression of the four-vector  $R^\mu$  which should also contain terms that are of second order in the thermodynamic fluxes. The truncation to first order in the flux  $q$  adopted in (6.28), *de facto* removes those terms which are necessary both for causality and stability, the two major drawbacks of CIT. Bearing this in mind, the most general algebraic form for the four-vector  $R^\mu$  which is at most second order in the fluxes is (Hiscock and Lindblom, 1983)

$$\begin{aligned} \mathcal{S}^\mu &= s\rho u^\mu + \frac{R^\mu}{T} \\ &= s\rho u^\mu + \frac{q^\mu}{T} - (\beta_0 \Pi^2 + \beta_1 q_\nu q^\nu + \beta_2 \pi_{\alpha\beta} \pi^{\alpha\beta}) \frac{u^\mu}{2T} + \alpha_0 \frac{\Pi q^\mu}{T} + \alpha_1 \frac{\pi^{\mu\nu} q_\nu}{T}. \end{aligned} \quad (6.81)$$

The new thermodynamic coefficients  $\beta_0$ ,  $\beta_1$  and  $\beta_2$  model the scalar, vector and tensor dissipative contributions to the entropy density, respectively. The other two coefficients,  $\alpha_0$  and  $\alpha_1$ , measure instead the changes in the entropy current due to possible couplings between viscosity and heat fluxes. Using the new expression (6.81), the entropy density measured in the local rest frame then becomes [*cf.* Eq. (6.32)]

$$-\mathcal{S}^\mu u_\mu = s\rho - \frac{1}{2T}(\beta_0 \Pi^2 + \beta_1 q_\mu q^\mu + \beta_2 \pi_{\mu\nu} \pi^{\mu\nu}), \quad (6.82)$$

which is clearly independent of  $\alpha_0$  and  $\alpha_1$ . The entropy generation rate associated to (6.81) follows from the continuity equation (3.52), the first law of thermodynamics Eq. (2.137) and from (6.23)–(6.25), and is given by (Hiscock and Lindblom, 1983)

$$\begin{aligned} T\nabla_\mu \mathcal{S}^\mu &= -\Pi \left[ \Theta + \beta_0 \dot{\Pi} - \alpha_0 \nabla_\mu q^\mu - \gamma_0 T q^\mu \nabla_\mu \left( \frac{\alpha_0}{T} \right) + \frac{1}{2} T \nabla_\mu \left( \frac{\beta_0}{T} u^\mu \right) \Pi \right] \\ &\quad - q^\mu \left[ \nabla_\mu \ln T + a_\mu + \beta_1 \dot{q}_\mu - \alpha_0 \nabla_\mu \Pi - \alpha_1 \nabla_\nu \pi^\nu_\mu \right. \\ &\quad \left. - (1 - \gamma_0) T \nabla_\mu \left( \frac{\alpha_0}{T} \right) \Pi - (1 - \gamma_1) T \pi^\nu_\mu \nabla_\nu \left( \frac{\alpha_1}{T} \right) + \frac{1}{2} T q_\mu \nabla_\nu \left( \frac{\beta_1}{T} u^\nu \right) \right] \\ &\quad - \pi^{\mu\nu} \left\langle \nabla_\mu u_\nu + \beta_2 \dot{\pi}_{\mu\nu} - \alpha_1 \nabla_\mu q_\nu - \gamma_1 T q_\mu \nabla_\nu \left( \frac{\alpha_1}{T} \right) + \frac{1}{2} T \pi_{\mu\nu} \nabla_\gamma \left( \frac{\beta_2}{T} u^\gamma \right) \right\rangle, \end{aligned} \quad (6.83)$$

where we have reintroduced the overdot symbol to indicate the *convective derivative*, i.e.,  $\dot{A} := u^\mu \nabla_\mu A$  [cf., Eq. (3.7)], and where the brackets  $\langle \rangle$  indicate the symmetric and trace-free part of the corresponding tensors [cf., Eq. (1.98)].

Equation (6.83) defines as *extended forces* the terms in the square brackets and contains terms which were neglected in the original formulation by Israel (1976). More specifically, these are the terms involving the gradients of the thermodynamic coefficients  $\alpha_i$  and  $\beta_i$ . While the former amount to spatial gradients, i.e.,  $\pi^{\mu\nu} \nabla_\nu (\alpha_1/T)$ , and cannot be ignored *a priori* if the fluid is not homogeneous (e.g., as in the interior of a relativistic star), the latter amount to time derivatives for a fluid at rest, i.e.,  $\nabla_\mu (\beta_1 u^\mu/T)$  and can sometimes be neglected (e.g., when considering small perturbations around an equilibrium state). Note also the introduction in Eq. (6.83) of two new thermodynamic coefficients,  $\gamma_0$  and  $\gamma_1$ , which are needed because of the ambiguity arising when factoring out the terms which involve the products  $\Pi q^\mu$  and  $\pi_{\mu\nu} q^\nu$ . Unfortunately, neither the physical meaning nor the magnitude of these coefficients is known *a priori*. This represents an obvious drawback of the formulation, since the terms in (6.83) involving the spatial gradients  $\pi^{\mu\nu} \nabla_\nu (\alpha_1/T)$  could be large even though the gradients themselves are small. For simplicity, in the rest of this section we will set  $\alpha_0 = \alpha_1 = 0$ , thus neglecting the coupling between the heat flux and viscosity, as well as  $\gamma_0 = \gamma_1 = 0$ . However, nonzero values of these coefficients will be considered in Section 6.6.2.

Within this approximation, and as done in the classical theory, the simplest way to satisfy the second law of thermodynamics (2.150) is to impose linear relations between the thermodynamic fluxes and the extended forces. In this case, however, the extended forces contain convective derivatives of the corresponding fluxes and the resulting *constitutive equations* replacing (6.36)–(6.38) are

$$\Pi = -\zeta \left[ \Theta + \beta_0 \dot{\Pi} + \frac{1}{2} T \nabla_\nu \left( \frac{\beta_0}{T} u^\nu \right) \Pi \right], \quad (6.84)$$

$$q_\nu = -\kappa \left[ \mathcal{D}_\nu \ln T + a_\nu + \beta_1 \dot{q}_\nu + \frac{1}{2} T \nabla_\mu \left( \frac{\beta_1}{T} u^\mu \right) q_\nu \right], \quad (6.85)$$

$$\begin{aligned} \pi_{\mu\nu} &= -2\eta \left\langle \nabla_\mu u_\nu + \beta_2 \dot{\pi}_{\mu\nu} + \frac{1}{2} T \nabla_\gamma \left( \frac{\beta_2}{T} u^\gamma \right) \pi_{\mu\nu} \right\rangle \\ &= -2\eta \left[ \sigma_{\mu\nu} + \beta_2 \dot{\pi}_{\mu\nu} + \frac{1}{2} T \nabla_\gamma \left( \frac{\beta_2}{T} u^\gamma \right) \pi_{\mu\nu} \right], \end{aligned} \quad (6.86)$$

which can also be rearranged as (Maartens, 1996)

$$\tau_0 \dot{\Pi} + \Pi = -\zeta \Theta - \left[ \frac{1}{2} \zeta T \nabla_\mu \left( \frac{\tau_0}{\zeta T} u^\mu \right) \Pi \right], \quad (6.87)$$

$$\tau_1 h^\nu_\mu \dot{q}_\nu + q_\mu = -\kappa T (\mathcal{D}_\mu \ln T + a_\mu) - \left[ \frac{1}{2} \kappa T^2 \nabla_\nu \left( \frac{\tau_1}{\kappa T^2} u^\nu \right) q_\mu \right], \quad (6.88)$$

$$\tau_2 h^\alpha_\mu h^\beta_\nu \dot{\pi}_{\alpha\beta} + \pi_{\mu\nu} = -2\eta \sigma_{\mu\nu} - \left[ \eta T \nabla_\gamma \left( \frac{\tau_2}{2\eta T} u^\gamma \right) \pi_{\mu\nu} \right], \quad (6.89)$$

where we have introduced the three *relaxation times*  $\tau_0, \tau_1, \tau_2$  as re-parameterisations of the transport coefficients  $\zeta, \kappa$  and  $\eta$ , i.e.,

$$\tau_0 := \zeta \beta_0, \quad \tau_1 := \kappa T \beta_1, \quad \tau_2 := 2\eta \beta_2. \quad (6.90)$$

Equations (6.87)–(6.89) are known as the *Israel–Stewart equations* of EIT. In many applications, the terms in square brackets on the right-hand side of Eqs. (6.87)–(6.89) are much smaller than the other terms and thus often neglected. The resulting equations, which represent the set of truncated Israel–Stewart equations, are sometimes reported in so-called *Maxwell–Cattaneo* form and can be written as (Maartens, 1996)

$$\tau_0 \dot{\Pi} + \Pi =: \tilde{\Pi} = -\zeta \Theta, \quad (6.91)$$

$$\tau_1 h^\nu_\mu \dot{q}_\nu + q_\mu =: \tilde{q}_\mu = -\kappa T (\mathcal{D}_\mu \ln T + a_\mu), \quad (6.92)$$

$$\tau_2 h^\alpha_\mu h^\beta_\nu \dot{\pi}_{\alpha\beta} + \pi_{\mu\nu} =: \tilde{\pi}_{\mu\nu} = -2\eta \sigma_{\mu\nu}, \quad (6.93)$$

where  $\tilde{\Pi}$ ,  $\tilde{q}_\alpha$  and  $\tilde{\pi}_{\alpha\beta}$  are the same equilibrium thermodynamic fluxes  $\Pi$ ,  $q_\alpha$  and  $\pi_{\alpha\beta}$  of CIT appearing on the right-hand side of (6.36)–(6.38). The Maxwell–Cattaneo form now makes it clear that  $\tau_0$ ,  $\tau_1$  and  $\tau_2$  are referred to as relaxation times because they measure the time-scales over which the system evolves to a new equilibrium. For example, considering Eq. (6.87) in the limit  $\Theta \rightarrow 0$  and for a homogeneous fluid, we obtain that  $\tau_0 \rightarrow -\Pi/\dot{\Pi}$ , thus measuring the time-scale over which bulk viscosity suppresses the fluid compression or expansion.

Whether written in the full form of Eqs. (6.87)–(6.89), or in the truncated form of Eqs. (6.91)–(6.93), the new evolution equations of EIT clearly represent a much more complex system than the corresponding one defined in CIT, *i.e.*, Eqs. (6.36)–(6.38). When coupled with the continuity and the energy–momentum equations, Eqs. (6.87)–(6.89) constitute a complete system of first-order-in-time partial differential equations in  $1+1+3+1+3+5 = 14$  unknowns<sup>11</sup> corresponding to the independent components among the variables  $\{\rho, e, u^\mu, \Pi, q^\mu, \pi^{\mu\nu}\}$ . For comparison, we note that the counting was  $1+1+3=5$  for a perfect fluid described by  $\{\rho, e, u^\mu\}$ .

The new character of the equations of EIT (whose hyperbolic nature we will prove in the following section), is highlighted by the presence of the relaxation times  $\tau_0$ ,  $\tau_1$  and  $\tau_2$ , which are needed to model, without violation of causality, all those phenomena for which an accurate description of the transition from one state to another one is essential. However, as shown by the definitions (6.90), the three relaxation times depend not only on the transport coefficients  $\zeta$ ,  $\kappa$  and  $\eta$ , and also on the coefficients  $\beta_0$ ,  $\beta_1$  and  $\beta_2$ , which are themselves not known and should, in principle, be calculated from kinetic theory and could vary, also considerably, from fluid to fluid. In practice, the relaxation times are simply estimated as mean collision times, *e.g.*,  $1/\tau_0 \sim n\Sigma_0 v$ , with  $\Sigma_0$  being the collision cross-section of the process involved in the time-scale  $\tau_0$ , and  $v$  being the mean free particle speed intervening in the generation of bulk viscosity.

The considerations made so far naturally lead to an important remark about EIT. As formulated, in fact, the theory is not complete and requires indispensable input from kinetic theory. After all, the assumption made in (6.81) that the entropy depends on the heat flux and on the shear stress tensor is rather unconventional from a phenomenological point of view. However, as shown by Mueller and Ruggeri (1998), kinetic theory does provide the correct interpretation of the equations presented here and will motivate a more consistent version of

<sup>11</sup>This approach represents the macroscopic counterpart of *Grad's 14-moment approximation* developed in kinetic theory (Grad, 1949) [see, *e.g.*, Israel and Stewart (1979)].

EIT, known as the divergence-type theories, or RET, whose basic features will be presented in Section 6.6.3.

### 6.6.2 Characteristic speeds of the Israel–Stewart formulation

As mentioned in the previous sections, obtaining a hyperbolic and causal theory describing the dynamics of non-perfect fluids was the main motivation to go beyond the first-order theory of CIT and has led to the derivation of the Israel–Stewart equations of EIT. In this section we verify that Eqs. (6.87)–(6.89) represent a set of hyperbolic equations and that the corresponding characteristic velocities can be calculated. In showing this we follow Hiscock and Lindblom (1983) and first consider a fluid in a background equilibrium state, *i.e.*, with  $\Pi = 0 = q^\mu = \pi^{\mu\nu}$ , and described by the variables  $\rho, e, u^\mu$ . Next, we introduce the perturbations about such an equilibrium state  $\delta\rho, \delta e, \delta u^\mu, \delta\Pi, \delta q^\mu, \delta\pi^{\mu\nu}$ , and work, for simplicity, within the so-called *Cowling approximation*, *i.e.*, not including perturbations in the space-time metric and thus setting  $\delta g_{\mu\nu} = 0$  (Cowling, 1941). As a result, the perturbed energy–momentum tensor and thermodynamic fluxes will take the explicit form<sup>12</sup>

$$\delta T^{\mu\nu} = (e + p)(\delta u^\mu u^\nu + u^\mu \delta u^\nu) + \delta e u^\mu u^\nu + (\delta p + \delta\Pi)h^{\mu\nu} + \delta q^\mu u^\nu + u^\mu \delta q^\nu + \delta\pi^{\mu\nu}, \quad (6.94)$$

$$\delta\Pi = -\zeta \left( \nabla_\mu \delta u^\mu + \beta_0 \dot{\delta\Pi} - \alpha_0 \nabla_\mu \delta q^\mu \right), \quad (6.95)$$

$$\begin{aligned} \delta q^\mu = -\kappa T h^{\mu\nu} & \left[ \nabla_\nu \left( \frac{\delta T}{T} \right) + \dot{\delta u}_\nu + \delta u^\alpha \nabla_\alpha u_\nu + \beta_1 \dot{\delta q}_\nu - \alpha_0 \nabla_\nu \delta\Pi - \alpha_1 \nabla_\gamma \delta\pi^\gamma_\nu \right. \\ & \left. - T \delta\Pi \nabla_\nu \left( \frac{\alpha_0}{T} \right) - T \delta\pi^\gamma_\nu \nabla_\gamma \left( \frac{\alpha_1}{T} \right) \right], \end{aligned} \quad (6.96)$$

$$\delta\pi^{\mu\nu} = -2\eta \left\langle \nabla^\mu \delta u^\nu + \delta u^\mu \dot{\delta u}^\nu + \beta_2 \dot{\delta\pi}^{\mu\nu} - \alpha_1 \nabla^\mu \delta q^\beta \right\rangle, \quad (6.97)$$

where  $\dot{\delta u}_\nu = u^\mu \nabla_\mu \delta u_\nu$ , etc. Inserting these perturbations into the conservation of rest mass (3.52) and of the energy–momentum tensor (3.53)

$$u^\mu \nabla_\mu \delta\rho + \nabla_\mu (\rho \delta u^\mu) = 0, \quad \nabla_\mu \delta T^{\mu\nu} = 0, \quad (6.98)$$

as well as in the new evolution laws for the thermodynamic fluxes (6.87)–(6.89), we can write the resulting system in the quasi-linear form [*cf.*, Eq. (4.6)<sub>2</sub>]

$$(\mathcal{A}^\mu)_B^A \nabla_\mu Y^B + \mathcal{B}_B^A Y^B = 0, \quad (6.99)$$

where

$$Y^B := \left( T \delta\tilde{\alpha}_f, \frac{\delta T}{T}, \delta\Pi, \delta u^1, \delta q^1, \delta\pi^{11}, \delta u^2, \delta q^2, \delta\pi^{21}, \delta u^3, \delta q^3, \delta\pi^{31}, \delta\pi^{22} - \delta\pi^{33}, \delta\pi^{23} \right) \quad (6.100)$$

<sup>12</sup>Given the difficulties in the physical interpretation of the coefficients  $\gamma_0$  and  $\gamma_1$ , we will consider them to be zero for this analysis, as done also by Hiscock and Lindblom (1983). On the other hand, we will not consider  $\alpha_0$  and  $\alpha_1$  to be zero.

is the vector of the 14 perturbed fields and where  $\tilde{\alpha}_f := \alpha_f k_B$  is the rescaled *fugacity* [cf., Eq. (2.122)].

In Section 4.1.1 we have presented a precise definition of a *hyperbolic* system of equations, and provided a systematic presentation of its mathematical properties. We here recall that a necessary (but not sufficient) condition for the quasi-linear system (6.99) to be hyperbolic is that the matrix  $(\mathcal{A}^\mu)_B^A$  admits a set of real eigenvalues, which, from a physical point of view, correspond to the speeds at which perturbations propagate within the fluid. In particular, such *eigenvalues* can be computed after solving the equation

$$\det(\mathcal{A}^\mu{}_B^A \nabla_\mu \phi) = 0, \quad (6.101)$$

where  $\phi = \text{const.}$  defines the characteristic surface, along which discontinuities in the initial data propagate, and, for compactness, we have dropped the round brackets in  $(\mathcal{A}^\mu)_B^A$ . As done in Section 4.1.1, we introduce  $\phi_\mu$  to denote  $\nabla_\mu \phi$ , and restrict our analysis to one spatial dimension introducing local coordinates such that  $\phi = \phi(x^0, x^1)$ . As a result, Eqs. (6.101) can be rewritten as

$$\det(\lambda \mathcal{A}^{A0}{}_B - \mathcal{A}^{A1}{}_B) = 0, \quad (6.102)$$

where we have defined  $\lambda := -\phi_0/\phi_1$ . After rather lengthy algebra, whose details can be found in Stewart (1977), and considering a fluid of identical particles of mass  $m$ , we can cast the set of equations (6.102) as

$$\lambda \mathcal{A}^{A0}{}_B - \mathcal{A}^{A1}{}_B = \begin{pmatrix} \mathbf{Q} & 0 & 0 & 0 \\ 0 & \mathbf{R} & 0 & 0 \\ 0 & 0 & \mathbf{R} & 0 \\ 0 & 0 & 0 & \mathbf{S} \end{pmatrix}, \quad (6.103)$$

where the matrices  $\mathbf{Q}$ ,  $\mathbf{R}$  and  $\mathbf{S}$  are defined as

$$\mathbf{Q} := \begin{pmatrix} \frac{\lambda}{mT} \left( \frac{\partial \rho}{\partial \tilde{\alpha}_f} \right)_T & \frac{\lambda}{T} \left( \frac{\partial e}{\partial \tilde{\alpha}_f} \right)_T & 0 & -\frac{\rho}{m} & 0 & 0 \\ \frac{\lambda}{T} \left( \frac{\partial e}{\partial \tilde{\alpha}_f} \right)_T & \lambda T \left( \frac{\partial e}{\partial T} \right)_{\tilde{\alpha}_f} & 0 & -(e+p) & -1 & 0 \\ 0 & 0 & \beta_0 \lambda & -1 & \alpha_0 & 0 \\ -\frac{\rho}{m} & -(e+p) & -1 & \lambda(e+p) & \lambda & -1 \\ 0 & -1 & \alpha_0 & \lambda & \beta_1 \lambda & \alpha_1 \\ 0 & 0 & 0 & -1 & \alpha_1 & \frac{3}{2} \beta_2 \lambda \end{pmatrix}, \quad (6.104)$$

$$\mathbf{R} := \begin{pmatrix} \lambda(e+p) & \lambda & -1 \\ \lambda & \beta_1\lambda & \alpha_1 \\ -1 & \alpha_1 & 2\beta_2\lambda \end{pmatrix}, \quad \mathbf{S} := \begin{pmatrix} 2\beta_2\lambda & 0 \\ 0 & \beta_2\lambda \end{pmatrix}. \quad (6.105)$$

Since the determinant of a block diagonal matrix is given by the products of the determinants of the single blocks, we can write

$$\det(\lambda \mathcal{A}^{A0} - \mathcal{A}^{A1}) = \det \mathbf{Q} (\det \mathbf{R})^2 \det \mathbf{S}, \quad (6.106)$$

where each determinant is given by

$$\det \mathbf{Q} = \frac{3}{2m} \lambda^2 (A\lambda^4 + B\lambda^2 + C) \left[ \left( \frac{\partial \rho}{\partial \tilde{\alpha}_f} \right)_T \left( \frac{\partial e}{\partial T} \right)_{\tilde{\alpha}_f} - \left( \frac{\partial \rho}{\partial T} \right)_{\tilde{\alpha}_f} \left( \frac{\partial e}{\partial \tilde{\alpha}_f} \right)_T \right], \quad (6.107)$$

$$\det \mathbf{R} = \lambda \{ 2\beta_2[\beta_1(e+p)-1]\lambda^2 - [(e+p)\alpha_1^2 + 2\alpha_1 + \beta_1] \}, \quad (6.108)$$

$$\det \mathbf{S} = 2\beta_2^2\lambda^2, \quad (6.109)$$

with the different terms having been grouped through the auxiliary definitions

$$A := \beta_0\beta_2[\beta_1(e+p)-1], \quad B := -(e+p)D - \beta_1E - 2F, \quad (6.110)$$

$$C := \frac{DE - F^2}{\beta_0\beta_2}, \quad D := \beta_0\beta_2 \left[ \frac{\alpha_0^2}{\beta_0} + \frac{2}{3} \frac{\alpha_1^2}{\beta_2} + \frac{1}{\rho T^2} \left( \frac{\partial T}{\partial s} \right)_\rho \right], \quad (6.111)$$

$$E := \beta_0\beta_2 \left[ (e+p) \left( \frac{\partial p}{\partial e} \right)_s + \frac{1}{\beta_0} + \frac{2}{3\beta_2} \right], \quad F := \beta_0\beta_2 \left[ \frac{\alpha_0}{\beta_0} + \frac{2}{3} \frac{\alpha_1}{\beta_2} - \frac{\rho}{T} \left( \frac{\partial T}{\partial \rho} \right)_s \right]. \quad (6.112)$$

The characteristic velocities which correspond to the *eigenvalues* of the system (6.99), can therefore be obtained after setting to zero the individual determinants (6.107)–(6.109). The matrix  $\mathbf{Q}$ , in particular, has six characteristic velocities, two of which vanish, while the remaining four are obtained as the solution of the following equation

$$Av_L^4 + Bv_L^2 + C = 0. \quad (6.113)$$

Such velocities are referred to as “longitudinal” since they are relative to perturbation variables that are orthogonal to the characteristic surface, with two of them corresponding approximately to the usual sound speed, while the other two correspond approximately to the propagation of temperature perturbations (*i.e.*, the second sound speed). The matrix  $\mathbf{R}$ , on the other hand, has three characteristic velocities, one of which vanishes, while the other two are given by

$$v_T^2 = \frac{(e+p)\alpha_1^2 + 2\alpha_1 + \beta_1}{2\beta_2[\beta_1(e+p)-1]}, \quad (6.114)$$

and they are referred to as “transverse” velocities, since they correspond to perturbation variables that are tangent to the characteristic surface and hence transverse to the direction of

propagation of a disturbance. Finally, the matrix  $S$  contributes with two additional characteristic velocities, both of which are zero.

Despite the general expressions (6.113) and (6.114), the proof that the characteristic velocities are all real and finite can only be made on a case-by-case basis, that is, after a specific equilibrium distribution function is considered and the corresponding unknown coefficients  $\alpha_i$  and  $\beta_i$  are computed. For example, Stewart (1977) has considered the case of a Maxwellian distribution and found that the transverse velocity lies in the range

$$\frac{7}{5} \leq \frac{v_T^2 m}{k_B T} \leq \frac{1}{5}, \quad (6.115)$$

while the longitudinal velocities are limited by

$$1.35 \leq \frac{v_{L,1}^2 m}{k_B T} \leq \frac{1}{3}, \quad 5.18 \leq \frac{v_{L,2}^2 m}{k_B T} \leq \frac{3}{5}. \quad (6.116)$$

### 6.6.3 Divergence-type theories

#### **Motivations and fundamental principles.**

The transport equations for the dissipative fluxes (6.87)–(6.89) have been derived under the assumption that the entropy current vector of CIT can be extended to include terms that are quadratic in the dissipative fluxes [*cf.*, Eq. (6.81)]. In spite of the promising features of the Israel–Stewart formulation, it is not straightforward to know whether the system of Eqs. (3.52)–(3.53) and Eqs. (6.87)–(6.89) is hyperbolic under all conditions. In this spirit, Hiscock and Lindblom (1983) performed a detailed analysis of the conditions under which the characteristic speeds computed in the previous section [*cf.*, Eq. (6.113)–(6.114)] are subluminal and found that such conditions impose a number of constraints on the coefficients  $\beta_i$ , whose physical significance is not always transparent and leaves the door open to causality violation under extreme regimes. Indeed, Hiscock and Lindblom (1988) showed that, when the physical state of a heat-conducting fluid deviates strongly from equilibrium, the Israel–Stewart formulation fails to be hyperbolic. In particular, it is possible to show that for values of the ratio  $|\vec{q}|/e > 0.08898$ , where  $|\vec{q}|$  is the modulus of the heat flux along a given direction, some of the characteristic speeds become complex, thus breaking hyperbolicity. Furthermore, for  $|\vec{q}|/e > 0.4$ , one of the real characteristic velocities is greater than the speed of light.

An alternative formulation of extended thermodynamics that overcomes these difficulties was suggested by Liu *et al.* (1986), and is built in such a way that it satisfies three different conditions: (*i*) the relativistic covariance property; (*ii*) the entropy principle (2.150); (*iii*) the requirement of hyperbolicity. This new formulation, which has also benefited from a close connection with the kinetic theory of gases, particularly through the *moment method* of Grad<sup>13</sup> (Grad, 1949), is called the *divergence-type formulation* of *Extended Irreversible Thermodynamics*, and is also known as *Rational Extended Thermodynamics* (RET).

<sup>13</sup>In the Grad model, proposed to solve the Boltzmann equation in non-equilibrium situations, the non-equilibrium distribution function  $f$  is replaced by its higher-order moments.

To review the main features of this formulation, which is treated thoroughly in the monograph by Mueller and Ruggeri (1998), we recall that within relativistic kinetic theory, the rest-mass density current  $J^\mu$ , the energy–momentum tensor  $T^{\mu\nu}$  and the tensor of fluxes  $F^{\mu\nu\sigma}$ , are defined respectively as the first, the second and the third moment of the distribution function  $f(x^\mu, p^\nu)$  [see Section 2.3.2 and *cf.*, Eqs. (2.94)–(2.96) where  $c \neq 1$ ], *i.e.*,

$$J^\mu := mN^\mu = m \int p^\mu f \frac{d^3 p}{p^0}, \quad (6.117)$$

$$T^{\mu\nu} := \int p^\mu p^\nu f \frac{d^3 p}{p^0}, \quad (6.118)$$

$$F^{\mu\nu\sigma} := \int p^\mu p^\nu p^\sigma f \frac{d^3 p}{p^0}, \quad (6.119)$$

where  $p^\mu$  is the four-momentum of the particle and of course  $f$  obeys the relativistic Boltzmann equation (2.86). Within divergence-type theories, the determination of the 14 fields represented by the components of  $J^\mu$  and  $T^{\mu\nu}$  is obtained after solving the following divergence-type laws (Liu *et al.*, 1986)

$$\nabla_\mu J^\mu = 0, \quad (2.118)$$

$$\nabla_\mu T^{\mu\nu} = 0, \quad (2.119)$$

$$\nabla_\mu F^{\mu\nu\sigma} = I^{\nu\sigma}, \quad (6.120)$$

where  $I^{\nu\sigma}$  is called the *production density tensor* and essentially represents the source term in the conservation of the third moment of the distribution function. Equations (2.118) and (2.119) are the usual continuity equation and the conservation laws of energy–momentum, whereas (6.120) is the “balance-law of fluxes”. Kinetic theory suggests that the tensors  $F^{\mu\nu\sigma}$  and  $I^{\nu\sigma}$  are algebraic functions of  $J^\mu$  and  $T^{\mu\nu}$ , and that  $F^{\mu\nu\sigma}$  is symmetric in all of its indices,<sup>14</sup> so that  $I^{\mu\nu}$  is also symmetric. We note that the condition

$$F^{\mu\nu}{}_\nu = mJ^\mu, \quad (6.121)$$

which is obtained from kinetic theory for a fluid of identical particles of mass  $m$ , implies, from Eqs. (2.118) and (6.120), that  $I^\mu{}_\mu = 0$  (Chernikov, 1964a; Chernikov, 1964b). Of course, at equilibrium, the production density will be zero, *i.e.*,  $I^{\mu\nu} = 0$ .

Within divergence-type theories, the constitutive equations are represented by relations among the tensors  $S^\mu$ ,  $I^{\mu\nu}$ ,  $F^{\mu\nu\sigma}$  and the fields  $J^\mu$  and  $T^{\mu\nu}$ , namely by relations of the type

$$S^\mu = \hat{S}^\mu(J^\alpha, T^{\alpha\beta}), \quad (6.122)$$

$$I^{\mu\nu} = \hat{I}^{\mu\nu}(J^\alpha, T^{\alpha\beta}), \quad (6.123)$$

$$F^{\mu\nu\sigma} = \hat{F}^{\mu\nu\sigma}(J^\alpha, T^{\alpha\beta}), \quad (6.124)$$

where the functions  $\hat{S}^\mu$ ,  $\hat{I}^{\mu\nu}$ , and  $\hat{F}^{\mu\nu\sigma}$  are called *constitutive functions*. If available, knowledge of the constitutive functions would make the set of equations (2.118), (2.119), (6.120),

<sup>14</sup>It should be stressed that such a symmetry assumption on  $F^{\mu\nu\sigma}$  limits the applicability of divergence-type theories to ideal gases (Kremer, 1985). In the alternative formulation of Geroch and Lindblom (1990), on the other hand,  $F^{\mu\nu\sigma}$  is symmetric only in the last two indices,  $\nu$  and  $\sigma$ .

and (6.122)–(6.124), an explicit set of equations whose solution formally defines a *thermodynamic process*. Of course, the determination of the functional form of  $\widehat{\mathcal{S}}^\mu$ ,  $\widehat{I}^{\mu\nu}$  and  $\widehat{F}^{\sigma\mu\nu}$  is the actual goal of a divergence-type formulation and is accomplished, as mentioned above, after using as guidelines relativistic covariance, the entropy principle (2.150), and the requirement of hyperbolicity. Below we will discuss how to do this in practice.

Let us first consider the requirement of relativistic covariance and recall that in Section 6.6.1 we have seen that the 14 fields equivalent to the determination of  $J^\mu$  and  $T^{\mu\nu}$  are the quantities  $\{\rho, e, u^\mu, \Pi, q^\mu, \pi^{\mu\nu}\}$ . When changing from one reference frame  $\mathcal{O}$  to another one  $\mathcal{O}'$ , the functional form of the constitutive relations cannot change, although the function arguments, *i.e.*, the tensors  $u^\mu, q^\mu, \pi^{\mu\nu}$ , and the constitutive tensors themselves will of course change. Requiring covariance between the two frames translates therefore into the following constraints

$$\mathcal{S}^\alpha = \widehat{\mathcal{S}}^\alpha(\rho, e, \Pi, u^\mu, q^\mu, \pi^{\mu\nu}), \quad \mathcal{S}^{\alpha'} = \widehat{\mathcal{S}}^{\alpha'}(\rho, e, \Pi, u^{\mu'}, q^{\mu'}, \pi^{\mu'\nu'}), \quad (6.125)$$

$$I^{\alpha\beta} = \widehat{I}^{\alpha\beta}(\rho, e, \Pi, u^\mu, q^\mu, \pi^{\mu\nu}), \quad I^{\alpha'\beta'} = \widehat{I}^{\alpha'\beta'}(\rho, e, \Pi, u^{\mu'}, q^{\mu'}, \pi^{\mu'\nu'}), \quad (6.126)$$

$$F^{\alpha\beta\gamma} = \widehat{F}^{\alpha\beta\gamma}(\rho, e, \Pi, u^\mu, q^\mu, \pi^{\mu\nu}), \quad F^{\alpha'\beta'\gamma'} = \widehat{F}^{\alpha'\beta'\gamma'}(\rho, e, \Pi, u^{\mu'}, q^{\mu'}, \pi^{\mu'\nu'}), \quad (6.127)$$

that is, the constitutive functions  $\widehat{\mathcal{S}}^\alpha$ ,  $\widehat{I}^{\alpha\beta}$  and  $\widehat{F}^{\alpha\beta\gamma}$  are the same in the two frames, while their arguments transform according to the usual coordinate transformations, *i.e.*, (see Section 1.3.4)

$$u^{\mu'} = \Lambda^{\mu'}_\nu u^\nu, \quad q^{\mu'} = \Lambda^{\mu'}_\nu q^\nu, \quad \pi^{\mu'\nu'} = \Lambda^{\mu'}_\alpha \Lambda^{\nu'}_\beta \pi^{\alpha\beta}, \quad (6.128)$$

where the matrices  $\Lambda$  are shorthand for coordinate transformations, *i.e.*,  $\Lambda^{\mu'}_\mu = \partial x^{\mu'}/\partial x^\mu$ . Similarly, the transformation rules for the constitutive functions are given by

$$\widehat{\mathcal{S}}^{\alpha'}(\rho, e, \Pi, \Lambda^{\mu'}_\nu u^\nu, \Lambda^{\mu'}_\nu q^\nu, \Lambda^{\mu'}_\alpha \Lambda^{\nu'}_\beta \pi^{\alpha\beta}) = \Lambda^{\alpha'}_\beta \widehat{\mathcal{S}}^\beta(\rho, e, \Pi, u^\mu, q^\mu, \pi^{\mu\nu}), \quad (6.129)$$

$$\widehat{I}^{\alpha'\beta'}(\rho, e, \Pi, \Lambda^{\mu'}_\nu u^\nu, \Lambda^{\mu'}_\nu q^\nu, \Lambda^{\mu'}_\alpha \Lambda^{\nu'}_\beta \pi^{\alpha\beta}) = \Lambda^{\alpha'}_\pi \Lambda^{\beta'}_\rho \widehat{I}^{\pi\rho}(\rho, e, \Pi, u^\mu, q^\mu, \pi^{\mu\nu}), \quad (6.130)$$

$$\widehat{F}^{\alpha'\beta'\pi'}(\rho, e, \Pi, \Lambda^{\mu'}_\nu u^\nu, \Lambda^{\mu'}_\nu q^\nu, \Lambda^{\mu'}_\alpha \Lambda^{\nu'}_\beta \pi^{\alpha\beta}) = \Lambda^{\alpha'}_\pi \Lambda^{\beta'}_\rho \Lambda^{\pi'}_\sigma \widehat{F}^{\pi\rho\sigma}(\rho, e, \Pi, u^\mu, q^\mu, \pi^{\mu\nu}). \quad (6.131)$$

Determining the general solution of the functional forms in Eqs. (6.129)–(6.131) represents a formidable task, which can be made easier if we follow a more pragmatic approach. In essence, this consists in considering the case when  $I^{\mu\nu}$  and  $F^{\mu\nu\sigma}$  are linear in the dissipative fluxes, *i.e.*, when they are written as

$$I^{\mu\nu} := B_1^\Pi \Pi(g^{\mu\nu} + 4u^\mu u^\nu) + B_3 \pi^{\mu\nu} + B_4(q^\mu u^\nu + q^\nu u^\mu), \quad (6.132)$$

$$\begin{aligned} F^{\mu\nu\sigma} := & - (C_1^0 + C_1^\Pi \Pi) \left[ u^\mu u^\nu u^\sigma + \frac{1}{6}(g^{\mu\nu} u^\sigma + g^{\nu\sigma} u^\mu + g^{\sigma\mu} u^\nu) \right] \\ & + \frac{1}{6} nm^2 (g^{\mu\nu} u^\sigma + g^{\nu\sigma} u^\mu + g^{\sigma\mu} u^\nu) + C_3 \left[ (g^{\mu\nu} q^\sigma + g^{\nu\sigma} q^\mu + g^{\sigma\mu} q^\nu) \right. \\ & \left. + 6(u^\mu u^\nu q^\sigma + u^\nu u^\sigma q^\mu + u^\sigma u^\mu q^\nu) \right] + C_5(\pi^{\mu\nu} u^\sigma + \pi^{\nu\sigma} u^\mu + \pi^{\sigma\mu} u^\nu), \end{aligned} \quad (6.133)$$

which then allows one to compute the coefficients of the linear and quadratic terms of the entropy current as

$$\mathcal{S}^\mu := (\rho s + A_1^\Pi \Pi + A_1^{\Pi^2} \Pi^2 + A_1^q q^\nu q_\nu + A_1^\pi \pi^{\alpha\beta} \pi_{\alpha\beta}) u^\mu + (A_2^0 + A_2^\Pi \Pi) q^\mu + A_3^0 \pi^{\mu\nu} q_\nu. \quad (6.134)$$

Clearly, the definitions (6.132)–(6.134) make use of a number of new coefficients, namely, the 14 coefficients

$$\{A_2^0, A_3^0, A_1^q, A_1^\Pi, A_1^{\Pi^2}, A_2^\Pi, A_1^\pi; B_3, B_4, B_1^\Pi; C_3, C_5, C_1^0, C_1^\Pi\}, \quad (6.135)$$

which are functions of  $\rho$  and  $e$ , and cannot depend on the dissipative fluxes.

It was objected above that the Israel–Stewart formulation of EIT, [*i.e.*, Eqs. (6.87)–(6.89)], had the drawback of the appearance of a large number of coefficients with a non-transparent physical significance. The same objection could be made also for the formulation of RET discussed so far, with the added complication that the number of coefficients has actually increased. Such an objection, however, can be easily overturned and indeed Liu *et al.* (1986) have shown that the unknown coefficients in (6.132)–(6.134) can actually be calculated, more or less straightforwardly, through statistical-mechanics techniques, thus allowing one to make the resulting representation fully explicit. In addition, the entropy principle (2.150) sets stringent constraints on the dependence of the coefficients (6.135) on the temperature  $T$  and on the fugacity  $\alpha_f$  [we recall that  $\alpha_f T$  is proportional to the Gibbs free energy or chemical potential; *cf.* Eq. (2.122)], provided that the equilibrium state functions  $\rho(\alpha_f, T)$ ,  $e(\alpha_f, T)$ ,  $p(\alpha_f, T)$ ,  $C_1^0(\alpha_f, T)$  and  $s(\alpha_f, T)$  are known.<sup>15</sup>

We next discuss the second constraint of a divergence-type formulation via the entropy principle. We do this by noticing that the condition expressed by the inequality (2.150),  $\nabla_\mu \mathcal{S}^\mu \geq 0$ , does not need to hold for all fields  $J^\mu$  and  $T^{\mu\nu}$ , but only for those that represent a thermodynamic process, that is, for those that satisfy the conservation/balance equations (2.118), (2.119), and (6.120). As a result, it is possible to generalise the entropy principle (2.150) in terms of new fields  $\Upsilon$ ,  $\Upsilon_\mu$  and  $\Upsilon_{\mu\nu}$  such that

$$\nabla_\mu \mathcal{S}^\mu + \Upsilon \nabla_\mu J^\mu + \Upsilon_\nu \nabla_\mu T^{\mu\nu} + \Upsilon_{\mu\nu} (\nabla_\sigma F^{\sigma\mu\nu} - I^{\mu\nu}) \geq 0, \quad (6.136)$$

holds for all fields  $J^\mu$  and  $T^{\mu\nu}$ , even if they are not solutions of the equations of motion. Following Liu *et al.* (1986), we refer to  $\Upsilon$ ,  $\Upsilon_\mu$  and  $\Upsilon_{\mu\nu}$  as to the *Lagrange multipliers*, and introduce the vector  $\chi^\mu$ , defined as

<sup>15</sup>We recall from Chapter 2 that the fugacity (or equivalently the chemical potential) and the temperature are natural variables of statistical thermodynamics. However, one can always switch to using the variables  $\rho$  and  $e$ , as long as an equation of state of the type  $p = p(\alpha_f, T)$  is known.

### 310 Relativistic Non-Perfect Fluids

$$\chi^\mu := \mathcal{S}^\mu + \Upsilon J^\mu + \Upsilon_\nu T^{\mu\nu} + \Upsilon_{\nu\sigma} F^{\mu\nu\sigma}, \quad (6.137)$$

so that, after using Eq. (6.136) and some tensor algebra, we find (see Problem 8)

$$\left( \frac{\partial \chi^\mu}{\partial \Upsilon} - J^\mu \right) \nabla_\mu \Upsilon + \left( \frac{\partial \chi^\mu}{\partial \Upsilon_\nu} - T^{\mu\nu} \right) \nabla_\mu \Upsilon_\nu + \left( \frac{\partial \chi^\mu}{\partial \Upsilon_{\nu\sigma}} - F^{\mu\nu\sigma} \right) \nabla_\mu \Upsilon_{\nu\sigma} - \Upsilon_{\mu\nu} I^{\mu\nu} \geq 0. \quad (6.138)$$

Because the quantities  $\Upsilon$ ,  $\Upsilon_\mu$  and  $\Upsilon_{\mu\nu}$  are completely general (the only specific condition being that  $\Upsilon_{\mu\nu}$  is symmetric and trace-free because so is  $I_{\mu\nu}$ ), the only way to satisfy Eq. (6.138) is that the terms in round brackets vanish, namely, that

$$J^\mu = \frac{\partial \chi^\mu}{\partial \Upsilon}, \quad (6.139)$$

$$T^{\mu\nu} = \frac{\partial \chi^\mu}{\partial \Upsilon_\nu}, \quad (6.140)$$

$$F^{\mu\nu\sigma} = \frac{\partial \chi^\mu}{\partial \Upsilon_{\nu\sigma}}, \quad (6.141)$$

and that, in addition,

$$-\Upsilon_{\mu\nu} I^{\mu\nu} \geq 0. \quad (6.142)$$

Furthermore, since the tensor  $T^{\mu\nu}$  is symmetric, it follows from Eq. (6.140) that the four-vector  $\chi^\mu$  can also be expressed as

$$\chi^\mu = \frac{\partial \chi}{\partial \Upsilon_\mu}, \quad (6.143)$$

where  $\chi = \chi(\Upsilon, \Upsilon_\mu, \Upsilon_{\mu\nu})$  is a scalar field, called the *generating function* (Geroch and Lindblom, 1990). As a result of this procedure, Eqs. (6.139)–(6.141) become

$$J^\mu = \frac{\partial^2 \chi}{\partial \Upsilon \partial \Upsilon_\mu}, \quad (6.144)$$

$$T^{\mu\nu} = \frac{\partial^2 \chi}{\partial \Upsilon_\mu \partial \Upsilon_\nu}, \quad (6.145)$$

$$F^{\mu\nu\sigma} = \frac{\partial^2 \chi}{\partial \Upsilon_\mu \partial \Upsilon_{\nu\sigma}}. \quad (6.146)$$

Equations (6.144)–(6.146) can effectively be regarded as a change of variables from the original fields  $J^\mu$  and  $T^{\mu\nu}$  to the new fields represented by the Lagrange multipliers  $\Upsilon$ ,  $\Upsilon_\mu$ , and  $\Upsilon_{\mu\nu}$ . In this way, a divergence-type formulation of the kind expressed by equations (2.118), (2.119), and (6.120), has been shown to admit a representation in terms of a single generating function,  $\chi$ , and of the production density tensor  $I^{\mu\nu}$ , both of which are expressed as functions of the new set of variables  $\Upsilon$ ,  $\Upsilon_\mu$ , and  $\Upsilon_{\mu\nu}$ . The expression of the entropy current in terms on the new variables, on the other hand, follows directly from Eqs. (6.137) and (6.143) and is given by

$$\mathcal{S}^\mu = \frac{\partial \chi}{\partial \Upsilon_\mu} - \Upsilon J^\mu - \Upsilon_\nu T^{\mu\nu} - \Upsilon_{\nu\sigma} F^{\mu\nu\sigma}, \quad (6.147)$$

so that the entropy-production rate amounts to

$$\nabla_\mu S^\mu = -\Upsilon_{\mu\nu} I^{\mu\nu}. \quad (6.148)$$

Because the fields  $J^\mu$ ,  $T^{\mu\nu}$  and  $F^{\mu\nu\sigma}$  can be obtained by differentiation of  $\chi$ , Eqs. (6.144)–(6.146) can then be seen as the constraints that the entropy principle imposes on the constitutive functions and thus on the unknown coefficients (6.135).

Finally, we consider the third requirement of a divergence-type formulation, namely that of hyperbolicity. To better appreciate how to enforce this constraint, it is convenient to introduce the symbolic vector  $\Upsilon_A$  to represent the whole set of dynamical Lagrange multipliers, namely, to define the components of  $\Upsilon$  such that  $\Upsilon_A := (\Upsilon, \Upsilon_\mu, \Upsilon_{\mu\nu})$ , where the index  $A$  runs from 1 to 14 (we recall that  $\Upsilon_{\mu\nu}$  is symmetric and trace-free, thus with nine independent components) so that, for instance,  $\Upsilon_9 = \Upsilon_{04}$ . Similarly, we also express the dissipation source vector  $I$  so that its components are given by  $I^A = (0, 0, I^{\mu\nu})$ . As a result, the balance laws (2.118), (2.119), and (6.120) may be written in the compact form

$$\frac{\partial^2 \chi^\mu}{\partial \Upsilon_A \partial \Upsilon_B} \nabla_\mu \Upsilon_B = M^{AB\mu} \nabla_\mu \Upsilon_B = I^A. \quad (6.149)$$

When regarded as a first-order system of equations in the unknown  $\Upsilon_B$ , the system (6.149) is symmetric in the indices  $A$  and  $B$ , just because of the commutation property of partial differentiation. Furthermore, a symmetric system is hyperbolic in the direction given by the four-velocity of the fluid  $u^\mu$  if  $M^{AB\mu} u_\mu$  is positive definite, namely, if

$$\left\| \frac{\partial^2 \chi^\mu}{\partial \Upsilon_A \partial \Upsilon_B} u_\mu \right\| \text{:: positive definite.} \quad (6.150)$$

The condition (6.150) states, therefore, that depending on the generating function, the property of hyperbolicity may or may not hold for a given formulation of irreversible thermodynamics. For example, the original formulation of CIT by Eckart, which in Section 6.4 we have discussed to be non-causal and not hyperbolic, does admit a divergence-type formulation in terms of a generating function (Geroch and Lindblom, 1990), but it does not fulfill the requirement given by the condition (6.150). On the other hand, the Israel–Stewart formulation presented in Section 6.6.1, admits a similar divergence-type representation in terms of a generating function, but is hyperbolic only for sufficiently small values of the variables  $\Upsilon_{\mu\nu}$ , *i.e.*, in the neighbourhood of the equilibrium state. These considerations highlight the fact that the construction of a formulation that is cast in a divergence-type is not, *per se*, sufficient to guarantee hyperbolicity.

Although all what we have discussed so far may appear rather generic and having little contact with the physical properties of the fluids normally considered in relativistic hydrodynamics, applications to more realistic conditions are possible. For example, starting from kinetic theory, Mueller and Ruggeri (1998) have computed the coefficients  $\{A_2^0, A_3^0, A_1^q, A_1^\Pi, A_1^{\Pi^2}, A_2^\Pi, A_1^\pi; C_3, C_5, C_1^0, C_1^\Pi\}$  appearing in Eqs. (6.132)–(6.134) in the case of a non-degenerate relativistic fluid (see Section 2.4.2). The claim made by Mueller and Ruggeri (1998) is that it is then possible to derive a complete set of relativistic-hydrodynamic equations for a non-perfect non-degenerate relativistic fluid in the variables  $\rho$ ,  $e$ ,  $u^\mu$ ,  $\Pi$ ,  $\pi^{\mu\nu}$  and  $q^\mu$ , which contains only one unknown function of one variable, *i.e.*,  $\mathcal{A} = \mathcal{A}(\alpha_f)$ , and three functions of  $\rho$

and  $e$ , *i.e.*, the three unknown coefficients  $B_1^\pi$ ,  $B_3$  and  $B_4$ . No prescription, however, is given on how to compute in practice the function  $\mathcal{A}$ , which is even conjectured to be zero.

#### **Extended thermodynamics of moments.**

The possible number of fields does not stop at 14, but can be extended to include even higher-order moments of the distribution function expressed as divergences in the spirit of Eq. (6.120). Relevant examples of this procedure can be found in Weiss and Müller (1995) and in Mueller (2008), who, in a non-relativistic context, have studied the interaction of light with matter and computed the scattering spectra after adopting a large number of moments. In the relativistic framework, on the other hand, Mascali and Romano (1997), have used the entropy principle to close the set of the moment radiation-hydrodynamic equations to a finite but arbitrary order.

Obviously, the extension to a large number of fields raises the question of their physical interpretation and it increases considerably the complexity of the set of equations, a non-trivial aspect especially when considering a numerical solution. More importantly, there is a serious potential drawback connected with this procedure, namely, the introduction of spurious characteristic speeds. Such unwanted speeds are due only to the truncation procedure, but obviously are not present in the relativistic kinetic description. A conclusion on the seriousness of this risk has not been reached yet. On the one hand, there are serious concerns about the possibility that non-physical discontinuities may appear in the solution of the equations. On the other hand, some numerical solutions indicate that such discontinuities could occur only at the highest characteristic speed [see, *e.g.*, Weiss (1995)]. Because the latter increases with the number of retained moments, the problem may be less severe than it appears at first.

## 6.7 Concluding remarks

The large flexibility of EIT has provided this theory with strong predictive power in experiments of light scattering, sound-wave dispersion, shock-wave structure, and non-equilibrium radiation, to mention a few of the applications in Newtonian regimes. In relativistic regimes, on the other hand, EIT has been successfully applied to astrophysical problems such as the gravitational collapse of relativistic spherical stars (Di Prisco *et al.*, 1996; Herrera *et al.*, 2009), the flow properties in the inner regions of accretion discs around black holes (Peitz and Appl, 1997), the analysis of dissipative effects in several cosmological scenarios (Romano and Pavón, 1993; Maartens, 1995; Maartens and Triginer, 1997), and the study of dissipative multifluid dynamics (Andersson and Comer, 2009). However, most of the recent interest in relativistic non-perfect fluids has come from the investigations of heavy-ion collisions, such as those that are performed at the BNL Relativistic Heavy Ion Collider or at the CERN Large Hadron Collider [see Section 11.10 for an extended description]. In these experiments, in fact, the necessity of a relativistic theory for treating non-perfect fluid effects has become crucial for explaining the spectra of particles produced in ultrarelativistic nucleus–nucleus collisions.

Much more limited has been the work done so far on the formulation of the equations of relativistic hydrodynamics of non-perfect fluids that would be suitable for numerical calculations. Within CIT, for instance, numerical simulations have been performed only by Yokosawa (1995), who studied the dynamical evolution of accretion flows onto black holes, and by Duez

*et al.* (2004), who investigated the evolution of rapidly rotating stars with shear viscosity in full general relativity. Within EIT, on the other hand, numerical simulations either in the Israel–Stewart formulation or in the divergence-type formulation, have been long hampered by the absence of an appropriate formulation of these equations in a form that could make them tractable in a numerical implementation. This lack of significant numerical progress has persisted even after the equations were recast in the 3 + 1 formalism (see Section 7.1) by Peitz and Appl (1999). Only very recently, and mainly due to the renewed interest coming from investigations of relativistic heavy-ion collisions, numerical simulations have been attempted. In most cases, however, traditional finite difference methods have been adopted (Romatschke, 2010; Muronga, 2007), which have well-known shortcomings when applied to nonlinear systems of equations (see Chapter 10). A more promising approach has been proposed by Takamoto and Inutsuka (2011), who solved the relativistic hydrodynamics equations for non-perfect fluids by resorting to numerical methods adopting finite-volume methods (see Chapter 11), treating the inevitable stiffness of the source terms via Strang-splitting methods.

Overall, therefore, while the physics and astrophysics of non-perfect fluids has seen comparatively limited progress over the last few decades, because of the recent advances in numerical techniques and in the ability to tackle complex multidimensional nonlinear problems (either in relativistic astrophysics or in heavy-ion collisions), we foresee that the next years will witness rapid progress both in the numerical solution of relativistic-hydrodynamic equations of non-perfect fluids and in the development of refined analytical formulations.

We close this section by summarising below the approaches (and their denominations) we have discussed so far to describe the dynamics of non-perfect fluids.

- *Classical (or Standard) Irreversible Thermodynamics (CIT)*  
(these are also known as *first-order theories*)  
Eckart (1940), Landau and Lifshitz (1987).
- *Extended Irreversible (or Causal) Thermodynamics (EIT)*  
(these are also known as *second-order theories*)
  - *Israel–Stewart formulation*  
Israel (1976), Stewart (1977)
  - *Divergence-type theories or Rational Extended Thermodynamics (RET)*  
Liu, Mueller and Ruggeri (1986), Mueller and Ruggeri (1998).

## 6.8 Further reading

- Hiscock, W. and Lindblom, L. (1983). Stability and causality in dissipative relativistic fluids. *Ann. Phys.* **151**, 466–496.
- Jou, D., Casas-Vázquez, J., and Lebon, G. (2009). *Extended Irreversible Thermodynamics*. Springer, Berlin.
- Landau, L. D. and Lifshitz, E. M. (1987). *Fluid Mechanics*. Course of Theoretical Physics, Vol. 6. Butterworth-Heinemann, Oxford.
- Liu, I-S., Mueller, I. and Ruggeri, T. (1986). Relativistic thermodynamics of gases. *Ann. Phys.* **169**, 191–219.
- Mihalas, D. and Mihalas, B. (1984). *Foundations of radiation hydrodynamics*. Dover, New York.
- Mueller, I. and Ruggeri, T. (1998). *Rational Extended Thermodynamics*. Springer, Berlin.
- Romatschke, P. (2010). New developments in relativistic viscous hydrodynamics. *Int. J. Mod. Phys. E*, **19**, 1–53.

## 6.9 Problems

1. Derive the identities (6.17) and (6.24) to be used in constructing the momentum-conservation equation for non-perfect fluids (6.23).
2. Derive the momentum-conservation equation for non-perfect fluids (6.23) making use of the identities (6.17) and (6.24).
3. Derive the Newtonian limit of the momentum-conservation equation (6.23) and show that it coincides with the Navier–Stokes equations (2.75) modulo an external force term.
4. Derive the identities (6.49) and (6.50).
5. Derive the identity (6.59).
6. Derive the energy-conservation equation for non-perfect fluids (6.25) making use of the identities (6.18), (6.26), and (6.27).
7. Derive the Newtonian limit of the energy-conservation equation (6.49) and show that it coincides with the heat-conduction equation (2.76).
8. Show that Eq. (6.138) can be derived from Eq. (6.137) after taking its total derivative and using Eq. (6.136).

# 7

## Formulations of the Einstein–Euler Equations

---

As remarked several times in this book, the complexity and nonlinearity of the combined system of the Einstein field equations and of the relativistic-hydrodynamic equations prevents, in general, the derivation of analytic solutions. In this scenario, therefore, the numerical solution remains the only avenue towards an accurate description of those phenomena that involve relativistic flows, either in flat or in highly curved spacetimes. This chapter is dedicated to the introduction to the 3+1 decomposition of spacetime and to a *brief* review of the several formulations of the equations that have been proposed over the years. Our goal here is to provide some essential information that can be of direct use in the numerical solution of the equations of relativistic hydrodynamics in dynamical and curved spacetimes, leaving the discussion of those aspects which we will not be able to detail here to the more dedicated works of Alcubierre (2008), Bona *et al.* (2009), Baumgarte and Shapiro (2010), and Gourgoulhon (2012).

More specifically, we will first discuss the formulations of the Einstein equations (1.218) assuming that the right-hand side is known or can be computed easily, as in the case of spherically symmetric formulations. We will then discuss the different formulations of the relativistic-hydrodynamic equations (2.118)–(2.119) when the background spacetime is known.

Before moving on, a note on the terminology and the title of this chapter. The set of equations (1.218) and (2.118)–(2.119) will be here referred to as the set of the *Einstein–Euler equations*. While this is a commonly-adopted terminology, it is far from being perfect. In the previous chapters, in fact, we have called the “Euler equations” the equations of conservation of linear momentum [*cf.*, Eqs. (2.66), (3.55)], while Eqs. (2.118)–(2.119) also include the conservation of rest mass and energy. Hence, the denomination “Einstein–Euler” equations is incomplete and the reader should bear in mind that this is mostly a historical heritage.

### 7.1 The 3+1 decomposition of spacetime

In Chapter 1 we have discussed how spacetime should be regarded as a four-dimensional differentiable manifold and, more loosely speaking, as a container of events which can be suitably parameterised in terms of coordinates to be assigned to each of the events. At the heart of Einstein’s theory of general relativity is the equivalence among all of these coordinates, so that the distinction of spatial and time coordinates is more an organisational matter than a strict requirement of the theory. Despite this “covariant view”, however, our experience, and the

laws of physics on sufficiently large scales, do suggest that a distinction of the time coordinate from the spatial ones is the most natural one in describing physical processes. Furthermore, while not strictly necessary, such a distinction of time and space is the simplest way to exploit a large literature on the numerical solution of hyperbolic partial differential equations as those of relativistic hydrodynamics.

Following this principle, a decomposition of spacetime into “time” and “space” was already proposed in the 1960s within a Hamiltonian formulation of general relativity and later as an aid to the numerical solution of the Einstein equations in vacuum.<sup>1</sup> The basic idea is rather simple and consists in “foliating” spacetime in terms of a set of non-intersecting space-like hypersurfaces  $\Sigma := \Sigma(t)$ , each of which is parameterised by a constant value of the coordinate  $t$ . In this way, the three spatial coordinates are split from the one temporal coordinate and the resulting construction is called the *3+1 decomposition* of spacetime (Misner *et al.*, 1973).

Given one such constant-time hypersurface,  $\Sigma_t$ , belonging to the *foliation*  $\Sigma$ , we can introduce a timelike four-vector  $n$  normal to the hypersurface at each event in the spacetime and such that its dual one-form  $\Omega := \nabla t$  is parallel to the gradient of the coordinate  $t$ , *i.e.*,

$$n_\mu = A\Omega_\mu = A\nabla_\mu t, \quad (7.1)$$

with  $n_\mu = \{A, 0, 0, 0\}$  and  $A$  a constant to be determined. If we now require that the four-vector  $n$  defines an observer and thus that it measures the corresponding four-velocity, then from the normalisation condition on timelike four-vectors,  $n^\mu n_\mu = -1$ , we find that

$$n^\mu n_\mu = g^{\mu\nu} n_\mu n_\nu = g^{tt} A^2 = -\frac{1}{\alpha^2} A^2 = -1, \quad (7.2)$$

where we have defined  $\alpha^2 := -1/g^{tt}$ . From the last equality in expression (7.2) it follows that  $A = \pm\alpha$  and we will select  $A = -\alpha$ , such that the associated vector field  $n^\mu$  is future directed. The quantity  $\alpha$  is commonly referred to as the *lapse* function, it measures the rate of change of the coordinate time along the vector  $n^\mu$  (see Fig. 7.1), and will be a building block of the metric in a 3+1 decomposition [*cf.* Eq. (7.12)].

The specification of the normal vector  $n$  allows us to define the metric associated to each hypersurface, *i.e.*,

$$\gamma_{\mu\nu} := g_{\mu\nu} + n_\mu n_\nu, \quad \gamma^{\mu\nu} := g^{\mu\nu} + n^\mu n^\nu, \quad (7.3)$$

where  $\gamma^{0\mu} = 0$ ,  $\gamma_{ij} = g_{ij}$ , but in general  $\gamma^{ij} \neq g^{ij}$ . Also note that  $\gamma^{ik}\gamma_{kj} = \delta_j^i$ , that is,  $\gamma^{ij}$  and  $\gamma_{ij}$  are the inverse of each other, so that the spatial metric  $\gamma$  can be used for raising and lowering the indices of purely spatial vectors and tensors.

The tensors  $n$  and  $\gamma$  provide us with two useful tools to decompose any four-dimensional tensor into a purely spatial part (hence contained in the hypersurface  $\Sigma_t$ ) and a purely timelike part (hence orthogonal to  $\Sigma_t$  and aligned with  $n$ ). Not surprisingly, the spatial part is readily obtained after contracting with the *spatial projection operator* (or *spatial projection tensor*)

$$\gamma^\mu{}_\nu := g^{\mu\alpha}\gamma_{\alpha\nu} = g^\mu{}_\nu + n^\mu n_\nu = \delta^\mu{}_\nu + n^\mu n_\nu, \quad (7.4)$$

<sup>1</sup>Indeed, many of the ideas behind the 3+1 decomposition of spacetime date back even earlier, to the works of Darmois (1927), Lichnerowicz (1939) and Foures-Bruhat (1948).

while the timelike part is obtained after contracting with the *time projection operator* (or *time projection tensor*)

$$N^\mu_\nu := -n^\mu n_\nu, \quad (7.5)$$

and where the two projectors are obviously orthogonal, *i.e.*,

$$\gamma^\alpha_\mu N^\mu_\nu = 0. \quad (7.6)$$

Hence, a generic four-vector  $\mathbf{U}$  can be decomposed as

$$U^\mu = \gamma^\mu_\nu U^\nu + N^\mu_\nu U^\nu, \quad (7.7)$$

where the *purely spatial* part  $\gamma^\mu_\nu U^\nu = V^\mu$  is still a four-vector that, by construction, has a zero contravariant time component, *i.e.*,  $V^t = 0$ , whereas it has the covariant time component,  $V_t = g_{\mu t} V^\mu$ , which is nonzero in general. Analogous considerations can be done about tensors of any rank.

We have already seen in Eq. (7.1) that the unit normal  $\mathbf{n}$  to a spacelike hypersurface  $\Sigma_t$  does not represent the direction along which the time coordinate changes, that is, it is not the direction of the time derivative. Indeed, if we compute the contraction of  $\mathbf{n}$  and  $\Omega$  we obtain

$$n^\mu \Omega_\mu = \frac{1}{A} n^\mu n_\mu = \frac{1}{\alpha} \neq 1. \quad (7.8)$$

We can therefore introduce a new vector,  $\mathbf{t}$ , along which to carry out the time evolutions and that is dual to the surface one-form  $\Omega$ . Such a vector is just the time-coordinate basis vector and is defined as the linear superposition of a purely temporal part (parallel to  $\mathbf{n}$ ) and of a purely spatial one (orthogonal to  $\mathbf{n}$ ), namely

$$\mathbf{t} = \mathbf{e}_t = \partial_t := \alpha \mathbf{n} + \boldsymbol{\beta}. \quad (7.9)$$

The purely spatial vector  $\boldsymbol{\beta}$  [*i.e.*,  $\beta^\mu = (0, \beta^i)$ ] is usually referred to as the *shift vector* and will be another building block of the metric in a 3+1 decomposition [*cf.* Eq. (7.12)]. The decomposition of the vector  $\mathbf{t}$  into a timelike component  $n\alpha$  and a spatial component  $\boldsymbol{\beta}$  is shown in Fig. 7.1.

We can check that  $\mathbf{t}$  is a coordinate basis vector by verifying that

$$t^\mu \Omega_\mu = \alpha n^\mu \Omega_\mu + \beta^\mu \Omega_\mu = \frac{\alpha}{\alpha} = 1, \quad (7.10)$$

from which it follows that the vector  $\mathbf{t}$  is effectively dual to the one-form  $\Omega$ . This guarantees that the integral curves of  $t^\mu$  are naturally parameterised by the time coordinate. As a result, all infinitesimal vectors  $t^\mu$  originating on one hypersurface  $\Sigma_t$  would end up on the same hypersurface  $\Sigma_{t+dt}$ . Note that this is not guaranteed for translations along  $\Omega_\mu$  and that since  $t^\mu t_\mu = g_{tt} = -\alpha^2 + \beta^\mu \beta_\mu$ , the vector  $\mathbf{t}$  is not necessarily timelike (the shift can in fact be superluminal).

In summary, the components of  $\mathbf{n}$  are given by

$$n_\mu = (-\alpha, 0, 0, 0), \quad n^\mu = \frac{1}{\alpha} (1, -\beta^i), \quad (7.11)$$

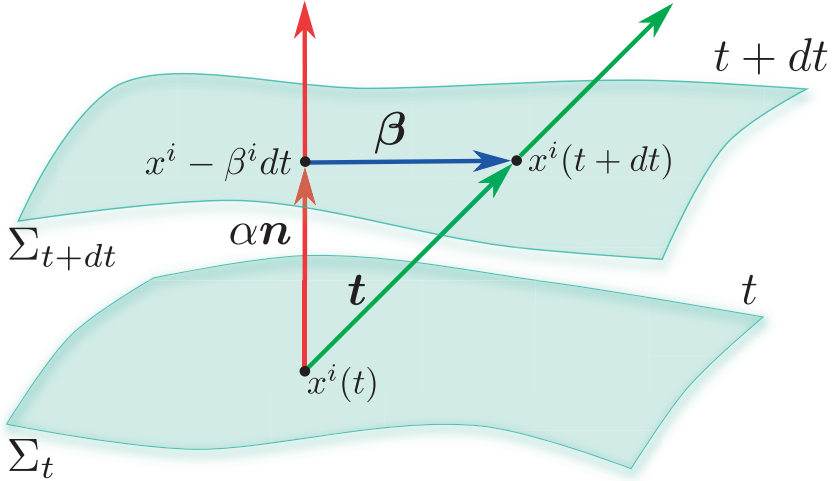


**Fig. 7.1** Schematic representation of the 3+1 decomposition of spacetime with hypersurfaces of constant time coordinate  $\Sigma_t$  and  $\Sigma_{t+dt}$  foliating the spacetime. The four-vector  $t$  represents the direction of evolution of the time coordinate  $t$  and can be split into a timelike component  $\alpha n$ , where  $n$  is a timelike unit normal to the hypersurface, and into a spacelike component, represented by the spacelike four-vector  $\beta$ . The function  $\alpha$  is the “lapse” and measures the proper time between adjacent hypersurfaces, while the components of the “shift” vector  $\beta^i$  measure the change of coordinates from one hypersurface to the subsequent one.

and we are now ready to deduce that the lapse function and the shift vector can be employed to express the generic *line element* in a 3+1 decomposition as

$$ds^2 = -(\alpha^2 - \beta_i \beta^i) dt^2 + 2\beta_i dx^i dt + \gamma_{ij} dx^i dx^j. \quad (7.12)$$

Expression (7.12) clearly emphasises that when  $\beta^i = 0 = dx^i$ , the lapse measures the proper time,  $d\tau$ , between two adjacent hypersurfaces [*cf.* Eq. (1.109)], *i.e.*,

$$d\tau^2 = \alpha^2(t, x^j) dt^2, \quad (7.13)$$

while the shift vector measures the change of coordinates of a point from the hypersurface  $\Sigma_t$  to the hypersurface  $\Sigma_{t+dt}$ , *i.e.*,

$$x^i_{t+dt} = x^i_t - \beta^i(t, x^j) dt. \quad (7.14)$$

Similarly, the covariant and contravariant components of the metric (7.12) can be written explicitly as

$$g_{\mu\nu} = \begin{pmatrix} -\alpha^2 + \beta_i \beta^i & \beta_i \\ \beta_i & \gamma_{ij} \end{pmatrix}, \quad g^{\mu\nu} = \begin{pmatrix} -1/\alpha^2 & \beta^i/\alpha^2 \\ \beta^i/\alpha^2 & \gamma^{ij} - \beta^i \beta^j/\alpha^2 \end{pmatrix}, \quad (7.15)$$

from which it is easy to obtain an important identity which will be used extensively hereafter, *i.e.*,

$$\sqrt{-g} = \alpha \sqrt{\gamma}, \quad (7.16)$$

where  $g := \det(g_{\mu\nu})$  and  $\gamma := \det(\gamma_{ij})$ .

When defining the unit timelike normal  $\mathbf{n}$  in Eq. (7.2), we have mentioned that it can be associated to the four-velocity of a special class of observers, which are referred to as *normal* or *Eulerian observers*. Although this denomination is somewhat confusing, since such observers are not at rest with respect to infinity but have a coordinate velocity  $dx^i/dt = n^i = -\beta^i/\alpha$ , we will adopt this traditional nomenclature also in the following and thus take an “Eulerian observer” as one with four-velocity given by (7.11).

When considering a fluid with four-velocity  $\mathbf{u}$ , the spatial four-velocity  $\mathbf{v}$  measured by an Eulerian observer will be given by the ratio between the projection of  $\mathbf{u}$  in the space orthogonal to  $\mathbf{n}$ , *i.e.*,  $\gamma^i_{\mu} u^\mu = u^i$ , and the *Lorentz factor* of  $\mathbf{u}$  as measured by  $\mathbf{n}$  (de Felice and Clarke, 1990)

$$-n_\mu u^\mu = \alpha u^t. \quad (7.17)$$

As a result, the spatial four-velocity of a fluid as measured by an Eulerian observer will be given by

$$\mathbf{v} := \frac{\gamma \cdot \mathbf{u}}{-\mathbf{n} \cdot \mathbf{u}}, \quad (7.18)$$

or, in component form, by

$$v^t = 0, \quad v^i = \frac{\gamma^i_{\mu} u^\mu}{\alpha u^t} = \frac{1}{\alpha} \left( \frac{u^i}{u^t} + \beta^i \right), \quad (7.19)$$

$$v_t = \beta_i v^i, \quad v_i = \frac{\gamma_{i\mu} u^\mu}{\alpha u^t} = \frac{u_i}{\alpha u^t} = \frac{\gamma_{ij}}{\alpha} \left( \frac{u^j}{u^t} + \beta^j \right). \quad (7.20)$$

Using now the normalisation condition  $u^\mu u_\mu = -1$  and indicating as usual with  $W$  the *Lorentz factor*, we obtain

$$\alpha u^t = -\mathbf{n} \cdot \mathbf{u} = \frac{1}{\sqrt{1 - v^i v_i}} = W, \quad u_t = W(-\alpha + \beta_i v^i), \quad (7.21)$$

so that the components (7.19)–(7.20) can finally be written as

$$v^i = \frac{u^i}{W} + \frac{\beta^i}{\alpha} = \frac{1}{\alpha} \left( \frac{u^i}{u^t} + \beta^i \right), \quad v_i = \frac{u_i}{W} = \frac{u_i}{\alpha u^t}, \quad (7.22)$$

where in the last equality we have exploited the fact that  $\gamma_{ij} u^j = u_i - \beta_i W/\alpha$ . Expressions (7.22) should also be compared with the corresponding special-relativistic definitions given in Eq. (1.114), to which they obviously reduce for  $\alpha = 1, \beta^i = 0$ . Finally, using expressions (7.18) and (7.21), it is also possible to write the fluid four-velocity as

$$u^\mu = W(n^\mu + v^\mu), \quad (7.23)$$

which highlights the split of  $\mathbf{u}$  into a temporal and a spatial part.

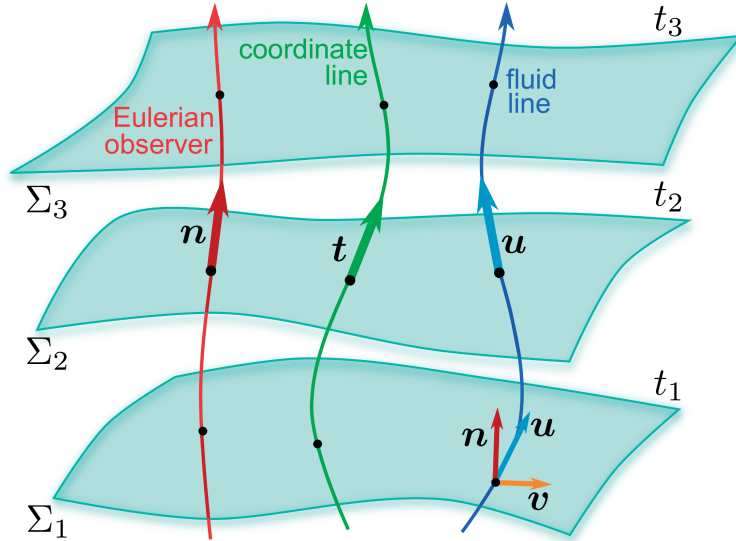


**Fig. 7.2** Schematic representation of the different unit vectors in a 3+1 decomposition of spacetime (see Fig. 7.1). The four-vectors  $n$ ,  $t$  and  $u$  represent the unit timelike normal, the time-coordinate basis vector and the fluid four-velocity, respectively. Shown are the associated worldlines, namely, the normal line, the coordinate line and the fluidline. Also shown is the spatial projection  $v$  of the fluid four-velocity  $u$  as measured by the (Eulerian) normal observer  $n$ .

The three different unit four-vectors in a 3+1 decomposition of spacetime are shown in Fig. 7.2, which should be compared with Fig. 7.1. The four-vectors  $n$ ,  $t$  and  $u$  represent the unit timelike normal, the time-coordinate basis vector and the fluid four-velocity, respectively. Also shown are the associated worldlines, namely, the *normal line* representing the worldline of an Eulerian observer, the *coordinate line* representing the worldline of a coordinate element, and the *fluidline*. Also shown is the spatial projection  $v$  of the fluid four-velocity  $u$ , thus highlighting that the  $v$  is the three-velocity as measured by the normal observer.

## 7.2 Formulations of the Einstein equations

The following five sections are dedicated to the discussion of different formulations that have been derived over the years to cast the Einstein equations (see Section 1.6)

$$R_{\mu\nu} - \frac{1}{2}g_{\mu\nu}R = 8\pi T_{\mu\nu} \quad (1.218)$$

into a form that is suitable for numerical calculation [see Sarbach and Tiglio (2012) for an extended review on the initial-value boundary problem for the Einstein equations]. Our review will lead us from the first formulations of the 1960s in spherical symmetry, to the more recent formulations in use in modern three-dimensional codes. As we will discuss, finding the

optimal formulation is harder than it may seem at first sight and we will explain why apparently correct choices can lead to undesired numerical behaviour. We will not worry here about the right-hand side of the Einstein equations and assume instead that the energy-momentum tensor is known. Later on, starting with Section 7.3, we will discuss how to deal also with the evolution of the right-hand side and hence with the numerical solution of the relativistic-hydrodynamic equations.

### 7.2.1 Spherically symmetric Lagrangian formulations

One of the first general-relativistic hydrodynamic codes was the one-dimensional Lagrangian code of May and White (1967), that solved numerically the *Lagrangian formulation* of Misner and Sharp (1964) and allowed for the first numerical modelling of a spherically symmetric collapse leading to black hole formation. The Misner–Sharp formulation, which is also known as the “cosmic time” formulation, was then subsequently improved by Hernandez and Misner (1966), who used instead as the time coordinate an “observer time”, that is, the time as measured by a distant observer. In this latter case, the foliation in time is obtained via a *null slicing* and this then allows one to extend the calculations also to later times for observers that are at large distances.

There is little doubt that for spherically symmetric systems, and short of using *adaptive mesh-refinement (AMR) techniques*, the Lagrangian approaches implementing either the Misner–Sharp or the Hernandez–Misner formulations have significant advantages with respect an Eulerian approach [see, e.g., Romero *et al.* (1996)]. In fact, because the mesh moves with the local fluid velocity, the Lagrangian approach is very efficient in capturing material interfaces sharply even in multifluid systems. However, such advantages are essentially lost when considering multidimensional problems, since the comoving grid of the Lagrangian coordinates is easily distorted in the presence of shear or vortex flows, thus requiring complicated remapping of the coordinates (*i.e.*, rezoning of the grid). Therefore, it is mainly for reasons of completeness that we present in this section the two most popular general-relativistic Lagrangian approaches in spherical symmetry, remarking that they are seldom used in multidimensional calculations.

#### **The Misner–Sharp formulation.**

As mentioned above, the formulation was originally proposed by Misner and Sharp (1964) and is particularly tailored for a spherically symmetric fluid configuration undergoing collapse (or expansion). The generic diagonal line element in spherical symmetry can then be written in the form

$$ds^2 = -a(r, t)^2 dt^2 + b(r, t)^2 dr^2 + R^2 (d\theta^2 + \sin^2 \theta d\phi^2), \quad (7.24)$$

where  $r$  and  $t$  are the radial and time coordinates, while  $R$  [not to be confused with the Ricci scalar (1.204) appearing in the Einstein equations (1.218)] is the Schwarzschild circumference coordinate, *i.e.*,  $4\pi R^2 := \int_{2\Sigma} \sqrt{g} d\sigma$ , where  $d\sigma$  is the surface element over the two-sphere  ${}^2\Sigma$  with metric determinant  ${}^2g$  [*cf.*, Eq. (1.81)].

For a fluid composed of particles with nonzero rest mass it is possible to replace the radial coordinate  $r$  with the rest mass  $\mu$  contained within a shell of radius  $r$ . On the other hand, for a fluid of massless particles (*e.g.*, the radiation fluid discussed in Section 2.4.8) it is convenient to introduce a conserved number of “unit comoving fluid elements” (Miller and Pantano,

### 326 Formulations of the Einstein–Euler Equations

1990). Denoting by  $\rho$  a “relative compression factor” for these fluid elements (equivalent to the rest-mass density in the standard treatment), one then has

$$d\mu = 4\pi\rho R^2 b dr, \quad (7.25)$$

and identifying the two radial coordinates  $\mu$  and  $r$ , it then gives

$$b = \frac{1}{4\pi R^2 \rho}. \quad (7.26)$$

Following the notation of Misner and Sharp (1964), we write the equations in terms of the operators

$$D_t := \frac{1}{a} \left( \frac{\partial}{\partial t} \right), \quad D_r := \frac{1}{b} \left( \frac{\partial}{\partial \mu} \right), \quad (7.27)$$

and applying these to  $R$  gives

$$D_t R = U, \quad D_r R = \Gamma, \quad (7.28)$$

where  $U$  is the radial component of the four-velocity in the associated Eulerian frame in which  $R$  is the radial coordinate and  $\Gamma$  is a generalisation of the Lorentz factor [*cf.* Eq. (7.34)]. A bit of algebra then allows us to write the Einstein–Euler equations in the Misner–Sharp formulation as (Musco *et al.*, 2005) (see Problem 1)

$$D_t U = - \left[ \frac{\Gamma}{(e + p)} D_r p + \frac{M}{R^2} + 4\pi R p \right], \quad (7.29)$$

$$D_t \rho = - \left( \frac{\rho}{\Gamma R^2} \right) D_r (R^2 U), \quad (7.30)$$

$$D_t e = \left( \frac{e + p}{\rho} \right) D_t \rho, \quad (7.31)$$

$$D_r a = - \left( \frac{a}{e + p} \right) D_r p, \quad (7.32)$$

$$D_r M = 4\pi \Gamma e R^2 = 4\pi \Gamma \rho (1 + \epsilon) R^2, \quad (7.33)$$

where  $\Gamma$  can be calculated either from (7.28) or from

$$\Gamma^2 = 1 + U^2 - \frac{2M}{R}. \quad (7.34)$$

The set of equations (7.28)–(7.33) can be seen as a set of four evolution equations for  $R$ ,  $U$ ,  $\rho$  and  $e$ , and two constraint equations for  $\Gamma$  and  $M$ . The latter also has an integral expression given by

$$M = 4\pi \int_0^{\mu_{\max}} \Gamma \rho (1 + \epsilon) R^2 \partial_\mu R d\mu, \quad (7.35)$$

where  $\mu_{\max}$  is the outer boundary of the matter distribution and can thus be seen as measuring the mass-energy contained inside the shell of mass  $\mu$ . Finally, there are of course also boundary conditions that need to be specified, some of which have a simple physical interpretation, *i.e.*,

$$M = 0, \quad R = 0, \quad u = 0, \quad \text{at } \mu = 0, \quad (7.36)$$

$$p = 0, \quad \rho = 0, \quad a = 1, \quad \text{at } \mu = \mu_{\max}. \quad (7.37)$$

The last condition in particular sets the coordinate time to be equal to the proper time of the comoving observer at the outer boundary.

Over the years, the original formulation of Misner and Sharp (1964) has inspired the development of a number of numerical codes to perform a wide class of simulations ranging from supernova and neutron-star collapse (Miralles *et al.*, 1990; Miller and Sciama, 1980), over to the calculation of the gravitational-wave emission from spherically symmetric backgrounds of collapsing stars (Seidel and Moore, 1987) and up to the study of phase-transitions in the early universe (Miller and Pantano, 1989; Rezzolla and Miller, 1994). Although Eulerian approaches have been proven to be much more effective when dealing with complex multidimensional scenarios, even recent applications of this formalism continue to be produced in modern research (Musco *et al.*, 2005; Fischer *et al.*, 2009).

### **The Hernandez–Misner formulation.**

Studying black-hole formation with the Misner–Sharp approach discussed above has the well-known drawback that singularities are typically formed rather early in the calculations, thus preventing the subsequent evolution. To compensate for this problem Hernandez and Misner (1966) used as time coordinate the time at which an outgoing radial light ray emanating from an event reaches a distant observer, *i.e.*, the “observer time”. This is also known as the *outward null slicing* (or outward null foliation) since it employs null hypersurfaces to foliate the spacetime and is particularly convenient for calculations involving black-hole formation in spherical symmetry. In this case, anything that could be seen by a distant observer placed at future null infinity and taking place before the formation of an apparent horizon can be calculated<sup>2</sup> [see, *e.g.*, Miller and Motta (1989) or Baumgarte *et al.* (1995) for some examples].

As with all formulations implementing a null foliation, also the Hernandez–Misner formulation suffers from the problem of the definition of initial data. While it is in fact natural to define initial conditions on a spacelike hypersurface at constant cosmic time, the calculation of the corresponding initial data on a null outward slice is less straightforward, although not overly complicated as we will discuss below. To derive the Hernandez–Misner formulation we start by considering an outgoing radial null ray, along which

$$a dt = b dr, \quad (7.38)$$

and we define the observer time  $u$  by the condition

$$f du := a dt - b dr, \quad (7.39)$$

with  $f$  being an integrating factor which needs to be determined and where  $1/f$  can be seen as the gravitational redshift at any event at  $(t, r)$ . Using this function, the metric (7.24) becomes

$$ds^2 = -f^2 du^2 - 2fb dr du + R^2 (d\theta^2 + \sin^2 \theta d\phi^2), \quad (7.40)$$

which is no longer diagonal. The differential operators equivalent to those in (7.27) are now given by

<sup>2</sup>A more sophisticated approach based on a “double-null” foliation is also possible and can be used to study, for instance, the interior of a black hole formed in the collapse of a scalar field (Harada *et al.*, 2002).

$$D_t := \frac{1}{f} \left( \frac{\partial}{\partial u} \right), \quad D_k := \frac{1}{b} \left( \frac{\partial}{\partial r} \right) = 4\pi\rho R^2 \left( \frac{\partial}{\partial \mu} \right), \quad (7.41)$$

where  $D_k$  is the radial derivative along the null slice and the corresponding derivative along the Misner–Sharp spacelike slice is given by

$$D_r = D_k - D_t. \quad (7.42)$$

As a result, the Einstein–Euler equations in the Hernandez–Misner formulation are given by (see Problem 2)

$$D_t U = -\frac{1}{1-c_s^2} \left[ \frac{\Gamma}{(e+p)} D_k p + \frac{M}{R^2} + 4\pi R p + c_s^2 \left( D_k U + \frac{2U\Gamma}{R} \right) \right], \quad (7.43)$$

$$D_t \rho = \frac{\rho}{\Gamma} \left( D_t U - D_k U - \frac{2U\Gamma}{R} \right), \quad (7.44)$$

$$D_t e = \left( \frac{e+p}{\rho} \right) D_t \rho, \quad (7.45)$$

$$D_k f = \frac{f}{\Gamma} \left( D_k U + \frac{M}{R^2} + 4\pi R p \right), \quad (7.46)$$

$$D_k M = 4\pi R^2 (e\Gamma - pU), \quad (7.47)$$

which are, again, four evolution equations [including Eq. (7.28)] and two spatial constraints. The generalised Lorentz factor  $\Gamma$  can be computed as before via Eq. (7.34), but also as

$$\Gamma = D_k R - U. \quad (7.48)$$

Note that using Eqs. (7.46), (7.47) and (7.34), it is possible to derive the following alternative equation for  $f$

$$D_k \left( \frac{\Gamma + U}{f} \right) = -4\pi R \frac{(e+p)}{f}. \quad (7.49)$$

In calculations of the collapse of an isolated fluid object in vacuum and for which the space-time is asymptotically flat, the observer time is taken to be the time of a static observer at future null infinity, so that  $f = 1$  and hence  $(\Gamma + U)/f = 1$  at infinity. It then follows from Eq. (7.49) that  $(\Gamma + U)/f = 1$  also at the surface of the collapsing object, since the right-hand side of (7.49) is zero there. The condition

$$f = \Gamma + U, \quad (7.50)$$

at the surface is then used as a boundary condition for  $f$ , while the values of  $f$  internal to the surface are then calculated from Eq. (7.46). In simulations of matter collapsing to a black hole it is of course important to be able to detect the formation of a *trapped surface*, that is, a surface on which the expansion of radially outgoing photons is zero (*cf.*, Section 12.4.1). In the Hernandez–Misner formulation this condition is simply expressed as

$$D_k R = 4\pi R^2 \partial_\mu R \leq 0. \quad (7.51)$$

It is a basic property of a solution obtained using an outward null slicing that, as a trapped surface forms, *i.e.*, as  $D_k R \rightarrow 0^+$ , the redshift factor  $1/f$  tends to infinity at the same location.

The conditions  $D_k R = 0$  and  $f = 0$  are reached only asymptotically in the future as seen by the distant observer and  $D_k R$  should in fact never become negative. In practice, care is required to avoid that negative values of  $D_k R$  appear and that the corresponding evolution becomes unphysical. In the case of an isolated collapsing object in vacuum, the use of the boundary condition (7.50) together with Eq. (7.46) ensures the correct behaviour, while Eq. (7.49), which guarantees synchronisation of  $D_k R \rightarrow 0$  and  $f \rightarrow 0$ , should be used for a spacetime which is not asymptotically flat [see, e.g., the discussion in Musco *et al.* (2005)].

We conclude this section by discussing the specification of initial data that, as anticipated above, requires some extra attention in the Hernandez–Misner formulation. In practice, initial data is first specified on a spacelike slice and thus at constant cosmic time. This data is then evolved using the Misner–Sharp equations (7.29)–(7.33) so as to generate a second set of initial data on a null slice and at constant observer time. To do this, an outgoing radial light ray is traced out from the centre and the corresponding values of time and position are saved as it passes the boundary of each grid zone. The second set of initial data, constructed in this way, is then evolved using the Hernandez–Misner equations (7.43)–(7.47).

### 7.2.2 The ADM formulation

The 3+1 decomposition introduced in Section 7.1 can be used not only to decompose tensors, but also equations and, in particular, the Einstein equations, which are then cast into an initial-value form suitable to be solved numerically. A 3+1 decomposition of the Einstein equations was presented by Arnowitt, Deser and Misner (Arnowitt *et al.*, 1962), but it is really the reformulation suggested by York (1979) that represents what is now widely known as the *ADM formulation* [see, e.g., Alcubierre (2008) and Gourgoulhon (2012) for a detailed and historical discussion]. As we will see in detail later on, in this formulation the Einstein equations are written in terms of purely spatial tensors that can be integrated forward in time once some constraints are satisfied initially.

To derive the ADM formulation we can start by noting that once a 3+1 decomposition is introduced as discussed in Section 7.1, it is then possible to define the *three-dimensional covariant derivative* after projecting the standard covariant derivative onto the space orthogonal to  $n^\mu$ , *i.e.*,

$$D_\nu := \gamma^\mu_\nu \nabla_\mu = (\delta^\mu_\nu + n_\nu n^\mu) \nabla_\mu, \quad (7.52)$$

which, as expected, is compatible with the spatial metric, *i.e.*,

$$D_\alpha \gamma^\beta_\delta = 0. \quad (7.53)$$

As an example, the three-dimensional covariant derivative of a mixed tensor  $T^\beta_\delta$  is simply obtained via the projection on  $\Sigma_t$  of all the indices of the four-dimensional covariant derivative

$$D_\alpha T^\beta_\delta = \gamma^\mu_\alpha \gamma^\beta_\nu \gamma^\rho_\delta \nabla_\mu T^\nu_\rho. \quad (7.54)$$

The entire four-dimensional tensor algebra can then be extended straightforwardly to the three-dimensional spatial slice so that, for instance, the three-dimensional connection coefficients can be expressed in terms of derivatives of the spatial metric [*cf.* Eq. (1.165)]

$${}^{(3)}\Gamma^\alpha_{\beta\gamma} = \frac{1}{2} \gamma^{\alpha\delta} (\partial_\beta \gamma_{\gamma\delta} + \partial_\gamma \gamma_{\delta\beta} - \partial_\delta \gamma_{\beta\gamma}). \quad (7.55)$$

### 330 Formulations of the Einstein–Euler Equations

where we will use the upper left index <sup>(3)</sup> to mark a purely spatial tensor.<sup>3</sup> Similarly, the three-dimensional Riemann tensor <sup>(3)</sup> $R_{\beta\mu\nu}^\alpha$  associated with  $\gamma$  is defined via the double three-dimensional covariant derivative of any spatial vector  $W$ , *i.e.*,

$$2D_{[\alpha}D_{\beta]}W_\delta = {}^{(3)}R_{\delta\beta\alpha}^\gamma W_\gamma, \quad (7.56)$$

where

$${}^{(3)}R_{\delta\alpha\beta}^\gamma n_\gamma = 0, \quad (7.57)$$

and where, in analogy with its four-dimensional counterpart the three-dimensional Riemann tensor has an explicit expression given by [*cf.*, Eq. (1.191)]

$${}^{(3)}R_{\nu\kappa\sigma}^\mu = \partial_\kappa {}^{(3)}\Gamma_{\nu\sigma}^\mu - \partial_\sigma {}^{(3)}\Gamma_{\nu\kappa}^\mu + {}^{(3)}\Gamma_{\lambda\kappa}^\mu {}^{(3)}\Gamma_{\nu\sigma}^\lambda - {}^{(3)}\Gamma_{\lambda\sigma}^\mu {}^{(3)}\Gamma_{\nu\kappa}^\lambda. \quad (7.58)$$

In a similar manner, the three-dimensional contractions of the three-dimensional Riemann tensor, *i.e.*, the three-dimensional Ricci tensor and the three-dimensional Ricci scalar, are defined respectively as their four-dimensional counterparts, *i.e.*,

$${}^{(3)}R_{\alpha\beta} := {}^{(3)}R_{\alpha\mu\beta}^\mu, \quad {}^{(3)}R := {}^{(3)}R_\mu^\mu. \quad (7.59)$$

Although it is easy to do so, it is important not to confuse the three-dimensional Riemann tensor <sup>(3)</sup> $R_{\nu\kappa\sigma}^\mu$  with the corresponding four-dimensional counterpart  $R_{\nu\kappa\sigma}^\mu$ . While the first one is purely spatial and is built with spatial derivatives of the spatial metric, the second one is a fully four-dimensional object containing also time derivatives of the full four-dimensional metric.

The information present in  $R_{\nu\kappa\sigma}^\mu$  and missing in <sup>(3)</sup> $R_{\nu\kappa\sigma}^\mu$  can be found in another symmetric tensor, the *extrinsic curvature*  $K_{\mu\nu}$ , which is purely spatial, *i.e.*,  $n^\mu K_{\mu\nu} = 0$ . Loosely speaking, the extrinsic curvature provides a measure of how the three-dimensional hypersurface  $\Sigma_t$  is curved with respect to the four-dimensional spacetime. In practice, this measure is made through the change of the normal vector  $n^\mu$  when it is parallel transported along the hypersurface and it is therefore defined as (see Section 1.5.4)

$$K_{\mu\nu} := -\gamma^\lambda_\mu \nabla_\lambda n_\nu = -(\delta_\mu^\lambda + n^\lambda n_\mu) \nabla_\lambda n_\nu. \quad (7.60)$$

This is illustrated schematically in Fig. 7.3, which shows that a normal vector  $\mathbf{n}$  at a point  $\mathcal{P}$  on  $\Sigma_t$  will be generically different from the corresponding normal  $\mathbf{n}'$  at a neighbouring point  $\mathcal{P} + \delta\mathcal{P}$ . The difference between  $\mathbf{n}'$  and the parallel-transported  $\mathbf{n}$  will give a measure of the extrinsic curvature of  $\Sigma_t$ . This is obviously zero if  $\Sigma_t$  is flat.

At least two more definitions of the extrinsic curvature are possible. The first one involves the “*acceleration*” of the Eulerian observers, which, in analogy with the fluid four-acceleration (3.1), is defined as

$$a_\nu := n^\mu \nabla_\mu n_\nu. \quad (7.61)$$

This is a purely spatial four-vector, *i.e.*,  $n^\mu a_\mu = 0$  since  $n^\mu \nabla_\nu n_\mu = 0$ , and satisfies the identity (see Problem 3)  $a_\nu = D_\nu \ln \alpha$  (York, 1979). Using the definition (7.61), the extrinsic curvature can then be written as

<sup>3</sup>An alternative notation is to mark with an upper left index <sup>(4)</sup> the four-dimensional tensors and to leave unmarked the three-dimensional ones (Baumgarte and Shapiro, 2010; Gourgoulhon, 2012).

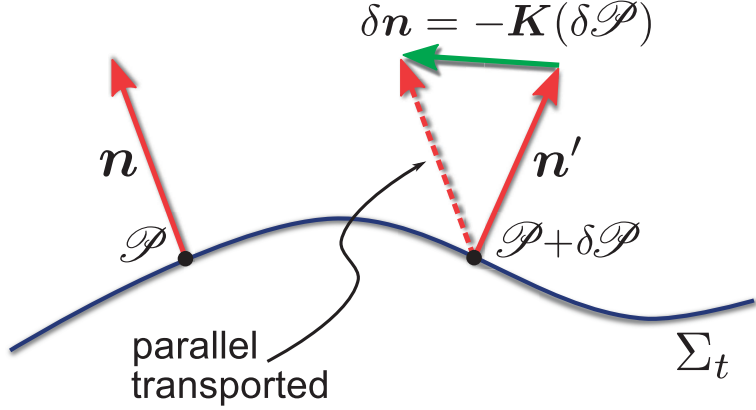


**Fig. 7.3** Schematic representation of the extrinsic curvature tensor of the spatial hypersurface  $\Sigma_t$ . A normal vector  $n$  at a point  $\mathcal{P}$  on  $\Sigma_t$  will be generically different from the corresponding normal  $n'$  at a neighbouring point  $\mathcal{P} + \delta\mathcal{P}$ . The difference between  $n'$  and the parallel-transported  $n$  will be a measure of the extrinsic curvature  $K$  of  $\Sigma_t$ .

$$K_{\mu\nu} = -\nabla_\mu n_\nu - n_\mu a_\nu = -\nabla_\mu n_\nu - n_\mu n^\gamma \nabla_\gamma n_\nu. \quad (7.62)$$

A third definition of the extrinsic curvature involves the spatial metric  $\gamma_{\mu\nu}$  and its Lie derivative along the local normal. More specifically, recalling the properties of the Lie derivative discussed in Section 1.5.1, it is easy to derive that

$$\begin{aligned} \mathcal{L}_n \gamma_{\mu\nu} &= n^\alpha \nabla_\alpha \gamma_{\mu\nu} + \gamma_{\mu\alpha} \nabla_\nu n^\alpha + \gamma_{\nu\alpha} \nabla_\mu n^\alpha \\ &= n^\alpha \nabla_\alpha (n_\mu n_\nu) + g_{\mu\alpha} \nabla_\nu n^\alpha + g_{\nu\alpha} \nabla_\mu n^\alpha \\ &= n^\alpha n_\mu \nabla_\alpha n_\nu + n^\alpha n_\nu \nabla_\alpha n_\mu + \nabla_\nu n_\mu + \nabla_\mu n_\nu \\ &= \gamma_\mu^\alpha \nabla_\alpha n_\nu + \gamma_\nu^\alpha \nabla_\alpha n_\mu = -2K_{\mu\nu}. \end{aligned} \quad (7.63)$$

Inverting expression (7.63) and restricting to (nonzero) spatial indices, the third and last expression for the extrinsic curvature is therefore given by

$$K_{ij} = -\frac{1}{2} \mathcal{L}_n \gamma_{ij}. \quad (7.64)$$

Expression (7.64) has now another simple interpretation of the extrinsic curvature  $K_{ij}$  as the rate of change of the three-metric  $\gamma_{ij}$  as measured by an Eulerian observer. We can now use the properties of the Lie derivative [*cf.* Eq. (1.140)], and recalling that  $\alpha n = t - \beta$  [*cf.* Eq. (7.9)], we can express the right-hand side of (7.64) as

$$\mathcal{L}_n = \frac{1}{\alpha} \mathcal{L}_{\alpha n} = \frac{1}{\alpha} (\mathcal{L}_t - \mathcal{L}_\beta) = \frac{1}{\alpha} (\partial_t - \mathcal{L}_\beta), \quad (7.65)$$

where we have exploited the fact that in the 3+1 decomposition  $\mathcal{L}_t = \partial_t$ . In this way, Eqs. (7.64) can be written as evolution equations for the three-metric (see Problem 4)

$$\partial_t \gamma_{ij} = -2\alpha K_{ij} + \mathcal{L}_\beta \gamma_{ij} \quad (7.66)$$

$$= -2\alpha K_{ij} + D_i \beta_j + D_j \beta_i. \quad (7.67)$$

Note that in deriving Eqs. (7.66) we have used exclusively geometrical quantities and have not employed the Einstein equations, which are instead going to provide information about the evolution of the extrinsic curvature. In fact, the extrinsic curvature is a purely *kinematic* measure that can be obtained either by parallel transporting the local normals [*cf.*, Eq. (7.60)], or through the time derivative of the spatial metric [*cf.*, Eq. (7.64)]. In this respect it can be considered as the extension of the concept of velocity (*i.e.*, of the time derivative of spatial coordinates as measured by Eulerian observers) in classical mechanics. However, just as in classical mechanics the equations of motion come through the time derivative of the velocity, so in general relativity the Einstein equations will prescribe the time derivative of the extrinsic curvature.

Before discussing the decomposition of the Einstein equations we need to express the twenty independent components of the Riemann tensor through a series of suitable projections of this tensor in the spatial and temporal directions. We start with projecting spatially all the indices of the Riemann tensor, so as to obtain what are also known as the *Gauss–Codazzi equations*, *i.e.*,

$$\gamma^\mu_\alpha \gamma^\nu_\beta \gamma^\rho_\delta \gamma^\sigma_\lambda R_{\mu\nu\rho\sigma} = {}^{(3)}R_{\alpha\beta\delta\lambda} + K_{\alpha\delta} K_{\beta\lambda} - K_{\alpha\lambda} K_{\beta\delta}. \quad (7.68)$$

Using the contraction of this relation on the indices  $\alpha$  and  $\delta$ , *e.g.*,  $\gamma^\mu_\alpha \gamma^\nu_\beta \rightarrow \gamma^\mu_\alpha \gamma^\alpha_\beta$ , and recalling that  $\gamma^\mu_\alpha \gamma^\alpha_\beta = \gamma^\mu_\beta = \delta^\mu_\beta + n^\mu n_\beta$ , we obtain the *contracted Gauss relations*

$$\gamma^\mu_\alpha \gamma^\nu_\beta R_{\mu\nu} + \gamma^\mu_\alpha \gamma^\rho_\beta n^\nu n^\sigma R_{\mu\nu\rho\sigma} = {}^{(3)}R_{\alpha\beta} + K K_{\alpha\beta} - K_{\alpha\delta} K^\delta_\beta. \quad (7.69)$$

Finally, contracting on all indices yields the so-called *scalar Gauss relation*

$$\gamma^{\alpha\mu} \gamma^{\beta\nu} R_{\alpha\beta\mu\nu} = R + 2R_{\mu\nu} n^\mu n^\nu = {}^{(3)}R + K^2 - K_{\mu\nu} K^{\mu\nu}, \quad (7.70)$$

where  $K := K^\mu_\mu$  is the *trace* of the extrinsic curvature. Equation (7.70) generalises Gauss’ “Theorema Egregium”, in which the measure of the intrinsic (Gaussian) curvature, expressed by the Ricci scalar  $R$ , is related to the extrinsic curvature, expressed by  $K^2 - K_{\mu\nu} K^{\mu\nu}$  [see, *e.g.*, (Gourgoulhon, 2012) for a detailed discussion].

Next, we apply three spatial projections and one temporal one to the Riemann tensor and obtain the so-called *Codazzi–Mainardi equations*, *i.e.*,

$$\gamma^\rho_\beta \gamma^\mu_\alpha \gamma^\nu_\lambda n^\sigma R_{\rho\mu\nu\sigma} = D_\alpha K_{\beta\lambda} - D_\beta K_{\alpha\lambda}. \quad (7.71)$$

Finally, we apply two spatial projections and two temporal ones and constrain the last six independent components of the Riemann tensor, *i.e.*,

$$\gamma^\alpha_\mu \gamma^\beta_\nu n^\delta n^\lambda R_{\alpha\delta\beta\lambda} = \mathcal{L}_n K_{\mu\nu} - \frac{1}{\alpha} D_\mu D_\nu \alpha + K^\lambda_\nu K_{\mu\lambda}. \quad (7.72)$$

We now have enough identities to rewrite the Einstein equations in a 3+1 decomposition. In particular, we can further use the Gauss–Codazzi equations to obtain the identity

$$\gamma^\alpha_\mu \gamma^\beta_\nu (n^\delta n^\lambda R_{\alpha\delta\beta\lambda} + R_{\alpha\beta}) = {}^{(3)}R_{\mu\nu} + KK_{\mu\nu} - K^\lambda_\nu K_{\mu\lambda}, \quad (7.73)$$

which we use together with Eq. (7.72) to obtain

$$\mathcal{L}_t K_{\mu\nu} - \mathcal{L}_\beta K_{\mu\nu} = -D_\mu D_\nu \alpha + \alpha \left( -\gamma^\alpha_\mu \gamma^\beta_\nu R_{\alpha\beta} + {}^{(3)}R_{\mu\nu} + KK_{\mu\nu} - 2K^\lambda_\nu K_{\mu\lambda} \right). \quad (7.74)$$

Writing out explicitly the Lie derivative along the shift direction and isolating the time derivative (recall that  $\mathcal{L}_t = \partial_t$ ), we can express Eq. (7.74) as

$$\begin{aligned} \partial_t K_{ij} &= -D_i D_j \alpha + \beta^k \partial_k K_{ij} + K_{ik} \partial_j \beta^k + K_{kj} \partial_i \beta^k \\ &\quad + \alpha \left( {}^{(3)}R_{ij} + KK_{ij} - 2K_{ik} K^k_j \right) + 4\pi\alpha [\gamma_{ij} (S - E) - 2S_{ij}], \end{aligned} \quad (7.75)$$

where the following definitions have been made for the “matter” quantities<sup>4</sup>

$$S_{\mu\nu} := \gamma^\alpha_\mu \gamma^\beta_\nu T_{\alpha\beta}, \quad (7.76)$$

$$S_\mu := -\gamma^\alpha_\mu n^\beta T_{\alpha\beta}, \quad (7.77)$$

$$S := S^\mu_\mu, \quad (7.78)$$

$$E := n^\alpha n^\beta T_{\alpha\beta}, \quad (7.79)$$

that is, for contractions of the energy–momentum tensor that would obviously be zero in vacuum spacetimes. The quantities  $S_{\mu\nu}$ ,  $S_\mu$ , and  $E$  are respectively: the *spatial part of the energy–momentum tensor* (*i.e.*,  $S_{ij} = T_{ij}$ ), the *momentum density* and the *energy density* as measured by the Eulerian observers with four-velocity  $\mathbf{n}$ . Here, and also in Sections 7.2.3 and 7.2.5, these quantities have to be considered simply as “known quantities” appearing on the right-hand side of the evolution equation for the extrinsic curvature on any hypersurface  $\Sigma_t$ .

Equations (7.75) determine six of the ten independent components of the Einstein tensor and the remaining four are obtained through a different set of equations that do not depend on time. To derive these equations we go back to the Gauss relation (7.70) and note that the left-hand side is also proportional to the Einstein tensor, *i.e.*,

$$\gamma^{\alpha\mu} \gamma^{\beta\nu} R_{\alpha\beta\mu\nu} = 2G_{\mu\nu} n^\mu n^\nu, \quad (7.80)$$

so that, using the Einstein equations (1.218) and the definition (7.79) we readily obtain (see Problem 5)

$${}^{(3)}R + K^2 - K_{ij} K^{ij} = 16\pi E. \quad (7.81)$$

Equation (7.81) does not contain time derivatives and is in fact a scalar elliptic partial differential equation on the hypersurface  $\Sigma_t$ , which is usually referred to as the *Hamiltonian* or

<sup>4</sup>Note that the definitions (7.76)–(7.79) are similar but distinct from the comoving projections (3.37)–(3.40). In fact, while the former are obtained with a projector orthogonal to the normal to a spacelike hypersurface  $\mathbf{n}$ , the latter are obtained with a projector orthogonal to the four-velocity  $\mathbf{u}$  (see Section 3.2).

*energy constraint.* Similarly, the mixed spatial-temporal contraction of the Einstein tensor and the contracted Codazzi–Mainardi equations (7.71) yield the identity

$$\gamma^{\alpha\mu} n^\nu G_{\mu\nu} = \gamma^{\alpha\mu} n^\nu R_{\mu\nu} = D^\alpha K - D_\mu K^{\alpha\mu}, \quad (7.82)$$

from which we finally obtain

$$D_j(K^{ij} - \gamma^{ij} K) = 8\pi S^i. \quad (7.83)$$

Also the three equations (7.83) do not contain time derivatives and indeed represent a vector elliptic partial differential equation on the hypersurface  $\Sigma_t$ , usually referred to as the *momentum constraints*. The constraints equations (7.81) and (7.83) do not depend on the lapse function  $\alpha$  and on the shift vector  $\beta^i$ . This is not surprising since both of these two gauge functions relate quantities on adjacent hypersurfaces, while the constraint equations are fully specified on a single hypersurface only. Because of this, the solution of the constraint equations on a given hypersurface  $\Sigma_t$  at, say,  $t = 0$  can provide the *initial data* for the evolution of the ADM equations to  $t > 0$ .

Overall, the six equations (7.75), together with the six equations (7.66) represent the time-evolving part of the ADM equations and prescribe how the three-metric and the extrinsic curvature change from one hypersurface to the following one. In contrast, Eqs. (7.81) and (7.83) are constraints that need to be satisfied on each hypersurface. This distinction into evolution equations and constraint equations is not unique to the ADM formulation and is indeed present also in classical electromagnetism, where the Maxwell equation can be similarly written as a set of evolution equations for the electric field  $\vec{E}$  and the magnetic field  $\vec{B}$ , together with a set of constraint equations expressing their divergence, *i.e.*,

$$\partial_t \vec{E} = \vec{\nabla} \times \vec{B} - 4\pi \vec{j}_e, \quad \partial_t \vec{B} = -\vec{\nabla} \times \vec{E}, \quad (7.84)$$

$$\vec{\nabla} \cdot \vec{E} = 4\pi \rho_e, \quad \vec{\nabla} \cdot \vec{B} = 0, \quad (7.85)$$

where  $\rho_e$  and  $\vec{j}_e$  are the electric charge density and current density, while  $\vec{\nabla} \cdot$  and  $\vec{\nabla} \times$  represent the standard flat-spacetime divergence and curl operators, respectively.

The analogy is indeed even deeper. In fact, just like in electrodynamics the divergence of the magnetic field remains zero if the field is divergence-free at the initial time, so the constraint equations (7.81) and (7.83), by virtue of the Bianchi identities, will remain satisfied during the evolution if they are satisfied initially (Frittelli, 1997). Of course, this concept is strictly true in the continuum limit, while numerically the situation is rather different. Firstly, for both the Maxwell and the Einstein equations, the constraint equations can never be satisfied but to a given precision (usually well below the machine precision). Secondly, the violation of these constraints usually grows in time as the error coming from the simple floating-point operations affects the evolved variables. As a result, techniques have been devised in which some or all of the constraint equations are actually solved during the evolution (Anderson and Matzner, 2005). This solution, which is referred to as a *constrained evolution*, is in general computationally very expensive (the solution of elliptic partial differential equations has a computational cost which is generically larger than that of the evolution equations) and is not frequently adopted in multidimensional simulations (however, see Section 7.2.6 for a discussion of a new, fully constrained formulation of the Einstein equations). Most numerical solutions of the Einstein–Euler equations, instead, are *free evolutions*, whereby the constraints

are simply monitored during the evolution to measure the amount of the violation and determine whether or not this is below a prescribed tolerance. Finally, other techniques involve instead the addition of suitable combinations of the constraint equations to the evolution equations (Tsuchiya *et al.*, 2011), or the use of damping terms to be added to the equations (Gundlach *et al.*, 2005), or the use of additional evolution equations that damp the growth of the constraint violations (Bona *et al.*, 2004; Alic *et al.*, 2012a). We will discuss these techniques further in Section 7.2.3.

Two remarks should be made before concluding this section. The first one is about the gauge quantities, namely, the lapse function  $\alpha$  and the shift vector  $\beta^i$ . Since they represent the four degrees of freedom of general relativity, they are not specified by the equations discussed above and indeed they can be prescribed arbitrarily, although great care must be taken in deciding which prescription is the most useful one. In Section 7.2.4 we will discuss the most common choices. The second comment is about the mathematical properties of the time-evolution ADM equations (7.75) and (7.66). The analysis of these properties can be found, for instance, in Reula (1998) or in Frittelli and Gómez (2000), reveals that such a system is only weakly hyperbolic with zero eigenvalues and, as such, not necessarily well-posed (see the discussion in Section 4.1.1 and Problem 6). The weak-hyperbolicity of the ADM equations explains why, while an historical cornerstone in the 3+1 formulation of the Einstein equations, they are rarely used in practice and have met only limited successes in multidimensional calculations (Cook *et al.*, 1998; Abrahams *et al.*, 1998). At the same time, the weak hyperbolicity of the ADM equations and the difficulty in obtaining stable evolutions, has motivated, and still motivates, the search for alternative formulations some of which are reported in the following two sections.

### 7.2.3 Conformal traceless formulations

The formulation of the Einstein equations that is most commonly used in numerical simulations is a savvy modification of the ADM equations that removes from the equations those parts that are responsible for their weak hyperbolicity. To better appreciate how to isolate and remove the “problematic” parts of the ADM equations, it is useful to go back to the Maxwell equations, which can also be written in a form where they are weakly hyperbolic<sup>5</sup> and thus equally problematic.

Let us start by introducing a four-vector potential  $A_\mu := (\Phi, A_i)$  such that  $B_i = \epsilon_{ijk} D^j A^k$ , and the Maxwell equations (7.84)–(7.85) can be then be written in coordinate form as

$$\partial_t A_i = -E_i - D_i \Phi, \quad (7.86)$$

$$\partial_t E_i = -D^j D_j A_i - D_i D^j A_j - 4\pi J_i, \quad (7.87)$$

$$D^i E_i = 4\pi \rho_e. \quad (7.88)$$

Taking a further time derivative of the first equation and replacing the time evolution of the electric field, it is simple to obtain the following equation for the spatial part of the vector potential

$$-\partial_t^2 A_i + D^j D_j A_i - D_i D^j A_j = D_i \partial_t \Phi - 4\pi J_i. \quad (7.89)$$

<sup>5</sup>See Section 4.1.1 for the definitions of hyperbolic and weakly hyperbolic equations.

The left-hand side of Eq. (7.89) would be a wave operator if it were not spoiled by the mixed-derivative term  $D_i D^j A_j$ , which impacts the principal part of the equation preventing it from being hyperbolic. This is not very different from the pathologies that the ADM equations suffer from, where the right-hand side of Eq. (7.75) contains the Ricci tensor and thus mixed derivatives of the three-metric of the type  $\gamma^{ab} \gamma^{cd} \partial_a \partial_c$ . Two different solutions are possible to bring Eq. (7.89) into hyperbolic form. The first one relies on a smart choice of gauges, *e.g.*, the Lorenz gauge  $\partial_t \Phi = -D^i A_i$ , such that Eq. (7.89) then becomes

$$\square A_i := (\partial_t^2 - D^j D_j) A_i = 4\pi J_i , \quad (7.90)$$

where  $\square$  is shorthand for the Dalambertian wave operator. The corresponding strategy in the case of the Einstein equations consists in the use of the harmonic (or generalised harmonic) gauge  $\square x^\mu = H^\mu$  and will be the subject of a detailed discussion in Section 7.2.5. The second approach to bring (7.89) into a hyperbolic form consists instead in defining a new variable, *e.g.*,  $\Gamma := D^i A_i$ , such that the equation is simply rewritten as

$$\square A_i = -D_i \Gamma - D_i \partial_t \Phi + 4\pi J_i . \quad (7.91)$$

Since now  $\Gamma$  is an independent evolution variable, whose evolution equation is given by

$$\partial_t \Gamma = \partial_t D^i A_i = D^i \partial_t A_i = -D^i E_i - D_i D^i \Phi = -4\pi \rho_e - D_i D^i \Phi , \quad (7.92)$$

it will no longer spoil the principal part of Eq. (7.89), which will therefore be hyperbolic and thus well-posed. Very similar logic can be applied also to the ADM equations, which can be recast into hyperbolic form after the introduction of a conformal transformation and of new suitable variables. This route will lead us to the *conformal traceless formulation* of the Einstein equations, which is now employed by the majority of numerical-relativity calculations, which has not been developed by following the logic above, but through a series of trial and error (Nakamura *et al.*, 1987; Shibata and Nakamura, 1995; Baumgarte and Shapiro, 1999).

### **The BSSNOK formulation.**

To obtain a conformal traceless formulation of the Einstein equations we obviously start by imposing a *conformal transformation* of the three-metric  $\gamma_{ij}$  as (Alic *et al.*, 2012a) [*cf.*, note 17 in Section 3.8]<sup>6</sup>

$$\tilde{\gamma}_{ij} = \phi^2 \gamma_{ij} , \quad \tilde{\gamma}^{ij} = \phi^{-2} \gamma^{ij} , \quad (7.93)$$

where the newly introduced conformal three-metric has been conveniently chosen so as to have unit determinant and *spatial volume element*,<sup>7</sup> *i.e.*,

$$\tilde{\gamma} := \det(\tilde{\gamma}_{ij}) = 1 . \quad (7.94)$$

<sup>6</sup>Other authors, *e.g.*, Alcubierre (2008) or Baumgarte and Shapiro (2010), set the conformal transformation (7.93) to be  $\tilde{\gamma}_{ij} = e^{-4\phi} \gamma_{ij}$ . To compare the corresponding equations with the ones reported here it is sufficient to perform the following transformations:  $\phi \rightarrow -(\ln \phi)/2$ ,  $\partial_t \phi \rightarrow -(\partial_t \ln \phi)/2$  and  $\partial_i \phi \rightarrow -(\partial_i \ln \phi)/2$ ; see also Problem 7 for the transformation of second derivatives.

<sup>7</sup>Although the definition of the spatial (proper) volume element obviously involves a volume integral over a three-dimensional domain  $\Omega$  of compact support, *i.e.*,  $V_\Omega := \int_\Omega \sqrt{\det(\gamma_{ij})} d^3x$  [*cf.* Eq. (1.81)], it is common to call the “volume element” simply the determinant of the three-metric.

so that the *conformal factor* is then given by

$$\phi := [\det(\gamma_{ij})]^{-1/6} = \gamma^{-1/6}. \quad (7.95)$$

The three-metric  $\tilde{\gamma}$  is referred to as the *conformally related spatial metric* (or simply “conformal three-metric”), while the three-metric  $\gamma$  is also referred to as the *physical spatial metric* (or simply “physical three-metric”). Of course, also the extrinsic curvature is subject to the same conformal transformation and in place of  $K_{ij}$  we first introduce the *trace-free extrinsic curvature* (hence the “traceless” character of this formulation)

$$A_{ij} := K_{ij} - \frac{1}{3}\gamma_{ij}K, \quad (7.96)$$

and then the corresponding conformal tensor

$$\tilde{A}_{ij} = \phi^2 A_{ij} = \phi^2(K_{ij} - \frac{1}{3}\gamma_{ij}K), \quad \tilde{A}^{ij} = \phi^{-2}A^{ij}, \quad (7.97)$$

where, after using  $\tilde{\gamma}$  to raise and lower the indices, the two tensors can be shown to satisfy the following identities

$$\tilde{A}^{ij}\tilde{A}_{ij} = A^{ij}A_{ij}, \quad \text{tr}(\tilde{A}_{ij}) = \gamma^{ij}\tilde{A}_{ij} = 0. \quad (7.98)$$

The introduction of the trace-free extrinsic curvature tensor has the consequence that the trace of the extrinsic curvature,  $K = \gamma^{ij}K_{ij}$ , needs now to be evolved as a new independent evolution variable. Other important new evolution variables are the *conformal factor*  $\phi$  and the “*Gammas*” (Alcubierre, 2008), which are defined as

$$\tilde{\Gamma}^i := \tilde{\gamma}^{jk}\tilde{\Gamma}_{jk}^i = \tilde{\gamma}^{ij}\tilde{\gamma}^{kl}\partial_l\tilde{\gamma}_{jk}, \quad (7.99)$$

where  $\tilde{\Gamma}_{jk}^i$  are the *Christoffel symbols* of the conformal three-metric, which in addition to the ordinary connection coefficients contains also derivatives of the conformal factor, *i.e.*,

$$\begin{aligned} \tilde{\Gamma}_{jk}^i &= \Gamma_{jk}^i - \frac{1}{3}(\delta_j^i\Gamma_{km}^m + \delta_k^i\Gamma_{jm}^m - \gamma_{jk}\gamma^{il}\Gamma_{lm}^m) \\ &= \Gamma_{jk}^i + 2(\delta_j^i\partial_k\ln\phi + \delta_k^i\partial_j\ln\phi - \gamma_{jk}\gamma^{il}\partial_l\ln\phi), \end{aligned} \quad (7.100)$$

and where we have used the identity  $\partial_i\ln\phi = -\frac{1}{6}\partial_i\ln\gamma = -\frac{1}{3}\Gamma_{im}^m$ .

In addition, using the new variables (7.99) we write the three-dimensional Ricci tensor as  ${}^{(3)}R_{ij} = {}^{(3)}\tilde{R}_{ij} + {}^{(3)}\tilde{R}_{ij}^\phi$ , that is, splitting it into a part containing conformal terms and another one containing space derivatives of the conformal factor

$${}^{(3)}\tilde{R}_{ij} := -\frac{1}{2}\tilde{\gamma}^{lm}\partial_l\partial_m\tilde{\gamma}_{ij} + \tilde{\gamma}_{k(i}\partial_{j)}\tilde{\Gamma}^k + \tilde{\Gamma}^k\tilde{\Gamma}_{(ij)k} + \tilde{\gamma}^{lm}\left(2\tilde{\Gamma}_{l(i}\tilde{\Gamma}_{j)km} + \tilde{\Gamma}_{im}^k\tilde{\Gamma}_{kj}^l\right), \quad (7.101)$$

$${}^{(3)}\tilde{R}_{ij}^\phi := \frac{1}{\phi^2}\left[\phi\left(\tilde{D}_i\tilde{D}_j\phi + \tilde{\gamma}_{ij}\tilde{D}^k\tilde{D}_k\phi\right) - 2\tilde{\gamma}_{ij}\tilde{D}^k\phi\tilde{D}_k\phi\right], \quad (7.102)$$

where  $\tilde{D}_i$  is the covariant derivative associated with the conformal metric  $\tilde{\gamma}$  (see Problem 7). Note that the split (7.101)–(7.102) has the important advantage that the only second-order differential operator on the right-hand side of (7.101) is a *Laplacian operator*, *i.e.*,  $\gamma^{lm}\partial_l\partial_m\tilde{\gamma}_{ij}$  and all the other problematic second-order mixed derivatives are “absorbed” by the first derivative of the Gammas (7.99), just as we have done for the Maxwell equations when introducing the variable  $\Gamma = D_i A^i$  in Eq. (7.91).

As a result, using the conformal decomposition (7.93) and the evolution variables  $\phi$ ,  $K$  and  $\tilde{\Gamma}^i$  we can rewrite the ADM equations (7.66), (7.75) as (see Problem 8)

$$\partial_t \tilde{\gamma}_{ij} = -2\alpha \tilde{A}_{ij} + 2\tilde{\gamma}_{k(i}\partial_{j)}\beta^k - \frac{2}{3}\tilde{\gamma}_{ij}\partial_k\beta^k + \beta^k\partial_k\tilde{\gamma}_{ij}, \quad (7.103)$$

$$\begin{aligned} \partial_t \tilde{A}_{ij} &= \phi^2 \left[ -D_i D_j \alpha + \alpha \left( {}^{(3)}R_{ij} - 8\pi S_{ij} \right) \right]^{\text{TF}} + \beta^k \partial_k \tilde{A}_{ij} + 2\tilde{A}_{k(i}\partial_{j)}\beta^k \\ &\quad + \alpha(\tilde{A}_{ij}K - 2\tilde{A}_{ik}\tilde{A}_j^k) - \frac{2}{3}\tilde{A}_{ij}\partial_k\beta^k, \end{aligned} \quad (7.104)$$

$$\partial_t \phi = \frac{1}{3}\phi\alpha K - \frac{1}{3}\phi\partial_i\beta^i + \beta^k\partial_k\phi, \quad (7.105)$$

$$\partial_t K = -D_i D^i \alpha + \alpha \left[ \tilde{A}_{ij}\tilde{A}^{ij} + \frac{1}{3}K^2 + 4\pi(E + S) \right] + \beta^i\partial_i K, \quad (7.106)$$

$$\begin{aligned} \partial_t \tilde{\Gamma}^i &= \tilde{\gamma}^{jk}\partial_j\partial_k\beta^i + \frac{1}{3}\tilde{\gamma}^{ik}\partial_k\partial_j\beta^j + \frac{2}{3}\tilde{\Gamma}^i\partial_j\beta^j - \tilde{\Gamma}^j\partial_j\beta^i - 2\tilde{A}^{ij}\partial_j\alpha + \beta^j\partial_j\tilde{\Gamma}^i \\ &\quad + 2\alpha \left( \tilde{\Gamma}_{jk}^i \tilde{A}^{jk} - 3\tilde{A}^{ij}\partial_j \ln \phi - \frac{2}{3}\tilde{\gamma}^{ij}\partial_j K \right) - 16\pi\alpha\tilde{\gamma}^{ij}S_j, \end{aligned} \quad (7.107)$$

where, we recall,  $D_i$  is the covariant derivative with respect to the physical metric  $\gamma_{ij}$ , and the index “TF” indicates that the trace-free part of the bracketed term is used. Note that we have used the Hamiltonian constraint (7.81) to eliminate the three-dimensional Ricci scalar on the right-hand side of Eq. (7.106), *i.e.*,

$${}^{(3)}R + K^2 = K^{ij}K_{ij} + 4\pi E = \tilde{A}_{ij}\tilde{A}^{ij} + \frac{1}{3}K^2 + 4\pi E, \quad (7.108)$$

and we have used the momentum constraints (7.83) to eliminate the divergence of the extrinsic curvature on the right-hand side of Eq. (7.107).

The *conformal traceless* evolution system (7.103)–(7.107) is a modern variant of what is also known as the *BSSNOK formulation* (from Baumgarte, Shapiro, Shibata, Nakamura, Oohara, and Kojima) (Nakamura *et al.*, 1987; Shibata and Nakamura, 1995; Baumgarte and Shapiro, 1999) and is again accompanied by the constraint subsystem (7.81) and (7.83) [see, *e.g.*, Baumgarte and Shapiro (2010) for a detailed discussion].

This system now being hyperbolic and hence well-posed, has all the desired features for a numerical implementation. Indeed, the BSSNOK formulation represents the standard implementation of the Einstein evolution equations in modern numerical-relativity codes, either in vacuum or in non-vacuum spacetimes.

When comparing the ADM evolution equations (7.66), (7.75) with the corresponding evolution equations (7.103)–(7.107), it is easy to realise that we have gone from having 12 evolutionary quantities, *i.e.*,  $\gamma_{ij}$ ,  $K_{ij}$ , to 15 variables, *i.e.*,  $\tilde{\gamma}_{ij}$ ,  $\tilde{A}_{ij}$ ,  $\phi$ ,  $K$ ,  $\tilde{\Gamma}^i$  (note that  $\tilde{\gamma}_{ij}$  and  $\tilde{A}_{ij}$ , have only five independent components each since they are traceless). The increased number

of equations is a very modest price to pay in exchange of the stability properties of the BSSNOK formulation. Furthermore, the use of the momentum constraint equations (but not of the energy constraint) in the evolution of the dynamical variables, which is crucial for ensuring strong hyperbolicity, provides the BSSNOK formulation with a certain “forgiveness”, so that the violation of the constraints does not grow rapidly even when constraint-violating boundary conditions are used near the strong-field region.

### The CCZ4 formulation.

Among many of the desirable features of the BSSNOK formulation, there is one which is less desirable and has to do with the fact that the constraint subsystem has a zero-speed characteristic for the Hamiltonian constraint (Bernuzzi and Hilditch, 2010). Stated differently, violations of the constraints do not propagate and if during a numerical calculation the violation of constraint equations increases (*e.g.*, because the spacetime is undergoing rapid and strong changes), then this violation will not decrease during the subsequent evolution, spoiling the overall accuracy of the solution. Clearly, formulations that have a constraint subsystem with nonzero characteristic speeds are highly desirable since in this way the constraint violations can propagate out of the numerical domain instead of residing on the domain once produced. These considerations have led a number of authors to seek formulations in which the evolution equations are modified by adding terms related to the constraint equations (which are zero at the continuum level) in such a way that the violations of the constraints (which are inevitably produced) are also damped dynamically (Bona *et al.*, 2003; Gundlach *et al.*, 2005).<sup>8</sup> These ideas are far from being academic and indeed the first successful calculations of the merger of binary black holes by Pretorius (2005a) have been made possible through the use of the constraint-damping terms.

Once again, before looking at the way *constraint-damping* techniques act on the Einstein equations, it is useful to go back to the simpler set of the Maxwell equations. Let us consider therefore the evolution and constraint equations for the magnetic field. An effective way of imposing a damping of the constraint  $(7.85)_2$  in the evolution equation  $(7.84)_2$ , consists in introducing a scalar function  $\psi$  such that Eqs.  $(7.85)_2$  and  $(7.84)_2$  are rewritten as

$$\partial_t B^i = -\epsilon^{ijk} \partial_j E_k + \gamma^{ij} \partial_j \psi, \quad (7.109)$$

$$\partial_t \psi = -a_1 \partial_i B^i - a_2 \psi, \quad (7.110)$$

where  $a_1 > 0$  and  $a_2 > 0$ . Clearly, the new system (7.109) coincides with the corresponding part of the Maxwell equations if

$$\psi(x^i, 0) = 0, \quad \partial_t \psi(x^i, 0) = 0. \quad (7.111)$$

However, if the conditions (7.111) are not satisfied at any later time, *i.e.*, if the magnetic field has nonzero divergence, they will drive exponentially the solution to be divergence-free over a time-scale given by  $1/a_2$ . In other words, the addition of the scalar function  $\psi$  and the introduction of an evolution equation for  $\psi$  “sourced” by the violation of the zero-divergence condition for the magnetic field generate a feedback loop acting whenever the violations grow

<sup>8</sup>In addition, an effort has also been made in the construction of constraint-preserving boundary conditions that prevent large constraint violations from propagating in from the outer boundary of the computational domain [see, *e.g.*, Rinne (2006); Seiler *et al.* (2008); Ruiz *et al.* (2011)].

and damping them away. This approach is also known as *divergence-cleaning* (Dedner *et al.*, 2002) and is a simple and effective choice to keep under control the violation of the zero-divergence constraint. Moreover, it is reasonably competitive also when compared with more sophisticated and accurate approaches, such as the *constraint-transport method* (Toth, 2000).

The logic illustrated above for the Maxwell equations can be extended also to the Einstein equations, both in the case of the generalised harmonic formulation that we will discuss in Section 7.2.5, and also in the case of the Z4 *formulation*. This formulation was introduced as a covariant extension of the Einstein equations (Bona *et al.*, 2003), where the original elliptic constraints are converted into algebraic conditions for a new four-vector  $Z_\mu$ . In the Z4 formulation the energy and momentum constraints become evolution equations for  $Z_\mu$ , modifying the principal part of the ADM system and converting it from weakly hyperbolic to hyperbolic (Bona *et al.*, 2004). Just like the scalar function  $\psi$  in the above example (7.109), the four-vector  $Z_\mu$  measures the deviation from the Einstein field equations and the algebraic constraints  $Z_\mu = 0$  amount therefore to the fulfilling of the standard Hamiltonian and momentum constraints (7.81)–(7.83). In order to control these constraints, the original system was supplemented with damping terms such that the true Einstein solutions (*i.e.*, the ones satisfying the constraint subsystem) become an attractor of the enlarged set of solutions of the Z4 system (Gundlach *et al.*, 2005).

The damped-Z4 formulation can be written in covariant form as

$$R_{\mu\nu} + 2\nabla_{(\mu}Z_{\nu)} + \kappa_1[2n_{(\mu}Z_{\nu)} - (1 + \kappa_2)g_{\mu\nu}n_\sigma Z^\sigma] = 8\pi \left( T_{\mu\nu} - \frac{1}{2}g_{\mu\nu}T \right), \quad (7.112)$$

where the constant coefficients  $\kappa_1, \kappa_2$  are free parameters related to the characteristic time of the exponential damping of constraint violations. Assuming conservation of the energy-momentum tensor, the Bianchi identities lead to the constraint-propagation system

$$\square Z_\mu + R_{\mu\nu}Z^\nu = -\kappa_1\nabla^\nu[2n_{(\mu}Z_{\nu)} + \kappa_2g_{\mu\nu}n_\sigma Z^\sigma], \quad (7.113)$$

which highlights the following important feature: the wave-like principal part in (7.113) ensures that any deviation from the original Einstein equations propagates along light cones, thus leaving the grid and not spoiling the overall accuracy of the solution as is the case of the BSSNOK formulation. It has also been shown that all the constraint-related modes are damped when  $\kappa_1 > 0$  and  $\kappa_2 > -1$  (Gundlach *et al.*, 2005).

A new variant of the Z4 system, *i.e.*, the *conformally and covariant Z4 formulation (or CCZ4)*, has been proposed to incorporate the constraint-violation damping features described above within a conformal and traceless framework very much alike the BSSNOK one.

As a first step towards deriving the CCZ4 formulation, we adapt the four-dimensional Z4 formulation to a 3+1 decomposition so as to obtain<sup>9</sup>

<sup>9</sup>Note that we use here the unit normal (7.11), *i.e.*,  $n_\mu = -\alpha\delta_\mu^0$ ,  $n^\mu = (1, -\beta^i)/\alpha$ , that is different from the one adopted in Alic *et al.* (2012a), where  $n_\mu = \alpha\delta_\mu^0$ ,  $n^\mu = (-1, \beta^i)/\alpha$ . As a result, a sign difference is present for the definitions of  $\Theta$  and  $S_i$ .

$$(\partial_t - \mathcal{L}_\beta) \gamma_{ij} = -2\alpha K_{ij}, \quad (7.114)$$

$$\begin{aligned} (\partial_t - \mathcal{L}_\beta) K_{ij} &= -D_i \alpha_j + \alpha \left[ {}^{(3)}R_{ij} + D_i Z_j + D_j Z_i - 2K_i^k K_{kj} + (K - 2\Theta) K_{ij} \right. \\ &\quad \left. - \kappa_1(1 + \kappa_2)\Theta \gamma_{ij} \right] - 8\pi\alpha \left[ S_{ij} - \frac{1}{2}(S - E)\gamma_{ij} \right], \end{aligned} \quad (7.115)$$

$$\begin{aligned} (\partial_t - \mathcal{L}_\beta) \Theta &= \frac{\alpha}{2} \left[ {}^{(3)}R + 2D_j Z^j + (K - 2\Theta)K - K^{ij}K_{ij} - 2\frac{Z^j \alpha_j}{\alpha} \right. \\ &\quad \left. - 2\kappa_1(2 + \kappa_2)\Theta - 16\pi E \right], \end{aligned} \quad (7.116)$$

$$(\partial_t - \mathcal{L}_\beta) Z_i = \alpha [D_j(K_i^j - \delta_i^j K) + \partial_i \Theta - 2K_i^j Z_j - \Theta \frac{\alpha_i}{\alpha} - \kappa_1 Z_i - 8\pi S_i], \quad (7.117)$$

where  $\mathcal{L}_\beta$  is again the Lie derivative along the shift vector  $\beta$  and  $\Theta$  is the projection of the Z4 four-vector along the normal direction [not to be confused with the fluid expansion introduced in Eq. (3.13)]

$$\Theta := -n_\mu Z^\mu = \alpha Z^0. \quad (7.118)$$

Note that the evolution variables are now  $\gamma_{ij}$ ,  $K_{ij}$ ,  $\Theta$ ,  $Z_i$  and that the constraint equations are automatically included in the evolution equations. Indeed, Eqs. (7.116) and (7.117) reduce to the standard constraint subsystem (7.81) and (7.83) if  $\Theta = 0 = Z_i$  (Bona *et al.*, 2004).

Next, we adopt the same conformal decomposition introduced in Eqs. (7.93)–(7.95) and after some algebra we arrive at the CCZ4 formulation given by the following system of evolution equations (see Problem 9)

$$\partial_t \tilde{\gamma}_{ij} = -2\alpha \tilde{A}_{ij} + 2\tilde{\gamma}_{k(i} \partial_{j)} \beta^k - \frac{2}{3}\tilde{\gamma}_{ij} \partial_k \beta^k + \beta^k \partial_k \tilde{\gamma}_{ij}, \quad (7.119)$$

$$\begin{aligned} \partial_t \tilde{A}_{ij} &= \phi^2 \left[ -D_i D_j \alpha + \alpha \left( {}^{(3)}R_{ij} + D_i Z_j + D_j Z_i - 8\pi S_{ij} \right) \right]^{\text{TF}} - 2\alpha \tilde{A}_{ik} \tilde{A}_j^k \\ &\quad + \alpha \tilde{A}_{ij} \left( K - 2\Theta \right) + 2\tilde{A}_{k(i} \partial_{j)} \beta^k - \frac{2}{3}\tilde{A}_{ij} \partial_k \beta^k + \beta^k \partial_k \tilde{A}_{ij}, \end{aligned} \quad (7.120)$$

$$\partial_t \phi = \frac{1}{3}\alpha \phi K - \frac{1}{3}\phi \partial_k \beta^k + \beta^k \partial_k \phi, \quad (7.121)$$

$$\begin{aligned} \partial_t K &= -D^j D_j \alpha + \alpha \left( {}^{(3)}R + 2D_j Z^j + K^2 - 2\Theta K \right) + \beta^j \partial_j K \\ &\quad - 3\alpha \kappa_1 (1 + \kappa_2) \Theta + 4\pi\alpha (S - 3E), \end{aligned} \quad (7.122)$$

$$\begin{aligned} \partial_t \hat{\Gamma}^i &= 2\alpha \left( \tilde{\Gamma}_{jk}^i \tilde{A}^{jk} - 3\tilde{A}^{ij} \partial_j \ln \phi - \frac{2}{3}\tilde{\gamma}^{ij} \partial_j K \right) - 2\tilde{A}^{ij} \partial_j \alpha + \tilde{\gamma}^{jk} \partial_j \partial_k \beta^i \\ &\quad + 2\tilde{\gamma}^{ij} \left( \alpha \partial_j \Theta - \Theta \partial_j \alpha - \frac{2}{3}\alpha K Z_j \right) + \frac{1}{3}\tilde{\gamma}^{ik} \partial_k \partial_j \beta^j + \frac{2}{3}\tilde{\Gamma}^i \partial_j \beta^j - \tilde{\Gamma}^j \partial_j \beta^i \\ &\quad + 2\kappa_3 \left( \frac{2}{3}\tilde{\gamma}^{ij} Z_j \partial_k \beta^k - \tilde{\gamma}^{jk} Z_j \partial_k \beta^i \right) + \beta^j \partial_j \hat{\Gamma}^i - 2\alpha \kappa_1 \tilde{\gamma}^{ij} Z_j - 16\pi\alpha \tilde{\gamma}^{ij} S_j, \end{aligned} \quad (7.123)$$

$$\begin{aligned} \partial_t \Theta &= \frac{1}{2}\alpha \left( {}^{(3)}R + 2D_j Z^j - \tilde{A}_{ij} \tilde{A}^{ij} + \frac{2}{3}K^2 - 2\Theta K \right) - Z^j \partial_j \alpha \\ &\quad + \beta^j \partial_j \Theta - \alpha \kappa_1 (2 + \kappa_2) \Theta - 8\pi\alpha E, \end{aligned} \quad (7.124)$$

where we have defined the new evolution variables

$$\hat{\Gamma}^i := \tilde{\Gamma}^i + 2\tilde{\gamma}^{ij}Z_j, \quad (7.125)$$

which clearly reduce to the standard “Gammas” (7.99) when  $Z_i = 0$  (Alic *et al.*, 2012a).

The implications of the *CCZ4 formulation* are numerous and can be summarised as follows:

- The CCZ4 equations (7.119)–(7.121) and (7.123) reduce to the corresponding equations (7.103)–(7.107) in the BSSNOK formulation when setting  $Z_i = 0 = \Theta$ . Equation (7.122), on the other hand, does not reduce to the corresponding Eq. (7.106), since it does not make use of the Hamiltonian constraint to remove the Ricci scalar from the right-hand side [*cf.* Eq. (7.108)].
- The choice made with the definition (7.125) is equivalent to the addition of the momentum constraint to the right-hand side of the evolution equation of  $\tilde{\Gamma}^i$  and amounts to replacing the vector  $Z_i$  by the quantities  $\hat{\Gamma}^i$  in the set of basic fields to be evolved.
- The coefficient  $\kappa_3$  in Eq. (7.123) has been introduced to improve the stability properties of the system. Although essentially arbitrary, a value of  $\kappa_3 = 1$  provides a fully covariant formulation of the equations, while  $\kappa_3 = 1/2$  has been shown by Alic *et al.* (2012a) to yield optimal results in the case of binary black-hole spacetimes. Experience has also shown that a value of  $\kappa_3 = 1$  is not problematic as long as no singularities are present [*e.g.*, as in the inspiral of neutron-star binaries (Kastaun *et al.*, 2013)].
- The CCZ4 system (7.119)–(7.123) is not fully equivalent to the Z4 system, since there are two extra fields, namely  $\det(\tilde{\gamma}_{ij})$  and  $\text{tr}(\tilde{A}_{ij})$ , that are not present in the Z4 system. These are not dynamical fields at the continuum level, where  $\det(\tilde{\gamma}_{ij}) = 1$  and  $\text{tr}(\tilde{A}_{ij}) = 0$  by construction. However, at the discrete level these constraints need to be monitored or imposed, *e.g.*, by replacing in Eq. (7.120) the numerically computed extrinsic curvature  $\tilde{A}_{ij}$  with its trace-removed part, *i.e.*,  $\tilde{A}_{ij} - \frac{1}{3}\tilde{\gamma}_{ij}\tilde{A}_{kl}\tilde{\gamma}^{kl}$  (Alic *et al.*, 2012a).
- Although the structure of the CCZ4 formulation is very similar to the BSSNOK one, there is an important difference in the evolution of the trace-free variable  $\tilde{A}_{ij}$ . In the BSSNOK formulation, in fact, the Hamiltonian constraint is assumed to be satisfied exactly and is used to eliminate the Ricci scalar from the right-hand side of the evolution equation for  $\tilde{A}_{ij}$  (Alcubierre *et al.*, 2003a). In the CCZ4 system, on the contrary, the evolution of  $\tilde{A}_{ij}$  follows directly from (the trace-free part of) the ADM evolution equation for  $K_{ij}$ , plus the extra terms in  $Z_i$  and  $\Theta$ .
- The trace of the extrinsic curvature in the BSSNOK formulation, which we here indicate as  $K^{\text{BSSNOK}}$ , and the corresponding quantity in the CCZ4 formulation, which we here indicate as  $K$ , do not coincide except in the continuum limit. In general, they are instead related as (Alic *et al.*, 2012a).

$$K^{\text{BSSNOK}} = K - 2\Theta. \quad (7.126)$$

Another conformal formulation of the Z4 system, *i.e.*, the *Z4c formulation*, has also been proposed recently by Bernuzzi and Hilditch (2010), which however does not include all of the non-principal terms coming from the covariant form of the Z4 equations, but aims at a system which is as close as possible to BSSNOK. The resulting set of equations has been applied

with success to spherically symmetric non-vacuum spacetimes, where it has shown its ability to damp and propagate away the violations of the constraints (Bernuzzi and Hilditch, 2010; Weyhausen *et al.*, 2012), and more recently also in generic spacetimes (Hilditch *et al.*, 2012).

The potential of the CCZ4 formulation has not yet been fully explored, but the recent calculations of the inspiral and merger of binary black holes (Alic *et al.*, 2012a) and of binary neutron stars (Kastaun *et al.*, 2013; Alic *et al.*, 2013), have shown that it leads not only to a stable evolution, but it also provides a violation of the constraints which is at least one order of magnitude smaller than the corresponding one obtained with the BSSNOK evolution. In addition, the CCZ4 formulation can efficiently recover from large violations of the constraints, with the damping terms rapidly removing constraint violations produced at the outer boundary. By contrast, evolutions with the BSSNOK formulation experiencing similar violations never recover from the boundary contamination, leading to an increasing violation and larger errors in the gravitational waves (Alic *et al.*, 2012a).

#### 7.2.4 Gauge conditions in 3+1 formulations

All of the 3+1 formulations discussed so far, independently of whether we are considering the evolution equations for the ADM, the BSSNOK, the Z4, or the CCZ4 formulations, represent a system of equations which is not yet closed, since two additional degrees of freedom need to be specified. These are: the lapse function  $\alpha$  and the shift vector  $\beta^i$ . More precisely, on each spatial hypersurface  $\Sigma_t$ , we need to specify a *slicing condition*, *i.e.*, prescribe the lapse (and possibly its evolution) and a *spatial shift condition*, *i.e.*, prescribe the shift vector (and possibly its evolution). These additional four degrees of freedom are genuinely arbitrary in the sense that they represent our choice of how to slice the spacetime and lay out coordinates on each hypersurface. The results of the numerical solution obtained with different gauge conditions will be different, but only in the “*gauge-dependent*” quantities. On the other hand, physical observables, such as scalar quantities or gravitational waves (when extracted in the wave zone) will not depend on the specific choice of gauge conditions, *i.e.*, they will be “*gauge-invariant*”.

The arbitrariness in the choice of gauge conditions is at the same time an advantage and a handicap. While in fact we are free to choose any prescription for  $\alpha$  and  $\beta^i$ , it is also true that some choices will lead in disastrous results when implemented numerically. Indeed, it is not an exaggeration to say that a savvy choice of gauge conditions makes the difference between a successful simulation and a rapid failure.

The first searches for suitable gauge conditions for the evolution of the Einstein equations date back essentially to the first formulations of the equations [see, *e.g.*, York (1979)] and this still represents a fertile field of research [see, *e.g.*, Mueller and Brügmann (2010); Schnetter (2010); Alic *et al.* (2010) for some more recent results]. It is not our intention to provide here a detailed discussion of the different classes of gauge conditions, which are instead illustrated in the more specialised books of Alcubierre (2008), Bona *et al.* (2009), Baumgarte and Shapiro (2010), and Gourgoulhon (2012). We will, however, briefly discuss what are the most important features that are sought after in gauge conditions and review those prescriptions that are more commonly employed in modern numerical simulations.

In essence, optimal gauge conditions should guarantee that the following three basic requirements are fulfilled:

- (i) if singularities are present in the spacetime under consideration (*e.g.*, if a black hole is present and is moving on the numerical grid), these singularities should be avoided;
- (ii) if coordinate distortions take place on the spatial grid as a result of the development of large spatial curvatures, these should be counteracted;
- (iii) if the gauges are prescribed, this should be done in a manner which is computationally the least expensive, that is, either through algebraic expressions or through the solution of simple evolution equations.

The first requirement is also referred to as the *singularity-avoiding slicing condition* and is accomplished essentially by slowing down the pace at which proper time evolves near the singularity, that is, by setting the lapse to be very small in the vicinity of the singularity. A mathematically precise manner of imposing this condition involves the trace of the extrinsic curvature  $K$  and requires that the coordinate volume elements associated with Eulerian observers will be not only maximal, *i.e.*,  $K = 0$ , but also will not change with time, *i.e.*,  $\partial_t K = 0$ . We recall that when  $K = 0$  the volume of any bounded portion  $\Omega$  on the spatial hypersurface  $\Sigma_t$  is at a maximum relative to small perturbations (York, 1979). Since in this case the hypersurface is said to be *maximal*, the condition

$$K = 0 = \partial_t K \quad (7.127)$$

is commonly referred to as the *maximal slicing condition* and it essentially requires that Eulerian observers in free fall (that is, with zero shift) do not “focus” there where the extrinsic curvature grows.

It is not difficult to show, using the ADM evolution equations (7.66), (7.75) and the Hamiltonian constraint (7.81), that imposing the maximal slicing condition amounts to the solution of the elliptic equation

$$D^2\alpha = \alpha [K_{ij}K^{ij} + 4\pi(E + S)] , \quad (7.128)$$

where  $D^2 := \gamma^{ij}\partial_i\partial_j$  is the Laplacian associated to the three-metric  $\gamma$ . Equation (7.128) needs to be solved on every spatial slice  $\Sigma_t$  after suitable boundary conditions are specified. In essence, we have translated the definition of an optimal slicing condition into an elliptic equation and thus into an operation that is computationally very costly in standard three-dimensional numerical-relativity codes. As a result, over the years alternative approaches have been sought that would provide singularity-avoiding properties similar to those coming with the maximal slicing condition, but not through the solution of an elliptic equation [see Alcubierre (2008) for a detailed historical account]. In particular, most of the modern 3+1 solutions of the Einstein equations adopt as hyperbolic slicing condition a member of the so-called *Bona–Massó* family of slicing conditions, which can be written generically as (Bona *et al.*, 1995)<sup>10</sup>

$$\partial_t\alpha - \beta^k\partial_k\alpha = -f(\alpha)\alpha^2(K - K_0) , \quad (7.129)$$

where  $f(\alpha) > 0$  and  $K_0 := K(t = 0)$ . By varying the expression of the generic function  $f(\alpha)$ , the slicing condition (7.129) recovers a number of well-known slicings. For example, by setting  $f = 1$  one recovers the so-called *harmonic slicing condition*, while, by setting

<sup>10</sup>It is not difficult to show that when using the Bona–Massó family of slicing conditions, the lapse follows an evolution equation with a wave-like principal part and hence a hyperbolic equation (Alcubierre, 2008).

$f = q/\alpha$  with  $q$  an integer, one obtains the generalised “1+log” slicing condition (Anninos *et al.*, 1995), where  $\alpha = h(x^i) + \ln \gamma^{q/2}$  and  $h(x^i)$  a positive but otherwise arbitrary time-independent function (see Problems 10 and 11). Finally, when  $f(\alpha)$  is taken to diverge, one recovers the maximal slicing condition to obtain a non-diverging lapse. In practice, most numerical simulations set  $f = 2/\alpha$ , thus adopting the 1+log slicing condition, which has been shown to be very robust and well-behaved not only in vacuum spacetimes representing isolated and binary black holes (Campanelli *et al.*, 2006; Baker *et al.*, 2006), but also in spacetimes describing isolated and binary neutron stars (Baiotti *et al.*, 2008; Yamamoto *et al.*, 2008). Furthermore, its singularity-avoiding properties have been thoroughly tested in the first three-dimensional simulations of the collapse of rotating stars to black holes without the aid of excision techniques (Baiotti and Rezzolla, 2006).

Much of what we have discussed for the slicing conditions applies also to the spatial shift conditions. In this case too, it is clear what an optimal shift condition should provide, but it is also clear that enforcing the optimal conditions amounts to the solution of elliptic equations which are computationally unsustainable in present three-dimensional codes. In fact, to fulfill the requirement (ii) above, we can exploit our freedom in laying out the spatial coordinates in such a way that the changes in size and shape of representative volume elements are minimised when moving from one spatial hypersurface to the next one. These changes can be measured through the spatial *metric strain tensor* along the time direction  $t$ , which is defined as (Smarr and York, 1978)

$$\Theta_{ij} := \frac{1}{2} \mathcal{L}_t \gamma_{ij} = \frac{1}{2} (\alpha \mathcal{L}_n + \mathcal{L}_\beta) \gamma_{ij} = -\alpha K_{ij} + \frac{1}{2} \mathcal{L}_\beta \gamma_{ij}. \quad (7.130)$$

Integrating the positive contraction of the strain tensor  $\Theta_{ij} \Theta^{ij}$  over the spatial slice  $\Sigma_t$  and minimising its variation then leads to the following *minimal-strain shift condition*

$$D_j \Theta_{ij} = 0, \implies D^2 \beta^i + D^i D_j \beta^j + R^i_j \beta^j = 2 D_j (\alpha K^{ij}). \quad (7.131)$$

As for the maximal slicing condition, Eqs. (7.131) represent three elliptic equations that need to be solved on every spatial slice  $\Sigma_t$  after the specification of appropriate boundary conditions. Once again, therefore, we have derived an excellent prescription, which however is very expensive in practice. Things do not improve much if instead we consider the *metric distortion tensor*, which measures uniquely the shape of the volume elements, independently of their size, and is defined as

$$\Sigma_{ij} := \Theta_{ij} - \frac{1}{3} \gamma_{ij} \Theta_{kl} \Theta^{kl} = \frac{1}{2} \gamma^{1/3} \mathcal{L}_t \bar{\gamma}_{ij}, \quad (7.132)$$

where  $\bar{\gamma}_{ij} := \gamma^{-1/3} \gamma_{ij}$  is the conformal metric. Also in this case, in fact, integrating the positive contraction of the strain tensor  $\Sigma_{ij} \Sigma^{ij}$  over the spatial slice and minimising its variation leads to the following three elliptic equations for the *minimal-distortion shift condition*

$$D_j \Sigma_{ij} = 0, \implies D^2 \beta^i + \frac{1}{3} D^i D_j \beta^j + R^i_j \beta^j = 2 D_j (\alpha A^{ij}), \quad (7.133)$$

where  $A_{ij}$  is again the trace-free extrinsic curvature [*cf.* Eq. (7.96)].

Not surprisingly, as had happened for the slicing condition, also in the case of a shift condition, a series of numerical improvements has led to the definition of hyperbolic expressions

### 346 Formulations of the Einstein–Euler Equations

for the shift vector which yield the desired properties of minimal grid distortions at a fraction of the computational cost that would be otherwise needed for the solution of the corresponding elliptic equations.

Most of the modern 3+1 solutions of the Einstein equations adopt as hyperbolic shift condition a variant of the so-called “*Gamma-driver*” shift condition proposed by Alcubierre *et al.* (2001), that essentially act so as to drive the Gammas  $\tilde{\Gamma}^i$  to remain approximately constant in time. In this respect, the Gamma-driver shift conditions are similar to the “*Gamma-freezing*” condition  $\partial_t \tilde{\Gamma}^k = 0$ , which, in turn, is closely related to the minimal-distortion shift condition (7.132).<sup>11</sup> In practice, the shift vector  $\beta^i$  is commonly evolved using the following set of first-order evolution equations (Alcubierre *et al.*, 2003a)<sup>12</sup>

$$\partial_t \beta^i - \beta^j \partial_j \beta^i = \frac{3}{4} B^i, \quad (7.134)$$

$$\partial_t B^i - \beta^j \partial_j B^i = \partial_t \tilde{\Gamma}^i - \beta^j \partial_j \tilde{\Gamma}^i - \eta B^i, \quad (7.135)$$

where  $B^i$  is simply an auxiliary variable. The coefficient  $\eta$  of the last term in (7.135) is usually referred to as the “damping term” and is introduced to avoid strong oscillations in the shift in those situations where there is a rapid and large variation in the gauges. In simulations of inspiralling compact binaries with total mass  $M$ , this damping term is typically set to be constant in space and time and equal to  $2/M$  for binaries of black holes, and equal to  $1/M$  for binaries of neutron stars (Rezzolla *et al.*, 2010). While this choice works well for binaries with comparable masses, it ceases to be a good one for binaries with unequal masses. The reason for this can be understood in terms of a simple dimensional argument: since the dimension of  $\eta$  is the inverse of a mass, a larger value of  $\eta$  will be needed for a smaller mass to maintain a similar damping effect and thus cannot be constant for binaries with different masses. Following this logic, a number of solutions have recently been proposed in which  $\eta$  is either prescribed to have a precise spatial fall-off with the distance from the black-hole/neutron star (Mueller and Brügmann, 2010; Schnetter, 2010) or is set to follow an additional evolution equation that drives it to a more accurate and smooth solution (Alic *et al.*, 2010).

In summary, while several more refined gauge conditions are possible, the use of a “1+log” slicing condition (7.129) and of a “*Gamma-driver*” shift condition (7.134)–(7.135), will provide robust and accurate solutions for most problems presently explored by numerical-relativity codes.

#### 7.2.5 The generalised harmonic formulation

Not all of the formulations of the Einstein equations currently employed in numerical calculations make use of the 3+1 decomposition. An important counterexample is offered by the *generalised harmonic formulation*, in which the metric is evolved in time as a four-dimensional object in a coordinate system which is harmonic or close to it. Other numerical approaches not

<sup>11</sup>Using the definition of the Gammas (7.99) and realising that the metric distortion tensor in (7.132) essentially measures the velocity of the conformal metric  $\tilde{\gamma}_{ij}$ , it is not difficult to conclude that the condition (7.133) essentially sets  $\partial_t \tilde{\Gamma}^k = 0$ .

<sup>12</sup>Evolution equations for the shift that are second order in time have also been used by Löffler *et al.* (2006).

adopting a 3+1 decomposition are those exploiting a 2+2 double-null foliation [see, *e.g.*, Winicour (2005) for a complete review on null (or characteristic) approaches in relativity], or the conformal formulation of the field equations proposed by Friedrich [see, *e.g.*, Frauendiener (2004) for a review]. In addition, recent work has cast the generalised harmonic formulation into a 3+1 decomposition to exploit the well-tested gauge conditions discussed in the previous section (Moesta, 2008).

We recall that *harmonic coordinates* were first introduced by de Donder (1921) to reduce the Einstein equations to 10 quasi-linear wave equations and they were later extensively developed by Fock (1959) and used by Choquet-Bruhat (1962) to give the first well-posed version of the Cauchy problem for the Einstein equations [see, *e.g.*, Choquet-Bruhat and Ruggeri (1983) for an extended discussion]. In a *harmonic gauge* the spacetime coordinates  $x^\mu$  (viewed as a set of four scalar functions) satisfy the curved-spacetime wave equation

$$\begin{aligned}\square x^\mu &:= \nabla_\alpha \nabla^\alpha x^\mu = \frac{1}{\sqrt{-g}} \partial_\alpha (\sqrt{-g} g^{\alpha\beta} \partial_\beta x^\mu) \\ &= \frac{1}{\sqrt{-g}} \partial_\alpha (\sqrt{-g} g^{\alpha\mu}) = 0.\end{aligned}\quad (7.136)$$

The importance of this choice is that in these coordinates the principal part of the Einstein equations reduces to a second-order hyperbolic form or to a first-order symmetric hyperbolic form. As discussed in Section 4.1.1, a hyperbolic formulation is then guaranteed to be well-posed and there is a vast literature dedicated to the solution of partial differential equations with a wave-equation principal part. Over the last decade a number of groups have implemented numerical evolution schemes for harmonic formulations of the Einstein equations (Garfinkle, 2002; Babiuc *et al.*, 2006a; Pretorius, 2005a; Lindblom *et al.*, 2006; Palenzuela *et al.*, 2007) and for the related Z4 formulation (Bona *et al.*, 2002; Bona *et al.*, 2005) (see also Section 7.2.3). Most of these formulations, however, do no impose a gauge choice which is purely harmonic and thus of the type (7.136). Rather, the common strategy is to use the so-called *generalised harmonic gauge* (Friedrich, 1996), in which the coordinates  $x^\mu = (t, x^i) = (t, x, y, z)$  satisfy instead the condition

$$-\square x^\mu = \Gamma^\mu = F^\mu, \quad (7.137)$$

where  $F^\mu(x^\alpha, g^{\alpha\beta})$  are the *gauge source functions*, which can be prescribed arbitrarily and may depend on the spacetime coordinates and on the metric. The four-vector  $\Gamma^\mu$  is defined as

$$\Gamma^\mu := g^{\alpha\beta} \Gamma_{\alpha\beta}^\mu = -\frac{1}{\sqrt{-g}} \partial_\nu \tilde{g}^{\mu\nu}, \quad (7.138)$$

where, following the formulation in Szilágyi *et al.* (2007), we have introduced the *densitised metric*  $\tilde{g}$  defined as

$$\tilde{g}^{\mu\nu} := \sqrt{-g} g^{\mu\nu}, \quad (7.139)$$

and which plays the role of the basic evolution variable. At a discrete level, the generalised harmonic condition (7.137) cannot be satisfied exactly, *i.e.*,  $\Gamma^\mu \simeq F^\mu$  only, and the difference between the two quantities is measured via the gauge functions

$$C^\mu := \Gamma^\mu - F^\mu = 0. \quad (7.140)$$

### 348 Formulations of the Einstein–Euler Equations

These functions also act as constraint equations, while the evolution system is based on the harmonic reduction of the Einstein tensor (Wald, 1984)

$$E^{\mu\nu} := G^{\mu\nu} - \nabla^{(\mu}\Gamma^{\nu)} + \frac{1}{2}g^{\mu\nu}\nabla_\alpha\Gamma^\alpha - 8\pi T^{\mu\nu}, \quad (7.141)$$

where  $\Gamma^\nu$  is treated as a four-vector in constructing the covariant derivative  $\nabla^\mu\Gamma^\nu$ . Provided the gauge source functions do not depend on derivatives of the metric, they do not enter the principal part of the system and do not affect its well-posedness or numerical stability. The evolution system (7.141) then takes the specific form of quasi-linear wave equations (Babiuc *et al.*, 2006a; Szilágyi *et al.*, 2007)

$$\begin{aligned} 2\sqrt{-g}E^{\mu\nu} &= \partial_\alpha(g^{\alpha\beta}\partial_\beta\tilde{g}^{\mu\nu}) \\ &- 2\sqrt{-g}g^{\alpha\beta}g^{\delta\lambda}\Gamma_{\alpha\delta}^\mu\Gamma_{\beta\lambda}^\nu - \sqrt{-g}(\partial_\alpha g^{\alpha\beta})(\partial_\beta g^{\mu\nu}) + \frac{g^{\alpha\beta}}{\sqrt{-g}}(\partial_\alpha g^{\mu\nu})(\partial_\beta g) \\ &+ \frac{1}{2}g^{\mu\nu}\left(\frac{g^{\alpha\beta}}{2g\sqrt{-g}}(\partial_\alpha g)(\partial_\beta g) + \sqrt{-g}\Gamma_{\alpha\beta}^\delta\partial_\delta g^{\alpha\beta} + \frac{1}{\sqrt{-g}}(\partial_\beta g)(\partial_\alpha g^{\alpha\beta})\right) \\ &+ 2\sqrt{-g}\nabla^{(\mu}F^{\nu)} - \sqrt{-g}g^{\mu\nu}\nabla_\alpha F^\alpha + \sqrt{-g}A^{\mu\nu} - 16\pi\sqrt{-g}T^{\mu\nu}, \end{aligned} \quad (7.142)$$

where the first line isolates the wave-like principal part. In analogy with the constraint-damping schemes discussed in Section 7.2.3, also for the generalised harmonic formulation it is possible to introduce a constraint-adjustment term that vanishes when the constraints are satisfied. In Eqs. (7.142) such a term is represented by the tensor  $A^{\mu\nu}$ , which does not affect the principal part of the evolution system and is generically defined as

$$A^{\mu\nu} := C^\alpha B^{\mu\nu}_\alpha, \quad (7.143)$$

with the term  $B^{\mu\nu}_\alpha$  being, in general, a function of position, of the metric and of its first derivative, *i.e.*,  $B^{\mu\nu}_\alpha = B^{\mu\nu}_\alpha(x^\delta, g_{\delta\gamma}, \partial_\tau g_{\delta\gamma})$ . The harmonic constraints (7.140) do not need to be enforced explicitly during a numerical evolution. Rather, it is possible to use the Bianchi identities, which imply that the constraints obey wave equations of the form

$$g^{\alpha\beta}\partial_\alpha\partial_\beta C^\mu + L^{\mu\alpha}_\beta\partial_\alpha C^\beta + M^\mu_\beta C^\beta = 0, \quad (7.144)$$

where the tensors  $L$  and  $M$  are functions of the metric and its first and second derivatives. Given constraint-preserving initial and boundary conditions, the uniqueness of the solutions to Eqs. (7.144) guarantees that the harmonic constraints will be conserved during the evolution. Expressions for the constraint adjustments  $A_{\mu\nu}$  have been investigated by Babiuc *et al.* (2006b) and employed for simulations of binary black holes in quasi-circular orbit by Szilágyi *et al.* (2007). They are expressed as

$$A^{\mu\nu} := -\frac{a_1}{\sqrt{-g}}C^\delta\partial_\delta\tilde{g}^{\mu\nu} + \frac{a_2C^\delta\nabla_\delta t}{\varepsilon + e_{\alpha\beta}C^\alpha C^\beta}C^\mu C^\nu - \frac{a_3}{\sqrt{-g}t}C^{(\mu}\nabla^{\nu)}t, \quad (7.145)$$

where  $a_i > 0$  are adjustable parameters,  $e_{\sigma\tau}$  is a metric of signature  $(+++)$  and  $\varepsilon$  is a small positive number chosen to ensure numerical regularity. The effects of these adjustments is to

suppress long-wavelength instabilities as shown in standardised tests with periodic boundary conditions by Babuć *et al.* (2006b).

As noted earlier, the gauge source functions  $F^\mu$  can be chosen to be arbitrary functions of the spacetime coordinates and of the metric and thus viewed as differential gauge conditions on the *densitised metric*  $\tilde{g}$ . However, in order not to affect the wave-like principal part, the gauge source functions cannot depend on the derivatives of the *metric*  $g$ . This represents a serious restriction as it does not allow for simple gauge prescriptions which would depend, for instance, on the location or shape of marginally trapped surfaces that may be present, or which would allow the coordinates to “respond” dynamically to the changes in the spacetime. A direct consequence of this restriction is that the generalised harmonic gauges cannot deal with the physical singularity inside the apparent horizon. As a result, at least for the gauges considered so far, *e.g.*, by Pretorius (2005b) or by Szilágyi *et al.* (2007), the evolution of black holes requires the use of *excision techniques*, that is, of techniques in which no solution is sought in the portion of the computational domain interior to an apparent horizon, which is then treated as an excision boundary. In turn, this requires the use of suitable and non-trivial numerical algorithms which allow one to excise a region of the computational domain whose position in general changes in time (Szilágyi *et al.*, 2007).

Because the gauge functions  $F^\mu$  do not have a direct geometrical interpretation, their specification is not simple and often they are the result of a series of trial and error. One example of gauge source functions successfully used in numerical simulations are (Szilágyi *et al.*, 2007)

$$F^\mu = \frac{\omega}{\sqrt{-g}} (\tilde{g}^{t\mu} - \eta^{t\mu}), \quad (7.146)$$

where  $\eta^{\mu\nu}$  is the flat spacetime metric and where  $\omega = \omega(x^i)$  is a smooth, spherically symmetric, time-independent weighting function with  $\omega = 1$  over most of the computational domain, but with  $\omega = 0$  in some neighbourhood of the outer boundary. When spatial derivatives are neglected and  $\omega = 1$ , the resulting gauge condition takes the simpler form

$$\partial_t \tilde{g}^{t\mu} = -(\tilde{g}^{t\mu} - \eta^{t\mu}), \quad (7.147)$$

showing that it forces the densitised lapse and shift to relax to their flat spacetime values.

As reported above, the evolution equations (7.142) are a second-order-in-time system of partial differential equations and a similar system has been employed for the first successful calculations of binary black holes (Pretorius, 2005a). However, it is often more convenient to reduce the system to first-order-in-time and employ techniques such as the “method of lines” to carry out the integration in time (see Section 9.5).<sup>13</sup> In this case, as is customary when reducing the order of a system of partial differential equations, we introduce the auxiliary variables

$$\hat{Q}^{\mu\nu} := g^{tt} \partial_t \tilde{g}^{\mu\nu} + w g^{ti} \partial_i \tilde{g}^{\mu\nu}, \quad (7.148)$$

where  $w = w(x^i)$ , just like  $\omega(x^i)$  in (7.146), is again a smooth weighting function which is unit over most of the computational domain but zero in a neighbourhood of the outer boundary.

<sup>13</sup>The reduction to first order in time can be done in a number of ways, with very different stability properties when discretised; see Szilágyi *et al.* (2007) for a discussion.

### 350 Formulations of the Einstein–Euler Equations

We next invert the definition (7.148) to obtain the time derivatives of  $\tilde{g}^{\mu\nu}$  in terms of  $\hat{Q}^{\mu\nu}$  and of the spatial derivatives of  $\tilde{g}^{\mu\nu}$

$$\partial_t \tilde{g}^{\mu\nu} = \frac{1}{g^{tt}} \left( \hat{Q}^{\mu\nu} - w g^{ti} \partial_i \tilde{g}^{\mu\nu} \right), \quad (7.149)$$

and use it to re-express the principal part of the harmonic evolution equations (7.142) as

$$\partial_\alpha (g^{\alpha\beta} \partial_\beta \tilde{g}^{\mu\nu}) = \partial_t \hat{Q}^{\mu\nu} + (1-w) \partial_t (g^{ti} \partial_i \tilde{g}^{\mu\nu}) + \partial_i (g^{it} \partial_t \tilde{g}^{\mu\nu}) + \partial_i (g^{ij} \partial_j \tilde{g}^{\mu\nu}). \quad (7.150)$$

Finally, using (7.149) to convert all time derivatives of  $\tilde{g}^{\mu\nu}$  in (7.150) and (7.142) into spatial derivatives, we obtain an equation of the form

$$\partial_t \hat{Q}^{\mu\nu} = F^{\mu\nu}(\tilde{g}, \partial_i \tilde{g}, \partial_{ij} \tilde{g}, \hat{Q}, \partial_i \hat{Q}), \quad (7.151)$$

which represents the basic evolution equations for the field variables  $\hat{Q}^{\mu\nu}$  and  $\tilde{g}^{\mu\nu}$ , respectively (Szilágyi *et al.*, 2007).

The determination of the initial data in the case of a generalised harmonic formulation is not very different from the one discussed in the previous section for the ADM system. In this case, however, since what is needed is the knowledge of the four-metric  $g_{\mu\nu}$  and of its time derivative  $\partial_t g_{\mu\nu}$ , the determination of the three-metric  $\gamma_{ij}$  and of the extrinsic curvature  $K_{ij}$  through Eqs. (7.81) and (7.83) will not be sufficient. Indeed, these quantities will have to be accompanied by a time derivative of the metric [which can be computed via Eq. (7.66)], and also by a prescription for the lapse function  $\alpha$  and for the shift vector  $\beta^i$ , and of their time derivatives [*cf.*, the line element (7.12)]. As we will discuss in Section 7.2.6, there are ways to prescribe the lapse and the shift (and their time derivatives), and hence fully specify the initial data within a generalised harmonic formulation.

The appealing mathematical properties of the generalised harmonic formulation have resulted in a number of successful numerical relativity calculations in vacuum [see, *e.g.*, Pretorius (2005b); Szilágyi *et al.* (2007)] and non-vacuum spacetimes [see, *e.g.*, Anderson *et al.* (2008); Duez *et al.* (2008); Stephens *et al.* (2011)]. At the same time, however, the need to excise parts of the computational domain and the delicate prescription of robust gauge conditions makes the generalised harmonic formulation less widely adopted than the conformal-traceless one discussed in Section 7.2.3.

#### 7.2.6 Constraint equations, initial data and constrained evolution

Computing accurate initial data represents of course the starting point of any numerical evolution and the variants to this problem are numerous, both in terms of the different mathematical prescriptions possible and of the various physical/astrophysical scenarios. When the fluid flow is relativistic but the fluid can be considered as non-selfgravitating on a known fixed spacetime, the specification of the initial data is simpler (though not trivial) and a number of examples will be illustrated in Chapter 11. On the other hand, when the fluid is selfgravitating and providing an important contribution to the spacetime curvature, the calculation of the initial conditions entails the solution of the constraint equations

$${}^{(3)}R + K^2 - K_{ij}K^{ij} = 16\pi E, \quad (7.81)$$

$$D_j(K^{ij} - \gamma^{ij}K) = 8\pi S^i. \quad (7.83)$$

In Section 7.2.2 we have anticipated that these can be written as a system of four elliptic equations that do not depend on time and whose solution on a given hypersurface  $\Sigma_t$  provides the *initial data* for the evolution of the Einstein equations to  $t > 0$ . It is not our interest here to provide a complete coverage of the various aspects of the complex ‘‘art’’ of specifying initial conditions, and we refer the interested reader to the comprehensive review of Cook (2000), or to the dedicated discussions by Alcubierre (2008), Baumgarte and Shapiro (2010) and Gourgoulhon (2012), where specific applications are presented. For completeness, however, we will introduce in this section those rudimentary concepts which can serve as a basis for more specialist discussions. These concepts will also provide us with the background necessary to introduce an interesting example of a formulation of the Einstein equations suited for *constrained evolutions*.

#### **The York–Lichnerowicz conformal traceless decomposition.**

We have seen that when cast into a 3+1 decomposition, the six time-dependent second-order Einstein equations can be written as two sets of evolution equations for, say, the three-metric,  $\gamma_{ij}$ , and the extrinsic curvature,  $K_{ij}$  (see Section 7.2.2). Since both tensors are symmetric, we generically end up with 12 evolution equations requiring the specification of 12 initial conditions. Clearly, the constraint equations (7.81) and (7.83) can provide information about only four, thus leaving the remaining eight unspecified. Four more initial values can be set after a choice for the gauges is made, so that the remaining four degrees of freedom represent the genuine degrees of freedom in the theory, *e.g.*, the two degrees of polarisation of a gravitational wave in general relativity. With the exception of some simple cases in linearised theory, however, the problem remains on how to select among the 12 initial values for  $\{\gamma_{ij}, K_{ij}\}$ , the eight ones that can be taken as ‘‘free’’ data and the four ones that need to be ‘‘constrained’’ via the Eqs. (7.81) and (7.83). In particular, a procedure is needed to select the ‘‘longitudinal’’ parts of the initial fields, which can be constrained on an initial slice, from the ‘‘transverse’’ parts of the fields, which being dynamical (*e.g.*, the gravitational-wave content) cannot be constrained initially. Although such a clean distinction is not possible under generic conditions because of the nonlinear nature of the Einstein equations, a procedure can be employed in which  $\gamma_{ij}$  and  $K_{ij}$  are decomposed into quantities that are constrained and into others that are freely specifiable. Such a procedure is also known as the York–Lichnerowicz conformal decomposition [Lichnerowicz (1944) and York (1971), York (1972)] and can be thought of as an approximate split of the longitudinal and transverse parts of the initial fields.

The starting point in the York–Lichnerowicz conformal decomposition is the introduction of a conformal metric, which we here indicate with a bar, and is given by

$$\bar{\gamma}_{ij} := \psi^{-4} \gamma_{ij}. \quad (7.152)$$

Note that we use a bar in place of a tilde and a different symbol ( $\psi$  instead of  $\phi$ ) for the conformal factor to distinguish the conformal transformation (7.152) from the similar but distinct one presented in Eq. (7.93) for the conformal traceless formulations of the Einstein evolution equations. Note also that the volume element of  $\bar{\gamma}$  is *not* assumed to be unit, as it was for  $\tilde{\gamma}$  [*cf.* Eq. (7.94)], so that the physical volume is fixed by

### 352 Formulations of the Einstein–Euler Equations

$$\bar{\gamma} := \det(\bar{\gamma}_{ij}) = \psi^{-12} \gamma. \quad (7.153)$$

Using now the trace-free part of the extrinsic curvature  $A^{ij} := K^{ij} - \frac{1}{3}\gamma^{ij}K$  [cf., Eq. (7.96)], we can rewrite the Hamiltonian constraint (7.81) as

$$8\bar{D}^2\psi - \bar{R}\psi + \psi^5 \left( A^{ij}A_{ij} - \frac{2}{3}K^2 \right) + 16\pi\psi^5 E = 0, \quad (7.154)$$

where  $\bar{D}_i$  is the covariant derivative with respect to  $\bar{\gamma}$  and where  $\bar{D}^2 := \bar{\gamma}^{ij}\bar{D}_i\bar{D}_j$  is the corresponding Laplacian. Similarly, the momentum constraints (7.83) can be expressed as

$$D_j A^{ij} - \frac{2}{3}D^i K - 8\pi S^i = 0. \quad (7.155)$$

Next, given a generic symmetric trace-free tensor  $U^{ij}$ , we decompose it into a transverse (*i.e.*, divergence-free) and longitudinal part

$$U^{ij} = U_{TT}^{ij} + U_L^{ij} = U_{TT}^{ij} + (\mathbf{LW})^{ij}, \quad (7.156)$$

where  $U_{TT}^{ij}$  is a *transverse* symmetric and trace-free tensor, *i.e.*,  $\gamma_{ij}U_{TT}^{ij} = 0 = D_j U_{TT}^{ij}$ , and  $\mathbf{L}$  is the *longitudinal operator* (or *conformal Killing operator*) acting on the generic vector  $W^i$  and defined as<sup>14</sup>

$$(\mathbf{LW})^{ij} := 2D^{(i}W^{j)} - \frac{2}{3}\gamma^{ij}D_k W^k. \quad (7.157)$$

Similarly, using the conformal metric (7.152), it is possible to rewrite the trace-free extrinsic curvature as

$$\bar{A}^{ij} = \psi^{10} A^{ij}, \quad \bar{A}_{ij} = \psi^2 A_{ij}, \quad (7.158)$$

where the power 10 in the conformal factor  $\psi$  of (7.158)<sub>1</sub> has been chosen because it leads to the simplest expression for the spatial covariant derivative of any symmetric trace-free tensor  $U^{ij}$ , which has the form

$$D_j U^{ij} = \psi^{-n} \bar{D}_j (\psi^n U^{ij}) + (10-n)U^{ij} \partial_j \ln \psi, \quad (7.159)$$

with  $n$  an integer. As a result, the momentum constraint equations (7.155) can be written as

$$\bar{D}_j \bar{A}^{ij} - \frac{2}{3}\psi^6 \bar{D}^i K - 8\pi\psi^{10} S^i = 0. \quad (7.160)$$

If we now split  $\bar{A}^{ij}$  into its transverse and longitudinal parts, *i.e.*,

$$\bar{A}^{ij} = \bar{A}_{TT}^{ij} + (\bar{\mathbf{L}}\bar{W})^{ij}, \quad (7.161)$$

where  $\bar{\mathbf{L}}$  is the conformal Killing operator relative to  $\bar{\gamma}$ , the first term of the differential operator in (7.160) will be trivial, *i.e.*,  $\bar{D}_j \bar{A}_{TT}^{ij} = 0$ , while the second one can be written as

<sup>14</sup>If  $W^i$  is such that  $(\mathbf{LW})^{ij} = 0$ , then the vector is said to be a *conformal Killing vector*.

$$\begin{aligned}\bar{D}_j(\bar{\mathbf{L}}\bar{W})^{ij} &:= (\bar{\Delta}_{\bar{\mathbf{L}}} W)^i = \bar{D}^2 W^i + \bar{D}_j \bar{D}^i W^j - \frac{2}{3} \bar{D}^i \bar{D}_j W^j \\ &= \bar{D}^2 \bar{W}^i + \frac{1}{3} \bar{D}^i \bar{D}_j \bar{W}^j + \bar{R}^i{}_j \bar{W}^j,\end{aligned}\quad (7.162)$$

where the operator  $\bar{\Delta}_{\bar{\mathbf{L}}}$  is the *vector Laplacian* and in the last equality we have made use of the conformal Ricci tensor  $\bar{R}^i{}_j$  to commute the covariant derivatives. Because the construction of a transverse tensor to be used as a free variable is not trivial, it is better to operate with a generic tensor,  $\bar{M}^{ij}$ , which is trace-free, symmetric and whose transverse trace-free part coincides with that of the conformal extrinsic curvature, *i.e.*,

$$\bar{M}_{TT}^{ij} = \bar{M}^{ij} - (\bar{\mathbf{L}}\bar{Y})^{ij} = \bar{A}_{TT}^{ij}, \quad (7.163)$$

where  $\bar{Y}^i$  is some vector to be specified. As a result, the conformal extrinsic curvature (7.161) can be expressed as

$$\bar{A}^{ij} = \bar{A}_{TT}^{ij} + (\bar{\mathbf{L}}\bar{W})^{ij} = \bar{M}^{ij} + (\bar{\mathbf{L}}\bar{V})^{ij}, \quad (7.164)$$

where

$$\bar{V}^i := \bar{W}^i - \bar{Y}^i, \quad (7.165)$$

and where we have made use of the property that the conformal Killing operator is linear, *i.e.*,  $(\bar{\mathbf{L}}W)^{ij} - (\bar{\mathbf{L}}Y)^{ij} = (\bar{\mathbf{L}}(W - Y))^{ij}$ . Collecting things together, we write the conformal traceless decomposition of the Hamiltonian and momentum constraints (7.81) and (7.83) respectively as

$$8\bar{D}^2\psi - \bar{R}\psi + \psi^{-7}\bar{A}^{ij}\bar{A}_{ij} - \frac{2}{3}\psi^5 K^2 + 16\pi\psi^5 E = 0, \quad (7.166)$$

$$(\bar{\Delta}_{\bar{\mathbf{L}}} V)^i + \bar{D}_j \bar{M}^{ij} - \frac{2}{3}\psi^6 \bar{D}^i K - 8\pi\psi^{10} S^i = 0. \quad (7.167)$$

We have therefore reached the goal of isolating a set of four *constrained* variables, *i.e.*,  $\psi$ ,  $W^i$ , and another set of *freely* specifiable ones, *i.e.*,  $\bar{\gamma}_{ij}$ ,  $K$ ,  $\bar{M}_{ij}$ ,  $E$ ,  $S_j$ . Once a solution for Eqs. (7.166)–(7.167) is found in terms of the constrained variables, the three-metric and extrinsic curvature can be reconstructed as

$$\gamma_{ij} = \psi^4 \bar{\gamma}_{ij}, \quad (7.168)$$

$$K^{ij} = \psi^{-10} \bar{A}^{ij} + \frac{1}{3} \gamma^{ij} K = \psi^{-10} [\bar{A}_{TT}^{ij} + (\bar{\mathbf{L}}\bar{W})^{ij}] + \frac{1}{3} \gamma^{ij} K, \quad (7.169)$$

with  $\bar{W}^i = \bar{V}^i + \bar{Y}^i$ . Because Eqs. (7.166)–(7.167) are coupled, it is often convenient to use in place of  $E$  and  $S_j$ , the conformally related quantities  $\bar{E} := \psi^8 E$  and  $\bar{S}^i := \psi^{10} S^i$ , where the exponents in the conformal factors are chosen so as to remove an explicit dependence from the conformal factor in the matter term of the momentum constraints and simplify the decoupling from the Hamiltonian constraint. A decoupling is obtained also when considering a foliation which maintains  $K$  constant on what is then referred to as a *constant mean curvature* hypersurface. In this case, in fact, the momentum constraint decouples from the Hamiltonian

constraint and it is possible to solve the latter to obtain the three vectors  $\bar{V}^i$ , to reconstruct from them the conformal extrinsic curvature  $\bar{A}^{ij}$  and eventually solve the Hamiltonian constraint to compute  $\psi$ .

The calculation of initial data via the solution of the constraints simplifies considerably if, in addition to the assumption of a constant  $K$ , the additional assumption of a *conformally flat* metric is made (*i.e.*,  $\bar{\gamma}_{ij} = \delta_{ij}$  in Cartesian coordinates). This choice suppresses the presence of gravitational radiative fields on the initial hypersurface, but has the advantage that the Hamiltonian constraint (7.166) reduces to

$$8\bar{D}_{\text{flat}}^2\psi + \psi^{-7}\bar{A}^{ij}\bar{A}_{ij} - \frac{2}{3}\psi^5K^2 + 16\pi\psi^5E = 0, \quad (7.170)$$

where  $\bar{D}_{\text{flat}}^2$  is the Laplacian in a flat spacetime. Furthermore, if the physical problem under consideration can be considered to have time symmetry, then  $K_{ij} = 0$  on the initial hypersurface, the momentum constraints (7.167) are automatically satisfied and the Hamiltonian constraint is the only constraint to be solved, reducing to

$$\bar{D}_{\text{flat}}^2\psi = 0, \quad (7.171)$$

in a vacuum spacetime, such as the one containing one or more black holes.

The conformal traceless decomposition (7.166)–(7.167) provides a simple and clear route to formulate the constraint equations and is indeed the most common formulation of the initial-data problem in numerical relativity. However, it is by no means the only possible one. At least two variants of the approach discussed above are possible. A first one in which the decomposition of the trace-free extrinsic curvature  $A^{ij}$  is not made in terms of the conformal metric  $\bar{\gamma}$  as in (7.161), but in terms of the physical three-metric  $\gamma$ , and is therefore called the *physical transverse decomposition*. A second one was proposed more recently by Pfeiffer and York (2003) and is referred to as the *weighted transverse decomposition*. This latter approach can be regarded as an extension of the conformal thin-sandwich decomposition that we will discuss in more detail in the next section.

### **The conformal thin-sandwich decomposition.**

We have already anticipated in Section 7.2.2 that the constraint equations (7.81) and (7.83) do not depend on the lapse function  $\alpha$  and on the shift vector  $\beta^i$ , since they are specified on a single hypersurface only while the gauge functions express relations between neighbouring hypersurfaces. Yet, it can sometimes be advantageous to use the constraint equations to obtain information on these gauge quantities and in particular on the shift. This is indeed one of the results of the so-called *conformal thin-sandwich decomposition* (York, 1999), whose basic idea is rather simple: the specification of a constraint-satisfying three-metric  $\gamma_{ij}$  on two neighbouring spatial hypersurfaces  $\Sigma_t$  and  $\Sigma_{t+dt}$  (*i.e.*, the two slices of the “sandwich”) can be seen as the specification of the time derivative of the three-metric in the limit  $dt \rightarrow 0$ . In this way we gain information not only on the three-metric, but also on its rate of change.

We start therefore from the same conformal transformation (7.152),  $\bar{\gamma}_{ij} := \psi^{-4}\gamma_{ij}$ , and measure the time derivative of the conformal three-metric in terms of a new tensor

$$\bar{u}_{ij} := \partial_t\bar{\gamma}_{ij}. \quad (7.172)$$

Furthermore, we use  $\bar{u}_{ij}$  to require that the time variation of the conformal volume element is momentarily zero, *i.e.*,

$$\bar{\gamma}^{ij}\bar{u}_{ij} = 0. \quad (7.173)$$

Note that since the determinants of the conformal and of the physical metric are related as  $\bar{\gamma} = \psi^{-12}\gamma$ , Eq. (7.173) can be used to derive the following relation between the conformal factor and the determinant of the physical metric

$$12\partial_t \ln \psi = \partial_t \ln \gamma. \quad (7.174)$$

Next, we define another tensor  $u_{ij}$ , which measures instead the rate of change of the traceless physical metric

$$\begin{aligned} u_{ij} &:= \partial_t \gamma_{ij} - \frac{1}{3}\gamma_{ij}(\gamma^{kl}\partial_t \gamma_{kl}) = \psi^4 \bar{u}_{ij} \\ &= -2\alpha A_{ij} + (\mathbf{L}\beta)_{ij}, \end{aligned} \quad (7.175)$$

where the second equality has been derived after using the evolution equation for the three-metric (7.67). We can then use Eqs. (7.174) and (7.175) to rewrite expression (7.172) as

$$\begin{aligned} \bar{u}_{ij} &= \partial_t(\psi^{-4}\gamma_{ij}) = \psi^{-4}(\partial_t \gamma_{ij} - 4\gamma_{ij}\partial_t \ln \psi) \\ &= \psi^{-4}(\partial_t \gamma_{ij} - \frac{1}{3}\gamma_{ij}\partial_t \ln \gamma), \end{aligned} \quad (7.176)$$

and invert Eq. (7.175) to write the trace-free extrinsic curvature as

$$A^{ij} = \frac{1}{2\alpha} [(\mathbf{L}\beta)^{ij} - u^{ij}] = \frac{\psi^{-4}}{2\alpha} [(\bar{\mathbf{L}}\beta)^{ij} - \bar{u}^{ij}]. \quad (7.177)$$

Recalling now that the conformal and the physical traceless extrinsic curvatures are related as  $A^{ij} = \psi^{-10}\bar{A}^{ij}$  [*cf.* Eq. (7.158)], we finally obtain the expression relating  $\bar{A}^{ij}$  and  $\bar{u}^{ij}$ , *i.e.*,

$$\bar{A}^{ij} = \frac{1}{2\bar{\alpha}} [(\bar{\mathbf{L}}\beta)^{ij} - \bar{u}^{ij}], \quad (7.178)$$

where we have introduced the *conformal lapse* function  $\bar{\alpha} := \psi^{-6}\alpha$ . Having obtained explicit expressions for all of the free variables, we can finally rewrite the constraint equations in the conformal thin-sandwich decomposition as

$$8\bar{D}^2\psi - \bar{R}\psi + \psi^{-7}\bar{A}^{ij}\bar{A}_{ij} - \frac{2}{3}\psi^5 K^2 + 16\pi\psi^5 E = 0, \quad (7.166)$$

$$\bar{D}_j \left[ \frac{1}{2\bar{\alpha}} [(\bar{\mathbf{L}}\beta)^{ij} - \bar{u}^{ij}] \right] - \frac{2}{3}\psi^6 \bar{D}^i K - 8\pi\psi^{10} S^i = 0. \quad (7.179)$$

Note that the Hamiltonian constraint (7.166) has the same form as in the conformal traceless decomposition [*cf.* Eq. (7.166)], while the momentum constraints derive directly from (7.160) after using (7.178). In essence, we have cast the initial-data problem into an elliptic one for the constrained variables  $\psi$  and  $\beta^i$ , with freely specifiable data given by the conformal metric  $\bar{\gamma}_{ij}$ , its time derivative  $\bar{u}_{ij}$ , the trace of the extrinsic curvature  $K$ , the conformal lapse  $\bar{\alpha}$  and,

of course, the matter terms  $E$  and  $S^i$ . As before, once a solution for the constrained variables is known, the three-metric and extrinsic curvature can be reconstructed as

$$\gamma_{ij} = \psi^4 \bar{\gamma}_{ij}, \quad (7.168)$$

$$K^{ij} = \psi^{-10} \bar{A}^{ij} + \frac{1}{3} \gamma^{ij} K, \quad (7.169)$$

where  $\bar{A}^{ij}$  is given by (7.178).

Within the conformal thin-sandwich decomposition, therefore, the solution of the constraints provides us not only with a three-metric and an extrinsic curvature, but also with a shift vector  $\beta^i$  and a *physical lapse*  $\alpha = \psi^6 \bar{\alpha}$ . We thus obtain also a full specification of the gauge conditions, which we can either adopt or discard without harm, since the three-metric and extrinsic curvature would still be solutions of the constraints. Note that because the conformal lapse is freely specifiable, we could simply set  $\bar{\alpha} = 1$ . On the other hand, if we find this choice unsatisfactory, we could also obtain  $\bar{\alpha}$  as the solution of an additional elliptic equation after we specify the time derivative of the trace of the extrinsic curvature,  $\partial_t K$  (York, 1999).

### **The fully constrained formulation.**

Much of the material presented so far on the use of the constraint equations and of their formulation after a conformal decomposition can be used now to introduce a rather recent approach to the solution of the Einstein equations that makes extensive use of the constraint equations to attain the evolution from one spacelike hypersurface to the next. This formulation is still based on the 3+1 decomposition of the Einstein equations, but is different from all other “*free-evolution*” formulations discussed so far in that it maximises the number of elliptic equations to be solved at each time-step and minimises the number of hyperbolic equations by choosing an appropriate gauge condition. Because of this, it is referred to as the *fully constrained formulation (or FCF)* (Bonazzola *et al.*, 2004) and is composed of an “elliptic sector” and of a “hyperbolic sector”, with the latter containing only two degrees of freedom, which, far from the matter sources, correspond to the two degrees of freedom of the gravitational-radiation in the system. As we will discuss below, the fully constrained formulation represents the natural extension of the purely elliptic approach to the solution of the Einstein equations in the conformally flat approximation. This approach, which was initially proposed in 1978 by Isenberg (2008) and later on developed independently by Wilson and Mathews (1989), is usually referred to as the *Isenberg–Wilson–Mathews (or IWM)* formulation and is also sometimes encountered as the “*waveless*” approximation or *conformally flat condition (or CFC)*, for reasons that will become obvious in what follows.

Following Bonazzola *et al.* (2004), we introduce a time-independent flat metric  $f_{ij}$ , which satisfies  $\mathcal{L}_t f_{ij} = \partial_t f_{ij} = 0$  and coincides with  $\gamma_{ij}$  at spatial infinity. As done in Section 7.2.6, we further introduce the conformal metric  $\bar{\gamma}$  [cf., Eq. (7.152)], such that

$$f := \det(f_{ij}) = \bar{\gamma} := \det(\bar{\gamma}_{ij}), \quad (7.180)$$

and that [cf., Eq. (7.153)]

$$\psi = (\gamma/\bar{\gamma})^{1/12} = (\gamma/f)^{1/12}. \quad (7.181)$$

The deviation of the conformal metric from the flat fiducial one is then measured via the tensor  $h^{ij}$  [not to be confused with the projection tensor used extensively in the book and defined in Eq. (3.9)].

$$h^{ij} := \tilde{\gamma}^{ij} - f^{ij}. \quad (7.182)$$

In addition to the maximal slicing condition,  $K = 0$  [cf., Eq. (7.127)], the fully constrained formulation makes use of the so-called *generalised Dirac gauge*,

$$\mathcal{D}_i \tilde{\gamma}^{ij} = \mathcal{D}_i h^{ij} = 0, \quad (7.183)$$

where  $\mathcal{D}_k$  denotes the spatial covariant derivative associated with the flat metric  $f_{ij}$  [see, e.g., Bonazzola *et al.* (2004) for details]. The Einstein equations then become a coupled elliptic–hyperbolic system, with the elliptic sector acting on the variables  $\psi$ ,  $\alpha$  and  $\beta^i$  and with the hyperbolic sector acting on  $h^{ij}$ . We note that in the original formulation of Bonazzola *et al.* (2004),  $h^{ij}$  is evolved through a second-order-in-time system and, more specifically, the hyperbolic part is cast in terms of the evolution of two scalar quantities satisfying wave-like equations, from which  $h^{ij}$  is reconstructed after imposing the gauge conditions. Here, we will instead follow the more recent formulation of Cordero-Carrión *et al.* (2008), where the hyperbolic part is reduced to a first-order system and the elliptic subsystem is enlarged in order to address the uniqueness problems potentially associated to the resolution of elliptic equations.

In analogy with what was done in Section 7.2.6, we introduce the conformal decomposition [cf., Eq. (7.158)<sub>1</sub>]

$$\hat{A}^{ij} := \psi^{10} K^{ij}, \quad (7.184)$$

and its decomposition in longitudinal and transverse–traceless parts [cf., Eq. (7.161)]

$$\hat{A}^{ij} = (\mathbf{L}W)^{ij} + \hat{A}_{TT}^{ij}, \quad (7.185)$$

where, again, we have introduced the conformal Killing operator [cf., Eq. (7.157)], but this time acting on  $f$ , *i.e.*,

$$(\mathbf{L}W)^{ij} := 2\mathcal{D}^{(i} W^{j)} - \frac{2}{3} f^{ij} \mathcal{D}_k W^k, \quad (7.186)$$

and  $\mathcal{D}_i \hat{A}_{TT}^{ij} = 0$ . As a final step, we define

$$w^{ij}{}_k := \mathcal{D}_k \tilde{\gamma}^{ij}, \quad (7.187)$$

with  $w^{ij}{}_i = 0$  in the Dirac gauge, so that the hyperbolic system for  $h^{ij}$  can be written as a first-order-in-time system for the tensors  $h^{ij}$ ,  $\hat{A}^{ij}$ ,  $w^{ij}{}_k$ , *i.e.*, (Cordero-Carrión *et al.*, 2009)

**358 Formulations of the Einstein–Euler Equations**

$$\partial_t h^{ij} = 2\alpha\psi^{-6}\hat{A}^{ij} + \beta^k w^{ij}_k - \tilde{\gamma}^{ik}\mathcal{D}_k\beta^j - \tilde{\gamma}^{kj}\mathcal{D}_k\beta^i + \frac{2}{3}\tilde{\gamma}^{ij}\mathcal{D}_k\beta^k, \quad (7.188)$$

$$\begin{aligned} \partial_t \hat{A}^{ij} = & \mathcal{D}_k \left( \frac{\alpha\psi^2}{2} \tilde{\gamma}^{kl} w^{ij}_l + \beta^k \hat{A}^{ij} \right) - \hat{A}^{kj}\mathcal{D}_k\beta^i - \hat{A}^{ik}\mathcal{D}_k\beta^j \\ & + \frac{2}{3}\hat{A}^{ij}\mathcal{D}_k\beta^k + 2\alpha\psi^{-6}\tilde{\gamma}_{kl}\hat{A}^{ik}\hat{A}^{jl} \\ & - 8\pi\alpha\psi^6 \left( \psi^4 S^{ij} - \frac{S\tilde{\gamma}^{ij}}{3} \right) + \alpha \left( \psi^2 \tilde{R}_*^{ij} + 8\tilde{\gamma}^{ik}\tilde{\gamma}^{jl}\mathcal{D}_k\psi\mathcal{D}_l\psi \right) \\ & + 4\psi \left( \tilde{\gamma}^{ik}\tilde{\gamma}^{jl}\mathcal{D}_k\psi\mathcal{D}_l\alpha + \tilde{\gamma}^{ik}\tilde{\gamma}^{jl}\mathcal{D}_k\alpha\mathcal{D}_l\psi \right) \\ & - \frac{1}{3} \left[ \alpha \left( \psi^2 \tilde{R} + 8\tilde{\gamma}^{kl}\mathcal{D}_k\psi\mathcal{D}_l\psi \right) + 8\psi\tilde{\gamma}^{kl}\mathcal{D}_k\psi\mathcal{D}_l\alpha \right] \tilde{\gamma}^{ij} \\ & - \frac{1}{2} \left( \tilde{\gamma}^{ik}w^{lj}_k + \tilde{\gamma}^{kj}w^{il}_k \right) \mathcal{D}_l(\alpha\psi^2) - \tilde{\gamma}^{ik}\tilde{\gamma}^{jl}\mathcal{D}_k\mathcal{D}_l(\alpha\psi^2) \\ & + \frac{1}{3}\tilde{\gamma}^{ij}\tilde{\gamma}^{kl}\mathcal{D}_k\mathcal{D}_l(\alpha\psi^2), \end{aligned} \quad (7.189)$$

$$\partial_t w^{ij}_k = \mathcal{D}_k \left( 2\alpha\psi^{-6}\hat{A}^{ij} + \beta^l w^{ij}_l - \tilde{\gamma}^{il}\mathcal{D}_l\beta^j - \tilde{\gamma}^{lj}\mathcal{D}_l\beta^i + \frac{2}{3}\tilde{\gamma}^{ij}\mathcal{D}_l\beta^l \right), \quad (7.190)$$

where

$$\tilde{R} := \frac{1}{4}\tilde{\gamma}^{kl}\mathcal{D}_k h^{mn}\mathcal{D}_l\tilde{\gamma}_{mn} - \frac{1}{2}\tilde{\gamma}^{kl}\mathcal{D}_k h^{mn}\mathcal{D}_n\tilde{\gamma}_{ml}, \quad (7.191)$$

$$\begin{aligned} \tilde{R}_*^{ij} := & \frac{1}{2} \left[ -w^{ik}_l w^{jl}_k - \tilde{\gamma}_{kl}\tilde{\gamma}^{mn} w^{ik}_m w^{jl}_n + \tilde{\gamma}_{nl} w^{mn}_k (\tilde{\gamma}^{ik} w^{jl}_m + \tilde{\gamma}^{jk} w^{il}_m) \right] \\ & + \frac{1}{4}\tilde{\gamma}^{ik}\tilde{\gamma}^{jl} w^{mn}_k \mathcal{D}_l\tilde{\gamma}_{mn}, \end{aligned} \quad (7.192)$$

and  $S_{ij} := T_{\mu\nu}\gamma^\mu_i\gamma^\nu_j$  [cf., Eq. (7.76)], with  $S := \gamma^{ij}S_{ij}$  its trace.

Furthermore, the elliptic sector of the FCF equations is given by the system of elliptic equations (Cordero-Carrión *et al.*, 2009)

$$\tilde{\gamma}^{kl}\mathcal{D}_k\mathcal{D}_l\psi = -2\pi\psi^{-1}E^* - \frac{\tilde{\gamma}_{il}\tilde{\gamma}_{jm}\hat{A}^{lm}\hat{A}^{ij}}{8\psi^7} + \frac{\psi\tilde{R}}{8}, \quad (7.193)$$

$$\tilde{\gamma}^{kl}\mathcal{D}_k\mathcal{D}_l(\alpha\psi) = \left[ 2\pi\psi^{-2}(E^* + 2S^*) + \left( \frac{7\tilde{\gamma}_{il}\tilde{\gamma}_{jm}\hat{A}^{lm}\hat{A}^{ij}}{8\psi^8} + \frac{\tilde{R}}{8} \right) \right] (\alpha\psi), \quad (7.194)$$

$$\begin{aligned} \tilde{\gamma}^{kl}\mathcal{D}_k\mathcal{D}_l\beta^i + \frac{1}{3}\tilde{\gamma}^{ik}\mathcal{D}_k\mathcal{D}_l\beta^l = & 16\pi\alpha\psi^{-6}\tilde{\gamma}^{ij}(S^*)_j + \hat{A}^{ij}\mathcal{D}_j(2\alpha\psi^{-6}) \\ & - 2\alpha\psi^{-6}\Delta^i_{kl}\hat{A}^{kl}, \end{aligned} \quad (7.195)$$

where  $S_i := -\gamma^\mu_i T_{\mu\nu} n^\nu$  [cf., Eq. (7.77)],  $E := T_{\mu\nu} n^\mu n^\nu$  [cf., Eq. (7.79)],  $E^* := \psi^6 E$ ,  $S^* := \psi^6 S$ ,  $(S^*)_i := \psi^6 S_i$ , and we have introduced the tensor

$$\Delta^k_{ij} := \frac{1}{2} \tilde{\gamma}^{kl} (\mathcal{D}_i \tilde{\gamma}_{lj} + \mathcal{D}_j \tilde{\gamma}_{il} - \mathcal{D}_l \tilde{\gamma}_{ij}) . \quad (7.196)$$

It should be noted that the decomposition introduced in Eq. (7.185) leads to an additional elliptic equation for the vector  $W^i$

$$\begin{aligned} \mathcal{D}_j \mathcal{D}^j W^i + \frac{1}{3} \mathcal{D}^i \mathcal{D}_k W^k + \tilde{\gamma}^{im} \left( \mathcal{D}_k \tilde{\gamma}_{ml} - \frac{\mathcal{D}_m \tilde{\gamma}_{kl}}{2} \right) (\mathbf{L}W)^{kl} \\ = 8\pi \tilde{\gamma}^{ij} (S^*)_j - \tilde{\gamma}^{im} \left( \mathcal{D}_k \tilde{\gamma}_{ml} - \frac{\mathcal{D}_m \tilde{\gamma}_{kl}}{2} \right) \hat{A}_{TT}^{kl} , \end{aligned} \quad (7.197)$$

so that the evolution equation (7.189) is effectively an evolution equation for the tensor  $\hat{A}_{TT}^{ij}$ . Although the fully constrained formulation is rather recent and not widely diffused, promising first results have been reported by Cordero-Carrión *et al.* (2010).

Note that because in the fully constrained formulation the radiative degrees of freedom associated with the gravitational-wave field are neatly encoded in the tensor  $h^{ij}$ , it can be useful to assume  $h^{ij} = 0$  in those situations in which the strength of the gravitational waves is so small so as not to influence the properties of the spacetime. In these cases, the resulting three-metric  $\gamma_{ij}$  is *conformally flat* [cf., Eq. (7.182)], the spacetime is “waveless” by construction,<sup>15</sup> and the fully constrained formulation coincides with the conformally flat approximation. As a result, the hyperbolic sector is entirely suppressed and Eqs. (7.193)–(7.197) reduce to the simpler set of eight elliptic equations

$$\Delta \psi + 2\pi \psi^{-1} E^* + \frac{f_{il} f_{jm} \hat{A}^{lm} \hat{A}^{ij}}{8\psi^7} = 0 , \quad (7.198)$$

$$\Delta(\alpha\psi) - 2\pi\alpha\psi^{-1}(E^* + 2S^*) - \alpha\psi^{-7} \frac{7f_{il} f_{jm} \hat{A}^{lm} \hat{A}^{ij}}{8} = 0 , \quad (7.199)$$

$$\Delta\beta^i + \frac{1}{3} f^{ij} \mathcal{D}_j \mathcal{D}_k \beta^k - \mathcal{D}_j \left( 2\alpha\psi^{-6} \hat{A}^{ij} \right) = 0 , \quad (7.200)$$

$$\Delta W^i + \frac{1}{3} f^{ij} \mathcal{D}_j \mathcal{D}_k W^k - 8\pi f^{ij} (S^*)_j = 0 , \quad (7.201)$$

where  $\Delta := f^{ij} \mathcal{D}_i \mathcal{D}_j$  is the flat Laplacian.

If the spacetime has a modest radiation content, then there are a number of advantages in the use of the conformally flat approximation. First of all, in spherical symmetry it coincides with general relativity, thus providing a very accurate solution in all those scenarios involving quasi-spherical objects, such as isolated neutron stars or the collapse of stellar cores [see, e.g., Cerdá-Durán *et al.* (2007) and Bucciantini and Del Zanna (2011) for some recent developments]. Second, although it is not a post-Newtonian approximation, it has many analogies with a first-order post-Newtonian theory [1PN, Kley and Schäfer (1994)], thus allowing us

<sup>15</sup>Conformal flatness is not a necessary condition for a spacetime to be waveless. The Kerr spacetimes is waveless but does not admit a conformally flat slicing, while the Schwarzschild spacetime is also waveless but admits a conformally flat slicing. If conformal flatness is imposed only on a single spacelike hypersurface, e.g., when computing initial data, this does not guarantee that the spacetime will be waveless. Only the evolution of the conformally flat initial data can provide this information; indeed, conformally flat initial data does generally lead to what is known as “*junk radiation*” when evolved in time.

to recover the Newtonian limit correctly in the case of weak gravity. Third, although the numerical solution of elliptic equations is in general more complex, in non-vacuum spacetimes the time-step is limited by the sound speed instead of the speed of light, thus also increasing the computational costs. However, together with these advantages, the conformally flat approximation also has the non-negligible disadvantage that the gravitational-wave content of the spacetime is suppressed by construction. As a result, the calculation of the gravitational-wave emission, which is often a very important observable in this type of calculation, must be performed using more approximate expressions, such as the Newtonian quadrupole formula (Misner *et al.*, 1973).

Although the conformally flat approximation has been originally employed in the study of neutron-star binaries (Wilson *et al.*, 1996; Oechslin *et al.*, 2002), by far the most common application has been the study of the collapse of stellar cores, starting from the work of Dimmelmeier *et al.* (2001) till the more recent work of Mueller *et al.* (2010).

### 7.3 Formulations of the hydrodynamic equations

In all of the previous sections in this chapter we have illustrated the most common formulations of the Einstein equations used in numerical calculations. In our discussion we have assumed that the right-hand side of the Einstein equations is known, that is, that the properties of the matter as described by the energy–momentum tensor are known. In practice, however, this requires the solution of the relativistic-hydrodynamic equations expressing the evolution in time of rest-mass density, momentum and energy, *i.e.*, (see Section 3.3)

$$\nabla_\mu(\rho u^\mu) = 0, \quad (3.52)$$

$$\nabla_\nu T^{\mu\nu} = 0. \quad (3.53)$$

In the following four sections we will discuss the different formulations that have been derived over the years to solve numerically the relativistic-hydrodynamic equations. We will start with the non-conservative formulations developed in the 1970s and arrive at the more recent formulations in use in modern three-dimensional codes. Also in the case of the relativistic-hydrodynamic equations, we will discuss how finding the optimal formulation is far from obvious and explain why some formulations, which are apparently suitable, may lead to undesired behaviour. Luckily, two theorems in Section 7.3.2 will provide us with guidance about the properties that robust formulations, such as the conservative ones, should have.

#### 7.3.1 The Wilson formulation

Already in the 1970s, Wilson was pioneering the numerical solution of the relativistic-hydrodynamic equations in multidimensional codes and curved spacetimes, developing and implementing an Eulerian formulation that has subsequently been used by many authors (Wilson, 1972; Wilson, 1979). A full account of the developments of the formulation can be found in the recent monograph by Wilson and Mathews (2003), but we here recall that, after defining

the “*transport velocity*” as  $V^\mu := u^\mu/u^t$ , with  $V^t = 1$ , Wilson introduced the following basic dynamical variables

$$D := \rho u^t, \quad (7.202)$$

$$S_\mu := \rho h u^t u_\mu, \quad (7.203)$$

$$E := \rho u^t \epsilon \quad (7.204)$$

where, we recall,  $e, p, \rho$  and  $h = (e + p)/\rho$  represent the energy density, the pressure, the rest-mass density and the specific enthalpy, respectively. Note that the quantities defined in (7.202)–(7.204) represent respectively the conserved rest-mass density, the covariant momentum and the generalised internal energy density. Using these variables, the equations of conservation of rest mass (3.52) and of conservation of energy and momentum (3.53) can be written as

$$\frac{1}{\sqrt{-g}} \partial_t (\sqrt{-g} D) + \frac{1}{\sqrt{-g}} \partial_i (\sqrt{-g} D V^i) = 0, \quad (7.205)$$

$$\frac{1}{\sqrt{-g}} \partial_t (\sqrt{-g} S_\mu) + \frac{1}{\sqrt{-g}} \partial_i (\sqrt{-g} S_\mu V^i) + \partial_\mu p + \frac{1}{2} (\partial_\mu g^{\alpha\beta}) \left( \frac{S_\alpha S_\beta}{S^t} \right) = 0, \quad (7.206)$$

$$\partial_t (\sqrt{-g} E) + \partial_i (\sqrt{-g} E V^i) + p \partial_\mu (\sqrt{-g} u^t V^\mu) = 0, \quad (7.207)$$

and represent what is usually referred to as the *Wilson formulation* of the equations of relativistic hydrodynamics (Wilson, 1972; Wilson, 1979).

Note that when solving in practice the system (7.205)–(7.207), the momentum density equation (7.206) is solved only for the three spatial components  $S_i$ , while the temporal one  $S_t$  can be obtained through the normalisation condition of the four-velocity (3.2), which then yields  $S_\mu S^\mu = -(\rho h u^t)^2$ . Equations (7.205)–(7.207) are essentially written as a set of coupled advection equations, where the terms containing the spatial and time derivatives of the pressure are treated as source terms.

The Wilson formulation is *not* in conservative form (see Section 4.1.2) and this fact ultimately imposes the use of numerical dissipation to stabilise the solution across discontinuities or large gradients (we will say more on the importance of conservative formulations in Section 7.3.2). As a result, the first attempts to solve the equations of relativistic hydrodynamics with the Wilson formulation required the combined use of finite-difference upwind techniques together with terms representing *artificial viscosity* (Wilson, 1972). The technical aspects of this numerical approach will be described in more detail in Section 8.4, but it is sufficient to mention here that artificial-viscosity techniques amount to introducing a viscosity term which is added to the pressure and which acts in the same way as a physical bulk viscosity. The addition of artificial viscosity mimics in many respects what actually takes place in nature, where viscosity converts into internal energy the kinetic energy associated with high-frequency acoustic disturbances. However, the explicit expression of the artificial viscosity is coupled nonlinearly to the fluid velocity and this could rapidly lead to inaccurate numerical solutions when the flow becomes ultrarelativistic. In the case of one-dimensional flows, these inaccuracies appear for Lorentz factors  $W \gtrsim 2$  (Centrella and Wilson, 1984), or for flows with  $W \sim 10$  if a series of careful improvements are implemented in the numerical solution (Norman and Winkler, 1986).

More recently, Anninos and Fragile (2003) have compared the results of special and general-relativistic multidimensional simulations using either artificial-viscosity schemes employing the Wilson formulation, or high-order non-oscillatory central schemes using a conservative formulation of the relativistic-hydrodynamic equations.<sup>16</sup> The result of these comparisons essentially confirmed the conclusions reached with previous, simpler and lower-dimensional codes using explicit schemes (see Section 8.3 for a definition), namely, that in shock-tube tests the numerical solution using artificial viscosity becomes increasingly unstable for shock velocities  $V_s/c \gtrsim 0.95$  or  $W_s \gtrsim 4$ . A somewhat different conclusion is drawn in Section 2.4.1 of the book by Wilson and Mathews (2003). Given the large freedom allowed by the definition of the artificial viscosity and the recent development of improved artificial-viscosity methods discussed in Wilson and Mathews (2003), additional comparisons may be needed to settle this issue convincingly.

Overall, the Wilson formulation represents one of the most widely used formulations of the relativistic-hydrodynamic equations and it has been historically employed in a number of hydrodynamic codes investigating a large variety of relativistic configurations. Among these we should mention the first studies of cosmological flows (Centrella and Wilson, 1984; Anninos *et al.*, 1998) and of axisymmetric stellar collapse (Nakamura, 1981; Stark and Piran, 1985; Evans, 1986), the investigation of accretion flows onto compact objects (Hawley *et al.*, 1984; Petrich *et al.*, 1989) and, more recently, the inspiral and merger of neutron-star binaries (Wilson *et al.*, 1996; Mathews and Wilson, 2000). Furthermore, the formulation has also been employed by McAbee and Wilson (1994) in its special-relativistic form to study heavy-ion collisions. As mentioned above, however, one distinguishing feature of the Wilson formulation is that it *does not* cast the equations in conservative form; as we will discuss in the following section, this is potentially an important drawback.

### 7.3.2 The importance of conservative formulations

In Section 4.1 we have seen how the equations of relativistic hydrodynamics can be written in the generic first-order-in-time form [*cf.*, Eq. (4.9)]

$$\partial_t \mathbf{U} + \mathbf{A} \cdot \nabla \mathbf{U} + \mathbf{B} = 0, \quad (4.9)$$

and that the system above is said to be *hyperbolic* if the matrix of coefficients  $\mathbf{A}$  is diagonalisable with a set of real eigenvalues, or *eigenspeeds*,  $\lambda_1, \dots, \lambda_N$  and a corresponding set of  $N$  linearly independent *right eigenvectors*  $\mathbf{R}^{(1)}, \dots, \mathbf{R}^{(m)}$ , such that  $\mathbf{A}\mathbf{R}^{(i)} = \lambda_i \mathbf{R}^{(i)}$ ,  $\mathbf{\Lambda} := \mathbf{R}^{-1} \mathbf{A} \mathbf{R} = \text{diag}(\lambda_1, \dots, \lambda_N)$  is the diagonal matrix of eigenvalues and  $\mathbf{R}$  the matrix of right eigenvectors.

We have also seen that the most important property of *hyperbolic equations* is that they are *well-posed*, hence suitable for numerical solution. Moreover, in Section 4.1.2 we have discussed that if the matrix  $\mathbf{A}(\mathbf{U})$  is the Jacobian of a *flux vector*  $\mathbf{F}(\mathbf{U})$  with respect to the state vector  $\mathbf{U}$ , namely if  $\mathbf{A}(\mathbf{U}) := \partial \mathbf{F} / \partial \mathbf{U}$ , then the homogeneous version of the system (4.9) can be written in *conservative form* as

$$\partial_t \mathbf{U} + \nabla \mathbf{F}(\mathbf{U}) = 0, \quad (4.27)$$

<sup>16</sup>Postponing a more detailed discussion to Section 9.2.2, we here recall that a numerical method is said to be *non-oscillatory* if it does not increase the number of local extrema of the solution (*i.e.*, its “oscillations”).

where  $\mathbf{U}$  is therefore called the vector of *conserved variables*.

What we have not yet discussed, however, is the importance of using a conservative form of the equations when dealing with problems admitting shocks or other discontinuities in the solution. Such importance hinges on two important theorems that explore complementary aspects of the same issue. However, before discussing the theorems, we need a definition that would allow us to handle also solutions which would be otherwise mathematically problematic. It is quite obvious, in fact, that a discontinuous function, such as a solution to the Euler equations admitting shocks and with derivatives that are not defined at the shock, would not satisfy the hyperbolic partial differential equation in conservation form (4.27). For this reason, an alternative *integral* formulation can be adopted in order to rewrite a differential equation in a form that would admit also non-smooth “solutions”. The basic idea, therefore, is that of multiplying the partial differential equation (4.27) by a smooth test function  $\phi$  with compact support in space and of integrating it by parts to move the derivatives from the function  $\mathbf{U}$  over to the test function  $\phi$ . More specifically, if we consider the simpler case of one spatial dimension only, Eq. (4.27) can be written as

$$\partial_t \mathbf{U} + \partial_x \mathbf{F} = 0, \quad (7.208)$$

so that if we multiply it by a continuously differentiable function  $\phi(x, t)$  of compact support, the integration over space, with  $x \in (-\infty, \infty)$ , and time, with  $t \in [0, \infty)$ <sup>17</sup>, will lead to

$$\int_0^\infty \int_{-\infty}^{+\infty} [\phi \partial_t \mathbf{U} + \phi \partial_x \mathbf{F}] dx dt = 0. \quad (7.209)$$

Integration by parts both in time and in space then leads to

$$\int_{-\infty}^{+\infty} \phi \mathbf{U} dx \Big|_{t=0}^{t=\infty} + \int_0^\infty \phi \mathbf{F} dt \Big|_{x=-\infty}^{x=+\infty} - \int_0^\infty \int_{-\infty}^{+\infty} [\mathbf{U} \partial_t \phi + \mathbf{F} \partial_x \phi] dx dt = 0, \quad (7.210)$$

and thus to

$$\int_0^\infty \int_{-\infty}^{+\infty} [\mathbf{U} \partial_t \phi + \mathbf{F} \partial_x \phi] dx dt = - \int_{-\infty}^{+\infty} \phi(x, 0) \mathbf{U}(x, 0) dx, \quad (7.211)$$

where we have used the property that  $\phi$  has compact support and therefore

$$\phi(x, t = \infty) = 0 = \phi(x = -\infty, t) = \phi(x = +\infty, t). \quad (7.212)$$

A function  $\mathbf{U}$  is then called a *weak solution* of the conservative equation (7.208) if it satisfies the so-called *weak formulation* (7.211) for all functions  $\phi$ . As a result, also solutions involving discontinuities can be taken as weak solutions of the conservation equation.

With this definition in mind, we are ready to discuss two theorems underlining the importance of a conservative formulation. The first one is due to Lax and Wendroff (1960) and loosely speaking states that: *conservative numerical schemes,<sup>18</sup> if convergent, do converge to*

<sup>17</sup>As done throughout the book, we are here assuming that  $t \in [0, \infty)$  but the arguments apply unchanged also if  $t \in (-\infty, \infty)$ , in which case the right-hand side of Eq. (7.211) is zero.

<sup>18</sup>The notion of a conservative numerical scheme will be made rigorous in Section 9.1, but for the time being it can be regarded simply as a numerical scheme based on the conservative formulation of the equations.

*the weak solution of the problem.* The second theorem is instead due to Hou and LeFloch (1994), and states instead that: *non-conservative schemes, i.e., schemes in which the equations are not written in the conservative form (4.27), do not converge to the correct solution if a shock wave is present in the flow.*

In other words, the two theorems above state that if a conservative formulation *is used*, then we are guaranteed that the numerical solution will converge to the correct one, while if a conservative formulation *is not used*, we are guaranteed to converge to the incorrect solution in the likely event in which the flow develops a discontinuity.

A well-known example of the importance of a conservative formulation is provided by the Burgers equation (see Section 4.2.3) whose non-conservative representation

$$\partial_t u + u \partial_x u = 0 \quad (4.72)$$

fails dramatically in providing the correct propagation velocity of a shock wave that might form during the evolution [see, *e.g.*, LeVeque (1992) for an extended discussion]. On the other hand, the solution of the conservative formulation of the Burgers equation (4.72), *i.e.*,

$$\partial_t u + \partial_x \left( \frac{1}{2} u^2 \right) = 0, \quad (7.213)$$

leads to the correct propagation velocity with essentially all numerical schemes evolving smooth initial data.

Overall, the two theorems above represent important guidelines for the use and development of conservative formulations of the relativistic-hydrodynamic equations, as we discuss below.

### 7.3.3 The 3+1 “Valencia” formulation

Starting in the 1990s, Martí, Ibáñez and Miralles (Martí *et al.*, 1991) presented an Eulerian formulation of the relativistic-hydrodynamic equations that distinguished itself from the Wilson formulation in being written in conservative form. The new formulation was aimed at taking advantage of the hyperbolic and conservative character of the equations to import a series of numerical tools already developed in classical (Newtonian) hydrodynamics and based on the characteristic fields of the system. Much of Chapter 9 will be dedicated to illustrating the mathematical and numerical properties of these schemes, which are collectively referred to as *high-resolution shock-capturing (HRSC) methods*. Here, on the other hand, we will concentrate on the derivation of the conservative formulation that has now become the most widely-used in relativistic-hydrodynamics codes and on illustrating its mathematical properties.

We start by recalling that Banyuls *et al.* (1997) showed that the system of equations of relativistic hydrodynamics (3.52), (3.53), can be cast in conservative form after the introduction of a suitable set of *conserved variables*. To understand the logic of the procedure that leads from the covariant formulation of the relativistic-hydrodynamic equations (3.52)–(3.53) over to the conservative one (4.27), let us consider first the continuity equation (3.52), which is indeed already in conservative form but does not make use of the conservative variables yet.

In this case the procedure is simple and all we need to do is to exploit the identity for the divergence of a four-vector to obtain [*cf.*, Eq. (1.166)]

$$\begin{aligned}\nabla_\mu(\rho u^\mu) &= \frac{1}{\sqrt{-g}}\partial_\mu(\sqrt{-g}\rho u^\mu) \\ &= \frac{1}{\sqrt{-g}}[\partial_t(\sqrt{-g}\rho u^t) + \partial_i(\sqrt{-g}\rho u^i)] = 0.\end{aligned}\quad (7.214)$$

It is now natural to define as *conserved variable* the quantity

$$D := \rho\alpha u^t = \rho W,\quad (7.215)$$

and to rewrite (7.214), using also the definition of the Eulerian three-velocity (7.22) and the identity (7.16), as

$$\partial_t(\sqrt{\gamma}D) + \partial_i[\sqrt{\gamma}D(\alpha v^i - \beta^i)] = 0.\quad (7.216)$$

Before considering the corresponding conservative form of the energy and momentum equations, it is useful to write the energy-momentum tensor in terms of quantities measured by normal observers in a 3+1 decomposition of spacetime. We can then recall that we have defined  $E := n_\mu n_\nu T^{\mu\nu}$  as the component of the energy-momentum tensor  $\mathbf{T}$  fully projected along the unit normal  $\mathbf{n}$  to the spatial hypersurface  $\Sigma_t$  [*cf.*, Eq. (7.79)], while  $S^{\mu\nu} := \gamma^\mu{}_\alpha \gamma^\nu{}_\beta T^{\alpha\beta}$  as the projection of  $\mathbf{T}$  in the space orthogonal to  $\mathbf{n}$  [*cf.*, Eq. (7.76)] and  $S^\mu := -\gamma^\mu{}_\alpha n_\beta T^{\alpha\beta}$  as the mixed parallel-transverse component of  $\mathbf{T}$  [*cf.*, Eq. (7.77)], we can rewrite the energy-momentum tensor of a perfect fluid as [*cf.*, Eq. (3.36)]

$$T^{\mu\nu} = (e + p)u^\mu u^\nu + pg^{\mu\nu}\quad (3.36)$$

$$= En^\mu n^\nu + S^\mu n^\nu + S^\nu n^\mu + S^{\mu\nu}.\quad (7.217)$$

In addition, we can also rewrite the equivalent expression (3.197) for the energy-momentum tensor by replacing the four-velocity by its decomposed form (7.23)  $u^\mu = W(n^\mu + v^\mu)$  and by replacing the metric with its 3+1 decomposed expression, namely,  $g^{\mu\nu} = \gamma^{\mu\nu} - n^\mu n^\nu$ . In this way we obtain

$$T^{\mu\nu} = \rho h u^\mu u^\nu + pg^{\mu\nu}\quad (3.197)$$

$$= \rho h W^2(n^\mu + v^\mu)(n^\nu + v^\nu) + p(\gamma^{\mu\nu} - n^\mu n^\nu).\quad (7.218)$$

After rearranging terms, a simple comparison between expressions (7.217) and (7.218) allows one to recognise that<sup>19</sup>

$$S^{\mu\nu} = \rho h W^2 v^\mu v^\nu + p \gamma^{\mu\nu},\quad (7.219)$$

$$S^\mu = \rho h W^2 v^\mu,\quad (7.220)$$

$$E = \rho h W^2 - p.\quad (7.221)$$

<sup>19</sup>Note that we use here the same symbol for  $S^\mu$  as in the Wilson formulation, although they obviously refer to different quantities [*cf.*, Eq. (7.203)].

### 366 Formulations of the Einstein–Euler Equations

The next step consists in writing the four-divergence of a symmetric rank-2 tensor as [see, e.g., Section 2.10 of de Felice and Clarke (1990)]

$$\nabla_\mu T^{\mu\nu} = g^{\nu\lambda} \left[ \frac{1}{\sqrt{-g}} \partial_\mu (\sqrt{-g} T^\mu_{\lambda}) - \frac{1}{2} T^{\alpha\beta} \partial_\lambda g_{\alpha\beta} \right], \quad (7.222)$$

which, when applied to the energy–momentum tensor and when using the conservation of energy and momentum (3.53), leads to

$$\frac{1}{\sqrt{-g}} \partial_\mu (\sqrt{-g} T^\mu_{\nu}) = \frac{1}{2} T^{\mu\lambda} \partial_\nu g_{\mu\lambda}. \quad (7.223)$$

It is now just a matter of substituting the decomposed form (7.217) in the above equation (7.223), restricting the free index  $\nu$  to a spatial index  $j$ , to obtain the conservative form of the momentum equation in a generically curved spacetime

$$\partial_t (\sqrt{\gamma} S_j) + \partial_i [\sqrt{\gamma} (\alpha S^i_j - \beta^i S_j)] = \frac{1}{2} \sqrt{-g} T^{\mu\nu} \partial_j g_{\mu\nu}. \quad (7.224)$$

The energy equation, on the other hand, is obtained after contracting (3.53) with  $n_\nu$ , namely

$$\nabla_\mu (T^{\mu\nu} n_\nu) - T^{\mu\nu} \nabla_\mu n_\nu = 0, \quad (7.225)$$

and by replacing  $T^{\mu\nu}$  with its decomposed form (7.217). After a bit of algebra it is then possible to obtain the conservative form of the energy equation in a generically curved spacetime

$$\partial_t (\sqrt{\gamma} E) + \partial_i [\sqrt{\gamma} (\alpha S^i - \beta^i E)] = -\sqrt{-g} T^{\mu\nu} \nabla_\mu n_\nu. \quad (7.226)$$

Both in Eq. (7.224) and in Eq. (7.226) there are *source terms* on the right-hand side that deserve some more attention. First of all, they do not contain differential operators acting on the thermodynamic variables of the fluid, a key feature to yield a conservative formulation and preserve the hyperbolic character of the system. Second, the source terms of the momentum equation (7.224) can be written more explicitly as

$$\begin{aligned} \frac{1}{2} \sqrt{-g} T^{\mu\nu} \partial_j g_{\mu\nu} &= \sqrt{-g} \left( \frac{1}{2} S^{ik} \partial_j \gamma_{ik} + S^\mu n^\nu \partial_j g_{\mu\nu} + \frac{1}{2} E n^\mu n^\nu \partial_j g_{\mu\nu} \right) \\ &= \sqrt{-g} \left( \frac{1}{2} S^{ik} \partial_j \gamma_{ik} + \frac{1}{\alpha} S_i \partial_j \beta^i - E \partial_j \ln \alpha \right), \end{aligned} \quad (7.227)$$

where we have used

$$\partial_j g_{\mu\nu} = \Gamma_{j\nu}^\kappa g_{\mu\kappa} + \Gamma_{j\mu}^\kappa g_{\kappa\nu}, \quad (7.228)$$

which follows from Eq. (1.164) and from the identity  $n^\mu \nabla_j n_\mu = 0$ . Finally, the source terms for the energy equation (7.226) can also be computed explicitly as

$$-\sqrt{-g} T^{\mu\nu} \nabla_\mu n_\nu = \sqrt{-g} (K_{ij} S^{ij} - S^i \partial_i \ln \alpha), \quad (7.229)$$

where  $K_{\mu\nu}$  is the extrinsic curvature as defined in (7.60) and where we have used the definition of the acceleration of normal observers (7.61).

By collecting Eqs. (7.214), (7.224) and (7.226), we can finally cast the conservative expressions of the relativistic-hydrodynamic equations in the compact form

$$\partial_t(\sqrt{\gamma} \mathbf{U}) + \partial_i(\sqrt{\gamma} \mathbf{F}^i) = \mathbf{S}, \quad (7.230)$$

where the vector of *conserved variables*  $\mathbf{U}$  and the corresponding *flux vector* in the  $i$ -direction  $\mathbf{F}^i$  are given by

$$\mathbf{U} = \begin{pmatrix} D \\ S_j \\ E \end{pmatrix} := \begin{pmatrix} \rho W \\ \rho h W^2 v_j \\ \rho h W^2 - p \end{pmatrix}, \quad \mathbf{F}^i := \begin{pmatrix} \alpha v^i D - \beta^i D \\ \alpha S_j^i - \beta^i S_j \\ \alpha S^i - \beta^i E \end{pmatrix}, \quad (7.231)$$

while the source vector has components

$$\mathbf{S} := \sqrt{\gamma} \begin{pmatrix} 0 \\ \frac{1}{2} \alpha S^{ik} \partial_j \gamma_{ik} + S_i \partial_j \beta^i - E \partial_j \alpha \\ \alpha S^{ij} K_{ij} - S^j \partial_j \alpha \end{pmatrix}. \quad (7.232)$$

Because much of the historical development of expressions (7.230)–(7.232) has taken place in Valencia, through the work of Ibáñez and of his collaborators, this formulation is also known as the “*Valencia formulation*” of the relativistic-hydrodynamic equations (see Problem 12).

There are a number of comments that should be made on these equations and that can be summarised as follows:

- Equations (7.230)–(7.232) are valid in any curved spacetime written in any coordinate systems, provided, of course, that the line element is in the form (7.12).
- Because linear combinations of *conserved variables* are still solutions of the equations in conservative form, the original formulation of Banyuls *et al.* (1997) used as conserved energy the quantity

$$\tau := \rho W(hW - 1) - p = E - D. \quad (7.233)$$

This choice has purely numerical motivations, *i.e.*, the conservation of  $\tau$  as a combination of two conserved quantities is more accurate than that of  $E$  only; because of this it is the one employed in most numerical codes (Baiotti *et al.*, 2005). Therefore, the corresponding new conserved variables and fluxes are given by

$$\mathbf{U} = \begin{pmatrix} D \\ S_j \\ \tau \end{pmatrix} := \begin{pmatrix} \rho W \\ \rho h W^2 v_j \\ \rho h W^2 - p - D \end{pmatrix}, \quad \mathbf{F}^i = \begin{pmatrix} \alpha v^i D - \beta^i D \\ \alpha S_j^i - \beta^i S_j \\ \alpha(S^i - Dv^i) - \beta^i \tau \end{pmatrix},$$

(7.234)

while the sources remain the same as in (7.232).

- Although the *conserved variables* (7.231)<sub>1</sub> can be readily expressed in terms of the *primitive variables*:  $\rho, v^i, \epsilon$ , the opposite is not true and a root-finding procedure is needed to obtain the primitive variables from the conserved ones that have been evolved in time.<sup>20</sup> This procedure, which is not necessary when considering the Newtonian hydrodynamic equations in conservative form, can be very involved, computationally expensive, and a source of numerical inaccuracies. All of these aspects will be discussed in more detail in Section D.1 of the Appendix D.
- By looking at the source terms (7.232), it is easy to realise that they do not involve derivatives of the fluid variables and are therefore finite even in the presence of physical shocks. Furthermore, all of the source terms vanish for a flat spacetime in *Cartesian coordinates*. This is the only case where the relativistic-hydrodynamic equations (7.230) can be cast in a strictly homogeneous conservative form [see, e.g., Font *et al.* (1994) for a detailed analysis of the equations in the case of a flat spacetime]. More generically, in fact, the system (7.230) takes the form of a “*flux-balanced*” set of equations (LeVeque, 1992) and this is the case even for flat spacetimes in curvilinear coordinates.
- If the spacetime is stationary, the term  $\alpha S^{ik} K_{ik}$  in the source vector (7.232) reduces to

$$\alpha S^{ik} K_{ik} = \frac{1}{2} S^{ik} \beta^j \partial_j \gamma_{ik} + S^j_i \partial_j \beta^i. \quad (7.235)$$

- Had we written the four-divergence of the energy–momentum tensor as

$$\nabla_\mu T^{\mu\nu} = \frac{1}{\sqrt{-g}} \partial_\mu (\sqrt{-g} T^{\mu\nu}) + \Gamma_{\mu\lambda}^\nu T^{\mu\lambda}, \quad (7.236)$$

instead of using its expression (7.222), then the source terms would have been expressed in terms of the *Christoffel symbols*, as in the original formulation of Banyuls *et al.* (1997). Although mathematically equivalent, the sources as written in Eq. (7.232) are of course much easier to implement in a numerical code in which the metric is a primary quantity (Del Zanna *et al.*, 2007).

<sup>20</sup>The recovery of the primitive variables is not mathematically necessary, but it is physically indispensable in order to interpret the results and to interface the evolution equations with the microphysical description coming from the equation of state, which is naturally expressed in terms of the primitive variables.

**Eigenstructure of the relativistic Euler equations.**

All the effort invested in rewriting the equations of relativistic hydrodynamics in the conservative form (4.27) is paid back in the simplifications emerging when studying the characteristic structure of the equations. This is fundamental in the implementation of those numerical methods that make use of the characteristic structure of the equations and that we will discuss in Section 9.3.1. In particular, it is straightforward to derive the form of the Jacobians of the flux vectors  $\mathbf{A}^{(i)}$  associated with the system (7.230). Below we report the expressions for the original formulation of Banyuls *et al.* (1997), that refer therefore to the choice of conserved variables given by Eq. (7.234)<sub>1</sub>.<sup>21</sup> In practice, the Jacobians  $\mathbf{A}^{(i)}$  are three (*i.e.*, one per spatial direction)  $5 \times 5$  matrices defined as [*cf.*, Eq. (4.26)]

$$\mathbf{A}^{(i)} = \frac{\partial(\sqrt{\gamma}\mathbf{F}^i)}{\partial(\sqrt{\gamma}\mathbf{U})} = \frac{\partial\mathbf{F}^i}{\partial\mathbf{U}}. \quad (7.237)$$

Fixing on, say, the  $x$ -direction, the *eigenvalues* of  $\mathbf{A}^{(x)}$  are then given by

$$\lambda_0 = \alpha v^x - \beta^x \quad (\text{triple eigenvalue}), \quad (7.238)$$

$$\lambda_{\pm} = \frac{\alpha}{1 - v^2 c_s^2} \left\{ v^x (1 - c_s^2) \pm c_s \sqrt{(1 - v^2)[\gamma^{xx}(1 - v^2 c_s^2) - v^x v^x (1 - c_s^2)]} \right\} - \beta^x, \quad (7.239)$$

and the corresponding set of *right eigenvectors* is [*cf.*, Eq. (4.10)]<sup>22</sup>

$$\mathbf{R}^{(01)} = \begin{pmatrix} \frac{\mathcal{K}}{hW} \\ v_x \\ v_y \\ v_z \\ 1 - \frac{\mathcal{K}}{hW} \end{pmatrix}, \quad \mathbf{R}^{(02)} = \begin{pmatrix} Wv_y \\ h(\gamma_{xy} + 2W^2 v_x v_y) \\ h(\gamma_{yy} + 2W^2 v_y v_y) \\ h(\gamma_{zy} + 2W^2 v_z v_y) \\ Wv_y(2hW - 1) \end{pmatrix}, \quad (7.240)$$

<sup>21</sup>Note that eigenvectors computed with respect to different sets of variables are related through Eq. (4.38).

<sup>22</sup>Note that the equivalent expressions in Banyuls *et al.* (1997) refer to a diagonal metric, *i.e.*, to  $\gamma_{ij} = 0$  for  $i \neq j$ . Hence, apart from an ignorable constant, the right eigenvectors (7.240)–(7.241) coincide with those in Banyuls *et al.* (1997) for a diagonal metric.

**370** *Formulations of the Einstein–Euler Equations*

$$\mathbf{R}^{(03)} = \begin{pmatrix} Wv_z \\ h(\gamma_{xz} + 2W^2v_xv_z) \\ h(\gamma_{yz} + 2W^2v_yv_z) \\ h(\gamma_{zz} + 2W^2v_zv_z) \\ Wv_z(2hW - 1) \end{pmatrix}, \quad \mathbf{R}^{(\pm)} = \begin{pmatrix} 1 \\ hW(v_x - \mathcal{V}_\pm^x) \\ hWv_y \\ hWv_z \\ hW\mathcal{A}_\pm^x - 1 \end{pmatrix}, \quad (7.241)$$

where  $\mathbf{R}^{(01)} - \mathbf{R}^{(03)}$  are the three right eigenvectors relative to the triple eigenvalue  $\lambda_0$  (hence the “zero”). As usual,  $c_s$  is the local sound speed, that for a generic equation of state  $p = p(\rho, \epsilon)$  can be computed as [*cf.*, Eq. (2.173)]

$$hc_s^2 = \chi + \frac{p}{\rho^2}\kappa, \quad (7.242)$$

where

$$\chi := \left( \frac{\partial p}{\partial \rho} \right)_\epsilon, \quad \kappa := \left( \frac{\partial p}{\partial \epsilon} \right)_\rho. \quad (7.243)$$

Other shorthand definitions used in the expressions for the right eigenvectors (7.240)–(7.241) are

$$\mathcal{K} := \frac{\tilde{\kappa}}{\tilde{\kappa} - c_s^2}, \quad \tilde{\kappa} := \frac{\kappa}{\rho}, \quad (7.244)$$

and<sup>23</sup>

$$\mathcal{V}_\pm^x := \frac{v^x - \Lambda_\pm^x}{\gamma^{xx} - v^x\Lambda_\pm^x}, \quad \mathcal{A}_\pm^x := \frac{\gamma^{xx} - v^xv^x}{\gamma^{xx} - v^x\Lambda_\pm^x}, \quad \Lambda_\pm^x := \frac{\lambda_\pm + \beta^x}{\alpha}. \quad (7.245)$$

Note that in the case of a barotropic equation of state,  $p = p(e)$  (see Section 2.4.10 for a definition),  $\tilde{\kappa} = (1/\rho)(\partial p/\partial \epsilon) = c_s^2$  and hence expression (7.244)<sub>1</sub> for  $\mathcal{K}$  is singular. The occurrence of this singularity in the characteristic decomposition is simply due to the fact that in a barotropic equation of state the conservation equations for the rest mass and for the energy are not independent. This is either because the rest-mass density does not play any role in the equation of state [*cf.*, Eq. (2.270)], or because the specific internal energy (and hence the energy density) can be trivially derived from the rest mass [*cf.*, Eq. (2.248)].<sup>24</sup> In practice, this case can be handled by suitably redefining the state vector so that the corresponding characteristic decomposition is regular (Mach and Piętka, 2010; Ibáñez *et al.*, 2012a).

As already anticipated in Section 4.1.1, the eigenvectors  $\mathbf{R}^{(\pm)}$  are associated with the eigenvalues  $\lambda_\pm$ , which measure the propagation speeds of the *acoustic waves* of the system.

<sup>23</sup>Note that the corresponding special-relativistic expressions (4.28), (4.30) and (4.32) are recovered after setting  $\alpha = 0$ ,  $\beta^x = 0$ , and  $\gamma_{ij} = \delta_{ij}$ .

<sup>24</sup>Indeed, in most numerical codes in adopting a polytropic equation of state, the energy equation is not evolved and the energy density is updated simply using the algebraic expression (2.248).

On the other hand, the remaining eigenvectors  $\mathbf{R}^{(01)} - \mathbf{R}^{(03)}$  are associated with the triply-degenerate eigenvalue  $\lambda_0$ , which measures the propagation speed of *matter waves*. Another important aspect of the relativistic eigenspeeds  $\lambda_0$  and  $\lambda_{\pm}$  is the intrinsic coupling of all the velocity components through the modulus of the three-velocity  $v^2 = \gamma_{ij}v^i v^j$ . This is a fundamental difference with respect to the Newtonian case (see the discussion below). Even in the purely one-dimensional case, in fact, the eigenspeeds  $\lambda_{\pm}$  do not involve the simple Galilean addition of the flow and of the sound speed, *i.e.*,  $v^i \pm c_s$ , but rather a relativistic composition of both velocities. As an example, considering for simplicity  $v^i = (v^x, 0, 0)$  and a flat spacetime, the eigenspeeds for acoustic waves (7.239) reduce to

$$\lambda_{\pm} = \frac{v^x \pm c_s}{1 \pm v^x c_s}, \quad (4.25)$$

which are the expressions for the relativistic law of velocity-composition [*cf.*, Eq. (1.115)]. Clearly, as long as the equation of state considered is causal, *i.e.*, with  $c_s \leq 1$ , then the eigenspeeds are always within the light cone.

All that has been said so far for the Jacobian matrix  $\mathbf{A}^{(x)}$  applies also for the other two Jacobian matrices  $\mathbf{A}^{(y)}$  and  $\mathbf{A}^{(z)}$ , with the obvious replacements of  $x \leftrightarrow y$  or  $x \leftrightarrow z$ , respectively. Similarly, the corresponding right eigenvectors are the same as in (7.240)–(7.241), but for the obvious exchange of  $x \leftrightarrow y$  or  $x \leftrightarrow z$  and with the second row being exchanged with the third or the fourth row, respectively. Finally, since some approximate Riemann solvers, such as the *Marquina solver* (or *Marquina flux formula*) that we will discuss in Section 9.4.2, make explicit use also of the *left eigenvectors*, we report them here for completeness [see, *e.g.*, Ibáñez *et al.* (2001) for a derivation]

$$\mathbf{L}^{(01)} = \frac{W}{\mathcal{K} - 1} \begin{pmatrix} h - W \\ Wv^x \\ Wv^y \\ Wv^z \\ -W \end{pmatrix}, \quad \mathbf{L}^{(02)} = \frac{1}{h\xi} \begin{pmatrix} -\gamma_{zz}v_y + \gamma_{yz}v_z \\ v^x(\gamma_{zz}v_y - \gamma_{yz}v_z) \\ \gamma_{zz}(1 - v_x v^x) + \gamma_{xz}v_z v^x \\ -\gamma_{yz}(1 - v_x v^x) - \gamma_{xz}v_y v^x \\ -\gamma_{zz}v_y + \gamma_{yz}v_z \end{pmatrix}, \quad (7.246)$$

$$\mathbf{L}^{(03)} = \frac{1}{h\xi} \begin{pmatrix} -\gamma_{yy}v_z + \gamma_{zy}v_y \\ v^x(\gamma_{yy}v_z - \gamma_{zy}v_y) \\ -\gamma_{zy}(1 - v_x v^x) - \gamma_{xy}v_z v^x \\ \gamma_{yy}(1 - v_x v^x) + \gamma_{xy}v_y v^x \\ -\gamma_{yy}v_z + \gamma_{zy}v_y \end{pmatrix}, \quad (7.247)$$

$$\mathbf{L}^{(\mp)} = \pm \frac{h^2}{\Delta} \begin{pmatrix} hW\mathcal{V}_\pm^x \xi + \mathcal{N}_\mp \\ \Gamma_{xx}(1 - \mathcal{K}\mathcal{A}_\pm^x) + (2\mathcal{K} - 1)\mathcal{V}_\pm^x(W^2 v^x \xi - \Gamma_{xx} v^x) \\ \Gamma_{xy}(1 - \mathcal{K}\mathcal{A}_\pm^x) + (2\mathcal{K} - 1)\mathcal{V}_\pm^x(W^2 v^y \xi - \Gamma_{xy} v^x) \\ \Gamma_{xz}(1 - \mathcal{K}\mathcal{A}_\pm^x) + (2\mathcal{K} - 1)\mathcal{V}_\pm^x(W^2 v^z \xi - \Gamma_{xz} v^x) \\ \mathcal{N}_\mp \end{pmatrix}, \quad (7.248)$$

where

$$\mathcal{N}_\mp := (1 - \mathcal{K})[-\gamma v^x + \mathcal{V}_\pm^x(W^2 \xi - \Gamma_{xx})] - \mathcal{K}W^2 \mathcal{V}_\pm^x \xi, \quad (7.249)$$

$$\mathcal{C}_\pm^x := v_x - \mathcal{V}_\pm^x, \quad \Delta := h^3 W (\mathcal{K} - 1) (\mathcal{C}_+^x - \mathcal{C}_-^x) \xi, \quad (7.250)$$

$$\xi := \Gamma_{xx} - \gamma(v^x)^2, \quad \Gamma_{xx} := \gamma_{yy} \gamma_{zz} - \gamma_{yz}^2, \quad (7.251)$$

$$\Gamma_{xy} := -(\gamma_{xy} \gamma_{zz} - \gamma_{xz} \gamma_{yz}), \quad \Gamma_{xz} := \gamma_{xy} \gamma_{yz} - \gamma_{yy} \gamma_{xz}, \quad (7.252)$$

and the following additional identities can be shown to hold (Ibáñez, 2012c)

$$1 - \mathcal{A}_\pm^x = v^x \mathcal{V}_\pm^x, \quad \mathcal{A}_\pm^x - \mathcal{A}_\mp^x = v^x (\mathcal{C}_\pm^x - \mathcal{C}_\mp^x), \quad (7.253)$$

$$\mathcal{C}_\pm^x - \mathcal{C}_\mp^x = \mathcal{V}_\mp^x - \mathcal{V}_\pm^x, \quad \mathcal{C}_\pm^x - \mathcal{C}_\mp^x = \mathcal{A}_\pm^x \mathcal{V}_\mp^x - \mathcal{A}_\mp^x \mathcal{V}_\pm^x. \quad (7.254)$$

Note that expressions (7.249) and (7.250) contain the determinant of the three-metric  $\gamma$ , which can also be expressed in terms of the following identities

$$\gamma = \gamma_{xx} \Gamma_{xx} + \gamma_{xy} \Gamma_{xy} + \gamma_{xz} \Gamma_{xz}, \quad \gamma v^x = \Gamma_{xx} v_x + \Gamma_{xy} v_y \Gamma_{xz} v_z. \quad (7.255)$$

The concluding remark in this section is that, although knowledge of the characteristic structure of the system is a fundamental one for a particular class of Riemann solvers, high-order numerical methods can also be implemented which do not require such information. We will introduce these concepts and methods in Chapter 10.

### **The Newtonian limit.**

In Section 4.1.1 we have already encountered the Newtonian equations of conservation of mass, momentum and energy in the absence of external forces and written them explicitly in Cartesian coordinates [*cf.*, Eqs. (3.83)–(3.89)]. We have also seen how they can be cast into a first-order matrix form [*cf.*, Eq. (4.1)]. Using a slightly different state vector, we now rewrite them in the conservative form that is commonly used in numerical calculations, *i.e.*,

$$\partial_t \mathbf{U} + \partial_x \mathbf{f}(\mathbf{U}) + \partial_y \mathbf{g}(\mathbf{U}) + \partial_z \mathbf{h}(\mathbf{U}) = 0, \quad (7.256)$$

where the five-dimensional (state) vector of conserved quantities is given by (Kulikovskii *et al.*, 2001)

$$\mathbf{U} := \begin{pmatrix} \rho \\ \rho v^i \\ e_N \end{pmatrix}. \quad (7.257)$$

As remarked several times already, the Newtonian energy density  $e_N$  includes kinetic-energy contributions and internal ones, *i.e.*, [cf., Eq. (2.68)]

$$e_N = \rho\epsilon + \frac{1}{2}\rho V^2, \quad (7.258)$$

where

$$V^2 := (v^x)^2 + (v^y)^2 + (v^z)^2. \quad (7.259)$$

Similarly, the fluxes in the  $x$ ,  $y$  and  $z$ -directions have explicit expressions given, respectively, by

$$\mathbf{f} := \begin{pmatrix} \rho v^x \\ p + \rho(v^x)^2 \\ \rho v^x v^y, \\ \rho v^x v^z \\ v^x(e_N + p) \end{pmatrix}, \quad \mathbf{g} := \begin{pmatrix} \rho v^y \\ \rho v^x v^y \\ p + \rho(v^y)^2 \\ \rho v^y v^z \\ v^y(e_N + p) \end{pmatrix}, \quad \mathbf{h} := \begin{pmatrix} \rho v^z \\ \rho v^x v^z \\ \rho v^y v^z \\ p + \rho(v^z)^2 \\ v^z(e_N + p) \end{pmatrix}. \quad (7.260)$$

It is then straightforward to obtain the characteristic speeds and fields of the Jacobian matrices associated with the above conservative equations. Again, taking the  $x$ -direction as an example, the eigenspeeds are given by

$$\lambda_0 = v^x, \quad (7.261)$$

$$\lambda_{\pm} = v^x \pm c_s, \quad (7.262)$$

which represent the Newtonian limits of the corresponding Eqs. (7.238) and (7.239) introduced above. Similarly, the Newtonian sound speed for a generic equation of state is now given by [cf., Eq. (7.242)]

$$c_s^2 = \chi + \frac{p}{\rho^2} \kappa = \frac{\gamma p}{\rho}, \quad (7.263)$$

with the second equality referring to an ideal-fluid equation of state [cf., Eq. (2.173)].

Finally, the associated right eigenvectors read (Kulikovskii *et al.*, 2001)

$$\mathbf{R}^{(01)} = \begin{pmatrix} 1 \\ v^x \\ v^y \\ v^z \\ h_N + \frac{1}{2}V^2 - \rho c_s^2 / \kappa \end{pmatrix}, \quad \mathbf{R}^{(02)} = \begin{pmatrix} 0 \\ 0 \\ 1 \\ 0 \\ v^y \end{pmatrix}, \quad (7.264)$$

$$\mathbf{R}^{(03)} = \begin{pmatrix} 0 \\ 0 \\ 0 \\ 1 \\ v^z \end{pmatrix}, \quad \mathbf{R}^{(\pm)} = \begin{pmatrix} 1 \\ v^x \pm c_s \\ v^y \\ v^z \\ h_N + \frac{1}{2}V^2 \pm v^x c_s \end{pmatrix}, \quad (7.265)$$

and are the Newtonian equivalent of the right eigenvectors (7.240)–(7.241). Note that they contain the Newtonian specific enthalpy  $h_N := \epsilon + p/\rho$  [cf., Eq. (2.147)] and, as remarked in Section 3.5,  $h_N$  does not represent the Newtonian limit of the relativistic specific enthalpy  $h$ , which is instead given by  $h \rightarrow 1$ .

### 7.3.4 The covariant formulation

A *covariant conservative formulation* of the general-relativistic hydrodynamics equations for ideal fluids was first reported by Eulderink and Mellema (1994) and subsequently extended by Eulderink and Mellema (1995) to study the propagation of relativistic jets that are “inertially” confined by axisymmetric matter distributions. Because they do not make use of a 3+1 decomposition of spacetime, the form of the equations is invariant with respect to spacetime foliation. As a result, the derivation of the covariant conservative form is straightforward and the final form follows immediately from the equations of conservation of rest mass (3.52), of energy and of momentum (3.53) after rewriting them as

$$\partial_\mu(\sqrt{-g}\rho u^\mu) = 0, \quad (7.266)$$

$$\partial_\mu(\sqrt{-g}T^{\mu\nu}) = S^\nu, \quad (7.267)$$

where  $S^\nu := -\sqrt{-g}\Gamma_{\mu\lambda}^{\nu} T^{\mu\lambda}$ . Equations (7.266) and (7.267) can be collectively expressed as

$$\partial_\mu \mathbf{F}^\mu = \partial_t \mathbf{F}^t + \partial_i \mathbf{F}^i = \hat{\mathbf{S}}, \quad (7.268)$$

where  $\mathbf{F}^\mu$  and  $\hat{\mathbf{S}}$  are five-dimensional vectors defined as

$$\mathbf{F}^\mu := \sqrt{-g} \begin{pmatrix} \rho u^\mu \\ T^{\mu t} \\ T^{\mu 1} \\ T^{\mu 2} \\ T^{\mu 3} \end{pmatrix}, \quad \hat{\mathbf{S}} := \begin{pmatrix} t \\ S^t \\ S^1 \\ S^2 \\ S^3 \end{pmatrix}, \quad (7.269)$$

and where  $\mathbf{F}^t = (\rho u^t, T^{tt}, T^{t1}, T^{t2}, T^{t3})^\top$  is the vector of conserved variables (*i.e.*, the state vector), while  $\mathbf{F}^i = (\rho u^i, T^{it}, T^{i1}, T^{i2}, T^{i3})^\top$  are the three flux vectors.

As discussed for the Valencia formulation (7.230), also the covariant formulation (7.268) contains a source term on the right-hand side that is zero only in flat spacetime, hence making it a *flux-balanced formulation* in general. However, also in this case the source term does not contain partial derivatives of the fluid variables and, as for the Valencia formulation (7.230), it does not spoil the conservative character of the formulation.

In the exhaustive work in which Eulderink and Mellema (1995) first introduced the covariant formulation (7.268), the set of equations was solved using a numerical method based on a generalisation of the Roe approximate Riemann solver, which we will discuss in more detail in Chapter 9. The performance of the method and of the general-relativistic Roe solver were tested by Eulderink and Mellema (1995) in a number of one-dimensional testbed problems, including relativistic and non-relativistic shock-tube tests and the spherical accretion onto a Schwarzschild black hole. In all the tests the method was shown to yield accurate results and to track correctly shocks even for ultrarelativistic flows with Lorentz factor  $W \simeq 300$ . Furthermore, in its special-relativistic version, the solver was used in the study of the confinement properties of relativistic jets (Eulderink and Mellema, 1994).

The considerable mathematical advantages of the covariant formulation (7.268), namely, its transparent conservative and hyperbolic form, as well as the simplicity of studying the corresponding eigenstructure, are to be contrasted with at least two difficulties. The first one is that it is not straightforward, although it is certainly possible, to couple the set of equations (7.268) with the solution of the Einstein equations within a 3+1 decomposition, since no use is made of the gauge information coming from the decomposition. The second difficulty is that, although the vector of conserved variables  $\mathbf{F}^t$  can be inverted analytically to yield the primitive variables, this operation involves the introduction of several auxiliary variables and the solution of a quartic polynomial that is computationally inefficient. Therefore, as for the Valencia formulation, numerical iterative methods are used to recover the primitive variables from the conserved ones (Eulderink and Mellema, 1995). Possibly as a result of these drawbacks, the covariant formulation (7.268) has not yet been employed to study strong-field, general-relativistic flows.

### 7.3.5 The light-cone formulation

The formulation of the relativistic-hydrodynamic equations that we discuss below is both similar and distinct from the one introduced in the previous sections. The similarity is that it is manifestly conservative, but it is also fundamentally different in the fact that it assumes the spacetime not to be foliated through a sequence of spacelike hypersurfaces, as we have seen so far for most formulations. Rather, it requires that the spacetime is decomposed into a sequence of (outgoing) null slices, thus providing the optimal conditions for the calculation of radiation, be it gravitational or electromagnetic [see, *e.g.*, Winicour (2005) for a review]. More specifically, the use of a null foliation implies that the line element is not of the generic 3+1 form (7.12) but is described in terms of a “radiative” metric. For example, in the simpler case of an axisymmetric and stationary spacetime, this is given by the *Bondi–Sachs (radiative) metric* (Bondi *et al.*, 1962; Sachs, 1962)

### 376 Formulations of the Einstein–Euler Equations

$$ds^2 = - \left( \frac{V}{r} e^{2\beta} - U^2 r^2 e^{2\gamma} \right) du^2 - 2e^{2\beta} dudr - 2Ur^2 e^{2\gamma} dud\theta + r^2 (e^{2\gamma} d\theta^2 + e^{-2\gamma} \sin^2 \theta d\phi^2), \quad (7.270)$$

where  $u$  is the outgoing null coordinate (*i.e.*, labelling outgoing light cones),  $r$  is the areal radial coordinate (*i.e.*, two-spheres will have area  $4\pi r^2$ ), and  $\theta, \phi$  are the usual angular coordinates, with  $\phi$  being the direction of the Killing vector. Because of stationarity and axisymmetry, the metric functions  $V, U, \beta$  and  $\gamma$  depend on the coordinates  $u, r$  and  $\theta$ .

The numerical procedures for the integration of the hydrodynamic equations in this foliation are much less common and we have already discussed in Section 7.2.1 some of the advantages and disadvantages of a null formulation by Hernandez and Misner (1966), for spherically symmetric spacetimes [see, *e.g.*, Isaacson *et al.* (1983) for some initial work with axisymmetric matter distributions]. However, once suitable initial data is specified (and this is particularly straightforward for stationary and axisymmetric spacetimes), then the use of a null foliation is not particularly more complex than a standard 3+1 one. Alternatively, it is also possible to “match” a spacelike interior section to a null exterior one. In this way, the specification of the initial data can be made following standard techniques, while the use of a null foliation provides an accurate calculation of the radiative fields. This approach has been employed by Dubal *et al.* (1998) for a spherical spacetime containing a perfect fluid and by Reisswig *et al.* (2009) for a spacetime with black-hole binaries.

A general formalism *light-cone formulation* of the equations of relativistic hydrodynamics has been developed by Papadopoulos and Font (1999b) and has been applied to a series of astrophysical problems involving accretion onto a black hole (Papadopoulos and Font, 1999a; Papadopoulos and Font, 2001). In this formulation, the vector of conserved quantities is then defined as

$$\mathbf{U} := \begin{pmatrix} D \\ S_j \\ E \end{pmatrix} = \begin{pmatrix} \rho u^t \\ \rho h u^t u^i + pg^{ti} \\ \rho h u^t u^t + pg^{tt} \end{pmatrix}, \quad (7.271)$$

where we have again overused the notation of the previous formulations to represent different physical quantities [*cf.* Eq. (7.203) or (7.231)]. With these definitions, the equations of general-relativistic hydrodynamics again take a conservative form

$$\partial_t (\sqrt{-g} \mathbf{U}) + \partial_i (\sqrt{-g} \mathbf{F}^i) = \mathbf{S}, \quad (7.272)$$

where the flux vectors  $\mathbf{F}^j$  are defined as

$$\mathbf{F}^j := \begin{pmatrix} J^j \\ T^{ji} \\ T^{j0} \end{pmatrix} = \begin{pmatrix} \rho u^j \\ \rho h u^i u^j + pg^{ij} \\ \rho h u^t u^j + pg^{tj} \end{pmatrix}, \quad (7.273)$$

while the source terms  $\mathbf{S}$  are given by

$$S := \begin{pmatrix} 0 \\ -\sqrt{-g} \Gamma_{\mu\lambda}^i T^{\mu\lambda} \\ -\sqrt{-g} \Gamma_{\mu\lambda}^0 T^{\mu\lambda} \end{pmatrix}. \quad (7.274)$$

As we have seen for the covariant formulation (7.268), also in this case the source terms are never zero, except in a flat spacetime and Cartesian coordinates. However, they do not contain derivatives of the fluid variables and hence they are regular even in the presence of shocks. A complete discussion of the characteristic structure of Eqs. (7.272) can be found in Papadopoulos and Font (1998), where the formulation was shown to be well suited for the numerical implementation of HRSC schemes.

One of the most appealing aspects of the light-cone formulation is that it allows for a simple and explicit recovery of the primitive variables by virtue of the particular form of the Bondi–Sachs metric (7.270). As a result, the formulation has found a number of applications both in spherical spacetimes (Papadopoulos and Font, 1998; Papadopoulos and Font, 2001; Linke *et al.*, 2001) and in axisymmetric ones (Siebel *et al.*, 2002; Siebel *et al.*, 2003). First steps have also been taken to extend the approach to generic three-dimensional spacetimes (Bishop *et al.*, 1999), although it is not obvious whether a purely null foliation will turn out to be more convenient than a purely spatial one or a mixed spatial-null foliation.

### 7.3.6 The discontinuous Galerkin formulation

Radice and Rezzolla (2011) have recently proposed a *discontinuous Galerkin formulation*, that is, a covariant *weak formulation* of the equations of general-relativistic hydrodynamics that is suitable for projection methods, such as *finite-elements methods* or *discontinuous Galerkin (DG) methods*, (see Section 10.3 for a detailed discussion of DG methods). As already anticipated in Section 7.3.2, also within the general class of finite-element numerical methods, the weak formulation of a set of equations consists in the multiplication by a test function, followed by an integration over a certain domain and by the use of Green’s formula to reduce the maximum order of partial derivatives present in the equation [see, *e.g.*, Solin (2006) for an extended discussion of finite-element methods]. This approach is well-suited also for general-relativistic hydrodynamics because of the covariant nature of finite-element methods [first pointed out by Meier (1999)] and can be extended to DG methods as well. In these methods the equations are formulated on reference elements mapped into the physical space via diffeomorphisms, thus removing any need for a preferred coordinate system (see also Section 10.3).

We introduce the discontinuous Galerkin formulation by referring to the relativistic hydrodynamics equations in covariant form, Eqs. (3.52)–(3.53), which should be intended here in the sense of distributions, such as Dirac deltas, since we have to allow for the solution to develop discontinuities. In general, we are interested in solving the equations on an open, regular,<sup>25</sup> finite domain  $\Omega$ , which is a subset of the four-dimensional manifold  $\mathcal{M}$  with suitable

<sup>25</sup>Chen *et al.* (2009) have presented a detailed discussion of the regularity requirements for a domain. In essence, this amounts to having a domain which has a normal defined everywhere except for at most a discrete set of points (vertexes). As an example, a cubic box is a regular domain.

### 378 Formulations of the Einstein–Euler Equations

initial and boundary data. A precise mathematical formulation of this problem can be done within the context of bounded divergence-measure vector fields using the theory developed by Chen and Frid (2003) and Chen *et al.* (2009). Anticipating a few concepts that will be further developed in Section 10.2.1, we first introduce a *triangulation* of  $N_e$  elements of  $\Omega$ ,  $\{\Omega_j\}_{j=1}^{N_e}$ , by selecting a family of diffeomorphisms  $\varphi_j: \mathcal{E} \subset \mathbb{R}^4 \rightarrow \Omega$ , with  $\Omega_j = \varphi_j(\mathcal{E})$  such that

$$\Omega = \bigcup_{j=1}^{N_e} \Omega_j, \quad \text{and} \quad \overset{\circ}{\Omega}_i \cap \overset{\circ}{\Omega}_j = \emptyset \quad \forall i \neq j, \quad (7.275)$$

where  $\mathcal{E}$  is a multidimensional reference element, *e.g.*, a “hypercube” or a four-dimensional simplex, while  $\overset{\circ}{\Omega}_j$  denotes the interior of  $\Omega_j$ . We also arrange the local coordinate system,  $\{x^\mu\}_j$ , induced by  $\varphi_j$ , so that  $\partial_t$  is timelike or null.

If we now look for solutions  $J^\alpha \in \mathcal{V}_h$ , where  $\mathcal{V}_h$  is the functional space of all bounded vector fields over  $\Omega$ , the continuity equation (3.52) is equivalent, in the sense of distributions, to

$$\sum_{j=1}^{N_e} \left[ \int_{\Omega_j} J^\alpha \nabla_\alpha \phi \epsilon_{\alpha\beta\gamma\delta} dx^\alpha dx^\beta dx^\gamma dx^\delta - \int_{\partial\Omega_i} \phi \mathcal{J}^\alpha \epsilon_{\alpha\beta\gamma\delta} dx^\beta dx^\gamma dx^\delta \right] = 0, \quad (7.276)$$

for all test functions  $\phi$ , where  $\epsilon_{\alpha\beta\gamma\delta} dx^\alpha dx^\beta dx^\gamma dx^\delta$  is the four-dimensional proper volume. The symbol  $\mathcal{J}^\alpha$  in expression (7.276) is the internal normal trace of  $J^\alpha$ . This object reduces simply to the rest-mass density current  $J^\alpha$ , when  $J^\alpha$  and  $\Omega_k$  are regular, but in general the second integral has to be intended as the action of a measure,  $\mathcal{J}^\alpha \epsilon_{\alpha\beta\gamma\delta} dx^\beta dx^\gamma dx^\delta$ , on  $\phi$  (Chen *et al.*, 2009). Similarly, if we look for solutions  $T^{\alpha\beta} \in \mathcal{V}_h \otimes \mathcal{V}_h$ , the equations (3.53) for the energy and the momentum are equivalent to

$$\sum_{j=1}^{N_e} \int_{\Omega_j} T^{\alpha\beta} \nabla_\beta \phi_\alpha \epsilon_{\alpha\beta\gamma\delta} dx^\alpha dx^\beta dx^\gamma dx^\delta = \sum_{j=1}^{N_e} \int_{\partial\Omega_j} \phi_\alpha \mathcal{T}^{\alpha\beta} \epsilon_{\beta\gamma\delta\mu} dx^\gamma dx^\delta dx^\mu, \quad (7.277)$$

again for all the test one-forms  $\phi_\alpha$ . Also in this case,  $\mathcal{T}^{\alpha\beta}$  is a generalisation of  $T^{\alpha\beta}$  and the integral has to be interpreted as the action of  $\mathcal{T}^{\alpha\beta} \epsilon_{\beta\gamma\delta\mu} dx^\gamma dx^\delta dx^\mu$  on  $\phi_\alpha$  in the non-smooth case. The solution of the relativistic-hydrodynamic equations consists then in finding

$$J^\alpha \in \mathcal{V}_h \quad \text{such that (7.276) holds } \forall \phi, \quad (7.278)$$

$$T^{\alpha\beta} \in \mathcal{V}_h \otimes \mathcal{V}_h \quad \text{such that (7.277) holds } \forall \phi_\alpha, \quad (7.279)$$

together with an equation of state and some proper boundary-initial data to be specified through  $\mathcal{J}^\alpha$  and  $\mathcal{T}^{\alpha\beta}$  on  $\partial\Omega$ .

As we will see in more detail in Section 10.3.1, a numerical scheme within the DG approach is then obtained by “projecting” the conditions (7.278)–(7.279) on a finite-dimensional

subspace  $V_h \subset \mathcal{V}_h$ . In general, this space is constructed starting from the space of piecewise polynomials, in particular we define

$$X_h := \{u \in L^\infty(\Omega) : u \circ \varphi_j \in \mathbb{P}_p(\mathcal{E}), j = 1, \dots, N_e\}, \quad (7.280)$$

where  $\mathbb{P}_p(K)$  is the space of polynomials with at most degree  $p$  on  $\mathcal{E}$ . The space  $V_h$  is taken as the space of all the vector fields “whose components are elements of  $X_h$ ”, or more precisely

$$V_h := \{u^\alpha \in \mathcal{V}_h : [\varphi_j]_* u^\alpha \in [\mathbb{P}_p(\mathcal{E})]^4, j = 1, \dots, N_e\}, \quad (7.281)$$

where  $[\mathbb{P}_p(\mathcal{E})]^4$  is the space of four-tuples of polynomials with at most degree  $p$  on  $\mathcal{E}$  and  $[\varphi_j]_*$  is the pull-back associated with  $\varphi_j$ . The DG approach is then simply the restriction of the conditions (7.278)–(7.279) to  $V_h$ , and it amounts to finding  $J^\alpha \in V_h$  and  $T^{\alpha\beta} \in V_h \otimes V_h$  such that (7.276) and (7.277) hold for suitable choices of the test functions  $\phi$  and of the one-forms  $\phi_\alpha$ .

As commented above, when no discontinuities are present, the fluxes  $\mathcal{J}^\alpha$  and  $\mathcal{T}^{\alpha\beta}$  are the restriction of  $J^\alpha$  and  $T^{\alpha\beta}$  to the boundaries  $\partial\Omega_j$ . As a result, denoting a possible set of primitives variables as  $\mathbf{V} = \{V^1, V^2, V^3, V^4, V^5\}$  and considering  $J^\alpha$  and  $T^{\alpha\beta}$  as functions of  $\mathbf{V}$ , then  $\mathcal{J}^\alpha = J^\alpha(\mathbf{V}^*)$  and  $\mathcal{T}^{\alpha\beta} = T^{\alpha\beta}(\mathbf{V}^*)$ ,  $\mathbf{V}^*$  being the restriction of  $\mathbf{V}$  on  $\partial\Omega_j$ , as the fluxes can only depend on the location in the spacetime through  $\mathbf{V}$ . In the general case,  $\mathcal{J}^\alpha$  and  $\mathcal{T}^{\alpha\beta}$  can be determined with causality considerations on spacelike boundaries or as solutions of generic Riemann problems (see Section 9.2.3) on timelike and null boundaries, as they are known as soon as  $\mathbf{V}^*$  is known on those boundaries. The computation of the fluxes is then obtained in the standard way by resorting to approximate Riemann solvers.

Once a method is chosen to compute the fluxes, the fully discrete equations are readily obtained by testing (7.276) and (7.277) on a set of linearly independent test functions,  $\phi \in X_h$  and  $\phi_\alpha \in V_h$ . To write down the method explicitly in every finite element  $\Omega_j$ , a set of conserved quantities  $\mathbf{U} = \{J^t, T^{t\mu}\}^{26}$  is first chosen (Papadopoulos and Font, 1999b). This provides a one-to-one relation between primitive and conserved variables, so that we can formally write  $J^i = J^i(\mathbf{U})$  and  $T^{i\mu} = T^{i\mu}(\mathbf{U})$ . A set of nonlinear equations for  $\mathbf{U} \in X_h$  can now be obtained by expanding the Galerkin conditions (7.276) and (7.277), *i.e.*,

$$\begin{aligned} & \sum_{j=1}^{N_e} \left[ \int_{\Omega_j} J^t \partial_t \phi \epsilon_{\alpha\beta\gamma\delta} dx^\alpha dx^\beta dx^\gamma dx^\delta + \int_{\Omega_j} J^i(\mathcal{C}) \partial_i \phi \epsilon_{\alpha\beta\gamma\delta} dx^\alpha dx^\beta dx^\gamma dx^\delta \right] = \\ & \sum_{j=1}^{N_e} \int_{\partial\Omega_j} \mathcal{J}^\mu \phi \epsilon_{\mu\alpha\beta\gamma} dx^\alpha dx^\beta dx^\gamma, \end{aligned} \quad (7.282)$$

where we have set  $\phi_\alpha = \phi \delta_\alpha^\mu$  and

<sup>26</sup>Other choices are possible; for example in the context of a 3+1 decomposition we could use the same conserved quantities as those used in the Valencia formulation.

$$\begin{aligned} \sum_{j=1}^{N_e} \left[ \int_{\Omega_j} T^{0\mu} \partial_0 \phi \epsilon_{\alpha\beta\gamma\delta} dx^\alpha dx^\beta dx^\gamma dx^\delta + \int_{\Omega_j} T^{i\mu}(\mathbf{U}) \partial_i \phi \epsilon_{\alpha\beta\gamma\delta} dx^\alpha dx^\beta dx^\gamma dx^\delta \right] = \\ \sum_{j=1}^{N_e} \left[ \int_{\partial\Omega_j} \mathcal{T}^{\nu\mu} \phi \epsilon_{\nu\alpha\beta\gamma} dx^\alpha dx^\beta dx^\gamma + \int_{\Omega_j} T^{\nu\lambda}(\mathbf{U}) \Gamma_{\lambda\nu}^\mu \phi \epsilon_{\alpha\beta\gamma\delta} dx^\alpha dx^\beta dx^\gamma dx^\delta \right], \end{aligned} \quad (7.283)$$

where  $\Gamma_{\beta\gamma}^\alpha$  are the Christoffel symbols [cf., Eq. (1.165)].

The key point of this treatment is that, as the functions are discontinuous across the boundaries  $\partial\Omega_i$ , the equations just obtained are local equations for a set of coefficients<sup>27</sup> within the  $\Omega_i$ 's and coupled only through the fluxes. In particular, this implies that if the computational grid “follows the causal structure of the spacetime”, in a sense that we clarify below, then the DG method becomes globally explicit. Under these conditions, in fact, the fluxes between the elements of the grid slice depend only on the data on the previous slice. Once these are computed, we are left with a set of formally decoupled equations involving the spectral coefficients of the numerical solution in the different elements.

#### **The discontinuous Galerkin formulation in the 3+1 decomposition.**

The generation of a triangulation which can follow the causal structure of the spacetime may become highly non-trivial, especially if the spacetime is evolved dynamically. For these reasons, instead of directly solving (7.282) and (7.283), one can use them to derive a fully explicit scheme. This can be accomplished by performing a 3+1 decomposition (see Section 7.1), according to which the spacetime is foliated along  $t = \text{const.}$  hypersurfaces,  $\Sigma_t$ . Once again, we consider a four-vector  $t^\mu$  such that  $t^\mu \nabla_\mu t = 1$  [cf., Eq. (7.10)] and define the three-volume form as  $\eta_{\alpha\beta\gamma} := \epsilon_{\delta\alpha\beta\gamma} t^\delta$ . We can use the integral lines of  $t^\alpha$  to identify points on  $\Sigma_t$  with points on  $\Sigma_{t+dt}$  and interpret the variation of the fields across the  $\Sigma_t$ 's as being the result of a dynamics on a three-manifold,  $\Sigma$ . The hydrodynamics equations are then studied in a world-tube  $\mathcal{S} \times (0, t)$ ,  $\mathcal{S} \subset \Sigma$  being an open, bounded, regular domain in  $\Sigma$ , again supplemented by proper boundary-initial conditions.

We can consider a triangulation  $\{\mathcal{S}_j\}_{j=1}^{N_e}$  of  $\mathcal{S}$  by selecting a family of diffeomorphisms  $\varphi_j: \mathcal{E} \subset \mathbb{R}^3 \rightarrow \Sigma$ , and  $\mathcal{S}_j = \varphi_j(\mathcal{E})$  such that

$$\mathcal{S} = \bigcup_{j=1}^{N_e} \mathcal{S}_j, \quad \dot{\mathcal{S}}_i \cap \dot{\mathcal{S}}_j = \emptyset \quad \forall i \neq j, \quad (7.284)$$

where  $\mathcal{E}$  is now a three-dimensional reference element, typically a cube or a tetrahedron. This induces a spacetime triangulation of  $\Omega$

$$\{\Omega_{j,n}\}_{j=1,n=1}^{N_e,Q} = \left\{ \mathcal{S}_j \times [n\Delta t, (n+1)\Delta t] \right\}_{j=1,n=1}^{N_e,Q}. \quad (7.285)$$

<sup>27</sup>In Chapter 10 we will learn that these coefficients are also called “degrees of freedom” or “spectral coefficients” within DG methods.

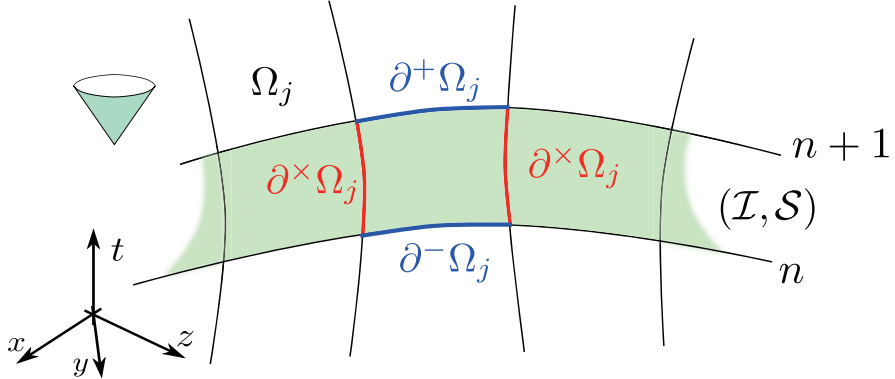


**Fig. 7.4** Schematic representation of a causal slice  $(\mathcal{I}, \mathcal{S})$  containing the element  $\Omega_j$ . The future and past boundaries  $\partial^\pm \Omega_j$ , as well as the timelike or null boundaries  $\partial^x \Omega_j$  of  $\Omega_j$ , are indicated with blue and red lines, respectively. Finally, the shaded region represents the causal slice [adapted from Radice and Rezzolla (2011)].

Because the concept of causal triangulation can be made rather rigorous, let us introduce a number of useful definitions. First of all, for every open set  $A$ , we introduce the notation  $\partial^+ A$ , to indicate the *future boundary* of  $A$ , that is the set of all the points  $\mathcal{P} \in \partial A$ , such that

$$J^+(\mathcal{P}) \cap A = \emptyset, \quad (7.286)$$

with  $J^+(\mathcal{P})$  being the causal future of  $\mathcal{P}$ . Analogously, we call the *past boundary* of  $A$ ,  $\partial^- A$ , the set of all points  $\mathcal{P} \in \partial A$  for which there exists an open neighbourhood,  $U$ , such that

$$J^+(\mathcal{P}) \cap U \subset \overline{A}, \quad (7.287)$$

where we have indicated with  $\overline{A}$  the closure of  $A$ . We now define the *slice of the triangulation* as any tuple  $(\mathcal{I}, \mathcal{S})$  where  $\mathcal{I} \subset \{1, 2, \dots, N_e\}$  and  $\mathcal{S} = \bigcup_{j \in \mathcal{I}} \Omega_j$  is connected. We will say that a slice  $(\mathcal{I}, \mathcal{S})$  is a *causal slice* if

$$\partial^x \mathcal{S} \subset \partial \Omega, \quad (7.288)$$

where  $\partial^+ \mathcal{S}$  and  $\partial^- \mathcal{S}$  are the future and past boundaries of  $\mathcal{S}$ , respectively and where

$$\partial^x \mathcal{S} = \partial \mathcal{S} \setminus [\partial^+ \mathcal{S} \cup \partial^- \mathcal{S}]. \quad (7.289)$$

An example of such a slice of the triangulation is given by the shaded region in Fig. 7.4, from which it follows that a causal slice is basically a slice whose timelike spatial boundaries  $\partial^+$  and  $\partial^-$  are parts of a Cauchy foliation of the spacetime. A causal slice  $(\mathcal{I}, \mathcal{S})$  is said to be a *minimal causal slice* if it also satisfies a CFL-like condition, here generalised as

$$\left[ \bigcup_{j \in \mathcal{I}} (\partial^x \Omega_j \cup \partial^- \Omega_j) \setminus \partial \Omega_k \right] \cap J^+(\Omega_k) = \emptyset \quad \forall k \in \mathcal{I}. \quad (7.290)$$

In other words, if the characteristics originating in each element  $\Omega_k$  only intersect the boundaries of the element itself  $\partial \Omega$ , or the future boundaries of the other elements in the slice.

Finally, then we say that a triangulation *follows the causal structure of the spacetime* if it can be written as the union of minimal causal slices. Put differently, a triangulation that follows the causal structure of the spacetime is one that can be sliced into minimal causal slices, which are grids associated with a Cauchy foliation of the spacetime and which satisfy a CFL condition on each hyper-surface of this foliation. For example, the triangulation (7.285) follows the causal structure of the spacetime on the  $n$ -th thin-sandwich  $\Omega_n = \mathcal{S} \times (t_n, t_n + \Delta t)$ , at least for small  $\Delta t$ .

Having introduced these concepts, we can obtain a fully explicit method by looking for  $J^\alpha$  and  $T^{\alpha\beta}$  such that (7.276) and (7.277) hold for all test functions  $\phi$  and all vector fields  $\phi^\alpha$ . When doing so, we do not allow the numerical solution to be discontinuous in time, so that the time integration can be performed with a standard solver for ordinary differential equations, *e.g.*, a Runge–Kutta scheme (see Section 9.5).

An explicit form for the continuity equation can be derived by projecting Eq. (7.282) with  $\phi$ , dividing both terms by  $\Delta t$  and by letting  $\Delta t \rightarrow 0$ , to obtain

$$\sum_{j=1}^{N_e} \partial_t \int_{\mathcal{S}_j} J^t \phi \boldsymbol{\eta} = \sum_{j=1}^{N_e} \left[ \int_{\mathcal{S}_j} J^i(\mathbf{U}) \partial_i \phi \boldsymbol{\eta} - \int_{\partial \mathcal{S}_j} \mathcal{J}^i \phi \eta_{i\alpha\beta} dx^\alpha dx^\beta \right]. \quad (7.291)$$

Analogously, we can derive an explicit discretisation of the energy–momentum equation starting from Eq. (7.283) to find

$$\begin{aligned} \sum_{j=1}^{N_e} \partial_t \int_{\mathcal{S}_j} T^{t\mu} \phi \boldsymbol{\eta} = \\ \sum_{j=1}^{N_e} \left[ \int_{\mathcal{S}_j} T^{i\mu}(\mathbf{U}) \partial_i \phi \boldsymbol{\eta} - \int_{\partial \mathcal{S}_j} \mathcal{T}^{i\mu} \phi \eta_{i\alpha\beta} dx^\alpha dx^\beta - \int_{\mathcal{S}_j} T^{\alpha\beta}(\mathbf{U}) \Gamma_{\beta\alpha}^\mu \phi \boldsymbol{\eta} \right]. \end{aligned} \quad (7.292)$$

As a result, the 3+1 DG formulation can be summarised as finding  $J^\alpha$  and  $T^{\alpha\beta}$  such that Eqs. (7.291) and (7.292) hold for all  $\phi$  and for all  $\phi^\alpha$ . This scheme can be interpreted as a higher-order generalisation of the light-cone formulation of relativistic hydrodynamics proposed by Papadopoulos and Font (1999b), which has the additional flexibility to work even with spacelike or null foliations. This aspect can be appreciated after considering the case in which  $p = 0$  [*cf.* Eq. (7.281)], namely, when looking for solutions that are constant over each element  $\mathcal{S}_j$ . In that case, a sufficient number of conditions can be obtained by choosing  $\phi = \chi_{\mathcal{S}_j}$  for  $j = 1, 2, \dots, N_e$ , where  $\chi_T$  is the *indicator function* of the set  $T$ , *i.e.*, a function which is equal to one in  $T$  and identically zero elsewhere. With this choice we finally obtain the set of equations

$$\partial_t \int_{\mathcal{S}_j} J^t \boldsymbol{\eta} + \int_{\partial \mathcal{S}_j} J^i(\mathbf{U}) \eta_{i\alpha\beta} dx^\alpha dx^\beta = 0, \quad (7.293)$$

$$\partial_t \int_{\mathcal{S}_j} T^{t\mu} \boldsymbol{\eta} + \int_{\partial \mathcal{S}_j} \mathcal{T}^{i\mu} \eta_{i\alpha\beta} dx^\alpha dx^\beta = - \int_{\mathcal{S}_j} T^{\alpha\beta}(\mathbf{U}) \Gamma_{\beta\alpha}^\mu \boldsymbol{\eta}, \quad (7.294)$$

for all  $j = 1, 2, \dots, N_e$ . It is easy to show that this corresponds to the finite-volume discretisation proposed by Papadopoulos and Font (1999b) in the light-cone formulation.

## 7.4 Further reading

- Alcubierre, M. (2008). *Introduction to 3 + 1 Numerical Relativity*. Oxford University Press, Oxford.
- Baumgarte, T. W. and Shapiro, S. L. (2010). *Numerical Relativity: Solving Einstein's Equations on the Computer*. Cambridge University Press, Cambridge.
- Bona, C., Palenzuela-Luque, C., and Bona-Casas, C. (2009). *Elements of Numerical Relativity and Relativistic Hydrodynamics: From Einstein's Equations to Astrophysical Simulations*. Lecture Notes in Physics. Springer, Berlin.
- Font, J. A. (2008). Numerical Hydrodynamics and Magnetohydrodynamics in General Relativity. *Living Rev. Relativ.*, **11**, 7.
- Gourgoulhon, É. (2012). *3+1 Formalism in General Relativity*. Volume 846, Lecture Notes in Physics, Springer, Berlin.
- Martí, J. M. and Müller, E. (2003). Numerical Hydrodynamics in Special Relativity. *Living Rev. Relativ.*, **6**, 7.
- Reula, O. (1998). Hyperbolic methods for Einstein's equations. *Living Rev. Relativ.*, **1**, 3.
- Sarbach, O. and Tiglio, M. (2012). Continuum and discrete initial-boundary value problems and Einstein's field equations. *Living Rev. Relativ.*, **15**, 9.
- Wilson, J. R. and Mathews, G. J. (2003). *Relativistic Numerical Hydrodynamics*. Cambridge University Press, Cambridge.

## 7.5 Problems

1. Derive the Misner–Sharp equations (7.29)–(7.33) from the Einstein equations and from the equations of motions.
2. Derive the Hernandez–Misner equations (7.43)–(7.47) from the Einstein equations and from the equations of motions.
3. Prove that  $a_\nu = D_\nu \ln \alpha$ . [Hint: expand directly the left- and right-hand sides by using the definitions  $a_\nu = n^\mu \nabla_\mu n_\nu$ ,  $n_\mu = -\alpha \nabla_\mu t$  and  $D_\nu \ln \alpha = \gamma^\mu_\nu \nabla_\mu \ln \alpha$ .]
4. Given a 3+1 decomposition of spacetime, derive the ADM evolution equations (7.67) and (7.75) from the projections of the Riemann tensor.
5. Given a 3+1 decomposition of spacetime, derive the ADM constraint equations (7.81) and (7.83) from the projections of the Riemann tensor.
6. It is not difficult to see why the numerical solution of a weakly hyperbolic system with zero-velocity modes, such as the ADM equations presented in Section 7.2.2, can become problematic. Consider for example a modified form of the advection equation (4.66), *i.e.*,

$$\partial_t u + v \partial_x u = \varepsilon u, \quad (7.295)$$

where  $\varepsilon > 0$  is a source term introduced by the numerical errors and which obviously vanishes in the continuum limit. Discuss what happens in the limiting cases when no numerical errors are present, *i.e.*, of  $\varepsilon \rightarrow 0$ , and in the other case when the solution also has “zero-velocity” modes, *i.e.*, when  $v \rightarrow 0$ . What can be done to prevent the development of a numerical “instability”?

7. Given the conformal transformation (7.93), show that the second covariant derivative of the conformal factor appearing in the split (7.102) is given by

$$\tilde{D}_i \tilde{D}_j \phi = \partial_i \partial_j \phi - \tilde{\Gamma}_{ij}^k \partial_k \phi,$$

and that the relation with the corresponding derivative in the physical metric is given by

$$D_i D_j \phi = -\frac{1}{2\phi} \tilde{D}_i \tilde{D}_j + \frac{1}{2\phi^2} \partial_i \phi \partial_j \phi.$$

8. Given the conformal transformation (7.93) and the evolution variables  $\tilde{\Gamma}^i$  defined in Eq. (7.99), rewrite the ADM equations (7.66), (7.75) in the BSSNOK formulation (7.103)–(7.107).

9. Given the conformal transformation (7.93) and the evolution variables  $\Theta$  and  $\hat{\Gamma}^i$  defined in Eqs. (7.118), (7.125), rewrite the ADM equations (7.66), (7.75) in the CCZ4 formulation of Eqs. (7.119)–(7.121) and (7.123).
10. Show that the harmonic slicing condition *i.e.*, Eq. (7.129) with  $f = 1$ , is only marginally singularity avoiding, *i.e.*, the lapse cannot be zero unless the space volume element is zero. [Hint: start by writing in a 3+1 decomposition the harmonic condition for the time coordinate  $\square x^0 = 0$ .]
11. Show that when using the “1+log” slicing condition, *i.e.*, Eq. (7.129) with  $f = 2/\alpha$ , the final volume element corresponding to  $\alpha = 0$  is around 60% of the initial one. [Hint: consider the initial lapse equal to be 1.]
12. Consider the Kerr spacetime, which is stationary and axisymmetric, in Boyer–Lindquist coordinates. Show that the sources (7.232) for the  $\phi$ -momentum vanish. Notice how this make the conservation of the angular momentum very transparent for an equilibrium fluid configuration sharing the same symmetries of the spacetime.

# 8

## Numerical Relativistic Hydrodynamics: Finite-Difference Methods

---

As shown in the previous chapter, the relativistic-hydrodynamic equations can be written as a quasi-linear hyperbolic system of conservative equations. The nonlinear nature of the equations, which is only amplified in relativistic regimes, makes the analytic solution of these equations a daunting task, if at all possible. Hence, numerical approaches remain the most convenient (if not the only) route to obtain a quantitative description of the dynamics. This chapter, and the two following it, are dedicated to the discussion of the methods needed for the numerical solution of the relativistic-hydrodynamic equations.<sup>1</sup> Note that we will distinguish numerical “*methods*” from numerical “*schemes*”, considering the former as a general class of the latter. In this sense, given a numerical method, we will present different numerical schemes meant as different implementations of the same method. As an example, the upwind (see Section 8.3.2) and the FTCS (see Section 8.3.3) schemes are different implementations of a finite-difference method.

In addition to their nonlinear character, the relativistic-hydrodynamic equations have the remarkable property of admitting the development of discontinuities even from smooth initial data (see Section 4.2). From a computational point of view, the appearance of discontinuities represents a serious obstacle for any numerical method. To see why this is the case, it is sufficient to recall that in traditional *finite-difference (non-conservative) methods* the solution  $u$  of a system of partial differential equations is assumed to be smooth and the derivatives of the solution  $u(x, t)$  at position  $x$  and at time  $t$  are approximated by using only values of  $u$  at a finite number of points near  $x$  and  $t$ . Clearly, such an approximation to a derivative, which is based on Taylor expansions, is incorrect in the presence of discontinuities, which are therefore reproduced with strong smearing or with very pronounced oscillations in their vicinity. Fortunately, the mathematical structure of the hyperbolic equations can be successfully exploited to develop numerical methods that are at the same time conservative (see Section 9.1) and upwind (see Sections 8.3.2 and 9.2), *i.e.*, they incorporate the information about the direction towards which perturbations propagate, thus resolving these discontinuities very efficiently. Such an approach will be extensively illustrated in the next chapter, which is entirely devoted to the so-called *high-resolution shock-capturing (HRSC)* methods. This chapter, on the other hand, is meant to serve as a first introduction to the basic aspects of the numerical solution of a system of hyperbolic equations, with a focus on finite-difference non-conservative

<sup>1</sup>All of the methods that we will present are valid in general for any *hyperbolic* partial differential equation.

methods and on those approaches that have been devised to cope with these shortcomings, *e.g.*, *artificial-viscosity methods*.

Hereafter we will focus on the so-called *grid-based methods*, that is, on methods in which the solution of a system of partial differential equations is evaluated at specific points in space and time, *i.e.*, the *gridpoints*. A radically different approach is the one in which the hydrodynamic equations are written in a coordinate-free sense, such as *smooth particle hydrodynamics* or *SPH* (Monaghan and Lattanzio, 1985). Within a Newtonian framework these methods, which are also called *particle-based methods*, offer many advantages over grid-based methods and a few disadvantages [see, *e.g.*, Falle *et al.* (2012) for a discussion]. This is particularly true when describing configurations which do not possess any symmetry or whose spatial extension can change considerably over the evolution [see, *e.g.*, Monaghan (1992) for a review]. However, no fully covariant formulation of smooth particle hydrodynamics has been derived yet and a number of approximations need to be introduced when simulating black holes. We will not comment further on these methods, but refer to the works of Oechslin *et al.* (2002), Rosswog (2010) and of Bauswein and Janka (2012), where important extensions to curved spacetimes have been made recently.

## 8.1 The discretisation process

Given a set of partial differential equations of hyperbolic type, the corresponding *Cauchy* or *initial-value problem (IVP)* consists in finding a solution at an arbitrary future time once the solution is known at an initial time, which is also referred to as the *initial data*. For simplicity, let us consider a well-posed initial-value problem in one spatial dimension and write it generically as (the generalisation to the multidimensional case is straightforward)

$$\mathcal{L}(u) - \mathcal{F} = 0, \quad (8.1)$$

where  $u = u(x, t)$  is a *smooth* function in the two variables  $x$  and  $t$ ,  $\mathcal{L}$  is a differential operator acting on  $u$ , and  $\mathcal{F} = \mathcal{F}(u)$  is a function of  $u$  only and not of its derivatives. To fix ideas, one could think that the generic expression (8.1) actually refers to an advection equation, so that  $\mathcal{L}(u) = (\partial_t + v\partial_x)u$  and  $\mathcal{F} = 0$ .

Independently of the specific numerical method employed, the numerical solution of (8.1) consists of three “discretisation steps”, *i.e.*,

- *Spacetime discretisation*: define a finite set of spacelike foliations of the spacetime “ordered” through the discrete time coordinate

$$t^n := t^0 + n\Delta t, \quad n = 0, 1, \dots, N_t, \quad (8.2)$$

where  $\Delta t$  represents the separation between two spacelike foliations and can, in general, be a function of space and time. On each of such foliations, say the one at  $t = t^n$ , “order” the spatial positions through the discrete coordinates

$$x_j := x_0 + j\Delta x, \quad j = 0, 1, \dots, J, \quad (8.3)$$

where we have simplified the notation, *i.e.*,  $x_j^n \rightarrow x_j$  and where also  $\Delta x$  can be a function of space and time. The set of spacetime points  $\{x_k^n\}$  is also referred to as *gridpoints*.

The points  $x_0$  and  $x_J$  mark the edges of the *computational domain*.

- *Variable discretisation*: replace the function  $u(x, t)$  with a discrete set of values  $\{u_j^n\}$  that approximate the *exact* pointwise values of  $u$  at the gridpoints  $\{x_j^n\}$ , i.e.,  $U_j^n$ , through the *gridfunction*  $\{u_j^n\}$  defined as

$$\{u_j^n\} \approx u(\{x_j^n\}) = u(x = x_j, t = t^n) =: \{U_j^n\}, \quad (8.4)$$

with  $n = 0, 1, \dots, N_t$ , and  $j = 0, 1, \dots, J$ . In this way, we can represent a generic solution  $u(x, t)$  of the generic equation (8.1) in the continuum spacetime with an infinite set of discretised solutions  $\{u_j^n\}$ , whose properties will depend both on the details of the discretisation (i.e., on  $\Delta t$  and  $\Delta x$ ) and on the method used to discretise the differential operator (see below).

- *Operator discretisation*: replace the continuous differential operator  $\mathcal{L}$  with a discretised one,  $L_h$ , that when applied to the gridfunction  $\{u_j^n\}$  gives an approximation to  $\mathcal{L}(u)$  in terms of differences between the set of values  $\{u_j^n\}$ .

Through this discretisation process, the *continuum* initial-value problem (8.1) is replaced by the *discrete* initial-value problem

$$\mathcal{L}(u) - \mathcal{F} = 0 \quad \longmapsto \quad L_h(U_j^n) - F_h = 0, \quad (8.5)$$

that is, by a discrete representation of *both* the differential operator  $\mathcal{L}$  and of the function  $u$ , where  $h := \Delta x$ . Note that the right-hand side of Eq. (8.5)<sub>2</sub> is zero because the differential operator acts on the numerical solution  $u_j^n$ , but this is no longer the case if the operator acts on the exact pointwise values of  $u$  at the gridpoints  $\{x_j^n\}$ , i.e.,

$$L_h(U_j^n) - F_h \neq 0. \quad (8.6)$$

The amount by which it differs from zero is actually very important as it reflects the *error* made in the discretisation of the operator, whose significance will be clarified below [cf., Eqs. (8.14), and (8.16)].

Many of the concepts discussed above on the discretisation process are shown schematically in Fig. 8.1, which describes the transition from a continuum space of solutions  $\Omega$ , on the left, to a discretised one  $\Omega_h$ , on the right. We denote respectively as  $\mathcal{I}$  and  $\mathcal{I}_h$  the initial data in each representation, and mark both of them with a thick dark red line. The blue solid lines on the left panel represent the edges,  $\partial\Omega$ , of the region of influence as marked by the local characteristics, whose slope is not necessarily constant (see Section 4.2.4 for a definition). Note that in the vast majority of numerical solutions, the spatial grid covers only a portion of the spacetime, so that the outer boundaries  $\delta\Omega_h$  (blue solid lines in the right panel) are effectively timelike boundaries. Since these boundaries are in causal contact with the space of solutions (they are in the region of the influence of the initial data), the corresponding initial-value problem becomes an *initial-value boundary problem (IVBP)*, to emphasise that also the boundaries can affect the solution.<sup>2</sup> Suitable boundary conditions need to be imposed on  $\delta\Omega_h$  to minimise their influence on the solution.

<sup>2</sup>In this classification, the solution of a set of *elliptic* partial differential equations is also referred to as a *boundary-value problem (BVP)*.

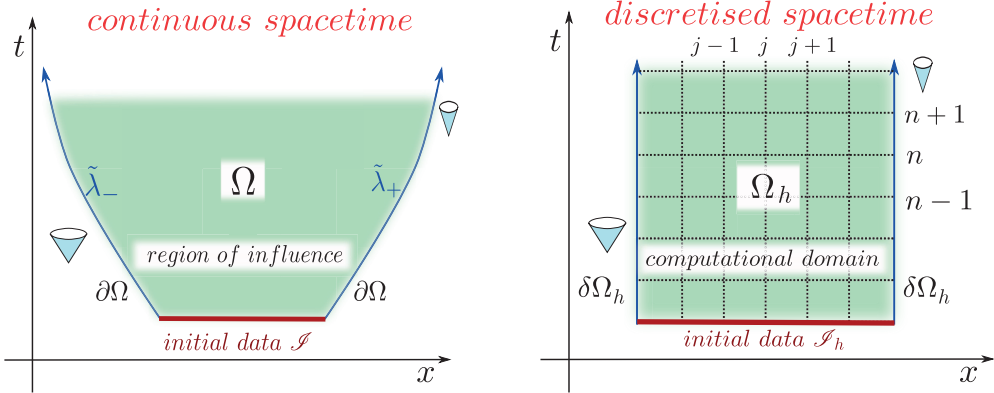


**Fig. 8.1** Schematic discretisation of a hyperbolic initial-value boundary problem. *Left panel:* Continuous spacetime and continuum space of solutions  $\Omega$ , whose edges  $\partial\Omega$  mark the limits of the region of influence (see Section 4.2.4 and *cf.*, Fig. 4.3). *Right panel:* Discretised spacetime and space of solutions  $\Omega_h$ , whose edges  $\delta\Omega_h$  are usually timelike boundaries in causal contact with the solution.

### Spatial norms.

A very useful tool in assessing the global properties of a discretised solution is offered by the (spatial) *discretised norms*. We recall that for a continuum function  $u(x, t)$ , smooth in the interval  $x \in [a, b]$ , the corresponding  $p$ -norm is defined as

$$\|u\|_p := \left( \frac{1}{(b-a)} \int_a^b |u(x, t)|^p dx \right)^{1/p}, \quad (8.7)$$

and has the same dimensions as the originating quantity  $u(x, t)$ . The extension of the definition (8.7) to a discretised space and time is straightforward and yields the following discretised norms most commonly used

$$\|u(t^n)\|_1 = \frac{1}{J} \sum_{j=0}^J |u_j^n| = \|u(t^n)\|, \quad :: \text{one--norm}, \quad (8.8)$$

$$\|u(t^n)\|_2 = \left( \frac{1}{J} \sum_{j=0}^J (u_j^n)^2 \right)^{1/2}, \quad :: \text{two--norm}, \quad (8.9)$$

$$\|u(t^n)\|_p = \left( \frac{1}{J} \sum_{j=0}^J |u_j^n|^p \right)^{1/p}, \quad :: p\text{-norm}, \quad (8.10)$$

$$\|u(t^n)\|_\infty = \max(|u_j^n|), \quad j = 0, \dots, J, \quad :: \text{infinity--norm}. \quad (8.11)$$

Note that the discretised two-norm  $\|u\|_2$  effectively corresponds to a root mean square of the discretised solution  $u_j^n$  and indeed it is often used as a measure of the average of the solution over the computational domain.

## 8.2 Numerical errors

Errors are an inevitable property of the numerical solution of a mathematical problem and their presence is not a nuisance as long as their origin is well understood and their behaviour matches the expected one. Like an experimental physicist, who has to determine all the sources of error in his measurements, so a computational physicist must determine all the contributions to his numerical solution that make it differ from the exact one, that is, the *numerical errors*. Three main errors will be discussed repeatedly in the following chapters and we briefly discuss them below.

### Machine-precision error.

The *machine-precision error* is a consequence of the fact that any machine will represent a rational number with a finite set of significant figures. It can be expressed in terms of the equality

$$\text{fp}(1.0) = \text{fp}(1.0) + \epsilon_M, \quad (8.12)$$

where  $\text{fp}(1.0)$  is the floating-point representation of the number 1. Stated differently, the machine-precision error reflects the ability of the machine to distinguish two floating-point numbers and is therefore a genuine property of the machine.

### Round-off error.

The *round-off error* is the accumulation of machine-precision errors as a result of  $N_{\text{FP}}$  floating-point operations. Because of the incoherent nature in which machine-precision errors add up, this error can be estimated to be

$$\epsilon_{\text{RO}} \approx \sqrt{N_{\text{FP}}} \epsilon_M. \quad (8.13)$$

When performing a numerical computation one should restrict the number of operations such that  $\epsilon_{\text{RO}}$  is below the error at which the results need to be determined.

### Truncation error.

The *truncation error* (either *local* or *global*) is fundamentally different from the previous two types of errors in that it is entirely under human control and reflects the decision made in discretising the continuum problem. As we will discuss below, the truncation error is the most important tool to assess the correct discretisation of a system of partial differential equations, and it is therefore useful to dedicate a brief discussion to this concept.

For simplicity, we consider a hyperbolic system of partial differential equations in one dimension with a discretisation  $\Delta t$  in time and  $\Delta x$  in space. If  $u(x, t)$  is the exact solution of the system (8.1) at  $t = t^n$  and  $x = x_j$ , we can measure the difference between the exact solution of the continuum problem,  $u(t^n, x_j)$ , and its numerical counterpart  $u_j^n$ , that is, using Eqs. (8.1) and (8.5), we can define the *local truncation error* (or “residual”) as [cf., Eq. (8.5)]

$$(\epsilon^{(h)})_j^n := [L_h(U_j^n) - F_h] - [\mathcal{L}(u) - \mathcal{F}] = L_h(U_j^n) - F_h, \quad (8.14)$$

where  $U_j^n := u(x = x_j, t = t^n)$  are the values of the continuum (exact) solution at the discretised locations in the spacetime [cf., Eq. (8.4)]. In other words, the local truncation error measures the difference from zero when the discretised operators are applied to the exact

solution. In this respect, it represents the error we have selected when a specific mathematical choice has been made in the discretisation of the differential operator  $\mathcal{L}$ . In general, the local truncation error can be written as a combination of an error associated with the *time discretion* and an error associated with the *spatial discretisation*, *i.e.*,

$$(\epsilon^{(h)})_j^n = \mathcal{O}(c_1 \Delta t^q + c_2 \Delta x^p), \quad (8.15)$$

where  $c_1$  and  $c_2$  are assumed to be two constant coefficients. The discretised problem (8.2) is then said to have a *local order of accuracy*  $r$ , where  $r = \min(p, q)$ . Note that in the above definition we have assumed that  $c_1 \sim c_2$ ; if the coefficients are very different, *e.g.*,  $c_1 \ll c_2$ , it is then possible that the order of accuracy is  $p$  even if  $p > q$ . This is actually the case in most practical numerical simulations, where the time discretisation has a smaller order of accuracy, but where the use of small time-steps makes the spatial discretisation the dominant truncation error.

It is quite clear that the truncation error is totally under human judgement and its measure is essential to guarantee that the discretisation operation has been made properly and that the discretised problem is therefore a faithful representation of the continuum one, but for the truncation error. Let us elaborate further on this concept and simplify our notation a bit. In the vast majority of discretisation methods for hyperbolic problems, a constraint requires that the time and spatial discretisation are comparable,<sup>3</sup> *i.e.*,  $\Delta x = \mathcal{O}(\Delta t)$ , so that we do not need to distinguish between the space and time discretisation and just consider a generic discretisation interval  $h := \Delta x \sim \Delta t$ . Let us then drop the index  $n$  referring to the time slice and indicate the local truncation error simply as

$$\epsilon_j^{(h)} = \tilde{C} h^{\tilde{p}_j} + \mathcal{O}(h^{\tilde{p}_j+1}), \quad (8.16)$$

with  $\tilde{C}$  a constant. Given the local numerical solution  $u_j^{(h)}$  obtained with grid spacing  $h$  and a discrete differential operator which is  $p$ -th order accurate at  $x_j$ , we can calculate the *local error*,  $E_j^{(h)}$ , as the difference between the exact and the numerical solution at  $x_j^n$ , *i.e.*,

$$E_j^{(h)} := U_j - u_j^{(h)}. \quad (8.17)$$

The local truncation error and the local error are clearly related and this relation is particularly simple to derive in the case of linear problem, where (see Problem 1)

$$E_j^{(h)} = (L_h)^{-1} \epsilon_j^{(h)} = Ch^{\tilde{p}_j} + \mathcal{O}(h^{\tilde{p}_j+1}), \quad (8.18)$$

so that we can immediately obtain a measure of the local error simply in term of the spacing of the discretisation.<sup>4</sup> If a different solution is computed with a grid spacing  $k < h$ , it will

<sup>3</sup>We will see below that this constraint is imposed by the *Courant–Friedrichs–Lewy (CFL) condition* (Courant *et al.*, 1967); see also footnote 8 in Section 8.3.1.

<sup>4</sup>Of course, for Eq. (8.18) to be valid, the inverse operator  $(L_h)^{-1}$  must not be singular for  $h \rightarrow 0$ ; a similar relation can be found also in the case of nonlinear problems (LeVeque, 1992).

then have, at the same time  $t = t^n$  and spatial position  $x_j$ , a corresponding error  $E_j^{(k)}$ , so that we can introduce the *error ratio* as

$$R_j(h, k) := \frac{E_j^{(h)}}{E_j^{(k)}} = \frac{h^{\tilde{p}_j}}{k^{\tilde{p}_j}} + \mathcal{O}(h^{\tilde{p}_j+1}), \quad (8.19)$$

from which we can compute the *numerical* local order of accuracy as

$$\tilde{p}_j := \frac{\log |R_j(h, k)|}{\log(h/k)}. \quad (8.20)$$

Note that  $p$  and  $\tilde{p}_j$  are conceptually similar but distinct. The first one represents the accuracy order in the continuum limit, while the second one is the accuracy order as *measured* from the numerical solution of the continuum problem at  $x = x_j$ . As we will comment later on, it is important to establish the relations between  $p$  and  $\tilde{p}_j$  as the resolution is changed. Assuming now that the two resolutions scale as  $k = h/\gamma$ , the error ratio (8.19) and the corresponding order of accuracy can be written respectively as

$$R_j(h, h/\gamma) = \gamma^{\tilde{p}_j} = 2^{\tilde{p}_j}, \quad \tilde{p}_j = \log |R_j(h, h/\gamma)| / \log(\gamma) = \log_2 |R_j|, \quad (8.21)$$

where the second equalities in (8.21) are written in the (rather common) case in which the grid spacing is simply halved, *i.e.*,  $\gamma = 2$ .

When defining the local error (8.17), we have assumed knowledge of the exact solution  $U_j$ , which, however, is in general not available. This does not represent a major obstacle and the local accuracy order can still be computed by simply employing a third (or more) numerical evaluation of the solution. We therefore exploit the fact that the difference between two numerical solutions does not depend on the actual exact solution and write

$$u_j^{(h)} - u_j^{(k)} = (U_j - E_j^{(h)}) - (U_j - E_j^{(k)}) = E_j^{(k)} - E_j^{(h)}, \quad (8.22)$$

where, of course, the two solutions  $u_j^{(h)}$  and  $u_j^{(k)}$  should be evaluated at the same gridpoint  $t = t^n, x = x_j$ . If one of the numerical solutions is not available at such a point (*e.g.*, because the spacing used is not uniform) a suitable interpolation is needed and attention must be paid that the error it introduces is much smaller than either  $E_j^{(h)}$  or  $E_j^{(k)}$  in order not to spoil the measurement of the order of accuracy.

Using the definition (8.17) and three different numerical solutions  $u_j^{(h)}, u_j^{(k)}, u_j^{(\ell)}$  with grid spacings  $h, k$  and  $\ell$  such that  $\ell < k < h$ , two different error ratios can then be defined as<sup>5</sup>

$$R_j(h, k; \ell) := \frac{u_j^{(h)} - u_j^{(\ell)}}{u_j^{(k)} - u_j^{(\ell)}} = \frac{E_j^{(h)} - E_j^{(\ell)}}{E_j^{(k)} - E_j^{(\ell)}} = \frac{h^{\tilde{p}_j} - \ell^{\tilde{p}_j}}{k^{\tilde{p}_j} - \ell^{\tilde{p}_j}}, \quad (8.23)$$

$$R_j(h, k, \ell) := \frac{u_j^{(h)} - u_j^{(k)}}{u_j^{(k)} - u_j^{(\ell)}} = \frac{E_j^{(h)} - E_j^{(k)}}{E_j^{(k)} - E_j^{(\ell)}} = \frac{h^{\tilde{p}_j} - k^{\tilde{p}_j}}{k^{\tilde{p}_j} - \ell^{\tilde{p}_j}}, \quad (8.24)$$

<sup>5</sup>Note the slight but important difference in the notation of Eqs. (8.23) and (8.24), *i.e.*,  $R_j(h, k; \ell)$  and  $R_j(h, k, \ell)$ .

where in (8.23) we have taken the numerical solution  $u_j^{(\ell)}$  with the associated error  $E_j^{(\ell)}$  as the “reference” solution, since it is the one with the smallest error. Assuming again for concreteness the different resolutions have the same ratio  $\gamma$ , *i.e.*, that  $k = h/\gamma$  and  $\ell = k/\gamma = h/\gamma^2$ , then the error ratios assume the simple expressions<sup>6</sup>

$$R_j(h, h/\gamma; h/\gamma^2) = \gamma^{\tilde{p}_j} + 1 = 2^{\tilde{p}_j} + 1, \quad R_j(h, h/\gamma, h/\gamma^2) = \gamma^{\tilde{p}_j} = 2^{\tilde{p}_j}, \quad (8.25)$$

where, again, the second equalities in (8.25) refer to the case in which the grid spacing is halved. As a result, the corresponding orders of numerical accuracy can be computed equivalently as (see Problem 2)

$$\tilde{p}_j = \frac{\log |R_j(h, h/\gamma; h/\gamma^2) - 1|}{\log(\gamma)} = \log_2 |R_j(h, h/2; h/4) - 1|, \quad (8.26)$$

or as

$$\tilde{p}_j = \frac{\log |R_j(h, h/\gamma, h/\gamma^2)|}{\log(\gamma)} = \log_2 |R_j(h, h/2, h/4)|. \quad (8.27)$$

All of our considerations so far have been “*local*”, in the sense that both the truncation error  $E_j^{(h)}$  and the order of accuracy  $\tilde{p}_j$  have been computed at a representative spatial position  $x = x_j$ . Of course, such considerations should apply equally for any position in the computational grid and therefore also in a “*global*” sense, that is, when the truncation error and the order of accuracy are computed relative to a “*global*” measurement in terms of quantities that can be considered as spatial averages of the solution. Any representative spatially averaged measure can be used, *e.g.*, a volume integral of the solution, but particularly useful are the spatial norms introduced in the previous section. For any spatial norm, therefore, it will be possible to define a *global truncation error* as the extension of the definition (8.14), *i.e.*,

$$\epsilon^{(h)} := \|\epsilon_j^{(h)}\| = \|L_h(U_j^n) - F_h\|, \quad (8.28)$$

as well as the *global error* as the extension of the definition (8.17), *i.e.*,

$$E^{(h)} := \|E_j^{(h)}\| = \|U_j - u_j^{(h)}\|. \quad (8.29)$$

These global measurements can then be used to define a *global order accuracy* as the extension of the definition (8.20), *i.e.*,

$$\tilde{p} := \frac{\log R(h, k)}{\log(h/k)}, \quad (8.30)$$

where now the *global* error ratio for two resolutions  $h$  and  $k$  is given by [*cf.*, (8.19)]

$$R(h, k) := \frac{E^{(h)}}{E^{(k)}} = \frac{h^{\tilde{p}}}{k^{\tilde{p}}} + \mathcal{O}(h^{\tilde{p}+1}), \quad (8.31)$$

and the errors  $\epsilon(h)$  and  $\epsilon(k)$  are computed via the norms (8.28). Following a logic which is identical to that followed before for the local order of accuracy, we can compute the global

<sup>6</sup>If the resolutions are not in a constant ratio, a nonlinear equation needs to be solved via a root-finding algorithm.

error ratio also when the exact solution is not known. More specifically, in this case, given three resolutions  $h, k$  and  $\ell$  with  $k = h/\gamma, \ell = k/\gamma$ , the *global orders of accuracy* can be computed equivalently as

$$\tilde{p} = \frac{\log |R(h, h/\gamma; h/\gamma^2) - 1|}{\log(\gamma)} = \log_2 |R(h, h/2; h/4) - 1|, \quad (8.32)$$

or as

$$\tilde{p} = \frac{\log |R(h, h/\gamma, h/\gamma^2)|}{\log(\gamma)} = \log_2 |R(h, h/2, h/4)|. \quad (8.33)$$

### 8.2.1 Consistency, convergence and stability

Many of the concepts and quantities introduced in the previous section represent the building blocks for two important definitions that will be presented here. Let us therefore go back to the hyperbolic partial differential equation [cf., Eq. (8.1)] where, we recall,  $\mathcal{L}$  is a quasi-linear differential operator and  $\mathcal{F}$  is a generic source term that depends on  $u$  but not on its derivatives. We indicate again with  $L_h$  the discretised representation of the continuum differential operator and with  $\epsilon^{(h)}$  the associated global truncation error [cf., Eq. (8.28)], which can be conveniently expressed as  $\epsilon^{(h)} = Ch^p = \mathcal{O}(h^p)$ , with  $C$  a real constant coefficient [cf., (8.16)]. The discretised representation  $L_h$  of the partial differential operator  $\mathcal{L}(u)$  is then said to satisfy the global *consistency condition* if (Richtmyer and Morton, 1994)

$$\lim_{h \rightarrow 0} \epsilon^{(h)} = 0. \quad (8.34)$$

In addition,  $L_h$  is said to satisfy the global *convergence condition* if

$$\lim_{h \rightarrow 0} E^{(h)} = \lim_{h \rightarrow 0} Ch^p = 0, \quad (8.35)$$

where the first equality follows from taking the norm of Eq. (8.18), and where  $p$  is then called the global *convergence order*. Note that local consistency conditions and local convergence can be defined in a very similar fashion by simply replacing  $\epsilon^{(h)}$  with  $\epsilon_j^{(h)}$  in Eq. (8.34), and  $E^{(h)}$  with  $E_j^{(h)}$  in Eq. (8.35), respectively. Of course, these changes would then lead to local convergence order  $\tilde{p}_j$ .

The convergence condition (8.35) can also be expressed in a different, more revealing way. Using in fact the definition of the numerical order of accuracy made in Eq. (8.20), the discretised operator  $L_h$  is said to be locally *convergent* if

$$\lim_{h \rightarrow 0} \tilde{p} := \frac{\log(E^{(h)})}{\log(Ch)} = p, \quad (8.36)$$

that is, if the accuracy order coincides with the convergence order, or, equivalently, if the measured numerical local truncation error coincides with the expected continuum one. Note that the convergence condition (8.35) is much more restrictive than the consistency one (8.34).

While both require the local truncation error to decrease with increasing resolution and to vanish in the continuum limit, the convergence condition requires that this happens at a very precise rate, that is, the *convergence rate*. Therefore, consistency is a necessary condition for convergence, but not a sufficient one.

A few remarks are worth making. First, in practice, there will be a minimum resolution,  $h_{\min}$ , below which the truncation error will dominate over the others, *e.g.*, round-off error. Clearly, one should expect convergence only for  $h < h_{\min}$  and the solution in this case is said to be in a *convergent regime*. Second, note that the consistency and convergence conditions (8.34) and (8.35), which have been expressed above for the *global* truncation error, can be easily extended to the *local* truncation error following the logic behind expressions (8.14) and (8.20). Third, when validating the correct discretisation of a partial differential equation, the convergence condition (8.35) is verified by computing the numerical solution at different resolutions and by estimating the truncation error through the exact solution [*cf.*, Eq. (8.21)]. This is usually referred to as the “*convergence test*”, with two resolutions being sufficient.<sup>7</sup> If the exact solution is not known, it is sufficient to perform an additional measurement at a third resolution, comparing the three different truncation errors to estimate the order of accuracy [*cf.*, Eq. (8.23)]. This is usually referred to as the “*self-convergence test*”.

We conclude this section with an important theorem that brings together many of the concepts discussed so far and provides a unique interpretation for the interplay between consistency, convergence and stability. Indeed, the measurement of a convergent discretisation also has another important aspect, which requires, however, yet another definition. Let us consider again the discretised representation  $L_h$  of the partial differential operator  $\mathcal{L}(u)$  and recall that its application across a time interval  $\Delta t$  introduces an associate truncation error  $\epsilon_j(h)$ . The evolution from time  $t = 0$  to  $t = t^n$  can then be thought of as the application  $n$ -times of the operator  $L_h$  to the corresponding solution  $u_j^m$  with  $m = 1, \dots, n$ . The application of this operator should be such that the error accumulated does not grow unbounded and we express this requirement through the condition of *numerical stability*. More specifically, indicating with  $L_h^n$  the  $n$ -th application of the operator  $L_h$ , the latter is said to be *numerically stable* if for each time  $T = t^n$  there is a constant  $C_s$  and a value  $h_0$  such that (LeVeque, 1992)

$$\|L_h^n\|_1 \leq C_s, \quad \text{for all } n h \leq T, \text{ and } h < h_0. \quad (8.37)$$

In essence, although our initial-value problem has been chosen to be well-posed, its discretisation can still lead to a solution that grows unbounded if an “unstable” numerical method is used. Hence, stability is a primary requirement for any discretised operator and the numerical solution of a well-posed initial-value problem is simply hopeless if performed with an unstable method.

Note that the operator is clearly stable if  $\|L_h\|_1 \leq 1$ , since  $\|L_h^n\|_1 \leq \|L_h\|_1^n \leq 1$ . In most practical situations, however, a certain growth is allowed, for instance if the solution intrinsically grows with time, so that the stability condition is enforced by requiring that  $\|L_h\|_1 \leq 1 + \gamma h$ , and

$$\|L_h\|_1^n \leq (1 + \gamma h)^n \leq e^{\gamma hn} \leq e^{\gamma T}. \quad (8.38)$$

Stated differently, the solution at later times is bounded to grow at most exponentially. With this definition in hand, we can state the following theorem

<sup>7</sup>In practice, the truncation errors measured with the two resolutions are used to draw a straight line in a log-log plot of  $\epsilon_j$  versus  $h$ , whose slope should match the expected one.

**Theorem** *Given a well-posed initial-value linear problem and a finite-difference approximation to it that satisfies the consistency condition, stability is a necessary and sufficient condition for convergence.*

This theorem, known as the *Lax equivalence theorem* (Lax and Richtmyer, 1956), shows that for an initial-value problem which has been discretised with a consistent finite-difference operator (which we will introduce in detail in the next section), the concept of *stability* and *convergence* are interchangeable. In principle, therefore, proving that the numerical solution is convergent will not only validate that the discrete form of the equations represents a faithful representation of the continuum ones, but also that the solution will be bounded at all times. In practice, however, since the theorem strictly holds only for linear partial differential equations, it has a limited impact for most of the problems of physical interest. A proof of the Lax equivalence theorem can also be found in Richtmyer and Morton (1967).

### 8.3 Finite-difference methods

Once a discretisation of space and time is introduced, *finite-difference methods* offer a very natural way to express a partial derivative (and hence a partial differential equation). The basic idea behind these techniques is that the solution of the differential equation  $u(x_j, t^n)$  at a given position  $x_j$  and at a given time  $t^n$  can be Taylor-expanded in the vicinity of  $(x_j, t^n)$ . Under this simple assumption, differential operators can be replaced by properly weighted differences of the solution evaluated at different points in the numerical grid. In what follows we review briefly the most elementary, but also pedagogical, algorithms employed to solve the simplest initial-value problem, namely, the one-dimensional scalar advection equation [*cf.*, Eq. (4.66)]

$$\partial_t u + \lambda \partial_x u = 0. \quad (8.39)$$

Here  $\lambda$  is the *advection velocity* and the general solution to Eq. (8.39) is  $u = u_0(x - \lambda t)$  [*cf.*, Eq. (4.71)]. An extensive presentation of finite-difference methods can be found in the monographs of Richtmyer and Morton (1994), Leveque (2007) and of Strikwerda (2004).

#### 8.3.1 Analysis of the numerical stability

Before going into the details of the various *numerical schemes* that will be discussed in the following section, it is useful to translate the concept of numerical stability introduced in Section 8.2.1 into *stability criteria* for a generic hyperbolic equation of the type (8.39).

##### **The CFL condition.**

A first and *necessary* condition for stability is the so-called *Courant–Friedrichs–Lewy (CFL) condition* (Courant *et al.*, 1928; Courant *et al.*, 1967), which applies essentially to all the numerical schemes that are “explicit” and “one-level” (see Section 8.3.2 for the corresponding definitions)<sup>8</sup>. From a *mathematical* point of view, it ensures that the domain of dependence of  $(x_j, t^{n+1})$  is contained in the *numerical domain of dependence* of  $(x_j, t^{n+1})$ . We recall that

<sup>8</sup>It should not go without a remark the fact that the CFL condition was first suggested back in 1927, when of course computers had still to be developed (Courant *et al.*, 1928).

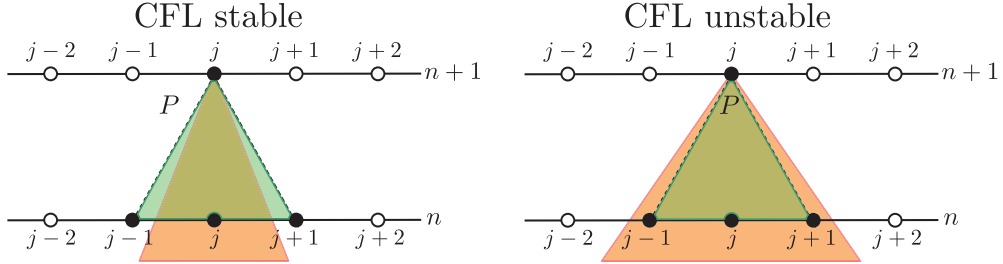


**Fig. 8.2** Schematic diagrams of CFL stable and CFL unstable choices of time discretisation. The left panel shows an example in which the domain of dependence (orange-shaded area) is smaller than the numerical one set by the stencil across the gridpoints  $j - 1, j + 1$  (green-shaded area), and is therefore stable. In the right panel, instead, the domain of dependence is larger and would therefore lead to a CFL unstable evolution.

the domain of dependence of a generic point  $(x_j, t^{n+1})$  was defined in Section 4.2.4 as the set of points at time  $t^n$  upon which the solution at  $(x_j, t^{n+1})$  depends. Its size is determined therefore by the slopes of the characteristics converging at  $(x_j, t^{n+1})$ . The numerical domain of dependence of  $(x_j, t^{n+1})$  is instead defined as the set of points at time  $t^n$  that are involved in the calculation of the solution at  $(x_j, t^{n+1})$ . Its size is entirely determined by the *stencil* of the method, that is, by the number of points involved in the scheme. From a *physical* point of view the CFL condition ensures that the propagation speed of any physical perturbation (e.g., the sound speed, or the speed of light) is always smaller than the numerical speed defined as  $\lambda_N := \Delta x / \Delta t$ , *i.e.*,

$$|\lambda| \leq \lambda_N := \frac{\Delta x}{\Delta t}. \quad (8.40)$$

In essence, therefore, the CFL condition prevents any physical signal from propagating for more than a fraction of a gridzone during a single time-step.

These concepts are summarised graphically in the diagrams in Fig. 8.2. The left panel shows an example of a time discretisation which is CFL stable, while the right panel shows one which is CFL unstable. Note that in the first case the domain of dependence (orange-shaded area) is smaller than the numerical one set by the stencil across the gridpoints  $j - 1, j + 1$  (green-shaded area), while it is larger than the numerical stencil for an unstable discretisation.

In all practical implementations, the CFL condition (8.40) is used to constrain the time-step  $\Delta t$  once  $\lambda$  is known and  $\Delta x$  has been chosen to achieve a certain accuracy. Moreover, since the CFL condition is only a necessary one, a constant dimensionless coefficient, usually referred to as the “CFL factor”,  $c_{\text{CFL}} \leq 1$ , is introduced to CFL-constrain the time-step and obtain an effectively stable evolution, *i.e.*,

$$\Delta t = c_{\text{CFL}} \frac{\Delta x}{|\lambda|}. \quad (8.41)$$

With this picture in mind, the generalisation of the CFL condition (8.41) to systems of equations is straightforward and essentially amounts to ensuring that, whatever the number of

equations, the fastest signal travels at most a fraction of the length of a *gridcell* (or *gridzone* or simply *cell*) between  $t = t^n$  and  $t = t^{n+1}$ , i.e.,

$$\Delta t = c_{\text{CFL}} \min_k \left( \frac{\Delta x}{|\lambda_k^n|} \right), \quad (8.42)$$

where the index  $k$  spans the set of possible different eigenvalues of the system, while the minimum value has to be computed after comparing the values of  $\lambda_k^n$  over the computational grid. The generalisation of the condition (8.41) to multidimensional spacetimes is straightforward and will be presented in Section 10.5 [cf., Eq. (10.110)]. Finally, note that since the CFL condition is necessary but not sufficient for stability, we will encounter in Section 8.3.3 a typical example of a numerical scheme that is unstable even when it satisfies the CFL condition.

### The von Neumann analysis.

Being based on the simple comparison between the mathematical and numerical domains of dependence, the CFL condition does not measure the stability properties of a given stable numerical scheme. To obtain such a measure, it is necessary to employ a more sophisticated approach, usually referred to as the *von Neumann stability analysis*, which represents a very useful tool for a first assessment of the stability properties of a numerical scheme. It is important to emphasise that the von Neumann stability analysis is “local” in the sense that: (a) it does not take into account boundary effects; (b) it assumes that the coefficients of the finite-difference equations vary sufficiently slowly to be considered constant in time and space; (c) it is just a *necessary* condition for stability.<sup>9</sup>

To highlight the basic logic of the von Neumann stability analysis, let us consider our reference hyperbolic differential equation (8.1) when written in a first-order-in-time homogeneous form as

$$\mathcal{L}(u) = 0 = \partial_t u - \mathcal{S}(u), \quad (8.43)$$

where  $\mathcal{S}$  represents a generic spatial differential operator acting on  $u$ . In full generality, and using a discretisation of the time derivative that will be made more rigorous in (8.49), we can then express the discretised representation of Eq. (8.43) as

$$u_j^{n+1} = u_j^n + \Delta t S_h(u_j^n, u_{j\pm 1}^n, \dots), \quad (8.44)$$

with  $S_h = S_h(\Delta x^p)$  being the discretised form of the spatial differential operator  $\mathcal{S}$  expressed at the order  $q$  in space and acting on the stencil with gridpoints  $u_j^n, u_{j\pm 1}^n, \dots$ . Let us now express the discretised solution to (8.43) as a sum of eigenmodes which, at each grid point, have the form

$$u_j^n = \xi^n e^{ikx_j} = \xi^n e^{ik(x_0 + j\Delta x)}, \quad (8.45)$$

where  $k$  is the spatial wavenumber and  $\xi = \xi(k)$  is a complex number. It then follows from Eqs. (8.45) and (8.44) that the time evolution of a single eigenmode is nothing but a succession of integer powers of the complex number  $\xi$ , which is therefore named the *amplification factor*.

<sup>9</sup>We note that under suitable conditions, which require a more involved mathematical analysis than the one carried out here, the von Neumann stability condition can also become a *sufficient* one (Morton and Mayers, 2005).

This naturally leads to a criterion of stability requiring that the modulus of the amplification factor is always less than or equal to one, *i.e.*,

$$|\xi|^2 = \xi \xi^* \leq 1. \quad (8.46)$$

In the following sections we will employ the von Neumann stability analysis to evaluate the amplification factor (8.46) for a series of well-known numerical methods and will learn how to use it for measuring the degree of dissipation.

### 8.3.2 The upwind scheme

The first discretisation algorithm we will consider is referred to as the *upwind scheme* and represents the building block of many others we will see in the remainder of this chapter and in the following one. Let us start the derivation of a finite-difference discrete representation of the advection equation (8.39) by first considering the derivative in time. Taylor-expanding the solution around  $(x_j, t^n)$  we readily obtain

$$u(x_j, t^n + \Delta t) = u(x_j, t^n) + \partial_t u(x_j, t^n) \Delta t + \mathcal{O}(\Delta t^2). \quad (8.47)$$

Replacing now the exact pointwise values of  $u(x_j, t^n)$  with their discrete approximation  $\{u_j^n\}$  and the continuous partial derivative  $\partial_t u(x_j, t^n)$  with the corresponding discretised operator  $\partial_t u|_j^n$ , we can rewrite (8.47) as

$$u_j^{n+1} = u_j^n + \partial_t u|_j^n \Delta t + \mathcal{O}(\Delta t^2). \quad (8.48)$$

Isolating the time derivative and dividing by  $\Delta t$  we obtain the first-order-in-time finite-difference representation of the time derivative as

$$\partial_t u|_j^n = \frac{u_j^{n+1} - u_j^n}{\Delta t} + \mathcal{O}(\Delta t). \quad (8.49)$$

In a similar way, we can derive a first-order, finite-difference approximation to the space derivative as

$$\partial_x u|_j^n = \frac{u_j^n - u_{j-1}^n}{\Delta x} + \mathcal{O}(\Delta x), \quad (8.50)$$

which however suffers from the ambiguity, not present in expression (8.49), that the first-order term in the Taylor expansion can be equally expressed in terms of  $u_{j+1}^n$  and  $u_j^n$ , that is, also as

$$\partial_x u|_j^n = \frac{u_{j+1}^n - u_j^n}{\Delta x} + \mathcal{O}(\Delta x). \quad (8.51)$$

As long as we are concerned with an advection equation, whose transport properties are known, this ambiguity is easily resolved if we think that the differential equation will simply translate each point in the initial solution to the new position  $x + \lambda \Delta t$  over a time interval  $\Delta t$ . In this case, it is natural to select the points in the solution at the time-level  $n$  that are “upwind” of the solution at the position  $j$  and at the time-level  $n + 1$ , as these are the ones causally connected with  $u_j^{n+1}$ . Depending then on the direction in which the solution is translated, and

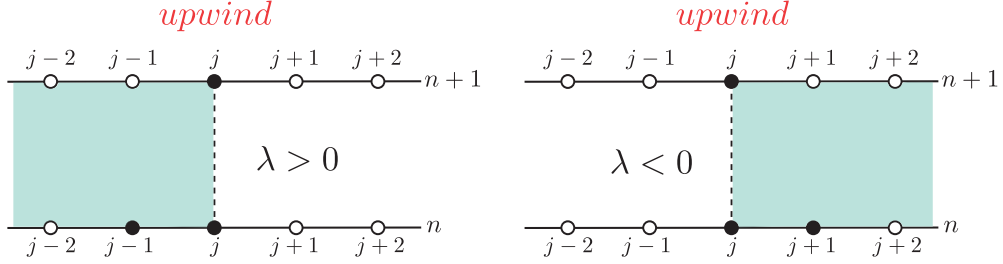


**Fig. 8.3** Schematic representation of the space and time stencils of the upwind scheme. Indicated with filled circles are the gridpoints used by the discrete differential operator, while dashed lines indicate a time evolution.

hence on the sign of the advection velocity  $\lambda$ , two different finite-difference representations of Eq. (8.39) can be given

$$\frac{u_j^{n+1} - u_j^n}{\Delta t} = -\lambda \left( \frac{u_j^n - u_{j-1}^n}{\Delta x} \right) + \mathcal{O}(\Delta t, \Delta x), \quad \text{if } \lambda > 0, \quad (8.52)$$

$$\frac{u_j^{n+1} - u_j^n}{\Delta t} = -\lambda \left( \frac{u_{j+1}^n - u_j^n}{\Delta x} \right) + \mathcal{O}(\Delta t, \Delta x), \quad \text{if } \lambda < 0, \quad (8.53)$$

respectively. As a result, the final finite-difference algorithms for determining the solution at the new time-level will have the form

$$u_j^{n+1} = u_j^n - \alpha(u_j^n - u_{j-1}^n) + \mathcal{O}(\Delta t^2, \Delta x \Delta t), \quad \text{if } \lambda > 0, \quad (8.54)$$

$$u_j^{n+1} = u_j^n - \alpha(u_{j+1}^n - u_j^n) + \mathcal{O}(\Delta t^2, \Delta x \Delta t), \quad \text{if } \lambda < 0, \quad (8.55)$$

where<sup>10</sup>

$$\alpha := \lambda \frac{\Delta t}{\Delta x}. \quad (8.56)$$

A schematic representation of the upwind scheme can be found in Fig. 8.3. Expressions (8.52)–(8.53) and (8.54)–(8.55) give us the opportunity for a general comment. When passing from the finite-difference representation of the equation [*i.e.*, (8.52)–(8.53)], over to the expression for the solution at the new *time-level* [*i.e.*, (8.54)–(8.55)], the truncation error has been decreased by  $\mathcal{O}(\Delta t) = \mathcal{O}(\Delta x)$ . Therefore, if  $p$  is the order of the *new solution*  $u_j^{n+1}$ , and if the time derivative is only first-order, then the order of the *scheme* is  $p - 1$ . As a result, the upwind scheme is first-order.

The upwind scheme is an example of an *explicit scheme*, that is, of a scheme where the solution at the new time-level  $n + 1$  can be calculated explicitly from the quantities that are already known at the previous time-level  $n$ , *i.e.*,

$$u_j^{n+1} = f(u_j^n, u_{j\pm 1}^n, u_{j\pm 2}^n, \dots, u_j^{n-m}, u_{j\pm 1}^{n-m}, u_{j\pm 2}^{n-m}, \dots) + \mathcal{O}(\Delta x^p), \quad (8.57)$$

with  $m < n$ , where the terms on the right-hand side represent the spatial and time *stencils* of the finite-difference operator, that is, the number of gridpoints around  $j$  and the number of

<sup>10</sup>Some authors refer to  $\alpha$  as the *Courant factor* (Toro, 2009).

time-levels before the  $n$ -th that are needed by the scheme. Clearly, the size of the stencil is a function of the order of the discretisation, and the schemes we will consider hereafter either have  $m = 1$  in (8.57), and are then referred to as “one-level” schemes, or have  $m = 2$ , and are then obviously named “two-level” schemes (see Fig. 8.5 for the schematic diagram of the two-level leapfrog scheme). In Section 9.5 we will also introduce a different technique for performing the time update, namely the *method of lines*, where a different (and more common approach) is adopted. Finally, the stencil is also said to be (spatially) *centred* if it involves an equal number of gridpoints relative to the  $j$ -th, while it is said to be *one-sided* if the gridpoints are placed all to the left or all to the right of the  $j$ -th (the stencils of the upwind scheme are clearly one-sided).

The behaviour of an explicit scheme as given in Eq. (8.57) should be contrasted with that of an *implicit scheme*, where the finite-difference representation of the differential equation has terms on the right-hand-side that are at the new time-level  $n + 1$ , *i.e.*,

$$u_j^{n+1} = f(u_j^n, u_{j\pm 1}^{n+1}, u_{j\pm 1}^n, u_{j\pm 2}^n, \dots, u_{j\pm 1}^{n+m}, u_{j\pm 2}^{n+m}, \dots) + \mathcal{O}(\Delta x^p). \quad (8.58)$$

These numerical methods have the important advantage of not being constrained by a CFL condition on the time-step size [*cf.* Eq. (8.40)], but require in general the solution of a number of coupled algebraic equations and will not be discussed further here [see, *e.g.*, Press *et al.* (1986) for a basic introduction].

Using the definition (8.38) and the von Neumann stability analysis introduced in Section 8.3.1, we can determine that the upwind scheme is stable. To do this, let us consider  $\lambda > 0$  and substitute (8.45) in (8.55) to obtain an amplification factor (see Problem 3)

$$\xi = 1 - \alpha [1 - \cos(k\Delta x)] - i\alpha \sin(k\Delta x). \quad (8.59)$$

Its squared modulus  $|\xi|^2 := \xi \xi^*$  is then

$$|\xi|^2 = 1 - 2\alpha(1 - \alpha)[1 - \cos(k\Delta x)], \quad (8.60)$$

so that the amplification factor (8.60) is less than one as long as

$$\alpha \leq 1, \quad (8.61)$$

where of course  $\alpha > 0$  [*cf.* Eq. (8.56)]. The condition (8.61) coincides with the CFL condition (8.40) and therefore it effectively sets a constraint on the size of the time-step. As a final remark we note that the upwind method is applicable as long as the corresponding continuum equations have a clear “transport direction”. This is obvious in the case of Eq. (8.39), but may not be the case for more generic hyperbolic equations, for which different strategies need to be adopted in order to preserve the upwind character of the method (see Section 9.2).

### 8.3.3 The FTCS scheme

Let us consider again the advection equation (8.39), but with a more accurate finite-difference approximation of the spatial derivative. To do this we can calculate the two Taylor expansions in  $x_j \pm \Delta x$

$$u(x_j + \Delta x, t^n) = u(x_j, t^n) + \partial_x u(x_j, t^n) \Delta x + \frac{1}{2} \partial_x^2 u(x_j, t^n) \Delta x^2 + \mathcal{O}(\Delta x^3), \quad (8.62)$$

$$u(x_j - \Delta x, t^n) = u(x_j, t^n) - \partial_x u(x_j, t^n) \Delta x + \frac{1}{2} \partial_x^2 u(x_j, t^n) \Delta x^2 + \mathcal{O}(\Delta x^3), \quad (8.63)$$

which we then subtract and divide by  $2\Delta x$  to eliminate first-order terms and obtain

$$\partial_x u|_j^n = \frac{u_{j+1}^n - u_{j-1}^n}{2\Delta x} + \mathcal{O}(\Delta x^2). \quad (8.64)$$

Using now the second-order accurate operator (8.64), we can finite-difference the advection equation (8.39) using a first-order approximation for the time derivative and a second-order approximation for the spatial one, *i.e.*,

$$\frac{u_j^{n+1} - u_j^n}{\Delta t} = -\lambda \left( \frac{u_{j+1}^n - u_{j-1}^n}{2\Delta x} \right) + \mathcal{O}(\Delta t, \Delta x^2). \quad (8.65)$$

The resulting algorithm is then referred to as the *FTCS (Forward-Time-Centred-Space) scheme*, so that the solution at the new time-level is given by

$$u_j^{n+1} = u_j^n - \frac{\alpha}{2}(u_{j+1}^n - u_{j-1}^n) + \mathcal{O}(\Delta t^2, \Delta x^2 \Delta t), \quad (8.66)$$

so that the FTCS scheme is also first-order. A schematic representation of the FTCS scheme can be found in Fig. 8.4. Disappointingly, the FTCS scheme is *unconditionally unstable* even though it may satisfy the CFL condition. In fact, the numerical solution will be destroyed by numerical errors which grow exponentially, independently of the choice made for the time-step. This conclusion can be easily reached by applying the definition (8.45) to Eq. (8.65) and carrying out a few algebraic steps to obtain an amplification factor (see Problem 3)

$$\xi = 1 - i\alpha \sin(k\Delta x), \quad (8.67)$$

whose squared modulus is

$$|\xi|^2 = 1 + (\alpha \sin(k\Delta x))^2 > 1. \quad (8.68)$$

Because of this, the FTCS scheme cannot be used for the solution of hyperbolic equations.<sup>11</sup>

### 8.3.4 The Lax–Friedrichs scheme

The unconditional instability of the FTCS scheme can be easily resolved with a minor modification of the algorithm. The basic idea was proposed by Lax and Friedrichs and consists in simply replacing in the FTCS formula (8.65), the term  $u_j^n$  with its spatial average, *i.e.*,  $u_j^n \rightarrow u_j^n = (u_{j+1}^n + u_{j-1}^n)/2 + \mathcal{O}(\Delta x^2)$ , so as to obtain for the advection equation (8.39) the expression

$$u_j^{n+1} = \frac{1}{2}(u_{j+1}^n + u_{j-1}^n) - \frac{\alpha}{2}(u_{j+1}^n - u_{j-1}^n) + \mathcal{O}(\Delta x^2), \quad (8.69)$$

so that also the *Lax–Friedrichs scheme* is first-order only. A schematic representation of the Lax–Friedrichs scheme can be found in Fig. 8.4. Note that the truncation error in Eq. (8.69)

<sup>11</sup>Interestingly, the FTCS scheme is conditionally stable when employed for the solution of parabolic equations.

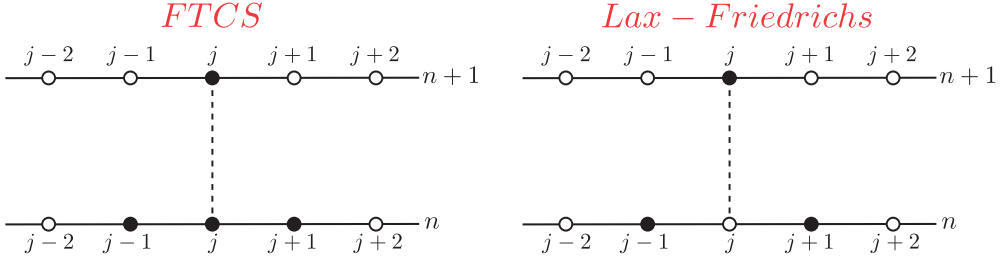


**Fig. 8.4** Schematic representation of the space and time stencils of the FTCS scheme (left panel) and of the Lax–Friedrichs scheme (right panel). Indicated with filled circles are the gridpoints used by the discrete differential operator, while dashed lines indicate a time evolution.

is reported to be  $\mathcal{O}(\Delta x^2)$  and not  $\mathcal{O}(\Delta t^2, \Delta x^2 \Delta t)$  because we are assuming that the CFL condition is satisfied<sup>12</sup> and hence  $\Delta t = \mathcal{O}(\Delta x)$ . We will maintain this assumption hereafter. Perhaps surprisingly, the algorithm (8.69) is now *conditionally stable*, as can be verified through a von Neumann stability analysis. Proceeding along the same lines followed for the FTCS scheme and using (8.45) in (8.69), we obtain an amplification factor whose modulus squared is (see Problem 3)

$$|\xi|^2 = 1 - \sin^2(k\Delta x) (1 - \alpha^2), \quad (8.70)$$

which is less than 1 as long as the CFL condition  $|\alpha| \leq 1$  is satisfied.

Although not obvious, the correction introduced by the Lax–Friedrichs scheme is equivalent to the introduction of a *numerical dissipation* (see also Section 8.3.7), which should not be confused however with the *artificial viscosity* (see also Section 8.4). To understand why a dissipative term has been introduced, we rewrite Eq. (8.69) so that it appears as a correction to (8.65), *i.e.*, as

$$\frac{u_j^{n+1} - u_j^n}{\Delta t} = -\lambda \left( \frac{u_{j+1}^n - u_{j-1}^n}{2\Delta x} \right) + \frac{1}{2} \left( \frac{u_{j+1}^n - 2u_j^n + u_{j-1}^n}{\Delta t} \right), \quad (8.71)$$

which, however, is the finite-difference representation at  $\mathcal{O}(\Delta t, \Delta x^2)$  of the *advection–diffusion equation*

$$\partial_t u + \lambda \partial_x u = \frac{1}{2} \left( \frac{\Delta x^2}{\Delta t} \right) \partial_x^2 u, \quad (8.72)$$

that is, of an advection equation with an additional diffusion term,  $\propto \partial_x^2 u$ . To prove this, we sum the two Taylor expansions (8.62)–(8.63) around  $x_j$  to eliminate the first-order derivatives and the  $\mathcal{O}(\Delta x^3)$  error terms, thus obtaining the second-order accurate representation of the second derivative, *i.e.*,

$$\partial_x^2 u|_j^n = \frac{u_{j+1}^n - 2u_j^n + u_{j-1}^n}{\Delta x^2} + \mathcal{O}(\Delta x^2). \quad (8.73)$$

Note that the second-order spatial derivative on the right-hand side of Eq. (8.72) is multiplied by  $\Delta x^2/\Delta t = \mathcal{O}(\Delta x)$ , so that the coefficient of the dissipative term is not constant and

<sup>12</sup>More generally, this result holds for any scheme having  $\Delta t \propto \Delta x$ .

$\mathcal{O}(\Delta x)$ . As a result, it goes to zero as  $\Delta x \rightarrow 0$ , thus guaranteeing that in the continuum limit the algorithm will converge to the correct solution of the advection equation.

To better appreciate the role played by numerical dissipation in the Lax–Friedrichs scheme, it is useful to bear in mind that a key aspect in any discrete representation is the determination of the length-scale  $L_s$  over which an accurate description is needed. If  $k$  is the wavenumber associated to this length-scale,  $k \propto 1/L_s$ , then the numerical description is accurate as long as the resolution  $\Delta x$  is such that  $k\Delta x \ll 1$ . In this case, expressions (8.67) and (8.70) clearly show that the amplification factor is very close to 1 and that the effects of dissipation are small both for the FTCS and for the Lax–Friedrichs schemes. On these scales the stable and unstable schemes are equally accurate. However, on the very small scales for which  $k\Delta x \sim 1$ , and which in general are not of interest, the stable and unstable schemes are radically different. The Lax–Friedrichs scheme will be simply inaccurate, while the FTCS will have exponentially growing errors destroying the solution. It is rather obvious that stability and inaccuracy are by far preferable to instability, especially if the accuracy is lost over wavelengths that are not of interest or when it can be recovered easily by using more refined grids.

### 8.3.5 The leapfrog scheme

Clearly, both the FTCS and the Lax–Friedrichs schemes are “one-level” schemes, with a first-order approximation for the time derivative and a second-order approximation for the spatial derivative. As a result, in order to achieve the desired accuracy,  $\lambda\Delta t$  should be taken significantly smaller than  $\Delta x$ , well below the limit imposed by the CFL condition. To improve on this and obtain second-order accuracy in time we simply need to employ a higher-order discretisation of the time derivative, *i.e.*, [cf., Eq. (8.64)]

$$\partial_t u|_j^n = \frac{u_j^{n+1} - u_j^{n-1}}{2\Delta t} + \mathcal{O}(\Delta t^2), \quad (8.74)$$

which, when applied to the FTCS scheme (8.66), leads to the *leapfrog scheme* for the advection equation (8.39)

$$u_j^{n+1} = u_j^{n-1} - \alpha(u_{j+1}^n - u_{j-1}^n) + \mathcal{O}(\Delta x^2). \quad (8.75)$$

Note that the factor 2 in  $\Delta x$  cancels the equivalent factor 2 in  $\Delta t$ , that the scheme is now second-order because of the second-order approximation of the time derivative in (8.74), and that it is a two-level scheme, requiring the storage of the values at time-levels  $n$  and  $n-1$  to obtain values at time-level  $n+1$ . Also in this case, a schematic representation of the leapfrog scheme can be found in Fig. 8.5.

Interestingly, in a leapfrog scheme which is CFL stable, there is no amplitude dissipation, *i.e.*,  $|\xi|^2 = 1$ . To reach this conclusion we use again a von Neumann stability analysis to obtain (see Problem 3)

$$\xi = -i\alpha \sin(k\Delta x) \pm \sqrt{1 - [\alpha \sin(k\Delta x)]^2}, \quad (8.76)$$

so that (see Problem 3)

$$|\xi|^2 = \alpha^2 \sin^2(k\Delta x) + \{1 - [\alpha \sin(k\Delta x)]^2\} = 1 \quad \forall \alpha \leq 1. \quad (8.77)$$

As a result, the squared modulus of amplification factor is always 1, provided the CFL condition  $|\alpha| \leq 1$  is satisfied. Note that a maximal amplification factor is not necessarily an

advantage, since a certain amount of dissipation can instead help in stabilising small errors introduced, for instance, by the outer boundaries in the computational domain, or by the use of meshes of different resolution.

### 8.3.6 The Lax–Wendroff scheme

The Lax–Wendroff scheme is the second-order accurate extension of the Lax–Friedrichs scheme. As for the case of the leapfrog scheme, in this case too we need two time-levels to obtain the solution at the new time-level. There are a number of different ways of deriving the *Lax–Wendroff scheme* but it is probably useful to look at it as a combination of the Lax–Friedrichs scheme and of the leapfrog scheme. In particular a Lax–Wendroff scheme for the advection equation (8.39) can be obtained as

- a Lax–Friedrichs “half-step” at fictitious intermediate spatial positions  $j \pm 1/2$  and half-time-level  $n + 1/2$ , *i.e.*,

$$u_{j \pm 1/2}^{n+1/2} = \frac{1}{2} (u_j^n + u_{j \pm 1}^n) \mp \frac{\alpha}{2} (u_{j \pm 1}^n - u_j^n) + \mathcal{O}(\Delta x^2), \quad (8.78)$$

where the coefficient  $\frac{1}{2}$  comes from having used a time-step  $\frac{1}{2}\Delta t$ ;

- a leapfrog “half-step”, so that the solution at the new time level  $n + 1$  will be

$$\begin{aligned} u_j^{n+1} &= u_j^n - \alpha (u_{j+1/2}^{n+1/2} - u_{j-1/2}^{n+1/2}) + \mathcal{O}(\Delta x^2) \\ &= u_j^n - \frac{\alpha}{2} (u_{j+1}^n - u_{j-1}^n) + \frac{\alpha^2}{2} (u_{j+1}^n - 2u_j^n + u_{j-1}^n) + \mathcal{O}(\Delta x^2), \end{aligned} \quad (8.79)$$

where expression (8.79) has been obtained after using the Lax–Friedrichs “half-step” (8.78).

Although described as a two-level scheme (*i.e.*, with information at time levels  $n$  and  $n + 1/2$ ), the Lax–Wendroff scheme can be effectively cast, via algebraic manipulations, as a one-level scheme. This is clear from expressions (8.79) where only quantities at time-levels  $n$  and  $n + 1$  appear. Again a schematic representation of its stencil can be found in Fig. 8.5.

Performing the usual von Neumann stability analysis on the Lax–Wendroff scheme reveals that the amplification factor is given by (see Problem 3)

$$\xi = 1 - i\alpha \sin(k\Delta x) - \alpha^2 [1 - \cos(k\Delta x)], \quad (8.80)$$

and the corresponding squared modulus is

$$|\xi|^2 = 1 - \alpha^2(1 - \alpha^2) [1 - \cos(k\Delta x)]^2. \quad (8.81)$$

As a result, the von Neumann stability criterion  $|\xi|^2 \leq 1$  is satisfied as long as  $\alpha^2 \leq 1$ , or equivalently, as long as the CFL condition is satisfied. It should be noticed, however, that unless  $\alpha^2 = 1$ , then  $|\xi|^2 < 1$  and some amplitude dissipation is present. In other words, the dissipative properties of the Lax–Friedrichs scheme are not completely lost in the Lax–Wendroff scheme, but are much smaller, being of  $\mathcal{O}(\alpha^2)$  only.

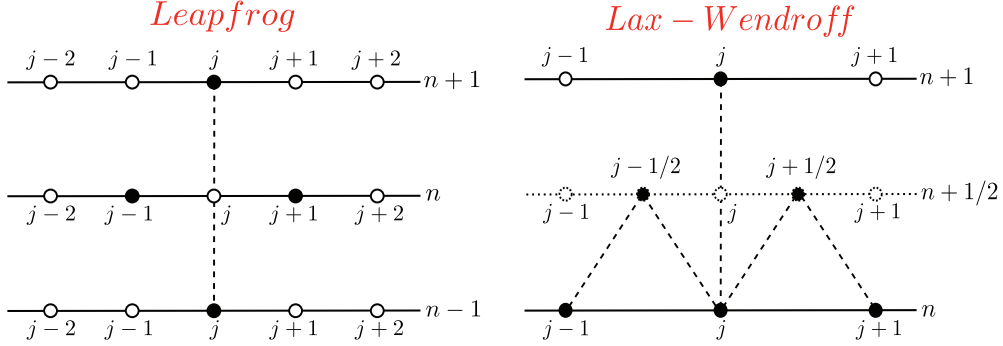


**Fig. 8.5** Schematic representation of the space and time stencils of the leapfrog scheme (left panel) and the Lax–Wendroff scheme (right panel). Indicated with filled circles are the gridpoints used by the discrete differential operator, while dashed lines indicate a time evolution. Note that the leapfrog stencil involves time-levels  $n$  and  $n-1$  to evolve the solution to time-level  $n+1$ .

With a bit of patience and a few more lines of algebra it is possible to show that the Lax–Wendroff scheme (8.79) provides a second-order accurate approximation to the advection equation (8.39), a second-order approximation to the advection–diffusion equation (8.72) with dissipation coefficient  $\varepsilon$ , and a third-order approximation to the equation

$$\partial_t u + \lambda \partial_x u = \varepsilon \partial_x^2 u + \beta \partial_x^3 u, \quad (8.82)$$

where

$$\varepsilon := \frac{\alpha \lambda \Delta x}{2}, \quad \beta := -\frac{\lambda \Delta x^2}{6} (1 - \alpha^2). \quad (8.83)$$

The simplest way of quantifying the effects introduced by the right-hand side of Eq. (8.82) is by using a single Fourier mode with angular frequency  $\omega$  and wavenumber  $k$ , propagating in the positive  $x$ -direction, *i.e.*,

$$u(x, t) = e^{i(kx - \omega t)}. \quad (8.84)$$

It is then easy to verify that in the continuum limit

$$\partial_t u = -i\omega u, \quad \partial_x u = iku, \quad \partial_x^2 u = -k^2 u, \quad \partial_x^3 u = -ik^3 u. \quad (8.85)$$

In the case in which the finite-difference scheme provides an accurate approximation to a purely advection equation [*cf.* Eq. (8.39)], the relations (8.85) lead to the obvious dispersion relation  $\omega = \lambda k$ , so that the *numerical* mode  $\tilde{u}(x, t)$  will have a solution

$$\tilde{u}(x, t) = e^{ik(x - \lambda t)}, \quad (8.86)$$

thus representing a mode propagating with *phase velocity*  $v_{\text{ph}} := \text{Re}(\omega/k) = \lambda$ , which coincides with the *group velocity*  $v_{\text{gr}} := \partial\omega/\partial k = \lambda$ . However, the advection–diffusion equation approximated by the Lax–Wendroff scheme (8.79) will have a corresponding solution

$$\tilde{u}(x, t) = e^{-\varepsilon k^2 t} e^{ik[x - (v + \beta k^2)t]}, \quad (8.87)$$

where the advective term is also accompanied by an exponentially decaying one and by an additional *dispersive* term,  $\sim \beta k^2 t$ , which produces different propagation speeds for modes

with different wavenumbers. This becomes apparent after calculating the phase and group velocities which are given by

$$v_{\text{ph}} = \frac{\omega}{k} = \lambda + \beta k^2, \quad v_{\text{gr}} = \frac{\partial \omega}{\partial k} = \lambda + 3\beta k^2. \quad (8.88)$$

Such a dispersive term is absent in the case of a Lax–Friedrichs scheme, which however has larger dissipation coefficient  $\varepsilon$ . Overall, these considerations show that, given a continuum (hyperbolic) partial differential equation, any discretisation scheme will introduce terms that are higher-order representations of dissipative and dispersive operators (*i.e.*, odd and even spatial partial derivatives). Although these corrections disappear in the continuum limit, they are present at a discrete level and their influence on the solution must be properly quantified.

As a final remark, we note that the Lax–Wendroff scheme can also be cast in a one-sided upwind version, which is also known as the *Beam–Warming scheme* and which we report below for completeness in its upwind version (this is also the only version in which it is essentially used)

$$u_j^{n+1} = u_j^n - \frac{\alpha}{2}(3u_j^n - 4u_{j-1}^n + u_{j-2}^n) + \frac{\alpha^2}{2}(u_j^n - 2u_{j-1}^n + u_{j-2}^n), \quad \text{if } \lambda > 0. \quad (8.89)$$

### 8.3.7 Kreiss–Oliger dissipation

We have already discussed that the finite-differencing in the Lax–Friedrichs scheme is equivalent to the introduction of a second-order spatial derivative, which has the effect of dissipating those contributions to the solution which appear at wavelengths comparable to or shorter than the grid spacing. We have also commented that, as long as the resolution used is sufficient to capture the relevant wavelengths of the problem at hand, a certain amount of dissipation is actually beneficial. Just like in a low-pass filter, in fact, it smooths out those high-frequency components of the solution we are not interested in and that can be introduced by a number of sources (outer boundaries, mesh-refinement boundaries, etc). It would therefore be useful to extend this feature of the Lax–Friedrichs scheme also to more generic discretisation. This is the spirit behind a very common form of *numerical dissipation* which is referred to as *Kreiss–Oliger dissipation* (Kreiss and Oliger, 1973).

The basic idea is simple and to illustrate it we can go back to our reference homogeneous hyperbolic equation in first-order form (8.43) with discretisation

$$u_j^{n+1} = u_j^n + \Delta t S_h(u_j^n, u_{j\pm 1}^n, \dots), \quad (8.44)$$

and think of adding to the spatial differential operator  $S_h$ , another operator  $D_h$ , with dissipative properties and such that the discretisation of (8.43) now becomes

$$u_j^{n+1} = u_j^n + \Delta t S_h(u_j^n, u_{j\pm 1}^n, \dots) - \varepsilon(-1)^N \Delta t \Delta x^{2N-1} D_h^{2N}(u_j^n, u_{j\pm 1}^n, \dots), \quad (8.90)$$

where  $\varepsilon > 0$ ,  $N \geq 1$  is an integer and  $D_h^{2N}$  is a centred difference operator approximating a partial spatial derivative of order  $2N$ , *e.g.*, a second- ( $N = 1$ ) or fourth-order ( $N = 2$ ) spatial derivative. Clearly, the discretisation (8.90) refers now to a continuum initial-value problem which is not given by Eq. (8.43), but rather by the first-order differential equation

$$\partial_t u = \mathcal{S}(u) - \varepsilon(-1)^N \Delta x^{2N-1} \partial_x^{2N} u. \quad (8.91)$$

Since we need Eq. (8.91) to represent a consistent approximation of the original equation (8.43), it is necessary that in the continuum limit the dissipative term  $D_h^{2N}u(u_j^n, u_{j\pm 1}^n, \dots)$  goes to zero together with — or possibly more rapidly than — the truncation error. Assuming that the latter is  $\epsilon^{(h)} = \mathcal{O}(\Delta x^p)$ , then it is clear that the coefficient in front of the dissipative term will have to be smaller than  $\epsilon^{(h)}$ , or, equivalently that  $N \geq (p+1)/2$ . This condition therefore sets a constraint on the order of the continuum partial differential operator  $\partial_x^{2N}u$  on the basis of the truncation error of the other continuum partial differential operator  $\mathcal{S}(u)$ . As a practical example, if  $\mathcal{S}(u)$  is discretised at fourth-order, *i.e.*,  $S_h = \mathcal{O}(\Delta x^4)$ , then the dissipative term must involve a sixth-order partial derivative, *i.e.*,  $N \geq 3$ .

If we are not interested in any of the specific finite-difference schemes discussed above and we simply want a finite-difference expression  $S_h(u_j^n)$  of a given differential operator,  $\mathcal{S}(u)$ , of differential order  $N$  and with a truncation error  $\mathcal{O}(\Delta x^p)$ , we can use rather simple recursive expressions. In particular, for a *centred* finite-difference scheme around  $x_j$  and over a numerical grid with *uniform* spacing  $h$ , we can approximate the  $N$ -th partial derivative in  $\mathcal{S}(u) = \partial_x^N u$  simply as (for compactness we drop the index  $n$  relative to the time-level)

$$\partial_x^N u|_{x=x_j} = \frac{1}{\Delta x^N} \sum_{k=1}^{k=s} c_k (u_{j+k} - u_{j-k}) + \mathcal{O}(\Delta x^p), \quad (8.92)$$

where  $s$  depends on the extent of the stencil and the coefficients  $c_k$  at the gridpoints  $x_{j+k}$  are given in Table 8.1 (see Problem 4).

For example, the centred finite-difference expressions for the first-order derivative at different orders of accuracy are simply given by

$$\partial_x f_j = \frac{1}{\Delta x} \left( \frac{1}{2} f_{j+1} - \frac{1}{2} f_{j-1} \right) + \mathcal{O}(\Delta x^2), \quad (8.93)$$

$$\partial_x f_j = \frac{1}{\Delta x} \left( -\frac{1}{12} f_{j+2} + \frac{2}{3} f_{j+1} - \frac{2}{3} f_{j-1} + \frac{1}{12} f_{j-2} \right) + \mathcal{O}(\Delta x^4), \quad (8.94)$$

while, for instance, the fourth-order accurate expression for the second derivative is

$$\partial_x^2 f_j = \frac{1}{\Delta x^2} \left( -\frac{1}{12} f_{j+2} + \frac{4}{3} f_{j+1} - \frac{5}{2} f_j + \frac{4}{3} f_{j-1} - \frac{1}{12} f_{j-2} \right) + \mathcal{O}(\Delta x^4). \quad (8.95)$$

Additional stencils for higher-order differential operators or for one-sided stencils can be found in Fornberg (1988). In a similar way, we can derive the finite-difference expression  $D_h^{2N}$  for the dissipative operator at  $x = x_j$ , which will instead take the simple expression (again, for compactness we drop the index  $n$  relative to the time-level)

$$D_h^{2N}|_{x=x_j} = \frac{1}{(2\Delta x)^{2N}} \left[ d_0 u_j + \sum_{k=1}^{k=s} d_k (u_{j+k} + u_{j-k}) \right] + \mathcal{O}(\Delta x^p), \quad (8.96)$$

where the coefficients  $d_k$  at the gridpoints  $x_{j+k}$  are given in Table 8.2.

As a final remark on Kreiss–Oliger dissipation, we note that while it is rarely used in the solution of the equations of relativistic hydrodynamics, it is however widely employed in the solution of the Einstein equations either in vacuum or non-vacuum spacetimes [see, *e.g.*, Baiotti and Rezzolla (2006) or Löffler *et al.* (2006)].

**Table 8.1** Coefficients  $c_k$  at gridpoints  $x_{j+k}$  for the centred finite-difference discretisation of the derivative  $\partial_x^N u$  at  $x_j$  and with truncation error  $\mathcal{O}(\Delta x^p)$ .

$N$	$\mathcal{O}(\Delta x^p)$	Approximation of $\partial_x^N u$ at $x_j$								
		-4	-3	-2	-1	0	+1	+2	+3	+4
1	2				$-\frac{1}{2}$	0	$+\frac{1}{2}$			
1	4			$+\frac{1}{12}$	$-\frac{2}{3}$	0	$+\frac{2}{3}$	$-\frac{1}{12}$		
1	6		$-\frac{1}{60}$	$+\frac{3}{20}$	$-\frac{3}{4}$	0	$+\frac{3}{4}$	$-\frac{3}{20}$	$+\frac{1}{60}$	
1	8	$+\frac{1}{280}$	$-\frac{4}{105}$	$+\frac{1}{5}$	$-\frac{4}{5}$	0	$+\frac{4}{5}$	$-\frac{1}{5}$	$+\frac{4}{105}$	$-\frac{1}{280}$
2	2				$+\frac{1}{1}$	$-\frac{2}{1}$	$+\frac{1}{1}$			
2	4			$-\frac{1}{12}$	$+\frac{4}{3}$	$-\frac{5}{2}$	$+\frac{4}{3}$	$-\frac{1}{12}$		
2	6		$+\frac{1}{90}$	$-\frac{3}{20}$	$+\frac{3}{2}$	$-\frac{49}{18}$	$+\frac{3}{2}$	$-\frac{3}{20}$	$+\frac{1}{90}$	
2	8	$-\frac{1}{560}$	$+\frac{8}{315}$	$-\frac{1}{5}$	$+\frac{8}{5}$	$-\frac{205}{72}$	$+\frac{8}{5}$	$-\frac{1}{5}$	$+\frac{8}{315}$	$-\frac{1}{560}$

## 8.4 Artificial-viscosity approaches

As mentioned in Section 7.3.1, when introducing the Wilson formulation of the relativistic-hydrodynamic equations, a non-conservative formulation requires the introduction of an *artificial viscosity*, usually indicated as  $Q$ , so as to channel high-frequency acoustic disturbances into internal energy where large compressions in the fluid take place. The corresponding numerical methods are then referred to as *artificial-viscosity methods* and have played an important role in the solution of the relativistic-hydrodynamic equations. Historically, the first implementations of artificial-viscosity methods were made by May and White (1967), basically extending to the relativistic regime the treatment of shock waves introduced by VonNeumann and Richtmyer (1950) for classical fluids, and were employed to study the gravitational collapse to a black hole in spherical symmetry adopting the Lagrangian formulation of Misner and Sharp (1964) (see Section 7.2.1). In practice, in these implementations the artificial viscosity  $Q_{\text{MW}}$  is activated only if there is a compression, *i.e.*, if  $\partial_t \rho > 0$ , and is simply added to the pressure. A prescription for  $Q_{\text{MW}}$  which has been extensively adopted in Lagrangian implementations is of the type

## 410 Numerical Relativistic Hydrodynamics: Finite-Difference Methods

**Table 8.2** Coefficients  $d_k$  at gridpoints  $x_{j+k}$  for the centred finite-difference discretisation of the derivative  $\partial_x^{2N} u$  (*i.e.*, of the dissipative Kreiss–Oliger operator) at  $x_j$  and with truncation error  $\mathcal{O}(\Delta x^p)$ .

$N$	Approximation of $\partial_x^{2N} u$ at $x_j$								
	Coefficients $d_k$ at $x_{j+k}$								
	-4	-3	-2	-1	0	+1	+2	+3	+4
1				+1	-2	+1			
2			-1	+4	-6	+4	-1		
3		+1	-6	+15	-20	+15	-6	+1	
4	-1	+8	-28	+56	-70	+56	-28	+8	-1

$$Q_{\text{MW}} = \begin{cases} k^2(e/\Gamma) [(\Delta\mu/R^2) \partial_\mu (uR^2)]^2 & \text{if } \partial_t \rho > 0, \\ 0 & \text{if } \partial_t \rho \leq 0, \end{cases} \quad (8.97)$$

where  $k$  is an adjustable coefficient [*e.g.*,  $k^2 = 2$  was used by Rezzolla and Miller (1994)] and where  $\mu$  is the rest mass contained within a shell of radius  $r$  and works as a radial comoving coordinate (see also Section 7.2.1). We recall that in Eq. (8.97)  $\mu$  represents the rest mass contained within a shell of radius  $r$  and plays the role of a comoving radial coordinate.

Artificial viscosity is used not only in Lagrangian but also in Eulerian formulations of the relativistic-hydrodynamic equations and indeed numerical codes using the Wilson formulation, which is *not* cast in a conservative form (see Section 7.3.1), have adopted numerical viscosity to stabilise the solution across discontinuities or large gradients (Wilson, 1972). The addition of artificial viscosity then has the effect of removing spurious oscillations which would develop across a shock, but at the cost of spreading the discontinuity over several grid-zones, sacrificing the ability to capture shocks sharply.

Poorly resolved shocks are not the only drawback of artificial-viscosity methods. As first pointed out by Centrella and Wilson (1984) and Norman and Winkler (1986), large errors can arise in the solution of relativistic flows according to how the artificial viscosity terms are included in the numerical implementation of the Wilson formulation. Originally, in fact, these terms were added only in specific parts of the equations, namely, to the pressure gradient in the source of the momentum equation (7.206) and at the divergence of the velocity in the source of the energy equation (7.207). This approach then led to errors which became larger for increasing bulk Lorentz factors. To compensate for these errors, Norman and Winkler (1986) proposed to add the artificial-viscosity terms in a relativistically consistent way, thus considering the *artificial* viscosity as a *physical* bulk viscosity. In this sense, the relativistic-hydrodynamic equations for a perfect fluid are rewritten in terms of a modified, artificial-viscosity energy-momentum tensor in the form [*cf.*, Eq. (3.36)]

$$T_{\text{AV}}^{\mu\nu} := (e + p + Q) u^\mu u^\nu + (p + Q) g^{\mu\nu}, \quad (8.98)$$

where  $Q$  is the *scalar* artificial-viscosity term<sup>13</sup> and is defined, for instance, as (Anninos and Fragile, 2003)

$$Q := (D + E + p\sqrt{-g}u^t)\ell(\nabla_i V^i)[k_{q2}\ell(\nabla_i V^i)(1 - \phi^2) - k_{q1}c_s], \quad (8.99)$$

where  $\ell$  is a length-scale (usually set to be the dimension of a typical gridzone), the coefficients  $k_{q2}$  and  $k_{q1}$  control the amount of viscosity which is either linear or quadratic in the velocity divergence, and  $\phi$  is a limiter between zero and one that can be applied to reduce the effect of artificial heating and narrow the width of shock fronts.

As a result of the new energy–momentum tensor (8.98), the *flat-spacetime* form of the momentum and energy equations in the Wilson formulation, *i.e.*, Eqs. (7.206)–(7.207), becomes (Norman and Winkler, 1986)

$$\partial_t[(\rho h + Q)W^2V_j] + \partial_i[(\rho h + Q)W^2V_jV^i] + \partial_j(p + Q) = 0, \quad (8.100)$$

$$\partial_t E + \partial_i(EV^i) + (p + Q)[\partial_t W + \partial_i(WV^i)] = 0, \quad (8.101)$$

where  $W := (1 - V^iV_i)^{-1/2}$  is the Lorentz factor, while the continuity equation remains unchanged.

Comparing the definition of the artificial-viscosity term (8.99), with the way it appears in the momentum equation (8.100), *i.e.*, as  $\sim QW^2V_jV^i$ , it is easy to realise that this prescription introduces a highly nonlinear coupling between the velocity field (and most importantly its derivatives) and the artificial-viscosity scalar. While this coupling mimics in many respects the one that actually takes place in nature, it also introduces a stiff dependence on this additional quantity, which could rapidly lead to inaccurate numerical solutions in ultrarelativistic flows. Furthermore, the fact that the artificial-viscosity  $Q$  appears in the momentum equation (8.99) mediated by the square of the Lorentz factor makes the coupling in relativistic flows much more severe than that in Newtonian flows, where artificial-viscosity techniques have also been widely used. Indeed Norman and Winkler (1986) had to resort to the use of implicit numerical methods (see Section 8.3 for a definition) and of an adaptive numerical grid in order to accurately solve ultrarelativistic flows with Lorentz factors  $W \sim 10$  in one-dimensional, flat-spacetime test calculations.

A final consideration before concluding this chapter. We have already remarked that strong shocks moving at relativistic speeds are typical manifestations of relativistic flows, whose propagation needs to be accurately captured in realistic simulations. On the other hand, standard artificial-viscosity methods tend to spread discontinuities over several gridzones, sacrificing their ability to capture shocks. As a result, over the last two decades artificial-viscosity methods have been in large part replaced by *high-resolution shock-capturing (HRSC)* methods, which exploit the conservative formulation of the equations to obtain an accurate description of the dynamics of discontinuities in the flow. The following chapter is dedicated to a detailed discussion of such numerical methods.

<sup>13</sup>Besides a scalar artificial viscosity, also a more general tensor version of the artificial viscosity can be introduced (Anninos and Fragile, 2003).

## 8.5 Further reading

- LeVeque, R. J. (1992). *Numerical Methods for Conservation Laws*. Birkhauser, Basel.
- LeVeque, R. J. (2007). *Finite Difference Methods for Ordinary and Partial Differential Equations*. SIAM, Philadelphia.
- Morton, K. W. and Mayers, D. F. (2005). *Numerical Solution of Partial Differential Equations*. Cambridge University Press, Cambridge.
- Richtmyer, R. D. and Morton, K.W. (1967). *Difference Methods for Initial Value Problems*. Interscience Publishers, New York.
- Richtmyer, R. D. and Morton, K. W. (1994). *Difference Methods for Initial Value Problems*. Second edition. Kreiger, Malabar.
- Strikwerda, J. C. (2004). *Finite differential schemes and partial differential equations*. Second edition. SIAM, Philadelphia
- Wilson, J. R. and Mathews, G. J. (2003). *Relativistic Numerical Hydrodynamics*. Cambridge University Press, Cambridge.

## 8.6 Problems

1. Using the definitions (8.14) and (8.17), and assuming a linear problem, obtain the relation between the local error  $E_j^{(h)}$  and the local truncation error  $\epsilon_j^{(h)}$ , as expressed by Eq. (8.18).
2. Derive expressions (8.26)–(8.27) and (8.32)–(8.27) for the local numerical accuracy orders.
3. Using the von Neumann stability analysis, derive the expressions for the amplification factor of the upwind, FTCS, Lax–Friedrichs, leapfrog and Lax–Wendroff numerical schemes. Compare your results with expressions (8.59), (8.67), (8.70), (8.76), and (8.80).
4. Derive the coefficients reported in Table 8.1 for the discretised expression of the first derivative with truncation errors of  $\mathcal{O}(\Delta x^4)$  and of  $\mathcal{O}(\Delta x^6)$ .
5. Show that finite-difference schemes of the type

$$u_j^{n+1} = a_1 u_{j-1}^n + a_2 u_{j+1}^n$$

are stable if  $|a_1| + |a_2| \leq 1$ . [Hint: start from  $\sum_{j=-\infty}^{\infty} |u_j^{n+1}|^2$  and prove that this is smaller than  $(|a_1| + |a_2|)^2 \sum_{j=-\infty}^{\infty} |u_j^n|^2$ , hence ...] From this conclude that the Lax–Friedrichs scheme is stable for  $|\alpha| \leq 1$ .

6. Write a numerical code that solves the linear advection equation (8.39) through the Lax–Friedrichs scheme and the Lax–Wendroff scheme. Compare the results in the two cases and verify the order of convergence.
7. After considering the one-dimensional wave equation

$$\partial_t^2 u - \lambda^2 \partial_x^2 u = 0,$$

where  $\lambda$  is constant, show that it can be reduced to a system of three coupled, first-order differential equations. Using a Gaussian as initial condition, write a numerical code that solves such a system with the FTCS, the Lax–Friedrichs, the leapfrog and the Lax–Wendroff schemes.

# 9

## Numerical Relativistic Hydrodynamics: HRSC Methods

---

When introducing the formal properties of conservation laws in Section 7.3.2, we commented on two fundamental results proved by Lax and Wendroff (1960) and by Hou and LeFloch (1994). Namely, that conservative numerical methods, if convergent, do converge to the weak solution of the problem, while non-conservative methods do not converge to the correct solution if the solution contains a discontinuity. Although we have already devoted some space to discussing the properties of hyperbolic partial differential equations in conservative form (see Sections 4.1 and 7.3.2), we have not yet introduced the definition of a *conservative numerical method*. This chapter is therefore dedicated to this important class of methods for the solution of hyperbolic equations.

We will distinguish those methods that evolve the *cell averages* of the solution in time, and that are therefore known as *finite-volume (conservative) methods*, from those that evolve instead the *pointwise values* of the solution, and that are instead known as *finite-difference (conservative) methods*. Because of their common conservative nature, both methods belong to a more general class of so-called *high-resolution shock-capturing (HRSC)* methods, which are particularly suited to reproduce accurately discontinuous features in the solution. Such methods can be also divided into *upwind methods*, which can be equally built with finite-volume and finite-differences algorithms, and *central schemes*. The first ones are methods that use the characteristic information after introducing local Riemann problems at the interfaces between adjacent gridzones, with *Godunov methods* representing the most celebrated example of this class of approaches. The second ones, on the other hand, do not use the characteristic information (with the exception of *central-upwind schemes*), but are considerably less expensive and often with comparable properties. Most of our attention in this chapter will be dedicated to upwind schemes, but we will also briefly discuss central schemes in Section 9.6. As in the previous chapter, we will restrict ourselves to the solution of problems which are one-dimensional in space, postponing the discussion of the multidimensional cases to Section 10.5.

### 9.1 Conservative schemes

#### 9.1.1 Rankine–Hugoniot conditions

Before going into the heart of conservative numerical schemes, it is useful to obtain a generalisation of the *Rankine–Hugoniot conditions*, introduced in Section 4.4.3, that is valid for any

system of hyperbolic equations written in conservative form. For convenience, let us consider again the prototype equation in one spatial dimension of the generic conservation equation (4.27), *i.e.*,

$$\partial_t \mathbf{U} + \partial_x \mathbf{F}(\mathbf{U}) = 0, \quad (9.1)$$

and assume that the solution admits a discontinuity moving with positive speed  $S$  along the spacetime curve  $(s(t), t)$ , and separating two constant states  $\mathbf{U}_L$  and  $\mathbf{U}_R$ . At any time  $t$ , we integrate Eq. (9.1) in space on the interval  $[x_L, x_R]$ , where  $x_L < s(t) < x_R$ , and obtain

$$\mathbf{F}(\mathbf{U}(x_L, t)) - \mathbf{F}(\mathbf{U}(x_R, t)) = \frac{d}{dt} \int_{x_L}^{x_R} \mathbf{U}(x, t) dx. \quad (9.2)$$

The spatial integration on the right-hand side of Eq. (9.2) contains the discontinuity at  $s = s(t)$ , and the integral can therefore be split as

$$\mathbf{F}(\mathbf{U}_L) - \mathbf{F}(\mathbf{U}_R) = \frac{d}{dt} \int_{x_L}^{s(t)} \mathbf{U}(x, t) dx + \frac{d}{dt} \int_{s(t)}^{x_R} \mathbf{U}(x, t) dx, \quad (9.3)$$

where we have defined  $\mathbf{F}(\mathbf{U}_L) := \mathbf{F}(\mathbf{U}(x_L, t))$  and  $\mathbf{F}(\mathbf{U}_R) := \mathbf{F}(\mathbf{U}(x_R, t))$ . The derivative of the integrals on the right-hand side of (9.3) yields<sup>1</sup>

$$\mathbf{F}(\mathbf{U}_L) - \mathbf{F}(\mathbf{U}_R) = S(\mathbf{U}_L - \mathbf{U}_R) + \int_{x_L}^{s(t)} \partial_t \mathbf{U}(x, t) dx + \int_{s(t)}^{x_R} \partial_t \mathbf{U}(x, t) dx, \quad (9.5)$$

where  $S = ds(t)/dt$  and the constant states  $\mathbf{U}_L$  and  $\mathbf{U}_R$  coincide with the left and right limits of  $\mathbf{U}(x, t)$  for  $x \rightarrow s(t)$ , *i.e.*,

$$\mathbf{U}_L = \lim_{x \rightarrow s^-(t)} \mathbf{U}(x, t), \quad \mathbf{U}_R = \lim_{x \rightarrow s^+(t)} \mathbf{U}(x, t). \quad (9.6)$$

When  $x_L \rightarrow s^-(t)$  and  $x_R \rightarrow s^+(t)$  the two integrals on the right-hand side of Eq. (9.5) vanish and we finally obtain the Rankine–Hugoniot condition

$$\mathbf{F}_L - \mathbf{F}_R = S(\mathbf{U}_L - \mathbf{U}_R). \quad (9.7)$$

If Eqs. (9.1) represent the hydrodynamic equations written in conservative form, then expressions (9.7) provide in a very concise form the *Rankine–Hugoniot conditions* across a discontinuity<sup>2</sup> and are often used to check whether a numerical method succeeds (or fails) in providing the correct propagation speed of discontinuity fronts. Although they are in a form that appears to be different from the one introduced in Section 4.4.3, the Rankine–Hugoniot conditions (9.7) are effectively equivalent to the conservation of rest mass, momentum and energy expressed by Eqs. (4.109)–(4.110) (Smoller and Temple, 1993). The only difference,

<sup>1</sup>Here we use the standard derivation of an integral depending on a parameter, *i.e.*,

$$\frac{d}{dt} \int_{x_1(t)}^{x_2(t)} Q(x, t) dx = \int_{x_1(t)}^{x_2(t)} \partial_t Q(x, t) dx + Q(x_2(t), t) \frac{dx_2(t)}{dt} - Q(x_1(t), t) \frac{dx_1(t)}{dt}. \quad (9.4)$$

<sup>2</sup>Note that the Rankine–Hugoniot conditions are valid even if the states  $\mathbf{U}_L$  and  $\mathbf{U}_R$  are not constant.

which is however a very important one, is that Eqs. (9.7) are not sufficient to select a solution which is physically admissible. This is particularly evident when more than one discontinuous weak solution is available. Consider, for example, the solution of the relativistic one-dimensional Riemann problem that we studied in Section 4.6. In addition to the solution reported in Fig. 4.12, another possible solution is given by the weak solution (see Section 7.3.2)

$$\mathbf{U}(x, t) = \begin{cases} \mathbf{U}_L & \text{if } x/t < S, \\ \mathbf{U}_R & \text{if } x/t > S, \end{cases} \quad (9.8)$$

and thus consisting of the initial condition propagating at the constant speed  $S$  as obtained from the solution of the system

$$\mathbf{F}_L - \mathbf{F}_R = S(\mathbf{U}_L - \mathbf{U}_R). \quad (9.7)$$

The solution (9.8) is usually referred to as an *expansion shock*, and is well-known to be non-physical (it only represents the translation of the discontinuous initial problem). Indeed, it does not guarantee that the entropy of the fluid increases as the fluid crosses the discontinuity, which we have discussed to be a fundamental property of physical shocks [see Eq. (4.123) in Section 4.4.3].

The example above clarifies the importance of introducing a mathematical criterion reflecting the physical principle of entropy increase across a discontinuity. From a mathematical point of view, however, it is not obvious what is the most appropriate criterion for excluding those weak solutions that do not correspond to a physically viable solution. One such criterion, and certainly the most celebrated one, is the so-called *entropy condition* of Lax (1990). In essence, given a system of hyperbolic equations with a set of eigenvalues  $\lambda_1 < \lambda_2 < \dots < \lambda_N$ , a weak solution admitting a discontinuity between states  $\mathbf{U}_L$  and  $\mathbf{U}_R$  is a shock if and only if there is an index  $p$ ,  $1 \leq p \leq N$ , associated to the characteristic  $\lambda_p$ , such that

$$\lambda_p(\mathbf{U}_L) > S > \lambda_p(\mathbf{U}_R), \quad (9.9)$$

and

$$\lambda_{p-1}(\mathbf{U}_L) < S < \lambda_{p+1}(\mathbf{U}_R). \quad (9.10)$$

In other words, the characteristic associated to the eigenvalue  $\lambda_p$  must collide with the discontinuity both from the left and from the right sides of the discontinuity, while the other characteristics collide with the discontinuity from one side only. The entropy conditions (9.9)–(9.10) are not the only criteria formulated to single-out physical discontinuities, and other versions of the entropy condition have been formulated based, for instance, on the introduction of a suitable *entropy function* (LeVeque, 2002). Overall, the study of the non-uniqueness of weak solutions represents an active field of research and some relevant progress has been made by Bressan and LeFloch (1997).

### 9.1.2 Finite-volume conservative numerical schemes

We are now ready to introduce the definition of a conservative numerical scheme and we do so by starting, once again, from the conservative form of a hyperbolic system in one spatial

dimension (9.1). On each time-slice let us discretise the spatial domain into  $J$  computing cells  $I_j = [x_{j-1/2}, x_{j+1/2}]$  of size  $\Delta x := x_{j+1/2} - x_{j-1/2}$ , with  $j = 1, \dots, J$ . In addition, we define a spacetime *control volume* as  $\Omega_j^{n+1/2} := I_j \times [t^n, t^{n+1}]$  and integrate Eq. (9.1) first in space over  $I_j$

$$\frac{d}{dt} \int_{x_{j-1/2}}^{x_{j+1/2}} \mathbf{U}(x, t) dx = \mathbf{F}(\mathbf{U}(x_{j-1/2}, t)) - \mathbf{F}(\mathbf{U}(x_{j+1/2}, t)), \quad (9.11)$$

where the partial time derivative has now become a total derivative, and then in time between  $t^n$  and  $t^{n+1}$  to obtain

$$\begin{aligned} \int_{x_{j-1/2}}^{x_{j+1/2}} \mathbf{U}(x, t^{n+1}) dx &= \int_{x_{j-1/2}}^{x_{j+1/2}} \mathbf{U}(x, t^n) dx \\ &\quad + \int_{t^n}^{t^{n+1}} \mathbf{F}(\mathbf{U}(x_{j-1/2}, t)) dt - \int_{t^n}^{t^{n+1}} \mathbf{F}(\mathbf{U}(x_{j+1/2}, t)) dt. \end{aligned} \quad (9.12)$$

Equation (9.12) represents the *integral form* of the conservative equations (9.1). We next define two new quantities, the *cell (volume) averages*

$$\mathbf{U}_j^n := \frac{1}{\Delta x} \int_{x_{j-1/2}}^{x_{j+1/2}} \mathbf{U}(x, t^n) dx, \quad (9.13)$$

and the *numerical fluxes*

$$\mathbf{F}_{j\pm 1/2} := \frac{1}{\Delta t} \int_{t^n}^{t^{n+1}} \mathbf{F}[\mathbf{U}(x_{j\pm 1/2}, t)] dt, \quad (9.14)$$

such that (9.12) is rewritten as

$$\mathbf{U}_j^{n+1} = \mathbf{U}_j^n + \frac{\Delta t}{\Delta x} (\mathbf{F}_{j-1/2} - \mathbf{F}_{j+1/2}). \quad (9.15)$$

Because of the volume averages introduced in the definition (9.13), the numerical methods that will be built in this way are known as *finite-volume methods*.

It is important to stress that although we have introduced a discretisation of space and time, expression (9.15) does not (yet) represent a numerical scheme and is indeed exact as no mathematical approximation has been done yet. The exact *mathematical method* (9.15) becomes an approximate *numerical method* only when an approximation (and hence a truncation error) is introduced for the computation of the cell averages  $\mathbf{U}_j$  and of the numerical fluxes  $\mathbf{F}_{j\pm 1/2}$ . In addition, the resulting scheme will be called a *conservative numerical scheme* if the numerical flux  $\mathbf{F}_{j+1/2}$  (and analogously  $\mathbf{F}_{j-1/2}$ ) depends on the values taken by  $\mathbf{U}$  on the neighbouring cells, namely if

$$\mathbf{F}_{j+1/2} = \mathcal{F}(\mathbf{U}_{j-q}^n, \mathbf{U}_{j-q+1}^n, \dots, \mathbf{U}_{j+r}^n), \quad (9.16)$$

where  $q$  and  $r$  are integers and  $\mathcal{F}$  is a numerical flux function of  $q+r+1$  arguments. A further requirement on the flux function  $\mathcal{F}$  of a conservative numerical scheme is that it reduces to the true physical flux in the case of constant flow, *i.e.*, it satisfies the *consistency condition*

$$\mathcal{F}(\mathbf{U}, \dots, \mathbf{U}) = \mathbf{F}(\mathbf{U}). \quad (9.17)$$

In practice, because for hyperbolic problems information propagates with finite speed and because the CFL condition on the time-step ensures that such information does not move across a single cell over a time-step (see Section 8.3.1), it is often convenient to assume that  $\mathbf{F}_{j+1/2}$  depends only on the values of  $\mathbf{U}$  in the two adjacent cells, *i.e.*,  $r = 0 = q$  and

$$\mathbf{F}_{j+1/2} = \mathcal{F}(\mathbf{U}_j^n, \mathbf{U}_{j+1}^n). \quad (9.18)$$

As an illustrative example, we note that the Lax–Friedrichs scheme, reported in Eq. (8.69) for the case of the scalar advection equation with speed  $\lambda$ , can be written as a (consistent) conservative finite-volume scheme with a numerical flux function given by

$$\mathbf{F}_{j+1/2} = \mathcal{F}(\mathbf{U}_j^n, \mathbf{U}_{j+1}^n) = \frac{1}{2} [\mathbf{F}(\mathbf{U}_j^n) + \mathbf{F}(\mathbf{U}_{j+1}^n)] - \frac{\Delta x}{2\Delta t} (\mathbf{U}_{j+1}^n - \mathbf{U}_j^n), \quad (9.19)$$

where  $\mathbf{U}_j^n = u_j^n$  and  $\mathbf{F}(\mathbf{U}_j^n) = \lambda u_j^n$ . Similarly, the Lax–Wendroff scheme described in Section 8.3.6 for the scalar advection equation [*cf.*, Eq. (8.79)] can be re-interpreted as a finite-volume scheme with a numerical flux function

$$\mathbf{F}_{j+1/2} = \mathcal{F}(\mathbf{U}_j^n, \mathbf{U}_{j+1}^n) = \mathbf{F}(\mathbf{U}_{\text{LW}}), \quad (9.20)$$

where

$$\mathbf{U}_{\text{LW}} = \frac{1}{2} (\mathbf{U}_j^n + \mathbf{U}_{j+1}^n) - \frac{\Delta t}{2\Delta x} [\mathbf{F}(\mathbf{U}_{j+1}^n) - \mathbf{F}(\mathbf{U}_j^n)]. \quad (9.21)$$

Since conservative numerical schemes rely on the conservative formulation of the equations, serious problems may arise when such a conservative formulation is not available and in particular for those solutions admitting discontinuous waves. In such cases, in fact, it is not obvious how to generalise the Rankine–Hugoniot condition (9.7) so that the discontinuities can propagate with the correct speed. A class of numerical methods introduced to account for systems of equations that cannot be cast in conservative form, and which are called *path-conservative methods*, was studied by Dal Maso *et al.* (1995). The interested reader can find in Pares (2006) and Castro *et al.* (2008) a comprehensive discussion of these methods.

### 9.1.3 Finite-difference conservative numerical schemes

As mentioned above, a conservative numerical scheme can be obtained also when expressing the differential operator via the finite-difference methods introduced in Chapter 8. In essence, rather than integrating Eq. (9.1) in space and time, we can write directly a finite-difference approximation of the spatial derivative as

$$\frac{d\mathbf{U}_j}{dt} = \frac{1}{\Delta x} (\hat{\mathbf{F}}_{j-1/2} - \hat{\mathbf{F}}_{j+1/2}), \quad (9.22)$$

where  $\hat{\mathbf{F}}_{j\pm 1/2}$  are quantities which will be defined more precisely below. Note that the right-hand side of Eq. (9.22) should be seen as a continuous function of time and this justifies the use of a continuous differential operator  $d\mathbf{U}_j/dt$  on the left-hand side.

In spite of the analogies between Eqs. (9.15) and (9.22), they differ in two fundamental respects. First of all,  $\mathbf{U}_j$  represents a *cell-averaged* quantity in Eq. (9.15) [cf., Eq. (9.13)], while it is the *pointwise approximation* of  $\mathbf{U}(x, t)$  at the position  $x = x_j$  in Eq. (9.22), namely

$$\mathbf{U}_j = \mathbf{U}(x_j, t) + \mathcal{O}(\Delta x^p), \quad (9.23)$$

where  $p$  is the order of the scheme. Because the average of a linear function over the interval  $[x_{j-1/2}, x_{j+1/2}]$  is equal to the point-value at the centre of the interval, finite-volume and finite-difference conservative schemes do coincide up to order  $p \leq 2$ . However, at orders  $p > 2$ , the two schemes truly differ, as will be discussed in Section 10.2. Secondly, the whole term on the right-hand side of (9.22) is an appropriate (high-order) approximation of the first derivative  $\partial_x \mathbf{F}(x)$  computed at  $x = x_j$ . The rationale behind this idea is the following. If we can find a function  $h(x)$  such that

$$\mathbf{F}(x) = \frac{1}{\Delta x} \int_{x-\Delta x/2}^{x+\Delta x/2} h(x') dx', \quad (9.24)$$

then we have

$$\partial_x \mathbf{F}(x) = \frac{1}{\Delta x} \left[ h\left(x + \frac{\Delta x}{2}\right) - h\left(x - \frac{\Delta x}{2}\right) \right]. \quad (9.25)$$

We can now identify the terms on the right-hand side of (9.22) as

$$\hat{\mathbf{F}}_{j\pm 1/2} = h(x_{j\pm 1/2}) + \mathcal{O}(\Delta x^p), \quad (9.26)$$

such that

$$\frac{1}{\Delta x} (\hat{\mathbf{F}}_{j+1/2} - \hat{\mathbf{F}}_{j-1/2}) = \partial_x \mathbf{F}(x_j) + \mathcal{O}(\Delta x^p). \quad (9.27)$$

Hence,  $\hat{\mathbf{F}}_{j\pm 1/2}$  provide a high-order approximation to the *primitives* of the physical fluxes, in the sense that, according to (9.24), the cell averages of  $\hat{\mathbf{F}}(x)$  must coincide with the point values  $\mathbf{F}_j$  of the flux function  $\mathbf{F}(x)$ . As for finite-volume methods, also for finite-difference ones we will demand that the numerical flux  $\hat{\mathbf{F}}_{j\pm 1/2}$  in Eq. (9.22) satisfies the same conservative property established by Eq. (9.16), namely that

$$\hat{\mathbf{F}}_{j+1/2} = \hat{\mathcal{F}}(\mathbf{U}_{j-q}^n, \mathbf{U}_{j-q+1}^n, \dots, \mathbf{U}_{j+r}^n), \quad (9.28)$$

accompanied by the consistency condition

$$\hat{\mathcal{F}}(\mathbf{U}, \dots, \mathbf{U}) = \hat{\mathbf{F}}(\mathbf{U}). \quad (9.29)$$

We will come back to the distinction between finite-volume and finite-difference conservative methods in Chapter 10 (see Section 10.2). We here just anticipate that both of them have their advantages and disadvantages. In particular, finite-difference schemes can be naturally implemented in a dimension-by-dimension fashion for multidimensional problems, while finite-volume schemes typically rely on expensive multidimensional reconstruction algorithms (see Section 9.3 for a definition). On the other hand, finite-volume schemes can also be implemented over irregular (unstructured) grids, while finite-difference schemes cannot (Shu, 2003). Because in the rest of this chapter we will limit our analysis to methods of order up to the second, the distinction between finite-difference and finite-volume methods will not be necessary.

## 9.2 Upwind methods

As anticipated above, finite-volume and finite-difference conservative schemes need an additional property to capture the position of discontinuities in the flow without excessive numerical dissipation. In Section 8.3.2 we have already described what an *upwind method* is for (non-conservative) finite-difference methods. We recall that in the case of a scalar advection equation (8.39), an upwind scheme required care in the selection of the stencil that reflected the direction of propagation of the advected wave. In practice, this reduced to the choice of the correct one-sided *stencil* according to the sign of the advection velocity, [cf., Eq. (8.54)–(8.55)]. A similar requirement is necessary also in the case of conservative finite-volume and finite-difference methods, where care is now required in the choice of the *numerical fluxes*.

For a system of *linear* equations this is not too difficult to do and upwind methods can still be obtained by resorting to *characteristic variables* [cf., Eq. (4.42)], namely, by first writing the original system as a set of decoupled advection equations according to Eq. (4.45), where special care has to be taken on the signs of the eigenvalues of the matrix  $\mathbf{A}$  in Eq. (4.9). As discussed in Chapter 4, in fact, the eigenvalues represent the velocities with which perturbations propagate in a system of hyperbolic equations, and the signs of the eigenvalues specify the direction of such propagation. If the eigenvalues have mixed signs, as is often the case in practice, the flux  $\mathbf{F}$  must be decomposed in two parts,  $\mathbf{F}^+$  and  $\mathbf{F}^-$ , in such a way that the corresponding Jacobian matrices  $\mathbf{A}^+ := \partial\mathbf{F}^+/\partial\mathbf{U}$  and  $\mathbf{A}^- := \partial\mathbf{F}^-/\partial\mathbf{U}$  contain, respectively, just the positive and negative eigenvalues of the original matrix  $\mathbf{A}$ . In this way, the upwind character of the resulting methods is guaranteed (LeVeque, 2002). These numerical methods are commonly referred to as *flux vector splitting methods*.

However, guaranteeing an upwind character is much more complicated for systems of *nonlinear* equations. Although the Flux Vector Splitting methods can still be applied [see, e.g., van Leer (1982) for the case of the Euler equations and the discussion in Section 10.2.3], by far the most successful strategy for obtaining an upwind (conservative) numerical scheme is the one due to Godunov (1959), who suggested solving a Riemann problem forward in time at each interface between adjacent cells. By providing all the necessary information about the *characteristic structure* of the problem, *i.e.*, the information on all the waves that will appear in the *Riemann fan* (see Section 4.5), the solution of the Riemann problem can effectively guarantee the upwind property of a numerical scheme, even for systems of nonlinear equations (van Leer, 2006).

### 9.2.1 Monotone methods

Before discussing in detail the idea behind Godunov methods, it is useful to introduce a number of important concepts that will be used extensively also in the following chapters and that are related to *monotonicity* of the solution, that is, to the appearance of oscillations. Given an explicit numerical method of the type

$$\mathbf{U}_j^{n+1} = f(\mathbf{U}_j^n, \mathbf{U}_{j\pm 1}^n, \mathbf{U}_{j\pm 2}^n, \dots, \mathbf{U}_j^{n-m}, \mathbf{U}_{j\pm 1}^{n-m}, \mathbf{U}_{j\pm 2}^{n-m}, \dots), \quad (8.57)$$

we will say that the method is *monotone* if

$$\frac{\partial f}{\partial \mathbf{U}_j^n} \geq 0 \quad \forall \mathbf{U}_j^n. \quad (9.30)$$

In other words,  $f$  must be a *non-decreasing* function of each of its arguments. The condition (9.30) has a simple equivalent expression when the method is *linear*, namely, when the solution can be expanded as

$$\mathbf{U}_j^{n+1} = \sum_{k=-K_L}^{k=K_R} c_k \mathbf{U}_{j+k}^n, \quad (9.31)$$

with  $c_k$  *constant* coefficients and with  $K_L$  and  $K_R$  the sizes of the stencils to the left and to the right of the cell centred at  $x_j$ . Under these conditions, the condition (9.30) translates into the requirement that all coefficients in the stencil are positive, *i.e.*,

$$c_k \geq 0 \quad \forall k \in [-K_L, K_R]. \quad (9.32)$$

Although we have started from an explicit method in (8.57), the definition given above can be extended also to implicit methods by defining a method as monotone if

$$\mathbf{V}_j^n \geq \mathbf{U}_j^n \implies \mathbf{V}_j^{n+1} \geq \mathbf{U}_j^{n+1} \quad \forall \mathbf{U}_j^n, \quad (9.33)$$

where  $\mathbf{V}_j^n$  and  $\mathbf{U}_j^n$  are the discretised evolutions of the two different initial conditions  $\mathbf{V}_0(x)$  and  $\mathbf{U}_0(x)$ . As a result, given the data  $\{\mathbf{U}_j^n\}$ , the solution  $\{\mathbf{U}_j^{n+1}\}$  obtained through a monotone method is such that

$$\max_j \{\mathbf{U}_j^{n+1}\} \leq \max_j \{\mathbf{U}_j^n\}, \quad \min_j \{\mathbf{U}_j^{n+1}\} \geq \min_j \{\mathbf{U}_j^n\}, \quad (9.34)$$

that is, the method does not introduce spurious new extrema in the solution as time evolves. It is left as an exercise to show that, for instance, the Lax–Friedrichs scheme is monotone while the Lax–Wendroff one is not (see Problem 2).

### 9.2.2 Total variation diminishing methods

The monotonicity property of a numerical scheme is closely related to the potential appearance of spurious oscillations in the solution across a discontinuity. We have already discussed this possibility before and we have seen that these oscillations can be attenuated through the introduction of an *artificial viscosity* (see Section 8.4). A way to make this concept more quantitative is through the notion of the *total variation* (TV) of the solution. More specifically, given a one-dimensional solution  $\mathbf{U}^n$  with values  $\{\mathbf{U}_j^n\}$  at time-level  $t^n$ , its total variation is defined as

$$TV(\mathbf{U}^n) := \sum_{j=-\infty}^{+\infty} |\mathbf{U}_j^n - \mathbf{U}_{j-1}^n|, \quad (9.35)$$

and thus “measures” the oscillations appearing in the solution  $\mathbf{U}$ . The requirement that a scheme does not produce spurious oscillations is then translated into the requirement that the total variation should not increase in time, or, equivalently, that the total variation at any time is uniformly bounded by the total variation of the initial data.<sup>3</sup> As an example, a two-level

<sup>3</sup>This requirement is so natural that the exact solution of scalar conservative laws in one dimension has non-increasing total variation.

numerical method is said to be *total-variation diminishing* (TVD) if, for any set of data  $\mathbf{U}^n$ , the values  $\mathbf{U}^{n+1}$  computed by the method satisfy the condition (Harten, 1983)<sup>4</sup>

$$TV(\mathbf{U}^{n+1}) \leq TV(\mathbf{U}^n), \quad (9.36)$$

from which, of course, it follows that

$$TV(\mathbf{U}^n) \leq TV(\mathbf{U}^{n-1}) \leq \dots \leq TV(\mathbf{U}^0). \quad (9.37)$$

In analogy with artificial-viscosity methods, also TVD methods aim at eliminating, or at least controlling, the appearance of oscillations in the solution. However, in contrast with artificial-viscosity methods, where viscous terms are introduced explicitly in the numerical scheme, the reduction of oscillations in modern TVD methods is rooted in the method itself and does not appear explicitly.

Another useful characterisation of a numerical method is in its ability to not introduce or increase the oscillations in the solution, *i.e.*, the property of “preserving the monotonicity”. In this regard, a method such that

$$\mathbf{U}_j^n \geq \mathbf{U}_{j+1}^n \quad \forall j, \quad (9.38)$$

is said to be *monotonicity preserving* if

$$\mathbf{U}_j^{n+1} \geq \mathbf{U}_{j+1}^{n+1} \quad \forall j. \quad (9.39)$$

This property is crucial in preventing the appearance of oscillations, since in the numerical evolution obtained with a monotonicity-preserving method no new local extrema can be produced, the value of a local minimum cannot decrease, and the value of a local maximum cannot increase.

An important result due to Harten (1983) is that any monotone numerical method (see definition in Section 9.2.1) is TVD, and any TVD method is monotonicity preserving, namely, the following chain of implications is true

$$\text{monotone method} \implies \text{TVD method} \implies \text{monotonicity-preserving method}.$$

TVD methods do not extend beyond second-order accuracy and, as we will see in Section 9.3.1, they reduce to first-order at local extrema. Moreover, to construct third- (and higher) order methods one must drop the total variation condition (9.36) and allow for an increase of the total variation, which is usually proportional to some power of the typical time-step. This is the case of some of the methods that we will introduce in Section 10.2.

In practice, the TVD property can be imposed either through *slope-limiter methods*, in which case the slope of the solution inside a cell is suitably limited, or through *flux-limiter methods*, in which case a smoothing strategy is applied directly to the numerical fluxes. In the following, we will concentrate exclusively on the first class of methods, referring to Sweby (1984) and to Toro (2009) for an exhaustive treatment of flux-limiter methods.

<sup>4</sup>Although universally known as “total-variation diminishing”, the condition (9.36) is really just requiring that the variation does not increase, with a constant variation still being acceptable. Indeed, it was proposed as a *total-variation non-increasing* condition (TVNI) in the original work of Harten (1983).

The concepts of monotonicity and monotonicity preservation play an important role in the following theorem proven by Godunov (1959), and expressing a relation between the monotonicity and the order of a numerical scheme, namely

**Theorem** *A linear (i.e., with constant coefficients) and monotonicity-preserving scheme is at most first-order accurate.*

This theorem,<sup>5</sup> which is traditionally referred to as *Godunov's theorem*, essentially states that high-order linear schemes and the absence of oscillations are two incompatible requirements. We will refer again to this theorem in Chapter 10, when discussing the strategies for obtaining a numerical scheme that is both non-oscillatory and with an order higher than the second.

### 9.2.3 Godunov methods

To illustrate how Godunov methods manage to guarantee the upwind property of conservative nonlinear equations it is useful to follow the logical steps behind Godunov's original idea.

#### **Godunov's original idea.**

Consider the finite-volume representation (9.15) of the conservation equation (9.1). The ingenious observation of Godunov was that at each interface between adjacent numerical cells the quantity  $\mathbf{U}_j^n$ , which is the volume average of  $\mathbf{U}(x, t)$  over the cell  $[x_{j-1/2}, x_{j+1/2}]$  at time  $t = t^n$ , manifests a *jump*, thus generating the “left” and “right” states of local Riemann problems. As a result, we can define as a *Godunov method* any method in which the fluxes  $\mathbf{F}_{j-1/2}$  and  $\mathbf{F}_{j+1/2}$  in Eq. (9.15) are calculated by solving a local Riemann problem at  $x_{j\pm 1/2}$ . Because this logic can be extended to any other cell, a Godunov method consists in the solution of a *sequence* of local Riemann problems (Godunov, 1959).

In its *original* form, Godunov's approach used as left and right states the piecewise-constant distribution of data given by (9.13), thus building the local Riemann problem [*cf.* Eq. (4.145)]

$$\mathbf{U}(x, 0) = \begin{cases} \mathbf{U}_j^n & \text{if } x < x_{j+1/2}, \\ \mathbf{U}_{j+1}^n & \text{if } x > x_{j+1/2}. \end{cases} \quad (9.40)$$

The formal solution of the local Riemann problem will then provide the terms  $\mathbf{U}(x_{j\pm 1/2}, t)$ , which can be used in Eq. (9.14) to calculate the fluxes  $\mathbf{F}_{j\pm 1/2}$ . In particular, because the solution of a Riemann problem is self-similar (indeed, it consists either of a set of piecewise-constant values or of a set of rarefaction waves, which are themselves self-similar) and therefore constant along the line  $x/t = 0$  emerging from the points  $(x_{j\pm 1/2}, t^n)$ , the two states  $\mathbf{U}(x_{j\pm 1/2}, t)$  are constant along the line  $x/t = 0$ . As a result, the time integrals on the right-hand side of (9.14) can be computed analytically as soon as the values  $\mathbf{U}(x_{j\pm 1/2}, t)$  are known.

<sup>5</sup>Note that the validity of Godunov's theorem is not limited to linear equations, as it is for the Lax equivalence theorem (see Section 8.2.1).

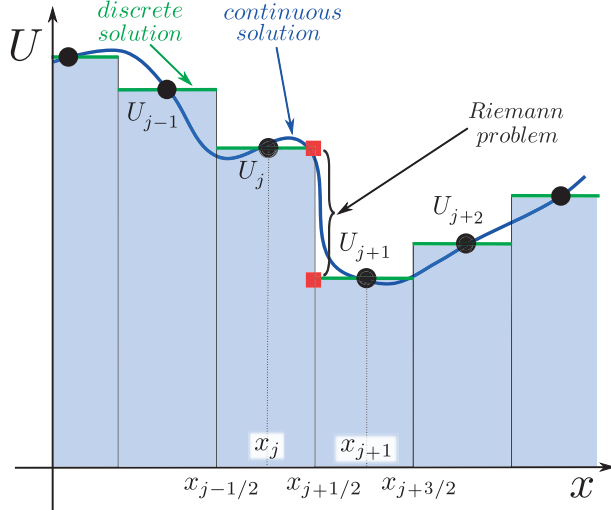


**Fig. 9.1** Schematic representation of local Riemann problems appearing at each cell interface in the original first-order Godunov method. Note that the continuous solution (blue solid line) is discretised as a constant value (green solid line) corresponding to the volume-average in the cell at  $x_j$ . As a result, a series of piecewise-constant states is produced, which can be seen as a sequence of (small) elementary Riemann problems, e.g., the one between the states  $U_j$  and  $U_{j+1}$  at  $x_{j+1/2}$ .

A schematic representation of the original Godunov method as a sequence of local Riemann problems is offered in Fig. 9.1, where the continuous solution (blue solid line) is discretised as a constant value corresponding to the volume-average in the cell at  $x_j$  and leading to a series of piecewise-constant states (green solid lines). The latter can be viewed as a sequence of (small) elementary Riemann problems as the one at  $x_{j+1/2}$  between the states  $U_j$  and  $U_{j+1}$ . The evolution of the Riemann problems depicted in Fig. 9.1 from  $t^n$  to  $t^{n+1}$  is shown schematically in Fig. 9.2, where we report the characteristic waves originating from each cell interface. These waves represent a local *Riemann fan* and comprise shock waves (blue solid lines), rarefaction waves (red solid lines) and contact discontinuities (green dotted lines) whose direction of propagation will be dictated by the initial conditions of the local Riemann problem (see also Figs. 4.10 and 4.11). Note that, because the time-step is constrained by the CFL condition through Eq. (8.42), it is possible that the characteristics emerging at time  $t^n$  from a given interface intersect with those emerging from the adjacent interface (this is indeed shown in Fig. 9.2 for the characteristic emanating from  $x_{j+1/2}$  and  $x_{j+3/2}$ ). However, as long as the new characteristics produced at the intersection point at a time between  $t^n$  and  $t^{n+1}$  are not faster than the original ones generated at time  $t^n$  (*i.e.*, there is no “wave acceleration”), the perturbation due to the wave interaction will have no time to reach the interface, leaving the computation of the numerical fluxes unaffected. Indeed, the condition that  $c_{\text{CFL}}$  needs to be chosen smaller than 1 in Godunov methods reflects the constraint on the choice of  $t^{n+1}$  that accounts for a possible wave acceleration.

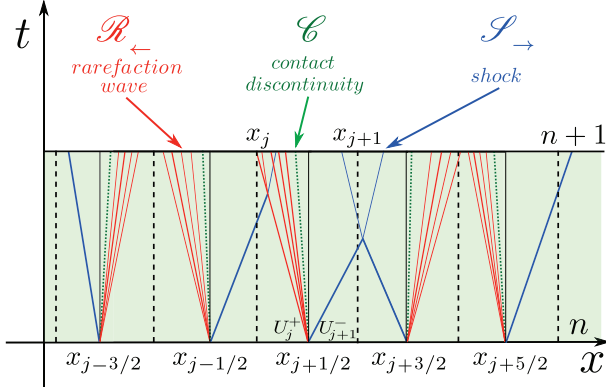


**Fig. 9.2** Schematic spacetime representation of the characteristic waves originating from each cell interface as a result of the evolution from  $t^n$  to  $t^{n+1}$  of the sequence of Riemann problems in the first-order Godunov scheme of Fig. 9.1 (see also Figs. 4.10 and 4.11). At each cell interface a Riemann fan will be opened comprising shock waves (blue solid lines), rarefaction waves (red solid lines) and contact discontinuities (green dotted lines).

A number of remarks can be made about the original Godunov scheme (9.15) with a piecewise-constant distribution of the data:

1. The scheme is *conservative* since it adopts the form (9.15) with a numerical flux function

$$\mathbf{F}_{j+1/2} = \frac{1}{\Delta t} \int_{t^n}^{t^{n+1}} \mathbf{F}[\mathbf{U}(x_{j+1/2}, t)] dt = \mathcal{F}(\mathbf{U}_j^n, \mathbf{U}_{j+1}^n), \quad (9.14)$$

in which  $\mathcal{F}$  is in the form prescribed by Eq. (9.18) because the solution of the Riemann problem only depends on the two (constant) states  $\mathbf{U}_j$  and  $\mathbf{U}_{j+1}$ .

2. The scheme is *upwind* since it adopts the solution of the Riemann problem for the computation of the fluxes  $\mathbf{F}_{j\pm 1/2}$ . The proof is indeed straightforward if we apply the scheme (9.15) to the linear advection equation with the flux given by  $\mathbf{F} = \lambda \mathbf{U}$ . In this case, the solution of each local Riemann problem at the generic cell interface  $x_{j+1/2}$  is given by  $\mathbf{U}_{j+1}^n$ , if  $\lambda < 0$ , and by  $\mathbf{U}_j^n$ , if  $\lambda > 0$ . Therefore, the resulting scheme is given by

$$\mathbf{U}_j^{n+1} = \mathbf{U}_j^n - \alpha(\mathbf{U}_j^n - \mathbf{U}_{j-1}^n), \quad \text{if } \lambda > 0, \quad (9.41)$$

and

$$\mathbf{U}_j^{n+1} = \mathbf{U}_j^n - \alpha(\mathbf{U}_{j+1}^n - \mathbf{U}_j^n), \quad \text{if } \lambda < 0, \quad (9.42)$$

where  $\alpha := \lambda \Delta t / \Delta x$  [cf. Eq. (8.40)]. The schemes (9.41) and (9.42) are nothing but the upwind methods first introduced by Courant *et al.* (1952) and already derived through Eqs. (8.54)–(8.53) for a scalar advection equation. For systems of nonlinear equations, the upwind property is guaranteed by the fact that the exact Riemann solver provides the full wave structure at each numerical interface, and therefore the resulting numerical flux respects the direction from which perturbations propagate.

3. The scheme is *monotone* and therefore non-oscillatory (see Section 9.2.1) as can be easily proved for a scalar advection equation by applying the criterion (9.30) to Eqs. (9.41)–(9.42).
4. The scheme is just *first-order accurate* in time and in space as a consequence of Godunov’s theorem (see Section 9.2.2) and as evident from Eqs. (9.41)–(9.42), which are indeed first-order schemes.
5. The scheme is *time-constrained* by the CFL condition even when applied to a system of  $N$  nonlinear equations. In other words, the time-step between  $n$  and  $n + 1$  must be such that  $\Delta t = c_{\text{CFL}} \min_k (\Delta x / |\lambda_k^n|)$ , where  $|\lambda_k^n|$  is the propagation velocity at time  $t = t^n$ , while the index  $1 \leq k \leq N$  spans the set of possible different eigenvalues of the system [cf., Eq. (8.42)].

From these considerations it emerges that the original Godunov method had the virtue of combining the least-accurate strategy for the calculation of the left and right states of the local Riemann problem (*i.e.*, the use of piecewise-constant data), with the most accurate strategy for the solution of such Riemann problems (*i.e.*, the use of an exact Riemann solver). Starting in the early 1970s, a great deal of effort has been dedicated to circumventing the strong limitations imposed by Godunov’s theorem (see Section 9.2.1), namely, that no linear and monotone scheme exists with order of accuracy higher than the first. Indeed, it was soon found that the limitations can be circumvented if the numerical method is made nonlinear. In practice, the spatial accuracy of the original first-order Godunov method can be improved if the left and right states of the Riemann problem solved at the interface  $x_{j+1/2}$  are not simply given by the constant values of  $\mathbf{U}_j$  and  $\mathbf{U}_{j+1}$ , but are rather obtained after *reconstructing* a higher-order polynomial representation of  $\mathbf{U}$  within each cell, starting from the averages  $\mathbf{U}_j$  of  $\mathbf{U}$  in a prescribed number of neighbouring cells (see Section 9.3). Of course, this reconstruction procedure should be done in a way that avoids the appearance of oscillations in the solution. At the same time, the accuracy in time can be increased either by adopting a Runge–Kutta (RK) method (see Section 9.5), or through the so-called *ADER* (for “arbitrary high order methods using derivatives”) approach of Titarev and Toro (2005) (see Section 10.4).

### **Modern Godunov methods.**

Modern Godunov methods, unlike the original one, combine sophisticated strategies for the computation of the left and right states of the local Riemann problems with approximate solutions of such Riemann problems. The resulting methods have become so widely adopted that they are collectively known as *high-resolution shock-capturing (HRSC)* methods *tout-court*, though HRSC methods also include non-upwind methods, like central schemes. In the rest of the chapter we will present the main ideas behind HRSC methods for schemes of order up to the second, leaving higher-order HRSC methods to Chapter 10.

Although several authors have contributed to the development of this field of research over the last two decades, particularly relevant is the first application of HRSC methods to the equations of relativistic hydrodynamics, which was made by Martí *et al.* (1991). Since then, the number of numerical techniques has grown considerably and there are often numerous different numerical methods to choose from when solving a specific problem. It is not our intention to give here a systematic presentation of all these methods [see, *e.g.*, Toro (2009), Trangenstein (2009)], which however all possess the following properties:

- at least second order of accuracy on smooth parts of the solution;
- sharp resolution of discontinuities without large smearing;
- absence of spurious oscillations in the solution;
- convergence to the “true” solution as the grid is refined;
- no use of artificial-viscosity terms.

Despite the large variety of flavours in which HRSC methods can be devised, three basic blocks are behind every HRSC method based on Godunov methods and represent the so-called “reconstruct-solve-update” steps, *i.e.*,

1. Reconstruction of the left and right states of a local Riemann problem at each cell boundary.
2. Use of an approximate Riemann solver, either complete or incomplete.
3. Use of a time-update algorithm of at least second order of accuracy.

In the following Sections 9.3, 9.4, and 9.5 we will detail each of these three steps.

### 9.3 Reconstruction techniques

In a piecewise-constant representation of the solution, any information about the behaviour of the quantities inside the numerical cell is lost. However, this information can be recovered if suitable techniques are employed, which, in turn, will also improve the spatial accuracy of a numerical method based on Riemann solvers. These techniques are generically called *reconstruction techniques* and all have the same goal of obtaining a polynomial representation of the solution within each cell, thus providing a better estimate for the calculation of the left and of the right state of the Riemann problem to be solved at the interface between two adjacent cells.<sup>6</sup>

It is important to stress that in finite-volume conservative schemes the reconstruction involves only the *conserved variables*, and is performed from cell averages to point values (see also Section 10.2.1). On the other hand, if finite-difference conservative schemes are used, the reconstruction can be done also on the *primitive variables*, or on the *numerical fluxes*, where it is performed from cell-centred point values to cell-interface point values (see also Section 10.2.3).

Let us be more precise about what we mean with the improvement of the spatial accuracy. We recall that a numerical method with space discretisation  $\Delta x$  is said to be accurate of order  $p$  in space if any norm of the truncation error vanishes like  $\mathcal{O}(\Delta x^p)$  (see Section 8.2). In HRSC methods, the order of convergence is essentially determined by the accuracy with which the profiles of the conserved (or primitive) quantities are reconstructed within each cell. For the linear reconstruction methods considered in this section, and with the exception of the *piecewise-parabolic method (PPM)* discussed in Section 9.3.2, we expect the convergence order to be  $p \approx 2$ .

<sup>6</sup>As a historical remark, we note that Kolgan was the first to introduce the idea of modifying the piecewise-constant data (9.13) to achieve higher than first-order spatial accuracy, while at the same time avoiding the annoying consequence of Godunov’s theorem (Kolgan, 1972; van Leer, 1976; van Leer, 1977). This approach is also sometimes called *MUSCL*, for monotone upstream-centred method for conservation laws.

### 9.3.1 Slope-limiter methods

As mentioned above, slope-limiter methods can be used to improve the representation of the solution within the cell and, at the same time, impose a TVD property on the methods. In practice, slope-limiter methods improve the simple piecewise-constant representation adopted in the original Godunov method by providing a piecewise-linear reconstruction of  $\mathbf{U}_j(x)$  inside each cell, *i.e.*, by prescribing  $\mathbf{U}_j^n(x)$  as

$$\mathbf{U}_j^n(x) = \mathbf{U}_j^n + \boldsymbol{\sigma}_j^n(x - x_j) \quad \text{with } x_{j-1/2} \leq x \leq x_{j+1/2}, \quad (9.43)$$

where  $x_j := (x_{j-1/2} + x_{j+1/2})/2$  is the coordinate value at the cell centre, while  $\boldsymbol{\sigma}_j^n$  is the “slope” of the linear reconstruction inside the cell. Several choices are possible for the slope and the most commonly adopted TVD slope limiters are listed below.<sup>7</sup>

- The *minmod slope limiter* (Kolgan, 1972; van Leer, 1979)

$$\boldsymbol{\sigma}_j^n := \text{minmod} \left( \frac{\mathbf{U}_j^n - \mathbf{U}_{j-1}^n}{\Delta x}, \frac{\mathbf{U}_{j+1}^n - \mathbf{U}_j^n}{\Delta x} \right), \quad (9.44)$$

where

$$\begin{aligned} \text{minmod}(\alpha, \beta) &:= \begin{cases} \alpha & \text{if } |\alpha| < |\beta| \text{ and } \alpha\beta > 0, \\ \beta & \text{if } |\beta| < |\alpha| \text{ and } \alpha\beta > 0, \\ 0 & \text{if } \alpha\beta \leq 0, \end{cases} \\ &:= \text{sign}(\alpha) \max\{0, \min\{|\alpha|, \beta \text{ sign}(\alpha)\}\}. \end{aligned} \quad (9.45)$$

- The *monotonised central-difference limiter* (MC) (van Leer, 1977)

$$\boldsymbol{\sigma}_j^n := \text{minmod} \left( \frac{\mathbf{U}_{j+1}^n - \mathbf{U}_{j-1}^n}{2\Delta x}, 2\frac{\mathbf{U}_j^n - \mathbf{U}_{j-1}^n}{\Delta x}, 2\frac{\mathbf{U}_{j+1}^n - \mathbf{U}_j^n}{\Delta x} \right). \quad (9.46)$$

where

$$\text{minmod}(\alpha, \beta, \gamma) := \begin{cases} \min(\alpha, \beta, \gamma) & \text{if } \alpha, \beta, \gamma > 0, \\ \max(\alpha, \beta, \gamma) & \text{if } \alpha, \beta, \gamma < 0, \\ 0 & \text{otherwise.} \end{cases} \quad (9.47)$$

- The *superbee limiter* (Roe, 1985)

$$\boldsymbol{\sigma}_j^n := \text{maxmod}(\boldsymbol{\sigma}_j^I, \boldsymbol{\sigma}_j^{II}), \quad (9.48)$$

where

$$\boldsymbol{\sigma}_j^I := \text{minmod} \left( 2\frac{\mathbf{U}_j^n - \mathbf{U}_{j-1}^n}{\Delta x}, \frac{\mathbf{U}_{j+1}^n - \mathbf{U}_j^n}{\Delta x} \right), \quad (9.49)$$

<sup>7</sup>To keep the notation simple in the following formulas we assume a uniform grid *i.e.*,  $\Delta x := x_{j+1/2} - x_{j-1/2} = \text{const.}$ , but the extension to non-uniform spacings is straightforward.

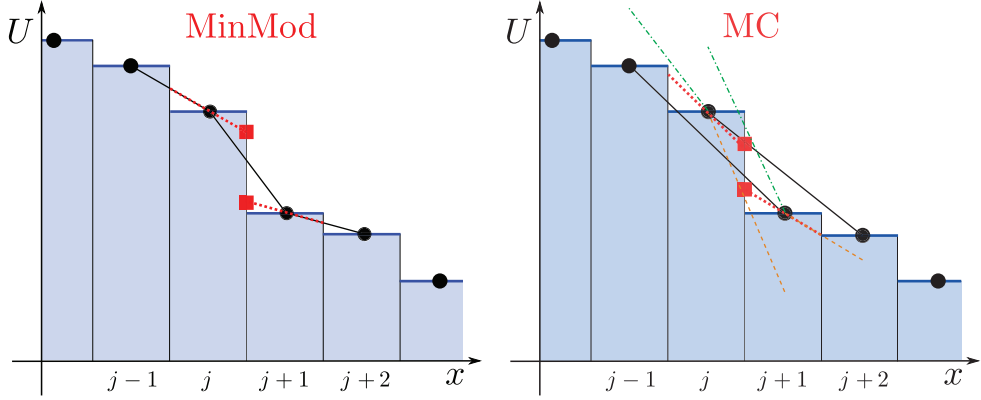


**Fig. 9.3** Schematic representation and comparison between two slope limiters: the minmod limiter (left panel) and the MC limiter (right panel), when acting on the same set of data (cf., Fig. 9.1). Shown with red dashed lines are the reconstructed final slopes, while solid red boxes represent the boundary-extrapolated values. In the case of the MC limiter, black dashed, dotted and dot-dashed lines represent the various slopes that can be computed.

$$\sigma_j^{\text{II}} := \text{minmod} \left( \frac{\mathbf{U}_j^n - \mathbf{U}_{j-1}^n}{\Delta x}, 2 \frac{\mathbf{U}_{j+1}^n - \mathbf{U}_j^n}{\Delta x} \right), \quad (9.50)$$

and

$$\text{maxmod}(\alpha, \beta) := \begin{cases} \alpha & \text{if } |\alpha| > |\beta| \text{ and } \alpha\beta > 0, \\ \beta & \text{if } |\beta| > |\alpha| \text{ and } \alpha\beta > 0, \\ 0 & \text{if } \alpha\beta \leq 0. \end{cases} \quad (9.51)$$

Figure 9.3 shows the comparison between the slopes provided by the minmod and the MC limiters. Note that minmod always takes the least steep among the slopes provided by the backward and the forward finite-difference. The MC limiter, on the other hand, compares three different slopes and it is slightly more involved. To fix ideas, let us consider the graphical representation of the MC algorithm when applied to the cell  $j + 1$ , as shown in the right panel of Fig. 9.3. The first slope that is considered is that among the values at  $x_j$  and  $x_{j+2}$ , reported with a black solid line; the second one has twice the slope of the straight line among the values at  $x_j$  and  $x_{j+1}$ , and is reported with the green dash-dotted line originating from the value at  $x_{j+1}$ ; finally, the third one has twice the slope of the straight line among the values at  $x_{j+1}$  and  $x_{j+2}$ , and is reported with the orange short-dashed line originating from the value at  $x_{j+1}$ . The resulting slope provided by the MC algorithm is the least steep among the above three, and is reported with the red dashed line inside the cell  $j + 1$ . This procedure is then repeated for each cell. Once  $\mathbf{U}_j(x)$  has been reconstructed, the values of  $\mathbf{U}_j(x)$  at the two extremes of each cell, also called the *boundary-extrapolated values*,

$$\mathbf{U}_j^- := \mathbf{U}_j(x_{j-1/2}), \quad \mathbf{U}_j^+ := \mathbf{U}_j(x_{j+1/2}), \quad (9.52)$$

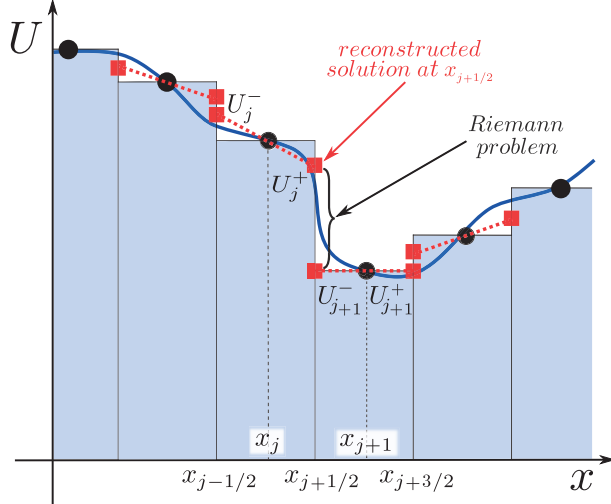


**Fig. 9.4** Schematic representation of the boundary-extrapolated values (red solid boxes) providing the left and right constant states of the Riemann problem that has to be solved at every cell interface (these are shown as red solid boxes in Fig. 9.3). For instance, at  $x_{j+1/2}$  the local Riemann problem is defined as

$$U(x, 0) = \begin{cases} U_j^+ & \text{if } x < x_{j+1/2}, \\ U_{j+1}^- & \text{if } x > x_{j+1/2}. \end{cases} \quad (9.53)$$

This configuration is represented schematically in Fig. 9.4, where  $U_j^+$  and  $U_{j+1}^-$  are the left and right states of the Riemann problem to be solved at  $x_{j+1/2}$ .

In spite of their success in modelling sharp discontinuities without producing oscillations, TVD slope-limiter methods suffer from excessive numerical dissipation near local extrema, where the reconstructed profile of the TVD method is a straight line with zero slope, thus reducing to the first-order Godunov method. This is illustrated in Fig. 9.4 for the values reconstructed in the cell at  $x_{j+1}$ . Examples of explicit implementations of the slope limiters discussed so far are presented in Appendix E and can be of aid in the construction of HRSC numerical codes.

### 9.3.2 The piecewise-parabolic method

Because of its relevance and popularity, in this section we will describe in the most concise way the so-called *piecewise-parabolic method (PPM)*, originally introduced by Colella and Woodward (1984), and later applied to relativistic hydrodynamics by Martí and Müller (1996).

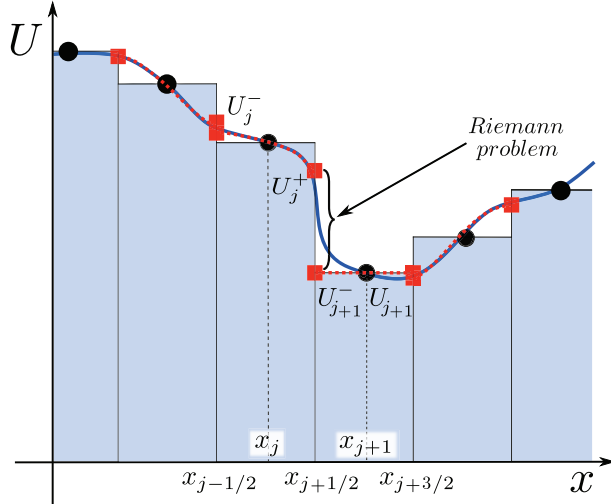


**Fig. 9.5** Schematic representation of the boundary-extrapolated values (red solid boxes) providing the left and right states of the Riemann problem at each cell interface. The reconstruction is made using the PPM method (*cf.* Fig. 9.1 for a piecewise-constant reconstruction and Fig. 9.4 for a piecewise-linear reconstruction).

and Mignone and Bodo (2005). We should note that the original procedure behind the PPM method is more than a simple reconstruction and that it also includes the time evolution using characteristic information (see Section 9.3.3). Here, however, we will follow the common practice of referring to the PPM method simply as to a higher-order reconstruction procedure which adopts a parabolic interpolation of the variables inside numerical cells. This is illustrated in Fig. 9.5, which reports a schematic representation of the boundary-extrapolated values (red solid boxes) providing the left and right states of the Riemann problem at each cell interface using the PPM reconstruction and improves on the piecewise-constant (see Fig. 9.1) and piecewise-linear (see Fig. 9.4) reconstructions.

Though not TVD, the PPM method uses specific monotonicity constraints to the extent of keeping the solution free from numerical oscillations. In addition, by using a quadratic reconstruction, the PPM method is nominally third-order accurate in regions of the flow that are smooth. In practice, however, the standard PPM method still deteriorates to a first-order method at local extrema, thus leading to a global order of accuracy which is rarely above the second<sup>8</sup> [see however some recent improvements by Colella and Sekora (2008)]. Indeed, it is because of its effective “low-order” accuracy in space that we discuss it here rather than in the next chapter, where higher-order methods will be presented.

<sup>8</sup>For instance, measurements of the convergence order of the PPM method in numerical-relativity simulations of binary neutron stars (see also Section 12.5) indicate that the PPM reconstruction yields an order of convergence  $\simeq 1.8$  in the absence of global shocks (Baiotti *et al.*, 2009).

We start again by considering the initial averaged values of the general quantity  $\mathbf{U}$  between  $x_{j-1/2}$  and  $x_{j+1/2}$  over a uniform spatial grid<sup>9</sup>

$$\mathbf{U}_j^n = \frac{1}{\Delta x} \int_{x_{j-1/2}}^{x_{j+1/2}} \mathbf{U}(x, t^n) dx, \quad (9.13)$$

where  $\Delta x := x_{j+1/2} - x_{j-1/2}$ . The basic idea of the PPM is to build an interpolating parabola  $\Phi(\xi)$  inside each cell, namely

$$\Phi(\xi) := \mathbf{a}\xi^2 + \mathbf{b}\xi + \mathbf{c}, \quad (9.54)$$

where  $\xi := (x - x_{j-1/2})/\Delta x_j$ ,  $x \in [x_{j-1/2}, x_{j+1/2}]$ , and  $\mathbf{a}, \mathbf{b}, \mathbf{c}$  are vectors of constant coefficients to be determined. The interpolation must of course be conservative, in the sense that

$$\mathbf{U}_j^n = \int_0^1 \Phi(\xi) d\xi. \quad (9.55)$$

Note that such a condition was automatically satisfied in the case of a linear reconstruction of the slope-limiter methods and hence did not require any special attention. Furthermore, because of the constraint (9.55), the PPM method makes sense only when applied to the conserved variables within finite-volume methods, for which a cell average does exist.

An additional constraint is that no new extrema appear in the interpolating function  $\Phi(\xi)$  which did not already appear in the  $\mathbf{U}_j^n$ 's. Since determining a parabola requires the calculation of the vectors of constants  $\mathbf{a}, \mathbf{b}, \mathbf{c}$  in Eq. (9.54), and one condition for their calculation is obtained from Eq. (9.55), we still have the freedom to choose the values  $\mathbf{U}_j^-$  and  $\mathbf{U}_j^+$  of the interpolating parabola at the left and right edges of the  $j$ -th numerical cell. In practice,  $\mathbf{U}_j^-$  and  $\mathbf{U}_j^+$  are found by imposing that

1. they do not fall outside the range of the two adjacent values  $\mathbf{U}_j^n$  and  $\mathbf{U}_{j+1}^n$ ;
2. in smooth parts, away from extrema,  $\mathbf{U}_{j+1}^- = \mathbf{U}_j^+ = \mathbf{U}_{j+1/2}^n$ , so that the interpolation function is continuous at  $x_{j+1/2}$ ;
3. the interpolating parabola is monotone in each cell.

The common procedure is to perform a polynomial Lagrangian interpolation on the values of the indefinite integral of  $\mathbf{U}$

$$\mathbf{U}^n(x) = \int_{-\infty}^x \mathbf{U}(x', t^n) dx', \quad (9.56)$$

whose value at the zone edges is given by the sum of the cell averages, *i.e.*,

$$\mathbf{U}^n(x_{j+1/2}) = \sum_{k=-\infty}^j \int_{x_{k-1/2}}^{x_{k+1/2}} \mathbf{U}(x', t^n) dx' = \sum_{k=-\infty}^j \mathbf{U}_k^n \Delta x_k. \quad (9.57)$$

As a result, the value of  $\mathbf{U}$  at the edge of the numerical cell can be calculated by differentiating (9.57), *i.e.*,

<sup>9</sup>The PPM method was originally proposed for generally non-uniform grids, but we treat uniform grids for simplicity.

$$\mathbf{U}_{j+1/2}^n = \frac{d\mathcal{U}^n}{dx} \Big|_{x_{j+1/2}}. \quad (9.58)$$

When the grid is uniform, it is possible to obtain a quartic interpolation through the points of the parabola  $(x_{j+k+1/2}, \mathcal{U}^n(x_{j+k+1/2}))$ , with  $k = 0, \pm 1, \pm 2$ , so as to obtain

$$\mathbf{U}_{j+1/2}^n = \frac{1}{2}(\mathbf{U}_j^n + \mathbf{U}_{j+1}^n) + \frac{1}{6}(\delta\mathbf{U}_j^n - \delta\mathbf{U}_{j+1}^n), \quad (9.59)$$

where  $\delta\mathbf{U}_j^n := \frac{1}{2}(\mathbf{U}_{j+1}^n - \mathbf{U}_{j-1}^n)$ . However, we can guarantee that  $\mathbf{U}_{j+1/2}^n$  meets the condition 1 listed above if we replace  $\delta\mathbf{U}_j^n$  with

$$\delta\mathbf{U}_j^n = \begin{cases} \min(|\delta\mathbf{U}_j^n|, 2|\mathbf{U}_j^n - \mathbf{U}_{j-1}^n|, 2|\mathbf{U}_{j+1}^n - \mathbf{U}_j^n|) \operatorname{sign}(\delta\mathbf{U}_j^n) & \text{if } \delta\mathbf{U}_{j+1/2}^n \delta\mathbf{U}_{j-1/2}^n > 0, \\ 0 & \text{otherwise,} \end{cases} \quad (9.60)$$

where  $\delta\mathbf{U}_{j\pm 1/2}^n := \pm \frac{1}{2}(\mathbf{U}_{j\pm 1}^n - \mathbf{U}_j^n)$ .

After computing  $\mathbf{U}_j^-$  and  $\mathbf{U}_j^+$ , the interpolating parabola can be written as

$$\Phi(\xi) = \mathbf{U}_j^- + \xi \left\{ (\mathbf{U}_j^+ - \mathbf{U}_j^-) + 6 \left[ \mathbf{U}_j^n - \frac{1}{2}(\mathbf{U}_j^+ + \mathbf{U}_j^-) \right] (1 - \xi) \right\}. \quad (9.61)$$

Because the function  $\Phi(\xi)$  within each numerical cell must be monotonic and thus without oscillations, the parabola in Eq. (9.61) is further modified according to the following cases:

- *Case I:* If  $\mathbf{U}_j^n$  is a local extremum, then the interpolating function is set to be a constant, *i.e.*,

$$\mathbf{U}_j^- = \mathbf{U}_j^+ = \mathbf{U}_j^n. \quad (9.62)$$

- *Case II:* If  $\mathbf{U}_j^n$  falls between  $\mathbf{U}_j^-$  and  $\mathbf{U}_j^+$  but is close to one of them, so that the interpolated parabola may take a value outside this range, namely, when

$$(\mathbf{U}_j^+ - \mathbf{U}_j^-) \left[ \mathbf{U}_j^n - \frac{1}{2}(\mathbf{U}_j^+ + \mathbf{U}_j^-) \right] > \frac{1}{6}(\mathbf{U}_j^+ - \mathbf{U}_j^-)^2, \quad (9.63)$$

then  $\mathbf{U}_j^-$  is reset as

$$\mathbf{U}_j^- = 3\mathbf{U}_j^n - 2\mathbf{U}_j^+, \quad (9.64)$$

so that the interpolating parabola is monotone and its derivative at the opposite edge of the zone is zero, *i.e.*,  $\Phi'(1) = 0$ .

- *Case III:* If  $\mathbf{U}_j^n$  falls between  $\mathbf{U}_j^-$  and  $\mathbf{U}_j^+$ , but is close to one of them, namely when

$$-\frac{1}{6}(\mathbf{U}_j^+ - \mathbf{U}_j^-)^2 > (\mathbf{U}_j^+ - \mathbf{U}_j^-) \left[ \mathbf{U}_j^n - \frac{1}{2}(\mathbf{U}_j^+ + \mathbf{U}_j^-) \right], \quad (9.65)$$

then  $\mathbf{U}_j^+$  is reset as

$$\mathbf{U}_j^+ = 3\mathbf{U}_j^n - 2\mathbf{U}_j^-, \quad (9.66)$$

again ensuring that the interpolating parabola is monotone and its derivative at the opposite edge of the zone is zero, *i.e.*,  $\Phi'(0) = 0$ .

Colella and Woodward (1984) also suggested additional modifications to improve the reconstruction, for instance, to obtain sharper profiles at contact discontinuities, and their implementation in a numerical-relativity code can be found in Baiotti (2004). Further technical details regarding the monotonicity part of the algorithm and the way in which spurious post-shock oscillations can be avoided near strong shocks is discussed by Martí and Müller (1996).

### 9.3.3 Reconstruction in characteristic variables

In Section 4.2 we discussed that hyperbolic linear systems written in conservative form<sup>10</sup> can always be rewritten in terms of *characteristic variables* as

$$\partial_t \mathbf{W} + \boldsymbol{\Lambda} \nabla \mathbf{W} = 0, \quad (4.45)$$

where  $\mathbf{W}$  is the *characteristic vector* and can be written either as

$$\mathbf{W} := \mathbf{R}^{-1} \mathbf{U}, \quad (4.42)$$

with  $\mathbf{U}$  representing the vector of conserved quantities and  $\mathbf{R}$  the matrix of right eigenvectors, or as

$$\mathbf{W}_p := \mathbf{R}_p^{-1} \mathbf{V}, \quad (9.67)$$

with  $\mathbf{V}$  representing the vector of primitive variables and  $\mathbf{R}_p$  the corresponding matrix of right eigenvectors. The diagonal matrix  $\boldsymbol{\Lambda}$ , on the contrary, is the same in the two cases and has elements given by the eigenvalues of the system.<sup>11</sup> When considering the numerical problem of reconstructing a profile of the unknown quantities starting from the average values, the form of the equations (4.45) and the accompanying definition (4.42) can provide a very powerful tool. In fact, even if the equations are nonlinear, at any given time  $t^n$  the average values inside each cell are, by definition, constant in that cell. As a result, such values define a fixed state around which the quasi-linear form of the equations can be linearised, leading to the form given by (4.45). It is therefore possible to perform the reconstruction on the characteristic variables given by Eq. (9.67), rather than on the usual conserved (or primitive) quantities. Note that this strategy can only be used to perform a “predictor step” and thus to compute the solution only at an intermediate time  $t = t^{n+1/2}$ .

The practical implementation of a *characteristic reconstruction* proceeds with the following steps:

1. The characteristic variables  $\mathbf{W}$  are reconstructed inside each numerical cell, thus obtaining the corresponding boundary-extrapolated values  $\mathbf{W}_j^{-,n}$  and  $\mathbf{W}_j^{+,n}$ , where we have added the superscript  $n$  to indicate that these refer to values at time-level  $t^n$ . The reconstruction can of course be performed with any method: TVD slope limiters, PPM, high-order methods, or others. In some cases, this first step followed by the transformation back to the conservative (or primitive) variables (*cf.*, step 3 below) is sufficient to obtain sharper profiles than those obtained with a direct reconstruction of the vector  $\mathbf{U}$  (or  $\mathbf{V}$ ). Indeed, some authors consider the *characteristic reconstruction* to consist only

<sup>10</sup>We recall that a linear system can always be cast in conservative form.

<sup>11</sup>We recall that such eigenvalues do not depend on the set of variables used to write the quasi-linear form of the system (see the discussion in Section 4.1.2).

of steps 1 and 3. However, since the advantages of this simplified procedure are not universal (*i.e.*, it does not always yields improvements), the next step becomes necessary to fully exploit the advantages of the characteristic reconstruction.

2. Once  $\mathbf{W}_j^{+,n}$  and  $\mathbf{W}_j^{-,n}$  have been computed, a discrete version of the characteristic equations (4.45) is used to perform a predictor step and compute each component of the characteristic variables at the cell interface and at time  $t^{n+1/2}$ . Let us for simplicity illustrate this procedure in one spatial dimension, recalling that the system (4.45) represents a set of decoupled  $N$  advection equations, *i.e.*,

$$\partial_t W^\alpha + \lambda^\alpha \partial_x W^\alpha = 0, \quad 1 \leq \alpha \leq N. \quad (9.68)$$

For ease of notation we drop momentarily the index  $\alpha$  denoting the characteristic and use the upwind finite-difference method (8.52) to find that for  $\lambda_j > 0$  (see Section 8.3.2)

$$\frac{W_j^{+,n+1/2} - W_j^{+,n}}{\Delta t / 2} + \lambda_j \frac{W_j^{+,n} - W_j^{-,n}}{\Delta x} = 0, \quad (9.69)$$

which then leads to

$$W_j^{+,n+1/2} = W_j^n + \frac{1}{2} \left( 1 - \lambda_j \frac{\Delta t}{\Delta x} \right) (W_j^{+,n} - W_j^{-,n}). \quad (9.70)$$

Similarly, after applying the alternative expression (8.53) for  $\lambda_{j+1} < 0$ , we obtain

$$W_{j+1}^{-,n+1/2} = W_{j+1}^n - \frac{1}{2} \left( 1 + \lambda_{j+1} \frac{\Delta t}{\Delta x} \right) (W_{j+1}^{+,n} - W_{j+1}^{-,n}). \quad (9.71)$$

3. Once the values of  $W_j^{\pm,n+1/2}$  have been computed, the corresponding conservative (or primitive) variables are recovered through the inverse of Eq. (4.42) or Eq. (9.67), namely as

$$\mathbf{U}^{n+1/2} = \mathbf{R}\mathbf{W}^{n+1/2} \quad (9.72)$$

or

$$\mathbf{V}^{n+1/2} = \mathbf{R}_p \mathbf{W}^{n+1/2}. \quad (9.73)$$

These quantities can now be used to build the left and right states of the local Riemann problems at each cell interface and use any Riemann solver to update the solution to the new time-level  $t^{n+1}$ .

We should stress that a few variants of the *predictor step* 2 described above have been presented in the literature, starting from the original formulations by Colella and Woodward (1984) and by Harten *et al.* (1983). Our description above followed that of Balsara (2001), though other solutions are also possible (Colella, 1990; Mignone *et al.*, 2012). When compared to the traditional reconstruction in primitive or conserved variables, the reconstruction in characteristic variables translates into an additional computational cost, related to the implementation of the spectral decomposition, but the advantages in terms of accuracy can be significant, especially for high-order methods.

## 9.4 Approximate Riemann solvers

As anticipated in Section 4.6, the general solution of the Riemann problem cannot be given in a closed analytic form even for one-dimensional Newtonian flows. Nevertheless, because it is possible to solve the Riemann problem numerically to any required accuracy, the corresponding solution is loosely called *exact*, even though it is not analytical. The exact solution of the Riemann problem is available both in Newtonian and in relativistic hydrodynamics (see Section 4.6), but the high computational costs associated with its solution at each cell interface make its application in present multidimensional codes unrealistic. As a result, a large number of *approximate Riemann solvers* have been proposed over the years that are computationally less expensive and yet give results that are in general very accurate.

, , Approximate Riemann solvers can be divided into *complete Riemann solvers* which contain all the characteristic fields of the exact solution, and *incomplete Riemann solvers* which contain only a subset of them. Such a distinction is a very relevant one, since only complete Riemann solvers are fully upwind and thus able to capture any discontinuity or wave that may form during the evolution. Incomplete Riemann solvers, on the other hand, are devised in such a way to be upwind only with respect to the fastest possible waves produced in the Riemann fan, but they can lose important information about intermediate waves. As a result, a Godunov scheme adopting an incomplete Riemann solver like Rusanov's (see Section 9.4.1) effectively behaves like a central-upwind scheme (see Section 9.6.2).

We should note that the distinction between complete and incomplete Riemann solvers also depends on the specific equations that are being solved, since different systems of equations typically have a different number of characteristic fields. For example, the HLLC Riemann solver that will be described in Section 9.4.2 is a complete Riemann solver for the equations of relativistic hydrodynamics, but is no longer so if used for the equations of magnetohydrodynamics. Similarly, the Rusanov solver is a one-wave solver and therefore complete when applied to a scalar advection equation, but it is an incomplete solver in general. In the rest of our discussion we will specifically refer to the equations of relativistic hydrodynamics in one spatial dimension and the classification is therefore appropriate for this system of equations. Finally, we remark that our discussion of Riemann solvers is not intended to be comprehensive or detailed, but rather aims at illustrating the main ideas behind these solvers, concentrating on those which are more commonly adopted in relativistic hydrodynamics nowadays. For an exhaustive treatment on this topic we refer to the more specialist book of Toro (2009).

### 9.4.1 Incomplete Riemann solvers

#### **The HLLE solver.**

A widely used approximate Riemann solver is the one first proposed by Harten et al. (1983) and later improved by Einfeldt (1988), namely, the so-called *HLLE Riemann solver*. The strength and simplicity of this solver is in the assumption that after the decay of the initial discontinuity of the local Riemann problem only two waves propagate in two opposite directions with velocities  $\lambda_L$  and  $\lambda_R$ , generating a *single* and *constant* state between them, *i.e.*,

$$\mathbf{U}(x, t) = \begin{cases} \mathbf{U}_L & \text{if } x/t < \lambda_L, \\ \mathbf{U}_{\text{HLLE}} & \text{if } \lambda_L < x/t < \lambda_R, \\ \mathbf{U}_R & \text{if } x/t > \lambda_R, \end{cases} \quad (9.74)$$

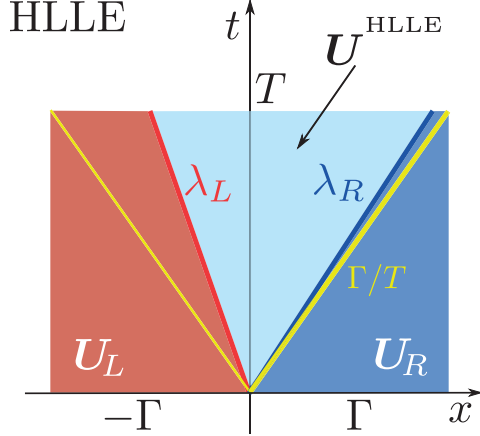


**Fig. 9.6** Spacetime control volume  $V := [-\Gamma, \Gamma] \times [0, T]$  for the computation of the approximate HLLE flux. The Riemann fan is composed of two waves only, with speeds  $\lambda_L$  and  $\lambda_R$ , delimiting a single constant state between them,  $\mathbf{U}^{\text{HLLE}}$  (*cf.*, Fig. 4.10).

where  $\lambda_L \leq 0$  and  $\lambda_R \geq 0$  are the smallest and the largest of the characteristic speeds resulting from the solution of the Riemann problem. Because it represents a basic building block in many numerical codes, we will discuss this approximate Riemann solver in more detail. We start by defining a spacetime *control volume* as  $V := [-\Gamma, \Gamma] \times [0, T]$ , where  $\Gamma > \max(|\lambda_L|, |\lambda_R|)T$ , while  $T$  is just a representative time interval. This is shown schematically in Fig. 9.6.

The integral form of the conservative equations (9.1) over such a control volume becomes

$$\begin{aligned} \int_{-\Gamma}^{\Gamma} \mathbf{U}(x, T) dx &= \int_{-\Gamma}^{\Gamma} \mathbf{U}(x, 0) dx + \int_0^T \mathbf{F}(\mathbf{U}(-\Gamma, t)) dt - \int_0^T \mathbf{F}(\mathbf{U}(\Gamma, t)) dt \\ &= \int_{-\Gamma}^0 \mathbf{U}_L dx + \int_0^{\Gamma} \mathbf{U}_R dx + \int_0^T \mathbf{F}(\mathbf{U}(-\Gamma, t)) dt - \int_0^T \mathbf{F}(\mathbf{U}(\Gamma, t)) dt \\ &= \Gamma(\mathbf{U}_L + \mathbf{U}_R) + T(\mathbf{F}_L - \mathbf{F}_R), \end{aligned} \quad (9.75)$$

where  $\mathbf{F}_L = \mathbf{F}(\mathbf{U}_L)$  and  $\mathbf{F}_R = \mathbf{F}(\mathbf{U}_R)$ . It is now possible to split the integral on the left-hand side of Eq. (9.75) into three integrals

$$\begin{aligned} \int_{-\Gamma}^{\Gamma} \mathbf{U}(x, T) dx &= \int_{-\Gamma}^{T\lambda_L} \mathbf{U}_L dx + \int_{T\lambda_L}^{T\lambda_R} \mathbf{U}^{\text{HLLE}} dx + \int_{T\lambda_R}^{\Gamma} \mathbf{U}_R dx \\ &= \mathbf{U}_L(T\lambda_L + \Gamma) + \mathbf{U}^{\text{HLLE}}(\lambda_R - \lambda_L)T + \mathbf{U}_R(\Gamma - T\lambda_R), \end{aligned} \quad (9.76)$$

and comparing the right-hand sides of Eq. (9.75) and Eq. (9.76), it is easy to find

$$\mathbf{U}^{\text{HLLE}} = \frac{(\lambda_R \mathbf{U}_R - \lambda_L \mathbf{U}_L + \mathbf{F}_L - \mathbf{F}_R)}{(\lambda_R - \lambda_L)}. \quad (9.77)$$

Thus the constant state  $\mathbf{U}^{\text{HLLE}}$  can be easily computed, provided the signal speeds  $\lambda_L$  and  $\lambda_R$  are known. Applying then the Rankine–Hugoniot conditions (9.7) across the left and the right waves, we obtain

$$\mathbf{F}_{L_*} = \mathbf{F}_L + \lambda_L (\mathbf{U}^{\text{HLLE}} - \mathbf{U}_L), \quad (9.78)$$

$$\mathbf{F}_{R_*} = \mathbf{F}_R + \lambda_R (\mathbf{U}^{\text{HLLE}} - \mathbf{U}_R). \quad (9.79)$$

Finally, by substituting (9.77) into (9.78) or into (9.79) we obtain the *HLLE flux*

$$\mathbf{F}_* := \frac{\lambda_R \mathbf{F}_L - \lambda_L \mathbf{F}_R + \lambda_L \lambda_R (\mathbf{U}_R - \mathbf{U}_L)}{\lambda_R - \lambda_L}, \quad (9.80)$$

to be used in the Godunov method according to the logic below (see Problem 3), *i.e.*,

$$\mathbf{F}^{\text{HLLE}} = \begin{cases} \mathbf{F}_L & \text{if } x/t < \lambda_L, \\ \mathbf{F}_* & \text{if } \lambda_L < x/t < \lambda_R, \\ \mathbf{F}_R & \text{if } x/t > \lambda_R. \end{cases} \quad (9.81)$$

The HLLE Riemann solver is clearly very simple, performs well at critical sonic rarefactions but produces excessive smearing at contact discontinuities due to the fact that middle waves are ignored in the solution. Obviously, it needs to be implemented with an algorithm for the calculation of the wave speeds  $\lambda_L$  and  $\lambda_R$ . In special-relativistic hydrodynamics, for example,  $\lambda_L$  and  $\lambda_R$  can be computed as<sup>12</sup>

$$\lambda_L := \min(0, \lambda_-(\mathbf{U}_L), \lambda_-(\mathbf{U}_R)), \quad (9.82)$$

$$\lambda_R := \max(0, \lambda_+(\mathbf{U}_L), \lambda_+(\mathbf{U}_R)), \quad (9.83)$$

with  $\lambda_-$  and  $\lambda_+$  given by Eqs. (4.24). Appendix E offers an example of the implementation of this solver with a simple pseudo-code (see Section E.2).

### The Rusanov solver.

The *Rusanov approximate Riemann solver* (Rusanov, 1961), also known as the *local Lax–Friedrichs flux* (Shu and Osher, 1989), is a special case of the HLLE solver where one imposes that  $\lambda_R = -\lambda_L = \lambda$ . In this case, the flux formula (9.80) reduces to

$$\mathbf{F}^{\text{Rusanov}} = \frac{1}{2}(\mathbf{F}_L + \mathbf{F}_R) - \frac{1}{2}\lambda(\mathbf{U}_R - \mathbf{U}_L), \quad (9.84)$$

where, as a simple choice for the single speed  $\lambda$ , one can take  $\lambda = \max(|\lambda_R|, |\lambda_L|)$ , with  $\lambda_L$  and  $\lambda_R$  given by Eq. (9.82)–(9.83). Although very simplified, this Riemann solver has been adopted successfully in a variety of computational applications, even in combination with high-order methods (Dumbser and Zanotti, 2009; Hidalgo and Dumbser, 2011). Also in this case, Appendix E offers an example of the implementation of this solver with a simple pseudo-code (see Section E.2).

<sup>12</sup>The notation here can be very confusing. Note that  $\lambda_L$  and  $\lambda_R$  are not the eigenvalues computed in the left and right states, as the indices seem to suggest. Rather, as expressed by their definitions (9.82) and (9.83), they are respectively the minimum of the left-propagating eigenvalues and the maximum of the right-propagating eigenvalues, when considered over *both* the left and right states.

### 9.4.2 Complete Riemann solvers

#### “Two-rarefaction” Riemann solver.

As discussed in detail in Section 4.6, finding the wave pattern in a Riemann problem is part of the solution procedure, but if one assumes *a priori* that both nonlinear waves are rarefactions, then the solution can be obtained analytically. The resulting approximate Riemann solver is very accurate for flow conditions near vacuum, when rarefaction waves indeed give the best approximation to the problem (Rezzolla and Zanotti, 2001). In the following we describe this procedure for a polytropic equation of state (see Section 2.4.7). The extension to a generic equation of state is of course possible but will not necessarily lead to an analytic solver.

We recall that in the exact solver of Rezzolla and Zanotti (2001), if the initial relative velocity  $(v_{12})_0$  falls in the interval given by (see Section 4.6.1)

$$(v_{12})_{\mathcal{R}}|_{p_3=0} < (v_{12})_0 \leq (v_{12})_{\mathcal{R}}|_{p_3=p_2} = (\tilde{v}_{12})_{\mathcal{R}}, \quad (4.178)$$

where  $(\tilde{v}_{12})_{\mathcal{R}}$  are the limiting velocities in several possible cases, then the initial conditions of the Riemann problem give rise to two rarefaction waves moving in opposite directions (Rezzolla and Zanotti, 2001). To derive a closed-form solution for the unknown pressure  $p_*$  in Eq. (4.155), we can use expression (2.173) for the sound speed and write the pressures  $p_3$  and  $p_{3'}$  as functions of the sound speeds  $c_s(p_3)$  and  $c_s(p_{3'})$  which, for convenience, hereafter we will denote as  $x$  and  $x'$  respectively, *i.e.*,

$$p_3 = K_1^{-1/(\Gamma-1)} \left[ \frac{x^2(\Gamma-1)}{\Gamma(\Gamma-1)-\Gamma x^2} \right]^{\Gamma/(\Gamma-1)}, \quad (9.85)$$

$$p_{3'} = K_2^{-1/(\Gamma-1)} \left[ \frac{(x')^2(\Gamma-1)}{\Gamma(\Gamma-1)-\Gamma(x')^2} \right]^{\Gamma/(\Gamma-1)}, \quad (9.86)$$

where  $K_1 = p_1/\rho_1^\Gamma$  and  $K_2 = p_2/\rho_2^\Gamma$  are the two polytropic constants. Since  $p_3 = p_{3'} = p_*$ , we can obtain the following relation between  $x'$  and  $x$

$$(x')^2 := \frac{\Gamma(\Gamma-1)x^2}{\Gamma x^2(1-\chi) + \chi\Gamma(\Gamma-1)}, \quad (9.87)$$

where  $\chi := (K_1/K_2)^{1/\Gamma}$ . The expression for the relative velocity (4.177) can also be written as

$$\frac{A_+(p_3)}{A_-(p_{3'})} = \frac{1 - (v_{12})_0}{1 + (v_{12})_0}. \quad (9.88)$$

We next use expressions (4.169) and (4.176) to expand the left-hand side of (9.88) and obtain, after a bit of algebra, that

$$\left( \frac{\bar{\Gamma} - x}{\bar{\Gamma} + x} \right) \left( \frac{\bar{\Gamma} - x'}{\bar{\Gamma} + x'} \right) = \left[ \frac{\bar{\Gamma} - c_s(p_2)}{\bar{\Gamma} + c_s(p_2)} \right] \left[ \frac{\bar{\Gamma} - c_s(p_1)}{\bar{\Gamma} + c_s(p_1)} \right] \left[ \frac{1 - (v_{12})_0}{1 + (v_{12})_0} \right]^{\bar{\Gamma}/2}, \quad (9.89)$$

where  $\bar{\Gamma}^2 := \Gamma - 1$ . The right-hand side of (9.89) is a constant and can be renamed as

$$\Pi := \left[ \frac{\bar{\Gamma} - c_s(p_2)}{\bar{\Gamma} + c_s(p_2)} \right] \left[ \frac{\bar{\Gamma} - c_s(p_1)}{\bar{\Gamma} + c_s(p_1)} \right] \left[ \frac{1 - (v_{12})_0}{1 + (v_{12})_0} \right]^{\bar{\Gamma}/2}. \quad (9.90)$$

Introducing now the auxiliary quantity

$$\Psi := \frac{1 + \Pi}{1 - \Pi}, \quad (9.91)$$

Eq. (9.89) can be rewritten as

$$(x')^2 = \left[ \frac{\bar{\Gamma}(x\Psi - \bar{\Gamma})}{x - \bar{\Gamma}\Psi} \right]^2. \quad (9.92)$$

Comparing Eqs. (9.87) and (9.92) yields a fourth-order equation in the unknown sound velocity  $x$ , *i.e.*,

$$a_0 x^4 + a_1 x^3 + a_2 x^2 + a_3 x + a_4 = 0, \quad (9.93)$$

where

$$a_0 := 1 - \Psi^2(1 - \chi), \quad a_1 := -2\bar{\Gamma}\chi\Psi, \quad (9.94)$$

$$a_2 := \bar{\Gamma}^2(1 - \chi)(\Psi^2 - 1), \quad a_3 := 2\bar{\Gamma}^3\chi\Psi, \quad (9.95)$$

$$a_4 := -\chi\bar{\Gamma}^4. \quad (9.96)$$

The analytic solution of Eq. (9.93) will yield at least two real roots for the pressure  $p_*$ , one of which is the physically acceptable one: *i.e.*, it is positive, leads to a subluminal sound speed, and falls in the interval  $0 < p_* < \min(p_1, p_2)$ . Once  $p_*$  has been computed, the corresponding  $v_*$  follows from Eq. (4.99) and all the remaining quantities on the back of the two rarefaction waves follow immediately (see Section 4.4.2). The last operation to be performed consists in sampling the position of the line  $x/t = 0$  emerging from the interface between adjacent cells with respect to the wave fan of the two-rarefaction wave solution. This provides the state  $\mathbf{U}(x_{j\pm1/2}, t)$ , to be used in the computation of the numerical flux through Eq. (9.14).

A two-rarefaction Riemann solver is also known within a Newtonian framework [see, *e.g.*, Toro (2009)], in which case Eq. (9.93) reduces to a second-order equation in the unknown sound velocity

$$\left( \frac{1}{\chi} - 1 \right) x^2 + 2\Sigma x - \Sigma^2 = 0, \quad (9.97)$$

where

$$\Sigma := c_s(p_1) + c_s(p_2) + \frac{(\Gamma - 1)}{2}(v_{12})_0, \quad (9.98)$$

and  $(v_{12})_0 := v_1 - v_2$ .

### **The HLLC solver.**

Although the HLLE approximate Riemann solver described in Section 9.4.1 is widely employed in numerical codes, it suffers from strong limitations in capturing contact or tangential waves. Its natural improvement, the so-called *HLLC Riemann solver*, was specifically introduced to restore the missing information about the intermediate contact discontinuity. The Newtonian version was first introduced by Toro *et al.* (1994), while the relativistic extension is due to Mignone and Bodo (2005). In this solver, a Riemann fan composed of three waves is

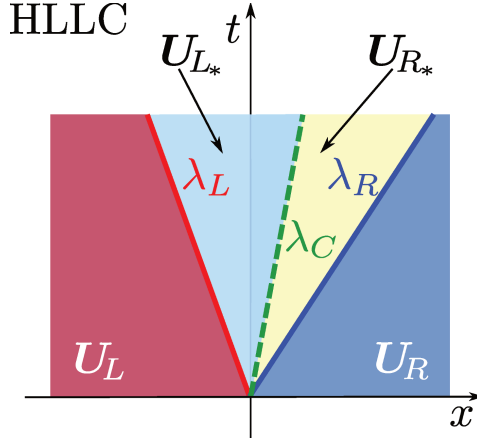


**Fig. 9.7** Spacetime control volume for the computation of the approximate HLLC flux. The Riemann fan is composed of two waves, with speeds  $\lambda_L$  and  $\lambda_R$ , plus an approximation to the contact discontinuity,  $\lambda_C$ . The three characteristics delimit two constant states between  $\mathbf{U}_{L*}$  and  $\mathbf{U}_{R*}$  (cf., Fig. 4.10).

constructed by defining two intermediate states  $\mathbf{U}_{L*}$  and  $\mathbf{U}_{R*}$ , such that the complete solution is given by

$$\mathbf{U}(x, t) = \begin{cases} \mathbf{U}_L & \text{if } x/t < \lambda_L, \\ \mathbf{U}_{L*} & \text{if } \lambda_L < x/t < \lambda_C, \\ \mathbf{U}_{R*} & \text{if } \lambda_C < x/t < \lambda_R, \\ \mathbf{U}_R & \text{if } x/t > \lambda_R, \end{cases} \quad (9.99)$$

where  $\lambda_L \leq 0$  and  $\lambda_R \geq 0$  are the smallest and the largest of the characteristics arising from the solution of the Riemann problem, while  $\lambda_C$  is the speed of the contact discontinuity, for which an approximate estimate needs to be given. A schematic representation of the corresponding control volume is reported in Fig. 9.7.

The intermediate state fluxes  $\mathbf{F}_{L*}$  and  $\mathbf{F}_{R*}$  are related to  $\mathbf{U}_{L*}$  and  $\mathbf{U}_{R*}$  through the Rankine–Hugoniot conditions (9.7), namely as

$$\mathbf{F}_{L*} - \mathbf{F}_L = \lambda_L(\mathbf{U}_{L*} - \mathbf{U}_L), \quad (9.100)$$

$$\mathbf{F}_{R*} - \mathbf{F}_R = \lambda_R(\mathbf{U}_{R*} - \mathbf{U}_R). \quad (9.101)$$

For a one-dimensional relativistic flow, with vectors of the conserved variables and of the fluxes given by Eq. (4.33), the Rankine–Hugoniot relations (9.100)–(9.101) represent a set of six equations. Provided an estimate of  $\lambda_C = v_*$  is available, the unknowns are given by the six components of the vectors  $\mathbf{U}_{L*}$  and  $\mathbf{U}_{R*}$ , thus yielding a well-posed problem. To fix ideas, let us consider Eq. (9.100), which we rewrite as

$$\lambda_L \mathbf{U}_{L*} - \mathbf{F}_{L*} = \lambda_L \mathbf{U}_L - \mathbf{F}_L = \mathbf{Q}, \quad (9.102)$$

or, explicitly as

$$\lambda_L \begin{pmatrix} D_{L_*} \\ S_{L_*} \\ E_{L_*} \end{pmatrix} - \begin{pmatrix} v_* D_{L_*} \\ S_{L_*} v_* + p_* \\ S_{L_*} \end{pmatrix} = \begin{pmatrix} Q_1 \\ Q_2 \\ Q_3 \end{pmatrix}, \quad (9.103)$$

where we should recall that  $S = (E + p)v$  [*cf.*, Eq. (4.33)]. As a result, the three unknowns in Eq. (9.103) are  $D_{L_*}$ ,  $E_{L_*}$  and  $p_*$ , with the first and third of Eqs. (9.103) being respectively

$$D_{L_*} = \frac{Q_1}{\lambda_L - \lambda_C}, \quad (9.104)$$

$$E_{L_*} = \frac{Q_3 + p_* \lambda_C}{\lambda_L - \lambda_C}. \quad (9.105)$$

Finally, after inserting Eq. (9.105) in the second of Eqs. (9.103), we obtain

$$p_* = \frac{1}{1 - \lambda_L \lambda_C} \left[ \frac{Q_2}{\lambda_C - \lambda_L} + Q_3 \lambda_C \right]. \quad (9.106)$$

Equations (9.104)–(9.106) complete our knowledge of the state  $\mathbf{U}_{L_*}$ , and in the same way we can obtain the state  $\mathbf{U}_{R_*}$ . Once these quantities are known, the corresponding numerical fluxes follow from Eqs. (9.100)–(9.101), so that the HLLC numerical flux is (see Problem 4)<sup>13</sup>

$$\mathbf{F}^{\text{HLLC}} = \begin{cases} \mathbf{F}_L & \text{if } x/t < \lambda_L, \\ \mathbf{F}_{L_*} & \text{if } \lambda_L < x/t < \lambda_C, \\ \mathbf{F}_{R_*} & \text{if } \lambda_C < x/t < \lambda_R, \\ \mathbf{F}_R & \text{if } x/t > \lambda_R. \end{cases} \quad (9.107)$$

Of course, the solution presented above requires an estimate for all the speeds  $\lambda_L$ ,  $\lambda_C$ , and  $\lambda_R$ . While for  $\lambda_L$  and  $\lambda_R$  we can follow the same strategy used in the case of the HLLE solver [*cf.*, Eqs. (9.82)–(9.83)], an estimate for  $\lambda_C$  can be obtained as the speed of the contact discontinuity in the analytic solution of the two-rarefaction Riemann solver.

As a final remark we note that although the HLLC solver has been shown to have superior performance when compared to the simpler HLLE solver, it has also been reported to suffer from the “carbuncle” phenomenon,<sup>14</sup> especially in multidimensional problems (Dumbser *et al.*, 2004; Wang *et al.*, 2008).

### The Roe solver.

Another widely used approximate Riemann solver is the one proposed by Roe (1981), that exploits the solution of the associated linearised Riemann problem. In Section 4.1.2 we have seen that a hyperbolic system expressed in conservative form can always be written in a quasi-linear form [*cf.*, Eq. (4.9)]<sup>15</sup>

$$\partial_t \mathbf{U} + \mathbf{A} \cdot \nabla \mathbf{U} = 0, \quad (9.108)$$

<sup>13</sup>The original presentation of the HLLC solver by Mignone and Bodo (2005) is intrinsically two-dimensional and thus differs slightly from the one reported here.

<sup>14</sup>The “carbuncle” phenomenon is a numerical instability that can affect the capturing of shocks and that leads to large distortions of the shock front (Pandolfi and D’Ambrosio, 2001).

<sup>15</sup>For simplicity we are here setting to zero the source terms  $\mathbf{S}$  in Eq. (4.9).

through the calculation of the Jacobian

$$\mathbf{A}(\mathbf{U}) := \frac{\partial \mathbf{F}}{\partial \mathbf{U}} . \quad (4.26)$$

The idea behind the *Roe Riemann solver* is then to compute the exact solution of a modified Riemann problem, namely the one obtained when the Jacobian matrix  $\mathbf{A}$  is replaced by a matrix of constant coefficients  $\tilde{\mathbf{A}}(\mathbf{U}_L, \mathbf{U}_R)$ . In the case of a constant Jacobian matrix, in fact, the system becomes linear, and the solution of the corresponding Riemann problem can be obtained easily [see the discussion below Eq. (9.118)]. We note that a linear system with matrix of constant coefficients  $\tilde{\mathbf{A}}$  corresponds to the following modified system in conservative form

$$\partial_t \tilde{\mathbf{U}} + \partial_x \tilde{\mathbf{F}}(\tilde{\mathbf{U}}) = 0 , \quad (9.109)$$

where the modified flux function is therefore just  $\tilde{\mathbf{F}} = \tilde{\mathbf{A}}\tilde{\mathbf{U}}$  and  $\tilde{\mathbf{U}}$  is the state vector of the modified Riemann problem. The candidate constant-coefficient matrix  $\tilde{\mathbf{A}}(\mathbf{U}_L, \mathbf{U}_R)$  must satisfy the following conditions:

1. It must be diagonalisable with a set of real eigenvalues  $\tilde{\lambda}_1, \dots, \tilde{\lambda}_N$  and a corresponding set of  $N$  linearly independent right eigenvectors  $\tilde{\mathbf{R}}^{(1)}, \dots, \tilde{\mathbf{R}}^{(N)}$ . This condition is necessary to guarantee that the modified system still remains hyperbolic.
2. It must satisfy the condition

$$\mathbf{F}_R - \mathbf{F}_L = \tilde{\mathbf{A}}(\mathbf{U}_R - \mathbf{U}_L) , \quad (9.110)$$

where  $\mathbf{F}_R = \mathbf{F}(\mathbf{U}_R)$  and  $\mathbf{F}_L = \mathbf{F}(\mathbf{U}_L)$ . As a result, if  $(\mathbf{U}_R, \mathbf{U}_L)$  satisfy the Rankine–Hugoniot conditions (9.7) for some scalar  $S$  (the propagation velocity of the discontinuity), then  $(\mathbf{U}_R - \mathbf{U}_L)$  is an eigenvector of  $\tilde{\mathbf{A}}$  with eigenvalue  $S$ . This is particularly important for the special case in which the initial states are connected by a single shock wave or a contact discontinuity. Under these conditions, in fact, the requirement (9.110) guarantees that also the approximate solution consists of a single jump.

3. It must be such that when  $\mathbf{U}_L \rightarrow \mathbf{U}_R \rightarrow \mathbf{U}$ , then  $\tilde{\mathbf{A}}(\mathbf{U}_L, \mathbf{U}_R) \rightarrow \mathbf{A}(\mathbf{U})$ , where  $\mathbf{A}$  is given by Eq. (4.26).

In practice, the computation of the constant matrix  $\tilde{\mathbf{A}}$  is normally avoided and, as we will show below, it is possible to evaluate the numerical flux directly (Roe and Pike, 1985). To do this we resort to Eq. (9.75), which we apply twice, once on the left and then on the right of the interface, to find

$$\int_{T\lambda_L}^0 \mathbf{U}(x, T) dx = -T\lambda_L \mathbf{U}_L + T(\mathbf{F}_L - \mathbf{F}_{0L}) , \quad (9.111)$$

$$\int_0^{T\lambda_R} \mathbf{U}(x, T) dx = T\lambda_R \mathbf{U}_R + T(\mathbf{F}_{0R} - \mathbf{F}_R) , \quad (9.112)$$

or, equivalently,

$$\mathbf{F}_{0L} = \mathbf{F}_L - \lambda_L \mathbf{U}_L - \frac{1}{T} \int_{T\lambda_L}^0 \mathbf{U}(x, T) dx , \quad (9.113)$$

$$\mathbf{F}_{0R} = \mathbf{F}_R - \lambda_R \mathbf{U}_R + \frac{1}{T} \int_0^{T\lambda_R} \mathbf{U}(x, T) dx, \quad (9.114)$$

where  $\mathbf{F}_{0L}$  and  $\mathbf{F}_{0R}$  are the numerical fluxes at the cell interface, say  $x_{j+1/2}$ , computed from the left or from the right side, respectively. We then repeat the volume integrals in Eqs. (9.111)–(9.112) acting on  $\tilde{\mathbf{U}}_{j+1/2}(x, t)$ , namely, on the exact solution of the modified Riemann problem, using however the same initial left and right states  $\mathbf{U}_L$  and  $\mathbf{U}_R$ . In this way we obtain that

$$\int_{T\lambda_L}^0 \tilde{\mathbf{U}}_{j+1/2}(x, T) dx = -T\lambda_L \mathbf{U}_L + T[\tilde{\mathbf{F}}_L - \tilde{\mathbf{F}}(\tilde{\mathbf{U}}_{j+1/2}(0))], \quad (9.115)$$

$$\int_0^{T\lambda_R} \tilde{\mathbf{U}}_{j+1/2}(x, T) dx = T\lambda_R \mathbf{U}_R + T[\tilde{\mathbf{F}}(\tilde{\mathbf{U}}_{j+1/2}(0)) - \tilde{\mathbf{F}}_R], \quad (9.116)$$

where  $\tilde{\mathbf{F}}_L := \tilde{\mathbf{F}}(\mathbf{U}_L)$ ,  $\tilde{\mathbf{F}}_R := \tilde{\mathbf{F}}(\mathbf{U}_R)$  and  $\tilde{\mathbf{U}}_{j+1/2}(0) := \tilde{\mathbf{U}}_{j+1/2}(x/t = 0)$ . We now approximate the integrals on the right-hand sides of Eqs. (9.113)–(9.114) with those obtained from Eqs. (9.115)–(9.116), to find

$$\mathbf{F}_{0L} = \mathbf{F}_L - \tilde{\mathbf{F}}_L + \tilde{\mathbf{F}}(\tilde{\mathbf{U}}_{j+1/2}(0)), \quad (9.117)$$

$$\mathbf{F}_{0R} = \mathbf{F}_R - \tilde{\mathbf{F}}_R + \tilde{\mathbf{F}}(\tilde{\mathbf{U}}_{j+1/2}(0)). \quad (9.118)$$

Equations (9.117)–(9.118) can be further expanded if we provide the exact solution to the Riemann problem  $\tilde{\mathbf{U}}_{j+1/2}(0)$  for the modified linear system. As commented above, the solution of the Riemann problem for systems of linear equations is readily available and we summarise it briefly as follows. First of all we expand the two states  $\mathbf{U}_L$  and  $\mathbf{U}_R$  with respect to the basis of the eigenvectors  $\tilde{\mathbf{R}}^{(1)}, \dots, \tilde{\mathbf{R}}^{(N)}$ , *i.e.*,

$$\mathbf{U}_L = \sum_{i=1}^N \tilde{\alpha}_i \tilde{\mathbf{R}}^{(i)}, \quad \mathbf{U}_R = \sum_{i=1}^N \tilde{\beta}_i \tilde{\mathbf{R}}^{(i)}, \quad (9.119)$$

where  $\tilde{\alpha}_i$  and  $\tilde{\beta}_i$  are constant coefficients. Because linear systems can be written as a set of decoupled advection equations in terms of the characteristic vector  $\tilde{\mathbf{W}}$  [*cf.* Eq. (4.42)], the solution to the  $k$ -th advection equation is given by a discontinuity in the characteristic vector propagating with the constant speed  $\tilde{\lambda}_i$ , namely

$$\tilde{W}^i(x, t) = \tilde{W}^i(x - \tilde{\lambda}_i t, 0) = \begin{cases} \tilde{\alpha}_i & \text{if } x - \tilde{\lambda}_i t < 0, \\ \tilde{\beta}_i & \text{if } x - \tilde{\lambda}_i t > 0. \end{cases} \quad (9.120)$$

For the generic point  $\mathcal{P}(x, t)$  inside the Riemann fan of the solution, there is always an eigenvalue  $\tilde{\lambda}_p$  such that  $\tilde{\lambda}_p < x/t < \tilde{\lambda}_{p+1}$ , and, combining Eq. (4.49) with Eq. (9.120), the solution of the Riemann problem can be written as a superposition of advection waves (*i.e.*, without a nonlinear wave such as a rarefaction)

$$\tilde{\mathbf{U}}(x, t) = \sum_{i=1}^p \tilde{\beta}_i \tilde{\mathbf{R}}^{(i)} + \sum_{i=p+1}^N \tilde{\alpha}_i \tilde{\mathbf{R}}^{(i)}. \quad (9.121)$$

In other words, the term  $\tilde{\mathbf{U}}_{j+1/2}(0)$  in Eqs. (9.117)–(9.118) can be written either as

$$\tilde{\mathbf{U}}_{j+1/2}(0) = \tilde{\mathbf{U}}_L + \sum_{i=1}^p (\tilde{\beta}_i - \tilde{\alpha}_i) \tilde{\mathbf{R}}^{(i)} = \tilde{\mathbf{U}}_L + \sum_{\tilde{\lambda}_i \leq 0} (\tilde{\beta}_i - \tilde{\alpha}_i) \tilde{\mathbf{R}}^{(i)}, \quad (9.122)$$

or as

$$\tilde{\mathbf{U}}_{j+1/2}(0) = \tilde{\mathbf{U}}_R - \sum_{i=p+1}^N (\tilde{\beta}_i - \tilde{\alpha}_i) \tilde{\mathbf{R}}^{(i)} = \tilde{\mathbf{U}}_R - \sum_{\tilde{\lambda}_i \geq 0} (\tilde{\beta}_i - \tilde{\alpha}_i) \tilde{\mathbf{R}}^{(i)}. \quad (9.123)$$

After substituting (9.122)–(9.123) into Eqs. (9.117)–(9.118), we obtain

$$\mathbf{F}_{0L} = \mathbf{F}_L + \sum_{\tilde{\lambda}_i \leq 0} \tilde{\omega}_i \tilde{\lambda}_i \tilde{\mathbf{R}}^{(i)}, \quad (9.124)$$

$$\mathbf{F}_{0R} = \mathbf{F}_R - \sum_{\tilde{\lambda}_i \geq 0} \tilde{\omega}_i \tilde{\lambda}_i \tilde{\mathbf{R}}^{(i)}, \quad (9.125)$$

where we have used the property that  $\tilde{\mathbf{F}} = \tilde{\mathbf{A}}\tilde{\mathbf{U}}$  and set  $\tilde{\omega}_i := \tilde{\beta}_i - \tilde{\alpha}_i$ , so that the quantities  $\tilde{\omega}_i$  represent the projection with the right eigenvectors of the jumps in the state-vector variables, *i.e.*, [*cf.*, Eqs. (9.119)]

$$\mathbf{U}_R - \mathbf{U}_L = \sum_{i=1}^N \tilde{\omega}_i \tilde{\lambda}_i \tilde{\mathbf{R}}^{(i)}. \quad (9.126)$$

Finally, after identifying both  $\mathbf{F}_{0L}$  and  $\mathbf{F}_{0R}$  with the sought Roe numerical flux, and summing them up, we obtain the *Roe flux formula*

$$\mathbf{F}^{\text{Roe}} = \frac{1}{2} \left[ \mathbf{F}_L + \mathbf{F}_R - \sum_{i=1}^N \tilde{\omega}_i \tilde{\lambda}_i \tilde{\mathbf{R}}^{(i)} \right]. \quad (9.127)$$

It is useful to emphasise that, provided an estimate of the quantities  $\tilde{\mathbf{R}}^{(i)}$ ,  $\tilde{\lambda}_i$  and  $\tilde{\omega}_i$  is available, the calculation of the Roe flux (9.127) bypasses completely the use of the matrix  $\tilde{\mathbf{A}}$ . The first implementation of the Roe solver in relativistic hydrodynamics dates back to Font *et al.* (1994) [see, *e.g.*, Eulderink and Mellema (1995), Banyuls *et al.* (1997), Font (2008)] who, for instance, adopted suitable averages of  $\tilde{\mathbf{R}}^{(i)}$ ,  $\tilde{\lambda}_i$  and  $\tilde{\omega}_i$ , starting from the analytic expressions of the known eigenvalues and eigenvectors of the original system.

### The Marquina solver

A basic disadvantage of the Roe solver is that the use of a linearised system prevents the formation of rarefaction waves and can also lead to discontinuities that violate the entropy condition (see Section 9.1.1).<sup>16</sup> An approach that seeks a remedy to this problem was suggested

<sup>16</sup>As proved by Einfeldt *et al.* (1991) for the Newtonian-hydrodynamic equations, under physical conditions approaching vacuum, a linearisation of the equations such as the one implied by Roe's Riemann solver always yields a negative density or pressure. In order to cope with this difficulty, Einfeldt *et al.* (1991) proposed a flux formula, also known as the *HLLEM flux*, which is a modification of the HLLE flux involving knowledge of the eigenvectors.

by Donat and Marquina (1996), via a flux formula that has a flux vector splitting structure (see Section 9.2) and leads to an upwind scheme. In practice, the first step in the *Marquina solver* (or *Marquina flux formula*) consists in computing the matrices of the right eigenvectors  $\mathbf{R}$  and the eigenvalues  $\lambda_i$  of the Jacobian matrix  $\partial\mathbf{F}/\partial\mathbf{U}$ , for both the left and right states of the Riemann problem. Then, in addition to the characteristic vector  $\mathbf{W}$  defined by Eq. (4.42), the vector of *characteristic fluxes* is introduced as

$$\phi := \mathbf{R}^{-1} \mathbf{F}, \quad (9.128)$$

and a choice on the flux is made according to the behaviour of each  $\lambda_i$  in the range of values of  $\mathbf{U}$  between  $\mathbf{U}_L$  and  $\mathbf{U}_R$ . Namely, if the eigenvalues  $\lambda_i(\mathbf{U}_L)$  and  $\lambda_i(\mathbf{U}_R)$  have the same sign, then

$$\phi_+^i = \phi_L^i, \quad \phi_-^i = 0, \quad \text{for } \lambda_i(\mathbf{U}_L) > 0, \quad (9.129)$$

and

$$\phi_+^i = 0, \quad \phi_-^i = \phi_R^i, \quad \text{for } \lambda_i(\mathbf{U}_L) < 0. \quad (9.130)$$

On the other hand, if the eigenvalues  $\lambda_i(\mathbf{U}_L)$  and  $\lambda_i(\mathbf{U}_R)$  do not have the same sign, then we set

$$\phi_+^i = \frac{1}{2}(\phi_L^i + \alpha_i W_L^i), \quad \phi_-^i = \frac{1}{2}(\phi_R^i - \alpha_i W_R^i), \quad (9.131)$$

where  $\alpha_i = \max |\lambda_i(\mathbf{U})|$ . The resulting Marquina flux formula is then given by

$$\mathbf{F}^{\text{Marquina}} = \sum_{i=1}^N [\phi_+^i \mathbf{R}^{(i)}(\mathbf{U}_L) + \phi_-^i \mathbf{R}^{(i)}(\mathbf{U}_R)]. \quad (9.132)$$

In the case of simple scalar equations, the flux given by Eq. (9.132) is a combination of the Roe flux and of the Lax–Friedrichs flux [*cf.* Eq. (9.19)]. Furthermore, Marquina’s flux reduces to the flux vector split formula proposed by Steger and Warming (1981) for systems of first-order quasi-linear partial differential equations with constant coefficients.

The Marquina flux formula (9.132) has been successfully adopted in many astrophysical contexts, including the simulation of relativistic jets (Martí *et al.*, 1995; Martí *et al.*, 1997), of the runaway instability in thick discs (Font and Daigne, 2002b) (see also Section 11.7.1) and in the long-term dynamics of stable and unstable fully relativistic stars (Font *et al.*, 2002; Baiotti *et al.*, 2005). Overall, the Marquina solver together with a third-order PPM reconstruction was shown by Donat *et al.* (1998) to avoid the carbuncle phenomenon and by Font *et al.* (2000) to be superior to other methods in maintaining a highly accurate angular velocity profile in relativistic rotating stars. At the same time, however, the additional computational costs associated with the calculation of the right eigenvectors (which are the same as those appearing in the Roe solver) does not make the Marquina solver (nor the Roe solver) the standard one in multidimensional numerical-relativity codes.

We conclude this section devoted to approximate Riemann solvers with an important comment. Riemann solvers that are based on the spectral decomposition of the Jacobian matrix, and therefore on knowledge of the eigenvectors as well as of the eigenvalues of the system,<sup>17</sup>

<sup>17</sup>Another very popular Riemann solver based on the spectral decomposition of the Jacobian matrix is that of Osher and Solomon (1982).

can exploit the mathematical structure of the equations. As a result, they perform generally better, providing more accurate representations of relativistic and discontinuous flows. At the same time, however, the intrinsic complexity, both mathematical and of technical implementation in multidimensional codes, can become a serious obstacle for more complicated systems of equations such as those of relativistic magnetohydrodynamics or of relativistic radiation hydrodynamics. As a result, over the last 10 years Riemann solvers that avoid the use of eigenvectors have become more and more popular in relativistic codes. For instance, Del Zanna and Bucciantini (2002) and Del Zanna *et al.* (2003) were the first to combine a third-order essentially non-oscillatory method (which we will discuss in more detail in Section 10.2) with a central Riemann solver such as HLLE. The corresponding numerical schemes is also known as the *central-upwind scheme* (Londrillo and Del Zanna, 2000; Kurganov *et al.*, 2001) and will be the focus of Section 9.6, which is dedicated to *central schemes* in general.

## 9.5 The method of lines

The reconstruction methods discussed in Section 9.3 guarantee that a prescribed order of accuracy is achieved in space. However, the need to retain a high-order accuracy also in time can complicate considerably the evolution from one time-level to the following one. A widespread strategy consists in considering the spatial and time discretisation processes as distinct. In practice, the continuum equations are first considered to be discretised in space only, while leaving the problem continuous in time. This is equivalent to transforming a set of partial differential equations (PDEs), such as (4.27), into a set of ordinary differential equations (ODEs), called the *semi-discrete equations*. The resulting system of ODEs can then be solved numerically with any stable solver. The whole approach is usually referred to as the *method of lines* and can be equally applied to finite-difference and finite-volume numerical schemes, with differences appearing if the equations do or do not contain “stiff” terms. We recall that an evolution system of partial differential equations is said to be *stiff* if the evolution proceeds over two considerably different time-scales, *i.e.*, a rapid dynamical one and a slow secular one, with the latter one posing serious restrictions on the size of the time-step (LeVeque, 1998; Solin, 2006). The prototypical stiff system of equations will therefore have the generic form

$$\partial_t \mathbf{U} = Q(\mathbf{U}) + \frac{1}{\tau} R(\mathbf{U}), \quad (9.133)$$

where  $Q(\mathbf{U})$  and  $R(\mathbf{U})$  contain spatial differential operators, and where  $\tau > 0$  is the *relaxation time*. In the limit of  $\tau \rightarrow \infty$ , the second term on the right-hand side of Eq. (9.133) vanishes and the system is then hyperbolic with a spectral radius  $c_h$  (*i.e.*, with  $c_h$  being the absolute value of the maximum eigenvalue). In the opposite limit of  $\tau \rightarrow 0$ , the first term on the right-hand side of Eq. (9.133) becomes negligible and the system then becomes stiff, since the time-scale  $\tau$  of the relaxation (or stiff) part  $R(\mathbf{U})$  is very different from the speeds  $c_h$  of the hyperbolic (or non-stiff) part  $Q(\mathbf{U})$ .

As we will discuss below, different strategies need to be employed depending on whether the system of equations is stiff or not, and we start by considering the simpler case of non-stiff systems, for which fully explicit methods are available.

### 9.5.1 Explicit Runge–Kutta methods

To illustrate first how the method of lines is used in the case of non-stiff equations, we consider a hyperbolic system of partial differential equations written in conservative form with source terms [cf., Eqs (4.27) and (9.133)]

$$\partial_t \mathbf{U} = -\partial_x \mathbf{F}(\mathbf{U}) + \mathbf{S}(\mathbf{U}) = Q(\mathbf{U}). \quad (9.134)$$

We then integrate it spatially over the cell  $I_j$ , obtaining the following ordinary differential equation

$$\begin{aligned} \frac{d\mathbf{U}_j(t)}{dt} &= \frac{1}{\Delta x} (\mathbf{F}[\mathbf{U}(x_{j-1/2}, t)] - \mathbf{F}[\mathbf{U}(x_{j+1/2}, t)]) + \mathbf{S}_j, \\ &=: \mathbf{L}(\mathbf{U}_j) + \mathbf{S}_j, \end{aligned} \quad (9.135)$$

where  $\mathbf{L}(\mathbf{U}_j)$  is the spatial differential operator and where we have introduced the spatial averages in the cell  $I_j$  of the solution and of the source term at time  $t$  [cf., Eq. (9.13)]

$$\mathbf{U}_j := \frac{1}{\Delta x} \int_{x_{j-1/2}}^{x_{j+1/2}} \mathbf{U}(x, t) dx, \quad \mathbf{S}_j := \frac{1}{\Delta x} \int_{x_{j-1/2}}^{x_{j+1/2}} \mathbf{S}(x, t) dx. \quad (9.136)$$

When comparing Eq. (9.135) with the similar one (9.15) (where of course  $\mathbf{S}_j = 0$ ), the essence of the method of lines then becomes clear. While in fact in Eq. (9.15) we have discretised both the space and the time differential operators, in Eq. (9.135) we have discretised only the first one, leaving the right-hand side as a *continuous* function of time, just as in an ODE.

The method of lines acquires the accuracy order of the time-integrator employed, provided that the discrete operator  $\mathbf{L}$  in Eq. (9.135) is of the same order in space or higher. At first order, (9.135) can be integrated through the so-called *Euler method* simply as (hereafter we will drop the index  $j$  for compactness)

$$\mathbf{U}^{n+1} = \mathbf{U}^n + \Delta t Q(\mathbf{U}^n), \quad (9.137)$$

which can be shown to be TVD, provided the time-step is restricted by a CFL condition. At higher orders, several time integrators are available, but the most popular one is the multi-step *Runge–Kutta method* (Runge, 1895; Kutta, 1901; Shu and Osher, 1988). In general, starting from time  $t = t^n$ , the method consists in the computation of a number of predictor steps, indicated as  $\mathbf{U}^{(i)}$  for the  $i$ -th substep, followed by the final update to time  $t = t^{n+1}$ , i.e.,

$$\mathbf{U}^{(i)} = \sum_{k=0}^{i-1} \left( \alpha_{ik} \mathbf{U}^{(k)} + \Delta t \beta_{ik} Q(\mathbf{U}^{(k)}) \right), \quad i = 1, \dots, n+1, \quad (9.138)$$

$$\mathbf{U}^{(0)} = \mathbf{U}^n, \quad (9.139)$$

where  $\alpha_{ik}$  and  $\beta_{ik}$  are constant coefficients. Particularly common are the second-order (*RK2*) and third-order (*RK3*) Runge–Kutta schemes, where the time update for the RK2 is given by

$$\mathbf{U}^{(1)} = \mathbf{U}^n + \Delta t Q(\mathbf{U}^n),$$

$$\mathbf{U}^{n+1} = \frac{1}{2} \left[ \mathbf{U}^n + \mathbf{U}^{(1)} + \Delta t Q(\mathbf{U}^{(1)}) \right], \quad (9.140)$$

while the update for the RK3 is given as<sup>18</sup>

$$\begin{aligned} \mathbf{U}^{(1)} &= \mathbf{U}^n + \Delta t Q(\mathbf{U}^n), \\ \mathbf{U}^{(2)} &= \frac{1}{4} \left[ 3\mathbf{U}^n + \mathbf{U}^{(1)} + \Delta t Q(\mathbf{U}^{(1)}) \right], \\ \mathbf{U}^{n+1} &= \frac{1}{3}\mathbf{U}^n + \frac{2}{3}\mathbf{U}^{(2)} + \frac{2}{3}\Delta t Q(\mathbf{U}^{(2)}). \end{aligned} \quad (9.141)$$

It is also possible to show that, under the conditions that

$$\alpha_{ik} \geq 0, \quad \beta_{ik} \geq 0, \quad \sum_{k=0}^{i-1} \alpha_{ik} = 1, \quad (9.142)$$

and the CFL constraint

$$c_{\text{CFL}} = \min_{i,k} \left( \frac{\alpha_{ik}}{\beta_{ik}} \right), \quad (9.143)$$

the Runge–Kutta methods (9.138) are TVD (Shu and Osher, 1988; Gottlieb and Shu, 1998).

For instance, both the second and the third-order Runge–Kutta schemes (9.140) and (9.141) are TVD with  $c_{\text{CFL}} = 1$ . On the contrary, there are no TVD Runge–Kutta schemes with order higher than the third that satisfy the conditions (9.142). However, when such conditions are relaxed, TVD Runge–Kutta schemes are possible even at fourth and fifth orders (Gottlieb *et al.*, 2001).

As we will comment in the following section, the algorithms above can be seen as special cases of the more general approach adopted for implicit–explicit Runge–Kutta methods.

### 9.5.2 Implicit-explicit Runge–Kutta methods

We next switch to considering the implementation of the method of lines in the case of stiff systems of equations. Numerous physical examples can be made of stiff equations, the most celebrated one being, of course, the relativistic-hydrodynamic equations of non-perfect fluids (see Chapter 6). However, stiff systems of equations appear also when solving the equations of relativistic resistive MHD (Palenzuela *et al.*, 2009; Bucciantini and Del Zanna, 2013; Dionysopoulou *et al.*, 2012), of force-free electrodynamics (Alic *et al.*, 2012b), and of relativistic radiation hydrodynamics (Roedig *et al.*, 2012).

In the following we present the *implicit-explicit (IMEX) Runge–Kutta* scheme, which has been recently shown to have great flexibility and robustness in the solution of relativistic systems of stiff equations.<sup>19</sup> The starting and crucial step in IMEX schemes is to split the conserved variables  $\mathbf{U}$  in Eq. (9.133) into two subsets  $\{\mathbf{X}, \mathbf{Y}\}$ , indicating with  $\mathbf{X}$  the *stiff*

<sup>18</sup>Note that both in (9.140) and in (9.141), the first substep  $\mathbf{U}^{(1)}$  corresponds to the *Euler method*, i.e., Eq. (9.137).

<sup>19</sup>IMEX schemes have been extensively discussed in a series of papers by Ascher *et al.* (1997) and Pareschi and Russo (2005). Traditional implicit Runge–Kutta schemes could also be used and we refer to Solin (2006) for a complete discussion about explicit and implicit Runge–Kutta schemes.

variables and with  $\mathbf{Y}$  the *non-stiff* variables.<sup>20</sup> This identification is not always obvious, especially for complicated systems of equations, but it then allows us to rewrite the system of equations (9.133) for the two subsets of variables  $\{\mathbf{X}, \mathbf{Y}\} = \mathbf{U}$  as

$$\partial_t \mathbf{Y} = Q_{\mathbf{Y}}(\mathbf{X}, \mathbf{Y}), \quad (9.144)$$

$$\partial_t \mathbf{X} = Q_{\mathbf{X}}(\mathbf{X}, \mathbf{Y}) + R_{\mathbf{X}}(\mathbf{X}, \mathbf{Y}). \quad (9.145)$$

The operator  $Q_{\mathbf{Y}}$  contains both the first-order spatial derivatives of  $\mathbf{Y}$  and the non-stiff source terms. The operator  $Q_{\mathbf{X}}$  contains instead both the first-order spatial derivatives of  $\mathbf{X}$  and the non-stiff source terms. Finally, the operator  $R_{\mathbf{X}}$  contains the stiff source terms affecting the variables  $\mathbf{X}$ . In this way, each Runge–Kutta substep of the IMEX scheme can be divided into two parts:

1. In the first part, the explicit intermediate values  $\{\mathbf{X}_*^{(i)}, \mathbf{Y}_*^{(i)}\}$  of each substep  $i$  are computed as

$$\mathbf{Y}_*^{(i)} = \mathbf{Y}^n + \Delta t \sum_{j=1}^{i-1} \tilde{a}_{ij} Q_{\mathbf{Y}}[\mathbf{U}^{(j)}], \quad (9.146)$$

$$\mathbf{X}_*^{(i)} = \mathbf{X}^n + \Delta t \sum_{j=1}^{i-1} \tilde{a}_{ij} Q_{\mathbf{X}}[\mathbf{U}^{(j)}] + \Delta t \sum_{j=1}^{i-1} a_{ij} R_{\mathbf{X}}[\mathbf{U}^{(j)}], \quad (9.147)$$

where it is crucial that the summation stops at  $(i - 1)$  to avoid the appearance of the implicit terms at this stage. The matrices with coefficients  $\tilde{a}_{ij}$  and  $a_{ij}$  are  $N_{\text{IMEX}} \times N_{\text{IMEX}}$  square matrices whose dimensions and values of the coefficients depend on the choice made for the accuracy of the scheme and on the number of the substeps taken (Pareschi and Russo, 2005).

2. In the second part, the non-stiff variables are directly promoted to the status of Runge–Kutta substep variables, namely

$$\mathbf{Y}^{(i)} = \mathbf{Y}_*^{(i)}. \quad (9.148)$$

The stiff variables, on the other hand, need to be corrected as

$$\begin{aligned} \mathbf{X}^{(i)} &= \mathbf{X}_*^{(i)} + a_{ii} \Delta t R_{\mathbf{X}}(\mathbf{X}^{(i)}, \mathbf{Y}_*^{(i)}), \\ &= \mathbf{X}_*^{(i)} + a_{ii} \Delta t \left[ \mathbf{A}(\mathbf{Y}_*^{(i)}) \mathbf{X}^{(i)} + \mathbf{K}_{\mathbf{X}}(\mathbf{Y}_*^{(i)}) \right], \end{aligned} \quad (9.149)$$

where the operator  $R_{\mathbf{X}}(\mathbf{X}, \mathbf{Y})$  has been decomposed as

$$R_{\mathbf{X}}(\mathbf{X}, \mathbf{Y}) = \mathbf{A}(\mathbf{Y}) \mathbf{X} + \mathbf{K}_{\mathbf{X}}(\mathbf{Y}), \quad (9.150)$$

so that the vector  $\mathbf{K}_{\mathbf{X}}(\mathbf{Y})$  does not depend on the stiff variables  $\mathbf{X}$ . Using now Eq. (9.149), it follows that

$$\mathbf{X}^{(i)} = \mathbf{M}(\mathbf{Y}_*^{(i)}) \left[ \mathbf{X}_*^{(i)} + a_{ii} \Delta t \mathbf{K}_{\mathbf{X}}(\mathbf{Y}_*^{(i)}) \right], \quad (9.151)$$

where the matrix  $\mathbf{M}$  is given by

$$\mathbf{M}(\mathbf{Y}_*) = [\mathbf{I} - a_{ii} \Delta t \mathbf{A}(\mathbf{Y}_*)]^{-1}, \quad (9.152)$$

and  $\mathbf{I}$  is the identity matrix.

<sup>20</sup>For compactness of notation we include the relaxation time-scale  $\tau$  in the definition of the stiff term  $R(\mathbf{U})$ .

For each Runge–Kutta substep, the two subsets of state vectors  $\{\mathbf{X}^{(i)}, \mathbf{Y}^{(i)}\}$  are computed as described above, after which the final time-update is performed as

$$\mathbf{U}^{n+1} = \mathbf{U}^n + \Delta t \sum_{i=1}^{N_{\text{IMEX}}} \tilde{w}_i F(\mathbf{U}^{(i)}) + \Delta t \sum_{i=1}^{N_{\text{IMEX}}} w_i R(\mathbf{U}^{(i)}), \quad (9.153)$$

where  $w_i$  and  $\tilde{w}_i$  are vectors with constant coefficients. A *strong stability preserving (SSP)* version<sup>21</sup> of the IMEX Runge–Kutta scheme is often implemented, for which the notation SSPk( $s, \sigma, p$ ) is adopted to specify the order of the SSP scheme (*i.e.*,  $k$ ), the number of stages of the implicit scheme (*i.e.*,  $s$ ), the number of stages of the explicit scheme (*i.e.*,  $\sigma$ ), and the order of the IMEX scheme (*i.e.*,  $p$ ) (Pareschi and Russo, 2005). Both explicit and implicit Runge–Kutta schemes can be written economically in terms of the *Butcher tableau* as [see, *e.g.*, Butcher (2008) for details]

$$\begin{array}{c|cccc} c_i & a_{ij} \\ \hline & (w_i)^T \end{array} \quad (9.154)$$

where the index  $T$  denotes transposition.<sup>22</sup> As an example, the explicit Butcher tableau of the SSP3(4,3,3) method is

$$\begin{array}{c|cccc} 0 & 0 & 0 & 0 & 0 \\ 0 & 0 & 0 & 0 & 0 \\ 1 & 0 & 1 & 0 & 0 \\ \hline 1/2 & 0 & 1/4 & 1/4 & 0 \\ \hline & 0 & 1/6 & 1/6 & 2/3 \end{array} \quad (9.155)$$

while the corresponding implicit Butcher tableau is

$$\begin{array}{c|cccc} q_1 & q_1 & 0 & 0 & 0 \\ 0 & -q_1 & q_1 & 0 & 0 \\ 1 & 0 & 1-q_1 & q_1 & 0 \\ \hline 1/2 & q_2 & q_3 & 1/2-q_1-q_2-q_3 & q_1 \\ \hline & 0 & 1/6 & 1/6 & 2/3 \end{array} \quad (9.156)$$

with

$$\begin{aligned} q_1 &:= 0.24169426078821, & q_2 &:= 0.06042356519705, \\ q_3 &:= 0.12915286960590. \end{aligned} \quad (9.157)$$

If we limit our attention to the explicit part of the algorithm, we note that the intermediate Runge–Kutta substeps of SSP3(4,3,3) are [*cf.*, Eq. (9.155)]

$$\mathbf{U}^{(1)} = \mathbf{U}^n, \quad (9.158)$$

<sup>21</sup>A *strong stability preserving (SSP)* scheme extends the TVD property to a general norm, not necessarily the one-norm (8.8) used in Eq. (9.35) (Gottlieb *et al.*, 2001).

<sup>22</sup>Note that the vectors of coefficients  $c_i$  and  $\tilde{c}_i$ , which are defined as  $c_i := \sum_{j=1}^s a_{ij}$  and  $\tilde{c}_i := \sum_{j=1}^s \tilde{a}_{ij}$ , are not used in the practical implementation of the IMEX scheme, while they are adopted in traditional implicit Runge–Kutta schemes [see, *e.g.*, Solin (2006)].

$$\mathbf{U}^{(2)} = \mathbf{U}^n, \quad (9.159)$$

$$\mathbf{U}^{(3)} = \mathbf{U}^n + \Delta t Q(\mathbf{U}^{(1)}), \quad (9.160)$$

$$\mathbf{U}^{(4)} = \mathbf{U}^n + \Delta t \left[ \frac{1}{4} Q(\mathbf{U}^{(2)}) + \frac{1}{4} Q(\mathbf{U}^{(3)}) \right], \quad (9.161)$$

$$\mathbf{U}^{n+1} = \mathbf{U}^n + \Delta t \left[ \frac{1}{6} Q(\mathbf{U}^{(2)}) + \frac{1}{6} Q(\mathbf{U}^{(3)}) + \frac{2}{3} Q(\mathbf{U}^{(4)}) \right], \quad (9.162)$$

From the substep (9.161) we then find that

$$\frac{1}{6} \Delta t Q(\mathbf{U}^{(3)}) = \frac{2}{3} \mathbf{U}^{(4)} - \frac{2}{3} \mathbf{U}^n - \frac{1}{6} \Delta t Q(\mathbf{U}^{(2)}), \quad (9.163)$$

and, after renaming  $\mathbf{U}^{(3)} \rightarrow \mathbf{U}^{(1)}$ , and  $\mathbf{U}^{(4)} \rightarrow \mathbf{U}^{(2)}$ , we can substitute it in the final substep (9.162) to obtain

$$\mathbf{U}^{n+1} = \frac{1}{3} \mathbf{U}^n + \frac{2}{3} \mathbf{U}^{(2)} + \frac{2}{3} \Delta t Q(\mathbf{U}^{(2)}), \quad (9.141)$$

which coincides with the well-known RK3 scheme encountered in Section 9.5.2. In other words, the general IMEX scheme presented above reduces to the standard explicit Runge–Kutta scheme when acting on the non-stiff part of the equations.

We conclude this section with an important remark. Runge–Kutta schemes, either explicit or implicit, become inefficient for orders of accuracy larger than four. This is due to the fact that the number of substeps starts growing faster than the accuracy of the scheme; this effect is known as the *Butcher barrier* (Butcher, 1987). Mainly for this reason, over the years numerical methods have been developed that avoid the Runge–Kutta time-stepping but preserve the high order of the scheme and are able to handle stiff source terms<sup>23</sup>. These methods will be discussed in the next chapter.

## 9.6 Central numerical schemes

Numerical schemes that sacrifice the upwind property while preserving the conservative form of the scheme, and therefore yielding the correct propagation speeds of all nonlinear waves appearing in the solution, are called *central schemes*.

This alternative class of methods has been developed in parallel with upwind HRSC schemes [see, *e.g.*, Roe (1981), Nessyahu and Tadmor (1990), Kurganov and Tadmor (2000)], and, broadly speaking, is based either on the Lax–Wendroff second-order scheme with additional dissipative terms, or on non-oscillatory high-order extensions of the Lax–Friedrichs first-order central scheme. As a result, this class of methods avoids altogether the use of Riemann solvers, either exact or approximate, while maintaining HRSC properties.

<sup>23</sup>See however Spiteri and Ruuth (2002) for an alternative class of optimal high-order SSP and low-storage SSP Runge–Kutta schemes with  $s > p$ .

### 9.6.1 Staggered central schemes

Central schemes can be introduced by rewriting the discretisation of the conservative equation (9.1) on a spatial control volume centred in  $x_{j+1/2}$  rather than  $x_j$  and with extremal points given by  $x_j$  and  $x_{j+1}$ , namely [*cf.*, Eq. (9.15)]

$$\mathbf{U}_{j+1/2}^{n+1} = \mathbf{U}_{j+1/2}^n - \frac{1}{\Delta x} \left[ \int_{t^n}^{t^{n+1}} \mathbf{F}[\mathbf{U}(x_{j+1}, t)] dt - \int_{t^n}^{t^{n+1}} \mathbf{F}[\mathbf{U}(x_j, t)] dt \right], \quad (9.164)$$

where a *staggered (volume) average* of the state vector is introduced, *i.e.*,

$$\mathbf{U}_{j+1/2}^n := \frac{1}{\Delta x} \int_{x_j}^{x_{j+1}} \mathbf{U}(x, t^n) dx. \quad (9.165)$$

Since at time-level  $t^n$  the solution consists of an approximation of  $\mathbf{U}(x, t^n)$  over a grid centred at  $x_j$ , the integral in the staggered average must be split as

$$\mathbf{U}_{j+1/2}^n := \frac{1}{\Delta x} \left[ \int_{x_j}^{x_{j+1/2}} \mathbf{p}_j^n(x) dx + \int_{x_{j+1/2}}^{x_{j+1}} \mathbf{p}_{j+1}^n(x) dx \right], \quad (9.166)$$

where  $\mathbf{p}_j^n(x)$  is a polynomial approximation to  $\mathbf{U}(x, t^n)$  at time  $t^n$ . A schematic representation of staggered averages in a central scheme is shown in Fig. 9.8, where the darker shading indicates the new volume averages  $\mathbf{U}_{j-1/2}^n$  and  $\mathbf{U}_{j+1/2}^n$  centred around  $x_{j-1/2}$  and  $x_{j+1/2}$ , respectively.

As remarked already, the key point of central schemes is that the computation of the numerical fluxes in Eq. (9.164) does not require the solution of a Riemann problem. In fact, provided the CFL condition is met, the mid-cell values  $\mathbf{U}(x_j, t)$  remain free of discontinuities, and the numerical fluxes involve only smooth “half-cell” integrals that can be solved with any quadrature rule to the desired accuracy. Let us for example assume that the numerical fluxes in (9.164) are computed through a second-order midpoint quadrature rule, *i.e.*,

$$\int_{t^n}^{t^{n+1}} \mathbf{F}[\mathbf{U}(x_j, t)] dt \simeq \Delta t \mathbf{F}[\mathbf{U}(x_j, t^{n+1/2})], \quad (9.167)$$

where  $\mathbf{U}(x_j, t^{n+1/2})$  is obtained with a simple Taylor expansion

$$\begin{aligned} \mathbf{U}_j^{n+1/2} &= \mathbf{U}(x_j, t^{n+1/2}) = \mathbf{U}(x_j, t^n) + \frac{\Delta t}{2} \partial_t \mathbf{U}(x_j, t^n) \\ &= \mathbf{U}(x_j, t^n) - \frac{\Delta t}{2} \partial_x \mathbf{F}[\mathbf{U}(x_j, t^n)]. \end{aligned} \quad (9.168)$$

Truncating now (9.168) to the first-order term, *i.e.*,  $\mathbf{U}_j^{n+1/2} = \mathbf{U}(x_j, t^n)$ , and choosing the polynomial  $\mathbf{p}_j^n(x)$  to be just the piecewise constant average over the cell, so that (9.166) becomes

$$\mathbf{U}_{j+1/2}^n = \frac{1}{2} (\mathbf{U}_j^n + \mathbf{U}_{j+1}^n), \quad (9.169)$$

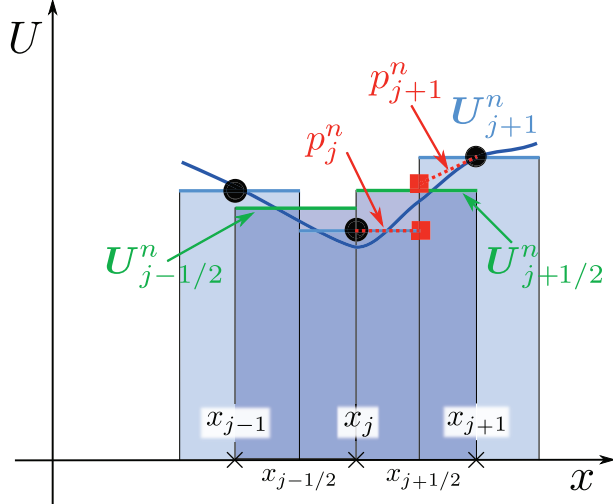


**Fig. 9.8** Schematic representation of staggered averages in a central scheme. Indicated with a darker shading are the volume averages  $\mathbf{U}_{j-1/2}^n$  and  $\mathbf{U}_{j+1/2}^n$  centred around  $x_{j-1/2}$  and  $x_{j+1/2}$ . Also indicated with red dashed lines are the reconstructions  $p_j^n(x)$  and  $p_{j+1}^n(x)$  in the two half-cells around  $x_{j+1/2}$ . Note that the solution is no longer discontinuous at the interface  $x_j$ , so that no Riemann problem needs to be solved there (*cf.* Fig. 9.1).

Eq. (9.164) then reduces to

$$\mathbf{U}_{j+1/2}^{n+1} = \frac{1}{2}(\mathbf{U}_j^n + \mathbf{U}_{j+1}^n) - \frac{\Delta t}{\Delta x} [\mathbf{F}(\mathbf{U}_{j+1}^n) - \mathbf{F}(\mathbf{U}_j^n)]. \quad (9.170)$$

The scheme just derived represents the simplest example of a central scheme over staggered grids. Note that the two sets of cells, the original and the staggered ones, alternate every other time-step. Namely, the centred averages  $\{\mathbf{U}_j^n\}$  are first used to obtain the staggered averages  $\{\mathbf{U}_{j+1/2}^{n+1}\}$  at the new time-level  $n + 1$ . Next,  $\{\mathbf{U}_{j+1/2}^{n+1}\}$  are used again in Eq. (9.170) to compute  $\{\mathbf{U}_j^{n+2}\}$  at  $n + 2$ , and the process repeats. We also note that, after replacing  $\mathbf{F} = \lambda \mathbf{U}$  in Eq. (9.170) and letting  $j + 1/2 \rightarrow j$ ,  $j \rightarrow j - 1$ ,  $\Delta x \rightarrow 2\Delta x$ , we obtain the first-order Lax–Friedrichs scheme described in Section 8.3.4 and given by Eq. (8.69) for the scalar advection equation. Hence the Lax–Friedrichs scheme can be viewed as the prototype of central schemes. Nessyahu and Tadmor (1990) were the first to introduce a second-order version of central schemes by taking a piecewise linear representation for the interpolating polynomial, namely  $p_j^n(x) = \mathbf{U}_j^n + \sigma_j^n(x - x_j)$ , where  $\sigma_j^n$  is the slope of the linear reconstruction inside the cell (see Section 9.3.1 and the red dashed lines in Fig. 9.8). The corresponding staggered average is given by

$$\mathbf{U}_{j+1/2}^n = \frac{1}{2}(\mathbf{U}_j^n + \mathbf{U}_{j+1}^n) + \frac{\Delta x}{8}(\sigma_j^n - \sigma_{j+1}^n). \quad (9.171)$$

Moreover, after substituting (9.171) into (9.164) with  $\mathbf{U}_{j+1/2}^n$  now retaining also the first-order term as on the right-hand side of (9.168), we obtain the second-order *Nessyahu–Tadmor*

central scheme

$$\mathbf{U}_{j+1/2}^{n+1} = \frac{1}{2}(\mathbf{U}_j^n + \mathbf{U}_{j+1}^n) + \frac{\Delta x}{8}(\boldsymbol{\sigma}_j^n - \boldsymbol{\sigma}_{j+1}^n) - \frac{\Delta t}{\Delta x} [\mathbf{F}(\mathbf{U}_{j+1}^{n+1/2}) - \mathbf{F}(\mathbf{U}_j^{n+1/2})], \quad (9.172)$$

where again the flux terms are computed using the Taylor expansion (9.168).

### 9.6.2 Non-staggered central schemes

A substantial drawback of staggered central schemes is that one is obliged to alternate between two staggered grids throughout the time evolution, with particular problems which inevitably arise at the border of the computational domain. To overcome these difficulties, Jiang *et al.* (1998) proposed a non-staggered version of central schemes. Moreover, Kurganov and Tadmor (2000) presented a class of non-staggered central schemes in semi-discrete form, suitable for integration through Runge–Kutta methods, which has become very popular over the years. As in the staggered version, no Jacobians and characteristic decompositions are needed, whereas it is sufficient to compute the local speed of propagation at cell interfaces, namely  $a_{j\pm 1/2}^n$ , which is again provided by the knowledge of the eigenvalues. After obtaining the boundary-extrapolated values  $\mathbf{U}_j^+$  and  $\mathbf{U}_{j+1}^-$  [cf., Eq. (9.52)] from a Taylor expansion as<sup>24</sup>

$$\mathbf{U}_j^+ = \mathbf{U}_j + \frac{\Delta x}{2}(\partial_x \mathbf{U})_j, \quad \mathbf{U}_{j+1}^- = \mathbf{U}_{j+1} - \frac{\Delta x}{2}(\partial_x \mathbf{U})_{j+1}, \quad (9.173)$$

where  $(\partial_x \mathbf{U})_j$  and  $(\partial_x \mathbf{U})_{j+1}$  are numerical approximations to the exact spatial derivatives, it is possible to write the central scheme in semi-discrete form as [see, e.g., Kurganov and Tadmor (2000) for details]

$$\begin{aligned} \frac{d\mathbf{U}_j}{dt} = & -\frac{1}{2\Delta x} [(\mathbf{F}(\mathbf{U}_{j+1}^-) + \mathbf{F}(\mathbf{U}_j^+)) - (\mathbf{F}(\mathbf{U}_j^-) + \mathbf{F}(\mathbf{U}_{j-1}^+))] \\ & + \frac{1}{2\Delta x} [a_{j+1/2} (\mathbf{U}_{j+1}^- - \mathbf{U}_j^+) - a_{j-1/2} (\mathbf{U}_j^- - \mathbf{U}_{j-1}^+)]. \end{aligned} \quad (9.174)$$

The discretisation provided by Eq. (9.174) can be written as a conservative numerical scheme (see Section 9.1.2), namely as

$$\frac{d\mathbf{U}_j}{dt} = \frac{1}{\Delta x} (\mathbf{F}_{j-1/2} - \mathbf{F}_{j+1/2}), \quad (9.175)$$

with a numerical flux function given by

$$\mathbf{F}_{j+1/2} = \frac{1}{2} [\mathbf{F}(\mathbf{U}_j^+) + \mathbf{F}(\mathbf{U}_{j+1}^-)] - \frac{1}{2} a_{j+1/2} (\mathbf{U}_{j+1}^- - \mathbf{U}_j^+). \quad (9.176)$$

The above formula is sometimes referred to as *Tadmor's flux formula*, it provides second-order accuracy in space, and can be successfully implemented in combination with any Runge–Kutta time update. After replacing  $\mathbf{U}_j^+ \rightarrow \mathbf{U}_L$  and  $\mathbf{U}_{j+1}^- \rightarrow \mathbf{U}_R$ , the flux formula (9.176),

<sup>24</sup>Note that  $\mathbf{U}_j^+$  and  $\mathbf{U}_{j+1}^-$  provide an approximation to  $\mathbf{U}$  at  $x = x_{j+1/2}$ , while  $\mathbf{U}_j^-$  and  $\mathbf{U}_j^+$  of Eq. (9.52) refer to values computed in two different locations.

reduces to the Rusanov flux formula (9.84), provided that  $a_{j+1/2}$  is identified with the maximum of the eigenvalues. This property clarifies that even limited information about the characteristic structure of the equations, such as that given by knowledge of the eigenvalues, is sufficient to provide a certain degree of the upwind property in central schemes. A central scheme that tries to recover the upwind property, of which (9.84) and (9.176) can be regarded as prototypes, is also known as a *central-upwind scheme*.

The considerable advantage of not requiring the costly solution of Riemann solvers has made central schemes very popular over the years, especially as simulations of relativistic astrophysics scenarios employ more and more complex systems of equations. Progress has been made both in increasing the accuracy, so that central schemes with orders higher than the second are now available (Liu and Tadmor, 1998; Jiang *et al.*, 1998; Arminjon and St-Cyr, 2003), and in extending them to unstructured grids (Toro *et al.*, 2009). The typical results obtained in the solution of the Newtonian hydrodynamic equations show a quality comparable to that of upwind HRSC schemes, at the expense of a small loss of sharpness at discontinuities (Toro, 2009; Kurganov and Tadmor, 2000). Relevant applications to relativistic hydrodynamics were considered by Del Zanna and Bucciantini (2002), Lucas-Serrano *et al.* (2004) and Shibata and Font (2005), where it was concluded that algorithms based on central schemes yield results of comparable accuracy, but at a smaller computational cost.

## 9.7 Further reading

- Font, J. A. (2008). Numerical Hydrodynamics and Magnetohydrodynamics in General Relativity. *Living Rev. Relativ.*, **11**, 7.
- LeVeque, R. J. (1992). *Numerical Methods for Conservation Laws*. Birkhauser, Basel.
- LeVeque, R. J. (2002). *Finite Volume Methods for Hyperbolic Problems*. Cambridge University Press. Cambridge, UK.
- LeVeque, R. J. (2007). *Finite Difference Methods for Ordinary and Partial Differential Equations*. SIAM, Philadelphia.
- Martí, J. M. and Müller, E. (2003). Numerical Hydrodynamics in Special Relativity. *Living Rev. Relativ.*, **6**, 7.
- Toro, E. (2009). *Riemann Solvers and Numerical Methods for Fluid Dynamics*. Springer, Berlin.
- Trangenstein, J. A. (2009). *Numerical Solution of Hyperbolic Partial Differential Equations*. Cambridge University Press, Cambridge.

## 9.8 Problems

1. Apply (9.20) and (9.21) to the scalar advection equation

$$\partial_t u + \lambda \partial_x u = 0,$$

to obtain the Lax–Wendroff scheme (8.79).

2. Show that in the case of the linear advection equation an evolution in which the new solution is expressed as

$$\mathbf{U}_j^{n+1} = \sum_{k=-K_L}^{k=K_R} c_k \mathbf{U}_{j+k}^n, \quad (9.177)$$

is monotone if and only if all the coefficients are  $c_k \geq 0$ . As a result, prove that the Lax–Friedrichs scheme is monotone, while the Lax–Wendroff scheme is not.

3. Starting from the conservative equations (9.1) and using the control volume defined as  $V := [-\Gamma, \Gamma] \times [0, T]$ , where  $\Gamma > \max(|\lambda_L|, |\lambda_R|)T$  and  $T$  is a representative time, obtain the HLLE flux (9.80).
4. Starting from the Rankine–Hugoniot equations (9.100)–(9.101) obtain the expressions (9.104)–(9.106) that describe the properties of the state  $\mathbf{U}_{L_*}$  in the HLLC approximate Riemann solver. Compute also the corresponding quantities for the state  $\mathbf{U}_{R_*}$  and finally the numerical fluxes (9.107).
5. Implement a numerical code that solves the following system of stiff linear ordinary differential equations

$$\begin{aligned} \frac{dy_1}{dt} &= -y_1(t), \\ \frac{dy_2}{dt} &= -100y_2(t), \end{aligned}$$

with initial conditions given by

$$\begin{aligned} y_1(0) &= 1, \\ y_2(0) &= 1. \end{aligned}$$

Show that the solution of this problem fails when the explicit RK2 scheme (9.140) is adopted, while it can be obtained with the implicit SSP2(2,2,2) scheme, which has explicit and implicit Butcher tableaux given by

$$\begin{array}{c|cc} 0 & 0 & 0 \\ 1 & 1 & 0 \\ \hline & 1/2 & 1/2 \end{array} \quad \begin{array}{c|cc} g & g & 0 \\ 1-g & 1-2g & g \\ \hline & 1/2 & 1/2 \end{array} \quad (9.178)$$

with  $g = 1 - 1/\sqrt{2}$ .

6. Implement a numerical code that solves the special-relativistic hydrodynamic equations (7.231) in one spatial dimension and in Cartesian coordinates. [Hint: use as reference the flow chart reported in Appendix E.3.]

# 10

## Numerical Relativistic Hydrodynamics: High-Order Methods

---

This chapter is devoted to the presentation of *high-order methods*, whereby we refer to those numerical methods with order of accuracy that is three or higher, both in time and in space (see Section 8.2 for the definition of the order of accuracy).

When discussing high-order methods a pivotal role is played by Godunov's theorem, stating that a numerical scheme of order larger than the first must be nonlinear, namely must depend on the solution itself, in order to avoid the appearance of numerical oscillations typical of linear methods (see Section 9.2.2). In most of the schemes that we will present in this chapter, the nonlinearity is introduced through reconstruction techniques that depend on the solution itself, just like it was done for the TVD limiters discussed in Section 9.3. The development of high-order numerical methods is a vast and very active area of research that we will not be able to cover in great detail here. Rather, in what follows we will provide a brief overview of those high-order methods for hyperbolic conservation laws that are commonly employed in numerical simulations and have made them the most promising tool for studying very complex flow structures. These include *essentially non-oscillatory methods (ENO)*, *weighted essentially non-oscillatory methods (WENO)*, *discontinuous Galerkin methods (DG)*, and *arbitrary high-order methods using derivatives (ADER)*.

### 10.1 Why high-order numerical methods?

A first question that arises naturally is: why bother with higher-order methods? After all, in the previous two chapters we have discussed many of the properties of second-order methods and seen that with such methods the error in the solution can be made as small as desired, provided that a sufficiently fine resolution is available. Furthermore, in the presence of a discontinuity in the solution (a very likely event in relativistic hydrodynamics), all methods deteriorate to being only first-order accurate near the discontinuity.

When considered more closely, however, it is easy to realise that there is a flaw in this logic. In reality, in fact, the large majority of numerical calculations are limited by the computational power available and, more specifically, by the available memory. Under these constraints, it is clearly advantageous to employ those numerical methods that provide the smallest truncation error for the largest discretisation and thus for the smallest use of the memory. However, also the logic of “the higher the order, the better”, has its shortcomings. As we

will see in this chapter, the use of high-order methods inevitably implies the use of numerical methods that are increasingly complex and memory intensive, thus more difficult to handle, especially on massively parallel supercomputing facilities. As a result, a subtle compromise between the order of the method and the complexity of its implementation needs in general to be found. It is under these constraints that the advantages of a high-order method over a second-order one become evident, as shown through specific examples by Shu (2003). The advantages of a high-order method become even more evident when using *adaptive mesh-refinement (AMR) techniques*, since for essentially the same computational costs of a low-order scheme, the truncation error decreases very rapidly in the regions at high resolution, where the accuracy needs to be particularly large.<sup>1</sup>

The considerations made above also make it clear that high-order methods are the only choice for those problems characterised by a wide range of length-scales. A classical example is that of *turbulent flows*, namely of those flows with chaotic velocity fluctuations superimposed on a main velocity field. This can happen, for instance, when the *Reynolds number* is above a critical value, thus triggering the instabilities that lead to *turbulence*.<sup>2</sup> Fluid turbulence is ubiquitous in nature, manifesting itself from the Earth's atmosphere over to the largest cosmological scales (Brandenburg and Nordlund, 2011). Because of the existence of a wide range of length-scales that need to be accounted for, the numerical modelling of a phenomenon like turbulence represents a formidable task, which, in spite of the progress in computational resources and techniques, still suffers from serious limitations and is essentially unexplored in relativistic regimes (Radice and Rezzolla, 2013; Zrake and MacFadyen, 2013).

## 10.2 ENO and WENO methods for hyperbolic conservation laws

When implementing a numerical scheme of order higher than the second, the TVD condition based on slope-limiter reconstructions and discussed in Section 9.3.1 turns out to be too restrictive. It produces excessive numerical dissipation in regions of smooth flow and reduces the order of accuracy to first-order near local extrema. These restrictions have led to looser criteria that allow for a small increase of the total variation near extremal points while suppressing oscillations when required. *Essentially non-oscillatory* (ENO) and *weighted essentially non-oscillatory* (WENO) methods have been devised precisely to meet these criteria.

Both ENO and WENO methods use the idea of adaptive stencils when performing the reconstruction of the numerical solution to achieve high-order accuracy and the non-oscillatory property near discontinuities. However, while the ENO method uses just one out of many candidate stencils for the reconstruction and in particular the “smoother” one, the WENO method uses a special combination of all the candidate stencils, with each being assigned a nonlinear weight depending on the local smoothness of the numerical solution on that stencil. The weights are then adjusted by the local smoothness of the solution, so that essentially zero weights are given to non-smooth stencils while optimal weights are prescribed in smooth

<sup>1</sup>The combination of high-order methods and AMR techniques is a very modern field of research, and interesting results have been obtained by Mignone *et al.* (2012) and Dumbser *et al.* (2012).

<sup>2</sup>We recall that the *Reynolds number*,  $Re$ , is defined as the dimensionless ratio  $Re := vL/\nu$ , where  $v$ ,  $L$  and  $\nu$  are the typical flow velocity, the length-scale of the problem and the kinematic viscosity, respectively (see Sections 6.2 and 11.8.3).

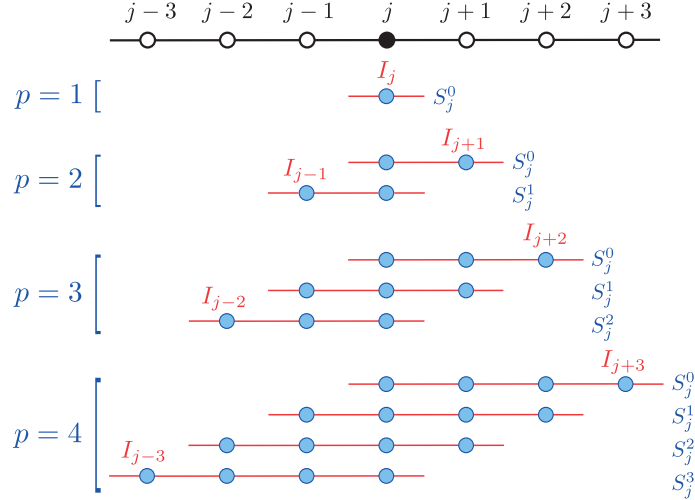


**Fig. 10.1** Schematic representation for the admissible stencils  $S_j^l$  around the gridpoint  $j$  and for different values of the polynomial order  $p - 1$ , where  $p = l + r + 1$  is the total number of cells in each stencil, while  $l$  and  $r$  are the number of cells to the left and to the right of  $j$ . Indicated with red are also the corresponding intervals  $I_i := [x_{i-1/2}, x_{i+1/2}]$  with  $i \in [j-l, j+r]$ .

regions. ENO and WENO methods have been developed both for finite-difference and for finite-volume methods, generating families of different numerical schemes that we will discuss separately below [see also Barth and Deconinck (1999)].

### 10.2.1 Finite-volume ENO schemes

A basic problem needs to be faced when adopting a high-order finite-volume numerical scheme. In general, the scheme will evolve the cell averages of the conserved quantities in time, but the computation of the fluxes requires the pointwise values of the solution at the interfaces between adjacent cells. Hence, a procedure is needed to reconstruct the pointwise values of the solution starting from the cell averages  $U_j^n$ .

The solution to this problem comes by defining a stencil  $S_j^l$  relative to the cell  $j$  for which the reconstruction needs to be performed. In the one-dimensional case, the stencil is just given by the union of the intervals, *i.e.*,

$$S_j^l := \bigcup_{i=j-l}^{j+r} I_i, \quad I_i := [x_{i-1/2}, x_{i+1/2}], \quad (10.1)$$

with  $l$  cells to the left of  $j$ ,  $r$  cells to the right of  $j$  and a total number of  $p = l + r + 1 \geq 1$  cells for each stencil. The admissible stencils  $S_j^l$  are shown schematically in Fig. 10.1

As a result, we search the polynomial  $P_l(x)$ , of degree  $p - 1$ , whose cell average in each of the cells  $I_i$  of the stencil  $S_j^l$  coincides with  $U_i^n$ , *i.e.*,

$$\mathbf{U}_i^n := \frac{1}{\Delta x} \int_{x_{i-1/2}}^{x_{i+1/2}} \mathbf{P}_l(\xi) d\xi, \quad \forall I_i \in S_j^l, \quad (10.2)$$

and such that it provides a  $p$ -th order accurate approximation to the true solution  $\mathbf{U}(x)$  at the cell boundaries, *i.e.*,

$$\mathbf{P}_l(x_{j\pm 1/2}) = \mathbf{U}(x_{j\pm 1/2}) + \mathcal{O}(\Delta x^p). \quad (10.3)$$

The interpolation procedure can in principle resort to any interpolation technique, but in practice there are two different *finite-volume ENO schemes* that are most commonly used and discussed below.

#### **Pointwise reconstruction at cell interfaces.**

As described by Shu (1997), a  $p$ -th order reconstruction of the solution at pointwise values can be obtained after performing a Lagrange interpolation of the primitive of the polynomial  $\mathbf{P}_l(x)$ . This idea is the same as the one expressed by Eqs. (9.56)–(9.58) in the context of the PPM (see Section 9.3.2). Unlike the logic behind the PPM method, however, no modifications are imposed on the reconstructed polynomials to keep them monotone. Following this strategy, it is possible to write the pointwise values of the solution at cell interfaces in terms of the cell averages as

$$\mathbf{U}_{j+1/2}^n = \sum_{i=0}^{p-1} c_{li} \mathbf{U}_{j-l+i}^n, \quad (10.4)$$

where  $c_{li}$  are constant coefficients that for a uniform grid are given by

$$c_{li} := \sum_{m=i+1}^p \frac{\sum_{k=0, k \neq m}^p \Pi_{q=0, q \neq m, k}^p (l - q + 1)}{\Pi_{k=0, k \neq m}^p (m - k)}. \quad (10.5)$$

To fix ideas, we report in Table 10.1 a few of the coefficients  $c_{li}$  for  $p$  up to 5. For example, when  $p = 3$ , the following stencils with corresponding reconstructed polynomials of degree 2 and approximations of order  $\mathcal{O}(\Delta x^3)$  can be built

$$S_j^0 = \{j, j+1, j+2\}, \quad \mathbf{U}_{j+1/2}^n = \frac{1}{3} \mathbf{U}_j^n + \frac{5}{6} \mathbf{U}_{j+1}^n - \frac{1}{6} \mathbf{U}_{j+2}^n, \quad (10.6)$$

$$S_j^1 = \{j-1, j, j+1\}, \quad \mathbf{U}_{j+1/2}^n = -\frac{1}{6} \mathbf{U}_{j-1}^n + \frac{5}{6} \mathbf{U}_j^n + \frac{1}{3} \mathbf{U}_{j+1}^n, \quad (10.7)$$

$$S_j^2 = \{j-2, j-1, j\}, \quad \mathbf{U}_{j+1/2}^n = \frac{1}{3} \mathbf{U}_{j-2}^n - \frac{7}{6} \mathbf{U}_{j-1}^n + \frac{11}{6} \mathbf{U}_j^n. \quad (10.8)$$

Note that, according to this procedure, the number of stencils considered is the same as the order of accuracy  $p$  of the scheme.

#### **Entire-polynomial reconstruction.**

Following a more modern approach, first proposed by Harten *et al.* (1987) and recently extended by Dumbser and Käser (2007) and Tsoutsanis *et al.* (2011) to the multidimensional case and also to unstructured grids, it is possible to reconstruct the required  $(p-1)$ -th degree

**Table 10.1** Coefficients  $c_{li}$  for a uniform grid, as given by Eq. (10.5) for a few values of  $p$ , which expresses both the order of accuracy of the reconstruction and the number of cells in each stencil. The degree of the reconstructed polynomial is  $p - 1$ , while  $l$  is the number of cells to the left of the reference element  $j$ .

$p$	$l$	$i = 0$	$i = 1$	$i = 2$	$i = 3$	$i = 4$
1	0	1				
2	0	1/2	1/2			
	1	-1/2	3/2			
3	0	1/3	5/6	-1/6		
	1	-1/6	5/6	1/3		
	2	1/3	-7/6	11/6		
4	0	1/4	13/12	-5/12	1/12	
	1	-1/12	7/12	7/12	-1/12	
	2	1/12	-5/12	13/12	1/4	
	3	-1/4	13/12	-23/12	25/12	
5	0	1/5	77/60	-43/60	17/60	-1/20
	1	-1/20	9/20	47/60	-13/60	1/30
	2	1/30	-13/60	47/60	9/20	-1/20
	3	-1/20	17/60	-43/60	77/60	1/5
	4	1/5	-21/20	137/60	-163/60	137/60

polynomial within the element  $I_j$  in terms of an expansion with respect to a basis of polynomials. In order to introduce this procedure, and because of its relevance in the rest of the chapter, let us first select a family of diffeomorphisms  $\varphi_i$  such that  $I_i = \varphi_i(\mathcal{E})$ , where  $\mathcal{E}$  is the so-called *reference element* (see also Section 7.3.6). In practice, in the one-dimensional case  $\mathcal{E}$  is just an interval,<sup>3</sup> e.g.,  $\mathcal{E} = [0, 1]$ , spanned by the local coordinate  $\xi \in \mathcal{E}$  and such that

$$x = x_{j-1/2} + \xi \Delta x, \quad 0 \leq \xi \leq 1. \quad (10.9)$$

As a result, the standard one-dimensional nonlinear conservation equation

$$\partial_t \mathbf{U} + \partial_x \mathbf{F}(\mathbf{U}) = 0, \quad (9.1)$$

can be rewritten as

$$\partial_t \mathbf{U} + \partial_\xi \mathbf{F}^*(\mathbf{U}) = 0, \quad (10.10)$$

with  $\mathbf{F}^* := (\partial_x \xi) \mathbf{F}(\mathbf{U}) = \mathbf{F}(\mathbf{U}) / \Delta x$ .

With this change of variables, the reconstruction of  $\mathbf{U}$  for each available stencil is obtained through the expansion

$$\mathbf{U}_{j,l}(\xi, t^n) = \sum_{k=0}^{p-1} \Psi_k(\xi) \hat{\mathbf{U}}_{k,l}(t^n), \quad l = 1, \dots, N_{\text{st}}, \quad (10.11)$$

<sup>3</sup>The reference element must have the same dimensions as the spatial ones in the problem, e.g., it will be a surface in two dimensions (e.g., a square or a triangle) and a volume in three dimensions (e.g., a cube or a tetrahedron).

where the index  $j$  still refers to the element  $I_j$  for which the reconstruction is performed, while  $N_{\text{st}}$  indicates the number of stencils considered. The functions  $\Psi_k(\xi)$  represent a basis of polynomials, which can either be a *nodal basis* (which we will introduce in Section 10.3.2) or a *modal basis*. In the latter case, which is the one we consider here,  $\Psi_k(\xi)$  is given by a set of  $p$  linearly independent polynomials, with degree from zero to the maximum one, *i.e.*,  $p - 1$ . The  $p$  coefficients  $\hat{\mathbf{U}}_{k,l}(t^n)$  of the expansion are often referred to as the “*degrees of freedom*” (or “*spectral coefficients*”). In practice, the polynomials  $\Psi_k(\xi)$  can be chosen among the orthogonal *Legendre polynomials* (Quarteroni and Valli, 1997), which, rescaled on the reference element  $\mathcal{E} = [0, 1]$ , are referred to as the *shifted Legendre polynomials* and are given by

$$\begin{aligned}\Psi_0(\xi) &= 1, \\ \Psi_1(\xi) &= 2\xi - 1, \\ \Psi_2(\xi) &= 6\xi^2 - 6\xi + 1, \\ \Psi_3(\xi) &= 20\xi^3 - 30\xi^2 + 12\xi - 1, \\ \Psi_4(\xi) &= 70\xi^4 - 140\xi^3 + 90\xi^2 - 20\xi + 1, \\ \Psi_5(\xi) &= 252\xi^5 - 630\xi^4 + 560\xi^3 - 210\xi^2 + 30\xi - 1, \\ &\vdots\end{aligned}\tag{10.12}$$

A few of them are reported for illustration in Fig. 10.2 (see also Fig. 10.3 for the corresponding polynomials in a modal basis).

Once again, the requirement expressed by Eq. (10.2) still holds, *i.e.*,  $\mathbf{U}_{j,l}(\xi, t^n)$  must return the average  $\mathbf{U}_i^n$  when integrated over each element of the stencil.<sup>4</sup> Of course, there are as many integrals to compute as the elements of the stencil and the condition (10.2) generates a linear system

$$\sum_{k=0}^{p-1} A_{ik} \hat{\mathbf{U}}_{k,l}(t^n) = \mathbf{U}_i^n, \quad \forall I_i \in S_j^l, \tag{10.13}$$

in the unknown coefficients  $\hat{\mathbf{U}}_{k,l}(t^n)$ , where

$$A_{ik} := \int_0^1 \Psi_k(\xi) d\xi, \quad \forall I_i \in S_j^l. \tag{10.14}$$

The system (10.13) can finally be solved with any linear solver to provide the full representation (10.11). The optimal situation for the solution of the system (10.13) is represented by the case in which there are as many cells in each stencil as the number  $p$  of the unknown degrees of freedom.<sup>5</sup>

<sup>4</sup>The reconstruction (10.11) is valid for the single interval  $I_j$ , while we require the integral conservation (10.2) for each interval  $I_i$  of the stencil  $S_j^l$  relative to  $I_j$ .

<sup>5</sup>In the case of unstructured grids, a number of cells in the stencil larger than  $p$  improves the robustness of the scheme (Barth and Frederickson, 1990; Kaeser and Iske, 2005).

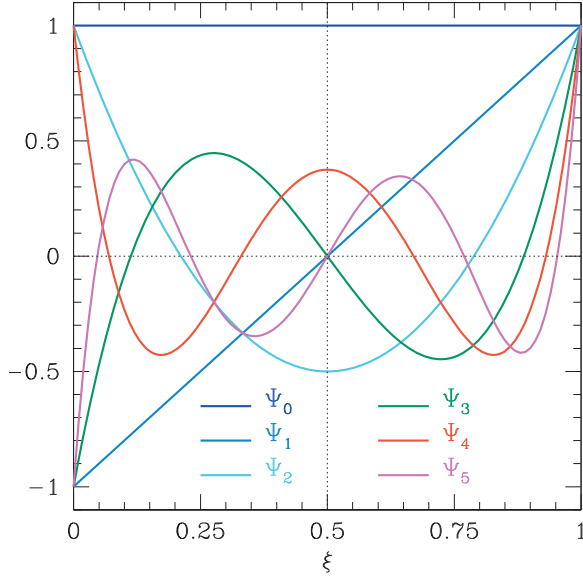


**Fig. 10.2** Functional behaviour of the first six shifted Legendre polynomials of a modal basis as given by expressions (10.12) (*cf.* Fig. 10.3 for the corresponding polynomials in a modal basis).

#### Choice of the “smoothest” stencil.

Once a polynomial has been reconstructed for each considered stencil, ENO’s philosophy is that of selecting among them the stencil that avoids any discontinuity, thus adopting the “smoothest” one. To perform this selection, an *oscillation indicator*  $\mathcal{OI}_l$  on the  $l$ -th candidate stencil is required, and a few of them are available as we list below.

1. For uniform grids, it is convenient to use the notion of *undivided differences*  $\Xi[\cdot, \cdot]$ , defined recursively as (Jiang and Shu, 1996)

$$\Xi[j, 0] := \Xi_j, \quad (10.15)$$

$$\Xi[j, l] := \Xi[j + 1, l - 1] - \Xi[j, l - 1]. \quad (10.16)$$

The undivided difference is then used to build the oscillation indicator of the  $l$ -th stencil as

$$\mathcal{OI}_l := \sum_{k=1}^{p-1} \sum_{i=1}^{p-k} \frac{(\mathbf{P}[j + l + i - p, k])^2}{p - k}, \quad (10.17)$$

where  $\mathbf{P}[j, 0]$  is the average of the reconstructed polynomial over the cell  $j$ , and hence  $\mathbf{U}_j^n$ .

2. For general grids and when entire reconstructed polynomials have been computed over the original  $x$ -grid, it is possible to adopt an oscillation indicator which is explicitly based on derivatives, *i.e.*, (Jiang and Shu, 1996)

$$\mathcal{OI}_l := \sum_{i=1}^{p-1} \int_{x_{j-1/2}}^{x_{j+1/2}} \left( \frac{d^i \mathbf{P}_l(x)}{dx^i} \right)^2 \Delta x^{2i-1} dx, \quad l = 0, \dots, p-1. \quad (10.18)$$

3. Again for general grids, and when entire reconstructed polynomials have been computed over the reference  $\xi$ -grid [cf., Eq. (10.11)], another oscillation indicator is adopted typically (Dumbser and Kaeser, 2007)

$$\mathcal{OI}_l := \sum_{k=1}^{p-1} \sum_{m=1}^{p-1} \sigma_{km} \hat{\mathbf{U}}_{k,l}(t^n) \hat{\mathbf{U}}_{m,l}(t^n), \quad (10.19)$$

where  $\sigma_{km}$  is the *oscillation indicator matrix* and is given by

$$\sigma_{km} = \sum_{i=1}^{p-1} \int_0^1 \frac{d^i \psi_k(\xi)}{d\xi^i} \frac{d^i \psi_m(\xi)}{d\xi^i} d\xi. \quad (10.20)$$

This last oscillation indicator has a significant advantage over (10.18), since it does not depend on the grid spacing, which instead enters (10.18) through the term  $\Delta x^{2i-1}$ .

Finally, once a measure of  $\mathcal{OI}_l$  is available, it is possible to select the “smoother” stencil as the polynomial  $\mathbf{P}_l(x)$ , among the available ones, which has the least value of  $\mathcal{OI}_l$ . This step is called ENO’s “*adaptivity strategy*”. It is exactly ENO’s adaptivity strategy, namely, the choice of a reconstruction stencil that depends on the solution itself, that introduces in the numerical scheme the nonlinearity necessary to bypass the limitations imposed by Godunov’s theorem on linear schemes (see Section 9.2.1).

### 10.2.2 Finite-volume WENO schemes

The idea behind the ENO method of using the smoothest stencil among the several candidates for performing the reconstruction is very good near discontinuities, since it completely excludes the information coming from stencils across which the function is discontinuous. Alternatively, however, one can assign a weight,  $\omega_l$ , to each candidate stencil  $S_j^l$  and use them to provide an approximation that is given by the combination of all the ENO reconstructions. In this way, by exploiting the information contained in the set of all the ENO polynomials, one can also expect to obtain an even more accurate approximation. This is the basic idea behind the WENO method. Also in this case, two different *finite-volume WENO schemes* are possible for the reconstruction, which we will illustrate below.

#### **Pointwise “optimal” WENO reconstruction.**

Having considered  $p$  candidate stencils, each providing the approximation (10.4), the WENO reconstruction combines them as a new approximation to the cell boundary value, which is then expressed as (Shu, 1997)

$$\mathbf{U}_{j+1/2}^n = \sum_{l=0}^{p-1} \omega_l \mathbf{U}_{j+1/2,l}^n, \quad (10.21)$$

where each term  $\mathbf{U}_{j+1/2,l}^n$ , computed through (10.4), has acquired the index  $l$  to stress that it refers to the specific stencil  $S_j^l$ . The choice of the weights is understandably crucial and is

**Table 10.2** Coefficients  $\lambda_l$ , with  $0 \leq l \leq p - 1$  in the optimal WENO reconstruction (10.21). The degree of the reconstructed polynomial is  $p - 1$ .

$p$	$l = 0$	$l = 1$	$l = 2$
1	1		
2	1/3	2/3	
3	1/10	3/5	3/10

done according to a number of criteria. First of all, for stability and consistency it is required that

$$\omega_l \geq 0, \quad \sum_{l=0}^{p-1} \omega_l = 1. \quad (10.22)$$

Second, if the function to be reconstructed is smooth in all the candidate stencils, which altogether contain  $(2p - 1)$  cells, then there are constants  $\lambda_l$  such that

$$\mathbf{U}_{j+1/2}^n = \sum_{l=0}^{p-1} \lambda_l \mathbf{U}_{j+1/2,l}^n = \mathbf{U}^n(x_{j+1/2}) + \mathcal{O}(\Delta x^{2p-1}), \quad (10.23)$$

with

$$\omega_l = \lambda_l + \mathcal{O}(\Delta x^{p-1}), \quad l = 0, \dots, p - 1. \quad (10.24)$$

On the other hand, if the solution has a discontinuity in one of the stencils, we then want to mimic the logic behind the ENO method and assign to the corresponding stencil a weight that is close to zero. Shu (1997) proposed the following choice for the coefficients  $\omega_l$ , which has remained essentially unaltered over the years, *i.e.*,

$$\omega_l = \frac{\tilde{\omega}_l}{\sum_{s=0}^{p-1} \tilde{\omega}_s}, \quad \tilde{\omega}_l = \frac{\lambda_l}{(\mathcal{OI}_l + \varepsilon)^2}, \quad (10.25)$$

where  $\varepsilon > 0$  is a small number introduced to avoid potential divisions by zero,<sup>6</sup>  $\mathcal{OI}_l$  is the oscillation indicator of the corresponding stencil, so that a large value of  $\mathcal{OI}_l$ , in combination with the exponent 2, has the net effect of making the WENO scheme behave very closely to the single-stencil ENO scheme.

The coefficients  $\lambda_l$  for a few representative values of  $p$  are reported in Table 10.2. At least formally, the pointwise WENO reconstruction is accurate at the  $(2p - 1)$ -th order in smooth regions of the solution [*cf.* Eq. (10.23)], thus considerably more accurate than the ENO reconstruction that is only  $p$ -th order accurate [*cf.* Eq. (10.3)]. Because of this, the original pointwise version of WENO just presented is often referred to as the “optimal” WENO.<sup>7</sup>

<sup>6</sup>See also Henrick *et al.* (2005) for an alternative approach which does not need to introduce  $\varepsilon$ .

<sup>7</sup>High-order monotonicity-preserving WENO methods have been developed by Balsara and Shu (2000).

### **Entire-polynomial WENO reconstruction.**

In the alternative entire-polynomial WENO reconstruction, the number of stencils considered,  $N_{\text{st}}$ , is not forced to be  $p$ , where  $p - 1$ , we recall, is the degree of the ENO reconstructed polynomial, and is actually typically less than that. A practical example will help us illustrate the strategy of this scheme. Let us assume, for simplicity, that the ENO entire-polynomial reconstruction (10.11) has been performed over three stencils, *i.e.*, an entirely left-sided stencil, a central stencil and an entirely right-sided stencil, providing the terms  $\mathbf{U}_{j,1}(\xi, t^n)$ ,  $\mathbf{U}_{j,2}(\xi, t^n)$  and  $\mathbf{U}_{j,3}(\xi, t^n)$ , respectively. The final non-oscillatory reconstructed polynomial within the element  $I_j$  is obtained as

$$\mathbf{U}_j(\xi, t^n) = \sum_{k=0}^{p-1} \Psi_k(\xi) \hat{\mathbf{U}}_k(t^n), \quad (10.26)$$

where the degrees of freedom  $\hat{\mathbf{U}}_k(t^n)$  result from a combination of the degrees of freedom for each stencil, *i.e.*,

$$\hat{\mathbf{U}}_k(t^n) = \omega_1 \hat{\mathbf{U}}_{k,1}(t^n) + \omega_2 \hat{\mathbf{U}}_{k,2}(t^n) + \omega_3 \hat{\mathbf{U}}_{k,3}(t^n). \quad (10.27)$$

The single nonlinear weights for each stencil, on the other hand, are computed according to similar arguments as for the optimal WENO reconstruction and are given by

$$\omega_l = \frac{\tilde{\omega}_l}{\tilde{\omega}_1 + \tilde{\omega}_2 + \tilde{\omega}_3}, \quad \tilde{\omega}_l = \frac{\tilde{\lambda}_l}{(\mathcal{OI}_l + \varepsilon)^q}, \quad l = 1, 2, 3, \quad (10.28)$$

where the oscillation indicator  $\mathcal{OI}_l$  is given by (10.19). Note that the linear weights  $\tilde{\lambda}_l$  are not the same as those of the optimal WENO reported in Table 10.2 and they can be chosen according to a more pragmatic approach. In particular, the weight  $\tilde{\lambda}_2$  of the central stencil is usually given a very large value, *e.g.*,  $\tilde{\lambda}_2 = 10^5$ , while  $\tilde{\lambda}_1$  and  $\tilde{\lambda}_3$  are set to 1. In addition, it has been shown that the numerical results are substantially independent of the two parameters  $\varepsilon$  and  $q$  (Liu *et al.*, 1994). As is apparent from Eq. (10.26), the accuracy of the entire-polynomial WENO reconstruction is determined by the maximum degree of the polynomial basis functions, *i.e.*, is  $p$ -th order accurate for polynomials up to the  $(p - 1)$ -th degree. Additional details about this implementation of WENO can be found in Friedrich (1996) and in Dumbser *et al.* (2008b).

An important final remark is that, by removing the conditional statements inherent in the ENO stencil choosing step, WENO schemes are computationally less expensive than ENO schemes and they are practically always preferred to the latter.

### **10.2.3 Finite-difference ENO schemes**

In analogy with what was discussed in Section 10.2.1 for finite-volume methods, a similar problem needs to be solved also when using finite-difference high-order schemes. Given the

pointwise values of the flux function,  $\mathbf{F}_j := \mathbf{F}(x_j)$ , in fact, it is necessary to provide a numerical flux function  $\hat{\mathbf{F}}_{j+1/2}$  such that the flux difference approximates the derivative  $\partial_x \mathbf{F}(x)$  to  $p$ -th order of accuracy (see Section 9.1.3), *i.e.*,

$$\frac{1}{\Delta x} (\hat{\mathbf{F}}_{j+1/2} - \hat{\mathbf{F}}_{j-1/2}) = \partial_x \mathbf{F}(x_j) + \mathcal{O}(\Delta x^p). \quad (9.27)$$

As we discuss below, there are two main *finite-difference ENO schemes* for obtaining such a high-order representation of the numerical fluxes at cell interfaces and which reflect the possibility of including or not including the solution of the Riemann problem.

### **Flux reconstruction.**

The first strategy consists in applying the ENO reconstruction operator directly to the flux function  $\mathbf{F}(x_j)$ . As already discussed in Section 9.1.3, this is possible because the pointwise values of  $\mathbf{F}$  are the cell averages of another function, *i.e.*,  $h(t)$  in Eq. (9.24). As a result, it is possible to perform the reconstruction from cell averages to pointwise values according to the standard ENO reconstruction, namely, by rewriting Eq. (10.4) as

$$\hat{\mathbf{F}}_{j+1/2} = \sum_{i=0}^{p-1} c_{li} \mathbf{F}_{j-l+i}, \quad (10.29)$$

where  $c_{li}$  are the same coefficients reported in Table 10.1. Such a reconstruction is repeated for each candidate stencil  $S_j^l$  defined by (10.1), and is then followed by the usual choice of the smoothest stencil based on a suitable oscillation indicator.

Clearly, no Riemann problem has been solved in this procedure, and consequently the resulting numerical scheme would lose the upwind property if no additional modifications are made. To avoid this drawback and preserve the upwind property,  $\mathbf{F}$  is split into a right-going and a left-going component, *i.e.*,

$$\mathbf{F} = \mathbf{F}^+ + \mathbf{F}^-, \quad (10.30)$$

where the corresponding Jacobian matrices  $\mathbf{A}^+ := \partial \mathbf{F}^+ / \partial \mathbf{U}$  and  $\mathbf{A}^- := \partial \mathbf{F}^- / \partial \mathbf{U}$  contain just the positive and negative eigenvalues (see Section 9.2).

In practice, the procedure outlined above is often combined with the information obtained from characteristic reconstruction, and can be applied through the following steps:

- An average state  $\bar{\mathbf{U}}_{j+1/2}$  between adjacent cells is computed, often with a simple arithmetic mean, *i.e.*,

$$\bar{\mathbf{U}}_{j+1/2} = \frac{1}{2} (\mathbf{U}_j + \mathbf{U}_{j+1}), \quad (10.31)$$

though more elaborate averages are also possible (Roe, 1981).

- Using the Jacobian matrix computed at the average state, *i.e.*,

$$\mathbf{A} = \left. \frac{\partial \mathbf{F}}{\partial \mathbf{U}} \right|_{\bar{\mathbf{U}}_{j+1/2}}, \quad (10.32)$$

its characteristic structure (the eigenvalues as well as the left and right eigenvectors) is computed, yielding

$$\bar{\mathbf{\Lambda}} = \mathbf{\Lambda}(\bar{\mathbf{U}}_{j+1/2}), \quad \bar{\mathbf{R}} = \mathbf{R}(\bar{\mathbf{U}}_{j+1/2}), \quad \bar{\mathbf{R}}^{-1} = \mathbf{R}^{-1}(\bar{\mathbf{U}}_{j+1/2}), \quad (10.33)$$

where  $\Lambda$  and  $R$  are the matrices of the eigenvalues and of the right eigenvectors, respectively.

- The characteristic fields related to the fluxes are defined as

$$\mathbf{Q}_j = \bar{\mathbf{R}}^{-1} \mathbf{F}(\mathbf{U}_j), \quad (10.34)$$

and a flux splitting of the kind of (10.30) is made on the transformed  $\mathbf{Q}$  rather than on  $\mathbf{F}$ .

- The ENO reconstruction is performed according to (10.29), so as to obtain  $\hat{\mathbf{Q}}_{j+1/2}^+$  and  $\hat{\mathbf{Q}}_{j+1/2}^-$ , which are then transformed back to find

$$\hat{\mathbf{F}}_{j+1/2}^\pm = \bar{\mathbf{R}} \hat{\mathbf{Q}}_{j+1/2}^\pm. \quad (10.35)$$

- Finally, it is possible to combine the two components to have

$$\hat{\mathbf{F}}_{j+1/2} = \hat{\mathbf{F}}_{j+1/2}^+ + \hat{\mathbf{F}}_{j+1/2}^-. \quad (10.36)$$

Further information and possible variants of this approach can be found in Shu (1997), and, more recently, in Zhang and MacFadyen (2006) and in Radice and Rezzolla (2012), who adopted it in the study of relativistic turbulent flows.

### Primitive variable reconstruction.

The second strategy for obtaining a high-order representation of the numerical flux function  $\hat{\mathbf{F}}_{j+1/2}$  is instead based on an interpolation of the *primitive (or conserved) variables* from pointwise values to pointwise values. Note that this strategy requires the solution of a Riemann problem.

In practice, from a stencil  $S_j^l$  relative to  $x_j$  and composed of  $p$  cells, the Lagrangian interpolation formula can be used to provide the polynomial approximation

$$\mathbf{P}_l(x) = \sum_{i=1}^p a_i \mathbf{V}_i, \quad (10.37)$$

where

$$a_i := \prod_{k=1, k \neq i}^p \frac{x - x_k}{x_i - x_k}. \quad (10.38)$$

Note that by construction  $\mathbf{P}_l(x_i) = \mathbf{V}_i := \mathbf{V}(x_i)$  and that, for convenience, we are considered to be working with the vector of primitive variables  $\mathbf{V}$ . The interpolation (10.37) is repeated for each candidate stencil  $S_j^l$ , followed by the standard ENO selection according to the smoothest oscillation indicator. This procedure ultimately provides the values of  $\mathbf{V}$  at the cell interfaces  $x_{j \pm 1/2}$ , after which the standard Riemann problem is solved, thus obtaining a sequence of values  $\mathbf{F}_{j \pm 1/2}$ . Such values, however, must be corrected in order to preserve the high-order accuracy of the scheme. We can do this by starting from a centred finite-difference approximation of the first derivative of the flux, which we write as

$$\begin{aligned} (\Delta x) \partial_x \mathbf{F}(x_j) &\approx \hat{\mathbf{F}}_{j+1/2} - \hat{\mathbf{F}}_{j-1/2} \\ &= a(\mathbf{F}_{j+1/2} - \mathbf{F}_{j-1/2}) + b(\mathbf{F}_{j+3/2} - \mathbf{F}_{j-3/2}) \\ &\quad + c(\mathbf{F}_{j+5/2} - \mathbf{F}_{j-5/2}) + \mathcal{O}(\Delta x^6), \end{aligned} \quad (10.39)$$

where we have truncated the approximation at the sixth order. The constant coefficients providing the finite-difference approximation of the derivatives of a generic function at  $x_j$  using the values at  $x_{j\pm 1/2}, x_{j\pm 3/2}, x_{j\pm 5/2}, \dots$  can be found in Table 2 of Fornberg (1988) (see also Section 8.3.7 for the equivalent coefficients at the cell centres), where they are tabulated up to the eighth order. We therefore know that at second order, namely with  $p = 2$ , the coefficients are:  $a = 1, b = c = 0$ ; similarly, at fourth order, namely with  $p = 4$ , they are:  $a = 9/8, b = -1/24, c = 0$ ; finally, at sixth order, namely with  $p = 6$ , they are:  $a = 75/64, b = -25/384, c = 3/640$ .

The next step is to write  $\hat{\mathbf{F}}_{j+1/2}$  as

$$\hat{\mathbf{F}}_{j+1/2} = d_0 \mathbf{F}_{j+1/2} + d_2 (\mathbf{F}_{j-1/2} + \mathbf{F}_{j+3/2}) + d_4 (\mathbf{F}_{j-3/2} + \mathbf{F}_{j+5/2}), \quad (10.40)$$

so that a comparison with Eq. (10.39) provides the relations

$$d_0 = a + b + c, \quad d_2 = b + c, \quad d_4 = c, \quad (10.41)$$

from which it follows that

$$\begin{aligned} d_0 &= 1, & d_2 &= 0, & d_4 &= 0, & \text{for } p = 2, \\ d_0 &= 13/12, & d_2 &= -1/24, & d_4 &= 0, & \text{for } p = 4, \\ d_0 &= 1067/960, & d_2 &= -29/480, & d_4 &= 3/640, & \text{for } p = 6. \end{aligned} \quad (10.42)$$

As a result, no extra high-order corrections on numerical fluxes are needed for schemes up to second order, for which  $\hat{\mathbf{F}}_{j+1/2} = \mathbf{F}_{j+1/2}$ . This conclusion can be reached also after rewriting Eq. (10.40) in the form

$$\hat{\mathbf{F}}_{j+1/2} = \mathbf{F}_{j+1/2} - \frac{1}{24} \Delta^{(2)} \mathbf{F}_{j+1/2} + \frac{3}{640} \Delta^{(4)} \mathbf{F}_{j+1/2}, \quad (10.43)$$

where  $\Delta^{(2)}$  and  $\Delta^{(4)}$  are, respectively, the second and fourth-order numerical derivatives defined as

$$\Delta^{(2)} \mathbf{F}_{j+1/2} := \mathbf{F}_{j-1/2} - 2\mathbf{F}_{j+1/2} + \mathbf{F}_{j+3/2}, \quad (10.44)$$

$$\begin{aligned} \Delta^{(4)} \mathbf{F}_{j+1/2} &:= \Delta^{(2)} \mathbf{F}_{j-1/2} - 2\Delta^{(2)} \mathbf{F}_{j+1/2} + \Delta^{(2)} \mathbf{F}_{j+3/2} \\ &= \mathbf{F}_{j-3/2} - 4\mathbf{F}_{j-1/2} + 6\mathbf{F}_{j+1/2} - 4\mathbf{F}_{j+3/2} + \mathbf{F}_{j+5/2}. \end{aligned} \quad (10.45)$$

Note that for  $p = 2$  only the first term in Eq. (10.43) is retained, while the second one is introduced for  $p = 4$ , and the complete expression is used for  $p = 6$ .

We should also stress that we have used here only derivative operators based on centred, symmetric stencils because we have assumed  $p$  to be an even number. However, the polynomial interpolation through Eq. (10.37) might have been performed, equivalently, with an odd value of  $p$ . Therefore, the correction through Eq. (10.43) with  $p = 4$  must be applied in the case of an ENO reconstruction of order three or four, while the correction with  $p = 6$  must be applied in case of an ENO reconstruction of order five or six, and so on.

Additional details about this procedure can be found in Del Zanna and Bucciantini (2002) and Del Zanna *et al.* (2007), where it was applied to equations of relativistic hydrodynamics and magnetohydrodynamics.

#### 10.2.4 Finite-difference WENO schemes

The *finite-difference WENO schemes* follow the same line of argument discussed for the ENO schemes. In particular, the same distinction between the two strategies illustrated in Section 10.2.3 still holds, and in both cases, the WENO philosophy assigns a weight to each candidate stencil. More specifically, for the first strategy, that is, the one based on a reconstruction from cell-averages to pointwise values, Eq. (10.21) is applied directly to the fluxes (Jiang and Shu, 1996; Shu, 2003), *i.e.*,

$$\hat{\mathbf{F}}_{j+1/2} = \sum_{k=0}^{p-1} \omega_k \mathbf{F}_{j+1/2,k}, \quad (10.46)$$

with optimal weights  $\omega_k$  that are the same as those computed in Section 10.2.2. On the other hand, for the second strategy, that is, the one based on a reconstruction from pointwise values to pointwise values, the weighting process is applied to the primitive variables, *i.e.*,

$$\mathbf{V}_{j+1/2}^n = \sum_{k=0}^{p-1} \bar{\omega}_k \mathbf{V}_{j+1/2,k}^n, \quad (10.47)$$

with optimal weights  $\bar{\omega}_k$  that are different from the weights  $\omega_k$  of Eq. (10.46) [see, *e.g.*, Londrillo and Del Zanna (2000) for an example].

### 10.3 Discontinuous Galerkin methods

Broadly speaking, *discontinuous Galerkin (DG) methods* can be considered as numerical methods for the *weak formulation* of the equations. They were first applied to first-order equations by Reed and Hill (1973), but their widespread use followed from the application to hyperbolic problems by Cockburn and collaborators in a series of articles (Cockburn and Shu, 1989; Cockburn *et al.*, 1990; Cockburn, 1998). In these works, the typical DG discretisation in space was combined with a stable high-order Runge–Kutta discretisation in time to solve nonlinear time-dependent conservation laws. Over the years, these methods have become increasingly popular in the solution of the hydrodynamics and magnetohydrodynamics equations, and in Section 7.3.6 we have already presented the DG formulation of the general-relativistic hydrodynamic equations, which can also be cast in a 3+1 representation. In the following we will first briefly review the basic idea behind DG schemes and then take advantage of our discussion in Section 7.3.6 to illustrate more extensively the specific case of DG schemes for relativistic hydrodynamics.

#### 10.3.1 The essence of DG methods

For simplicity, let us consider the standard nonlinear conservation equation in one dimension and without source terms, *i.e.*,

$$\partial_t \mathbf{U} + \partial_x \mathbf{F}(\mathbf{U}) = 0. \quad (9.1)$$

The one-dimensional computational domain  $I$  is partitioned into the union of a number of intervals  $I_j$ , i.e.,  $I = \bigcup_j I_j$ , with  $I_j := [x_{j-1/2}, x_{j+1/2}]$ ,<sup>8</sup> so that Eq. (9.1) can now be rewritten on the spatial reference element  $\mathcal{E} = [0, 1]$  as

$$\partial_t \mathbf{U} + \partial_\xi \mathbf{F}^*(\mathbf{U}) = 0. \quad (10.10)$$

In the DG approach, the  $p$ -th order accurate solution approximating  $\mathbf{U}$  can be expanded over a polynomial basis as

$$\mathbf{U}_j(\xi, t) = \sum_{k=0}^{p-1} \hat{\mathbf{U}}_k(t) \Psi_k(\xi), \quad (10.48)$$

where the basis functions  $\Psi_k$  contain the spatial dependence only and belong to a finite functional space  $V_h$ , while the coefficients  $\hat{\mathbf{U}}_k(t)$  contain the temporal dependence only and are again called the *degrees of freedom*. A weak formulation of Eq. (10.10) is now obtained after multiplying it by a test function<sup>9</sup>  $\Psi_l \in V_h$ , and then integrating over the reference element  $\mathcal{E}$ , to obtain

$$\int_0^1 (\Psi_l \partial_t \mathbf{U} + \Psi_l \partial_\xi \mathbf{F}^*) d\xi = 0. \quad (10.49)$$

Integration by parts in space then gives

$$\int_0^1 \Psi_l \partial_t \mathbf{U} d\xi + \left[ \Psi_l \mathbf{F}^* \right]_0^1 - \int_0^1 \mathbf{F}^* d_\xi \Psi_l d\xi = 0, \quad (10.50)$$

where the representation in terms of the test functions  $\Psi_l$ , which usually have jumps at the edges of the reference element  $\mathcal{E}$ , is ultimately responsible for jumps in the solution itself and explain why the method is qualified as “*discontinuous*”. Substituting (10.48) into (10.50) yields the expression

$$\sum_{k=0}^{p-1} \left( \int_0^1 \Psi_l \Psi_k d\xi \right) d_t \hat{\mathbf{U}}_k + \left[ \Psi_l \mathbf{F}^* \right]_0^1 - \int_0^1 \mathbf{F}^* (\mathbf{U}(\xi, t)) d_\xi \Psi_l d\xi = 0, \quad (10.51)$$

which represents a system of (coupled) ordinary differential equations in time for the degrees of freedom  $\hat{\mathbf{U}}_l(t)$ . The advantage of this procedure is that the basis functions  $\Psi_l$  are known analytically, so that also their derivatives,  $d_\xi \Psi_l$ , are also known analytically. As a result, the integral in the first term in (10.51) is analytic and needs to be calculated only once. As an example, let us consider the case of a fourth-order representation, namely with  $p = 3$ , of the function  $\mathbf{U}(\xi, t)$  with respect to the modal basis of orthogonal Legendre polynomials already introduced in Section 10.2.1, [cf., Eqs. (10.12)] i.e.,

$$\mathbf{U}(\xi, t) = \hat{\mathbf{U}}_0(t) \Psi_0(\xi) + \hat{\mathbf{U}}_1(t) \Psi_1(\xi) + \hat{\mathbf{U}}_2(t) \Psi_2(\xi) + \hat{\mathbf{U}}_3(t) \Psi_3(\xi). \quad (10.52)$$

<sup>8</sup>Note the distinction between the interval  $I_i$  of the stencil  $S_j^l$  introduced in Eq. (10.1) and the interval  $I_j$  of the one-dimensional grid.

<sup>9</sup>In general, the functional space  $V_h$  of functions over which  $\mathbf{U}$  is expanded can be different from that of the test functions  $\Psi_l$ . When this happens the method is more appropriately referred to as the *Petrov–Galerkin method*.

The corresponding system of (coupled) ordinary differential equations obtained from (10.51) is

$$\frac{d\hat{\mathbf{U}}_0}{dt} + \mathbf{F}^*(1) - \mathbf{F}^*(0) = 0, \quad (10.53)$$

$$\frac{1}{3} \frac{d\hat{\mathbf{U}}_1}{dt} + \Psi_1(1)\mathbf{F}^*(1) - \Psi_1(0)\mathbf{F}^*(0) - \int_0^1 \mathbf{F}^*(\mathbf{U}(\xi, t)) d_\xi \Psi_1 d\xi = 0, \quad (10.54)$$

$$\frac{1}{5} \frac{d\hat{\mathbf{U}}_2}{dt} + \Psi_2(1)\mathbf{F}^*(1) - \Psi_2(0)\mathbf{F}^*(0) - \int_0^1 \mathbf{F}^*(\mathbf{U}(\xi, t)) d_\xi \Psi_2 d\xi = 0, \quad (10.55)$$

$$\frac{1}{7} \frac{d\hat{\mathbf{U}}_3}{dt} + \Psi_3(1)\mathbf{F}^*(1) - \Psi_3(0)\mathbf{F}^*(0) - \int_0^1 \mathbf{F}^*(\mathbf{U}(\xi, t)) d_\xi \Psi_3 d\xi = 0, \quad (10.56)$$

and can be solved through a standard Runge–Kutta discretisation in time (see Section 9.5), leading to a *Runge–Kutta discontinuous Galerkin scheme*, i.e., a RKDG scheme.

A number of interesting aspects of this strategy should be highlighted. The first one is that, to first order, namely when considering only Eq. (10.53), the RKDG scheme coincides with a first-order finite-volume scheme. Secondly, the values of the fluxes at the cell borders,  $\mathbf{F}^*(0)$  and  $\mathbf{F}^*(1)$ , can be obtained by solving a Riemann problem, thus incorporating the upwind property into the RKDG scheme. Thirdly, at least in principle, the solution of such Riemann problems does not require any spatial reconstruction at the interface between adjacent cells. The value of  $\mathbf{U}$  at the cell borders is in fact naturally provided by the expansion (10.48) computed at the proper locations. However, if the discontinuities are strong, the scheme generates significant oscillations. The problem is therefore circumvented by borrowing the technique of slope limiters from finite-volume methods and using it after each Runge–Kutta substep to control the solution in those numerical cells that require special attention (Cockburn and Shu, 1989; Qiu and Shu, 2005; Balsara *et al.*, 2007). Moreover, the spatial integrals in Eq. (10.53)–(10.56) are evaluated using *Gaussian quadrature points* of the appropriate order, where  $\mathbf{F}^*$  is expressed in terms of the polynomial expansion (10.48), i.e.,  $\mathbf{F}^*(\mathbf{U}(\xi, t)) = \mathbf{F}^*(\sum_{k=0}^{p-1} \hat{\mathbf{U}}_k \Psi_k)$  [see, e.g., Press *et al.* (1986) for a basic introduction to Gaussian quadrature]. The increasing success of RKDG schemes, and of DG methods in general, relies on their flexibility and adaptivity strategy in handling complex geometries, and in the efficiency of parallel implementation (Biswas *et al.*, 1994). These properties essentially reflect the fact that RKDG schemes advance the solution in time by using information only from the immediate neighbouring cells.

A disadvantage of RKDG schemes is that the number of degrees needed increases dramatically with increasing orders, especially in multiple dimensions. If  $p - 1$  is the maximum order of the Legendre polynomials in the expansion (10.48), the number of degrees of freedom to take into account is easily shown to be  $p$  in one-dimensional problems,  $p(p + 1)/2 \sim p^2$  in two-dimensional problems and  $p(p + 1)(p + 2)/6 \sim p^3$  in three-dimensional problems.<sup>10</sup> Moreover, the time-step has a tighter CFL condition, which is expressed by (Dumbser, 2005)

$$\Delta t \leq \frac{c_{\text{CFL}}}{2p - 1} \left( \frac{\Delta x}{\lambda_{\max}} \right), \quad (10.57)$$

<sup>10</sup>Indeed, the number of degrees of freedom is given by  $(1/D!) \prod_{j=1}^D (p - 1 + j)$  in  $D$  spatial dimensions.

where, as usual,  $\lambda_{\max}$  represents the maximum eigenvalue admitted by the system of equations considered. Although the constraint imposed by Eq. (10.57) may appear very severe and such as to make RKDG methods of little practical use, especially at high orders, this limitation is mitigated by two properties of RKDG methods. The first one is that discretisation with spacings much larger than those used in lower-order methods can be used with success. The second one is that *local time-stepping* can be performed, whereby each element is updated in time at its own maximum stable time-step, with a potential speedup that is progressively higher if only a small fraction of elements requires a small time-step [see, *e.g.*, Hesthaven and Warburton (2007) for details].

### 10.3.2 An example: a RKDG scheme in spherical symmetry

Following Radice and Rezzolla (2011), we consider an instructive example of the above formalism for the general-relativistic hydrodynamic equations in a spherically symmetric space-time (see Section 7.3.6). In a radial-polar gauge the metric can be written as

$$ds^2 = -\alpha^2 dt^2 + A^2 dr^2 + r^2(d\theta^2 + \sin^2\theta d\phi^2), \quad (10.58)$$

where  $\alpha$  and  $A$  are functions of  $t$  and  $r$  only. We next introduce the Bondi mass function,  $m$ , and the metric potential,  $\nu$ , defined as

$$A(t, r) := \left(1 - \frac{2m(t, r)}{r}\right)^{-1/2}, \quad \alpha(t, r) := e^{\nu(t, r)}. \quad (10.59)$$

Following Romero *et al.* (1996), we define the velocity as  $v := Au^r/\alpha u^t$ , where  $W = \alpha u^t = (1 - v^2)^{-1/2}$  is the Lorentz factor [*cf.* Eq. (7.21)<sub>1</sub>]. Furthermore, we introduce new conserved quantities<sup>11</sup>

$$\mathcal{D} := \alpha A J^t = \rho AW, \quad (10.60a)$$

$$S := \alpha T^{tr} = \rho h W^2 v, \quad (10.60b)$$

$$E := \alpha^2 T^{tt} = \rho h W^2 - p, \quad (10.60c)$$

$$\tau := E - \mathcal{D}, \quad (10.60d)$$

so that the Einstein equations can be rewritten in terms of the Hamiltonian constraint

$$\partial_r m = 4\pi r^2 E, \quad (10.61)$$

and of the slicing condition  $\partial_t K_{\theta\theta} = K_{\theta\theta} = 0$ , which becomes

$$\partial_r \nu = A^2 \left[ \frac{m}{r^2} + 4\pi r(p + Sv) \right], \quad (10.62)$$

where  $K_{ij}$  is the extrinsic curvature. These equations have to be integrated with the boundary conditions given by  $m(0) = 0$ , and by the requirement that  $\nu$  matches the Schwarzschild solution at the outer boundary of the computational domain.

<sup>11</sup>The pressure  $p$  in the equations below should not be confused with the number of degrees of freedom  $p$  extensively used in this chapter.

In order to discretise the DG equations in the spacetime given by Eq. (10.58), we consider a sphere  $\mathcal{S} = [0, R]$ , such that  $[0, R] = \bigcup_{j=1}^{N_e} \mathcal{S}_j$ , where the  $N_e$  elements  $\mathcal{S}_j$  are taken to be the spherical shells with radii  $r_j < r < r_{j+1}$ , and where  $\mathcal{S}_j = \varphi_j(\mathcal{E})$  and  $\mathcal{E} = [0, 1]$ . In this way, the relativistic-hydrodynamic equations (7.291) and (7.292) can be written in terms of the conserved quantities (10.60) and specialised for the metric (10.58) by substituting the explicit expression for the Christoffel symbols and the determinant of the metric to obtain

$$\begin{aligned} \sum_{j=1}^{N_e} \int_{r_j}^{r_{j+1}} \partial_t \mathbf{U} \phi r^2 dr = \\ \sum_{j=1}^{N_e} \left\{ \int_{r_j}^{r_{j+1}} X \mathbf{F}^r(\mathbf{U}) \partial_r \phi r^2 dr - \left[ r^2 X \mathcal{F}^r \phi \right]_{r_j}^{r_{j+1}} + \int_{r_j}^{r_{j+1}} \mathbf{S}(\mathbf{U}) \phi r^2 dr \right\}, \end{aligned} \quad (10.63)$$

where  $\phi$  is a generic test function. Other quantities introduced are  $X := \alpha/A$ , the conserved variables  $\mathbf{U} = (\mathcal{D}, S, \tau)$ , and  $\mathcal{F}^r$ , which is an estimate of  $\mathbf{F}^r$  at  $r_{j+1}$  and  $r_j$ , usually computed through the solution of a Riemann problem. The explicit expression for the fluxes is given by

$$\mathbf{F}^r = (\mathcal{D}v, Sv + p, S - \mathcal{D}v), \quad (10.64)$$

while the source terms are

$$\mathbf{S} = \left( 0, (Sv - \tau - \mathcal{D}) \left( 8\alpha A \pi r p + \alpha A \frac{m}{r^2} \right) + \alpha A p \frac{m}{r^2} + 2 \frac{\alpha p}{Ar}, 0 \right). \quad (10.65)$$

In the derivation of Eq. (10.63), the momentum constraint was used to substitute the derivatives of the metric in the source term and a factor  $X$  was absorbed into the test function in the derivation of the equation for  $\tau$ .

It is also convenient to introduce a *nodal basis* of polynomials,<sup>12</sup> formed by a set of  $p$  polynomials, all of degree  $p - 1$ , which are effectively the Lagrange polynomials  $\{\Phi_i(\xi)\}_{i=0}^{p-1}$  interpolating the  $p$  Gaussian quadrature points, also known as nodal points, within the reference element  $\mathcal{E} = [0, 1]$ . A few of these polynomials are reported for illustration in Fig. 10.3 and they should be compared with those in Fig. 10.2, which refer instead to a modal basis.

We recall that the abscissas of the nodal points for the  $(p - 1)$ -th degree nodal basis are the zeros of the Legendre polynomial of order  $p$  [*cf.* Eqs. (10.12)]. By construction, these polynomials are such that  $\Phi_i(\xi_k) = \delta_{ik}$  for  $i, k = 0, 1, \dots, p - 1$ , where  $\xi_k$  are the abscissas of the nodal points. Table 10.3 reports the abscissas of the  $p$  nodal points  $\xi_k$  and the corresponding weights  $w_k$  for the nodal basis of degree  $p - 1$  over the reference element  $\mathcal{E} = [0, 1]$ .

As a result, spatial integrals over the reference element can be computed through the Gaussian quadrature

$$\int_0^1 f(\xi) d\xi \approx \sum_{k=0}^{p-1} w_k f(\xi_k), \quad (10.66)$$

where  $w_k$  are a set of weights (see Table 10.3) given by

$$w_k = \int_0^1 \Phi_k(\xi) d\xi, \quad k = 0, 1, \dots, p - 1. \quad (10.67)$$

<sup>12</sup>See Section 10.2.1 for the alternative notion of *modal basis*.

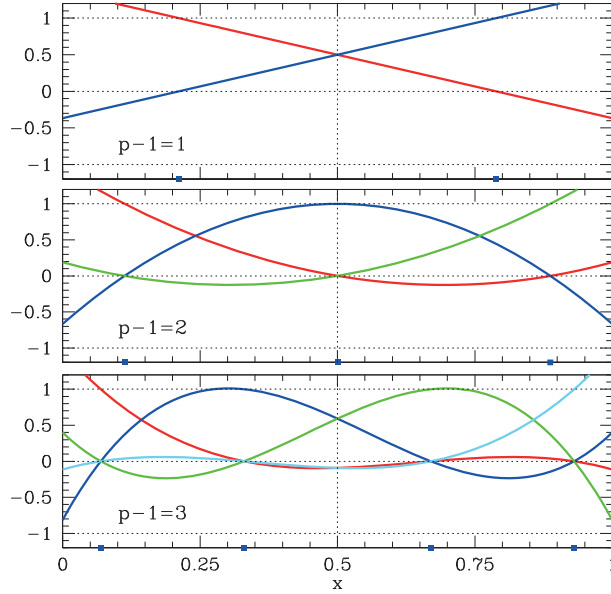


**Fig. 10.3** Functional behaviour of the first polynomials of the nodal basis of degree  $p - 1$ . The blue squares along the  $x$ -axis indicate the abscissas of the  $p$  Gaussian quadrature points (cf., Fig. 10.2 for the corresponding polynomials in a modal basis).

**Table 10.3** Abscissas of the  $p$  nodal points  $\xi_k$  and the corresponding weights  $w_k$  for the nodal basis of degree  $p - 1$  over the reference element  $\mathcal{E} = [0, 1]$ .

$p - 1$	$\xi_0$	$\xi_1$	$\xi_2$	$\xi_3$	$\xi_4$
0	0.50000				
1	0.21132	0.78867			
2	0.11270	0.50000	0.88730		
3	0.06943	0.33000	0.66999	0.93056	
4	0.04691	0.23076	0.50000	0.76923	0.95309

$p - 1$	$w_0$	$w_1$	$w_2$	$w_3$	$w_4$
0	1.00000				
1	0.50000	0.50000			
2	0.27778	0.44444	0.27778		
3	0.17392	0.32607	0.32607	0.17392	
4	0.11846	0.23931	0.28444	0.23931	0.11846

Given two regular functions  $f_1$  and  $f_2$  in  $r \in (0, R)$ , we define their scalar product as

$$[f_1, f_2] := \int_0^R f_1(r) f_2(r) r^2 dr, \quad (10.68)$$

which is then approximated through the quadrature formula (10.66) to obtain

$$[f_1, f_2] = \sum_{j=1}^{N_e} [f_1, f_2]_{\mathcal{S}_j} \approx \sum_{j=1}^{N_e} \left( \sum_{k=0}^{p-1} w_k |\varphi'_j| f_1[\varphi_j(\xi_k)] f_2[\varphi_j(\xi_k)] \right), \quad (10.69)$$

where  $|\varphi'_j|$  is the Jacobian of the affine transformation  $\varphi_j: [0, 1] \rightarrow \mathcal{S}_j$ . It is convenient to assume that  $\varphi_j$  is just an affine connection, so that the transformation between the reference element  $\mathcal{E}$  and the finite element  $\mathcal{S}_j$  is given by

$$\varphi_j(\xi) = \xi r_{j+1} + (\xi - 1)r_j, \quad (10.70)$$

and  $|\varphi'_j| = |r_{j+1} + r_j|$ . With these preliminary definitions, a fully discrete system can be constructed by looking for solutions  $\mathcal{D}, S, \tau$  and computing the integrals in (10.63) using the Gaussian quadrature (10.66) over each element. In particular, using the notation (10.69), we obtain

$$[r^2 \partial_t \mathbf{U}, \phi] = [r^2 X \mathbf{F}^r, \partial_r \phi] - \sum_{j=1}^{N_e} \left[ r^2 X \mathcal{F}^r \phi \right]_{r_j}^{r_{j+1}} + [r^2 \mathbf{S}, \phi], \quad (10.71)$$

where  $r_j$  is the left vertex of the  $j$ -th element in the discretisation of the radial coordinate in the line element (10.58). We consider now test functions with support contained within a given element,  $\mathcal{S}_j$ , e.g.,

$$\phi(r) = \Phi_k(\varphi_j^{-1}(r)) \chi_{[r_j, r_{j+1}]}(r), \quad (10.72)$$

where  $\Phi_k(\varphi_j^{-1}(r))$  is the Lagrange polynomial of order  $k$  evaluated at  $x = \varphi_j^{-1}(r)$  of the reference element mapped into  $r$ , while  $\chi_{[r_j, r_{j+1}]}$  is the *indicator function* and thus equal to one in the interval  $[r_j, r_{j+1}]$  and zero elsewhere. Expanding  $\mathbf{U}$  over the Lagrange basis of  $\mathcal{S}_j$

$$[\mathbf{U} \circ \varphi_j](\xi) = \sum_{k=0}^{p-1} \mathbf{U}_{jk} \Phi_k(\xi), \quad (10.73)$$

we obtain a set of coupled ordinary differential equations for the coefficients  $\mathbf{U}_{jk}$

$$r_{jk}^2 d_t \mathbf{U}_{jk} = \left[ r^2 X \mathbf{F}^r, \partial_r \Phi_k \right]_{\mathcal{S}_j} - \frac{1}{w_k |\varphi'_j|} \left[ r^2 X \mathcal{F}^r \Phi_k \right]_{r_j}^{r_{j+1}} + r_{jk}^2 \mathbf{S}_{jk}, \quad (10.74)$$

where  $r_{jk} = \varphi_j(\xi_k)$  and we used the fact that  $[\Phi_i, \Phi_k]_{\mathcal{S}_j} = \delta_{ik}$ .

The system of equations (10.74) can be closed with an EOS and coupled with the equations for the evolution of the metric quantities.<sup>13</sup> As usual, the computation of the fluxes  $\mathcal{F}^r$  requires that an approximate Riemann solver is used, while the time update can be done with a Runge–Kutta scheme (see Section 9.5).

<sup>13</sup>The application of the DG approach to numerical relativity, though still in its infancy, has already been attempted with promising results (Zumbusch, 2009; Field *et al.*, 2010).

## 10.4 The ADER approach

In Section 9.5.2 we anticipated that the efficiency of the Runge–Kutta time discretisation decreases dramatically for orders of accuracy larger than four because of the so-called “Butcher barrier”, which causes the number of intermediate steps to become larger than the formal order of accuracy. To circumvent the problem, a new method, called *ADER* (for “arbitrary high-order schemes using derivatives”) approach has been proposed by Titarev and Toro (2002) and Toro and Titarev (2005), where the update in time is performed through a single step, while preserving the high-order accuracy of the scheme.<sup>14</sup>

### 10.4.1 The original formulation

The key ingredients of the original ADER scheme are: (i) the definition of a *generalised Riemann problem* at the interfaces between adjacent cells, with initial data that is no longer piecewise constant but piecewise polynomial; (ii) a Taylor expansion in time of the state at each interface for the solution of such generalised Riemann problems; (iii) the so-called *Cauchy–Kovalewski* or Lax–Wendroff, procedure, consisting of the replacement of the time derivatives with space derivatives using repeatedly the governing conservation law in differential form. Let us illustrate each of these steps in more detail.

1. In order for the solution of the Riemann problem to preserve the high-order accuracy of the scheme at order  $p$ , the constant left and right states of the Riemann problem are replaced by left and right polynomials of order  $p - 1$ , thus generating a *generalised Riemann problem* (Ben-Artzi and Falcovitz, 1984; Floch and Raviart, 1988).

$$\mathbf{U}(x, 0) = \begin{cases} \mathbf{U}_L(x) = \mathbf{P}_j(x) & \text{if } x < x_{j+1/2}, \\ \mathbf{U}_R(x) = \mathbf{P}_{j+1}(x) & \text{if } x > x_{j+1/2}, \end{cases} \quad (10.75)$$

where  $\mathbf{P}_j(x)$  and  $\mathbf{P}_{j+1}(x)$  are the polynomials of order  $p - 1$  reconstructed in the cells  $[x_{j-1/2}, x_{j+1/2}]$  and  $[x_{j+1/2}, x_{j+3/2}]$ , respectively. Expression (10.75) should be compared with the definition (4.145) of the standard Riemann problem. In practice, while in the standard Riemann problem the left and right states are given by the boundary-extrapolated values of the reconstructed polynomials  $\mathbf{P}_j(x)$  and  $\mathbf{P}_{j+1}(x)$ , in the generalised Riemann problem one wants to keep all the information provided by the polynomials, which is typically obtained via a high-order reconstruction technique. The exact solution of the generalised Riemann problem is considerably more complicated than that of the standard Riemann problem and is available only for a limited set of equations (Menshov, 1990; Ben Artzi and Falcovitz, 2003). The solution, in fact, is no longer self-similar, the characteristics are no longer straight lines and centred rarefactions are not necessarily isentropic (see Fig. 10.4 for a schematic representation and Fig. 4.10 for a comparison with the standard Riemann problem).

<sup>14</sup>This approach was already suggested in the original formulation of the ENO method (Harten *et al.*, 1983).

2. An approximate solution of the generalised Riemann problem is obtained by Taylor-expanding in time the state  $\mathbf{U}$  at the cell interface. More precisely, after introducing the local time  $t' := t - t^n$ , this amounts to computing

$$\mathbf{U}(x_{j+1/2}, t') = \mathbf{U}(x_{j+1/2}, 0) + \sum_{k=1}^{p-1} \frac{(t')^k}{k!} \partial_t^{(k)} \mathbf{U}(x_{j+1/2}, 0). \quad (10.76)$$

The leading term  $\mathbf{U}(x_{j+1/2}, 0)$  represents the solution of the standard Riemann problem<sup>15</sup> with constant left and right states given by the boundary-extrapolated values of the reconstructed polynomials  $\mathbf{U}_L(x)$  and  $\mathbf{U}_R(x)$ , *i.e.*, of the Riemann problem with initial conditions given by

$$\mathbf{U}(x, 0) = \begin{cases} \mathbf{U}_L(x_{j+1/2}) & \text{if } x < x_{j+1/2}, \\ \mathbf{U}_R(x_{j+1/2}) & \text{if } x > x_{j+1/2}. \end{cases} \quad (10.77)$$

3. The time derivatives in the series expansion (10.76) are then replaced with space derivatives by resorting repeatedly to the governing evolution equation in conservative form. This is what is referred to as the *Cauchy–Kovalewski* procedure. In practice, for a system of equations in the conservative form (9.1), the following expressions are needed in order to compute the time derivatives of (10.76)

$$\partial_t \mathbf{U} = - \left( \frac{\partial \mathbf{F}}{\partial \mathbf{U}} \right) \partial_x \mathbf{U}, \quad (10.78)$$

$$\partial_{tx} \mathbf{U} = - \left( \frac{\partial^2 \mathbf{F}}{\partial \mathbf{U}^2} \right) (\partial_x \mathbf{U})^2 - \left( \frac{\partial \mathbf{F}}{\partial \mathbf{U}} \right) \partial_{xx} \mathbf{U}, \quad (10.79)$$

$$\partial_t^2 \mathbf{U} = - \left( \frac{\partial^2 \mathbf{F}}{\partial \mathbf{U}^2} \right) \partial_x \mathbf{U} \partial_t \mathbf{U} - \left( \frac{\partial \mathbf{F}}{\partial \mathbf{U}} \right) \partial_{xt} \mathbf{U}, \quad (10.80)$$

⋮

where we could use the identities (10.78) and (10.79) to further remove the terms  $\partial_t \mathbf{U}$  and  $\partial_{xt} \mathbf{U}$  involving time derivatives on the right-hand side of (10.80).

Although we have removed the time derivatives from the Taylor expansion (10.76), we still have to compute the spatial derivatives  $\partial_x^{(k)} \mathbf{U}(x_{j+1/2}, 0)$  appearing in the identities (10.78)–(10.80). These can be obtained after solving a sequence of  $p - 1$  standard *linear* Riemann problems for the equations

$$\partial_t \left[ \partial_x^{(k)} \mathbf{U}(x_{j+1/2}, 0) \right] + \tilde{\mathbf{A}} \partial_x \left[ \partial_x^{(k)} \mathbf{U}(x_{j+1/2}, 0) \right] = 0 \quad k = 1 \dots p - 1, \quad (10.81)$$

where  $\tilde{\mathbf{A}} := \mathbf{A}(\mathbf{U}(x_{j+1/2}, 0))$ , while the initial left and right states of such Riemann problems are obtained after taking spatial derivatives of the reconstructed polynomials (Toro and Titarev, 2002), *i.e.*,

<sup>15</sup>Note that  $\mathbf{U}(x_{j+1/2}, 0)$  should be regarded as the solution of the standard Riemann problem in the limit of  $t \rightarrow 0$ , namely it accounts for the “first-instant” interaction.

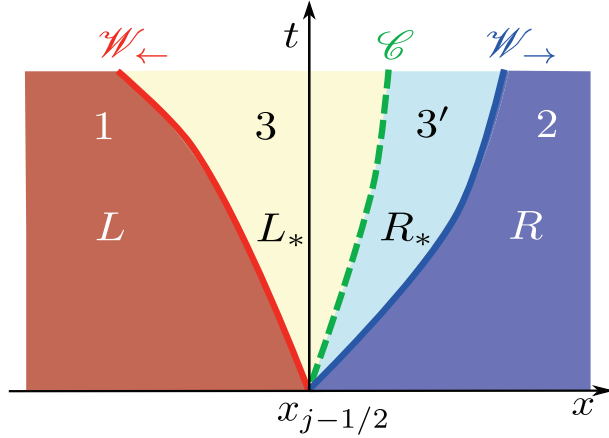


**Fig. 10.4** Spacetime diagram, or “Riemann fan”, of the evolution of a generalised Riemann problem, for which characteristics are no longer straight lines. This figure should be compared with the corresponding one for a standard Riemann problem, *cf.*, Fig. 4.10.

$$\partial_x^{(k)} \mathbf{U}(x, 0) = \begin{cases} \partial_x^{(k)} \mathbf{U}_L(x)|_{x_{j+1/2}} & \text{if } x < x_{j+1/2}, \\ \partial_x^{(k)} \mathbf{U}_R(x)|_{x_{j+1/2}} & \text{if } x > x_{j+1/2}. \end{cases} \quad (10.82)$$

We should stress that the coefficients of the matrix  $\tilde{\mathbf{A}}$  are the same for all the derivatives and must be computed only once. Being linear, the solution of the  $p - 1$  Riemann problems (10.81) does not represent a problem and can be readily obtained through the procedure discussed in Section 9.4.2. Having found an approximate solution of the generalised Riemann problem through (10.76), namely a temporal evolution of the state  $\mathbf{U}$  at each interface, the numerical flux function is computed directly from

$$\mathbf{F}_{j\pm 1/2} = \frac{1}{\Delta t} \int_{t^n}^{t^{n+1}} \mathbf{F}[\mathbf{U}(x_{j\pm 1/2}, t)] dt, \quad (9.14)$$

which requires a Gaussian quadrature in time of appropriate order.

4. A one-step time-update scheme can then be constructed by direct application of (9.15), and this completes the description of the ADER scheme in its original formulation (Toro *et al.*, 2001).

Given the complexity of the algorithm described above, there is nothing better than an example to fix ideas. Let us consider the conservation law to be given by the linear scalar advection equation for the function  $u(x, t)$  [*cf.*, Eq. (4.66)]

$$\partial_t u + \lambda \partial_x u = 0. \quad (10.83)$$

Then the time derivatives are simply given by

$$\partial_t^{(k)} u = (-\lambda)^k \partial_x^{(k)} u, \quad (10.84)$$

so that the state (10.76) becomes

$$u(x_{j+1/2}, t') = u(x_{j+1/2}, 0) + \sum_{k=1}^{p-1} \frac{(-\lambda t')^k}{k!} \partial_x^{(k)} u(x_{j+1/2}, 0). \quad (10.85)$$

Finally, the whole procedure leads to

$$u_j^{n+1} = u_j^n - \sum_{k=0}^{p-1} \frac{(\Delta t)^{k+1}}{\Delta x (k+1)!} \lambda \left( q_{j+1/2}^{(k)} - q_{j-1/2}^{(k)} \right), \quad (10.86)$$

where

$$q_{j+1/2}^{(k)} := (-\lambda)^k \partial_x^{(k)} u(x_{j+1/2}). \quad (10.87)$$

Of course, if  $p = 1$  (zeroth-order polynomial), and assuming  $\lambda > 0$ , then the scheme reduces to the first-order Godunov upwind method, *i.e.*, [cf. Eq. (9.41)]

$$u_j^{n+1} = u_j^n - \frac{\Delta t}{\Delta x} \lambda (u_j - u_{j-1}). \quad (10.88)$$

In essence, therefore, the solution of generalised Riemann problems is reduced to the formulation of a standard nonlinear Riemann problem, *i.e.*, (10.77), and to a sequence of  $p - 1$  linear Riemann problems (10.82), that must be solved at each interface. This procedure can of course be applied to nonlinear conservation laws and in fact the method that we have briefly outlined here has been successfully used to solve the Newtonian Euler equations in multiple dimensions (Toro and Titarev, 2005; Dumbser *et al.*, 2007).

It should be remarked, however, that the application of the original ADER approach to the equations of relativistic hydrodynamics introduces additional difficulties and has not yet been tempted. In general coordinates, in fact, even the special-relativistic equations have nonzero source terms that make the application of the Cauchy–Kovalewski procedure (10.78)–(10.80) very cumbersome. For these reasons, in the following section we present an alternative approach for determining the time evolution of the reconstructed polynomial, which avoids the Cauchy–Kovalewski procedure altogether, while still providing a one-step time-update numerical scheme. It is in this modified form that the ADER approach is nowadays usually referred to.

#### 10.4.2 The local spacetime DG scheme

As a valuable alternative to the Cauchy–Kovalewski procedure presented in the previous section for the construction of high-order, one-step time-update schemes, it is possible to perform the time evolution of the reconstructed polynomial locally for each cell, that is, without taking into account the contribution of the fluxes from the neighbouring cells. This can be done through the DG approach and has the additional benefit that it allows one to treat even systems of equations with stiff source terms; the resulting scheme is usually referred to as the *local spacetime DG scheme*. Following the original idea presented by Dumbser *et al.* (2008b), but using the more convenient nodal basis suggested by Hidalgo and Dumbser (2011), we

consider a general nonlinear system of hyperbolic equations written in conservative form as [cf., Eq. (4.27)]

$$\partial_t \mathbf{U} + \partial_x \mathbf{F}(\mathbf{U}) = \mathbf{S}(\mathbf{U}), \quad (10.89)$$

which we rewrite in terms of the reference local spatial coordinate  $\xi$  defined by Eq. (10.9) and of the analogous reference local temporal coordinate,  $\tau$ , defined as

$$t = t^n + \tau \Delta t, \quad 0 \leq \tau \leq 1, \quad (10.90)$$

so that Eq. (10.89) becomes

$$\partial_\tau \mathbf{U} + \partial_\xi \mathbf{F}^*(\mathbf{U}) = \mathbf{S}^*(\mathbf{U}), \quad (10.91)$$

with<sup>16</sup>

$$\mathbf{F}^* := \mathbf{F}^*(\mathbf{U}) = \mathbf{F}(\mathbf{U}) \frac{\Delta t}{\Delta x}, \quad (10.92)$$

$$\mathbf{S}^* := \Delta t \mathbf{S}. \quad (10.93)$$

We next assume that an entire-polynomial ENO or WENO reconstruction has been performed at time-level  $t^n$  according to the procedure described in Section 10.2, for example through Eq. (10.26), so that

$$\mathbf{U}_j(\xi, t^n) = \sum_{k=0}^{p-1} \Phi_k(\xi) \hat{\mathbf{U}}_k(t^n), \quad (10.94)$$

where, however, we have used the nodal basis  $\Phi_k(\xi)$  of polynomials introduced in Section 10.3.2. In addition, the solution within every *spacetime* reference control volume is expanded as

$$\mathbf{U}(\xi, \tau) = \sum_{l=1}^{N_d} \Theta_l(\xi, \tau) \hat{\mathbf{U}}_l, \quad (10.95)$$

where the spacetime polynomials  $\Theta_l(\xi, \tau)$  are given by the product of the nodal basis polynomials  $\Phi_i(\xi)$  and  $\Phi_j(\tau)$ , *i.e.*,

$$\Theta_l = \Theta_l(\xi, \tau) := \Phi_i(\xi) \Phi_j(\tau), \quad l = 1, \dots, N_d = p^2, \quad i, j = 0, \dots, p-1, \quad (10.96)$$

while the  $\hat{\mathbf{U}}_l$  are just constant, yet unknown, coefficients. In a similar way, the fluxes and the sources are also expanded and computed as

$$\mathbf{F}^*(\xi, \tau) := \sum_{l=1}^{N_d} \Theta_l(\xi, \tau) \hat{\mathbf{F}}_l^*, \quad (10.97)$$

$$\mathbf{S}^*(\xi, \tau) := \sum_{l=1}^{N_d} \Theta_l(\xi, \tau) \hat{\mathbf{S}}_l^*, \quad (10.98)$$

where

$$\hat{\mathbf{F}}_l^* = \mathbf{F}^*(\hat{\mathbf{U}}_l), \quad \hat{\mathbf{S}}_l^* = \mathbf{S}^*(\hat{\mathbf{U}}_l). \quad (10.99)$$

<sup>16</sup>Note that the flux  $\mathbf{F}^*$  in Eq. (10.91) is different from the flux in Eq. (10.10), where it was defined as  $\mathbf{F}^* = \mathbf{F}(\mathbf{U})/\Delta x$ .

Equation (10.91) can now be multiplied by the basis functions  $\Theta_k(\xi, \tau)$  and then integrated in space over the cell and in time from  $t^n$  to  $t^{n+1}$ , to obtain

$$\int_0^1 \int_0^1 (\Theta_k \partial_\tau \mathbf{U} + \Theta_k \partial_\xi \mathbf{F}^*) d\xi d\tau = \int_0^1 \int_0^1 \Theta_k \mathbf{S}^* d\xi d\tau. \quad (10.100)$$

The key step at this point is to perform an integration by parts in time, while keeping a local formulation in space, thus yielding

$$\begin{aligned} & \left( \int_0^1 \Theta_k \mathbf{U} d\xi \right)^{n+1} - \left( \int_0^1 \Theta_k \mathbf{U} d\xi \right)^n - \int_0^1 \int_0^1 \mathbf{U} \partial_\tau \Theta_k d\xi d\tau + \int_0^1 \int_0^1 \Theta_k \partial_\xi \mathbf{F}^* d\xi d\tau = \\ & \int_0^1 \int_0^1 \Theta_k \mathbf{S}^* d\xi d\tau. \end{aligned} \quad (10.101)$$

In this way, the various expansions introduced so far, namely, (10.94) at time-level  $t^n$ , and the three spacetime ones (10.95), (10.97), and (10.98), are inserted in (10.101) to give

$$\begin{aligned} & \sum_{l=1}^{N_d} ([\Theta_k, \Theta_l]^{n+1} - \langle \partial_\tau \Theta_k, \Theta_l \rangle) \hat{\mathbf{U}}_l - \sum_{l=0}^{p-1} [\Theta_k, \Phi_l]^n \hat{\mathbf{U}}_l(t^n) + \sum_{l=1}^{N_d} \langle \Theta_k, \partial_\xi \Theta_l \rangle \hat{\mathbf{F}}_l^* = \\ & \sum_{l=1}^{N_d} \langle \Theta_k, \Theta_l \rangle \hat{\mathbf{S}}_l^*, \end{aligned} \quad (10.102)$$

where, just for compactness and in analogy to the notation of Eq. (10.68), we have abbreviated the integrals over the spatial and spacetime reference element as

$$\langle f_1, f_2 \rangle := \int_0^1 \int_0^1 f_1 f_2 d\xi d\tau, \quad (10.103)$$

$$[f_1, f_2] := \int_0^1 f_1 f_2 d\xi. \quad (10.104)$$

Equation (10.102) represents a nonlinear system to be solved in the unknown  $\hat{\mathbf{U}}_l$ , while the terms  $\hat{\mathbf{U}}_l(t^n)$  are known and given by the coefficients of the expansion provided by the reconstruction operator.<sup>17</sup> Moreover, the space and spacetime integrals of the basis functions, namely the matrices  $[\Theta_k, \Theta_l]^{n+1}$ ,  $\langle \partial_\tau \Theta_k, \Theta_l \rangle$ ,  $[\Theta_k, \Phi_l]^n$ ,  $\langle \Theta_k, \partial_\xi \Theta_l \rangle$ , and  $\langle \Theta_k, \Theta_l \rangle$ , are analytic and can be computed once for all. The computation of the coefficients  $\hat{\mathbf{U}}_l$ , which makes the representation (10.95) fully determined, should be regarded as a predictor step alternative to the Cauchy–Kovalewski procedure described in the previous section, whose final result was to provide the time evolution of the reconstructed polynomials at cell boundaries. The state  $\mathbf{U}(\xi, \tau)$  as given by (10.95) cannot of course be used to determine the true solution at the time-level  $t^{n+1}$ , which instead requires taking into account the coupling of the cells through

<sup>17</sup> We should stress that the particularly simple computation of the coefficients  $\hat{\mathbf{F}}_l^*$  and  $\hat{\mathbf{S}}_l^*$  provided by (10.99) is due to the choice of the nodal basis. When a modal basis is instead adopted,  $\hat{\mathbf{F}}_l^*$  and  $\hat{\mathbf{S}}_l^*$  can only be obtained after performing a time-consuming “L2-projection”, *i.e.*, after solving for  $\langle \Theta_k, \Theta_l \rangle \hat{\mathbf{F}}_l^* = \langle \Theta_k, \mathbf{F}^*(\mathbf{U}) \rangle$ .

the numerical fluxes. However, fluxes and sources can now be easily obtained through the expressions

$$\mathbf{F}_{j+1/2}^* = \int_0^1 \mathcal{F}(\mathbf{U}_j(1, \tau), \mathbf{U}_{j+1}(0, \tau)) d\tau, \quad (10.105)$$

$$\mathbf{S}_j^* = \int_0^1 \int_0^1 \mathbf{S}(\mathbf{U}_j(\xi, \tau)) d\xi d\tau, \quad (10.106)$$

where  $\mathcal{F}$  is a numerical flux requiring the solution of the Riemann problem with left and right states given by  $\mathbf{U}_j(1, \tau)$  and  $\mathbf{U}_{j+1}(0, \tau)$ . After transforming back via Eqs. (10.92)–(10.93), the overall scheme will finally adopt the form

$$\mathbf{U}_j^{n+1} = \mathbf{U}_j^n + \frac{\Delta t}{\Delta x} (\mathbf{F}_{j-1/2} - \mathbf{F}_{j+1/2}) + \Delta t \mathbf{S}_j, \quad (10.107)$$

and therefore appear as a high-order, one-step time-update scheme, with no need for Runge–Kutta substeps.

This idea can be further developed to produce a class of hybrid numerical schemes which unify in a single framework both the finite-volume and the DG approach, and the interested reader is referred to Dumbser *et al.* (2008a) for further details. What is worth stressing here is that because of the local feature of the predictor step, the local spacetime DG scheme is also suitable for treating stiff source terms and indeed it has been successfully applied to the solution of the relativistic resistive magnetohydrodynamic equations to study magnetic reconnection in relativistic regimes (Zanotti and Dumbser, 2011).

## 10.5 Extension to multidimensional problems

All of the discussions made so far about numerical methods for the solution of hyperbolic equations, *i.e.*, the content of Chapters 8–10, has been focused on algorithms valid in one spatial dimension only. Our goal was in fact to illustrate the basic features of the different methods in the simplest scenario possible. It is obvious, however, that none of the schemes illustrated so far would be of great practical use if it could not be extended easily to two and three spatial dimensions. In this section, which cannot be comprehensive but is sufficient to give a first idea, we will deal with the extension to multidimensional systems of hyperbolic equations written in conservative form, *i.e.*, *multidimensional conservation laws*. In logical analogy with the one-dimensional case, we express a generic conservation law in Cartesian coordinates as

$$\partial_t \mathbf{U} + \partial_x \mathbf{F} + \partial_y \mathbf{G} + \partial_z \mathbf{H} = \mathbf{S}(\mathbf{U}). \quad (10.108)$$

Despite the common conservative form, a clear distinction needs to be made between finite-difference schemes and finite-volume schemes, which we will discuss separately below.

### 10.5.1 Finite-difference multidimensional schemes

The most natural strategy for extending finite-difference conservative numerical schemes to multidimensions is to apply to Eq. (10.108) the same discretisation in space made in the one-dimensional case so as to obtain the *semi-discrete equations* [cf., Eq. (9.22)]

$$\frac{d\mathbf{U}_{i,j,k}}{dt} = \frac{1}{\Delta x} (\hat{\mathbf{F}}_{i-1/2,j,k} - \hat{\mathbf{F}}_{i+1/2,j,k}) + \frac{1}{\Delta y} (\hat{\mathbf{G}}_{i,j-1/2,k} - \hat{\mathbf{G}}_{i,j+1/2,k}) + \frac{1}{\Delta z} (\hat{\mathbf{H}}_{i,j,k-1/2} - \hat{\mathbf{H}}_{i,j,k+1/2}) + \mathbf{S}_{i,j,k}, \quad (10.109)$$

where  $\mathbf{S}_{i,j,k}$  is the source function at point  $(x_i, y_j, z_k)$ , while  $\hat{\mathbf{F}}_{i\pm 1/2,j,k}$ ,  $\hat{\mathbf{G}}_{i,j\pm 1/2,k}$  and  $\hat{\mathbf{H}}_{i,j,k\pm 1/2}$  are the numerical fluxes at points  $(x_{i\pm 1/2}, y_j, z_k)$ ,  $(x_i, y_{j\pm 1/2}, z_k)$ , and  $(x_i, y_j, z_{k\pm 1/2})$ , respectively. As for Eq. (9.22), also in this case the right-hand side of Eq. (10.109) should be thought of as a continuous function of time, thus justifying the use of a continuous differential operator on the left-hand side.

In practice, each of the fluxes entering (10.109) is computed after performing a *dimension-by-dimension reconstruction* along the corresponding direction, *i.e.*,

- a first reconstruction along the  $x$ -direction to obtain the fluxes  $\hat{\mathbf{F}}_{i\pm 1/2,j,k}$ ,
- a second reconstruction along the  $y$ -direction to obtain the fluxes  $\hat{\mathbf{G}}_{i,j\pm 1/2,k}$ ,
- a third reconstruction along the  $z$ -direction to obtain the fluxes  $\hat{\mathbf{H}}_{i,j,k\pm 1/2}$ .

It is important to stress that the same reconstruction operator is applied to each direction and, as discussed in Section 10.2.3, the reconstruction can either be performed to provide directly the numerical flux, thus avoiding the solution of the Riemann problem, or be performed so as to incorporate the solution of the Riemann problem. When all the terms on the right-hand side of Eq. (10.109) have been computed, the same time integrator introduced for one-dimensional problems can be used also to update  $\mathbf{U}_{i,j,k}$ . In most cases, this will be chosen among Runge–Kutta methods, such as those discussed in Section 9.5.

Attention needs to be paid to the choice of the time-step  $\Delta t$ . In fact, the generalisation of the CFL condition (8.42) to systems of equations and to multidimensional spacetimes with  $D$  spatial dimensions amounts to ensuring that, whatever the number of equations and of spatial directions considered, the fastest signal travels at most a fraction of the length of a cell in that direction, *i.e.*, (Titarev and Toro, 2005)

$$\Delta t = \frac{c_{\text{CFL}}}{D} \min_k \left( \frac{\Delta x}{|\lambda_{k,x}^n|}, \frac{\Delta y}{|\lambda_{k,y}^n|}, \frac{\Delta z}{|\lambda_{k,z}^n|} \right), \quad (10.110)$$

where  $|\lambda_{k,i}^n|$  are the eigenvalues admitted by the system at time-level  $t^n$  over the whole computational grid, with the index  $k$  spanning the set of possible eigenvalues, and with the index  $i$  marking the various spatial directions.

### 10.5.2 Finite-volume multidimensional schemes

By trivially following the same line of argument that allowed us to derive the one-dimensional finite-volume scheme in Eq. (9.15), it is possible to extend it to multidimensions in the semi-discrete form and thus express Eq. (10.108) as<sup>18</sup>

$$\begin{aligned} \frac{d\mathbf{U}_{i,j,k}}{dt} = & \frac{1}{\Delta x} (\mathbf{F}_{i-1/2,j,k} - \mathbf{F}_{i+1/2,j,k}) + \frac{1}{\Delta y} (\mathbf{G}_{i,j-1/2,k} - \mathbf{G}_{i,j+1/2,k}) + \\ & \frac{1}{\Delta z} (\mathbf{H}_{i,j,k-1/2} - \mathbf{H}_{i,j,k+1/2}) + \mathbf{S}_{i,j,k}, \end{aligned} \quad (10.111)$$

where

$$\mathbf{U}_{i,j,k} := \frac{1}{\Delta x} \frac{1}{\Delta y} \frac{1}{\Delta z} \int_{x_{i-1/2}}^{x_{i+1/2}} \int_{y_{j-1/2}}^{y_{j+1/2}} \int_{z_{k-1/2}}^{z_{k+1/2}} \mathbf{U}(x, y, z, t) dz dy dx, \quad (10.112)$$

is the spatial average of the solution at time  $t$  in the spatial element

$$I_{i,j,k} = [x_{i-1/2}, x_{i+1/2}] \times [y_{j-1/2}, y_{j+1/2}] \times [z_{k-1/2}, z_{k+1/2}], \quad (10.113)$$

while

$$\mathbf{F}_{i\pm 1/2,j,k} := \frac{1}{\Delta y} \frac{1}{\Delta z} \int_{y_{j-1/2}}^{y_{j+1/2}} \int_{z_{k-1/2}}^{z_{k+1/2}} \mathbf{F}[\mathbf{U}(x_{i\pm 1/2}, y, z, t)] dz dy, \quad (10.114)$$

$$\mathbf{G}_{i,j\pm 1/2,k} := \frac{1}{\Delta x} \frac{1}{\Delta z} \int_{x_{i-1/2}}^{x_{i+1/2}} \int_{z_{k-1/2}}^{z_{k+1/2}} \mathbf{G}[\mathbf{U}(x, y_{j\pm 1/2}, z, t)] dz dx, \quad (10.115)$$

$$\mathbf{H}_{i,j,k\pm 1/2} := \frac{1}{\Delta x} \frac{1}{\Delta y} \int_{x_{i-1/2}}^{x_{i+1/2}} \int_{y_{j-1/2}}^{y_{j+1/2}} \mathbf{H}[\mathbf{U}(x, y, z_{k\pm 1/2}, t)] dy dx, \quad (10.116)$$

$$\mathbf{S}_{i,j,k} := \frac{1}{\Delta x} \frac{1}{\Delta y} \frac{1}{\Delta z} \int_{x_{i-1/2}}^{x_{i+1/2}} \int_{y_{j-1/2}}^{y_{j+1/2}} \int_{z_{k-1/2}}^{z_{k+1/2}} \mathbf{S}[\mathbf{U}(x, y, z, t)] dy dx dz \quad (10.117)$$

are the fluxes and sources, respectively. Just like in Section 9.1.2, it is important to remark here that expression (10.111) becomes a numerical scheme only after an approximation is introduced for the computation of the fluxes. Such an approximation can effectively be performed by computing expressions (10.114)–(10.116), *e.g.*, by means of Gaussian quadratures. Focusing for simplicity just on the flux along the  $x$ -direction, we would then obtain

$$\mathbf{F}_{i\pm 1/2,j,k} = \frac{1}{\Delta y} \frac{1}{\Delta z} \sum_{m=1}^{N_G} \sum_{n=1}^{N_G} \mathbf{F}(\mathbf{U}(x_{i\pm 1/2}, y_m, z_n)) w_m w_n, \quad (10.118)$$

where the summation is taken over the  $N_G$  different Gaussian integration points, with  $w_m$  and  $w_n$  being the corresponding weights. The term  $\mathbf{F}(\mathbf{U}(x_{i\pm 1/2}, y_m, z_n))$  will be typically obtained after solving a Riemann problem at  $(x_{i\pm 1/2}, y_m, z_n)$ , which means that the left and

<sup>18</sup>A different approach is possible in which the time update is performed through a sequence of incremental time updates, each valid along a given direction. This approach is referred to as *dimensional splitting* or *method of fractional steps* and details of its implementation can be found in Toro (2009).

right states of the vector  $\mathbf{U}(x_{i\pm 1/2}, y_m, z_n)$  are needed. It is at this stage that the flexibility of finite-volume methods can be fully appreciated. Indeed, even if a dimension-by-dimension reconstruction is still possible [see, *e.g.*, Titarev and Toro (2004), or Tchekhovskoy *et al.* (2007) in the relativistic context], the very nature of finite-volumes allows (and suggests) performing a genuine multidimensional reconstruction with stencils that will cover a surface in the two-dimensional case and a volume in the three-dimensional case (Balsara *et al.*, 2009). One of the main advantages of this approach is that also grids with arbitrary triangulations can be treated (Dumbser and Käser, 2007). In this latter case, however, the computational costs are also considerably larger and only a few applications to relativistic problems have been done so far [see, *e.g.*, Zanotti and Dumbser (2011)], although more are expected as these methods are further developed.

Finally, it should also be stressed that, at least in principle, the Riemann solver adopted should be intrinsically multidimensional. This is particularly relevant for relativistic hydrodynamics and marks an important difference with respect to Newtonian hydrodynamics. As shown by Rezzolla and Zanotti (2002), in fact, the presence of tangential velocities along the remaining (or passive) directions can even change the wave pattern produced in a relativistic Riemann problem. In practice, however, due to the high computational costs related to the implementation of exact Riemann solvers, standard one-dimensional approximate Riemann solvers are used in most of the practical implementations. This does not mean that such one-dimensional Riemann solvers ignore completely the presence of the passive directions. Even a simplified but robust Riemann solver such as HLLE (see Section 9.4.1), requires knowledge of the eigenvalues of the system, thus incorporating some information about the multidimensionality of the problem, through the coupling among velocities introduced by the Lorentz factor. What should be kept in mind, though, is that for relativistic hydrodynamics the approximation inherent in the choice of an approximate Riemann solver, especially an incomplete Riemann solver, is larger in multidimensional problems than in one-dimensional ones.

## 10.6 Further reading

- Barth, T. and Deconinck, H. (1999). *High-Order Methods for Computational Physics*. Springer, Berlin.
- Ben Artzi, M. and Falcovitz, J. (2003). *Generalised Riemann Problems in Computational Fluid Dynamics*. Cambridge University Press, Cambridge.
- Hesthaven, J. S. and Warburton, T. (2007). *Nodal Discontinuous Galerkin Methods: Algorithms, Analysis, and Applications*. Texts in Applied Mathematics. Springer, Berlin.
- LeVeque, R. J. (2002). *Finite Volume Methods for Hyperbolic Problems*. Cambridge University Press, Cambridge.
- Quarteroni, A. and Valli, A. (2008). *Numerical Approximation of Partial Differential Equations*. Springer Series in Computational Mathematics. Springer, Berlin.
- Toro, E. (2009). *Riemann Solvers and Numerical Methods for Fluid Dynamics*. Springer, Berlin.
- Trangenstein, J. A. (2009). *Numerical Solution of Hyperbolic Partial Differential Equations*. Cambridge University Press, Cambridge.

## 10.7 Problems

1. Show that up to  $p = 2$ , the two oscillation indicators (10.17) and (10.18) give the same results, while they differ for  $p \geq 3$ .
2. Show that for  $p = 3$ , Eq. (10.18) gives

$$\begin{aligned}\mathcal{OI}_0 &= \frac{13}{12}(\mathbf{U}_{j-2}^n - 2\mathbf{U}_{j-1}^n + \mathbf{U}_j^n)^2 + \frac{1}{4}(\mathbf{U}_{j-2}^n - 4\mathbf{U}_{j-1}^n + 3\mathbf{U}_j^n)^2, \\ \mathcal{OI}_1 &= \frac{13}{12}(\mathbf{U}_{j-1}^n - 2\mathbf{U}_j^n + \mathbf{U}_{j+1}^n)^2 + \frac{1}{4}(\mathbf{U}_{j-1}^n - \mathbf{U}_{j+1}^n)^2, \\ \mathcal{OI}_2 &= \frac{13}{12}(\mathbf{U}_j^n - 2\mathbf{U}_{j+1}^n + \mathbf{U}_{j+2}^n)^2 + \frac{1}{4}(3\mathbf{U}_j^n - 4\mathbf{U}_{j+1}^n + \mathbf{U}_{j+2}^n)^2.\end{aligned}$$

3. Using Table 10.3, take the abscissas of the nodal points  $\xi_0$ ,  $\xi_1$  and  $\xi_2$  to compute the coefficients of the three polynomials forming the nodal basis of degree 2. [Hint: use the property that  $\Phi_i(\xi_k) = \delta_{ik}$ .]
4. Considering the modal basis of orthogonal Legendre polynomials (10.12) and the nodal basis associated to the Gaussian quadrature points of Table 10.3, find the relation among the components of a polynomial with respect to the two bases. In particular, find the matrix  $\mathbf{B}$  that performs the transformation

$$\hat{\mathbf{U}}_{\text{nodal}} = \mathbf{B}\hat{\mathbf{U}}_{\text{modal}},$$

where  $\hat{\mathbf{U}}_{\text{nodal}}$  and  $\hat{\mathbf{U}}_{\text{modal}}$  are the vectors of the components with respect to the two bases.

5. Implement a numerical code that solves the special-relativistic hydrodynamic equations (7.231) in one spatial dimension and in Cartesian coordinates adopting the Runge–Kutta discontinuous Galerkin scheme as described in Section 10.3.1. Apply the code to solve the Riemann problem with initial conditions given by  $p_L = 1.0$ ,  $\rho_L = 1.0$ ,  $v_L = 0$  and  $p_R = 0.1$ ,  $\rho_R = 0.125$ ,  $v_R = 0$ , and compare the result with that obtained using any TVD limiter.
6. Write a simple one-dimensional code that solves the linear scalar advection equation (4.66) through the original ADER scheme, *i.e.*, with Eq. (10.86), to third-order accuracy. Choosing a few different initial conditions, compare the solutions with those obtained using the first-order Godunov scheme [*cf.*, Eq. (9.41)–(9.42)].

# 11

## Relativistic Hydrodynamics of Non-Selfgravitating Fluids

---

Chapters 2–6 have been used to build a general mathematical framework describing relativistic fluids. However, the expressions we have derived in those chapters are more than elegant tensorial equations and actually open the way to the study of relativistic fluids in a large variety of physical scenarios. This chapter is dedicated to the investigation of some of these scenarios. For convenience we will distinguish between non-selfgravitating and selfgravitating fluids, depending respectively on whether the simultaneous solution of the Einstein equations needs to be added to the solution of the relativistic-hydrodynamic equations or not.

More specifically, we define as *non-selfgravitating fluids* those fluids whose associated total mass and energy is sufficiently small that they do not provide a source for the right-hand side of the Einstein equations (1.218). As a result, although the energy–momentum tensor is strictly nonzero, the Einstein equations reduce to their form in vacuum<sup>1</sup>

$$R_{\mu\nu} - \frac{1}{2}Rg_{\mu\nu} = R_{\mu\nu} = 0. \quad (11.1)$$

The only equations we need to solve are therefore those for the conservation of the rest mass and of the energy and momentum [*cf.*, (2.118)–(2.119)], *i.e.*,

$$\nabla_\mu(\rho u^\mu) = 0, \quad (3.52)$$

$$\nabla_\mu T^{\mu\nu} = 0, \quad (3.53)$$

where the covariant derivatives are taken on the *background spacetime* solution of (11.1). Under these conditions, the spacetime can be considered fixed and the flow dynamics that of a *test fluid*. The case of selfgravitating fluids will be considered in the next chapter.

We should note that although somewhat idealised, the solutions that will be discussed here are very relevant for two different reasons. First, they often capture the basic physical processes behind an otherwise complicated and obscure phenomenology. Second, they provide important testbeds for numerical codes solving the relativistic-hydrodynamic equations. Indeed, a code cannot be considered fully tested if it does not reproduce accurately many of the solutions discussed hereafter.

<sup>1</sup>In vacuum, it is straightforward to show that, after contracting both sides of Eqs. (1.218) with the metric, the Ricci scalar is zero, *i.e.*,  $R^\mu_\mu - \frac{1}{2}Rg^{\mu\nu}g_{\mu\nu} = R - 2R = -R = 0$ .

## 11.1 Similar and self-similar flows

The Newtonian equations of hydrodynamics and those of special-relativistic hydrodynamics admit *similarity transformations*, that is, transformation that describe flows which are similar to each other and that can be derived from each other by simply changing the basic scales of length, time and density [see, e.g., Zel'dovich and Raizer (2002)]. The concept of *similarity* is widely used in mechanics and hydrodynamics and relies on the possibility of modelling a physical phenomenon by the study of an analogous phenomenon whose properties can be suitably rescaled. In this way, by exploiting the properties of similarity, it is possible to perform in reduced and inexpensive laboratory conditions experiments that would otherwise require considerably larger effort. As in the conversion from a system of units to another one, the properties of a specific phenomenon can then be deduced from the properties of another phenomenon when the latter is *similar* to the first one (Sedov, 1959).

Of course, not all phenomena can be scaled in a similar way and the definition of some *similarity criteria* is therefore relevant. For this purpose, let a given phenomenon be described by a number  $n$  of parameters, some of which are dimensionless while others are dimensional physical quantities. Moreover, assume that the dimensions of the physical quantities are expressed by means of  $k$  fundamental units with  $k \leq n$ . In general then, it is evident that  $n - k$  is the maximum number of independent dimensionless combinations out of the  $n$  parameters. In other words, all of the dimensionless properties of the given phenomenon can be expressed in terms of the  $n - k$  independent dimensionless combinations. It follows then, that a necessary and sufficient condition for two phenomena to be similar is that the number of independent dimensionless combinations of parameters is the same for the two phenomena (Sedov, 1959).

Let us make some examples to fix ideas. A special-relativistic system can be described in terms of two dimensional fundamental quantities (or parameters) given by *length* and *time* (*i.e.*,  $n = 2$ ), which collapse to a single fundamental quantity (*i.e.*,  $k = 1$ ), *e.g.*, a length, when expressed in geometrical units, *i.e.*, units in which  $c = 1$ . As a result, all dimensional quantities can be thought of as lengths, while all the dimensionless quantities can be thought of as velocities. When considering a general-relativistic system, instead, in addition to lengths and times, another dimensional fundamental quantity needs to be considered and is given by the *mass* of the spacetime. Also in this case, the three fundamental quantities can be collapsed into a single one, *e.g.*, a length, when expressed in geometrical units, *i.e.*, units in which  $c = G = 1$ , where  $G$  is the gravitational constant.

While the condition of similarity is useful to establish a relation between two types of flows, the condition of *self-similarity* describes a similarity of the flow with itself and is useful to establish a relation within the same flow at two different positions or at two different times. From a more formal point of view, a solution to a hydrodynamic problem is said to be *self-similar* when it can be described by no more than two quantities with independent dimensions other than space and time. When this is the case, all of the physical quantities representative of the problem can be rewritten as a function of a *similarity variable*, which is usually a combination of the spatial and time coordinates. Although a self-similar solution does evolve in time (*i.e.*, it is not stationary), it nevertheless evolves in such a way that the solution at any instant is *similar* (in the sense defined above) to the solutions at neighbouring instants (Batchelor, 2000; Zel'dovich and Raizer, 2002). An obvious conclusion that can be drawn is that a self-similar solution can be realised in practice only in a physical system that does not possess intrinsic length- or time-scales, since the latter could not be expressed in

terms of the similarity variable.

There are at least two important reasons to look for hydrodynamic self-similar solutions. The first one is that it is much simpler to find an analytical solution to a given hydrodynamic problem when the relevant equations are written in terms of a *self-similar* or *similarity variable*. The second reason is that, in the absence of intrinsic length- or time-scales, nature seems to prefer solutions which have self-similar properties. In this sense, the search for self-similar behaviour does not represent the search for an exotic and unrealistic solution, but rather the search for that specific behaviour that the system would “naturally” tend to assume in the absence of length- or time-scales.

Before discussing the properties of non-selfgravitating self-similar flows, it is useful to make a remark which serves to qualify self-similarity also within a general-relativistic context. All that has been discussed so far about self-similarity, in fact, applies to what is usually referred to as *physical* self-similarity and should be regarded as a property of the fluid in a given fixed background spacetime. In general relativity, however, the concept of self-similarity can be applied also to the spacetime as a whole. This second self-similarity is referred to as *geometrical*, is in general distinct from physical self-similarity and reflects the fact that the properties of the spacetime can be similar at different positions and times. Examples in this respect are critical solutions in gravitational collapse (Choptuik, 1993), or some classes of cosmological solutions (Carr and Coley, 1999). Although distinct, geometrical and physical self-similarities are in general related and it is possible to show that if the spacetime admits a *homothetic vector*, namely a four-vector  $\xi$  such that

$$\mathcal{L}_\xi g_{\mu\nu} = 2g_{\mu\nu}, \quad (11.2)$$

where  $\mathcal{L}_\xi$  is the Lie derivative along  $\xi$  (see Section 1.5.1), then the existence of a geometrical self-similarity implies also the existence of a physical self-similarity. In essence, “homothety” (or “homothetic motion”) is meant to capture the geometric concept of invariance under scale transformations, so that a portion of the spacetime will be similar to itself also when subject to a scale transformation.

Following the spirit of this chapter, which is devoted to non-selfgravitating fluids, in the following sections we will restrict ourselves not only to physical self-similarity, but also to flat background spacetimes. However, the interested reader will find in Carr and Coley (1999) an enjoyable review of self-similarity in general relativity.

### 11.1.1 One-dimensional self-similar flows

In order to obtain self-similar solutions we first write the special-relativistic form of the conservation equations (3.52) and (3.53)<sup>2</sup>

$$\nabla_\mu(\rho u^\mu) = 0, \quad (11.3)$$

$$\nabla_\mu T^{\mu\nu} = 0, \quad (11.4)$$

<sup>2</sup>Although we are considering a flat spacetime, we use the covariant derivatives in Eqs. (3.52) and (3.53) to allow for coordinates that are not Cartesian.

**496 Relativistic Hydrodynamics of Non-Selfgravitating Fluids**

for one-dimensional flows (*i.e.*, for  $\mu = 0, 1$ ) in a geometry-independent form to obtain the conservation equation for the rest mass, the linear momentum and the energy as

$$\partial_t (W\rho) + \partial_{x^1} (\rho W v) = -\frac{j}{x^1} \rho W v, \quad (11.5)$$

$$\partial_t [(e + p) W^2 v] + \partial_{x^1} [(ev^2 + p) W^2] = -\frac{j}{x^1} [(e + p) W^2 v^2], \quad (11.6)$$

$$\partial_t [(e + pv^2) W^2] + \partial_{x^1} [(e + p) W^2 v] = -\frac{j}{x^1} [(e + p) W^2 v], \quad (11.7)$$

where  $u^\mu = W(1, v)$ ,  $W$  is the Lorentz factor  $W = (1-v^2)^{-1/2}$ , and, as usual,  $e$ ,  $p$ , and  $\rho$  are the energy density, the pressure and the rest-mass density, respectively. In the equations above  $j = 0, 1, 2$  distinguishes situations with planar, cylindrical or spherical symmetry, respectively. As a result, for  $j = 0$  we have  $x^1 = x$  in a Cartesian coordinate system  $(t, x, y, z)$ , for  $j = 1$  we have  $x^1 = \varpi$  in a cylindrical coordinate system  $(t, \varpi, \phi, z)$ , and for  $j = 2$ ,  $x^1 = r$  in a spherical polar coordinate system  $(t, r, \theta, \phi)$ .

It is now convenient to introduce a *similarity variable* which, because in geometrised units all quantities can be set to be either lengths or times, can only be a function of  $x^1$  and  $t$ , *e.g.*,

$$\xi := \pm \frac{x^1}{t}, \quad (11.8)$$

where  $-1 \leq \xi \leq 1$ . The dimensionless similarity variable  $\xi$  can be viewed either as the position of a point in the solution at a given time, as a time at a given position in the solution, or as the velocity a given feature in the solution is moving at (*e.g.*, the velocity of a discontinuity surface). This velocity is to be distinguished from the fluid velocity  $v$  at the point described by  $\xi$ . For example, a self-similar flow which is linearly expanding with time is naturally described in terms of a positive similarity variable  $\xi$  (*i.e.*,  $\xi \in [0, 1]$ ), while a self-similar contracting flow should be described in terms of negative values of  $\xi$  (*i.e.*,  $\xi \in [-1, 0]$ ).

We next express the conservation equations for the rest-mass density, the momentum and the energy (11.5)–(11.7) in terms of the similarity variable, that is, we search for solutions of the type  $e = e(\xi)$ ,  $\rho = \rho(\xi)$ , and  $v = v(\xi)$ , where we use the definition (2.168) of the sound speed  $c_s$  to remove the dependence on the pressure. To this end we introduce the new dimensionless variables

$$f := \frac{1+v}{1-v}, \quad v = \frac{f-1}{1+f}, \quad (11.9)$$

$$z := \frac{1+\xi}{1-\xi}, \quad \xi = \frac{z-1}{1+z}, \quad (11.10)$$

so that Eqs. (11.5)–(11.7) can be rewritten as

$$\frac{(z+f)(f+1)}{2f} f' - (z-f)\rho' + j \frac{(f-1)}{(z-1)} \rho = 0, \quad (11.11)$$

$$\frac{z}{f}(e+p)f' + f(e-p)' - z(e+p)' + \frac{j}{z-1}(e+p)(f-1) = 0, \quad (11.12)$$

$$(e+p)f' + f(e+p)' - z(e-p)' + \frac{j}{z-1}(e+p)(f-1) = 0, \quad (11.13)$$

where

$$' := \frac{\partial}{\partial z}. \quad (11.14)$$

Note that Eqs. (11.12)–(11.13) can be combined to yield an energy equation which is coordinate independent

$$\frac{e'}{e} = 2 \left( \frac{z-f}{z+f} \right) \frac{f'}{f}, \quad (11.15)$$

and a momentum equation which involves only terms related to the velocity

$$(f^2 - 4zf + z^2) \frac{f'}{f} = j \left( \frac{f-1}{z-1} \right) (z+f). \quad (11.16)$$

Using now the relations

$$\frac{\partial}{\partial \xi} := \frac{(1+z)^2}{2} \frac{\partial}{\partial z}, \quad (11.17)$$

$$v' := \left( \frac{1+z}{1+f} \right)^2 f', \quad (11.18)$$

it is possible to rewrite Eqs. (11.11)–(11.13) in the following self-similar form (Steinhardt, 1982; Kurki-Suonio, 1985)

$$\frac{1}{\rho} \frac{d\rho}{d\xi} = \frac{1}{(e+p)} \frac{de}{d\xi}, \quad (11.19)$$

$$[(c_s^2 \xi^2 - 1)v^2 + 2\xi(1 - c_s^2)v + c_s^2 - \xi^2] \frac{dv}{d\xi} = -j \frac{v}{\xi} c_s^2 (1 - v^2) (1 - \xi v), \quad (11.20)$$

$$\frac{c_s^2}{(e+p)} \frac{de}{d\xi} = \left( \frac{\xi - v}{1 - \xi v} \right) \left( \frac{1}{1 - v^2} \right) \frac{dv}{d\xi}. \quad (11.21)$$

Equation (11.19) shows that the self-similar solution of the rest-mass density (or of the number density if the fluid is ultrarelativistic) is proportional to that of the energy density divided by the enthalpy density. As a result, hereafter we will consider only Eqs. (11.20)–(11.21) since the expression for  $\rho$  can be obtained trivially once that for  $e$  is known. Furthermore, note that these equations are invariant under the simultaneous transformations

$$\xi \rightarrow -\xi \quad \text{and} \quad v \rightarrow -v, \quad (11.22)$$

so that it is necessary to solve them only in one of the half-planes  $\xi \in [0, \pm 1]$  in order to know the solution in the whole interval  $\xi \in [-1, 1]$ .

Under generic conditions, the system of equations (11.19)–(11.21) does not have analytic solutions and a numerical approach is therefore necessary to study the properties of these equations. However, before illustrating the result of such numerical solutions, it is useful to

## 498 Relativistic Hydrodynamics of Non-Selfgravitating Fluids

consider some analytic expressions which can be derived under suitable conditions for the velocity equation. In fact, in the limit of small velocities [*i.e.*, neglecting terms  $\mathcal{O}(v^2, vdv/d\xi)$ ], we can approximate Eq. (11.20) as

$$(c_s^2 - \xi^2) \frac{dv}{d\xi} = -j \frac{v}{\xi} c_s^2, \quad (11.23)$$

which can be integrated analytically and has solution

$$v(\xi) = \frac{A}{\xi^j} (\xi^2 - c_s^2)^{j/2} = A \left( 1 - \frac{c_s^2}{\xi^2} \right), \quad (11.24)$$

where  $A$  is an integration constant and where the second equality refers to a spherical self-similar flow (*i.e.*,  $j = 2$ ). Expression (11.24) clearly shows that  $v \rightarrow 0$  for  $\xi \rightarrow c_s$  and indeed this represents an *attractor* for the solutions of Eq. (11.20), which will all go through the point  $\xi = c_s$ ,  $v = 0$ . In the neighbourhood of this point, which is commonly referred to as the *sonic radius*, we can Taylor expand in terms of the small quantity  $|u| \ll 1$ , such that (Kurki-Suonio, 1985)

$$\xi = c_s + u, \quad d\xi = du. \quad (11.25)$$

In this way, neglecting terms  $\mathcal{O}(v^2, uv, vdv/d\xi, udv/d\xi)$ , we can approximate Eq. (11.20) as

$$[u - v(1 - c_s^2)] \frac{dv}{du} = j \frac{v}{2}. \quad (11.26)$$

Equation (11.26) is most easily solved in terms of  $u(v)$  and yields the following analytic solution near the sonic radius

$$u = Av - \frac{2}{3}v \ln |v| = \xi - c_s, \quad (11.27)$$

where  $A > 0$  for  $\xi > c_s$  and  $A < 0$  for  $\xi < c_s$ . Further expanding the logarithmic term for  $v > 0$  and  $v \ll 1$ , we obtain

$$v \simeq \frac{3}{3A+2}(\xi - c_s) = B(\xi - c_s), \quad (11.28)$$

where  $B := 3/(3A+2)$  is a new constant coefficient such that  $B > 0$  for  $\xi > c_s$  and  $B < 0$  for  $\xi < c_s$ . Stated differently, for expanding systems (*i.e.*,  $\xi > 0$ ) the fluid velocity  $v$  decreases/increases linearly in the left/right neighbourhood of  $\xi = c_s$ , while it decreases/increases linearly in the left/right neighbourhood of  $\xi = -c_s$  for contracting systems (*i.e.*,  $\xi < 0$ ) (see Fig. 11.1).

The results of the numerical integration of Eqs. (11.20) and (11.21) are shown in Fig. 11.1 for the velocity  $v(\xi)$  and in Fig. 11.2 for the energy density  $e(\xi)$ , which we assume to be always positive. Note that all of the self-similar solutions for the velocity go through the points  $v(+\xi_s) = 0 = v(-\xi_s)$ , where  $\pm \xi_s := \pm c_s$  are the sonic radii and the solution is approximated as in Eq. (11.28). However, as we will comment below, also other values for the velocity are possible in the neighbourhood of  $\xi_s$ .

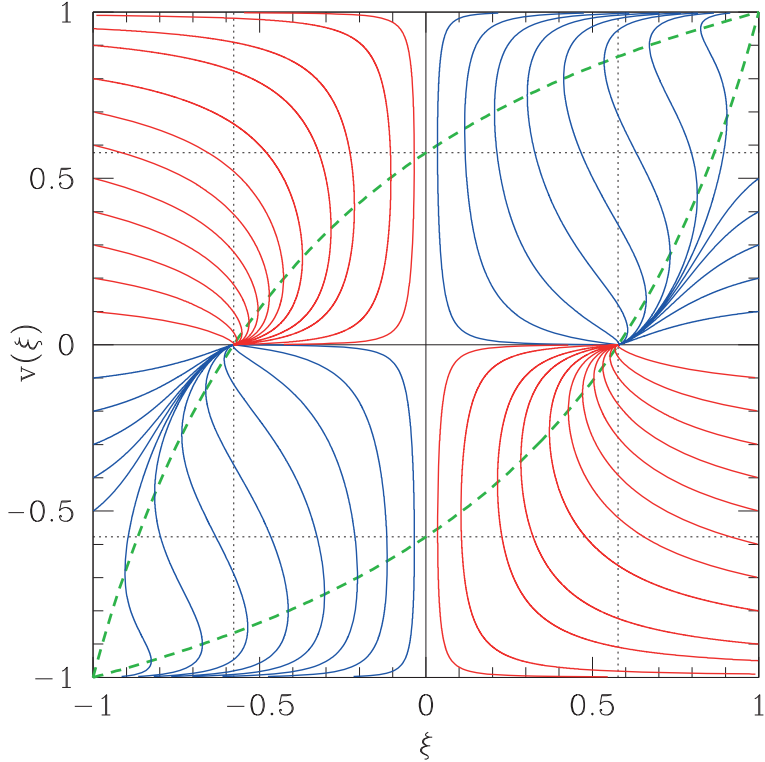


**Fig. 11.1** Solutions of the similarity equations (11.20)–(11.21) for the velocity  $v(\xi)$ . The portions of the diagrams relative to positive values of  $\xi$  refer to expanding systems (e.g., bubbles), while those relative to negative values of  $\xi$  refer to contracting systems (e.g., drops). The green dashed lines represent the set of points where the fluid velocity is equal to the speed of sound as measured by an observer moving at  $\xi$  [cf. Eq. (11.30)], while the dotted lines mark the sound speed for an ultrarelativistic fluid ( $\xi_s = 1/\sqrt{3}$ ). Parts of the solutions in these panels are used to build the self-similar velocity in Fig. 11.3 [adapted from Rezzolla *et al.* (1995)].

For concreteness, in Fig. 11.2 we have considered the case of an ultrarelativistic fluid, such that  $p = \frac{1}{3}e$  and the sound speed is simply  $c_s = 1/\sqrt{3} \simeq 0.577$  (see Section 2.4.4) (Kurki-Suonio, 1985; Rezzolla *et al.*, 1995).<sup>3</sup>

The green dashed lines in Fig. 11.1 represent the points for which the derivative  $dv/d\xi$  in (11.20) diverges, that is, they mark the values for which

$$(c_s^2 \xi^2 - 1)v^2 + 2\xi(1 - c_s^2)v + c_s^2 - \xi^2 = 0. \quad (11.29)$$

The roots of Eq. (11.29) are given by the two velocities

<sup>3</sup>This choice for the sound speed is common in the study of self-similar solutions for phase transitions in the early universe (Steinhardt, 1982; Kurki-Suonio, 1985; Rezzolla *et al.*, 1995), when the plasma is radiation dominated and the equation of state is that of an ultrarelativistic fluid (see the discussion in Section 2.4.9).

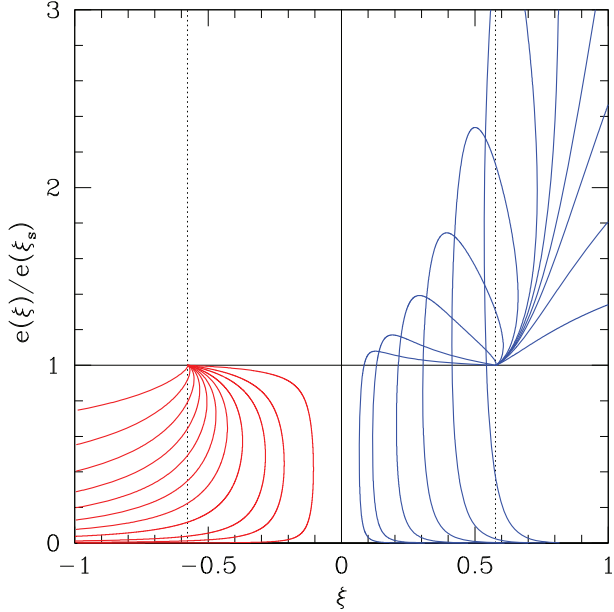


**Fig. 11.2** The same as in Fig. 11.1 but for the energy density  $e(\xi)$  (right panel), which we assume to be always positive. Parts of the solutions in these panels are used to build the self-similar energy-density profiles in Fig. 11.4 [adapted from Rezzolla *et al.* (1995)].

$$v = \frac{\xi \pm c_s}{1 \pm c_s \xi}, \quad (11.30)$$

which, being the special-relativistic formula for velocity composition, expresses the fact that the fluid velocity, as measured by an observer moving at  $\xi$ , is equal to the speed of sound.

A physical solution for  $v(\xi)$  cannot be extended across these points, since it would then be double valued and a discontinuity needs to be introduced. The upper right quadrant of Fig. 11.1 shows the solutions of the similarity equations for an expanding system, *i.e.*, for  $v > 0$ ,  $\xi > 0$ . Similarly, the upper left quadrant shows the equivalent solutions for a contracting system, *i.e.*, for  $v > 0$ ,  $\xi < 0$ . The lower quadrants reflect the invariance under the transformation  $\xi \rightarrow -\xi$ ,  $v \rightarrow -v$  [*cf.* Eq. (11.22)] and provide the corresponding solutions for negative values of the fluid velocity; note that these solutions do not necessarily represent physically realistic configurations.

The only self-similar flow solution in Figs. 11.1 and 11.2 which can be taken to extend to all values of  $\xi$  is the trivial solution, *i.e.*,  $v = 0$ ,  $e = \text{const.}$ , which is obviously of limited interest. Any other solution must be the result of a “patching” of different solution curves with the joints being either via a *weak discontinuity* (*i.e.*, where the function is continuous but has a derivative of some order which is not continuous), or via a *discontinuity* proper (*i.e.*, where the function itself is not continuous). The first type of discontinuity is relevant in the case of the edge of a rarefaction or compression wave (see Section 4.4.2), while the second one occurs in the case of shocks or combustion fronts (see Section 4.4.3). To focus our discussion,

in the following two sections we will discuss how to construct such self-similar solutions for an expanding bubble (Section 11.1.2) or a contracting fluid drop (Section 11.1.3).

### 11.1.2 Self-similar hydrodynamics of a bubble

A rather interesting and non-trivial class of self-similar solutions for an expanding spherically symmetric flow, *i.e.*, with  $\xi > 0$ ,  $v > 0$ , is offered by *boiling bubbles*. We recall that boiling bubbles are also known as *vapour bubbles*, *i.e.*, bubbles whose interiors contain only vapour of the surrounding fluid and that are normally nucleated in a superheated fluid. They should be distinguished from *cavitation bubbles*, which are also vapour bubbles but nucleated within a cool fluid (*e.g.*, behind the propellers in a ship). The classical (Newtonian) dynamics of *boiling bubbles* within first-order phase transitions has been widely studied and represents valuable background for the discussion of the growth of the low-temperature phase bubbles during cosmological phase transitions. The main results of the theory of Newtonian bubble dynamics are contained in a number of works (Plessset and Zwick, 1954; Plessset and Prosperetti, 1977), which represent further development of the work of Rayleigh (1917).

Because of the different properties of the fluid and of the vapour, the bubble surface should be treated as a reaction front (see Chapter 5) and the self-similar growth of bubbles in first-order cosmological transitions has been considered in the literature both in the case of *detonation fronts* (see Section 5.3) and of *deflagration fronts* (see Section 5.4). Of course, for bubble expansion, self-similar motion can appear only when the bubble radius is small enough so that there is no interaction between neighbouring bubbles, but also large enough so that the corrections introduced by the *surface tension* effects are negligible.<sup>4</sup> This is also the regime we consider here.

In the case of a spherical growing bubble whose surface is represented by a weak deflagration front, the point  $\xi = 0$  represents the centre of the bubble at any given time,  $\xi_s = c_s$  is the *expanding sonic radius* and determines the position of a possible weak discontinuity, while  $\xi = 1$  is the edge of the future light cone. Symmetry requires that the conditions  $v = 0$ ,  $e = \text{const.}$  should be satisfied at the centre of the bubble and a similar requirement could be made for the unperturbed fluid far away from the surface of the bubble. As a consequence, for a non-trivial solution, *at least* two discontinuities should be introduced in the interval  $\xi \in [0, 1]$ , and junction conditions for the conservation of energy, momentum and particle number need to be imposed across any discontinuity which is not a weak one.

As discussed in Section 5.4, weak deflagrations are under-determined reaction fronts for which a further equation, usually establishing the motion of the interface in terms of the local fluid conditions, needs to be provided. Doing this restricts the analysis to those situations for which a reasonable knowledge of the properties of the interface exists. For a cosmological first-order phase transition there are a number of ways of accomplishing this, *e.g.*, either by means of the energy flux across the phase interface (Miller and Pantano, 1989) or by using a parameter related to the entropy production across the front (Ignatius *et al.*, 1994). What is relevant is that it is in principle possible to specify an expression for the velocity of the deflagration front, so that the construction of a self-similar solution can be obtained after imposing

<sup>4</sup>For a bubble in equilibrium, the surface tension  $\sigma$  is proportional to the pressure jump between the interior and exterior pressures and the radius  $R_b$  of the bubble, *i.e.*,  $\sigma = 2R_b(p_{\text{in}} - p_{\text{out}})$  (Degrand and Kajantie, 1984). Since the surface tension has the dimensions of the inverse of a length, it introduces a length-scale  $\sim \sigma^{-1}$ , thus breaking the self-similarity condition.

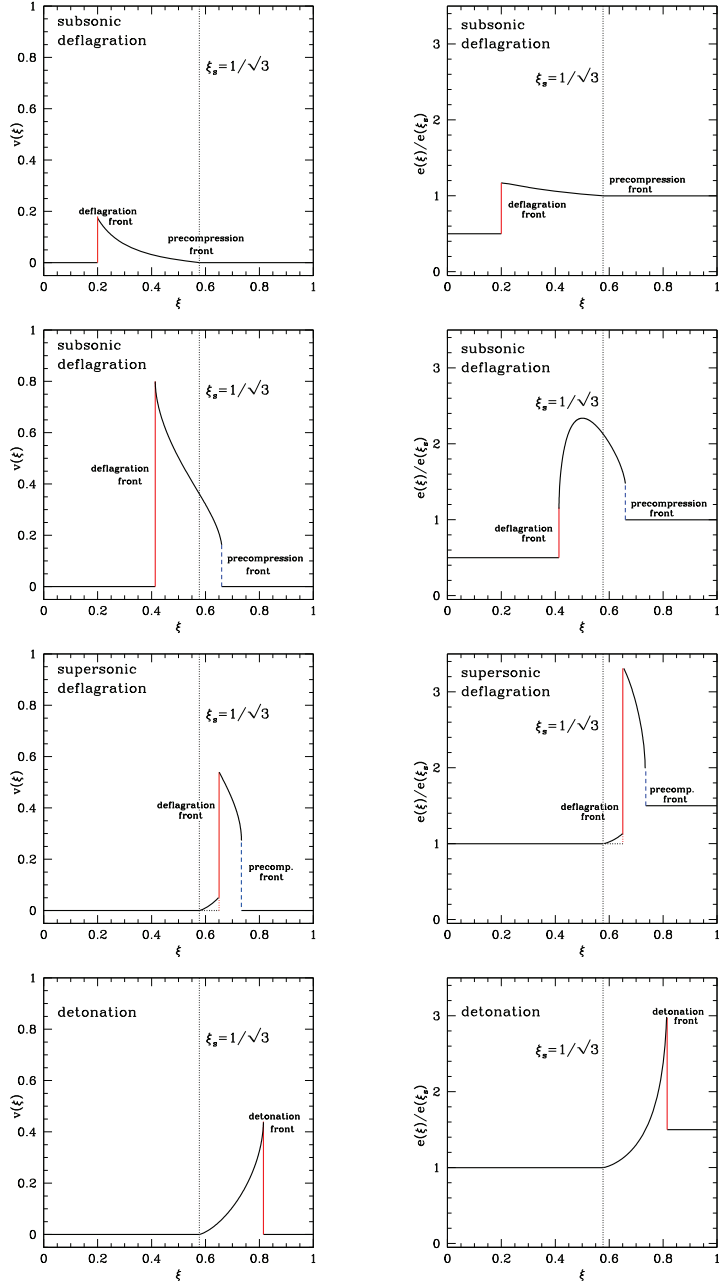


**Fig. 11.3** Examples of expanding-bubble solutions obtained by patching together pieces of the self-similar solutions (11.20)–(11.21). For increasingly large velocities of the deflagration front (vertical red line), the left panels show the self-similar velocity field, while the right panels show the self-similar energy density. In all panels the vertical dotted line marks the expanding sonic radius. Starting from the top, the first two rows refer to *subsonic deflagrations*, the third row refers to a *supersonic deflagration*, and the bottom row refers to a *detonation*. An ultrarelativistic equation of state  $p = \frac{1}{3}e$  has been assumed.

junction conditions across suitably located discontinuity surfaces. In this way, it is possible to obtain the whole one-parameter family of solutions for a spherical weak deflagration where the parameter is set by the velocity of the interface.

Figure 11.3 shows some representative examples of expanding-bubble solutions which can be constructed by patching together pieces of the self-similar solutions (11.20)–(11.21). The left panels of Fig. 11.3 refer to the velocity field, while the right panels refer to the energy density (normalised to its value at the sonic point), for increasingly large velocities of the deflagration front (shown as a vertical red line). In all panels the vertical dotted line marks the sonic radius for an ultrarelativistic equation of state. Note that because these solutions refer to expanding fronts, one should think of the reaction fronts as moving from left to right.

Starting from the top, the first two rows refer to a *subsonic deflagration*, in which the deflagration front is always subsonic, but the precompression front can either be moving at the sound speed (first row), or at supersonic velocities (second row). In the first case, the velocity at the precompression front is continuous but with discontinuous derivatives, while in the second case the velocity itself is discontinuous. In either case, the solution has two discontinuity surfaces. Note also that while the velocity is zero both at the centre of the bubble and at large distances, the energy density cannot be the same in the states ahead and behind the deflagration front and, in particular, we have assumed that  $e_2 > e_1$ . This example is in close analogy with what could have happened in the early universe during a first-order quark–hadron phase transition, in which case, subsonic deflagrations would have been produced as a consequence of a small supercooling of the quark phase (Kurki-Suonio, 1985; Miller and Pantano, 1989; Rezzolla *et al.*, 1995). Furthermore, the energy density before the deflagration front need not be monotonic and can also decrease ahead of the front.

The third row, on the other hand, refers to a *supersonic deflagration*, as indicated by the fact that in this case both the reaction front and the precompression front are to the right of the sonic radius. Interestingly, depending on the specific properties of the deflagration process, the state behind the deflagration front can be set to have zero velocity (dotted lines to the left of the deflagration front) or nonzero velocity, in which case the flow is followed by a rarefaction wave whose tail is at the sonic point (solid lines to the left of the deflagration front). As a result, supersonic deflagrations should have *at least two* discontinuities.

As mentioned in Section 5.4, supersonic deflagrations take place when the strength of the precompression shock front is rather large and the fluid is in a highly energetic state before being processed by the reaction front. In this case, the speed of the deflagration front increases steadily, catching up with the precompression front, thus leading to a single supersonic reaction front which compresses and accelerates the fluid. This is clearly a *detonation* and it is shown in the fourth row of Fig. 11.3. Note the analogies between the subsonic deflagration solution in the first row with the supersonic detonation of the last row, with the presence, in either case, of a weak discontinuity at the sonic radius.

Finally, we note that within a cosmological context, the possibility of obtaining a supersonic deflagration or a detonation depends on the degree of supercooling of the high-temperature phase, *e.g.*, the quark phase in a quark–hadron phase transition. As the degree of supercooling reached by the metastable phase is increased, the resulting reaction front goes from a subsonic deflagration, over to a supersonic deflagration and up to a detonation (Steinhardt, 1982; Gyulassy *et al.*, 1984; Kurki-Suonio, 1985; Miller and Pantano, 1990).

### 11.1.3 Self-similar hydrodynamics of a drop

An equally interesting class of self-similar solutions for a spherically symmetric contracting flow, *i.e.*, with  $\xi < 0$ ,  $v > 0$ , is represented by *evaporating drops*, which share several of the features discussed in the previous section for expanding bubbles. Also in this case we expect that self-similar motion should set in when the drop radius is reasonably smaller than the mean distance among neighbouring drops so that one can neglect the interaction among them, but large enough so that surface tension effects are negligible. At the same time, however, the new and different boundary conditions emerging in the dynamics of drops can influence significantly the properties of reaction fronts, preventing the occurrence of some of the solutions encountered for expanding systems, most notably, detonations (see below). The first self-similar solutions for a relativistic evaporating drop were presented by Rezzolla *et al.* (1995), where additional information on these systems can be found.

Note that because in the case of a contracting system we need to consider solutions with  $\xi < 0$ , the use of a positive time coordinate would lead us to describe the physical system in terms of negative spatial dimensions. This rather counter-intuitive point of view can be abandoned if we consider time as progressing through *negative* values and tending to zero as the radius of the contracting drop tends to zero. In this way, the instant  $t = 0$  represents an asymptotic limit in time and we can describe the dynamics of the system since  $t = -\infty$ . The point  $\xi = 0$  then represents the centre of the drop at any given time,  $\xi_s = -c_s$  marks, in analogy with what we have seen for a bubble, the position of the *contracting sonic radius*, and  $\xi = -1$  finally represents the edge of the past light cone.

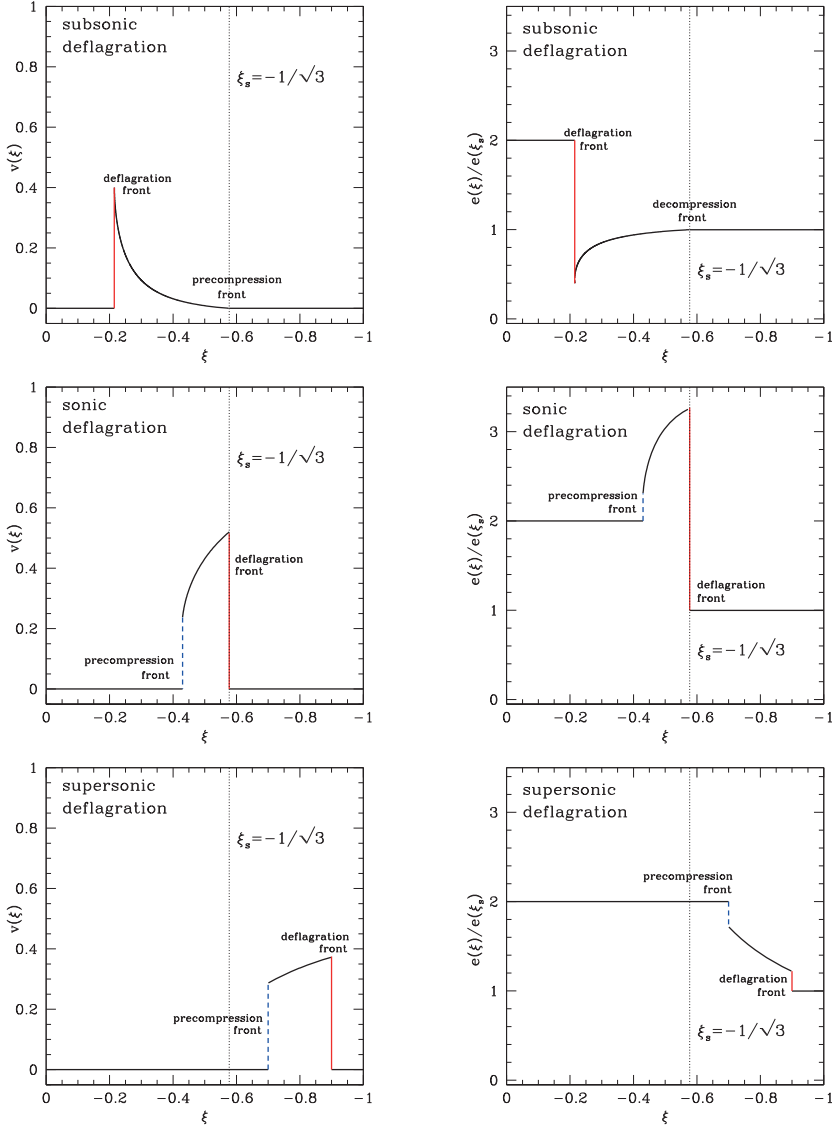
As for growing bubbles, self-similar solutions for contracting drops moving as weak deflagrations can be found only after a further equation, establishing the motion of the front, is provided. When this is done and the velocity of the deflagration front is specified, junction conditions across the relevant discontinuity surfaces, together with the continuous solution of Eqs. (11.20) and (11.21), provide the whole one-parameter family of self-similar solutions.

Figure 11.4 shows some representative examples of contracting-drop solutions, *e.g.*, a burning drop of an inflammable fluid, which can be constructed by patching together pieces of the self-similar solutions (11.20)–(11.21). As in Fig. 11.3, the left panels refer to the velocity field, while the right panels refer to the energy density (normalised to its value at the sonic radius), for increasingly large velocities of the deflagration front (shown as a vertical red line). In all panels the vertical dotted line marks the contracting sonic radius. Note that because these solutions refer to contracting fronts, one should think of the reaction fronts as moving from right to left.

The first row, in particular, refers to a subsonic deflagration, with the reaction front proceeding at subsonic speeds and the energy density inside the drop being larger than that at large distances. The self-similar solution behind the front is represented by a simple wave,<sup>5</sup> in which the fluid that was accelerated and expanded by the deflagration front is progressively slowed down until it is eventually taken to rest at the contracting sonic radius.

Although not obvious, the solution for the fluid behind the deflagration front is effectively going through a *compression* wave. This is due to the fact that a fluid element crossing the deflagration front is strongly decompressed from its original state, but is subsequently and

<sup>5</sup>We recall that a simple wave is defined as a region of smooth flow which is always adjacent to a flow region of constant state. Examples of simple waves are rarefaction and compression waves (see the discussion in Section 4.4.1).



**Fig. 11.4** Representative examples of contracting-drop solutions that can be constructed by patching together pieces of the self-similar solutions (11.20)–(11.21). For increasingly large velocities of the deflagration front (vertical red line), the left panels show the self-similar velocity field, while the right panels show the self-similar energy density. In all panels the vertical dotted line marks the contracting sonic radius. Starting from the top, the first row refers to a *subsonic deflagration*, the second row to a *sonic deflagration*, which is however *not possible* in practice, while the bottom row refers to a *supersonic deflagration*. Note the presence of a precompression front that is behind/ahead of the reaction front in the case of subsonic/supersonic deflagrations.

progressively compressed up to the value in the unperturbed fluid as it moves away from the front. At the sonic radius, the solution joins via a weak discontinuity onto another one with zero velocity and constant energy density, with the value of the latter coinciding with the background value of the reacted fluid (see the top right panel of Fig. 11.4). As a result, the sonic radius can be thought of as tracing the edge of the perturbed flow region at any given time.

When looking at the upper quadrants of the diagrams in Fig. 11.1, one may think that another self-similar solution is possible for a weak deflagration besides the one shown in the first row of Fig. 11.4. In fact, since all of the solutions of (11.20) and (11.21) converge from the right to the point  $\xi = -c_s$  with positive first derivatives [*cf.*, Eq. (11.28)], and since the only requirement for a weak deflagration front is that it has to be subsonic, one may be tempted to introduce a precompression front ahead of the reaction front, as shown in the second row of Fig. 11.4, where the deflagration is chosen to be at the sonic radius. While mathematically acceptable, this solution is *not possible* in reality. Such a precompression front, in fact, would be a genuine discontinuity and it cannot move at subsonic speeds, as shown instead in Fig. 11.4. As a result, a drop contracting via a weak deflagration cannot be preceded by a precompression front. This is an important feature and points out that there are *at most* two discontinuities in the self-similar solution for a contracting drop. This is quite different from what we have seen for the solution of growing bubbles, where there had to be *at least* two discontinuities.

The limitations discussed above for the presence of a precompression shock ahead of a contracting subsonic deflagration front cease to apply when the latter is supersonic. In this case, in fact, the supersonic deflagration front can be preceded by another supersonic but slower precompression shock front, with the joint between the two being given by the continuous solutions of Eqs. (11.20) and (11.21). The fluid ahead of the precompression shock, as well as the fluid behind the supersonic deflagration front, would then be at rest with constant but different energy densities. As a result, solutions for supersonic evaporating drops can be constructed out of deflagration waves and representative solutions for this case are shown in the third row of Fig. 11.4.

Finally, it is important to emphasise that, since the fluid behind the deflagration front is at rest and since the latter is supersonic, the fluid behind the deflagration front moves at supersonic speed relative to the front rest frame (*i.e.*,  $v_2 = -v_{\text{def}} > c_s$ ). This means that the solution of a supersonic deflagration drop would effectively correspond to a supersonic strong deflagration which, however, cannot be realised in practice because of negative entropy production (see the discussion in Section 5.4). As a consequence, it is *not possible to construct self-similar solutions for drops moving as detonations*. A simple way of proving this result is by recalling that a supersonic deflagration naturally evolves into a detonation when the deflagration front “catches up” with its supersonic precompression shock front (see Section 5.4). However, if this were the case, then the self-similar solution would differ from a trivial solution only at the detonation front, which would effectively represent the only feature of the otherwise unphysical solution, *i.e.*, the solution would be constant but for an infinitesimal discontinuity. Another way of reaching the same conclusion is to realise that if a discontinuity surface were to be added behind the detonation front, then it would correspond to a “decompressive shock”, which is an impossible process in practice.

We conclude this section with a concrete example of a one-parameter family of self-similar subsonic deflagration solutions illustrated in Fig. 11.5. These curves have been computed for

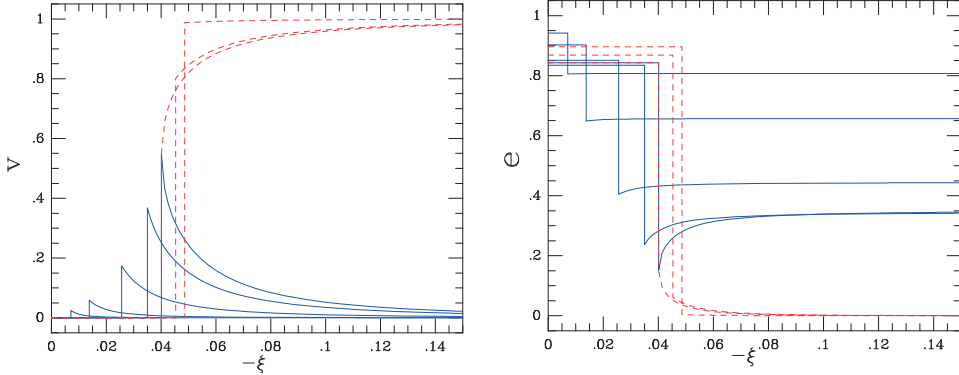


**Fig. 11.5** Self-similar curves for the velocity and the energy density profiles of relativistic subsonic deflagrations. The solid lines represent weak deflagration solutions with the rightmost solid curve being a Chapman–Jouguet deflagration. The dashed curves represent strong deflagration solutions beyond the Chapman–Jouguet limit and are physically forbidden [adapted from Rezzolla *et al.* (1995)].

the self-similar motion of a disconnected quark drop during the cosmological quark–hadron phase transition (Rezzolla *et al.*, 1995). The velocity of the interface has been determined after specifying the temperature in the hadron phase adjacent to the phase interface. This temperature, which is also related to the degree of supercooling of the high-temperature phase, effectively ranges between  $0.95 T_c$  for the leftmost solid curve and  $0.61 T_c$  for the rightmost solid curve, where  $T_c$  is the critical temperature for the transition (Rezzolla *et al.*, 1995).

Different curves correspond to different values of the velocity of the drop surface. Solid lines are representative of subsonic weak deflagration waves, while dashed lines show the solution of subsonic strong deflagrations (note that the sonic radius is at  $-\xi_s = 1/\sqrt{3} \simeq 0.577$ ). The rightmost solid curve and the leftmost dashed curve correspond to adjacent but distinct values of the velocity of the drop surface. In particular, the rightmost solid curve represents a *Chapman–Jouguet deflagration*, for which the front moves at the sound speed relative to the fluid behind (see Section 5.4). This marks the transition from subsonic weak deflagrations (which are physically realistic) to subsonic strong deflagrations (which are physically forbidden). Note that the solution for the medium behind a subsonic strong deflagration front differs from that behind a subsonic weak deflagration front since in this case the medium behind the front is accelerated away, reaching a velocity approaching the velocity of light at infinity, while the energy density decreases through a rarefaction wave, going to zero at infinity.

## 11.2 Relativistic blast waves

Another very common use of self-similar solutions is in the study of “*blast waves*”, that is, of very rapid flows produced after an impulsive injection of large amounts of energy in a uniform medium at rest. Since these conditions are common to ordinary explosions, it is not surprising that this problem has a long history [see, *e.g.*, Zel'dovich and Raizer (2002)] and that, in contrast to the detonations discussed in the previous section, is usually treated without

the complication of considering a chemical change in the states of the fluid ahead and behind the discontinuity. Astrophysical phenomena also offer a number of scenarios in which self-similar blast waves are expected to be produced and indeed blast waves have been studied extensively when interpreting the phenomenology behind *gamma-ray bursts* (GRBs) (see also Section 11.9). These are extremely energetic astrophysical events, detected in the gamma-ray band of the electromagnetic spectrum and capable of accelerating particles to Lorentz factors of the order of  $W \sim 10^2 - 10^3$  (Gehrels *et al.*, 2009). A particularly important self-similar solution for relativistic blast waves was found early on by Blandford and McKee (1976) and still represents, at least as a first approximation, an excellent tool to understand the most salient aspects of an impulsive ejection of energy in a uniform medium [see, *e.g.*, Sari (2006) for some recent developments].

For simplicity, in our derivation we will neglect radiative losses and use spherical coordinates to rewrite the one-dimensional special-relativistic hydrodynamic equations of conservation of rest mass, momentum and energy, *i.e.*, Eqs. (11.5)–(11.7) with  $j = 2$ , as

$$\partial_t(W\rho) + \frac{1}{r^2}\partial_r(r^2\rho Wv) = 0, \quad (11.31)$$

$$\partial_t[(e+p)W^2v] + \frac{1}{r^2}\partial_r[r^2(e+p)W^2v^2] + \partial_rp = 0, \quad (11.32)$$

$$\partial_t[(e+pv^2)W^2] + \frac{1}{r^2}\partial_r[r^2(e+p)W^2v] = 0. \quad (11.33)$$

Given the extreme conditions of the fluid in the blast wave, it is reasonable to assume an ultrarelativistic equation of state (see Section 2.4.4), where  $p = \frac{1}{3}e$ , so that Eqs. (11.32)–(11.33) become

$$\partial_t(pW^4) + v\partial_r(pW^4) = W^2\partial_tp, \quad (11.34)$$

$$\partial_t\ln(p^3W^4) + v\partial_r\ln(p^3W^4) = -\frac{4}{r^2}\partial_r(r^2v). \quad (11.35)$$

As a result of the explosion, which we assume to release a large amount of energy over a very short period, a strong spherical shock is formed which propagates outwards with velocity  $V_s$  and corresponding Lorentz factor  $W_s = (1 - V_s^2)^{-1/2}$ . The Rankine–Hugoniot junction conditions given by Eqs. (4.136)–(4.139) are helpful to derive a number of relations that are particularly convenient for this problem. For example, expression (4.136) provides the Lorentz factor of the unshocked fluid as measured in the shock frame and thus effectively provides  $W_s$ . Similarly, expression (4.138) gives the Lorentz factor  $W_{ab}$  of the shocked fluid with respect to the unshocked one, so that using Eq. (4.138) together with (4.139) we obtain<sup>6</sup>

$$W_{ab}^2 = \frac{4(1 - W_s^2)W_s^2}{9(1 - 8W_s^2/9)}, \quad (11.36)$$

and in the ultrarelativistic limit of  $W_s \gg 1$  the jump in the Lorentz factor across the shock is simply given by

$$W_{ab}^2 = \frac{1}{2}W_s^2. \quad (11.37)$$

<sup>6</sup>We recall that the indices  $a$  and  $b$  refer to the states “ahead” and “behind” the shock, respectively (see Section 4.4.3).

Similarly, it is easy to see that in the same limit the following conditions hold for the pressure and rest-mass density in the shocked fluid

$$p_b = \frac{2}{3} h_a \rho_a W_s^2, \quad (11.38)$$

$$\rho_b W_{ab} = 2 \rho_a W_s^2. \quad (11.39)$$

We can now seek a self-similar solution by expressing Eqs. (11.37)–(11.39) through three unknown functions  $f(\chi)$ ,  $g(\chi)$  and  $h(\chi)$  of a (yet undetermined) similarity variable  $\chi$ , and such that the pressure, the Lorentz factor and the rest-mass density in the shocked fluid are given by<sup>7</sup>

$$p_b = \frac{2}{3} h_a \rho_a W_s^2 f(\chi), \quad (11.40)$$

$$W_{ab}^2 = \frac{1}{2} W_s^2 g(\chi), \quad (11.41)$$

$$\rho_b W_{ab} = 2 \rho_a W_s^2 h(\chi). \quad (11.42)$$

The search for the correct choice for the similarity variable  $\chi$  can be aided by considering the same spherical blast-wave problem in Newtonian physics. This was done originally by Sedov (1959), who assumed that at time  $t = 0$  an amount of energy  $E$  is released isotropically in an ambient medium at rest with uniform rest-mass density  $\rho_0$ . After the explosion, a shock front of radius  $R_s(t)$ , propagates outwards and it is not difficult to deduce, on the basis of dimensional arguments only, that the functional behaviour of the shock radius should behave as

$$R_s(t) = \bar{a} \left( \frac{Et^2}{\rho_0} \right)^{1/5}, \quad (11.43)$$

where  $\bar{a}$  is a constant coefficient. The shock speed is then trivially obtained through a time derivative of  $R_s(t)$  and thus amounts to

$$V_s = \frac{dR_s}{dt} = \frac{2}{5} \left( \frac{R_s}{t} \right) = \frac{2}{5} \bar{a} \left( \frac{E}{\rho_0 t^3} \right)^{1/5}. \quad (11.44)$$

Expressions (11.43) and (11.44) represent the classical *Sedov solution* for a spherical blast wave and show that, apart from the constant coefficient  $\bar{a}$ , it is possible to derive the correct propagation speed without having to solve a differential equation, simply collecting the three distinct dimensional quantities in the problem, namely  $E$ ,  $\rho_0$  and  $t$ .

Using the Sedov solution as a guideline also in a relativistic framework, we can assume that the shock four-velocity  $u_s^\mu = dx^\mu/d\tau = W_s(1, V_s, 0, 0)$  [cf. Eq. (1.113)] has a radial component given by

$$u_s^1 = \frac{dx_s^1}{d\tau} = \frac{2}{5} \left( \frac{x_s^1}{\tau} \right), \quad (11.45)$$

where  $\tau$  is the proper time in the rest frame of the shock front, while the proportionality constant  $2/5$  has been chosen to preserve the Newtonian limit (11.44). Equation (11.45) can then be integrated directly to give

<sup>7</sup>The function  $h$  should not be confused with the specific enthalpy for which we have used the same symbol in the rest of the book.

## 510 Relativistic Hydrodynamics of Non-Selfgravitating Fluids

$$x_s^1 = A\tau^{2/5}, \quad (11.46)$$

with  $A$  an integration constant. It is then straightforward to deduce that

$$\frac{dx_s^1}{d\tau} = \frac{2}{5}A\tau^{-3/5} = W_s V_s, \quad (11.47)$$

and finally that

$$\tau = \left( \frac{5V_s W_s}{2A} \right)^{-5/3}. \quad (11.48)$$

The time interval in the Eulerian frame,  $dt$ , will be Lorentz dilated when compared to the proper-time interval in the shock frame,  $d\tau$ , so that [cf., Eq. (1.110)]

$$dt = W_s d\tau, \quad (11.49)$$

which, combined with Eq. (11.48) and in the limit of  $W_s \gg 1$ , can be integrated to yield

$$W_s \propto t^{-3/2}, \quad V_s \propto (1 - t^3)^{1/2}, \quad (11.50)$$

for  $t > 0$ . Once again, note how the simplicity of the physical conditions has allowed us to derive expressions (11.50), which are the relativistic equivalents of Eq. (11.44) and which describe the deceleration of the shock front with time, without actually solving the equations of motion. As a result, we can compute the expression for the shock radius simply as

$$R_s(t) = \int_0^t V_s(t') dt' \approx \int_0^t \left( 1 - \frac{1}{2W_s^2} \right) dt' = t \left( 1 - \frac{1}{8W_s^2} \right), \quad (11.51)$$

for  $t < 8W_s^2$ . Next, in the rest frame of the shock we introduce the coordinate  $d$  to measure distances from the shock, from which we build the local similarity variable [cf., Eq. (11.8)]

$$\xi := \frac{d}{\tau}. \quad (11.52)$$

The distance  $d$  will be Lorentz contracted when compared to the equivalent expression in the Eulerian frame, *i.e.*,

$$d = W_s(R_s - r), \quad (11.53)$$

where  $r$  is the radial coordinate having its origin at the centre of the blast wave. We can use Eq. (11.48) in the limit of high  $W_s$  to show that the similarity variable in the Eulerian frame is given by

$$\xi = W_s^2 \left( \frac{R_s - r}{R_s} \right). \quad (11.54)$$

We are now ready to determine the similarity variable  $\chi$  appearing in expressions (11.40)–(11.42) and regulating the solution of the pressure, Lorentz factor and rest-mass density behind the shock. Following Blandford and McKee (1976), we set it to be

$$\chi = 1 + 8\xi = 1 + 8W_s^2 \left( \frac{R_s - r}{R_s} \right) \approx (1 + 8W_s^2) \left( 1 - \frac{r}{t} \right), \quad (11.55)$$

so that  $\chi = 1$  corresponds to  $r = R_s$ , and  $\chi = 1 + 8W_s^2$  to  $r = 0$ . Furthermore, it is now possible to perform a change of coordinates from  $(r, t)$  to  $(W_s^2, \chi)$  through the relations

$$\frac{\partial}{\partial \ln t} = -3 \frac{\partial}{\partial \ln W_s^2} + [4(2W_s^2 - \chi) + 1] \frac{\partial}{\partial \chi}, \quad (11.56)$$

$$t \frac{\partial}{\partial r} = -[1 + 8W_s^2] \frac{\partial}{\partial \chi}, \quad (11.57)$$

and thus express the solution entirely as a function of  $\chi$  and  $W_s^2$ , the latter playing the role of a free parameter. Using these transformations, we can now write the three equations (11.31), (11.34) and (11.35) as ordinary differential equations for the three unknown functions  $f$ ,  $g$  and  $h$ , *i.e.*,

$$\frac{1}{g} \frac{d \ln f}{d \chi} = \frac{16 + g\chi}{4(4 - 8g\chi + g^2\chi^2)}, \quad (11.58)$$

$$\frac{1}{g} \frac{d \ln g}{d \chi} = \frac{17 - 5g\chi}{4(4 - 8g\chi + g^2\chi^2)}, \quad (11.59)$$

$$\frac{1}{g} \frac{d \ln h}{d \chi} = \frac{38 - 18g\chi + g^2\chi^2}{4(4 - 8g\chi + g^2\chi^2)(2 - g\chi)}. \quad (11.60)$$

Surprisingly enough, once supplemented with the boundary conditions at the shock front resulting from Eqs. (11.37)–(11.39), *i.e.*,

$$g(1) = f(1) = h(1) = 1, \quad (11.61)$$

the differential equations (11.58)–(11.60) admit the following analytic *Blandford–McKee solution* for the pressure, Lorentz factor and rest-mass density in a self-similar relativistic blast wave

$$f = \chi^{-17/12}, \quad g = \chi^{-1}, \quad h = \chi^{-7/4}. \quad (11.62)$$

The functional behaviour of the solution is reported in Fig. 11.6, whose left panel shows  $f$ ,  $g$  and  $h$  as a function of the similarity variable  $\chi$ , so that  $\chi = 1$  represents the position of the shock and  $\chi = 1 + 8W_s^2$  the centre of the blast wave. The right panel shows instead the same quantities as a function of dimensionless radial position  $r/R_s$  for a shock with  $W_s = 50$ , and where the inset shows a magnified view just behind the shock. Note that the slope of  $f$ ,  $g$  and  $h$  near the shock front increases with the shock speed and that, for instance, more than 90% of the mass and energy is confined in a very small region behind the shock, with a radial width  $\Delta r/R_s \sim 9/(8W_s^2)$  (see Problem 1).

Using the Blandford–McKee solution (11.62) it is then possible to derive all of the quantities in the shocked fluid, so that, for instance, the specific internal energy for an ultrarelativistic fluid  $\epsilon = e/\rho - 1 \sim e/\rho$  and is given by [*cf.*, Eq. (2.206)]

$$\epsilon = \frac{3p}{\rho} = \frac{h_a W_s}{\sqrt{2}} \left( \frac{f(\chi)g(\chi)^{1/2}}{h(\chi)} \right) = \frac{h_a W_s}{\sqrt{2}\chi^{1/6}}. \quad (11.63)$$

As mentioned above, we have so far considered the case in which the blast wave is produced by an impulsive injection of energy  $E$  over a very short time, thus leading to a shock evolution given by Eq. (11.50). However, more general conditions can also be considered,

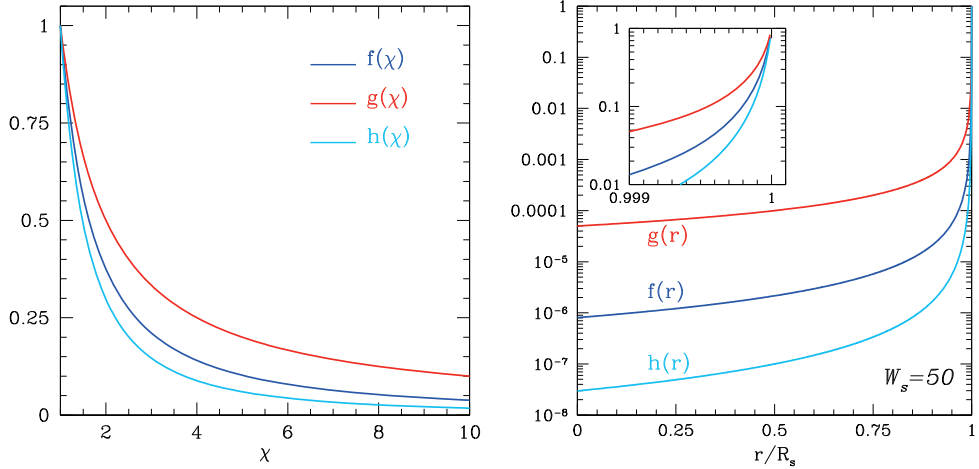


**Fig. 11.6** Dependence of the functions  $f$ ,  $g$ , and  $h$  behind the shock and expressing the pressure, the Lorentz factor and the rest-mass density, respectively. The left panel shows the quantities as a function of the similarity variable  $\chi$ , while the right panel shows the same quantities as a function of dimensionless radial position  $r/R_s$  for a shock with  $W_s = 50$ .

which can account, for instance, for blast-wave solutions with a sustained energy supply. In this case, Eq. (11.50) is generalised by a power law of the type  $W_s^2 \propto t^{-m}$ , with  $m \leq 3$ , where  $m = 3$  represents the case considered so far, in which the energy supply is only instantaneous or “impulsive”. As a result, the governing equations (11.58)–(11.60) take the more general form (Blandford and McKee, 1976)

$$\frac{1}{g} \frac{d \ln f}{d \chi} = \frac{8(m-1) - (m-4)g\chi}{(m+1)(4-8g\chi + g^2\chi^2)}, \quad (11.64)$$

$$\frac{1}{g} \frac{d \ln g}{d \chi} = \frac{(7m-4) - (m+2)g\chi}{(m+1)(4-8g\chi + g^2\chi^2)}, \quad (11.65)$$

$$\frac{1}{g} \frac{d \ln h}{d \chi} = \frac{2(9m-8) - 2(5m-6)g\chi + (m-2)g^2\chi^2}{(m+1)(4-8g\chi + g^2\chi^2)(2-g\chi)}, \quad (11.66)$$

whose solution is in general found via direct numerical integration.

As a final remark we note that although very simplified, the Blandford–McKee solution highlights that extreme physical conditions can be generated near the shock front and that, in astrophysical scenarios, these can be responsible for efficient mechanisms of particle acceleration. In turn, these trigger non-thermal emission processes, such as synchrotron radiation and inverse Compton scattering, which are often revealed by astronomical observations. It is indeed in combination with a proper treatment of the radiation produced near the shock that blast-wave models have been used extensively in the literature to interpret the phenomenology of GRBs (Cohen *et al.*, 1998; Chiang and Dermer, 1999; Downes *et al.*, 2002) and other explosive astrophysical phenomena.

### 11.3 Spherical flows onto and out of a compact object

The problem of spherical flows onto and out of a compact gravitating object is both a very old and a very important one. While many of the details of these flows depend sensitively on the precise boundary conditions of the flow at spatial infinity and near the compact object, some very general results about the properties of these flows can be derived from the simple considerations that we will make in this section. Because of the qualitative nature of these considerations and of the corresponding definitions, we can consider the simpler case of Newtonian flows and yet not lose generality in our conclusions.

Let us assume therefore a stationary spherical flow with positive-definite radial velocity  $u := |dr/dt|$  on a gravitating compact object of mass  $M$ , with the fluid obeying a polytropic equation of state (see Section 2.4.7). As discussed in Section 3.6.1, under these conditions the equations of motion reduce to the Bernoulli equation (3.96), which for a polytropic fluid we rewrite as

$$\frac{1}{2}u^2 + \phi + h_N = \text{const.} = \frac{1}{2}u^2 - \frac{M}{r} + \frac{c_s^2}{\Gamma - 1}, \quad (11.67)$$

where  $h_N := \epsilon + p/\rho$  is the Newtonian specific enthalpy and we have expressed the gravitational potential and the sound speed as  $\phi = -M/r$ ,  $c_s^2 = \Gamma p/\rho$ , respectively. The system is then closed via the continuity equation, which allows us to express the mass accretion rate  $\dot{M}$  as

$$\dot{M} := \frac{dM}{dt} = 4\pi r^2 \rho u = \text{const.} \quad (11.68)$$

For any fixed radial position  $r = \bar{r}$ , the Bernoulli equation (11.67) represents an ellipse in the  $(u, c_s)$  plane, such as those indicated with dashed lines in Fig. 11.7 (Zel'dovich and Novikov, 1971; Novikov and Thorne, 1973). Similarly, the continuity equation (11.68) represents a hyperbola in the same plane, as indicated by the solid lines in Fig. 11.7.<sup>8</sup> The flow will exist if both equations are satisfied at any radius  $\bar{r}$ , so that the condition for the existence of a solution can be translated geometrically into whether or not the ellipses and hyperbolas meet for a given  $\bar{r}$ . Clearly this intersection does not always happen as, for instance, when the mass accretion rate is too large or too small. Because no smooth solution can be found under these conditions, we will not consider this possibility further. Rather, we will consider as relevant those cases in which the ellipses and hyperbolas do meet at each radial position.

When an intersection is possible, this can happen in two different ways:

- (i) at two distinct points, each on either side of the line  $u = c_s$  bisecting the  $(u, c_s)$  plane (red dashed line in Fig. 11.7) and then also at a single point on the  $u = c_s$  line, where the two curves meet tangentially; the radial position where this happens represents the *sonic radius* and, as will be discussed in the next section, it also represents a critical point for the solution.
- (ii) at two distinct points, each on either side of the line  $u = c_s$ , but never at a single point.

The loci of these intersections are shown respectively in the right and left panels of Fig. 11.8 and lead to the four different classes of spherical flows onto and out of a compact object. The

<sup>8</sup>Strictly speaking, the continuity equation (11.68) represents a hyperbola only for  $\Gamma = 3$ . For any other value of  $\Gamma$ , the equation will scale like  $u \propto Mr^{-2}c_s^{-2/(\Gamma-1)}$ .

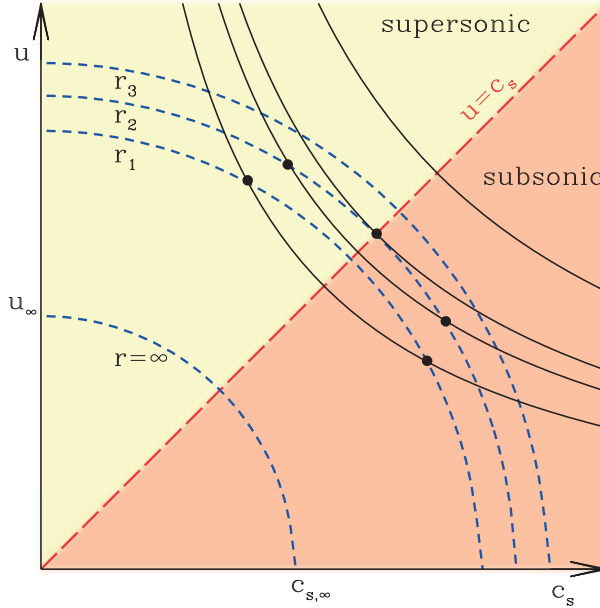


**Fig. 11.7** Geometric characterisation of the spherical flows onto and out of a compact object. On the  $(u, c_s)$  plane, the Bernoulli and the continuity equations (11.67)–(11.68) at fixed radii represent ellipses and hyperbolae, respectively, while the sonic line  $u = c_s$  distinguishes supersonic flows from subsonic flows. For a solution to exist, at any radial position the ellipse and the hyperbola must intersect, either at two points (one above and one below the sonic line) or at a single point. The loci of these intersections represent the four different types of solution.

first one is referred to as an *accretion* solution and is characterised by a flow which is subsonic at large distances (*i.e.*,  $u_\infty/c_{s,\infty} < 1$ ),<sup>9</sup> it reaches sound speed at the sonic radius and then becomes supersonic near the compact object (*i.e.*,  $u_0/c_{s,0} > 1$ );<sup>10</sup> this solution is indicated as (A) in the left panel of Fig. 11.8. The second type of flow is referred to as an *outflow* (or *wind*) solution and is characterised by a flow which is subsonic near the compact object (*i.e.*,  $u_0/c_{s,0} < 1$ ), reaches the sound speed at the sonic radius, and then becomes supersonic at large distances (*i.e.*,  $u_\infty/c_{s,\infty} > 1$ ); this solution, which is commonly observed in massive stars, is indicated as (B) in the left panel of Fig. 11.8. Note that when the compact object is a black hole and not a star, this type of flow cannot extend from the black-hole horizon, where the flow must necessarily be ingoing and supersonic.

The remaining two solutions are considerably less common astrophysically and have the basic property of being always either supersonic or subsonic. The first one is referred to as the *ejection* solution and requires suitable accelerating mechanisms near the compact object to produce a supersonic flow even in the strong gravitational field regime; this solution is

<sup>9</sup>Note that we are here assuming that there is fluid at infinity and hence  $c_{s,\infty} \neq 0$ . Furthermore, while  $u_\infty = 0$  is the most sensible condition for the flow velocity at infinity, it can in principle also be nonzero.

<sup>10</sup>We generically indicate with an index 0 either the surface of the compact object or the event horizon in the case of a black hole.

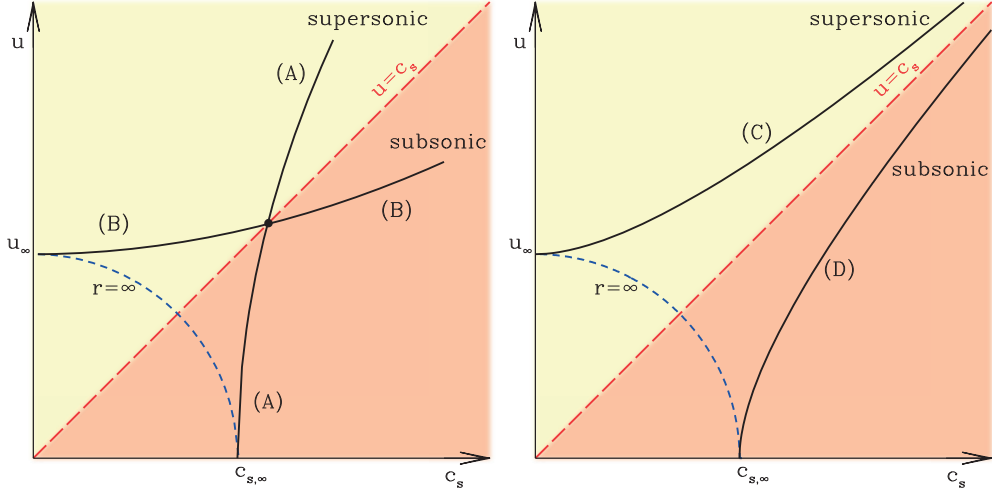


**Fig. 11.8** The four possible classes of spherical flows onto and out of a compact object. *Left panel:* (A) *accretion* solution, characterised by a flow which is subsonic at large distances, it equals the sound speed at the sonic radius and then becomes supersonic near the compact object; (B) *outflow* or *wind* solution, characterised by a flow which is supersonic at large distances, it equals the sound speed at the sonic radius and then becomes subsonic near the compact object. *Right panel:* (C) *ejection* solution, characterised by a flow which is always supersonic; (D) *settling* solution, characterised by a flow which is always subsonic at large distances, reaches the sound speed at the sonic radius and then becomes subsonic near the compact object.

indicated as (C) in the right panel of Fig. 11.8. The last solution is instead referred to as the *settling* solution and requires a suitable decelerating mechanism near the compact object. While this mechanism could be offered by the resistance exerted by the radiation pressure, a settling flow cannot extend down to the horizon in the case of a black hole. It can however exist as a global solution in the case of a neutron star (Medvedev and Narayan, 2001). This solution is indicated as (D) in the right panel of Fig. 11.8.

In the table below we summarise the four different types of spherical flows which are possible onto and out of a compact object.

$$\begin{array}{ll}
 \text{(A)} & u_\infty/c_{s,\infty} < 1, u_0/c_{s,0} > 1 : \text{ accretion solution} \\
 \text{(B)} & u_\infty/c_{s,\infty} > 1, u_0/c_{s,0} < 1 : \text{ outflow solution} \\
 \text{(C)} & u_\infty/c_{s,\infty} > 1, u_0/c_{s,0} > 1 : \text{ ejection solution} \\
 \text{(D)} & u_\infty/c_{s,\infty} < 1, u_0/c_{s,0} < 1 : \text{ settling solution}
 \end{array} \quad (11.69)$$

All of the considerations made so far ignore the fact that as the fluid approaches the compact object it will emit radiation, whose momentum exchange with the inflowing matter will resist the flow. Taking this into account requires a proper redefinition of the Bernoulli equation and does not have a simple general solution. However, an approximate but important limit can be obtained in the case in which the fluid is represented by a fully ionised plasma in which protons and electrons are coupled through electromagnetic forces. The Newtonian gravitational force

## 516 Relativistic Hydrodynamics of Non-Selfgravitating Fluids

exerted by the spherically symmetric object of mass  $M$  on the coupled proton electron pair at distance  $r$  is given by

$$F_{\text{grav}} = \frac{GM(m_p + m_e)}{r^2} \approx \frac{GMm_p}{r^2}, \quad (11.70)$$

where  $m_p \simeq 1.67 \times 10^{-30}$  g is the rest mass of the proton, which is much larger than the mass of the electron  $m_e$ . At equilibrium, such a force must be balanced by the force exerted through the radiation pressure, which can be written in terms of the radiation energy flux  $f$  as (Rybicki and Lightman, 1986)

$$F_{\text{rad}} = \frac{f}{c} \sigma_{T,e}, \quad (11.71)$$

where  $\sigma_{T,e} \simeq 6.65 \times 10^{-25}$  cm $^2$  is the Thomson cross-section of electrons.<sup>11</sup> After introducing the luminosity  $L$  to write the radiation flux as  $f = L/4\pi r^2$ , we can equate the two forces (11.70) and (11.71), to obtain what is known as the *Eddington luminosity*, *i.e.*,

$$\begin{aligned} L_{\text{Edd}} &:= 4\pi GcM \left( \frac{m_p}{\sigma_{T,e}} \right) \simeq 3.46 \times 10^{-22} \left( \frac{M}{M_\odot} \right) \\ &\simeq 1.26 \times 10^{38} \left( \frac{M}{M_\odot} \right) \text{ erg s}^{-1} \simeq 3.27 \times 10^4 \left( \frac{M}{M_\odot} \right) L_\odot, \end{aligned} \quad (11.72)$$

where the first line provides the luminosity in geometrised units (*cf.* Appendix A) and  $L_\odot \simeq 3.85 \times 10^{33}$  erg s $^{-1}$  is the luminosity of the Sun. Equation (11.72) establishes a limit, *i.e.*, the *Eddington limit*, to the luminosity produced through accretion onto a source of mass  $M$ . This limit is most often expressed in terms of the corresponding *Eddington accretion rate* (for convenience we report the speed of light explicitly)

$$\begin{aligned} \dot{M}_{\text{Edd}} &:= \frac{L_{\text{Edd}}}{c^2} \simeq 3.46 \times 10^{-22} \left( \frac{M}{M_\odot} \right) \\ &\simeq 1.39 \times 10^{17} \left( \frac{M}{M_\odot} \right) \text{ g s}^{-1} \simeq 2.21 \times \left( \frac{M}{10^9 M_\odot} \right) M_\odot \text{ yr}^{-1}, \end{aligned} \quad (11.73)$$

where again the first line provides the accretion rate in geometrised units (and is obviously the same as  $L_{\text{Edd}}$ ) and where  $M_\odot \simeq 1.98 \times 10^{33}$  g. Both the Eddington luminosity and the Eddington accretion rate should be taken as approximate upper limits to the luminosity and accretion rate in stationary conditions. While most astronomical objects are below these limits, specific conditions can lead to super-Eddington luminosities and accretion rates.

## 11.4 Spherical accretion onto a black hole

The problem of spherically symmetric accretion onto a selfgravitating object was first discussed by Bondi (1952) within a Newtonian treatment and the corresponding solution is

<sup>11</sup>We recall that the Thomson cross-sections of electrons and protons are related as  $\sigma_{T,p} = (m_e/m_p)^2 \sigma_{T,e}$ .

known as the *Bondi solution*. As anticipated in the previous section, this solution is characterised by the presence of a critical *accretion radius* marking the transition of the flow from subsonic to supersonic velocities. The relativistic generalisation of the Bondi solution is due to Michel (1972) and is often referred to as the *Michel solution*. While this solution is idealised, it can be described in great part analytically, thus with the obvious benefit that it allows for a better interpretation of the properties of the solution. As we will see later on, the possibility of having analytic solutions decreases very rapidly with the complexity of the hydrodynamic problem. We provide here a presentation of the properties of spherical accretion flows following in part the analysis made by Straumann (1984), adjusting for the different signature (and correcting some typos).

Consider therefore the metric of a Schwarzschild black hole (1.221) with mass  $M$ , which for convenience we rewrite as

$$ds^2 = -(1 - 2M/r) dt^2 + (1 - 2M/r)^{-1} dr^2 + r^2 d\Omega^2, \quad (11.74)$$

and a flow which is also spherically symmetric and stationary, *i.e.*,  $u^\mu = (u^t, u^r, 0, 0)$ . The continuity equation (3.52) can then be written as [*cf.*, Eq. (1.166)]

$$\partial_\mu(\sqrt{-g}\rho u^\mu) = 0 = \partial_r(r^2\rho u), \quad (11.75)$$

where we have introduced  $u := -u^r$  to avoid an overloading of indices when we consider this quantity at infinity or at the event horizon. Also, since we will restrict our attention to *accretion solutions*, it follows that  $u > 0$  by construction and the mass accretion rate is a positive number. However, the recovery of the wind solution is straightforward after a suitable change of the boundary conditions at the black-hole event horizon and at spatial infinity.

As discussed in Section 3.6.2, the existence of a timelike Killing vector  $\xi^\mu = (1, 0, 0, 0)$  reduces the momentum-conservation equation to the Bernoulli equation (3.98)

$$\mathcal{L}_u(hu_\mu\xi^\mu) = 0 = \partial_r(hu_\mu\xi^\mu) = \partial_r(h\mathcal{W}), \quad (11.76)$$

where, we recall,  $\mathcal{L}_u$  stands for the Lie derivative along  $u$  (see Section 1.5.1) and  $h$  is the specific enthalpy [*cf.*, Eq. (2.141)]. Using the normalisation condition  $u^\mu u_\mu = -1$  [*cf.*, Eq. (3.2)] and the fact that for a Schwarzschild metric  $g_{tt} = -1/g_{rr}$ , we obtain that

$$\mathcal{W} := u_\mu\xi^\mu = u_t = g_{tt}u^t = -(-g_{tt} + u^2)^{1/2} = -\left(1 - \frac{2M}{r} + u^2\right)^{1/2}. \quad (11.77)$$

The quantity  $\mathcal{W}$  is closely related to the Lorentz factor  $W$  of the fluid velocity as measured by an *Eulerian observer* (*i.e.*, an observer stationary at a given spatial position), and in the spacetime (11.74) this relation is given by [*cf.*, Eq. (7.21)]

$$\mathcal{W} = -(-g_{tt})^{1/2}W = -(g_{rr})^{-1/2}W. \quad (11.78)$$

Direct integration of the continuity equation (11.75) and of the Bernoulli equation (11.76) then leads to the mass accretion rate (or simply “accretion rate”)  $\dot{M}$  and to the Bernoulli constant to be expressed respectively as

**518 Relativistic Hydrodynamics of Non-Selfgravitating Fluids**

$$\dot{M} = 4\pi r^2 \rho u = \text{const.}, \quad (11.79)$$

$$-h\mathcal{W} = \text{const.} = h_\infty = \frac{e_\infty + p_\infty}{\rho_\infty}, \quad (11.80)$$

where we have assumed that  $p_\infty \neq 0, \rho_\infty \neq 0$  but  $u_\infty = 0$ . Taking now full differentials of Eqs. (11.79) and (11.80), we obtain the two equations

$$\frac{d\rho}{\rho} + \frac{du}{u} + 2\frac{dr}{r} = 0, \quad (11.81)$$

$$\frac{d(e+p)}{e+p} + \frac{d\mathcal{W}}{\mathcal{W}} - \frac{d\rho}{\rho} = 0, \quad (11.82)$$

which can be combined into a single (Pfaffian) equation

$$\frac{d(e+p)}{e+p} + \left(1 + \frac{u^2}{\mathcal{W}^2}\right) \frac{du}{u} + \left(2 + \frac{M}{r\mathcal{W}^2}\right) \frac{dr}{r} = 0, \quad (11.83)$$

after removing the dependence of the rest-mass density  $d\rho/\rho$  and after using the relation

$$\frac{d\mathcal{W}}{\mathcal{W}} = \frac{M}{r^2\mathcal{W}} dr + \frac{u}{\mathcal{W}} du. \quad (11.84)$$

If the fluid is isentropic, we can use the definition of the sound speed (2.172) to rewrite the first term in Eq. (11.83) as

$$\begin{aligned} \frac{d(e+p)}{e+p} &= \frac{d(\rho h)}{\rho h} = \left[1 + \left(\frac{\partial \ln h}{\partial \ln \rho}\right)_s\right] d\ln \rho \\ &= (1 + c_s^2) d\ln \rho = -(1 + c_s^2) \left(\frac{du}{u} + 2\frac{dr}{r}\right), \end{aligned} \quad (11.85)$$

where we have used Eq. (11.81) in the last equality. Inserting (11.85) in (11.83) we finally obtain a single differential equation for the fluid velocity

$$\left(c_s^2 - \frac{u^2}{\mathcal{W}^2}\right) \frac{du}{u} + \left(2c_s^2 - \frac{M}{r\mathcal{W}^2}\right) \frac{dr}{r} = 0. \quad (11.86)$$

The solutions of Eq. (11.86) are curves in the  $(u, r)$  plane representing the solution from spatial infinity, where it is defined in terms of  $u_\infty, c_{s,\infty}$  (*i.e.*,  $p_\infty, \rho_\infty$ ),  $\mathcal{W}_\infty$ , down to the black-hole event horizon,  $u_h, a_h$  (*i.e.*,  $p_h, \rho_h$ ),  $\mathcal{W}_h$ . Denoting the Lorentz factor as [*cf.* Eq. (7.21)]

$$W := (-g_{tt})^{1/2} u^t = -\mathcal{W}/(-g_{tt})^{1/2}, \quad (11.87)$$

the quantity  $v^r := u^r/W$  then represents the coordinate component of the fluid velocity as measured by an Eulerian observer [*cf.* Eq. (7.22)]. As a result, the square of the Eulerian radial velocity is given by

$$v^2 := v^r v_r = g_{rr}(v^r)^2 = \frac{u^2}{\mathcal{W}^2}. \quad (11.88)$$

Stated differently, the quantity  $v := u/|\mathcal{W}|$  represents the fluid velocity as measured by an observer stationary at a given radial position. Using the definition (11.77), the right-hand side

of expression (11.88) indicates that at the event horizon (*i.e.*,  $r = 2M$ )  $\mathcal{W}_h = -u_h$  and hence  $v_h = 1$ , as expected for any fluid crossing the horizon. At the same time, note that the coordinate Eulerian velocity vanishes at the horizon, *i.e.*,  $(v^r)_h = 0$ , and that although  $u$  cannot go to zero at the horizon, it could be zero if the accretion were to happen on a stellar surface.

With this in mind, it is easy to recognise that the quantity  $(c_s^2 - u^2/\mathcal{W}^2)$  appearing in the first term of (11.86) effectively measures whether the flow relative to an Eulerian observer is *subsonic*, *i.e.*,  $c_s^2 > u^2/\mathcal{W}^2$ , or *supersonic*, *i.e.*,  $c_s^2 < u^2/\mathcal{W}^2$ . It is also clear that a solution that will start subsonically at infinity with  $u_\infty/\mathcal{W}_\infty = 0$  and will have to become supersonic  $u_h/|\mathcal{W}_h| = 1$  at the horizon, will necessarily pass through a *sonic point*, where  $u/|\mathcal{W}| = c_s$ , where the slope of the solution  $du/dr$  will diverge [*cf.* Eq. (11.86)].<sup>12</sup> To avoid this, a suitable regularity condition must be imposed at the sonic radius for the mass accretion rate.

Since the accretion rate (11.79) is constant in space, its asymptotic value is difficult to determine given that near spatial infinity  $r \rightarrow \infty$  and  $u \rightarrow 0$ . As a way around this, we introduce the *accretion radius*,  $r_{\text{acc}}$ , as the radial position marking the region of the fluid which is in sonic contact. In practice, this is defined as the radius at which the relativistic *escape velocity*  $v_{\text{esc}}$  (which interestingly coincides with the Newtonian expression)

$$v_{\text{esc}} := \left( \frac{2M}{r} \right)^{1/2}, \quad (11.89)$$

is equal to the local sound speed, that is

$$r_{\text{acc}} := \frac{2M}{c_s^2}. \quad (11.90)$$

Using expression (11.90) we can easily evaluate the accretion radius on the basis of the physical conditions of the accreting flow and hence impose a regularity condition (see Problem 2 to estimate the accretion radius for the candidate supermassive black hole at the centre of our Galaxy, Sgr A\*).

### **Solution at the critical radius.**

Because  $r_{\text{acc}}$  is never diverging unless we are in vacuum (note we are assuming  $c_{s,\infty} \neq 0$ ), we can now parameterise the radial coordinate in terms of the accretion radius, *i.e.*,  $r \rightarrow \zeta r_{\text{acc}}$  and the fluid velocity in terms of the local sound speed, *i.e.*,  $u \rightarrow \eta c_s$ . With these parameterisations we can express the asymptotic value of the mass flux  $r^2 \rho u$  as

$$\lim_{r \rightarrow \infty} r^2 \rho u = \lambda \left( \frac{M}{c_{s,\infty}^2} \right)^2 \rho_\infty c_{s,\infty}, \quad (11.91)$$

where  $\lambda := 4\zeta^2 \eta$  is just a coefficient to parameterise the accretion rate (11.79) as

$$\dot{M} = 4\pi \lambda \left( \frac{M}{c_{s,\infty}^2} \right)^2 \rho_\infty c_{s,\infty}. \quad (11.92)$$

<sup>12</sup>If we relax the condition of isentropy in the fluid, then *discontinuous* solutions are also allowed, at least in principle. In this case, a subsonic solution at spatial infinity is joined via a shock to another subsonic solution near the event horizon. Although such “standing-shock” solutions are not frequently encountered in numerical simulations of accretion flows, a detailed discussion of their properties can be found in Chakrabarti (1990).

In essence, expression (11.92) states that once the properties of the fluid at infinity are fixed via  $\rho_\infty$  and  $c_{s,\infty}$ , the mass accretion rate of a black hole of mass  $M$  depends only on the value chosen for  $\lambda$ . In the reasonable case in which  $u_\infty = 0$  (*i.e.*, a fluid at rest at infinity), different values of  $\lambda$  will define different curves in the  $(r, u)$  plane, each labelled by a specific value of  $\lambda$ , but only one of these will yield a solution that is regular at the sonic point. This is obtained after requiring that at the sonic point *both* conditions

$$c_{s,c}^2 = \frac{u_c^2}{\mathcal{W}_c^2}, \quad 2c_{s,c}^2 = \frac{M}{r_c \mathcal{W}_c^2} \quad (11.93)$$

are satisfied or, equivalently, using Eq. (11.77), that the following conditions are met

$$u_c^2 = \frac{1}{2} \frac{M}{r_c}, \quad c_{s,c}^2 = \frac{u_c^2}{1 - 3u_c^2}. \quad (11.94)$$

In order to express these conditions in an explicit form we need to specialise our considerations to an equation of state and, because of the condition of isentropy, we can make use of the simple polytropic equation of state  $p = K\rho^\Gamma$  (see Section 2.4.7). The sound speed in this case can be written as [*cf.*, Eq. (2.249)]

$$c_s^2 = \left( \frac{1}{\Gamma K \rho^{\Gamma-1}} + \frac{1}{\Gamma - 1} \right)^{-1}, \quad (11.95)$$

so that

$$\Gamma K \rho^{\Gamma-1} = \frac{(\Gamma - 1)c_s^2}{\Gamma - 1 - c_s^2}. \quad (11.96)$$

We can therefore write the Bernoulli equation (11.80) as

$$\left( 1 + \frac{\Gamma K}{\Gamma - 1} \rho^{\Gamma-1} \right)^2 \left( 1 - \frac{2M}{r} + u^2 \right) = \left( 1 + \frac{\Gamma K}{\Gamma - 1} \rho_\infty^{\Gamma-1} \right)^2, \quad (11.97)$$

or, after using expression (11.96), as

$$\begin{aligned} \left( 1 - \frac{c_{s,\infty}^2}{\Gamma - 1} \right)^2 &= \left( 1 - \frac{c_{s,c}^2}{\Gamma - 1} \right)^2 \left( \frac{1}{1 - 3u_c^2} \right) \\ &\simeq \left( 1 - \frac{c_{s,c}^2}{\Gamma - 1} \right)^2 (1 + 3c_{s,c}^2), \end{aligned} \quad (11.98)$$

where in the second equality we have assumed that the critical radius is sufficiently far from the black hole so that  $\mathcal{W}_c \simeq -1$  and thus  $u_c \simeq c_{s,c}$ . The following analysis will need to distinguish the case in which the fluid has polytropic index  $\Gamma \neq 5/3$  from those cases in which instead  $\Gamma = 5/3$ , as for a degenerate relativistic fluid (see the discussion in Section 2.4.7).

First we express the right-hand side of expression (11.98) in a series expansion in terms of  $c_{s,c} \ll 1$ , and thus derive that the value of the sound speed at the sonic point is given by

$$c_{s,c} = \begin{cases} c_{s,\infty} \left( \frac{2}{5-3\Gamma} \right)^{1/2} & \text{for } \Gamma \neq 5/3, \\ \left( \frac{2}{3} c_{s,\infty} \right)^{1/2} & \text{for } \Gamma = 5/3, \end{cases} \quad (11.99)$$

where the expression for  $\Gamma = 5/3$  requires the expansion to be truncated at second order. The radial position of the critical radius is then straightforward to compute recalling that far from the black hole  $u_c^2 \simeq c_{s,c}^2 \simeq \frac{1}{2}M/r$ , so that

$$r_c = \begin{cases} \left( \frac{5-3\Gamma}{4} \right) \frac{M}{c_{s,\infty}^2} & \text{for } \Gamma \neq 5/3, \\ \frac{3}{4} \frac{M}{c_{s,\infty}} & \text{for } \Gamma = 5/3. \end{cases} \quad (11.100)$$

Note that  $r_c|_{\Gamma=5/3} \ll r_c|_{\Gamma \neq 5/3}$ , thus locating the sonic radius much closer to the horizon when  $\Gamma = 5/3$ . Furthermore, using as reasonable asymptotic sound speed a value of  $c_{s,\infty} \simeq 10^{-4}$ , expressions (11.100) indicate that  $r_c \simeq 10^8 M$  when  $\Gamma \neq 5/3$ , thus confirming the assumption that the fluid is only mildly relativistic at the sonic point.

Next, we calculate the mass accretion rate at the sonic point, which, by definition, is

$$\dot{M}_c := 4\pi r_c^2 \rho_c u_c, \quad (11.101)$$

and approximate the sound speed at the sonic point in terms of the rest-mass density as  $c_{s,c}^2 \simeq \Gamma K \rho_c^{\Gamma-1}$  [cf. Eq. (11.95)], so that

$$\left( \frac{c_{s,c}}{c_{s,\infty}} \right)^2 \simeq \left( \frac{\rho_c}{\rho_\infty} \right)^{\Gamma-1}. \quad (11.102)$$

Using now the two equivalent expressions for the mass accretion rate (11.92) and (11.101), we can determine the *critical accretion rate* via the parameter

$$\lambda_c \simeq \frac{1}{4} \left( \frac{5-3\Gamma}{2} \right)^{(3\Gamma-5)/[2(\Gamma-1)]}. \quad (11.103)$$

To fix ideas, let us consider the typical conditions of the interstellar medium, which has a density of 1 particle  $\text{cm}^{-3} \sim 10^{-24} \text{ g cm}^{-3}$ , a sound speed  $c_{s,\infty} \sim 10 \text{ km s}^{-1}$ , so that the corresponding critical mass accretion rate for a fluid with  $\Gamma = 5/3$  is

$$\dot{M}_c \simeq 2.17 \times 10^{-24} \left( \frac{M}{M_\odot} \right)^2 \left( \frac{\rho_\infty}{10^{-24} \text{ g cm}^{-3}} \right) \left( \frac{c_{s,\infty}}{10 \text{ km s}^{-1}} \right)^{-3} M_\odot \text{ yr}^{-1}. \quad (11.104)$$

This is much smaller than the maximum accretion rate, *i.e.*, the Eddington accretion rate  $\dot{M}_{\text{Edd}} \simeq 2.2 \times 10^{-9} (M/M_\odot) M_\odot \text{ yr}^{-1}$ , expressing the rate above which the radiation pressure is so large that it prevents accretion [cf. Eq. (11.73)].

**Solution at the horizon.**

The analysis carried out so far for quantities at the sonic point can be extended to the horizon and once again we need to distinguish the case of generic values of the polytropic index from the case when  $\Gamma = 5/3$ . In the first case, *i.e.*, for  $\Gamma \neq 5/3$ , we can first compute the velocity profile by recalling that Eq. (11.97) can be written as [*cf.*, Eq. (11.96)]

$$\left(\frac{\Gamma - 1}{\Gamma - 1 - c_s^2}\right)^2 \left(1 - \frac{2M}{r} + u^2\right) = \left(\frac{\Gamma - 1}{\Gamma - 1 - c_{s,\infty}^2}\right)^2. \quad (11.105)$$

Since inside the sonic radius the fluid velocity is much larger than the sound speed, we can take  $c_s^2 \rightarrow 0$  in Eq. (11.105), which then reduces to

$$1 - 2M/r + u^2 \simeq 1, \quad (11.106)$$

which once evaluated at the horizon yields the obvious result that  $u_h = 1$ . Once again, since the mass accretion rate is constant, we can write its expression at the horizon as [*cf.*, Eqs. (11.92), (11.103)]

$$4u_h\rho_h = \lambda_c \frac{\rho_\infty}{c_{s,\infty}^3}, \quad (11.107)$$

from which we can compute the rest-mass density at the horizon as

$$\rho_h = \frac{\lambda_c}{4} \frac{\rho_\infty}{u_h c_{s,\infty}^3} = \frac{\lambda_c}{4} \frac{\rho_\infty}{c_{s,\infty}^3}. \quad (11.108)$$

Interestingly, for reasonable values of the asymptotic sound speed, the density increase at the horizon is not infinite, but of order  $\rho_h/\rho_\infty \simeq 10^{11}$ . Even more interesting is the determination of the density profile, which can be computed after expressing the fluid velocity inside the sonic radius as  $u^2 \simeq 2M/r$  [*cf.*, Eq. (11.106)], and after using the mass accretion rate to obtain

$$\frac{\rho}{\rho_\infty} = \frac{\lambda_c}{\sqrt{2}} \left(\frac{M}{r c_{s,\infty}^2}\right)^{3/2}. \quad (11.109)$$

Note that because the flow velocity is not constant, the density near the horizon scales like  $r^{-3/2}$  rather than like  $r^{-2}$ , as for a free-falling flow with constant final velocity.

In the case in which  $\Gamma = 5/3$ , instead, Eq. (11.99) reduces to  $u^2 \simeq c_s^2 \simeq c_{s,\infty}^2$ , so that we can evaluate the Bernoulli constant (11.80) at the horizon as

$$u_h \left(1 + \frac{\Gamma K}{\Gamma - 1} \rho_h^{\Gamma - 1}\right) \simeq 1. \quad (11.110)$$

We can remove the dependence on the rest-mass density in (11.110) by noting that in this case  $\lambda_c \simeq 1/4$  [*cf.*, Eq. (11.103)], so that Eq. (11.108) then yields

$$\rho_h \simeq \frac{1}{16} \frac{\rho_\infty}{u_h c_{s,\infty}^3}. \quad (11.111)$$

Using now Eq. (11.111) we can rewrite (11.110) as

$$\begin{aligned} 1 &\simeq u_h \left[ 1 + \frac{c_{s,\infty}^{5-3\Gamma}}{\Gamma-1} \left( \frac{\lambda_c}{4u_h} \right)^{\Gamma-1} \right] \\ &\simeq u_h + \frac{3}{2^{11/3}} u_h^{1/3}. \end{aligned} \quad (11.112)$$

Solving for  $u_h$  finally gives the desired estimate  $u_h \simeq 0.78$  and thus  $\rho_h \simeq 0.08 (\rho_\infty / c_{s,\infty}^3)$ . This result may appear surprising but this is just because we are looking at the radial component of the four-velocity. However, at the horizon,  $\mathcal{W}_h = -u_h$  [cf., Eq. (11.77)] and the Eulerian radial velocity at the horizon is  $v_h = u_h / |\mathcal{W}_h| = 1$  [cf., Eq. (11.88)], as expected.

Clearly, as the fluid falls towards the black hole, it will be compressed and, in the absence of radiative losses, it will increase its temperature. Considering a classical monatomic fluid with an equation of state  $p = \rho k_B T / m$  [cf., Eq. (2.235)], we can compute the temperature increase in terms of the rest-mass density amplification as

$$\frac{T}{T_\infty} = \left( \frac{\rho}{\rho_\infty} \right)^{\Gamma-1} \simeq \left( \frac{\lambda}{\sqrt{2}} \right)^{\Gamma-1} \left( \frac{M}{rc_{s,\infty}^2} \right)^{3(\Gamma-1)/2}, \quad (11.113)$$

which is valid only in the case of  $\Gamma \neq 5/3$  [cf., Eq. (11.109)].<sup>13</sup> Similarly, we can exploit the expressions for the rest-density density at the horizon (11.108) and (11.111), to obtain the corresponding values of the temperature

$$\frac{T_h}{T_\infty} \simeq \begin{cases} \left( \frac{\lambda_c}{4c_{s,\infty}^3} \right)^{\Gamma-1} & \text{for } \Gamma \neq 5/3, \\ \frac{1}{2^{8/3}} \frac{1}{c_{s,\infty}^2} & \text{for } \Gamma = 5/3. \end{cases} \quad (11.114)$$

Note that at spatial infinity the fluid is non-relativistic and hence with  $c_{s,\infty}^2 = \Gamma(p/\rho)_\infty$ , and that the temperature can be also expressed in terms of the same ratio of rest-mass densities, *i.e.*,  $T_\infty = (m/k_B)(p/\rho)_\infty$ . As a result, in the case  $\Gamma = 5/3$ , the temperature at the horizon is simply

$$T_h = \frac{m}{k_B} \frac{1}{2^{8/3} \Gamma} \simeq 0.1 \frac{m}{k_B}, \quad (11.115)$$

and is therefore independent of  $T_\infty$ . A direct estimate of (11.114)<sub>2</sub> yields  $T_h \simeq 10^{11}$  K, which is a reasonable first approximation for the temperatures of accreting flows near a black hole (see Problem 3).

### An example of a numerical solution.

As mentioned at the beginning of the section, the Michel spherical-accretion solution represents an excellent first testbed of a relativistic-hydrodynamic numerical code and is used extensively also in multidimensional codes. In principle, for any given black hole of mass  $M$ , the setup of this test would require the specification of the critical accretion rate  $\lambda_c$  and of the

<sup>13</sup>The density profile when  $\Gamma = 5/3$  is difficult to compute analytically since the sonic radius is much closer to the horizon and no simple approximate expression can be derived for the flow velocity  $u$ .

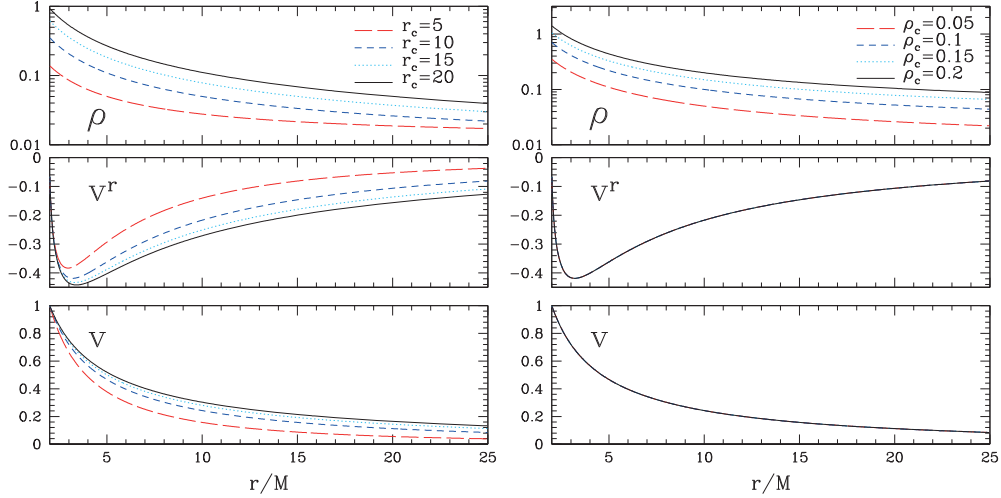


**Fig. 11.9** Representative solutions of the spherical accretion problem. *Left panels:* Solutions having different values of the critical radius but the same critical rest-mass density ( $\rho_c = 0.05$ ). *Right panels:* Solutions having different values of the critical rest-mass density but the same critical radius ( $r_c/M = 10$ ). In either case the top row reports the rest-mass density  $\rho$ , the middle one shows the Eulerian coordinate velocity  $v^r$ , while the bottom one shows the Eulerian proper velocity  $v$ .

Bernoulli constant  $h_c \mathcal{W}_c$ . In practice, it is much simpler to select the critical radius  $r_c$  and the density at the critical radius  $\rho_c$ . This choice fixes  $u_c$  through Eq. (11.94)<sub>1</sub> and the sound speed  $c_{s,c}$  through Eq. (11.94)<sub>2</sub> (the pressure follows trivially via the equation of state). This is sufficient to complete the determination of the fluid properties at the critical point and hence to fix the mass accretion rate  $\dot{M}_c$  and the Bernoulli constant  $h_c \mathcal{W}_c$ . The solution away from the critical point follows after inserting the fluid velocity expressed as  $u = \dot{M}_c / (4\pi r^2 \rho)$  in the Bernoulli equation  $h\mathcal{W} = h_c \mathcal{W}_c$ . The latter becomes therefore a nonlinear equation in the rest-mass density  $\rho$ , which can be solved with a root-finder.

Figure 11.9 shows some example solutions of the fluid velocity and of the rest-mass density for flows having different values of the critical radius but the same critical rest-mass density (left panels), or for flows having different values of the critical density but the same critical radius (right panels). Note that in this case the radial velocity does not depend on  $\rho_c$  since  $\dot{M}_c$  does not depend on  $\rho_c$ . For both panels, the top row reports the rest-mass density  $\rho$ , the middle one shows the coordinate radial velocity  $v^r$ , while the bottom row reports the proper Eulerian velocity  $v$ .

## 11.5 Non-spherical accretion onto a moving black hole

Non-spherical accretion flows are astrophysically relevant in all those situations where strong winds with a small amount of angular momentum are able to transport considerable amounts of matter towards an accreting compact object, *e.g.*, a black hole or a neutron star. Examples

include the case of massive X-ray binaries in which a compact object accretes from the wind of an early-type star, or the case of young stellar systems orbiting in the gravitational potential of their birth cluster and accreting from the dense molecular interstellar medium. The following two sections are dedicated to the analysis of this type of flow in a “crescendo” of complexity but also of realism.

### 11.5.1 Accreting potential flows

As discussed in Section 3.7.4, also in a relativistic framework, potential flows lack important features that characterise realistic fluids. However, there is an application of relativistic potential flow in the context of the stationary accretion problem onto a moving black hole that, although idealised, is remarkable since it can be solved exactly. This solution was first investigated by Petrich *et al.* (1988), and is so exceptional in relativistic hydrodynamics that we will report its derivation below. Consider therefore a Schwarzschild black-hole spacetime of mass  $M$  (this is a restriction for the sake of clarity but the solution can be easily extended to other spacetimes), described by the metric (1.221). Assuming an ultrastiff equation of state  $p = e$  with  $e \propto \rho^2$  and a sound speed equal to the speed of light (see Section 2.4.9), the equation for an irrotational flow  $\nabla_\mu \nabla^\mu \Psi = 0$ , where  $h u_\mu =: \partial_\mu \Psi$  [cf. Eqs. (3.126), (3.131)] can then be written as

$$\left(1 - \frac{2M}{r}\right)^{-1} \partial_t^2 \Psi = \frac{1}{r^2} \partial_r \left[ \left(1 - \frac{2M}{r}\right) r^2 \partial_r \Psi \right] + \frac{1}{r^2} \left[ \frac{1}{\sin \theta} \partial_\theta (\sin \theta \partial_\theta \Psi) + \frac{1}{\sin^2 \theta} \partial_\phi^2 \Psi \right]. \quad (11.116)$$

The asymptotic expressions of the potential  $\Psi$  can be obtained by requiring that at infinity the spacetime is flat and the fluid is homogeneous and hence with constant rest-mass density and specific enthalpy, which we can simply set to be  $h_\infty = 1 = \rho_\infty$ , specifying their actual values later on after a normalisation. In this case, Eq. (3.126) can be integrated and the asymptotic value of the potential can be expressed as

$$\Psi_\infty = (u_\mu x^\mu)_\infty = -W_\infty t + (u_i x^i)_\infty, \quad (11.117)$$

where  $x^\mu$  are Cartesian coordinates, while  $W_\infty$  is the asymptotic Lorentz factor of the asymptotic three-velocity magnitude  $v_\infty$ , so that

$$W_\infty = (1 - v_\infty^2)^{-1/2}, \quad u_\infty^\mu = W_\infty (1, \vec{v}_\infty). \quad (11.118)$$

The resulting asymptotic expression is therefore

$$\Psi_\infty = \lim_{r \rightarrow \infty} \Psi = -W_\infty t + u_\infty r [\cos \theta \cos \theta_0 + \sin \theta \sin \theta_0 \cos(\phi - \phi_0)], \quad (11.119)$$

where  $(\theta_0, \phi_0)$  select the arbitrary direction in which  $\vec{v}_\infty$  is pointing and where  $u_\infty$  is defined as

$$u_\infty := |\vec{v}_\infty| W_\infty = v_\infty W_\infty = (1/v_\infty^2 - 1)^{-1/2}, \quad (11.120)$$

and  $W_\infty^2 = 1 + u_\infty^2$ . Note that the potential  $\Psi$  must be, both asymptotically and anywhere in space, linearly dependent on  $t$  to guarantee the time independence of the flow velocity. As a result, the solution to (11.116) for stationary flows can be expressed as

$$\Psi = -W_\infty t + \sum_{\ell,m} A_{\ell m} R_\ell(r) Y_{\ell m}(\theta, \phi), \quad (11.121)$$

where we have expanded the spatial part in terms of spherical harmonics  $Y_{\ell m}(\theta, \phi)$ , and where the radial part  $R_\ell$  is the solution of the equation

$$\frac{1}{r^2} \frac{d}{dr} \left[ \left( 1 - \frac{2M}{r} \right) r^2 \frac{dR_\ell}{dr} \right] - \frac{\ell(\ell+1)}{r^2} R_\ell = 0. \quad (11.122)$$

The general solution of Eq. (11.122) can be expressed as a superposition of Legendre functions  $P_\ell$  and  $Q_\ell$ , so that the general solution (11.121) can be written as

$$\Psi = -W_\infty t + \sum_{\ell,m} [A_{\ell m} P_\ell(\xi) + B_{\ell m} Q_\ell(\xi)] Y_{\ell m}(\theta, \phi), \quad (11.123)$$

where  $\xi := r/M - 1$ , with  $\xi = 1$  on the horizon, and the coefficients  $A_{\ell m}, B_{\ell m}$  are determined after specifying the boundary conditions on the flow both at spatial infinity and on the horizon. Using now the definition (3.126), we can easily compute the four-velocity components as

$$\frac{\rho}{\rho_\infty} u_t = \rho u_t = -W_\infty, \quad (11.124)$$

$$\frac{\rho}{\rho_\infty} u_r = \rho u_r = \frac{1}{M} \sum_{\ell,m} [A_{\ell m} P'_\ell(\xi) + B_{\ell m} Q'_\ell(\xi)] Y_{\ell m}(\theta, \phi), \quad (11.125)$$

$$\frac{\rho}{\rho_\infty} u_\theta = \rho u_\theta = \sum_{\ell,m} [A_{\ell m} P_\ell(\xi) + B_{\ell m} Q_\ell(\xi)] \partial_\theta Y_{\ell m}(\theta, \phi), \quad (11.126)$$

$$\frac{\rho}{\rho_\infty} u_\phi = \rho u_\phi = \sum_{\ell,m} [A_{\ell m} P_\ell(\xi) + B_{\ell m} Q_\ell(\xi)] \partial_\phi Y_{\ell m}(\theta, \phi), \quad (11.127)$$

where the first equation results from requiring that the flow is stationary and irrotational, so that  $\partial_t(\partial_i \Psi) = \partial_i(\partial_t \Psi) = 0$  and thus  $\partial_t \Psi = -W_\infty$  everywhere. Once the solution is known, we can use the normalisation condition on the four-velocity [*cf.*, Eq. (3.2)] to compute the distribution of the rest-mass density as [*cf.*, (3.129)]

$$\rho^2 = \left( 1 - \frac{2M}{r} \right)^{-1} (\rho u_t)^2 + \left( 1 - \frac{2M}{r} \right) (\rho u_r)^2 - \frac{(\rho u_\theta)^2}{r^2} - \frac{\csc^2 \theta (\rho u_\phi)^2}{r^2}, \quad (11.128)$$

which is divergent at  $r = 2M$ . Such a divergence can be cured if one of the spatial components of the four-velocity is also suitably divergent there. More specifically, near the horizon, *i.e.*, for  $\xi \rightarrow 1$ , the limiting properties of the Legendre functions imply that

$$\rho^2 \rightarrow \left( 1 - \frac{2M}{r} \right)^{-1} \left[ W_\infty^2 - \left( \frac{1}{4M} \sum_{\ell,m} B_{\ell m} Y_{\ell m}(\theta, \phi) \right)^2 \right], \quad (11.129)$$

or, equivalently, that all the coefficients  $B_{\ell m}$  are zero, with the exception of the first one, which is then given by  $B_{00} Y_{00} = 4M W_\infty$ , and where the positive sign is chosen since we are

considering an accretion scenario. Imposing this boundary condition, the resulting expression for the potential becomes

$$\begin{aligned}\Psi &= -W_\infty t - 2MW_\infty \ln \left( 1 - \frac{2M}{r} \right) \sum_{\ell,m} A_{\ell m} P_\ell(\xi) Y_{\ell m}(\theta, \phi) \\ &= -W_\infty t - 2MW_\infty \ln \left( 1 - \frac{2M}{r} \right) + u_\infty(r - M) \cos \theta,\end{aligned}\quad (11.130)$$

where the second line in (11.130) comes from considering the asymptotic condition (11.119) with  $\theta_0 = 0 = \phi_0$ . In this case, in fact, all the coefficients  $A_{\ell m}$  are zero, with the exception of  $A_{10}$ . Using now the form of the potential function (11.130), we can derive the velocity field components as

$$\rho u_t = -W_\infty, \quad (11.131)$$

$$\rho u_r = -\frac{4M^2}{r(r-2M)} W_\infty + u_\infty \cos \theta, \quad (11.132)$$

$$\rho u_\theta = -u_\infty(r-M) \sin \theta, \quad (11.133)$$

$$\rho u_\phi = 0, \quad (11.134)$$

and thus the corresponding rest-mass density distribution as

$$\begin{aligned}\rho^2 &= W_\infty^2 \left[ 1 + \frac{2M}{r} + \left( \frac{2M}{r} \right)^2 + \left( \frac{2M}{r} \right)^3 \right] \\ &\quad - u_\infty^2 \left[ 1 - \frac{2M}{r} + \left( \frac{M \sin \theta}{r} \right)^2 \right] + 8 \left( \frac{M}{r} \right)^2 W_\infty u_\infty \cos \theta.\end{aligned}\quad (11.135)$$

Two remarks are worth making about the velocity field (11.131)–(11.134). First, the whole solution is specified in terms of a single parameter  $W_\infty$ , or equivalently,  $u_\infty$ . Second, while  $u_\theta$  is always nonzero away from the infalling direction,  $\theta = 0, \pi$ , the radial component  $u_r$  vanishes at one point in the downstream region of the flow and for  $\theta = \pi$ , *i.e.*, at

$$r_s = M \left[ 1 + \left( 1 + \frac{4}{v_\infty} \right)^{1/2} \right]. \quad (11.136)$$

A particle placed at such a point, which is also referred to as a *stagnation point*, will either accrete onto the black hole or escape downwind to spatial infinity. Figure 11.10 shows a plot of the streamlines of the three-velocity field,  $v^i$ , measured by static observers outside the event horizon for a flow moving from left to right with  $u_\infty = 0.75$  ( $v_\infty = 0.6$ ). The different red contour lines mark the values of  $v = (v^i v_i)^{1/2}$  with a spacing of 0.1 and with the largest value of 0.9 near the event horizon (dark circle), while the green star shows the location of the stagnation point (see Problems 4 and 5).<sup>14</sup> This figure should be compared with the similar

<sup>14</sup>This velocity field is measured in a local orthonormal tetrad which removes locally the spacetime curvature (see Section 1.5.1) and thus has the same physical significance as if it were performed in a flat spacetime. We will encounter such tetrads also in Section 11.8 and indeed the velocity field in Fig. 11.10 has been obtained using the tetrad (11.205) for a non-rotating black hole. The resulting expressions are:  $v^r = \sqrt{g_{rr}} v^r = \sqrt{g_{rr}} u^r / W$  and  $v^\theta = \sqrt{g_{\theta\theta}} v^\theta = \sqrt{g_{\theta\theta}} u^\theta / W$ , with  $W$  the Lorentz factor.

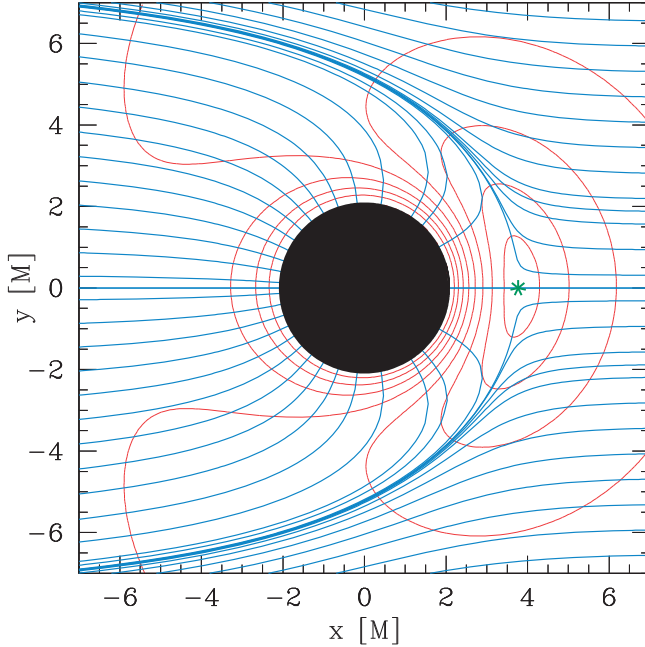


**Fig. 11.10** Streamlines of the three-velocity field,  $\hat{v}^i$ , measured by static observers outside the event horizon for a flow moving from left to right with  $u_\infty = 0.75$  ( $v_\infty = 0.6$ ). The different red contour lines mark the values of  $v = (v^i v_i)^{1/2}$  with the largest value of 0.9 near the event horizon (dark circle), while the green star shows the location of the stagnation point.

ones obtained for generic fluid motion, where a shock cone appears downstream of the flow (cf., Fig. 11.11).

Finally, we can calculate the rest-mass accretion rate across a closed surface  $\Sigma$  as

$$\dot{M} := - \int_{\Sigma} \rho u^i \sqrt{-g} dS_i = \int_{\Sigma} \partial_r \Psi g^{rr} \sqrt{-g} d\Omega = 16\pi M^2 \rho_\infty W_\infty , \quad (11.137)$$

which corrects, therefore, the spherical mass accretion rate by a factor  $W_\infty$ , accounting for the motion at large distance of the fluid. The solution just discussed can be extended to the case of a Kerr black hole, but also to a variety of other objects (e.g., a hard sphere, an infinite cylinder, a cosmic string) and the interested reader will find details in Petrich *et al.* (1988), and Shapiro (1989). These idealised but prototypical solutions will offer insight when studying more generic stationary and non-stationary supersonic accretion flows onto black holes that have been investigated in Petrich *et al.* (1989), Font and Ibáñez (1998), Dönmez (2011), Zanotti *et al.* (2011), and that we will review below.

### 11.5.2 Bondi–Hoyle–Lyttleton flows

One of the most celebrated and best-studied types of non-spherical accretion flows is the *Bondi–Hoyle–Lyttleton accretion* (BHL) (Hoyle and Lyttleton, 1939; Bondi and Hoyle, 1944), which develops when a compact object moves relative to a uniform gas cloud.<sup>15</sup> The BHL flow has been the subject of several numerical investigations, starting from Matsuda *et al.* (1987) and followed by Fryxell and Taam (1988), Sawada *et al.* (1989), and Benensohn *et al.* (1997). As a summary of the bulk of work done so far on this topic, Table 1 of Foglizzo *et al.* (2005) reports an overview of published numerical simulations of BHL accretion over the last 30 years and lists more than 40 works. The first two-dimensional simulations of BHL accretion in a relativistic regime were performed by Petrich *et al.* (1989) and subsequently extended by Font and Ibáñez (1998), Font *et al.* (1998), Font *et al.* (1999) and more recently by Dönmez (2011), Zanotti *et al.* (2011), and Cruz-Osorio *et al.* (2012). These investigations considered flows in axisymmetry and in the equatorial plane, while a fully general-relativistic investigation of the BHL accretion in three dimensions has been considered recently by Farris *et al.* (2010) in the context of the merger of supermassive black-hole binaries.

Some of the features of this flow have already been discussed in the previous section, where we have pointed out the presence of an upstream part of the flow, which is in great part accreted, and of a wake, characterised by a *stagnation point*, downstream of which the flow is unbound. However, as noted in the previous section, the speed of sound in the case considered in Section 11.5.1 is equal to the speed of light and the flow speed must be *subsonic* everywhere, with no shock waves being allowed to form. For more realistic and less extreme conditions, the flow is expected to be *supersonic* at least somewhere, so that shocks can be produced. Indeed, in general, when a homogeneous flow of matter moves non-radially towards a compact object, a shock wave is likely to form in the neighbourhood of the accretor. Recalling that the relativistic *Mach number* is defined as (see Section 4.7.5)

$$\mathcal{M} := \frac{Wv}{W_s c_s}, \quad (4.218)$$

where  $v$  is the flow velocity,  $W$  the associated Lorentz factor and  $W_s$  the Lorentz factor of the sound speed, *i.e.*,  $W_s := (1 - c_s^2)^{-1/2}$ , the position of the shock will depend on the properties of the flow. Using the metric (11.142) to represent a generic black-hole spacetime, numerical simulations are usually performed after specifying the initial velocity field components in terms of an asymptotic velocity  $v_\infty$  (Font *et al.*, 1998)

$$v^r = \sqrt{\gamma^{rr}} v_\infty \cos \phi, \quad (11.138)$$

$$v^\phi = -\sqrt{\gamma^{\phi\phi}} v_\infty \sin \phi, \quad (11.139)$$

where  $\gamma^{rr} = g^{rr}$  and  $\gamma^{\phi\phi} = g^{\phi\phi} - (g^{t\phi})^2/g^{tt}$ . These relations guarantee that the velocity of the injected gas reproduces a continuous parallel wind at large distances, while  $v^2 := v_i v^i = v_\infty^2$  everywhere in the flow. As matter is continuously injected from the outer boundary in the upstream region with components (11.138) and (11.139), the value of  $v_\infty$  can be chosen to investigate different regimes of the flow and consider therefore either subsonic or supersonic

<sup>15</sup>We recall that Hoyle and Lyttleton (1939) first considered the accretion by a point mass moving at a constant speed through an infinite gas cloud within a Newtonian treatment. Later on, Bondi and Hoyle (1944) extended the analysis to include the accretion column, *i.e.*, the wake following the point mass.

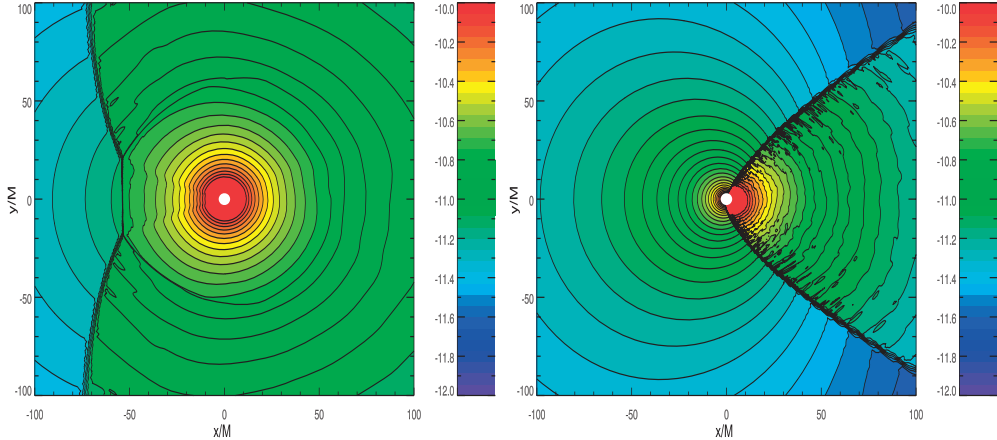


**Fig. 11.11** Rest-mass density in cgs units on a logarithmic colour scale and with isodensity contours for two supersonic flows having the same adiabatic index  $\Gamma = 5/3$ , the same asymptotic sound speed, the same asymptotic rest-mass density, but different asymptotic velocities and thus Mach numbers. The left panel refers to a model  $v_\infty = 0.09$ ,  $\mathcal{M}_\infty = 1.28$  and shows the appearance, once a stationary state has been reached, of a *detached shock*. The right panel refers instead to a model with  $v_\infty = 0.10$ ,  $\mathcal{M}_\infty = 1.42$ , which shows the appearance of a *shock cone*. In both cases the black hole is non-rotating with mass  $M = 3.6 \times 10^6 M_\odot$  [adapted from Zanotti *et al.* (2011)].

accretion. The initial density and pressure profiles, which can be specified freely, are usually adjusted to set the sound speed to a given value.

In the case of an ideal-fluid equation of state (a very reasonable approximation for a fluid at large distances from a compact object) once the asymptotic sound speed is chosen (*e.g.*,  $c_{s,\infty} = 0.1$ ), the rest-mass density can be set to be a constant (*e.g.*,  $\rho_\infty = 1$ ) and then the pressure is derived from the relativistic definition of the sound speed [*cf.*, Eq. (2.249)]

$$p = \left[ \frac{\Gamma - 1}{\Gamma(\Gamma - 1) - c_{s,\infty}^2 \Gamma} \right] c_{s,\infty}^2 \rho_\infty. \quad (11.140)$$

Within this general setup, the main properties of the flow can be controlled after acting on the adiabatic index  $\Gamma$  and on the asymptotic Mach number  $\mathcal{M}_\infty$ . In particular, numerical simulations reveal that for any given value of  $\mathcal{M}_\infty$ , there is a critical adiabatic index  $\Gamma \simeq 2$ , below which a shock wave of conic shape, *i.e.*, a *shock cone*, forms downstream of the accretor. On the other hand, for increasingly stiff fluids and thus for values of the adiabatic index larger than the critical one, a *bow shock* forms upstream of the accretor.<sup>16</sup> In this case, the accretion is almost spherical and because the bow shock does not reach the horizon of the black hole, it is often referred to as a *detached shock*. The same phenomenology of the appearance of either a shock cone or of a detached shock is observed if the adiabatic index is kept constant and the varying parameter is instead the asymptotic Mach number.

This is shown in Fig. 11.11, which reports the rest-mass density accreting onto a Schwarzschild black hole with mass  $M = 3.6 \times 10^6 M_\odot$ , for two different models having the same

<sup>16</sup>A complete discussion of bow waves in Newtonian hydrodynamics can be found in Landau and Lifshitz (1987).

asymptotic sound speed ( $c_{s,\infty} = 0.07$ ), the same asymptotic rest-mass density ( $\rho_\infty = 3.22 \times 10^{-12}$  g cm $^{-3}$ ) and the same adiabatic index ( $\Gamma = 5/3$ ), but different asymptotic velocities and thus Mach numbers. Note that if a (strong) shock is produced, the accretion rate is no longer guaranteed to be negative everywhere and the spherical accretion radius  $r_{\text{acc}}$  [*cf.*, (11.90)] needs to be replaced by the *Bondi–Hoyle–Lyttleton radius*  $r_{\text{BHL}}$ , which is therefore defined as the radial position where the accretion rate (as a function of radius) becomes negative. In practice, numerical simulations [*e.g.*, of Dönmmez (2011)] show that the BHL is very well approximated by the expression [*cf.*, Eq. (11.90)]

$$r_{\text{BHL}} \approx \frac{2M}{v_\infty^2 + c_{s,\infty}^2}. \quad (11.141)$$

The left panel of Fig. 11.11 refers to a model with  $v_\infty = 0.09$ ,  $\mathcal{M}_\infty = 1.28$  and shows the appearance, once a stationary state has been reached, of a detached shock. Note that in this case the accretion is almost spherical and thus  $r_{\text{acc}} \simeq r_{\text{BHL}}$ . The flow morphology in the left panel should be contrasted with that in the right panel, which instead refers to a model with  $v_\infty = 0.10$ , and  $\mathcal{M}_\infty = 1.42$ , that shows instead the appearance of a shock cone. When the latter is produced,  $r_{\text{acc}} \simeq r_{\text{BHL}}$ , and matter from the upstream region crosses the shock front, undergoes a strong deceleration and is ultimately accreted if inside the accretion radius  $r_{\text{BHL}}$ . As a result, the maximum rest-mass density in the downstream region is always larger than the corresponding one in the upstream region and, consequently, the mass accretion rate is significantly non-spherical and larger in the downstream part of the flow.

It is important to remark that the shape of the shock cone depends sensitively on the spin of the black hole. If the black hole is not spinning, in fact, the shock cone is perfectly symmetric about the  $\phi = 0$  direction, where  $\phi$  is azimuthal coordinate. On the other hand, if the black hole is spinning, the induced frame-dragging effect produces a “wrapping” of the shock cone, as first shown by Font *et al.* (1999). Interestingly, such wrapping involves not only the part of the flow outside the event horizon but it extends also inside it, as shown by Font *et al.* (1999) in simulations using event-horizon-penetrating coordinates such as the Kerr–Schild coordinates [*cf.*, Eqs (1.259)].

The main features of the stationary pattern of the shock cone around a rotating black hole are summarised in Fig. 11.12, which shows the rest-mass density distribution on the equatorial plane in geometrised units and logarithmic colour scale (left panel) and the corresponding Lorentz factor (right panel) for a supersonic flow with adiabatic index  $\Gamma = 4/3$  and asymptotic properties:  $c_{s,\infty} = 0.1$ ,  $\rho_\infty = 1$ ,  $v_\infty = 0.5$ , and  $\mathcal{M}_\infty = 5$ , accreting onto a black hole with spin  $a/M = 0.9$  (Dönmmez , 2011). As is evident from the isodensity contours, the accretion in the upstream region is essentially spherical, while a well-defined shock cone, characterised by a strong density gradient, forms in the downstream region. The accretion rate is largest in the shock cone, which is distorted by the spin of the black hole, with an opening angle that slightly decreases with increasing distance from the centre. Furthermore, the maximum rest-mass density in the shock cone increases with the spin of the black hole. The right panel of Fig. 11.12 also shows that the overall flow is only very mildly relativistic, with a maximum Lorentz factor  $W_{\max} \lesssim 3$ , even ahead of the shock front and in the vicinity of the black hole. Similarly, accretion within the shock cone takes place only with a very small Lorentz factor (Dönmmez , 2011).

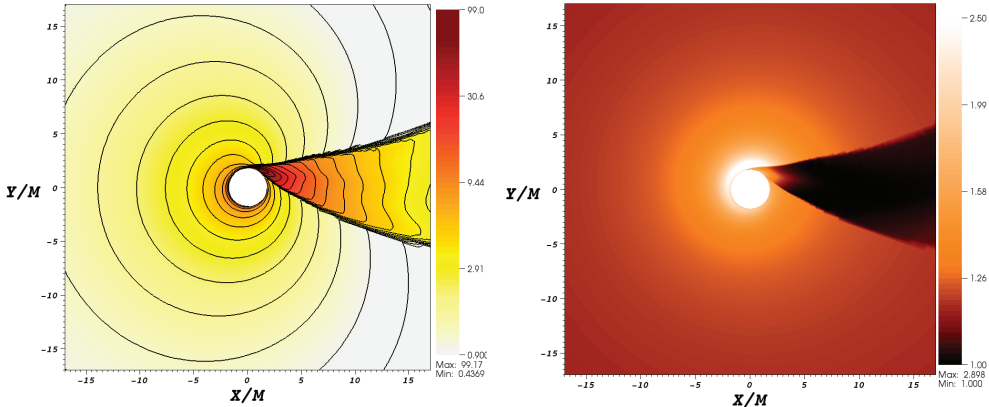


**Fig. 11.12** Rest-mass density distribution in geometrised units on a logarithmic colour scale and with isodensity contours (left panel) and Lorentz factor distribution (right panel) for a supersonic flow with adiabatic index  $\Gamma = 4/3$  and asymptotic properties:  $v_\infty = 0.5$ ,  $\mathcal{M}_\infty = 5$ , accreting onto a rotating black hole with spin  $a/M = 0.9$  (here  $c_{s,\infty} = 0.1$ ,  $\rho_\infty = 1$ ). In the downstream region a clear shock cone forms which is distorted by the non-vanishing spin of the black hole. Both panels refer to the equatorial plane of the black hole. [From Dönmel (2011).]

A more quantitative description of the flow is shown in Fig. 11.13, which reports one-dimensional profiles of the rest-mass density at different radial shells. The left panel refers to a Schwarzschild black hole, while the right panel shows a rotating black hole with spin  $a/M = 0.9$ . A sharp transition in the density exists at the border of the shock cone and this is particularly evident for the non-rotating black hole. Note also the amount of asymmetry in the azimuthal direction, which is present in the case of a rotating black hole. As already mentioned above, the opening angle of the shock cone is only weakly dependent on the radial distance, reducing slightly when moving away from the black hole.

Besides the development of the shock cone, there are at least two other relevant physical processes that may manifest themselves in BHL accretion flows. The first one is the onset of the so-called *flip-flop instability*, that is, an instability leading to the oscillation of the shock cone from one side to the other of the accretor. The second one is the development of *quasi-periodic oscillations (QPOs)* of sonic nature inside the shock cone, which provides a natural cavity for the confinement of such oscillations. We will discuss both processes in what follows.

### **The flip-flop instability.**

As shown through numerical simulations performed by several authors over the years in Newtonian physics, the BHL accretion flow is subject to the so-called *flip-flop* instability, namely an instability of the shock cone to tangential velocities, which produces large-scale periodic oscillations of the shock cone as a whole. Such instability was first discovered by Matsuda *et al.* (1987) in two-dimensional axisymmetric Newtonian simulations, and later confirmed

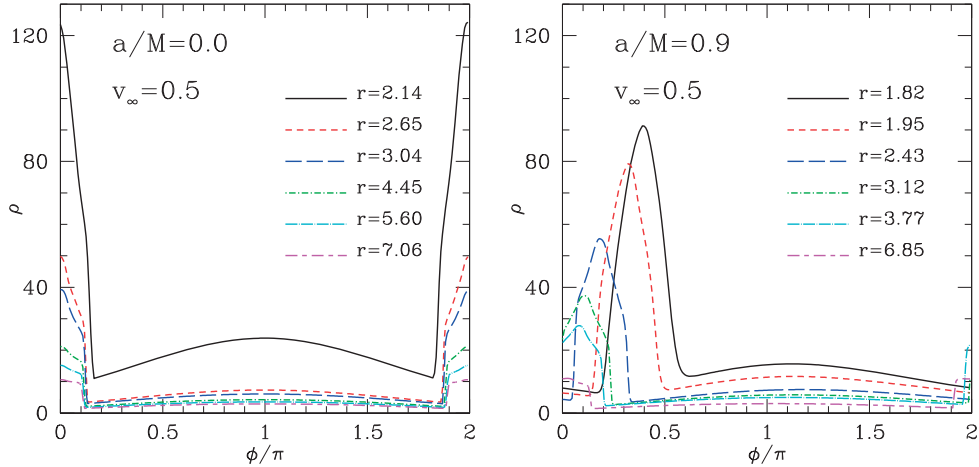


**Fig. 11.13** One-dimensional profiles of the rest-mass density in geometrised units showing the location of the shock at different radial positions (expressed in units of  $M$ ) for a supersonic flow with adiabatic index  $\Gamma = 4/3$  and asymptotic properties:  $v_\infty = 0.5$ ,  $\mathcal{M}_\infty = 5$ . The left panel refers to a Schwarzschild black hole, while the right panel shows a rotating black hole with spin  $a/M = 0.9$ . Note that in this latter case the shock is distorted and is no longer symmetric as a result of shock “wrapping”. [From Dönmelz (2011).]

and further investigated by several authors (Fryxell and Taam, 1988; Sawada *et al.*, 1989; Benennohn *et al.*, 1997; Foglizzo and Ruffert, 1999; Pogorelov *et al.*, 2000). Three-dimensional simulations were performed by Ishii *et al.* (1993) and Ruffert (1997), who confirmed the occurrence of the instability, although with deformations of the shock cone only very close to the accreter.

Possibly because of the small growth rate of the instability, which forces simulations to be carried out on very long time-scales, none of the early relativistic calculations were able to report the development of the flip-flop instability in a relativistic regime. Recently, however, the first evidence for the occurrence of the instability in a relativistic regime was obtained by Dönmelz (2011). Figure 11.14 reports four snapshots taken from Dönmelz (2011) of the rest-mass density in a long-term evolution of a BHL accretion flow leading to the instability. The data refers to a supersonic flow with adiabatic index  $\Gamma = 4/3$ , asymptotic properties  $c_{s,\infty} = 0.1$ ,  $\rho_\infty = 1$ ,  $v_\infty = 0.4$ , and  $\mathcal{M}_\infty = 4$ , accreting onto a black hole with spin  $a/M = 0.5$ . Note that the shock cone in the downstream region oscillates back and forth in the orbital plane with a period of  $\sim 1000 M$ .

In spite of all these investigations, the nature and the physical origin of the flip-flop instability remain obscure. According to Foglizzo and Ruffert (1999), for example, local instabilities, such as the Rayleigh–Taylor or the Kelvin–Helmholtz instabilities (Chandrasekhar, 1981), should not play a significant role and cannot account for the flip-flop instability. On the other hand, Soker (1990) showed through a Wentzel–Kramers–Brillouin (WKB) analysis that the two-dimensional axisymmetric accretion flow can be unstable against tangential modes, as well as against radial modes. When extending these results to three-dimensional simula-

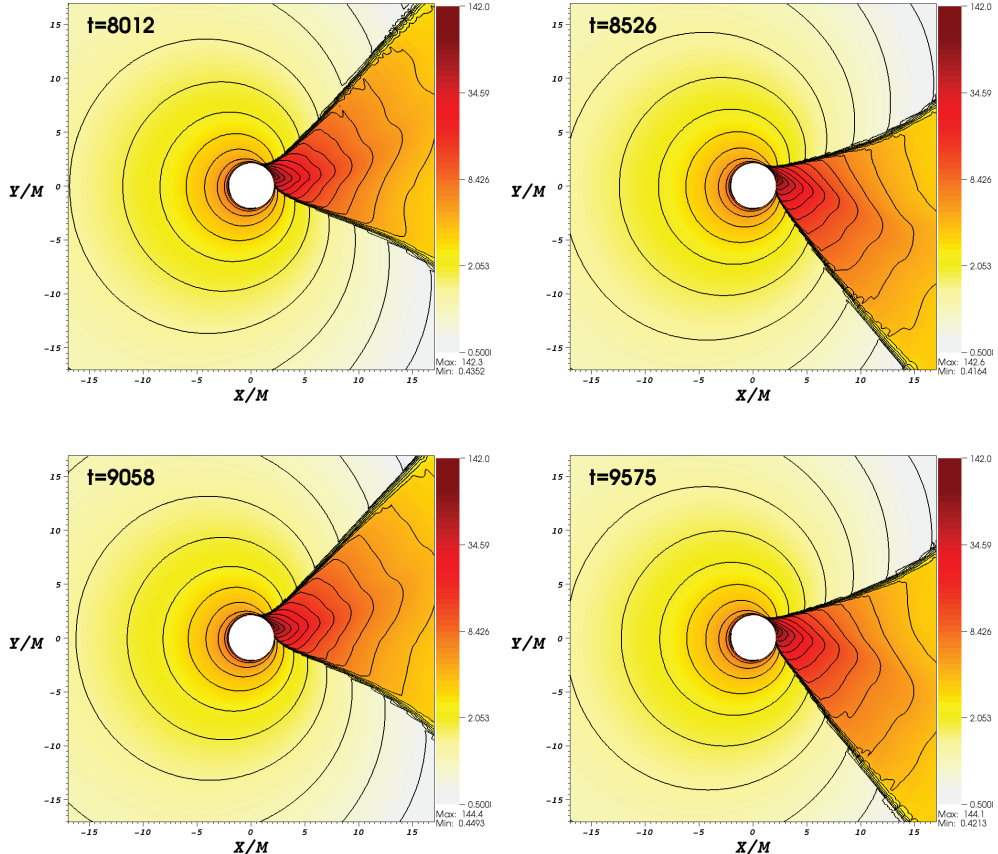


**Fig. 11.14** Logarithm of the rest-mass density on the equatorial plane expressed in geometrised units and at different times for a supersonic flow with adiabatic index  $\Gamma = 4/3$ , asymptotic properties  $c_{s,\infty} = 0.1$ ,  $\rho_\infty = 1$ ,  $v_\infty = 0.4$ ,  $\mathcal{M}_\infty = 4$ , accreting onto a black hole with spin  $a/M = 0.5$ . The flip-flop instability manifests itself after the shock cone has reached a stationary state and it causes the shock cone to oscillate back and forth with an oscillation period around  $1000 M$ . [From Dönmez (2011).]

tions, however, the persistence of such instabilities has not been fully clarified yet. Overall, it is still unclear whether the physical mechanisms driving the instabilities in two- and three-dimensional simulations is the same or not, and recent investigations even attribute the origin of the instability to the choice of coordinates (Cruz-Osorio *et al.*, 2012).

#### Quasi-periodic oscillations in the shock cone.

Possibly one of the most interesting properties of a BHL accretion is the development of QPOs in the shock cone that forms in the downstream region once the system has relaxed to the stationary state. Indeed, because a stationary state is necessary for the development of the

QPOs, the latter are not found when the flip-flop instability develops.

An extensive Fourier analysis of the different dynamical quantities (*e.g.*, the mass accretion rate) has been recently performed by Dönmez (2011) and has revealed that the oscillations measured numerically are global eigenmodes of the system, with power spectral densities which are essentially independent of the position inside the shocked cone. Besides the first fundamental modes, the power spectra also show peaks associated with nonlinear couplings, as is typical of physical systems governed by nonlinear equations in the limit of small oscillations (Landau and Lifshitz, 1976; Zanotti *et al.*, 2005). Overall, the first fundamental frequencies appear in the integer ratios 2:1 and 3:1, and show a scaling both with the mass of the black hole (black holes with larger masses lead to linearly smaller frequencies) and with its spin (black holes with larger spins lead to linearly larger frequencies). The precise identification of these oscillation modes within a perturbative analysis is made difficult by the absence of an analytic solution for the stationary flow inside the shock cone, but would obviously be of great importance.

Furthermore, when the flip-flop instability is triggered and develops, the power spectrum of the oscillations inside the shock cone changes considerably and in these cases only the periodicity of the shock-cone oscillation can be found, which is then accompanied by the usual nonlinear couplings. In general, therefore, the effect of the flip-flop instability is that of suppressing most of the oscillations inside the shock cone.

Finally, we note that the phenomenology discussed for the QPOs in the shock cone shows strong similarities with the one reported for perturbed relativistic tori orbiting around a black hole (Zanotti *et al.*, 2003). In that case, in fact, it was shown that the eigenfunctions and eigenfrequencies were those corresponding to the  $p$  modes of the torus (Rezzolla *et al.*, 2003b; Rezzolla *et al.*, 2003a; Zanotti *et al.*, 2005; Montero *et al.*, 2007). Such modes have pressure gradients and centrifugal forces as the main restoring forces and are closely related to the propagation of sound waves in a perturbed rotating fluid, that is, *inertial-acoustic waves*. The major difference in the physical conditions met with tori orbiting black holes and those found in BHL accretion flows is that in the latter centrifugal forces play a negligible role. Apart from this, the physical nature of the modes is very similar in the two cases.

### **Interaction with a radiation field.**

A final remark in this section is dedicated to the interaction of the accreting BHL flow with a radiation field, which is expected to be produced as a consequence of increased density and temperature of the fluid as it moves towards the black hole. All of the discussion made so far, in fact, has assumed the non-spherical accretion to be a purely hydrodynamic process, with the fluid remaining sufficiently cold so as not to emit any radiation, or, equivalently, that if radiation is produced, this is instantaneously lost without affecting the dynamics of the BHL flow.

This is clearly an approximation and a first attempt to go beyond this idealisation has recently been made by Zanotti *et al.* (2011). Numerical simulations have been carried out in which the radiation field has been treated as fully coupled with the fluid and thus treated in the optically thick approximation (see the discussion in Section 3.11.1), with the opacity provided by Thomson scattering and by thermal bremsstrahlung. This approach has allowed us to perform a systematic comparison between purely hydrodynamic simulations and simulations with a coupled matter-radiation fluid, thus revealing significant differences once the system

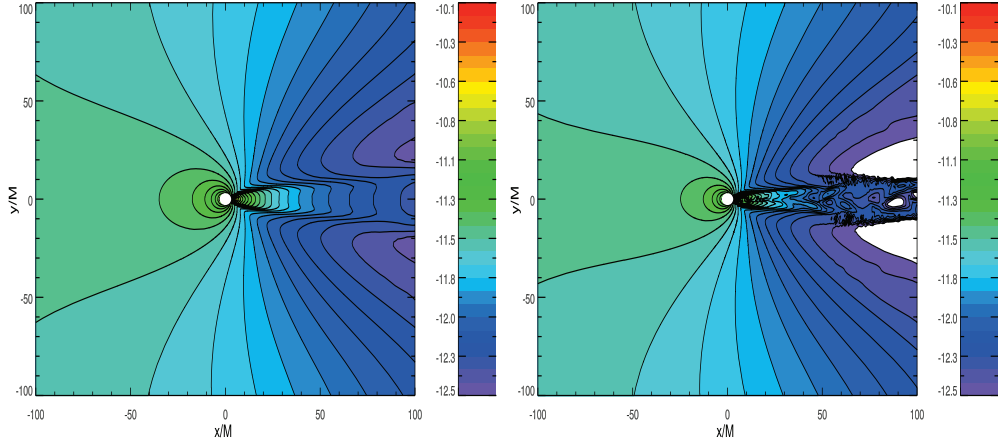


**Fig. 11.15** The same physical conditions as in Fig. 11.11 when, however, the fluid is coupled to radiation in the optically thick regime. Note that the introduction of a radiation pressure greatly reduces the density of the fluid in the vicinity of the black hole (the white regions in the two panels above correspond to densities below the threshold for the colour-code at around  $10^{-12} \text{ g cm}^{-3}$ ). The left panel refers to the flow with smaller Mach number and is characterised by a shock cone downstream of the accretor, rather than by a detached shock as in the hydrodynamic solution. The right panel refers to a flow with a larger Mach number. In both cases a “reduced” shock cone is produced [adapted from Zanotti *et al.* (2011)].

relaxes to a radiation-pressure dominated regime. More specifically, the accretion rates have been found to be about two orders of magnitude smaller than in the purely hydrodynamic case. Furthermore, when increasing the Mach number of the inflowing gas, the accretion rates become smaller because of the smaller cross-section of the black hole, but the luminosities increase as a result of a stronger emission in the shocked regions.

Two representative examples of the quantitative and qualitative differences introduced by the interaction with a radiation field are shown in Fig. 11.15, which reports the rest-mass distribution for flows with the same physical conditions as in Fig. 11.11. Note that the colour-code scales are the same in the two figures, thus highlighting that the introduction of a radiation pressure greatly reduces the density of the fluid in the vicinity of the black hole, suppressing the accretion rates as an obvious consequence. As in Fig. 11.11, the left panel refers to the flow with smaller Mach number, but, in contrast with the purely hydrodynamic evolution, it shows a shock cone rather than a detached shock. This behaviour can be explained by recalling that the effective adiabatic index of the fluid-plus-radiation medium in the radiation-pressure dominated regime is smaller than that of the fluid alone [*cf.*, Eq. (2.279)]. As a result, the rest-mass density jumps across shock fronts are increased and the generation of the shock cone downstream of the accretor is favoured [see, *e.g.*, Ruffert (1996) and Font and Ibáñez (1998) for similar behaviour in purely hydrodynamic simulations]. Moreover, the two shock cones of Fig. 11.15 have a much smaller opening angle than in the hydrodynamic solution, thus giving rise to a “reduced” shock cone, possibly accompanied by instabilities and turbulence.

## 11.6 Fluids in circular motion around a black hole

We have seen in the previous sections that the motion of a fluid in the vicinity of a black hole is in general accompanied by an accretion process and that the efficiency of this process depends both on the properties of the flow and on those of the black hole. However, there are also fluid configurations that, despite being around a black hole, are stationary and in equilibrium, thus *non-accreting*. The existence of these solutions may appear not particularly surprising if one bears in mind that there exist stable test-particle trajectories around a black hole, as we have discussed in detail in Sections 1.7.1 and 1.7.2. However, it is also not obvious that these stability properties should apply also to the case of an extended fluid, and the following Section 11.7 is dedicated to illustrate what such properties are. Before going into that, however, and because rotation is a fundamental ingredient for any stable fluid motion around a black hole, it is useful to spend a few words and review an important theorem that applies for fluids in circular motion around a source of gravity.

### 11.6.1 von Zeipel cylinders

To appreciate the properties of a fluid rotating in a black-hole spacetime we first need to obtain an expression for the acceleration of a fluid element in circular motion. Using a spherical polar coordinate system  $(t, r, \theta, \phi)$ , we write the metric of a compact object (*e.g.*, a rotating black hole with mass  $M$  and spin parameter  $a := J/M$ ) in the generic form [see Eqs. (1.251) and (1.252) for the explicit expressions of the metric functions in the case of a Kerr black hole]

$$ds^2 = g_{tt} dt^2 + 2g_{t\phi} dt d\phi + g_{rr} dr^2 + g_{\theta\theta} d\theta^2 + g_{\phi\phi} d\phi^2, \quad (11.142)$$

and assume that the spacetime admits two commuting Killing vectors,  $\eta$  and  $\xi$ , associated with the stationarity and the axisymmetry of the metric, namely

$$\eta^\mu = \delta_t^\mu = (1, 0, 0, 0), \quad \eta_\mu = (g_{tt}, 0, 0, g_{t\phi}), \quad (11.143)$$

$$\xi^\mu = \delta_\phi^\mu = (0, 0, 0, 1), \quad \xi_\mu = (g_{t\phi}, 0, 0, g_{\phi\phi}) \quad (11.144)$$

[see also Section 1.5.3]. The four-velocity for purely circular motion (*i.e.*,  $u^r = 0 = u^\theta$ ) can then be written as

$$u^\mu = \frac{dx^\mu}{d\tau} = u^t(\eta^\mu + \Omega\xi^\mu), \quad (11.145)$$

where we recall that  $\tau$  is the proper time of an observer comoving with the fluid and the coordinate angular velocity of the fluid is defined as

$$\Omega := \frac{u^\phi}{u^t} = \frac{d\phi}{dt}. \quad (11.146)$$

The normalisation condition (3.2) for the four-velocity  $u$  in the metric (11.142) can then be written as a condition for the contravariant time component of the four-velocity, *i.e.*,

$$(u^t)^{-2} = -(g_{tt} + 2\Omega g_{t\phi} + \Omega^2 g_{\phi\phi}). \quad (11.147)$$

Using now the properties of the Killing vectors in the metric (11.142) [*cf.*, Eqs. (1.172)–(1.175)]

$$\eta^\nu \nabla_\nu \eta_\mu = -\frac{1}{2} \nabla_\mu (\eta^\nu \eta_\nu) = -\frac{1}{2} \partial_\mu g_{tt}, \quad (11.148)$$

$$\xi^\nu \nabla_\nu \xi_\mu = -\frac{1}{2} \nabla_\mu (\xi^\nu \xi_\nu) = -\frac{1}{2} \partial_\mu g_{\phi\phi}, \quad (11.149)$$

$$\xi^\nu \nabla_\nu \eta_\mu = \eta^\nu \nabla_\nu \xi_\mu = -\frac{1}{2} \nabla_\mu (\xi^\nu \eta_\nu) = -\frac{1}{2} \partial_\mu g_{t\phi}, \quad (11.150)$$

we can compute the acceleration experienced by the fluid,  $a_\mu := u^\nu \nabla_\nu u_\mu$ , as

$$a_\mu = \frac{1}{2} \frac{\partial_\mu g_{tt} + 2\Omega \partial_\mu g_{t\phi} + \Omega^2 \partial_\mu g_{\phi\phi}}{g_{tt} + 2\Omega g_{t\phi} + \Omega^2 g_{\phi\phi}} \quad (11.151)$$

$$= \frac{1}{2} \frac{\partial_\mu (g_{tt} + 2\Omega g_{t\phi} + \Omega^2 g_{\phi\phi})}{g_{tt} + 2\Omega g_{t\phi} + \Omega^2 g_{\phi\phi}} - \frac{(g_{t\phi} + \Omega g_{\phi\phi}) \partial_\mu \Omega}{g_{tt} + 2\Omega g_{t\phi} + \Omega^2 g_{\phi\phi}} \\ = -\partial_\mu \ln |u^t| + \frac{\ell}{1 - \Omega \ell} \partial_\mu \Omega, \quad (11.152)$$

where we have used  $\partial_A u^t = 0 = \partial_A \Omega$ , for  $A = t, \phi$ , as a result of stationarity and axisymmetry, and where we have defined the (dimensionless) *specific angular momentum* as

$$\ell := -\frac{u_\phi}{u_t}, \quad (11.153)$$

with

$$\frac{\ell}{1 - \Omega \ell} = -\frac{g_{t\phi} + \Omega g_{\phi\phi}}{g_{tt} + 2\Omega g_{t\phi} + \Omega^2 g_{\phi\phi}} = u^t u_\phi. \quad (11.154)$$

We should note that alternative definitions of the specific angular momentum are possible, *e.g.*,  $\ell = h u_\phi$ , as adopted in Eq. (3.73) when discussing fluids in symmetric spacetimes. While both definitions lead to the same Newtonian limit, *i.e.*,  $\ell_N = \Omega r^2$ , the definition (11.153) is preferable over (3.73), as it satisfies the condition of giving a zero epicyclic frequency for orbital motion around a Schwarzschild black hole with constant specific angular momentum [*cf.*, Eq. (45) of Rezzolla *et al.* (2003b)].

After using the following identities (which are a consequence of the normalisation condition)

$$u^t u_t = -\frac{1}{1 - \Omega \ell}, \quad u^\phi u_\phi = \frac{\Omega \ell}{1 - \Omega \ell}, \quad (11.155)$$

we can rewrite Eq. (11.152) in the more convenient form

$$a_\mu = \partial_\mu \ln |u_t| - \frac{\Omega}{1 - \Omega \ell} \partial_\mu \ell, \quad (11.156)$$

which now involves only partial derivatives of the specific angular momentum and the latter is in general a freely specifiable function [*cf.*, Eq. (11.180)]. When the motion is purely geodetic, the acceleration  $a_\mu$  must vanish, and specialising Eq. (11.151) to the case of a rotating black

hole, it is easy to show that the angular velocity of an *equatorial* circular motion is then just the *Keplerian angular velocity* (or *Keplerian frequency*; see Problems 6 and 7)

$$\Omega_{\text{K}}^{\pm}(r) = \pm \frac{M^{1/2}}{r^{3/2} \pm a M^{1/2}}, \quad (11.157)$$

with the  $\pm$  sign referring to a fluid which is corotating or counter-rotating with respect to the compact object, respectively.

As discussed in Section 3.3 when illustrating Eq. (3.55), the fluid acceleration (11.156) represents one of the two terms in the momentum-conservation equations. We can therefore use the expression just derived for the acceleration experienced by a fluid element rotating around a compact object to obtain the Euler equations for the case we are considering, *i.e.*,

$$\partial_{\mu} \ln |u_t| - \left( \frac{\Omega}{1 - \Omega \ell} \right) \partial_{\mu} \ell = - \frac{1}{\rho h} \partial_{\mu} p. \quad (11.158)$$

Expression (11.158) now provides the basis to deduce an important theorem valid in the case of stationary and axisymmetric fluid motions around a compact object. In fact, if we take the covariant derivative of (11.158) and then contract it with the Levi-Civita tensor  $\epsilon^{\mu\nu\lambda\kappa}$  [*cf.*, Eq. (1.63)], all of the symmetric terms in  $\mu$  and  $\nu$  vanish, so that the remaining expression is

$$-\epsilon^{\mu\nu\lambda\kappa} \partial_{\mu}(\ell) \partial_{\nu} \left( \frac{\Omega}{1 - \Omega \ell} \right) = \epsilon^{\mu\nu\lambda\kappa} \frac{1}{(\rho h)^2} \partial_{\mu}(p) \partial_{\nu}(\rho h). \quad (11.159)$$

If the fluid is barotropic, that is, if  $e = e(\rho)$  and thus  $p = p(e) = p(\rho)$  (see Section 2.4.10), then the derivative of the enthalpy is proportional to the derivative of the pressure, *i.e.*,

$$\partial_{\mu}(\rho h) = \partial_{\mu}(e + p) = \left( \frac{de}{dp} + 1 \right) \partial_{\mu}p, \quad (11.160)$$

so that the right-hand side of (11.159) is symmetric in its derivatives and thus zero when contracted with the antisymmetric tensor  $\epsilon^{\mu\nu\lambda\kappa}$ . In turn, this implies that the left-hand side of (11.159) must also vanish, and this, apart from the trivial cases of rigid rotation or constant specific angular momentum, proves the thesis of the *relativistic von Zeipel's theorem* (Abramowicz, 1971), namely, that

$$\Omega = \Omega(\ell). \quad (11.161)$$

Stated differently, in stationary and axisymmetric circular flow of a barotropic fluid around a compact object, the surfaces of constant angular velocity  $\Omega$  coincide with the surfaces of constant specific angular momentum  $\ell$ . Such surfaces are also known as *von Zeipel cylinders*. This theorem was originally formulated in Newtonian gravity and stated that, within a rotating selfgravitating object, *isodensity* (or *isopycnic*, *i.e.*, at constant rest-mass density) and *isobaric* (*i.e.*, at constant pressure) surfaces coincide if and only if the angular velocity is a function of the distance from the rotation axis only [see, *e.g.*, Von Zeipel (1924), Tassoul (2007)]. As a result, the Newtonian von Zeipel cylinders are indeed *cylinders*. In a black-hole spacetime, however, the general-relativistic version of the theorem, which is due to Abramowicz (1971), reveals that this is no longer true and that the von Zeipel cylinders are cylindrical surfaces only asymptotically.

To determine their shape we can derive closed expressions for  $\ell$  and  $\Omega$  as functions of the metric, *i.e.*,

$$\ell(r, \theta) = -\frac{g_{t\phi} + g_{\phi\phi}\Omega}{g_{tt} + g_{t\phi}\Omega}, \quad (11.162)$$

$$\Omega(r, \theta) = -\frac{g_{t\phi} + g_{tt}\ell}{g_{\phi\phi} + g_{t\phi}\ell}, \quad (11.163)$$

where the second expression can be obtained after noting that the inverse of the top left corner of the metric, *i.e.*, of

$$\begin{pmatrix} g_{tt} & g_{t\phi} \\ g_{\phi t} & g_{\phi\phi} \end{pmatrix} \quad (11.164)$$

is given by

$$\begin{pmatrix} g^{tt} & g^{t\phi} \\ g^{\phi t} & g^{\phi\phi} \end{pmatrix} = \frac{1}{g_{tt}g_{\phi\phi} - (g_{t\phi})^2} \begin{pmatrix} g_{\phi\phi} & -g_{\phi t} \\ -g_{t\phi} & g_{tt} \end{pmatrix}. \quad (11.165)$$

Finally, combining Eqs. (11.162) and (11.163), we obtain the equation for the von Zeipel cylinders as

$$g_{tt}\ell + g_{t\phi}(1 + \Omega\ell) + \Omega g_{\phi\phi} = 0. \quad (11.166)$$

Hence, the locus of points  $(r, \theta)$  that satisfy Eq. (11.166), for a given pair of  $\Omega$  and  $\ell$ , selects a von Zeipel cylinder. Suppose we fix  $\ell_0$  as the value of  $\ell(r, \theta)$  on the equatorial plane at  $r_0$ , *i.e.*,  $\ell_0 := \ell(r_0, \pi/2)$ . The corresponding value of  $\Omega_0$  is

$$\Omega_0 = -\frac{\tilde{g}_{t\phi} + \tilde{g}_{tt}\ell_0}{\tilde{g}_{\phi\phi} + \tilde{g}_{t\phi}\ell_0}, \quad (11.167)$$

where the tilde over the metric function is a shorthand to remind us that they are computed at  $r = r_0, \theta = \pi/2$ . By rewriting Eq. (11.166) for the pair  $(\Omega_0, \ell_0)$  we obtain the expression

$$\ell_0^2(g_{tt}\tilde{g}_{t\phi} - g_{t\phi}\tilde{g}_{tt}) + \ell_0(g_{tt}\tilde{g}_{\phi\phi} - g_{\phi\phi}\tilde{g}_{tt}) + g_{t\phi}\tilde{g}_{\phi\phi} - g_{\phi\phi}\tilde{g}_{t\phi} = 0, \quad (11.168)$$

which defines the set of points  $(r, \theta)$  of that particular von Zeipel cylinder intersecting the equatorial plane at  $r_0$ . This expression simplifies considerably in a Schwarzschild spacetime, where  $g_{t\phi} = 0$ , the equation for the von Zeipel cylinders does not depend on the distribution of the angular momentum and it is simply given by

$$g_{tt}\tilde{g}_{\phi\phi} - g_{\phi\phi}\tilde{g}_{tt} = 0. \quad (11.169)$$

Examples of such cylinders for a Schwarzschild black hole are shown in Fig. 11.16, where the left panel shows a magnification near the event horizon and the existence of a critical cylinder with a cusp at  $r = 3M$  on the equatorial plane (see also Problem 8). The right panel, on the other hand, gives a view on a large scale and highlights the fact that the von Zeipel cylinders attain a cylindrical shape as they move away from the black hole.

As a final remark we stress that the conditions of the von Zeipel theorem (11.168) are not specific to a black hole, but apply equally to any compact object, *e.g.*, a relativistic star, as long as the corresponding metric can be cast in the form (11.142).

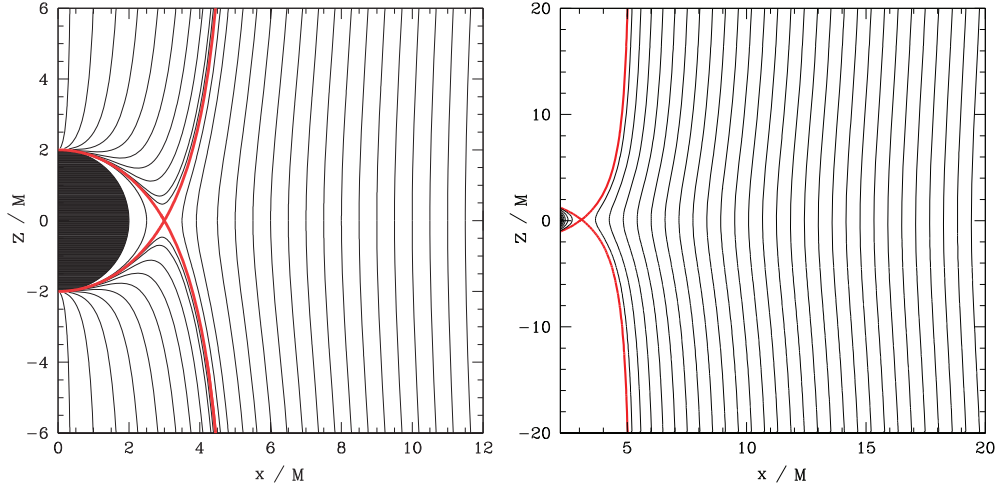


**Fig. 11.16** Examples of von Zeipel cylinders for a Schwarzschild black hole. The left panel shows a magnification near the event horizon and the existence of a critical cylinder with a cusp at  $r = 3 M$  on the equatorial plane. The right panel gives a view on a large scale and shows that the von Zeipel cylinders attain a cylindrical shape far from the black hole [adapted from Font and Daigne (2002b)].

## 11.7 Geometrically thick tori

The theory of non-geodesic, perfect-fluid, *relativistic tori* orbiting a black hole has a long history dating back to fundamental work in the 1970s (Fishbone and Moncrief, 1976; Abramowicz *et al.*, 1978; Kozłowski *et al.*, 1978). As for any stationary fluid with compact support in a gravitational field, its equilibrium is mainly determined by the balance of gravitational forces, pressure gradients and centrifugal forces. A spherical topology is natural in those configurations in which the contributions coming from the centrifugal force are much smaller than those due to pressure gradients and gravitational forces (*e.g.*, in a star). On the other hand, a toroidal topology is inevitable when the contributions to the force balance coming from the pressure gradients are smaller than those due to the centrifugal and gravitational forces. These are indeed the conditions of the fluid flow which we will consider in this section, and the interested reader will find in Nishida *et al.* (1996), Shibata (2007), and Stergioulas (2011) the extension of our analysis to geometrically thick *selfgravitating* tori.

There are at least two good reasons to discuss the properties of these fluid configurations. The first one is that, as we will show, there exist stationary axisymmetric configurations in which the matter is contained within ‘‘constant-pressure’’ equipotential surfaces. Furthermore, under rather generic conditions, these surfaces possess a sharp cusp on the equatorial plane. The existence of this cusp does not depend on the choice of the specific angular momentum distribution and introduces important dynamical differences with respect to the standard model of thin accretion discs. The second reason is instead offered by recent general-relativistic simulations of the coalescence and merger of binary neutron stars, that have shown the formation after the merger of a rapidly rotating black hole of mass  $\simeq 2 - 3 M_\odot$ , surrounded by large-scale tori with masses  $M_{\text{tor}} \lesssim 0.2 M_\odot$  (Shibata and Taniguchi, 2006; Anderson *et al.*, 2008; Baiotti *et al.*, 2008; Liu *et al.*, 2008; Giacomazzo *et al.*, 2009). Even larger masses can be pre-

dicted for binaries with unequal masses (Kiuchi *et al.*, 2009; Rezzolla *et al.*, 2010). These tori are typically axisymmetric with a quasi-Keplerian distribution of angular momenta, evolving on secular time-scales and not exhibiting dynamical instabilities (see the discussion in Section 11.7.1). As we will discuss in the remainder of this section, these properties are very close to those encountered in geometrically thick tori.

Let us therefore start by considering a background metric corresponding to a Kerr black hole in Boyer–Lindquist coordinates (see Section 1.7.2),<sup>17</sup> written in the general form (11.142). We can now take advantage of the analysis of the circular motion carried out in the previous section and assume that the fluid obeys a barotropic equation of state, such that the von Zeipel theorem holds, namely that surfaces of constant  $\ell$  and of constant  $\Omega$  coincide. In this case, the differential form  $dp/(\rho h)$  is an exact differential, so that the compatibility condition  $\partial_r \partial_\theta p = \partial_\theta \partial_r p$  is automatically fulfilled. Hence, the integration of Eq. (11.158) does not depend on the path of integration and we can write

$$\mathcal{W} - \mathcal{W}_{\text{in}} = \ln |u_t| - \ln |(u_t)_{\text{in}}| - \int_{\ell_{\text{in}}}^{\ell} \frac{\Omega d\ell'}{1 - \Omega\ell'} , \quad (11.170)$$

where the subscript “in” refers to the inner edge of the disc (in the equatorial plane), where the pressure vanishes, and is taken as a free parameter. Hereafter we will assume that the equatorial plane of the torus will in general coincide with the equatorial plane of the black hole when the latter is rotating. However, interesting dynamical effects are produced also when the black holes are “tilted” relative to the equatorial plane of the torus (Fragile and Anninos, 2005; Fragile, 2009; McKinney *et al.*, 2013).

The *effective potential*  $\mathcal{W}$  is defined as

$$\mathcal{W} - \mathcal{W}_{\text{in}} := - \int_0^p \frac{dp'}{\rho h} , \quad (11.171)$$

so that, in the Newtonian limit,  $\mathcal{W}$  represents the effective potential of a test particle in a central potential (*i.e.*, the combination of the centrifugal and gravitational potential) and Eq. (11.171) is the integral form of the equation of hydrostatic equilibrium.

Equations (11.158) simplify considerably if one considers fluid configurations with constant specific angular momentum, that is, fluids for which<sup>18</sup>

$$\ell = \pm \mathcal{U} = \text{const.} , \quad (11.172)$$

where the  $\pm$  sign reflects fluid motion which is either corotating or counter-rotating with respect to the spin of the compact object. The constant  $\mathcal{U}$ , which is assumed to be strictly positive, cannot be arbitrary, but must satisfy

$$\ell_{\text{ms}} < \mathcal{U} < \ell_{\text{mb}} , \quad (11.173)$$

where  $\ell_{\text{ms}}$  and  $\ell_{\text{mb}}$  are the specific angular momenta of the *marginally stable* and of the *marginally bound* (circular) orbit, respectively (see Section 1.7.1 and Problem 9). For a non-rotating black hole,  $\ell_{\text{ms}}/M = 3\sqrt{6}/2 \sim 3.67$  and  $\ell_{\text{mb}}/M = 4$ , while they depend on the

<sup>17</sup>Much of what we will present here is valid also for a more generic metric that is stationary and axisymmetric.

<sup>18</sup>Hereafter, when referring to the specific angular momentum we will consider the values it assumes on the equatorial plane, *i.e.*,  $\ell(r) = \ell_{\text{eq}}(r) = \ell(r, \pi/2)$ .

black-hole spin for a Kerr black hole [see, *e.g.*, Daigne and Font (2004) for a systematic discussion]. One of the advantages of configurations with constant specific angular momentum is that the angular velocity is a simple expression of the metric functions [*cf.*, Eq. (11.163)], and the equipotential surfaces can be computed directly through the metric coefficients and the value of the specific angular momentum. For example, considering again the case of a Schwarzschild black hole it is straightforward to compute that [see, *e.g.*, Daigne and Font (2004) for the equivalent expressions in the case of a Kerr black hole]

$$u_t = -r \sin \theta \sqrt{\frac{r-2}{r^3 \sin^2 \theta - \ell^2(r-2)}}, \quad (11.174)$$

so that the equipotential surfaces are simply given by [*cf.*, Eq. (11.170), (11.171)]

$$\mathcal{W}(r, \theta) = \ln |u_t| = \frac{1}{2} \ln \left[ \frac{r^2(r-2) \sin^2 \theta}{r^3 \sin^2 \theta - \ell^2(r-2)} \right], \quad (11.175)$$

where we have set  $\mathcal{W}_{\text{in}} = \ln |(u_t)_{\text{in}}|$ . Note that at any point in the  $(r, \theta)$  plane, the potential  $\mathcal{W}$  can either be positive (indicating equipotential surfaces that are open) or negative (indicating equipotential surfaces that are closed). The case  $\mathcal{W} = 0$  refers to that special equipotential surface which is closed at infinity. Interestingly, closed equipotential surfaces contain local extrema and in the equatorial plane these mark two very important points. There, in fact,  $a_\mu = \partial_\mu \mathcal{W} = 0 = \partial_\mu p$ , the motion is geodetic and an orbiting fluid element would not experience any net acceleration, with the centrifugal force balancing the gravitational force exactly.

These points correspond to the (radial) positions of the *cusp*,  $r_{\text{cusp}}$ , and of the *centre* of the torus,  $r_{\text{max}}$  (*i.e.*, where the pressure has its maximum).<sup>19</sup> At these radial positions the specific angular momentum must be that of a Keplerian geodesic circular orbit, that is (see Problem 10)

$$\ell_K^2(r) = \frac{Mr^3}{(r-2M)^2}, \quad (11.176)$$

where  $\ell_K(r)$  is the *Keplerian specific angular momentum* of a particle located at a radius  $r$  in the equatorial plane. When  $\ell = \text{const.} = \mathcal{C}$ , Eq. (11.176) can effectively be used to calculate the position of both the centre and the cusp as  $\ell_K(r) = \mathcal{C}$ . The Keplerian specific angular momentum is shown as a black solid line in the left panel of Fig. 11.17 (top part) and the intersections with  $\ell = \text{const.}$  determine the positions of the cusp  $r_{\text{cusp}}$  and of the pressure maximum  $r_{\text{max}}$  (*i.e.*, the torus’ “centre”). The figure also illustrates that the position of the cusp is necessarily located between  $r_{\text{mb}}$  and  $r_{\text{ms}}$ , as can be easily shown (Abramowicz *et al.*, 1978). Also reported in the left panel of Fig. 11.17 (bottom part) is the equatorial section of the effective potential  $\mathcal{W}_{\text{eq}}$ , illustrating how  $r_{\text{cusp}}$  and  $r_{\text{max}}$  mark the two local extrema of the effective potential, while  $r_{\text{out}}$  represents the outer edge of the torus.

Note that the green shaded areas represent the regions on the equatorial plane which can be filled up by fluid. More specifically, the light-green shaded area shows the region occupied

<sup>19</sup>The terminology can be a bit confusing here. The cusp of a torus is not a single point, but rather the circle produced by the rotation of the equivalent of the  $L_1$  Lagrangian point in a binary system around the symmetry axis.

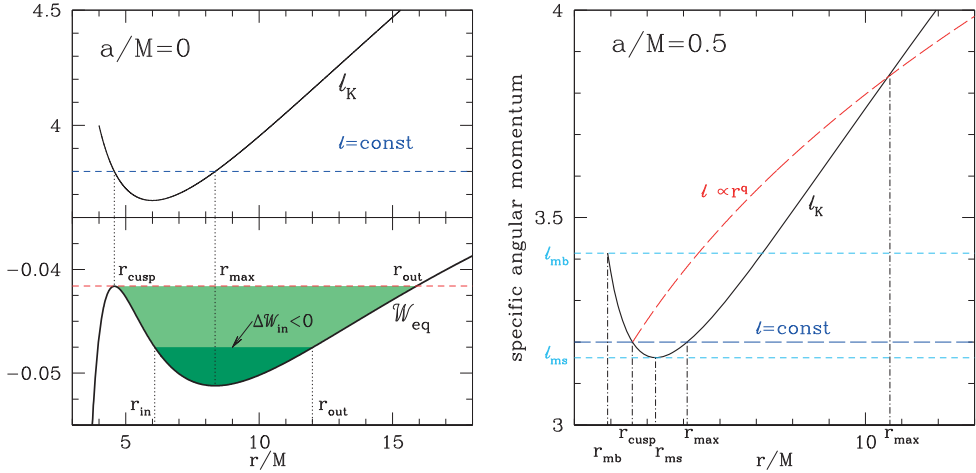


**Fig. 11.17** *Left panel:* Representative behaviour on the *equatorial plane* of the Keplerian specific angular momentum (top part) and of the effective potential  $\mathcal{W}_{\text{eq}}$  (bottom part) of a Schwarzschild black hole ( $a/M = 0$ ). The intersections of  $\ell_K$  with  $\ell = \text{const.}$  determine the positions of the cusp  $r_{\text{cusp}}$ , of the pressure maximum (*i.e.*, the torus’ “centre”)  $r_{\text{max}}$ , while  $r_{\text{out}}$  represents the outer edge of the torus. The shaded areas represent the regions which can be filled up by fluid. *Right panel:* Schematic representation on the *equatorial plane* of a Kerr black hole with  $a/M = 0.5$  of the position of the relevant radii in the cases of “constant” (purple dashed line) and “power-law” distributions of specific angular momentum (red dashed line), compared with the corresponding Keplerian one (black solid line). The relevant radii are the same as in the left panel, with  $r_{\text{mb}}$  and  $r_{\text{ms}}$  indicating the positions of the marginally bound and marginally stable orbits [adapted from Montero *et al.* (2004)].

by the fluid when this fills the outermost closed equipotential surface of the torus (*i.e.*, its “Roche lobe”),<sup>20</sup> while the dark-green shaded area refers to a fluid well inside the outermost closed equipotential surface. In either case the fluid orbital motion is *super-Keplerian* in the inner part of the torus, *i.e.*,  $\ell > \ell_K$  for  $r_{\text{in}} < r < r_{\text{max}}$ , while it is *sub-Keplerian* in the outer part of the torus, *i.e.*,  $\ell < \ell_K$  for  $r_{\text{max}} < r < r_{\text{out}}$ . In either region, the pressure gradients act to balance the excess centrifugal acceleration, with the sign of such gradients changing according to whether the motion is sub- or super-Keplerian.

The position of the *inner edge* of the torus  $r_{\text{in}}$  and the position of the cusp  $r_{\text{cusp}}$  do not necessarily coincide and, in fact,  $r_{\text{in}}$  can be chosen to be anywhere between the cusp and the centre. In practice, the inner edge is set by specifying the value of the effective potential on the equatorial plane  $\mathcal{W}(r_{\text{in}})$ , which then also automatically determines the position of the outer edge of the torus on the equatorial plane through the constraint that both points must belong to the same equipotential surface, *i.e.*,  $\mathcal{W}(r_{\text{out}}) = \mathcal{W}(r_{\text{in}})$ . Interestingly, the specification of  $\mathcal{W}(r_{\text{in}})$  provides a simple parameter to distinguish three classes of configurations in terms of the energy jump, or “*potential gap*”, between the cusp and the inner edge, *i.e.*,

<sup>20</sup>As with the cusp, note that this surface effectively represents the axisymmetric generalisation of the Roche lobe in a binary system.

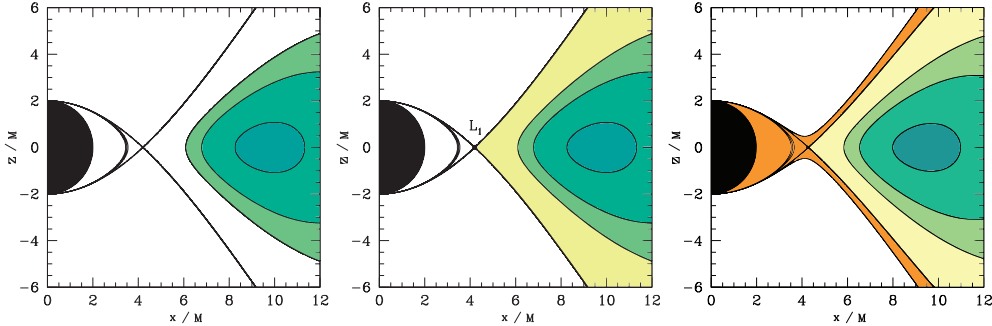


**Fig. 11.18** Different regimes for a geometrically thick torus around a Schwarzschild black hole as obtained by setting different values for  $\Delta\mathcal{W}_{\text{in}}$ . The left panel refers to the case in which  $\Delta\mathcal{W}_{\text{in}} < 0$ , thus representing a torus fully inside its “Roche lobe” and for which no mass transfer is possible. The middle panel, instead, refers to the case  $\Delta\mathcal{W}_{\text{in}} = 0$ , corresponding to a disc filling its “Roche lobe” and showing the appearance of an axisymmetric  $L_1$  Lagrangian point. Finally, the right panel refers to the case  $\Delta\mathcal{W}_{\text{in}} > 0$ , corresponding to a disc overflowing its “Roche lobe”. In all panels the black solid lines refer to equipotential surfaces of  $\mathcal{W}$  and hence also to isodensity contours if filled with matter [adapted from Font and Daigne (2002b)].

$$\Delta\mathcal{W}_{\text{in}} := \mathcal{W}_{\text{in}} - \mathcal{W}_{\text{cusp}}. \quad (11.177)$$

These three different classes of geometrically thick tori are shown in Fig. 11.18, where the black solid lines refer to equipotential surfaces of  $\mathcal{W}$ . In particular, the left panel refers to the case in which  $\Delta\mathcal{W}_{\text{in}} < 0$ , thus representing a torus fully inside its “Roche lobe” and for which no mass transfer is possible; indeed an energy input larger than  $\Delta\mathcal{W}_{\text{in}}$  is necessary to trigger the accretion in this case. The middle panel, instead, refers to the case  $\Delta\mathcal{W}_{\text{in}} = 0$ , corresponding to a disc filling its “Roche lobe” and showing the appearance of an axisymmetric  $L_1$  Lagrangian point<sup>21</sup> (see also Section 11.7.1 for a further discussion of this case). Finally, the right panel refers to the case  $\Delta\mathcal{W}_{\text{in}} > 0$ , corresponding to a disc overflowing its “Roche lobe”. This configuration received considerable attention in the 1970s, since it suggested the existence of a mechanism for triggering disc accretion onto a black hole even in the absence of a shear viscosity.

If we now restrict our attention to the case of isentropic fluids obeying a polytropic equation of state with  $p = K\rho^\Gamma$  (see Section 2.4.7), then  $dp/(\rho h) = dh/h$  and Eq. (11.171) can be integrated analytically to yield

$$h = \exp(\mathcal{W}_{\text{in}} - \mathcal{W}), \quad (11.178)$$

where we have used the fact that  $h_{\text{in}} = 1$  since  $p_{\text{in}} = 0 = e_{\text{in}}$ . Another important advantage of configurations with  $\ell = \text{const.}$  and a polytropic equation of state is that the rest-mass density distribution can be specified *analytically* and has the form

$$\rho(r, \theta) = \left[ \left( \frac{\Gamma - 1}{K\Gamma} \right) [\exp(\mathcal{W}_{\text{in}} - \mathcal{W}(r, \theta)) - 1] \right]^{1/(\Gamma-1)}. \quad (11.179)$$

<sup>21</sup>Note that as with the cusp, also the Lagrangian point is effectively a circle.

Expression (11.179) gives us the opportunity for three important remarks. First, it highlights that surfaces with constant rest-mass density (and thus isobaric surfaces given the barotropic equation of state) coincide with surfaces of constant effective potential  $\mathcal{W}$ . Second, the geometrical properties of the fluid quantities are dictated by the effective potential and since the latter is intrinsically two-dimensional [*cf.*, Eq. (11.175)], the corresponding configurations will be necessarily extended also in the vertical direction,<sup>22</sup> *i.e.*, they will be *geometrically thick tori*. This is a distinctive character imprinted on the fluid by the presence of non-negligible pressure gradients also in the vertical direction and that distinguishes this class of fluid configurations from the quasi-Keplerian ones that will be discussed in Section 11.8. Finally, since the effective potential does not depend on the microphysical properties of the fluid but only on its kinematic properties, Eq. (11.179) shows that tori with the *same physical extents but different masses* (both gravitational and rest-mass) are simply obtained after varying the polytropic index  $\Gamma$  and constant  $K$ . This rather peculiar property (we could in fact build tori with the same radial extensions but with enormous differences in the mass by simply changing the value of  $K$ ), is obviously a consequence of the test-fluid assumption and will have an important consequence on the sound speed (see Section 11.7.2).

An example of such a distribution is shown in Fig. 11.19, which reports the density distribution of a torus with constant specific angular momentum orbiting around a Schwarzschild black hole. The thin solid lines are the equipotential surfaces  $\mathcal{W}(r, \theta)$ , which are either open and intersect the black-hole horizon, or are closed and never intersect the event horizon. The thick solid line marks the outermost such closed surface, revealing the presence of a cusp.

While advantageous for a number of reasons, the condition of constant specific angular momentum (11.172) is also an idealised one. A much better approximation to the configurations that are expected to be astrophysically realistic [*e.g.*, such as those resulting from the merger of a binary system of neutron stars (Rezzolla *et al.*, 2010)] is a distribution of the angular momentum that on the equatorial plane is a simple power law of the type

$$\ell_{\text{eq}}(r) = \pm \mathcal{U} r^q. \quad (11.180)$$

An example of such a distribution is shown in the right panel of Fig. 11.17 as a red dashed line. Note that in this case the outer radius is generically placed at larger radii (*i.e.*, where the red-dashed line intersects the black solid line of the Keplerian specific angular momentum), while it may happen that  $r_{\text{cusp}} > r_{\text{ms}}$ , depending on the choice of the parameters  $\mathcal{U}$  and  $q$  in Eq. (11.180).

Clearly, the Ansatz (11.180) is very general and almost arbitrary. One constraint limiting the space of parameters comes from requiring that the tori correspond to stable fluid configurations. In Newtonian gravity this constraint is expressed by the simple *Rayleigh criterion* for stability against axisymmetric perturbations for rotating inviscid fluids, *i.e.*, (Tassoul, 2007)

$$\frac{d}{dr} [\ell_{\text{eq}}^2(r, \pi/2)] = \frac{d}{dr} (\Omega^2 r^4) > 0. \quad (11.181)$$

The situation in a general-relativistic framework is more complex. In particular, the condition of stability requires that the gradient of the specific angular momentum must never point toward the interior of the quasi-circular level surfaces of  $\ell$  (Seguin, 1975; Abramowicz and

<sup>22</sup>Here we adopt a terminology common in the disc-accretion literature, where “horizontal” and “vertical” refer respectively to the equatorial direction and to the plane perpendicular to it (Frank *et al.*, 2002; Kato *et al.*, 2008).

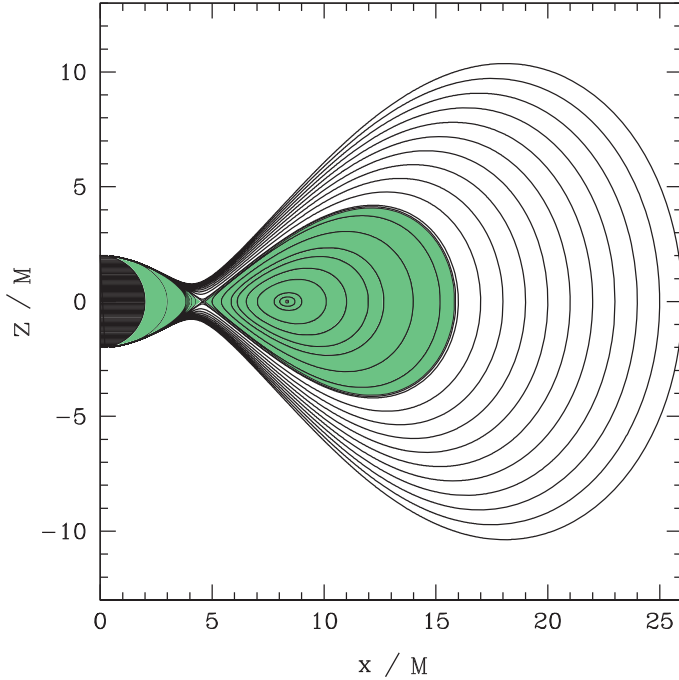


**Fig. 11.19** Prototypical torus with constant specific angular momentum and orbiting around a Schwarzschild black hole. Shown with thin solid lines are the equipotential surfaces of  $\mathcal{W}(r, \theta)$ , which are either open and intersect the black-hole horizon, or are closed and never intersect the event horizon. Marked with a thick solid line is the outermost such closed surface, revealing the presence of a cusp. This surface is the axisymmetric equivalent of a Roche lobe in a binary system [adapted from Font and Daigne (2002b)].

Prasanna, 1990). In practice, the Rayleigh stability condition translates into the constraint that  $q \geq 0$ , so that a constant angular momentum distribution is stable, although only marginally [this condition is indeed satisfied in simulations generating tori from the inspiral and merger of binary neutron stars; see Fig. 10 of Rezzolla *et al.* (2010)]. Additional constraints can be obtained after requiring that the tori possess a cusp, a centre, and with a closed equipotential through the cusp. These conditions are satisfied only when  $0 \leq q < 1/2$  and when  $|\mathcal{U}_{\text{ms}}| < |\mathcal{U}| < |\mathcal{U}_{\text{mb}}|$ , where  $\mathcal{U}_{\text{ms}}$  and  $\mathcal{U}_{\text{mb}}$  are two limiting values that are non-trivial functions of the black-hole spin and of the slope  $q$  [see, e.g., Daigne and Font (2004) for a definition of  $\mathcal{U}_{\text{ms}}$ ,  $\mathcal{U}_{\text{mb}}$  and a detailed discussion of their properties].

When the specific angular momentum is not constant, the calculation of equilibrium models, although more involved, still proceeds through the calculation of the effective potential via Eq. (11.170). As a first step, the value of  $\ell$  at any given point of coordinates  $(r, \theta)$  can be computed by solving Eq. (11.168) in the unknown  $r_0$ , which amounts to finding the position  $r_0$  where the von Zeipel cylinder through  $(r, \theta)$  intersects the equatorial plane. Once  $r_0$  has been found, the specific angular momentum at that particular point is simply  $\ell(r, \theta) = \pm \mathcal{U} r_0^q$ , while the angular velocity  $\Omega(r, \theta)$  comes from (11.163). The integration of Eq. (11.170), how-

ever, is not possible unless the functional dependence  $\Omega = \Omega(\ell)$  is known explicitly. Since this is very seldom the case, the effective potential is computed on the equatorial plane through the expression

$$\mathcal{W}_{\text{eq}}(r) = - \int_r^{+\infty} \left[ \partial_r \ln |u_t| - \left( \frac{\Omega}{1 - \Omega \ell} \right) \partial_r \ell \right] dr, \quad (11.182)$$

where we have used the condition that  $\mathcal{W}(r, \pi/2) = 0$  for  $r \rightarrow +\infty$ . In particular, the equatorial potential can be computed at the same radius  $r_0$  where the von Zeipel cylinder that passes through the point of coordinates  $(r, \theta)$  intersects the equatorial plane. Since  $d\ell = 0$  along a von Zeipel cylinder, the potential  $\mathcal{W}(r, \theta)$  at the point  $(r, \theta)$  is just

$$\mathcal{W}(r, \theta) = \mathcal{W}_{\text{eq}}(r_0) + \ln \left| \frac{u_t(r, \theta)}{u_t(r_0, \pi/2)} \right|, \quad (11.183)$$

and the density distribution is again fully described by Eq. (11.179), at least in the isentropic case. Note that also for non-constant distributions of specific angular momentum, the same considerations about the existence of local extrema and of an axisymmetric cusp in the effective potential (11.183) apply unmodified.

Independently of the specific angular momentum considered, once the rest-mass density distribution is known, *e.g.*, as in (11.179), the total *rest mass* of the torus can be easily calculated as

$$M_{T,b} := 2\pi \int \rho(r, \theta) \sqrt{-g} u^t dr d\theta, \quad (11.184)$$

where  $g$  is the determinant of the metric. As commented above when discussing Eq. (11.179), since  $\rho(r, \theta) \propto [(\Gamma - 1)/(K\Gamma)]^{1/(\Gamma-1)}$ , the rest mass of the torus can be simply rescaled via  $\Gamma$  and  $K$  for tori filling the same outermost equipotential surface. Similarly, the total *mass-energy* in the torus is computed as (see Problem 11)

$$M_T := 2\pi \int (T_r^r + T_\phi^\phi + T_\theta^\theta - T_t^t) \sqrt{-g} dr d\theta. \quad (11.185)$$

### 11.7.1 The “runaway” instability

It is useful to go back to the classification of the different classes of tori in terms of the energy gap at the inner edge,  $\Delta\mathcal{W}_{\text{in}}$ , to point out the potential development of an instability in the case in which  $\Delta\mathcal{W}_{\text{in}} \geq 0$  and a small amount of mass can be lost through the cusp. To appreciate why this process can lead to an instability, consider that when matter flows through the cusp, it will be on orbits below the marginally stable orbit and therefore forced to accrete onto the black hole. In turn, this would increase the mass of the black hole and change its angular momentum (either increasing or decreasing it according to whether the torus is corotating or counter-rotating), thus affecting the equipotential surfaces and the location of the cusp. If, as a result of this process, the cusp moved to *smaller* radial positions, the new configuration *would be* in equilibrium and no further accretion would follow. If, on the other hand, the cusp moved to *larger* radial positions, the new configuration *would not be* in equilibrium and additional material (which was previously in equilibrium) would accrete onto the black hole which, in turn, would further increase its mass. This process could trigger a runaway mechanism in

which more and more mass is accreted onto the black hole, evacuating the whole torus on a dynamical time-scale of a few orbital periods. This is usually referred to as the *runaway instability* of geometrically thick tori (Abramowicz *et al.*, 1983).

Although this instability was first studied in the 1980s (Abramowicz *et al.*, 1983; Wilson, 1984), time-dependent hydrodynamic simulations have been performed only recently, either with SPH techniques and pseudo-Newtonian potentials (Masuda and Eriguchi, 1997), or with HRSC techniques in general relativity (Font and Daigne, 2002*b*; Zanotti *et al.*, 2003). These investigations have shown that, under the assumption of constant specific angular momentum distributions and that the torus mass falling onto the black hole instantaneously increases its mass, relativistic tori around Schwarzschild and Kerr black holes are generically unstable to the runaway instability, if non-selfgravitating. However, the inclusion of more generic initial conditions can disfavour the occurrence of the instability. More recently, Font and Daigne (2002*a*), Zanotti *et al.* (2003), and Daigne and Font (2004), have shown through numerical simulations that the runaway instability is suppressed when a non-constant distribution of the angular momentum is assumed, a result which is in agreement with studies based on a recent perturbative analysis (Rezzolla *et al.*, 2003*a*; Rezzolla *et al.*, 2003*b*). Although a final conclusion on the occurrence of this instability in astrophysically realistic conditions has not yet been reached, recent fully general-relativistic simulations seem to converge on the evidence that this instability does not take place in practice, at least for non-magnetised perfect fluids and generic distribution of angular momentum. In fact, simulations performed either in axisymmetry (Montero *et al.*, 2010) or in three dimensions (Rezzolla *et al.*, 2010; Korobkin *et al.*, 2011), under controlled initial conditions (Montero *et al.*, 2010; Korobkin *et al.*, 2011) or as a result of fully dynamical situations (Rezzolla *et al.*, 2010), all indicate that the tori are stable over time-scales of the order of the orbital time-scale or longer (see also the related discussion in Section 12.5.3). However, some room for the development of the instability may be open in the case of selfgravitating tori with constant specific angular momentum (Korobkin *et al.*, 2013).

### 11.7.2 On the sound speed in polytropic tori

We have already discussed that the rest mass of a non-selfgravitating, polytropic fluid configuration orbiting in hydrostatic equilibrium around a compact object can be rescaled simply by changing the polytropic constant  $K$ , or the polytropic exponent  $\Gamma$ . This peculiar aspect of these configurations is accompanied by another one, equally intriguing. Indeed, a geometrically thick disc around a compact object has a sound speed which is *invariant* under changes of the polytropic constant  $K$  (Rezzolla *et al.*, 2003*b*).

To prove this result it is convenient to consider the Schwarzschild metric in cylindrical coordinates  $(t, \varpi, \phi, z)$  and retain the zeroth-order terms in the ratio  $(z/\varpi)$  as done by Novikov and Thorne (1973), *i.e.*,

$$ds^2 = -e^{2\nu(\varpi)} dt^2 + e^{2\lambda(\varpi)} d\varpi^2 + dz^2 + \varpi^2 d\phi^2, \quad (11.186)$$

where

$$e^{2\nu(\varpi)} := 1 - \frac{2M}{\varpi} =: e^{-2\lambda(\varpi)}. \quad (11.187)$$

Without loss of generality, we can rewrite the equivalent expressions for the acceleration (11.152) and (11.156) as (Montero and Zanotti, 2012)

$$\begin{aligned}\partial_i \ln |u_t| - \frac{\Omega}{1 - \Omega\ell} \partial_i \ell &= -\partial_t \ln |u^t| + \frac{\ell}{1 - \Omega\ell} \partial_i \Omega \\ &= \frac{(u^t)^2}{2} (\partial_i g_{tt} + 2\Omega \partial_i g_{t\phi} + \Omega^2 \partial_i g_{\phi\phi}),\end{aligned}\quad (11.188)$$

which thus involves only derivative of the metric functions. Using now expressions (11.187), we can write the radial part of the hydrostatic equilibrium equations (11.158) as

$$\frac{\partial_\varpi p}{e + p} = -\frac{e^{2\nu} \partial_\varpi \nu - \Omega^2 \varpi}{e^{2\nu} - \Omega^2 \varpi^2} = f(\varpi). \quad (11.189)$$

The right-hand side of Eq. (11.189) depends only on the kinematic and geometric properties of the disc, namely on the angular momentum distribution (through  $\Omega$ ) and on the external gravitational field of the central black hole (through the metric function  $e^\nu$ ). Both of these quantities depend on  $\varpi$  only. Recalling that the polytropic index  $N_p$  is defined as  $N_p = 1/(\Gamma - 1)$  (see Section 2.4.7) and introducing the Emden function  $\Pi$  (not to be confused with the viscous bulk pressure introduced in Section 6.2), such that  $\Pi := \rho^{1/N_p}$ , we can write the polytropic equation of state (2.242) as

$$p = K\Pi^{N_p+1}, \quad (11.190)$$

so that Eq. (11.189) effectively becomes

$$\frac{\partial_\varpi \psi}{1 + \psi} = f(\varpi), \quad (11.191)$$

where we have defined

$$\psi := K(N_p + 1)\Pi. \quad (11.192)$$

Equation (11.191) can be integrated analytically to give

$$\psi(\varpi) = \mathcal{C} \exp \left[ \int_{\varpi_{\text{in}}}^{\varpi} f(\varpi') d\varpi' \right] - 1, \quad (11.193)$$

where  $\mathcal{C}$  is an arbitrary constant. The important result contained in Eq. (11.193) is that  $\psi$  is a function of  $\varpi$  only and will not depend, therefore, on the specific value chosen for  $K$ . As a result, once  $\Gamma$  (and thus  $N_p$ ) is fixed, any transformation  $K \rightarrow K\alpha$ , where  $\alpha$  is an arbitrary constant, must be accompanied by a corresponding transformation  $\Pi \rightarrow \Pi/\alpha$ . An important consequence of this is that all of the quantities given by

$$\frac{p}{\rho}, \quad \frac{dp}{d\rho}, \quad \frac{p}{e}, \quad \frac{dp}{de}, \quad (11.194)$$

are invariant under changes in  $K$ . Hence, the sound speed, which, we recall, is defined as  $c_s^2 := (dp/d\epsilon)_s$  [cf. Eq. (2.168)], is also *invariant* under such a transformation (Rezzolla *et al.*, 2003b).

Interestingly, therefore, once the parameters of the background model for the geometrically thick disc have been fixed, *i.e.*, the distribution of angular momentum and the potential gap, different choices for  $K$  will yield tori with different rest-mass density distributions and hence rest masses, but with the same extensions and the same sound speed. Finally, note that this result can be shown to apply also in Newtonian physics, when the central black hole is replaced by a generic spherically symmetric gravitational potential.

### 11.7.3 Thick tori in Schwarzschild–de Sitter spacetimes

We have so far considered geometrically thick tori around compact objects, *e.g.*, black holes and neutron stars, as described by the metric (11.142). While these are the cases that are astrophysically relevant, it is also interesting to consider stationary and axisymmetric fluid motions in less trivial spacetimes and a good example in this sense is offered by a *Schwarzschild–de Sitter* spacetime. In what follows we briefly recall the main features of stationary configurations in such spacetimes referring the reader to Stuchlík *et al.* (2000) and Rezzolla *et al.* (2003c) for a more complete discussion. We start by recalling that within a spherical coordinate system  $(t, r, \theta, \phi)$  the metric of a Schwarzschild–de Sitter spacetime reads

$$ds^2 = - \left( 1 - \frac{2M}{r} - y \frac{r^2}{M^2} \right) dt^2 + \left( 1 - \frac{2M}{r} - y \frac{r^2}{M^2} \right)^{-1} dr^2 + r^2(d\theta^2 + \sin^2 \theta d\phi^2), \quad (11.195)$$

where  $M$  is the mass of the black hole and the cosmological constant  $\Lambda$  is incorporated in the dimensionless parameter  $y$  defined as

$$y := \frac{1}{3} \Lambda M^2. \quad (11.196)$$

This parameter has to be smaller than a critical value  $y < y_c := 1/27$  in order to produce static regions of the spacetime where equilibrium configurations can be found. Once  $M$  and  $\Lambda$  have been prescribed, the explicit expression for the potential  $\mathcal{W}(r, \theta)$  in the Schwarzschild–de Sitter spacetime for a torus with  $\ell = \text{const.}$  [*cf.*, Eq. (11.172)] is given by (Stuchlík *et al.*, 2000)

$$\mathcal{W}(r, \theta) = \frac{1}{2} \ln \left[ \frac{(1 - 2M/r - yr^2/M^2)r^2 \sin^2 \theta}{r^2 \sin^2 \theta - (1 - 2M/r - yr^2/M^2)\ell^2} \right], \quad (11.197)$$

which obviously reduces to Eq. (11.175) in the case in which  $y = 0$ .

The new potential  $\mathcal{W}(r, \theta)$  shows *three* local extrema in the equatorial plane, that is, one more than in the case of a Schwarzschild spacetime. Ordering these points with increasing values of  $r$ , the first extremum corresponds to the position of the inner cusp,  $r_{ci}$  (this was named  $r_{cusp}$  in a Schwarzschild black hole), where the equipotential surface has a self-crossing point in the  $(r, \theta)$  plane. The second extremum corresponds to the position of the “centre” of the torus,  $r_{\max}$ , where the internal pressure of the torus has its maximum. The third extremum marks instead the position of the outer cusp,  $r_{co}$ , which is not present in the Schwarzschild spacetime and represents the distinctive contribution of the nonzero cosmological constant (see Fig. 11.20 for a schematic diagram and contrast it with Fig. 11.17).<sup>23</sup> Also in this case, the fluid motion at  $r_{ci}$ ,  $r_{\max}$  or  $r_{co}$  is purely geodetic, with the specific angular momentum given by the Keplerian one for a point-like particle at that radius (Stuchlík *et al.*, 2000)

$$\ell_K^2(r, y) := \frac{r^3 M (1 - yr^3/M^3)}{(r - 2M - yr^3/M^2)^2}, \quad (11.198)$$

which again reduces to Eq. (11.176) when  $y = 0$  (see also Problems 6 and 7).

<sup>23</sup>Note that because of the smallness of the cosmological constant as deduced from recent cosmological observations, *i.e.*,  $\Lambda \sim 10^{-56} \text{ cm}^{-2}$ , the outer cusp would be at  $\sim 50\text{--}100$  kpc for supermassive black holes with masses in the range  $\sim 10^8\text{--}10^9 M_\odot$ . In other words, astrophysical tori of these sizes are possible in principle, but are not realistic and have never been observed so far.

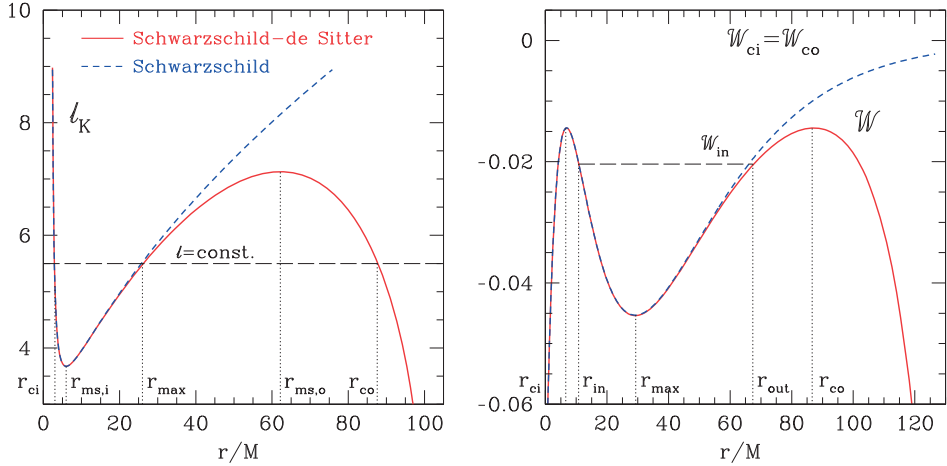


**Fig. 11.20** Schematic diagram for the Keplerian specific angular momentum  $\ell_K$  in a Schwarzschild–de Sitter spacetime (left panel) and the corresponding effective potential  $\mathcal{W}$  (right panel) once a constant value for  $\ell$  has been chosen (*cf.* Fig. 11.17). Reported are the radial locations of the inner and outer cusp points  $r_{ci}$ ,  $r_{co}$ , the inner and outer radii for the torus  $r_{in}$ ,  $r_{out}$ , the inner and outer marginally stable orbits  $r_{ms,i}$ ,  $r_{ms,o}$ , and the location of the maximum pressure in the torus  $r_{max}$ . Note that  $r_{ci}$ ,  $r_{co}$  and  $r_{max}$  are determined once a value for the constant specific angular momentum has been chosen (this is shown with the long-dashed line in the left panel) and that the inner and outer radii need not coincide with the corresponding locations of the cusps but are set by the value chosen for the potential  $\mathcal{W}_{in}$  (long-dashed line in the right panel). Reported for comparison with a short-dashed line are  $\ell_K$  and  $\mathcal{W}$  in a Schwarzschild spacetime, which was discussed in Fig. 11.17 [adapted from Rezzolla *et al.* (2003c)].

The space of possible values for a constant specific angular momentum distribution is considerably more complex in the case of a Schwarzschild–de Sitter spacetime, since it is necessary to take into account also the constraints on the acceptable values for  $y$ . A detailed discussion of this issue is provided by Stuchlík *et al.* (2000), and we here recall only that a toroidal configuration of finite size is obtained for values of the specific angular momentum that satisfy

$$\ell_{ms,i} < \ell < \ell_{ms,o}, \quad (11.199)$$

where now  $\ell_{ms,i}$  and  $\ell_{ms,o}$  represent the values of the specific angular momentum at the inner and outer marginally stable radii, respectively, and correspond to the local minimum and maximum of the Keplerian specific angular momentum given by Eq. (11.198) (see Fig. 11.20). Hence,  $\ell_{ms,i}$  and  $\ell_{ms,o}$  provide the minimum and maximum values of  $\ell(r, y)$  for which stable Keplerian circular orbits exist. Note that the very existence of these stable circular orbits depends on the values of  $y$  and these can be found only if  $y < y_{ms} < y_c$ , where  $y_{ms} = 12/15^4$ . In other words, given a value for the dimensionless parameter  $\bar{y} < y_{ms}$ , circular orbits can exist for  $\ell_{ms,i}(\bar{y}) < \ell < \ell_{ms,o}(\bar{y})$ . Clearly, these orbits will be at radii smaller than the static radius  $r_s/M := \bar{y}^{-1/3}$ , at which the angular momentum (11.198) is zero and where the

gravitational attraction of the black hole is exactly balanced by the cosmological repulsion.<sup>24</sup>

Once values for the cosmological parameter and for the angular momentum have been fixed, Eq. (11.158), supplemented for instance by the polytropic equation of state, can be integrated analytically for any  $r \leq r_s$  to yield the rest-mass density distribution inside the torus via expression (11.179). Numerical simulations of geometrically thick, constant specific angular momentum tori in Schwarzschild–de Sitter spacetimes have been recently reported by Rezzolla *et al.* (2003c), where it was shown that the runaway instability is no longer the only evolution possible for these systems, but that their dynamics is rather the end-result of the interplay between the mass outflows at the inner and the outer cusps. On the one hand, initial models for which the cosmological constant has a weak influence have negligible mass outflows to infinity while maintaining large mass outflows onto the black hole through the *inner cusp*, which then lead to the development of the runaway instability. On the other hand, initial models which are significantly influenced by the cosmological constant develop mass outflows through the *outer cusp* which are much larger than those appearing at the inner cusp and do not develop the runaway instability. Placed between these two classes of initial configurations, there exist initial models for which the mass outflows from the inner and outer cusps are more closely balanced. In these cases the runaway instability may or may not develop [see, *e.g.*, Rezzolla *et al.* (2003c) for a detailed discussion].

## 11.8 Relativistic accreting discs

In addition to the stationary axisymmetric solutions discussed in the previous section for fluids orbiting around a black hole, other solutions are possible in which the fluid is allowed to accrete onto the black hole on a time-scale which is set by dissipative processes and is therefore much larger than the orbital time-scale. In this case, there are three basic classes of models of accretion discs, which have been proposed over the years to reproduce the observed properties of AGNs (active galactic nuclei) and galactic X-ray binaries. These disc models can be classified in terms of their geometrical “thickness”  $H(r)$ , when the latter is compared with the distance  $r$  from the black hole. It is then possible to consider a first class of accreting disc models called “*thin discs*”, which have  $H(r) \ll r$  and are described by the Shakura and Sunyaev (1973) solution in Newtonian gravity and by the Novikov and Thorne (1973) solution in general relativity. Similarly, another class is represented by the so-called “*thick discs*”, which have instead  $H(r) \gg r$ , and that we have illustrated in detail in the previous section. Finally, an intermediate and third class is represented by the so-called “*slim discs*” (Abramowicz *et al.*, 1988), which have  $H(r) \lesssim r$  and that will be the focus of this section.

Independently of the geometry of the accreting disc, the mechanism effectively determining the accretion of matter onto the black hole is still a matter of intense research, but it has already appeared quite early in accretion-disc theory that microscopic transport phenomena (*i.e.*, based on simple molecular viscosity) are too inefficient to account for the observed properties [see, *e.g.*, Treves *et al.* (1989)]. At the same time, it has also emerged that turbulent

<sup>24</sup>Note that the Keplerian specific angular momentum (11.198) is not defined for  $r > r_s$ , where its square is negative.

transport of angular momentum, most likely mediated by magnetic fields and magnetohydrodynamic instabilities, such as the *magnetorotational instability (MRI)*, must play a fundamental role [see, *e.g.*, Balbus and Hawley (1998)]. We will not address here the magnetohydrodynamic aspects of disc-accretion theory and concentrate instead on purely hydrodynamic ones, as they represent an excellent arena in which to make use of many of the tools and concepts developed in Chapter 6 on the relativistic hydrodynamics of non-perfect fluids. Our presentation is similar but distinct from that of advection-dominated accretion flows around Kerr black holes given in Abramowicz *et al.* (1996).<sup>25</sup> A more comprehensive discussion of the theory and phenomenology of accreting discs can be found in Frank *et al.* (2002), Kato *et al.* (2008) and Abramowicz and Fragile (2013).

Before entering into the details of the mathematical framework needed to describe a relativistic slim-disc model, it is useful to emphasise two important features that distinguish slim discs from their quasi-Keplerian equivalents, *i.e.*, thin discs. First, the angular velocity of fluid elements in slim discs is not assumed *a priori* to be Keplerian (as it is for thin discs) and the pressure gradient in the horizontal (radial) direction is therefore dynamically important. As a result, slim-disc models are described by a set of ordinary differential equations containing one equation more than for thin discs (*i.e.*, the radial Euler equation) and, in the case of stationary models, one must explicitly solve the eigenvalue problem connected with a regularity condition at the sonic radius. Second, while for thin-disc models a local heat balance is assumed (*i.e.*, the heat generated by viscous stresses is radiated away at the same radius through the disc surface), heat transport in the horizontal direction via advection represents an important cooling mechanism in slim-disc models.<sup>26</sup>

Let us consider now a fixed background spacetime and, as in the previous sections of this chapter, we will assume that the disc has a mass much smaller than that of the black hole, so that the metric will be simply that of a Kerr black hole. Furthermore, since we are interested in the portion of the spacetime in the vicinity of the equatorial plane (*i.e.*, for values of the spherical angular coordinate  $|\theta - \pi/2| \ll 1$ ), we write the Kerr metric in the Boyer–Lindquist coordinates  $(t, r, \theta, \phi)$  and introduce the cylindrical vertical coordinate  $z = r \cos \theta \simeq r(\pi/2 - \theta)$  to define quantities very close to the equatorial plane, where  $z \approx 0$ . In this way, the Kerr metric (1.251) can be expanded around the equatorial plane and the resulting form at zeroth order in the ratio  $(z/r)$  was first derived by Novikov and Thorne (1973) to be [see, *e.g.*, Riffert and Herold (1995) for an expression to second order in  $(z/r)$ ]

$$ds^2 = -\frac{r^2 \Delta}{A} dt^2 + \frac{A}{r^2} (d\phi - \omega dt)^2 + \frac{r^2}{\Delta} dr^2 + dz^2, \quad (11.200)$$

where

$$\Delta := r^2 - 2Mr + a^2, \quad (11.201)$$

$$A := r^4 + r^2 a^2 + 2Mra^2 = (r^2 + a^2)^2 - a^2 \Delta, \quad (11.202)$$

<sup>25</sup>A time-dependent, non-vertically integrated version of the equations presented here can be found in Rezzolla (1996a).

<sup>26</sup>When advection represents the most important cooling mechanism, it is possible to construct solutions for optically thin-disc models whose luminosity is much smaller than that of standard thin discs with the same accretion rate.

$$\omega := -\frac{g_{t\phi}}{g_{\phi\phi}} = \frac{2Mar}{A}, \quad (11.203)$$

and a bit of algebra and several simplifications can show that  $g_{tt} = -(1 - 2M/r)$ . We recall that in (11.201),  $M$  is the gravitational mass of the black hole and  $a/M$  is the dimensionless Kerr parameter, so that the black-hole angular momentum can be expressed as  $J = aM$ .

Physical quantities that will often be used in the following are the angular velocity with respect to stationary observers at infinity,  $\Omega$ , [cf., Eq. (11.146)], and the angular velocity  $\omega$  [cf., Eq. (1.256)] of local non-rotating observers, *i.e.*, the zero angular momentum observers, ZAMOs, introduced by Bardeen *et al.* (1972). Because of the preferred direction introduced by the spin of the black hole, there will be corotating (+) and counter-rotating (−) angular frequencies for Keplerian orbits  $\Omega_{\text{K}}^{\pm}$  [cf., Eq. (11.157)], having a Keplerian specific angular momentum given by [cf., Eqs. (11.176) and (11.198), and see Problem 12 for a derivation]

$$\ell_{\text{K}}^{\pm} = \pm \frac{M^{1/2}(r^2 \mp 2aM^{1/2}r^{1/2} + a^2)}{r^{3/4}(r^{3/2} - 3Mr^{1/2} \pm 2aM^{1/2})^{1/2}}. \quad (11.204)$$

Note that  $\ell_{\text{K}}^{\pm}$  has a minimum at the marginally stable orbit  $r_{\text{ms}}^{\pm}$  [cf., Eq. (1.267) and Fig. 11.17].

Within the metric (11.200), vector and tensor quantities can be evaluated in several frames, with the optimal choice changing from case to case. Relevant frames are the *locally non-rotating* or ZAMO frame, which is at fixed  $r, z$  coordinates and rotates at the angular velocity of a particle which has zero angular momentum at infinity; the *orbiting* frame, which is at fixed  $r, z$  coordinates and corotates with matter in the disc; and the *comoving* frame, which is the “infalling” equivalent of the orbiting frame and thus only at constant  $z$  coordinate. If orthonormal tetrads are introduced in all of these frames, it is then possible to express the relevant quantities in a form familiar from special relativity.

We start with the ZAMO tetrad,  $(e_{\hat{t}}, e_{\hat{r}}, e_{\hat{z}}, e_{\hat{\phi}})$ , which we express in terms of the coordinate basis  $(e_t, e_r, e_z, e_\phi)$  as (Rezzolla, 1996a)

$$e_{\hat{t}} = \frac{1}{r} \sqrt{\frac{A}{\Delta}} (e_t + \omega e_\phi), \quad e_{\hat{r}} = \frac{\sqrt{\Delta}}{r} e_r, \quad (11.205)$$

$$e_{\hat{z}} = e_z = \frac{1}{r} e_\theta, \quad e_{\hat{\phi}} = \frac{r}{\sqrt{A}} e_\phi, \quad (11.206)$$

while the corresponding one-forms are given by

$$\omega^{\hat{t}} = r \sqrt{\frac{\Delta}{A}} dt, \quad \omega^{\hat{r}} = \frac{r}{\sqrt{\Delta}} dr, \quad (11.207)$$

$$\omega^{\hat{z}} = dz, \quad \omega^{\hat{\phi}} = \frac{\sqrt{A}}{r} (d\phi - \omega dt). \quad (11.208)$$

In the ZAMO frame, the components of the three-velocity are indicated with “hats” and are defined as [cf., Eq. (1.114)]<sup>27</sup>

<sup>27</sup>The definition of three-velocity adopted in this section is slightly different from the one used in numerical simulations, which refers to the three-velocity measured by normal observers and is defined by Eq. (7.19).

**556 Relativistic Hydrodynamics of Non-Selfgravitating Fluids**

$$v^{\hat{i}} := \frac{u^{\hat{i}}}{u^{\hat{t}}} = \frac{\omega_{\alpha}^{\hat{i}} u^{\alpha}}{\omega_{\alpha}^{\hat{t}} u^{\alpha}}, \quad (11.209)$$

so that, for a four-velocity describing an orbiting fluid which is also (slowly) accreting with  $u := u^r$  and  $u^z \simeq 0$ , *i.e.*,  $u^\mu = (u^t, u, 0, u^\phi)$ , the relevant components of the three-velocity are<sup>28</sup>

$$v^{\hat{r}} = \frac{u^{\hat{r}}}{u^{\hat{t}}} = \frac{\sqrt{A}}{u^t \Delta} u = \frac{1}{\gamma} \left( \frac{\Delta}{r^2} + u^2 \right)^{-1/2} u, \quad (11.210)$$

$$v^{\hat{\phi}} = \frac{u^{\hat{\phi}}}{u^{\hat{t}}} = \frac{A}{r^2 \sqrt{\Delta}} (\Omega - \omega) = \mathcal{R}(\Omega - \omega) = \mathcal{R}\tilde{\Omega}, \quad (11.211)$$

where

$$\gamma := \left[ 1 - (v^{\hat{\phi}})^2 \right]^{-1/2} = \left[ 1 - \frac{A^2}{r^4 \Delta} (\Omega - \omega)^2 \right]^{-1/2}. \quad (11.212)$$

The quantity  $\mathcal{R}$  in Eq. (11.211) is the *radius of gyration*, whose definition

$$\mathcal{R} := \left( \frac{g_{\phi\phi}^2}{g_{t\phi}^2 - g_{tt}g_{\phi\phi}} \right)^{1/2} = \frac{A}{r^2 \sqrt{\Delta}} \quad (11.213)$$

is a relativistic generalisation of the corresponding Newtonian quantity [Eq. (11.211) does indeed have the same form of the equivalent Newtonian expression] and it represents a useful tool for analysing rotational effects in strong gravitational fields (Abramowicz *et al.*, 1993). Using Eqs. (11.210) and (11.211), it is possible to define the Lorentz factor with respect to the ZAMO observer as

$$W := \left[ 1 - (v^{\hat{r}})^2 - (v^{\hat{\phi}})^2 \right]^{-1/2} = \frac{r}{\sqrt{\Delta}} \left( \frac{\Delta}{r^2} + u^2 \right)^{1/2} \gamma. \quad (11.214)$$

Note that while  $W$  represents the standard Lorentz factor and is divergent at the horizon (*i.e.*, at  $r = r_+ = M + \sqrt{M^2 - a^2}$ ),  $\gamma$  accounts for a velocity boost produced by the difference in angular velocity between the matter in the disc and the ZAMO, and is equal to one at the horizon, where  $\Omega - \omega = 0$ .

Using now Eqs. (11.210), (11.211), and (11.214), we can express the normalisation condition for the fluid four-velocity  $u^\mu u_\mu = -1$  [*cf.* Eq. (3.2)] as

$$u^t = \frac{W}{r} \sqrt{\frac{A}{\Delta}}, \quad u = \frac{W \sqrt{\Delta}}{r} v^{\hat{r}}. \quad (11.215)$$

In a similar way, we can compute the nonzero components of the *orbiting tetrad* as these will be useful later on when discussing vertical hydrostatic equilibrium. We express the tetrad

<sup>28</sup>Note that at the horizon  $\Delta = 0 = \Omega - \omega$ , so that  $v^{\hat{r}} = 1$ ,  $v^{\hat{\phi}} = 0$ , as expected for a flow that can only be luminal and radial at the horizon.

of the orbiting frame ( $\mathbf{e}_{\bar{t}}$ ,  $\mathbf{e}_{\bar{r}}$ ,  $\mathbf{e}_{\bar{z}}$ ,  $\mathbf{e}_{\bar{\phi}}$ ) in terms of the coordinate basis and of the ZAMO tetrad as<sup>29</sup>

$$\mathbf{e}_{\bar{t}} = \frac{\gamma}{r} \sqrt{\frac{A}{\Delta}} (\mathbf{e}_t + \Omega \mathbf{e}_\phi) = \gamma \left( \mathbf{e}_{\hat{t}} + v^{\hat{\phi}} \mathbf{e}_{\hat{\phi}} \right), \quad (11.218)$$

$$\mathbf{e}_{\bar{r}} = \frac{\sqrt{\Delta}}{r} \mathbf{e}_r = \mathbf{e}_{\hat{r}}, \quad (11.219)$$

$$\mathbf{e}_{\bar{z}} = \frac{1}{r} \mathbf{e}_z = \mathbf{e}_{\hat{z}}, \quad (11.220)$$

$$\mathbf{e}_{\bar{\phi}} = \gamma \left[ \frac{r}{\sqrt{A}} \mathbf{e}_\phi + \frac{v^{\hat{\phi}}}{r} \sqrt{\frac{A}{\Delta}} (\mathbf{e}_t + \omega \mathbf{e}_\phi) \right] = \gamma \left( v^{\hat{\phi}} \mathbf{e}_{\hat{t}} + \mathbf{e}_{\hat{\phi}} \right). \quad (11.221)$$

Indicating now with “bars” the components of any tensor with respect to this orbiting tetrad, it is then easy to show that<sup>30</sup>

$$v^{\bar{r}} = \gamma v^{\hat{r}} = \left( \frac{\Delta}{r^2} + u^2 \right)^{-1/2} u, \quad v^{\bar{\phi}} = 0. \quad (11.222)$$

Our discussion so far has been rather general [the only exception being the expanded metric (11.200)], but a number of assumptions are needed to make the problem tractable at an analytic level. Therefore, we will assume that:

- (i) the plane of the disc coincides with the equatorial plane of the black hole.
- (ii) the disc is geometrically thin, *i.e.*,  $H(r) \ll r$ , where  $H(r)$  is the disc thickness at  $r$ .
- (iii) the accretion flow is quasi-stationary, so that if we define the average

$$\langle \Psi \rangle := \frac{1}{2\pi\delta r\delta t} \int_0^{2\pi} \int_{r-\delta r/2}^{r+\delta r/2} \int_{t-\delta t/2}^{t+\delta t/2} \Psi d\phi dr' dt', \quad (11.223)$$

for any physical quantity  $\Psi$ , then

$$\mathcal{L}_\eta \langle \Psi \rangle = 0, \quad (11.224)$$

where  $\mathcal{L}_\eta$  is the Lie derivative along the timelike Killing vector  $\eta$  [*cf.* Eq. (11.143)]. The average in (11.223) is meant to be done over a length-scale comparable with the thickness of the disc and over a time-scale comparable with the accretion time-scale over the same length-scale, *i.e.*,

$$\delta r \simeq 2H/\sqrt{g_{rr}}, \quad \delta t \simeq \sqrt{g_{rr}}\delta r/(v^{\hat{r}}\sqrt{g_{rr}}) = 2H/(v^{\hat{r}}\sqrt{g_{rr}}). \quad (11.225)$$

<sup>29</sup>For completeness we report also the tetrad of the comoving frame ( $\mathbf{e}_{\bar{t}}$ ,  $\mathbf{e}_{\bar{r}}$ ,  $\mathbf{e}_{\bar{z}}$ ,  $\mathbf{e}_{\bar{\phi}}$ ) when expressed in terms of the ZAMO tetrad, *i.e.*,

$$\mathbf{e}_{\bar{t}} = W \left( \mathbf{e}_{\hat{t}} + v^{\hat{r}} \mathbf{e}_{\hat{r}} + v^{\hat{\phi}} \mathbf{e}_{\hat{\phi}} \right), \quad \mathbf{e}_{\bar{r}} = W v^{\hat{r}} \mathbf{e}_{\hat{t}} + \left[ (W-1)n^{\hat{r}}n^{\hat{r}} + 1 \right] \mathbf{e}_{\hat{r}} + (W-1)n^{\hat{\phi}}n^{\hat{r}} \mathbf{e}_{\hat{\phi}}, \quad (11.216)$$

$$\mathbf{e}_{\bar{z}} = \mathbf{e}_{\hat{z}}, \quad \mathbf{e}_{\bar{\phi}} = W v^{\hat{\phi}} \mathbf{e}_{\hat{t}} + (W-1)n^{\hat{\phi}}n^{\hat{r}} \mathbf{e}_{\hat{r}} + \left[ (W-1)n^{\hat{\phi}}n^{\hat{\phi}} + 1 \right] \mathbf{e}_{\hat{\phi}}, \quad (11.217)$$

where  $\hat{v}^2 := v_j v^j$ , and  $n^i := v^i/\hat{v}$ .

<sup>30</sup>In Abramowicz *et al.* (1996), the radial velocity in the orbiting frame,  $v^{\bar{r}}$  is related to the (rescaled) radial velocity  $V$ , which is defined as  $V/\sqrt{1-V^2} = W v^{\hat{r}} = ru/\sqrt{\Delta}$ .

## 558 Relativistic Hydrodynamics of Non-Selfgravitating Fluids

(iv) the motion of the fluid elements is very nearly geodesic with a predominantly azimuthal flow, *i.e.*,

$$0 \simeq |v^{\hat{z}}| \ll |v^{\hat{r}}| \ll |v^{\hat{\phi}}| \simeq (M/r)^{1/2}. \quad (11.226)$$

(v) the internal energy density is much smaller than the gravitational binding energy density, *i.e.*,  $\rho\epsilon \ll \rho(1 - E)$ , where  $E = E(r)$  is the specific energy of the orbit at radius  $r$ .

It is useful to remark that within a Newtonian framework of balances of forces, conditions (iv) and (v) can be interpreted as being equivalent to the statement that pressure gradients and shear stresses play a minor role in the balance and that instead gravity is very nearly balanced by the centrifugal force (Novikov and Thorne, 1973). More specifically, if  $T^{\mu\nu}$  is the energy-momentum tensor of the fluid, then near-geodesic motion is equivalent to requiring that

$$\frac{\partial_r(T^{\hat{i}\hat{j}}(r, z))}{\rho(r, z)} \sim \partial_r\left(\frac{T^{\hat{i}\hat{j}}(r, z)}{\rho(r, z)}\right) \ll \partial_r(1 - E(r)), \quad (11.227)$$

where the different terms in (11.227) account for the pressure gradient, the shear and the “gravitational acceleration”, respectively. Now, since  $\epsilon \sim T^{\hat{i}\hat{j}}/\rho$ , the condition (11.227) implies that  $\partial_r(\epsilon + E(r)) \ll 1$  and because at infinity  $\epsilon \simeq 0 \simeq E$ , we can deduce that  $\epsilon \simeq |E| \ll 1$  everywhere, so that assumption (v) can be recast as  $e = \rho(1 + \epsilon) \approx \rho$ .

Using this setup, and within a purely hydrodynamic framework, we can now cast the problem of the relativistic flow of a disc accreting onto a black hole in terms of the standard conservation laws of rest mass, momentum and energy. Further physical input can come from the specification of the microphysics via an equation of state, as well as from the solution of the radiative transfer problem of the radiation emitted across the disc or leaving it. The following subsections are dedicated to a detailed discussion of such conservation laws.

### 11.8.1 Rest-mass conservation

The general expression of the continuity equation (3.52) has a simple form for the specific conditions of the flow considered here [*i.e.*, those expressed by (11.226)] and for the assumption made of axisymmetry, thus reducing to

$$\partial_\mu(\sqrt{-g}\rho u^\mu) = 0 = \partial_t(\rho u^t) + \frac{1}{r}\partial_r(r\rho u), \quad (11.228)$$

where again  $u := u^r$  and the metric (11.200) has determinant  $g = -r^2$ . If we further impose stationarity in the sense of (11.224) and define  $\dot{M}\delta t$  as the amount of matter passing across an arbitrary closed surface around the black hole, then the continuity equation simply becomes [cf., Eq. (11.79)]

$$\dot{M} := -2\pi r\Sigma u = -2\pi\Sigma\sqrt{\Delta}Wv^{\hat{r}} = \text{const.}, \quad (11.229)$$

where the constant is strictly positive for accretion flows<sup>31</sup> and

<sup>31</sup>Note that the definition (11.229) differs from the one in Eq. (11.68) since here we do not need to assume that  $u$  is strictly positive and indeed  $u < 0$  for accretion flows.

$$\Sigma(r) := \int_{-H}^{+H} \langle \rho(r, z) \rangle dz \approx 2H(r)\rho, \quad (11.230)$$

is the integrated surface rest-mass density.

### 11.8.2 Radial momentum conservation

Next, we consider the conservation of the radial momentum (or radial Euler equation), which can be written by requiring that the projection in the radial direction of the four-divergence of the energy–momentum tensor is zero, *i.e.*,

$$h_{r\mu} \nabla_\nu T^{\mu\nu} = 0. \quad (11.231)$$

The energy–momentum tensor in (11.231) cannot be that of a perfect fluid as it must account both for viscous dissipation and for the transport of energy across the disc and out of it. Most (if not all) of the accretion-disc models describe dissipative processes within the framework of Classical Irreversible Thermodynamics (see Section 6.4), rather than in the more consistent one provided by Extended Irreversible Thermodynamics (see Section 6.6). Because of its simplicity, we will also follow here this traditional approach and recall that the general expression for the energy–momentum tensor of non-perfect fluids is (see Section 6.2) is

$$T^{\mu\nu} = eu^\mu u^\nu + (p + \Pi)h^{\mu\nu} + q^\mu u^\nu + q^\nu u^\mu + \pi^{\mu\nu}, \quad (6.13)$$

where we recall that  $\Pi$ ,  $q^\mu$  and  $\pi^{\mu\nu}$  are, respectively, the *viscous bulk pressure*, the *heat flux* and the *anisotropic stress tensor*, while  $h_{\mu\nu} := g_{\mu\nu} + u_\mu u_\nu$  is the standard projection tensor orthogonal to the four-velocity  $\mathbf{u}$  [*cf.*, Eq. (3.9)]. At this point, a certain amount of algebra and integration in the vertical direction leads to

$$u \frac{du}{dr} = -\frac{a^2 - Mr}{r\Delta} u^2 - \frac{AMW^2\mathcal{K}}{r^2\Delta} \left( \frac{\Delta}{r^2} + u^2 \right) - \frac{1}{\Sigma} \left( \frac{\Delta}{r^2} + u^2 \right) \frac{dp}{dr} + Q^r, \quad (11.232)$$

where we have defined

$$\mathcal{K} := \frac{(\Omega - \Omega_K^+)(\Omega - \Omega_K^-)}{\Omega_K^+ \Omega_K^-}, \quad (11.233)$$

with  $\Omega_K^\pm$  being the Keplerian angular velocities as defined in Eq. (11.157). The last term on the right-hand side of (11.232) is defined as

$$Q^r := \int_{-H}^{+H} \langle h_{r\mu}^r \nabla_\nu \pi^{\mu\nu} \rangle dz, \quad (11.234)$$

and represents the contribution of the viscous part of the energy–momentum tensor (6.13) to the conservation of radial momentum. However, assuming that the azimuthal shear stress

$\sigma_{r\phi} \sim r \sigma_{\hat{r}\hat{\phi}}$  is the only nonzero component of the shear tensor and that the bulk viscosity for the fluid is essentially zero,<sup>32</sup> it is easy to conclude that

$$Q^r = \left[ \left( 1 + \frac{r^4 u^2}{\Delta^2} \right) \nabla_\mu \pi^{r\mu} + uu_0 \nabla_\mu \pi^{0\mu} \right] \approx \nabla_i \pi^{ri} \approx \nabla_\phi \pi^{r\phi} \approx 0. \quad (11.235)$$

The comparison of Eq. (11.232) with its Newtonian counterpart

$$u \frac{du}{dr} = - \left( \frac{M}{r^2} - \frac{\ell_N^2}{r^3} \right) - \frac{1}{\Sigma} \frac{dp}{dr} + Q^r, \quad (11.236)$$

where  $\ell_N := \Omega r^2$  is the Newtonian specific angular momentum, provides a simple physical interpretation of the different terms. In particular, it is easy to realise that the second term on the right-hand side of (11.232) reflects the competition between the centrifugal and the gravitational force and corresponds to the term in round brackets of (11.236), while the first term on the right-hand side represents a purely relativistic correction.

### 11.8.3 Angular momentum conservation

For the equation of conservation of angular momentum we could proceed here in analogy with the previous section and require that the projection in the  $\phi$ -direction of the four-divergence of the energy-momentum tensor is zero. However, it is more convenient to exploit the presence of a spacelike Killing vector  $\xi$  associated with the axisymmetry of the metric [*cf.*, Eq. (11.143)] and define an associated conserved current  $\mathcal{J}^\mu := T^{\mu\nu} \xi_\nu$ , so that the conservation of angular-momentum can be expressed in terms of a current-conservation equation, *i.e.*, [*cf.*, Eq. (3.63)]

$$h_{\phi\mu} \nabla_\nu T^{\mu\nu} = 0, \quad \Longleftrightarrow \quad \nabla_\mu \mathcal{J}^\mu = 0. \quad (11.237)$$

After a bit of algebra and integration in the vertical direction, the explicit form of (11.237) is

$$u \frac{d\mathcal{J}}{dr} = \frac{2H}{r\Sigma} \nabla_r (r\pi_{\phi}^r) - \frac{F^-}{\Sigma} \mathcal{J}, \quad (11.238)$$

where  $\mathcal{J}$  is defined as<sup>33</sup>

$$\mathcal{J} := -u_\phi = \frac{W}{r^3} \sqrt{\frac{A^3}{\Delta}} (\Omega - \omega), \quad (11.239)$$

and coincides, in the Newtonian limit, with the Newtonian specific angular momentum  $\ell_N$ , *i.e.*,  $\mathcal{J} \rightarrow \ell_N = \Omega r^2$ . The last term on the right-hand side of Eq. (11.238) represents the angular momentum lost through radiative fluxes, where  $F^-$  is the vertically integrated outgoing energy flux, *i.e.*, the *radiative cooling*, and is defined as

$$F^- := \int_{-H(r)}^{+H(r)} \partial_z (q^z) dz = 2q^z. \quad (11.240)$$

As discussed by Abramowicz *et al.* (1996), neglecting these losses in Eq. (11.238) would greatly simplify the calculations, but it would also represent a dangerous approximation since

<sup>32</sup>Both of these assumptions are customarily made in accretion-disc theory.

<sup>33</sup>As remarked in Section 11.6.1, the specific angular momentum as defined in Eq. (11.153),  $\ell = -u_\phi/u_t$ , and  $\mathcal{J}$  have the same Newtonian limit.

$F^-$  can provide a sizeable contribution to the total angular momentum loss. Examples of the radiative cooling processes that intervene in determining  $F^-$  have been presented for a two-temperature plasma cooled by synchrotron radiation, inverse-Compton process, and bremsstrahlung emission in Narayan and Yi (1995) and more recently in Sadowski *et al.* (2011).

A more important role in Eq. (11.238) is played by the viscous shear stresses,  $\pi_{\phi}^r$ , which are at the heart of any accretion-disc model, already in a Newtonian regime. These terms, in fact, account for the loss of angular momentum via shear viscosity and allow distant fluid elements, orbiting in almost Keplerian orbits, to get closer to the black hole and eventually fall into it. The definition of a suitable expression for  $\pi_{\phi}^r$  raises a number of problems. The first one is merely algebraic and reflects the fact that the complete analytic expression for  $\pi_{\phi}^r$  is rather complex for generic fluid motions and two examples are provided below. The second problem is more severe and reflects the fact that no definitive prescription is actually known for the shear viscosity of the matter in the disc. A number of phenomenological approaches have already been proposed in Newtonian models [*cf.*, the following expression (11.245)], but none of these expressions follows from first-principle considerations. Notwithstanding our ignorance on the microphysical details of these dissipative mechanisms, we can calculate explicitly the relativistic expressions for the azimuthal shear stress in two specific conditions. The first one is offered by fluid elements that move in azimuthal geodesic orbits, *i.e.*,  $u^\mu := (u^t, 0, u^\phi, 0)$ , in which case the azimuthal shear is given by [*cf.*, Eq. (3.12) for a definition of the shear tensor and Section 6.2 for a discussion of non-perfect fluids]

$$\sigma_{r\phi} = \sqrt{\frac{A^3}{\Delta}} \left( \frac{\gamma^3}{2r^3} \right) \frac{d\Omega}{dr}, \quad (11.241)$$

and the corresponding expression in the ZAMO and orbiting frames has the form (Novikov and Thorne, 1973)

$$\sigma_{\hat{r}\hat{\phi}} = \sigma_{\mu\nu} e_{\hat{r}}^\mu e_{\hat{\phi}}^\nu = \left( \frac{A\gamma^3}{2r^3} \right) \frac{d\Omega}{dr} = \sigma_{\bar{r}\bar{\phi}}, \quad (11.242)$$

where the proof of the last equality is the subject of Problem 13. It is straightforward to evaluate (11.242) in the case of motion on a radial geodesic orbit with  $\Omega = \Omega_K$  to obtain

$$\sigma_{\hat{r}\hat{\phi}} = \sigma_{\bar{r}\bar{\phi}} = -\frac{3}{4} AW_{\hat{\phi}}^2 \left( \frac{M}{r^3} \right)^{1/2} \stackrel{N}{=} -\frac{3}{4} \sqrt{\frac{M}{r^3}} \stackrel{N}{=} -\frac{3}{4} \Omega_K, \quad (11.243)$$

where the last equalities (indicated with “ $\stackrel{N}{=}$ ”) refer to the Newtonian limit. It follows from Eq. (11.241) that the expression for the viscous-tensor component  $\pi_{\phi}^r$  can be computed to be<sup>34</sup>

$$-r\pi_{\phi}^r = 2\eta \frac{\Delta}{r} \sigma_{r\phi} = \eta \frac{\sqrt{A^3\Delta}}{r^4} \gamma^3 \frac{d\Omega}{dr} = \left( \frac{\nu\Sigma}{2H} \right) \frac{\sqrt{A^3\Delta}}{r^4} \gamma^3 \frac{d\Omega}{dr}, \quad (11.244)$$

where  $\nu := \eta/\rho$  is the *kinematic viscosity* coefficient and in the last equality in (11.244) we have used the relation  $\eta \approx \nu\Sigma/(2H)$  [*cf.*, Eq. (11.230)]. We recall that the standard “alpha”

<sup>34</sup>We recall that for a non-perfect fluid, the anisotropic stress and shear tensors are related by  $\pi_{\mu\nu} = -2\eta\sigma_{\mu\nu}$  [*cf.*, Eq. (6.38)].

*prescription* for the kinematic viscosity coefficient in accretion discs can be derived from dimensional arguments to be

$$\nu = \frac{2}{3} \alpha c_s H(r), \quad (11.245)$$

which is also known as the “alpha-law” of the Shakura–Sunyaev disc model (Shakura and Sunyaev, 1973), where  $0 < \alpha < 3/2$  is a dimensionless constant coefficient.

The second explicit expression for the azimuthal shear stress can be derived if radial motions cannot be neglected and the four-velocity is then  $u^\mu := (u^t, u, u^\phi, 0)$ . In this case, the azimuthal shear stress has the more complex form

$$\begin{aligned} \sigma_{r\phi} \simeq & \frac{r}{2} \left\{ u \mathcal{J} \frac{d}{dr} \left( \frac{ur^2}{\Delta} \right) - \frac{2aMu^t}{r^2} (1 + u^t \Omega \mathcal{J}) + \left( 1 + \frac{u^2 r^2}{\Delta} \right) \frac{d\mathcal{J}}{dr} \right. \\ & \left. - u^t \Omega \left( r - \frac{a^2 M}{r^2} \right) (2 + u^t \Omega \mathcal{J}) - \frac{u^2 r}{\Delta^2} (a^2 - Mr) \mathcal{J} + \frac{(u^t)^2 M}{r^2} \mathcal{J} \right\}. \end{aligned} \quad (11.246)$$

#### 11.8.4 Hydrostatic vertical equilibrium

Also in this case, the calculation of the conservation of momentum in the  $z$ -direction would follow the same logic presented in Section 11.8.2 for the radial Euler equation and can be derived by writing the explicit expression for  $h_{z\mu} \nabla_\nu T^{\mu\nu} = 0$ . In practice, however, it is much simpler to *assume* that the conservation of vertical momentum can be *approximated* with a hydrostatic vertical equilibrium (Novikov and Thorne, 1973; Abramowicz *et al.*, 1996). The condition for hydrostatic equilibrium is a *local* one and can be obtained by requiring that the vertical pressure-gradient in a local inertial frame is balanced by the vertical component of the tidal gravitational acceleration, which can be written in terms of the  $R_{tzt}^z$  component of the Riemann tensor for the metric (11.200) at  $z = 0$ . This was first suggested by Novikov and Thorne (1973) who, however, approximated such a frame with one moving along circular Keplerian orbits in the equatorial plane.<sup>35</sup> This is reasonable in the most distant parts of the disc, but is a rather poor approximation in the innermost parts, where the infalling flow becomes supersonic and the angular velocity is not Keplerian; as a result, the expression proposed by Novikov and Thorne is singular on the circular photon orbit. This singularity can be moved to a less worrisome location if the vertical balance is computed in the comoving frame, that is, in the frame which is not only corotating with the fluid but it is also accreting with it (Abramowicz *et al.*, 1996). Doing this then yields

$$\frac{1}{\rho} \frac{dp}{dz} = z(R_{\tilde{t}\tilde{z}\tilde{t}}^{\tilde{z}}) = W^2 \frac{M}{r^3} \left[ \frac{(r^2 + a^2)^2 + 2a^2 \Delta}{(r^2 + a^2)^2 - a^2 \Delta} \right] z, \quad (11.247)$$

where we have indicated with a tilde the components of the Riemann tensor in the comoving frame (see Section 1.5.5). Note that in such a frame  $v^{\tilde{r}} = v^{\tilde{\phi}} = v^{\tilde{z}} = 0$ . For most of its practical applications, the differential equation (11.247) can be approximated as

<sup>35</sup>Such a Keplerian orbiting frame is not inertial because of the Coriolis and centrifugal forces produced by rotation. However, these forces do not influence the vertical structure and we can regard the orbiting frame essentially as locally inertial.

$$p \approx W^2 \frac{M}{r^3} H^2 \rho \left[ \frac{(r^2 + a^2)^2 + 2a^2\Delta}{(r^2 + a^2)^2 - a^2\Delta} \right], \quad (11.248)$$

thus providing an algebraic equation for the thickness of the disc  $H(r)$ . Also expression (11.247) is singular, although only at the horizon, where  $\Delta = 0$  and  $W \rightarrow \infty$ , and where the flow is causally disconnected from that at larger radii. This singularity is again a consequence of assuming hydrostatic equilibrium of the flow down to the horizon, which of course implicitly requires an infinite boost at the horizon. However, the singularity in (11.248) can be removed if a suitable expansion in the ratio  $z/r$  is assumed for the hydrodynamic quantities, *e.g.*, the pressure (Abramowicz *et al.*, 1997). This is certainly an assumption, but a reasonable one, which then yields

$$-2 \frac{p}{\rho} + \left( \frac{H}{r} \right)^2 \left( \frac{1}{r^2} \right) \left[ \mathcal{J}^2 + a^2(1 - u_t^2) - \Delta u \frac{du}{dr} \right] = 0. \quad (11.249)$$

Expression (11.249) represents therefore the non-singular approximation of the vertical-equilibrium equation for slim discs orbiting around Kerr black holes [see, *e.g.*, Sadowski *et al.* (2011) for the inclusion of a vertical radiative energy transport].

### 11.8.5 Energy conservation

We conclude the derivation of the hydrodynamic equations for relativistic slim discs by writing the standard energy conservation equation for the matter in the disc, *i.e.*,

$$u_\nu \nabla_\mu T^{\mu\nu} = 0, \quad (11.250)$$

which, using the first law of thermodynamics, can written as [*cf.* Eq. (6.25) and the discussion in Section 6.3.1]

$$\rho T u^\mu \partial_\mu s = 2\eta \sigma^{\alpha\beta} \sigma_{\alpha\beta} - \nabla_\mu q^\mu - a_\mu q^\mu, \quad (11.251)$$

where  $s$  is the specific entropy and  $a_\mu$  is the fluid four-acceleration [*cf.* Eq. (3.1)]. Note that we have neglected the bulk viscous pressure term  $\Pi$ , while we have replaced the anisotropic stress tensor  $\pi^{\mu\nu}$  with its expression (6.38) within the context of Classical Irreversible Thermodynamics. The last term in (11.251) is a special-relativistic correction to  $\vec{\nabla} \cdot \vec{q}$  and will be assumed to be always negligible as long as the accelerations of the fluid elements are small, which is indeed the case for near-geodesic motion. For stationary flows,  $\sigma_{tt} \sim \sigma^{tt} \sim 0$ , so that we can simplify the contraction of the shear tensor in (11.251) as

$$\sigma^{\alpha\beta} \sigma_{\alpha\beta} \approx 2\sigma^{ta} \sigma_{ta} + \sigma^{ij} \sigma_{ij}. \quad (11.252)$$

If we further assume that the fluid elements in the disc move along near-geodesic circular orbits so that Eq. (11.241) holds exactly, then the property  $\sigma^{\alpha\beta} u_\alpha = 0$  with  $u^\alpha = (u^t, 0, u^\phi, 0)$  provides two useful identities

$$\sigma_{t\alpha} = -\Omega \sigma_{\phi\alpha}, \quad (11.253)$$

$$\sigma^{t\alpha} = -\frac{u_\phi}{u_t} \sigma^{\phi\alpha}, \quad (11.254)$$

from which (11.252) can be rewritten as [cf., Eq. (11.162)]

$$\sigma^{\alpha\beta} \sigma_{\alpha\beta} \approx 2\Omega \left( \frac{g_{t\phi} + g_{\phi\phi}\Omega}{g_{tt} + g_{t\phi}\Omega} \right) \sigma^{\phi a} \sigma_{\phi a} + \sigma^{ij} \sigma_{ij}. \quad (11.255)$$

Finally, assuming that the azimuthal shear stresses are dominant over the radial and vertical ones, *i.e.*,

$$\sigma^{\phi a} \sigma_{\phi a} \approx \sigma^{\phi r} \sigma_{\phi r}, \quad \sigma^{ij} \sigma_{ij} \approx 2\sigma^{\phi r} \sigma_{\phi r}, \quad (11.256)$$

the viscous contribution to the entropy increase (11.255) can finally be approximated as [cf., Eq. (11.241)]

$$\begin{aligned} \sigma^{\alpha\beta} \sigma_{\alpha\beta} &\approx 2 \left[ 1 + \Omega \left( \frac{g_{t\phi} + g_{\phi\phi}\Omega}{g_{tt} + g_{t\phi}\Omega} \right) \right] \sigma^{\phi r} \sigma_{\phi r} \\ &= 2 \frac{\Delta}{A\gamma^2} (\sigma_{\phi r})^2 = \frac{A^2 \gamma^4}{2r^6} \left( \frac{d\Omega}{dr} \right)^2. \end{aligned} \quad (11.257)$$

As a result, and after the usual vertical integration, the equation for the conservation of energy (11.250) can be cast in its final form

$$u\Sigma T \frac{ds}{dr} = \nu\Sigma \left( \frac{A^2 \gamma^4}{r^6} \right) \left( \frac{d\Omega}{dr} \right)^2 - \frac{2H}{r} \frac{d}{dr} (rq^r) - F^-, \quad (11.258)$$

which shows the distinct contributions to the time variation of the specific entropy coming respectively from viscous stresses (the first term on the right-hand side), from energy advection (the second term on the right-hand side) and from radiative cooling from the disc (the third term on the right-hand side). Equation (11.258) can also be written as a balance equation of the type

$$F^{\text{adv}} = F^+ - F^-, \quad (11.259)$$

where  $F^+$  is the surface heat generation rate

$$F^+ := \nu\Sigma \left( \frac{A^2 \gamma^4}{r^6} \right) \left( \frac{d\Omega}{dr} \right)^2, \quad (11.260)$$

while  $F^{\text{adv}}$  is the advective cooling rate due to the infall of matter onto the black hole and is defined as

$$F^{\text{adv}} := u\Sigma T \frac{ds}{dr} + \frac{2H}{r} \frac{d}{dr} (rq^r) \approx -\frac{\dot{M}}{2\pi r} T \frac{ds}{dr}. \quad (11.261)$$

The last equality results from considering the conductive radial flux to be much smaller than the advected fluxes (*i.e.*,  $d(rq^r)/dr \ll ds/dr$ ) and after using the mass accretion rate as given

by Eq. (11.229). An explicit expression for the radiative cooling  $F^-$  can be found in Narayan and Yi (1995) and Abramowicz *et al.* (1996) in the case in which the matter in the disc is composed of two distinct fluids of electrons and ions, and the cooling is due to synchrotron radiation, inverse-Compton processes, and bremsstrahlung emission. In the simple case in which the matter in the disc is optically thick and emitting as a black-body at temperature  $T$ , the radiative cooling can be approximated as (Abramowicz *et al.*, 1996)

$$F^- \approx \frac{2}{3} \frac{a_R T^4}{\kappa \rho H}, \quad (11.262)$$

where  $\kappa$  is the mean opacity in the disc (Frank *et al.*, 2002) and  $a_R$  is the radiation constant [*cf.* Eq. (2.269)].

In summary, Eq. (11.258), together with Eqs. (11.232), (11.238) and (11.249) completely describe the flow properties of a relativistic, vertically integrated, stationary slim-disc model. Once the properties of the matter in the disc have been specified and a detailed radiative cooling recipe has been prescribed for the radiative cooling  $F^-$ , the corresponding set of coupled ordinary differential equations can be solved numerically to yield all the relevant information about the hydrodynamic and thermodynamic properties of the disc. Details and subtleties about the boundary conditions to be imposed at the inner edge of the disc are discussed, for instance, by Novikov and Thorne (1973), Abramowicz *et al.* (1997) and Sadowski *et al.* (2011). In addition, an extended review on accretion-disc theory, including the results of numerical simulations, has been compiled recently by Abramowicz and Fragile (2013).

## 11.9 Relativistic jets

The denomination *relativistic jets* was first used in the extragalactic context by Baade and Minkowski (1954), who observed in the optical waveband knots emerging from the nucleus of the galaxy M87 on an angular scale of  $20''$ . However, it was only after the advent of radio astronomy and the construction of the Very Large Array (VLA), that relativistic jets have been recognised as a very common phenomenon in high-energy astrophysics, responsible, for instance, of the apparently superluminal motions of radio blobs within radio galaxies.

Relativistic jets are observed in AGNs, where they are expected to be connected to accretion onto a supermassive black hole, in galactic binaries (*microquasars*), where they are expected to be associated with the mass loss by a normal star onto a compact object, and in GRBs, where they are expected to accompany a catastrophic event and the formation of a stellar-mass black hole. Because the phenomenology and physical nature of these classes of sources is indeed very different, it is useful to distinguish relativistic jets in AGNs and microquasars from those associated with GRBs. The latter are short and extremely energetic bursts of high-energy radiation releasing in a few seconds as much energy as does the entire Galaxy over one year [see, *e.g.*, Zhang and Mészáros (2004) for a review]. They are presently detected with a rate of about one event per day and their extragalactic location was unequivocally clarified by the BATSE detector onboard the Compton gamma-ray observatory (Meegan *et al.*, 1992). The energy spectra are non-thermal, with most of the power emitted in the 100–500 keV range, even though photons up to 18 GeV have been reported. Arguments involving

opacity to pair creation or electron scattering for the high-energy photons (Lithwick and Sari, 2001) suggest that GRBs are non-spherical explosions with collimated relativistic jets having Lorentz factors as large as  $W \sim 10^2 - 10^3$ , which can be described, at least in the initial *fireball* phase, with a thermal acceleration mechanism (Cavollo and Rees, 1978) that we will review below. A basic property of these relativistic jets is that the emission is beamed in a cone with opening angle  $\theta_{\text{op}} \simeq 1/W$ , which is smaller than the geometrical opening angle, at least in the initial phases of the expansion (Wygoda *et al.*, 2011). Specific aspects of GRB jet dynamics are inevitably connected with the underlying physics of the progenitor, for which we cannot provide a comprehensive discussion here, although we will reconsider this topic again in Section 11.9.3.

Both in AGNs, microquasars and GRBs, relativistic jets are thought to reflect the interplay between an accretion disc and a compact object (which is always a supermassive black hole for AGNs), leading to a collimated outflow moving near the speed of light and with Lorentz factors usually observed in the range  $W \sim 2-100$  (Lister *et al.*, 2009).

Despite decades of observations, the physics of the “*central engine*” powering the jet, the stability of the jet and what is responsible for their collimation and acceleration, remain open theoretical challenges. Possibly the only firm point in this scenario is that magnetic fields are widely recognised to play a *fundamental* role both in accelerating and in collimating relativistic flows (Camenzind, 1986; Krasnopolsky *et al.*, 1999; Bogovalov and Tsinganos, 2001; Komissarov *et al.*, 2009; Tchekhovskoy *et al.*, 2011). As such, the physics of relativistic jets is connected with that of magnetic fields and no satisfactory description can be obtained in a purely hydrodynamic context, such as the one covered by this book. Nevertheless, there are some aspects of relativistic-jet acceleration that, albeit idealised, can be discussed in a purely hydrodynamic framework and that can serve either as pedagogical applications of relativistic hydrodynamics or for a better understanding of flows in realistic relativistic jets. We will review the most salient of these aspects in the following sections.

### 11.9.1 Apparently superluminal jets

Using simple kinematic arguments, Rees (1966) predicted that radio jets should manifest an apparent superluminal motion, a fact that was confirmed soon after through astronomical radio observations. An example is presented in Fig. 11.21, which reports the computed radio maps of a compact relativistic jet, showing at five different times the evolution of a superluminal component as it moves along the jet as observed by a distant observer.

In general, observations of this type imply a relativistic velocity of some internal pattern or structure within the jet, which can either be a blob or a knot and not, as it may appear at first, of the plasma forming the jet. The two velocities may well coincide under certain conditions, but the Lorentz factor of the radio pattern  $W_p$ , which is responsible for the observed apparent superluminal velocity, should really be distinguished from the Lorentz factor  $W_b$  of the bulk plasma flow, which is instead responsible for the amplification of the observed radiation, namely the *Doppler boosting* (Homan *et al.*, 2009) [see also Eq. (11.264)].

The kinematic interpretation proposed by Rees proceeds as follows. First imagine a radio blob, which is stationary with respect to an observer at infinity, and a second radio blob, that is moving with velocity  $\beta_p := v_p$  along a direction forming an angle  $\theta$  with the line of sight (see the left panel of Fig. 11.22 for a diagram). At time  $t = 0$  the two blobs are in the same

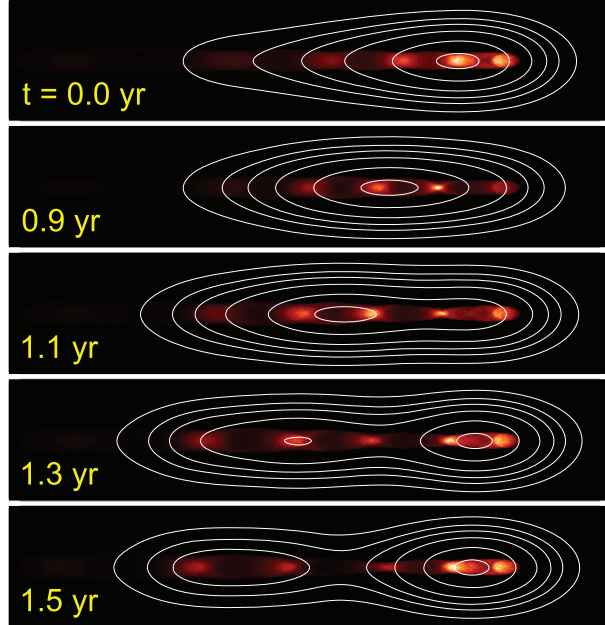


**Fig. 11.21** Computed radio maps of a compact relativistic jet showing the evolution of a superluminal component as it moves along the jet. The white contours refer to the present VLBI resolution while the orange colour-coding refers to the resolution provided by the numerical simulation. The times refer to the observer's rest frame, the contour levels are 0.1, 0.2, 0.3, 0.45, 0.7 and 0.95 of the peak intensity, and the maps extend longitudinally by an angle of 0.90 mas [adapted from Martí and Müller (2003)].

position and emit a radio signal; at a later time,  $\Delta t$ , the moving blob, which in the meanwhile has moved a projected distance  $\Delta x = \beta_p \Delta t \sin \theta$  in the transverse direction, sends another signal. It is then easy to show that the apparent transverse velocity is just the ratio between the apparent distance  $\Delta x$  and the time interval between the two emissions after the latter has been corrected for the fact that the blob is also moving towards the observer (*i.e.*, it effectively does not need to run a distance  $\beta_p \Delta t \cos \theta$ ). The resulting expression is then

$$\beta_{\text{app}} = \frac{\beta_p \sin \theta}{1 - \beta_p \cos \theta}. \quad (11.263)$$

Although not obvious, Eq. (11.263) is a special-relativistic expression, but because it combines only quantities measured by an observer at infinity, no Lorentz transformation is necessary and a simple linear composition of the time intervals is sufficient.

The dependence of the apparent blob velocity on the viewing angle and on different effective velocities of the blob is reported in the right panel of Fig. 11.22. Note that the apparent velocity has a maximum value given by  $\beta_{\text{app},\text{max}} = W_p \beta_p$  for  $\sin \theta_{\text{max}} = 1/W_p$ . Hence, if an apparent superluminal velocity is observed, *i.e.*, if  $\beta_{\text{app}} > 1$  for a viewing angle  $\theta \approx \theta_{\text{max}}$ , we can conclude that it must be  $W_p \beta_p > 1$  and therefore that  $\beta_p > 1/\sqrt{2} \approx 0.71$ . Stated differently, relativistic velocities for the radio blobs within the jet of the order of  $\beta_p \gtrsim 0.71$  are necessary in order to account for the observation of superluminal jets.

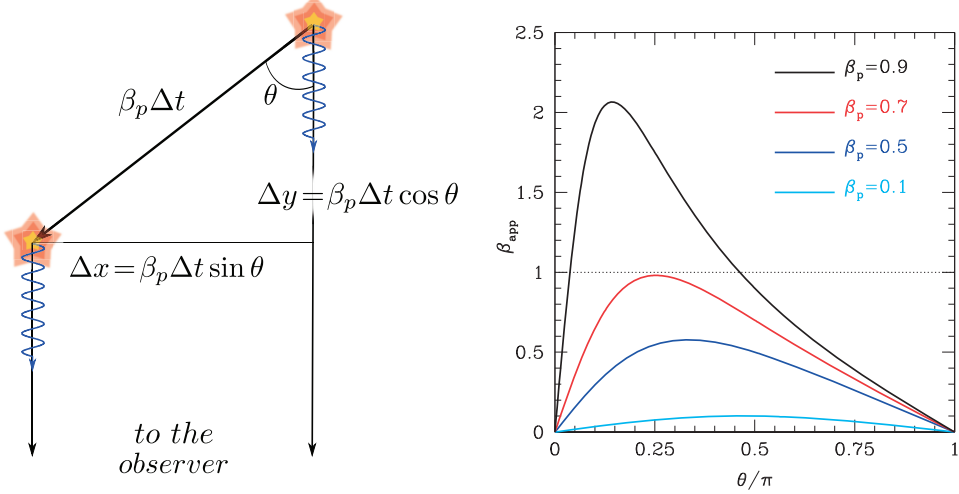


**Fig. 11.22** *Left panel:* Geometry for explaining the apparent superluminal motion. A radio blob, indicated in red, moves along the diagonal with velocity  $\beta_p c$  while the projected displacement measured by the observer is given by  $\Delta x$ . *Right panel:* Curves of apparent velocity  $\beta_{\text{app}}$  shown as a function of the viewing angle  $\theta$  for different values of the blob velocity  $\beta_p$ .

Relativistic speeds are responsible not only for the apparent superluminal motion, but also for an enhancement of the observed radiation intensity, according to the law

$$I_{\text{ob}} = \delta^n(\theta, W_b) I_{\text{em}}, \quad (11.264)$$

where  $I_{\text{em}}$  is the intensity of the emitted radiation as measured by an observer comoving with the plasma and  $\delta$  is the *Doppler factor*,<sup>36</sup> which is related to the Lorentz factor of the plasma by (Ghisellini *et al.*, 1993)

$$\delta = \frac{1}{W_b(1 - \beta_b \cos \theta)}. \quad (11.265)$$

The index  $n$  in Eq. (11.264) depends on the geometry of the emission and on the spectral properties of the emitted radiation. Assuming a simple power-law spectrum with  $I_{\text{em}} \propto \nu^{-\alpha}$ , the exponent of the Doppler boost is  $n = 3 + \alpha$  in the case of an optically thin sphere, while it is  $n = 2 + \alpha$  for a continuous jet (Scheuer and Readhead, 1979). Note that the maximum value of the Doppler factor is obtained for  $\theta = 0$  and is given by  $\delta_{\max} = W_b(1 + \beta_b)$ . As a result, if an observational estimate of the Doppler factor  $\delta$  is available, the condition  $\delta \leq \delta_{\max}$  can be used to obtain a lower limit for the Lorentz factor of the plasma, *i.e.*,

$$W_b \geq \frac{1}{2} \left( \delta + \frac{1}{\delta} \right). \quad (11.266)$$

We have already mentioned the importance of distinguishing between the Lorentz factor of the bulk flow  $W_b$  and the Lorentz factor  $W_p$  of specific features, *e.g.*, blobs, within the jet.

<sup>36</sup>This is the same Doppler factor as in the standard relativistic Doppler effect.

There are observational situations, however, where different radio structures within the jet are observed to move at roughly the same speed, so that it is reasonable to assume that there is a single Lorentz factor  $W_p$  for each element in the jet and that  $W_p \simeq W_b = W$ . When this simplifying assumption can be made (as is often the case in astronomical observations), Eqs. (11.263) and (11.265) can be used to express the so-called *beaming parameters*  $W$  and  $\tan \theta$ , in terms of the observable  $\beta_{\text{app}}$  and  $\delta$ , namely<sup>37</sup>

$$W = \frac{\beta_{\text{app}}^2 + \delta^2 + 1}{2\delta}, \quad (11.267)$$

$$\tan \theta = \frac{2\beta_{\text{app}}}{\beta_{\text{app}}^2 + \delta^2 - 1}. \quad (11.268)$$

High-energy astronomical observations suggest several different approaches for deriving the Doppler factor in terms of additional observational quantities (we recall that the apparent velocity  $\beta_{\text{app}}$  is directly available from radio observations). As a final remark we note that over the last few years it has become clear that, although originally discovered in the radio-band, relativistic jets emit most of their radiation at the other extreme of the electromagnetic spectrum, namely in X-rays and gamma-rays.

### 11.9.2 Hydrodynamic acceleration mechanisms

Soon after relativistic jets were discovered, several models were proposed to account for their extremely high propagation speeds. Although such jets are expected to be generated near a black hole or a neutron star, their propagation takes place on scales that are much larger than that of the compact object. As a result, and for all practical purposes, when describing large-scale relativistic jets we can consider the spacetime to be flat and thus work in a special-relativistic regime. With this assumption in mind, in the following we will discuss the basic features of three acceleration models that are purely hydrodynamic.

#### **Thermal acceleration of a conical jet.**

A first model for the thermal acceleration of a relativistic jet was pointed out by Flammang (1982) and later on developed by Derishev *et al.* (1999) in the context of GRBs. The model considers the conical expansion of a high-temperature relativistic fluid obeying a polytropic equation of state with index  $\Gamma = 4/3$  (see Section 2.4.6). Under these conditions, and after recalling that in special relativity  $u_t$  is just the Lorentz factor  $W$ , the Bernoulli equation (3.98) implies that

$$\left(1 + 4\frac{p}{\rho}\right) W = \text{const.} \quad (11.269)$$

Assuming further that the flow is confined to a conical jet and is essentially radial there, the four-velocity inside the jet is given by  $u^\mu = W(1, v^r, 0, 0)$  and the continuity equation (3.52) for a stationary flow is simply expressed as [*cf.*, Eq. (11.75)]

<sup>37</sup>In practice,  $\beta_{\text{app}}$  is normally deduced from the angular speed  $\mu$  on the radio map via the expression  $\beta_{\text{app}} = \mu D_A (1+z)/c$ , where  $D_A$  is the angular size distance while  $z$  is the redshift of the hosting galaxy (Homan *et al.*, 2009).

$$\rho W v^r r^2 = \text{const.} \quad (11.270)$$

If the flow is ultrarelativistic, then  $v^r \approx 1$ , and after exploiting the conical geometry of the expansion, Eq. (11.270) reduces to the relation  $\rho \sim W^{-1} r_{\text{jet}}^{-2}$ , where  $r_{\text{jet}}$  is the cylindrical radius of the jet. In the absence of shocks we can express the pressure in terms of the rest-mass density and hence find that

$$\frac{p}{\rho} = K \rho^{1/3} \sim \frac{1}{(W r_{\text{jet}}^2)^{1/3}}. \quad (11.271)$$

In the case of a high-temperature ultrarelativistic flow, for which  $p \gg \rho$ , the first term in (11.269) can be neglected and this leads to the conclusion that (Komissarov, 2011)

$$W \sim r_{\text{jet}}. \quad (11.272)$$

Expression (11.272) highlights that as long as the conditions behind the Bernoulli equation apply, the Lorentz factor increases with the cylindrical radius, thus naturally leading to very large accelerations. The problem with this mechanism is that while it can be very efficient on length-scales comparable with the gravitational radius of the central object, for example when applied to the fireball phase in GRBs (Vlahakis and Königl, 2003), it does not work on the much larger scales that are usually associated with extragalactic jets. As shown by Derishev *et al.* (1999), in fact, the Lorentz factor on much larger distance scales reaches a saturation value that is well below the values currently observed in astrophysical jets. The failure of this mechanism was indeed one of the main motivations for resorting to the contributions of magnetic fields also in jets associated with GRBs.

### **The twin-exhaust model.**

The *twin-exhaust model* introduced by Blandford and Rees (1974) can be regarded as a modification of the thermal-expansion model presented in the previous section. Its main motivation was to address the acceleration problem mentioned above, leaving aside the issue of the injection, which is expected to be provided in some way by the “central engine”. The model assumes that two channels of fluid (*i.e.*, the twin exhaust) are expelled in opposite directions from a rotating central object, either a black hole or a neutron star.<sup>38</sup> The left panel of Fig. 11.23 shows a schematic diagram of one of these channels, with the direction of the fluid motion being oriented along the rotation axis; shown as dashed lines are representative isobaric surfaces. The motion is assumed to be one-dimensional, with the four-velocity of the fluid given in a Cartesian coordinates system by  $u^\mu = W(1, v, 0, 0)$ , and the cross-sectional area of the channel  $\mathcal{S}$  is not constant (the channel is not a cylinder), but it adjusts to the varying pressure and velocity so as to act as a relativistic *de Laval nozzle*.

The flow is assumed to be stationary and the fluid to be ultrarelativistic and to follow a polytropic equation of state with adiabatic index  $\Gamma = 4/3$  (see Section 2.4.7). As a result, the Bernoulli equation (3.98) reduces to [*cf.* Eq. (11.269)]

$$\frac{4p}{\rho} W = \text{const.}, \quad (11.273)$$

<sup>38</sup>Rotation is here useful just to establish a direction in the flow but is not relevant for the acceleration mechanism.

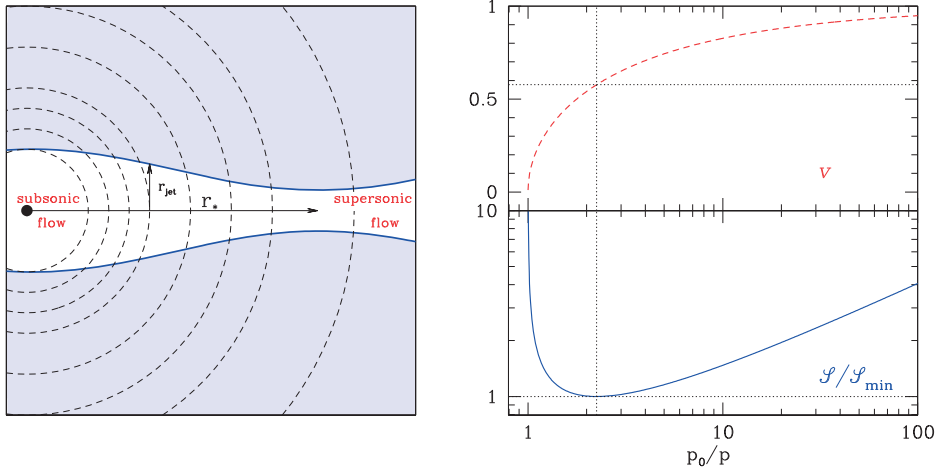


**Fig. 11.23** *Left panel:* Schematic modelling of the twin-exhaust model, showing the transition from subsonic to supersonic flow at the stagnation point where the cross-sectional area is minimum. The dashed lines are representative isobaric surfaces [adapted from Blandford and Rees (1974)]. *Right panel:* Velocity along the jet shown as a function of the pressure jump  $p_0/p$  (red dashed line) and cross-sectional area normalised to its minimal value (blue solid line). Note that the flow becomes supersonic at  $p_0/p = 9/4$ , which marks the minimum cross-section and the position of the nozzle.

from which it follows that

$$p = p_0 W^{-4}, \quad (11.274)$$

where  $p_0$  is the *stagnation pressure*, that is the value of the pressure when the flow has zero velocity, such that at the stagnation point  $W_0 = 1$ . The one-dimensional special-relativistic laws of conservation of rest mass and energy require that the following conditions are met [*cf.*, Eqs. (11.5) and (11.7)]

$$J := \rho W v \mathcal{S} = \text{const.}, \quad (11.275)$$

$$E := 4pW^2v\mathcal{S} = \text{const.}. \quad (11.276)$$

As a result, using Eq. (11.276) we can express the variation of the cross-sectional area as

$$\mathcal{S} = \left( \frac{E}{4p_0} \right) \frac{(p_0/p)^{3/4}}{\sqrt{(p_0/p)^{1/2} - 1}}, \quad (11.277)$$

and, using Eq. (11.274), we can express the flow velocity along the jet as

$$v = \sqrt{1 - \left( \frac{p}{p_0} \right)^{1/2}}. \quad (11.278)$$

It is now easy to realise that  $\mathcal{S}$  reaches the minimum value of

$$\mathcal{S}_{\min} = \frac{3\sqrt{3}}{8} \frac{E}{p_0} \quad \text{when} \quad p = p^* := \frac{4}{9} p_0, \quad (11.279)$$

so that a nozzle forms in this point. This is shown in Fig. 11.23, whose right panel reports the velocity along the jet shown as a function of the pressure jump  $p_0/p$  (red dashed line) and of the cross-sectional area normalised to its minimal value (blue solid line). At the nozzle,  $p_0/p^* = 9/4$  and the Lorentz factor of the flow is  $W^* = \sqrt{3/2}$ , to which corresponds a bulk velocity  $v^* = 1/\sqrt{3}$ . Because this value corresponds to the sound speed of an ultrarelativistic fluid [*cf.* Eq. (2.207)], it highlights that the flow becomes supersonic past the nozzle.

The stagnation pressure at the injection point represents therefore the maximum pressure within the jet, which then decreases moving outwards along the jet. A suitable adjustment of the cross-section, resulting from the balance between internal and external pressure, then provides the conditions for jet acceleration, with a transition from subsonic flow near the compact object, over to supersonic flow past the nozzle, where the pressure is about half that at the injection point [*i.e.*,  $p^* = (4/9)p_0 \simeq p_0/2$ ].

As a final note we remark that although the bulk flow is assumed to be one-dimensional, the walls of the jet are not parallel to it and, as a result, the fluid can exchange momentum with the walls. The linear momentum carried by the flow is [*cf.* Eq. (11.6)]

$$Q := (4pW^2v^2 + p)\mathcal{S}, \quad (11.280)$$

and it cannot be constant along the jet, although it is still conserved. Rather it must adjust according to

$$Q = E \left( v + \frac{1}{4W^2v} \right) = \frac{Q^*}{2} \left( \frac{v}{v^*} + \frac{v^*}{v} \right), \quad (11.281)$$

where

$$Q^* := \frac{\sqrt{3}}{4} E = \frac{1}{4v^*} E \quad (11.282)$$

is the value of  $Q$  at the nozzle.

The twin-exhaust model of Blandford and Rees has the value of providing an analytic solution to describe a possible acceleration mechanism behind relativistic jets. At the same time, the model is also overly simplified and it has been shown to suffer from a number of difficulties, such as the development of the Kelvin–Helmholtz instability at the nozzle (Smith *et al.*, 1983). In addition, lacking the stabilising contribution of magnetic fields, it clearly represents only an idealised realisation of a phenomenon which is in reality much more complex.

### **The tangential-velocity booster.**

Another purely hydrodynamic mechanism, which is sometimes referred to as the *Aloy–Rezzolla booster* (Aloy and Rezzolla, 2006), was proposed recently to accelerate very efficiently and to relativistic velocities the high-energy plasma observed in jets. As for the other booster, this one also lacks the contribution of magnetic fields and hence cannot be considered as a realistic jet model. However, it serves to highlight how purely relativistic and hydrodynamic effects can easily provide large Lorentz factors in relativistic jets. Extensions of this mechanism to

include magnetic fields have been considered by Mizuno *et al.* (2009) and Komissarov *et al.* (2009), but these extensions do not alter the basic mechanism at the core of the booster.

To illustrate the basic mechanism behind the booster it is useful to think that the dynamics of a relativistic hydrodynamic jet in an external medium can be assimilated to the motion of two fluids, the inner one being much hotter and at higher (or equal) pressure than the outer one and moving with a large tangential velocity with respect to the cold, slowly moving outer fluid. In this scenario, a blob of hot plasma moving outwards along the jet generically produces in the direction perpendicular to the motion a hydrodynamic structure composed of a “forward” shock (moving away from the jet axis) and of a “reverse” shock (moving towards the jet axis). Consistent with the notation introduced in Section 4.5, this pattern of nonlinear waves may be indicated as  $\mathcal{S}_\leftarrow \mathcal{C} \mathcal{S}_\rightarrow$  [cf., Eq. (4.148)], where  $\mathcal{S}_\leftarrow$  refers to the reverse shock,  $\mathcal{S}_\rightarrow$  to the forward one, and  $\mathcal{C}$  is the contact discontinuity between the two.

As discussed in Section 4.7.4, genuine special-relativistic effects, not present in Newtonian hydrodynamics, can cause this wave pattern to change for sufficiently large tangential velocities, replacing the inward-moving shock by a rarefaction wave, thus leading to a  $\mathcal{R}_\leftarrow \mathcal{C} \mathcal{S}_\rightarrow$  wave pattern [cf., Eq. (4.149)]. Convincing evidence that this process is likely to occur under realistic conditions has emerged from special-relativistic calculations of extragalactic jets (Aloy *et al.*, 2003), as well as from general-relativistic, multidimensional simulations of progenitors of short GRBs (Aloy *et al.*, 2005). The development of a  $\mathcal{R}_\leftarrow \mathcal{C} \mathcal{S}_\rightarrow$  wave pattern is schematically shown in Fig. 11.24, which reports the flow structure produced in numerical simulations involving a thick accretion torus around a black hole and in which an ultrarelativistic outflow is generated.

At the heart of the Aloy–Rezzolla booster is exactly this change of wave pattern in a Riemann problem as a result of large tangential velocities, which was first pointed out by Rezzolla and Zanotti (2002). We recall that a Riemann problem consists of determining the evolution of a fluid which is composed at some initial time by two uniform states (*i.e.*, a “left” and a “right” state) with different and discontinuous hydrodynamic properties (see Section 4.7 for an extended discussion). Using this initial setup and the equations of special-relativistic hydrodynamics, Rezzolla and Zanotti (2002) revealed that a smooth transition from one wave-pattern to another can be produced by simply varying the velocities which are tangential to the initial discontinuity  $v^t$ , while maintaining the initial states unmodified (Rezzolla *et al.*, 2003). More specifically, for each set of initial states there exists a critical value for the initial tangential velocity  $(v_L^t)_c$  at which a *shock* is transformed into a *rarefaction wave* or vice versa<sup>39</sup>. When this happens, the local Lorentz factor

$$W := [1 - (v^t)^2 - (v^n)^2]^{-1/2}, \quad (11.283)$$

where  $v^n$  is the velocity normal to the initial discontinuity, can undergo a large amplification, thus leading to a boost in the fluid spanned by the rarefaction wave.

To illustrate how this process can lead to an accelerating mechanism in relativistic jets, it is useful to consider a Riemann problem with initial states that would mimic the conditions in an astrophysical relativistic jet. This can be done by considering a left state which is much hotter, with larger pressure and smaller rest-mass density than the right one. Keeping the initial states fixed, we can then use the tangential velocity in the left state  $v_L^t$  as a free parameter

<sup>39</sup>Note that because the total velocity in the each state is  $v = [(v^t)^2 + (v^n)^2]^{1/2} \leq 1$ , a critical threshold for the tangential component also translates into a critical threshold for the normal component, as discussed below.

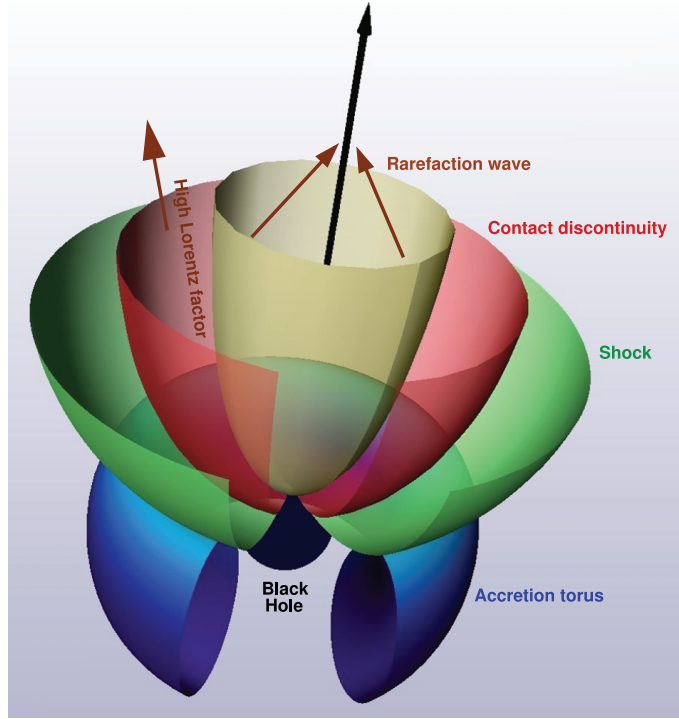


**Fig. 11.24** Schematic illustration of the flow structure in the acceleration of a short GRB produced by an accretion torus orbiting around a stellar-mass black hole. The arrows mark the direction of fluid velocity at the rarefaction head (yellow paraboloidal surface), indicating that collimation of the fluid tends towards the black-hole rotation axis (black arrow). A large boost is produced in the region between the rarefaction head and the contact discontinuity (red surface) separating the relativistic outflow from the shocked external medium. [From Aloy and Rezzolla (2006), reproduced by permission of the AAS.]

and tune it to go from one wave-pattern to the other. More specifically, let us consider the right state to be a cold fluid with a large rest-mass density and essentially at rest, *i.e.*, with initial hydrodynamic properties:  $p_R \approx 10^{-6} \rho_{\text{ext}}$ ,  $\rho_R \approx 10^{-2} \rho_{\text{ext}}$ ,  $v_R^n \approx 0$ ,  $v_R^t \approx 0$ , where  $\rho_{\text{ext}}$  is a normalisation constant, which can be specified when considering the astrophysical implications of the boosting mechanism [see, *e.g.*, Aloy and Rezzolla (2006) for some astrophysical examples]. The left state will have comparable but larger pressure, will be underdense, with a small initial tangential velocity and a normal one close to the speed of light, *i.e.*,  $p_L \gtrsim p_R$ ,  $\rho_L \ll \rho_R$ ,  $v_L^n \approx 1$ ,  $v_L^t \approx 0$ .

The solution of the Riemann problem produced by these two states is shown in the left panel of Fig. 11.25 and is of type  $\mathcal{S}_\leftarrow \mathcal{C} \mathcal{S}_\rightarrow$ , thus consisting of a shock propagating to the left, of a shock propagating to the right and of a contact discontinuity at  $x \approx 0.39$  separating

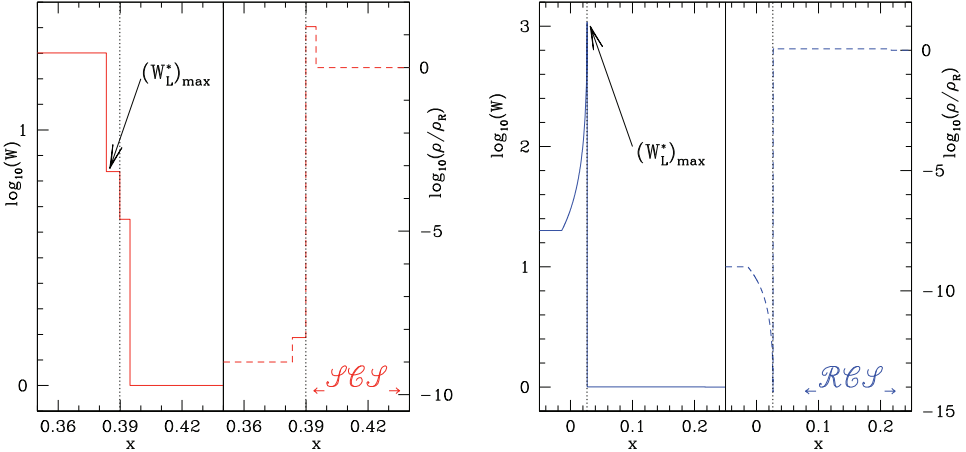


**Fig. 11.25** *Left panel:* Profiles of the Lorentz factor (blue solid line) and rest-mass density (red dashed line) resulting from a prototypical Riemann problem yielding a  $\mathcal{S}\leftarrow\mathcal{C}\mathcal{S}\rightarrow$  pattern; the vertical dotted line marks the position of the contact discontinuity. Note that no boost is produced at the contact discontinuity, *i.e.*,  $(W_L^*)_{\max} < W_L$ . *Right panel:* The same as in the left panel but for a prototype  $\mathcal{R}\leftarrow\mathcal{C}\mathcal{S}\rightarrow$  wave-pattern. Note the very large boost, *i.e.*,  $(W_L^*)_{\max} \gg W_L$ , which peaks at the contact discontinuity [adapted from Aloy and Rezzolla (2006)].

the two waves.<sup>40</sup> This double-shock structure has a well-known Newtonian counterpart and is commonly observed in numerical simulations when there is an almost pressure-match between the jet and the environment. Note that the acceleration at the transition layer between the jet and the external medium is very small and that the Lorentz factor reached in the state between the left-propagating shock and the contact discontinuity,  $W_L^*$ , is smaller than the initial Lorentz factor in the left state  $W_L$ . This is indicated as  $(W_L^*)_{\max}$  in Fig. 11.25 and reaches a value  $(W_L^*)_{\max} \approx 6.87$  against an initial one in the left state  $W_L = 20$ .

While keeping the same right state, we can now consider the jet to be considerably over-pressured and with almost no velocity component perpendicular to the jet direction. The left state can then be parameterised as:  $p_L \gg p_R$ ,  $\rho_L \ll \rho_R$ ,  $v_L^n \approx 0$ ,  $v_L^t \approx 1$ , and the solution of the Riemann problem in this case is shown in the right panel of Fig. 11.25.<sup>41</sup> This is now of type  $\mathcal{R}\leftarrow\mathcal{C}\mathcal{S}\rightarrow$  and thus consists of a rarefaction wave propagating to the left, of a contact discontinuity at  $x \approx 0.026$  and of a shock propagating to the right. This change in wave-pattern is accompanied by a large increase of the Lorentz factor across the rarefaction wave, with the maximum value  $(W_L^*)_{\max} \approx 10^3$  reached at the contact discontinuity.

As a result, the production of a very strong rarefaction near the contact discontinuity *and* the combined conservation across such a wave of the specific enthalpy and of the Lorentz

<sup>40</sup>The initial states in this Riemann problem are given by:  $(p_L, \rho_L, v_L^n, W_L) = (10^{-3}, 10^{-4}, 0.99, 20)$  and  $(p_R, \rho_R, v_R^n, W_R) = (10^{-6}, 10^{-2}, 0, 1)$ .

<sup>41</sup>The initial states in this Riemann problem are instead given by:  $(p_L, \rho_L, v_L^n, W_L) = (10^3, 10^{-4}, 0, 20)$  and  $(p_R, \rho_R, v_R^n, W_R) = (10^{-6}, 10^{-2}, 0, 1)$ .

factor, *i.e.*, [cf., Eqs. (4.188) and (4.189)]

$$\llbracket hW \rrbracket = 0, \quad (11.284)$$

has the consequence of accelerating the fluid to ultrarelativistic regimes with  $W \sim 10^4$  or larger. In essence, this boosting mechanism efficiently converts into kinetic energy the work done on the jet by the external medium.

We should stress that the occurrence of these large fluid accelerations is not the result of the peculiar initial conditions considered above, or of a simplified hydrodynamic flow such as the one offered by a Riemann problem. Rather, accelerations produced through this effect are a robust feature observed in several numerical simulations of relativistic jets (Aloy *et al.*, 2003; Aloy *et al.*, 2005). Indeed, it is easy to illustrate on more general grounds how the final fluid acceleration depends on the initial conditions by assuming that the right state is held fixed. In this way, in fact, the transition from one wave-pattern to the other and the boost in the flow depends on two distinct but related factors: the value of the pressure in the left state  $p_L$  and the value of the tangential velocity there,  $v_L^t$ . In particular, for very small left-state pressures (*i.e.*, for  $p_L \lesssim 10^{-6}$  and the initial states used above) the system evolves to produce a wave pattern of the type  $\mathcal{S}_\leftarrow \mathcal{C} \mathcal{S}_\rightarrow$  also when the normal velocity is zero (*i.e.*,  $v_L^n \approx 0$ ). On the other hand, for very large left-state pressures (*i.e.*, for  $p_L > 1$  and the initial states used above), the system evolves to produce a Riemann structure of the type  $\mathcal{R}_\leftarrow \mathcal{C} \mathcal{S}_\rightarrow$  also when the normal velocity is ultrarelativistic (*i.e.*,  $v_L^n \approx 1$ ). For all the values of  $p_L$  within this range, a critical normal velocity  $(v_L^n)_c$  exists below which the left-propagating shock is replaced by a rarefaction wave and a large boost takes place.

This is summarised in Fig. 11.26, where the maximum values of the Lorentz factors are shown as functions of the initial value of the normal velocity in the left state  $v_L^n$  (note that the value of  $W_L$  is held fixed so that the increase of  $v_L^n$  corresponds to a decrease of  $v_L^t$ ). Different curves refer to different values of the pressure in the left state  $p_L$ , with blue solid lines indicating solutions of the Riemann problem of the type  $\mathcal{R}_\leftarrow \mathcal{C} \mathcal{S}_\rightarrow$ , red dashed lines solutions of the type  $\mathcal{S}_\leftarrow \mathcal{C} \mathcal{S}_\rightarrow$ , and filled circles marking the critical normal velocity  $(v_L^n)_c$  at which one wave-pattern transforms into the other. Clearly, Lorentz factors as large as  $10^3$  can be reached even with moderate values of the tangential velocity.

One of the most important implications of this boosting mechanism is that *less extreme* conditions are required at the launching sites of relativistic jets and GRBs. This hydrodynamic mechanism, in fact, can boost a fluid to ultrarelativistic regimes very efficiently and thus the Lorentz factors either expected or observed in astrophysical sources can be explained with initial “left-states” that have considerably smaller pressures and are thus easier to produce in practice (Aloy and Rezzolla, 2006). A second astrophysical implication is that under suitable but realistic conditions, ultrarelativistic regimes can be reached *very close* to the jet-launching site. Furthermore, while the boost originates and is larger in a small region at the interface between the jet and the external material, it is not restricted to a thin boundary layer but can rapidly involve the whole jet. This is because the left-going rarefaction wave can sweep up the jet material at relativistic speeds and thus rapidly accelerate a considerable mass fraction in the jet (Aloy and Rezzolla, 2006). In contrast, in other thermal acceleration mechanisms that also exploit the existence of a fluid with very large specific enthalpy (*e.g.*, the fireball model for GRBs) some time is needed to speed up the flow, with ultrarelativistic regimes being reached far from the launching site.

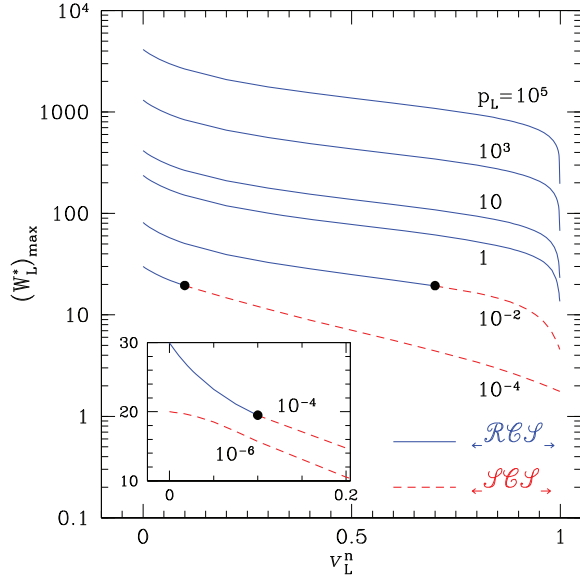


**Fig. 11.26** Maximum Lorentz factors  $(W_L^*)_{\max}$  produced in the Riemann problem as a function of the normal velocity in the left state  $v_L^n$ . The right state is held fixed and is given by  $(p_R, \rho_R, v_R^n, W_R) = (10^{-6}, 10^{-2}, 0, 1)$ . The left state has fixed values in the rest-mass density and Lorentz factor  $(\rho_L, W_L) = (10^{-4}, 20)$ , while the pressure  $p_L$  is varied for each curve as indicated by the different labels. Blue solid lines refer to a  $\mathcal{R}_- \mathcal{C} \mathcal{S}_+$  pattern, while red dashed lines refer to a  $\mathcal{S}_- \mathcal{C} \mathcal{S}_+$ ; filled circles mark the critical normal velocity  $(v_L^n)_c$  [adapted from Aloy and Rezzolla (2006)].

As a final remark, we note that large hydrodynamic boosts of the type discussed here may also be detected with laboratory experiments involving heavy-ion collisions. In these experiments, heavy ions are accelerated to ultrarelativistic velocities and collided. If the two beams are chosen to have different specific enthalpies and to collide with a nonzero impact parameter, an acceleration of the interacting layer could be produced as a result of the relativistic boosting discussed here (see Section 11.10 for an extended discussion).

### 11.9.3 Numerical modelling of relativistic jets

Over the last 20 years the development of time-dependent relativistic-hydrodynamic codes has allowed for the simulation of jet propagation both in AGNs and in GRBs. Relativistic jets from AGNs, in particular, can now be studied numerically over larger and larger distance scales. Several dynamical and morphological features can be reproduced successfully in this way, such as, for example, the generation of superluminal components triggered by small perturbations in steady jets (Gomez *et al.*, 1998). In addition, simulations using equations of state that account for an arbitrary mixture of electrons, protons and electron–positron pairs, can help us understand whether relativistic jets are made of electron–positron pairs or, rather, of

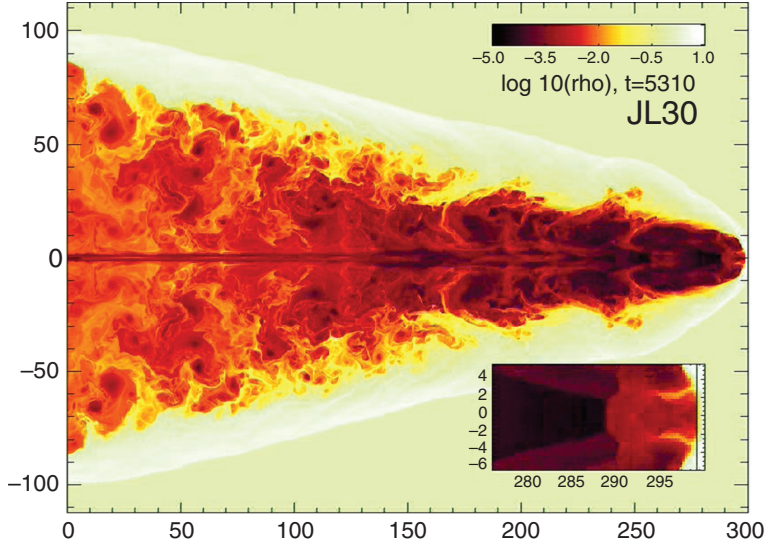


**Fig. 11.27** Logarithm of the density normalised to the density of the ambient medium for a relativistic hot leptonic jet as computed in a two-dimensional numerical simulation. The scale is in units of the size of the beam at the injection point. [From Scheck *et al.* (2002).]

electrons and protons (Scheck *et al.*, 2002). An example of such simulations is reported in Fig. 11.27, which shows the logarithm of the density normalised to the density of the ambient medium for a relativistic hot leptonic jet as computed in a two-dimensional numerical simulation. Note that the jet is considerably less dense than the surrounding medium.

On the kiloparsec scale, moreover, a number of numerical analyses have shown that beams with large internal energies but relatively small speeds have little internal structure and small cocoons, resulting in a *termination shock* that remains well-defined as the jet propagates (Marti *et al.*, 1994; Marti *et al.*, 1995; Komissarov and Falle, 1998). Highly relativistic flows, on the other hand, show extended cocoons that can play a role in confining the jet (Marti *et al.*, 1995). Furthermore, on length-scales that are larger than a few kiloparsecs, the interaction with the surrounding extragalactic medium has strong effects on the dynamics of the flow, being probably responsible for the classical dichotomy between the so-called Faranoff–Riley classes I and II (Faranoff and Riley, 1974).

Another direction along which hydrodynamic numerical simulations have helped in understanding the dynamics and properties of astrophysical relativistic jets is represented by the study of perturbations and instabilities within the jets. In this respect, it is commonly believed that most of the features observed in real jets are due to the growth of Kelvin–Helmholtz normal modes (Bodo *et al.*, 1994; Hardee, 2006). By combining numerical simulations with linear analysis, it was possible to find a number of interesting results which can be summarised as follows:

- (i) *cold and slow jets* are unstable and are easily disrupted after the formation of a shock front crossing the boundary between the jet and the ambient medium.

(ii) *hot and slow* jets are also unstable, but they are disrupted and mixed in a continuous way by the growth of the mixing layer down to the jet axis.

(iii) *hot and fast* jets develop short-wavelength, high-order modes, which grow in the shear layer and saturate without significant loss of collimation [see, e.g., Hardee *et al.* (1998), Perucho *et al.* (2004), Osmanov *et al.* (2008), and Perucho *et al.* (2010) for details].

When considering instead relativistic jets from GRBs, highly relativistic outflows are expected from several of the models that have been proposed over the years, such as a binary compact object merger (Paczynski, 1986; Eichler *et al.*, 1989; Rezzolla *et al.*, 2011), which is possibly best-suited for the subclass of short-duration GRBs, a young, highly magnetised pulsar (Usov, 1992) or a hypernova/collapsar (Paczynski, 1998; MacFadyen and Woosley, 1999), which is best-suited for the subclass of long-duration GRBs. The latter model, in particular, relies on the idea that a significant fraction of the gravitational binding energy is converted into neutrino and antineutrino pairs, which in turn annihilate into a fireball of electron–positron pairs. One potential problem in this scenario is the so-called “baryon loading”, that is, whether baryons can be efficiently excluded from the flow, so as to avoid a strong deceleration in the jet and thus reach the Lorentz factors  $W \gtrsim 100$  needed to explain the observations. Recent, fully general-relativistic simulations of the inspiral and merger of magnetised binary neutron stars have revealed for the first time that the result of this process is a rapidly spinning black hole surrounded by a hot and highly magnetised torus. Furthermore, magnetohydrodynamic instabilities in the torus amplify an initially turbulent magnetic field of  $\sim 10^{12}$  G to produce an ordered poloidal field of  $\sim 10^{15}$  G along the black-hole spin axis, within a half-opening angle of  $\sim 30^\circ$ , which may naturally launch a relativistic jet (Rezzolla *et al.*, 2011). The very low rest-mass densities measured inside the jet seem to indicate that the baryon-loading may not represent a serious limitation for the acceleration to relativistic speeds of the material inside the jet.

In addition to these fully general-relativistic studies, the time-dependent numerical modelling of relativistic jets from GRB explosions in fixed (flat or curved) spacetimes, where the details of the “central engine” are ignored or mimicked with some phenomenological prescription, has a long history. Over the years, in fact, several aspects of the above mentioned GRB models have been investigated numerically and a complete review of the main results obtained can be found in the excellent review by Martí and Müller (2003). Worth noting are the first multidimensional simulations of relativistic jets from GRBs. These were performed by Aloy *et al.* (2000), where the propagation of an axisymmetric jet through the envelope of a collapsing star was studied, and where it was found that the maximum Lorentz factor reached by the jet when it touches the surface of the progenitor star is  $W \sim 20$ . This result was essentially confirmed by several other authors, e.g., Zhang *et al.* (2003). On the whole, all of these numerical analyses should be regarded as the first steps towards a better understanding of GRB phenomena, which is likely to be achieved only through accurate and realistic numerical simulations in the years to come.

## 11.10 Relativistic heavy-ion collisions

Modern nuclear-physics experiments accelerating and colliding heavy ions (*i.e.*, nuclei with an atomic weight heavier than carbon), such as those carried out at the Relativistic Heavy Ion Collider (RHIC) at Brookhaven (USA), at the GSI (Helmholtzzentrum für Schwerionenforschung) facility at Darmstadt (Germany), or at the Large Hadron Collider (LHC) at CERN, may appear rather distant from the astrophysical application of relativistic hydrodynamics we have investigated so far in this chapter. However, it is sufficient to recall that one of the goals of heavy-ion collisions at ultrarelativistic energies is to study and test quantum chromodynamics (QCD) in a dense, thermally equilibrated, strongly interacting system, namely, the *quark-gluon plasma* (QGP), which can be very conveniently described as an ultrarelativistic fluid.

We recall that QCD is the theory of the strong interaction and it predicts a phase transition from a state of confined hadronic constituents to a plasma of deconfined quarks and gluons if the energy density exceeds a critical value. These conditions are expected to have been present at about  $10^{-5}$  s after the big bang, when the universe had a mean density of the order of nuclear matter density,  $\rho \sim 10^{15} \text{ g cm}^{-3}$ , a temperature of the order of 100–200 MeV (*i.e.*,  $\sim 10^{12} \text{ K}$ ) and a particle horizon of the order of a solar mass [*i.e.*,  $r_H \sim 10^5 \text{ cm}$ , Bonometto and Pantano (1993)]. Heavy-ion collisions at ultrarelativistic speeds offer, therefore, the possibility not only to study nuclear matter under conditions comparable with those of the early universe or of collapsed stars, but also to explore under controlled experimental conditions the properties of relativistic hydrodynamics.

In what follows we will briefly review the most salient aspects of the relativistic hydrodynamics of heavy-ion collisions, recalling the basic features of these flows and avoiding the more subtle details, such as the role played by energy fluxes and dissipative processes during the hydrodynamic stage of the collision. The interested reader will find more on these topics in the very good reviews of Huovinen and Ruuskanen (2006), Ollitrault (2008) and Romatschke (2010), while a detailed discussion of the numerical methods normally employed in these calculations can be found in the comprehensive review of Rischke *et al.* (1995).

### 11.10.1 Basic concepts

We start by noting that the units that are better suited to heavy-ion collisions calculations are those obtained after setting  $h_p = c = k_B = 1$ , which we will use in the remainder of this chapter. Moreover, there are a few fundamental parameters and corresponding reference values that are worth recalling. Obviously very important are:

- the mass of the nucleon pair  $m_{NN}$ ;
- the centre-of-mass collision energy per nucleon pair,  $\sqrt{s_{NN}} := \sqrt{\tilde{s}/m_{NN}}$ , where we indicate as  $\tilde{s} := s\rho = \bar{s}n = S/V$  the *entropy density* [cf., Eq. (2.274)<sub>2</sub>];
- the mean energy density  $e_0$ ;
- the mean size and the geometry of the colliding nuclei. In particular, if  $A$  is the atomic mass number, then the typical length-scale in the collision can be defined in terms of the *nuclear radius*  $R_A \sim 1.2 A^{1/3} \text{ fm}$  (Baym *et al.*, 1983), so that, for instance, gold nuclei are typically larger than copper ones.

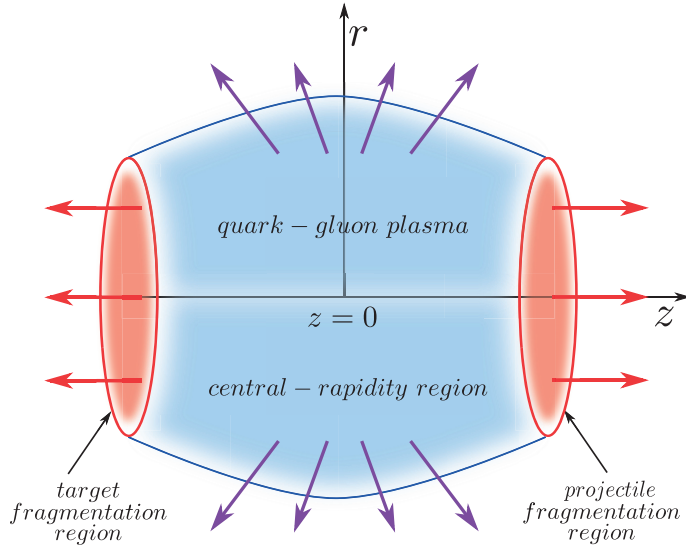


**Fig. 11.28** Schematic view in the centre-of-mass frame of the central collision of two highly Lorentz-contracted ultrarelativistic heavy ions moving along the  $z$ -direction. Shown are the target and fragmentation regions (shaded areas) and the central rapidity region, where the baryon number is very small and the energy density very high. Note that the central-rapidity region also expands in the perpendicular direction,  $r$ .

The collisions are then said to be *relativistic* if the centre-of-mass energy is larger than the rest mass of the nuclei, that is, if  $\sqrt{s_{NN}}/2 \gtrsim m_{NN}$ . The corresponding Lorentz factor  $W$  of the collision is then computed as (Romatschke, 2010)

$$W = \frac{E_{\text{tot}}}{m_{NN}} \simeq \frac{\sqrt{s_{NN}}}{2 \text{ GeV}}. \quad (11.285)$$

For typical energies of  $\sqrt{s_{NN}} \simeq 100\text{--}200 \text{ GeV}$  (this is the highest energy achieved so far for Au-Au collisions at the RHIC),<sup>42</sup> Eq. (11.285) indicates that  $W \simeq 100\text{--}200$ . In the laboratory frame the two nuclei are thus highly Lorentz-contracted in the direction of motion and we should therefore think of the collision not as happening between two spheres, but, rather, between two “pancakes” approaching each other at a speed  $\beta \simeq 0.9999$ .

At these ultrarelativistic energies, the nuclei are essentially transparent to nucleons, so that during the collision the nuclei pass through each other producing two highly excited nuclear fragmentation regions containing the net baryon number of the system, one corresponding to the “target” and the other to the “projectile” (Baym *et al.*, 1983). These are illustrated schematically in Fig. 11.28, where we have assumed the two nuclei to move along the  $z$ -direction and where we have indicated as shaded in red the nuclear-fragmentation regions. Also shown as shaded in blue is the *central-rapidity region*, which joins the target and the projectile, and where the net baryon number is very small, but where the energy density is

<sup>42</sup>Energies as high as  $\sqrt{s_{NN}} \simeq 2.7 \text{ TeV}$  have instead been obtained at the LHC.

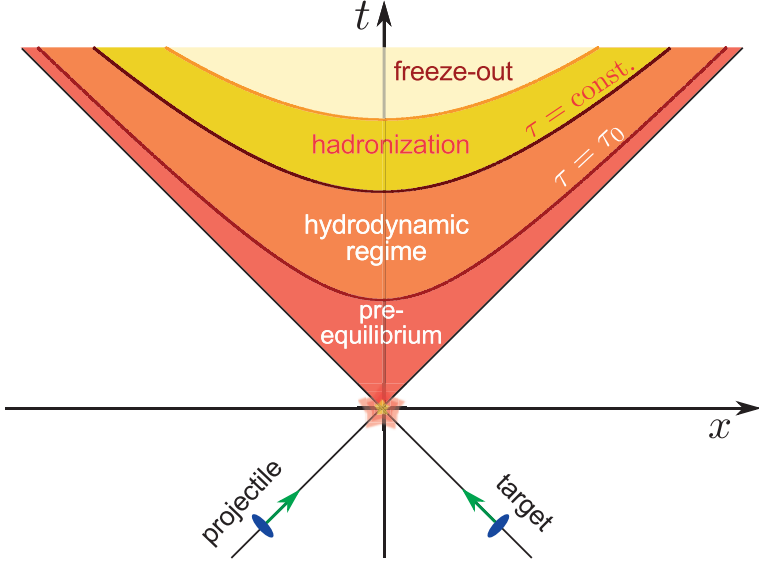


**Fig. 11.29** Spacetime diagram of the collision between a projectile and a target moving at ultrarelativistic speeds along the  $z$ -direction. The collision takes place at  $z = 0$ ,  $t = 0$  and the diagram reports the different stages after the collision: pre-equilibrium, hydrodynamic evolution, hadronisation and freeze-out. The proper time  $\tau$  is constant along hyperbolae.

very high and above the deconfinement transition. Note that the central-rapidity region also expands in the perpendicular direction, which we indicate as  $r$ .

The purely spatial schematic diagram in Fig. 11.28 can be contrasted with the  $(t, z)$  centre-of-mass spacetime diagram shown in Fig. 11.29, representing the different stages of the collision. More specifically, in such a diagram, the target and the projectile nuclei follow trajectories close to the past light cone and collide at  $z = 0$ ,  $t = 0$ , with the proper time being defined as

$$\tau := (t^2 - z^2)^{1/2}, \quad (11.286)$$

and therefore constant on the hyperbolae given by Eq. (11.286).

At very short (proper) times after the collision, the degrees of freedom excited are weakly interacting, the constituents rescatter, but their distributions are not thermal, so that they move essentially freely with velocity  $v_z$  away from the centre of the collision; this is indicated as the *pre-equilibrium* region in Fig. 11.29 and would correspond to straight lines with velocity  $z/t$  from  $z = 0$  in the spacetime diagram. Later on, at a proper time  $\tau_0 \sim 1 \text{ fm} \sim 3.3 \times 10^{-24} \text{ s}$ , the interactions become sufficiently strong to establish local thermodynamic equilibrium and thus allow for the possibility of hydrodynamic flow. For collisions with energies in the range 100–270 GeV, the post-collision energy density is (Baym *et al.*, 1983)

$$e_0 \sim (0.3 - 0.4) A^{1/3} / t \sim 2 \text{ GeV/fm}^3, \quad (11.287)$$

where  $t$  is expressed in fm and where we have considered  $A \sim 238$ . Assuming now that the matter at  $\tau_0$  consists of a thermalised mixture of quarks and antiquarks ( $q, \bar{q}$ ) and gluons

(*g*) with equal numbers of ups and downs,  $u$ ,  $\bar{u}$ ,  $d$ ,  $\bar{d}$ , and neglecting interaction effects and strange quarks, an energy density of  $e_0 \sim 2 \text{ GeV/fm}^3$  corresponds to a temperature of  $T_0 \approx 160 e_0^{1/4} \text{ MeV}$  and to a number density of quanta (Baym *et al.*, 1983)

$$n_0 = n_q + n_{\bar{q}} + n_g \simeq 2.1 e_0^{3/4} \text{ fm}^{-3} \simeq 3.5 \text{ fm}^{-3}. \quad (11.288)$$

In turn, this large number density implies that the mean free path  $\lambda$  is much smaller than the typical transverse dimension of the central-rapidity region  $R_A \sim 10 \text{ fm}$  at  $\tau_0$ , *i.e.*,

$$\lambda \simeq \frac{1}{n_0 \sigma} \sim \frac{0.47}{e_0^{3/4} \sigma_{\text{fm}}} \sim \frac{1}{4 \sigma_{\text{fm}}} \sim 0.1 \text{ fm} \ll A^{1/3}, \quad (11.289)$$

where  $\sigma_{\text{fm}} \sim \mathcal{O}(1-10) \text{ fm}^2$  is the mean scattering cross-section in  $\text{fm}^2$ . In practice, expression (11.289) shows that  $R_A/\lambda \gtrsim 100$  and hence that once a thermodynamic equilibrium has been reached in the central-rapidity region, a relativistic hydrodynamics approach is justified; this is indicated as the *hydrodynamic regime* in Fig. 11.29.

For proper times  $\tau_0 < \tau \lesssim R_A/c_s \sim 4 \text{ fm}$ , that is, for proper times larger than  $\tau_0$  but smaller than the sound crossing time, the dominant motion is the longitudinal recession of the two nuclear pancakes. In addition to this longitudinal motion, there is also an expansion in the plane transverse to the incident direction (*i.e.*, the  $r$ -direction in Fig. 11.28), which begins with the outward propagation of a rarefaction wave from  $r \simeq R_A$ . Clearly, both the longitudinal and the transverse expansions lead to cooling and the matter, which is in the deconfined QGP phase, will rapidly go through a transition to confined hadronic matter; this is indicated as *hadronisation transition* in Fig. 11.29.<sup>43</sup> At this point, the hadronic fluid becomes sufficiently rarefied that local thermodynamic equilibrium is no longer maintained, the hadrons decouple from each other and stream freely eventually reaching the detector. In such a regime, the hydrodynamic approximation ceases to be valid and the problem of the subsequent evolution should be treated within a kinetic-theory approach. This regime is indicated as *freeze-out* in Fig. 11.29.

Hereafter we will obviously focus only on the hydrodynamic regime and will do so by assuming that the QGP can be treated as a perfect fluid and hence as obeying the laws of relativistic hydrodynamics discussed in Chapter 3. This is a reasonable first approximation, which is sufficient to model the main properties of the flows in heavy-ion collisions and indeed viscosity is neglected in most applications of relativistic hydrodynamics to heavy-ion collisions. For example, simulations of Au-Au collisions at the RHIC based on perfect-fluid hydrodynamics reproduce well the observed large-size and impact-parameter dependence of elliptic flow as long as the collisions are sufficiently central, *i.e.*, with impact parameter  $\lesssim 7 \text{ fm}$  (Ackermann *et al.*, 2001). We recall that, in contrast to central collisions, in which the particle production is azimuthally isotropic, in non-central collisions the reaction zone is not isotropic, but has an elongated elliptical shape. If the produced particles rescatter, those moving in the direction of the longer axis of the ellipse are more likely to change their direction than the particles moving in the direction of the shorter axis, thus leading to an azimuthally anisotropic particle distribution, *i.e.*, an *elliptic flow* (Huovinen and Ruuskanen, 2006). On

<sup>43</sup>If a first-order phase transition takes place between the QGP and the hadronic phase, a reaction front is expected to be present in the form of a deflagration (see Chapter 6 for a discussion of reaction fronts). On the other hand, the phase transition could also be a smooth cross-over.

the other hand, shear viscosity, bulk viscosity, heat conductivity are important properties of QCD matter and their influence emerges clearly in experiments with largely non-central collisions or at lower collision energies (Baier *et al.*, 2006). Under these conditions, which are much harder to handle in an ultrarelativistic regime, the theory of relativistic hydrodynamics of non-perfect fluids discussed in Chapter 6 needs to be employed. Indeed, these scenarios are among the strongest motivations to develop and employ dissipative relativistic hydrodynamics. A complete discussion of the state-of-the-art of the research in this area can be found in Romatschke (2010).

### 11.10.2 One-dimensional Bjorken flow

As a first approach to the flow properties of relativistic heavy-ion collisions we consider purely one-dimensional flows and assume that the projectile and target approach each other along the  $z$ -axis and have infinitesimal dimensions in this direction. Furthermore, we will assume that the gravitational corrections are unimportant,<sup>44</sup> so that we can consider a flat spacetime metric (1.103) and express the conservation of baryon number, energy and momentum (2.118)–(2.119) simply as

$$\nabla_\mu(nu^\mu) = 0, \quad \nabla_\mu T^{\mu\nu} = 0. \quad (11.290)$$

Since in the central-rapidity region the local baryon density is nearly zero, we can assume the energy density and pressure to be evaluated at zero net baryon density, or equivalently at zero baryon chemical potential, *i.e.*,  $\mu_b = 0$ . As a result, the temperature  $T$  is the only independent variable and we can write the energy density and pressure differentials as [*cf.*, Eqs. (2.139) and (2.140)]

$$d(\rho\epsilon) = Td\tilde{s}, \quad dp = \tilde{s}dT. \quad (11.291)$$

The equation of state is that of an ultrarelativistic fluid, *i.e.*,  $p = \frac{1}{3}\epsilon$  (see Section 2.4.4) and the sound speed is therefore given by [*cf.*, Eq. (2.274)]

$$c_s^2 = \frac{dp}{de} = \frac{\tilde{s}}{T} \frac{\partial T}{\partial \tilde{s}} = \frac{1}{3}. \quad (11.292)$$

Under these assumptions, the conservation of energy and momentum are simply expressed as

$$\nabla_\mu(\tilde{s}u^\mu) = 0, \quad (11.293)$$

$$u^\mu \nabla_\mu(Tu_\nu) + \nabla_\nu T = 0, \quad (11.294)$$

which, in a cylindrical coordinate system  $(t, r, \phi, z)$ , we can also write as

$$\partial_t(\tilde{s} \cosh y) + \partial_z(\tilde{s} \sinh y) = 0, \quad (11.295)$$

$$\partial_t(T \sinh y) + \partial_z(T \cosh y) = 0, \quad (11.296)$$

<sup>44</sup>While this is a reasonable first approximation at low energies, it also hides general-relativistic effects which could be important at sufficiently high energies. As an example, numerical-relativity simulations have shown that black holes can be produced in the collision of two solitons or fluid stars when boosted to ultrarelativistic energies (Choptuik and Pretorius, 2010; Rezzolla and Takami, 2013; East and Pretorius, 2013).

where we have introduced the *longitudinal rapidity* defined as  $y := \tanh^{-1} v_z$  and where the *longitudinal Lorentz factor* is defined as  $W := (1 - v_z^2)^{-1/2}$ .

Equations (11.295)–(11.296) can be easily solved once an initial value for the longitudinal velocity  $v_z$  is chosen. In a simplified, but not unrealistic picture first proposed by Bjorken (1983), the longitudinal thickness of the colliding nuclei approaches zero when  $v_z \rightarrow 1$ . In this limit, also the longitudinal size of the collision zone tends to zero and thus the system does not have a longitudinal scale at all. As a result, the longitudinal collective velocity of the matter/particles emerging from the collision zone around  $z = 0 = t$  has to have a scaling law in which the velocity increases with the distance  $z$ , *i.e.*,  $v_z = z/t$  (note that  $v_z = 0$  at  $t = 0$  for all values of  $z$  and  $v_z = 0$  at  $z = 0$  at all times, as it should be as a result of the collision). Interestingly, this uniform-flow prescription is “boost invariant”, that is, if a Lorentz transformation with velocity  $v$  is made along the  $z$ -axis, all quantities  $v_z$ ,  $z$ , and  $t$  will be transformed in the new frame, but the transformation will leave unchanged the fluid velocity  $v_z = z/t$ . This is not surprising, since if the motion is uniform it should remain uniform also after a Lorentz transformation. This “boost-invariant” flow is also referred to as *Bjorken flow* (Bjorken, 1983) and, although only a toy-model valid for  $\tau \lesssim \tau_0$ , it represents an important reference solution that reproduces the experimental data at later time reasonably well [see, *e.g.*, Ollitrault (2008) and Romatschke (2010) for an extended discussion].

The boost-invariance condition on  $v_z$  can also be expressed in terms of the four-velocity as (Baym *et al.*, 1983)

$$u^\mu = (u^t, 0, 0, u^z) = \tau^{-1}(t, 0, 0, z), \quad (11.297)$$

so that  $\sinh y = z/\tau$ ,  $\cosh y = t/\tau$  and Eq. (11.296) then implies that  $T(t, z)$  is a function of  $\tau$  only. Furthermore, the energy conservation equation (11.295) can be rewritten as

$$\frac{d\tilde{s}}{d\tau} + \frac{\tilde{s}}{\tau} = 0, \quad \frac{de}{d\tau} + \frac{e+p}{\tau} = 0, \quad (11.298)$$

where the second equation is obtained after recalling that for an ultrarelativistic fluid  $\tilde{s} \propto e^{3/4}$  [*cf.*, Eq. (2.274)]. The resulting solutions can be easily integrated and are simple scaling relations of the type

$$\tilde{s} = \tilde{s}_0 \frac{\tau_0}{\tau}, \quad e = e_0 \left( \frac{\tau_0}{\tau} \right)^{1+c_s^2} = e_0 \left( \frac{\tau_0}{\tau} \right)^{4/3}. \quad (11.299)$$

Expressions (11.299) highlight that in a Bjorken flow the entropy and energy densities decrease with proper time as  $\tilde{s} \sim \tau^{-1}$  and  $e \sim \tau^{-4/3}$ , respectively. The global cooling of the QGP that results from this longitudinal expansion is therefore responsible for the phase transition to a confined fluid of hadrons. Viscous corrections to the solutions (11.299) have been considered by several authors and a review of the main results can be found in Romatschke (2010).

### 11.10.3 Cylindrically symmetric flows

Although a useful first approximation, the Bjorken flow discussed in the previous section is one-dimensional and neglects the description of the transverse expansion of the central-rapidity region, whose main overall effect is a more rapid cooling leading to shorter lifetime of

the thermal system than with the longitudinal expansion alone. Accounting for this correction is of course of great importance to compare with the experimental data, especially in non-central collisions. No analytic solution is known in more than one dimension and even in the simpler case of a two-dimensional flow, the set of relativistic-hydrodynamic equations needs to be solved numerically.

Let us therefore assume that the collision preserves a cylindrical symmetry around the collision axis  $z$ , so that in cylindrical coordinates, the fluid four-velocity is given by (Baym *et al.*, 1983)

$$u^\mu = \left( u^0, u^r, u^\phi, u^z \right) = f(\tau, r) \left( t, g(\tau, r), 0, z \right), \quad (11.300)$$

where the second equality simplifies the search for a form of the four-velocity which is invariant under a boost along the  $z$ -direction. Such an invariance is obtained by setting

$$v_z(t, z) = \frac{z}{t}, \quad v_r(t, r, z) = \frac{g(\tau, r)}{t}, \quad f^2(\tau, r) := \frac{1}{\tau^2 - g^2}, \quad (11.301)$$

so that, if we know the transverse velocity at  $z = 0$ , *i.e.*,  $v_r(t, r, 0)$ , we can deduce it at any other position along the  $z$ -direction as

$$v_r(t, r, z) = \frac{\tau}{t} v_r(\tau, r, 0). \quad (11.302)$$

As a result, although the problem is intrinsically two-dimensional, the use of the boost invariance makes it effectively one-dimensional and the only relevant coordinate is therefore the transverse one,  $r$ .

In this coordinate system and with this velocity field, the conservation equations (11.293) and (11.294) take the explicit form (Baym *et al.*, 1983)

$$\partial_t(\tilde{s}W_r) + \partial_r(\tilde{s}W_r v_r) + \tilde{s}W_r \left( \frac{v_r}{r} + \frac{1}{t} \right) = 0, \quad (11.303)$$

$$\partial_t(TW_r v_r) + \partial_r(TW_r) = 0, \quad (11.304)$$

where  $W_r := (1 - v_r^2)^{-1/2}$  is the transverse Lorentz factor. Introducing now the *transverse rapidity*  $\alpha := \tanh^{-1} v_r$ , Eqs. (11.303) and (11.304) can be written in the more compact form

$$\partial_t(rt\tilde{s}\cosh\alpha) + \partial_r(rt\tilde{s}\sinh\alpha) = 0, \quad (11.305)$$

$$\partial_t(T\sinh\alpha) + \partial_r(T\cosh\alpha) = 0, \quad (11.306)$$

which is similar to that of Eqs. (11.295)–(11.296) in cylindrical symmetry. Equations (11.305) and (11.306) can be conveniently reduced to a single equation after introducing the potential  $\Phi(T)$

$$d\Phi := \frac{d\ln T}{c_s} = c_s d\ln \tilde{s}, \quad (11.307)$$

and the function

$$a_\pm(t, r) := \exp(\Phi \pm \alpha), \quad (11.308)$$

so as to obtain

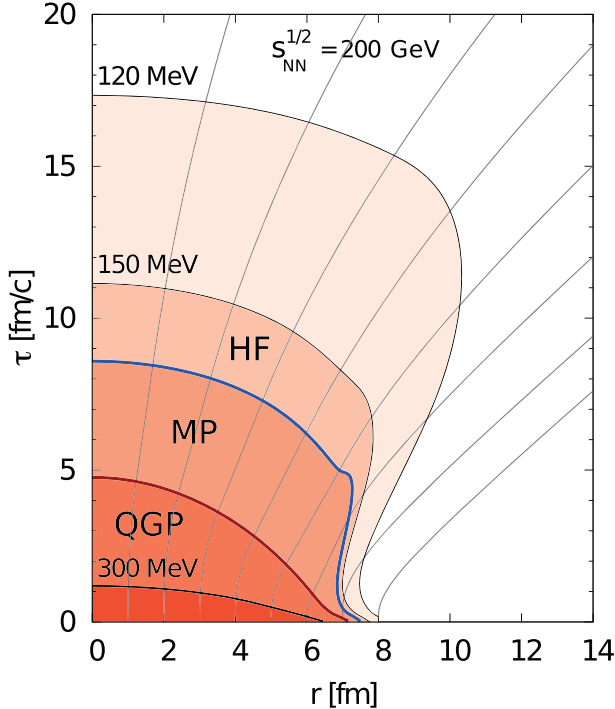


**Fig. 11.30** Temperature contours marking the boundaries of the various regions of the flow: quark–gluon plasma (QGP), mixed phase (MP) and hadron fluid (HF), with  $T_c = 167$  MeV. The data refers to a calculation with initial energies  $\sqrt{s_{NN}} = 200$  GeV. Flow lines are also shown as thin grey lines [adapted from Huovinen and Ruuskanen (2006)].

$$\partial_t a_{\pm} + \left( \frac{v_r \pm c_s}{1 \pm v_r c_s} \right) \partial_r a_{\pm} + \left( \frac{c_s}{1 \pm v_r c_s} \right) \left( \frac{v_r}{r} + \frac{1}{t} \right) a_{\pm} = 0. \quad (11.309)$$

This change of variables is particularly useful, since it provides regular solutions of the type  $a_{\pm} \rightarrow 0$  as  $T \rightarrow 0$  and  $\Phi(T) \sim \ln T \rightarrow -\infty$ . Furthermore, once the solution in  $a_{\pm}$  is found, the temperature and the expansion velocity are simply given by

$$\Phi(T) = \frac{1}{2} \ln(a_+ a_-), \quad v_r = \frac{a_+ - a_-}{a_+ + a_-}. \quad (11.310)$$

The procedure followed above is useful because we can now find an explicit analytic solution of Eq. (11.309) if it is taken to represent a one-dimensional relativistic Riemann problem in a reference  $x$ -direction, where the initial left state goes from  $x = -\infty$  up to  $x = R > 0$  and the initial right state from  $x = R$  to  $x = \infty$  (*i.e.*, the expansion of a semi-infinite slab of matter). If the velocities in the two states are taken to be zero and the left state is taken to have a uniform temperature  $T_0$  which drops to zero in the right state, then the evolution of the Riemann problem is that of a rarefaction wave moving at the speed of sound to the right of  $R$ . The derivation of the explicit solution can be found in Baym *et al.* (1983) and we report here only its form at late times, which is given by

$$\alpha(t, x) = \frac{1}{2} \ln \left( \frac{t+x}{t-x} \right), \quad T = T_0 \left( \frac{\tau_0^2}{t^2 - x^2} \right)^{c_s^2/2}, \quad (11.311)$$

where  $v_x(x=0) = 0$  at all times. Such solution is often used as a basis for interpreting the numerical solutions and to construct approximate analytic solutions.

We conclude this section by illustrating the actual results of a (one-dimensional) numerical calculation of the transverse expansion in a heavy-ion collision at an energy  $\sqrt{s_{NN}} = 200$  GeV (Huovinen and Ruuskanen, 2006) [see, e.g., Eskola *et al.* (2005) for additional details]. This is shown in the spacetime diagram of Fig. 11.30, which reports the boundaries of the QGP (which is taken to be a deflagration), those of the hadron fluid (marked as HF), and of the mixed phase separating the two (marked as MP). The calculations have assumed that the phase transition from quarks to hadrons is of first order, with the mixed phase being composed, for instance, of hadronic droplets in the QGP. A conclusive view on the precise order of the phase transition has not yet been reached, although the most recent lattice-gauge calculations indicate that it is not of first order, but rather a smooth cross-over (Rischke, 2004; Huovinen, 2005). Also reported are the isothermal contours at 300, 150 and 120 MeV and the fluidlines of representative tracers, with the slope of the fluidlines obviously indicating the local velocity. These calculation shows that the maximum lifetime of the QGP phase is  $\sim 5$  fm, while that of the mixed phase is  $\sim 8$  fm. At small distances  $r$  from the collision point, the gradients are small and the fluidlines are only slightly bent. However, as the distance increases, the pressure gradients also become larger and the fluidlines have larger velocities, close to the speed of light at the edge of the expanding flow (Huovinen and Ruuskanen, 2006).

### 11.11 Further reading

- Font, J. A. (2008). Numerical Hydrodynamics and Magnetohydrodynamics in General Relativity. *Living Rev. Relativ.*, **11**, 7.
- Frank, J., King, A., and Raine, D. J. (2002). *Accretion Power in Astrophysics: Third Edition*. Cambridge University Press, Cambridge.
- Kato, S., Fukue, J., and Mineshige, S. (2008). *Black-Hole Accretion Disks - Towards a New Paradigm*. Kyoto University Press, Kyoto.
- Landau, L. D. and Lifshitz, E. M. (1987). *Fluid Mechanics*. Course of Theoretical Physics, Vol. 6. Butterworth-Heinemann, Oxford.
- Martí, J. M. and Müller, E. (2003). Numerical Hydrodynamics in Special Relativity. *Living Rev. Relativ.*, **6**, 7.
- Straumann, N. (1984). *General Relativity and Relativistic Astrophysics*. Springer, Berlin.
- Zel'dovich and Novikov, I. D. (1971). *Relativistic Astrophysics, Vol. I (Stars and Relativity)*. University of Chicago Press, Chicago.

## 11.12 Problems

1. Using the Blandford–McKee solution (11.62), show that a fraction  $\varepsilon < 1$  of the mass and energy is confined in a shell of relative thickness

$$\frac{\Delta r}{R_s} = \frac{\varepsilon}{8 W_s^2 (1 - \varepsilon)},$$

so that  $\Delta r/R_s \sim 10^{-4}$  for  $\varepsilon = 90\%$  and  $W_s \sim 100$ . [Hint: use expression (11.55) to relate a radial position to the value at which  $f(\chi) = 1 - \varepsilon$ .]

2. Compute the accretion radius of the black hole assumed to be at the centre of our Galaxy, Sgr A\*, assuming  $M \approx 3.6 \times 10^6 M_\odot$  and  $c_{s,\infty} \approx 1000 \text{ kms}^{-1}$ .
3. Compute the spherically symmetric accretion solution onto a Schwarzschild black hole using the same parameters as Fig. 11.9, namely assuming a critical radius  $r_c = 8.0M$  and a critical density  $\rho_c = 0.0625$ .
4. Compute the streamlines of the potential flow onto a moving Schwarzschild black hole after fixing a value for  $u_\infty$ . [Hint: streamlines can be computed after solving a partial differential equation for the velocity field once the initial positions and the values of the slopes  $dx/dz$  are specified, *i.e.*,

$$\frac{dx}{dz} = \frac{v^x}{v^z} = \frac{u^x}{u^z}.$$

The most convenient frame to express such a velocity field is the local orthonormal tetrad of a static observer as used in Fig. 11.10. In this case, within a Cartesian coordinate system and restricting our attention to the  $(x, z)$  plane, *i.e.*,  $\phi = 0$ , the streamlines can be computed as

$$\frac{dx}{dz} = \frac{v^{\hat{x}}}{v^{\hat{z}}} = \frac{\Pi^{\hat{x}}_{\hat{\alpha}} v^{\hat{\alpha}}}{\Pi^{\hat{z}}_{\hat{\alpha}} v^{\hat{\alpha}}} = \frac{\Pi^{\hat{x}}_{\hat{r}} v^{\hat{r}} + \Pi^{\hat{x}}_{\hat{\theta}} v^{\hat{\theta}}}{\Pi^{\hat{z}}_{\hat{r}} v^{\hat{r}} + \Pi^{\hat{z}}_{\hat{\theta}} v^{\hat{\theta}}} = \frac{\sin \theta v^{\hat{r}} + \cos \theta v_{\hat{\theta}}}{\cos \theta v^{\hat{r}} - \sin \theta v_{\hat{\theta}}},$$

where  $\Pi^{\hat{i}}_{\hat{j}}$  is the rotation matrix in the orthonormal basis and

$$v^{\hat{r}} := \mathbf{e}_{\hat{r}} \cdot \mathbf{v}, \quad v^{\hat{\theta}} := \mathbf{e}_{\hat{\theta}} \cdot \mathbf{v},$$

and where  $v^i = u^i/W$  [*cf.* Eq. (7.22)], with the tetrad  $\mathbf{e}_{\hat{\alpha}}$  given by Eqs. (11.205) in the limit of a non-rotating black hole.]

5. Using the results of Problem 4, consider now a coordinate frame, *i.e.*,

$$\frac{dx}{dz} = \frac{\Lambda_r^x g^{rr} u_r + \Lambda_\theta^x g^{\theta\theta} u_\theta}{\Lambda_r^z g^{rr} u_r + \Lambda_\theta^z g^{\theta\theta} u_\theta} = \frac{\sin \theta (1 - 2M/r) u_r + \cos \theta r^{-2} u_\theta}{\cos \theta (1 - 2M/r) u_r - \sin \theta r^{-2} u_\theta},$$

where  $\Lambda_j^i$  is the transformation matrix from polar to Cartesian coordinates and where  $u_r$  and  $u_\theta$  are given by Eqs. (11.132) and (11.133), respectively. What happens to the streamlines in the limit of  $u_\infty = 0$  and for initial positions such that  $\sin \theta = \cos \theta$ ?

6. Consider circular motion with four-velocity  $u^\mu = u^t(\eta^\mu + \Omega\xi^\mu)$ , where  $\Omega$  is the angular velocity and  $\eta^\mu = \delta_t^\mu$  and  $\xi^\mu = \delta_\phi^\mu$  are the Killing vectors associated to the stationarity and axisymmetry of the spacetime. Show that if the motion is geodetic the rotation law follows after solving the following quadratic equation in  $\Omega$

$$\Omega^2 \nabla_\mu g_{\phi\phi} + 2\Omega \nabla_\mu g_{t\phi} + \nabla_\mu g_{tt} = 0.$$

[Hint: starting from the condition  $u^\mu \nabla_\mu u^\nu = 0$ , use the properties (1.173).]

7. Using the results of Problem 6, show that the solution of the equation above on the equatorial plane of the Kerr spacetime (both in Boyer–Lindquist and in Kerr–Schild coordinates) gives the Keplerian rotation law [*cf.*, Eq. (11.157)]

$$\Omega_K = \pm \frac{M^{1/2}}{r^{3/2} \pm a/M^{1/2}}.$$

This proves that an equatorial circular motion is geodetic if and only if the rotation law is Keplerian.

8. Compute the specific angular momentum  $\ell$  at a generic point of coordinates  $(r, \theta)$  knowing the distribution of  $\ell_{\text{eq}}(r)$  on the equatorial plane. [Hint: Use Eq. (11.168), evaluated at  $(r, \theta)$ , to obtain  $r_0$ .]
9. Compute the radius of the marginally stable orbit  $r_{\text{ms}}$  for a Kerr black hole using the condition  $d\ell_K/dr = 0$  and compare the result with expression (1.267).
10. Using the definitions (11.146) and (11.153), and the expression for the Keplerian angular frequency (11.157), derive expression (11.176) for the Keplerian specific angular momentum around a Schwarzschild black hole.
11. The total energy of a gravitating system in a spacetime admitting a timelike Killing vector  $\xi^\mu$  can be computed as (Komar, 1959)

$$\mathcal{E} = 2 \int_{\Sigma} \left( T^\beta{}_\alpha - \frac{1}{2} \delta_\alpha^\beta T^\mu{}_\mu \right) \xi^\alpha n_\beta \sqrt{\gamma} d^3 x,$$

where the integration is performed over the three-dimensional hypersurface  $\Sigma$  in which the energy-momentum tensor  $T^{\alpha\beta} \neq 0$ ,  $\sqrt{\gamma}$  is the determinant of the induced metric on  $\Sigma$  and  $n^\mu$  is the unit normal to  $\Sigma$  (see Section 7.1). Use the expression above to deduce Eq. (11.185) for the mass energy of a thick disc. [Hint: use  $\xi^\mu = \delta_t^\mu$  and  $n_\mu = (-\alpha, 0, 0, 0)$ .]

12. Using the relation (11.162) between the specific angular momentum  $\ell$  and the orbital angular  $\Omega$ , and exploiting the corresponding expression (11.157) in the case of Keplerian motion, derive the expression for the Keplerian specific angular momentum (11.204).

**592 Relativistic Hydrodynamics of Non-Selfgravitating Fluids**

13. Using the definition of the shear tensor (3.12) and the components of the ZAMO tetrad (11.218), prove Eq. (11.242), that is, prove that the following identity is true

$$\sigma_{\hat{r}\hat{\phi}} = \sigma_{\mu\nu} e_r^\mu e_{\hat{\phi}}^\nu = \left( \frac{A\gamma^3}{2r^3} \right) \frac{d\Omega}{dr} = \sigma_{\bar{r}\bar{\phi}}.$$

## 12

# Relativistic Hydrodynamics of Selfgravitating Fluids

---

Chapter 11 was devoted to illustrating a number of scenarios in which the relativistic dynamics of fluids can be studied without having to resort to the solution of the Einstein equations. For such *non-selfgravitating fluid* (or test fluids), in fact, the total mass and energy are sufficiently small that they do not provide a significant source for the right-hand side of the Einstein equations (1.218). As a result, the equations of relativistic hydrodynamics can be solved on a background spacetime that does not evolve in time. However, there are often conditions in which the assumptions made above are not valid, as is the case for *selfgravitating fluids*. When this is the case, the equations to be solved are the combination of the Einstein equations and of those of conservation of rest mass, energy and momentum, *i.e.*, the Einstein–Euler equations

$$R_{\mu\nu} - \frac{1}{2}R g_{\mu\nu} = 8\pi T_{\mu\nu}, \quad (12.1)$$

$$\nabla_\mu(\rho u^\mu) = 0, \quad (3.52)$$

$$\nabla_\mu T^{\mu\nu} = 0, \quad (3.53)$$

where in Eqs. (12.1) we have intentionally neglected the cosmological constant [*cf.*, Eq. (1.218)], as its role is normally negligible on the scale of astrophysical compact objects.

This chapter is therefore devoted to the analysis of relativistic selfgravitating fluids and we will first discuss some examples of stationary objects, *e.g.*, isolated stars, before moving on to more dynamical configurations, *e.g.*, the collapse to a black hole or the merger of compact stars in a binary system. As will become apparent, the nonlinearity of the equations will make analytic solutions increasingly difficult to obtain, leaving room only for complex numerical simulations. At the same time, our description will become more and more phenomenological as much of our present understanding of these regimes depends on the still poor realism of the simulations. Because the realism will increase as larger computational resources become available and better numerical approaches are employed, part of what is described in this chapter as “state of the art” will need to be updated.

### 12.1 Spherical stars

The first example of a selfgravitating fluid configuration is offered by a *spherical star* in static equilibrium. Despite its simplicity, this still represents a basic benchmark of general-relativistic codes. Before going into the details of the derivation of the equations describing

the relativistic equilibrium, it is convenient to recall the solution of this problem in Newtonian gravity. In this case, in fact, the hydrostatic equilibrium equation follows from the equation of conservation of momentum, *i.e.*, the Euler equations, under the assumption of zero velocity and stationarity. Using Eq. (2.66) it is straightforward to obtain

$$\vec{\nabla} p = \rho \vec{g} = -\rho \vec{\nabla} \phi_N, \quad (12.2)$$

where  $\vec{g}$  represents the *gravitational acceleration* vector, which can be expressed as the gradient of the *gravitational potential*  $\phi_N$ . In turn, the gravitational potential is the solution of the elliptic *Poisson equation* having the rest-mass density distribution  $\rho = \rho(r)$  as a source, *i.e.*,

$$\nabla^2 \phi_N = 4\pi\rho. \quad (1.215)$$

The importance of Eq. (12.2) lies in showing that an equilibrium is possible in a selfgravitating fluid as long as the gravitational forces (which are inwardly directed) are balanced by pressure gradients (which are outwardly directed). Equations (12.2) and (1.215) can be combined as

$$\vec{\nabla} \cdot \left( \frac{\vec{\nabla} p}{\rho} \right) = \frac{1}{r^2} \frac{d}{dr} \left( \frac{r^2}{\rho} \frac{dp}{dr} \right) = -4\pi\rho, \quad (12.3)$$

thus leading to a second-order ordinary differential equation in the pressure  $p(r)$ . Once an equation of state  $p = p(\rho)$  is specified, Eq. (12.3) can be integrated, for instance, from the stellar centre, up to the position  $r = R$ , where  $p(R) = 0$ . For a polytropic equation of state  $p = K\rho^\Gamma$  (see Section 2.4.7), the differential equation above can be written solely in terms of  $\rho$  as the *Lane–Emden equation* and can even be solved analytically for certain values of the adiabatic index, *i.e.*, for  $\Gamma = 6/5, 3/2, \infty$  (Chandrasekhar, 1939).

Let us move now to discuss the corresponding hydrostatic equilibrium equations in relativistic gravity. Part of the solution is already known and is provided by *Birkhoff's theorem* introduced in Section 1.7.1, stating that the Schwarzschild solution is the *only* solution of the Einstein equations in a spherically symmetric spacetime in vacuum. As a result, we already know that the metric tensor outside the relativistic star is simply given by Eq. (1.221), where  $M$  must be a measure of the (gravitational) mass of the star. The interior metric, on the other hand, needs to be determined, but we already know that in a spherical and static spacetime the metric can always be cast in the form

$$ds^2 = -e^{2\phi} dt^2 + e^{2\lambda} dr^2 + r^2 d\Omega^2, \quad (12.4)$$

where  $\phi$  and  $\lambda$  are functions of  $r$  only. It is also convenient to introduce a re-parameterisation of the radial metric component  $g_{rr}$  via the function

$$m(r) := \frac{1}{2}r \left( 1 - \frac{1}{g_{rr}} \right) = \frac{1}{2}r(1 - e^{-2\lambda}), \quad (12.5)$$

so that

$$g_{rr} = e^{2\lambda} = \left( 1 - \frac{2m(r)}{r} \right)^{-1}. \quad (12.6)$$

As in Newtonian gravity, we first derive an equation that expresses the equilibrium of forces or, equivalently, the conservation of linear momentum. We consider therefore the stellar matter to be represented by a perfect fluid with energy–momentum tensor

$$T^{\mu\nu} = (e + p)u^\mu u^\nu + pg^{\mu\nu}, \quad (2.95)$$

where, we recall,  $e$ ,  $u^\mu$  and  $p$  are the total mass-energy density, the fluid four-velocity and the pressure, respectively (see Section 2.3.2). The stellar configuration will therefore be a solution of the hydrodynamics equations for the conservation of the rest-mass density, momentum and energy, *i.e.*,

$$\nabla_\mu(\rho u^\mu) = 0, \quad (3.52)$$

$$\nabla_\mu T^{\mu\nu} = 0. \quad (3.53)$$

Projecting now Eq. (3.53) in the direction orthogonal to the fluid four-velocity through the projector operator  $h^{\mu\nu} := g^{\mu\nu} + u^\mu u^\nu$  [*cf.* Eq. (3.9)], we obtain the general-relativistic Euler equations [*cf.* Eq. (3.56)]

$$(e + p)a_\mu = -h_\mu^\nu \partial_\nu p, \quad (12.7)$$

where  $a_\mu := u^\nu \nabla_\nu u_\mu$  is the fluid four-acceleration [*cf.* Eq. (3.1)]. Imposing now the conditions of stationarity and spherical symmetry, the only non-trivial Euler equation reduces to<sup>1</sup>

$$\frac{dp}{dr} = -(e + p) \frac{d\phi}{dr}. \quad (12.8)$$

Comparison between Eqs. (12.2) and (12.8) highlights the analogies, but also the differences, between Newtonian and relativistic gravity, with the mass density in Newtonian physics  $\rho$  being replaced in general relativity by the combined contribution of the energy density and of the pressure  $e + p$ .

Given the metric (12.4), it is a simple exercise to show that the only non-trivial Einstein equations (1.218) for a spherically symmetric and static perfect fluid reduce to (see Problem 1)

$$\frac{dm}{dr} = 4\pi r^2 e, \quad (12.9)$$

$$-(e + p) \frac{d\phi}{dr} = -\frac{(e + p)(m + 4\pi r^3 p)}{r(r - 2m)} = \frac{dp}{dr}, \quad (12.10)$$

where the second equality in Eq. (12.10) follows from Eq. (12.8). Also in this case, a comparison between Eqs. (12.10) and (1.215) shows the analogies between the Newtonian gravitational potential  $\phi_N$  and the metric function  $\phi$ , which in general relativity has both the energy density and the pressure as sources.<sup>2</sup> Note also that the relativistic pressure gradient scales like  $1/r^2$  only if  $m(r) = \text{const.}$ , which is the case only at large distances. We can reach this conclusion through the physical interpretation of the function  $m(r)$ , which was introduced before simply for mathematical convenience. Recalling in fact that outside the star the solution must match the Schwarzschild solution, it is clear that  $m(r)$  represents the gravitational mass-energy inside a sphere of radius  $r$ , so that its integral from the centre of the star to infinity is just [*cf.* Eq. (12.9)]

$$M = \int_0^\infty 4\pi r^2 e dr = \int_0^R 4\pi r^2 e dr, \quad (12.11)$$

where  $r = R$  marks the position where  $e(R) = 0$ .

<sup>1</sup>With a little algebra it is easy to show that  $a_r = \Gamma_{tr}^t = d\phi/dr$ .

<sup>2</sup>Interestingly, Eq. (12.10) also follows from extremising the entropy in a Schwarzschild background (Gao, 2011).

Equations (12.8), (12.9), and (12.10), together with an equation of state,  $p = p(\rho, \epsilon)$ , are known as the *Tolmann–Oppenheimer–Volkoff (TOV) equations* (Tolman, 1939; Oppenheimer and Volkoff, 1939) and their solutions requires, in general, numerical integration. In practice, using an equation of state to relate the energy density and the pressure, it is convenient to start integrating the equations from the origin,  $r = 0$ , after specifying the central density  $\epsilon_c$ , which therefore acts as a free parameter, and to proceed up to the stellar surface,  $r = R$ , where the following boundary conditions need to be met

$$m(R) = M, \quad p(R) = 0, \quad (12.12)$$

$$\phi(R) = \frac{1}{2} \log \left( 1 - \frac{2M}{R} \right), \quad \lambda(R) = -\frac{1}{2} \log \left( 1 - \frac{2M}{R} \right). \quad (12.13)$$

The boundary condition for  $\phi$ , in particular, ensures a smooth match to the Schwarzschild metric at the stellar surface.

Figure 12.1 shows the results of the numerical solution of the TOV equations for a number of cold equations of state inspired by nuclear physics theory, namely: APR (Akmal *et al.*, 1998), BBS1 (Baldo *et al.*, 2000), GM1 (Glendenning and Moszkowski, 1991), MPA1 (Müther *et al.*, 1987), SLy4 (Douchin and Haensel, 2001), and WFF1 (Wiringa *et al.*, 1988).<sup>3</sup> The left panel shows the behaviour of the gravitational mass  $M$  (hereafter simply “mass”) as a function of the central rest-mass density  $\rho_c$ , reporting in the inset the difference for the APR equation of state between  $M$  and the baryon mass  $M_b$ . Note that the latter is always larger as it does not account for the (negative) contribution of the binding energy. Finally, shown with a horizontal shaded stripe is the range for the largest reported mass for a neutron star, *i.e.*,  $M = 2.01 \pm 0.4 M_\odot$  (Antoniadis *et al.*, 2013) [see also Demorest *et al.* (2010) for a pulsar with mass  $M = 1.97 \pm 0.4 M_\odot$ ]. The right panel on the other hand, shows the mass as a function of the stellar radius for stable stellar models. Note that in contrast with ordinary stars, the radius of compact stars generally decreases with the mass, thus leading to more and more compact objects.

All the curves on the left panel of Fig. 12.1 exhibit a local maximum, *i.e.*, a value of the central density where  $dM/d\rho_c = 0$ . This central density marks the onset of a dynamical instability to the fundamental radial mode and thus distinguishes *stable* stars, *i.e.*, with  $dM/d\rho_c > 0$ , from *unstable* ones, *i.e.*, with  $dM/d\rho_c < 0$ . While a formal proof that for each sequence the *turning point* marks the limit of stable models can be found in Misner *et al.* (1973), it is easy to see why this should be the case. Consider, in fact, a stellar configuration with relatively small central density and mass, which is however undergoing accretion. The addition of a small amount of rest mass will lead to an increase of the central density and of the mass, corresponding to a new equilibrium. This process, however, cannot continue indefinitely and at the maximum of the sequence the addition of a single atom will not yield a new equilibrium with a larger mass. Indeed, at that point we will have reached the limit of stability and the star will have to evolve dynamically towards a black-hole solution. As a result, models on the “*unstable branch*” of the sequence of equilibrium configurations cannot be produced in nature through a series of quasi-stationary transformations, *e.g.*, through secular mass accretion, but can be produced through some catastrophic event, *e.g.*, through the collision of two stars, as discussed by Kellerman *et al.* (2010). The fate of such configurations will then

<sup>3</sup>All models were computed by Francesco Pannarale.

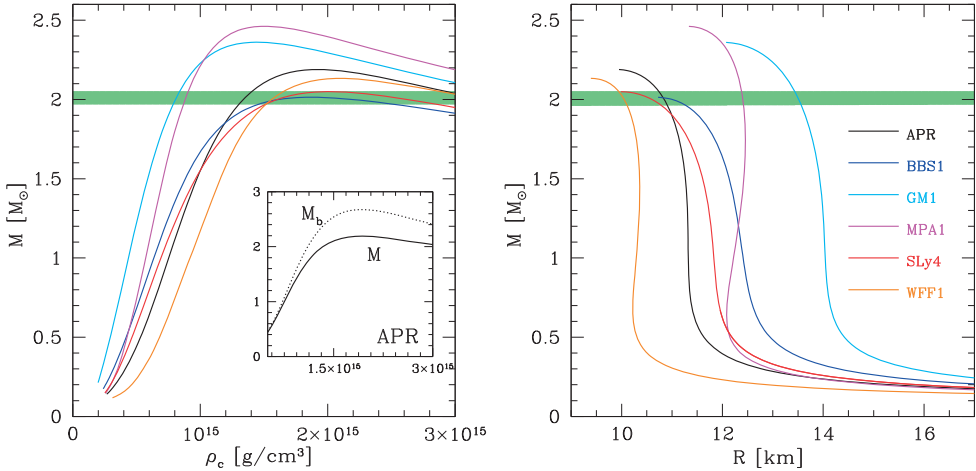


**Fig. 12.1** *Left panel:* Gravitational mass,  $M$ , as a function of the central rest-mass density,  $\rho_c$ , for a number of cold nuclear physics equations of state. Shown in the inset is the difference for the APR equation of state between the gravitational mass and the baryon mass  $M_b$ , the latter being always larger. The horizontal shaded stripe refers to the range for the largest reported mass for a neutron star, *i.e.*,  $M = 2.01 \pm 0.4 M_\odot$ . *Right panel:* Gravitational mass as a function of the stellar radius for stable stellar models. Note that the compactness  $M/R$  increases with the mass.

be determined by the type of perturbations they will be subject to and they can either move to larger central densities through the collapse to a black hole, or ‘‘migrate’’ to the ‘‘stable branch’’ of configurations, while conserving the rest-mass density. Because the corresponding dynamics is highly nonlinear and in the strong-field regime, the so-called ‘‘migration test’’ is very often used as a benchmark for numerical-relativity codes [see, *e.g.*, Font *et al.* (2002) for the first implementation in three dimensions].

#### Uniform-density solution and Buchdahl’s limit.

While a numerical integration is normally needed, the TOV equations admit an analytic solution in the simplified case of a spherically symmetric star with uniform energy density  $\bar{e}$ . Despite being a rather idealised configuration, this solution is useful to derive a general result on the minimum radius of a relativistic star of given mass. To obtain this result we first recall that Birkhoff’s theorem guarantees that the exterior spacetime is the Schwarzschild spacetime and since the gravitational mass of the star is trivially given by  $M = 4\pi R^3 \bar{e}/3$ , we deduce that the relevant metric functions can be expressed as (see also the right panel of Fig. 12.3)

$$g_{rr} = e^{2\lambda} = \begin{cases} \left(1 - \frac{2}{r} \frac{4\pi r^3}{3} \bar{e}\right)^{-1} & \text{for } r \leq R, \\ \left(1 - \frac{2M}{r}\right)^{-1} & \text{for } r \geq R, \end{cases} \quad (12.14)$$

and

$$\sqrt{-g_{tt}} = e^\phi = \begin{cases} \frac{3}{2} \left(1 - \frac{2M}{R}\right)^{1/2} - \frac{1}{2} \left(1 - \frac{2Mr^2}{R^3}\right)^{1/2} & \text{for } r \leq R, \\ \left(1 - \frac{2M}{r}\right)^{1/2} & \text{for } r \geq R. \end{cases} \quad (12.15)$$

Note that the value for the energy density can be fixed after a choice of the mass and radius of the star, *i.e.*,  $\bar{e} = 3M/(4\pi R^3)$ , but also that  $M$  and  $R$  are not linearly independent. Rather, their ratio is upper bounded. This conclusion can be reached after realising that although the energy density is uniform within the star, the pressure is not and is instead given by the integral of Eq. (12.10), *i.e.*,

$$p = p(r) = \bar{e} \left[ \frac{(1 - 2Mr^2/R^3)^{1/2} - (1 - 2M/R)^{1/2}}{3(1 - 2M/R)^{1/2} - (1 - 2Mr^2/R^3)^{1/2}} \right], \quad (12.16)$$

(this solution is reported in the left panel of Fig. 12.3 with a red dashed line). As a result, the central pressure,  $p_c := p(r = 0)$ , is given by

$$p_c = \bar{e} \left[ \frac{1 - (1 - 2M/R)^{1/2}}{3(1 - 2M/R)^{1/2} - 1} \right], \quad (12.17)$$

while the stellar radius is simply the position at which  $p(R) = 0$ , *i.e.*,

$$R = \sqrt{\frac{3}{8\pi\bar{e}} \left[ 1 - \frac{(\bar{e} + p_c)^2}{(\bar{e} + 3p_c)^2} \right]}. \quad (12.18)$$

Equation (12.17) reveals that the central pressure depends only on the stellar mass and radius, but also that it diverges for  $M/R \rightarrow 4/9$ . In other words, if we define the *stellar compactness* as the dimensionless ratio  $C := M/R$ , then an infinite pressure is necessary to support a star with a compactness larger than the critical one,  $C_{\text{crit}} := 4/9 \simeq 0.444$ . If the stellar matter is compressed to reach a compactness  $C_{\text{crit}}$  or larger, it can only collapse to produce a black hole. The importance of this result, which is also known as *Buchdahl's limit*, is that although we have derived it for a constant energy-density star, a theorem by Buchdahl (1959) proves that it holds for *any* equation of state, so that the radius of *any relativistic star* must be larger than the critical one

$$R > R_{\text{crit}} := \frac{9}{8} R_s = \frac{9}{4} M, \quad (12.19)$$

where  $R_s := 2M$  is the *Schwarzschild radius*<sup>4</sup>. The condition (12.19) may appear as a very restrictive one, but this is really the case only for compact stars. To fix ideas, the critical radius for the Sun is  $\sim 3$  km, while it is as small as  $\sim 1$  cm for the Earth. In practice, most realistic equations of state lead to neutron-star models with compactness  $0.1 \lesssim C \lesssim 0.2$ .

As a final remark we note that the discussion has so far been limited to static models of spherical stars. While all these configurations are in *equilibrium* in the sense that they are solutions of the Einstein and hydrodynamic equations in equilibrium, they are not guaranteed

<sup>4</sup>A simple proof of Buchdahl's theorem can be found in Weinberg (1972).

to be in *stable* equilibrium. When the assumption of staticity is relaxed and the stars are perturbed, in fact, some of these models could develop dynamical instabilities, such as the one leading to gravitational collapse [see, *e.g.*, the introductory discussion by Rezzolla (2003)]. The dynamics of these unstable stars will be discussed in more detail in Section 12.4.

## 12.2 Gravastars

The TOV stars discussed in the previous section are not the only possible relativistic solutions of selfgravitating fluids which are static and spherically symmetric. As pointed out recently by Mazur and Mottola (2004), in fact, another ingenious solution is possible, namely that of a “gravitational star” or *gravastar*. In practice, the original gravastar model is a spherically symmetric and static “five-layer” solution of the Einstein equations, including two infinitesimally thin shells needed by the junction conditions of the metric (Israel, 1966). Broadly speaking, a gravastar is a very compact matter object whose radius would be very close to the Schwarzschild radius (indeed arbitrarily close to it) without having an event horizon or a central singularity. For a gravastar to be produced, it is conjectured that during the gravitational collapse marking the end of the life of a massive star, a phase transition takes place at or near the location where the event horizon would have otherwise been formed. The interior of what would have been the black hole is then replaced by a suitably chosen portion of a de Sitter spacetime with an equation of state  $p = -e$ , surrounded by a thin shell of ultra-stiff matter, *i.e.*, a “crust” with equation of state  $p = +e$  (see Section 2.4.9), which is then suitably matched to a Schwarzschild vacuum as dictated by *Birkhoff’s theorem*.

Without entering into the debate about the physical processes that would lead to the formation of a gravastar or the astronomical evidence in support of their existence, the gravastar model, for as much as it is ingenious, also challenges one of the most cherished foundations of modern astrophysics: *i.e.*, the existence of astrophysical black holes. Gravastars, in fact, can be constructed to be arbitrarily compact, with an external surface which is only infinitesimally larger than the horizon of a black hole with the same mass. As a result, the electromagnetic emission from the surface of a gravastar will suffer essentially from the same gravitational redshift as that of a black hole, making it difficult, if possible at all, to distinguish the two when only electromagnetic radiation is available.

Fortunately, the prospects are not so grim if gravitational radiation is available. Chirenti and Rezzolla (2007) have shown, in fact, that the quasi-normal mode spectra of a gravastar and of a black hole of the same mass differ considerably.<sup>5</sup> In particular, while it is always possible to construct a gravastar model that has the same oscillation frequency as that of a black hole with the same mass, the corresponding decaying time will be different. As a result, the gravitational radiation produced by an oscillating gravastar can be used to distinguish it, beyond dispute, from a black hole of the same mass.

In what follows we briefly review the main features of the original model of gravastar proposed by Mazur and Mottola (2004) with an *infinitesimally thin* shell and then extend it to

<sup>5</sup>When perturbed through non-spherically symmetric perturbations, black holes and relativistic stars emit gravitational waves with a precise spectrum of frequencies and decaying times, *i.e.*, the *quasi-normal modes (QNMs)*; see also the footnote 18.

the case of gravastars with finite thickness. Also in this case, the starting point is a static and spherically symmetric line element, which we write as [*cf.*, Eqs. (12.4)]

$$ds^2 = -e^{2\phi} dt^2 + e^{2\lambda} dr^2 + r^2 d\Omega^2 = -f(r)dt^2 + \frac{dr^2}{g(r)} + r^2 d\Omega^2. \quad (12.20)$$

In addition, the Einstein equations must be solved for a perfect fluid at rest in such a way that there are three different regions with three different equations of state

- I. Interior:  $0 \leq r \leq R_i$ ,  $e = -p$ ,
  - II. Shell:  $R_i \leq r \leq R$ ,  $e = +p$ ,
  - III. Exterior:  $R \leq r$ ,  $e = 0 = p$ ,
- (12.21)

where  $R_i$  and  $R$  mark the inner and outer radii of the shell, respectively. In region I, the energy density  $e$  is a constant which we express as  $e := 3H_0^2/8\pi$  with  $H_0$  an integration constant [*cf.*, (12.30)<sub>2</sub>], the pressure is negative and the metric is that of a de Sitter spacetime, so that (see Section 1.7.3)

$$f(r) = Cg(r) = C(1 - H_0^2r^2), \quad 0 \leq r \leq R_i, \quad (12.22)$$

where  $C$  is another integration constant whose value will be determined later [*cf.*, Eq. (12.30)]. In region II we introduce a new dimensionless variable  $w := 8\pi r^2 p$ , so as to obtain the following set of effective TOV equations

$$\frac{dr}{r} = \frac{dg}{1 - w - g}, \quad (12.23)$$

$$\frac{dg}{g} = - \left( \frac{1 - w - g}{1 + w - 3g} \right) \frac{dw}{w}, \quad (12.24)$$

where Eq. (12.23) is the only non-trivial of the Einstein equations, while Eq. (12.24) derives from the conservation of energy and momentum. In the case of a very thin shell, *i.e.*, for

$$\frac{R_i}{R} \simeq 1, \quad 0 < g \ll 1, \quad (12.25)$$

an analytical solution to Eqs. (12.23)–(12.24) can be obtained. It is in fact easy to see that if we take  $g = 1 - \bar{m}/r$ , with  $\bar{m}$  reminiscent of the mass function introduced in (12.5) and  $d\bar{m}(r) = 8\pi r^2 dr = wdr$ , and if we neglect terms  $\mathcal{O}(g)$  on the right-hand side of (12.24), the latter can be integrated analytically to yield

$$g := 1 - \frac{\bar{m}}{r} \simeq \varepsilon \frac{(1+w)^2}{w} \ll 1, \quad (12.26)$$

where  $\varepsilon \ll 1$  is an integration constant, while Eq. (12.23) reduces to

$$\frac{dr}{r} \simeq -\varepsilon \frac{(1+w)}{w^2} dw \ll 1. \quad (12.27)$$

This implies that the coordinate radius  $r$  changes only slightly in region II and  $r \simeq R_i$  there. The remaining metric function can be computed from the condition that  $ef = wf/r^2 = \text{const.}$ , from which we deduce that

$$f(r) \simeq \frac{w_i}{w} f_i. \quad (12.28)$$

Finally, in region III, Birkhoff's theorem can be used to deduce that the spacetime is described by the Schwarzschild metric and hence with

$$f(r) = g(r) = 1 - \frac{2M}{r}, \quad R \leq r. \quad (12.29)$$

A bit of algebra and imposing the continuity of the metric functions  $f$  and  $g$  at  $R_i$  and  $R$ , provides the integration constants  $\varepsilon$ ,  $C$ ,  $M$  and  $H_0$  in terms of  $R_i$ ,  $R$ ,  $w_R := w(r = R)$  and  $w_i := w(r = R_i)$  through the relations (see Problem 2)

$$\varepsilon = -\ln\left(\frac{R}{R_i}\right) \left[ \ln\left(\frac{w_R}{w_i}\right) - \frac{1}{w_R} + \frac{1}{w_i} \right]^{-1}, \quad C = \left(\frac{1+w_R}{1+w_i}\right)^2, \quad (12.30)$$

$$M := m(R) = \frac{R}{2} \left[ 1 - \frac{\varepsilon(1+w_R)^2}{w_R} \right], \quad H_0^2 = \frac{1}{R_i^2} \left[ 1 - \frac{\varepsilon(1+w_R)^2}{w_i} \right]. \quad (12.31)$$

The infinitesimally thin condition (12.25) and the corresponding Eqs. (12.23)–(12.24), provide an accurate solution to the TOV equations for shell thickness  $\delta := R - R_i \lesssim 0.1 M$ . Gravastar models with a *thin* shell can also be computed numerically through the solution of the TOV equations for  $e(r) = p(r)$  and  $m(r)$ . By specifying  $R_i$ ,  $R$ , as well as the initial conditions for the pressure  $p(R_i)$  and mass  $m(R_i) < R_i/2$ , the numerical solution of the TOV equations provides  $m(r)$  and  $e(r)$  for  $R_i < r \leq R$ . Note that each shell thickness  $\delta$  selects a maximum compactness  $\mathcal{C}$  for the gravastar above which no solution of the TOV equations can be found. This is shown in the left panel of Fig. 12.2, which reports in the shaded area the region in the  $(\mathcal{C}, \delta)$  plane where thin-shell gravastars can be built. Overall, it is not possible to build a very compact gravastar with a very thick matter shell. Rather, gravastars have either large compactness and thin shells, or small compactness and thicker shells (Chirenti and Rezzolla, 2007). Further note that gravastars can be built with compactness arbitrarily close to the Schwarzschild limit, *i.e.*, with  $\mathcal{C} \rightarrow 1/2$  and thus with the outer radius  $R$  being only infinitesimally larger than the corresponding Schwarzschild radius. It is exactly this property that would make gravastars hard to distinguish from a black hole if only electromagnetic radiation is available.

One of the disadvantages of the original thin-shell model of Mazur and Mottola (2004) is that both the energy density  $\rho(r)$  and the pressure  $p(r)$  are discontinuous at  $R_i$  and at  $R$ . Using the TOV equation (12.10) to express the pressure gradient, it is not difficult to realise that the only way to avoid such discontinuities is to require that the fluid in the shell has anisotropic pressures (see Section 3.2), whereby a *radial pressure*,  $p_r$ , is accompanied also by a *tangential pressure*,  $p_t$  (Cattoen *et al.*, 2005). The latter essentially replaces the surface tension introduced by the matching of the metric in the infinitesimally thin shells. Although this expedient requires the specification of the functional form for the energy density  $e = e(r)$  in the fluid shell and an equally arbitrary equation of state for the radial pressure  $p_r = p_r(e)$ , anisotropic pressures have the appealing property of being continuous. In turn, this allows one to build equilibrium models without the presence of infinitesimally thin shells, and thus to address the issue of the stability of these objects.

In essence, the derivation of equilibrium configurations for gravastars with anisotropic pressures follows the same route discussed above and in Section 12.1. The spacetime is still

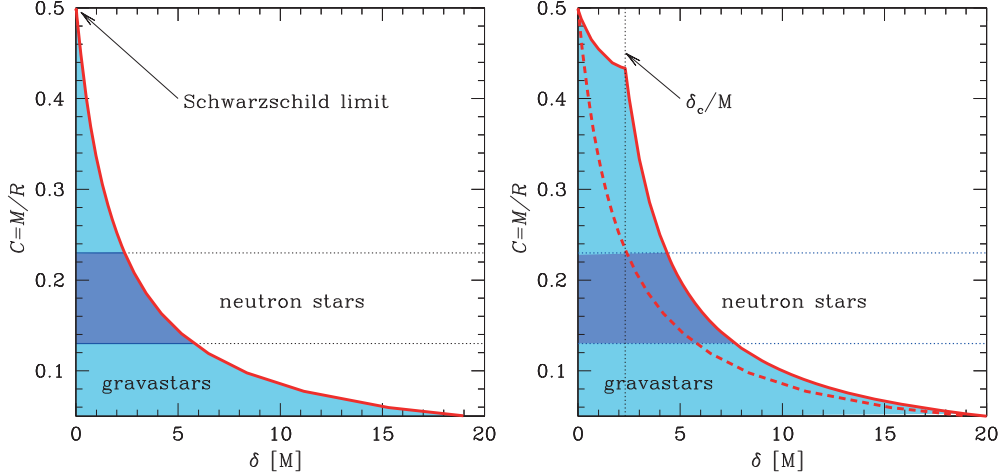


**Fig. 12.2** *Left panel:* Limits in the compactness  $C$  and thickness  $\delta$  of a gravastar with a thin shell and isotropic pressure. The red curve marks the maximum compactness for a given thickness of the shell, so that solutions are possible only in the shaded area below the curve. Marked with a blue-shaded area is the typical range of compactness for neutron stars. *Right panel:* The same as in the left panel but for a gravastar with a thick shell and anisotropic pressure. The red dashed line still marks the limit in the case of thin-shell gravastars [adapted from Chirenti and Rezzolla (2007)].

distinguished into the three regions (12.21), but the fluid shell is now assumed to be represented by an anisotropic perfect fluid with energy-momentum tensor  $T^{\mu\nu} = \text{diag}(e, p_r, p_t, p_t)$  [cf., Eq. (3.32)]. The only difference is in the equation for the pressure (12.10), which becomes

$$\frac{dp_r}{dr} = -\frac{(e + p_r)(m + 4\pi r^3 p_r)}{r(r - 2m)} + \frac{2(p_t - p_r)}{r}, \quad (12.32)$$

in the presence of a tangential pressure and which coincides with (12.10) for a star with isotropic pressure, *i.e.*,  $p_r = p = p_t$  (see Problem 3). Once the solutions for the energy density and the radial pressure are known, the tangential pressure  $p_t$  can be computed through Eq. (12.32) as

$$p_t(r) = p_r + \frac{r}{2} \left( \frac{dp_r}{dr} \right) + \frac{1}{2}(p_r + e) \left[ \frac{m + 4\pi r^3 p_r}{r(1 - 2m/r)} \right]. \quad (12.33)$$

The behaviour of the energy density and of the pressures is shown in the left panel of Fig. 12.3 for a representative thick-shell gravastar model with anisotropic pressure. The model has  $M = 1$ ,  $R_i = 1.8 M$ ,  $R = 2.2 M$ , and thus with  $\delta/M = 0.4$  and  $C = 0.4545 > 4/9$ . The right panel on the same figure, instead, shows the mass function and the metric coefficient  $g_{rr}$  for the same representative model. Also shown with dashed lines in the two panels are the corresponding quantities for a highly relativistic, constant-density star with compactness  $C = 0.44$  [cf., Eqs. (12.14) and (12.16)].

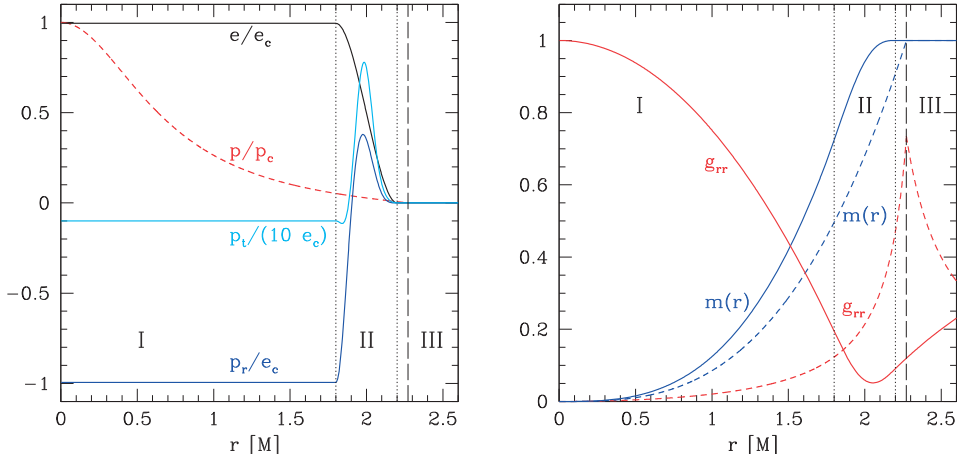


**Fig. 12.3** *Left panel:* Radial dependence of the energy density and of the pressures for a representative thick-shell gravastar model with  $M = 1$ ,  $R_i = 1.8 M$  and  $R = 2.2 M$ . *Right panel:* Mass function  $m(r)$  and the metric coefficient  $g_{rr}$  for the same representative model. The dashed lines in the two panels show instead the corresponding quantities for a constant-density star with  $C = 0.44$  (see Section 12.1).

The modified set of TOV equations (12.8), (12.9), and (12.33) determines therefore a “thick-shell” gravastar model with a finite core described by the de Sitter metric, a crust of ultrastiff matter, and an exterior described by the Schwarzschild solution. Note however that the TOV equations alone are not sufficient to guarantee that the metric functions are continuous and differentiable. Indeed, additional constraints need to be imposed to ensure that the metric functions  $g_{tt}$  and  $g_{rr}$ , and their first derivatives, have the expected properties once a choice for the equation of state  $p_r(e)$  and  $e(r)$  is made. In addition, the three free parameters  $M$ ,  $R_i$  and  $R$  cannot be chosen arbitrarily, but in such a way that  $g_{rr}$  is always positive. An incorrect choice of  $R_i$  and  $R$ , in fact, can lead to negative values for  $g_{rr}$  and thus to the unphysical appearance of an event horizon.

With a reasonable but yet arbitrary equation of state, Chirenti and Rezzolla (2007) have carried out a systematic investigation of this problem and constructed a large number of gravastar models with varying compactness  $C$  and thickness  $\delta$ . In this way it is possible to extend the diagram presented in the left panel of Fig. 12.2 and define the region in the  $(\delta, C)$  plane where equilibrium models of thick-shell gravastars with anisotropic pressure can be found. Introducing the parameter  $\varepsilon$  as the dimensionless distance of the gravastar’s surface from a Schwarzschild horizon, *i.e.*,  $\varepsilon := R/M - 2$ , then it was found that for  $\varepsilon > \varepsilon_c \approx 0.3085$  the thickness  $\delta$  can be as large as  $R$  (*i.e.*,  $R_i$  can also be taken to be zero). On the other hand, for  $\varepsilon \leq \varepsilon_c$  there exists a critical thickness  $\delta_c = \delta_c(R, M) \approx 2.31 M$ , above which equilibrium models cannot be found because of the appearance of horizons. The resulting allowed space of equilibria is shown with a shaded area in the right panel of Fig. 12.2. Also reported with a red dashed line is the corresponding region for a thin-shell, isotropic pressure gravastar model.

## 12.3 Rotating stars

The assumption of spherical symmetry, which has characterised the selfgravitating configurations in the previous two sections, will now be abandoned to consider the less restrictive and more realistic case of axisymmetric and stationary spacetimes, and thus study equilibrium models of *rotating stars*. This rather small mathematical change brings in an enormous variety in the classes and properties of possible solutions, both stationary and dynamical. It is not possible to cover such a variety with our brief review and we thus refer the reader to the monographs by Meinel *et al.* (2008) and by Friedman and Stergioulas (2012) for a more detailed discussion of the many facets of relativistic rotating stars. An extended discussion of Newtonian stars can also be found in the classical book of Tassoul (2007).

### 12.3.1 Uniformly rotating stars

The starting point for the discussion of selfgravitating rotating relativistic fluids is the line element describing a stationary and axisymmetric spacetime in spherical quasi-isotropic coordinates  $(t, r, \theta, \phi)$ , *i.e.* (Komatsu, Eriguchi and Hachisu, 1989)

$$ds^2 = -e^{\gamma+\varrho} dt^2 + e^{\gamma-\varrho} r^2 \sin^2 \theta (d\phi - \omega dt)^2 + e^{2\xi} (dr^2 + r^2 d\theta^2), \quad (12.34)$$

where  $\varrho$  (not to be confused with the rest-mass density),  $\gamma$ ,  $\omega$  and  $\xi$  are functions of  $r$  and  $\theta$ . The Einstein equations are then given by the following elliptic equations for the metric potentials

$$\nabla^2(\varrho e^{\gamma/2}) = S_\nu(r, \mu), \quad (12.35)$$

$$\left( \nabla^2 + \frac{1}{r} \partial_r - \frac{1}{r^2} \mu \partial_\mu \right) \gamma e^{\gamma/2} = S_\gamma(r, \mu), \quad (12.36)$$

$$\left( \nabla^2 + \frac{2}{r} \partial_r - \frac{2}{r^2} \mu \partial_\mu \right) \omega e^{(\gamma-2\varrho)/2} = S_\omega(r, \mu), \quad (12.37)$$

where  $\mu := \cos \theta$ , and  $\nabla^2$  is the Laplacian in flat spacetime and in a spherical polar coordinate system, *i.e.*,  $\nabla^2 := \partial_r^2 + (2/r)\partial_r^2 + (1/r^2)\partial_\theta^2 + (\cot \theta/r^2)\partial_\theta + [1/(r^2 \sin^2 \theta)]\partial_\phi^2$ . The right-hand sides of Eqs. (12.35)–(12.37) are rather lengthy differential expressions and are given by (Komatsu, Eriguchi and Hachisu, 1989)

$$\begin{aligned} S_\nu(r, \mu) &= e^{\gamma/2} \left\{ 8\pi e^{2\xi} (e + p) \frac{1 + v^2}{1 - v^2} + r^2 (1 - \mu^2) e^{-2\varrho} \left[ \partial_r \omega^2 + \frac{1 - \mu^2}{r^2} \partial_\mu \omega^2 \right] \right. \\ &\quad \left. + \frac{\partial_r \gamma}{r} - \frac{\mu \partial_\mu \gamma}{r^2} + \frac{\varrho}{2} \left[ 16\pi e^{2\xi} p - \partial_r \gamma \left( \frac{\partial_r \gamma}{2} + \frac{1}{r} \right) \right. \right. \\ &\quad \left. \left. - \frac{\partial_\mu \gamma}{r^2} \left( \frac{\partial_\mu \gamma (1 - \mu^2)}{2} - \mu \right) \right] \right\}, \end{aligned} \quad (12.38)$$

$$S_\gamma(r, \mu) = e^{\gamma/2} \left[ 16\pi e^{2\xi} p + \frac{\gamma}{2} \left( 16\pi e^{2\xi} p - \frac{\partial_r \gamma^2}{2} - \frac{1}{2r^2} (1 - \mu^2) \partial_\mu \gamma^2 \right) \right], \quad (12.39)$$

$$S_\omega(r, \mu) = e^{\gamma/2-\varrho} \left\{ -16\pi e^{2\xi} \frac{(\Omega - \omega)(e + p)}{1 - v^2} + \omega \left[ -8\pi e^{2\xi} \frac{(1 + v^2)e + 2v^2 p}{1 - v^2} \right. \right. \\ \left. \left. - \frac{1}{r} \left( 2\partial_r \varrho + \frac{\partial_r \gamma}{2} \right) + \frac{\mu}{r^2} \left( 2\partial_\mu \varrho + \frac{\partial_\mu \gamma}{2} \right) + \partial_r \varrho^2 - \frac{\partial_r \gamma^2}{4} \right. \right. \\ \left. \left. + \frac{1}{4r^2} (1 - \mu^2) (4\partial_\mu \varrho^2 - \partial_\mu \gamma^2) - r^2 (1 - \mu^2) e^{-2\varrho} \left( \partial_r \omega^2 + \frac{1 - \mu^2}{r^2} \partial_\mu \omega^2 \right) \right] \right\}, \quad (12.40)$$

where  $\Omega := u^\phi/u^t$  is the rotation frequency as measured at spatial infinity and  $v$  is the fluid velocity relative to a ZAMO observer (see Section 11.8), *i.e.*,

$$v := (\Omega - \omega)r \sin \theta e^{-\varrho}. \quad (12.41)$$

Indicating as usual the Lorentz factor as  $W := (1 - v^2)^{-1/2}$  [*cf.* Eq. (1.107)], the complete expression for the fluid four-velocity is therefore given by

$$u^\alpha = e^{-(\gamma+\varrho)/2} W \left( 1, 0, 0, \Omega \right). \quad (12.42)$$

In addition to the Einstein equations, hydrostatic equilibrium is governed by the balance equation [*cf.* Eq. (12.10)]

$$\partial_i p + (e + p) \left[ \partial_i \nu + \left( \frac{1}{1 - v^2} \right) \left( -v \partial_i v + \frac{v^2 \partial_i \Omega}{\Omega - \omega} \right) \right] = 0. \quad (12.43)$$

No general analytic solution is known for Eqs. (12.35)–(12.37), which therefore need to be solved numerically using one of the several approaches possible [see, *e.g.*, Nozawa *et al.* (1998) for a discussion]. A particularly popular method is the so-called KEH approach [after the original proponents: Komatsu, Eriguchi and Hachisu (1989)], which recasts the differential equations into an integral form after the introduction of a representation in terms of three-dimensional Green's functions of the sources  $S_\nu$ ,  $S_\gamma$ ,  $S_\omega$ . In practice, the KEH approach converges robustly to a solution, if it exists. A stellar model is usually selected with a choice of two parameters, *e.g.*, the central pressure  $p_c$  (or, equivalently, the energy density) and the ratio between the polar and equatorial radii  $r_p/r_e$  (or, equivalently, the rotation rate  $\Omega$ ).

Once an equilibrium solution is obtained, a number of related quantities can be computed within the  $3 + 1$  decomposition of spacetime (see Section 7.1). These quantities are: the *rest mass* (or baryon mass)  $M_b$ , the *gravitational mass*  $M$ , the *angular momentum*  $J$ , the *rotational kinetic energy*  $T$ , the gravitational *binding energy*  $\mathcal{W}$ , and their ratio  $\beta$ , defined respectively as

$$M_b := \int \rho W \sqrt{\gamma} d^3x, \quad (12.44)$$

$$M := \int (-2T^t{}_t + T^\mu{}_\mu) \alpha \sqrt{\gamma} d^3x, \quad (12.45)$$

$$E_{\text{int}} := \int \rho W \epsilon \sqrt{\gamma} d^3x, \quad (12.46)$$

$$J := \int T_\phi^t \alpha \sqrt{\gamma} d^3x, \quad (12.47)$$

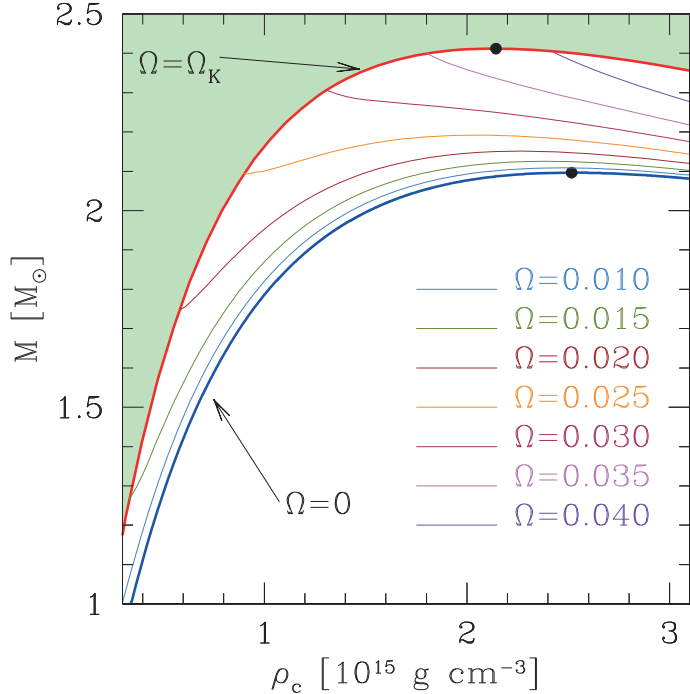


**Fig. 12.4** Representative examples of equilibrium solutions of relativistic rotating stars. The solutions have been obtained for a polytropic equation of state with  $K = 100$  and  $\Gamma = 2$ . The equilibrium models are shown along sequences of constant angular frequency, with the thick blue line indicating the sequence of non-rotating models and the thick red line indicating the sequence of models at the Keplerian frequency. Marked with filled circles are the maximum masses for the spherically symmetric sequence and for the mass-shedding one (*cf.*, left panel of Fig. 12.1). No solutions can be found in the green-shaded area as these would be beyond the break-up limit.

$$T := \frac{1}{2} \int \Omega T_\phi^t \alpha \sqrt{\gamma} d^3x, \quad (12.48)$$

$$\mathcal{W} := T + E_{\text{int}} + M_b - M < 0, \quad (12.49)$$

$$\beta := T/|\mathcal{W}|, \quad (12.50)$$

where  $\sqrt{\gamma}$  is the square root of the determinant of the three-metric  $\gamma_{ij}$ ,  $\alpha$  is the “lapse” function, and  $W = \alpha u^t$  is the fluid Lorentz factor (see Section 7.1). Note that the definitions (12.44)–(12.50) are meaningful only in the case of stationary axisymmetric configurations.

Representative examples of equilibrium solutions of relativistic rotating stars are presented in Fig. 12.4, which reports the gravitational mass as a function of the central rest-mass density.<sup>6</sup> The solutions have been obtained for a polytropic equation of state with  $K = 100$  in geometrised units and  $\Gamma = 2$  (see Section 2.4.7) so as to have a maximum non-rotating mass

<sup>6</sup>All models were computed by Kentaro Takami.

$M_{\max} = 2.1 M_{\odot}$ . The figure shows equilibrium models along sequences of constant angular frequency  $\Omega$ , with the thick blue line indicating the sequence of (spherical) models with  $\Omega = 0$ , [cf., left panel of Fig. 12.1], while lines of different colours refer to sequences of stars having the rotation rate indicated in the legend.<sup>7</sup>

Note that for any central density, larger rotation rates allow us to produce models with larger masses as a consequence of the additional centrifugal support to the hydrostatic equilibrium. Note also that the different sequences terminate abruptly at low central densities when the spin frequency is such that the star would shed mass if it were spun-up even infinitesimally. The corresponding star is then said to be spinning at the *mass-shedding frequency* or *Keplerian frequency* (or *break-up frequency*),  $\Omega_K$ , to emphasise that at this frequency the motion of a fluid element on the stellar equator is geodetic (or Keplerian). The locus of these frequencies is indicated with a thick red line and the green-shaded region above it represents the portion of the  $(\rho_c, M)$  diagram in which no equilibrium stationary models can be found as they would be shedding mass at the equator. As a first approximation, the Keplerian frequency can be estimated to be  $\Omega_K \sim (2/3)\sqrt{\pi\bar{\rho}}$ , where  $\bar{\rho}$  is the volume-averaged rest-mass density.

Marked with filled circles are the maximum masses for the spherically symmetric sequence, *i.e.*,  $M_{\max}(\Omega = 0)$ , and for the mass-shedding one, *i.e.*,  $M_{\max}(\Omega = \Omega_K)$ . It is important to remark that  $M_{\max}(\Omega = \Omega_K) > M_{\max}(\Omega = 0)$ , but also that  $M_{\max}(\Omega = \Omega_K)$  is the largest mass for uniformly rotating models. As a result, any (uniformly rotating) model with mass  $M$  such that

$$M_{\max}(\Omega = 0) < M_{\text{supra}} \leq M_{\max}(\Omega = \Omega_K), \quad (12.51)$$

will be referred to as a *supramassive star* to emphasise the fact that it has a mass larger than the maximum allowed for spherical star. Should this star lose its angular momentum while conserving its rest mass, *e.g.*, through dissipative processes, it will move to progressively larger central densities up to the point where no equilibrium will be possible and the star will have to collapse to a black hole (see the discussion in Section 12.4.2). Finally, Fig. 12.5 reports the same models as in Fig. 12.4, but when collected along sequences of constant angular momentum  $J$  as indicated in the legend,<sup>8</sup> while black dotted lines refer to sequences of models with constant baryon mass.

As noted above, but as is clearer in this representation, for any central density, models with larger angular momentum also have larger masses. Furthermore, for a given angular momentum, the mass-shedding model will also be the one with the smallest central density. Also shown with black dot-dashed lines are sequences of constant baryon mass, *i.e.*,  $M_b = 1.60, 1.92, 2.08, 2.24, 2.30, 2.40, 2.56 M_{\odot}$ . Finally, marked with a black dotted line is the locus of maximum masses for each  $J = \text{const.}$  sequence, *i.e.*,  $(\partial M / \partial \rho_c)_J = 0$ . As will be discussed in Section 12.4.2, this line can be used as a first approximation for the location of the dynamically unstable models (Friedman *et al.*, 1988), although the actual boundary is at slightly smaller central densities (Takami *et al.*, 2011).

<sup>7</sup>The angular velocity  $\Omega$  is expressed in geometrised units (see Appendix A), but a conversion to cgs units is simply given by  $\Omega_{\text{cgs}} \simeq 2.030 \times 10^5 (M_{\odot}/M) \Omega$ , where  $\Omega_{\text{cgs}}$  is expressed in rad s<sup>-1</sup>.

<sup>8</sup>The angular momentum  $J$  is expressed in gravitational geometrised units (see Appendix A), but a conversion to cgs units is simply given by  $J_{\text{cgs}} \simeq 8.804 \times 10^{48} (M/M_{\odot})^2 J$ , where  $J_{\text{cgs}}$  is expressed in g cm<sup>2</sup> s<sup>-1</sup>.

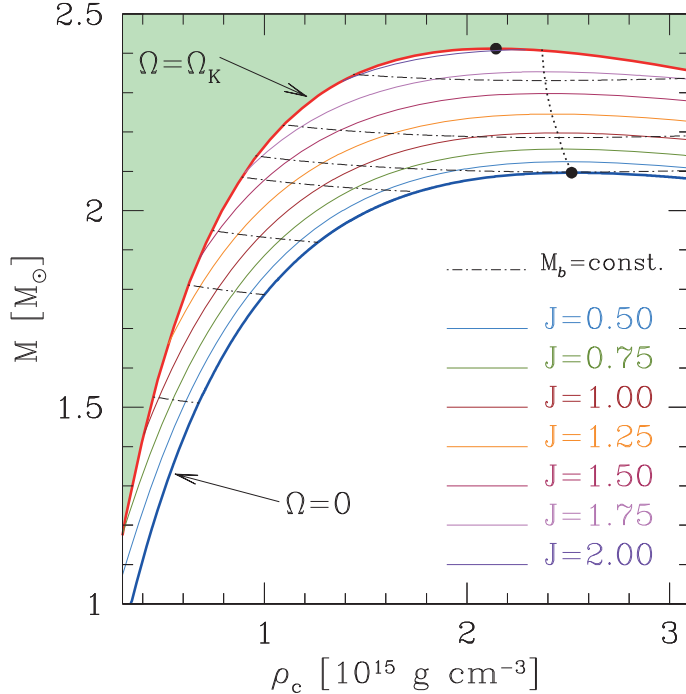


**Fig. 12.5** The same models as in Fig. 12.4, but when collected along sequences of constant angular momentum  $J$ . The black dotted line marks the “turning-point” of the different sequences, *i.e.*,  $(\partial M / \partial \rho_c)_J = 0$ , and provides a first approximation for the location of the dynamically unstable models. Also shown with black dot-dashed lines are sequences of constant baryon mass, *i.e.*,  $M_b = 1.60, 1.92, 2.08, 2.24, 2.30, 2.40, 2.56 M_\odot$ .

### 12.3.2 Differentially rotating stars

An additional degree of freedom in the construction of equilibrium models of relativistic stars can be introduced through *differential rotation*, that is, through the possibility that the spin frequency, although axisymmetric, is not a constant but depends on the distance from the rotation axis. While differential rotation is not expected to be present in old and cold neutron stars, which are indeed expected to rotate uniformly, differential rotation will likely accompany the formation of proto-neutron stars, where it could lead to a number of non-axisymmetric instabilities [see, *e.g.*, Stergioulas (2003)]. Similarly, differentially rotating objects are expected to be produced in the merger of binary neutron stars, where again it could lead to a rich phenomenology (see the discussion in Section 12.5). For the time being, however, we can consider differential rotation simply as an additional dimension in the space of parameters in which to look for equilibrium models and comment on the peculiar properties that these new models have.

Since no observational constraints exist on the properties of the law of differential rotation, we can either specify a recipe which is mathematically simple and with a clear physical interpretation, or rely on the numerical results of dynamical simulations to deduce a more

realistic law of differential rotation [this is indeed the approach followed by Galeazzi *et al.* (2012)]. Following the first route, we consider here the relativistic version of the *j*-constant law of differential rotation, which amounts to assuming an angular-velocity distribution of the form

$$\Omega_c - \Omega = \frac{1}{\hat{A}^2 r_e^2} \left[ \frac{(\Omega - \omega) r^2 \sin^2 \theta e^{-2\rho}}{1 - (\Omega - \omega)^2 r^2 \sin^2 \theta e^{-2\rho}} \right], \quad (12.52)$$

where  $\Omega_c$  is the frequency on the rotation axis, *i.e.*,  $\Omega_c = \Omega(r \sin \theta = 0)$ , and  $\hat{A}$  is a coefficient that provides a measure of the degree of differential rotation. Expression (12.52) represents the general-relativistic equivalent of the simpler Newtonian *j*-constant law introduced by Eriguchi and Mueller (1985)

$$\Omega_c - \Omega = \frac{\Omega_c r^2 \sin^2 \theta}{\hat{A}^2 r_e^2 + r^2 \sin^2 \theta}. \quad (12.53)$$

Clearly, the case when  $\hat{A} \rightarrow \infty$  corresponds to a star in uniform rotation, while  $\hat{A} \rightarrow 0$  corresponds to a star with increasing degree of differential rotation. As a reference,  $\hat{A} = 1$  yields a star with an angular-velocity profile which varies by a factor  $\sim 3$  between the centre and the surface of the star.

A large collection of representative equilibrium models with a polytropic equation of state with  $K = 100$  and  $\Gamma = 2$  is shown in Fig. 12.6, which can be seen as the extension of Fig. 12.4 to differentially rotating relativistic stars.<sup>9</sup> The figure is composed of four different panels, each showing the gravitational mass as a function of the central rest-mass density for a fixed degree of differential rotation  $\hat{A}$ . For each subpanel, we show sequences of constant and increasing angular momentum  $J$  and, as for Fig. 12.4, the thick blue line indicates the sequence of non-rotating models, *i.e.*,  $\Omega = 0$ , while the thick red line marks the sequence of models at the Keplerian frequency, *i.e.*,  $\Omega = \Omega_K$ . Also shown with a thick green dashed line is the mass-shedding sequence for uniformly rotating models, *i.e.*,  $\Omega = \Omega_K(\hat{A} = \infty)$ , which of course coincides with the thick red line in Fig. 12.4. It is quite apparent that as the degree of differential rotation is increased, models with substantially larger masses can be constructed (note that the scale in masses of the top subpanels is smaller than that in the bottom ones), and that mass-shedding models can be found with masses which are almost twice as large as the maximum mass of the non-rotating sequence.

In analogy with what was done in the case of uniformly rotating models, it is possible to introduce the definition of a *hypermassive star* as a star with a gravitational mass larger than the maximum allowed for a uniformly rotating star, *i.e.*, with mass

$$M_{\text{hyper}} \geq M_{\max}(\Omega = \Omega_K, \hat{A} = \infty). \quad (12.54)$$

As the differential rotation will be lost through dissipative processes, either viscous or electromagnetic, the hypermassive star will find itself with a mass too large to be supported via uniform rotation and will therefore be forced to collapse to a black hole. The formation of a metastable *hypermassive neutron star*, or HMNS, is expected to occur frequently in the merger of a binary system of neutron stars (see the discussion in Section 12.5).

Three important remarks need to be made at this point. First, as the degree of differential rotation is increased, it is harder to build models with large masses and large central densities.

<sup>9</sup>All models were computed by Roberto De Pietri.

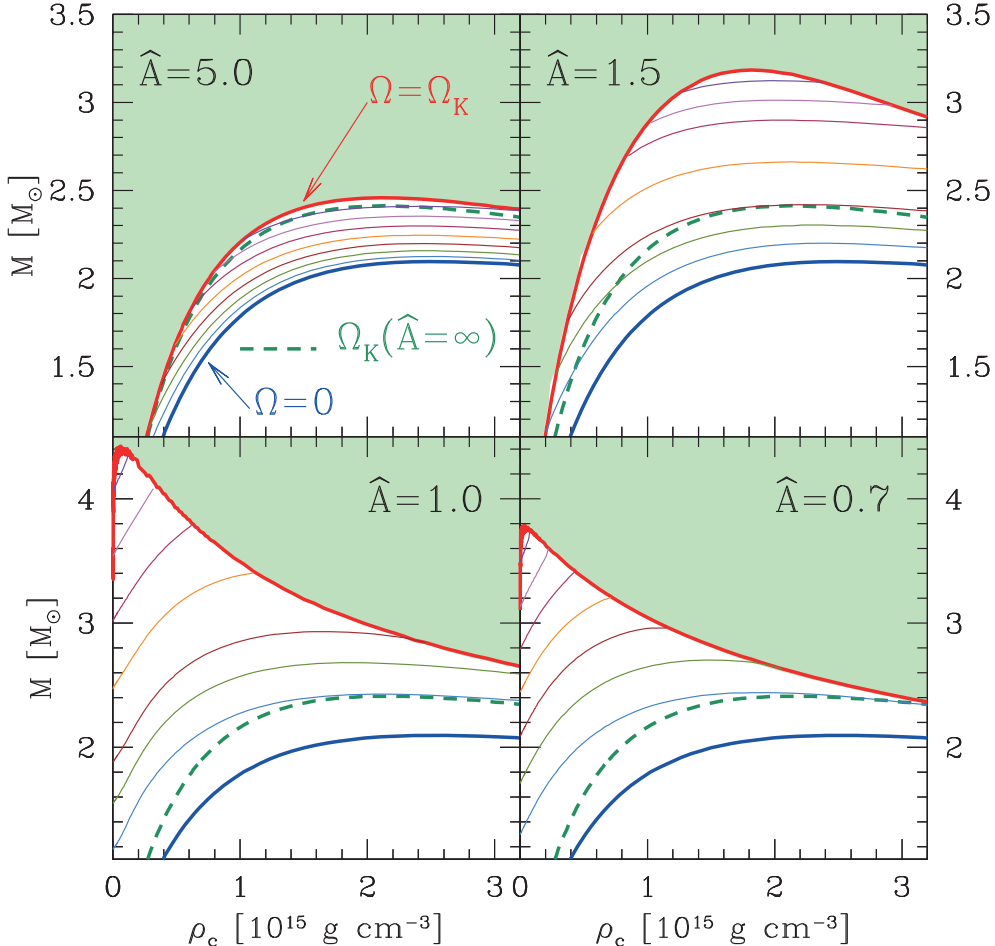


**Fig. 12.6** Representative examples of equilibrium solutions of relativistic differentially rotating stars. The solutions have been obtained for a polytropic equation of state with  $K = 100$  and  $\Gamma = 2$ . The four panels refer to different and fixed degrees of differential rotation as measured by the parameter  $\hat{A}$ . As for Fig. 12.4, the thick blue line indicates the sequence of non-rotating models, while the thick red line marks the sequence of models at the Keplerian frequency. Also shown with a thick green dashed line is the corresponding mass-shedding sequence for uniformly rotating models.

Indeed, for very large degrees of differential rotation the mass-shedding line tends to coincide with the corresponding line in the case of uniform rotation, so that only low-mass models can have large central densities (*cf.*, lower right panel of Fig. 12.6). Second, the maximum value of the rest-mass density does not necessarily coincide with the central one. This is because as differential rotation tends to increase the angular momentum in the outer layers, the star undergoes a transition from an (oblate) spheroidal topology to a “toroidal” one, in which the maximum rest-mass density is located somewhere off the rotation axis (see the bottom

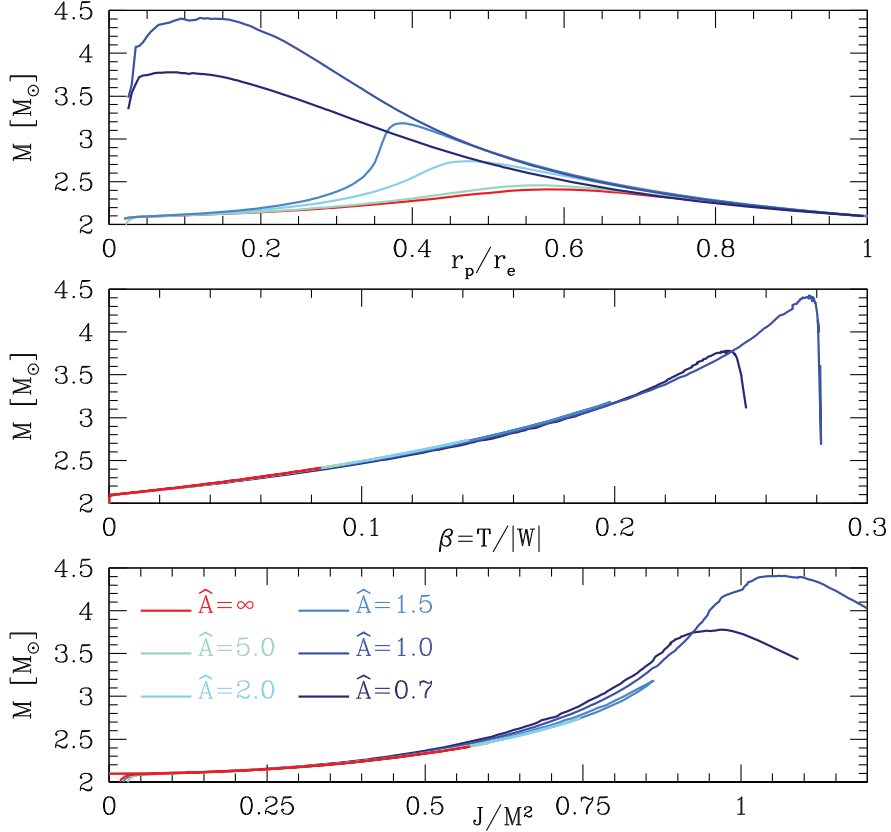


**Fig. 12.7** Maximum masses as a function of the axis ratio,  $r_p/r_e$  (top panel) of the dimensionless kinetic energy,  $\beta = T/|W|$  (middle panel), and of the dimensionless angular momentum,  $J/M^2$  (bottom panel).

left panel of Fig. 12.12 for a representative example). Finally, the mass of the hypermassive models tends to increase with differential rotation, but not monotonically with  $\hat{A}$ . Comparing in fact the bottom panels of Fig. 12.6 it is evident that the maximum mass of the hypermassive stars is larger for  $\hat{A} = 1$ , than it is for  $\hat{A} = 0.7$ .

Interestingly, the maximum mass is not reached for  $\rho_c \rightarrow 0$ , but for a small nonzero value of the central density. Indeed, for large differential rotation, the curve marking the mass-shedding models exhibits a local maximum (not very evident in Fig. 12.6), thus indicating that two models with the same gravitational mass can be obtained for different values of  $\rho_c$ . These models correspond to two configurations differing in the degree of oblateness, as shown in Fig. 12.7. This figure reports the maximum masses<sup>10</sup> for different degrees of differential rotation and as a function of the ratio of the polar and equatorial radii  $r_p/r_e$  (top panel), of the dimensionless kinetic energy  $\beta = T/|W|$  (middle panel), and of the dimensionless

<sup>10</sup>Note that the maximum mass reported here is larger than the mass of a Keplerian model with the same axis ratio.

angular momentum  $J/M^2$  (bottom panel). Comparing with Fig. 12.6 it then becomes evident that configurations having central densities  $\rho_c \lesssim 0.1 \times 10^{15} \text{ g cm}^{-3}$  can have equilibria either with a markedly toroidal topology, *i.e.*,  $r_p/r_e \lesssim 0.1$ , or with a roughly spheroidal one, *i.e.*,  $r_p/r_e \gtrsim 0.2$ . Note also that the highly differentially rotating models have not only the largest masses, but are also able to sustain the largest amount of rotation, with  $\beta \gtrsim 0.25$  and  $J/M^2 \gtrsim 1$ . [We recall that  $\beta \simeq 0.25$  marks the threshold for the dynamical bar mode instability (Baiotti *et al.*, 2007a) and that  $\beta \simeq 0.16$  marks instead the threshold for the secular bar mode instability (Chandrasekhar, 1969).] A recent and extended discussion on the different classes of solutions of differentially rotating stars can be found in Ansorg *et al.* (2009).

The final comment of this section is dedicated to the issue of the stability of differentially rotating models. In contrast with the situation for uniformly rotating models, where a number of investigations have been carried out over the years (Friedman *et al.*, 1988) and some progress has been obtained recently by Takami *et al.* (2011), very little is still known about the stability properties of differentially rotating models. A discussion of this issue will be presented in the following section, when illustrating the dynamics of rotating models undergoing gravitational collapse to rotating black holes.

## 12.4 Collapse of a compact star to a black hole

So far we have concentrated on stationary configurations, but we have also stressed that not all *equilibrium* configurations will also be *stable* and that, under sufficiently large compactness, the only fate awaiting a selfgravitating fluid configuration is that of the collapse to a black hole. This area of research in general relativity is enormously vast, with the initial works dating back to May and White (1967) and with new results being obtained continuously (see also Section 7.2.1). It is clearly not possible to report here the great bulk of work covered over these 45 years and thus we will limit ourselves to a very personal selection of the most important results. The interested reader will find a more complete discussion in the review of Fryer and New (2011) and in the comprehensive numerical analysis of Baiotti *et al.* (2007b).

### 12.4.1 Dust collapse: the Oppenheimer–Snyder solution

Also in the case of the gravitational collapse to a black hole, it is useful to start by studying a simplified scenario such as the one offered by the collapse of a star composed of uniform-density, pressureless *dust* (see Section 2.4 for a definition). This is also known as the *Oppenheimer–Snyder (OS) collapse*. In this case, in fact, the fluid motion is particularly simple, *i.e.*, it is the motion of collisionless particles with a collective geodetic flow in the same (radial) direction. Furthermore, because of Birkhoff’s theorem, the only portion of the spacetime that is undergoing an evolution is the one interior to the star, since the exterior always remains a Schwarzschild solution, although with a dynamical boundary.

We have already encountered the combined assumptions of homogeneity and spherical symmetry in Chapter 1, when studying some exact solutions of the Einstein equations. We have seen in Section 1.7.3 that in spherical symmetry the dynamical spacetime of a collapsing/expanding region occupied by a homogeneous distribution of matter is a *Friedmann–Robertson–Walker (FRW) universe*, whose line element is given by Eq. (1.270). Hence, combining two basic results, such as the Birkhoff theorem and the FRW solution, we gain a very

precise idea of what should be the properties of a spacetime undergoing an OS collapse: it will be a contracting FRW universe dynamically matched to a Schwarzschild solution.

While in a cosmological context the line element (1.270) can take three different forms according to the value of the constant curvature  $\kappa$  of the spatial slice (*i.e.*,  $\kappa = -1$ , curved open universe;  $\kappa = 0$ : flat open universe,  $\kappa = 1$ ; curved closed universe), the relevant solution in the context of an OS collapse is the one with positive constant curvature,  $\kappa = 1$ . In this case, the line element (1.270) can be expressed in terms of comoving *hyperspherical coordinates*  $(\chi, \theta, \phi)$

$$ds^2 = -d\tau^2 + a^2(\tau) (\chi^2 + \sin^2 \chi d\Omega^2) , \quad (12.55)$$

where  $\chi := \sin^{-1} r$ , and where we have indicated the time coordinate with  $\tau$  to recall that this coincides with the proper time of a comoving observer. Besides using the coordinate system in (12.55), it is useful to introduce a new conformal time coordinate (or ‘‘cycloid parameter’’),  $\eta \in [0, \pi]$ , defined as  $d\eta := d\tau/a$  and such that  $\eta = 0$  at the beginning of collapse, and  $\eta = \pi$  at the end. Using this coordinate, the scale factor  $a$ , and the proper time  $\tau$  can be parameterised as

$$a = \frac{a_{\max}}{2} (1 + \cos \eta) , \quad \tau = \frac{a_{\max}}{2} (\eta + \sin \eta) , \quad (12.56)$$

where  $\tau(\eta = 0) = 0$ , and  $a_{\max} := a(\eta = 0)$ . An important difference between the FRW universe and the spacetime of an OS collapse is that in the latter case not all of the spacetime is occupied by matter. If the dust star initially has a finite radial size  $R_0$ , matching conditions in the metric can be imposed between the interior FRW spacetime and the exterior Schwarzschild one. In spherical symmetry, this matching is attained by requiring the continuity of the proper circumference at  $R_0$ , *i.e.*,

$$\mathcal{C}_{\text{Schw.}} = \int_0^{2\pi} \sqrt{g_{\phi\phi}} d\phi = 2\pi R_0 = \mathcal{C}_{\text{FRW}} = 2\pi a \sin \chi_0 , \quad (12.57)$$

and since the condition (12.57) must hold at all times, it is easy to deduce that

$$R_0 = a_{\max} \sin \chi_0 . \quad (12.58)$$

Because each of the collisionless particles of the dust star is effectively following a radial ingoing geodesic, the equation of motion of the outermost shell is simply given by

$$R = \frac{R_0}{2} (1 + \cos \eta) , \quad (12.59)$$

and, of course, we could have chosen any other shell at initial radius  $kR_0$  with  $k < 1$ . Using now Eq. (12.59) and the matching condition (12.57), it is possible to deduce that the scale factor is related to the total mass  $M$  and the initial radius  $R_0$  through the simple relations

$$a_{\max} = \left( \frac{R_0^3}{2M} \right)^{1/2} , \quad \chi_0 = \sin^{-1} \left( \frac{2M}{R_0} \right)^{1/2} . \quad (12.60)$$

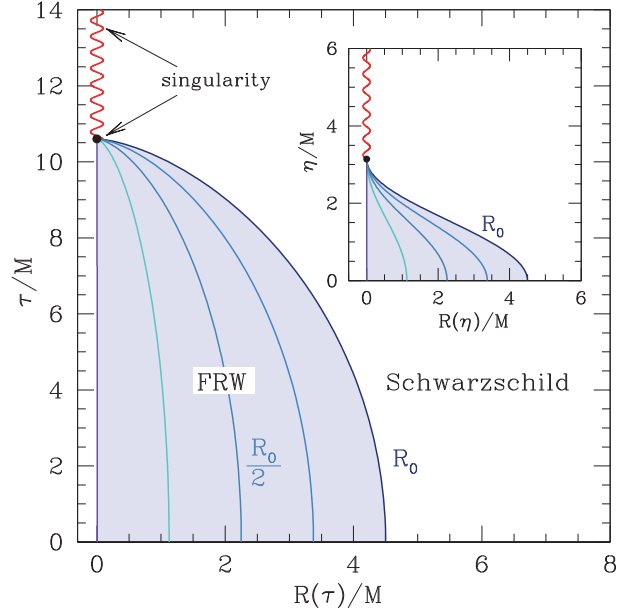


**Fig. 12.8** Schematic diagram showing the worldlines of different collapsing radial shells in a  $(R, \tau)$  spacetime diagram. The various lines refer to shells initially at  $0, (1/4)R_0, (1/2)R_0, (3/4)R_0$ , and  $R_0$ , and the lavender shaded area represents the stellar interior. Note that they all reach the singularity at the same proper time  $\tau = \frac{\pi}{2} \left( \frac{R_0^3}{2M} \right)^{1/2}$ . Also reported in the inset are the same worldlines but shown as a function of the cycloid parameter  $\eta$ .

Note that because  $R_0 = R_0(\tau)$ , also  $a_{\max}$  and  $\chi_0$  are functions of the proper time  $\tau$ . We can now calculate the (finite) proper time that an observer comoving with the stellar surface will measure when going from  $R_0$  to  $R = 0$  and that amounts to

$$\tau = \frac{\pi}{2} \left( \frac{R_0^3}{2M} \right)^{1/2}. \quad (12.61)$$

This time will be the same for *all* initial radial positions  $R$  and this is a trivial consequence of the uniformity in density, for which the ratio  $R^3/m(R) = \text{const}$ . A schematic diagram showing the worldlines of different collapsing radial shells in a  $(R, \tau)$  spacetime diagram is shown in Fig. 12.8 for a dust star with  $M = 1$  and  $R_0 = (9/2)M$ . The various lines refer to shells initially at  $0, (1/4)R_0, (1/2)R_0, (3/4)R_0, R_0$ , with the latter marking the dynamical border between the interior FRW spacetime (lavender shaded area) and the exterior Schwarzschild one. Note that all worldlines reach the *singularity*, *i.e.*, the event at which the energy density diverges, at the same proper time (12.61). Also shown in the inset are the same worldlines but reported as a function of the cycloid parameter  $\eta$ .

Finally, it is interesting to calculate the proper time  $\tau$  at which a shell initially at  $R_0$  reaches  $R = 2M$ . This can be computed straightforwardly from (12.56) and is given by

$$\tau_{2M} = \frac{1}{2} \left( \frac{R_0^3}{2M} \right)^{1/2} (\eta_{2M} + \sin \eta_{2M}), \quad (12.62)$$

where  $\eta_{2M} := \cos^{-1}(4M/R_0 - 1)$ . This expression will be useful below, where we discuss what happens to outgoing photons as the collapse proceeds and that may never reach null infinity.

### Trapped surfaces.

The end-result of the spherical collapse described above will be a Schwarzschild black hole, in which case the physical singularity at  $r = 0$  will be covered by an *event horizon* at  $r = 2M$ , *i.e.*, a null surface that photons cannot leave (see Section 1.7.1). This is indeed the essence of the *cosmic censorship* hypothesis (Penrose, 1979), which conjectures that singularities produced in the solutions of Einstein's equations from generic initial conditions are hidden within event horizons, and thus cannot be seen from the rest of spacetime. Such singularities are therefore “dressed” by the event horizon, in contrast to “naked” singularities, which are not covered by an event horizon.

However, the Schwarzschild solution will be reached only asymptotically and it is interesting to study how the event horizon is formed during the collapse and what are its properties before it becomes the event horizon of a static non-rotating black hole. In practice, we would need to compute the trajectory of the outermost outgoing photon that was not able to reach null infinity. This is of course possible, but it also requires knowledge of the whole spacetime (the event horizon is a global property of a spacetime and it cannot be computed on a spatial slice without knowing the future development of that slice). Alternatively, we can try and locate at any instant of time the two-surface that photons cannot leave, at least locally. This is a “marginally outer trapped surface” (or MOTS) and is defined as a smooth closed two-surface whose future-pointing outgoing null geodesics have zero expansion, *i.e.*, a surface from which photons cannot propagate outwards. An *apparent horizon* is then defined as the outermost MOTS and is always contained within an event horizon [see, *e.g.*, Gourgoulhon and Jaramillo (2006) for a complete discussion]. Computing the location of the *apparent horizon* in numerical-relativity calculations can be accomplished in a number of different ways [see, *e.g.*, Thornburg (2007) for a review], but it essentially amounts to the expensive solution of an elliptic equation for the outward-pointing unit three-vector normal to the trapping surface. Fortunately, however, the solution is much simpler and indeed analytical in the case of an OS collapse.

To compute it, let us start by considering the worldline of a radially moving photon. In this case,  $ds^2 = 0 = d\theta = d\phi$ , and the line element (12.55) then yields the curves

$$\frac{d\chi}{d\tau} = \pm \frac{1}{a(\tau)}, \quad (12.63)$$

where the  $\pm$  sign distinguishes *outgoing* (+) from *ingoing* (-) photons. Using now the cycloid parameter  $\eta$  [*cf.*, Eq. (12.56)], it is easy to show that these photons propagate along straight lines in the  $(\chi, \eta)$  plane, *i.e.*,

$$\frac{d\chi}{d\eta} = \pm 1, \quad (12.64)$$

or, equivalently, they follow curves of the type

$$\chi = \chi_e \pm (\eta - \eta_e), \quad (12.65)$$

where  $\chi_e$  and  $\eta_e$  are the “place” and “time” of emission, respectively. A swarm of outgoing photons will be *trapped* if their proper area will not grow in time, *i.e.*, if

$$\frac{d\mathcal{A}}{d\eta} \leq 0, \quad (12.66)$$

where  $\mathcal{A} := \int \sqrt{g_{\theta\theta}g_{\phi\phi}} d\theta d\phi$ . Writing out explicitly the condition (12.66) then yields

$$\eta_e \geq \pi - 2\chi_e, \quad (12.67)$$

which indicates that any outgoing photon emitted at a position  $\chi_e$  and at a time  $\eta_e$  will be able to propagate out if and only if  $\eta_e$  is smaller than  $\pi - 2\chi_e$ . Photons emitted above the line  $\eta_e = \pi - 2\chi_e$  in the  $(\chi, \eta)$  plane, will instead be trapped. As mentioned above, out of all the possible trapped surfaces, the most important one is the outermost, since it will discriminate between the photons that will propagate to null infinity from those that will be trapped. Such a surface selects the apparent horizon and since  $\chi_e \leq \chi_0$  (the photons must be emitted from within the star) it is simply expressed as

$$\eta_{\text{AH}} = \pi - 2\chi_0 = \pi - 2 \sin^{-1} \left( \frac{2M}{R_0} \right)^{1/2} = 2 \cos^{-1} \left( \frac{2M}{R_0} \right)^{1/2}. \quad (12.68)$$

Note that  $\eta_{\text{AH}} = \cos^{-1}(4M/R_0 - 1) = \eta_{2M}$  and hence the apparent horizon first forms when the stellar surface crosses  $R = 2M$  and then progressively moves inwards till reaching the singularity at  $\tau$  given by Eq. (12.61). Note also that this condition is true only in the OS collapse and that the apparent horizon is in general formed earlier in the case of a fluid collapse (see Section 12.4.2).

Finally, we consider the evolution of the event horizon which is defined as the surface for which the equality in condition (12.66) holds. Using the constraint that the event horizon is always outside or coincides with the apparent horizon, we can set  $\chi_{\text{EH}} = \chi_{\text{AH}} = \chi_0$  when  $\eta = \eta_{\text{AH}}$ , so that the worldline for the event horizon is given by

$$\chi_{\text{EH}} = \chi_0 + (\eta - \eta_{\text{AH}}), \quad (12.69)$$

for  $\eta \leq \eta_{\text{AH}}$ . We can re-express this condition in terms of the more intuitive  $\tau$  and  $R$  coordinates, and thus obtain the worldline of the event horizon as

$$R_{\text{EH}} = \frac{1}{2} \left( \frac{R_0^3}{2M} \right)^{1/2} (1 + \cos \eta) \sin(\chi_0 + \eta - \eta_{\text{AH}}). \quad (12.70)$$

An important property that can be deduced from (12.70) is that the event horizon starts from a zero radius and then progressively grows to reach  $R = 2M$ ; this should be contrasted with what happens for the apparent horizon, which is first formed with a nonzero radial size.

The dynamics of the trapped surfaces is summarised in Fig. 12.9, which is similar to Fig. 12.8, but where we have reported the worldline of the stellar surface  $R_0(\tau)$  (dark blue line), that of the event horizon (green dashed line) and of the apparent horizon (orange solid line). Note that the event horizon grows from zero size and reaches the value  $2M$  when the

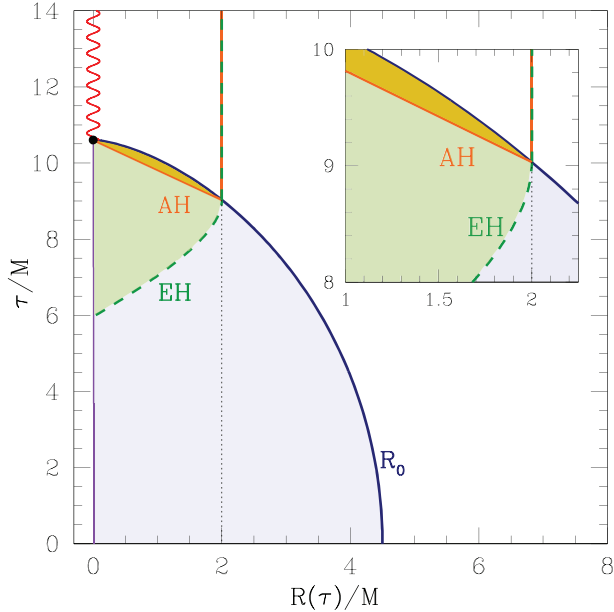


**Fig. 12.9** Schematic diagram showing the worldlines of the event horizon (EH), of the apparent horizon (AH) and of the stellar surface ( $R_0$ ). The inset offers a magnified view, where it is possible to note that the event and apparent horizons coincide after the stellar surface has reached  $R = 2M$ .

stellar surfaces is at that position. This also marks the time when the inward-expanding apparent horizon is formed, which then shrinks to zero size as the dust star approaches the “covered” singularity. Note also that another outward expanding apparent horizon is formed at  $\tau_{2M}$ , but this then coincides with the event horizon. The trapped regions inside the event horizon and outside the shrinking apparent horizon are marked with a light-green and with an orange shaded area, respectively. Much of what we have learnt about the dynamics of trapped surfaces in the OS collapse continues to hold true also in the case of the collapse of a perfect fluid, where however the apparent horizon is also formed earlier because of the additional contribution of the fluid compression.

### 12.4.2 Fluid collapse

We next discuss the dynamics of gravitational collapse to a rotating black hole in the case of a fluid star, and it is useful to remark that the problem of the stability of a star against collapse to a black hole is obviously absent in Newtonian physics and is one of the most intriguing aspects introduced by general relativity. While the stability properties of non-rotating stars are reasonably well understood [see, e.g., Misner *et al.* (1973)], this is not the case for rotating stars and is particularly obscure when the stars are rapidly rotating. An important contribution in this context is represented by the *turning-point criterion* for secular stability proposed by Friedman *et al.* (1988), who proved that a sequence of uniformly rotating barotropic stars is secularly unstable on one side of a turning point (*i.e.*, an extremum of mass along a sequence

of constant angular momentum, or an extremum of angular momentum along a sequence of constant rest mass). They then argued, based on the expectation that viscosity leads to uniform rotation, that the turning point should identify the onset of a secular instability.<sup>11</sup> While for a non-rotating star the turning point does coincide with the secular-instability point (and with the dynamical-instability point for a barotropic star if the perturbation satisfies the same equation of state as the equilibrium model), for rotating stars it is only a sufficient condition for secular instability. Yet, because of its simplicity, the turning-point criterion is routinely used to find a dynamical instability in simulations (Baiotti *et al.*, 2005).

A better understanding of the dynamical instability of relativistic stars in uniform rotation has been reached recently through the investigations of Takami *et al.* (2011), who have determined the *neutral-stability line*, that is, the line in the  $(M, \rho_c)$  plane corresponding to stellar models whose frequency of the fundamental mode of quasi-radial oscillation (*i.e.*, the  $F$ -mode) is vanishingly small. By construction, this line marks the threshold for stability to gravitational collapse and, surprisingly, it was found that the neutral-stability line coincides with the turning point for spherical stars, but not for rotating stars, with the difference increasing with the angular momentum. This difference is not in contrast with the predictions of the turning-point criterion, since the latter is only a sufficient condition for secular instability and not a necessary condition for secular and dynamical instability. Hence, a stellar model which is stable according to the turning-point criterion, can nevertheless be dynamically unstable, as shown by Takami *et al.* (2011) through dynamical simulations.

In the following we will discuss separately the gravitational collapse of uniformly and of differentially rotating stars, with the latter case being distinguished in models with mass  $M$  and angular momentum  $J$  that are *sub-Kerr*, *i.e.*, with  $J/M^2 \leq 1$ , from models that are *supra-Kerr*, *i.e.*, with  $J/M^2 > 1$ . We will also use the neutral-stability line to guide us in the selection of models that are known to be dynamically unstable, or close to the instability threshold, so that a numerical simulation of the collapse is actually possible (collapsing a stable model requires quite an effort!).

The initial models considered in our discussion are nicely collected in Fig. 12.10, which again shows the gravitational mass as a function of the central-density (*cf.*, Figs. 12.4 and 12.6), together with the non-rotating and mass-shedding sequences. We have also marked the position of the representative models whose dynamics we will discuss, namely: the uniformly rotating models D1–D4 (solid light-blue circles) and the differentially rotating models A1–A3 and B1 (purple triangles). Finally, shown with a black dotted line and with a dashed purple line are the turning-point line and the neutral-stability line, respectively. Note that all the uniformly rotating models are at larger densities than the neutral-stability line and hence within the unstable region of the  $(M, \rho_c)$  plane.

### **Uniformly rotating models.**

The range of behaviours in the gravitational collapse of uniformly rotating models is well illustrated when considering the dynamics of two extreme models, namely, models D1 and D4 (see the inset in Fig 12.10). The first one is a slowly-rotating model and almost spherical, *i.e.*, with

<sup>11</sup>Besides a *dynamical instability*, which is purely hydrodynamic and with a growth time which is comparable with the dynamical one, a *secular instability* is also possible in rotating compact stars. This class of instabilities is triggered by dissipative processes, such as viscosity or radiation emission. If the dissipative mechanism is the emission of gravitational radiation, then the secular instability is also known as Chandrasekhar–Friedman–Schutz or *CFS instability* (Chandrasekhar, 1970; Friedman and Schutz, 1978).

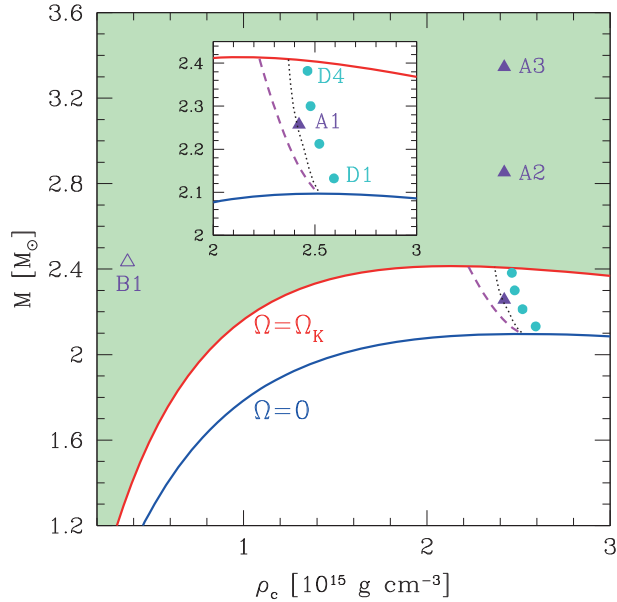


**Fig. 12.10** Initial equilibrium models of uniformly rotating (filled light-blue circles) and of differentially rotating models (purple triangles). Together with the non-rotating and mass-shedding sequences, we report with a black dotted line and with a dashed purple line the turning-point line and the neutral-stability line, respectively. Note that all the uniformly rotating models are within the unstable region of the  $(M, \rho_c)$  plane [adapted from Giacomazzo *et al.* (2011)].

$r_p/r_e = 0.95$ , while the second one is rapidly rotating and close to the mass-shedding limit, with an axis ratio  $r_p/r_e = 0.65$ . Simulations relative to these models, either with a polytropic or an ideal-fluid equation of state, have been considered in detail by Baiotti *et al.* (2005) and reveal that, after the introduction of a small perturbation,<sup>12</sup> the gravitational collapse of model D1 takes place in an almost spherical manner, without evidence of shock formation, which could prevent the prompt collapse to a black hole, nor appreciable deviations from axisymmetry. As the collapse proceeds, an apparent horizon is found and all of the matter is rapidly accreted by the newly formed black hole.

When considering instead the dynamics of model D4, which is initially considerably more oblate than D1, it was observed that significant differences appear because the infall is no longer spherically symmetric. Indeed, the parts of the star around the rotation axis that are experiencing smaller centrifugal forces collapse more promptly and, as a result, the configuration increases its oblateness and the ratio between polar and equatorial proper radii becomes as small as 0.45 at the time when the matter on the rotation axis is inside the apparent horizon. Indeed, by this stage, the star has flattened considerably, all of the matter near the rotation axis has fallen inside the apparent horizon, but a disc of low-density matter remains near the equatorial plane, orbiting at very high velocities  $\gtrsim 0.2$ . However, the disc formed outside the

<sup>12</sup>The simplest of these perturbations consists in reducing the polytropic constant of the initial model by a small amount, e.g.,  $\lesssim 2\%$  (Baiotti *et al.*, 2005).

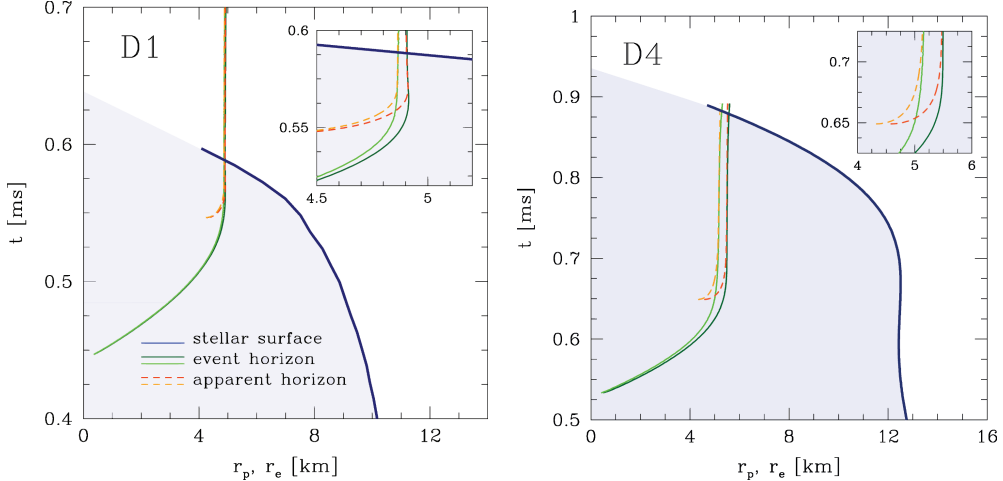


**Fig. 12.11** Evolution of the most relevant surfaces during the collapse for the cases D1 and D4. Solid, dashed and dotted lines represent the worldlines of the circumferential radii of the event horizon, of the apparent horizon and of the stellar surface, respectively. Note that for the horizons we plot both the equatorial and the polar circumferential radii, while only the equatorial circumferential radius is shown for the stellar surface. Shown in the insets are the magnified views of the worldlines during the final stages of the collapse [adapted from Baiotti *et al.* (2005)].

apparent horizon is not dynamically stable and it rapidly accretes onto the newly-formed black hole. This is simply due to the fact that the outer edge of the disc is well within the ISCO of the newly formed Kerr black hole and hence the stellar matter there can only accrete onto the black hole.<sup>13</sup>

The qualitative differences in the dynamics of slowly and rapidly rotating models can also be appreciated by studying the worldlines of the most representative surfaces during the collapse, namely those of the equatorial stellar surface, of the apparent horizon and of the event horizon. These are shown in Fig. 12.11, whose left and right panels refer to the collapse of models D1 and D4, respectively. The different lines indicate the worldlines of the circumferential radius of the stellar surface (thick blue solid lines), as well as of the apparent horizon (orange dashed lines) and of the event horizon (green solid lines). Note that for the horizons we show both the equatorial and the polar circumferential radii, with the latter being always smaller than the former. Note also that in both panels of Fig. 12.11 the event horizon grows from an essentially zero size to its asymptotic value. In contrast, the apparent horizon grows from an initially finite size and is always contained within the event horizon. At late times the worldlines merge, as expected (see Fig. 12.9).

A rapid look at the two panels of Fig. 12.11 is sufficient to appreciate the different properties in the dynamics of models D1 and D4. First, in the case of model D1, the differences between the equatorial and polar circumferential radii of the two trapped surfaces are very small and emerge only in the inset which offers a magnified view of the worldlines during

<sup>13</sup>Note that simple point-like particle motion in stationary spacetimes is a sufficient approximation to the dynamics of the matter of this rapidly rotating model for which pressure gradients cannot play an important role.

the final stages of the collapse. This is not the case for model D4, for which the differences are much more evident and can be appreciated also in the main panel. Second, the worldlines of the stellar surface are very different in the two cases. In particular, for the slowly rotating model, the star collapses smoothly and the worldline always has a negative slope, thus reaching progressively smaller radii as the evolution proceeds. By time  $t \simeq 0.59$  ms, the stellar equatorial circumferential radius has shrunk below the corresponding value of the event horizon. In the case of the rapidly rotating model D4, on the other hand, this is no longer true and after an initial phase which is similar to the one described for D1, the worldline does not reach smaller radii. Rather, the stellar surface slows its inward motion and at around  $t \sim 0.6$  ms the stellar equatorial circumferential radius does not vary appreciably. Indeed, the right panel of Fig. 12.11 shows that at this stage the stellar surface moves to slightly larger radii. This behaviour marks the phase in which a flattened configuration has been produced and the material at the outer edge of the disc experiences a stall. As the collapse proceeds, however, also this material will not be able to sustain its orbital motion and after  $t \sim 0.7$  ms the worldline moves to smaller radii again. By a time  $t \simeq 0.9$  ms, the stellar equatorial circumferential radius has shrunk below the corresponding value of the event horizon.

### Differentially rotating models.

The dynamics in the gravitational collapse of differentially rotating models differs enormously on whether the models are sub- or supra-Kerr. Hereafter, we will concentrate on the sub-Kerr model A2 (see the inset in Fig 12.10) and on the supra-Kerr model B1. The latter is particularly interesting because, if the *cosmic censorship* hypothesis is expected to hold, this model cannot collapse promptly to a Kerr black hole, which are limited to  $J/M^2 \leq 1$ . The properties of the two models can be found in Giacomazzo *et al.* (2011) and in essence model A2 has an axis ratio  $r_p/r_e = 0.33$  and a dimensionless spin  $J/M^2 = 0.8151$ , while model B1 is slightly less flat with  $r_p/r_e = 0.39$  and a dimensionless spin  $J/M^2 = 1.0865$ . The dynamics of the sub-Kerr model A2 is summarised in the various panels of Fig. 12.12, where we show the isodensity contours in the  $(x, y)$  plane (top row) and  $(x, z)$  plane (bottom row).<sup>14</sup> Note that the star has initially a pronounced toroidal shape as a result of its strong differential rotation. In practice, the evolution to a rotating black hole is rather similar to what was already observed for the uniformly rotating models and especially for model D4. The collapse is axisymmetric and leads to the formation of a black hole, as indicated by the appearance of an apparent horizon (red dashed line). At this time, the star has assumed the shape of a disc which rapidly accretes until no matter is left outside, as one can see from the last column of panels in Fig. 12.12.

The supra-Kerr model B1, on the hand, shows very different dynamical behaviour, as reported in Fig. 12.13. First, the model was found to be very far from the putative instability threshold for differentially rotating models, so that it was necessary to force its collapse by *artificially* reducing the initial pressure by 99% (smaller pressure reductions were found to be insufficient to trigger the collapse and no changes were made to the total angular momentum). Of course this is physically quite unlikely to happen, but serves here the purpose of assess-

<sup>14</sup>Note that the density is expressed in geometrised units (see Appendix A), but a conversion to cgs units is simply given by  $\rho_{\text{cgs}} \simeq 6.1776 \times 10^{17} \rho$ , where  $\rho_{\text{cgs}}$  is expressed in  $\text{g cm}^{-3}$ . Furthermore, the time is expressed also in units of the initial central rotation period of the star,  $P_{\text{rot,c}}$ .

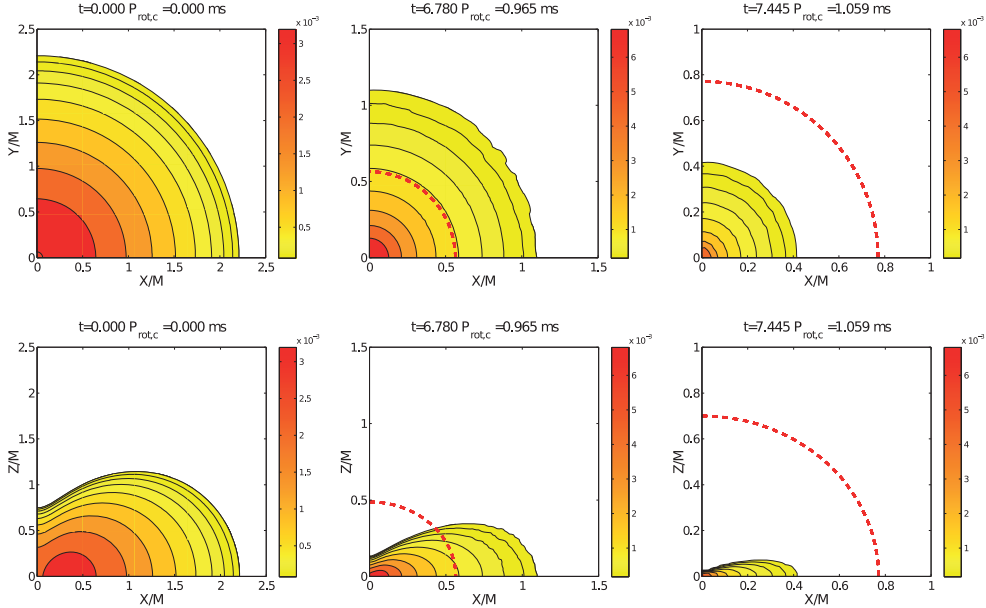


**Fig. 12.12** Snapshots of the rest-mass density in the equatorial ( $x, y$ ) plane (top row) and in the polar ( $x, z$ ) plane (bottom row) for the sub-Kerr model A2. The apparent horizon (red dashed line) is found at time  $t_{\text{AH}} = 6.71 P_{\text{rot},c}$ , where  $P_{\text{rot},c}$  is the initial central rotation period of the star. This figure should be contrasted with the equivalent Fig. 12.13 for the supra-Kerr model B1. [Reprinted with permission from Giacomazzo *et al.* (2011). © 2011 by the American Physical Society.]

ing what is the flow dynamics under these extreme conditions and whether the matter can successfully collapse to a black hole.

With its pressure support essentially removed, the model immediately flattens along the  $z$ -direction and collapses toward the centre on the equatorial plane, producing a strong shock. After a first bounce, due to the centrifugal barrier produced by the large angular momentum, a quasi-toroidal structure forms, which rapidly fragments into four clumps (see the snapshots in the middle column of Fig. 12.13).

The fragmentation of the collapsing matter with a predominant  $m = 4$  Fourier mode could be either physical and only triggered by the use of a Cartesian grid, or entirely due to the Cartesian coordinate system. However, later on, the four fragments merge and a new collapse and bounce follows, with the formation of a new quasi-toroidal structure, which eventually settles to a new stable configuration with a dominant  $m = 2$  oscillation. Interestingly, the collapse leads to an even larger degree of differential rotation than the initial one and the new equilibrium is very close to a Keplerian configuration in its outer layers. This is the result of having essentially removed pressure forces, leaving the centrifugal forces the only ones responsible for the equilibrium. Interestingly, the fact that it was not possible to force model B1 to collapse to a black hole, even when artificially reducing the pressure by 99%, confirms that supra-Kerr models cannot directly collapse to a black hole. Indeed, the evidence that even when forced to collapse the supra-Kerr model does not produce a black hole, but redistributes its angular

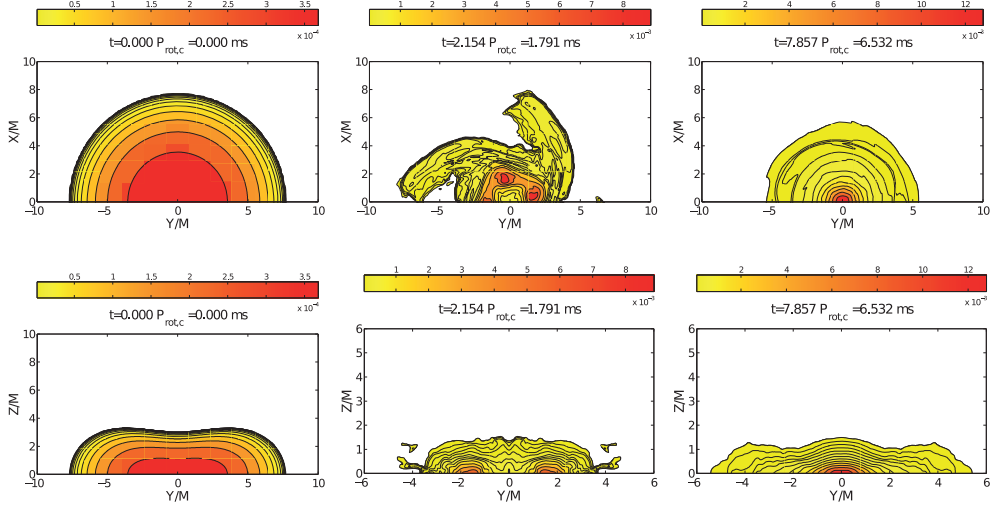


**Fig. 12.13** The same as in Fig. 12.12, but for the supra-Kerr model B1. Note that no black hole is found in this case. [Reprinted with permission from Giacomazzo *et al.* (2011). © 2011 by the American Physical Society.]

momentum to reach a stable and axisymmetric stellar configuration, provides strong evidence that cosmic censorship is not violated and that rather generic conditions for a supra-Kerr progenitor do not lead to a naked singularity.

## 12.5 Dynamics of binary neutron stars

### 12.5.1 Broadbrush picture

The study of the dynamics of *binary neutron stars* requires little justification. Despite this being a rather simple “two-body” problem, *i.e.*, the problem of the dynamics of two massive objects interacting gravitationally, it is one of the most challenging problems in classical general relativity and the perfect arena for relativistic hydrodynamics (and magnetohydrodynamics!). A number of astronomical observations reveal that binary neutron stars exist and for some of the systems in our own Galaxy, general-relativistic effects in the binary orbit have been measured to high precision (Kramer *et al.*, 2004). The inspiral and merger of two neutron stars in binary orbit is the inevitable fate of close-binary evolution, whose main dissipation mechanism is the emission of gravitational radiation. An important part of the interest in the study of coalescing systems of compact objects comes from the richness of general-relativistic effects that accompany these processes and, most importantly, from the gravitational-wave emission. Detection of gravitational waves from neutron-star binaries, in fact, will provide a wide variety of physical information on the component stars, including their mass, spin, radius and equations of state (Oechslin and Janka, 2007; Andersson *et al.*, 2011). Furthermore, neutron-star binary systems are expected to produce signals of amplitude large enough to be relevant

for Earth-based gravitational-wave detectors and to be sufficiently frequent sources to be detectable over the time-scale in which the detectors are operative. Advanced interferometric detectors are in fact expected to observe these sources at a rate of  $\sim 0.4\text{--}400$  events per year, with a most realistic rate of  $\sim 40$  per year (Abadie *et al.*, 2010).

However, the study of neutron-star binary systems goes beyond the impact they have on gravitational-wave astronomy and also aims at understanding the origin of a class of *gamma-ray bursts (GRBs)*, whose short rise times suggest that their central sources have to be highly relativistic objects. As anticipated in Section 11.9, after the observational confirmation that GRBs have a cosmological origin it has been estimated that the central sources powering these bursts must provide a large amount of energy, *i.e.*,  $\sim 10^{48\text{--}50}$  erg, in a very short time-scale, going from one millisecond to one second. It has long been suggested that the merger of neutron-star binaries could be a likely candidate for the powerful central source of GRBs, at least for this class of “short” GRBs. The typical scenario assumes that a system composed of a rotating black hole and a surrounding massive torus is formed after the merger. If the disc had a mass  $\gtrsim 0.01\text{--}0.1 M_\odot$ , it could provide the large amount of energy observed in GRBs, either through neutrino processes or by extracting the rotational energy of the black hole via magnetic fields (Paczynski, 1986; Eichler *et al.*, 1989; Rezzolla *et al.*, 2011).

The total gravitational masses of the known galactic neutron-star binaries are in the narrow range  $\sim 2.65\text{--}2.85 M_\odot$  and the present observational evidence indicates that the masses of the two stars are nearly equal. If this is the general situation, neutron stars in binary systems will not be tidally disrupted except just before the merger. As a result, the mass loss from the binary systems is expected to be small during the evolution and the mass of the merged object will be approximately equal to the initial mass of the binary system [indeed, numerical simulations indicate that the amount of matter lost during the inspiral is  $\lesssim 10^{-4} M_\odot$  (Rezzolla *et al.*, 2010)]. Unless the progenitor stars have very small masses (*e.g.*,  $M \lesssim M_{\max}/2$ ) and depending on the equation of state, the compact objects formed just after the merger of these binary systems are expected in general to collapse to a black hole, either promptly after the merger or after a certain “delay”. More precisely, the merged object is expected to be a *HMNS*, *i.e.*, a differentially rotating hypermassive neutron star (see Section 12.3.2), whose collapse to a black hole will be prevented on a time-scale over which dissipative effects like viscosity, magnetic fields or gravitational-wave emission bring the star towards a configuration which is unstable to gravitational collapse. During this time, if the merged object has a sufficiently high ratio of rotational to gravitational binding energy, it could also become dynamically unstable to nonlinear instabilities leading to a bar-mode deformation.

The different stages in the possible evolution of a binary system of neutron stars is shown as a cartoon in Fig. 12.14.<sup>15</sup> The diagram shows the different stages of the life of the binary as a function of time (horizontal axis) and of the ratio of the mass of the binary,  $M$ , to the maximum mass of an isolated spherical star,  $M_{\max}$ . Also indicated are the typical frequencies at which the corresponding gravitational waves are expected to be emitted. Note that in all cases, once formed, the binary system evolves on the *radiation-reaction time-scale*, *i.e.*, on the time-scale set by the loss of energy and angular momentum via gravitational radiation. This stage could last for millions of years before the binary reaches a separation small enough that the changes in the orbits take place on a time-scale of a few seconds only. At this point,

<sup>15</sup>The cartoon was made using images from fully general-relativistic numerical simulations. The images were produced by R. Kaelher (AEI/ZIB) and L. Rezzolla.

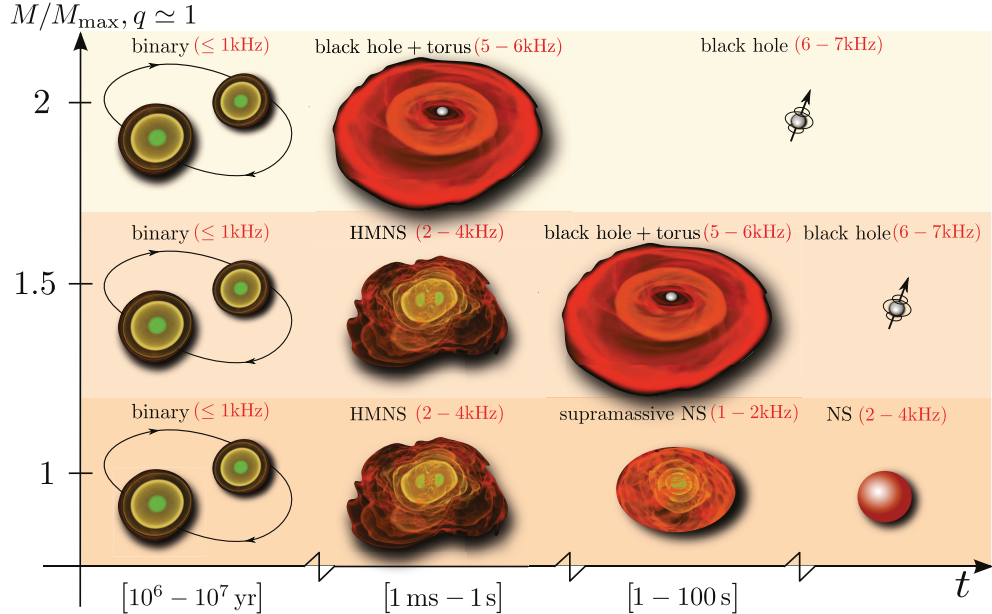


**Fig. 12.14** Schematic diagram illustrating the various stages in the evolution of an equal-mass binary system of neutron stars and indicating how the dynamics changes in time as a function of the initial mass of the binary. Depending on the initial mass, the binary can either collapse promptly to a black hole surrounded by a torus, or give rise to a HMNS which ultimately collapses to a black hole and torus, or lead to a HMNS which eventually yields a supramassive neutron star. Also indicated in red are the typical frequencies at which gravitational waves are expected to be emitted.

finite-size effects and relativistic regimes impose the numerical solution of the equations of relativistic hydrodynamics in fully dynamical spacetimes. After the merger, and depending on the initial mass, the binary can either collapse promptly (*i.e.*, over a time-scale of a few ms) to a black-hole surrounded by a torus (*i.e.*, for  $M/M_{\max} \gtrsim 1.5$ ), or give rise to a HMNS which eventually (*i.e.*, over a time-scale of 10–1000 ms) collapses to a black hole with a torus (*i.e.*, for  $1 \lesssim M/M_{\max} \lesssim 1.5$ ). In both cases, the torus will ultimately accrete onto the black hole and this will take place on a time-scale set by the most efficient process removing angular momentum, *i.e.*, gravitational radiation, magnetic fields or viscous processes, and which can be roughly estimated to be of the order of 1–100 s, or more.<sup>16</sup> A final possibility arises for systems with rather small masses (*i.e.*, for  $M/M_{\max} \lesssim 1$ ), in which case the merger leads to an object which gradually loses much of its angular momentum and differential rotation, eventually becoming a hot, axisymmetric and supramassive neutron star.<sup>17</sup> When the supra-

<sup>16</sup>The uncertainty in determining this time-scale is clearly very large. This is due particularly to the difficulty of performing accurate numerical simulations over these very long time-scales.

<sup>17</sup>It is also conceivable that the merged object may not be a supramassive star, *e.g.*, if  $M \ll M_{\max}/2$ . In this case, once the object has lost all of its angular momentum, it will end up as a non-rotating star on the stable branch of the equilibrium configurations.

massive star will have lost all of its rotational energy, *e.g.*, because of dissipative or radiative losses, its only possible fate will be that of collapsing to a black hole.

Although the broadbrush picture described above and illustrated in Fig. 12.14 is now well established and supported by a number of numerical simulations carried out by several groups, the details of the picture are still far from being clear. In particular, the properties of the intermediate product of the merger are known only very approximately, as these depend not only on the equation of state for high-density neutron matter, but also on the rotational profile of the merged object and on the physical processes through which the object can lose angular momentum and energy. Both magnetic fields (Giacomazzo *et al.*, 2011) and radiative processes (Sekiguchi *et al.*, 2011) can modify significantly the lifetime of the HMNS and hence change the properties of the black hole and of the surrounding torus.

What is clear however is that the highly nonlinear regimes encountered during merger of the two stars prevent any perturbative or approximate approach, forcing instead the numerical solution of the Einstein equations together with those of relativistic hydrodynamics. We have already discussed in detail in Chapters 8–10 how to do this in practice, and we here simply remark that because of the complexity of the merger and post-merger phases, several groups worldwide have developed numerical codes able to solve the equations of relativistic hydrodynamics together with the Einstein equations and to model the coalescence and merger of neutron star binaries. Starting from the first successful simulations of binary neutron star mergers by Shibata and Uryū (2000), who employed analytic equations of state and stopped when an apparent horizon was found and up to the more recent simulations of Hotokezaka *et al.* (2011) adopting nuclear physics equations of state, the ability to model binary neutron stars has steadily increased, providing a complete (although not necessarily realistic) description of the inspiral and merger of a neutron-star binary leading to the prompt or delayed formation of a black hole and to its ringdown<sup>18</sup> (Baiotti *et al.*, 2008).

All modern numerical simulations of binary neutron stars in full general relativity share a number of aspects which are essential for an accurate modelling of this process. These are: (*i*) high-order finite-differencing or pseudo-spectral techniques for the solution of the Einstein equations (see Chapter 8); (*ii*) high-resolution shock-capturing methods for the solution of the hydrodynamic/MHD equations (see Chapter 9); (*iii*) adaptive mesh-refinement techniques that provide higher resolution around the orbiting stars; (*iv*) consistent initial data representing a system of binary neutron stars in quasi-circular orbits;<sup>19</sup> and (*v*) analysis of the properties of the black holes produced in the merger, *e.g.*, through the calculation of trapped surfaces.

Given the complexity of the numerical infrastructure and the variety of the physical scenarios considered, it is difficult to review here the large literature produced over the last decade on the inspiral and merger of binary neutron stars and that is likely to be further developed in the coming years. As done in the previous sections, we will restrict ourselves to providing here a brief overview of the most salient (and robust) aspects of the simulations, leaving the details

<sup>18</sup> A perturbed black hole will respond to the perturbation by emitting radiation, which will be either scalar, electromagnetic or gravitational according to the perturbing agent. The corresponding oscillations will have amplitudes with a characteristic exponential decay in time, *i.e.*, a *ringdown*, as is typical of ordinary bells. The properties of these *quasi-normal modes* (*QNMs*), *i.e.*, the frequencies of the oscillations and their decay times, provide direct information on the black-hole mass and spin.

<sup>19</sup> A common choice is to consider binaries that are “irrotational”, that is, with a velocity field having a zero vorticity [see Section 3.7 and Gourgoulhon *et al.* (2001) for a discussion on this type of initial data]. However, also initial configurations of spinning binaries have been evolved recently (Kastaun *et al.*, 2013).

to the complete review of Faber and Rasio (2012). We will further distinguish the dynamics of equal-mass binaries from that of unequal-mass binaries as these two classes are those that offer the largest differences.

### 12.5.2 Dynamics of equal-mass binaries

We first start discussing the dynamics of equal-mass binaries as these represent by far the best studied case and already provide many of the most important aspects discussed above. Much of what is presented below is taken from Baiotti *et al.* (2008), where a systematic investigation of this problem was made using analytic equations of state and initial irrotational binaries. More specifically, Baiotti *et al.* (2008) considered binaries modelled either with a “cold”, *i.e.*, polytropic, equation of state (see Section 2.4.7), or with a “hot”, *i.e.*, ideal-fluid, equation of state (see Section 2.4.6). Although the polytropic equation of state is isentropic and thus unrealistic for describing the post-merger evolution, it provides an adequate description of the inspiral phase, during which the neutron stars are expected to interact only gravitationally. Moreover, because these two equations of state are mathematically equivalent in the absence of shocks, their use offers the important advantage of allowing one to employ the *same* initial data and thus of comparing directly the influence that the equation of state has on the evolution. Also, because they represent “extremes” of the possible fluid behaviour, these equations of state offer insights into the expected range in dynamical behaviour.

We now move on to discussing the dynamics of binary inspiral and merger when using the ideal-fluid equation of state. As discussed in Section 2.4.6, while this is an idealised equation of state, it has the important property of being non-isentropic and thus of allowing for changes in the internal energy also as a result of shock heating. As we will show in the remainder of this section, this difference can alter significantly the properties and dynamics of the HMNS produced by the merger. We concentrate therefore on the evolution of a “high-mass” binary, in which each neutron star has a baryon mass of  $M_b = 1.625 M_\odot$  (the total mass is  $M_{\text{tot}} = 2.998 M_\odot$ ) and an initial coordinate separation of 45 km, and we collect in Fig. 12.15 some representative isodensity contours in the equatorial plane. A time stamp in ms is shown in the top of each panel, while the colour-code bar is shown on the right in units of  $\text{g cm}^{-3}$ , with the thick dashed line in the bottom two panels representing the apparent horizon.

Once the evolution is started, the binary slowly starts its inspiral, which then progressively speeds up as the separation decreases. In the 3–4 orbits that are needed before the merger, and as the two neutron stars approach each other, tidal waves produced by the tidal interaction become visible at the surface (see the second and third panels in Fig. 12.15), with their amplitude increasing with the mass of the binary. As a result, oscillations in the central rest-mass density appear, accompanied by comparatively larger amounts of matter that are stripped from the surface in the form of winds. This process is at the same time the result of a consistent solution of the relativistic-hydrodynamic equations and a nuisance. When using a non-isentropic equation of state, in fact, the evolution during the inspiral is accompanied by the production of small shocks in the very low-density layers of the stars as these orbit around each other. These small shocks channel some of the orbital kinetic energy into internal energy, leading to small ejections of matter (*i.e.*, of the order of  $\sim 10^{-6} M_\odot$ ). These shocks would appear quite independently of the fact that the neutron stars are surrounded by an atmosphere, since they represent the evolution of small sound waves that propagate from the central regions of the

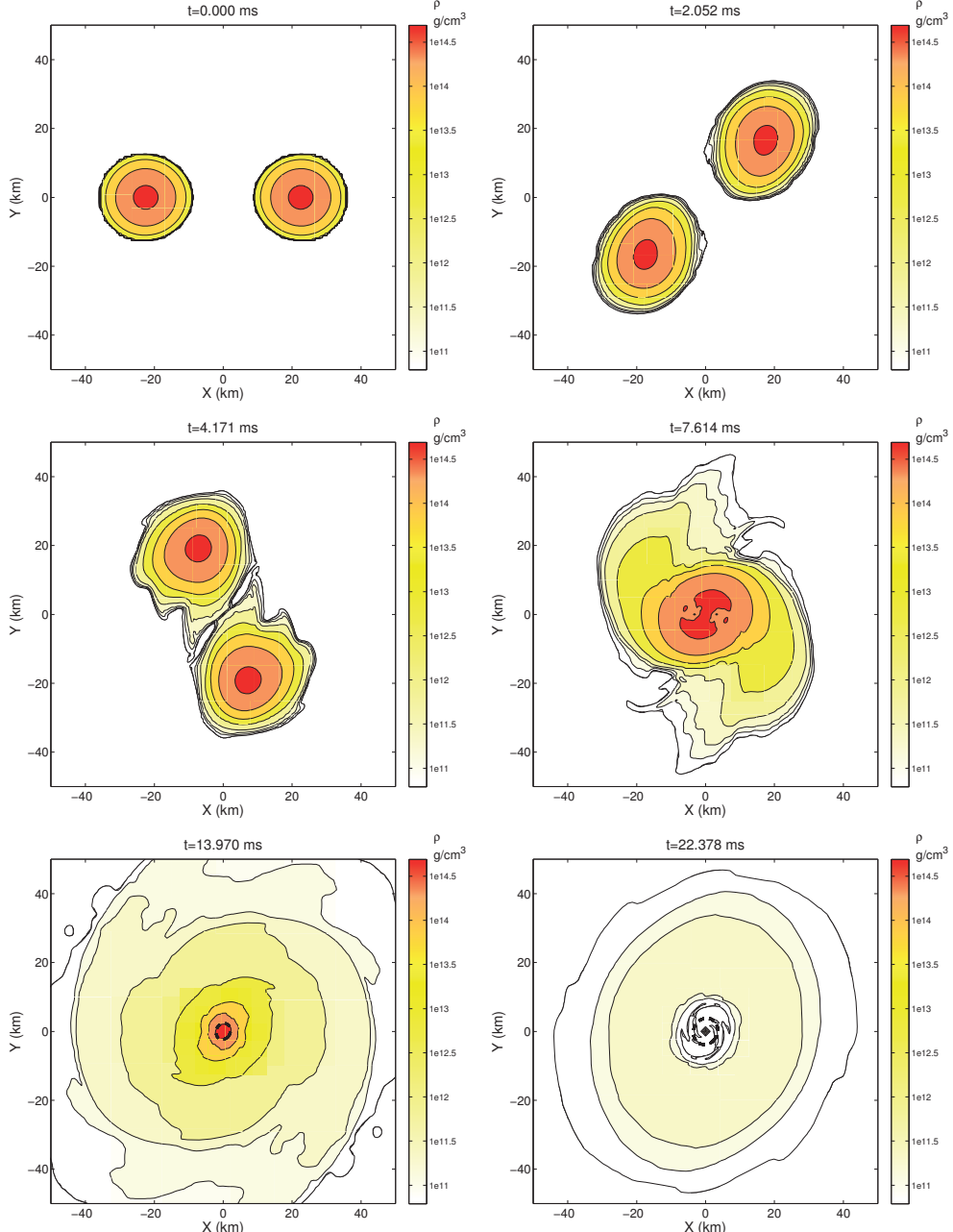


**Fig. 12.15** Isodensity contours in the  $(x, y)$  plane for the evolution of a high-mass binary with an ideal-fluid equation of state. The time stamp in ms is shown on the top of each panel, while the colour-code bar is shown on the right in units of  $\text{g cm}^{-3}$ , with the thick dashed line representing the apparent horizon. [Reprinted with permission from Baiotti *et al.* (2008). © 2008 by the American Physical Society.]

stars, steepening as they move outwards in regions of smaller rest-mass density (Stergioulas *et al.*, 2004).

At the merger, the two stars collide with a rather large impact parameter. This reduces significantly the strength of the shocks, but it also produces a considerable amount of shear, which could then lead to a series of interesting dynamical instabilities such as the Kelvin–Helmholtz instability (see also the discussion below). Even in the case of a high-mass binary such as the one considered here, the HMNS produced from the merger does not collapse promptly to a black hole, but rather undergoes very large oscillations with variations of 100% in the maximum of the rest-mass density (see the left panel of Fig. 12.17). These oscillations, which have a dominant  $m = 2$  non-axisymmetric character (Stergioulas *et al.*, 2011), are the result of a dynamical bar mode instability which develops and is suppressed at least four times during the post-merger phase. More specifically, after the first initial merger, the two stellar cores break up again to produce a bar-deformed structure, which rotates for several periods before disappearing. As this process takes place, the merged object becomes increasingly more compact as it loses angular momentum and thus spins progressively faster, further emitting gravitational waves and contracting in a runaway manner. The process ends when the HMNS is sufficiently compact that a rotating black hole is produced with a mass  $M_\bullet = 2.94 M_\odot$  and a dimensionless spin  $a := J_\bullet/M_\bullet^2 = 0.85$ , where  $J_\bullet$  is the black-hole spin.

After an apparent horizon is first found, the amount of matter outside of it is still quite large and has the largest specific angular momentum. This leads to the formation of an accretion torus with an average density between  $10^{12}$  and  $10^{13} \text{ g cm}^{-3}$ , a vertical size of  $\sim 20 \text{ km}$ , but a much larger horizontal size, *i.e.*,  $\sim 60 \text{ km}$ . The torus has an initial rest mass of  $(M_T)_0 \simeq 0.6 M_\odot$ , which however decreases rapidly to become  $(M_T)_{3 \text{ ms}} = 0.0726 M_\odot$  only 3 ms later. The dynamics of the torus are summarised in Fig. 12.16, which shows the isodensity contours in the  $(x, z)$  plane; also in this case the time stamp is shown on the top of each panel, while the colour-code bar is shown on the right in units of  $\text{g cm}^{-3}$ . Note that the panels refer to times between  $\sim 14.0 \text{ ms}$  and  $22.4 \text{ ms}$  after the evolution is started.

Overall, the torus has a dominant  $m = 0$  (axisymmetric) structure but because of its violent birth, it is very far from equilibrium. As a result, it is subject to large oscillations, mostly in the radial direction, as it tries to compensate between the excess of angular momentum and the intense gravitational field produced by the black hole. In doing so, it triggers quasi-periodic oscillations with a period of  $\sim 2 \text{ ms}$ , during which the torus moves in towards the black hole, which accretes a part of its mass. The quasi-periodic dynamics of the torus represents a generic response of the fluid to a quasi-radial oscillation with a frequency reminiscent of the epicyclic frequency for point-like particles in a gravitational field (Rezzolla *et al.*, 2003a). Furthermore, because of the large quadrupole moment possessed by the torus and its large variations produced by the oscillations, a non-negligible amount of gravitational radiation can be produced as a result of this process (Zanotti *et al.*, 2005). As mentioned above, the existence of a massive torus around the newly formed rotating black hole is a key ingredient in the modelling of short GRBs, and the ability of reproducing this feature through a fully nonlinear simulation starting from consistent initial data is a measure of the maturity of simulations of this type (Rezzolla *et al.*, 2011).

The dynamics of the inspiral and merger is also nicely summarised in the left panel of Fig. 12.17, which reports the evolution of the maximum rest-mass density normalised to its initial value and which, after the apparent horizon is found, refers to the region outside the

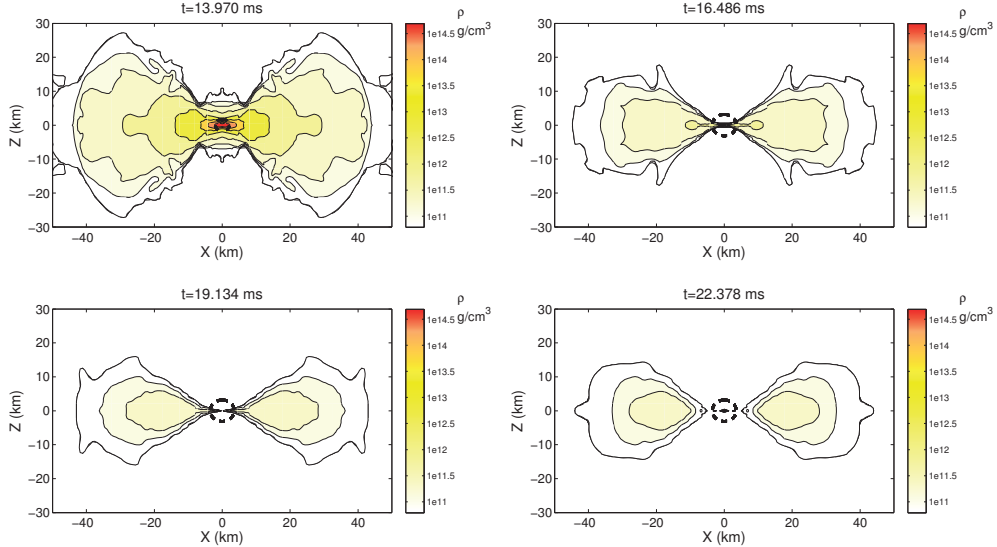


**Fig. 12.16** Isodensity contours in the  $(x, z)$  plane highlighting the formation of a torus surrounding the central black hole, whose apparent horizon is indicated with a thick dashed line. The data refer to the high-mass binary and this torus should be compared with the larger one obtained with an unequal-mass binary in Fig. 12.22. [Reprinted with permission from Baiotti *et al.* (2008). © 2008 by the American Physical Society.]

apparent horizon. Note that together with the large variations, the rest-mass density also experiences a secular growth and the increased compactness eventually leads, at  $t \sim 14$  ms, to the collapse to a rotating black hole. Despite the high mass of the system, the ability of the HMNS of delaying its collapse to a black hole is simply due to the large increase in the internal energy produced by the shock heating when the stars collide. The shocks produced at the merger, in fact, are responsible for a local and global increase of the temperature, which will produce a global expansion of the HMNS and thus a reduction of its compactness. This stabilising effect is not present in the case of an isentropic equation of state and, in fact, a binary with the same mass collapses essentially at the merger (Baiotti *et al.*, 2008). A simple estimate reveals that the HMNS has an initial temperature of  $\simeq 5 \times 10^{10}$  K, which rapidly increases to  $\simeq 5 \times 10^{11}$  K following the compression of the cores. The additional shocks produced by the large oscillations in the post-merger phase can increase the temperature above these values, with maximum values that can reach  $\simeq 2 \times 10^{12}$  K locally.

Clearly, the efficiency in converting the orbital kinetic energy into internal energy will depend on the microphysical properties of the neutron-star matter, which will therefore introduce a dependence of the lifetime of the HMNS on its equation state. However, the equation of state is not the only degree of freedom determining the dynamics of the HMNS. Another degree of freedom, which is equally important, is given by the initial mass of the binary, which will set the merged object closer or farther away from the stability limit to gravitational collapse. This is very eloquently indicated in the right panel of Fig. 12.17, which reports again the evolution of the maximum rest-mass density, but for a “low-mass” binary, *i.e.*, a binary in which

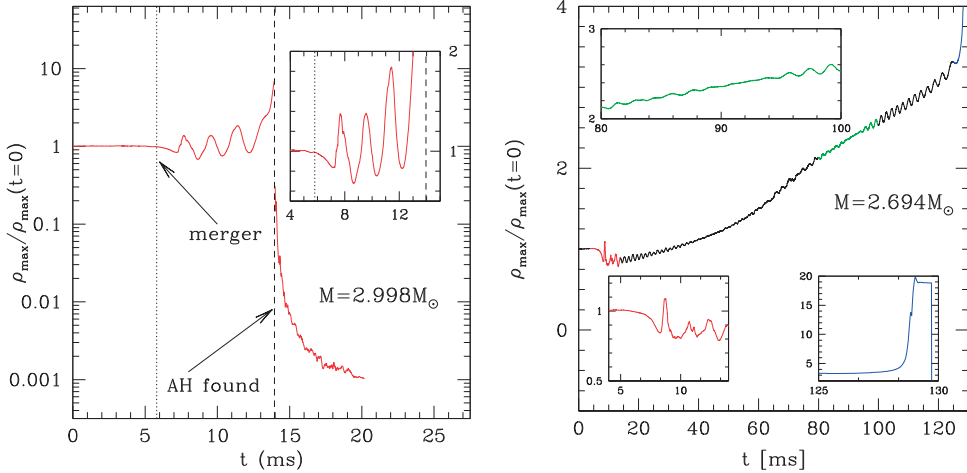


**Fig. 12.17** *Left panel:* Evolution of the maximum rest-mass density normalised to its initial value for a high-mass binary using the ideal-fluid equation of state. Indicated with a dotted vertical line is the time at which the binary merges, while a vertical dashed line shows the time at which an apparent horizon is found. After this time, the maximum rest-mass density is computed in a region outside the apparent horizon [adapted from Baiotti *et al.* (2008)]. *Right panel:* The same as in the left panel but for a low-mass binary. Note that the evolution is much longer in this case and that different colours are used to denote the different parts of the evolution (see insets) [adapted from Rezzolla *et al.* (2010)].

each star has a baryon mass of  $M_b = 1.456 M_\odot$  (the total mass is  $M_{\text{tot}} = 2.694 M_\odot$ ), and hence only about 10% smaller than in the left panel. Although the initial separation and the equation of state are the same as in the left panel of Fig. 12.17, the evolution is quantitatively very different. Shown with different colours are the different parts of the evolution, which are also magnified in the different insets (*cf.*, the time-scale to associate the insets to the three parts of the evolution). They refer to the immediate formation of the HMNS (red line), to the secular evolution of the HMNS as a contracting bar-deformed object (green line) and to the exponential growth when the threshold to black-hole formation has been crossed (blue line). Note that the time-scale over which the evolution is reported is  $\sim 140$  ms and thus a factor  $\sim 6$  larger than that for the high-mass binary (*cf.*, left panel). Yet, the qualitative behaviour is the same and essentially the one described in Fig. 12.14.

In addition to the equation of state and the initial total mass of the binary, the storyboard portrayed in Fig. 12.14 also has at least two more degrees of freedom that can influence significantly the evolution of the HMNS and the subsequent torus, namely: radiative effects and magnetic fields. Let us consider both of them in somewhat more detail.

At the very high temperatures reached at the merger and later on in the torus, radiative losses, either via photons or neutrinos, can become very important and lead to a qualitative change from the evolution described above. While first attempts at introducing the contribution of radiative losses in general-relativistic calculations have been made recently [see, *e.g.*, Farris *et al.* (2008), Zanotti *et al.* (2011), Kiuchi *et al.* (2012)], we are still far from a physically accurate treatment of these processes. For the time being it is sufficient to emphasise that,

while it is clear that the inclusion of radiative processes will lead to a decrease in the survival time of the HMNS after the merger, determining this time with any reasonable precision will require not only the inclusion of radiative transport, but also of a more realistic treatment of the equation of state and of the scattering properties of the matter in the HMNS.<sup>20</sup> Leaving to future numerical simulations the task of assessing in detail the effects of the radiative cooling via neutrinos, we can perform some simpler back-of-the-envelope calculations to assess the importance of radiative cooling in the post-merger phase. Let us therefore assume that the core of the HMNS is approximately spherical with an average radius of  $R_{\text{HMNS}} \sim 20$  km, a mass of  $M_{\text{HMNS}} \sim 3.2 M_{\odot}$  and thus an average rest-mass density which is essentially the nuclear rest-mass density, *i.e.*,  $\rho_{\text{HMNS}} \sim \rho_{\text{nuc}} \sim 3 \times 10^{14} \text{ g cm}^{-3}$ . We can now consider two different cooling processes acting either via modified-URCA emission (Shapiro and Teukolsky, 1983) or through the more efficient direct-URCA emission (Lattimer *et al.*, 1991). Assuming an initial average temperature of  $T_{\text{HMNS}} \sim 10^{11}$  K, the HMNS would cool down via modified-URCA processes to  $T_{\text{HMNS}} \sim 10^{10}$  ( $10^9$ ) K in about 20 s (1 yr). On the other hand, if the cooling takes place through the much more efficient direct-URCA processes, the cooling time would be  $\sim 3$  ms (1 min). In this case, the radiative losses would act well before the HMNS collapses to a black hole, significantly modifying the timing of events in Fig. 12.14.

Finally, the very strong magnetic fields (*i.e.*,  $10^8$ – $10^{10}$  G) that are expected to endow the neutron stars before the merger and which will be inherited by the HMNS, can redistribute the angular momentum, transporting it outwards and reducing the amount of differential rotation that is essential in supporting the HMNS against gravitational collapse. The ratio between the magnetic tension and the pressure gradients scales like the ratio between the magnetic pressure and the gas pressure, and this ratio increases (although remaining less than one) after the merger because the magnetic fields are stronger and the HMNS is more extended and with smaller pressure gradients (Giacomazzo *et al.*, 2011). As a result, magnetic fields can “accelerate” the collapse of the HMNS, but only if sufficiently strong for the magnetic tension to be comparable to or larger than the normal pressure gradients. Hence, the efficiency in angular-momentum redistribution will be proportional to the intensity of the (square of the) magnetic field and thus essentially unchanged for small magnetic fields, such as  $B_0 \lesssim 10^8$  G. For larger values, however, the magnetic fields will also introduce a magnetic pressure providing an additional pressure support and thus either compensating or even dominating the angular-momentum redistribution, with an overall delay of the collapse (Giacomazzo *et al.*, 2011). We should also remark that the HMNS could be subject to a magnetorotational instability (MRI), which could then increase exponentially the strength of the magnetic field (Duez *et al.*, 2006; Siegel *et al.*, 2013).

The conclusion to be drawn from these considerations is that the dynamics of the HMNS is the result of a number of highly nonlinear and intertwined processes which determine the fine balance among pressure forces, centrifugal forces, magnetic forces and gravitational forces. It is hard to imagine that analytic or semi-analytic approximations will be able to disentangle this complex knot, leaving the answer to increasingly realistic and accurate numerical simulations.

### **Gravitational-wave emission.**

The matter dynamics described so far in the various stages of the evolution of a binary system

<sup>20</sup>The cooling process, in fact, depends sensitively on the fraction of electrons which are present in the different regions of the HMNS and that can be tracked only with realistic equations of state.

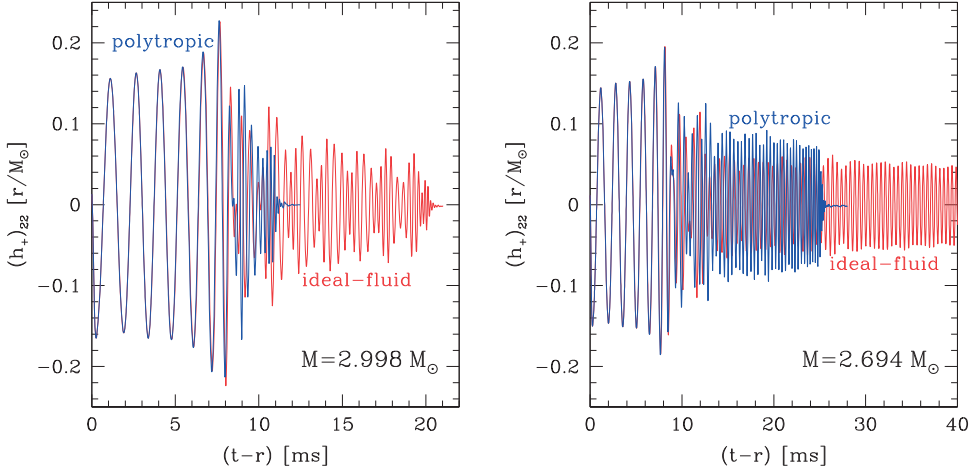


**Fig. 12.18** Gravitational-wave amplitudes in the plus polarisation corresponding to the  $\ell = 2, m = 2$  multipoles, as obtained for two equations of state and for two binaries with different masses. The left panel shows  $h_+$  for a high-mass binary when evolved using either the polytropic equation of state (blue line) or the ideal-fluid one (red line), while the right one shows the same quantities but for a low-mass binary. Note that significant differences emerge after the merger [adapted from Baiotti *et al.* (2008)].

of neutron stars and summarised in Fig. 12.14 is imprinted in the gravitational-wave signal and can be used to extract important information on the properties of the neutron star. Indeed, a trained eye can easily recognise the different stages in the two panels of Fig. 12.18, which report the largest multipoles, *i.e.*,  $\ell = m = 2$ , of the gravitational-wave amplitudes in the plus polarisation [*cf.* Eqs. (1.302)] for two equations of state and for two binaries with different masses. In particular, the left panel shows the evolution in retarded time of the  $\ell = m = 2$  amplitude in the  $h_+$  polarisation for the high-mass binary when evolved using either the polytropic equation of state (blue line) or the ideal-fluid one (red line). The initial data is exactly the same in the two cases and differences are expected to emerge only after the merger. Indeed the very good overlap during the inspiral confirms this expectation. As the two stars collide, however, the dynamics is significantly different, and while the polytropic binary very rapidly collapses to a black hole, the ideal-fluid one can use the extra pressure support produced by the shock heating at the merger to postpone the collapse by several milliseconds. Note that before this happens the gravitational-wave signal shows a beating and an increase in frequency. This is because the HMNS repeatedly undergoes a dynamical bar mode instability, which develops and is suppressed at least four times during the post-merger phase as the two stellar cores merge. Furthermore, because the HMNS becomes increasingly more compact as it loses angular momentum, it spins progressively faster, leading to the observed increase in the gravitational-wave frequency. In both cases, a black hole is eventually formed and when this happens the gravitational-wave signal dies out exponentially as a result of the black hole ringdown. We should note that although neither of the two equations of state used is realistic, both a polytropic and an ideal-fluid equation of state can be considered as the extremes of the possible behaviour, with either a perfectly adiabatic evolution in which shocks cannot occur,

or of an evolution in which local increases of the temperature through shocks are allowed but cannot lead to radiative processes.

The right panel of Fig. 12.18 refers instead to the low-mass binary and again shows the  $h_+$  amplitude for the two equations of state. The interpretation is straightforward: in the case of the isentropic equation of state, the HMNS at merger has a small  $m = 2$  deformation and is still rather far from the instability threshold of collapse to a black hole. However, after about 15 ms, the HMNS has lost sufficient angular momentum to contract and collapse to a black hole (note that because of the contraction, the HMNS will actually spin up before producing a black hole). Conversely, in the case of the ideal-fluid equation of state, the HMNS is too far from the stability threshold to collapse over the 40 ms reported in the figure; the bar deformation, in fact, persists for more than 110 ms before collapsing to a black hole and has been reported in the right panel of Fig. 12.17 (Rezzolla *et al.*, 2010).

Much of what has been discussed so far when considering the gravitational-wave signal as a time-series applies also when it is considered in the frequency domain and this can be quantified by computing the power spectral density (PSD) of the *effective amplitude*  $\tilde{h}(f)$  for the different masses and equations of state. After defining the PSD as

$$\tilde{h}(f) := \sqrt{\frac{\tilde{h}_+^2(f) + \tilde{h}_\times^2(f)}{2}}, \quad (12.71)$$

where  $f$  is the gravitational-wave frequency and where

$$\tilde{h}_{+,\times}(f) := \int_0^\infty e^{2\pi i f t} h_{+,\times}(t) dt \quad (12.72)$$

are the Fourier transforms of the gravitational-wave amplitudes  $h_{+,\times}(t)$ , we can compare the PSDs with the sensitivity curves of modern and future gravitational-wave detectors.

This is shown in Fig. 12.19, which refers to the  $\ell = m = 2$  multipole, and whose left panel shows the scaled PSDs  $\tilde{h}(f)f^{1/2}$  for either a high-mass (left panel) or a low-mass binary (right panel) at a distance of 300 Mpc. Also in this case, blue and red lines refer to the polytropic and the ideal-fluid equation of state, respectively, while dot-dashed lines report the slope of the tracks following the post-Newtonian approximation, *i.e.*,  $\propto f^{-7/6}$ . Finally, shown with a black line is the phenomenological evolutionary track obtained using numerical-relativity calculations for a non-rotating black-hole binary with total mass  $M = 200 M_\odot$  (Ajith *et al.*, 2007). The PSDs are computed over the time-scale of survival of the HMNS and are compared to the sensitivity curves of present and future detectors: Virgo (dotted magenta line), advanced LIGO (green dot-dashed line), and Einstein Telescope (ET) [cyan long-dashed line, Punturo *et al.* (2010)].

After what was discussed above, the left panel of Fig. 12.19 is quite simple to interpret. It shows that besides the large power at low frequencies corresponding to the inspiral, there is a peak at  $f \approx 4$  kHz corresponding to the rapid merger of the two neutron stars. For the polytropic equation of state (blue line), where the merger is not mediated by increased pressure forces via shock heating, the gravitational-wave signal terminates abruptly with a prompt collapse to a black hole and a cutoff corresponding to the fundamental QNM frequency of the black hole at  $f_{\text{QNM}} \simeq 6.7$  kHz (Kokkotas and Schmidt, 1999). In contrast, the PSD for the ideal-fluid equation of state (red line) is more complex, with the inspiral peak being accompanied by a number of other peaks, the two most prominent, at  $f \approx 1.75$  kHz and  $f \approx 3$  kHz,

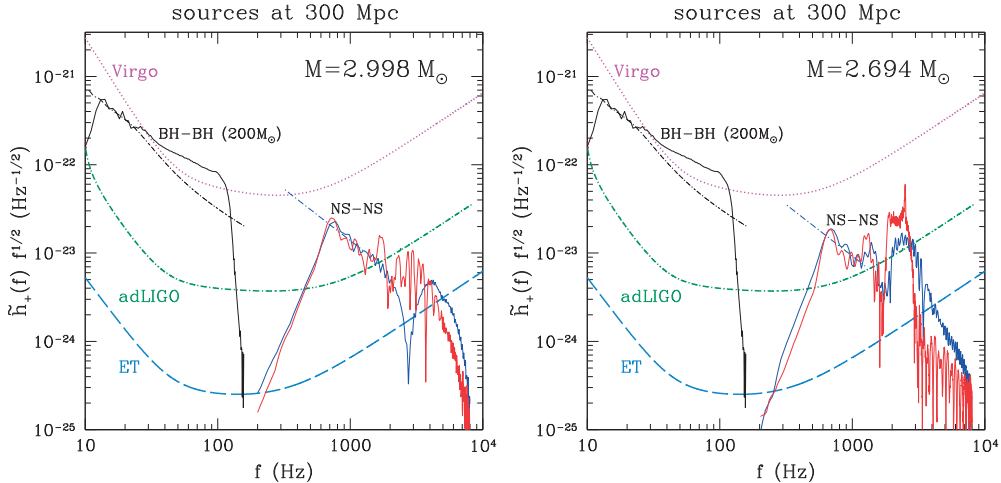


**Fig. 12.19** Left panel: PSD of the  $\ell = m = 2$  component of  $\tilde{h}(f)f^{1/2}$  for a high-mass binary when evolved with the polytropic (blue solid line) or with the ideal-fluid (red line) equation of state. Shown for comparison is the corresponding PSD for a black-hole binary (black solid line). Right panel: The same as in the left panel but for a low-mass binary, with the red line referring to the PSD computed when the HMNS survives for  $\sim 120$  ms. In both panels the dot-dashed lines indicate evolutionary tracks obtained using the post-Newtonian approximation [adapted from Andersson *et al.* (2011)].

having almost comparable amplitude. These additional peaks are related to the post-merger phase and to the dynamics of the HMNS, *i.e.*, the repeated merger-and-bounce of the two stellar cores. Eventually, the HMNS collapses to a black hole, leaving a signature at  $f \approx 4$  kHz. The fundamental QNM frequency at  $f_{\text{QNM}} \simeq 7.0$  kHz marks the cutoff of the signal also in this case.

The PSDs of the low-mass binaries in the right panel of Fig. 12.19 can be interpreted in a similar way, with the isentropic equation of state (blue line) showing a broad peak between  $f \approx 2$  kHz and  $\approx 3.5$  kHz, and related to the dynamics of the bar-shaped HMNS that persists for several milliseconds after the merger. A small excess at  $f \gtrsim 4$  kHz is associated with the collapse to a black hole, whose fundamental QNM has a frequency of  $f_{\text{QNM}} \simeq 7.3$  kHz.

Conversely, the PSD for the ideal-fluid equation of state (red line) does not show the broad peak, but a very narrow and high-amplitude peak around  $f \approx 2.5$  kHz, which is related to the long-lived HMNS. Since the latter is able to prevent the collapse to a black hole for  $\sim 110$  ms and since it is spinning at a rate of  $\sim 1.25$  kHz, it will perform  $N \sim 150$  revolutions, thus increasing the overall signal by a factor  $\sim \sqrt{N} \simeq 12$ . Besides the local increase in the gravitational-wave PSD, the *peak frequency* produced by the HMNS is also a faithful tracer of the stellar properties (*i.e.*, mass and radius) and hence a very good proxy to deduce the equation of state (Bauswein and Janka, 2012).

Three main conclusions can be drawn from the results shown in Fig. 12.19. First of all, with the exception of very massive neutron stars (in which case the collapse of the HMNS occurs essentially simultaneously with the merger), the gravitational-wave signal from binary neutron stars is considerably richer (and more complex) than that from binary black holes.

Second, while small differences between the two equations of state already appear during the inspiral, it is really the post-merger phase that is markedly different. Hence, an accurate description of the post-merger evolution is *essential* not only to detect this part of the signal, but also to extract information concerning the neutron-star interior structure. Finally, the parts of the PSD that are most interesting and more likely to yield fundamental clues to the physics beyond nuclear density, are also at very high frequencies and thus possibly only marginally detectable by detectors like advanced LIGO. As a result, third-generation detectors, such as ET, may provide the first realistic opportunity to use gravitational waves as a “Rosetta stone” to decipher the stellar structure and equation of state (Andersson *et al.*, 2011).

### **Vortex sheet and Kelvin–Helmholtz instability.**

As mentioned above, when the two stars come into contact, a *vortex sheet* (or *shear interface*) develops, where the tangential component of the velocity exhibits a discontinuity (*i.e.*, the  $x$  and  $y$  components of the three-velocity in our setup). This condition is known to be unstable to very small perturbations and it can develop a *Kelvin–Helmholtz instability*, which will curl the interface forming a series of vortices at all wavelengths (Chandrasekhar, 1981; Bodo *et al.*, 1994). Even if this instability is purely hydrodynamic and it is likely to be important only for binaries with very similar masses, it can have strong consequences when the stars are endowed with magnetic fields. Indeed, as suggested by Price and Rosswog (2006) with Newtonian simulations, in the presence of an initially poloidal magnetic field, this instability may lead to an exponential growth of the toroidal component. Such a growth is the result of the exponentially rapid formation of vortices that can curl magnetic field lines that were initially purely poloidal. The fully general-relativistic MHD simulations carried out by Giacomazzo *et al.* (2011) have shown that a strong toroidal component is indeed formed at the vortex sheet and that it reaches values that are comparable to or larger than the poloidal component, but its energy is not in equipartition with the kinetic energy in the layer. However, despite the exponential growth caused by the Kelvin–Helmholtz instability, the overall amplification of the magnetic field was found to be of one order of magnitude at most. This is in different from what was reported by Price and Rosswog (2006), where an amplification of several orders of magnitude in the magnetic field of the HMNS was observed.

In the left panel of Fig. 12.20 we show the isodensity contours and the velocity vector field on the equatorial plane for the high-mass binary evolved with a polytropic equation of state at a time  $t = 6.091$  ms, when the presence of vortices is particularly evident (very similar results were obtained also for an ideal-fluid equation of state). The density is shown in units of  $\text{g cm}^{-3}$  and in the bottom-right part of the plot an arrow is used as a reference for the values of the velocity in terms of the speed of light. Furthermore, in order to highlight the formation of the shear interface, we have removed from the total velocity field the orbital angular velocity defined as the angular velocity of the stellar centres. The vector-field representation shows rather clearly that the vortex sheet goes from the bottom-left corner of the plot to the upper-right one. Along this sheet one can observe at least four main vortices and two smaller ones with a scale of  $\gtrsim 2$  km. Of course, vortices of even smaller scales are expected to be produced down to the dissipative scale of the neutron-star matter; although the latter is highly uncertain at these physical conditions, it is at least six orders of magnitude smaller.

A different way of showing the presence of a vortex sheet and of the consequent development of a Kelvin–Helmholtz instability is offered in the right panel of Fig. 12.20, which shows

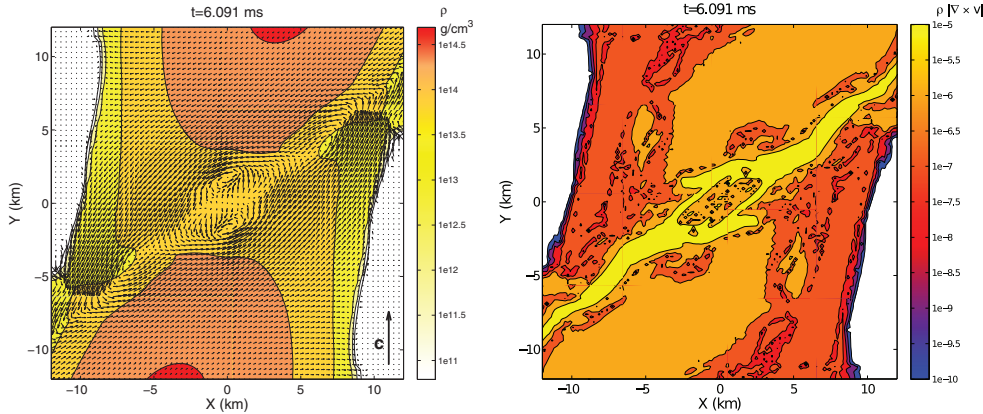


**Fig. 12.20** *Left panel:* Isodensity contours and velocity vector field in the  $(x, y)$  (equatorial) plane at a selected time soon after the merger (note that the orbital motion has been removed). Notice the presence of localised vortices in the shear layer between the two stars. *Right panel:* Contours of the weighted vorticity  $\rho |\vec{\nabla} \times \vec{v}|^z$  for the same time shown in the left panel. Both panels refer to a high-mass binary evolved with the polytropic equation of state. [Reprinted with permission from Baiotti *et al.* (2008). © 2008 by the American Physical Society.]

the contours of the ‘‘weighted vorticity’’ on the equatorial plane *i.e.*,  $\rho |\nabla \times \mathbf{v}|^z$ . Although this vector represents the Newtonian limit of the general-relativistic *kinematic vorticity tensor*  $\omega_{\mu\nu}$  [*cf.*, Eq. (3.11)], it serves the purpose here of being proportional to the latter and also of simpler calculation. The colour-code, which is in a logarithmic scale, highlights that the vorticity is not uniform in the merged object, but that its value in the vortex sheet is up to three orders of magnitude larger than in the bulk of the stars. Indeed, it is possible to compute the actual growth rate of the vorticity,  $\sigma \sim \pi v / \lambda$ , where  $v$  is the value of the velocity at the shear interface and  $\lambda$  is the wavelength of the smallest growing mode; for  $v \sim 10^{-2}$  and  $\lambda \sim 2$  km, the growth rate measured from the simulations is  $\sigma \simeq 10^3$  s<sup>-1</sup> (Baiotti *et al.*, 2008).

### 12.5.3 Dynamics of unequal-mass binaries

As mentioned in Section 12.5.1, binary neutron stars are expected to be produced with masses that are very similar and in this case the description given in the previous section is rather adequate. However, it is also obvious that a certain asymmetry in the mass is to be expected and hence it is interesting to discuss how the dynamics of the flow is affected in this case. Much of what is presented below is taken from Rezzolla *et al.* (2010), where additional details can be found. A representative example of the dynamics of an unequal-mass binary with an ideal-fluid equation of state is shown in Fig. 12.21, which reports isodensity contours in the equatorial plane for the inspiral and merger of a binary with a *mass ratio*<sup>21</sup>  $q := M_2/M_1 = 0.7$  and a total (gravitational) mass  $M_{\text{tot}} := M_2 + M_1 = 3.07 M_\odot$  (the corresponding rest mass

<sup>21</sup>Note that we define the mass ratio  $q := M_2/M_1$  in such a way that  $M_2$  always refers to the ‘‘secondary’’, *i.e.*, the less massive star. In this way the mass ratio is bounded between zero and one.

is instead  $M_{b,\text{tot}} = 3.37 M_\odot$ ). The asymmetry of the binary system is already apparent at the initial time, with the more massive star being more compact than the less massive companion, which is already deformed at the initial distance by tidal forces. During the inspiral phase, the heavier and more compact star is only slightly affected by its companion, whereas the latter is decompressed rapidly while being accreted onto the heavier star (see the three intermediate panels of Fig. 12.21).

The tidal disruption of the lower-mass neutron star, when it still retains a large fraction of its angular momentum, torques the high-mass star resulting in an extended tidal tail, which, unlike what happens in the equal-mass case, transfers angular momentum outwards very efficiently. In turn, this leads to the formation of large spiral arms extending well beyond the domain shown in Fig. 12.21 and ultimately to a more rapid ejection of matter. Quite generically, the matter which travels along the spiral arms away from the central object and is still gravitationally bound, will form an accretion torus around the central black hole that is considerably more massive than for equal-mass binary systems.

Because of the large initial mass of the system, the merged object rapidly collapses to a black hole. In contrast to the case of equal-mass binaries, where the black-hole properties do not change significantly after its formation, variations in the mass and spin of the black hole as large as 5% are possible for unequal-mass systems during the subsequent evolution. In addition, the black hole also has a recoil as a result of the asymmetrical emission of gravitational radiation in the final stages of the inspiral, although the velocity is  $\lesssim 100 \text{ km s}^{-1}$  and much smaller than what observed in black-hole simulations [see, *e.g.*, Koppitz et al. (2007)]. Yet, such a recoil could still yield astrophysically interesting results, being comparable to or larger than the escape velocity from the core of a globular cluster, that is,  $v_{\text{esc}} \sim 50 \text{ km s}^{-1}$  (Webbink, 1985).

In Fig. 12.22 we show the continuation of the dynamics reported in Fig. 12.21, but concentrating on the properties of the torus, both in the  $(x, y)$  plane (upper rows) and in the  $(x, z)$  plane (lower rows). The snapshots in the left column in Fig. 12.22, in particular, correspond to the time  $t \sim 10 \text{ ms}$  when the system enters the regime of quasi-stationary accretion (QSA), shortly after the formation of the black hole, while those in the right column refer to the final time of the evolution,  $t \sim 21 \text{ ms}$ . These panels allow for a closer view of the morphological features of the torus, its spatial dimensions and thickness and should be compared with the corresponding ones obtained with the equal-mass binary in Fig. 12.16.

The significant morphological differences between equal- and unequal-mass binaries are clearly visible when comparing these two figures. At black-hole formation, in fact, the equal-mass model produces a highly symmetric disc, while the unequal-mass model is characterised by the presence of a large spiral arm, which has not yet been accumulated onto the central disc surrounding the formed black hole. The asymmetry in the matter distribution at this stage is also apparent from the colour-map of the rest-mass density, and only much later the disc acquires a more axisymmetric shape. The diameters of the tori and their heights differ significantly between the two models; using the isodensity contour at  $\rho = 10^{10} \text{ g cm}^{-3}$  as the reference value below which material is not considered part of the disc, an equal-mass binary yields in general tori with diameters of  $\sim 50 \text{ km}$ , while these are of  $\sim 150 \text{ km}$  for unequal-mass binaries;<sup>22</sup> similarly, the corresponding vertical scales are  $\sim 5 \text{ km}$  and  $\sim 35 \text{ km}$ , respectively. Furthermore, if the tori differ by about a factor  $\sim 3$  in size, they differ by

<sup>22</sup>These numbers depend on the cutoff density and are more useful in a relative sense than in an absolute sense.

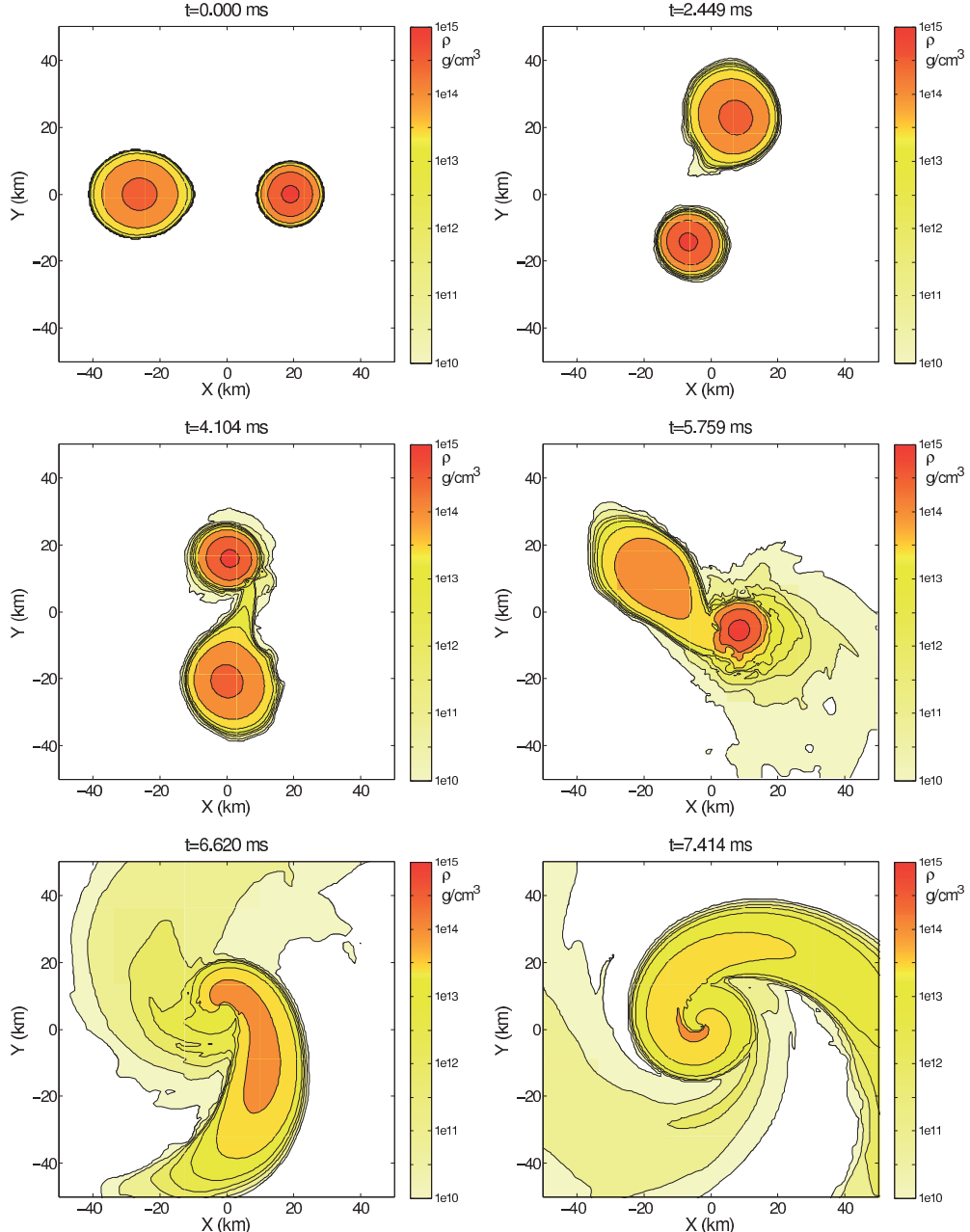


**Fig. 12.21** Isodensity contours in the  $(x, y)$  plane for the inspiral and merger of a binary with mass ratio  $q = 0.7$  and total mass  $M_{\text{tot}} = 3.07 M_{\odot}$ . The corresponding times are shown on the top of the different panels, while the colour-code for the rest-mass density is indicated on the right of each plot. The third frame shows the onset of the merger and the last two frames show the behaviour of the system during the collapse to a black hole. [From Rezzolla *et al.* (2010), reproduced by permission of IOP Publishing Ltd.]

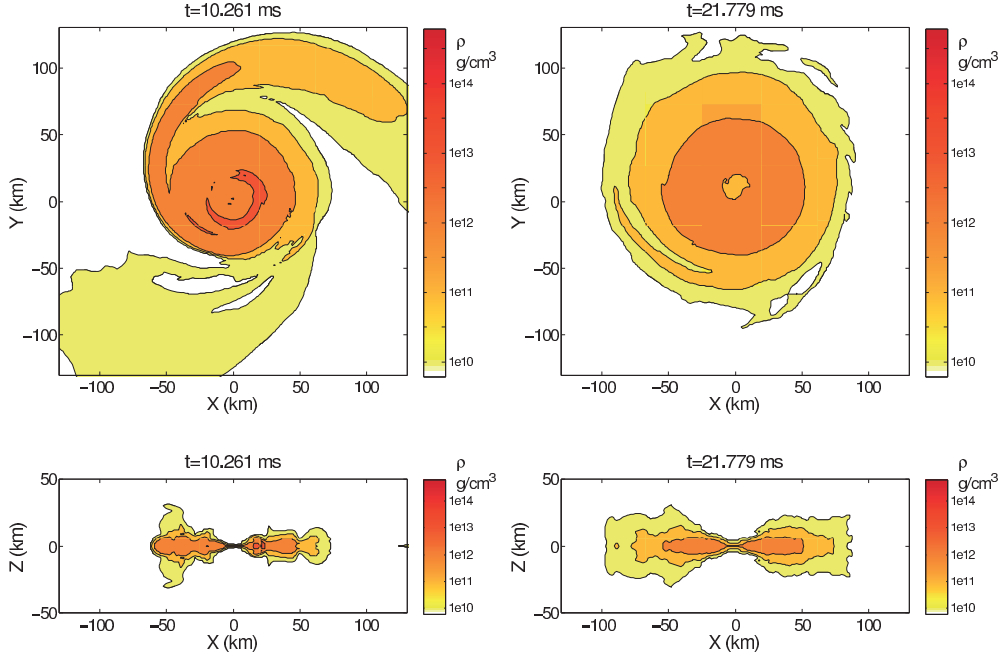


**Fig. 12.22** As in Fig. 12.21 but concentrating on the morphology of the tori at the onset of the QSA in the  $(x, y)$  plane (upper rows) and in the  $(x, z)$  plane (lower rows). Note that the colour-map used here is different from the one in Fig. 12.21; this torus should be compared with the smaller one obtained with an equal-mass binary in Fig. 12.16. [From Rezzolla *et al.* (2010), reproduced by permission of IOP Publishing Ltd.]

a factor  $\sim 200$  in mass, while having comparable mean rest-mass densities (see the further discussion below).

### Matter evolution and torus mass.

Once the black hole is formed, an effective potential well builds up in which the torus undergoes radial oscillations. In the case of an equal-mass binary, the well is essentially axisymmetric, with the corresponding dynamics that is very well approximated by that of oscillating relativistic tori in equilibrium and in axisymmetry (see the discussion in Section 11.7). The work of Zanotti *et al.* (2005) and Montero *et al.* (2007) has shown that, upon the introduction of perturbations in the tori, a long-term oscillatory behaviour is found, lasting for tens of orbital periods. These oscillations correspond to axisymmetric  $p$ -mode oscillations whose lowest-order eigenfrequencies are in the harmonic sequence 2:3. This harmonic sequence is present with a variance of  $\sim 10\%$  for tori with a constant distribution of specific angular momentum and of  $\sim 20\%$  for tori with a power-law distribution of specific angular momentum. The dynamics of the black hole–torus system produced by the merger of an equal-mass binary is considerably more complicated than that considered in the test-fluid studies, for which initial configurations in stable equilibrium could be found. Nevertheless, much of the phenomenology reported for test fluids continues to apply, with the evidence for a 2:3 harmonic relation

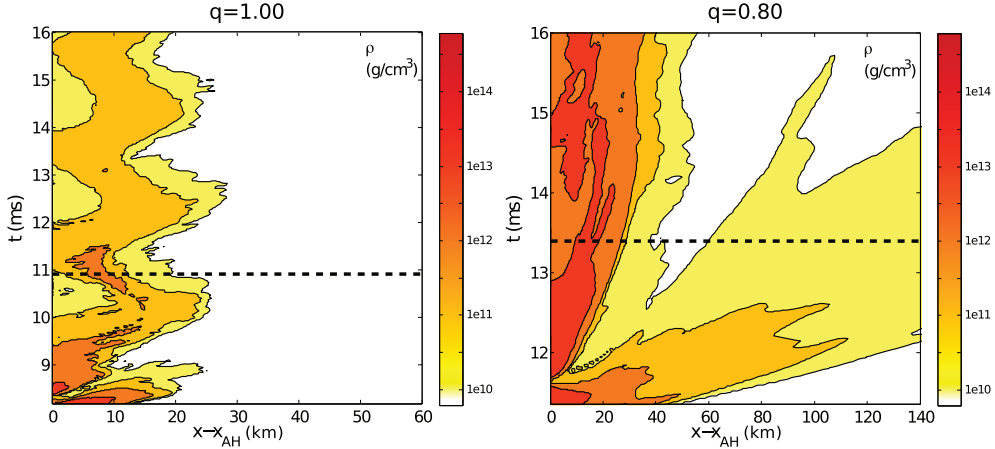


**Fig. 12.23** Evolution of the rest-mass density  $\rho$  along the positive  $x$ -axis in a frame comoving with the black hole. The panels show the colour-coded rest-mass density embedded in a spacetime diagram with the  $(x - x_{\text{AH}})$  coordinate on the horizontal axis,  $x_{\text{AH}}$  being the position of the apparent horizon, and the coordinate time  $t$  on the vertical axis. For each model, the dotted horizontal line marks the onset of the regime of QSA, with the left and right panels referring to an equal- and an unequal-mass binary with mass ratio  $q = 0.8$  [adapted from Rezzolla *et al.* (2010)].

between the oscillation frequencies, both for the density in the tori and for the accretion rate. Of course, the quality of the oscillations (*i.e.*, their amplitude and periodicity) is smaller for binaries with different masses, since in this case the tidal disruption during the merger leads to more asymmetric tori, which have a more complex dynamics. Interestingly, such oscillations seem to become more regular as the torus reaches a more axisymmetric configuration.

A useful way to analyse the evolution of the tori and gain some insight into their dynamics is offered by spacetime diagrams relative to an observer comoving with the black hole. These are shown in Fig. 12.23, which reports the evolution of the colour-coded rest-mass density embedded in a spacetime diagram with the  $(x - x_{\text{AH}})$  coordinate on the horizontal axis, where  $x_{\text{AH}}$  is the position of the apparent horizon, and with the coordinate time  $t$  on the vertical axis. To highlight the difference introduced by the mass asymmetry, the left panel refers to an equal-mass binary with total rest mass  $M_{b,\text{tot}} = 3.56 M_{\odot}$ , while the right panel refers to an unequal-mass binary with  $M_{b,\text{tot}} = 3.37 M_{\odot}$  and mass ratio  $q = 0.8$  (Rezzolla *et al.*, 2010).

By comparing the two spacetime diagrams for the two models it is evident that only the equal-mass model shows a global oscillatory movement with respect to the location of the black-hole horizon. The oscillation is indeed global as all the isodensity contours plotted vary simultaneously and the maximum and minimum radial extensions reached by the disc (as signalled by the location of the  $10^{10} \text{ g cm}^{-3}$  contour) are  $\sim 25 \text{ km}$  and  $\sim 15 \text{ km}$ , respectively. These oscillations are effectively producing the  $p$ -mode oscillations discussed above.

The unequal-mass binary, on the other hand, shows very rapid expansions corresponding to the ejection of the large spiral waves discussed above. Most of this matter is still bound but it nevertheless reaches distances which are several hundreds of km away from the black hole, leading to tori that have spatial dimensions as large as  $\sim 80 \text{ km}$ . Furthermore, noticeably

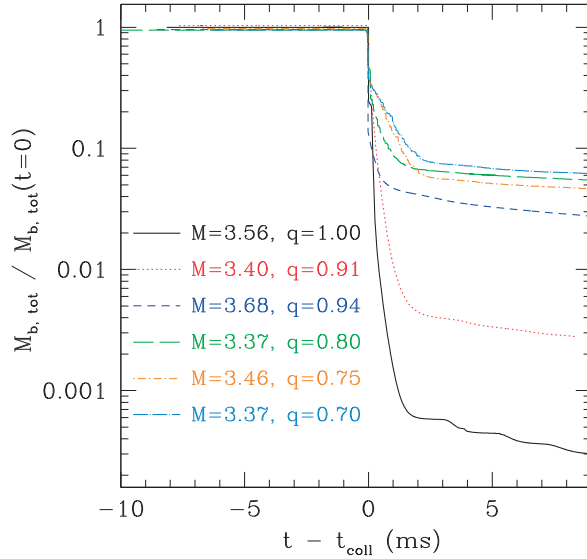


**Fig. 12.24** Evolution of the total rest masses normalised to their initial values for a number of unequal-mass binaries. The order of magnitude of the mass fraction in the accretion torus can be read off the logarithmic mass scale on the vertical axis. The curves referring to different models have been shifted in time to coincide at  $t_{\text{coll}}$ , which represents the time when the very rapid decrease of the total rest mass takes place. The mass in the legend is in solar masses [adapted from Rezzolla *et al.* (2010)].

higher average rest-mass densities are reached near the black hole, with maximum densities as high as  $\sim 10^{14}$  g cm $^{-3}$ . As a result, while tidal disruption sweeps away a large fraction of the external layers of the less massive star in the binary, the tori that are produced have matter with large specific angular momentum and can therefore sustain comparatively larger densities. We finally note that, because the matter in the spiral arms is bound, it will eventually fall back onto the tori, where it may lead to enhanced accretion and possibly lead a new and *delayed* gamma-ray emission (Giuliani *et al.*, 2010). Determining the dynamics of the fall-back material is therefore of great importance astrophysically.

Equally important is the matter that is actually accreted onto the black hole and which depends sensitively on the asymmetry in the mass of the binary. This is shown in Fig. 12.24, which reports the evolution of the total rest mass [defined as in Eq. (12.44)] for a number of binaries with different masses and mass ratios. All curves have been shifted in time to coincide at  $t_{\text{coll}}$ , which represents the (collapse) time, when a rapid decrease of the total rest mass takes place following the formation of a black hole. Note that the collapse time is not the same in different models, ranging from around 6 ms for the model with mass ratio  $q = 0.7$ , to around 11 ms for the model with  $q = 0.8$ . Overall, Fig. 12.24 shows that all models conserve the baryon mass almost perfectly (*i.e.*, with losses of  $\lesssim 10^{-6}$ ) up until the formation of the apparent horizon, after which most of the rest mass disappears in the singularity. The mass of the resulting accretion disc is larger for smaller values of  $q$ , but this trend is not

entirely monotonic as it is also influenced by the initial total baryon mass of the binary (see the additional discussion below). Of course, the mere definition of the torus mass is somewhat arbitrary, as the torus is continuously accreting. However, it is possible to determine a time when the disc enters a regime of quasi-steady accretion (QSA) and use this time for a robust measurement of the mass of the torus. This time will be different from binary to binary; just as different is the mass-accretion rate, which is systematically smaller for comparable-mass systems; however, all binaries will show a time when the accretion settles to a quasi-stationary stage and a meaningful measure is possible.

Using the results of a number of simulations and some simple physical considerations, Rezzolla *et al.* (2010) have built a phenomenological expression that reproduces reasonably well the mass distribution of tori produced in the merger of unequal-mass binaries, *i.e.*,

$$M_{b,\text{tor}} = [c_1(1 - q) + c_2][c_3(1 + q) - M_{\text{tot}}/M_{\text{max}}], \quad (12.73)$$

where  $M_{\text{tot}}$  and  $M_{\text{max}}$  are the (gravitational) mass of the binary and the maximum mass for an isolated neutron star with the same equation of state, respectively. The coefficients  $c_1 = 2.974 \pm 3.366$ ,  $c_2 = 0.11851 \pm 0.07192$ , and  $c_3 = 1.1193 \pm 0.1579$  were determined by fitting Eq. (12.73) to the results of the fully general-relativistic simulations of Baiotti *et al.* (2008) and Rezzolla *et al.* (2010), but rescaled to allow for a value of  $M_{\text{max}} = 2.20 M_{\odot}$  to be more consistent with current observations of neutron-star masses (see also Problem 4 for an interpretation of the physical significance of the coefficients). Overall, expression (12.73) indicates that: (1) the mass of the torus increases with the asymmetry in the mass ratio; (2) such an increase is not monotonic and for sufficiently small mass ratios the tidal disruption leads to tori that have a smaller mass for binaries with the same total mass; (3) tori with masses  $\lesssim 0.21 M_{\odot}$  have been measured and even more massive ones, *i.e.*, with masses up to  $\sim 0.35 M_{\odot}$ , are possible for mass ratios  $q \sim 0.75 - 0.85$ . This information has been recently exploited to set a relation between observations of the energy emitted by short GRBs and the mass of the tori presumed to feed them (Giacomazzo *et al.*, 2013).

### **Matter ejection.**

An important aspect of the formation and evolution of the tori is whether or not part of the rest mass of the system is ejected during the merger and the subsequent evolution. To determine whether a fluid particle is bound or unbound, it is possible to use the covariant time component of the four-velocity  $u_t$ . We recall that in a stationary spacetime, the value of  $u_t$  for a particle moving along a geodesic is conserved (see Section 1.5.4). If the particle is unbound, it will move outwards and have  $-u_t = W > 1$  at infinity. Stated differently, if a particle reaches infinity it is because it has  $u_t < -1$ . Furthermore, this condition is exact only in a stationary spacetime and, with the exception of the final stages of the evolution, the spacetime in a merging binary is far from being stationary. Nevertheless, this is a useful condition for a first estimate of the amount of matter ejected.

Figure 12.25 shows the evolution of  $u_t$  embedded in a spacetime diagram much like the ones presented before for the rest-mass density in Fig. 12.24. Clearly, for the equal-mass binary the criterion  $u_t > -1$  is well fulfilled (no parts appear in red), so that all the matter in the torus is bound. However, this is not the case for the unequal-mass binary with  $q = 0.80$ , which shows that in the early stages of its evolution a certain amount of unbound matter is ejected before reaching the regime of QSA (see the portion of the spacetime shaded in red).

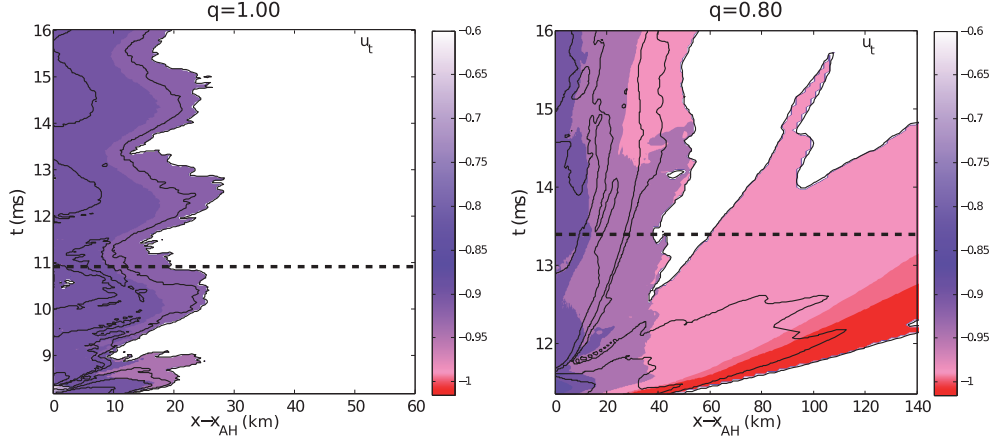


**Fig. 12.25** The same spacetime diagrams as in Fig. 12.23 but for the evolution of the local fluid energy  $u_t$ , so that regions in red indicate unbound matter. Note that the isocontours in this case refer to the rest-mass density and are the same as in Fig. 12.23 [adapted from Rezzolla *et al.* (2010)].

In practice, also for the outermost, very low-density regions of the tori (which are not shown in the spacetime diagrams of Fig. 12.25) values of  $u_t \leq -1$  are encountered and are probably a manifestation of an outflowing wind caused by the very large temperatures of those regions.

Note that although the total amount of matter ejected in this way is rather small and only of the order of  $\sim 10^{-4} M_\odot$ , it can nevertheless act as the site for the production of the neutron-rich heavy elements that are formed by rapid neutron capture, *i.e.*, the *r-processes* [see, *e.g.*, Freiburghaus *et al.* (1999) and more recently Korobkin *et al.* (2012)]. Performing such calculations and thus determining to what extent binary neutron star mergers contribute to the observed r-processed material in the interstellar medium requires a complete nuclear-reaction network, and is likely to be one of the most interesting aspects of binary neutron star mergers of future calculations.

#### Specific angular-momentum evolution.

Besides the rest-mass density, another quantity whose evolution can be very useful to understand the dynamics of the tori is the specific angular momentum. This quantity plays an important role in defining the dynamics of point particles around black holes and in defining the equilibrium of non-selfgravitating tori around black holes (see Section 11.7). As first discussed in Section 11.6.1, we define the specific angular momentum as  $\ell := -u_\phi/u_t$  [*cf.*, Eq. (11.153)], with the corresponding Newtonian limit being given by  $\ell_N = \Omega r^2$  (see Section 11.6.1). Figure 12.26 then shows, in analogy with Figs. 12.23 and 12.25, the evolution of the specific angular momentum for an equal- and an unequal-mass binary as measured by an observer comoving with the black hole. The most striking feature to note in Fig. 12.26 is that the radial distribution changes radically when going from the equal-mass binary on the left over to the unequal-mass binary on the right. In particular, while the specific angular momentum is decreasing outwards for the equal-mass model, it is essentially Keplerian and increasing outwards as  $\sim x^{1/2}$  for the unequal-mass model. Furthermore, the matter located

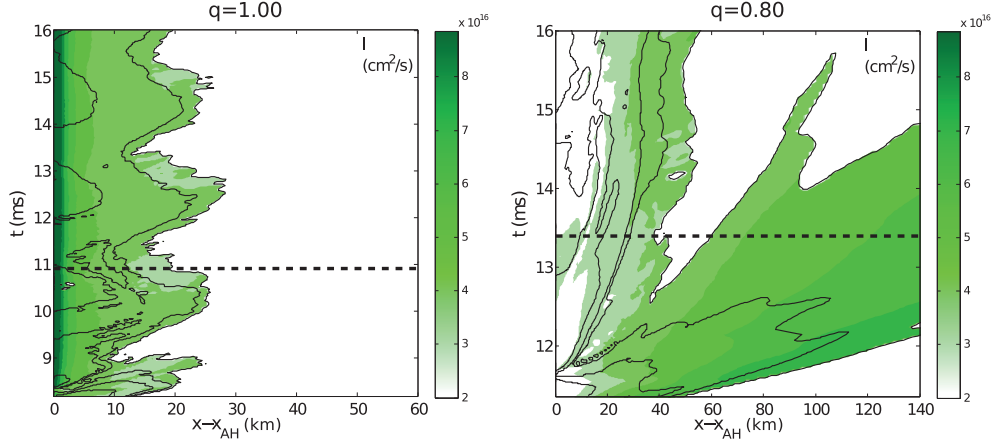


**Fig. 12.26** The same spacetime diagrams as in Fig. 12.23 but for the evolution of the specific angular momentum  $\ell = -u_\phi/u_t$ . Note that the isocontours in this case refer to the rest-mass density and are the same as in Fig. 12.23 [adapted from Rezzolla *et al.* (2010)].

in the outer regions of the torus, some of which is unbound, also acquires the largest values of the specific angular momentum. Broadly speaking, therefore, the simulations show that, the smaller the value of  $q$ , the more the angular momentum is transported outwards by a torque from the non-axisymmetric object that forms after the merger.

Interestingly, the Rayleigh criterion against axisymmetric perturbations of rotating fluids requires that  $d\ell/dx \geq 0$  for dynamical stability [see, *e.g.*, Tassoul (2007) and the discussion in Section 11.7]. While this criterion is clearly satisfied by the model with  $q = 0.80$ , it is also clearly violated by the equal-mass model, which is nevertheless stable on the dynamical time-scales explored by the simulations. This difference is probably due to the fact that the Rayleigh criterion assumes the motion to be stationary and purely azimuthal. While this is essentially the case for the unequal-mass binary, which does not show clear evidence of epicyclic oscillations, it does not hold true for the equal-mass binary, which shows instead large radial epicyclic oscillations. The nonlinear stability of the equal-mass model seems therefore to indicate that the Rayleigh criterion can and should be extended to account for fluids which are subject to large radial excursions. The conclusion that can be drawn from these simulations of unequal-mass binaries is that selfgravitating tori around black holes are stable at least on the dynamical time-scales investigated (see also the related discussion about the runaway instability in Section 11.7.1).

As a final remark, we note that a similar analysis can be carried out also for the evolution of the angular velocity  $\Omega := u^\phi/u^t$ . In this case, simulations indicate that, while the equal-mass binary has an exponentially decaying profile, *i.e.*, with  $\Omega \propto \exp[-k(x - x_{\text{AH}})] \sim \exp[-0.07(x - x_{\text{AH}})]$ , which does not change significantly with time, the unequal-mass binary reaches at the end of the simulation a profile which is essentially Keplerian, *i.e.*, with  $\Omega_K \sim x^{-3/2}$ , especially in the outer parts. This feature, which is also shared by the other low- $q$  binaries, explains the scaling of the specific angular momentum as  $\ell \sim x^{1/2}$  and provides firm evidence that the tori produced in this case will be dynamically stable.

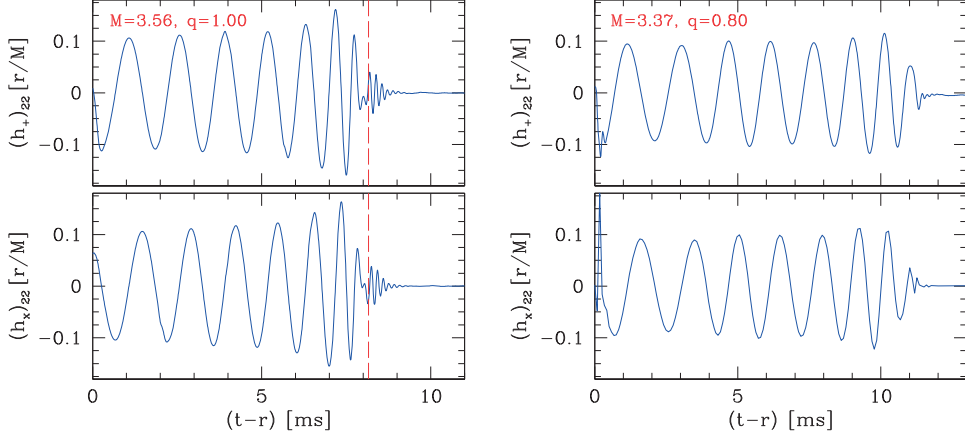


**Fig. 12.27** Gravitational waveforms in the two polarisations  $h_+$  (upper panels) and  $h_\times$  (lower panels) as computed from the lowest  $\ell = m = 2$  multipole for two binaries, whose total mass in the legend is expressed in solar masses. The vertical dashed lines mark the time of the first detection of the apparent horizon. As in previous figures, the left and right panels refer to an equal- and an unequal-mass binary with  $q = 0.80$ , respectively [adapted from Rezzolla *et al.* (2010)].

#### Gravitational-wave emission.

Figure 12.27 shows the waveforms in the two polarisations of the gravitational-wave amplitude  $(h_+)_\text{22}$  (upper panels) and  $(h_\times)_\text{22}$  (lower panels) for the two models considered also in the previous figures, *i.e.*, an equal-mass binary and an unequal-mass binary with  $q = 0.80$ . Note that the initial part of the inspiral of the unequal-mass binary shows contamination from an initial spurious burst of radiation, which is due to the larger initial violation of the constraint equations, despite the fact that the initial data is a consistent solution of the Einstein equations. The behaviour of the waveforms is straightforward to interpret: because of the very high total mass of the systems, no transient HMNS forms and the post-merger waveform is essentially the one corresponding to the collapse of the HMNS to a black hole. Indeed, the part of the waveform produced by the newly formed black hole starts essentially with the end of the inspiral (see Fig. 12.18).

While the ringdown of the black hole created after the merger can be identified in the waveform of the equal-mass binary, it becomes much less clear with decreasing mass ratio and it seems almost absent for mass ratios  $q \lesssim 0.7$ . Indeed it is necessary to examine the waveforms on a logarithmic scale in order to appreciate the presence of an exponential ringdown (Rezzolla *et al.*, 2010). This is due to the copious accretion of mass after the formation of the apparent horizon, which becomes increasingly large as the mass ratio decreases. As mentioned before, in fact, the mass accretion rate is highly sensitive to the mass ratio and inversely proportional to it (see Fig. 12.24). Under these conditions of very intense mass accretion, the black hole is continuously “hit” flows of matter that are generically non-spherical and prevent its natural ringdown, essentially “choking” it. Papadopoulos and Font (2001) have performed a detailed analysis of the role played by mass accretion on the properties of the ringdown.

Because of the intrinsically perturbative nature of their approach, a ringdown was always observed, independently of the mass-accretion rate. Hence, the different dynamics observed in Fig. 12.27 points to an interesting and novel nonlinear response of the black hole, which was not accessible to the perturbative work of Papadopoulos and Font (2001). Finally, we note that although the choking of the ringdown implies a net loss of signal, the latter is normally at rather high frequencies, so that the corresponding signal-to-noise ratio is not significantly smaller (Rezzolla *et al.*, 2010).

## 12.6 Dynamics of black-hole–neutron-star binaries

Another astrophysical system that represents an equally formidable arena of relativistic hydrodynamics is that of a binary composed of a black hole and a neutron star, *i.e.*, a *mixed binary*.

Many of the considerations made above about binary neutron stars continue to apply also for this type of binary. In particular, both the characteristic energy reservoir available in the system and the typical time-scales for the evolution of the binaries, make them suitable candidates to explain the phenomenology observed in short GRBs. Not differently from binary neutron stars, in fact, also this system could lead to the formation of a torus orbiting around a spinning black hole, which could supply a large amount of energy by neutrino processes or by extracting the rotational energy from the black hole. Finally, also in this case the binaries represent very strong sources of gravitational waves and advanced interferometric detectors are expected to observe these sources at a rate which is smaller than that for binary neutron stars, but still of  $\sim 0.2\text{--}300$  events per year, with a most realistic rate of  $\sim 10$  per year (Abadie *et al.*, 2010).

Also for this type of binary, the nonlinearity of the flow dynamics imposes the numerical solution of the equations of relativistic hydrodynamics in fully dynamical spacetimes for any accurate prediction, even though simplified toy models are surprisingly good at capturing the most salient aspects [see, *e.g.*, Pannarale *et al.* (2011)]. Fortunately, the same numerical techniques adopted in simulations of binary neutron stars in full general relativity can be adopted when computing the dynamics of mixed binaries (see the discussion in Section 12.5.1). On the other hand, simulations of this type have a much shorter history [see, *e.g.*, Löffler *et al.* (2006) for the first simulation in this respect] and a smaller space of parameters has been investigated so far. As a result, the level of maturity and accuracy of these simulations is in general somewhat smaller than for binary neutron stars. As an example, no direct comparison among different codes has yet been made [in contrast with what has happened for binary neutron stars (Baiotti *et al.*, 2010)] and the results of the simulations from different codes are sometimes not in agreement. In summary, while the broadbrush picture of the dynamics is by now clear, many of the details are not yet fully defined and will have to await further studies. In view of this, hereafter we will limit ourselves to provide only a brief overview of those aspects of the dynamics that are more robust and leave the details to the complete review of Shibata and Taniguchi (2011) for a complete discussion of the state of the art.

### 12.6.1 Broadbrush picture

In spite of the many dynamical aspects shared by neutron-star and mixed binaries, there are also some important differences, the most obvious one being that one member of the binary is now a black hole. In turn, this has two important implications. The first one is that the mass ratio,  $q := M/M_\bullet \leq 1$ , where  $M$  and  $M_\bullet$  are respectively the masses of the neutron star and of the black hole, cannot be close to one in this case. Rather, typical values to be expected in astrophysically realistic systems are in the range

$$0.10 \leq q \leq 0.33. \quad (12.74)$$

Furthermore, the most recent estimates for the mass accreted onto the primary compact object during the common-envelope phase are rather low and thus the black-hole masses in close black-hole–neutron-star binaries are likely to fall primarily on values near  $M_\bullet \simeq 10 M_\odot$  (Belczynski *et al.*, 2007). As a result, for a fiducial neutron star with mass  $M = 1.4 M_\odot$ , the most likely binary systems would have a mass ratio that is  $q \simeq 0.14$ . The second important difference brought in by the presence of a black hole is that the space of parameters acquires a new degree of freedom. In fact, in addition to the mass ratio, the equation of state (and hence the compactness of the star), and the strength of the magnetic fields, the dynamics of the binary will also be influenced by the spin of the black hole.<sup>23</sup>

The way in which the presence of the black hole modifies the dynamics of the binary can be appreciated, at least qualitatively, through some simple semi-Newtonian considerations. Let us therefore calculate the binary separation at which the tidal force experienced by a point particle on the surface of the neutron star will balance exactly the gravitational force exerted by the star. This separation is defined as the *tidal radius* and it is easy to derive that is given by (see Problem 5)

$$\frac{r_{\text{tide}}}{M_\bullet} = \left( \frac{M}{M_\bullet} \right)^{2/3} \frac{R}{M} = \frac{q^{2/3}}{\mathcal{C}}, \quad (12.75)$$

where, we recall,  $\mathcal{C} := M/R$  is the *stellar compactness* and  $R$  the stellar radius when the star is assumed as non-rotating and isolated. Overall, the tidal radius increases with the mass ratio and decreases with the stellar compactness. More specifically, at fixed black hole masses, small-compactness (*i.e.*, “Newtonian”) stars can be tidally disrupted at comparatively larger radii, while for fixed compactness the tidal break-up will happen at larger radii for more massive black holes.

The length-scale set by  $r_{\text{tide}}$  should be compared with another important one, namely the radius at which a point particle will no longer be able to have a stable circular orbit around the black hole. We have seen in Section 1.7.1 that this radius is that of the *innermost marginally stable orbit* or *ISCO*,  $r_{\text{ISCO}}$ , whose explicit expression for a generic black hole is given by Eqs. (1.267)–(1.268). Comparing now these two radii provides us with the two possible scenarios of the final stages of the binary. In fact, if  $r_{\text{ISCO}} \gtrsim r_{\text{tide}}$ , then the tidal forces exerted by the black hole will act only when the neutron star is very close to the horizon and the star will be “swallowed” essentially intact before entering the horizon. On the other hand, if  $r_{\text{ISCO}} \lesssim r_{\text{tide}}$ , then the neutron star will be tidally disrupted well before reaching the ISCO

<sup>23</sup>Note that as for binary neutron stars, the condition of irrotational flow for the neutron-star matter implies that the spin of the star is very small and dynamically negligible.

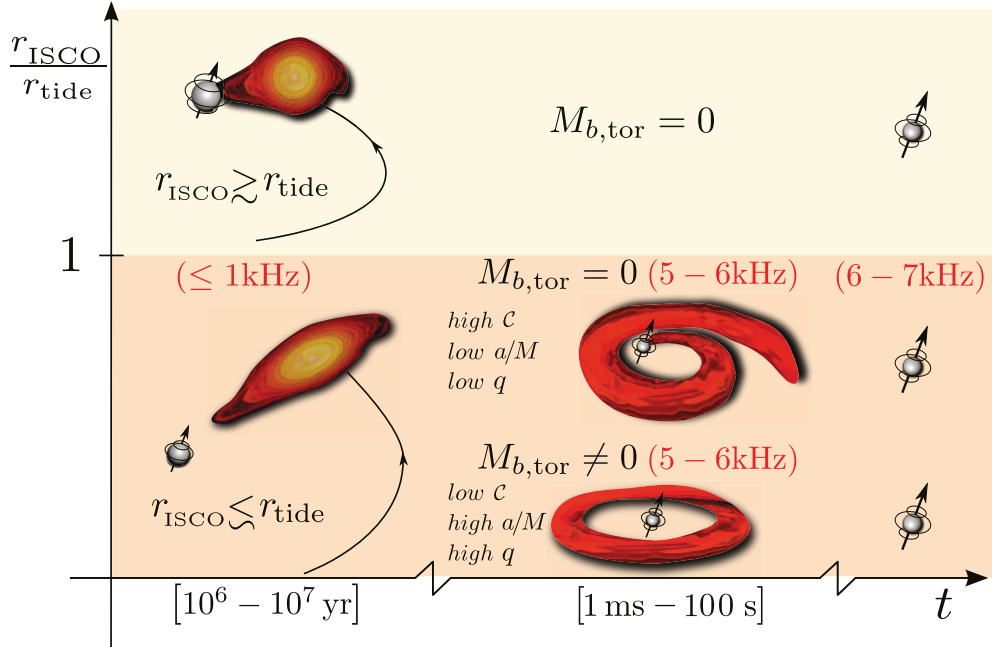


**Fig. 12.28** Schematic diagram illustrating the various stages in the evolution of black-hole–neutron-star binary and indicating how the dynamics changes in time as a function of the relative importance of the tidal radius (cf., Fig. 12.14). Two main scenarios are possible: global accretion, i.e.,  $r_{\text{ISCO}}/r_{\text{tide}} \gtrsim 1$  (top part), or tidal disruption, i.e.,  $r_{\text{ISCO}}/r_{\text{tide}} \lesssim 1$  (bottom part). In this latter case, the formation of a stable torus is possible for stars with low compactness, rapidly rotating black holes and high mass ratios. The typical frequencies at which gravitational waves are expected are indicated in red.

and its material will then either give rise to a spiral flow which will be accreted rapidly, or organise itself into an almost axisymmetric torus around the black hole. In this latter case, many of the properties of the flow dynamics discussed in the previous section for binary neutron stars apply unchanged here and do not need additional discussion.

As was done for binary neutron stars, we summarise in a cartoon in Fig. 12.28 the different stages in the possible evolution of a mixed binary system.<sup>24</sup> The diagram shows the different stages of the life of the binary as a function of time (horizontal axis) and of the ratio of the ISCO and tidal radius. Again, indicated in red are the typical frequencies of the gravitational-wave signal expected to be emitted. The two main scenarios considered in the figure refer to binaries in which either  $r_{\text{ISCO}}/r_{\text{tide}} \gtrsim 1$  (top part) or  $r_{\text{ISCO}}/r_{\text{tide}} \lesssim 1$  (bottom part). In both cases, the binary evolves for millions of years before reaching a separation small enough for tidal effects to become important.

Note that the dynamics is extremely simple in the case in which there is no tidal disruption (top part), namely: the star reaches the event horizon essentially whole (albeit highly

<sup>24</sup>The cartoon was made using images from fully general-relativistic numerical simulations. The images were produced by M. Koppitz (AEI/ZIB) and L. Rezzolla. The simulations were performed by Aaryn Tonita.

deformed) and is accreted on a time-scale  $\lesssim 1$  ms. Very little of the stellar matter is lost to infinity and the gravitational-wave signal is very similar to that of a point particle falling onto the black hole (Davis *et al.*, 1971) and, indeed, this scenario is more likely to take place for binaries with small mass ratios. On the other hand, two scenarios are possible when the tidal disruption happens outside the ISCO. These scenarios depend both on the properties of the star, most notably its compactness, and on the black-hole spin. In particular, the disrupted stellar matter is accreted rapidly over a time-scale of a few ms for stars that have large compactness and for black holes that are slowly rotating in binaries with small mass ratio; these conditions increase both the tidal radius and the location of the ISCO, but the former more than the latter (see the discussion below). The end-result of the process is therefore an isolated and rapidly rotating black hole in vacuum.

Conversely, for stars with small compactness and for black holes that are rapidly spinning in binaries with large mass ratios, the spiral flow of the disrupted star will be able to attain “closed” orbits, since in this case the ISCO moves to very small radii and the tidal radius is comparatively much larger. As a result, an approximately axisymmetric torus will be formed, whose dynamics will be rather similar to the one already discussed in the previous section for binary neutron stars. Once again, the torus will eventually accrete onto the black hole on a time-scale set by the most efficient process in removing angular momentum, namely, either gravitational radiation, magnetic fields or viscous processes, and which, again, can be estimated to be of the order of 1–100 s, or more. The final product is therefore a rapidly rotating black hole in vacuum.

Examples of numerical simulations are offered in Figs. 12.29 and 12.30, which report the isodensity contours in the  $(x, y)$  plane for two black hole-neutron star binaries.<sup>25</sup> In the binary shown in Fig. 12.29, in particular, the neutron star is modelled using an ideal-fluid equation of state with  $\Gamma = 2$  (see Section 2.4.6), and has a mass  $M = 1.40 M_\odot$  ( $M_b = 1.51 M_\odot$ ), with a rather realistic compactness of  $\mathcal{C} = 0.15$ . The black hole, instead, is non-rotating and with a mass  $M_\bullet = 7 M_\odot$ , so that the mass ratio is  $q = 0.2$ . The initial binary has a separation of  $d_0 \sim 100$  km and satisfies an irrotational-flow condition, so that the initial spin of the black hole is essentially zero (Grandclément, 2006). Despite the fact that the initial data uses an excision boundary condition at the apparent horizon, the interior solution can be filled smoothly by using a spectral extrapolation and requiring continuity and differentiability at the excision boundary (Brown *et al.*, 2009). This approach has been shown to be simple and effective in a number of different cases (Brown *et al.*, 2007; Etienne *et al.*, 2007).

As illustrated in Fig. 12.29, although the neutron star is already tidally disrupted at a distance of  $\gtrsim 50$  km, the bulk of the stellar matter does not find stable circular orbits and is forced to accrete onto the black hole through tight spiral orbits. This is particularly clear when reporting in the top right panel of Fig. 12.29 the position of the ISCO (blue dashed line), which is at  $r_{\text{ISCO}} \simeq 63$  km. Clearly, most of the stellar matter is within this radius and thus already on orbits that are unstable. Of course, the dynamics is more complex than the one that can be deduced from the motion of test particles and the position of the ISCO will change in time as a result of the accreted rest mass and angular momentum. Nevertheless, these considerations are sufficient to grasp the qualitative behaviour of the matter. At the end of the simulation, the black hole has a final mass  $M_{\bullet,f} = 8.26 M_\odot$ , a final dimensionless spin  $a/M_\bullet \simeq 0.42$ ,

<sup>25</sup>The simulations were performed by Aaryn Tonita.

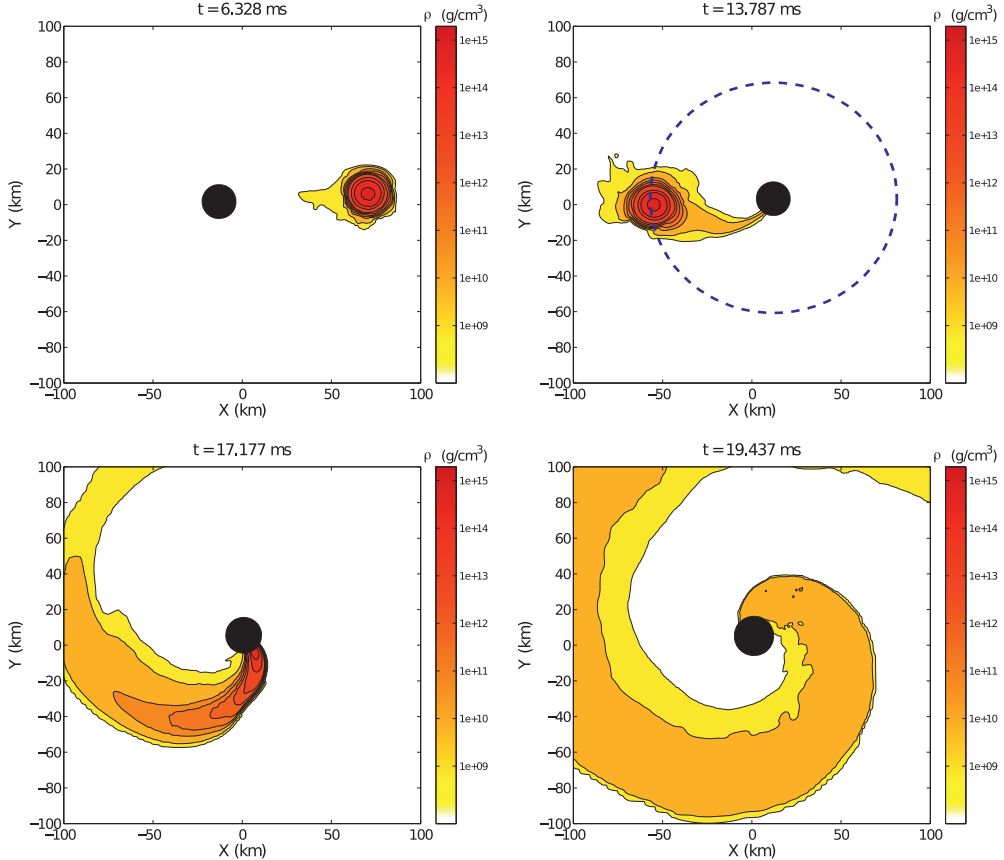


**Fig. 12.29** Isodensity contours in the  $(x, y)$  plane for the evolution of a mixed binary with mass ratio  $q = 0.2$ , when evolved with an ideal-fluid equation of state with  $\Gamma = 2$ . The black circle represents the apparent horizon of the black hole, which is non-rotating and with mass  $M_\bullet = 7 M_\odot$ . The star has a mass  $M = 1.40 M_\odot$  and a compactness  $\mathcal{C} = 0.15$ ; the blue dashed line in the top right panel marks the ISCO at that time. Note that a torus is not formed in this case because a large portion of the star is inside the ISCO at the tidal break-up (*c.f.*, Fig. 12.30).

while the rest mass left orbiting outside the black hole, and hence the rest mass of the torus, is vanishingly small.

The dynamics illustrated in Fig. 12.29, should be contrasted with the similar but distinct one shown in Fig. 12.30, where the binary shares most of the properties of the previous one, *i.e.*,  $M_\bullet = 7 M_\odot$ ,  $M = 1.40 M_\odot$  ( $M_b = 1.47 M_\odot$ ),  $q = 0.2$ ,  $d_0 \sim 100$  km, but also has an important difference, namely: a smaller compactness of  $\mathcal{C} = 0.10$ , as obtained after suitably specifying the polytropic constant (see Section 2.4.7). The tidal radius in this case is larger and the star, which is more “Newtonian”, can be disrupted at larger radii. More importantly, most of the stellar matter at disruption is outside the ISCO (see the top left panel of Fig. 12.29), and will therefore be able to find stable circular orbits, leading to the formation

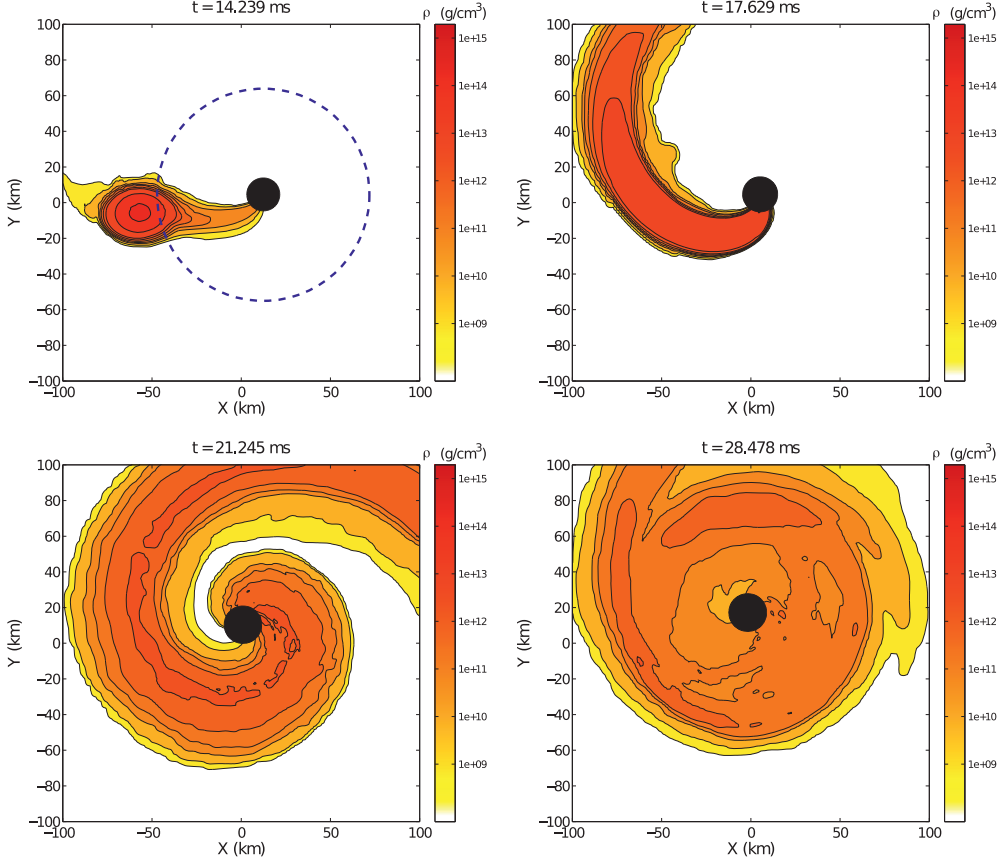


**Fig. 12.30** The same as in Fig. 12.29, but for a binary having the same black-hole mass and the same neutron-star mass, but with a compactness  $C = 0.10$ ; the blue dashed line in the top left panel marks the ISCO at that time. Note that a torus is formed in this case because a large portion of the star is outside the ISCO at the tidal break-up (*cf.*, Fig. 12.29).

of a torus around the black hole. At the end of the simulation, the black hole has a final mass  $M_{\bullet,f} = 8.09 M_{\odot}$ , a final dimensionless spin  $a/M_{\bullet} \simeq 0.37$ , while the torus has a rest mass  $M_{b,\text{tor}} \simeq 0.23 M_{\odot}$ . Interestingly, the black hole in this case has a slightly smaller mass but a considerably smaller dimensionless spin despite the fact that only part of the star has been accreted. The reason behind this counter-intuitive result is that the dimensionless spin is the ratio between the angular momentum acquired and the square of the associated mass. As a result, although the small-compactness star deposits more angular momentum onto the black hole, its mass is also larger and hence  $a/M_{\bullet}$  is smaller.

#### Matter evolution and torus mass.

We have already commented that the production of a massive torus orbiting stably around a rotating black hole is a necessary ingredient in all models that explain short GRBs in terms of

the coalescence of binary systems involving at least one neutron star. The accurate calculation of this mass inevitably requires the use of numerical-relativity simulations, which, however, are still very expensive and have so far been applied only to a small patch of the space of parameters. Furthermore, the higher dimensionality of the mixed-binary problem can only make the prospects less optimistic. As a result, two distinct approaches have been developed recently that try to solve the problem of determining the amount of rest mass in the torus without actually performing a numerical-relativity simulation.

In the first of these approaches, Pannarale *et al.* (2011) have constructed a toy model in which the neutron star is assumed to be a tri-axial ellipsoid, which is tidally distorted as it orbits in the tidal field of a rotating black hole and is described by the relativistic *affine model* (Carter and Luminet, 1982; Ferrari *et al.*, 2009). When the star is disrupted, it is decomposed into a system of non-interacting “fluid particles” which move on geodesics whose initial properties are known from the affine model. The mass of the torus can then be computed as the integral of the masses of the particles which do not fall into the black hole. This toy model has only one free parameter: the radius at which the tidal disruption takes place. While this cannot be deduced within the affine model, it can be tuned with the aid of numerical-relativity simulations, as long as the latter are accurate.

The predictions of this toy model are rather straightforward: high black-hole spins, small mass ratios and small neutron star compactness, all enhance the mass of the remnant torus. As a result, tori with masses as large as  $M_{b,\text{tor}} \simeq 1.33 M_\odot$  are predicted for a very extended star with a stellar compactness  $\mathcal{C} \simeq 0.1$  inspiralling around a black hole with dimensionless spin  $a/M_\bullet = 0.85$  and mass ratio  $q \simeq 0.3$ . However, when considering a more astrophysically reasonable mass ratio  $q \simeq 0.14$  and a conservative but realistic value of the compactness  $\mathcal{C} \simeq 0.145$ , the predictions set a considerably smaller upper limit of  $M_{b,\text{tor}} \lesssim 0.34 M_\odot$ . An example of this behaviour is shown in the left panel of Fig. 12.31, which shows the rest mass of the torus as a function of the stellar compactness  $\mathcal{C}$  and of the binary mass ratio  $q$  for a black hole with dimensionless spin  $a/M_\bullet = 0.4$ . Note that a mixed binary with a large mass ratio and a small compactness maximises the yields in terms of torus mass. For the same reasons, a binary with small mass ratio and large compactness will yield the smallest tori.

The second approach is even simpler and does not require any tuning of free parameters. More specifically, Foucart (2012) has derived a linear fit to the data of numerical simulations which expresses the torus mass in terms the mass of the star, its compactness and the location of the ISCO, *i.e.*,

$$M_{b,\text{tor}} = \left( \frac{M_b}{M} \right) \left[ c_1 \left( \frac{3}{q} \right)^{1/3} (1 - 2\mathcal{C})M - c_2 \mathcal{C} r_{\text{ISCO}} \right], \quad (12.76)$$

where  $c_1 = 0.288 \pm 0.011$  and  $c_2 = 0.148 \pm 0.007$ . Expression (12.76) requires knowledge of the ratio between the gravitational and baryon mass of the neutron star,  $M/M_b$ , for which no analytic expression is available, as it depends on the chosen equation of state. However, a large number of equations of state indicate that  $M/M_b \simeq 0.89\text{--}0.92$ , so that  $M/M_b \simeq 0.90$  is a reasonable first approximation. A representative cut of the torus mass as a function of the stellar compactness and of the black-hole’s spin is shown in the right panel of Fig. 12.31, for the most likely mass ratio of  $q = 0.14$  and a representative stellar mass  $M_b = 1.4 M_\odot$ . Note that the largest tori are obtained for the smallest compactness and for the largest spin, but

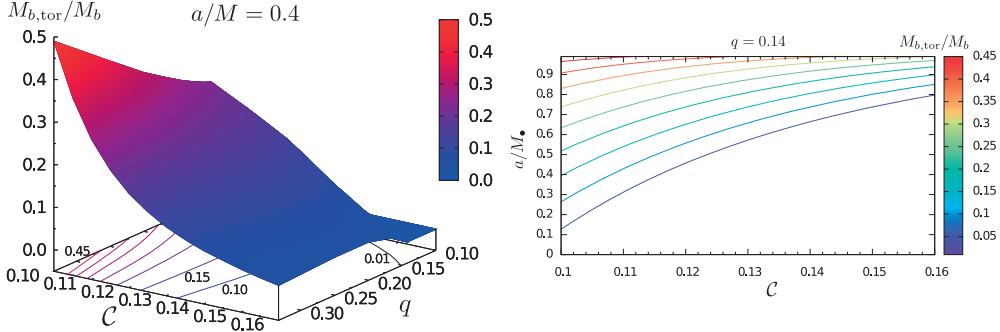


**Fig. 12.31** *Left panel:* Torus rest mass in units of the stellar mass,  $M_{b,\text{tor}}/M_b$ , shown as a function of the compactness  $\mathcal{C}$  and of the mass ratio  $q$ , for a black hole with spin parameter  $a/M_\bullet = 0.4$ . The data has been computed using a toy model. [From Pannarale *et al.* (2011), reproduced by permission of the AAS.] *Right panel:* Isocontours showing the torus rest mass in units of the stellar mass,  $M_{b,\text{tor}}/M_b$ , when presented as a function of the compactness  $\mathcal{C}$  and of the black-hole spin  $a/M_\bullet$ . The data is computed using expression (12.76) for a reference mass ratio of  $q = 0.14$  and a star with  $M_b = 1.4 M_\odot$ .

also that for realistic compactness, *e.g.*,  $\mathcal{C} \simeq 0.145$ , even very rapidly spinning black holes, *i.e.*,  $a/M_\bullet \gtrsim 0.95$ , would produce tori with masses not larger than  $M_{b,\text{tor}} \lesssim 0.42 M_\odot$ .

The qualitative predictions of the two approaches discussed above are obviously the same, although the fit presented by Foucart (2012) is more accurate since it provides a closer match to the numerical simulations (it is indeed a lower-order fit) and has been tuned with more accurate simulations than those used by Pannarale *et al.* (2011). As mentioned above, expression (12.76) has recently been used by Giacomazzo *et al.* (2013) in a study combining numerical simulations of compact binary mergers and a sample of short GRBs with measured energies, to constrain the mass of the tori that could be powering them. In particular, assuming a constant efficiency in the conversion of the torus mass into jet energy, it was found that most of the tori have masses smaller than  $0.01 M_\odot$ , thus favouring the idea that these tori result from the merger of binary neutron stars with large masses, *i.e.*, with total masses  $M_{\text{tot}} \gtrsim 1.5 M_{\text{max}}$ .

This conclusion has important consequences for the gravitational-wave signals that may be detected in association with short GRBs, since “high-mass” systems do not form a long-lived HMNS after the merger. Furthermore, while black-hole–neutron-star systems cannot be excluded from being the engine of at least some of the short GRBs, the black hole would need to have a very high initial dimensionless spin, *i.e.*,  $\sim 0.9$  or higher (Giacomazzo *et al.*, 2013).

### Gravitational-wave emission.

The concluding remark in this section will be dedicated to the gravitational radiation that is produced in the inspiral and merger of a black-hole–neutron-star binary. This is shown in Fig. 12.32, which reports the waveforms in the cross-polarisation  $h_x$  as computed from the lowest  $\ell = m = 2$  multipole for three representative binaries. All panels refer to binaries having the same total gravitational mass,  $M_{\text{tot}} = 8.34 M_\odot$ , the same neutron-star mass  $M = 1.40 M_\odot$ , but different compactnesses, *i.e.*,  $\mathcal{C} = 0.100, 0.125$  and  $0.150$ , from

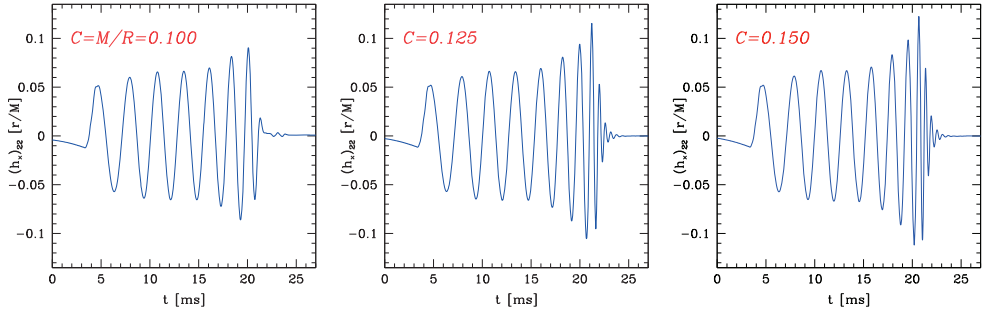


**Fig. 12.32** Gravitational waveforms in the cross-polarisation  $h_x$  as computed from the lowest  $\ell = m = 2$  multipole for three representative black-hole–neutron-star binaries. From left to right the panels refer to binaries having the same total gravitational mass,  $M_{\text{tot}} = 8.34 M_{\odot}$ , the same neutron-star mass  $M = 1.40 M_{\odot}$ , but different compactnesses, *i.e.*,  $C = 0.100, 0.125$  and  $0.150$ , respectively. Note that the ringdown is very clear for large  $C$ , but is choked for small  $C$ .

left to right.<sup>26</sup> What is quite clear when looking at these waveforms is that the black-hole ringdown is essentially absent in the case of the low-compactness binary (left panel), while it is quite clear for the high-compactness binary (right panel). As commented above for the gravitational-wave emission of unequal-mass binaries (see Fig. 12.27), this is due to the fact that a low-compactness star is easily destroyed tidally and in the case of small black-hole spin, most of its matter is on unstable orbits and hence accreting onto the black hole. The very high mass-accretion onto the black hole is then effectively preventing the black hole from ringing down, resulting in the waveform shown in the left panel of Fig. 12.32, but also in the right panel of Fig. 12.27.

When examined in frequency space, the gravitational waveforms shown in Fig. 12.32 are characterised by two fundamental frequencies: the *tidal frequency*  $f_{\text{tide}}$ , *i.e.*, the frequency marking the onset of *mass shedding*, and the *cutoff frequency*  $f_{\text{cutoff}}$ , *i.e.*, the frequency at which the gravitational-wave spectrum decays exponentially. Note that the latter incorporates the stellar ability to resist tidal deformations and reflects the genuine gravitational-wave emission of the dense stellar matter as it “plunges” onto the black hole. Hence, it is upper-limited but distinct from the fundamental QNM of the black hole,  $f_{\text{QNM}}$ , which can be easily estimated through an analytic expression derived from perturbation theory (Leaver, 1985; Echeverria, 1989)

$$f_{\text{cutoff}} \lesssim f_{\text{QNM}} \approx 3.23 \left( \frac{M_{\bullet}}{10 M_{\odot}} \right)^{-1} \left[ 1 - 0.63 \left( 1 - \frac{a}{M_{\bullet}} \right)^{0.3} \right] \text{ kHz}. \quad (12.77)$$

In turn, both of these frequencies are related respectively to the two orbital frequencies at which the star is first disrupted and at which it is fully accreted. These frequencies are clearly very close to each other but not identical, because the tidal disruption is not instantaneous and the gravitational-wave frequency changes rapidly in time, so that the transition

<sup>26</sup>The waveforms were computed by Aaryn Tonita.

from a chirping signal to an exponentially decaying one is pushed to higher frequencies. Numerical simulations indicate that a simple relation exists between the two frequencies, *i.e.*,  $f_{\text{cutoff}} \simeq (1.2 - 1.5)f_{\text{tide}}$  [see, *e.g.*, Shibata and Taniguchi (2011) for an extended discussion]. Furthermore, the difference between  $f_{\text{tide}}$  and  $f_{\text{cutoff}}$  increases as  $f_{\text{tide}}$  approaches the gravitational-wave frequency at the innermost stable circular orbit,  $f_{\text{ISCO}}$ . The latter is defined as the frequency yielded by the minimum of the binding energy of the binary system as expressed at the third order of the post-Newtonian approximation to general relativity (Vines *et al.*, 2011). In general, therefore, the four frequencies are such that<sup>27</sup>

$$f_{\text{tide}} \lesssim f_{\text{ISCO}} \lesssim f_{\text{cutoff}} \lesssim f_{\text{QNM}} . \quad (12.78)$$

The reason why the difference between the two frequencies  $f_{\text{tide}}$  and  $f_{\text{cutoff}}$  increases with  $f_{\text{ISCO}}$  is simple to explain: the tidal disruption takes place near the ISCO, *i.e.*,  $f_{\text{tide}} \sim f_{\text{ISCO}}$  only for rather compact stars that once destroyed will be more effective in perturbing the black hole, raising the cutoff frequency to  $f_{\text{cutoff}} \sim f_{\text{QNM}}$ .

The cutoff frequency for a mixed binary has the same importance that we have discussed for the *peak frequency* when considering the merger of two neutron stars. Also in this case, in fact, the cutoff frequency can be related to the stellar properties (*i.e.*, mass and radius) and hence acts as a proxy to deduce the equation of state. To assess whether  $f_{\text{cutoff}}$  is a faithful tracer of the stellar nuclear matter and can be used effectively to gain information on the equation of state, Pannarale *et al.* (2011) have recently computed the gravitational-wave phase evolution of mixed binaries when tidal effects are taken into account within a post-Newtonian approximation and compared it with the one expected when both the black hole and the neutron star are treated as point particles. The conclusion emerging from this investigation is that the tidal corrections to the evolution of the gravitational-wave phase depend sensitively on the equation of state, and also that such tidal corrections are generally small. As a result, for binaries at a generic distance of 100 Mpc, advanced interferometric detectors will be essentially “blind” to tidal effects and may be able to reveal them only for neutron stars with a particularly stiff equation of state and in large-mass-ratio binaries, *i.e.*, for  $q \gtrsim 0.2$  (Pannarale *et al.*, 2011).

<sup>27</sup>Note that at least in principle it is possible to consider binary systems in which  $f_{\text{tide}} \gtrsim f_{\text{ISCO}}$ , that is binaries in which  $r_{\text{ISCO}} \gtrsim r_{\text{tide}}$  [see, *e.g.*, Pannarale *et al.* (2011)]. However, as discussed in Fig. 12.28, in such systems the neutron star is accreted essentially intact and hence the concept of  $f_{\text{tide}}$  loses its significance.

### 12.7 Further reading

- Baumgarte, T. W. and Shapiro, S. L. (2010). *Numerical Relativity: Solving Einstein's Equations on the Computer*. Cambridge University Press, Cambridge.
- Faber, J. A. and Rasio, F. A. (2012). Binary neutron star mergers. *Living Rev. Relativ.*, **15**, 8.
- Font, J. A. (2008). Numerical Hydrodynamics and Magnetohydrodynamics in General Relativity. *Living Rev. Relativ.*, **11**, 7.
- Friedman, J. L. and Stergioulas, N. (2013). *Relativistic Rotating Stars*. Cambridge University Press, Cambridge.
- Shibata, M. and Taniguchi, K. (2011). Coalescence of black hole-neutron star binaries. *Living Rev. Relativ.*, **14**, 6.
- Stergioulas, N. (2003). Rotating stars in relativity. *Living Rev. Relativ.*, **6**, 3.

## 12.8 Problems

1. Starting from the Einstein equations (1.218) for a spherically symmetric, static perfect fluid, show that the only non-trivial equations reduce to Eqs. (12.9) and (12.10).
2. Starting from a spherically symmetric configuration such as the one in (12.21), show that for a gravastar with infinitesimally thick shell, the Einstein equations and the equation of energy–momentum conservation reduce to (12.23) and (12.24). In addition, show that the continuity of the metric functions  $f$  and  $h$  at  $R_i$  and  $R$ , provides the integration constants (12.30).
3. Show that in the case of a perfect fluid with anisotropic pressure described by the energy–momentum tensor (3.32), the Einstein equation and the equation of energy–momentum conservation reduce to Eq. (12.32).
4. Show that the coefficients  $c_2$  and  $c_3$  introduced in expression (12.73) have a direct physical interpretation. [Hint:  $c_2$  is proportional to the mass of the torus for equal-mass binaries, while  $c_3$  parameterises the excess of maximum mass that can be supported in the binary because of the stabilising effect produced by the nonzero spin of the stars and of the tidal potential.]
5. Use the Newtonian expression for the tidal force exerted by a black hole of mass  $M_\bullet$  and experienced by a point particle. Compare this with the gravitational force experienced on the stellar surface, with  $M$  and  $R$  being the stellar mass and radius, respectively. Show that this leads to expression (12.75).

# Appendix A

## Geometrised System of Units

---

The main motivation for choosing a geometrised system of units in general relativity is that, by providing a geometrical description of gravity, it turns out to be very natural to express every quantity in terms of lengths. The way this is obtained in practice depends on the number of quantities that one wants to “geometrise”. Suppose, for instance, that we are dealing with a physical system involving only three quantities, namely time, length and mass. The geometrisation is then obtained by selecting two physical constants of nature that contain those three quantities (and not other ones) and setting them to a *pure number*.<sup>1</sup> As far as the geometrisation of time, length and mass is concerned, the most obvious choice is to set to pure numbers the speed of light

$$c = 2.99792458 \times 10^{10} \text{ cm s}^{-1}, \quad (\text{A.1})$$

and the gravitational constant<sup>2</sup>

$$G = 6.67384 \times 10^{-8} \text{ cm}^3 \text{ g}^{-1} \text{ s}^{-2}. \quad (\text{A.2})$$

This implies that seconds and grams of the “cgs” system can be written as

$$1 \text{ s} = 2.99792458 \times 10^{10} \left( \frac{1}{c} \right) \text{ cm}, \quad (\text{A.3})$$

$$1 \text{ g} = 7.42565 \times 10^{-29} \left( \frac{c^2}{G} \right) \text{ cm}. \quad (\text{A.4})$$

Within this general setup in which all quantities are converted to lengths, it may still be useful to introduce a unit. In a gravitational context the most natural choice for such a unit is the *gravitational radius*  $r_g \equiv GM/c^2$ , with  $M$  being the mass of the source of the gravitational field. The mass itself can be expressed in units of the mass of the Sun,  $M_\odot$ , *i.e.*,

$$M = nM_\odot, \quad (\text{A.5})$$

with  $n$  a real number. From the physical measurement of the solar mass, *i.e.*,

<sup>1</sup>For a general physical system involving  $N$  quantities, the geometrisation will require selecting  $N - 1$  constants of nature involving those  $N$  quantities (and not more) and setting them to a pure number.

<sup>2</sup>The gravitational constant  $G$ , whose first measurement was performed by Cavendish in 1797–1798, is probably the least accurate among the physical constants. The value given in (A.2) is the one provided by CODATA (The Task Group on Fundamental Constants of the Committee on Data for Science and Technology) in June 2011 [see Milyukov and Fan (2012)].

$$M_\odot = 1.9884 \times 10^{33} \text{ g}, \quad (\text{A.6})$$

and from expressions (A.3)–(A.4), it is possible to find the relation between the cgs units and the new unit of length  $r_g$ , *i.e.*,

$$1 \text{ cm} = 6.77269 \times 10^{-6} \left( \frac{M_\odot}{M} \right) r_g, \quad (\text{A.7})$$

$$1 \text{ s} = 2.03040 \times 10^5 \left( \frac{1}{c} \right) \left( \frac{M_\odot}{M} \right) r_g, \quad (\text{A.8})$$

$$1 \text{ g} = 5.02916 \times 10^{-34} \left( \frac{c^2}{G} \right) \left( \frac{M_\odot}{M} \right) r_g. \quad (\text{A.9})$$

It is also useful to write explicitly the conversion between the cgs and *geometrised* systems of units for a generic length  $d$ , a time  $t$ , a mass  $m$ , a frequency  $f$ , a velocity  $v$ , a rest-mass density  $\rho$ , a pressures  $p$ , and a luminosity  $L$ , *i.e.*,

$$d_{\text{cgs}} = 1.47651 \times 10^5 \left( \frac{M}{M_\odot} \right) d_{\text{geo}} \quad (\text{A.10})$$

$$t_{\text{cgs}} = 4.92513 \times 10^{-6} c \left( \frac{M}{M_\odot} \right) t_{\text{geo}}, \quad (\text{A.11})$$

$$m_{\text{cgs}} = 1.9884 \times 10^{33} \left( \frac{G}{c^2} \right) \left( \frac{M}{M_\odot} \right) m_{\text{geo}}, \quad (\text{A.12})$$

$$f_{\text{cgs}} = 2.03040 \times 10^5 \left( \frac{1}{c} \right) \left( \frac{M_\odot}{M} \right) f_{\text{geo}}, \quad (\text{A.13})$$

$$v_{\text{cgs}} = 2.99792458 \times 10^{10} \left( \frac{1}{c} \right) v_{\text{geo}}, \quad (\text{A.14})$$

$$\rho_{\text{cgs}} = 6.17714 \times 10^{17} \left( \frac{G}{c^2} \right) \left( \frac{M_\odot}{M} \right)^2 \rho_{\text{geo}}, \quad (\text{A.15})$$

$$p_{\text{cgs}} = 5.55173 \times 10^{38} \left( \frac{G}{c^4} \right) \left( \frac{M_\odot}{M} \right)^2 p_{\text{geo}}, \quad (\text{A.16})$$

$$L_{\text{cgs}} = 3.62849 \times 10^{59} \left( \frac{G}{c^5} \right) L_{\text{geo}}, \quad (\text{A.17})$$

where the indices “cgs” and “geo” refer to the pure numbers expressing the generic quantity in the cgs system and in the geometrised system, respectively.

As a final remark we note that, in the traditional geometrised system,  $c$  and  $G$  are set equal to unity. However, this is just one of the possible choices and for specific physical applications, *e.g.*, where very low rest-mass densities are encountered, the corresponding value of  $\rho_{\text{geo}}$  may become excessively small to be used in numerical calculations. In these cases, it is more convenient to assume a smaller value for the gravitational constant, *e.g.*,  $G = 10^{-10}$ .

# Appendix B

## Notable Thermodynamic Expressions

---

### B.1 Thermodynamic quantities and potentials

Collected below is a list of the thermodynamic quantities and potentials that are often encountered when dealing with relativistic fluids.

$U$ :	internal energy,	$H$ :	enthalpy,
$G$ :	Gibbs free energy,	$F$ :	Helmholtz free energy,
$S$ :	entropy,	$T$ :	temperature,
$N$ :	particle number,	$V$ :	volume,
$e$ :	(total) energy density,	$\epsilon$ :	specific internal energy,
$\rho$ :	rest-mass density,	$p$ :	pressure,
$n$ :	number density,	$m$ :	particle mass,
$h$ :	specific enthalpy,	$s$ :	specific entropy,
$\bar{s}$ :	entropy per particle,	$\tilde{s}$ :	entropy density,
$\mu$ :	chemical potential,	$f$ :	specific Helmholtz free energy,
$c$ :	speed of light,	$c_s$ :	sound speed,
$c_V$ :	specific heat at const. volume,	$c_p$ :	specific heat at const. pressure,
$\gamma$ :	adiabatic index,	$\Gamma$ :	polytropic index,
$K$ :	polytropic constant,	$k_B$ :	Boltzmann constant,
$\zeta_c$ :	relativistic coldness,	$\alpha_f$ :	fugacity,
$a_R$ :	radiation constant.		

## 662 Notable Thermodynamic Expressions

Some notable algebraic relations among these quantities are:

$$e := \rho(1 + \epsilon), \quad (\text{B.1})$$

$$h := \frac{e + p}{\rho}, \quad (\text{B.2})$$

$$s := \frac{S}{Nm} = \frac{\bar{s}n}{\rho} = \frac{\tilde{s}}{\rho}, \quad (\text{B.3})$$

$$H := mNh = N \frac{(e + p)}{n}, \quad (\text{B.4})$$

$$G := \mu N, \quad (\text{B.5})$$

$$F := G - pV = U - TS, \quad (\text{B.6})$$

$$f := \frac{F}{Nm}, \quad (\text{B.7})$$

$$c_v := \left( \frac{\partial \epsilon}{\partial T} \right)_V = T \left( \frac{\partial s}{\partial T} \right)_V, \quad (\text{B.8})$$

$$c_p := c_v + \left[ \left( \frac{\partial \epsilon}{\partial \rho} \right)_T - \frac{p}{\rho^2} \right] \left( \frac{dp}{dT} \right)_p = \left( \frac{\partial h}{\partial T} \right)_p = T \left( \frac{\partial s}{\partial T} \right)_p, \quad (\text{B.9})$$

$$\gamma := \frac{c_p}{c_v} > 1, \quad (\text{B.10})$$

$$\alpha_f := \frac{m}{k_B T} \left( \frac{e + p}{\rho} - Ts \right), \quad (\text{B.11})$$

$$\zeta_c := \frac{mc^2}{k_B T}, \quad (\text{B.12})$$

$$c_s^2 := \left( \frac{dp}{d\epsilon} \right)_s = \frac{1}{h} \left[ \left( \frac{\partial p}{\partial \rho} \right)_\epsilon + \frac{p}{\rho^2} \left( \frac{\partial p}{\partial \epsilon} \right)_\rho \right], \quad (\text{B.13})$$

$$p = \rho\epsilon(\gamma - 1), \quad (\text{ideal fluid}) \quad (\text{B.14})$$

$$T = \frac{m}{k_B}(\gamma - 1)\epsilon = \frac{m}{k_B} \left( \frac{p}{\rho} \right), \quad (\text{ideal fluid}) \quad (\text{B.15})$$

$$c_s^2 = \frac{\gamma p}{\rho h} = \frac{\gamma(\gamma - 1)p}{\rho(\gamma - 1) + \gamma p}, \quad (\text{ideal fluid}) \quad (\text{B.16})$$

$$p = K\rho^\Gamma, \quad (\text{polytropic fluid}) \quad (\text{B.17})$$

$$\epsilon = \frac{K\rho^{\Gamma-1}}{\Gamma - 1}, \quad (\text{polytropic fluid}) \quad (\text{B.18})$$

$$c_s^2 = \left( \frac{1}{\Gamma K \rho^{\Gamma-1}} + \frac{1}{\Gamma - 1} \right)^{-1}, \quad (\text{polytropic fluid}) \quad (\text{B.19})$$

$$e_R = a_R T^4, \quad (\text{radiation fluid}) \quad (\text{B.20})$$

$$p_R = \frac{1}{3}a_R T^4 = \frac{1}{3}e_R, \quad (\text{radiation fluid}) \quad (\text{B.21})$$

$$S = \frac{4}{3}a_R T^3 V, \quad (\text{radiation fluid}) \quad (\text{B.22})$$

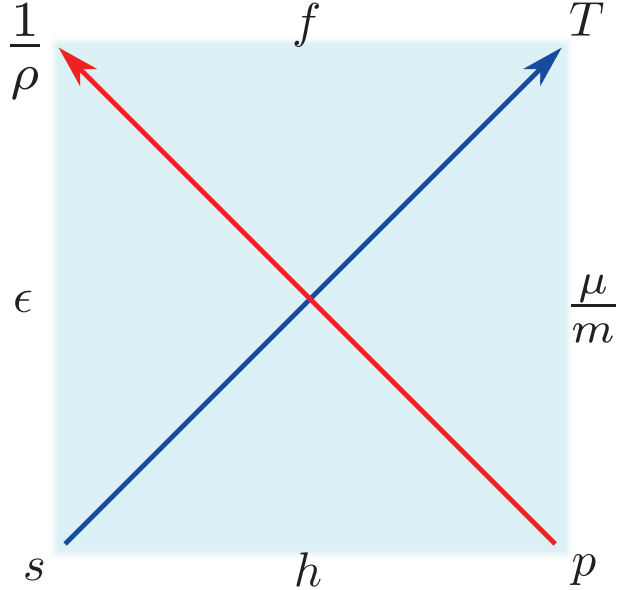


**Fig. B.1** The relativistic thermodynamic square. Using a simple algorithm, it allows one to derive straightforwardly a number of thermodynamic relations (see text).

## B.2 Maxwell relations

Several additional thermodynamic relations, including the first law of thermodynamics and the so-called *Maxwell relations*, can be obtained from the *thermodynamic square*, reported in Fig. B.1. The sides of the square correspond to the specific internal energy  $\epsilon$ , to the specific enthalpy  $h$ , to the specific chemical potential  $\mu/m$  and to the specific free Helmholtz energy  $f := F/(Nm)$ . The corners of the square, on the other hand, correspond to the specific volume  $1/\rho$ , to the specific entropy  $s$ , to the pressure  $p$  and to the temperature  $T$ .

The first law of thermodynamics can be expressed in four different forms, one for each side of the square. As an example, let us select the left vertical side, corresponding to  $\epsilon$ . Its differential  $d\epsilon$  will be written in terms of the differentials of the adjacent corners, namely,  $d(1/\rho)$  and  $ds$ . To find the coefficients for these differentials, it is necessary to follow the diagonals to the opposite corners and use the sense of the arrows to find the correct sign. In this way we obtain [cf., Eq. (2.137)]

$$d\epsilon = Tds - pd\left(\frac{1}{\rho}\right). \quad (\text{B.23})$$

The same logic applied to the bottom horizontal side allows us to obtain an equivalent form of the first law of thermodynamics

$$dp = \rho dh - \rho Tds. \quad (\text{B.24})$$

As mentioned above, the thermodynamic square can also be used to find the *Maxwell relations*, that is, a series of relations in terms of the derivatives of the thermodynamic quantities.

## 664 Notable Thermodynamic Expressions

In practice, any quantity along a given side must be regarded as a function of the two adjacent corners, *e.g.*,  $h = h(s, p)$ . The derivative of the side with respect to one corner, while keeping the other corner fixed, is obtained after looking at the quantity at the end of the diagonal, with the sign established by the orientation of the arrow. As an example, this simple rule allows us to find the following Maxwell relations

$$T = \left( \frac{\partial h}{\partial s} \right)_p , \quad \frac{1}{\rho} = \left( \frac{\partial h}{\partial p} \right)_s , \quad (\text{B.25})$$

$$T = \left( \frac{\partial \epsilon}{\partial s} \right)_\rho , \quad p = \rho^2 \left( \frac{\partial \epsilon}{\partial \rho} \right)_s , \quad (\text{B.26})$$

$$s = - \left( \frac{\partial(\mu/m)}{\partial T} \right)_p , \quad \frac{1}{\rho} = \left( \frac{\partial(\mu/m)}{\partial p} \right)_T , \quad (\text{B.27})$$

$$p = \rho^2 \left( \frac{\partial f}{\partial \rho} \right)_T , \quad s = - \left( \frac{\partial f}{\partial T} \right)_\rho . \quad (\text{B.28})$$

A bit of patience allows one to derive several additional relations, some of which are reported by Hiscock and Lindblom (1983) (pages 480–483), which represent a perfect exercise to become familiar with the Maxwell relations.

# Appendix C

## Notable Tensors

---

We report below the most relevant tensors, in their component notation, that have been used in the derivation of the relativistic-hydrodynamic equations.

### C.1 Relativistic expressions

A detailed discussion of the properties of the tensors presented here can be found in Sections 3.1.1 and 3.7.4.

$$\Theta := \nabla_\mu u^\mu , \quad (\text{expansion scalar}) \quad (\text{C.1})$$

$$a^\mu := u^\nu \nabla_\nu u^\mu , \quad (\text{kinematic acceleration four-vector}) \quad (\text{C.2})$$

$$\omega_{\mu\nu} := \nabla_{[\nu} u_{\mu]} + a_{[\mu} u_{\nu]} , \quad (\text{kinematic vorticity tensor}) \quad (\text{C.3})$$

$$\omega^\mu := \frac{1}{2} \eta^{\mu\nu\alpha\beta} \omega_{\alpha\beta} u_\nu , \quad (\text{kinematic vorticity four-vector}) \quad (\text{C.4})$$

$$\Omega_{\mu\nu} := 2 \nabla_{[\nu} h u_{\mu]} , \quad (\text{vorticity tensor}) \quad (\text{C.5})$$

$$\Omega^\mu{}_\mu = 0 , \quad (\text{trace of vorticity tensor}) \quad (\text{C.6})$$

$$\Omega^\mu := \frac{1}{2} \eta^{\mu\nu\alpha\beta} \Omega_{\alpha\beta} u_\nu , \quad (\text{vorticity four-vector}) \quad (\text{C.7})$$

$$\omega := \left( \frac{1}{2} \omega^{\mu\nu} \omega_{\mu\nu} \right)^{\frac{1}{2}} , \quad (\text{vorticity scalar}) \quad (\text{C.8})$$

$$\sigma_{\mu\nu} := \nabla_{(\mu} u_{\nu)} + a_{(\mu} u_{\nu)} - \frac{1}{3} \Theta h_{\mu\nu} , \quad (\text{shear tensor}) \quad (\text{C.9})$$

$$\sigma^\mu{}_\mu = 0 , \quad (\text{trace of shear tensor}) \quad (\text{C.10})$$

**666 Notable Tensors**

$$\sigma := \left( \frac{1}{2} \sigma^{\mu\nu} \sigma_{\mu\nu} \right)^{\frac{1}{2}}, \quad (\text{shear scalar}) \quad (\text{C.11})$$

$$\nabla_\nu u_\mu = \omega_{\mu\nu} + \sigma_{\mu\nu} + \frac{1}{3} \Theta h_{\mu\nu} - a_\mu u_\nu, \quad (\text{irreducible decomposition}) \quad (\text{C.12})$$

$$h_{\mu\nu} := g_{\mu\nu} + u_\mu u_\nu, \quad (\text{projection tensor}) \quad (\text{C.13})$$

$$T^{\mu\nu} = eu^\mu u^\nu + (p + \Pi)h^{\mu\nu} + q^\mu u^\nu + q^\nu u^\mu + \pi^{\mu\nu}, \quad (\text{C.14})$$

$$= (e + p)u^\mu u^\nu + pg^{\mu\nu} \quad \text{if} \quad q^\mu = 0 = \Pi = \pi^{\mu\nu}, \quad (\text{C.15})$$

(energy-momentum tensor)

$$q^\mu := -h^\mu{}_\alpha T^{\alpha\nu} u_\nu, \quad (\text{energy flux}) \quad (\text{C.16})$$

$$p + \Pi := \frac{1}{3} h_{\mu\nu} T^{\mu\nu}, \quad (\text{isotropic pressure and viscous bulk pressure}) \quad (\text{C.17})$$

$$\pi^{\mu\nu} := h^\mu{}_\alpha h^\nu{}_\beta T^{\alpha\beta} - (p + \Pi)h^{\mu\nu}, \quad (\text{anisotropic shear tensor}) \quad (\text{C.18})$$

$$\Pi = -\zeta \Theta, \quad (\text{C.19})$$

$$q_\mu = -\kappa T(h^\nu{}_\mu \nabla_\nu \ln T + a_\mu), \quad (\text{C.20})$$

$$\pi_{\mu\nu} = -2\eta \sigma_{\mu\nu}, \quad (\text{C.21})$$

where  $\eta$  and  $\zeta$  are the *shear viscosity* and the *bulk viscosity*, respectively.

## C.2 Newtonian expressions

To aid comparison with classical textbooks, *e.g.*, Landau and Lifshitz (1980), we report below the Newtonian expressions of the most relevant hydrodynamic tensors. A detailed discussion of the properties of the tensors presented here can be found in Section 2.2.6.

$$\theta := \partial_k v^k, \quad (\text{expansion scalar}) \quad (\text{C.22})$$

$$\omega_{\text{N}}^i := \epsilon^{ijk} \partial_j v_k, \quad (\text{vorticity vector}) \quad (\text{C.23})$$

$$\Lambda_{ij} := \frac{1}{2} (\partial_i v_j + \partial_j v_i), \quad (\text{strain tensor}) \quad (\text{C.24})$$

$$\Lambda_i^i = \theta, \quad (\text{trace of strain tensor} = \text{expansion}) \quad (\text{C.25})$$

$$\Lambda_{ij}^{\text{TF}} := \Lambda_{ij} - \frac{1}{3} \theta \delta_{ij}, \quad (\text{shear tensor}) \quad (\text{C.26})$$

$$P_{ij} := p \delta_{ij} - 2\eta \Lambda_{ij}^{\text{TF}}, \quad (\text{pressure tensor}) \quad (\text{C.27})$$

$$P_i^i = 3p, \quad (\text{trace of pressure tensor}) \quad (\text{C.28})$$

$$\mathcal{S}_{ij} := 2\eta \Lambda_{ij}^{\text{TF}} + \zeta \theta \delta_{ij} = -P_{ij} + (p + \zeta \theta) \delta_{ij}, \quad (\text{viscous stress tensor}) \quad (\text{C.29})$$

$$\mathcal{S}_i^i = 3\zeta \theta, \quad (\text{trace of viscous tensor}) \quad (\text{C.30})$$

$$\Sigma_{ij} := -p \delta_{ij} + \mathcal{S}_{ij} = -P_{ij} + \zeta \theta \delta_{ij}, \quad (\text{stress tensor}) \quad (\text{C.31})$$

$$\Sigma_i^i = 3(\zeta \theta - p). \quad (\text{trace of stress tensor}) \quad (\text{C.32})$$

# Appendix D

## Common Practices in Numerical Relativistic Hydrodynamics

---

This appendix is devoted to the discussion of a number of common practices in the numerical solution of the equations of relativistic hydrodynamics that are not easily found in the literature and that can make the difference between a successful or a failed simulation. We will first illustrate two optimised algorithms for the calculation of the primitive variables from the conserved ones (Section D.1), then move to the treatment of a low-density region, *i.e.*, of an “*atmosphere*” (Section D.2) and finally conclude with a discussion of how to effectively excise a region of the computational domain (Section D.4).

### D.1 Conversion from conserved to primitive variables

As mentioned in Section 7.3.3, the variables employed in the numerical solution of the relativistic-hydrodynamic equations when written in conservative form are of course the *conserved variables*  $D, S_i, \tau$  [*cf.*, Eqs. (7.231)<sub>1</sub> and (7.233)]. On the other hand, the fluxes and source terms are computed also in terms of the *primitive variables*  $\rho, v^i, p$ , and these represent the physical quantities we are most interested in. While the conversion from primitive to conservative variables can be done analytically through the relations (7.231)<sub>1</sub> and (7.233), *i.e.*, as

$$D := \rho W, \tag{D.1}$$

$$S_j := \rho h W^2 v_j, \tag{D.2}$$

$$E := \rho h W^2 - p, \tag{D.3}$$

$$\tau := D(hW - 1) - p = E - D, \tag{D.4}$$

the opposite conversion is not possible analytically and a numerical solution is needed to obtain the primitive variables from the conserved ones. In the following we describe the generic strategy behind this conversion, distinguishing between the case in which the equation of state is available in analytic form (Section D.1.1) from the one in which it is tabulated (Section D.1.2).

#### D.1.1 Analytic equations of state

Although several different routes are possible to perform the conversion, not all are equally efficient and robust. In the following we will discuss the well-tested procedures adopted in the numerical-relativity Whisky code (Baiotti *et al.*, 2005).

- We first consider a generic equation of state  $p = p(\rho, \epsilon)$ , e.g., the *ideal-fluid* equation of state (2.228) (see Section 2.4.6). In this case, the starting point is the solution to the following equation

$$p - \bar{p}[\rho(\mathbf{U}, p), \epsilon(\mathbf{U}, p)] = 0, \quad (\text{D.5})$$

where  $p$  is the value of the pressure to be found and  $\bar{p}[\rho(\mathbf{U}, p), \epsilon(\mathbf{U}, p)]$  is the pressure as obtained through the equation of state in terms of the conserved variables  $\mathbf{U}$  and of  $p$  itself. This can be done by inverting Eqs. (7.231)<sub>1</sub> to express  $\rho$  and  $\epsilon$  in terms of the conserved variables and of the pressure only, i.e.,

$$\rho = \frac{D}{\tau + p + D} \sqrt{(\tau + p + D)^2 - S^2}, \quad (\text{D.6})$$

$$\epsilon = D^{-1} \left( \sqrt{(\tau + p + D)^2 - S^2} - p \frac{\tau + p + D}{\sqrt{(\tau + p + D)^2 - S^2}} - D \right), \quad (\text{D.7})$$

where  $S^2 = \gamma^{ij} S_i S_j$ . Using these expressions it is then possible to solve numerically Eq. (D.5) with any root-finding algorithm [see Press *et al.* (1986) for several possible options]. If a derivative of (D.5) with respect to the pressure is necessary (e.g., as in the Newton–Raphson algorithm), this can be obtained as

$$\frac{d}{dp} \left\{ p - \bar{p}[\rho(\mathbf{U}, p), \epsilon(\mathbf{U}, p)] \right\} = 1 - \frac{\partial \bar{p}(\rho, \epsilon)}{\partial \rho} \frac{\partial \rho}{\partial p} - \frac{\partial \bar{p}(\rho, \epsilon)}{\partial \epsilon} \frac{\partial \epsilon}{\partial p}, \quad (\text{D.8})$$

where

$$\frac{\partial \rho}{\partial p} = \frac{DS^2}{\sqrt{(\tau + p + D)^2 - S^2}(\tau + p + D)^2}, \quad (\text{D.9})$$

$$\frac{\partial \epsilon}{\partial p} = \frac{pS^2}{\rho [(\tau + p + D)^2 - S^2](\tau + p + D)}, \quad (\text{D.10})$$

and where  $\partial \bar{p}/\partial \rho$  and  $\partial \bar{p}/\partial \epsilon$  can be easily calculated from the analytic equation of state. Once the pressure is found, the other variables follow simply through expressions (D.6) and (D.7), while the velocity is obtained after inverting (D.2).

- If the flow evolution is mainly smooth, with no or very moderate generation of shocks, the flow can be considered isentropic and the energy equation (3.57) can be replaced by the entropy conservation equation (3.61), which, after using the continuity equation, may also be rewritten as [cf., Eq. (7.230)]

$$\partial_t(\sqrt{\gamma} s D) + \partial_i [\sqrt{\gamma} s D (\alpha v^i - \beta^i)] = 0. \quad (\text{D.11})$$

It is then possible to define a new conserved variable  $\Sigma := sD = (p/\rho^{\Gamma-1})W$  [cf., Eq. (2.251)], in terms of which we can compute

$$Z := \rho h W^2 = W \left[ D + \frac{\Gamma}{\Gamma-1} \Sigma \left( \frac{D}{W} \right)^{\Gamma-1} \right]. \quad (\text{D.12})$$

Now squaring Eq. (D.2), we obtain

$$(Z^2 - S^2)W^2 = Z^2, \quad (\text{D.13})$$

and substituting  $Z$  from Eq. (D.12) into Eq. (D.13) provides a single equation in the unknown  $W$ , which can be solved with any root solver.

- A considerably simpler situation is the one in which the equation of state is still analytic and given by the polytropic expression (2.242). In this case, in fact, it is not even necessary to evolve the conserved energy  $\tau$ , which can be computed algebraically from the other quantities. Indeed, since  $d\epsilon = hdp$  for an isentropic transformation, the relativistic equation for the energy, Eq. (3.59), is automatically satisfied. It is therefore possible to solve only the nonlinear equation for the rest-mass density  $\rho$

$$\rho\tilde{W} - D = 0, \quad (\text{D.14})$$

where the pressure, the specific internal energy and the enthalpy are computed from the equation of state, *i.e.* (see Section 2.4.7)

$$p = K\rho^\Gamma, \quad \epsilon = \frac{K\rho^{\Gamma-1}}{\Gamma-1}, \quad h = 1 + \frac{\Gamma K \rho^\Gamma}{(\Gamma-1)\rho}, \quad (\text{D.15})$$

and the Lorentz factor is computed from Eqs. (7.231)<sub>1</sub> as

$$\tilde{W} = \sqrt{1 + \frac{S^2}{(Dh)^2}}. \quad (\text{D.16})$$

Equation (D.14) can then be solved numerically with a root-finding algorithm and in the case in which the Newton–Raphson algorithm is used, the derivative of (D.14) with respect to the density can be computed as

$$\frac{d}{d\rho}(\rho\tilde{W} - D) = \tilde{W} - \frac{\rho S^2 h'}{\tilde{W} D^2 h^3}, \quad (\text{D.17})$$

where

$$h' := \frac{\partial h}{\partial \rho} = \frac{1}{\rho} \frac{\partial p}{\partial \rho}, \quad (\text{D.18})$$

follows directly from Eq. (2.142) in the case of isentropic transformations. Once the rest-mass density is found, the other variables follow simply through expressions (D.15) and (D.16), while the velocity is obtained again after inverting (D.2).

### D.1.2 Tabulated equations of state

The use of a “realistic” tabulated equation of state (*e.g.*, of an equation of state for neutron-star matter that is the result of some nuclear-physics microscopic description) is considerably more complicated than the ones discussed so far. Firstly, while the calculation of the partial derivatives  $\partial\bar{p}/\partial\rho$  and  $\partial\bar{p}/\partial\epsilon$  needed in expression (D.8) is trivial in the case of an analytic equation of state, the corresponding calculation can be rather inaccurate in the case of a tabulated equation of state that is not sufficiently smooth, or whose derivatives are very small (this is a more common problem than one may think!). Overall, this aspect discourages one from using root-finding methods which require a derivative, *e.g.*, Newton–Raphson. Secondly, the space of the conserved quantities can easily contain large regions which do not correspond to physically valid values of the primitive variables.<sup>1</sup> In the following, we describe a scheme that detects unphysical conditions, allows for adjustments to physical conditions if desired, is robust also for extreme cases, and allows for a tight initial bracketing of the solution.

The approach discussed here is originally due to Kastaun (2012) and is suited to equations of state that depend also on the electron fraction  $Y_e$ , *i.e.*,  $p = p(\rho, \epsilon, Y_e)$  [*e.g.*, Lattimer and Swesty (1991) or Shen *et al.* (1998)]. To keep the notation compact, a few additional variables can be introduced, namely

$$a := \frac{p}{e}, \quad z := Wv = W\sqrt{v^i v_i}, \quad S := \sqrt{S^i S_i}, \quad (\text{D.19})$$

$$r := \frac{S}{D}, \quad q := \frac{\tau}{D}, \quad k := \frac{S}{\tau + D} = \frac{r}{1 + q}. \quad (\text{D.20})$$

Adopting the definitions above, the following identities hold

$$W = \sqrt{1 + z^2}, \quad W - 1 = \frac{z^2}{W + 1}, \quad z = \frac{r}{h}, \quad (\text{D.21})$$

$$\epsilon = Wq - zr + W - 1, \quad h = (1 + \epsilon)(1 + a) = (W - zk)(1 + q)(1 + a). \quad (\text{D.22})$$

Equally important are the definitions of the physical bounds of the different quantities which should be actively enforced, *i.e.*,

$$\epsilon \geq 0, \quad h \geq 1, \quad 0 \leq a \leq 1, \quad (\text{D.23})$$

while other bounds are less obvious and require a few lines of algebra. In particular, it is possible to show that the velocity is bounded to be

$$\frac{1}{2}k \leq v \leq k < 1, \quad (\text{D.24})$$

while the generalised “specific momentum”  $k = S/(\tau + D)$  is bounded to be

$$k < k_{\max} = \frac{2v_{\max}}{1 + v_{\max}^2} < 1, \quad (\text{D.25})$$

<sup>1</sup>Of course also analytic equations of state can have regions which are not physically valid, but the problem in that case is much easier to handle.

where  $v_{\max}$  is the maximum velocity expected. We note that a bound on  $k$  is much less problematic than bounds on other similar quantities, such as  $z$ . The latter can in fact become problematic because for realistic equations of state the energy density does not go to zero in the limit of zero rest-mass density at nonzero temperatures. As a result,  $h$  diverges in the same limit, leading to values of  $z$  that, although not divergent (no cell has zero rest-mass density as we will discuss in Section D.2), can nevertheless reach extremely high values and thus lead to expensive root-finding iterations. Finally, a bound can be found for the generalised ‘‘specific energy’’  $q$  as

$$q = Wh - 1 - \frac{p}{W\rho} \geq W - 1 + W\epsilon \geq 0, \quad (\text{D.26})$$

where  $q = 0$  holds only for  $r = 0$ .

Using the definitions (D.19)–(D.20) and the bounds (D.23)–(D.26), the conversion of the conserved variables to the primitive variables then consists of finding the root of the equation

$$f(z) = z - \frac{r}{\bar{h}(z)}, \quad (\text{D.27})$$

where

$$\bar{h}(z) = (1 + \bar{\epsilon}(z))(1 + \bar{a}(z)), \quad (\text{D.28})$$

$$\bar{a}(z) = \tilde{a}(\bar{\rho}(z), \bar{\epsilon}(z)), \quad (\text{D.29})$$

$$\bar{\rho}(z) = \frac{D}{\bar{W}(z)}, \quad (\text{D.30})$$

$$\bar{\epsilon}(z) = \bar{W}(z)q - zr + \frac{z^2}{1 + \bar{W}(z)}. \quad (\text{D.31})$$

Note that the function  $\tilde{a}$  first limits  $\bar{\rho}(z)$  and  $\bar{\epsilon}(z)$  to their allowed ranges and then computes the ratio  $a = p/e$  using the equation of state.

It is important that the expression for  $\bar{\epsilon}$  is written as above, which is accurate even for small velocities. Computing  $\bar{\epsilon}$  as in (D.22)<sub>1</sub>, in fact, would involve the quantity  $W - 1$ , which can lead to large cancellation errors in the limit of small velocities. Although these functions are well behaved for all values of  $z$ , they can produce unphysical values, *e.g.*,  $\bar{\epsilon} < 0$ , and thus the strategy is that of first finding the root [which can always be obtained given expressions (D.28)–(D.31)] and then to check if the solution is physically valid.

Note that Eq. (D.27) always admits a root, *i.e.*, a solution  $z_0$  such that  $f(z_0) = 0$ , and with a bit of algebra, it is also possible to show that it then falls in the rather tight interval  $z_0 \in [z_-, z_+]$ , where

$$z_- := \frac{k/2}{\sqrt{1 - k^2/4}}, \quad z_+ := \frac{k}{\sqrt{1 - k^2}}, \quad (\text{D.32})$$

since

$$f(z_-) \leq -\frac{W_- v_-^3}{1 - 2v_-^2} \leq 0, \quad f(z_+) \geq 0. \quad (\text{D.33})$$

Also in this case, once the solution  $z_0$  is found at the required precision, it is necessary to check that it is physically meaningful. If so, the other variables can be computed simply.

The advantage of the method discussed so far is that, besides introducing a function which is well-behaved, it offers a naturally tight bracketing. In turn, this removes the need of root-finding algorithms that require derivatives, such as Newton–Raphson. In practice, the use of the “regula–falsi” method, which decreases the bracketing around the root at each step, needs no derivatives, never evaluates the function outside the initial interval, provides super-linear convergence, and has been found to be efficient and robust in essentially all conditions commonly found in relativistic-hydrodynamic codes (Kastaun, 2012).

## D.2 Treatment of atmospheres

It is often the case, when modelling flows of selfgravitating relativistic fluids with Eulerian schemes, that some parts of the numerical domain will refer to portions of the space where the density and hence the pressure are expected to be zero. A standard example are the regions outside neutron stars, either when considered as isolated or in binary systems, which should represent regions that are nominally in vacuum. Configurations of this type are particularly common in general-relativistic simulations, where it is necessary to resolve well objects that are intrinsically compact (*e.g.*, neutron stars or black holes) and at the same time place the outer boundaries at very large distances from the compact object so as to be able to extract the gravitational radiation emitted. Ideally, such regions should be treated as in vacuum, *i.e.*, with zero values of the fluid pressure, density and velocity. In practice, however, the equations of relativistic hydrodynamics are not defined in vacuum, the speed of sound tends to zero as the density vanishes and the HRSC schemes discussed in Chapter 11 will inevitably fail.

A simple solution to this problem consists of the introduction of a tenuous “*atmosphere*”, that is, of a low-density and low-pressure region filling the supposedly vacuum regions around the compact objects. In this way, the equations of relativistic hydrodynamics can be solved equally in *all* gridzones, thus without resorting to a costly and cumbersome discrimination of vacuum and non-vacuum cells. The first implementations of this technique in numerical-relativity HRSC codes is due to Font *et al.* (2002) and it has been subsequently investigated systematically by Baiotti *et al.* (2005), becoming a common approach in essentially all numerical-relativity codes [see Kastaun (2006) for a notable exception].

While the treatment of the atmosphere can vary from code to code, in practice, what is done in most codes [*e.g.*, in the Whisky code of Baiotti *et al.* (2005)] is to check, before computing the fluxes necessary for the time-update of the equations of relativistic hydrodynamics in conservative form [*cf.*, Eqs. (9.15)], whether the conserved rest-mass density  $D$  is below some minimum value  $D_{\text{th}}$ , or whether an evolution step might push it below such a value<sup>2</sup> [these estimates can be done easily with a rough approximation of Eqs. (7.230)]. If this is the case, the relevant cell is not evolved and the hydrodynamic variables at that point are set to “atmospheric values”, namely, the conserved rest mass is set to  $D_{\text{atmo}} < D_{\text{th}}$ , the conserved momenta  $S_j$  are set to zero (so as to avoid the atmosphere accreting onto the compact object), and the conserved energy  $E$  is reset to be consistent with  $D_{\text{atmo}}$  through the adopted equation of state.

<sup>2</sup>A similar validation can also be performed equivalently on the conserved energy  $E$  [*cf.*, Eqs. (7.231)].

A similar check is performed also when converting from conserved variables to primitive variables, as discussed in Section D.1. More specifically, an attempt is made to convert the conserved variables to the primitive ones. If the iterative algorithm returns a value of the rest-mass density  $\rho$  which is negative or below a threshold  $\rho_{\text{th}}$ , then  $\rho$  is reset to the atmosphere value  $\rho_{\text{atmo}} \leq \rho_{\text{th}}$ , the velocities are set to zero and  $p, \epsilon$  are reset to be consistent with  $\rho_{\text{atmo}}$  using the equation of state. Once the primitive variables are set to the atmospheric values, the conserved ones are also reset through their definition [*cf.* Eqs. (7.231)]. As a result of this procedure, at the end of the time-update, a fraction of the cells in the numerical domain will be filled with matter corresponding to the atmosphere.

In principle, choosing the correct values for  $D_{\text{atmo}}$  or  $\rho_{\text{atmo}}$  will depend on the specific problem under consideration and on the resolution used, the only requirement being that the contributions of the atmosphere to the total energy and momentum content of the spacetime should be negligibly small. In practice, if  $D_{\max}$  or  $\rho_{\max}$  are the maximum values of the conserved or primitive rest-mass density on the whole numerical domain, the atmosphere is set to be between eight and ten orders of magnitude smaller, *i.e.*,  $D_{\text{atmo}}/D_{\max} = \rho_{\text{atmo}}/\rho_{\max} \sim 10^{-8} - 10^{-10}$ . On the other hand, the difference between the threshold value and the atmospheric one is in general much smaller, *i.e.*,  $D_{\text{th}}/D_{\text{atmo}} = \rho_{\text{th}}/\rho_{\text{atmo}} \sim 1.1-1.2$ . Indeed, a threshold value slightly larger than the atmospheric one is introduced simply because if the variables were set precisely to the atmospheric ones, then very small errors (generated, for instance, in the recovery from the conserved values) would start to move certain cells above the atmosphere values. This would then lead to “waves” of matter accreting onto the compact object which, despite the extremely low density, could influence its evolution. As an example, in the case of isolated neutron stars, this effect produces visible secondary overtones in the stellar oscillations (Baiotti *et al.*, 2005).

It is important to emphasise that although the approach described above turns out to be effective and robust, it needs care nevertheless. Indeed, since the use of an atmosphere amounts *de facto* to the imposition of a series of boundary conditions in all the gridzones filled with the atmosphere, it is imperative to validate that the results are not influenced by the physical properties of the atmosphere. For example, it is important to verify that the presence of an atmosphere does not have an impact on the formation of thermal winds from the compact objects, that it does not distort the oscillation properties and that, under all circumstances, the atmospheric rest-mass contribution to the field equations (both for the evolution and the constraint equations) is always negligibly small.

### D.3 Guaranteeing the positivity of pressure

A problem related to the one discussed in the previous section, but also distinct from it, is represented by the necessity of maintaining pressure and density positive during a numerical simulation. This problem is recurrent in those situations in which a high-density medium propagates into a second medium whose density is known to be smaller, but is still high enough to affect its dynamics. This can, for instance, be the case of a jet propagating in an ambient medium, or of the corona surrounding a relativistic accretion disc. Under such conditions, a treatment like the one presented in Section D.2 would not be adequate, as it would inevitably alter the interaction between the high-density and the low-density media, which is part of the problem one actually wants to investigate.

A possible strategy that can be adopted consists of replacing the energy equation, namely the fifth of Eqs. (7.231), with the equation for the evolution of the specific entropy  $s$ , *i.e.*, Eq. (D.11), where  $\Sigma := sD = (p/\rho^{\Gamma-1})W$  is the new conserved variable replacing the total energy [*cf.* Eq. (7.233)]. In contrast to Eq. (D.11), this replacement is not made across the whole computational domain but only in those cells where the standard recovery of the primitive variables produces a negative pressure. Since it has the same form of the continuity equation, Eq. (D.11) is much more robust and less likely to yield a negative value for the pressure. Such a procedure, combined with the use of a linearised Riemann solver and the use of suitable criteria for identifying in advance the “risky” numerical cells, was proposed by Balsara and Spicer (1999), who applied it in the context of Newtonian magnetohydrodynamics. The major drawback of this approach is that it is based on the assumption that the specific entropy remains constant along a fluid line. Although this is certainly the case for a perfect fluid in the absence of shocks, this condition is violated precisely in those regions experiencing large density gradients and where shocks may effectively form.

Pressure positivity-preserving schemes have been studied in detail and on more rigorous mathematical grounds for the non-relativistic Euler equations. Starting from Perthame and Shu (1996), a large number of different techniques have been proposed, which ultimately aim at reducing the variation of the evolved variables, while preserving the accuracy of the scheme (Zhang and Shu, 2010; Balsara, 2012). While the extension of these ideas to the relativistic case has not yet been reported, work is in progress.

## D.4 Domain excision

It is not unusual, when performing numerical-relativity simulations of compact objects, that one may wish to remove from the computational domain those regions where the solution is either physically unimportant (*e.g.*, inside an apparent horizon), or prone to large numerical errors (*e.g.*, close to a physical singularity), or simply too expensive computationally (*e.g.*, in numerical codes based on spherical coordinates which have the most severe CFL restriction coming from the innermost cells). In these cases, *excision boundaries* can be introduced, by means of which spatial parts of the computational domain can be removed from the time-update algorithms. The technique of domain excision is based on the principle that a region of spacetime that is causally disconnected can be ignored without affecting the solution in the remaining portion of the spacetime (see Fig. 4.3). Although this is true for signals and perturbations travelling at physical speeds (*i.e.*, the sound speed or the speed of light), numerical calculations may violate this assumption and disturbances, such as gauge waves, may travel at superluminal speeds, thus leaving the physically disconnected regions.

Since in general the propagation speeds of metric fields and of fluid disturbances are different, the corresponding excision boundaries are also different. For the fluid quantities, in fact, all characteristics emanating from an event in spacetime will propagate within the *sound cone* at that event, and, for physically realistic equations of state, this sound cone will always be contained within the *light cone* at that event. As a result, if a region of spacetime contains trapped surfaces, both the hydrodynamic and the metric fields will be causally disconnected

and both can be excised there.<sup>3</sup> On the other hand, there may be situations (*e.g.*, when the bulk flow is locally supersonic but no trapped surfaces are present) in which it is at least in principle possible to excise the hydrodynamic fields without being allowed to do the same for the metric fields.<sup>4</sup>

A first naive implementation of an excision algorithm within a HRSC method could consist in extrapolating from data outside the excision region to construct the flux at the excision boundary. This may appear to be a good idea since HRSC methods naturally change the stencils depending on the data locally, but this approach is not guaranteed to reduce the total variation of the solution. Indeed, it has been observed that this is not the case and simple examples may be produced that fail with this boundary condition (Baiotti *et al.*, 2005; Hawke *et al.*, 2005). An effective solution, however, is not much more complicated and can be obtained by applying at the excision boundary the simplest outflow boundary condition (*i.e.*, flow into the excision region). In practice, it is sufficient to apply a zeroth-order extrapolation to all variables at the excision boundary, *i.e.*, a simple copy of the hydrodynamic variables across the boundary. Furthermore, if the reconstruction method requires more cells inside the excision region, the stencil is forced to consider only the data in the exterior and the first interior cell.

This is illustrated in Fig. D.1, which reports a schematic view of the excision algorithm, with the excision boundary being represented by the green vertical dashed line. The left panel represents an example of the discretised solution when a piecewise linear reconstruction is used outside the excised region (indicated as the dark-blue shaded region) and a zeroth-order extrapolation is employed from the active region (indicated as the light-blue shaded region) across the excision boundary and via a suitable modification of the reconstruction method. The right panel shows the spacetime diagram of the evolution of the solution, remarking how the characteristics are all oriented in the same direction inside the excised spacetime. This figure should be compared with the equivalent Fig. 9.2 for regular non-excised solutions.

Although the actual implementation of this excision technique may depend on the reconstruction method used, the working principle is always the same and can be summarised as follows (Baiotti *et al.*, 2005; Baiotti, 2004):

- (i) all cells for which all possible reconstruction stencils are not contained within the excision region are evolved in the normal fashion;
- (ii) all cells within the excision region are not evolved and the fluid variables are extrapolated from the nearest non-excised cell;
- (iii) those cells that are not in the excised region but that have stencils containing at least one excised point, turn their stencil into a one-sided one in such a way that it does not contain excised points (see below).
- (iv) those cells that are on the excision boundary are not computed using Riemann solvers since all the characteristic information must come from the exterior of the excised region.

<sup>3</sup>In general the excision boundary is placed a few cells (typically four) within a surface which is typically  $\sim 60\%$  of the size of the apparent horizon (Baiotti *et al.*, 2005; Hawke *et al.*, 2005).

<sup>4</sup>While possible, this type of excision is rarely done and the hydrodynamic excision is always made within regions of the domain inside trapped surfaces. On the other hand, within a trapped surface it is sometimes possible to excise the fluid variables but without excising the metric ones.

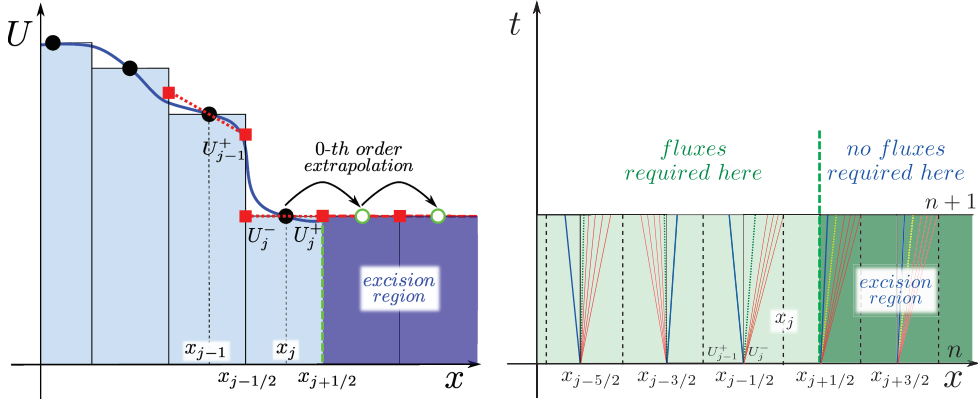


**Fig. D.1** Schematic view of the excision algorithm. *Left panel:* discretised solution when a piecewise linear reconstruction is used outside the excised region and a zeroth-order extrapolation is employed across the excision boundary (green vertical dashed line) with a modification of the reconstruction method. *Right panel:* spacetime diagram of the evolution of the solution, showing how the characteristics are all oriented in the same direction inside the excised spacetime [cf., Fig. 9.2].

Hence, the fluxes are computed from the exterior reconstruction only.<sup>5</sup>

For completeness we also discuss how the stencil is altered when different reconstruction methods are used (Hawke *et al.*, 2005; Baiotti, 2004):

- *Slope-limited TVD reconstruction (Section 9.3.1):* only the reconstructions at  $x_{B \pm 1/2}$ , where the subscript “\$B\$” indicates the point on the excision boundary, are affected by the excision region. Thus setting  $\sigma_B = 0$  in Eq. (9.43) ensures that only data outside the excision region are used, which is consistent with the TVD reconstruction.
- *PPM reconstruction (Section 9.3.2):* at the moment no third-order modification of the PPM reconstruction in the presence of an excision boundary is known. Hence, the simplest solution is to use the same reconstruction as in the TVD case. Since this provides a second-order stable reconstruction at an outflow boundary, it should not affect the order of accuracy in the rest of the domain.
- *ENO reconstruction (Section 10.2):* since the ENO methods use a stencil of width \$k\$ for an order \$k\$ accuracy, the reconstruction in the cells centred between  $x_B$  and  $x_{B-k+2}$  are affected by the excision region. However, it is easy to ensure that the stencil chosen by the ENO reconstruction does not include points from inside the excision region. In essence, the undivided differences are checked for the stencil giving the smoothest solution and if it contains an excised cell it is then discarded, passing over the next smoothest stencil not containing excised cells.

<sup>5</sup>This procedure would also be equivalent to solving a *trivial* Riemann problem on the excision boundary as well, but after having set the excised points next to the points on the excision boundary to the values of the points on the excision boundary themselves.

# Appendix E

## Numerical Building Blocks

---

### E.1 TVD slope limiters

As discussed in Section 9.3.1, TVD slope-limiter methods provide a piecewise-linear reconstruction of  $U_j(x)$  inside each cell, thus producing a better representation of the solution than the simple piecewise constant, as initially suggested in the Godunov method. Hereafter,  $U(j-1)$ ,  $U(j)$ , and  $U(j+1)$  denote respectively the values of the variable  $U$  at the centres of the cells  $j-1$ ,  $j$  and  $j+1$ , i.e., at  $x = x_{j-1}$ ,  $x_j$  and  $x_{j+1}$ . The reconstruction is performed for a total of  $NC$  cells. On return,  $UL(j)$  is the left state of the local Riemann problem at  $x_{j+1/2}$ , i.e.,  $U_j^+$ , while  $UR(j-1)$  is the right state of the local Riemann problem at  $x_{j-1/2}$ , i.e.,  $U_j^-$  (see Fig. 9.4).

We report below some “pseudo-code” examples for the simplest reconstructions schemes, starting with the elementary *minmod slope limiter* [see Section 9.3.1, Eqs. (9.44)–(9.45)]

```
!-----!  
! minmod slope limiter !  
!-----!  
do j = 1, NC  
    Ujm1 = U(j-1)  
    Uj   = U(j )  
    Ujp1 = U(j+1)  
    sp   = Ujp1 - Uj  
    sm   = Uj   - Ujm1  
    ssp  = sign(1.0,sp)  
    ssm  = sign(1.0,sm)  
    asp  = abs(sp)  
    asm  = abs(sm)  
    dU   = 0.25*(ssp+ssm)*min(aspm,asm)  
    Ujp  = Uj + dU  
    Ujm  = Uj - dU  
    UL(j ) = Ujp  
    UR(j-1) = Ujm  
end do
```

Next, we report the pseudo-code example for the *monotonised central-difference limiter* (*MC*) [see Section 9.3.1, Eq. (9.46)].

```

!-----!
! monotonised central-difference limiter (MC) !
!-----!
do j = 1, NC
    Ujm1 = U(j-1)
    Uj   = U(j  )
    Ujp1 = U(j+1)
    sp   = Ujp1 - Uj
    sm   = Uj   - Ujm1
    ssp  = sign(1.0,sp)
    ssm  = sign(1.0,sm)
    asp  = abs(sp)
    asm  = abs(sm)
    dU   = 0.25*(ssp+ssm)*min(2.0*asp,2.0*asm,0.5*abs(sp+sm))
    Ujp  = Uj + dU
    Ujm  = Uj - dU
    UL(j  ) = Ujp
    UR(j-1) = Ujm
end do

```

Finally, we report the pseudo-code example for the *superbee limiter* [see Section 9.3.1, Eq. (9.48)].

```

!-----!
! superbee slope limiter !
!-----!
do j = 1, NC
    Ujm1 = U(j-1)
    Uj   = U(j  )
    Ujp1 = U(j+1)
    sp   = Ujp1 - Uj
    sm   = Uj   - Ujm1
    ssp  = sign(1.0,sp)
    ssm  = sign(1.0,sm)
    asp  = abs(sp)
    asm  = abs(sm)
    dU   = 0.25*(ssp+ssm)*min(2.0*asp,2.0*asm,max(asp,asm))
    Ujp  = Uj + dU
    Ujm  = Uj - dU
    UL(j  ) = Ujp
    UR(j-1) = Ujm
end do

```

## E.2 Basic Riemann solvers

Let us now assume that a reconstruction has been obtained and indicate respectively with  $UL(j)$  and  $UR(j)$  the left and the right states in conserved variables of the local Riemann

problem at  $x_{j+1/2}$ , *i.e.*,  $U_j^+$  and  $U_{j+1}^-$  (see Fig. 9.4). Note that if the reconstruction is performed on the primitive variables  $\mathbf{V}$ , then  $UL(j)$  and  $UR(j)$  are obtained directly from  $VL(j)$  and  $VR(j)$  through Eq. (7.231). On the other hand, if the reconstruction is performed on the conserved variables, it is then necessary to perform a recovery of the primitive variables  $VL(j)$  and  $VR(j)$  following the procedure described in Section D.1.

Once  $VL(j)$  and  $VR(j)$  have been obtained, it is possible to compute the physical fluxes  $FL(j)$  and  $FR(j)$  through Eq. (7.231). A virtual subroutine named `Eigenvalues` then uses as input the vector of primitive variables, computes the two eigenvalues from Eq. (7.239), and stores them in the vectors `lambdaL(1:2)` and `lambdaR(1:2)`, *i.e.*,

$$\begin{aligned}\text{lambdaL}(1:2) &= (\lambda_+(VL), \lambda_-(VL)), \\ \text{lambdaR}(1:2) &= (\lambda_+(VR), \lambda_-(VR)).\end{aligned}$$

Using this information, it is then possible to employ an approximate Riemann solver formula to compute the numerical flux at  $x_{j+1/2}$ . As an example, below we report the pseudo-code expression for the *HLLE Riemann solver* [see Section 9.4.1 in Eq. (9.80), where  $al = \lambda_L$  and  $ar = \lambda_R$ ]

```
!-----!
! HLLE flux formula !
!-----!
do j = 1, NC
    call Eigenvalues(VL(j), lambdaL)
    call Eigenvalues(VR(j), lambdaR)
    al = min(0.0, lambdaL(2), lambdaR(2))
    ar = max(0.0, lambdaL(1), lambdaR(1))
    a = 1.0/(ap - am)
    F(j) = a*(ar*FL(j) - al*FR(j) + ar*al*(UR(j) - UL(j)))
end do
```

Similarly, using instead the *Rusanov Riemann solver* [see Section 9.4.1; Eq. (9.84) the flux can be computed as

```
!-----!
! Rusanov flux formula !
!-----!
do j = 1, NC
    call Eigenvalues(VL(j), lambdaL)
    call Eigenvalues(VR(j), lambdaR)
    al = min(0.0, lambdaL(2), lambdaR(2))
    ar = max(0.0, lambdaL(1), lambdaR(1))
    a = max(abs(ar), abs(al))
    F(j) = 0.5*(FL(j) + FR(j)) - 0.5*a*(UR(j) - UL(j))
end do
```

### E.3 Reference one-dimensional pseudo-code

Problem 6 of Chapter 9 suggested building a one-dimensional code to solve the special-relativistic hydrodynamic equations (7.231) in Cartesian coordinates. A pseudo-code using

TVD reconstruction (see Section 9.2.2) and Runge–Kutta time-stepping (see Section 9.5.1) is presented below.

```

main program
!-----
! Build the grid !
!-----
Setup_Grid
!-----
! Assign the initial conditions !
!-----
Setup_Initial_Data
!-----
! Start the time iteration !
!-----
do iter = 1, nt_steps
    !-----
    ! Compute the time-step Delta t [Eq. (8.41)] !
    !-----
    CFL_Condition
    !-----
    ! Advance the time coordinate !
    !-----
    time = time + dt
    !-----
    ! Start the Runge--Kutta sub-steps !
    !-----
    do irk = 1, rkindx
        !-----
        ! Sweep in spatial direction !
        !-----
        do j = 1, NC
            !-----
            ! Reconstruct variables at cell boundaries [Section 9.3] !
            !-----
            TVD_Reconstruct
            !-----
            ! Compute the numerical fluxes [Eq. (7.232)] !
            !-----
            Riemann_Solver
            !-----
            ! Compute Runge-Kutta time update [Section 9.5.1] !
            !-----
            Time_Update
            !-----
            ! Recover the primitive variables [Appendix D.1] !
            !-----
            Cons_to_Prim
        end do
    end do
    !-----
    ! Apply boundary conditions at grid edges !
    !-----
end do
end main program

```

# References

- Abadie, J., Abbott, B. P., Abbott, R., *et al.* (2010). Topical review: Predictions for the rates of compact binary coalescences observable by ground-based gravitational-wave detectors. *Class. Quant. Grav.*, **27**, 173001.
- Abrahams, A. M. and Price, R. H. (1996). Applying black hole perturbation theory to numerically generated spacetimes. *Phys. Rev. D*, **53**, 1963–1971.
- Abrahams, A. M., Rezzolla, L., Rupright, M. E., *et al.* (1998). Gravitational wave extraction and outer boundary conditions by perturbative matching. *Phys. Rev. Lett.*, **80**, 1812–1815.
- Abramowicz, M., Jaroszynski, M., and Sikora, M. (1978). Relativistic, accreting disks. *Astron. Astrophys.*, **63**, 221–224.
- Abramowicz, M. A. (1971). The relativistic von Zeipel's theorem. *Acta Astronom.*, **21**, 81–85.
- Abramowicz, M. A., Calvani, M., and Nobili, L. (1983). Runaway instability in accretion disks orbiting black holes. *Nature*, **302**, 597–599.
- Abramowicz, M. A., Chen, X.-M., Granath, M., and Lasota, J.-P. (1996). Advection-dominated accretion flows around Kerr black holes. *Astrophys. J.*, **471**, 762–773.
- Abramowicz, M. A., Czerny, B., Lasota, J. P., and Szuszkiewicz, E. (1988). Slim accretion disks. *Astrophys. J.*, **332**, 646–658.
- Abramowicz, M. A. and Fragile, P. C. (2013). Foundations of black hole accretion disk theory. *Living Rev. Relativ.*, **16**, 1.
- Abramowicz, M. A., Lanza, A., and Percival, M. J. (1997). Accretion disks around Kerr black holes: Vertical equilibrium revisited. *Astrophys. J.*, **479**, 179–183.
- Abramowicz, M. A., Miller, J. C., and Stuchlík, Z. (1993). Concept of radius of gyration in general relativity. *Phys. Rev. D*, **47**, 1440–1447.
- Abramowicz, M. A. and Prasanna, A. R. (1990). Centrifugal force reversal near a Schwarzschild black hole. *Mon. Not. Roy. Soc.*, **245**, 720–728.
- Abramowitz, M. and Stegun, I. A. (1968). *Handbook of Mathematical Functions with Formulas, Graphs and Mathematical Tables*. Dover, New York.
- Ackermann, K. H., Adams, N., Adler, C., *et al.* (2001). Elliptic flow in Au+Au collisions at  $\sqrt{s_{NN}} = 130\text{GeV}$ . *Phys. Rev. Lett.*, **86**, 402–407.
- Ajith, P., Babak, S., Chen, Y., *et al.* (2007). Phenomenological template family for black hole coalescence waveforms. *Class. Quant. Grav.*, **24**, S689–S700.
- Akmal, A., Pandharipande, V. R., and Ravenhall, D. G. (1998). Equation of state of nucleon matter and neutron star structure. *Phys. Rev. C*, **58**, 1804–1828.
- Alcubierre, M. (2008). *Introduction to 3 + 1 Numerical Relativity*. Oxford University Press, Oxford.
- Alcubierre, M., Brügmann, B., Diener, P., Koppitz, M., Pollney, D., Seidel, E., and Takahashi, R. (2003a). Gauge conditions for long-term numerical black hole evolutions without excision. *Phys. Rev. D*, **67**, 084023.

- Alcubierre, M., Brügmann, B., Pollney, D., Seidel, E., and Takahashi, R. (2001). Black hole excision for dynamic black holes. *Phys. Rev. D*, **64**, 061501(R).
- Alcubierre, M., Corichi, A., González, J. A., Núñez, D., and Salgado, M. (2003b). A hyperbolic slicing condition adapted to killing fields and densitized lapses. *Class. Quant. Grav.*, **20**, 3951–3968.
- Alic, D., Bona-Casas, C., Bona, C., Rezzolla, L., and Palenzuela, C. (2012a). Conformal and covariant formulation of the Z4 system with constraint-violation damping. *Phys. Rev. D*, **85**, 064040.
- Alic, D., Moesta, P., Rezzolla, L., Zanotti, O., and Jaramillo, J. L. (2012b). Accurate simulations of binary black hole mergers in force-free electrodynamics. *Astrophys. J.*, **754**, 36.
- Alic, D., Rezzolla, L., Hinder, I., and Mösta, P. (2010). Dynamical damping terms for symmetry-seeking shift conditions. *Class. Quant. Grav.*, **27** (24), 245023.
- Alic, D., Kastaun, W., and Rezzolla, L. (2013). Constraint-damping of the CCZ4 formulation in simulations of binary neutron stars. *arXiv:1305.0000*.
- Aloy, M.-Á., Janka, H.-T., and Müller, E. (2005). Relativistic outflows from remnants of compact object mergers and their viability for short gamma-ray bursts. *Astron. Astrophys.*, **436**, 273–311.
- Aloy, M.-Á., Martí, J.-M., Gómez, J.-L., Agudo, I., Müller, E., and Ibáñez, J.-M. (2003). Three-dimensional simulations of relativistic precessing jets probing the structure of superluminal sources. *Astrophys. J.*, **585**, L109–L112.
- Aloy, M. Á., Müller, E., Ibáñez, J. M., Martí, J. M., and MacFadyen, A. (2000). Relativistic jets from collapsars. *Astrophys. J.*, **531**, L119–L122.
- Aloy, M. Á. and Rezzolla, L. (2006). A powerful hydrodynamic booster for relativistic jets. *Astrophys. J.*, **640**, L115–L118.
- Anderson, M., Hirschmann, E. W., Lehner, L., Liebling, S. L., Motl, P. M., Neilsen, D., Palenzuela, C., and Tohline, J. E. (2008). Simulating binary neutron stars: Dynamics and gravitational waves. *Phys. Rev. D*, **77**, 024006.
- Anderson, M. and Matzner, R. A. (2005). Extended lifetime in computational evolution of isolated black holes. *Found. Phys.*, **35**, 1477–1495.
- Andersson, N. and Comer, G. L. (2001). On the dynamics of superfluid neutron star cores. *Mon. Not. R. Astron. Soc.*, **328**, 1129–1143.
- Andersson, N. and Comer, G. L. (2007). Relativistic fluid dynamics: Physics for many different scales. *Living Rev. Relativ.*, **10**, 1.
- Andersson, N. and Comer, G. L. (2010). Variational multi-fluid dynamics and causal heat conductivity. *Proc. R. Soc. London, Ser. A*, **466**, 1373–1387.
- Andersson, N., Ferrari, V., Jones, D. I., Kokkotas, K. D., Krishnan, B., Read, J., Rezzolla, L., and Zink, B. (2011). Gravitational waves from neutron stars: Promises and challenges. *Gen. Rel. Grav.*, **43**, 409–436.
- Anile, A. M. (1989). *Relativistic Fluids and Magneto-fluids*. Cambridge University Press, Cambridge.
- Anile, A. M., Miller, J. C., and Motta, S. (1980). Damping of relativistic shocks in an expanding universe. *Nuovo Cimento Lett.*, **29**, 268–272.
- Anile, A. M., Miller, J. C., and Motta, S. (1983). Formation and damping of relativistic strong shocks. *Phys. Fluids*, **26**, 1450–1460.

- Anile, A. M. and Russo, G. (1986). Corrugation stability for plane relativistic shock waves. *Phys. Fluids*, **29**, 2847–2852.
- Anile, A. M. and Russo, G. (1987). Linear stability for plane relativistic shock waves. *Phys. Fluids*, **30**, 1045–1051.
- Anile, A. M., Pavón, D., and Romano, V. (1998). The Case for Hyperbolic Theories of Dissipation in Relativistic Fluids. *arXiv:gr-qc/9810014*.
- Anninos, P., Camarda, K., Libson, J., Massó, J., Seidel, E., and Suen, W.-M. (1998). Finding apparent horizons in dynamic 3D numerical spacetimes. *Phys. Rev. D*, **58**, 024003.
- Anninos, P., Camarda, K., Massó, J., Seidel, E., Suen, W.-M., and Towns, J. (1995). Three-dimensional numerical relativity: The evolution of black holes. *Phys. Rev. D*, **52**, 2059–2082.
- Anninos, P. and Fragile, P. C. (2003). Nonoscillatory central difference and artificial viscosity schemes for relativistic hydrodynamics. *Astrophys. J. Supp.*, **144**, 243–257.
- Ansorg, M., Gondek-Rosińska, D., and Villain, L. (2009). On the solution space of differentially rotating neutron stars in general relativity. *Mon. Not. R. Astron. Soc.*, **396**, 2359–2366.
- Anton, L. (2008). *Magnetohidrodinamica relativista numérica: Aplicaciones en relatividad especial y general*. PhD Thesis, Universitat de Valencia, Valencia, Spain.
- Antoniadis, J., Freire, P., Wex, N. et al. (2013). A Massive Pulsar in a Compact Relativistic Binary. *Science*, **340**, 1233232–1–9.
- Applegate, J. H. and Hogan, C. J. (1985). Relics of cosmic quark condensation. *Phys. Rev. D*, **31**, 3037–3045.
- Arminjon, P. and St-Cyr, A. (2003). Nessyahu–Tadmor-type central finite volume methods without a predictor for 3D cartesian and unstructured tetrahedral grids. *Applied Numerical Mathematics*, **46**, 135–155.
- Arnowitt, R., Deser, S., and Misner, C. W. (1962). The dynamics of general relativity. In *Gravitation: An Introduction to Current Research* (Ed. L. Witten), 227–265. John Wiley, New York.
- Ascher, U. M., Ruuth, S. J., and Spiteri, R. J. (1997). Implicit–explicit Runge–Kutta methods for time-dependent partial differential equations. *Applied Numerical Mathematics*, **25**, 151–167. Special Issue on Time Integration.
- Baade, W. and Minkowski, R. (1954). On the identification of radio sources. *Astrophys. J.*, **119**, 215–231.
- Babiuc, M. C., Szilágyi, B., and Winicour, J. (2006a). Harmonic initial-boundary evolution in general relativity. *Phys. Rev. D*, **73**, 064017.
- Babiuc, M. C., Szilágyi, B., and Winicour, J. (2006b). Testing numerical relativity with the shifted gauge wave. *Class. Quant. Grav.*, **23**, S319–S342.
- Baier, R., Romatschke, P., and Wiedemann, U. A. (2006). Dissipative hydrodynamics and heavy-ion collisions. *Phys. Rev. C*, **73**, 064903.
- Baiotti, L. (2004). *Numerical relativity simulations of non-vacuum spacetimes in three dimensions*. PhD Thesis, SISSA, International School for Advanced Studies.
- Baiotti, L., De Pietri, R., Manca, G. M., and Rezzolla, L. (2007a). Accurate simulations of the dynamical bar-mode instability in full general relativity. *Phys. Rev. D*, **75**, 044023.
- Baiotti, L., Giacomazzo, B., and Rezzolla, L. (2008). Accurate evolutions of inspiralling neutron star binaries: Prompt and delayed collapse to a black hole. *Phys. Rev. D*, **78**, 084033.
- Baiotti, L., Giacomazzo, B., and Rezzolla, L. (2009). Accurate evolutions of inspiralling

- neutron star binaries: Assessment of the truncation error. *Class. Quant. Grav.*, **26**, 114005.
- Baiotti, L., Hawke, I., Montero, P. J., Löffler, F., Rezzolla, L., Stergioulas, N., Font, J. A., and Seidel, E. (2005). Three-dimensional relativistic simulations of rotating neutron star collapse to a Kerr black hole. *Phys. Rev. D*, **71**, 024035.
- Baiotti, L., Hawke, I., and Rezzolla, L. (2007b). On the gravitational radiation from the collapse of neutron stars to rotating black holes. *Class. Quant. Grav.*, **24**, S187–S206.
- Baiotti, L. and Rezzolla, L. (2006). Challenging the paradigm of singularity excision in gravitational collapse. *Phys. Rev. Lett.*, **97**, 141101.
- Baiotti, L., Shibata, M., and Yamamoto, T. (2010). Binary neutron star mergers with Whisky and SACRA: First quantitative comparison of results from independent general-relativistic hydrodynamics codes. *Phys. Rev. D*, **82**, 064015.
- Baker, J. G., Centrella, J., Choi, D.-I., Koppitz, M., and van Meter, J. (2006). Gravitational wave extraction from an inspiraling configuration of merging black holes. *Phys. Rev. Lett.*, **96**, 111102.
- Balbus, S. A. and Hawley, J. F. (1998). Instability, turbulence, and enhanced transport in accretion disks. *Rev. Mod. Phys.*, **70**, 1–53.
- Baldo, M., Burgio, G. F., and Schulze, H.-J. (2000). Hyperon stars in the Brueckner–Bethe–Goldstone theory. *Phys. Rev. C*, **61**, 055801.
- Balsara, D. (2001). Total variation diminishing scheme for relativistic magnetohydrodynamics. *Astrophys. J. Suppl. Ser.*, **132**, 83–101.
- Balsara, D. S. (2012). Self-adjusting, positivity preserving high order schemes for hydrodynamics and magnetohydrodynamics. *J. Comput. Phys.*, **231**, 7504–7517.
- Balsara, D. S., Altmann, C., Munz, C.-D., and Dumbser, M. (2007). A sub-cell based indicator for troubled zones in RKDG schemes and a novel class of hybrid RKDG+HWENO schemes. *J. Comput. Phys.*, **226**, 586–620.
- Balsara, D. S., Rumpf, T., Dumbser, M., and Munz, C.-D. (2009). Efficient, high accuracy ADER-WENO schemes for hydrodynamics and divergence-free magnetohydrodynamics. *J. Comput. Phys.*, **228**, 2480–2516.
- Balsara, D. S. and Shu, C.-W. (2000). Monotonicity preserving weighted essentially non-oscillatory schemes with increasingly high order of accuracy. *J. Comput. Phys.*, **160**, 405–452.
- Balsara, D. S. and Spicer, D. (1999). Maintaining pressure positivity in magnetohydrodynamic simulations. *J. Comput. Phys.*, **148**, 133–148.
- Banyuls, F., Font, J. A., Ibáñez, J. M., Martí, J. M., and Miralles, J. A. (1997). Numerical 3+1 general-relativistic hydrodynamics: A local characteristic approach. *Astrophys. J.*, **476**, 221–231.
- Bardeen, J. M., Press, W. H., and Teukolsky, S. A. (1972). Rotating black holes: Locally non-rotating frames, energy extraction, and scalar synchrotron radiation. *Astrophys. J.*, **178**, 347–370.
- Barth, T. J. and Frederickson, P. O. (Ed.) (1990). *Higher order solution of the Euler equations on unstructured grids using quadratic reconstruction*. In AIAA, 28th Aerospace Sciences Meeting, Reno, NV.
- Barth, T. and Deconinck, H. (1999). *High-Order Methods for Computational Physics*. Springer, Berlin, Heidelberg, New York.
- Batchelor, G. K. (2000). *An Introduction to Fluid Dynamics*. Cambridge University Press,

- Cambridge.
- Battaner, E. (1996). *Astrophysical Fluid Dynamics*. Cambridge University Press, Cambridge.
- Baumgarte, T. W. and Shapiro, S. L. (1999). On the numerical integration of Einstein's field equations. *Phys. Rev. D*, **59**, 024007.
- Baumgarte, T. W. and Shapiro, S. L. (2010). *Numerical Relativity: Solving Einstein's Equations on the Computer*. Cambridge University Press, Cambridge.
- Baumgarte, T. W., Shapiro, S. L., and Teukolsky, S. A. (1995). Computing supernova collapse to neutron stars and black holes. *Astrophys. J.*, **443**, 717–734.
- Bauswein, A., Janka, H.-T., and Oechslin, R. (2010). Testing approximations of thermal effects in neutron star merger simulations. *Phys. Rev. D*, **82**, 084043.
- Bauswein, A. and Janka, H.-T. (2012). Measuring neutron star properties via gravitational waves from neutron star mergers. *Phys. Rev. Lett.*, **108**, 011101.
- Baym, G., Friman, B. L., Blaizot, J.-P., Soyeur, M., and Czyż, W. (1983). Hydrodynamics of ultra-relativistic heavy ion collisions. *Nucl. Phys. A*, **407**, 541–570.
- Baym, G., Pethick, C., and Pines, D. (1969). Superfluidity in neutron stars. *Nature*, **224**, 673–674.
- Belczynski, K., Taam, R. E., Kalogera, V., Rasio, F., and Bulik, T. (2007). On the rarity of double black hole binaries: Consequences for gravitational wave detection. *Astrophys. J.*, **662**, 504–511.
- Ben-Artzi, M. and Falcovitz, J. (1984). A second-order Godunov-type scheme for compressible fluid dynamics. *J. Comput. Phys.*, **55**, 1–32.
- Ben Artzi, M. and Falcovitz, J. (2003). *Generalized Riemann Problems in Computational Fluid Dynamics*. Cambridge University Press, Cambridge.
- Benensohn, J. S., Lamb, D. Q., and Taam, R. E. (1997). Hydrodynamical studies of wind accretion onto compact objects: two-dimensional calculations. *Astrophys. J.*, **478**, 723–733.
- Bernuzzi, S. and Hilditch, D. (2010). Constraint violation in free evolution schemes: Comparing BSSNOK with a conformal decomposition of Z4. *Phys. Rev. D*, **81**, 084003.
- Binney, J. and Tremaine, S. (1987). *Galactic dynamics*. Princeton University Press, Princeton, NJ.
- Birkhoff, G. D. (1923). *Relativity and Modern Physics*. Harvard University Press. Cambridge, Mass.
- Bishop, N. T., Gómez, R., Lehner, L., Maharaj, M., and Winicour, J. (1999). Incorporation of matter into characteristic numerical relativity. *Phys. Rev. D*, **60**, 024005.
- Biswas, R., Devine, K. D., and Flaherty, J. E. (1994). Parallel, adaptative finite element methods for conservation laws. *Appl. Numer. Math.*, **14**, 255–283.
- Bjorken, J. D. (1983). Highly relativistic nucleus–nucleus collisions: The central rapidity region. *Phys. Rev. D*, **27**, 140–151.
- Blair, D. G., Howell, E.J., Ju, L., and Zhao, C. (2012). *Advanced Gravitational Wave Detectors*. Cambridge University Press, Cambridge.
- Blandford, R. D. and McKee, C. F. (1976). Fluid dynamics of relativistic blast waves. *Phys. Fluids*, **19**, 1130–1138.
- Blandford, R. D. and Rees, M. J. (1974). A “twin-exhaust” model for double radio sources. *Mon. Not. R. Astron. Soc.*, **169**, 395–415.
- Blandford, R. D. and Znajek, R. L. (1977). Electromagnetic extraction of energy from Kerr black holes. *Mon. Not. R. Astron. Soc.*, **179**, 433–456.

- Bodo, G., Massaglia, S., Ferrari, A. and Trussoni, E. (1994). Kelvin-Helmholtz instability of hydrodynamic supersonic jets. *Astron. Astrophys.*, **283**, 655–676.
- Bogovalov, S. and Tsinganos, K. (2001). Magnetic collimation of relativistic jets. *Astro-nomical and Astrophysical Transactions*, **20**, 303–309.
- Bolejko, K. and Lasky, P. D. (2008). Pressure gradients, shell-crossing singularities and acoustic oscillations—application to inhomogeneous cosmological models. *Mon. Not. R. Astron. Soc.*, **391**, L59–L63.
- Boltzmann, L. (1872). Weitere Studien über das Wärmegleichgewicht unter Gasmolekülen. *Wiener Berichte*, **66**, 275.
- Bona, C., Ledvinka, T., Palenzuela, C., and Zacek, M. (2003). General-covariant evolution formalism for numerical relativity. *Phys. Rev. D*, **67**, 104005.
- Bona, C., Ledvinka, T., Palenzuela, C., and Zacek, M. (2004). A symmetry-breaking mechanism for the Z4 general-covariant evolution system. *Phys. Rev. D*, **69**, 064036.
- Bona, C., Ledvinka, T., Palenzuela, C., and Zacek, M. (2005). Constraint-preserving boundary conditions in the Z4 numerical relativity formalism. *Class. Quant. Grav.*, **22**, 2615–2634.
- Bona, C., Massó, J., Seidel, E., and Stela, J. (1995). New formalism for numerical relativity. *Phys. Rev. Lett.*, **75**, 600–603.
- Bona, C., Palenzuela, C., and Bona-Casas, C. (2009). *Elements of Numerical Relativity and Relativistic Hydrodynamics: From Einstein's Equations to Astrophysical Simulations*. Lecture Notes in Physics. Springer, Berlin.
- Bona, C., T., Ledvinka., and Palenzuela, C. (2002). A 3+1 covariant suite of numerical relativity evolution systems. *Phys. Rev. D*, **66**, 084013.
- Bonazzola, S., Gourgoulhon, É., Grandclement, P., and Novak, J. (2004). A constrained scheme for Einstein equations based on Dirac gauge and spherical coordinates. *Phys. Rev. D*, **70**, 104007.
- Bondi, H. (1952). On spherically symmetric accretion. *Mon. Not. R. Astron. Soc.*, **112**, 195–204.
- Bondi, H. and Hoyle, F. (1944). On the mechanism of accretion by stars. *Mon. Not. R. Astron. Soc.*, **104**, 273–282.
- Bondi, H., van der Burg, M. G. J., and Metzner, A. W. K. (1962). Gravitational waves in general relativity. VII. Waves from axi-symmetric isolated systems. *Proc. R. Soc. London, Ser. A*, **269**, 21–52.
- Bonometto, S. A. and Pantano, O. (1993). Physics of the cosmological quark–hadron transition. *Phys. Rep.*, **228**, 175–252.
- Brandenburg, A. and Nordlund, A. (2011). Astrophysical turbulence modeling. *Rep. Prog. Phys.*, **74**, 046901.
- Bressan, A. and LeFloch, P. (1997). Uniqueness of weak solutions to systems of conservation laws. *Arch. Ration. Mech. An.*, **140**, 301–317.
- Brown, D., Diener, P., Sarbach, O., Schnetter, E., and Tiglio, M. (2009). Turduckening black holes: An analytical and computational study. *Phys. Rev. D*, **79**, 044023.
- Brown, D., Sarbach, O., Schnetter, E., Tiglio, M., Diener, P., Hawke, I., and Pollney, D. (2007). Excision without excision. *Phys. Rev. D*, **76**, 081503(R).
- Bucciantini, N. and Del Zanna, L. (2011). General relativistic magnetohydrodynamics in axisymmetric dynamical spacetimes: The X-ECHO code. *Astron. Astrophys.*, **528**, A101.

- Bucciantini, N. and Del Zanna, L. (2013). A fully covariant mean-field dynamo closure for numerical 3 + 1 resistive GRMHD. *Mon. Not. R. Astron. Soc.*, **428**, 71–85.
- Buchdahl, H. A. (1959). General relativistic fluid spheres. *Phys. Rev.*, **116**, 1027–1034.
- Buckmaster, J. D., Ludford, G. S. S., and Emmons, H. W. (1982). Theory of laminar flames. Cambridge University Press, Cambridge.
- Burstein, S. Z., Lax, P. D., and Sod, G. A. (1978). *Lectures on Combustion Theory*. New York University, Courant Mathematics and Computing Laboratory, New York.
- Butcher, J. C. (2008). *Numerical Methods for Ordinary Differential Equations*. John Wiley, New York.
- Butcher, J. C. (1987). *The Numerical Analysis of Ordinary Differential Equations: Runge–Kutta and General Linear Methods*. John Wiley, New York.
- Calder, A. C., Townsley, D. M., Seitenzahl, I. R., et al. (2007). Capturing the fire: Flame energetics and neutrinization for Type Ia supernova simulations. *Astrophys. J.*, **656**, 313–332.
- Camenzind, M. (1986). Centrifugally driven MHD-winds in active galactic nuclei. *Astron. Astrophys.*, **156**, 137–151.
- Campanelli, M., Lousto, C. O., Marronetti, P., and Zlochower, Y. (2006). Accurate evolutions of orbiting black hole binaries without excision. *Phys. Rev. Lett.*, **96**, 111101.
- Caprini, C., Durrer, R., and Servant, G. (2008). Gravitational wave generation from bubble collisions in first-order phase transitions: An analytic approach. *Phys. Rev. D*, **77**, 124015.
- Carmeli, M. (2001). *Classical Fields: General Relativity and Gauge Theory*. World Scientific, River Edge, NJ.
- Carr, B. J. and Coley, A. A. (1999). Topical review: Self-similarity in general relativity. *Class. Quant. Grav.*, **16**, R31–R71.
- Carter, B. (1968). Global structure of the Kerr family of gravitational fields. *Phys. Rev.*, **174**, 1559–1571.
- Carter, B. (1973). Elastic perturbation theory in general relativity and a variation principle for a rotating solid star. *Commun. Math. Phys.*, **30**, 261–286.
- Carter, B. (1989). Covariant theory of conductivity in ideal fluid or solid media. In *Relativistic Fluid Dynamics* (Ed. A. Anile and Y. Choquet-Bruhat), Volume 1385, Lecture Notes in Mathematics, 1–64. Springer, Berlin.
- Carter, B. and Gaffet, B. (1988). Standard covariant formulation for perfect-fluid dynamics. *J. Fluid Mech.*, **186**, 1–24.
- Carter, B. and Langlois, D. (1998). Relativistic models for superconducting-superfluid mixtures. *Nucl. Phys. B*, **531**, 478–504.
- Carter, B. and Luminet, J. P. (1982). Pancake detonation of stars by black holes in galactic nuclei. *Nature*, **296**, 211–214.
- Castro, M. J., LeFloch, P. G., Muoz-Ruiz, M. L., and Pars, C. (2008). Why many theories of shock waves are necessary: Convergence error in formally path-consistent schemes. *J. Comput. Phys.*, **227**, 8107–8129.
- Cattaneo, C. (1948). *Sulla Conduzione Del Calore*. Atti Semin. Mat. Fis. della Universitá di Modena, Vol. 3, 3.
- Cattoen, C., Faber, T., and Visser, M. (2005). Gravastars must have anisotropic pressures. *Class. Quant. Grav.*, **22**, 4189–4202.
- Cavallo, G. and Rees, M. J. (1978). A qualitative study of cosmic fireballs and gamma-ray

- bursts. *Monthly Notices of the Royal Astronomical Society*, **183**, 359–365.
- Centrella, J. and Wilson, J. R. (1984). Planar numerical cosmology. II. The difference equations and numerical tests. *Astrophys. J. SS*, **54**, 229–245.
- Cercignani, C. and Kremer, G. M. (2002). *The Relativistic Boltzmann Equation: Theory and Applications*. Birkhäuser, Boston.
- Cerdá-Durán, P., Font, J. A., and Dimmelmeier, H. (2007). General relativistic simulations of passive-magneto-rotational core collapse with microphysics. *Astron. Astrophys.*, **474**, 169–191.
- Chakrabarti, S. K. (1990). *Theory of Transonic Astrophysical Flows*. World Scientific, Singapore.
- Chamel, N. and Haensel, P. (2008). Physics of neutron star crusts. *Living Rev. Relativ.*, **11**, 10.
- Chandrasekhar, S. (1931). The maximum mass of ideal white dwarfs. *Astrophys. J.*, **74**, 81–82.
- Chandrasekhar, S. (1939). *An Introduction to the Study of Stellar Structure*. Dover, New Haven. Revised Edition 1958.
- Chandrasekhar, S. (1969). *Ellipsoidal Figures of Equilibrium*. Yale University Press, New Haven. Revised Edition 1987.
- Chandrasekhar, S. (1970). Solutions of two problems in the theory of gravitational radiation. *Phys. Rev. Lett.*, **24**, 611–615.
- Chandrasekhar, S. (1981). *Hydrodynamic and Hydromagnetic Stability*. Dover, New York.
- Chapman, S. and Cowling, T. G. (1970). *The Mathematical Theory of Non-uniform Gases. An Account of the Kinetic Theory of Viscosity, Thermal Conduction and Diffusion in Gases*. Cambridge University Press, Cambridge.
- Chen, G.-Q. and Frid, H. (2003). Extended divergence-measure fields and the Euler equations for gas dynamics. *Commun. Math. Phys.*, **236**, 251–280.
- Chen, G.-Q., Ziemer, W. P., and Torres, M. (2009). Gauss-Green theorem for weakly differentiable vector fields, sets of finite perimeter, and balance laws. *Commun. Pur. Appl. Math.*, **62**, 242–304.
- Chernikov, N. (1964a). Equilibrium distribution of the relativistic gas. *Acta Phys. Polonica*, **26**, 1069.
- Chernikov, N. (1964b). Microscopic foundation of relativistic hydrodynamics. *Acta Phys. Polonica*, **27**, 465.
- Chiang, J. and Dermer, C. D. (1999). Synchrotron and synchrotron self-Compton emission and the blast-wave model of gamma-ray bursts. *Astrophys. J.*, **512**, 699–710.
- Chirenti, C. B. M. H. and Rezzolla, L. (2007). How to tell a gravastar from a black hole. *Class. Quant. Grav.*, **24**, 4191–4206.
- Choptuik, M. W. (1993). Universality and scaling in gravitational collapse of massless scalar field. *Phys. Rev. Lett.*, **70**, 9–12.
- Choptuik, M. W. and Pretorius, F. (2010). Ultrarelativistic particle collisions. *Phys. Rev. Lett.*, **104**, 111101.
- Choquet-Bruhat, Y. (1962). The Cauchy problem. In *Gravitation: An Introduction to Current Research* (Ed. L. Witten), 130–168. John Wiley, New York.
- Choquet-Bruhat, Y. and Ruggeri, T. (1983). Hyperbolicity of the 3+1 system of Einstein equations. *Comm. Math. Phys.*, **89**, 269–275.

## 690 References

- Chorin, A. J. and Marsden, J. E. (1979). *A Mathematical Introduction to Fluid Mechanics*. Texts in Applied Mathematics, Springer, Berlin.
- Choudhuri, A. R. (1998). *The Physics of Fluids and Plasmas: An Introduction for Astrophysicists*. Cambridge University Press, Cambridge.
- Ciaraldi-Schoolmann, F., Schmidt, W., Niemeyer, J. C., Röpke, F. K., and Hillebrandt, W. (2009). Turbulence in a three-dimensional deflagration model for Type Ia supernovae. I. Scaling properties. *Astrophys. J.*, **696**, 1491–1497.
- Cockburn, B. and Shu, C.-W. (1989). Runge–Kutta local projection discontinuous Galerkin finite element method for scalar conservation laws. II. General framework. *Math. Comp.*, **52**, 411–435.
- Cockburn, B., How, S., and Shu, C.-W. (1990). Runge–Kutta local projection discontinuous Galerkin finite element method for conservation laws IV. The multidimensional case. *Math. Comp.*, **54**, 545–581.
- Cockburn, B. (1998). The Runge–Kutta discontinuous Galerkin method for conservation laws V. multidimensional systems. *J. Comput. Phys.*, **141**, 199–224.
- Cohen, E., Piran, T., and Sari, R. (1998). Fluid dynamics of semiradiative blast waves. *Astrophys. J.*, **509**, 717–727.
- Colella, P. (1990). Multidimensional upwind methods for hyperbolic conservation laws. *J. Comput. Phys.*, **87**, 171–200.
- Colella, P. and Sekora, M. D. (2008). A limiter for PPM that preserves accuracy at smooth extrema. *J. Comput. Phys.*, **227**, 7069–7076.
- Colella, P. and Woodward, P. R. (1984). The piecewise parabolic method (PPM) for gas-dynamical simulations. *J. Comput. Phys.*, **54**, 174–201.
- Coles, P. and Lucchin, F. (2002). *Cosmology: The Origin and Evolution of Cosmic Structure*. Second edition. John Wiley, New York.
- Comer, G. L. and Langlois, D. (1994). Hamiltonian formulation for relativistic superfluids. *Class. Quant. Grav.*, **11**, 709–721.
- Cook, G. B. (2000). Initial data for numerical relativity. *Living Rev. Relativ.*, **3**, 5.
- Cook, G. B., Huq, M. F., Klasky, S. A., et al. (1998). Boosted three-dimensional black hole evolutions with singularity excision. *Phys. Rev. Lett.*, **80**, 2512–2516.
- Cook, G. B., Shapiro, S. L., and Teukolsky, S. A. (1992). Spin-up of a rapidly rotating star by angular momentum loss—Effects of general relativity. *Astrophys. J.*, **398**, 203–223.
- Cordero-Carrión, I., Cerdá-Durán, P., Dimmelmeier, H., Jaramillo, J. L., Novak, J., and Gourgoulhon, E. (2009). Improved constrained scheme for the Einstein equations: An approach to the uniqueness issue. *Phys. Rev. D*, **79**, 024017.
- Cordero-Carrión, I., Cerdá-Durán, P., and María Ibáñez, J. (2010). Dynamical spacetimes and gravitational radiation in a fully constrained formulation. *JPCS*, **228**, 012055.
- Cordero-Carrión, I., Ibáñez, J. M., Gourgoulhon, E., Jaramillo, J. L., and Novak, J. (2008). Mathematical issues in a fully constrained formulation of the Einstein equations. *Phys. Rev. D*, **77**, 084007.
- Coulson, C. A. and Jeffrey, A. (1977). *Waves: A Mathematical Approach to the Common Types of Wave Motion*. Longman, Harlow.
- Courant, R., Friedrichs, K., and Lewy, H. (1928). Über die partiellen Differenzengleichungen der mathematischen Physik. *Mathematische Annalen*, **100**, 32–74.
- Courant, R., Friedrichs, K., and Lewy, H. (1967). On the partial difference equations of

- mathematical physics. *IBM J. Res. Develop.*, **11**, 215–234.
- Courant, R. and Friedrichs, K. O. (1948). *Supersonic Flow and Shock Waves*. Springer, Berlin.
- Courant, R. and Friedrichs, K. O. (1976). *Supersonic Flow and Shock Waves*. Springer, Berlin.
- Courant, R. and Hilbert, D. (1962). *Methods of Mathematical Physics*. John Wiley, New York.
- Courant, R., Isaacson, E., and Rees, M. (1952). On the solution of nonlinear hyperbolic differential equations by finite differences. *Communications on Pure and Applied Mathematics*, **5** 243–255.
- Cowling, T. G. (1941). The non-radial oscillations of polytropic stars. *Mon. Not. R. Astron. Soc.*, **101**, 367–375.
- Creighton, J. D. E. and Anderson, W. G. (2012). *Gravitational-Wave Physics and Astronomy: An Introduction to Theory, Experiment and Data Analysis*. John Wiley, New York.
- Cruz-Osorio, A., Lora-Clavijo, F. D., and Guzmán, F. S. (2012). Is the flip-flop behaviour of accretion shock cones on to black holes an effect of coordinates? *Mon. Not. R. Astron. Soc.*, **426**, 732–738.
- Daigne, F. and Font, J. A. (2004). The runaway instability of thick discs around black holes – II. Non-constant angular momentum discs. *Mon. Not. R. Astron. Soc.*, **349**, 841–868.
- Dal Maso, G., LeFloch, P. G., and Murat, F. (1995). Definition and weak stability of non-conservative products. *J. Math. Pure. Appl.*, **74**, 483–548.
- Danielewicz, P. and Gyulassy, M. (1985). Dissipative phenomena in quark–gluon plasmas. *Phys. Rev. D*, **31**, 53–62.
- Danielewicz, P. and Ruuskanen, P. V. (1987). Shock phenomena in baryonless strongly interacting matter. *Phys. Rev. D*, **35**, 344–354.
- Darmois, G. (1927). Les équations de la gravitation Einsteinienne, Mémorial des Sciences Mathématiques 25, Gauthier-Villars, Paris (1927).
- Davis, M., Ruffini, R., Press, W. H., and Price, R. H. (1971). Gravitational radiation from a particle falling radially into a Schwarzschild black hole. *Phys. Rev. Lett.*, **27**, 1466–1469.
- de Donder, T. (1921). *La Gravifique Einsteinienne*. Gauthiers-Villars, Paris.
- de Felice, F. (1980). Angular momentum and separation constant in the Kerr metric. *J. Phys. A; Math. Gen.*, **13**, 1701–1708.
- de Felice, F. and Clarke, C. J. S. (1990). *Relativity on Curved Manifolds*. Cambridge University Press, Cambridge.
- Dedner, A., Kemm, F., Kröner, D., Munz, C. D., Schnitzer, T., and Wesenberg, M. (2002). Hyperbolic divergence cleaning for the MHD equations. *J. Comput. Phys.*, **175**, 645–673.
- Degrand, T. and Kajantie, K. (1984). Supercooling, entropy production, and bubble kinetics in the quark–hadron phase transition in the early universe. *Phys. Lett. B*, **147**, 273–278.
- Del Zanna, L. and Bucciantini, N. (2002). An efficient shock-capturing central-type scheme for multidimensional relativistic flows. I. Hydrodynamics. *Astron. Astrophys.*, **390**, 1177–1186.
- Del Zanna, L., Bucciantini, N., and Londrillo, P. (2003). An efficient shock-capturing central-type scheme for multidimensional relativistic flows. II. Magnetohydrodynamics. *Astron. Astrophys.*, **400**, 397–413.
- Del Zanna, L., Zanotti, O., Bucciantini, N., and Londrillo, P. (2007). ECHO: A Eulerian

- conservative high-order scheme for general relativistic magnetohydrodynamics and magnetodynamics. *Astron. Astrophys.*, **473**, 11–30.
- Demorest, P. B., Pennucci, T., Ransom, S. M., Roberts, M. S. E., and Hessels, J. W. T. (2010). A two-solar-mass neutron star measured using Shapiro delay. *Nature*, **467**, 1081–1083.
- Derishev, E. V., Kocharovskiy, V. V., and Kocharovskiy, V. V. (1999). The neutron component in fireballs of gamma-ray bursts: Dynamics and observable imprints. *Astrophys. J.*, **521**, 640–649.
- Di Prisco, A., Herrera, L., and Esculpi, M. (1996). Radiating gravitational collapse before relaxation. *Class. Quant. Grav.*, **13**, 1053–1068.
- Dimmelmeier, H., Font, J. A., and Müller, E. (2001). Gravitational waves from relativistic rotational core collapse. *Astrophys. J.*, **560**, L163–166.
- Dimmelmeier, H., Font, J. A., and Müller, E. (2002). Relativistic simulations of rotational core collapse. I. Methods, initial models, and code tests. *Astron. Astrophys.*, **388**, 917–935.
- d’Inverno, Ray (1992). *Introducing Einstein’s Relativity*. Oxford University Press, Oxford.
- Dionysopoulou, K., Alic, D., Palenzuela, C., Rezzolla, L., and Giacomazzo, B. (2013). General-relativistic resistive magnetohydrodynamics in three dimensions: Formulation and tests. *Phys. Rev. D*, **88**, 044020.
- Donat, R., Font, J. A., Ibáñez, J. M., and Marquina, A. (1998). A flux-split algorithm applied to relativistic flows. *J. Comput. Phys.*, **146**, 58–81.
- Donat, R. and Marquina, A. (1996). Capturing shock reflections: An improved flux formula. *J. Comput. Phys.*, **125**, 42.
- Dönmez, O., Zanotti, O., and Rezzolla, L. (2011). On the development of quasi-periodic oscillations in Bondi–Hoyle accretion flows. *Mon. Not. R. Astron. Soc.*, **412**, 1659–1668.
- Douchin, F. and Haensel, P. (2001). A unified equation of state of dense matter and neutron star structure. *Astron. Astrophys.*, **380**, 151–167.
- Downes, T. P., Duffy, P., and Komissarov, S. S. (2002). Relativistic blast waves and synchrotron emission. *Mon. Not. R. Astron. Soc.*, **332**, 144–154.
- Drago, A., Lavagno, A., and Parenti, I. (2007). Burning of a hadronic star into a quark or a hybrid star. *Astrophys. J.*, **659**, 1519–1535.
- Dubal, M. R., D’inverno, R. A., and Vickers, J. A. (1998). Combining Cauchy and characteristic codes. V. Cauchy-characteristic matching for a spherical spacetime containing a perfect fluid. *Phys. Rev. D*, **58**, 044019.
- Duez, M. D., Foucart, F., Kidder, L. E., Pfeiffer, H. P., Scheel, M. A., Teukolsky, S. A. (2008). Evolving black hole-neutron star binaries in general relativity using pseudospectral and finite difference methods. *Phys. Rev. D*, **78**, 104015.
- Duez, M. D., Liu, Y. T., Shapiro, S. L., Shibata, M., and Stephens, B. C. (2006). Evolution of magnetized, differentially rotating neutron stars: Simulations in full general relativity. *Phys. Rev. D*, **73**, 104015.
- Duez, M. D., Liu, Y. T., Shapiro, S. L., and Stephens, B. C. (2004). General relativistic hydrodynamics with viscosity: Contraction, catastrophic collapse, and disk formation in hypermassive neutron stars. *Phys. Rev. D*, **69**, 104030.
- Dumbser, M., Moschetta, J. M., and Gressier, J. (2004). A matrix stability analysis of the carbuncle phenomenon. *J. Comput. Phys.*, **197**, 647–670.
- Dumbser, M. (2005). *Arbitrary high order schemes for the solution of hyperbolic conservation laws in complex domains*. PhD Thesis, Institut fur Aerodynamik und Gasdynamik,

- Stuttgart. Shaker Verlag, Aachen.
- Dumbser, M., Käser, M., Titarev, V. A., and Toro, E. F. (2007). Quadrature-free non-oscillatory finite volume schemes on unstructured meshes for nonlinear hyperbolic systems. *J. Comput. Phys.*, **226**, 204–243.
- Dumbser, M. and Käser, M. (2007). Arbitrary high order non-oscillatory finite volume schemes on unstructured meshes for linear hyperbolic systems. *J. Comput. Phys.*, **221**, 693–723.
- Dumbser, M., Balsara, D. S., Toro, E. F., and Munz, C.-D. (2008a). A unified framework for the construction of one-step finite volume and discontinuous Galerkin schemes on unstructured meshes. *J. Comput. Phys.*, **227**, 8209–8253.
- Dumbser, M., Enaux, C., and Toro, E. F. (2008b). Finite volume schemes of very high order of accuracy for stiff hyperbolic balance laws. *J. Comput. Phys.*, **227**, 3971–4001.
- Dumbser, M. and Zanotti, O. (2009). Very high order PNPM schemes on unstructured meshes for the resistive relativistic MHD equations. *J. Comput. Phys.*, **228**, 6991–7006.
- Dumbser, M., Zanotti, O., Hidalgo, A., and Balsara, D. S. (2012). ADER-WENO finite volume schemes with space-time adaptive mesh refinement. *J. Comput. Phys.*, **248**, 257–286.
- D'yakov, S. P. (1954). On the stability of shock waves. *Zh. Eksp. Teor. Fiz.*, **27**, 288.
- East, W. E., and Pretorius, F. (2013). Ultrarelativistic Black Hole Formation. *Phys. Rev. Lett.*, **110**, 101101.
- Echeverria, F. (1989). Gravitational-wave measurements of mass and angular momentum of a black hole. *Phys. Rev. D*, **40**, 3194.
- Eckart, C. (1940). The thermodynamics of irreversible processes. III: Relativistic theory of the simple fluid. *Phys. Rev.*, **58**, 919.
- Ehlers, J. (1971). General Relativity and Kinetic Theory. In *General Relativity and Cosmology*, 1–70. Proceedings of the Varenna Summer School on Relativistic Astrophysics. Academic Press, New York.
- Eichler, D., Livio, M., Piran, T., and Schramm, D. N. (1989). Nucleosynthesis, neutrino bursts and gamma-rays from coalescing neutron stars. *Nature*, **340**, 126–128.
- Einfeldt, B. (1988). On Godunov-type methods for gas dynamics. *SIAM J. Numer. Anal.*, **25**, 294–318.
- Einfeldt, B., Roe, P. L., Munz, C. D., and Sjogreen, B. (1991). On Godunov-type methods near low densities. *J. Comput. Phys.*, **92**, 273–295.
- Ellis, G. F. R., Maartens, R., and MacCallum, M. A. H. (2012). *Relativistic Cosmology*. Cambridge University Press, Cambridge.
- Engquist, B., Luskin, M. B., Majda, A. (1988). *Computational Fluid Dynamics and Reacting Gas Flows*. Springer, Berlin.
- Eriguchi, Y. and Mueller, E. (1985). A general computational method for obtaining equilibria of self-gravitating and rotating gases. *Astron. Astrophys.*, **146**, 260–268.
- Ernst, F. J. (1968). New formulation of the axially symmetric gravitational field problem. *Phys. Rev.*, **167**, 1175–1177.
- Erpenbeck, J. J. (1962). Stability of step shocks. *Phys. Fluids*, **5**, 1181–1187.
- Eskola, K. J., Honkanen, H., Niemi, H., Ruuskanen, P. V., and Räsänen, S. S. (2005). Predictions for low- $p_T$  and high- $p_T$  hadron spectra in nearly central Pb+Pb collisions at  $\sqrt{s_{NN}}=5.5$  TeV tested at  $\sqrt{s_{NN}}=130$  and 200 GeV. *Phys. Rev. D*, **72**, 044904.

- Etienne, Z. B., Faber, J. A., Liu, Y. T., Shapiro, S. L., and Baumgarte, T. W. (2007). Filling the holes: Evolving excised binary black hole initial data with puncture techniques. *Phys. Rev. D*, **76**, 101503.
- Eulderink, F. and Mellema, G. (1994). Special relativistic jet collimation by inertial confinement. *Astron. and Astrophys.*, **284**, 654–662.
- Eulderink, F. and Mellema, G. (1995). General relativistic hydrodynamics with a Roe solver. *Astron. Astrophys. Suppl.*, **110**, 587–623.
- Evans, C. (1986). An approach for calculating axisymmetric gravitational collapse. In *Dynamical Spacetimes and Numerical Relativity* (Ed. J. Centrella), 3–39. Cambridge University Press, Cambridge.
- Faber, J. A. and Rasio, F. A. (2012). Binary neutron star mergers. *Living Rev. Relativ.*, **15**, 8.
- Falle, S., Hubber, D., Goodwin, S., and Boley, A. (2012). Comparison Between AMR and SPH. In *Numerical Modeling of Space Plasma Flows* (Ed. N. V. Pogorelov, J. A. Font, E. Audit, and G. P. Zank), **459**, Astronomical Society of the Pacific Conference Series, 298.
- Falle, S. A. E. G. and Komissarov, S. S. (2001). On the inadmissibility of non-evolutionary shocks. *J. Plasma Phys.*, **65**, 29–58.
- Fanaroff, B. L. and Riley, J. M. (1974). The morphology of extragalactic radio sources of high and low luminosity. *Mon. Not. R. Astron. Soc.*, **167**, 31P–36P.
- Farris, B. D., Li, T. K., Liu, Y. T., and Shapiro, S. L. (2008). Relativistic radiation magnetohydrodynamics in dynamical spacetimes: Numerical methods and tests. *Phys. Rev. D*, **78**, 024023.
- Farris, B. D., Liu, Y. T., and Shapiro, S. L. (2010). Binary black hole mergers in gaseous environments: “Binary Bondi” and “binary Bondi–Hoyle–Lyttleton” accretion. *Phys. Rev. D*, **81**, 084008.
- Ferrari, V., Gualtieri, L., and Pannarale, F. (2009). A semi-relativistic model for tidal interactions in BH-NS coalescing binaries. *Class. Quant. Grav.*, **26**, 125004.
- Feynman, R. P. (1964). *Feynman Lectures on Physics. Volume 2: Mainly Electromagnetism and Matter*, Addison-Wesley, San Francisco.
- Fickett, W. and Davis, C. (1979). *Detonation: Theory and Experiment*. Dover, New York.
- Field, S. E., Hesthaven, J. S., Lau, S. R., and Mroue, A. H. (2010). Discontinuous Galerkin method for the spherically reduced Baumgarte–Shapiro–Shibata–Nakamura system with second-order operators. *Phys. Rev. D*, **82**, 104051.
- Fischer, T., Whitehouse, S. C., Mezzacappa, A., Thielemann, F.-K., and Liebendörfer, M. (2009). The neutrino signal from protoneutron star accretion and black hole formation. *Astron. Astrophys.*, **499**, 1–15.
- Fishbone, L. G. and Moncrief, V. (1976). Relativistic fluid disks in orbit around Kerr black holes. *Astrophys. J.*, **207**, 962–976.
- Flammang, R. A. (1982). Stationary spherical accretion into black holes. II. Theory of optically thick accretion. *Mon. Not. R. Astron. Soc.*, **199**, 833–867.
- Floch, P. Le and Raviart, P. A. (1988). An asymptotic expansion for the solution of the generalized Riemann problem. Part I: General theory. *Annales de l'institut Henri Poincaré (C) Analyse non linéaire*, **5**, 179–207.
- Fock, V. (1959). *The Theory of Space, Time, and Gravitation*. Pergamon, New York.
- Foglizzo, T., Galletti, P., and Ruffert, M. (2005). A fresh look at the unstable simulations of Bondi–Hoyle–Lyttleton accretion. *Astron. Astrophys.*, **435**, 397–411.

- Foglizzo, T. and Ruffert, M. (1999). An analytic study of Bondi–Hoyle–Lyttleton accretion. II. Local stability analysis. *Astron. Astrophys.*, **347**, 901–914.
- Font, J. A., Ibáñez, J. M., Martí, J. M., and Marquina, A. (1994). Multidimensional relativistic hydrodynamics: Characteristic fields and modern high-resolution shock-capturing schemes. *Astron. Astrophys.*, **282**, 304.
- Font, J. A. (2008). Numerical hydrodynamics in general relativity. *Living Rev. Relativ.*, **11**, 7.
- Font, J. A. and Daigne, F. (2002a). On the stability of thick accretion disks around black holes. *Astrophys. J.*, **581**, L23–L26.
- Font, J. A. and Daigne, F. (2002b). The runaway instability of thick discs around black holes-I. The constant angular momentum case. *Mon. Not. R. Astron. Soc.*, **334**, 383–400.
- Font, J. A., Goodale, T., Iyer, S., Miller, M., Rezzolla, L., Seidel, E., Stergioulas, N., Suen, W. M., and Tobias, M. (2002). Three-dimensional general relativistic hydrodynamics. II. Long-term dynamics of single relativistic stars. *Phys. Rev. D*, **65**, 084024.
- Font, J. A., Ibáñez, J. M., and Papadopoulos, P. (1998). A “horizon-adapted” approach to the study of relativistic accretion flows onto rotating black holes. *Astrophys. J.*, **507**, L67–L70.
- Font, J. A., Ibáñez, J. M., and Papadopoulos, P. (1999). Non-axisymmetric relativistic Bondi–Hoyle accretion on to a Kerr black hole. *Mon. Not. R. Astron. Soc.*, **305**, 920–936.
- Font, J. A. and Ibáñez, J. M. (1998). A numerical study of relativistic Bondi–Hoyle accretion onto a moving black hole: Axisymmetric computations in a Schwarzschild background. *Astrophys. J.*, **494**, 297.
- Font, J. A., Stergioulas, N., and Kokkotas, K. D. (2000). Nonlinear hydrodynamical evolution of rotating relativistic stars: Numerical methods and code tests. *Mon. Not. R. Astron. Soc.*, **313**, 678.
- Fornberg, B. (1988). Generation of finite difference formulas on arbitrarily spaced grids. *Mathematics of Computation*, **51** (184), 699–706.
- Foucart, F. (2012). Black hole–neutron star mergers: Disk mass predictions. *Phys. Rev. D*, **86**, 124007.
- Fourés-Bruhat, Y. (Choquet-Bruhat, Y.) (1948). Sur l’intégration des équations d’Einstein. *C. R. Acad. Sci. Paris*, **226**, 1071.
- Fragile, P. C. (2009). Effective inner radius of tilted black hole accretion disks. *Astrophys. J.*, **706**, L246–L250.
- Fragile, P. C. and Anninos, P. (2003). Hydrodynamic stability of cosmological quark-hadron phase transitions. *Phys. Rev. D*, **67**, 103010.
- Fragile, P. C. and Anninos, P. (2005). Hydrodynamic simulations of tilted thick-disk accretion onto a Kerr black hole. *Astrophys. J.*, **623**, 347–361.
- Frank, J., King, A., and Raine, D. J. (2002). *Accretion Power in Astrophysics*. Third edition. Cambridge University Press, Cambridge.
- Frankel, T. (2004). *The Geometry of Physics: An Introduction*. Second Edition. Cambridge University Press, Cambridge.
- Frauendiener, J. (2004). Conformal infinity. *Living Rev. Relativ.*, **7**, 1.
- Freiburghaus, C., Rosswog, S., and Thielemann, F.-K. (1999). R-process in neutron star mergers. *Astrophys. J.*, **525**, L121–L124.
- Friedman, A. (1922). Über die Krümmung des Raumes. *Z. Phys. A*, **10**, 377–386.

## 696 References

- Friedman, J. L., Ipser, J. R., and Sorkin, R. D. (1988). Turning-point method for axisymmetric stability of rotating relativistic stars. *Astrophys. J.*, **325**, 722–724.
- Friedman, J. L. and Schutz, B. F. (1978). Secular instability of rotating Newtonian stars. *Astrophys. J.*, **222**, 281–296.
- Friedman, J. L. and Stergioulas, N. (2012). *Relativistic Rotating Stars*. Cambridge University Press, Cambridge.
- Friedrich, H. (1996). Hyperbolic reductions for Einstein’s equations. *Class. Quant. Grav.*, **13**, 1451–1469.
- Friedrich, O. (1998). Weighted Essentially Non-Oscillatory Schemes for the Interpolation of Mean Values on Unstructured Grids. *J. Comput. Phys.*, **144**, 194–212.
- Frittelli, S. (1997). Note on the propagation of the constraints in standard 3+1 general relativity. *Phys. Rev. D*, **55**, 5992–5996.
- Frittelli, S. and Gómez, R. (2000). Ill-posedness in the Einstein equations. *J. Math. Phys.*, **41**, 5535–5549.
- Fryer, C. L. and New, K. C. B. (2011). Gravitational waves from gravitational collapse. *Living Rev. Relativ.*, **14**, 1.
- Fryxell, B. A. and Taam, R. E. (1988). Numerical simulation of nonaxisymmetric adiabatic accretion flow. *Astrophys. J.*, **335**, 862–880.
- Galeazzi, F., Yoshida, S., and Eriguchi, Y. (2012). Differentially-rotating neutron star models with a parametrized rotation profile. *Astron. Astrophys.*, **541**, A156.
- Gao, S. (2011). General maximum entropy principle for self-gravitating perfect fluid. *Phys. Rev. D*, **84**, 104023.
- Garfinkle, D. (2002). Harmonic coordinate method for simulating generic singularities. *Phys. Rev. D*, **65**, 044029.
- Gehrels, N., Ramirez-Ruiz, E., and Fox, D. B. (2009). Gamma-ray bursts in the Swift era. *Annu. Rev. Astron. Astr.*, **47**, 567–617.
- Geroch, R. and Lindblom, L. (1990). Dissipative relativistic fluid theories of divergence type. *Phys. Rev. D*, **41**, 1855–1861.
- Ghisellini, G., Padovani, P., Celotti, A., and Maraschi, L. (1993). Relativistic bulk motion in active galactic nuclei. *Astrop. J.*, **407**, 65–82.
- Giacomazzo, B., Perna, R., Rezzolla, L., Troja, E., and Lazzati, D. (2013). Compact binary progenitors of short gamma-ray bursts. *Astrophys. J.*, **762**, L18.
- Giacomazzo, B. and Rezzolla, L. (2007). WhiskyMHD: A new numerical code for general relativistic magnetohydrodynamics. *Class. Quant. Grav.*, **24**, S235–S258.
- Giacomazzo, B., Rezzolla, L., and Baiotti, L. (2009). Can magnetic fields be detected during the inspiral of binary neutron stars? *Mon. Not. R. Astron. Soc.*, **399**, L164–L168.
- Giacomazzo, B., Rezzolla, L., and Baiotti, L. (2011). Accurate evolutions of inspiralling and magnetized neutron stars: Equal-mass binaries. *Phys. Rev. D*, **83**, 044014.
- Giacomazzo, B., Rezzolla, L., and Stergioulas, N. (2011). Collapse of differentially rotating neutron stars and cosmic censorship. *Phys. Rev. D*, **84**, 024022.
- Giuliani, A., Fuschino, F., Vianello, G., et al. (2010). AGILE detection of delayed gamma-ray emission from the short gamma-ray burst GRB 090510. *Astrophys. J.*, **708**, L84–L88.
- Glendenning, N. K. and Moszkowski, S. A. (1991). Reconciliation of neutron star masses and binding of the lambda in hypernuclei. *Phys. Rev. Lett.*, **67**, 2414–2417.
- Godunov, S. K. (1959). A difference method for numerical calculations of discontinuous

- solutions of the equations of hydrodynamics. *Mat. Sb.*, **47**, 271. (In Russian).
- Gomez, J.-L., Marscher, A. P., Alberdi, A., Marti, J. M. A., and Ibanez, J. M. A. (1998). Sub-parsec polarimetric radio observations of 3C 120: A close-up look at superluminal motion. *Astrophys. J.*, **499**, 221–226.
- Gorenstein, M. I. and Zhdanov, V. I. (1987). Shock stability criterion in relativistic hydrodynamics and quark–gluon plasma hadronization. *Z. Phys. C*, **34**, 79–84.
- Gottlieb, S. and Shu, C. (1998). Total variation diminishing Runge–Kutta schemes. *Math. Comp.*, **67**, 73–85.
- Gottlieb, S., Shu, C.-W., and Tadmor, E. (2001). Strong stability-preserving high-order time discretization methods. *SIAM Review*, **43**, 89–112.
- Gourgoulhon, É. (2006). An introduction to relativistic hydrodynamics. *EAS Publications Series*, **21**, 43–79.
- Gourgoulhon, É. (2012). *3+1 Formalism in General Relativity*. Volume 846, Lecture Notes in Physics. Springer, Berlin.
- Gourgoulhon, É., Grandclément, P., Taniguchi, K., Marck, J. A., and Bonazzola, S. (2001). Quasiequilibrium sequences of synchronized and irrotational binary neutron stars in general relativity: Method and tests. *Phys. Rev. D*, **63**, 064029.
- Gourgoulhon, É. and Jaramillo, J.-L. (2006). A 3 + 1 perspective on null hypersurfaces and isolated horizons. *Phys. Rep.*, **423** (4–5), 159–294.
- Grad, H. (1949). On the kinetic theory of rarefied gases. *Communications on Pure and Applied Mathematics*, **2**, 331–407.
- Grandclément, P. (2006). Accurate and realistic initial data for black hole–neutron star binaries. *Phys. Rev. D*, **74**, 124002.
- Groot, S. R., Leeuwen, W. A., and van Weert, C. G. (1980). *Relativistic kinetic theory: Principles and applications*. North-Holland, Amsterdam.
- Gundlach, C., Martin-Garcia, J. M., Calabrese, G., and Hinder, I. (2005). Constraint damping in the Z4 formulation and harmonic gauge. *Class. Quant. Grav.*, **22**, 3767–3774.
- Gyulassy, M., Kajantie, K., Kurki-Suonio, H., and McLerran, L. (1984). Deflagrations and detonations as a mechanism of hadron bubble growth in supercooled quark–gluon plasmas. *Nucl. Phys. B*, **237**, 477–501.
- Harada, T., Goymer, C., and Carr, B. J. (2002). Tolman–Bondi collapse in scalar-tensor theories as a probe of gravitational memory. *Phys. Rev. D*, **66**, 104023.
- Hardee, P. E. (2006). AGN jets: A review of stability and structure. In *Relativistic Jets: The Common Physics of AGN, Microquasars, and Gamma-Ray Bursts* (Ed. P. A. Hughes and J. N. Bregman), **856**, American Institute of Physics Conference Series, 57–77.
- Hardee, P. E., Rosen, A., Hughes, P. A., and Duncan, G. C. (1998). Time-dependent structure of perturbed relativistic jets. *Astrophys. J.*, **500**, 599–609.
- Harten, A. (1983). High resolution schemes for hyperbolic conservation laws. *J. Comput. Phys.*, **49**, 357–393.
- Harten, A., Engquist, B., Osher, S., and Chakravarthy, S. R. (1987). Uniformly high order accurate essentially non-oscillatory schemes. III. *J. Comput. Phys.*, **71**, 231–303.
- Harten, A., Lax, P. D., and van Leer, B. (1983). On upstream differencing and Godunov-type schemes for hyperbolic conservation laws. *SIAM Rev.*, **25**, 35–61.
- Hartle, J. B. (2003). *Gravity: An introduction to Einstein’s general relativity*. Addison Wesley, San Francisco.

- Hawke, I., Löffler, F., and Nerozzi, A. (2005). Excision methods for high resolution shock capturing schemes applied to general relativistic hydrodynamics. *Phys. Rev. D*, **71**, 104006.
- Hawking, S. W. and Ellis, G. F. R. (1973). *The Large Scale Structure of Spacetime*. Cambridge University Press, Cambridge.
- Hawley, J. F., Smarr, L. L., and Wilson, J. R. (1984). A numerical study of nonspherical black hole accretion. I. Equations and test problems. *Astrophys. J.*, **277**, 296–311.
- Henrick, Andrew K., Aslam, Tariq D., and Powers, Joseph M. (2005). Mapped weighted essentially non-oscillatory schemes: Achieving optimal order near critical points. *J. Comput. Phys.*, **207**, 542–567.
- Hernandez, Jr., W. C. and Misner, C. W. (1966). Observer time as a coordinate in relativistic spherical hydrodynamics. *Astrophys. J.*, **143**, 452–464.
- Herrera, L., di Prisco, A., Fuenmayor, E., and Troconis, O. (2009). Dynamics of viscous dissipative gravitational collapse: A full causal approach. *Int. J. Mod. Phys. D*, **18**, 129–145.
- Herzog, M. and Röpke, F. K. (2011). Three-dimensional hydrodynamic simulations of the combustion of a neutron star into a quark star. *Phys. Rev. D*, **84**, 083002.
- Hesthaven, J. S. and Warburton, T. (2007). *Nodal Discontinuous Galerkin Methods: Algorithms, Analysis, and Applications*. Texts in Applied Mathematics. Springer, Berlin.
- Hidalgo, A. and Dumbser, M. (2011). ADER schemes for nonlinear systems of stiff advection–diffusion–reaction equations. *J. Sci. Comput.*, **48**, 173–189.
- Hilditch, D., Bernuzzi, S., Thierfelder, M., Cao, Z., Tichy, W., and Bruegmann, B. (2012). Compact binary evolutions with the Z4c formulation. *arXiv:1212.2901*.
- Hiscock, W. A. and Lindblom, L. (1983). Stability and causality in dissipative relativistic fluids. *Ann. Phys.*, **151**, 466–496.
- Hiscock, W. A. and Lindblom, L. (1985). Generic instabilities in first-order dissipative relativistic fluid theories. *Phys. Rev. D*, **31**, 725–733.
- Hiscock, W. A. and Lindblom, L. (1988). Nonlinear pathologies in relativistic heat-conducting fluid theories. *Phys. Lett. A*, **131**, 509–513.
- Hoeflich, P., Wheeler, J. C., and Thielemann, F. K. (1998). Type IA supernovae: Influence of the initial composition on the nucleosynthesis, light curves, and spectra and consequences for the determination of omega M and lambda. *Astrophys. J.*, **495**, 617–629.
- Holm, D. (1989). Hamiltonian techniques for relativistic fluid dynamics and stability theory. In *Relativistic Fluid Dynamics* (Ed. A. Anile and Y. Choquet-Bruhat), **1385**, Lecture Notes in Mathematics, 1–64. Springer, Berlin.
- Homan, D. C., Kadler, M., Kellermann, K. I., Kovalev, Y. Y., Lister, M. L., Ros, E., Savolainen, T., and Zensus, J. A. (2009). MOJAVE: Monitoring of Jets in Active Galactic Nuclei with VLBA Experiments. VII. Blazar jet acceleration. *Astrophys. J.*, **706**, 1253–1268.
- Horedt, G. P. (2004). *Polytropes—Applications in Astrophysics and Related Fields*, Volume 306, Astrophysics and Space Science Library. Kluwer Academic Publishers, Dordrecht.
- Hotokezaka, K., Kyutoku, K., Okawa, H., Shibata, M., and Kiuchi, K. (2011). Binary neutron star mergers: Dependence on the nuclear equation of state. *Phys. Rev. D*, **83**, 124008.
- Hou, T. Y. and LeFloch, P. G. (1994). Why nonconservative schemes converge to wrong solutions: Error analysis. *Math. Comp.*, **62**, 497–530.
- Hoyle, F. and Lyttleton, R. A. (1939). The effect of interstellar matter on climatic variation.

- Proceedings of the Cambridge Philosophical Society*, **35**, 405–415.
- Hsieh, S.-H. and Spiegel, E. A. (1976). The equations of photohydrodynamics. *Astrophys. J.*, **207**, 244–252.
- Huang, K. (1987). *Statistical Mechanics*, Second Edition. John Wiley, New York.
- Hubble, E. P. (1926). Extragalactic nebulae. *Astrophys. J.*, **64**, 321–369.
- Huet, P., Kajantie, K., Leigh, R. G., Liu, B.-H., and McLerran, L. (1993). Hydrodynamic stability analysis of burning bubbles in electroweak theory and in QCD. *Phys. Rev. D*, **48**, 2477–2492.
- Huovinen, P. (2005). Anisotropy of flow and the order of phase transition in relativistic heavy ion collisions. *Nucl. Phys. A*, **761**, 296–312.
- Huovinen, P. and Ruuskanen, P. V. (2006). Hydrodynamic models for heavy ion collisions. *Annual Review of Nuclear and Particle Science*, **56**, 163–206.
- Huynh, H. T. (1995). Accurate upwind methods for the Euler equations. *SIAM J. Numer. Anal.*, **32**, 1565–1619.
- Ibáñez, J. M. and Miralles, J. A. (1985). Anisotropic effects on the collapse of white dwarfs. *Astrophys. J.*, **299**, 21–23.
- Ibáñez, J. M., Aloy, M.-A., Font, J. A., Martí, J. M., Miralles, J. A., and Pons, J. A. (2001). Riemann solvers in general relativistic hydrodynamics. In *Godunov methods: Theory and Applications* (Ed. E. Toro). Kluwer Academic Publishers, Dordrecht.
- Ibáñez, J. M., Cordero-Carrión, I., and Miralles, J. A. (2012a). On numerical relativistic hydrodynamics and barotropic equations of state. *Class. Quant. Grav.*, **29**, 157001.
- Ibáñez, J. M., Cordero-Carrión, I., Martí, J. M. and Miralles, J. A. (2012b). On the convexity of relativistic hydrodynamics. *Class. Quant. Grav.*, **30**, 057002.
- Ibáñez, J. M. (2012c). Notes on the eigenstructure of the Valencia conservative formulation. Private communication.
- Ignatius, J., Kajantie, K., Kurki-Suonio, H., and Laine, M. (1994). Growth of bubbles in cosmological phase transitions. *Phys. Rev. D*, **49**, 3854–3868.
- Isaacson, R., Welling, J., and Winicour, J. (1983). Null cone computation of gravitational radiation. *J. Math. Phys.*, **24**, 1824–1834.
- Isenberg, J. A. (2008). Waveless approximation theories of gravity. *Int. J. Mod. Phys. D*, **17**, 265–273.
- Ishii, T., Matsuda, T., Shima, E., Livio, M., Anzer, U., and Boerner, G. (1993). Numerical simulations of two-dimensional and three-dimensional wind accretion flows of an isothermal gas. *Astrop. J.*, **404**, 706–716.
- Israel, W. (1966). Singular hypersurfaces and thin shells in general relativity. *Nuovo Cimento B Serie*, **44**, 1–14.
- Israel, W. (1967). Event horizons in static vacuum space-times. *Phys. Rev. D*, **164**, 1776–1779.
- Israel, W. (1976). Nonstationary irreversible thermodynamics: A causal relativistic theory. *Ann. Phys.*, **100**, 310–331.
- Israel, W. and Stewart, J. M. (1979). Transient relativistic thermodynamics and kinetic theory. *Ann. Phys.*, **118**, 341–372.
- Janka, H.-T. and Mueller, E. (1995). The first second of a Type II supernova: Convection, accretion, and shock propagation. *Astrophys. J.*, **448**, L109+.
- Janka, H.-Th., Zwerger, T., and Mönchmeyer, R. (1993). Does artificial viscosity destroy

- prompt Type-II supernova explosions? *Astron. Astrophys.*, **268**, 360–368.
- Jebsen, J. T. (1921). On the General Spherically Symmetric Solutions of Einstein's Gravitational Equations in Vacuo. *Ark. Mat. Ast. Fys.*, **15**, 18.
- Jeffrey, A. (1976). *Quasilinear Hyperbolic Systems and Waves*. Pitman, London.
- Jiang, G., Levy, D., Lin, C., Osher, S., and Tadmor, E. (1998). High-resolution nonoscillatory central schemes with nonstaggered grids for hyperbolic conservation laws. *SIAM J. Numer. Anal.*, **35**, 2147–2168.
- Jiang, G.-S. and Shu, C.-W. (1996). Efficient implementation of weighted ENO schemes. *J. Comput. Phys.*, **126**, 202–228.
- Jordan, IV, G. C., Fisher, R. T., Townsley, D. M., Calder, A. C., Graziani, C., Asida, S., Lamb, D. Q., and Truran, J. W. (2008). Three-dimensional simulations of the deflagration phase of the gravitationally confined detonation model of Type Ia supernovae. *Astrophys. J.*, **681**, 1448–1457.
- Jou, D., Casas-Vázquez, J., and Lebon, G. (2009). *Extended Irreversible Thermodynamics*. Springer, Berlin.
- Jüttner, F. (1911). Das Maxwellsche Gesetz der Geschwindigkeitsverteilung in der Relativtheorie. *Annalen der Physik*, **339**, 856–882.
- Kaeser, M. and Iske, A. (2005). ADER schemes on adaptive triangular meshes for scalar conservation laws. *J. Comput. Phys.*, **205**, 486–508.
- Kamenshchik, A., Moschella, U., and Pasquier, V. (2001). An alternative to quintessence. *Phys. Lett. B*, **511**, 265–268.
- Kamionkowski, M. and Freese, K. (1992). Instability and subsequent evolution of electroweak bubbles. *Phys. Rev. Lett.*, **69**, 2743–2746.
- Kantor, E. M. and Gusakov, M. E. (2009). Damping of sound waves in superfluid nucleon-hyperon matter of neutron stars. *Phys. Rev. D*, **79**, 043004.
- Kastaun, W. (2006). High-resolution shock capturing scheme for ideal hydrodynamics in general relativity optimized for quasistationary solutions. *Phys. Rev. D*, **74**, 124024.
- Kastaun, W. (2012). Private communication.
- Kastaun, W., Galeazzi, F., Alic, D., Rezzolla, L., and Font, J. A. (2013). On the black hole from merging binary neutron stars: How fast can it spin? *Phys. Rev. D*, **88**, R021501.
- Kato, S., Fukue, J., and Mineshige, S. (2008). *Black Hole Accretion Disks – Towards a New Paradigm*. Kyoto University Press, Kyoto.
- Katz, J. (1984). Relativistic potential vorticity. *Philos. T. Roy. Soc. A*, **391** (1801), 415–418.
- Kellerman, T., Rezzolla, L., and Radice, D. (2010). Critical phenomena in neutron stars. II. Head-on collisions. *Class. Quant. Grav.*, **27** (23), 235016.
- Kerr, R. P. (1963). Gravitational field of a spinning mass as an example of algebraically special metrics. *Phys. Rev. Lett.*, **11**, 237–238.
- Khokhlov, A. M. (1991). Delayed detonation model for Type IA supernovae. *Astron. Astrophys.*, **245**, 114–128.
- Khokhlov, A. M., Oran, E. S., and Wheeler, J. C. (1997). Deflagration-to-detonation transition in thermonuclear supernovae. *Astrophys. J.*, **478**, 678.
- Kiuchi, K., Sekiguchi, Y., Kyutoku, K., and Shibata, M. (2012). Gravitational waves, neutrino emissions and effects of hyperons in binary neutron star mergers. *Class. Quant. Grav.*, **29**, 124003.
- Kiuchi, K., Sekiguchi, Y., Shibata, M., and Taniguchi, K. (2009). Longterm general rel-

- ativistic simulation of binary neutron stars collapsing to a black hole. *Phys. Rev. D*, **80**, 064037.
- Kley, W. and Schäfer, G. (1994). Post-Newtonian oscillations of a rotating disk of dust. *Phys. Rev. D*, **50**, 6217–6226.
- Königl, A. (1980). Relativistic gasdynamics in two dimensions. *Phys. Fluids*, **23**, 1083–1090.
- Kokkotas, K. D. and Schmidt, B. G. (1999). Quasi-normal modes of stars and black holes. *Living Rev. Relativ.*, **2**, 2.
- Kolgan, V. P. (1972). Application of the minimum-derivative principle in the construction of finite-difference schemes for numerical analysis of discontinuous solutions in gas dynamics. *Transactions of the Central Aerohydrodynamics Institute*, **3**, 68–77. (In Russian).
- Komar, A. (1959). Covariant conservation laws in general relativity. *Phys. Rev.*, **113**, 934–936.
- Komatsu, H., Eriguchi, Y., and Hachisu, I. (1989). Rapidly rotating general relativistic stars. I. Numerical method and its application to uniformly rotating polytropes. *Mon. Not. R. Astron. Soc.*, **237**, 355–379.
- Komissarov, S. S. (2011). Magnetic acceleration of relativistic jets. *Memorie della Società Astronomica Italiana*, **82**, 95–103.
- Komissarov, S. S. and Falle, S. A. E. G. (1998). The large-scale structure of FR-II radio sources. *Mon. Not. R. Astron. Soc.*, **297**, 1087–1108.
- Komissarov, S. S., Vlahakis, N., Königl, A., and Barkov, M. V. (2009). Magnetic acceleration of ultrarelativistic jets in gamma-ray burst sources. *Mon. Not. R. Astron. Soc.*, **394**, 1182–1212.
- Kontorovich, V. M. (1958). Concerning the stability of shock waves. *J. Exp. Theor. Phys.*, **6**, 1179.
- Koppitz, M., Pollney, D., Reisswig, C., Rezzolla, L., Thornburg, J., Diener, P., and Schnetter, E. (2007). Getting a kick from equal-mass binary black hole mergers. *Phys. Rev. Lett.*, **99**, 041102.
- Korobkin, O., Abdikamalov, E. B., Schnetter, E., Stergioulas, N., and Zink, B. (2011). Stability of general-relativistic accretion disks. *Phys. Rev. D*, **83**, 043007.
- Korobkin, O., Rosswog, S., Arcones, A., and Winteler, C. (2012). On the astrophysical robustness of the neutron star merger r-process. *Mon. Not. R. Astron. Soc.*, **426**, 1940–1949.
- Korobkin, O., Abdikamalov, E. B., Stergioulas, N., Schnetter, E., Zink, B., Rosswog S., and Ott, C. D., (2013). The runaway instability in general relativistic accretion discs. *Mon. Not. R. Astron. Soc.*, **431**, 349–354.
- Kozłowski, M., Jaroszynski, M., and Abramowicz, M. A. (1978). The analytic theory of fluid disks orbiting the Kerr black hole. *Astron. and Astrophys.*, **63**, 209–220.
- Kramer, M., Lyne, A.G., Burgay, M., et al. (2005). The double pulsar—a new testbed for relativistic gravity. In *Binary Pulsars* (Ed. Rasio and Stairs), *Astr. Soc P.*, **328**, 59.
- Krasinski, A. (1997). *Inhomogeneous Cosmological Models*. Cambridge University Press, Cambridge.
- Krasnopol'sky, R., Li, Z.-Y., and Blandford, R. (1999). Magnetocentrifugal launching of jets from accretion disks. I. Cold axisymmetric flows. *Astrophys. J.*, **526**, 631–642.
- Kreiss, H. O. and Oliger, J. (1973). *Methods for the Approximate Solution of Time Dependent*

- Problems.* GARP publication series No. 10, Geneva.
- Kremer, G. M. (1985). *Expanded thermodynamics of ideal, dense gases.* PhD. Thesis, Technische Universitaet, Berlin.
- Kulikovskii, A. G., Pogorelov, N. V., and Semenov, A. Yu. (2001). *Mathematical Aspects of Numerical Solution of Hyperbolic Systems.* Chapman and Hall/CRC, Boca Raton.
- Künzle, H. P. and Nester, J. M. (1984). Hamiltonian formulation of gravitating perfect fluids and the Newtonian limit. *J. Math. Phys.*, **25**, 1009–1018.
- Kurganov, A. and Tadmor, E. (2000). New high-resolution central schemes for nonlinear conservation laws and convection–diffusion equations. *J. Comput. Phys.*, **160**, 241–282.
- Kurganov, A., Noelle, S., and Petrova, G. (2001). Semidiscrete central-upwind schemes for hyperbolic conservation laws and Hamilton–Jacobi equations. *SIAM J. Sci. Comp.*, **23**, 707–740.
- Kurki-Suonio, H. (1985). Deflagration bubbles in the quark–hadron phase transition. *Nucl. Phys. B*, **255**, 231–252.
- Kurki-Suonio, H. and Laine, M. (1995). Supersonic deflagrations in cosmological phase transitions. *Phys. Rev. D*, **51**, 5431–5437.
- Kutta, M. (1901). Beitrag zur näherungsweisen integration totaler differentialgleichungen. *Z. für Math. u. Phys.*, **46**, 435–453.
- Laine, M. (1994). Bubble growth as a detonation. *Phys. Rev. D*, **49**, 3847–3853.
- Lake, K. and Pim, R. (1985). Development of voids in the thin-wall approximation. I. General characteristics of spherical vacuum voids. *Astrophys. J.*, **298**, 439–447.
- Lamb, H. (1993). *Hydrodynamics.* Cambridge University Press, Cambridge.
- Landau, L. D. (1944). On the theory of slow combustion. *Acta Physicochimica USSR*, **19**, 77–85.
- Landau, L. D. and Lifshitz, E. M. (1975). *The Classical Theory of Fields.* Course of Theoretical Physics, Vol. 2. Butterworth-Heinemann, Oxford.
- Landau, L. D. and Lifshitz, E. M. (1976). *Mechanics.* Course of Theoretical Physics, Vol. 1. Butterworth-Heinemann, Oxford.
- Landau, L. D. and Lifshitz, E. M. (1980). *Statistical Physics.* Course of Theoretical Physics, Vol. 5. Butterworth-Heinemann, Oxford.
- Landau, L. D. and Lifshitz, E. M. (1987). *Fluid Mechanics.* Course of Theoretical Physics, Vol. 6. Butterworth-Heinemann, Oxford.
- Langlois, D., Sedrakian, D. M., and Carter, B. (1998). Differential rotation of relativistic superfluid in neutron stars. *Mon. Not. R. Astron. Soc.*, **297**, 1189–1201.
- Lanza, A., Miller, J. C., and Motta, S. (1985). Formation and damping of relativistic strong shocks in a Synge gas. *Phys. Fluids*, **28**, 97–103.
- Lattimer, J. M., Pethick, C. J., Prakash, M., and Haensel, P. (1991). Direct URCA process in neutron stars. *Phys. Rev. Lett.*, **66**, 2701–2704.
- Lattimer, J.M. and Swesty, F. D. (1991). A generalized equation of state for hot, dense matter. *Nucl. Phys. A*, **535**, 331–376.
- Lax, P. D. (1990). *Hyperbolic Systems of Conservation Laws and the Mathematical Theory of Shock Waves.* Society for Industrial and Applied Mathematics, Philadelphia.
- Lax, P. D. and Richtmyer, R. D. (1956). Survey of the stability of linear finite difference equations. *Communications on Pure and Applied Mathematics*, **9**, 267–293.
- Lax, P. D. and Wendroff, B. (1960). Systems of conservation laws. *Commun. Pure Appl.*

- Math.*, **13**, 217–237.
- Leaver, E.W. (1985). An analytic representation for the quasi-normal modes of Kerr black holes. *Proc. R. Soc. London, Ser. A*, **402**, 285–298.
- Lee, H. I. and Stewart, D. S. (1990). Calculation of linear detonation instability: One-dimensional instability of plane detonation. *J. Fluid Mech.*, **216**, 103–132.
- Leitao, L., Mégevand, A., and Sánchez, A. D. (2012). Gravitational waves from the electroweak phase transition. *JCAP*, **10**, 24.
- Letelier, P. S. (1980). Anisotropic fluids with two-perfect-fluid components. *Phys. Rev. D*, **22**, 807–813.
- LeVeque, R. J. (1992). *Numerical Methods for Conservation Laws*. Birkhäuser, Basel.
- LeVeque, R. J. (1998). In *Computational Methods for Astrophysical Fluid Flow* (Ed. S. O. and G. A.). Springer, Berlin.
- LeVeque, R. J. (2002). *Finite Volume Methods for Hyperbolic Problems*. Cambridge University Press, Cambridge.
- LeVeque, R. J. (2007). *Finite Difference Methods for Ordinary and Partial Differential Equations*. SIAM, Philadelphia.
- Lewis, B. and Elbe, G.V. (1987). *Combustion, Flames, and Explosions of Gases*. Cambridge University Press, Cambridge.
- Liang, E. P. T. and Baker, K. (1977). Damping of relativistic shocks. *Phys. Rev. Lett.*, **39**, 191–193.
- Liboff, R. L. (2003). *Kinetic Theory: Classical, Quantum, and Relativistic Descriptions*. Springer, Berlin.
- Lichnerowicz, A. (1939). Sur certains problèmes globaux relatifs aux système des équations d'Einstein. Paris, Université, Diss.; Herman Paris; Actual. Sci. Ind., **833**, 1.
- Lichnerowicz, A. (1944). L'intégration des équations de la gravitation relativiste et la problème des n corps. *J. Math. Pures et Appl.*, **23**, 37–63.
- Lichnerowicz, A. (1967). *Relativistic Hydrodynamics and Magnetohydrodynamics*. Benjamin, New York.
- Lichnerowicz, A. and Marrot, R. (1940). Propriétés statistiques des ensembles de particules en relativité restreinte. *C. R. Acad. Sci. Paris*, **210**, 759–761.
- Liebendörfer, M., Rampp, M., Janka, H.-T., and Mezzacappa, A. (2005). Supernova simulations with Boltzmann neutrino transport: A comparison of methods. *Astrophys. J.*, **620**, 840–860.
- Lindblom, L., Scheel, M. A., Kidder, L. E., Owen, R., and Rinne, O. (2006). A new generalized harmonic evolution system. *Class. Quant. Grav.*, **23**, S447–S462.
- Link, B. (1992). Deflagration instability in the quark–hadron phase transition. *Phys. Rev. Lett.*, **68**, 2425–2428.
- Linke, F., Font, J. A., Janka, H.-T., Müller, E., and Papadopoulos, P. (2001). Spherical collapse of supermassive stars: Neutrino emission and gamma-ray bursts. *Astron. Astrophys.*, **376**, 568–579.
- Lister, M. L., Cohen, M. H., Homan, D. C., et al. (2009). MOJAVE: Monitoring of Jets in Active Galactic Nuclei with VLBA Experiments. VI. Kinematics analysis of a complete sample of blazar jets. *Astron. Journ.*, **138**, 1874–1892.
- Lithwick, Y. and Sari, R. (2001). Lower limits on Lorentz factors in gamma-ray bursts. *Astrop. J.*, **555**, 540–545.

- Liu, I.-S. and Mueller, I. (1983). Extended thermodynamics of classical and degenerate ideal gases. *Arch. Ration. Mech. An.*, **83**, 285–332.
- Liu, I.-S., Mueller, I., and Ruggeri, T. (1986). Relativistic thermodynamics of gases. *Ann. Phys.*, **169**, 191–219.
- Liu, X.-D., Osher, S., and Chan, T. (1994). Weighted essentially non-oscillatory schemes. *J. Comput. Phys.*, **115**, 200–212.
- Liu, X.-D. and Tadmor, E. (1998). Third order nonoscillatory central scheme for hyperbolic conservation laws. *Numer. Math.*, **79**, 397–425.
- Liu, Y. T., Shapiro, S. L., Etienne, Z. B., and Taniguchi, K. (2008). General relativistic simulations of magnetized binary neutron star mergers. *Phys. Rev. D*, **78**, 024012.
- Löffler, F., Rezzolla, L., and Ansorg, M. (2006). Numerical evolutions of a black hole-neutron star system in full general relativity: Head-on collision. *Phys. Rev. D*, **74**, 104018.
- Londrillo, P. and Del Zanna, L. (2000). High-order upwind schemes for multidimensional magnetohydrodynamics. *Astrophys. J.*, **530**, 508–524.
- Lucas-Serrano, A., Font, J. A., Ibáñez, J. M., and Martí, J. M. (2004). Assessment of a high-resolution central scheme for the solution of the relativistic hydrodynamics equations. *Astron. Astrophys.*, **428**, 703–715.
- Maartens, R. (1995). Dissipative cosmology. *Class. Quant. Grav.*, **12**, 1455–1465.
- Maartens, R. (1996). Causal thermodynamics in relativity. Lectures given at the Hanno Rund Workshop on Relativity and Thermodynamics, South Africa 1996; astro-ph/9609119.
- Maartens, R. and Triginer, J. (1997). Density perturbations with relativistic thermodynamics. *Phys. Rev. D*, **56**, 4640–4650.
- MacFadyen, A. I. and Woosley, S. E. (1999). Collapsars: Gamma-ray bursts and explosions in “failed supernovae”. *Astrophys. J.*, **524**, 262–289.
- Mach, P. (2012). Instabilities of the Riemann problem in relativistic hydrodynamics. In *American Institute of Physics Conference Series* (Ed. J. Beltrán Jiménez, J. A. Ruiz Cembranos, A. Dobado, A. López Maroto, and A. De la Cruz Dombriz), American Institute of Physics Conference Series, **1458**, 459–462.
- Mach, P. and Piętka, M. (2010). Exact solution of the hydrodynamical Riemann problem with nonzero tangential velocities and the ultrarelativistic equation of state. *Phys. Rev. E*, **81**, 046313.
- Maeda, K. (1986). Bubble dynamics in the expanding universe. *General Relativity and Gravitation*, **18**, 931–951.
- Maeda, K. and Sato, H. (1983). Expansion of a thin shell around a void in an expanding universe. *Prog. Theor. Phys.*, **70**, 772–782.
- Maggiore, M. (2007). *Gravitational Waves: Volume 1: Theory and Experiments*. Oxford University Press, New York.
- Mak, M. K. and Harko, T. (2003). Anisotropic stars in general relativity. *Proc. R. Soc. London, Ser. A* **459**, No 2030, 393–408.
- Mann, P.J. (1985). Some mixed finite element-finite difference methods for spherically symmetric relativistic collapse. *J. Comput. Phys.*, **58** 377–394.
- Markstein, G. H. (1951). Experimental and theoretical studies of flame-front stability. *J. Aeronaut. Sci.*, **18**, 199–209.
- Martí, J. M., Ibáñez, J. M., and Miralles, J. A. (1991). Numerical relativistic hydrodynamics: Local characteristic approach. *Phys. Rev. D*, **43**, 3794.

- Marti, J. M., Müller, E., and Ibáñez, J. M. (1994). Hydrodynamical simulations of relativistic jets. *Astron. Astrophys.*, **281**, L9–L12.
- Martí, J. M. and Müller, E. (1994). The analytical solution of the Riemann problem in relativistic hydrodynamics. *J. Fluid Mech.*, **258**, 317–333.
- Martí, J. M. and Müller, E. (1996). Extension of the piecewise parabolic method to one-dimensional relativistic hydrodynamics. *J. Comput. Phys.*, **123**, 1–14.
- Martí, J. M. and Müller, E. (2003). Numerical hydrodynamics in special relativity. *Living Rev. Relativ.*, **6**, 7.
- Martí, J. M., Müller, E., Font, J. A., Ibáñez, J. M., and Marquina, A. (1997). Morphology and dynamics of relativistic jets. *Astrophys. J.*, **479**, 151–163.
- Marti, J. M. A., Müller, E., Font, J. A., and Ibáñez, J. M. (1995). Morphology and dynamics of highly supersonic relativistic jets. *Astrophys. J.*, **448**, L105–L108.
- Mascali, G. and Romano, V. (1997). Maximum entropy principle in relativistic radiation hydrodynamics. *Ann. Inst. Henri Poincaré*, **67**, 123–144.
- Masuda, N. and Eriguchi, Y. (1997). Three-dimensional simulations of runaway instability of self-gravitating accretion disks. *Astrophys. J.*, **489**, 804–818.
- Mathews, G. J. and Wilson, J. R. (2000). Revised relativistic hydrodynamical model for neutron star binaries. *Phys. Rev. D*, **61**, 127304.
- Mathews, W. G. (1971). The hydromagnetic free expansion of a relativistic gas. *Astrophys. J.*, **165**, 147–164.
- Matsuda, T., Inoue, M., and Sawada, K. (1987). Spin-up and spin-down of an accreting compact object. *Mon. Not. Roy. Astr. Soc.*, **226**, 785–811.
- May, M. M. and White, R. H. (1967). Stellar dynamics and gravitational collapse. In *Methods in Computational Physics*, **7**, 129.
- Mazur, P. O. and Mottola, E. (2004). Gravitational vacuum condensate stars. *Proceedings of the National Academy of Science*, **101**, 9545–9550.
- McAbee, T. L. and Wilson, J. R. (1994). Mean-field pion calculations of heavy-ion collisions at Bevalac energies. *Nucl. Phys. A*, **576**, 626–638.
- McKinney, J. C., Tchekhovskoy, A., and Blandford, R. D. (2013). Alignment of magnetized accretion disks and relativistic jets with spinning black holes. *Science*, **339**, 49–52.
- Medvedev, M. V. and Narayan, R. (2001). Self-similar hot accretion flow onto a neutron star. *Astrophys. J.*, **554**, 1255–1267.
- Meegan, C. A., Fishman, G. J., Wilson, R. B., Horack, J. M., Brock, M. N., Paciesas, W. S., Pendleton, G. N., and Kouveliotou, C. (1992). Spatial distribution of gamma-ray bursts observed by BATSE. *Nature*, **355**, 143–145.
- Meier, D. L. (1999). Multidimensional astrophysical structural and dynamical analysis. I. Development of a nonlinear finite element approach. *Astrophys. J.*, **518**, 788–813.
- Meinel, R., Ansorg, M., Kleinwächter, A., Neugebauer, G., and Petroff, D. (2008). *Relativistic Figures of Equilibrium*. Cambridge University Press, Cambridge.
- Mendell, G. (1991). Superfluid hydrodynamics in rotating neutron stars. I. Nondissipative equations. II. Dissipative effects. *Astrophys. J.*, **380**, 515–540.
- Menikoff, R. and Plohr, B. J. (1989). The Riemann problem for fluid flow of real materials. *Rev. Mod. Phys.*, **61**, 75–130.
- Menshov, I. S. (1990). Increasing the order of approximation of Godunov's scheme using solution of the generalized Riemann problem. *USSR J. Comput. Math. and Math. Phys.*, **30**,

- 54–65.
- Meyer, R. E. (1999). *Introduction to Mathematical Fluid Dynamics*. Second edition. Dover, New York.
- Mezzacappa, A., Liebendörfer, M., Messer, O. E. Bronson, Hix, W. Raphael, Thielemann, F.-K., and Bruenn, S. W. (2001). Simulation of the spherically symmetric stellar core collapse, bounce, and postbounce evolution of a star of 13 solar masses with Boltzmann neutrino transport, and its implications for the supernova mechanism. *Phys. Rev. Lett.*, **86**, 1935–1938.
- Michel, F. C. (1972). Accretion of matter by condensed objects. *Astrophys. Spa. Sci.*, **15**, 153–160.
- Mignone, A. and Bodo, G. (2005). An HLLC Riemann solver for relativistic flows. I. Hydrodynamics. *Mon. Not. R. Astron. Soc.*, **364**, 126–136.
- Mignone, A. and McKinney, J. C. (2007). Equation of state in relativistic magnetohydrodynamics: Variable versus constant adiabatic index. *Mon. Not. R. Astron. Soc.*, **378**, 1118–1130.
- Mignone, A., Zanni, C., Tzeferacos, P., van Straalen, B., Colella, P., and Bodo, G. (2012). The PLUTO code for adaptive mesh computations in astrophysical fluid dynamics. *Astrophys. J. Suppl. Ser.*, **198**, 7–37.
- Mihalas, D. and Mihalas, B. (1984). *Foundations of Radiation Hydrodynamics*. Dover, New York.
- Miller, J. C. and Motta, S. (1989). Computations of spherical gravitational collapse using null slicing. *Class. Quant. Grav.*, **6**, 185–193.
- Miller, J. C. and Pantano, O. (1989). Hydrodynamics of the cosmological quark–hadron transition. *Phys. Rev. D*, **40**, 1789–1797.
- Miller, J. C. and Pantano, O. (1990). Computations of the growth of hadronic bubbles during the cosmological quark–hadron transition. *Phys. Rev. D*, **42**, 3334–3343.
- Miller, J. C. and Sciama, D. W. (1980). Gravitational collapse to the black hole state. In *General Relativity and Gravitation, II* (Ed. H. A.), 359–391. Plenum Press, New York.
- Milyukov, V. and Fan, S. H. (2012). The Newtonian gravitational constant: Modern status of measurement and the new codata value. *Gravitation and Cosmology*, **18**, 216–224.
- Miralles, J. A., Ibanez, J. M., Martí, J. M., and Perez, A. (1990). Incompressibility of hot nuclear matter and general relativistic stellar collapse. *Astron. Astrophys.*, **237**, 97–102.
- Misner, C. W. and Sharp, D. H. (1964). Relativistic equations for adiabatic, spherically symmetric gravitational collapse. *Phys. Rev.*, **136**, B571–B576.
- Misner, C. W., Thorne, K. S., and Wheeler, J. A. (1973). *Gravitation*. W. H. Freeman, San Francisco.
- Mizuno, Y., Zhang, B., Giacomazzo, B., Nishikawa, K.-I., Hardee, P. E., Nagataki, S., and Hartmann, D. H. (2009). Magnetohydrodynamic effects in propagating relativistic jets: Reverse shock and magnetic acceleration. *Astrophys. J.*, **690**, L47–L51.
- Moesta, P. (2008). *Puncture evolutions within the harmonic framework*. Master's thesis, University of Kassel and Albert-Einstein-Institut, Potsdam.
- Monaghan, J. J. (1992). Smoothed particle hydrodynamics. *Annu. Rev. Astron. Astr.*, **30**, 543–574.
- Monaghan, J. J. and Lattanzio, J. C. (1985). A refined particle method for astrophysical problems. *Astron. Astrophys.*, **149**, 135–143.

- Moncrief, V. (1974). Gravitational perturbations of spherically symmetric systems. I. The exterior problem. *Ann. Phys.*, **88**, 323–342.
- Moncrief, V. (1980). Stability of stationary, spherical accretion onto a Schwarzschild black hole. *Astrophys. J.*, **235**, 1038–1046.
- Montero, P. J., Font, J. A., and Shibata, M. (2010). Influence of self-gravity on the runaway instability of black-hole-torus systems. *Phys. Rev. Lett.*, **104**, 191101.
- Montero, P. J., Rezzolla, L., and Yoshida, S. (2004). Oscillations of vertically integrated relativistic tori. II. Axisymmetric modes in a Kerr space-time. *Mon. Not. R. Astron. Soc.*, **354**, 1040–1052.
- Montero, P. J. and Zanotti, O. (2012). Oscillations of relativistic axisymmetric tori and implications for modelling kHz-QPOs in neutron star X-ray binaries. *Mon. Not. R. Astron. Soc.*, **419**, 1507–1514.
- Montero, P. J., Zanotti, O., Font, J. A., and Rezzolla, L. (2007). Dynamics of magnetized relativistic tori oscillating around black holes. *Mon. Not. R. Astron. Soc.*, **378**, 1101–1110.
- Morton, K. W. and Mayers, D. F. (2005). *Numerical Solution of Partial Differential Equations*. Cambridge University Press, Cambridge.
- Mueller, B., Janka, H.-T., and Dimmelmeier, H. (2010). A new multi-dimensional general relativistic neutrino hydrodynamic code for core-collapse supernovae. I. Method and code tests in spherical symmetry. *Astrophys. J. Suppl. Ser.*, **189**, 104–133.
- Mueller, D. and Brügmann, B. (2010). Toward a dynamical shift condition for unequal mass black hole binary simulations. *Class. Quant. Grav.*, **27**, 114008.
- Mueller, I. (1966). *Zur Ausbreitungsgeschwindigkeit von Störungen in kontinuierlichen Medien*. PhD Thesis, Aachen, T. H., Math.-naturwiss. F.
- Mueller, I. (1967). Zum Paradoxon der Wärmeleitungstheorie. *Zeitschrift für Physik*, **198**, 329–344.
- Mueller, I. (2008). Extended thermodynamics: A theory of symmetric hyperbolic field equations. *Entropy*, **10**, 477–492.
- Mueller, I. and Ruggeri, T. (1998). *Rational Extended Thermodynamics*. Springer, Berlin.
- Muronga, A. (2007). Relativistic dynamics of nonideal fluids: Viscous and heat-conducting fluids. I. General aspects and 3+1 formulation for nuclear collisions. *Phys. Rev. C*, **76**, 014909.
- Musco, I., Miller, J. C., and Rezzolla, L. (2005). Computations of primordial black hole formation. *Class. Quant. Grav.*, **22**, 1405–1424.
- Müther, H., Prakash, M., and Ainsworth, T. L. (1987). The nuclear symmetry energy in relativistic Brueckner–Hartree–Fock calculations. *Phys. Lett. B*, **199**, 469–474.
- Nagar, A. and Rezzolla, L. (2005). Gauge-invariant non-spherical metric perturbations of Schwarzschild black hole spacetimes. *Class. Quant. Grav.*, **22**, R167–R192. erratum-*ibid.* **23**, 4297, (2006).
- Nakamura, T. (1981). General relativistic collapse of rotating supermassive stars. *Prog. Theor. Phys.*, **66**, 2038–2051.
- Nakamura, T., Oohara, K., and Kojima, Y. (1987). General relativistic collapse to black holes and gravitational waves from black holes. *Prog. Theor. Phys. Suppl.*, **90**, 1–218.
- Narayan, R. and Yi, I. (1995). Advection-dominated accretion: Underfed black holes and neutron stars. *Astrophys. J.*, **452**, 710–735.
- Nessyahu, H. and Tadmor, E. (1990). Non-oscillatory central differencing for hyperbolic

- conservation laws. *J. Comput. Phys.*, **87**, 408–463.
- Newman, E. T. and Penrose, R. (1962). An approach to gravitational radiation by a method of spin coefficients. *J. Math. Phys.*, **3**, 566–578. erratum in *J. Math. Phys.*, **4**, 998 (1963).
- Nishida, S., Lanza, A., Eriguchi, Y., and Abramowicz, M. A. (1996). Runaway instability and gamma-ray bursts. *Mon. Not. R. Astron. Soc.*, **278**, L41–L45.
- Norman, M. L. and Winkler, K-H. A. (1986). *Astrophysical Radiation Hydrodynamics*. Kluwer Academic Publishers, Dordrecht.
- Novikov, I. D. and Thorne, K. S. (1973). Astrophysics of black holes. In *Black Holes (Les Astres Occlus)*, 343–450.
- Nozawa, T., Stergioulas, N., Gourgoulhon, É., and Eriguchi, Y. (1998). Construction of highly accurate models of rotating neutron stars—comparison of three different numerical schemes. *Astron. Astrophys. Suppl.*, **132**, 431–454.
- Oechslin, R. and Janka, H. Th. (2007). Gravitational waves from relativistic neutron star mergers with mycrophysical equations of state. *Phys. Rev. Lett.*, **99**, 121102.
- Oechslin, R., Rosswog, S., and Thielemann, F. K. (2002). Conformally flat smoothed particle hydrodynamics: Application to neutron star mergers. *Phys. Rev. D*, **65**, 103005.
- Ohanian, H. C. (1976). *Gravitation and spacetime*. Norton, New York.
- Oleinik, O. A. and Samokhin, V. N. (1999). *Mathematical Models in Boundary Layer Theory*. Applied Mathematics and Mathematical Computation, Chapman and Hall/CRC, Boca Raton.
- Ollitrault, J.-Y. (2008). Relativistic hydrodynamics for heavy-ion collisions. *Eur. J. Phys.*, **29**, 275–302.
- Oppenheimer, J. R. and Volkoff, G. (1939). On massive neutron cores. *Phys. Rev.*, **55**, 374–381.
- Osher, S. and Solomon, F. (1982). Upwind difference schemes for hyperbolic conservation laws. *Math. Comput.*, **38**, 339–374.
- Osmanov, Z., Mignone, A., Massaglia, S., Bodo, G., and Ferrari, A. (2008). On the linear theory of Kelvin–Helmholtz instabilities of relativistic magnetohydrodynamic planar flows. *Astron. Astrophys.*, **490**, 493–500.
- Ou, S., Ji, J., Liu, L., and Peng, X. (2007). Disk–planet interaction simulations. I. Baroclinic generation of vortensity and nonaxisymmetric Rossby wave instability. *Astrophys. J.*, **667**, 1220–1228.
- Paczynski, B. (1986). Gamma-ray bursters at cosmological distances. *Astrophys. J.*, **308**, L43–L46.
- Paczynski, B. (1998). Are gamma-ray bursts in star-forming regions? *Astrophys. J.*, **494**, L45–L48.
- Palenzuela, C., Lehner, L., Reula, O., and Rezzolla, L. (2009). Beyond ideal MHD: Towards a more realistic modelling of relativistic astrophysical plasmas. *Mon. Not. R. Astron. Soc.*, **394**, 1727–1740.
- Palenzuela, C., Olabarrieta, I., Lehner, L., and Liebling, S. L. (2007). Head-on collisions of boson stars. *Phys. Rev. D*, **75**, 064005.
- Pandolfi, M. and D’Ambrosio, D. (2001). Numerical instabilities in upwind methods: Analysis and cures for the “carbuncle” phenomenon. *J. Comput. Phys.*, **166**, 271–301.
- Pannarale, F., Rezzolla, L., Ohme, F., and Read, J. S. (2011). Will black hole-neutron star binary inspirals tell us about the neutron star equation of state? *Phys. Rev. D*, **84**, 104017.

- Pannarale, F., Tonita, A., and Rezzolla, L. (2011). Black hole-neutron star mergers and short GRBs: A relativistic toy model to estimate the mass of the torus. *Astrophys. J.*, **727**, 95–107.
- Papadopoulos, P. and Font, J. A. (2001). Imprints of accretion on gravitational waves from black holes. *Phys. Rev. D*, **63**, 044016.
- Papadopoulos, P. and Font, J. A. (1998). Relativistic hydrodynamics around black holes and horizon adapted coordinate systems. *Phys. Rev. D*, **58**, 024005.
- Papadopoulos, P. and Font, J. A. (1999a). Matter flows around black holes and gravitational radiation. *Phys. Rev. D*, **59**, 044014.
- Papadopoulos, P. and Font, J. A. (1999b). Relativistic hydrodynamics on spacelike and null surfaces: Formalism and computations of spherically symmetric spacetimes. *Phys. Rev. D*, **61**, 024015.
- Pares, C. (2006). Numerical methods for nonconservative hyperbolic systems: A theoretical framework. *SIAM J. Numer. Anal.*, **44**, 300–321.
- Pareschi, L. and Russo, G. (2005). Implicit-explicit Runge–Kutta schemes and applications to hyperbolic systems with relaxation. *J. Sci. Comput.*, **25**, 129–155.
- Peebles, P. J. E. (1993). *Principles of Physical Cosmology*. Princeton University Press, Princeton, NJ.
- Peitz, J. and Appl, S. (1997). Viscous accretion discs around rotating black holes. *Mon. Not. R. Astron. Soc.*, **286**, 681–695.
- Peitz, J. and Appl, S. (1999). Dissipative fluid dynamics in the 3 + 1 formalism. *Class. Quant. Grav.*, **16**, 979–989.
- Penrose, R. (1969). Gravitational collapse: The role of general relativity. *Riv. Nuovo Cimento*, **1**, 252.
- Penrose, R. (1979). Singularities and time-asymmetry. In *General Relativity: An Einstein Centenary Survey* (Ed. S. Hawking and W. Israel), 581–635. Cambridge University Press, Cambridge.
- Perlmutter, S., Aldering, G., Goldhaber, G., and The Supernova Cosmology Project (1999). Measurements of omega and lambda from 42 high-redshift supernovae. *Astrop. J.*, **517**, 565–586.
- Perthame, B. and Shu, C. (1996). On positivity preserving finite volume schemes for Euler equations. *Numerische Mathematik*, **73**, 119–130.
- Perucho, M., Martí, J. M., Cela, J. M., Hanasz, M., de La Cruz, R., and Rubio, F. (2010). Stability of three-dimensional relativistic jets: Implications for jet collimation. *Astron. Astrophys.*, **519**, A41.
- Perucho, M., Martí, J. M., and Hanasz, M. (2004). Stability of hydrodynamical relativistic planar jets. II. Long-term nonlinear evolution. *Astron. Astrophys.*, **427**, 431–444.
- Peshkov, V (1944). Second sound in helium II. *J. Phys.*, **8**, 381.
- Petrich, L. I., Shapiro, S. L., Stark, R. F., and Teukolsky, S. A. (1989). Accretion onto a moving black hole—a fully relativistic treatment. *Astrophys. J.*, **336**, 313–349.
- Petrich, L. I., Shapiro, S. L., and Teukolsky, S. A. (1988). Accretion onto a moving black hole—an exact solution. *Phys. Rev. Lett.*, **60**, 1781–1784.
- Pfeiffer, H. P. and York, J. W. (2003). Extrinsic curvature and the Einstein constraints. *Phys. Rev. D*, **67**, 044022.
- Pitaevskii, L. P. and Lifshitz, E. M. (1981). *Physical Kinetics*. Course of Theoretical Physics, Vol. 10. Pergamon Press, Oxford.

## 710 References

- Planck Collaboration, Ade, P. A. R., Aghanim, N., Armitage-Caplan, C. *et al.* (2013). Planck 2013 results. XVI. Cosmological parameters. *arXiv:1303.5076*.
- Plesset, M. S. and Prosperetti, A. (1977). Bubble dynamics and cavitation. *Annual Review of Fluid Mechanics*, **9**, 145–185.
- Plesset, M. S. and Zwick, S. A. (1954). The growth of vapor bubbles in superheated liquids. *J. Appl. Phys.*, **25**, 493–500.
- Pogorelov, N. V., Ohsugi, Y., and Matsuda, T. (2000). Towards steady-state solutions for supersonic wind accretion on to gravitating objects. *Mon. Not. R. Astron. Soc.*, **313**, 198–208.
- Poisson, E. (2004). *A Relativist's Toolkit: The Mathematics of Black Hole Mechanics*. Cambridge University Press, Cambridge.
- Pomraning, G. C. (1973). *The Equations of Radiation Hydrodynamics*. Pergamon Press, Oxford.
- Pons, J. A., Font, J. A., Ibanez, J. M., Martí, J. M., and Miralles, J. A. (1998). General relativistic hydrodynamics with special relativistic Riemann solvers. *Astron. Astrophys.*, **339**, 638–642.
- Pons, J. A., Martí, J. M., and Müller, E. (2000). The exact solution of the Riemann problem with non-zero tangential velocities in relativistic hydrodynamics. *J. Fluid Mech.*, **422**, 125–139.
- Press, W. H., Flannery, B. P., Teukolsky, S. A., and Vetterling, W. T. (1986). *Numerical Recipes*. Cambridge University Press, Cambridge.
- Preti, G., de Felice, F., and Masiero, L. (2009). On the Galilean non-invariance of classical electromagnetism. *Eur. J. Phys.*, **30**, 381–391.
- Pretorius, F. (2005a). Evolution of binary black hole spacetimes. *Phys. Rev. Lett.*, **95**, 121101.
- Pretorius, F. (2005b). Numerical relativity using a generalized harmonic decomposition. *Class. Quant. Grav.*, **22**, 425–452.
- Pretorius, F. (2006). Simulation of binary black hole spacetimes with a harmonic evolution scheme. *Class. Quant. Grav.*, **23**, S529–S552.
- Price, R. H. and Rosswog, S. (2006). Producing ultrastrong magnetic fields in neutron star mergers. *Science*, **312**, 719–722.
- Prix, R., Comer, G. L., and Andersson, N. (2002). Slowly rotating superfluid Newtonian neutron star model with entrainment. *Astron. Astrophys.*, **381**, 178–196.
- Prix, R., Novak, J., and Comer, G. L. (2005). Relativistic numerical models for stationary superfluid neutron stars. *Phys. Rev. D*, **71**, 043005.
- Punturo, M., Abernathy, M., Acernese, F. *et al.* (2010). The third generation of gravitational wave observatories and their science reach. *Class. Quant. Grav.*, **27**, 084007.
- Qiu, J. and Shu, C. (2005). Runge–Kutta discontinuous Galerkin methods using WENO limiters. *SIAM J. Sci. Comp.*, **26**, 907–929.
- Quarteroni, A. and Valli, A. (2008). *Numerical Approximation of Partial Differential Equations*. Springer, Berlin.
- Radice, D. and Rezzolla, L. (2011). Discontinuous Galerkin methods for general-relativistic hydrodynamics: Formulation and application to spherically symmetric spacetimes. *Phys. Rev. D*, **84**, 024010.
- Radice, D. and Rezzolla, L. (2012). THC: A new high-order finite-difference high-resolution

- shock-capturing code for special-relativistic hydrodynamics. *Astron. Astrophys.*, **547**, A26.
- Radice, D. and Rezzolla, L. (2013). Universality and Intermittency in Relativistic Turbulent Flows of a Hot Plasma. *Astrophys. J.*, **766**, L10–L14.
- Rayleigh, L. (1917). On the dynamics of revolving fluids. *Proc. R. Soc. London, Ser. A*, **93**, 148–154.
- Read, J. S., Lackey, B. D., Owen, B. J., and Friedman, J. L. (2009a). Constraints on a phenomenologically parametrized neutron star equation of state. *Phys. Rev. D*, **79**, 124032.
- Read, J. S., Markakis, C., Shibata, M., Uryu, K., Creighton, J. D. E., and Friedman, J. L. (2009b). Measuring the neutron star equation of state with gravitational wave observations. *Phys. Rev. D*, **79**, 124033.
- Reed, W. H and Hill, T. R. (1973). Triangular mesh methods for the neutron transport equation. Technical report, Los Alamos Scientific Laboratory, Los Alamos.
- Rees, M. J. (1966). Appearance of relativistically expanding radio sources. *Nature*, **211**, 468–470.
- Reichl, L. E. (1998). *A Modern Course in Statistical Physics*. Second edition. John Wiley, New York.
- Reif, F. (1965). *Fundamentals of Statistical and Thermal Physics*. McGraw-Hill, Boston.
- Reisswig, C., Bishop, N. T., Pollney, D., and Szilagyi, B. (2009). Unambiguous determination of gravitational waveforms from binary black hole mergers. *Phys. Rev. Lett.*, **103**, 221101.
- Rendall, A. D. (2004). The Einstein-Vlasov system. In P. T. Chrusciel and H. Friedrich, editors, *The Einstein equations and the large scale behavior of gravitational fields*. Birkhauser, Basel, 2004.
- Reula, O. (1998). Hyperbolic methods for Einstein's equations. *Living Rev. Relativ.*, **1**, 3.
- Rezzolla, L. (1996a). *General-relativistic hydrodynamics of compressible multicomponent fluids: Developments and applications*. PhD Thesis, SISSA, International School for Advanced Studies, Trieste.
- Rezzolla, L. (1996b). Stability of cosmological detonation fronts. *Phys. Rev. D*, **54**, 1345–1358.
- Rezzolla, L. (2003). Gravitational waves from perturbed black holes and relativistic stars. In *Summer School on Astroparticle Physics and Cosmology*, Volume 3, ICTP Lecture Series, arXiv:gr-qc/0302025.
- Rezzolla, L., Baiotti, L., Giacomazzo, B., Link, D., and Font, J. A. (2010). Accurate evolutions of unequal-mass neutron star binaries: Properties of the torus and short GRB engines. *Class. Quant. Grav.*, **27**, 114105.
- Rezzolla, L., Giacomazzo, B., Baiotti, L., Granot, J., Kouveliotou, C., and Aloy, M. A. (2011). The missing link: Merging neutron stars naturally produce jet-like structures and can power short gamma-ray bursts. *Astrophys. J.*, **732**, L6–L11.
- Rezzolla, L. and Miller, J. C. (1994). Relativistic radiative transfer for spherical flows. *Class. Quant. Grav.*, **11**, 1815–1832.
- Rezzolla, L. and Miller, J. C. (1996). Evaporation of cosmological quark drops and relativistic radiative transfer. *Phys. Rev. D*, **53**, 5411–5425.
- Rezzolla, L., Miller, J. C., and Pantano, O. (1995). Evaporation of quark drops during the cosmological quark–hadron transition. *Phys. Rev. D*, **52**, 3202–3213.
- Rezzolla, L. and Takami, K. (2013). Black hole production from ultrarelativistic collisions.

- Class. Quant. Grav.*, **30**, 012001.
- Rezzolla, L., Yoshida, S., Maccarone, T. J., and Zanotti, O. (2003a). A new simple model for high-frequency quasi-periodic oscillations in black hole candidates. *Mon. Not. R. Astron. Soc.*, **344**, L37–L41.
- Rezzolla, L., Yoshida, S., and Zanotti, O. (2003b). Oscillations of vertically integrated relativistic tori. I. Axisymmetric modes in a Schwarzschild space-time. *Mon. Not. R. Astron. Soc.*, **344**, 978–992.
- Rezzolla, L. and Zanotti, O. (2001). An improved exact Riemann solver for relativistic hydrodynamics. *J. Fluid Mech.*, **449**, 395–411.
- Rezzolla, L. and Zanotti, O. (2002). New relativistic effects in the dynamics of nonlinear hydrodynamical waves. *Phys. Rev. Lett.*, **89**, 114501.
- Rezzolla, L., Zanotti, O., and Font, J. A. (2003). Dynamics of thick discs around Schwarzschild-de Sitter black holes. *Astron. Astrophys.*, **412**, 603–613.
- Rezzolla, L., Zanotti, O., and Pons, J. A. (2003). An improved exact Riemann solver for relativistic hydrodynamics with non-zero tangential velocities. *Journ. of Fluid Mech.*, **479**, 199–219.
- Richtmyer, R. D. and Morton, K.W. (1967). *Difference Methods for Initial Value Problems*. Interscience Publishers, New York.
- Richtmyer, R. D. and Morton, K. W. (1994). *Difference Methods for Initial Value Problems*. Second edition. Kreiger, Malabar.
- Riess, A. G., Filippenko, A. V., Challis, P. et al. (1998). Observational evidence from supernovae for an accelerating universe and a cosmological constant. *Astron. Journ.*, **116**, 1009–1038.
- Riffert, H. and Herold, H. (1995). Relativistic accretion disk structure revisited. *Astrophys. J.*, **450**, 508–511.
- Rinne, O. (2006). Stable radiation-controlling boundary conditions for the generalized harmonic Einstein equations. *Class. Quant. Grav.*, **23**, 6275.
- Rischke, D. H. (2004). The quark-gluon plasma in equilibrium. *Progress in Particle and Nucl. Phys.*, **52**, 197–296.
- Rischke, D. H., Bernard, S., and Maruhn, J. A. (1995). Relativistic hydrodynamics for heavy-ion collisions. I. General aspects and expansion into vacuum. *Nucl. Phys. A*, **595**, 346–382.
- Robertson, H. P. (1935). Kinematics and world-structure. *Astrophys. J.*, **82**, 284–301.
- Robinson, D. C. (1975). Uniqueness of the Kerr black hole. *Phys. Rev. Lett.*, **34**, 905–906.
- Roe, P. L. (1981). Approximate Riemann solvers, parameter vectors and difference schemes. *J. Comput. Phys.*, **43**, 357–372.
- Roe, P. L. (1985). Some contributions to the modelling of discontinuous flows. In *Large-Scale Computations in Fluid Mechanics* (Ed. R. L. Lee, R. L. Sani, T. M. Shih, and P. M. Gresho), 163–193.
- Roe, P. L. and Pike, J. (1985). Efficient construction and utilisation of approximate Riemann solutions. In *Proceedings of the Sixth International Symposium on Computing Methods in Applied Sciences and Engineering, VI*, pp. 499–518. North-Holland, Amsterdam.
- Roedig, C., Zanotti, O., and Alic, D. (2012). General relativistic radiation hydrodynamics of accretion flows. II. Treating stiff source terms and exploring physical limitations. *Mon. Not. R. Astron. Soc.*, **426**, 1613–1631.
- Romano, V. and Pavón, D. (1993). Causal dissipative Bianchi cosmology. *Phys. Rev. D*, **47**,

- 1396–1403.
- Romatschke, P. (2010). New developments in relativistic viscous hydrodynamics. *Int. J. Mod. Phys. E*, **19**, 1–53.
- Romero, J. V., Ibáñez, J. M., Martí, J. M., and Miralles, J. A. (1996). A new spherically symmetric general relativistic hydrodynamical code. *Astrophys. J.*, **462**, 839–854.
- Rosswog, S. (2010). Conservative, special-relativistic smoothed particle hydrodynamics. *J. Comput. Phys.*, **229** (22), 8591–8612.
- Roytburd, V. (1991). *Fluid Dynamical Aspects of Combustion Theory*, Volume 223, Pitman Research Notes in Mathematics Series, 184. Ed. Onofri, M. and Tesei, A., Pitman, Harlow.
- Ruffert, M. (1996). Three-dimensional hydrodynamic Bondi–Hoyle accretion. V. Specific heat ratio 1.01, nearly isothermal flow. *Astron. Astrophys.*, **311**, 817–832.
- Ruffert, M. (1997). Non-axisymmetric wind-accretion simulations. I. Velocity gradients of 3% and 20% over one accretion radius. *Astron. Astrophys.*, **317**, 793–814.
- Ruiz, M., Hilditch, D., and Bernuzzi, S. (2011). Constraint preserving boundary conditions for the Z4c formulation of general relativity. *Phys. Rev. D*, **83**, 024025.
- Runge, C. (1895). Über die numerische auflösung von differentialgleichungen. *Math. Ann.*, **46**, 167–178.
- Rusanov, V. V. (1961). Calculation of interaction of non-steady shock waves with obstacles. *J. Comput. Math. Phys. USSR*, **1**, 267–279.
- Russo, G. and Anile, A. M. (1987). Stability properties of relativistic shock waves—Basic results. *Phys. Fluids*, **30**, 2406–2413.
- Rybicki, G. B. and Lightman, A. P. (1986). *Radiative Processes in Astrophysics*. John Wiley, New York.
- Sachs, R. K. (1962). Gravitational waves in general relativity. VIII. Waves in asymptotically flat space-time. *Proc. Roy. Soc. London, Ser. A*, **270**, 103–126.
- Sandvik, H. B., Tegmark, M., Zaldarriaga, M., and Waga, I. (2004). The end of unified dark matter? *Phys. Rev. D*, **69**, 123524.
- Sapone, D. (2010). Dark energy in practice. *Int. J. Mod. Phys. A*, **25**, 5253–5331.
- Sarbach, O. and Tiglio, M. (2012). Continuum and discrete initial-boundary value problems and einstein’s field equations. *Living Rev. Relativ.*, **15**, 9.
- Sari, R. (2006). First and second type self-similar solutions of implosions and explosions containing ultrarelativistic shocks. *Phys. Fluids*, **18**, 027106.
- Sawada, K., Matsuda, T., Anzer, U., Boerner, G., and Livio, M. (1989). Inhomogeneous wind accretion—comparison between 3D and 2D computations. *Astron. and Astrophys.*, **221**, 263–272.
- Sądowski, A., Abramowicz, M., Bursa, M., Kluźniak, W., Lasota, J.-P., and Różańska, A. (2011). Relativistic slim disks with vertical structure. *Astron. Astrophys.*, **527**, A17.
- Scheck, L., Aloy, M. A., Martí, J. M., Gómez, J. L., and Müller, E. (2002). Does the plasma composition affect the long-term evolution of relativistic jets? *Mon. Not. R. Astron. Soc.*, **331**, 615–634.
- Scheuer, P. A. G. and Readhead, A. C. S. (1979). Superluminally expanding radio sources and the radio-quiet QSOs. *Nature*, **277**, 182–185.
- Schmid, L. A. (1970). Effects of heat exchange on relativistic fluid flow. In *A Critical Review of Thermodynamics* (Ed. E. B. Stuart, A. J. Brainard, and B. G. Or), 161. Mono Book, Baltimore.

- Schnetter, E. (2010). Time step size limitation introduced by the BSSN Gamma Driver. *Class. Quant. Grav.*, **27**, 167001.
- Schutz, B. F. (1970). Perfect fluids in general relativity: velocity potentials and a variational principle. *Phys. Rev. D*, **2**, 2762–2773.
- Schutz, B. F. (1971). Hamiltonian theory of a relativistic perfect fluid. *Phys. Rev. D*, **4**, 3559–3566.
- Schutz, B. F. (1985). *A First Course in General Relativity*. Cambridge University Press, Cambridge.
- Schutz, B. F. and Sorkin, R. (1977). Variational aspects of relativistic field theories, with application to perfect fluids. *Ann. Phys.*, **107**, 1–43.
- Schwarzschild, K. (1916). Über das Gravitationsfeld eines Massenpunktes nach der Einsteinchen Theorie. *Sitzungsber. Dtsch. Akad. Wiss. Berlin, Kl. Math. Phys. Tech.*, **1**, 189–196.
- Sedov, L. I. (1959). *Similarity and Dimensional Methods in Mechanics*. Academic Press, New York.
- Sedrakian, A. D. and Sedrakian, D. M. (1995). Superfluid core rotation in pulsars. I. Vortex cluster dynamics. *Astrophys. J.*, **447**, 305–323.
- Seguin, F. H. (1975). The stability of nonuniform rotation in relativistic stars. *Astrophys. J.*, **197**, 745–765.
- Seibert, D. (1985). Dynamical hadronization transition and hydrodynamical stability. *Phys. Rev. D*, **32**, 2812–2821.
- Seidel, E. and Moore, T. (1987). Gravitational radiation from realistic relativistic stars: Odd-parity fluid perturbations. *Phys. Rev. D*, **35**, 2287.
- Seiler, J., Szilagyi, B., Pollney, D., and Rezzolla, L. (2008). Constraint-preserving boundary treatment for a harmonic formulation of the Einstein equations. *Class. Quant. Grav.*, **25**, 175020.
- Sekiguchi, Y., Kiuchi, K., Kyutoku, K., and Shibata, M. (2011). Gravitational waves and neutrino emission from the merger of binary neutron stars. *Phys. Rev. Lett.*, **107**, 051102.
- Seliger, R. L. and Whitham, G. B. (1968). Variational principles in continuum mechanics. *Proceedings of the Royal Society of London. Series A. Mathematical and Physical Sciences*, **305** (1480), 1–25.
- Service, A. T. (1986). Fitting formulae for the equation of state of a perfect, semirelativistic Boltzmann gas. *Astrop. J.*, **307**, 60–61.
- Shakura, N. I. and Sunyaev, R. A. (1973). Black holes in binary systems. Observational appearance. *Astron. Astrophys.*, **24**, 337–355.
- Shapiro, S. L. (1989). Potential flows in general relativity: Some exact solutions. *Phys. Rev. D*, **39**, 2839–2847.
- Shapiro, S. L. and Teukolsky, S. A. (1983). *Black Holes, White Dwarfs, and Neutron Stars*. John Wiley, New York.
- Shen, H., Toki, H., Oyamatsu, K., and Sumiyoshi, K. (1998). Relativistic equation of state of nuclear matter for supernova and neutron star. *Nucl. Phys. A*, **637**, 435–450.
- Shibata, M. (2007). Rotating black hole surrounded by self-gravitating torus in the puncture framework. *Phys. Rev. D*, **76**, 064035.
- Shibata, M. and Font, J. A. (2005). Robustness of a high-resolution central scheme for hydrodynamic simulations in full general relativity. *Phys. Rev. D*, **72**, 047501.

- Shibata, M., Kiuchi, K., Sekiguchi, Y., and Suwa, Y. (2011). Truncated moment formalism for radiation hydrodynamics in numerical relativity. *Prog. Theor. Phys.*, **125**, 1255–1287.
- Shibata, M. and Nakamura, T. (1995). Evolution of three-dimensional gravitational waves: Harmonic slicing case. *Phys. Rev. D*, **52**, 5428.
- Shibata, M. and Taniguchi, K. (2006). Merger of binary neutron stars to a black hole: Disk mass, short gamma-ray bursts, and quasinormal mode ringing. *Phys. Rev. D*, **73**, 064027.
- Shibata, M. and Taniguchi, K. (2011). Coalescence of black hole-neutron star binaries. *Living Rev. Relativ.*, **14**, 6.
- Shibata, M., Taniguchi, K., and Uryū, K. (2005). Merger of binary neutron stars with realistic equations of state in full general relativity. *Phys. Rev. D*, **71**, 084021.
- Shibata, M. and Uryū, K. (2000). Simulation of merging binary neutron stars in full general relativity:  $\Gamma = 2$  case. *Phys. Rev. D*, **61**, 064001.
- Shu, C. W. (2003). High order finite difference and finite volume WENO schemes and discontinuous Galerkin methods for CFD. *Int. J. Comput. Fluid. D.*, **17**, 107–118.
- Shu, C. W. (1997). Essentially non-oscillatory and weighted essentially non-oscillatory schemes for hyperbolic conservation laws. Lecture notes ICASE Report 97-65; NASA CR-97-206253, NASA Langley Research Center.
- Shu, C.-W. and Osher, S. (1989). Efficient implementation of essentially non-oscillatory shock-capturing schemes, II. *J. Comput. Phys.*, **83**, 32–78.
- Shu, C. W. and Osher, S. J. (1988). Efficient implementation of essentially non-oscillatory shock-capturing schemes. *J. Comput. Phys.*, **77**, 439–471.
- Siebel, F., Font, J. A., Müller, E., and Papadopoulos, P. (2002). Simulating the dynamics of relativistic stars via a light-cone approach. *Phys. Rev. D*, **65**, 064038.
- Siebel, F., Font, J. A., Mueller, E., and Papadopoulos, P. (2003). Axisymmetric core collapse simulations using characteristic numerical relativity. *Phys. Rev. D*, **67**, 124018.
- Siegel, D., Ciolfi, R., Harte, A. I., and Rezzolla, L. (2013). On the magnetorotational instability in relativistic hypermassive neutron stars. *Phys. Rev. D*, **87**, R121302.
- Smarr, L. and York, J. W. (1978). Kinematical conditions in the construction of spacetime. *Phys. Rev. D*, **17**, 2529–2552.
- Smith, M. D., Smarr, L., Norman, M. L., and Wilson, J. R. (1983). Bubbles, jets, and clouds in active galactic nuclei. *Astrophys. J.*, **264**, 432–445.
- Smoller, J. and Temple, B. (1993). Global solutions of the relativistic Euler equations. *Commun. Math. Phys.*, **156**, 67–99.
- Smoller, J. and Temple, B. (1995). Astrophysical shock-wave solutions of the einstein equations. *Phys. Rev. D*, **51**, 2733–2743.
- Sod, G. A. (1978). A survey of several finite difference methods for systems of nonlinear hyperbolic conservation laws. *J. Comput. Phys.*, **27**, 1–31.
- Soker, N. (1990). Stability analysis of the accretion line. *Astrop. J.*, **358**, 545–550.
- Solin, P. (2006). *Partial Differential Equations and the Finite Element Method*. Pure and Applied Mathematics. John Wiley, New York.
- Spergel, D. N., Bean, R., Doré, O. et al. (2007). Three-year Wilkinson Microwave Anisotropy Probe (WMAP) observations: Implications for Cosmology. *Astrop. J. Supp.*, **170**, 377–408.
- Spiteri, R. J. and Ruuth, S. J. (2002). A new class of optimal high-order strong-stability-preserving time discretization methods. *SIAM J. Numer. Anal.*, **40**, 469–491.

## 716 References

- Stark, R. F. and Piran, T. (1985). Gravitational-wave emission from rotating gravitational collapse. *Phys. Rev. Lett.*, **55**, 891–894.
- Steger, J. L. and Warming, R. F. (1981). Flux vector splitting of the inviscid gasdynamic equations with application to finite-difference methods. *J. Comput. Phys.*, **40**, 263–293.
- Steinhardt, P. J. (1982). Relativistic detonation waves and bubble growth in false vacuum decay. *Phys. Rev. D*, **25**, 2074–2085.
- Stephani, H. (2000). *General Relativity*, Second edition. Cambridge University Press, Cambridge.
- Stephens, B. C., East, W. E., and Pretorius, F. (2011). Eccentric black hole-neutron star mergers. *Astrophys. J.*, **737**, L5–L9.
- Stergioulas, N. (2003). Rotating stars in relativity. *Living Rev. Relativ.*, **6**, 3.
- Stergioulas, N. (2011). An improved method for constructing models of self-gravitating tori around black holes. *Int. J. Mod. Phys. D*, **20**, 1251–1263.
- Stergioulas, N., Apostolatos, T. A., and Font, J. A (2004). Non-linear pulsations in differentially rotating neutron stars: Mass-shedding-induced damping and splitting of the fundamental mode. *Mon. Not. R. Astron. Soc.*, **352**, 1089–1101.
- Stergioulas, N., Bauswein, A., Zagkouris, K., and Janka, H.-T. (2011). Gravitational waves and non-axisymmetric oscillation modes in mergers of compact object binaries. *Mon. Not. R. Astron. Soc.*, **418**, 427–436.
- Stern, D. P. (1970). Euler potentials. *Am. J. Phys.*, **38**, 494–501.
- Stewart, J. M. (1971). *Non-Equilibrium Relativistic Kinetic Theory*. Volume 10, Lecture Notes in Physics, Springer, Berlin.
- Stewart, J. M. (1977). On transient relativistic thermodynamics and kinetic theory. *Royal Society of London Proceedings Series A*, **357**, 59–75.
- Straumann, N. (1984). *General Relativity and Relativistic Astrophysics*. Springer, Berlin.
- Strikwerda, J. C. (2004). *Finite Differential Schemes and Partial Differential Equations*. Second edition. SIAM, Philadelphia.
- Stuchlík, Z., Slány, P., and Hledík, S. (2000). Equilibrium configurations of perfect fluid orbiting Schwarzschild–de Sitter black holes. *Astron. Astrophys.*, **363**, 425–439.
- Sweby, P. K. (1984). High resolution schemes using flux limiters for hyperbolic conservation laws. *SIAM J. Numer. Anal.*, **21**, 995–1011.
- Synge, J. L. (1957). *The Relativistic Gas*. North-Holland, Amsterdam.
- Synge, J. L. (2002). “Golden Oldie”: Relativistic Hydrodynamics. *Gen. Rel. Grav.*, **34**, 2177–2216.
- Szilágyi, B., Pollney, D., Rezzolla, L., Thornburg, J., and Winicour, J. (2007). An explicit harmonic code for black hole evolution using excision. *Class. Quant. Grav.*, **24**, S275–S293.
- Takami, K., Rezzolla, L., and Yoshida, S. (2011). A quasi-radial stability criterion for rotating relativistic stars. *Mon. Not. R. Astron. Soc.*, **416**, L1–L5.
- Takamoto, M. and Inutsuka, S.-I. (2011). A fast numerical scheme for causal relativistic hydrodynamics with dissipation. *J. Comput. Phys.*, **230**, 7002–7017.
- Tassoul, J.-L. (2007). *Stellar Rotation*. Cambridge University Press, Cambridge.
- Taub, A. H. (1948). Relativistic Rankine–Hugoniot equations. *Phys. Rev.*, **74**, 328–334.
- Taub, A. H. (1954). General relativistic variational principle for perfect fluids. *Phys. Rev.*, **94**, 1468–1470.

- Tchekhovskoy, A., McKinney, J. C., and Narayan, R. (2007). Wham: A WENO-based general relativistic numerical scheme. I. Hydrodynamics. *Monthly Notices of the Royal Astronomical Society*, **379**, 469.
- Tchekhovskoy, A., Narayan, R., and McKinney, J. C. (2011). Efficient generation of jets from magnetically arrested accretion on a rapidly spinning black hole. *Mon. Not. R. Astron. Soc.*, **418**, L79–L83.
- Teukolsky, S. A. (1973). Perturbations of a rotating black hole. I. Fundamental equations for gravitational, electromagnetic, and neutrino-field perturbations. *Astrophys. J.*, **185**, 635–647.
- Thompson, K. W. (1986). The special relativistic shock tube. *J. Fluid Mech.*, **171**, 365–375.
- Thompson, P. A., Kim, Y.-G., and Carofano, G. C. (1986). Shock waves and phase changes in a large-heat-capacity fluid emerging from a tube. *J. Fluid Mech.*, **166**, 57–92.
- Thornburg, J. (2007). Event and apparent horizon finders for 3+1 numerical relativity. *Living Rev. Relativ.*, **10**, 3.
- Thorne, K. S. (1973). Relativistic shocks: The taub adiabat. *Astrophys. J.*, **179**, 897–908.
- Thorne, K. S. (1981). Relativistic radiative transfer—Moment formalisms. *Mon. Not. R. Astron. Soc.*, **194**, 439–473.
- Titarev, V. A. and Toro, E. F. (2002). ADER: Arbitrary high order Godunov approach. *J. Sci. Comput.*, **17**, 609.
- Titarev, V. A. and Toro, E. F. (2004). Finite-volume WENO schemes for three-dimensional conservation laws. *J. Comput. Phys.*, **201**, 238–260.
- Titarev, V. A. and Toro, E. F. (2005). ADER schemes for three-dimensional non-linear hyperbolic systems. *J. Comput. Phys.*, **204**, 715–736.
- Tokareva, I., Nusser, A., Gurovich, V., and Folomeev, V. (2005). Relativistic model of detonation transition from neutron to strange matter. *Int. J. Mod. Phys. D*, **14**, 33–50.
- Tolman, R. C. (1939). Static solutions of Einstein’s field equations for spheres of fluids. *Phys. Rev.*, **55**, 364–373.
- Toro, E. F. (2009). *Riemann Solvers and Numerical Methods for Fluid Dynamics*. Springer, Berlin.
- Toro, E. F., Hidalgo, A., and Dumbser, M. (2009). FORCE schemes on unstructured meshes I: Conservative hyperbolic systems. *J. Comput. Phys.*, **228**, 3368–3389.
- Toro, E. F., Millington, R. C., and Nejad, L. A. M. (2001). Towards very high-order Godunov schemes. In *Godunov Methods: Theory and Applications. Conference in Honour of S. K. Godunov*, 897–902. Kluwer Academic Publishers, Dordrecht.
- Toro, E. F., Spruce, M., and Speares, W. (1994). Restoration of the contact surface in the HLL-Riemann solver. *Shock Waves*, **4**, 25–34.
- Toro, E. F. and Titarev, V. A. (2002). Solution of the generalized Riemann problem for advection-reaction equations. *Proc. Roy. Soc. London, Ser. A*, **458** (2018), 271–281.
- Toro, E. F. and Titarev, V. A. (2005). ADER schemes for scalar non-linear hyperbolic conservation laws with source terms in three-space dimensions. *J. Comput. Phys.*, **202**, 196–215.
- Toth, G. (2000). The  $\nabla \cdot B = 0$  constraint in shock-capturing magnetohydrodynamics codes. *J. Comput. Phys.*, **161**, 605–652.
- Trangenstein, J. A. (2009). *Numerical Solution of Hyperbolic Partial Differential Equations*. Cambridge University Press, Cambridge.
- Treves, A., Maraschi, L., and Abramowicz, M. (1989). *Accretion. A Collection of Influential*

- Papers.* Volume 5.
- Tsoutsanis, P., Titarev, V. A., and Drikakis, D. (2011). WENO schemes on arbitrary mixed-element unstructured meshes in three space dimensions. *J. Comput. Phys.*, **230**, 1585–1601.
- Tsuchiya, T., Yoneda, G., and Shinkai, H.-A. (2011). Constraint propagation of C<sup>2</sup>-adjusted formulation: Another recipe for robust ADM evolution system. *Phys. Rev. D*, **83**, 064032.
- Tsumura, T., Kunihiro, T., and Ohnishi, K. (2007). Derivation of covariant dissipative fluid dynamics in the renormalization-group method. *Phys. Lett. B*, **646**, 134–140.
- Uehling, E. A. and Uhlenbeck, G. E. (1933). Transport phenomena in Einstein–Bose and Fermi–Dirac gases. I. *Phys. Rev.*, **43**, 552–561.
- Usov, V. V. (1992). Millisecond pulsars with extremely strong magnetic fields as a cosmological source of gamma-ray bursts. *Nature*, **357**, 472–474.
- van Leer, B. (1976). MUSCL, a new approach to numerical gas dynamics. In *Computing in Plasma Physics and Astrophysics*, p. 1., (Ed. D. Biskamp), North-Holland, Amsterdam.
- van Leer, B. (1977). Towards the ultimate conservative difference scheme. IV. A new approach to numerical convection. *J. Comput. Phys.*, **23**, 276–299.
- van Leer, B. (1979). Towards the ultimate conservative difference scheme. V. A second-order sequel to godunov’s method. *J. Comput. Phys.*, **32**, 101–136.
- van Leer, B. (1982). Flux-vector splitting for the Euler equations. In *Eighth International Conference on Numerical Methods in Fluid Dynamics* (Ed. E. Krause), Volume 170, Lecture Notes in Physics, 507–512. Springer, Berlin.
- van Leer, B. J. (2006). Upwind and high-resolution methods for compressible flow: From donor cell to residual-distribution schemes. *Commun. Comput. Phys.*, **1**, 192–206.
- Vardanyan, G. A. and Sedrakian, A. D. (1981). Superfluid core rotation in pulsars. I. Vortex cluster dynamics. *Soviet Phys.-JETP*, **54**, 919–921.
- Vines, J., Flanagan, E. E., and Hinderer, T. (2011). Post-1-Newtonian tidal effects in the gravitational waveform from binary inspirals. *Phys. Rev. D*, **83**, 084051.
- Vlahakis, N. and Königl, A. (2003). A model for GRB jets. *Astrophys. Space Sci.*, **287**, 249–252.
- Voje, N. and Ravndal, F. (2006). On the discovery of Birkhoff’s theorem. *Gen. Rel. Grav.*, **38**, 537–540.
- Von Neumann, J. and Richtmyer, R. D. (1950). A method for the numerical calculation of hydrodynamical shocks. *J. Appl. Phys.*, **21**, 232–237.
- Von Zeipel, H. (1924). The radiative equilibrium of a rotating system of gaseous masses. *Mon. Not. Roy. Soc.*, **84**, 665–683.
- Wald, R. M. (1984). *General Relativity*. University of Chicago Press, Chicago.
- Walker, A. G. (1935). On the formal comparison of Milne’s kinematical system with the systems of general relativity. *Mon. Not. Roy. Soc.*, **95**, 263–269.
- Wang, P., Abel, T., and Zhang, W. (2008). Relativistic hydrodynamic flows using spatial and temporal adaptive structured mesh refinement. *Astrophys. J. Suppl. Ser.*, **176**, 467–483.
- Webbink, R. F. (1985). Structure parameters of galactic globular clusters. In *Dynamics of Star Clusters* (Ed. J. Goodman and P. Hut), Volume 113, IAU Symposium, 541–577.
- Weinberg, S. (1972). *Gravitation and Cosmology: Principles and Applications of the General Theory of Relativity*. John Wiley, New York.
- Weiss, W. (1995). Continuous shock structure in extended thermodynamics. *Phys. Rev. E*, **52**, 5760.

- Weiss, W. and Müller, I. (1995). Light scattering and extended thermodynamics. *Continuum Mechanics and Thermodynamics*, **7**, 123–177.
- Weyhausen, A., Bernuzzi, S., and Hilditch, D. (2012). Constraint damping for the Z4c formulation of general relativity. *Phys. Rev.*, **D85**, 024038.
- Whitham, G. B. (1974). *Linear and Nonlinear Waves*. Pure and Applied Mathematics. John Wiley, New York.
- Will, C. M. (1992). *Theory and Experiment in Gravitational Physics*. Cambridge University Press, Cambridge.
- Williams, F. A. (1965). *Combustion Theory*. Addison-Wesley, San Francisco.
- Wilson, D. B. (1984). A runaway instability in thick accretion disks? *Nature*, **312**, 620–621.
- Wilson, J. R. (1972). Numerical study of fluid flow in a Kerr space. *Astrophys. J.*, **173**, 431–438.
- Wilson, J. R. (1979). A numerical method for relativistic hydrodynamics. In *Sources of Gravitational Radiation* (Ed. L. Smarr), 423. Cambridge University Press, Cambridge.
- Wilson, J. R. and Mathews, G. J. (1989). Relativistic hydrodynamics. In *Frontiers in Numerical Relativity* (Ed. C. R. Evans, L. S. Finn, and D. W. Hobill), 306–314.
- Wilson, J. R. and Mathews, G. J. (2003). *Relativistic Numerical Hydrodynamics*. Cambridge University Press, Cambridge.
- Wilson, J. R., Mathews, G. J., and Marronetti, P. (1996). Relativistic numerical model for close neutron star binaries. *Phys. Rev. D*, **54**, 1317–1331.
- Winicour, J. (2005). Characteristic evolution and matching. *Living Rev. Relativ.*, **15**, 2.
- Wiringa, R. B., Fiks, V., and Fabrocini, A. (1988). Equation of state for dense nucleon matter. *Phys. Rev. C*, **38**, 1010–1037.
- Wygoda, N., Waxman, E., and Frail, D. A. (2011). Relativistic jet dynamics and calorimetry of gamma-ray bursts. *Astrophys. J.*, **738**, L23–L28.
- Yamamoto, T., Shibata, M., and Taniguchi, K. (2008). Simulating coalescing compact binaries by a new code SACRA. *Phys. Rev. D*, **78**, 064054–1–38.
- Yokosawa, M. (1995). Structure and dynamics of an accretion disk around a black hole. *Publ. Astron. Soc. Japan*, **47**, 605–615.
- York, J. W. (1971). Gravitational degrees of freedom and the initial-value problem. *Phys. Rev. Lett.*, **26**, 1656–1658.
- York, J. W. (1972). Role of conformal three-geometry in the dynamics of gravitation. *Phys. Rev. Lett.*, **28**, 1082–1085.
- York, J. W. (1979). Kinematics and dynamics of general relativity. In *Sources of Gravitational Radiation* (Ed. L. L. Smarr), 83–126. Cambridge University Press, Cambridge.
- York, J. W. (1999). Conformal ‘thin-sandwich’ data for the initial-value problem of general relativity. *Phys. Rev. Lett.*, **82**, 1350–1353.
- Zanotti, O. (2002). *Numerical Relativistic Hydrodynamics: New ideas and applications*. PhD Thesis, SISSA, International School for Advanced Studies, Trieste.
- Zanotti, O. and Dubser, M. (2011). Numerical simulations of high Lundquist number relativistic magnetic reconnection. *Mon. Not. R. Astron. Soc.*, **418**, 1004–1011.
- Zanotti, O., Font, J. A., Rezzolla, L., and Montero, P. J. (2005). Dynamics of oscillating relativistic tori around Kerr black holes. *Mon. Not. R. Astron. Soc.*, **356**, 1371–1382.
- Zanotti, O., Rezzolla, L., Del Zanna, L., and Palenzuela, C. (2010). Electromagnetic counterparts of recoiling black holes: General relativistic simulations of non-Keplerian discs.

- Astron. Astrophys.*, **523**, A8.
- Zanotti, O., Rezzolla, L., and Font, J. A. (2003). Quasi-periodic accretion and gravitational waves from oscillating “toroidal neutron stars” around a Schwarzschild black hole. *Mon. Not. Roy. Soc.*, **341**, 832–848.
- Zanotti, O., Roedig, C., Rezzolla, L., and Del Zanna, L. (2011). General relativistic radiation hydrodynamics of accretion flows. I. Bondi–Hoyle accretion. *Mon. Not. R. Astron. Soc.*, **417**, 2899–2915.
- Zel'dovich and Novikov, I. D. (1971). *Relativistic Astrophysics, Vol. I (Stars and Relativity)*. University of Chicago Press, Chicago.
- Zel'dovich, Y. B. and Raizer, Y. P. (2002). *Physics of Shock Waves and High-Temperature Hydrodynamic Phenomena*. Dover, New York.
- Zeldovich, Ya. B., Barenblatt, G. I., Librovich, V. B., and Makhviladze, G. M. (1985). *The Mathematical Theory of Combustion and Explosions*. Consultants Bureau, New York.
- Zhang, B. and Mészáros, P. (2004). Gamma-ray bursts: Progress, problems and prospects. *Int. J. Mod. Phys. A*, **19**, 2385–2472.
- Zhang, W. and MacFadyen, A. I. (2006). RAM: A relativistic adaptive mesh refinement hydrodynamics code. *Astrophys. J. Suppl. Ser.*, **164**, 255–279.
- Zhang, W., Woosley, S. E., and MacFadyen, A. I. (2003). Relativistic jets in collapsars. *Astrophys. J.*, **586**, 356–371.
- Zhang, X. and Shu, C.-W. (2010). On positivity-preserving high order discontinuous Galerkin schemes for compressible Euler equations on rectangular meshes. *J. Comput. Phys.*, **229**, 8918–8934.
- Zrake, J. and MacFadyen, A. I. (2013). Spectral and intermittency properties of relativistic turbulence. *Astrophys. J.*, **763**, L12–L16.
- Zumbusch, G (2009). Finite element, discontinuous Galerkin, and finite difference evolution schemes in spacetime. *Class. Quant. Grav.*, **26**, 175011.
- Zwerger, T. and Müller, E. (1997). Dynamics and gravitational wave signature of axisymmetric rotational core collapse. *Astron. Astrophys.*, **320**, 209–227.

# Index

- j*-constant law, 609  
1+log slicing condition, 345  
3+1 decomposition, 65, 196, 244, **319**, 329, 346, 351, 356, 365, 374, 379
- ## A
- absolute Maxwellian distribution, 82  
absolute space, 4  
absolute time, 4  
acceleration, Eulerian observer, 330  
accretion (flow solution), 515  
accretion discs  
    slim, 553  
    thick, 553  
    thin, 553  
accretion radius, 517, **519**  
accuracy  
    global order, 393  
    local order, 391  
acoustic, 209  
acoustic wave, *see* sound wave  
action, 169  
action, Einstein–Hilbert, 47, **173**  
active galactic nuclei, 59, **553**, 565  
adaptive mesh-refinement (AMR), 325, **460**  
adaptivity strategy, ENO, 466  
ADER method, 426, 459, **479**, 481, 482, 490  
adiabatic fluid, 103, **120**, 144  
adiabatic index, **106**, 116, 119  
adiabatic index, of polytrope, 119  
ADM, *see* Arnowitt–Deser–Misner formulation  
advection equation, 203  
advection velocity, **203**, 396  
advection–diffusion equation, 403  
affine connection coefficients, 35  
affine model, 653  
affine parameter, 39  
Aloy–Rezzolla booster, 572; *see also* relativistic jet  
amplification factor, 398  
amplitude tensor, 63; *see also* gravitational wave  
anelastic collision, 73  
angular momentum, 605; *see also* specific angular momentum  
anisotropic perfect fluid, **141**, 601  
anisotropic pressure, 141, **601**  
anisotropic stress tensor, **288**, 559  
anti-de Sitter cosmological model, 61  
antisymmetric tensor, 18  
apparent horizon, **615**, 619; *see also* horizon
- approximate Riemann solver, **436**, 680  
Arnowitt–Deser–Misner (ADM) formulation, 329;  
    *see also* Einstein–Euler formulation  
artificial viscosity, 361, 403, **409**, 421  
artificial-viscosity methods, 387, **409**  
atlas, 6  
atmosphere, 673  
attractor, 498  
average speed, 83
- ## B
- baroclinic fluid, 153  
barotropic equation of state, 128  
baryon mass, 605  
basis covectors, 15  
basis vectors, 14  
basis  
    coordinate, 14  
    coordinate orthonormal, 22  
    modal, **464**, 476  
    nodal, **464**, 476  
    non-coordinate, 34  
    tetrad, 34  
Baumgarte–Shapiro–Shibata–Nakamura–Oohara–Kojima (BSSNOK) formulation, 338;  
    *see also* Einstein–Euler formulation  
Beam–Warming scheme, 407  
beaming parameters, 569  
Bernoulli equation  
    classical, 151  
    relativistic, 152  
Bernoulli's constant, 151  
Bernoulli's theorem  
    classical, 151  
    relativistic, 152  
Bianchi identities, **44**, 45, 97  
Bianchi identities, contracted, **46**, 97  
big bang, **67**, 580  
binary collisions  
    elastic, **71**, 73  
    anelastic, 73  
binary system (compact objects)  
    black holes, **339**, 342, 343, 345, 349  
    mass ratio, 637  
    mixed, 647  
    neutron stars, 342, 541, 579, **623**, 626, 633, 637, 644, 647, 650  
binding energy, 605  
Birkhoff's theorem, **49**, 54, 594, 597, 599, 601, 612

- Bjorken flow, 584  
 black-body radiation, 123  
 black hole  
     accretion onto, 515–565  
     from collapse, 612–623  
     from binary neutron stars, 624–647  
     from mixed binaries, 647–656  
     Kerr, 54  
     Kerr extremal, 58  
     Schwarzschild, 50  
     Schwarzschild–de Sitter, 551  
 Blandford–McKee solution, 511  
 blast waves, 507  
 boiling bubbles, 501  
 Boltzmann constant, 81  
 Boltzmann equation  
     classical, 68, 73  
     relativistic, 90  
 Bona–Massó slicing condition, 344  
 Bondi solution, 517  
 Bondi–Hoyle–Lyttleton accretion, 529  
 Bondi–Hoyle–Lyttleton radius, 531  
 Bondi–Sachs metric, 375  
 book notation, 4  
 boost, 24; *see also* Lorentz transformations  
 Bose–Einstein integral, 123  
 Bose–Einstein statistics, 100, 123  
 boundary surface, 252  
 boundary-value problem (BVP), 388  
 bow shock, 530  
 Boyer–Lindquist coordinates, 55, 542, 554, 591  
 break-up frequency, 607  
 BSSNOK, *see* Baumgarte–Shapiro–Shibata–  
     Nakamura–Oohara–Kojima  
     formulation  
 BVP, *see* boundary-value problem  
 Buchdahl’s limit, 598  
 bulk viscosity, 88, 288  
 Burgers equation, 204  
 Burgers equation, implicit, 206  
 Butcher barrier, 452  
 Butcher tableau, 451
- C**
- Carter constant, 57  
 Carter–Lichnerowicz equation, 156  
 Cauchy data, 207  
 Cauchy problem, 193, 387  
 Cauchy–Kovalewski procedure, 479, 480, 482  
 causal slice, 381  
 Causal Thermodynamics, *see* Extended Irreversible  
     Thermodynamics (EIT)  
 caustics, 204  
 CCZ4 formulation, 340, 342; *see also* Z4  
     formulation  
 cell, 398; *see also* spacetime discretisation  
 cell averages, 417  
 central schemes, 426, 447, 452  
 central-rapidity region, 581
- central-upwind scheme, 414, 436, 447, 456  
 centred stencil, 401  
 CFC, *see* conformally flat condition  
 CFL condition, 391, 396, 424  
 CFL factor, 397  
 CFS instability, 618  
 Chandrasekhar mass, 115  
 Chaplygin fluid, 128  
 Chapman–Enskog, 87  
 Chapman–Jouguet deflagration, 262, 267, 507  
 Chapman–Jouguet detonation, 261, 263  
 Chapman–Jouguet hypothesis, 264  
 characteristic  
     curve, 199, 203  
     equations, 199  
     fluxes, 446  
     hypersurface, 194  
     matrix, 193  
     phase, 200  
     reconstruction, 434  
     speed, 203  
     variables, 198, 420, 434  
     vector, 198, 434, 444  
 chart, 6; *see also* coordinates  
 chemical potential, 98, 101, 109, 182, 183, 185, 309,  
     584  
 Christoffel symbols, 35, 36, 337, 368  
 circulation, 154  
 circulation tensor, 155  
 CIT, *see* Classical Irreversible Thermodynamics  
 Classical Irreversible Thermodynamics (CIT), 291  
 classical monatomic fluid, 81, 106, 111, 112, 115  
 closure relation, 104  
 Codazzi–Mainardi equations, 332  
 coldness, *see* relativistic coldness  
 collision integral, 74, 78, 91  
 collisional fluid, 85  
 collisionally invariant quantity, 78  
 collisionless Boltzmann equation, 72  
 collisionless fluid, 85  
 collisions  
     binary elastic, 71, 73  
     binary anelastic, 73  
 comoving frame, 555  
 comoving gauge, 59  
 compatibility conditions, 216  
 complete Riemann solver, 436  
 completely degenerate Fermi fluid, 114  
 completely degenerate non-relativistic Fermi fluid,  
     115, 118  
 completely degenerate ultrarelativistic Fermi fluid,  
     115  
 components (tensor), 10; *see also* tensor  
 compressibility, 119  
 compressible fluid, 69  
 compression, 209  
 computational domain, 388  
 condensation discontinuities, 263  
 conformal factor, 337, 351, 355  
 conformal Killing operator, 352, 357

- conformal Killing vector, 352  
 conformal metric, **163**, 337, 338  
 conformal metric, Christoffel symbols, 337  
 conformal thin-sandwich decomposition, 354  
 conformal traceless formulation, **336**, 338  
 conformal transformation, 336  
 conformally flat formulation, 354; *see also*  
     Einstein–Euler formulation  
 conformally flat condition, **356**, 360  
 congruence, 31  
 conjugate four-momenta, 180  
 connection coefficients, 35  
 conservation equation  
     energy (classical), 86  
     linear momentum (classical), 86  
     mass (classical), 86  
     Boltzmann, 78  
     energy, 97  
     linear momentum, 97  
     rest mass, 97  
 conservation of circulation, 154  
 conservative form, **196**, 362  
 conservative numerical method, **414**, 417  
 conservative numerical scheme  
     finite-difference, 418  
     finite-volume, 417  
 conserved energy, 196  
 conserved momentum, 196  
 conserved rest-mass density, 196  
 conserved variables, **196**, 363, 367, 427, 470, 668  
 consistency condition, **394**, 417  
 constant mean curvature, 353  
 constitutive equations, 289  
     Classical Irreversible Thermodynamics, 293  
     divergence-type theories, 307  
     Extended Irreversible Thermodynamics, 301  
 constitutive functions, 307  
 constrained evolution, *see* Einstein–Euler  
     formulation  
 constrained variables, 353  
 constraint damping, 339  
 constraint-transport method, 340  
 contact discontinuity, **222**, 223, 424, 575  
 continuity equation, 97  
     classical, 86  
     relativistic, 143  
 continuous parameterisation, 5  
 contracted Bianchi identities, **46**, 97  
 contracted Gauss relations, 332  
 contravariant index, 10  
 contravariant tensor, 16  
 contravariant vector, 10  
 control volume, **417**, 437  
 convective derivative, **32**, 38, 80, 135, 301  
 convergence condition, 394  
 convergence order, 394  
 convergent regime, 395  
 convex equation of state, **108**, 218  
 coordinate basis, **14**, 33  
 coordinate line, 324  
 coordinate time, 134  
 coordinate transformation, 7  
 coordinate transformation, inverse, 7  
 coordinate-components approach, 4  
 coordinates, 6  
     Boyer–Lindquist, **55**, 542, 554, 591  
     hyperspherical, 613  
     Kerr–Schild, **56**, 531, 591  
     map, 6  
     patch, 6  
     Schwarzschild, 49  
 Copernican principle, 59  
 corrugation, 247, **276**; *see also* shock stability  
 corrugation instability, 275  
 cosmic censorship, **615**, 621, 623  
 cosmological constant, **47**, 60, 127  
 cosmological principle, 59  
 cosmological redshift, 126  
 coupled multifluid, **175**, 176, 180, 182, 185  
 coupling scalar, 182  
 covariant  
     equations, 20  
     derivative, 35  
     derivative, three-dimensional, 329  
     formulation, 374; *see also*  
         relativistic-hydrodynamic equations  
 index, 10  
 tensor, 16  
 vector, 12  
 covector, 12  
 Cowling approximation, 303  
 critical accretion rate, 521  
 critical energy density, 60  
 critical radius, 517  
 Crocco equation, 157  
 curvature invariant, 45  
 curvature radius, 45  
 curvature scalar, 44  
 curvature tensor, 41; *see also* Riemann tensor  
 curve, 9  
 curved spacetime, 29  
 cusp (torus), 543  
 cutoff frequency (mixed binary), 655  
 cutoff frequency (QNM), 634  
 cyclic coordinate, 38

## D

- Dalambertian, **62**, 336  
 dark energy, **61**, 126  
 dark matter, **61**, 104, 126  
 dark-energy fluid, **126**, 128, 129  
 dark-matter fluid, **126**, 175  
 DDT, *see* deflagration-to-detonation  
 de Broglie wavelength, 68  
 de Laval nozzle, 570  
 de Sitter cosmological model, 61  
 deflagration, **260**, 501  
     Chapman–Jouguet, **262**, 267  
     strong, **262**, 267

- deflagration (*cont.*)  
     supersonic, 267  
     weak, **262**, 267
- deflagration-to-detonation (DDT), 267
- degeneracy factor, 98
- degenerate fluid, 99
- degenerate relativistic fluid, 109
- degenerate ultrarelativistic fluid, 113
- degree of under-determinacy, 245
- degrees of freedom, 380, **464**
- densitised metric, 347
- density, 79
- density parameter, 60
- derivative  
     convective, 38  
     covariant, 35  
     fundamental, 108  
     Lagrangian, **80**, 148  
     Lie, 31  
     Thomas, 249
- detached shock, 530
- detonation, **260**, 501  
     Chapman–Jouguet, **261**, 263  
     strong, **261**, 263  
     weak, **261**, 263
- DG, *see* discontinuous Galerkin method
- differential rotation, 608
- differential-geometry approach, 4
- dilatational viscosity, 88
- dimension-by-dimension reconstruction, 486
- dimensional splitting, 487
- dimensionless momentum, 104
- Dirac, generalised gauge, 357
- discs (accretion)  
     slim, 553  
     thick, 553  
     thin, 553
- discontinuity, 500
- discontinuity surface, 209
- discontinuous Galerkin formulation, 377; *see also* relativistic-hydrodynamic equations
- discontinuous Galerkin method, **377** 459, 472, 475, 485
- discontinuous wave, 209
- discretisation  
     operator, 388  
     spacetime, 387  
     spatial, 391  
     time, 391  
     variable, 388
- displacement vector, 134
- distribution function, **68**, 70
- divergence formula, 36
- divergence-cleaning method, 340
- divergence-type theories, **299**, 306
- domain excision, *see* excision technique
- domain of dependence, 206
- domain of dependence, numerical, 396
- domain of determinacy, 207
- dominant energy condition, 93
- Doppler boosting, 566
- Doppler factor, 568
- double-bracket notation, **215**, 252
- downstream, 214
- dual, 12
- dual space, 12
- duality, 22
- dynamical instability (relativistic star), 618
- ## E
- Eckart frame, 287
- Eckart's theory, 293; *see also* Relativistic Irreversible Thermodynamics (RET)
- Eddington  
     accretion rate, 516  
     limit, 516  
     luminosity, 516
- effective amplitude, 634
- effective potential (Kerr), 542
- effective potential (Schwarzschild), 51
- effective potential (Schwarzschild–de Sitter), 551
- effective potential, turning point, 52
- Ehrenfest's theorem, 68
- eigenspeeds, 362
- eigenvalue problem, 193
- eigenvalues, **192**, 195, 198, 304, 305, 369
- eigenvector matrix, 192
- eigenvectors, left, 371
- eigenvectors, right, **192**, 193, 198, 362, 369, 373
- Einstein equations, 46; *see also* Einstein–Euler formulation
- Einstein tensor, 46
- Einstein–Euler equations, **319**, 593
- Einstein–Euler formulation  
     ADM, 329  
     BSSNOK, 338  
     CCZ4, 342  
     conformal traceless, 336  
     conformally flat, **356**, 360  
     constrained evolution, **334**, 356  
     free evolution, **334**, 360  
     fully constrained,  
         generalised harmonic, 346  
     Hernandez–Misner, 327  
     IWM, 356  
     Lagrangian, 325  
     Misner–Sharp, 325  
     Z4, 340  
     Z4c, 342
- Einstein–Hilbert action, 47, **173**
- Einstein–Vlasov equation, 69
- EIT, *see* Extended Irreversible Thermodynamics
- ejection (flow solution), 515
- elastic collision, **71**, 73
- elliptic system of equations, 388
- emissivity, 178
- energy condition, 92  
     dominant, 93, **127**  
     strong, 93, **127**

- energy condition (*cont.*)
  - weak, 93, **127**
- energy constraint, 334
- energy density, **98**, 102, 140
  - Eulerian observer, 333
  - Newtonian, 102
  - total, 93
  - total (Newtonian), 86
- energy frame, 287
- energy
  - binding, 605
  - relativistic, 28
  - rotational kinetic, 605
    - specific internal, **79**, 102, 117, 175, 370, 511
- energy-momentum equation, relativistic, 143
- energy-momentum tensor, 47, 92, **138**, 145, 184, 216, 252, 286, **289**, 307, 333, **365**, 411
  - energy-momentum tensor, spatial part, 333
  - energy-conservation equation, 144
- ENO, *see* essentially non-oscillatory method
- enthalpy, 102
  - radiation, 124
  - specific, 102
- enthalpy current, **156**, 158
- entrainment function, 182
- entrainment matrix, 181
- entrainment parameters, 182
- entropy, 75, **77**, 94
  - entropy condition, 416
  - entropy current, 94
- entropy density, **124**, 292, 580
- entropy per particle, 113
- entropy principle, **103**, 286, 306, 308, 311; *see also* second law of thermodynamics
- equation of state, 69, **104**
  - ideal fluid, 669
  - Gamma-law, 116
  - barotropic, 128
  - convex, **108**, 218
  - hybrid, 121
  - ideal fluid, **116**, 618, 627, 650
  - non-convex, **108**, 218
  - piecewise polytropic, 120
  - polytropic, **118**, 120, 520, 545, 550, 627, 650
  - soft, 119
  - stiff, 119
  - ultrastiff, 127
- equation
  - advection, 203
  - advection-diffusion, 403
  - Bernoulli (classical), 151
  - Bernoulli (relativistic), 152
  - Boltzmann (classical), 73
  - Boltzmann (relativistic), 90
  - Burgers, 204
  - Burgers (implici), 206
  - Carter-Lichnerowicz, 156
  - Crocco, 157
  - continuity, 97
  - elliptic, 388
- Einstein-Vlasov, 69
- Ernst, 54
- Fokker-Planck, 74
- geodesic, 39
- geodesic-deviation, 43
- heat-condution, 80
- hyperbolic, 192
- Lane-Emden, 594
- Poisson, 46
- telegraph, 297
- transport (classical), 78
- transport (relativistic), 95
- Vlasov-Maxwell, 68
- equations
  - characteristic, 199
  - Codazzi-Mainardi, 332
  - constitutive, 289
  - Einstein, 47
  - Euler (classical), 86
  - Euler (relativistic), 144
  - Euler-Lagrange, 51
  - Friedmann, 60
  - Gauss-Codazzi, 252
  - Helmholtz, 164
  - Israel-Stewart, 302
  - Killing, 37
  - Maxwell-Cattaneo, 302
  - momentum, 80
  - Navier-Stokes, **88**, 294
  - radiation-hydrodynamic, 178
  - relativistic-hydrodynamic, 143
  - semi-discrete, 447
  - Tolmann-Oppenheimer-Volkoff (TOV), 595
- equilibrium distribution, **69**, 75
- equilibrium state, 291
- equivalence principle, 5, **29**, 37, 101
- ergoregion, 56
- ergosphere, 56
- Ernst equation, 54; *see also* Kerr black hole
- error ratio, 392
- escape velocity, 519
- essentially non-oscillatory method (ENO), **460**, 468
- Euler equations, **144**, 319, 539, 559, 562, 595
- Euler equations, classical, **86**, 420
- Euler method, 448
- Euler potentials, 166
- Euler-Lagrange equations, 51
- Eulerian observer, 80, **323**, 330, 344, 517
- evaporating drops, 504
- event (spacetime), 4
- event horizon, **50**, 616; *see also* apparent horizon
- evolutionary reaction front, 269
- evolutionary shock, 245
- excision boundary, **349**, 675
- excision technique, 345, **349**, 675
- expansion scalar, **135**, 288
- expansion scalar, classical 87
- expansion shock, 416
- explicit scheme, 400
- extended forces, 301

- Extended Irreversible Thermodynamics (EIT), 291, **299**, 306  
 Extended Irreversible Thermodynamics,  
     divergence-type theories, 299, **306**  
 external forces, 149  
 extrinsic curvature, 330  
 extrinsic curvature, trace, 332
- F**
- Fermi momentum, 114  
 Fermi–Dirac statistics, 100  
 finite-difference methods, 386, **396**, 414  
 finite-difference scheme  
     ENO, 469  
     WENO, 472  
 finite-elements methods, 377  
 finite-volume methods, 414, **417**  
 finite-volume scheme  
     ENO scheme, 462  
     WENO scheme, 466  
 fireball, 566  
 first law of thermodynamics, 101  
 first moment (distribution function), 91  
 first-order approximation, 87; *see also* Boltzmann  
     equation  
 flat spacetime, 25  
 flip-flop instability, 532  
 flowline, *see* fluidline  
 fluid velocity, 74  
 fluid  
     classical monatomic, **81**, 106, 111, 115  
     collisionless, 85  
     completely degenerate Fermi, 114  
     completely degenerate non-relativistic Fermi,  
         115  
     completely degenerate ultrarelativistic Fermi,  
         115  
     degenerate relativistic, 109  
     degenerate ultrarelativistic, 113  
     description, 69  
 dust, **104**, 127, 142, 175, 612  
 non-degenerate non-relativistic, 111  
 non-degenerate relativistic, 110  
 non-degenerate ultrarelativistic, 113  
 non-selfgravitating, 493  
 pressureless, 104  
 selfgravitating, 593  
 Synge, 110  
 ultrarelativistic, 107  
 fluidline, **80**, 135, 145, 151, 154, 157, 159, 206, 324  
 flux vector, **195**, 362, 367  
 flux vector splitting method, 420  
 flux-balanced formulation, 368, **375**  
 flux-limiter methods, 422  
 Fokker–Planck equation, 74  
 foliation, 320  
 formulation, flux-balanced, 375  
 four-acceleration, **133**, 288  
 four-force, **40**, 91, 95
- four-momentum, 28  
 four-vector, purely spatial, 321  
 four-velocity, **27**, 133  
 four-velocity, non-perfect fluid, 285  
 Fourier law, **88**, 296  
 frame dragging, 56  
 frame  
     comoving, 555  
     Eckart, 287  
     energy, 287  
     inertial, 24  
     Landau, 287  
     Lorentz (global), 64  
     orbiting, 555  
     particle, 287  
     ZAMO, 555  
 free evolution, *see* Einstein–Euler formulation  
 frequency  
     break-up, 607  
     cutoff (mixed binary), 655  
     cutoff (QNM), 634  
     Keplerian, **539**, 554, 606  
     mass-shedding, 607  
     peak (HMNS), 635  
     tidal (mixed binary), 655  
 Friedmann equations, 60  
 Friedmann cosmological models, 61  
 Friedrichs’ theorem, 209  
 Friedmann–Robertson–Walker (FRW) spacetime,  
     **38**, 59  
 FRW, *see* Friedmann–Robertson–Walker spacetime  
 FTCS scheme, **386**, 402, 413  
 fugacity, **98**, 105, 114, 293, 304,  
 fundamental derivative, 108  
 future boundary, 381  
 future domain of dependence, 207  
 future light cone, *see* light cone
- G**
- Galilean transformations, 24  
 Galilean velocity composition law, 28  
 Gamma-driver shift condition, 346  
 Gamma-law equation of state, 116  
 gamma-ray burst, 508, 573, 579, **624**, 643, 653  
 Gammas, 337  
 gas, *see* fluid  
 gauge changes, 63  
 gauge, 343  
     generalised Dirac, 357  
     generalised harmonic, 347  
     harmonic, 347  
     infinitesimal transformation, 64  
     Lorenz, 62  
     transverse–traceless (TT), 64  
 Gauss divergence theorem, **96**, 103  
 Gauss contracted relations, 332  
 Gauss scalar relation, 332  
 Gauss Theorema Egregium, 332  
 Gauss–Codazzi equations, 211, **252**, 332

- Gaussian curvature, *see* intrinsic curvature  
 Gaussian quadrature, **474**, 481,  
*see also* Gaussian quadrature points  
 generalised Dirac gauge, 357  
 generalised harmonic formulation, 346; *see also*  
     Einstein–Euler formulation  
 generalised harmonic gauge, 347  
 generalised pressure, 182  
 generating function, 310  
 geodesic curve, 39  
 geodesic deviation equation, 43  
 geodesic equation, 39  
 geometrically slim tori, 546  
 geometrically thick tori, 546  
 geometrically thin tori, 546  
 geometrised units, 659  
 Gibbs free energy, 98  
 global order, accuracy, 393  
 Godunov method, 423  
 Godunov’s theorem, **423**, 426, 459  
 Grad’s approximation, 302  
 gradient, 12  
 gravastar, 599  
 gravitational  
     acceleration, 594  
     collapse (dust: OS), 612  
     collapse (fluid), 612  
     mass, 605  
     potential, 594  
     radiation, *see* gravitational wave  
     radius, 659  
     redshift, 50  
     wave, **61**, 632, 646 654  
 GRB, *see* gamma-ray burst  
 grid-based methods, 387  
 gridcell, *see* gridzone  
 gridfunction, 388  
 gridpoint, 387  
 gridzone, 398; *see also* spacetime discretisation  
 group velocity, **298**, 406  
 gyration radius, 556
- H**
- H-theorem  
     classical, 75  
     relativistic, 93  
 Hamiltonian constraint, 334  
 harmonic coordinates, 347  
 harmonic gauge, 347  
 harmonic slicing condition, 344  
 heat, 101  
 heat flux, **80**, 88, 286, 288, 559  
 heat-conduction equation, **88**, 296  
 heat-diffusion equation, 88  
 heat-flux law, 296  
 Helmholtz equations, 164  
 Helmholtz free energy, 253  
 Hernandez–Sharp formulation, 327; *see also*  
     Einstein–Euler formulation
- high-order method, 459  
     ADER, 426 **479**  
     discontinuous Galerkin (DG), **377**, 459, **472**,  
         475, 482  
     Essentially Non-Oscillatory (ENO), **460**, 469  
     Petrov–Galerkin, 473  
     Runge–Kutta discontinuous Galerkin  
         (RKDG), **474**, 490  
     Weighted Essentially Non-Oscillatory  
         (WENO), **460**, 466, 472  
 high-order scheme, local spacetime DG, 482  
 high-resolution shock-capturing (HRSC) method,  
     364, 411, **414**–427  
 HLLC flux, 442  
 HLLC Riemann solver, 436, **440**, 458  
 HLLE flux, 438  
 HLLE Riemann solver, **436**, 438, 440, 442, 447,  
     458, 488, 680  
 HLLEM Riemann solver, 445  
 HMNS, *see* hypermassive neutron star  
 homogeneous system, 192  
 homothetic vector, 495  
 horizon  
     apparent, 615  
     event, 50  
 HRSC, *see* high-resolution shock-capturing method  
 Hubble parameter, 60  
 Hugoniot adiabat, 216  
 hybrid equation of state, 121  
 hybrid star, 259  
 hydrodynamics, *see* fluid description  
 hyperbolic equation, **192**, 285, 336  
     strictly, 193  
     strongly, *see* hyperbolic form  
     weakly, **193**, 335, 340  
 hyperbolic, system of equations, **192**, 304, 362  
 hypermassive neutron star (HMNS), **609**, 624, 629  
 hyperspherical coordinates, 613  
 hypersurface, **9**, 320, 330, 343  
 hypersurface, characteristic, 194
- I**
- ideal fluid, 89  
 ideal-fluid equation of state, **116**, 618, 627, 650  
 IMEX, *see* implicit-explicit Runge–Kutta scheme  
 implicit-explicit Runge–Kutta scheme, 449  
 implicit scheme, 401  
 implicit Burgers equation, 206  
 incomplete Riemann solver, 436  
 incompressible fluid, 69, 127, **144**  
 indicator function, 382, **478**  
 inertial frame, 24  
 inertial-acoustic waves, 535  
 initial data, **193**, 334, **350**, 387  
 initial-value boundary problem (IVBP), 388  
 initial-value problem (IVP), **193**, 387  
 innermost stable circular orbit (ISCO), **53**, 57, 542,  
     555, 648

instability  
 corrugation, 275  
 dynamical (relativistic star), 618  
 flip-flop, 532  
 Kelvin–Helmholtz, 572, **636**  
 magnetorotational (MRI), **554**, 632  
 runaway, 548  
 secular (relativistic star), 618  
 integral curves, 201  
 integral form, 417  
 interacting multifluid, 175, **179**, 183  
 internal energy, 101  
 internal energy density, **112**, 186, 558  
 internal energy density, classical, 295  
 internal energy equation, 86  
 invariant, 14  
 inviscid fluid, 88  
 irreducible decomposition, 135  
 irreversibility, 78  
 Irreversible Thermodynamics, Classic (CIT), 291  
 Irreversible Thermodynamics, Extended (EIT), **291**, 299  
 Irreversible Thermodynamics, Standard (SIT), 291  
 irrotational binaries, 626  
 irrotational flow, 152  
 irrotational fluid, 156  
 ISCO, *see* innermost stable circular orbit  
 isentrope, 108  
 isentropic fluid, 120, **145**  
 isobaric, 539  
 isodensity, 539  
 isopycnic, 539  
 isotropic perfect fluid, 141  
 isotropic pressure, 85  
 isotropic radiation fluid, 127  
 Isenberg–Wilson–Mathews formulation (IWM), 356; *see also* Einstein–Euler formulation  
 Israel–Stewart equations, 302  
 IVP, *see* initial-value problem  
 IVBP, *see* initial-value boundary problem  
 IWM, *see* Isenberg–Wilson–Mathews formulation

**J**

Jacobian, 8, 195  
 jet (relativistic), 152, 243, **565**, 572  
 jet acceleration model  
   tangential booster, 572  
   thermal acceleration, 569  
   twin-exhaust, 570  
 junction conditions, Rankine–Hugoniot, **214**, 415  
 junk radiation, 359; *see also* gravitational wave

**K**

k-essence, 127  
 Kelvin–Helmholtz instability, 572, **636**  
 Kelvin–Helmholtz theorem, 154  
 Keplerian angular velocity, *see* Keplerian frequency

Keplerian frequency, **539**, 554, 606  
 Keplerian specific angular momentum, **543**, 551, 555; *see also* specific angular momentum  
 Kerr black hole, 54  
 Kerr–Schild coordinates, **56**, 531, 591  
 Killing equations, 37  
 Killing vector, **37**, 145, 293  
 kinematic acceleration four-vector, 133  
 kinematic viscosity, 561  
 kinematic vorticity four-vector, 136  
 kinematic vorticity tensor, **135**, 156, 637  
 kinetic energy, 80  
 Knudsen number, **69**, 85  
 Kreiss–Oliger dissipation, 407  
 Kronecker delta, **11**, 19

**L**

Lagrange multiplier, **169**, 173, 309  
 Lagrangian, 40, **50**, 170, 174  
 Lagrangian density, 164, **169**, 174, 180  
 Lagrangian derivative, **80**, 148  
 Lagrangian formulation, 325; *see also* Einstein–Euler formulation  
 Lagrangian observer, 80  
 laminar flow, 80  
 Landau frame, 287  
 Lane–Emden equation, 594  
 Laplacian operator, 46, 338, **344**, 352, 359  
 lapse function, **320**, 322, 334, 343, 350, 354, 385  
 lapse function, conformal, 355  
 lapse function, physical, 356  
 Lax’s theorem, 396  
 Lax–Friedrichs scheme, **402**, 413  
 Lax–Friedrichs, local flux, 438  
 Lax–Wendroff scheme, **405**, 413  
 leapfrog scheme, 404  
 least-action principle, *see* variational principle  
 Legendre polynomials, 464  
 Lemaitre cosmological models, 61  
 Levi–Civita tensor, **19**, 157, 160, 539  
 Lie brackets, 33  
 Lie derivative, 31  
 limiter, *see* slope-limiter method  
 light cone, **26**, 208, 675  
 light-cone formulation, 376; *see also* relativistic-hydrodynamic equations  
 line element, 21; *see also* metric tensor  
 linear Riemann problem, **444**, 480  
 Liouville’s theorem, 91  
 liquid, *see* fluid  
 local error, 391  
 local Maxwellian distribution, 82  
 local order, accuracy, 391  
 local spacetime DG scheme, 482  
 Local Thermodynamic Equilibrium (LTE), 85  
 local time-stepping, 475  
 longitudinal operator, 352  
 longitudinal rapidity, 585

## Lorentz

factor, 25, 208, 323, 517, 556, 572  
invariant, 90  
transformation matrix, 25  
transformations, 25  
global frame, 64  
length contraction, 26

## Lorenz gauge, 62

**M**

Mach number, 243, 529  
machine-precision error, 390  
magnetorotational instability (MRI), 554, 632  
manifold, 5, 14, 17, 20, 29, 37, 41, 44  
manifold, maximally symmetric, 38  
mapping, 6; *see also* coordinates  
marginally bound orbit, 53, 57, 542  
marginally stable orbit, 53, 57, 542, 555, 648  
marginally stable radius, 53  
Marquina flux formula, 371, 446  
Marquina Riemann solver, *see* Marquina flux formula  
mass flux, 216, 220, 235, 260, 519  
mass matrix, 181  
mass shedding, 607, 655  
mass  
    baryon, 605  
    gravitational, 605  
    particle, 70  
    rest, 28, 70, 605  
mass-shedding frequency, 607  
material derivative, 80  
material waves, *see* matter wave  
matter wave, 195, 371  
maximal slicing condition, 344, 357  
maximally symmetric manifold, 38  
Maxwell relations, 663  
Maxwell–Boltzmann distribution, 81, 132  
Maxwell–Boltzmann distribution, relativistic, 98  
Maxwell–Cattaneo equations, 302  
Maxwell–Jüttner distribution, 98  
Maxwellian distribution, 81  
    absolute, 82  
    local, 82, 85  
MC, *see* monotonised central-difference limiter  
mean free path, 84  
mean intensity, 123  
mean macroscopic velocity, 74  
mean opacity, 565  
method of fractional steps, 487  
method of lines (MOL), 401, 447  
metric distortion tensor, 345  
metric strain tensor, 345  
metric tensor, 21, 25, 49, 57, 59, 322, 376, 604, 613  
metric, conformal, 337  
metric, conformally flat, 359  
metric, radiative, 375  
Michel solution, 517  
microquasars, 565

## migration test, 597

minimal causal slice, 381  
minimal-distortion shift condition, 345  
minimal-strain shift condition, 345  
Minkowski spacetime, 24  
minmod slope limiter, 428, 678; *see also* slope-limiter method  
Misner–Sharp formulation, 325; *see also* Einstein–Euler formulation  
mixed binary, 647; *see also* binary system (compact objects)  
mixed tensor, 16  
modal basis, 464, 476  
MOL, *see* method of lines  
moment equations, 80  
moment method, 306  
moments (radiation field), 177  
momentum constraints, 334  
momentum density, 333  
momentum flux, 79  
momentum-conservation equations, 144  
monotone method, 420  
monotonicity-preserving method, 422  
monotonised central-difference limiter (MC), 428, 678; *see also* slope-limiter method  
most probable velocity, 83

MOTS, 615; *see also* trapped surface  
MRI, *see* magnetorotational instability  
multicomponent fluid, *see* multifluid  
multidimensional conservation laws, 485  
multifluid, 101, 125, 156, 168, 175  
    coupled, 175, 180, 182, 185  
    interacting, 175, 179, 181, 183  
    non-interacting, 175  
    relative velocity, 181  
MUSCL method, 427

**N**

Navier–Stokes equations, 88, 294  
Nessyahu–Tadmor scheme, 455; *see also* central schemes  
neutral-stability line, 618  
neutron star, 593, 596, 602, 604, 608  
Newman–Penrose formalism, 46, 65  
Newman–Penrose scalar, 65  
Newtonian energy flux density vector, 86  
nodal basis, 464, 476  
non-convex equation of state, 108, 218  
non-coordinate basis, 34  
non-degenerate fluid, 97  
non-degenerate non-relativistic fluid, 111  
non-degenerate relativistic fluid, 110  
non-degenerate ultrarelativistic fluid, 113  
non-interacting multifluid, 175  
non-oscillatory, 362  
non-perfect fluid, 87, 285, 290, 554, 559, 561  
non-rotating star, 593  
non-selfgravitating fluid, 493, 593  
non-upwind method, 426

normal line, 324  
 normal observer, 323  
 norm, continuum, 389  
 norm, discretised, 389  
 null interval, 26  
 null separated events, 26  
 null slicing, 327, 375  
 null vector, 27  
 number density, 74, 91, 109, 112, 114, 123, 180  
 number-density current, 91  
 numerical dissipation, 403, 407  
 numerical domain of dependence, 396  
 numerical error  
     machine-precision, 390  
     round-off, 390  
     truncation, 390, 393, 408  
 numerical fluxes, 417, 420, 441, 444, 453,  
 numerical method, 386  
     artificial-viscosity, 387, 409  
     central schemes, 452  
     conservative, 414, 417  
     Euler, 448  
     finite-difference, 386, 414  
     finite-elements, 377  
     finite-volume, 414, 417  
     flux vector splitting, 420  
     flux-limiter, 422  
     fractional steps, 487  
     Godunov, 423  
     high-order, 459  
     HRSC, 414  
     monotone, 420  
     monotonicity preserving, 422  
     MUSCL, 427  
     non-upwind, 426  
     path-conservative, 418  
     PPM, 427, 430,  
     Runge–Kutta (RK), 448  
     slope-limiter, 422  
     total-variation diminishing (TVD), 421, 428  
     upwind, 420  
 numerical scheme, 386  
     Beam–Warming, 407  
     central-upwind, 414, 436, 447, 456  
     finite-difference ENO, 469  
     finite-difference WENO, 472  
     finite-volume ENO, 462  
     finite-volume WENO, 466  
     FTCS, 401  
     Lax–Friedrichs, 402  
     Lax–Wendroff, 405  
     leapfrog, 404  
     Nessyahu–Tadmor, 455  
     Runge–Kutta IMEX, 449  
     Tadmor’s formula, 455; *see also*  
         Nessyahu–Tadmor scheme  
     upwind, 399  
 numerical stability, 395  
 numerical stencil, *see* stencil

## O

observer  
     Eulerian, 80, 323  
     Lagrangian, 80  
 one-form, 12  
 one-sided stencil, 401  
 opacity, 178  
 operator discretisation, 388  
 Oppenheimer–Snyder (OS) collapse, 612  
 optically thick regime, 178  
 optically thin regime, 178  
 orbit  
     capture, 52  
     circular stable, 52  
     circular unstable, 52  
     elliptic, 52  
     innermost circular, 53  
     marginally bound, 53, 543  
     marginally stable, 543, 548, 555, 648  
 orbiting frame, 555, 561  
 orthogonal vectors, 20  
 OS, *see* Oppenheimer–Snyder collapse  
 oscillation indicator, 465  
 oscillation indicator matrix, 466  
 outer product, 17  
 outflow (flow solution), 514; *see also* wind

## P

parabolic equation, 285, 296  
 parallel transport, 39  
 particle currents, 180  
 particle frame, 287  
 particle mass, 70  
 particle number, 77  
 particle-based method, 387  
 past boundary, 381  
 past light cone, *see* light cone  
 patch, 6; *see also* coordinates  
 path, 9  
 path-conservative method, 418  
 Pauli’s exclusion principle, 99  
 peak frequency (HMNS), 635, 656  
 peculiar velocity, 85  
 perfect fluid, 101  
 perfect fluid classical, 88  
 permutation tensors, 19  
 Petrov–Galerkin method, 473  
 phantom models, 127  
 phase space, 68  
 phase velocity, 297, 406  
 photon fluid, 123  
 physical transverse decomposition, 354  
 piecewise parabolic method (PPM), 427, 430, 462,  
     677  
 piecewise polytropic equation of state, 120; *see also*  
     polytropic equation of state  
 piecewise-constant states, 423  
 Planck function, 123

Poisson adiabat, 218  
 Poisson equation, 46, 147, 185, 594  
 polarisation amplitudes, 65  
 polytropic  
 polytropic constant, 118  
 polytropic equation of state, 118, 120, 520, 545, 550, 627, 650  
 polytropic exponent, 118  
 polytropic index, 118  
 polytropic transformation, 118  
 potential flow, 153  
 precompression wave, 266  
 predictor step, 435  
 pressure  
   anisotropic, 141; *see also* anisotropic perfect fluid  
   isotropic, 85  
   radial, 141; *see also* anisotropic perfect fluid  
   scalar, 79  
   tangential, 141; *see also* anisotropic perfect fluid  
   tensor, 79  
   tensor (classical), trace, 667  
 pressureless fluid, 104  
 primitive variables, 197, 368, 427, 470, 668  
 principle  
   Copernican, 59  
   cosmological, 59  
   entropy, 103, 286, 306, 308, 311  
   of equivalence, 5, 29, 37, 101  
   of inertia, 24  
   of least action, *see* variational principle  
   Pauli's, 99  
   variational, 164, 168, 174, 179  
 production density tensor, 307  
 projection tensor, 23, 135, 192, 252, 288, 320, 559  
 proper  
   distance, 21, 49  
   time, 27, 39, 133, 170, 322  
   volume, 21

## Q

QNM, *see* quasi-normal mode  
 QPO, *see* quasi-periodic oscillation  
 quality factor, 249  
 quark star, 259  
 quark-gluon plasma, 580  
 quasi periodic oscillation (QPO), 532, 535  
 quasi-linear system, 192  
 quasi-linear system, order, 192  
 quasi-normal mode (QNM), 599, 626, 634, 655  
 quintessence, 127

## R

r-processes, 644  
 radial pressure, 141; *see also* anisotropic perfect fluid

radiation  
   constant, 124, 179, 565  
   energy density, 177  
   flux, 177  
   four-force density, 177  
   stress tensor, 177  
 radiation-hydrodynamic equations, 178  
 radiation-reaction time-scale, 624  
 radius  
   accretion, 517, 519  
   Bondi–Hoyle–Lyttleton, 531  
   critical, 517  
   curvature, 45  
   gravitational, 659  
   gyration, 556  
   marginally bound orbit, 53  
   marginally stable, 53  
   Schwarzschild, 50  
   sonic, 498  
   static, 552  
   tidal, 648  
 rank (tensor), 16; *see also* tensor  
 Rankine–Hugoniot junction conditions, 214, 415  
 rarefaction tail, 211  
 rarefaction head, 211  
 rarefaction wave, 211, 223, 231, 236, 423, 439, 573  
 Rational Extended Thermodynamics (RET), 299, 306  
 Rayleigh criterion, 546, 645  
 reaction adiabat, 259  
 reaction front, *see* reaction wave  
 reaction wave, 210, 258, 501  
 reaction wave, stability, 268  
 reconstruction technique, 427  
 reconstruction, dimension-by-dimension, 486  
 reference element, 463, 473  
 region of influence, 207  
 relativistic  
   relativistic Bernoulli's constant, 152  
   relativistic Bernoulli's theorem, 152  
   relativistic circulation, 159  
   relativistic coldness, 99, 111, 114  
   relativistic conservation equation (Boltzmann), 95  
   relativistic energy, 28  
   relativistic H-theorem, 93; *see also* H-theorem  
     classical  
   relativistic jet, 152, 243, 565, 572  
   relativistic Kelvin–Helmholtz theorem, 159  
   relativistic Maxwell–Boltzmann equation, 90  
   relativistic potential vorticity, 160  
   relativistic torus, 541  
   relativistic transport fluxes, 91  
   relativistic velocity composition laws, 28  
   relativistic velocity potential, 158  
   relativistic von Zeipel's theorem, 539  
   relativistic hydrodynamics, v  
   relativistic-hydrodynamic equations 143  
     covariant formulation, 374  
     discontinuous Galerkin (DG) formulation, 377  
     light-cone formulation, 376

- relativistic-hydrodynamic equations (*cont.*)  
     Valencia formulation, 364  
     velocity-potential formulation, 166  
     Wilson formulation, 361
- relaxation time, 297, 301, 447
- rest energy, 28, 147
- rest mass, 28, 70, 147, 548, 605
- rest-mass density, 98
- rest-mass density current, 92, 139
- RET, *see* Rational Extended Thermodynamics
- Reynolds number, 460
- Ricci identities, 41
- Ricci scalar, 44, 62, 252, 325, 330, 338, 342, 493
- Ricci tensor, 44, 46, 62, 93, 137, 330, 336, 353
- Riemann fan, 223, 420, 424, 436
- Riemann invariants, 201, 209, 213
- Riemann problem, 222  
     exact, 227, 436  
     generalised, 223, 479  
     linear, 444, 480
- Riemann solver  
     approximate, 436  
     complete, 436  
     HLLC, 440  
     HLLE, 436  
     HLLEM, 445  
     incomplete, 436  
     Marquina, 371  
     Roe, 443  
     Rusanov, 438
- Riemann tensor, 41, 43, 137
- ringdown, 626, 655; *see also* quasi-normal mode
- RK, *see* Runge–Kutta method
- RK2, second-order Runge–Kutta scheme, 448
- RK3, third-order Runge–Kutta scheme, 448
- RKDG, *see* Runge–Kutta discontinuous Galerkin method
- Roe flux formula, 445
- Roe Riemann solver, 443
- root mean square velocity, 82
- rotating star, 604
- rotational kinetic energy, 605
- round-off error, 390
- runaway instability, 548, 645
- Runge–Kutta (RK) method, 426, 448, 455
- Runge–Kutta discontinuous Galerkin method (RKDG), 474, 490
- Rusanov Riemann solver, 438, 680
- S**
- scalar Gauss relation, 332
- scalar product, 20
- scale factor, 59, 126
- Schwarzschild black hole, 50; *see also* black hole
- Schwarzschild coordinates, 49
- Schwarzschild radius, 50, 598
- Schwarzschild–de Sitter, 551
- second law of thermodynamics, 103; *see also* entropy principle
- second moment (distribution function), 92
- second sound speed, 297, 305
- secular instability (relativistic star), 618
- Sedov solution, 509
- self-similar flow, 211
- self-similar variable, 495
- self-similarity, 494
- selfgravitating fluids, 593
- semi-discrete equations, 447, 486
- settling (flow solution), 515
- shear interface, 636
- shear scalar, 137
- shear tensor, 135, 288, 294, 560
- shear tensor, trace, 137
- shear viscosity, 88, 288, 545, 561
- shift condition, 343  
     Gamma-driver, 346  
     minimal-distortion, 345  
     minimal-strain, 345
- shift vector, 321, 343, 346, 350, 356
- shifted Legendre polynomials, 464
- shock  
     damping time, 248  
     cone, 528, 530, 535  
     detector, 243  
     evolutionary, 245  
     front, *see* shock wave  
     heating, 120, 630, 633  
     wave, 120, 205, 210, 214, 235, 243, 263, 266, 416, 573,  
         stability, 245, 271
- shock-tube problem, 227, 362, 375
- signature, 21; *see also* metric tensor
- similarity, 494
- similarity transformations, 494
- similarity variable, 211, 495
- simple wave, 200, 209, 504
- singular hypersurface, 211, 250,
- singular-hypersurface method, 249
- singularity, 50, 614
- singularity-avoiding slicing condition, 344
- SIT, *see* Standard Irreversible Thermodynamics
- slice of the triangulation, 381
- slicing condition, 343  
     1+log, 345  
     harmonic, 344  
     maximal, 344, 357  
     singularity avoiding, 344
- slim discs, 553
- slope-limiter method, 422, 428  
     MC, 428, 678  
     minmod, 428, 678  
     superbee, 428, 679
- smooth particle hydrodynamics (SPH), 387, 549
- Sod problem, 226
- soft equation of state, 119
- sonic deflagration, 505
- sonic point, 519
- sonic radius, 498, 501, 503, 506, 514
- sound cone, 208, 246, 270, 675

- sound speed, **107**, 111, 116, 119, 126, 175, 183, 209, 212, 269, 305, **370**, 529, 549, 584  
     Newtonian, 107  
     second, **297**, 305  
 sound wave, 61, 107, **209**  
 source term (hyperbolic equation), **192**, 366  
 spacelike interval, 26  
 spacelike vector, 27  
 spacetime 4  
     curved, 30  
     decomposition, *see* 3+1 decomposition  
     discretisation, 387  
     flat, 24  
     Friedmann–Robertson–Walker (FRW), 59  
     interval, *see* line element  
     Kerr, 54  
     Minkowski, 24  
     Schwarzschild, 50  
     Schwarzschild–de Sitter, 551  
 spatial discretisation, 391  
 spatial momentum density, 141  
 spatial projection operator, 320  
 spatial projection tensor, **320**, 329, 332  
 spatial tensor, 320  
 specific angular momentum, **538**, 541, 546, 551, 560, 591, 640, 642, 644  
 specific angular momentum (particle), 52  
 specific energy, 98  
 specific energy (particle), **51**, 558  
 specific enthalpy, 102, 116, 149, 158, 163, 165, 576  
 specific enthalpy, Newtonian, **103**, 149, 151, 374  
 specific entropy, 98, **102**, 120, 145, 159, 161, 164, 169, 209, 218, 563, 675  
 specific four-momentum, 156  
 specific heat, 105  
     at constant pressure, **106**, 112  
     at constant pressure (particle), 111  
     at constant volume, **106**, 112, 116  
     at constant volume (particle), 111  
 specific Helmholtz free energy, 169  
 specific intensity, 176  
 specific internal energy, **79**, 102, 117, 119, 175  
 specific volume, 102  
 spectral coefficients, **380**, 464  
 speed of light, 4  
 SPH, *see* smooth particle hydrodynamics  
 spherical flows, 513  
 spherical star, *see* non-rotating star  
 spin parameter, 55  
 SSP, *see* strong stability preserving scheme  
 SSPk, *see* strong stability preserving Runge–Kutta scheme  
 stability analysis, von Neumann, 398  
 stability criteria, 396  
 stability, numerical, 395  
 staggered average, 453  
 stagnation point, **153**, 527, 529  
 Standard Irreversible Thermodynamics (SIT), 291  
 star, non-rotating, 593  
 star, rotating, 604  
 state vector, 191  
 static radius, 552  
 stationary flow, 80, **150**  
 Stefan–Boltzmann constant, 124  
 stellar compactness, **598**, 648  
 stencil, **397**, 400  
     centred, 401  
     one-sided, 401  
 stiff equation of state, 119  
 stiff system of equations, **447**, 449, 452  
 Stokes' theorem, **154**, 215  
 strain, *see* strain tensor, trace  
 strain tensor, **80**, 136  
 strain tensor, trace, 667  
 streamline, **80**, 135; *see also* fluidline  
 stress tensor, 87  
     classical, 88  
     relativistic, 141  
     classical, trace, 667  
     viscous, 288  
 stress–energy tensor, *see* energy–momentum  
 strictly hyperbolic system, 193  
 strong deflagration, **262**, 267  
 strong detonation, **261**, 263  
 strong energy condition, 93  
 strong shock, 220, **222**, 249, 622  
 strong stability preserving (SSP) scheme, 451  
 strong stability preserving Runge–Kutta (SSPk) scheme, 451  
 strongly degenerate Fermi fluid, 115  
 strongly hyperbolic system, *see* hyperbolic system  
 structure coefficients, 33  
 sub-Keplerian, 544  
 sub-Kerr stellar models, 618  
 subsonic flow, 220  
 subsonic deflagration, **267**, 503, 505  
 super-Keplerian, 544  
 superbee limiter, **428**, 679; *see also* slope-limiter method  
 superfluid, **159**, 179, 181  
 superluminal jet, 566; *see also* relativistic jet  
 supersonic deflagration, **267**, 502, 505  
 supersonic flow, 219  
 supra-Kerr stellar models, 618  
 supramassive star, 607  
 surface energy, **211**, **253**, 279  
 surface energy tensor, 252  
 surface layer, 252  
 surface tension, **211**, **253**, 501  
 symmetric hyperbolic system, 193  
 symmetric tensor, 18  
 Synge fluid, 110  
 system of equations  
     elliptic, 388  
     hyperbolic, 192  
     linear with constant coefficients, 192  
     linear with variable coefficients, 192  
     nonlinear, 192  
     parabolic, 296  
     quasi-linear, 192

- system of equations (*cont.*)  
 stiff, 447, 449, 452  
 strictly hyperbolic, 193  
 strongly hyperbolic, *see* hyperbolic  
 symmetric hyperbolic, 193  
 weakly hyperbolic, 193
- T**
- Tadmor's flux formula, 455  
 tangent space, 11  
 tangent vector, 9  
 tangential pressure, 141; *see also* anisotropic perfect fluid  
 tangential velocity, 234  
 Taub adiabat, 216, 259  
 Taub's inequality, 116  
 Taub's junction conditions, 216  
 telegraph equation, 297  
 temperature, 81  
 temporal tensor, 320, 323  
 tensor, 16  
   equations, 20  
   field, 17  
   antisymmetric, 18  
   Einstein, 47  
   energy-momentum, 47  
   index lowering, 21  
   index raising, 21  
   rank, 16  
   Ricci, 44  
   Riemann, 41  
   spatial, 320, 323  
   symmetric, 18  
   temporal, 320, 323  
   trace, 22  
   Weyl, 46  
 termination shock, 578  
 test fluid, 210, 249, 493  
 tetrad, 34  
 theorem  
   Bernoulli's, classical, 150  
   Bernoulli's, relativistic, 152  
   Birkhoff's, 49  
   Ehrenfest's, 68  
   Friedrichs', 209  
   Godunov's, 423  
   H, classical, 75  
   H, relativistic, 93  
   Kelvin–Helmholtz, classical, 154  
   Kelvin–Helmholtz, relativistic, 159  
   Lax's, 396  
   Liouville's, 91  
   Stokes', 154  
   von Zeipel's, 539  
 thermal conductivity, 293  
 thermal conductivity, coefficient, 88  
 thermal radiation energy density, 123  
 thermal waves, 297  
 thermodynamic fluxes, 289  
 thermodynamic process, 308  
 thermodynamic square, 158, 663  
 thermodynamics, first law, 101  
 thermodynamics, second law, 103  
 thick discs, 553  
 thin discs, 553  
 third moment (distribution function), 92  
 Thomas derivative, 249  
 three-metric, 606  
 three-vector, 14  
 three-velocity, 24  
 tidal frequency (mixed binary), 655  
 tidal radius, 648  
 time discretisation, 391  
 time projection operator, 321  
 time-level, 400  
 timelike interval, 26  
 timelike vector, 27  
 Tolmann–Oppenheimer–Volkoff (TOV) equations, 595  
 torsion, 36, 41, 137  
 torus, 541  
   centre, 543  
   cusp, 543  
   inner edge, 544  
 total energy density, 93, 98  
 total energy density (Newtonian), 86  
 total variation, 421  
 total-variation diminishing method (TVD), 421, 428, 430, 434, 448, 451, 459, 490, 677, 681  
 totally antisymmetric symbol, 19  
 trace, 22  
 trace, extrinsic curvature, 332  
 trace-free extrinsic curvature, 337  
 transformation matrix, 7  
 transport  
   coefficients, 293, 302  
   equation, 95, 132  
   equation (classical), 78  
   fluxes, 91  
   parallel, 39  
   velocity, 361  
 transverse rapidity, 586  
 transverse tensor, 352  
 transverse–traceless (TT) gauge, 64  
 trapped surface, 328, 615  
 triangulation, 378  
 triangulation, elements, 378  
 truncation error, global, 390  
 truncation error, local, 390  
 TT, *see* transverse–traceless gauge  
 turbulence, 460  
 turning point (effective potential), 52  
 turning-point stability criterion, 596, 617  
 TVD, *see* total-variation diminishing method  
 twin-exhaust model, 570  
 twist, 135  
 two-form, 16  
 two-sphere, 5, 45, 325

**U**

ultrarelativistic Fermi fluid, 118  
 ultrarelativistic fluid, 107  
 ultrastiff equation of state, 127, 525  
 ultrastiff fluid, 127  
 under-determinacy degree, 245  
 undivided differences, 465, 677  
 upstream, 214  
 upwind method, 420  
 upwind scheme, 399, 414

**V**

Valencia formulation, 364, 375, 379; *see also*  
     relativistic-hydrodynamic equations  
 vapour bubbles, 501  
 variable discretisation, 388  
 variational principle, 164, 168, 174, 179  
 vector field, 16  
 vector Laplacian, 353  
 velocity  
     potential, 153  
     flow, 74  
     group, 298  
     mean macroscopic, 74  
     most probable, 83  
     peculiar, 85  
     phase, 297  
     root mean square, 82  
 velocity-potential formulation, 166; *see also*  
     relativistic-hydrodynamic equations  
 viscosity  
     bulk, 88, 288  
     dilatational, 88  
     shear, 88, 288, 545, 561  
 viscous bulk pressure, 288, 559  
 viscous fluid, 88  
 viscous stress tensor, 288  
 viscous stress tensor (classical), trace, 667  
 Vlasov–Maxwell equation, 68  
 volume element, spatial, 336  
 von Neumann analysis, 398  
 von Zeipel cylinder, 539  
 von Zeipel's, theorem, 539  
 vortensity, 153  
 vortex, 155  
 vortex lines, 155, 166  
 vortex sheet, 636  
 vorticity  
     four-vector, 157  
     scalar, 137

tensor, 155, 290  
 tensor, kinematic, 135  
 tensor, trace, 137  
 two-form, 155  
 vector, 152

**W**

wave  
     pattern, 223  
     steepening, 206  
     acoustic; *see* sound wave  
     gravitational, *see* gravitational wave  
     material, *see* matter wave  
     matter, *see* matter wave  
     sound, *see* sound wave  
     thermal, 297  
 wavevector, 297  
 weak  
     weak deflagration, 262, 267  
     weak detonation, 261, 263  
     weak discontinuity, 218, 263, 500  
     weak energy condition, 93  
     weak formulation, 363, 377, 472  
     weak shock, 218, 222, 249  
     weak solution, 363  
     weakly hyperbolic form, 193, 335, 340  
     weighted essentially non-oscillatory method  
         (WENO), 459, 466, 472, 483  
     weighted transverse decomposition, 354  
     well-posedness, 193  
     WENO, *see* weighted essentially non-oscillatory  
     Weyl tensor, 46, 65, 137  
     white dwarfs, 115  
     Wilson formulation, 361; *see also*  
         relativistic-hydrodynamic equations  
 wind (flow solution), 514, 517  
 worldline, 5, 9, 26, 40, 71, 81, 134, 169, 213, 221,  
     247, 263, 266, 269, 324, 614, 620

**Z**

Z4 formulation, 340; *see also* Einstein–Euler  
     formulation  
 Z4c formulation, 342; *see also* Z4 formulation  
 ZAMO frame, 555, 561  
 ZAMO observer, 56, 555, 605  
 ZAMO tetrad, 556, 592  
 zero tensor, 18  
 zero-order approximation, 84; *see also* Boltzmann  
     equation